AFRL-AFOSR-VA-TR-2016-0242

Representative Structural Element - A New Paradigm for Multi-Scale Structural Modeling

Ling Liu
UTAH STATE UNIVERSITY
2400 OLD MAIN HILL
LOGAN, UT 84322-0001

07/05/2016
Final Report

Air Force Research Laboratory
AF Office Of Scientific Research (AFOSR)/RTA1

Arlington, Virginia 22203
Air Force Materiel Command

REPORT DOCUMENTATION PAGE

Form Approved
OMB No. 0704-0188

PLEASE DO NOT RETURN YOUR FORM TO THE ABOVE ORGANIZATION.

1. REPORT DATE *(DD-MM-YYYY)*	2. REPORT TYPE	3. DATES COVERED *(From - To)*
29-06-2016	Final Report	March 2013 - March 2016

4. TITLE AND SUBTITLE
Representative Structural Element - A New Paradigm for Multi-Scale Structural Modeling

5a. CONTRACT NUMBER

5b. GRANT NUMBER
FA9550-13-1-0148

5c. PROGRAM ELEMENT NUMBER

6. AUTHOR(S)
Ling Liu, and Wenbin Yu

5d. PROJECT NUMBER

5e. TASK NUMBER

5f. WORK UNIT NUMBER

7. PERFORMING ORGANIZATION NAME(S) AND ADDRESS(ES)
UTAH STATE UNIVERSITY
2400 OLD MAIN HILL
LOGAN UT 84322-0001

8. PERFORMING ORGANIZATION REPORT NUMBER

9. SPONSORING/MONITORING AGENCY NAME(S) AND ADDRESS(ES)
USAF, AFRL DUNS 143574726
AF OFFICE OF SCIENTIFIC RESEARCH
875 N, RANDOLPH ST ROOM 3112
ARLINGTON VA 22203

10. SPONSOR/MONITOR'S ACRONYM(S)
AFOSR

11. SPONSOR/MONITOR'S REPORT NUMBER(S)

12. DISTRIBUTION/AVAILABILITY STATEMENT
Distribution A

13. SUPPLEMENTARY NOTES

14. ABSTRACT
Under the sponsorship of AFOSR, we have successfully achieved the objective to establish a new paradigm for multiscale structural modeling to provide a systematic approach for efficient high-fidelity modeling of aerospace structures featuring multiscale heterogeneities and anisotropy. The proposed approach uses the concept of representative structural element, later renamed to be structure genome (SG) to emphasize the potential of this concept to bridge materials genome and structural analysis, and to better align with the Materials Genome Initiative (MGI). In this project, we have formulated the general theory for mechanics of structure genome (MSG), carried out a critical assessment of the proposed approach, and applied this approach to predict static failure and imperfect interfaces, construct models for hyperelastic materials, elastoplastic materials, viscoplastic materials, damaged materials, smart laminates, aperiodic materials, and last but not least, applied this approach to create new theories for laminates and micromechanics, and to provide a versatile solution for general free-edge stress problems.

15. SUBJECT TERMS
Multiscale structural modeling; heterogeneity; anisotropy; efficiency; representative structural element; micromechanics.

16. SECURITY CLASSIFICATION OF:			17. LIMITATION OF ABSTRACT	18. NUMBER OF PAGES	19a. NAME OF RESPONSIBLE PERSON
a. REPORT	b. ABSTRACT	c. THIS PAGE			Ling Liu
U	U	U	UU	469	19b. TELEPHONE NUMBER *(Include area code)* 435-797-9149

Reset

Standard Form 298 (Rev. 8/98)
Prescribed by ANSI Std. Z39.18
Adobe Professional 7.0

INSTRUCTIONS FOR COMPLETING SF 298

1. REPORT DATE. Full publication date, including day, month, if available. Must cite at least the year and be Year 2000 compliant, e.g. 30-06-1998; xx-06-1998; xx-xx-1998.

2. REPORT TYPE. State the type of report, such as final, technical, interim, memorandum, master's thesis, progress, quarterly, research, special, group study, etc.

3. DATES COVERED. Indicate the time during which the work was performed and the report was written, e.g., Jun 1997 - Jun 1998; 1-10 Jun 1996; May - Nov 1998; Nov 1998.

4. TITLE. Enter title and subtitle with volume number and part number, if applicable. On classified documents, enter the title classification in parentheses.

5a. CONTRACT NUMBER. Enter all contract numbers as they appear in the report, e.g. F33615-86-C-5169.

5b. GRANT NUMBER. Enter all grant numbers as they appear in the report, e.g. AFOSR-82-1234.

5c. PROGRAM ELEMENT NUMBER. Enter all program element numbers as they appear in the report, e.g. 61101A.

5d. PROJECT NUMBER. Enter all project numbers as they appear in the report, e.g. 1F665702D1257; ILIR.

5e. TASK NUMBER. Enter all task numbers as they appear in the report, e.g. 05; RF0330201; T4112.

5f. WORK UNIT NUMBER. Enter all work unit numbers as they appear in the report, e.g. 001; AFAPL30480105.

6. AUTHOR(S). Enter name(s) of person(s) responsible for writing the report, performing the research, or credited with the content of the report. The form of entry is the last name, first name, middle initial, and additional qualifiers separated by commas, e.g. Smith, Richard, J, Jr.

7. PERFORMING ORGANIZATION NAME(S) AND ADDRESS(ES). Self-explanatory.

8. PERFORMING ORGANIZATION REPORT NUMBER. Enter all unique alphanumeric report numbers assigned by the performing organization, e.g. BRL-1234; AFWL-TR-85-4017-Vol-21-PT-2.

9. SPONSORING/MONITORING AGENCY NAME(S) AND ADDRESS(ES). Enter the name and address of the organization(s) financially responsible for and monitoring the work.

10. SPONSOR/MONITOR'S ACRONYM(S). Enter, if available, e.g. BRL, ARDEC, NADC.

11. SPONSOR/MONITOR'S REPORT NUMBER(S). Enter report number as assigned by the sponsoring/ monitoring agency, if available, e.g. BRL-TR-829; -215.

12. DISTRIBUTION/AVAILABILITY STATEMENT. Use agency-mandated availability statements to indicate the public availability or distribution limitations of the report. If additional limitations/ restrictions or special markings are indicated, follow agency authorization procedures, e.g. RD/FRD, PROPIN, ITAR, etc. Include copyright information.

13. SUPPLEMENTARY NOTES. Enter information not included elsewhere such as: prepared in cooperation with; translation of; report supersedes; old edition number, etc.

14. ABSTRACT. A brief (approximately 200 words) factual summary of the most significant information.

15. SUBJECT TERMS. Key words or phrases identifying major concepts in the report.

16. SECURITY CLASSIFICATION. Enter security classification in accordance with security classification regulations, e.g. U, C, S, etc. If this form contains classified information, stamp classification level on the top and bottom of this page.

17. LIMITATION OF ABSTRACT. This block must be completed to assign a distribution limitation to the abstract. Enter UU (Unclassified Unlimited) or SAR (Same as Report). An entry in this block is necessary if the abstract is to be limited.

Representative Structural Element - A New Paradigm for Multi-Scale Structural Modeling

Abstract

Under the sponsorship of AFOSR, we have successfully achieved the objective to establish a new paradigm for multiscale structural modeling to provide a systematic approach for efficient high-fidelity modeling of aerospace structures featuring multiscale heterogeneities and anisotropy. The proposed approach uses the concept of *representative structural element*, later renamed to be ***structure genome*** (SG) to emphasize the potential of this concept to bridge materials genome and structural analysis, and to better align with the Materials Genome Initiative (MGI). In this project, we have formulated the general theory for mechanics of structure genome (MSG), carried out a critical assessment of the proposed approach, and applied this approach to predict static failure and imperfect interfaces, construct models for hyperelastic materials, elastoplastic materials, viscoplastic materials, damaged materials, smart laminates, aperiodic materials, and last but not least, applied this approach to create new theories for laminates and micromechanics, and to provide a versatile solution for general free-edge stress problems.

Introduction

This grant has been active since April 2013 with Dr. Wenbin Yu, a former employee of Utah State University (USU), as the PI, who joined the faculty of the School of Aeronautics and Astronautics at Purdue University in August 2013. The grant is consequently modified so that Dr. Ling Liu becomes the USU PI and a subcontract is issued to Purdue with Dr. Wenbin Yu as the subcontract PI taking care of all the technical responsibilities. The subcontract was not approved and effective until 11/10/2014. During 15-month funding gap (8/2013-11/2014), Dr. Yu's Purdue startup funds was used to support a postdoc and three graduate students who are working on this project.

All work done will be summarized and papers written under grant sponsorship will be appended to provide the technical details. The goal of this research is to establish a new paradigm for multiscale structural modeling. The importance of such a research stems from pervasive use of composites structures in USAF platforms, for which efficient high-fidelity predictive modeling capability is the key for future advance. These structures are usually heterogeneous and anisotropic at the material level and/or structural level. Although these structures can still be macroscopically modeled as beams, plates, shells, or 3D elements, their performance and failure greatly depend on the engineered heterogeneities. This poses formidable obstacles for mathematical modeling of these structures, which must be overcome before we can reap the full benefits of heterogeneous structures. Furthermore, to rapidly yet confidently evaluate

[1] Assistant Professor, Department of Mechanical and Aerospace Engineering, Utah State University, Logan, Utah 84332-4130.

[2]Associate Professor, School of Aeronautics and Astronautics, Purdue University, West Lafayette, Indiana 47907-2045.

new structural concepts with engineered heterogeneities, the designers must be equipped with versatile computational tools to accurately capture the right physics at the speed of computational design. This calls for efficient high-fidelity physics-based models for heterogeneous structures to deliver the best possible accuracy within desirable efficiency. We have successfully completed the three research tasks originally proposed in the proposal:

- Introduced RSE [1,2] as a new concept to provide a unified treatment for structural mechanics and micromechanics and establish the basic requirements for the RSE-based multi-scale structural modeling from fundamental mechanics principles. RSE generalizes the well-known representative volume element (RVE) concept in micromechanics and naturally connects the micromechanical analysis with the macroscopic structural analysis. RSE was renamed as SG later to better align with MGI [3,4].
- Constructed efficient high-fidelity models for heterogeneous composite structures. Exploiting the smallness of thickness and heterogeneity using the variational asymptotic method (VAM) [5], mechanics of structure genome (MSG) [6,7,8] was formulated to mathematically split the original structural analysis including heterogeneous details into a constitutive modeling analysis and a macroscopic structural analysis without heterogeneous details. The constitutive modeling analysis provides effective properties for the macroscopic structural analysis and dehomogenization relations for obtaining the microscopic behavior. MSG has been implemented into a general-purpose, multiscale constitutive modeling code called SwiftComp using the finite element technique to facilitate technology transfer of this fundamental research.
- Validated the models and the companion computer code SwiftComp developed in this research extensively using existing results in the literature, direct finite element analyses with meshing all the heterogeneous details, and experiments through collaboration with AFRL researchers. Particularly, we collaborated with AFRL researchers to design and analyze a unique sandwich configuration pursued by AFRL as a viable candidate for hybrid thermal protection systems [9, 10, 11].

We have also carried out a critical assessment of the proposed approach [12,13,14], and applied this approach to predict static failure [15, 16] and imperfect interfaces [17], to construct models for hyperelastic materials [18, 19], elastoplastic materials [20], viscoplastic materials [21,22], damaged materials including both continuum damage mechanics [23-27] and cohesive zone modeling [28-30], smart laminates [31, 32], to create new theories for micromechanics [33-36] and laminates [37, 38], to analyze low cycle and high cycle fatigue [39, 40], to treat aperiodic materials [41], and last but not least, applied this approach to provide a versatile solution for general free-edge stress problems [42]. A total of 24 technical papers have been published based on the results from this research including 4 peer reviewed journal articles, 19 conference papers, and 1 book chapter. Additional 12 conference abstracts were included in various national/international conferences. We are in the process to convert several conference papers for journal publications. In the following, we briefly summarize all the work we have accomplished under this grant.

Work Accomplished

The project team supported one postdoc and several PhD students, we have made the following major accomplishments during the past three years (4/2013-3/2016)[3].

[3] Due to the transition from USU to Purdue, the PhD could only start at Jan 1st 2015 due to availability of funding.

Establish SG concept and its mechanics

Motivated by materials genome initiative [4], we defined Structure Genome (SG) as the *smallest mathematical* building block of the structure. SG is built upon the concept of the representative structural element (RSE) initially introduced in [1, 2], to emphasize the fact that it contains all the constitutive information needed for a structure the same fashion as the genome contains all the intrinsic information for an organism's growth and development. SG generalizes from the RVE concept in micromechanics with the following three fundamental differences:

- SG is defined as smallest mathematical building block and its dimension only depends on the microstructure while RVE dimension is usually determined by heterogeneity and what type of properties required for the structural analysis. For example, if 3D properties are needed for 3D structural analysis of continuous unidirectional fiber reinforced composites, a 3D RVE is usually required. However, only a 2D SG is required to compute the 3D properties.
- SG for beams/plates/shells can be naturally chosen and structural modeling is rigorously unified with the micromechanical modeling.
- Boundary conditions in terms of displacements and tractions indispensable in RVE-based models are not needed for SG-based models.

Details of the SG concept and the Mechanics of Structure Genome have been presented at 2015 AIAA SciTech conference [3], 2015 MACH Conference [6], 13th US National Congress on Computational Mechanics [7]. The complete formulation can be found at the recently accepted journal paper [8].

Critical Assessment of the Proposed Approach

To show the strength of MSG, we carried a comprehensive evaluation of the proposed approach when it is applied to micromechanics with GMC/HFGMC, a micromechanics approach well known in the aerospace community. It is find out that our proposed approach consistently achieves the best accuracy for all microstructures and for some cases, our approach can achieve a better accuracy with even a better efficiency than GMC. This assessment was initially presented on the 2013 ASME IMECE conference [12], and the complete results was later documented [13] and presented on the 2014 AIAA SciTech conference. We also invited all micromechanics simulation tools to participate the micromechanics simulation challenge. Results for various composites including fiber reinforced composites, particle reinforced composites, laminates, woven composites, short fiber composites from several readily available micromechanics simulation tools include MAC/GMC, MAC/HFGMC, FVDAM, MDS, DIGIMAT, SwiftComp, ESI VPS are compiled. The accuracy and efficiency of each tool are compared with 3D FEA of RVE with periodic boundary conditions using either ABAQUS or ANSYS. The results are documented in [14] and presented in 2015 Annual Technical Meeting of the American Society of Composites. All the data generating the report are hosted in a live database at https://cdmhub.org/members/project/mmsimulationchalleng.

Modeling of Static Failure of Composites

The excellent stress predictive capability of the proposed approach is used to improve prediction for the static failure strength and the initial failure envelop of composites obeying various failure criteria. The failure is evaluated locally at integration points under both uniaxial and combined loading conditions. These evaluations are performed using several representative examples of heterogeneous materials such

as continuous fiber reinforced composite, particle reinforced composite, discontinuous fiber reinforced composite, and woven composite. This work was initially presented on the 2014 ASME IMECE conference [15], and later documented in [16] and presented on the 2015 AIAA SciTech conference. This capability is implemented into the official release version of SwiftComp and a journal version of the conference paper [16] is also under preparation.

Modeling of Imperfect Interface

The proposed approach is used to predict the effective properties and the failure strength of heterogeneous materials with imperfect interface. The imperfect interface is modeled using linear elastic traction displacement model obeying small infinitesimal displacement jump across the interface. These predictions are performed using several representative examples of heterogeneous materials such as continuous fiber reinforced composite, particle reinforced composite, discontinuous fiber reinforced composite, and woven composite. Finally, the predictions of the proposed approach is compared with the predictions of Finite Element Analysis (FEA) and the predictions obtained from other published papers. This work was documented and presented on the 2015th AIAA SciTech conference [17]. We are also revising the conference paper for journal publication.

Modeling of Hyperelastic Materials

The proposed approaches is used to develop a micromechanics approach to homogenizing hyperelastic heterogeneous materials undergoing finite deformation. A variational statement for homogenization is formulated using the variational asymptotic method, discretized in a finite-dimensional space, and solved using a multilevel Newton-Raphson method. The versatility and accuracy of the present approach are demonstrated through homogenizing several typical heterogeneous materials. The proposed approach is found to be capable of handling various microstructures, complex material models, and complex loading conditions. This work was initially presented on the 2013 ASME IMECE conference [18] and the complete work was presented on the 2014 AIAA SciTech conference and documented in the corresponding conference paper [19]. A significantly revised journal version of this work is currently under preparation.

Modeling of Elastoplastic Materials

The proposed modeling approach is applied to develop a micromechanics approach to homogenizing elastoplastic composites. A rigorous second-order radial return algorithm, which can handle elastic and plastic anisotropy and nonlinear kinematic hardening, is developed. A variational statement for homogenization is formulated using the variational asymptotic method, discretized in a finite-dimensional space, and solved using a multilevel Newton–Raphson method. The versatility and accuracy of the present approach are demonstrated through homogenizing long fiber-, particle-, and short fiber-reinforced metal matrix composites (MMCs). Different types of reinforcement are found to differently affect the response of MMCs. The present approach is found to be capable of handling various microstructures, complex material models, complex loading conditions, and complex loading paths. More sophisticated material models can be implemented in it. This work was published in the Journal of Composites Structures [20].

Modeling of Elastoviscoplastic Behavior of Composites

The proposed approach is used to develop a micromechanics approach to homogenize elasto-viscoplastic heterogeneous materials. An affine formulation of the constitutive relations for an elasto-viscoplastic constituent, which exhibits viscoplastic anisotropy and combined isotropic–kinematic hardening, is derived. The weak form of the problem is derived using an asymptotic method. An affine formulation of the constitutive relations for the constituents is derived. The Perzyna model, Hill's yield criterion, the Voce hardening law, and the Chaboche model are implemented into the affine formulation to enable it to couple the effects of viscoplasticity, plastic anisotropy, nonlinear isotropic hardening, and nonlinear kinematic hardening. The applicability, power, and accuracy of the proposed approach are validated using examples such as predicting the stress-strain hysteresis loops of fiber reinforced composites consisting of matrices of various material properties, subject to various loading conditions. This work was initially presented on the 2013 SDM conference [21] and later published in the International Journal of Solids and Structures [22].

Modeling of Damaged Materials

The constitutive relations which are capable of coupling anisotropic damage, damage hardening, (visco)plastic anisotropy, and isotropic/kinematic hardening are developed. The constitutive relations in the undamaged configuration, the damage evolution law, and the constitutive relations in the damaged configuration are subsequently derived. The applicability and power of the proposed constitutive relations are validated using examples such as predicting the stress-strain and damage factor-strain curves of damaged elastoplastic and elastoviscoplastic materials of various material properties. These thermodynamically consistent constitutive relations for damaged elastoplastic materials were documented in [23]. These constitutive relations for damaged elastoviscoplastic materials was initially presented on the 2014 ASME IMECE conference [24] followed by complete work presented on the 2015 SciTech conference [25]. The constitutive relations for damaged elastoplastic materials are also along with the proposed approach for multiscale constitutive modeling to construct micromechanics models for damaged elasto-visco-plastic materials [26, 27].

A Thermodynamically Consistent Cohesive Zone Model

A thermodynamically consistent cohesive zone model is developed for mixed-mode fracture, which enables a cohesive element to exhibit designated behaviors when subject to mixed-mode loading. The cohesive law in the undamaged configuration, the damage evolution law, and the cohesive law in the damaged configuration are subsequently derived, and a novel delamination criterion is proposed. The applicability and power of the proposed cohesive zone model are demonstrated using examples such as predicting the traction-relative displacement and damage factor-relative displacement curves of cohesive elements of various cohesive properties. The work was initially presented on the 2013 ASME IMECE conference [28], a follow on work was presented on the 2014 SciTech conference [29] and implemented as a UMAT in ABAQUS [30].

Modeling Smart Laminates

The proposed approach is used to model a general anisotropic laminated plate with thermal deformation and two-way coupled piezoelectric effect and pyroelectric effect. Total potential energy contains strain energy, electric potential energy and energy caused by temperature change and external loads. The feature of small thickness and large in-plane dimension of plate structures helped to asymptotically simplify the three-dimensional analysis to a two-dimensional analysis on the reference surface and a one-dimensional analysis through the thickness. This work was originally presented on 2015 ASC conference [31] and later published on the Journal of Smart Materials and Structures [32].

Modeling Aperiodic Materials and Structures

MSG was originally developed for periodic materials. During this research, we found out that MSG can be extended to deal with aperiodic materials and structures. This finding is documented in an ASC conference paper [33]. This discovery also enabled us to develop a micromechanics theory without boundary conditions which was presented on the 2015 ASME IMECE conference [34]. figured out the equivalence between asymptotic homogenization theory and RVE analysis which was also presented on the 2015 ASME IMECE conference [35]. The equivalence and difference between asymptotic homogenization theory, RVE analysis and MSG are documented in a book chapter [36]. MSG is further extended to model aperiodic structures (beams/plates/shells) which is documented in an ASC conference paper [42].

Remove Homogeneous Layer Assumption for Modeling Composite Laminates

A fundamental assumption in modeling composite laminates is the homogeneous layer assumption. We have discovered that MSG can enable to remove this fundamental assumption. This finding is documented in an ASC conference paper [37]. It was later used to point out the basic philosophy and fallacies of composite mechanics on the 2015 ASME IMECE conference [38]. This enables us to provide a true multiscale modeling for composite laminates without artificial separation of scales.

Modeling Fatigue Life of Composites

The proposed approach is used to model high cycle and low cycle fatigue life of heterogeneous materials, which was documented in 2016 AIAA SciTech conference papers [39] and [40], respectively. In this study, local continuum damage mechanics approach is employed to model and analyze the evolution of fatigue damage. The constitutive law for elastic damage analysis is derived. The evolution of anisotropic fatigue damage is iteratively approximated by incremental algorithm at each numerical integration point using weighted averaged local field. The fatigue damage and life are estimated for continuous fiber-reinforced composite.

Solving the Generalized Free-Edge Stress Problem

By serendipity, we discovered that MSG can be used to formulate and solve general free-edge stress problems of composite laminates. Due to its semi-analytical nature, MSG can converge to the singular free-edge stresses much faster than 3D FEA with similar discretization. MSG and the companion code SwiftCompare applied to the free-edge stress analysis of several composite laminates with arbitrary layups and general loads including extension, torsion, in-plane and out-of-plane bending and their combinations. The results of MSG are compared with various existing solutions for symmetric angle-ply laminates. New results are presented for the free-edge stress fields in general laminates for combined mechanical loads and compared with three dimensional (3D) finite element analysis (FEA) results, which agree very well. All the results are documented in a forthcoming 2016 ASC conference paper [41].

AFRL Interaction

We have interacted with AFRL researchers in a regular base. Particularly, we have worked closely with Dr. Ming Chen (Materials Directorate, AFRL, WPAFB) on efficient high-fidelity thermomechanical modeling of sandwich panels considered for hypersonic applications on the Rapid Development and Insertion of Hypersonic Materials program (RDIHM). The results of this collaboration are documented in

[9,10,11]. Prof. Yu was invited to give a seminar with the same title of this project at AFRL WPAFB (Nov. 4, 2013). The host is Dr. Steve Clay of Aerospace System Directorate. Prof. Yu also had frequent interaction with Dr. Clay regarding damage modeling of composite laminates. He has kindly provided the experimental data of his Damage Tolerance Design Principles (DTDP) program for Prof. Yu's research group to validate their models.

Technology Transfer and Dissemination

To facilitate technology transfer of the fundamental results from this research into practical engineering tools, we have implemented MSG into a general-purpose multiscale constitutive modeling called SwiftComp. SwiftComp has been commercialized by Purdue Research Foundation and licensed to AnalySwift LLC for fielding into various industries related with composites. SwiftComp represents a revolutionary, general-purpose computational approach for modeling composite materials and structures. It can be used independently as a tool for virtual testing of composites or as a plugin to power conventional finite element analysis (FEA) codes with efficient high-fidelity multiscale modeling for composites. SwiftComp enables engineers to model composites similarly to metals, capturing details as needed and affordable. This saves orders of magnitude in computing time and resources without sacrificing accuracy, while enabling engineers to tackle complex problems impossible with other approaches. SwiftComp can be used as a standalone code with a GUI developed based on Gmsh, or as a plugin for conventional finite element packages such as Abaqus, and Ansys. It can also be used as a module to be directly linked to other composite simulation environments. SwiftComp can be freely launched in the cloud at https://cdmhub.org/resources/scstandard on any device connected to internet through a browser. Within less than one year after its initial release, SwiftComp has reached a user base of several hundred.

The results from this research are broadly disseminated. In additional to traditional venues of dissemination such conference presentations, publications and archive journals, we also disseminated this research through workshops/short courses, keynote lectures and invited seminars. Such disseminations are listed below:

1. "Mechanics of Composites," A three-hour lecture given *at the cdmHUB hands-on workshop*, Purdue, Aug. 5-7, 2014.
2. "Composites Simulation Workshop," A two-day workshop taught *at the cdmHUB annual workshop*, Purdue, Nov. 3-5, 2015.
3. "Multiscale Structure Mechanics," A two-day short course taught at Department of Aerospace Engineering, Politecnico di Torino, Italy, Nov. 20-21, 2015.
4. Yu, W.: "Representative Structural Element: a New Paradigm for Multiscale Structural Modeling," *Aerospace Systems Directorate, Wright Patterson Air Force Base/AFRL*, Dayton, Ohio, Nov. 4th, 2013.
5. Yu, W.: "Unify Structural Mechanics with Micromechanics Using the Concept of Representative Structural Element," *Sunday Meeting of AIAA Structures Technical Committee*, National Harbor, Maryland, Jan. 12, 2014.
6. Yu, W.: "RSE: a New Paradigm for Multiscale Structural Modeling," *Department of Mechanical and Aerospace Engineering*, Ohio State University, Feb. 28, 2014.
7. Yu, W.: "Mechanics of Structure Genome," *Center for Laser-based Manufacturing*, Purdue University, Jan. 30, 2015.
8. Yu, W.: "Mechanics of Structure Genome," *Center for Computational & Applied Mathematics*, Purdue University, Feb. 6, 2015.
9. Yu, W.: "Mechanics of Structures Genome: Reproduce 3D FEA Using Simple Structural Models for Aero Structures," Boeing Community of Excellence, Sept. 10, 2015.

10. Yu, W.: "Mechanics of Structure Genome," Italian Association of Aeronautics and Astronautics – XXIII Conference, Nov. 19, 2015, Torino, Italy. (Plenary talk)
11. Yu, W.: "Structure Genome: Fill the Gap between Materials Genome and Structural Analysis," Department of Mechanical Engineering, Michigan State University, March 15, 2016.
12. Yu, W.: "Mechanics of Structure Genome: Fill the Gap between Materials Genome and Structural Analysis," Solid Mechanics Seminar, Purdue University, May 25, 2016.

Personnel Support

This project involves two faculty members: Prof. Wenbin Yu (USU before 08/2013, Purdue) and Prof. Ling Liu (USU, supported nominally to manage the subcontract from USU after Prof. Yu moved to Purdue), one postdoctoral fellow: Dr. Liang Zhang (08/2013-). Several students were also partially supported during the course of this project including Bo Peng (PhD student), Haiqiang She (PhD student), and Yufei Long (MS). Another PhD student Hamsasew M Sertse moved with Prof. Yu from USU to Purdue. He has been working on research related with this grant. He is supported by other resources at Purdue.

Conclusions and Further Work

We have accomplished the goal of this project: establish a new paradigm for multiscale structural modeling. The newly discovered Mechanics of Structure Genome is so overarching that it can be used to define any building block for all structures including 3D structures, beams, plates, and shells. And also the proposed approaches have been applied to construct models for failure prediction, capture effects of imperfect interface, and various nonlinear behavior including damage. It can handle both periodic and aperiodic structures and materials and can be used to solve the traditional problems such as composite laminates and the free-edge stress problems in a new way. MSG along with its companion code represents a unique and powerful approach to multiscale constitutive modeling of composites. Because of its versatility and generality, enormous applications are anticipated. Unfortunately, due to the PI's transition from USU to Purdue and inability of AFOSR to approve the no-cost extension, we lose about 15 months of opportunity to further develop this theory and demonstrate its power in many other applications.

Acknowledgements

This research is supported by the Air Force Office of Scientific Research, USAF, under grant FA9550-13-1-0148. The views and conclusions contained herein are those of the authors and should not be interpreted as necessarily representing the official policies or endorsement, either expressed or implied, of AFOSR or the US Government.

References

1. Yu, W.: "Representative Structural Element: a New Paradigm for Multiscale Structural Modeling," *Proceedings of the 54th Structures, Structural Dynamics, and Materials Conference*, Boston, Massachusetts, Apr. 8-11, 2013.
2. Yu, W.: "Representative Structural Element: a New Paradigm for Multiscale Structural Modeling," *Proceedings of the 2013 ASME International Mechanical Engineering Congress and Exposition*, San Diego, California, Nov. 15-21, 2013.
3. Yu, W.: "Structure Genome: Fill the Gap between Materials Genome and Structural Analysis," *Proceedings of the 56th Structures, Structural Dynamics, and Materials Conference*, Kissimmee, Florida, Jan. 5-9, 2015.

4. White House, *Materials Genome Initiative for Global Competitiveness*, Technical Report, http://www.whitehouse.gov/sites/default/files/microsites/ostp/materials_genome_initiative-final.pdf Executive Office of the President National Science and Technology Council, Washington, DC, 2011.
5. Berdichevsky, V. L.: *Variational Principles of Continuum Mechanics, Vol. 2*, Springer, 2009.
6. Yu, W.: "Mechanics of Structure Genome," Proceedings of *the 2015 MACH Conference*, Annapolis, Maryland, Apr. 8-10, 2015.
7. Yu, W.: "Mechanics of Structure Genome," Proceedings of *the 13th US National Congress on Computational Mechanics*, San Diego, California, July. 26-30, 2015.
8. Yu, W.: "A Unified Theory for Constitutive Modeling of Composites," *Journal of Mechanics of Materials and Structures*, to appear.
9. Ye, Z.; Yu, W., Tseng, C. and Chen, M. Y.: "Effective Thermomechanical Properties of the Silicon Carbide Foam," *Proceedings of the 2013 ASME International Mechanical Engineering Congress and Exposition*, San Diego, California, Nov. 15-21, 2013.
10. Ye, Z.; Jiang, F. and Yu, W.: "Thermomechanical Sizing of Various Core Options for a Structural Thermal Protection System," *Proceedings of the 2013 ASME International Mechanical Engineering Congress and Exposition*, San Diego, California, Nov. 15-21, 2013.
11. Jiang, F.; Ye, Z.; Yu, W.; Kerans, R. and Chen, M. Y.: "Analysis of Reusable Integrated Thermal Protection Panel Elements with Various Insulating Core Options," *Proceedings of the 55th Structures, Structural Dynamics, and Materials Conference*, National Harbor, Maryland, Jan. 13-17, 2014.
12. Sertse, H. and Yu, W.: "A Critical Assessment of MOC/GMC/HFGMC and VAMUCH," *Proceedings of the 2013 ASME International Mechanical Engineering Congress and Exposition*, San Diego, California, Nov. 15-21, 2013.
13. Sertse, H.; Zhang, L.; Yu, W. and Ye, Z. "A Comprehensive Evaluation of the Predictive Capabilities of Several Advanced Micromechanics Approaches," *Proceedings of the 55th Structures, Structural Dynamics, and Materials Conference*, National Harbor, Maryland, Jan. 13-17, 2014.
14. Ritchey, A.; Goodsell, J.; Sertse, H.; Yu, W.; and Pipes, R B: "Challenge Problems for the Benchmarking of Micromechanics Analysis," *Proceedings of the American Society for Composites 30th Technical Conference*, East Lansing, Michigan, Sept. 28-30, 2015.
15. Sertse, H. and Yu, W.: "A Micromechanical Approach to Static Failure Prediction of Heterogeneous Materials," *Proceedings of the 2014 ASME International Mechanical Engineering Congress and Exposition*, Montreal, Canada, Nov. 14-20, 2014.
16. Sertse, H. and Yu, W. "A Micromechanical Approach to Static Failure Prediction of Heterogeneous Materials," *Proceedings of the 56th Structures, Structural Dynamics, and Materials Conference*, Kissimmee, Florida, Jan. 5-9, 2015.
17. Sertse, H. and Yu, W. "A Micromechanical Approach to Imperfect Interface Analysis of Heterogeneous Materials," *Proceedings of the 56th Structures, Structural Dynamics, and Materials Conference*, Kissimmee, Florida, Jan. 5-9, 2015.
18. Zhang, L. and Yu, W.: "A Variational Asymptotic Method for Unit Cell Homogenization of Hyperelastic Heterogeneous Materials," *Proceedings of the 2013 ASME International Mechanical Engineering Congress and Exposition*, San Diego, California, Nov. 15-21, 2013.
19. Zhang, L. and Yu, W.: "A Variational Asymptotic Method for Unit Cell Homogenization of Hyperelastic Heterogeneous Materials," *Proceedings of the 55th Structures, Structural Dynamics, and Materials Conference*, National Harbor, Maryland, Jan. 13-17, 2014.
20. Zhang, L. and Yu, W.: "Variational Asymptotic Homogenization of Elastoplastic Composites," *Composite Structures*, vol 133, 2015, 947-958.
21. Zhang, L. and Yu, W.: "A Variational Asymptotic Method for Unit Cell Homogenization of Elasto-Viscoplastic Heterogeneous Materials," *Proceedings of the 54th Structures, Structural Dynamics, and Materials Conference*, Boston, Massachusetts, Apr. 8-11, 2013.
22. Zhang, L. and Yu, W.: "A Micromechanics Approach to Homogenizing Elasto-viscoplastic Heterogeneous Materials," *International Journal of Solids and Structures*, vol. 51, 2014, pp. 3878-3888.

23. Zhang, L. and Yu, W.: "On the Constitutive Relations for Damaged Elastoplastic Materials Coupling Anisotropic Damage and Plasticity," *Proceedings of the 55th Structures, Structural Dynamics, and Materials Conference*, National Harbor, Maryland, Jan. 13-17, 2014.
24. Zhang, L. and Yu, W.: "An Affine Formulation of the Constitutive Relations for Damaged Elasto-Viscoplastic Materials," *Proceedings of the 2014 ASME International Mechanical Engineering Congress and Exposition*, Montreal, Canada, Nov. 14-20, 2014.
25. Zhang, L. and Yu, W.: "On the Constitutive Relations for Damaged Elasto-Viscoplastic Materials Coupling Anisotropic Damage and Viscoplasticity," *Proceedings of the 56th Structures, Structural Dynamics, and Materials Conference*, Kissimmee, Florida, Jan. 5-9, 2015.
26. Zhang, L. and Yu, W.: "A Micromechanics Approach to Homogenizing Damaged Elastoplastic Heterogeneous Materials," *Proceedings of the 2014 ASME International Mechanical Engineering Congress and Exposition*, Montreal, Canada, Nov. 14-20, 2014.
27. Zhang, L. and Yu, W.: "A Micromechanics Approach to Homogenizing Damaged Elastoplastic Heterogeneous Materials," *Proceedings of the 56th Structures, Structural Dynamics, and Materials Conference*, Kissimmee, Florida, Jan. 5-9, 2015.
28. Zhang, L. and Yu, W.: "A Thermodynamically Consistent Cohesive Zone Model for Mixed-Mode Fracture," *Proceedings of the 2013 ASME International Mechanical Engineering Congress and Exposition*, San Diego, California, Nov. 15-21, 2013.
29. Zhang, L. and Yu, W.: "A Thermodynamically Consistent Cohesive Zone Model for Mixed-Mode Fracture," *Proceedings of the 55th Structures, Structural Dynamics, and Materials Conference*, National Harbor, Maryland, Jan. 13-17, 2014.
30. Gao, Z.; Zhang, L. and Yu, W.: "Simulating the Mixed-Mode Progressive Delamination in Composite Laminates," *Proceedings of the American Society for Composites 30th Technical Conference*, East Lansing, Michigan, Sept. 28-30, 2015.
31. Long, Y.; and Yu, W.: "Asymptotical Modelling of Thermopiezoelastic Laminates," *Proceedings of the American Society for Composites 30th Technical Conference*, East Lansing, Michigan, Sept. 28-30, 2015.
32. Long, Y. and Yu, W.: "Asymptotical Modelling of Thermopiezoelastic Laminates," *Smart Materials and Structures*, vol. 25, 2016, 015002.
33. Peng, B.; and Yu, W.: "A New Micromechanics Theory for Homogenization and Dehomogenization of Heterogeneous Materials," *Proceedings of the American Society for Composites 30th Technical Conference*, East Lansing, Michigan, Sept. 28-30, 2015.
34. Yu, W.: "A Boundaryless Micromechanics Theory," *Proceedings of the 2015 ASME International Mechanical Engineering Congress and Exposition*, Houston, Texas, Nov. 13-19, 2015.
35. Yu, W.: "Equivalence of Asymptotic Homogenization and RVE-Analysis with Periodic Boundary Conditions," *Proceedings of the 2015 ASME International Mechanical Engineering Congress and Exposition*, Houston, Texas, Nov. 13-19, 2015.
36. Yu, W.: "An Introduction to Micromechanics," Chapter 1 of Composite Materials and Structures in Aerospace Engineering, Applied Mechanics and Materials, Volume 828, pp. 3-24, 2016, edited by Erasmo Carrera.
37. Peng, B.; and Yu, W.: "Remove Homogeneous Layer Assumption from Lamination Theories," *Proceedings of the American Society for Composites 30th Technical Conference*, East Lansing, Michigan, Sept. 28-30, 2015.
38. Yu, W.: "Philosophies and Fallacies in Modeling of Composite Structures," *Proceedings of the 2015 ASME International Mechanical Engineering Congress and Exposition*, Houston, Texas, Nov. 13-19, 2015.
39. Sertse, H. and Yu, W.: "A Micromechanical Approach to Low Cycle Fatigue Analysis and Life Prediction of Heterogeneous Materials," *Proceedings of the 57th Structures, Structural Dynamics, and Materials Conference*, San Diego, California, Jan. 4-8, 2016.

40. Sertse, H. and Yu, W.: "A Micromechanical Approach to High Cycle Fatigue Analysis and Life Prediction of Heterogeneous Materials," *Proceedings of the 57th Structures, Structural Dynamics, and Materials Conference*, San Diego, California, Jan. 4-8, 2016.
41. Peng, B.; A; Goodsell, J.; Pipes, R. B. and Yu, W.: "Generalized Free-Edge Stress Analysis Using Mechanics of Structure Genome," *Proceedings of the American Society for Composites 31st Technical Conference*, Williamsburg, Virginia, Sept. 19-22, 2016.
42. Peng, B. and Yu, W.: "Modeling Aperiodic Dimensionally Reducible Structures Using Mechanics of Structure Genome," *Proceedings of the American Society for Composites 31st Technical Conference*, Williamsburg, Virginia, Sept. 19-22, 2016.

AIAA SciTech
5-9 January 2015, Kissimmee, Florida
56th AIAA/ASCE/AHS/ASC Structures, Structural Dynamics, and Materials Conference

Structure Genome: Fill the Gap between Materials Genome and Structural Analysis

Wenbin Yu*

A new concept, Structure Genome (SG), is proposed to fill the gap between materials genome and structural analysis. SG acts as the basic building block of the structure connecting materials to structures and the mechanics of SG governs the necessary information to link materials genome and structural analysis. SG also enables a powerful approach to construct efficient yet high-fidelity constitutive models for composite structures over multiple length scales. No apriori assumptions will be used in the formulation and multiscale constitutive modeling is mathematically decoupled from the structural analysis. A general-purpose computer code called SwiftComp$^{\text{TM}}$ is developed to implement the mechanics of Structure Genome along with various examples to demonstrate its application and power. SwiftComp$^{\text{TM}}$ can be used as plug-in for commercial finite element codes to treat composites as "black aluminum" in structural design and analysis with negligible loss of accuracy.

I. Introduction

The recently launched Materials Genome Initiative (MGI)[1], resonating the challenges pointed out earlier in the National Research Council report on Integrated Computational Materials Engineering (ICME)[2], aims to deliver the required infrastructure and training to accelerate discovery, developing, manufacturing, and deploying of advanced materials in a more expeditious and economical way. It is true that accelerating the pace of discovery and deployment of advanced materials is crucial to achieving global competitiveness as materials with nonexisting properties will bring transformative changes in science and technology. However, material by definition is a matter from which a thing can be made of. For example, structural materials are substances used to make structures. Ultimately speaking, it is not the material performance, but the structural performance or rather system performance we are after. Thus, materials genome must integrate with structural analysis to maximize the benefits of accelerated development of advanced structural materials to be delivered by MGI and ICME.

Nowadays, structural analyses are routinely carried out using the finite element analysis (FEA) in terms of three-dimensional (3D) solid elements, two-dimensional (2D) plate or shell elements or one-dimensional (1D) beam elements (see Figure 1). For structures made of isotropic homogeneous materials, material properties characterized in materials genome are direct inputs for solid elements, and these properties combined with geometric properties of the structure can be used for plate/shell/beam elements. This implies that materials genome can be directly linked with structural analysis. However, such simplicity does not exist for structures made of composites which are usually anisotropic and heterogeneous. Consider structural analysis of the UH-60 (8 ton helicopter) all composite rotor blade. The blade is of length 8.6 m, and chord 0.72 m. Main D-spar is composed of 60 graphite/epoxy plies, and each ply has thickness of 125 μm. To directly use the properties of graphite/epoxy composite tape delivered by materials genome in structural analysis, we need to use at least one 3D solid element through the ply thickness. Supposing we use 20-noded brick elements with a 1 to 10 thickness-length ratio, it is estimated that around 11.5 billions of degrees of freedom is needed for the blade analysis[3] Such a huge FEA model is too costly for effective structural design and analysis. The standard practice in helicopter industry is to model rotor blades as beams[4] To this end, models are needed to take the material properties out of materials genome as inputs to compute the beam properties needed for the structural analysis and recover the 3D stress fields within the original material for failure prediction

*Associate Professor, School of Aeronautics and Astronautics, Purdue University, West Lafayette, Indiana 47907-2045. Associate Fellow, AIAA. Fellow, ASME.

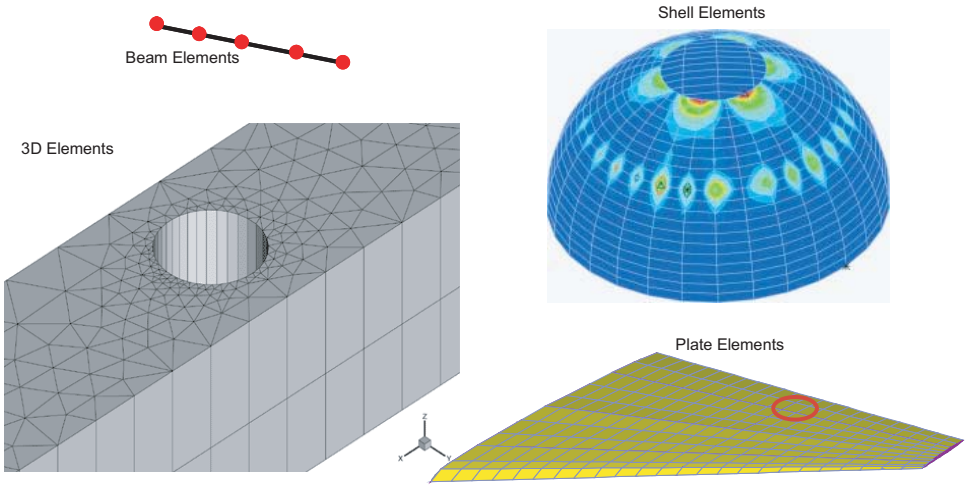

Figure 1. Typical structural elements

according to the allowables and failure criteria characterized by materials genome. Clearly there is a gap existing between materials genome and structural analysis.

In the past several decades, many models have been proposed to fill this gap, including both micromechanics models and structural mechanics models. These models are mainly based on various apriori assumptions. Models are either efficient but too simplistic to be predictive, or accurate but too computationally intensive to be used for effective design. These models usually cannot be used in general industrial settings particularly in the situations where the apriori assumptions will be violated. Moreover, structural mechanics models are not seamlessly unified with micromechanics models, creating difficulty for rigorous modeling of composite structures which are multiscale in nature. The present modeling capabilities for realistic composite structures are still very limited, and lagging much behind of their manufacturing techniques. For example, the recent world-wide failure analysis proved that prediction of strength for composites laminates, one of the simplest composite structures, has been elusive.[5,6] Nevertheless, we have been successfully designed and manufactured composites in many engineering systems. We do so with the conservative Edisonian approach based on exhaustive testings. This not only attributes to the expensive development cost of composites relative to conventional materials, but also causes significant delay in time-to-market of a product.

It is thus encouraging to see that ICME and MGI try to improve our modeling capability through an integrated computational framework. However, one should be careful about what integrated computational framework entails for predictive modeling. Simply linking models at different scales and streamlining information passing between different models are not sufficient. Unpinning theory must be formulated in such a way that provides a unified way for the passing of information between models. And also material modeling must be performed with the corresponding structural analysis in mind. This is particularly true for composites as the traditional boundary between materials and structures is quickly disappearing. Some modeling should be done at the material level through ICME and MGI, but some modeling must be done at the structural level. For example, for composite laminated plates, it is reasonable to expect ICME or MGI to deliver us the properties of fiber, matrix, their interfaces, and even those of each lamina (composite tapes), but it is out of the scope of ICME or MGI to obtain plate properties for the laminate for the structural analysis using plate elements.

Another significant disadvantage of most approaches to composite structural analyses is that they lack a direct connection with the analysis of structures made of isotropic homogeneous materials. FEA has been very successful and well established for design and analysis of these structures and commercial codes such as NASTRAN, ABAQUS, ANSYS, etc. are industrial standard. However, such success has not been transplanted to composite structures. The main reason is that most models for composite structures are very different from those models used for structures made of isotropic homogeneous materials and require special purpose structural elements not available in conventional FEA. Note that many commercial codes are adding a separate composites module into their packages but those modules are different analysis codes implementing special purpose structural elements. The direct connection with conventional structural elements is missing.

II. Structure Genome

To fill the gap between materials genome and composite structural analysis, avoid the disadvantages of current modeling approaches of composites, and enable a direct connection with conventional FEA, this paper will present the Structure Genome (SG) concept. According to MGI,[1]

> A genome is a set of *information* encoded in the language of DNA that serves as a blueprint for an organism's growth and development. The world genome, when applied in non-biological contexts, connotes a *fundamental building block* toward a larger purpose.

Motivated by this description, we define Structure Genome (SG) as the *smallest mathematical* building block (or a cell in biological contexts) of the structure containing many such building blocks. SG not only describes the matter but also carries the information bridging materials genome and structural analysis. SG is build upon the concept of the representative structural element (RSE),[7,8] to emphasize the fact that it contains all the constitutive information needed for a structure the same fashion as the genome contains all the intrinsic information for an organism's growth and development. For periodic structures, it is easy to identify the SG as described later. However, for real structures in engineering, we rely on the expert opinion of the analysts to determine what will be the smallest, representative building block of the structure. This liberal definition is intended for maximizing the freedom in choosing the SG. It can be justified from the view point of material characterization using experiments. When experimentalists want to find properties of a material, they cut representative pieces of the material according to their own judgment and do the testing to get the properties and associated statistics. As we are not doing physical experiments, SG is thus defined as the smallest *mathematical* building block.

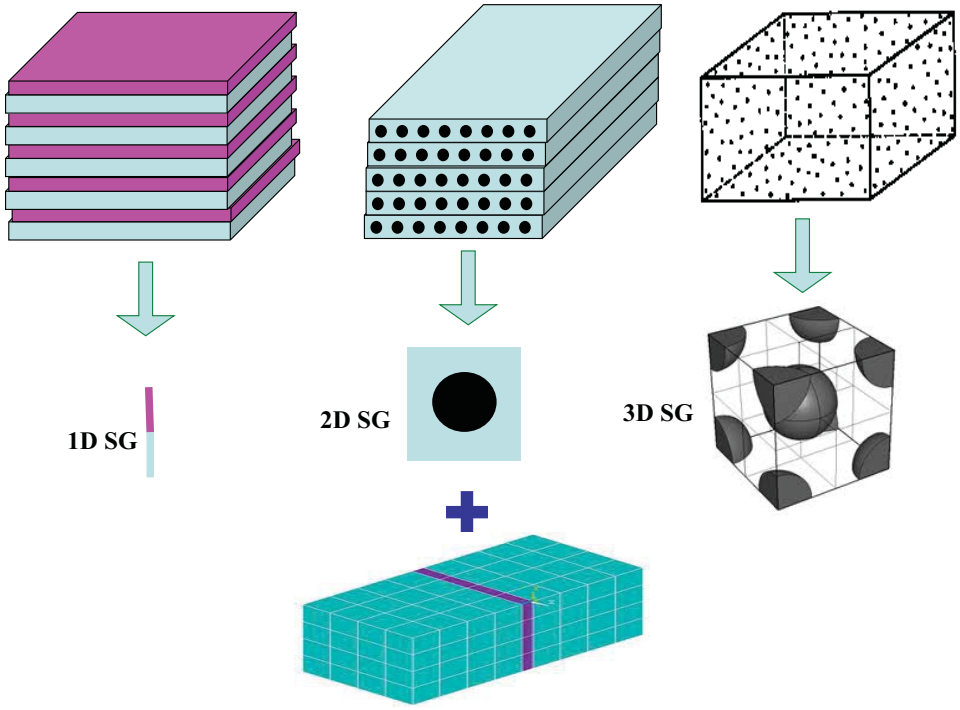

Figure 2. SG for 3D structure

A. SG for 3D Structures

If the structural analysis uses 3D solid elements (Figure 2), SG serves a similar role as representative volume element (RVE), a concept well known in micromechanics. However, they are fundamentally different. For example, for a structure made of composites featuring 1D heterogeneity (e.g. binary composites made of two alternating layers), SG will be a straight line with two segments denoting corresponding phases. Mathematically speaking, we can repeat this straight line in plane to build the two layers of the binary

composite, then we can repeat the binary composite out of plane to build the entire structure. For a structure made of composites featuring 2D heterogeneity (e.g. continuous unidirectional fiber reinforced composites), the SG will be a 2D domain, and for a structure made of composites featuring 3D heterogeneity (e.g. particle reinforced composites), the SG will be a 3D volume. Despite of the dimensionality of SGs, the effective properties should remain 3D for the 3D macroscopic structural analysis. For example, for linear elastic behavior, one should be able to carry out a micromechanical analysis over the 1D SG to obtain the complete 6×6 stiffness matrix. Clearly, SG uses the lowest dimension, thus highest efficiency, to describe the heterogeneity, while RVE dimension is determined by heterogeneity and by what type of properties required for the macroscopic structural analysis. If 3D properties are needed for a 3D structural analysis of continuous unidirectional fiber reinforced composites, a 3D RVE is usually required [9].

B. SG for Dimensionally Reducible Structures

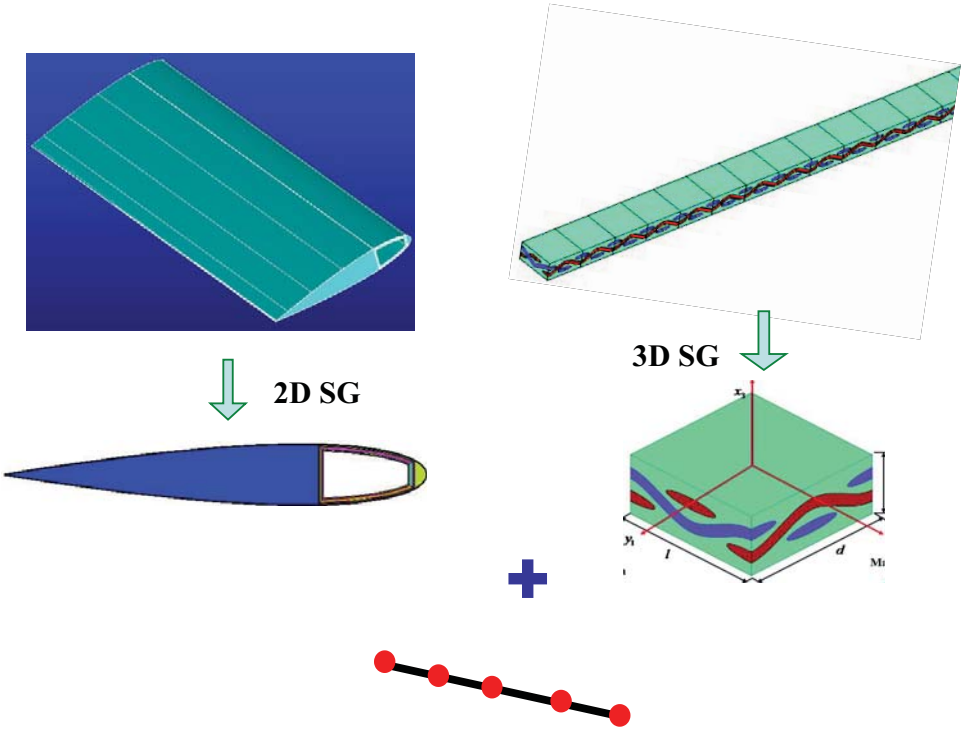

Figure 3. SG for beam-like structures

Another feature of SG not available in RVE is that SG allows direct connection with the macroscopic structural analysis, particularly for dimensionally reducible structures which have one or two dimensions much smaller than the other dimensions. For example, the structural analysis of slender structures (beam-like structures) can use beam elements (Figure 3). If the beam has uniform cross-sections which could be made of homogeneous materials or composites, its SG is the 2D cross-sectional domain as we can repeat the cross-section along the beam reference line to build the entire structure. This inspires an *astoundingly new perspective* toward beam theories, an important traditional branch of structural mechanics. If we consider the beam reference line as a 1D continuum, every material point of this continuum has a 2D cross-section as its microstructure. In other words, *structural mechanics can be effectively viewed as a specific application of micromechanics.* If the beam is also heterogeneous in the spanwise direction, we need a 3D SG to describe the microstructure of the 1D continuum, the behavior of which is governed by the 1D macroscopic beam analysis.

If the structural analysis uses plate/shell elements, SG can also be chosen properly. For illustrative purpose, typical SGs of plate-like structures are sketched in Figure 4. If the plate-like structures feature no in-plane heterogeneities such as composite laminates, the SG is a material line along the thickness direction with each segment denoting the corresponding material of each layer. For a sandwich panel with a core cor-

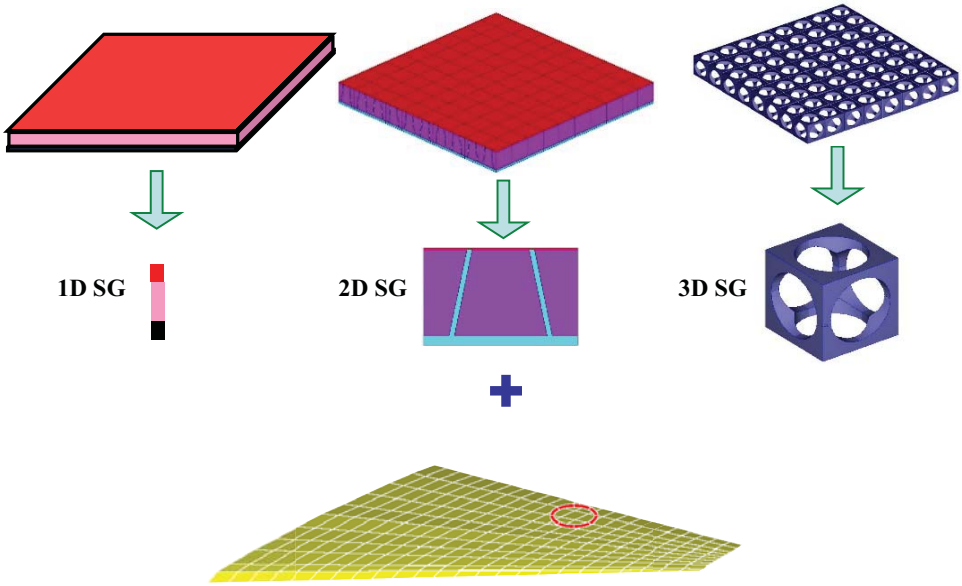

Figure 4. SG for plate-like structures

rugated in one direction, the SG is 2D, and if the panel is heterogeneous in both in-plane directions, the SG is 3D. Despite of different dimensions of SG, what we want out of the constitutive modeling is structural properties for the corresponding structural analysis (such as A, B, D matrices for the classical plate theory) and recovery relations to express the original 3D fields in terms of the global behavior (e.g. moments, curvatures, etc.) obtained from the plate/shell analysis. We know that theories of beams, plates, shells traditionally belong to structural mechanics, the SG concept enables us to treat them as special micromechanics theories. For a plate/shell-like structure, if we consider the reference surface as a 2D continuum, every material point of this continuum has the SG as its microstructure. Plate/shell theory constructed using the SG concept can handle buildup structures (see Figure 5) as long as their external contours look like plates or shells, that is, the thickness is much smaller than the in-plane dimensions.

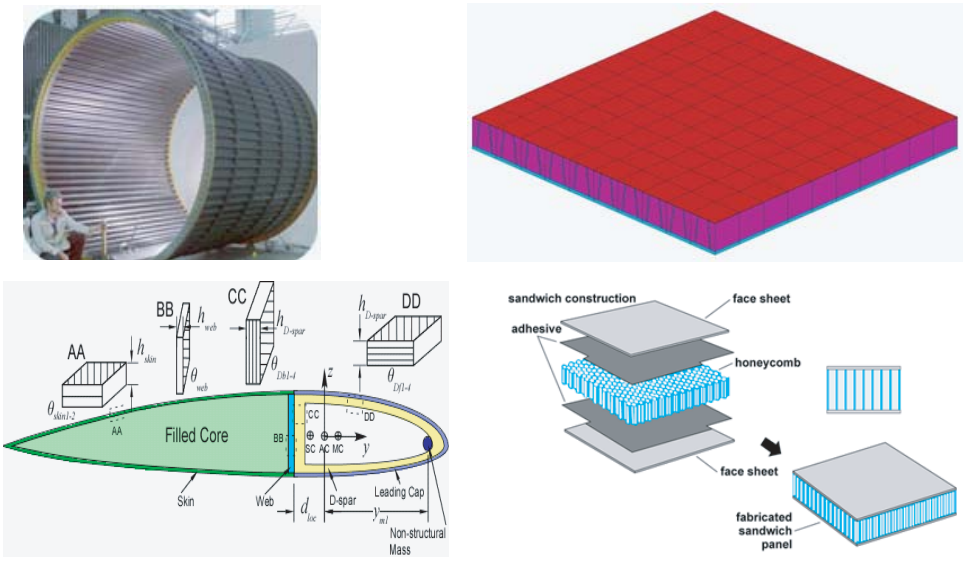

Figure 5. Typical buildup structures

Clearly SG can serve as the fundamental building block of a structure, no matter whether it is a 3D

structure, beam, plate, or shell. SG also bridges materials genome and structural analysis as SG itself is formed by materials. For SG to not merely remain as a concept, we need to develop the theory necessary to govern SG so that there is a two-way communication between materials genome and structural analysis: information from materials genome can be rigorously passed to structural analysis to predict structural performance and information from structural analysis can be passed back for material failure prediction according to materials genome. We develop such a theory with the objective to directly connect with structural analysis and minimize the loss of information from materials genome to structural analysis. As mentioned previously, structures are usually analyzed using structural elements in FEA. Underpinning each element type, there is a corresponding structural model containing three types of equations describing kinematics, kinetics, and constitutive relations. Kinematics deals with strain-displacement relations, and compatibility equations, kinetics deals with stress and equations of motion. Constitutive relations deal with stress-strain relations. Both kinematics and kinetics can be formulated exactly within the framework of continuum mechanics. Constitutive relations are ultimately approximate as we are using a hypothetical continuum to approximate the underlining atomic structure of matter. Some criterion is needed for us to minimize the loss of information between materials genome and structural analysis. For elastic materials, this can be achieved by minimizing the difference between the strain energy of the materials stored in SG and that stored in the structural model of structural analysis. The mechanics of Structure Genome is derived below.

III. Mechanics of Structure Genome

SG serves as the link of the original heterogeneous structures with microscopic details and the hypothetical homogeneous continuum used in the macroscopic structural analysis. Thus, we need to formulate its mechanics in such a way that the kinematics and energetics of the original heterogeneous structure can be expressed in terms of those of the final macroscopic structural model. Note that the final macroscopic homogenized structures are imaginary and are created by analysts to approximate the original heterogeneous structures. For this very reason, we call the final macroscopic homogenized structure as the macroscopic structural model.

A. Kinematics

The first step in formulating the mechanics of SG is to express the kinematics, including the displacement field and the strain field, of the original heterogeneous structures in terms of those of the macroscopic structural model. Although the SG concept is applicable to heterogeneous structures made of materials admitting general continuum description such as the Cosserat continuum,[10] we are focusing on materials admitting the Cauchy continuum description: the displacement field in a 3D space is described in terms of three translations and the corresponding strain field can be defined in terms of the stretch tensor obtained through the polar decomposition of the deformation gradient tensor.

Let us use x_i, called macro coordinates here, to denote the coordinates describing the original heterogeneous structure. The coordinates could be general curvilinear coordinates. However, without loss of generality, we choose an orthogonal system of arc-length coordinates. If the structure is dimensionally reducible, some of the macro coordinates x_α, called eliminated coordinates here, correspond to the dimensions eliminated in the macroscopic structural model. (Here and throughout the paper, Greek indices assume values corresponding to the eliminated macro coordinates, Latin indices k, l, m assume values corresponding to the macro coordinates remaining in the macroscopic structural model, and other Latin indices assume 1, 2, 3. Repeated indices are summed over their range except where explicitly indicated).

For beam-like structures, only x_1, describing the beam reference line, will remain in the final beam model, and x_2, x_3, the cross-sectional coordinates, will be the eliminated coordinates; for plate/shell-like structures, x_1 and x_2, describing the plate/shell reference surface, remain in the final plate/shell model, and x_3, the thickness coordinate, will be the eliminated coordinate. For this reason, we also call the beam model as 1D continuum model as all the unknown fields are functions of x_1 only although the 1D beam model could predict 3D behavior such as translations in three directions. Similarly, we call the plate/shell model as 2D continuum model as all the unknown fields are functions of x_1 and x_2 although the 2D plate/shell model can predict 3D behavior.

In view of the fact that the size of SG is much smaller than the overall size of the macroscopic structure, we introduce a set of micro coordinates $y_i = x_i/\varepsilon$ with ε being a small parameter to describe the SG. This

basically enables a zoom-in view of the SG at the size similar as the macroscopic structure. If the SG is 1D, only y_3 is needed; if the SG is 2D, y_2 and y_3 are needed; if the SG is 3D, all three coordinates y_1, y_2, y_3 are needed.

In multiscale structural modeling, it is postulated that all the information can be obtained from the SG in combination with the macroscopic structural model. In other words, a field function of the original heterogeneous structure can be generally written as a function of the macro coordinates x_k which remain in the macroscopic structural model and the micro coordinates y_j. The partial derivative of a function $f(x_k, y_j)$ can be expressed as

$$\frac{\partial f(x_k, y_j)}{\partial x_i} = \frac{\partial f(x_k, y_j)}{\partial x_i}|_{y_j=\text{const}} + \frac{1}{\varepsilon}\frac{\partial f(x_k, y_j)}{\partial y_i}|_{x_k=\text{const}} \equiv f_{,i} + \frac{1}{\varepsilon}f_{|i} \tag{1}$$

Note ε is just a book keeping parameter here to facilitate the asymptotic analysis. It has no significance in the numerical implementation. Choosing an ε will fix the corresponding SG domain. εy_i together remain invariant as equal to x_i.

Letting $\boldsymbol{b}_k$ denote the tangent vector to x_k for the undeformed configuration, one is then free to chose $\boldsymbol{b}_\alpha$ tangent to x_α to form an orthonormal triad $\boldsymbol{b}_i$. Note $\boldsymbol{b}_i$ chosen this way are functions of x_k only. For example, for beam-like structures, we chose $\boldsymbol{b}_1$ to be tangent to the beam reference line x_1, and $\boldsymbol{b}_2$ and $\boldsymbol{b}_3$ as unit vectors tangent to the cross-sectional coordinates x_α. We can describe the position of any material point of the heterogeneous structure by its position vector $\boldsymbol{r}$ relative to a point O fixed in an inertial frame such that

$$\boldsymbol{r}(x_k, y_\alpha) = \boldsymbol{r}_o(x_k) + \varepsilon y_\alpha \boldsymbol{b}_\alpha(x_k) \tag{2}$$

where $\boldsymbol{r}_o$ is the position vector from O to a material point of the macroscopic structural model. Note here x_k denote only those coordinates remaining in the final macroscopic structural model, and y_α correspond to eliminated coordinates x_α. Repeated index implies summation over its own range. Because x_k is the arc-length coordinate, we have

$$\boldsymbol{b}_k = \frac{\partial \boldsymbol{r}_o}{\partial x_k} \tag{3}$$

For beam-like structures, the undeformed configuration can be described as

$$\boldsymbol{r}(x_1, y_2, y_3) = \boldsymbol{r}_o(x_1) + \varepsilon y_2 \boldsymbol{b}_2(x_1) + \varepsilon y_3 \boldsymbol{b}_3(x_1) \tag{4}$$

because the dimensions along x_2 and x_3, corresponding to εy_2 and εy_3, are eliminated in the macroscopic structural model, no matter whether the SG is 2D or 3D (see Figure 3).

For plate/shell-like structures, the undeformed configuration can be described as

$$\boldsymbol{r}(x_1, x_2, y_3) = \boldsymbol{r}_o(x_1, x_2) + \varepsilon y_3 \boldsymbol{b}_3(x_1, x_2) \tag{5}$$

because the thickness dimension along x_3, corresponding to εy_3, is eliminated in the macroscopic structural model, no matter whether the SG is 1D, 2D, or 3D (see Figure 4).

For 3D structures, the undeformed configuration can be described as

$$\boldsymbol{r}(x_1, x_2, x_3) = \boldsymbol{r}_o(x_1, x_2, x_3) \tag{6}$$

because all the macro coordinates remain in the macroscopic structural model, no matter whether the SG is 1D, 2D, or 3D (see Figure 2).

When the heterogeneous structure deforms, the particle that had position vector $\boldsymbol{r}$ in the undeformed configuration now has position vector $\boldsymbol{R}$ in the deformed configuration, such as

$$\boldsymbol{R}(x_k, y_j) = \boldsymbol{R}_o(x_k) + \varepsilon y_\alpha \boldsymbol{B}_\alpha(x_k) + \varepsilon w_i(x_k, y_j)\boldsymbol{B}_i(x_k) \tag{7}$$

where $\boldsymbol{R}_o$ denotes the position vector of the deformed homogenized structure, y_j are the micro coordinates used to describe the SG, $\boldsymbol{B}_i$ forms a new orthonormal triad for the deformed configuration, and εw_i are fluctuating functions introduced to accommodate all possible deformation other than those described by $\boldsymbol{R}_o$ and $\boldsymbol{B}_i$. The small parameter ε is added due to traditional reasons. But as it is mentioned previously, it is not a number of significance and εw_i remain as the unique solution. Note w_i are usually called warping functions in structural mechanics and we call them as fluctuating functions for the reason that structural

mechanics can be viewed as a special application of micromechanics using the concept of SG. $\boldsymbol{B}_i$ can be related with $\boldsymbol{b}_i$ through a direction cosine matrix, $C_{ij} = \boldsymbol{B}_i \cdot \boldsymbol{b}_j$, subject to the requirement that these two triads are the same in the undeformed configuration.

For beam-like structures featuring 2D SGs, the deformed configuration can be described as

$$\boldsymbol{R}(x_1, y_2, y_3) = \boldsymbol{R}_o(x_1) + \varepsilon y_2 \boldsymbol{B}_2(x_1) + \varepsilon y_3 \boldsymbol{B}_3(x_1) + \varepsilon w_i(x_1, y_2, y_3)\boldsymbol{B}_i(x_1) \tag{8}$$

For beam-like structures featuring 3D SGs, the deformed configuration can be described as

$$\boldsymbol{R}(x_1, y_1, y_2, y_3) = \boldsymbol{R}_o(x_1) + \varepsilon y_2 \boldsymbol{B}_2(x_1) + \varepsilon y_3 \boldsymbol{B}_3(x_1) + \varepsilon w_i(x_1, y_1, y_2, y_3)\boldsymbol{B}_i(x_1) \tag{9}$$

For plate/shell-like structures featuring 1D SGs, the deformed configuration can be described as

$$\boldsymbol{R}(x_1, x_2, y_3) = \boldsymbol{R}_o(x_1, x_2) + \varepsilon y_3 \boldsymbol{B}_3(x_1, x_2) + \varepsilon w_i(x_1, x_2, y_3)\boldsymbol{B}_i(x_1, x_2) \tag{10}$$

For plate/shell-like structures featuring 2D SGs, the deformed configuration can be described as

$$\boldsymbol{R}(x_1, x_2, y_2, y_3) = \boldsymbol{R}_o(x_1, x_2) + \varepsilon y_3 \boldsymbol{B}_3(x_1, x_2) + \varepsilon w_i(x_1, x_2, y_2, y_3)\boldsymbol{B}_i(x_1, x_2) \tag{11}$$

For plate/shell-like structures featuring 3D SGs, the deformed configuration can be described as

$$\boldsymbol{R}(x_1, x_2, y_1, y_2, y_3) = \boldsymbol{R}_o(x_1, x_2) + \varepsilon y_3 \boldsymbol{B}_3(x_1, x_2) + \varepsilon w_i(x_1, x_2, y_1, y_2, y_3)\boldsymbol{B}_i(x_1, x_2) \tag{12}$$

For 3D structures featuring 1D SGs, the deformed configuration can be described as

$$\boldsymbol{R}(x_1, x_2, x_3, y_3) = \boldsymbol{R}_o(x_1, x_2, x_3) + \varepsilon w_i(x_1, x_2, x_3, y_3)\boldsymbol{B}_i(x_1, x_2, x_3) \tag{13}$$

For 3D structures featuring 2D SGs, the deformed configuration can be described as

$$\boldsymbol{R}(x_1, x_2, x_3, y_2, y_3) = \boldsymbol{R}_o(x_1, x_2, x_3) + \varepsilon w_i(x_1, x_2, x_3, y_2, y_3)\boldsymbol{B}_i(x_1, x_2, x_3) \tag{14}$$

For 3D structures featuring 3D SGs, the deformed configuration can be described as

$$\boldsymbol{R}(x_1, x_2, x_3, y_1, y_2, y_3) = \boldsymbol{R}_o(x_1, x_2, x_3) + \varepsilon w_i(x_1, x_2, x_3, y_1, y_2, y_3)\boldsymbol{B}_i(x_1, x_2, x_3) \tag{15}$$

Note in Eq. (7), we actually express $\boldsymbol{R}$ in terms of $\boldsymbol{R}_o$, $\boldsymbol{B}_i$, and w_i, which is six times redundant. Six constraints are needed to ensure a unique mapping. These constraints are directly related with how we define $\boldsymbol{R}_o$ and $\boldsymbol{B}_i$ in terms of $\boldsymbol{R}$. For example, it is natural for us to define

$$\boldsymbol{R}_o = \langle\langle \boldsymbol{R} \rangle\rangle - \langle\langle \varepsilon y_\alpha \rangle\rangle \boldsymbol{B}_\alpha(x_k) \tag{16}$$

where $\langle\langle \cdot \rangle\rangle$ indicates average over SG. If y_α is chosen such that $\langle\langle \varepsilon y_\alpha \rangle\rangle = 0$, position vector of a material point in the macroscopic structural model $\boldsymbol{R}_o$ is defined as the average of the position vector of the original heterogeneous structure. This definition implies following three constraints on the fluctuating functions:

$$\langle\langle w_i \rangle\rangle = 0 \tag{17}$$

The other three constraints can be used to specify $\boldsymbol{B}_i$ in a certain fashion. For 3D structures, we already have three constraints from the definition $\boldsymbol{B}_k = \boldsymbol{R}_{o,k}$.

For plate/shell-like structures, we can select $\boldsymbol{B}_3$ in such a way that

$$\boldsymbol{B}_3 \cdot \boldsymbol{R}_{o,1} = 0 \qquad \boldsymbol{B}_3 \cdot \boldsymbol{R}_{o,2} = 0 \tag{18}$$

which provides two constraints implying that we choose $\boldsymbol{B}_3$ normal to the reference surface of the deformed plate/shell. It should be noted that this choice has nothing to do with the well-known Kirchhoff hypothesis. In the Kirchhoff assumption, the transverse normal can only rotate rigidly without any local deformation. However, in the present formulation, we allow all possible deformation, classifying all deformation other than those described by $\boldsymbol{R}_o$ and $\boldsymbol{B}_i$ in terms of the fluctuating function $w_i\boldsymbol{B}_i$. The last constraint can be specified by the rotation of $\boldsymbol{B}_\alpha$ around $\boldsymbol{B}_3$ such that

$$\boldsymbol{B}_1 \cdot \boldsymbol{R}_{o,2} = \boldsymbol{B}_2 \cdot \boldsymbol{R}_{o,1} \tag{19}$$

This constraint actually defines the macro strains for a plate/shell model as defined in Eq. (48) later to be symmetric.

For beam-like structures, we can select $\boldsymbol{B}_\alpha$ in such a way that

$$\boldsymbol{B}_2 \cdot \boldsymbol{R}_{o,1} = 0 \qquad \boldsymbol{B}_3 \cdot \boldsymbol{R}_{o,1} = 0 \tag{20}$$

which provides two constraints implying that we choose $\boldsymbol{B}_1$ to be tangent to the reference line of deformed beam. Note that this choice is not the well-known Euler-Bernoulli assumption as the present formulation allows us to describe all the deformation of the cross-section. We can also prescribe the rotation of $\boldsymbol{B}_\alpha$ around $\boldsymbol{B}_1$ such that

$$\boldsymbol{B}_3 \cdot \frac{\partial \boldsymbol{R}}{\partial x_2} - \boldsymbol{B}_2 \cdot \frac{\partial \boldsymbol{R}}{\partial x_3} = 0 \tag{21}$$

which implies the following constraint on the fluctuating functions

$$\left\langle \langle w_{2|3} - w_{3|2} \rangle \right\rangle = 0 \tag{22}$$

This constraint actually defines the twist angle of the macroscopic beam model in terms of the original position vector as pointed out in Ref. [4].

Thus the fluctuating functions are constrained according to Eq. (17) for 3D structures or plate/shell-structures, for beam structures, they are also constrained according to Eq. (22).

If the original heterogeneous structure is made of materials described using a Cauchy continuum and if the local rotation (the real rotation of a material point of the original heterogeneous structure subtracting the rotation needed for bringing $\mathbf{b}_i$ to $\mathbf{B}_i$) is small, it is convenient to use the Jauman-Biot-Cauchy strain according to the decomposition of rotation tensor:[11]

$$\Gamma_{ij} = \frac{1}{2}\left(F_{ij} + F_{ji}\right) - \delta_{ij} \tag{23}$$

where δ_{ij} is the Kronecker symbol and F_{ij} is the mixed-basis component of the deformation gradient tensor defined as

$$F_{ij} = \mathbf{B}_i \cdot \mathbf{G}_a \mathbf{g}^a \cdot \mathbf{b}_j = \mathbf{B}_i \cdot \left(\mathbf{G}_k \mathbf{g}^k + \mathbf{G}_\alpha \mathbf{g}^\alpha\right) \cdot \mathbf{b}_j \tag{24}$$

Here $\mathbf{g}^a$ are the 3D contravariant base vectors of the undeformed configuration and $\mathbf{G}_a$ are the 3D covariant basis vectors of the deformed configuration.

The contravariant base vector $\mathbf{g}^a$ is defined as

$$\mathbf{g}^a = \frac{1}{2\sqrt{g}} e_{aij} \boldsymbol{g}_i \times \boldsymbol{g}_j \tag{25}$$

with e_{aij} as the 3D permutation symbol and

$$\boldsymbol{g}_i = \frac{\partial \boldsymbol{r}}{\partial x_i} \tag{26}$$

as the covariant base vector of the undeformed configuration. g is the determinant of the metric tensor of the undeformed configuration, defined as

$$g = \det(\boldsymbol{g}_i \cdot \boldsymbol{g}_j) \tag{27}$$

From the undeformed configuration in Eq. (2), corresponding to the remaining macro coordinate x_k, we obtain the covariant base vector as

$$\boldsymbol{g}_k = \frac{\partial \boldsymbol{r}}{\partial x_k} = \boldsymbol{b}_k + \varepsilon y_\alpha \frac{\partial \boldsymbol{b}_\alpha}{\partial x_k} = \boldsymbol{b}_k + \varepsilon y_\alpha \boldsymbol{k}_k \times \boldsymbol{b}_\alpha = \boldsymbol{b}_k + e_{i\alpha j} \varepsilon y_\alpha k_{ki} \boldsymbol{b}_j \tag{28}$$

Here $\boldsymbol{k}_k = k_{ki}\boldsymbol{b}_i$ is the initial curvature vector corresponding to the remaining macro coordinate x_k. This definition is consistent with those defined for initial curvatures of shells in Ref. [12], k_{kl}^{2D}, if we let

$$k_{kl}^{\mathrm{2D}} = \alpha_{lm} k_{km} \qquad k_{k3}^{\mathrm{2D}} = k_{k3} \tag{29}$$

with α_{lm} as the 2D permutation symbol so that $\alpha_{11} = \alpha_{22} = 0, \alpha_{12} = -\alpha_{21} = 1$.

From the undeformed configuration in Eq. (2), corresponding to the eliminated macro coordinate x_α, we obtain the covariant base vector as

$$\boldsymbol{g}_\alpha = \frac{\partial \boldsymbol{r}}{\partial x_\alpha} = \frac{\partial \varepsilon y_\alpha}{\partial x_\alpha}\boldsymbol{b}_\alpha = \boldsymbol{b}_\alpha \tag{30}$$

Specifically, for beam-like structures, we have

$$\mathbf{g}_1 = (1 - \varepsilon y_2 k_{13} + \varepsilon y_3 k_{12})\mathbf{b}_1 - \varepsilon y_3 k_{11}\mathbf{b}_2 + \varepsilon y_2 k_{11}\mathbf{b}_3 \tag{31}$$

$$\mathbf{g}_2 = \mathbf{b}_2 \tag{32}$$

$$\mathbf{g}_3 = \mathbf{b}_3 \tag{33}$$

$$\sqrt{g} = 1 - \varepsilon y_2 k_{13} + \varepsilon y_3 k_{12} \tag{34}$$

$$\mathbf{g}^1 = \frac{1}{\sqrt{g}}\mathbf{b}_1 \tag{35}$$

$$\mathbf{g}^2 = \mathbf{b}_2 + \frac{\varepsilon y_3 k_{11}}{\sqrt{g}}\mathbf{b}_1 \tag{36}$$

$$\mathbf{g}^3 = \mathbf{b}_3 - \frac{\varepsilon y_2 k_{11}}{\sqrt{g}}\mathbf{b}_1 \tag{37}$$

For prismatic beams, $k_{11} = k_{12} = k_{13} = 0$, and $\boldsymbol{g}_i = \boldsymbol{g}^i = \boldsymbol{b}_i$.

For plate/shell-like structures, one is free to chose the lines of curvatures to be the arc-length coordinates x_1 and x_2, so that $k_{11} = k_{22} = 0$. If such a choice is made, the covariant base vectors can be obtained in the following simple form:

$$\mathbf{g}_1 = (1 + \varepsilon y_3 k_{12})\mathbf{b}_1 \tag{38}$$

$$\mathbf{g}_2 = (1 - \varepsilon y_3 k_{21})\mathbf{b}_2 \tag{39}$$

$$\mathbf{g}_3 = \mathbf{b}_3 \tag{40}$$

$$\sqrt{g} = (1 + \varepsilon y_3 k_{12})(1 - \varepsilon y_3 k_{21}) \tag{41}$$

$$\mathbf{g}^1 = \frac{\mathbf{b}_1}{1 + \varepsilon y_3 k_{12}} \tag{42}$$

$$\mathbf{g}^2 = \frac{\mathbf{b}_2}{1 - \varepsilon y_3 k_{21}} \tag{43}$$

$$\mathbf{g}^3 = \mathbf{b}_3 \tag{44}$$

For plates, $k_{12} = k_{21} = 0$, we have $\boldsymbol{g}_i = \boldsymbol{g}^i = \boldsymbol{b}_i$.

For 3D structures, we have $\boldsymbol{g}_i = \boldsymbol{g}^i = \boldsymbol{b}_i$ according to Eq. (6).

The 3D covariant basis vectors of the deformed configuration $\mathbf{G}_i$ are defined as

$$\boldsymbol{G}_i = \frac{\partial \boldsymbol{R}}{\partial x_i} \tag{45}$$

From the deformed configuration in Eq. (7), corresponding to the remaining macro coordinate x_k, we obtain the covariant base vector $\mathbf{G}_k$ as

$$\boldsymbol{G}_k = \frac{\partial \boldsymbol{R}}{\partial x_k} = \frac{\partial \boldsymbol{R}_o}{\partial x_k} + \varepsilon y_\alpha \frac{\partial \boldsymbol{B}_\alpha}{\partial x_k} + \varepsilon \frac{\partial w_i}{\partial x_k}\boldsymbol{B}_i + \varepsilon w_i \frac{\partial \boldsymbol{B}_i}{\partial x_k} \tag{46}$$

From the deformed configuration in Eq. (7), corresponding to the eliminated macro coordinate x_α, we obtain the covariant base vector as

$$\boldsymbol{G}_\alpha = \frac{\partial \boldsymbol{R}}{\partial x_\alpha} = \frac{\partial (\varepsilon y_\beta)}{\partial x_\alpha}\boldsymbol{B}_\beta + \varepsilon \frac{\partial w_i}{\partial x_\alpha}\boldsymbol{B}_i = \boldsymbol{B}_\alpha + \frac{\partial w_i}{\partial y_\alpha}\boldsymbol{B}_i \tag{47}$$

A proper definition of the generalized strain measures for the macroscopic structural model is needed for purpose of formulating our macroscopic structural analysis in an intrinsic form. Following Refs. [4, 12, 13], we introduce the following definitions:

$$\begin{aligned} \epsilon_{kl} &= \boldsymbol{B}_l \cdot \frac{\partial \boldsymbol{R}_o}{\partial x_k} - \delta_{kl} \\ \kappa_{ki} &= \frac{1}{2} e_{iaj} \boldsymbol{B}_j \cdot \frac{\partial \boldsymbol{B}_a}{\partial x_k} - k_{ki} \end{aligned} \tag{48}$$

where ϵ_{kl} is the Lagrangian stretch tensor and κ_{ki} is the Lagrangian curvature strain tensor. This definition corresponds to the kinematics of a nonlinear Cosserat continuum[10] which allows six independent degrees of freedom (three translations and three rotations) for each material point no matter whether the macroscopic structural model is 1D, 2D, or 3D.

For beam-like structures, these definitions reproduce the 1D generalized strain measures of the Timoshenko beam model defined in Ref. [14]. If we restrict $\boldsymbol{B}_1$ to be tangent to $\boldsymbol{R}_o$, Eq. (20), these definitions reproduce the 1D generalized strain measures of the Euler-Bernoulli beam model defined in Ref. [14].

For plate/shell-like structures, if we uses Eq. (19), we will have the symmetry $\epsilon_{12} = \epsilon_{21}$ as a constraint for the kinematics of the final plate/shell model. These definitions reproduce the 2D generalized strain measures of the Reissner-Mindlin model defined in Ref. [12]. If we further restrain $\boldsymbol{B}_3$ to be normal to the reference surface, Eq. (18), these definitions reproduce the 2D generalized strain measures of the Kirchhoff-Love model defined in Ref. [15].

For 3D structures, these definitions correspond to the natural strain measures defined in Ref. [13] for non-linear Cosserat continuum. Although the SG kinematics formulated this way has the potential to construct a Cosserat continuum model for the 3D macroscopic structural model, we will restrict ourselves to the classical Cauchy continuum model for 3D structures in this paper. In other words, we are seeking a symmetric Lagrangian stretch tensor ϵ_{kl} and negligible curvature strain tensor κ_{ki}. This can be achieved by constraining the global rotation needed for bringing $\mathbf{b}_i$ to $\mathbf{B}_i$ in a specific way, which can be illustrated more clearly using an invariant form of the definitions in Eq. (48). According to Ref. [13, 16], these definitions can be rewritten as

$$\begin{aligned} \boldsymbol{\epsilon} &= \boldsymbol{C}^T \cdot \boldsymbol{F} - \boldsymbol{I} \\ \boldsymbol{\kappa}^T &= -\frac{1}{2}\boldsymbol{e} : \left(\boldsymbol{C}^T \cdot \frac{\partial \boldsymbol{C}}{\partial x_k} \boldsymbol{b}_k \right) \end{aligned} \tag{49}$$

where $\boldsymbol{\epsilon}$ is the Lagrangian stretch tensor, $\boldsymbol{\kappa}$ the Lagrangian curvature strain tensor (or so-called wryness tensor), $\boldsymbol{C} = \boldsymbol{B}_i \boldsymbol{b}_i$ is the global rotation tensor bringing $\boldsymbol{b}_i$ to $\boldsymbol{B}_i$, $\boldsymbol{F}$ is the deformation gradient tensor, $\boldsymbol{I} = \boldsymbol{b}_i \boldsymbol{b}_i$ is the second-order identity tensor, and $\boldsymbol{e} = -\boldsymbol{I} \times \boldsymbol{I}$ is the third-order skew Ricci tensor. If we constrain the global rotation tensor $\boldsymbol{C}$ to be that can be decomposed from $\boldsymbol{F}$ according to the polar decomposition theorem such that

$$\boldsymbol{F} = \boldsymbol{C} \cdot \boldsymbol{U} \tag{50}$$

where $\boldsymbol{U}$ is a second-order positive symmetric tensor, then the definitions in Eq. (49) become

$$\begin{aligned} \boldsymbol{\epsilon} &= \boldsymbol{C}^T \cdot (\boldsymbol{C} \cdot \boldsymbol{U}) - \boldsymbol{I} = \boldsymbol{U} - \boldsymbol{I} \\ \boldsymbol{\kappa}^T &= -\frac{1}{2}\boldsymbol{e} : \left(\boldsymbol{C}^T \cdot \frac{\partial \boldsymbol{C}}{\partial x_k} \boldsymbol{b}_k \right) \end{aligned} \tag{51}$$

Clearly, the Lagrangian stretch tensor $\boldsymbol{\epsilon}$ becomes symmetric and is the definition of Jauman-Biot-Cauchy strain tensor. Lagrangian curvature strain tensor $\boldsymbol{\kappa}$ corresponds to higher order terms, gradient of the deformation gradient, which is commonly neglected in a Cauchy continuum.

To facilitate the derivation of the covariant vectors $\boldsymbol{G}_i$, we can rewrite the definitions in Eq. (48) as

$$\begin{aligned} \frac{\partial \boldsymbol{R}_o}{\partial x_k} &= \boldsymbol{B}_k + \epsilon_{kl} \boldsymbol{B}_l \\ \frac{\partial \boldsymbol{B}_i}{\partial x_k} &= (\kappa_{kj} + k_{kj}) \boldsymbol{B}_j \times \boldsymbol{B}_i \end{aligned} \tag{52}$$

Note $\epsilon_{13} = \epsilon_{23} = 0$ for plate/shell-like structures due to Eq. (18) and $\epsilon_{12} = \epsilon_{13} = 0$ for beam-like structures due to Eq. (20).

Substituting Eq. (52) into Eq. (46), we can obtain more detailed expressions for the covariant base vectors of the deformed configuration $\boldsymbol{G}_k$ as follows:

$$\begin{aligned} \boldsymbol{G}_k &= \boldsymbol{B}_k + \epsilon_{kl}\boldsymbol{B}_l + \varepsilon y_\alpha \frac{\partial \boldsymbol{B}_\alpha}{\partial x_k} + \varepsilon \frac{\partial w_l}{\partial x_k}\boldsymbol{B}_l + \varepsilon \frac{\partial w_\alpha}{\partial x_k}\boldsymbol{B}_\alpha + \varepsilon w_l \frac{\partial \boldsymbol{B}_l}{\partial x_k} + \varepsilon w_\alpha \frac{\partial \boldsymbol{B}_\alpha}{\partial x_k} \\ &= \left(\delta_{kl} + \epsilon_{kl} + \varepsilon \frac{\partial w_l}{\partial x_k} \right) \boldsymbol{B}_l + \varepsilon \left(y_\alpha + w_\alpha \right) \frac{\partial \boldsymbol{B}_\alpha}{\partial x_k} + \varepsilon \frac{\partial w_\alpha}{\partial x_k}\boldsymbol{B}_\alpha + \varepsilon w_l \frac{\partial \boldsymbol{B}_l}{\partial x_k} \\ &= \left(\delta_{kl} + \epsilon_{kl} + \varepsilon \frac{\partial w_l}{\partial x_k} \right) \boldsymbol{B}_l + \varepsilon \left[e_{ij\alpha} \left(y_\alpha + w_\alpha \right) \left(\kappa_{kj} + k_{kj} \right) + \frac{\partial w_\alpha}{\partial x_k}\delta_{\alpha i} + e_{ijl} w_l (\kappa_{kj} + k_{kj}) \right] \boldsymbol{B}_i \end{aligned} \tag{53}$$

Note in this expressions for $\boldsymbol{G}_k$, according to Eq. (1), we have

$$\varepsilon\frac{\partial w_i(x_k,y_j)}{\partial x_k}=\varepsilon\frac{\partial w_i(x_k,y_j)}{\partial x_k}|_{y_j=\text{const}}+\frac{\partial w_i(x_k,y_j)}{\partial y_k}|_{x_k=\text{const}}\equiv\varepsilon w_{i,k}+w_{i|k} \tag{54}$$

Now, we are ready to write out the explicit expressions of $\boldsymbol{G}_i$ for beam-like structures, plate/shell-like structures, or 3D structures.

For beam-like structures, we have

$$\begin{aligned}\boldsymbol{G}_1=&\left[1+\epsilon_{11}+\varepsilon\frac{\partial w_1}{\partial x_1}-\varepsilon(y_2+w_2)(\kappa_{13}+k_{13})+\varepsilon(y_3+w_3)(\kappa_{12}+k_{12})\right]\boldsymbol{B}_1\\&+\varepsilon\left[\frac{\partial w_2}{\partial x_1}-(y_3+w_3)(\kappa_{11}+k_{11})+w_1(\kappa_{13}+k_{13})\right]\boldsymbol{B}_2\\&+\varepsilon\left[\frac{\partial w_3}{\partial x_1}+(y_2+w_2)(\kappa_{11}+k_{11})-w_1(\kappa_{12}+k_{12})\right]\boldsymbol{B}_3\end{aligned} \tag{55}$$

$$\boldsymbol{G}_2=\frac{\partial w_1}{\partial y_2}\boldsymbol{B}_1+\left(1+\frac{\partial w_2}{\partial y_2}\right)\boldsymbol{B}_2+\frac{\partial w_3}{\partial y_2}\boldsymbol{B}_3 \tag{56}$$

$$\boldsymbol{G}_3=\frac{\partial w_1}{\partial y_3}\boldsymbol{B}_1+\frac{\partial w_2}{\partial y_3}\boldsymbol{B}_2+\left(1+\frac{\partial w_3}{\partial y_3}\right)\boldsymbol{B}_3 \tag{57}$$

For plate/shell-like structures, we have

$$\begin{aligned}\boldsymbol{G}_1=&\left[1+\epsilon_{11}+\varepsilon\frac{\partial w_1}{\partial x_1}+\varepsilon(y_3+w_3)(\kappa_{12}+k_{12})-\varepsilon w_2(\kappa_{13}+k_{13})\right]\boldsymbol{B}_1\\&+\left[\epsilon_{12}+\varepsilon\frac{\partial w_2}{\partial x_1}-\varepsilon(y_3+w_3)\kappa_{11}+\varepsilon w_1(\kappa_{13}+k_{13})\right]\boldsymbol{B}_2\\&+\varepsilon\left[\frac{\partial w_3}{\partial x_1}-w_1(\kappa_{12}+k_{12})+w_2\kappa_{11}\right]\boldsymbol{B}_3\end{aligned} \tag{58}$$

$$\begin{aligned}\boldsymbol{G}_2=&\left[\epsilon_{21}+\varepsilon\frac{\partial w_1}{\partial x_2}+\varepsilon(y_3+w_3)\kappa_{22}-\varepsilon w_2(\kappa_{23}+k_{23})\right]\boldsymbol{B}_1\\&+\left[1+\epsilon_{22}+\varepsilon\frac{\partial w_2}{\partial x_2}-\varepsilon(y_3+w_3)(\kappa_{21}+k_{21})+\varepsilon w_1(\kappa_{23}+k_{23})\right]\boldsymbol{B}_2\\&+\varepsilon\left[\frac{\partial w_3}{\partial x_2}-w_1\kappa_{22}+w_2(\kappa_{21}+k_{21})\right]\boldsymbol{B}_3\end{aligned} \tag{59}$$

$$\boldsymbol{G}_3=\frac{\partial w_1}{\partial y_3}\boldsymbol{B}_1+\frac{\partial w_2}{\partial y_3}\boldsymbol{B}_2+\left(1+\frac{\partial w_3}{\partial y_3}\right)\boldsymbol{B}_3 \tag{60}$$

For 3D structures, we have

$$\boldsymbol{G}_k=\left(\delta_{ki}+\epsilon_{ki}+\varepsilon\frac{\partial w_i}{\partial x_k}\right)\boldsymbol{B}_i \tag{61}$$

Note for 3D structures, we are focusing on a Cauchy continuum, thus the initial curvatures vanish and curvature strain tensors are higher order terms and thus neglected.

Using the expressions for $\boldsymbol{g}^a$ and $\boldsymbol{G}_a$, and dropping nonlinear terms due to the product of the curvature strains and the fluctuating functions, the 3D strain field defined in Eq. (23) can be written in the following matrix form

$$\Gamma=\Gamma_h w+\Gamma_\epsilon\bar{\epsilon}+\varepsilon\Gamma_l w+\varepsilon\Gamma_R w \tag{62}$$

where $\Gamma=\lfloor\Gamma_{11}\ \ \Gamma_{22}\ \ \Gamma_{33}\ \ 2\Gamma_{23}\ \ 2\Gamma_{13}\ \ 2\Gamma_{12}\rfloor^T$, $w=\lfloor w_1\ \ w_2\ \ w_3\rfloor^T$, $\bar{\epsilon}$ is a column matrix containing the generalized strain measures for the macroscopic structural model. For example, if the macroscopic structural model is a beam model we have $\bar{\epsilon}=\lfloor\epsilon_{11}\ \ \kappa_{11}\ \ \kappa_{12}\ \ \kappa_{13}\rfloor^T$ with ϵ_{11} denoting the extensional strain and κ_{11} the twist, κ_{12} and κ_{13} the bending curvatures. If the macroscopic structural model is a plate/shell model we have $\bar{\epsilon}=\lfloor\epsilon_{11}\ \ 2\epsilon_{12}\ \ \epsilon_{22}\ \ \kappa_{11}\ \ \kappa_{12}+\kappa_{21}\ \ \kappa_{22}\rfloor^T$ with $\epsilon_{\alpha\beta}$ denoting the in-plane strains and $\kappa_{\alpha\beta}$ denoting the curvature strains. To be consistent with our previous work on plate/shell modeling,[12] the curvature strains

are defined according to Eq. (29). If the macroscopic structural model is a 3D continuum model we have $\bar{\epsilon} = \lfloor \epsilon_{11} \;\; \epsilon_{22} \;\; \epsilon_{33} \;\; 2\epsilon_{23} \;\; 2\epsilon_{13} \;\; 2\epsilon_{12} \rfloor^T$ with ϵ_{ij} denoting the Biot strain measures in a Cauchy continuum.

Γ_h is an operator matrix which depends on the dimensionality of the SG. If the SG is 3D, we have

$$\Gamma_h = \begin{bmatrix} \frac{1}{\sqrt{g_1}}\frac{\partial}{\partial y_1} & 0 & 0 \\ 0 & \frac{1}{\sqrt{g_2}}\frac{\partial}{\partial y_2} & 0 \\ 0 & 0 & \frac{\partial}{\partial y_3} \\ 0 & \frac{\partial}{\partial y_3} & \frac{1}{\sqrt{g_2}}\frac{\partial}{\partial y_2} \\ \frac{\partial}{\partial y_3} & 0 & \frac{1}{\sqrt{g_1}}\frac{\partial}{\partial y_1} \\ \frac{1}{\sqrt{g_2}}\frac{\partial}{\partial y_2} & \frac{1}{\sqrt{g_1}}\frac{\partial}{\partial y_1} & 0 \end{bmatrix} \tag{63}$$

where $\sqrt{g_1} = \sqrt{g_2} = 1$ for plate-like structures or 3D structures, $\sqrt{g_1} = 1 - \varepsilon y_2 k_{13} + \varepsilon y_3 k_{12}$ and $\sqrt{g_2} = 1$ for beam-like structures, $\sqrt{g_1} = 1 + \varepsilon y_3 k_{12}$ and $\sqrt{g_2} = 1 - \varepsilon y_3 k_{21}$ for shell-like structures.

If the SG is a lower-dimensional one, one just needs to vanish the corresponding term corresponding to the micro coordinates which are not used in describing the SG. For example, if the SG is 2D, we have

$$\Gamma_h = \begin{bmatrix} 0 & 0 & 0 \\ 0 & \frac{1}{\sqrt{g_2}}\frac{\partial}{\partial y_2} & 0 \\ 0 & 0 & \frac{\partial}{\partial y_3} \\ 0 & \frac{\partial}{\partial y_3} & \frac{1}{\sqrt{g_2}}\frac{\partial}{\partial y_2} \\ \frac{\partial}{\partial y_3} & 0 & 0 \\ \frac{1}{\sqrt{g_2}}\frac{\partial}{\partial y_2} & 0 & 0 \end{bmatrix} \tag{64}$$

If the SG is 1D, we have

$$\Gamma_h = \begin{bmatrix} 0 & 0 & 0 \\ 0 & 0 & 0 \\ 0 & 0 & \frac{\partial}{\partial y_3} \\ 0 & \frac{\partial}{\partial y_3} & 0 \\ \frac{\partial}{\partial y_3} & 0 & 0 \\ 0 & 0 & 0 \end{bmatrix} \tag{65}$$

Γ_ϵ is an operator matrix the form of which depends on the macroscopic structural model. If the macroscopic structural model is the 3D Cauchy continuum model, Γ_ϵ is the 6×6 identity matrix.

If the macroscopic structural model is a beam model, we have

$$\Gamma_\epsilon = \frac{1}{\sqrt{g_1}} \begin{bmatrix} 1 & 0 & \varepsilon y_3 & -\varepsilon y_2 \\ 0 & 0 & 0 & 0 \\ 0 & 0 & 0 & 0 \\ 0 & 0 & 0 & 0 \\ 0 & \varepsilon y_2 & 0 & 0 \\ 0 & -\varepsilon y_3 & 0 & 0 \end{bmatrix} \tag{66}$$

If the macroscopic structural model is a plate/shell model, we have

$$\Gamma_\epsilon = \begin{bmatrix} \frac{1}{\sqrt{g_1}} & 0 & 0 & \frac{\varepsilon y_3}{\sqrt{g_1}} & 0 & 0 \\ 0 & 0 & \frac{1}{\sqrt{g_2}} & 0 & 0 & \frac{\varepsilon y_3}{\sqrt{g_2}} \\ 0 & 0 & 0 & 0 & 0 & 0 \\ 0 & 0 & 0 & 0 & 0 & 0 \\ 0 & 0 & 0 & 0 & 0 & 0 \\ 0 & \frac{1}{2}\left(\frac{1}{\sqrt{g_1}} + \frac{1}{\sqrt{g_2}}\right) & 0 & 0 & \frac{1}{2}\left(\frac{\varepsilon y_3}{\sqrt{g_1}} + \frac{\varepsilon y_3}{\sqrt{g_2}}\right) & 0 \end{bmatrix} \tag{67}$$

Note the above expression is obtained with the understanding that the difference between κ_{12} and κ_{21} is of higher order and negligible if we are not seeking a higher-order approximation of the initial curvatures.

Γ_l is an operator matrix the form of which depends on the macroscopic structural model. If the macroscopic structural model is 3D, Γ_l has the same form as Γ_h in Eq. (68) with $\frac{\partial}{\partial y_k}$ replaced with $\frac{\partial}{\partial x_k}$, that is

$$\Gamma_l = \begin{bmatrix} \frac{1}{\sqrt{g_1}}\frac{\partial}{\partial x_1} & 0 & 0 \\ 0 & \frac{1}{\sqrt{g_2}}\frac{\partial}{\partial x_2} & 0 \\ 0 & 0 & \frac{\partial}{\partial x_3} \\ 0 & \frac{\partial}{\partial x_3} & \frac{1}{\sqrt{g_2}}\frac{\partial}{\partial x_2} \\ \frac{\partial}{\partial x_3} & 0 & \frac{1}{\sqrt{g_1}}\frac{\partial}{\partial x_1} \\ \frac{1}{\sqrt{g_2}}\frac{\partial}{\partial x_2} & \frac{1}{\sqrt{g_1}}\frac{\partial}{\partial x_1} & 0 \end{bmatrix} \tag{68}$$

Of course for 3D structures, we have $\sqrt{g_1} = \sqrt{g_2} = 1$.

If the macroscopic structural model is a lower-dimensional one, one just needs to vanish the corresponding term corresponding to the macro coordinates which are not used in describing the macroscopic structural model. For example, if the macroscopic structural model is a 2D plate/shell model, we have

$$\Gamma_l = \begin{bmatrix} \frac{1}{\sqrt{g_1}}\frac{\partial}{\partial x_1} & 0 & 0 \\ 0 & \frac{1}{\sqrt{g_2}}\frac{\partial}{\partial x_2} & 0 \\ 0 & 0 & 0 \\ 0 & 0 & \frac{1}{\sqrt{g_2}}\frac{\partial}{\partial x_2} \\ 0 & 0 & \frac{1}{\sqrt{g_1}}\frac{\partial}{\partial x_1} \\ \frac{1}{\sqrt{g_2}}\frac{\partial}{\partial x_2} & \frac{1}{\sqrt{g_1}}\frac{\partial}{\partial x_1} & 0 \end{bmatrix} \tag{69}$$

If the macroscopic structural model is the 1D beam model, we have

$$\Gamma_l = \begin{bmatrix} \frac{1}{\sqrt{g_1}}\frac{\partial}{\partial x_1} & 0 & 0 \\ 0 & 0 & 0 \\ 0 & 0 & 0 \\ 0 & 0 & 0 \\ 0 & 0 & \frac{1}{\sqrt{g_1}}\frac{\partial}{\partial x_1} \\ 0 & \frac{1}{\sqrt{g_1}}\frac{\partial}{\partial x_1} & 0 \end{bmatrix} \tag{70}$$

Γ_R is an operator matrix existing only for those heterogeneous structures featuring initial curvatures. For prismatic beams, plates or 3D structures, Γ_R vanishes. For those structures having initial curvatures such as initially twisted/curved beams or shells, the form of Γ_R depends on the macroscopic structural model. If the macroscopic structural model is a 1D beam model,

$$\Gamma_R = \frac{1}{\sqrt{g_1}} \begin{bmatrix} k_{11}\left(y_3\frac{\partial}{\partial y_2} - y_2\frac{\partial}{\partial y_3}\right) & -k_{13} & k_{12} \\ 0 & 0 & 0 \\ 0 & 0 & 0 \\ 0 & 0 & 0 \\ -k_{12} & k_{11} & k_{11}\left(y_3\frac{\partial}{\partial y_2} - y_2\frac{\partial}{\partial y_3}\right) \\ k_{13} & k_{11}\left(y_3\frac{\partial}{\partial y_2} - y_2\frac{\partial}{\partial y_3}\right) & -k_{11} \end{bmatrix} \tag{71}$$

If the macroscopic structural model is a 2D shell model,

$$\Gamma_R = \begin{bmatrix} 0 & \frac{-k_{13}}{\sqrt{g_1}} & \frac{k_{12}}{\sqrt{g_1}} \\ \frac{k_{23}}{\sqrt{g_2}} & 0 & \frac{-k_{21}}{\sqrt{g_2}} \\ 0 & 0 & 0 \\ 0 & \frac{k_{21}}{\sqrt{g_2}} & 0 \\ \frac{-k_{12}}{\sqrt{g_1}} & 0 & 0 \\ \frac{k_{13}}{\sqrt{g_1}} & -\frac{k_{23}}{\sqrt{g_2}} & 0 \end{bmatrix} \tag{72}$$

B. Variational Statement for SG

Although the SG concept can be used to analyze various type of behavior of heterogeneous structures, we are instead focusing on the elastostatic behavior of the original heterogeneous structure for illustrative purpose in this paper, which is governed by the following variational statement

$$\delta U = \overline{\delta W} \tag{73}$$

δ is the usual Lagrangean variation, U is the strain energy and $\overline{\delta W}$ is the virtual work of applied loads. The bars over variations are used to indicate that the virtual quantity needs not be the variation of a functional. For a linear elastic material characterized using a 6×6 stiffness matrix D, the strain energy can be written as

$$U = \frac{1}{2} \int \frac{1}{\omega} \left\langle \Gamma^T D \Gamma \right\rangle \mathrm{d}\Omega \tag{74}$$

where Ω is the volume of the domain spanned by x_k remaining in the macroscopic structural model. The notation $\langle \bullet \rangle = \int \bullet \sqrt{g} \mathrm{d}\omega$ is used to denote a weighted integration over the domain of the SG, ω, where g is the determinant of the metric tensor of the undeformed configuration spanned by x_1, x_2, x_3, as defined previously. ω also denotes the volume of the domain spanned by y_k corresponding to the coordinates x_k remaining in the macroscopic structural model. If none of y_k are needed in the SG, then $\omega = 1$. For example, if a heterogeneous beam-like structure features a 3D SG, ω is the length of the SG in the y_1 direction, corresponding to x_1 remaining in the macroscopic beam model. If the heterogeneous beam-like structure features a 2D SG (uniform cross-section), y_1 is not needed for the SG and $\omega = 1$. If a heterogeneous plate/shell-like structure features a 3D SG, ω is the area of the SG in the $y_1 - y_2$ plane, corresponding to x_1 and x_2 remaining in the macroscopic plate/shell model. If the heterogeneous plate/shell-like structure features a 2D SG, y_2 and y_3 are needed for the SG and ω is equal to the length of SG in y_2 direction. If the heterogeneous plate/shell-like structure features a 1D SG, only y_3 is needed for the SG and $\omega = 1$. If a 3D heterogeneous structure features a 3D SG, ω is the physical volume of SG spanned by y_1, y_2, and y_3. If a 3D heterogeneous structure features a 2D SG, ω is the area of SG spanned by y_2 and y_3. If a 3D heterogeneous structure features a 1D SG, ω is the length of SG in y_3 direction.

For a Cauchy continuum, there may exist applied loads from tractions and body forces. The virtual work done by these applied loads can be calculated as

$$\overline{\delta W} = \int \frac{1}{\omega} \left(\langle \mathbf{p} \cdot \delta \mathbf{R} \rangle + \int_s \mathbf{Q} \cdot \delta \mathbf{R} \sqrt{c} \mathrm{d}s \right) \mathrm{d}\Omega \tag{75}$$

where s denotes the boundary surfaces of the SG where the traction force per unit area $\mathbf{Q} = Q_i \mathbf{B}_i$ is applied and $\mathbf{p} = p_i \mathbf{B}_i$ denotes the applied body force per unit undeformed volume. $\sqrt{c}$ is equal to 1 except for some degenerated cases where s is only a boundary curve of the SG and one of coordinates x_k is required to form the physical surfaces on which the load is applied. In this case, the differential area of the physical surface is equal to $\sqrt{c}\mathrm{d}s\mathrm{d}x_k$ with $\mathrm{d}s$ as the differential arc length along the boundary curve of SG. For example for beam-like structures featuring a 2D SG, the SG boundary is the curve encircling the cross-section, and $\sqrt{c} = \sqrt{g + \left(y_2 \frac{\mathrm{d}y_2}{\mathrm{d}s} + y_3 \frac{\mathrm{d}y_3}{\mathrm{d}s} \right)^2 k_{11}^2}$. $\delta \mathbf{R}$ is the Lagrangian variation of the displacement field in Eq. (7), such that

$$\delta \mathbf{R} = \overline{\delta q}_i \mathbf{B}_i + \varepsilon y_\alpha \delta \mathbf{B}_\alpha + \varepsilon \delta w_i \mathbf{B}_i + \varepsilon w_i \delta \mathbf{B}_i \tag{76}$$

We may safely ignore products of the fluctuating function and virtual rotation in $\delta\mathbf{R}$, because the fluctuating functions are small. The last term of the above equation is then dropped so that

$$\delta\mathbf{R} = \overline{\delta q}_i\mathbf{B}_i + \varepsilon y_\alpha\delta\mathbf{B}_\alpha + \varepsilon\delta w_i\mathbf{B}_i \tag{77}$$

The virtual displacements and rotations of the macroscopic structural model are defined as

$$\overline{\delta q}_i = \delta\mathbf{R}_o\cdot\mathbf{B}_i \qquad \delta\mathbf{B}_\alpha = \overline{\delta\psi}_j\mathbf{B}_j\times\mathbf{B}_\alpha \tag{78}$$

where $\overline{\delta q}_i$ and $\overline{\delta\psi}_i$ contain the components of the virtual displacement and rotation in the $\mathbf{B}_i$ system, respectively. They are functions of x_k only. Note $\overline{\delta\psi}_j$ are restrained to be derivable from $\overline{\delta q}_i$ and are higher order terms neglected in a 3D structure described using the Cauchy continuum.

Then we can rewrite Eq. (77) as

$$\delta\mathbf{R} = \left(\overline{\delta q}_i + \varepsilon e_{j\alpha i}y_\alpha\overline{\delta\psi}_j + \varepsilon\delta w_i\right)\mathbf{B}_i \tag{79}$$

Finally, we express the virtual work due to applied loads as

$$\overline{\delta W} = \overline{\delta W}_H + \varepsilon\,\overline{\delta W}^* \tag{80}$$

where $\overline{\delta W}_H$ is the virtual work not related with the fluctuating functions w_i and $\overline{\delta W}^*$ is the virtual work related with the fluctuating functions. Specifically, they are

$$\overline{\delta W}_H = \int\left(f_i\overline{\delta q}_i + m_i\overline{\delta\psi}_i\right)\mathrm{d}\Omega \qquad \overline{\delta W}^* = \int\frac{1}{\omega}\left(\langle p_i\delta w_i\rangle + \oint Q_i\delta w_i\sqrt{c}\,\mathrm{d}s\right)\mathrm{d}\Omega \tag{81}$$

with the generalized forces f_i and moments m_i defined as

$$f_i = \frac{1}{\omega}\left(\langle p_i\rangle + \int Q_i\sqrt{c}\,\mathrm{d}s\right) \qquad m_i = \frac{e_{i\alpha j}}{\omega}\left(\langle\varepsilon y_\alpha p_j\rangle + \int\varepsilon y_\alpha Q_j\sqrt{c}\,\mathrm{d}s\right) \tag{82}$$

If we assume that p_i and Q_i are independent of the fluctuating functions, then we can rewrite $\overline{\delta W}^*$ as

$$\overline{\delta W}^* = \delta\int\frac{1}{\omega}\left(\langle p_iw_i\rangle + \int Q_iw_i\sqrt{c}\,\mathrm{d}s\right)\mathrm{d}\Omega \tag{83}$$

In view of the strain energy in Eq. (74) and virtual work in Eq. (80) along with Eq. (81), the variational statement in Eq. (73) can be rewritten as

$$\int\frac{1}{\omega}\delta\left[\frac{1}{2}\left\langle\Gamma^TD\Gamma\right\rangle - \varepsilon\left(\langle p_iw_i\rangle - \int Q_iw_i\sqrt{c}\,\mathrm{d}s\right)\right] - \left(f_i\overline{\delta q}_i + m_i\overline{\delta\psi}_i\right)\mathrm{d}\Omega = 0 \tag{84}$$

If we attempt to solve this variational statement directly, we will meet the same difficulty as solving the original problem of heterogeneous structures. The main complexity comes from the fluctuating functions w_i which are unknown functions of both micro and macro coordinates. The common practice in the literature is to assume the fluctuating functions, a priori, in terms of some unknown functions (displacements, rotations, and/or strains) of x_k and some known functions of y_k, to straightforwardly reduce the original continuum model into a macroscopic structural model. However, for arbitrary heterogeneous structures made with general composites, the imposition of such ad hoc assumptions may introduce significant errors. Fortunately, variational asymptotic method (VAM)[17] provides a useful technique to obtain the fluctuating functions through an asymptotical analysis of the variational statement in Eq. (84) in terms of the small parameter ε inherent in the heterogeneous structure to construct asymptotically correct macroscopic structural models. As the last two terms in Eq. (84) are not functions of w_i, we can conclude that the fluctuating function is governed by the following variational statement instead:

$$\delta\left[\frac{1}{2}\left\langle\Gamma^TD\Gamma\right\rangle - \varepsilon\left(\langle p_iw_i\rangle - \int Q_iw_i\sqrt{c}\,\mathrm{d}s\right)\right] = 0 \tag{85}$$

which can be considered as a variational statement for the SG as it is posed over the SG domain only.

According to VAM, we can neglect the terms in the order of ε to construct the first approximation of the variational statement in Eq. (85) as

$$\delta\frac{1}{2}\left\langle(\Gamma_h w+\Gamma_\epsilon\bar{\epsilon})^T D(\Gamma_h w+\Gamma_\epsilon\bar{\epsilon})\right\rangle=0 \tag{86}$$

For very simple cases, this variational statement can be solved analytically, while for general cases we need to turn to numerical techniques such as the finite element method for solution. To this end, we need to express w using shape functions defined over SG as

$$w(x_k,y_j)=S(y_j)V(x_k) \tag{87}$$

where S represents the shape functions and V a column matrix of the nodal values of the fluctuating functions.

Substituting Eq. (87) into Eq. (86), we obtain the the following discretized version of the strain energy functional:

$$U=\frac{1}{2}\left(V^T EV+2V^T D_{h\epsilon}\bar{\epsilon}+\bar{\epsilon}^T D_{\epsilon\epsilon}\bar{\epsilon}\right) \tag{88}$$

where

$$E=\left\langle(\Gamma_h S)^T D(\Gamma_h S)\right\rangle\quad D_{h\epsilon}=\left\langle(\Gamma_h S)^T D\Gamma_\epsilon\right\rangle\quad D_{\epsilon\epsilon}=\left\langle\Gamma_\epsilon^T D\Gamma_\epsilon\right\rangle \tag{89}$$

Minimizing U in Eq. (88) subject to the constraints, gives us the following linear system

$$EV=-D_{h\epsilon}\bar{\epsilon} \tag{90}$$

It is clear that V will linearly depend on $\bar{\epsilon}$, and the solution can be symbolically written as

$$V=V_0\bar{\epsilon} \tag{91}$$

Substituting Eq. (91) back into Eq. (88), we can calculate the strain energy storing in the SG as the first approximation as

$$U=\frac{1}{2}\bar{\epsilon}^T\left(V_0^T D_{h\epsilon}+D_{\epsilon\epsilon}\right)\bar{\epsilon}\equiv\frac{\omega}{2}\bar{\epsilon}^T\bar{D}\bar{\epsilon} \tag{92}$$

where $\bar{D}$ is the effective stiffness to be used in the macroscopic structural model.

Substituting the solved strain energy stored in the SG into Eq. (84), we can rewrite the variational statement governing the original heterogeneous structures as

$$\int\left[\delta\left(\frac{1}{2}\bar{\epsilon}^T\bar{D}\bar{\epsilon}\right)-f_i\overline{\delta q}_i-m_i\overline{\delta\psi}_i\right]\mathrm{d}\Omega=0 \tag{93}$$

This variational statement governs the macroscopic structural model as it involves only fields which are unknown functions of macro coordinates x_k. The first term is the variation of the strain energy of the macroscopic structural model and the last terms are the virtual work done by generalized forces and moments. This variational statement governs the C^1 structural elements and 3D solid elements implemented in most commercial FEA software packages.

We are not only interested in obtaining the effective stiffness and macroscopic structural behavior. We are also interested in obtaining the local fields within the original heterogeneous structure. First knowing $\bar{\epsilon}$, we can compute the fluctuating function as

$$w=SV_0\bar{\epsilon} \tag{94}$$

The local displacement field can be obtained as

$$u_i=\bar{u}_i+\varepsilon y_\alpha(C_{\alpha i}-\delta_{\alpha i})+\varepsilon w_j C_{ji} \tag{95}$$

where u_i is the local displacement, $\bar{u}_i$ is the macroscopic displacement.

The local strain field can be obtained as

$$\Gamma=\left(\Gamma_h SV_0+\Gamma_\epsilon\right)\bar{\epsilon}. \tag{96}$$

The local stress field can be obtained directly using the Hooke's law as

$$\sigma=D\Gamma. \tag{97}$$

IV. Numerical Examples

The Mechanics of Structure Genome developed in this paper is implemented into a computer code called SwiftComp$^{\text{TM}}$ using the modern Fortran language. Although still in its early development stage, SwiftComp$^{\text{TM}}$ has demonstrated a great potential for multiscale constitutive modeling of composites as it represents a unique unified approach for modeling composites structures and materials. A few examples are used here to demonstrate the application and validity of the Mechanics of Structure Genome and the companion code SwiftComp$^{\text{TM}}$. As it can be theoretically shown that one can specialize the Mechanics of Structure Genome to reproduce the theories the author and his co-workers have developed over the years for composite beams (Variational Asymptotic Beam Sectional analysis (VABS)), composite plates/shells (Variational Asymptotic Plate And Shell analysis (VAPAS)), and micromechanics (Variational Asymptotic Method for Unit Cell Homogenization (VAMUCH)). We have verified that SwiftComp$^{\text{TM}}$ can reproduce all the results of VAMUCH, and the classical models of VABS and VAPAS. Here, we just study a few examples which have been studied before in our previous publication to demonstrate the application of SwiftComp$^{\text{TM}}$.

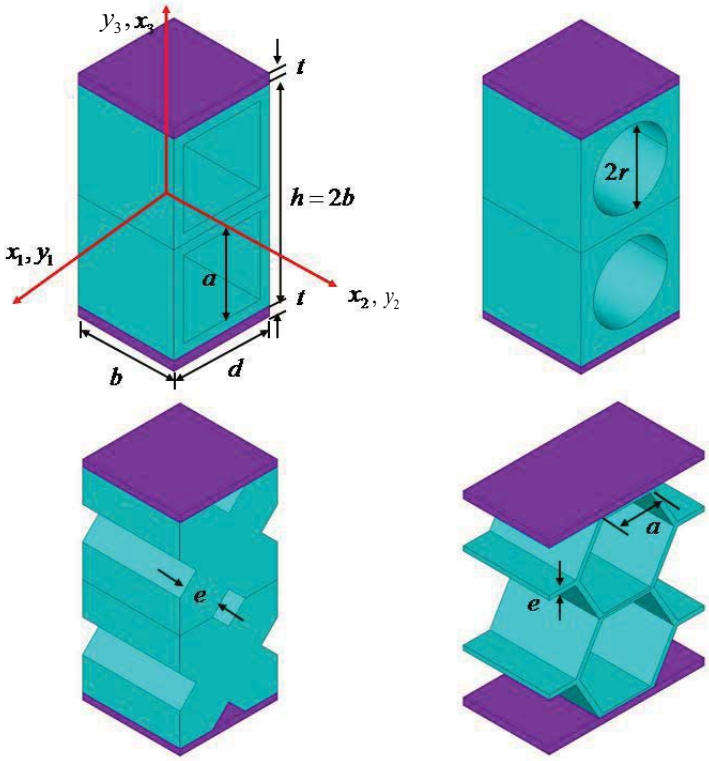

Figure 6. Structure genome for sandwich beam with various cross-sections

A. Sandwich Beam with Periodically Variable Cross-Section

The first example is to analyze a sandwich beam with periodically variable cross-section studied in Ref. [18]. The geometric parameters for each configuration are given below:

- For the sandwich beam with square holes, the geometric variables are given by $b = d = 1.5$ m, $t = 0.1$ m, $a = 1$ m (Figure 6 : top-left)
- For the sandwich beam with circular holes, the geometric variables are given by $b = d = 1.5$ m, $t = 0.1$ m, $r = 0.5614$ m (Figure 6 : top-right)
- For the sandwich beam with cross holes, the geometric variables are given by $b = d = 1.5$ m, $t = 0.1$ m, $e = 0.7071$ m (Figure 6 : bottom-left)

- For the sandwich beam with hexagonal holes, the geometric variables are given by $b = 1.23745$ m, $d = 2b$, $t = 0.1$ m, $a = 0.7887$ m, $e = 0.6431$ m (Figure 6 : bottom-right)

Note although all the SG in Figure 6 are uniform along y_2, the SG must be 3D as they are used to form a beam structure and y_2 is one of the cross-section domain which is finite, see Figure 7. All sandwich beams in the above cases have the same core material properties (material indicated by blue color in the figure) of $E_c = 3.5$ GPa, $\nu_c = 0.34$ and face sheet material properties (indicated by purple color in the figure) of $E_f = 70$ GPa, $\nu_c = 0.34$. Note although these beams are studied in [19], only bending stiffness is given. In fact, the effective stiffness for the classical beam model in general should be represented by a fully populated 4×4 matrix. The effective bending stiffnesses predicted by the analytical formulas in [19] and SwiftComp$^{\text{TM}}$ are listed in Table 1.

Table 1. Effective beam bending stiffness of sandwich beams predicted by different methods ($\times 10^{10}$ N.m^2)

	Ref. [19]	SwiftComp$^{\text{TM}}$
Rectangle Holes	5.669	5.576
Circular Holes	5.176	5.537
Cross Holes	5.486	5.805
Hexagon Holes	2.875	2.888

As can be observed, SwiftComp$^{\text{TM}}$ predictions are slightly different from those in [19]. However, the present approach is more versatile than that in [19] because [19] only provides analytic formulas for bending stiffness of beams made of materials characterized only by one material constant, the Young's modulus, while SwiftComp$^{\text{TM}}$ can estimate all the engineering beam constants represented by a 4×4 stiffness matrix, possibly fully populated, for the most general anisotropic materials by factorizing the coefficient material in the linear system, Eq. (90), only once.

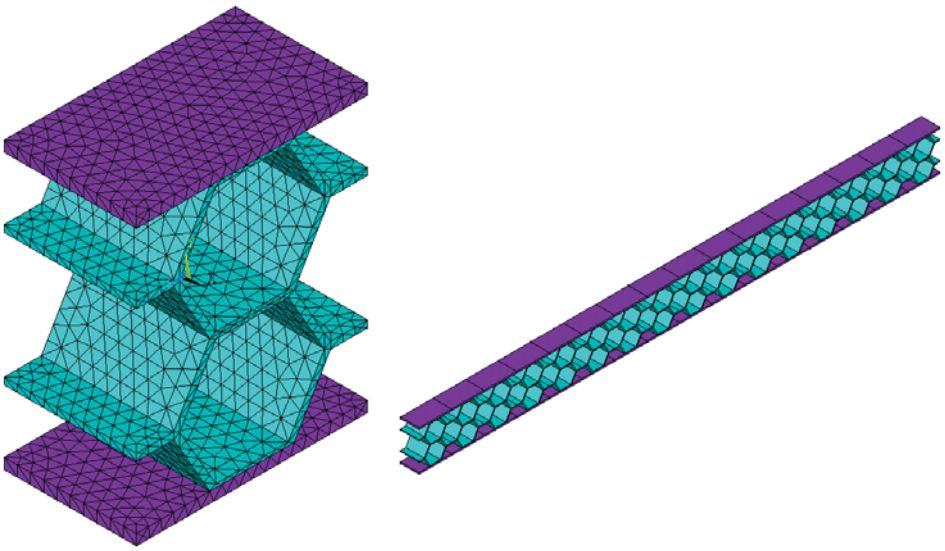

Figure 7. A sandwich beam with hexagonal holes

B. Sandwich Panel with a Corrugated Core

The second example is to model a corrugated-core sandwich panel, a concept used for Integrated Thermal Protection System (ITPS) studied in [20, 21]. The ITPS panel along with the details of the SG is sketched in Figure 8. The geometry parameters are $t_T = 1.2$ mm, $t_B = 7.49$ mm, $t_W = 1.63$ mm, $p = 25$ mm, $d = 70$ mm, and $\theta = 85°$. Both materials are isotropic with $E_1 = 109.36$ GPa, $\nu_1 = 0.3$, $E_2 = 209.482$ GPa, $\nu_2 = 0.063$. Although 3D unit cells are needed for the study in [20], only a 2D SG is necessary for

SwiftComp^{TM} as it is uniform along one of the in-plane directions. The effective stiffness for the classical plate model can be represented using A, B and D matrices known in classical lamination theory. Results obtained in Ref. [20] are compared with SwiftComp^{TM}in Tables 2, 3 and 4. SwiftComp^{TM} predictions agree very well with those in Ref. [20] with the biggest difference (around 1%) appearing for the extension-bending coupling stiffness (B_{11}). However, the present approach is much more efficient because using the approach in [20] one needs to carry out six analyses of a 3D unit cell under six different sets of boundary conditions and load conditions and postprocess the 3D stresses to compute the plate stress resultants, while using the present approach, one only needs to carry out one analysis of a 2D SG without any postprocessing.

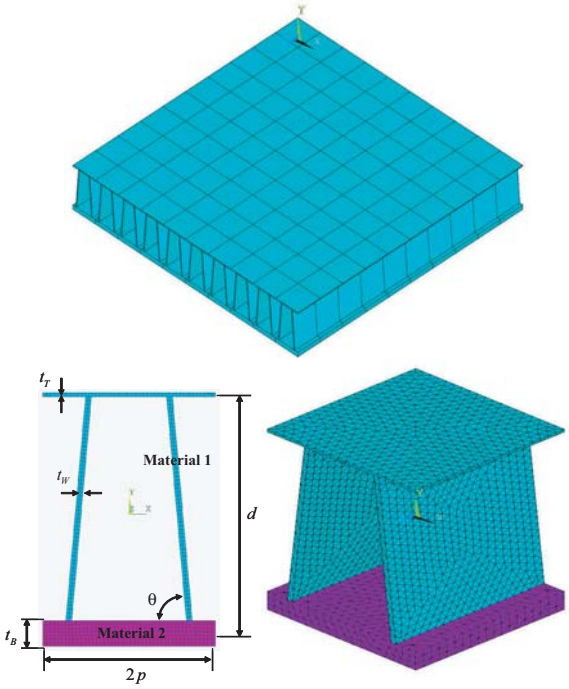

Figure 8. Sketch of the ITPS panel and its SG

Table 2. Effective extension stiffness of ITPS ($\times 10^9$ N/m)

	A_{11}	A_{13}	A_{22}	A_{33}
Ref. [20]	2.83	0.18	1.07	2.33
SwiftComp^{TM}	2.80	0.18	1.08	2.33

Table 3. Effective bending stiffness of ITPS ($\times 10^6$ N.m)

	D_{11}	D_{13}	D_{22}	D_{33}
Ref. [20]	3.06	0.22	1.32	2.85
SwiftComp^{TM}	3.03	0.22	1.32	2.87

V. Conclusion

This paper introduces the concept of structure genome (SG) to bridge materials genome and structural analysis. SG facilitates a mathematical decoupling of the original complex analysis of composite structures

Table 4. Effective coupling stiffness of ITPS ($\times 10^6$ N)

	B_{11}	B_{13}	B_{22}	B_{33}
Ref. [20]	-71.45	-3.36	-34.05	-71.45
SwiftComp$^{\text{TM}}$	-70.67	-3.31	-34.06	-71.42

into a constitutive modeling over SG and a macroscopic structural analysis. The constitutive modeling will not only perform homogenization to obtain the constitutive relations for the macroscopic structural analysis but also perform dehomogenization to obtain the local fields within the microstructure. This paper not only formulated the mechanics of structure genome but also implemented the theory in a computer code called SwiftComp$^{\text{TM}}$. Mechanics of SG presented in this paper enables a multiscale constitutive modeling approach with the following unique features:

- Use SG to fill the gap between materials genome and structural analysis. Intellectually, SG enables us to view structural mechanics as an application of micromechanics. Technically, SG empowers us to systematically model complex buildup structures with heterogeneities of a length scale comparable to the smallest structural dimension.
- Use VAM to avoid apriori assumptions commonly invoked in other approaches, providing the most mathematical rigor and the best engineering generality.
- Decouple the original problem into two sets of analyses: a constitutive modeling and a structural analysis. This allows the structural analysis to be formulated exactly as a general (1D, 2D, or 3D) continuum, the analysis of which is readily available in commercial FEA software packages and confines all approximations to the constitutive modeling, the accuracy of which is guaranteed to be the best by VAM.

A general-purpose computer code called SwiftComp$^{\text{TM}}$ is developed to implement the Mechanics of Structure Genome along with several examples to demonstrate its application and power.

VI. Acknowledgments

This research is supported, in part, by the Air Force Office of Scientific Research and by the Army Vertical Lift Research Center of Excellence at Georgia Institute of Technology and its affiliate program through subcontract at Purdue University. The technical monitors are Dr. David Stargel and Dr. Mahendra J Bhagwat. The views and conclusions contained herein are those of the authors and should not be interpreted as necessarily representing the official policies or endorsement, either expressed or implied, of the sponsor.

References

[1] "Materials Genome Initiative for Global Competitiveness," Tech. Rep. `http://www.whitehouse.gov/sites/default/files/microsites/ostp/materials_genome_initiative-final.pdf`, Executive Office of the President National Science and Technology Council, Washington, DC, 2011.

[2] "Integrated Computational Materials Engineering: a Transformational Discipline for Improved Competitiveness and National Security," Tech. Rep. `http://www.nap.edu/catalog.php?record_id=12199`, National Research Council, 2008.

[3] Han, S., *Integration of Flexible Multibody Dynamic Analysis with Dimensional Reduction Techniques*, Ph.D. thesis, Shanghai Jiao Tong University, 2014.

[4] Yu, W., Hodges, D. H., and Ho, J. C., "Variational Asymptotic Beam Sectional Analysis - An Updated Version," *International Journal of Engineering Science*, Vol. 59, 2012, pp. 40–64.

[5] Kaddour, A. S. and Hinton, M. J., "Evaluation of Theories for Predicting Failure in Polymer Composite Laminates under 3-D States of Stress: Part A of the Second World-Wide Failure Exercise (WWFE-II)," *Journal of Composite Materials*, Vol. 46, 2012, pp. 19 – 20.

[6] Kaddour, A. S. and Hinton, M. J., "Evaluation of Theories for Predicting Failure in Polymer Composite Laminates under 3-D States of Stress: Part B of the Second World-Wide Failure Exercise (WWFE-II)," *Journal of Composite Materials*, Vol. 47, 2013, pp. 6 – 7.

[7] Yu, W., "Unifying Structural Mechanics with Micromechanics Using the Concept of Representative Structural Element," *Proceedings of the American Society for Composites 27th Technical Conference*, Arlington, Texas, Oct. 1 – 3 2012.

[8]Yu, W., "Representative Structural Element: a New Paradigm for Multiscale Structural Modeling," *Proceedings of the 54th Structures, Structural Dynamics and Materials Conference*, AIAA, Boston, Massachusetts, Apr. 8-11 2013.

[9]Sun, C. T. and Vaidya, R. S., "Prediction of Composite Properties from a Representative Volume Element," *Composites Science and Technology*, Vol. 56, 1996, pp. 171 – 179.

[10]Cosserat, B. and Cosserat, F., *Théorie des Corps Deformables*, Hermann, Paris, 1909.

[11]Danielson, D. and Hodges, D., "Nonlinear Beam Kinematics by Decomposition of the Rotation Tensor," *Journal of Applied Mechanics*, Vol. 54, 1987, pp. 258–262.

[12]Yu, W. and Hodges, D. H., "A Geometrically Nonlinear Shear Deformation Theory for Composite Shells," *Journal of Applied Mechanics*, Vol. 71, No. 1, 2004, pp. 1 – 9.

[13]Pietraszkiewicz, W. and Eremeyev, V. A., "On Natural Strain Measures of the Non-Linear Micropolar Continuum," *International Journal of Solids and Structures*, Vol. 46, 2009, pp. 774–787.

[14]Hodges, D., *Nonlinear Composite Beam Theory*, AIAA, Washington, D.C., 2006.

[15]Yu, W., Hodges, D. H., and Volovoi, V. V., "Asymptotic Generalization of Reissner-Mindlin Theory: Accurate Three-dimensional Recovery for Composite Shells," *Computer Methods in Applied Mechanics and Engineering*, Vol. 191, No. 44, Oct. 2002, pp. 5087 – 5109.

[16]Pietraszkiewicz, W. and Eremeyev, V. A., "On Vectorially Parameterized Natural Strain Measures of the Non-Linear Cosserat Continuum," *International Journal of Solids and Structures*, Vol. 46, 2009, pp. 2477–2480.

[17]Berdichevsky, V., *Variational Principles of Continuum Mechanics*, Vol. 1 and 2, Springer Berlin, 2009.

[18]Lee, C.-Y. and Yu, W., "Variational Asymptotic Modeling of Composite Beams with Spanwise Heterogeneity," *Computers & Structures*, Vol. 89, 2011, pp. 1503–1511.

[19]Dai, G. and Zhang, W., "Size effects of basic cell in static analysis of sandwich beams," *International Journal of Solids and Structures*, Vol. 45, 2008, pp. 2512–2533.

[20]Sharma, A., Sankar, B. V., and Haftka, R. T., "Homogenization of Plates with Microstructure and Application to Corrugated Core Sandwich Panels," *Proceedings of the 51st AIAA/ASME/ASCE /AHS/ASC Structures, Structural Dynamics, and Materials Conference*, AIAA, Orlando, Florida, Apr. 12–15 2010.

[21]Lee, C.-Y. and Yu, W., "Homogenization and Dimensional Reduction of Composite Plates with In-Plane Heterogeneity," *International Journal of Solids and Structures*, Vol. 48, No. 10, 2011, pp. 1474–1484.

A Unified Theory for Constitutive Modeling of Composites

Wenbin Yu[a]
Purdue University, West Lafayette, IN 47907-2045, USA

A unified theory for multiscale constitutive modeling of composites is developed using the concept of structure genome. Generalized from the concept of representative volume element, a structure genome is defined as the smallest mathematical building block of a structure. The mechanics of structure genome governs the necessary information to bridge the microstructure length scale of composites and macroscopic length scale of structural analysis and provides a unified theory to construct constitutive models for structures including three-dimensional structures, beams, plates, and shells over multiple length scales. For illustration, this paper is restricted to construct Euler-Bernoulli beam model, Kirchhoff-Love plate/shell model, and the Cauchy continuum model for structures made of linear elastic materials. Geometrical nonlinearity is systematically captured for beams, plates/shells, and Cauchy continuum using a unified formulation. A general-purpose computer code called SwiftComp (accessible at https://cdmhub.org/resources/scstandard) implements this unified theory and is used in a few example cases to demonstrate its application.

I. Introduction

Structural analyses are routinely carried out using the finite element analysis (FEA) in terms of three-dimensional (3D) solid elements, two-dimensional (2D) plate or shell elements or one-dimensional (1D) beam elements (see Fig. 1). Here, the notation of 1D, 2D, or 3D refers to the number of coordinates needed to describe the analysis domain. It is not related with the dimen-

[a] Associate Professor, School of Aeronautics and Astronautics, Purdue University.

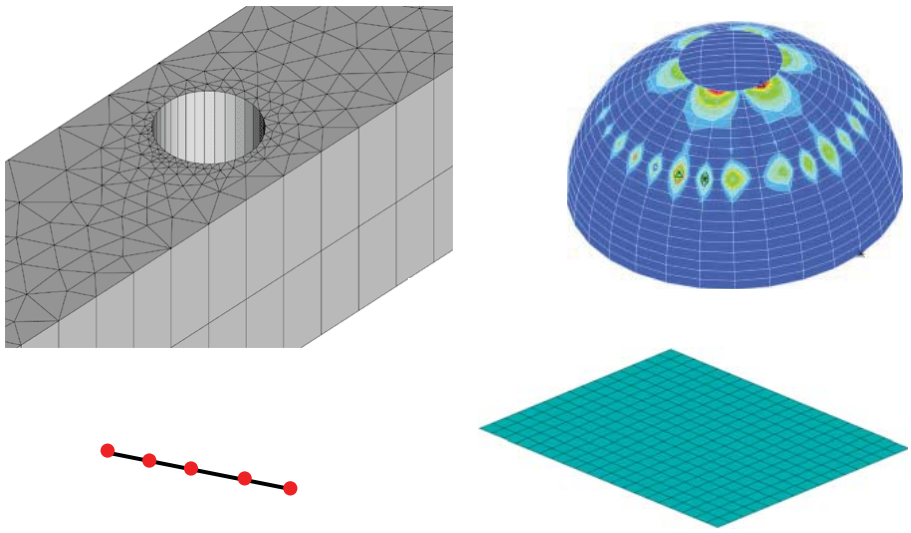

Fig. 1 Typical structural elements: a) 3D solid elements; b) 2D shell elements; c) 1D beam elements; d) 2D plate elements.

sionality of the behavior. For example, a beam element can have three-dimensional behavior as it can deform in three directions. A constitutive relation is needed for the corresponding structural element. For isotropic homogeneous structures, material properties such as Young's modulus and Poisson's ratio are direct inputs for structural analysis using solid elements, and these properties combined with the geometry of the structure can be used for plate/shell/beam elements. However, such straightforwardness does not exist for composite structures featuring anisotropy and/or heterogeneity. Consider a typical composite rotor blade of length 8.6 m, and chord 0.72 m with a main D-spar composed of 60 graphite/epoxy plies each with a ply thickness of 125 μm. To directly use the properties of graphite/epoxy composite plies in the blade analysis, at least one 3D solid element through the ply thickness should be used. Sometimes several layers are commonly lumped together into a single element with "smeared properties", however, it will result in approximate solutions that would negate the supposed accuracy advantage gained by the use of 3D solid elements. Suppose one uses 20-noded brick elements with a 1 to 10 thickness-length ratio, it is estimated that around ten billion degrees of freedom are needed for the blade analysis. Such a huge FEA model is too costly for effective blade design and analysis. A possible alternative is to model rotor blades as beams [1] with models to bridge the material properties of composite plies and the beam properties, and

compute the stress fields within each layer for failure and safety predictions.

Sometimes, it might be desirable to start the modeling process of composite structures from the fiber (usually in the size of a few microns) and matrix. A multiscale modeling approach is needed to link micromechanics [2–5] and structural mechanics [6–8]. Many micromechanics models have been introduced to provide either rigorous bounds, such as the rules of mixtures [9], Hashin-Shtrikman bounds [10], third-order bounds [11], and higher-order bounds [12], or approximate predictions such as Mori-Tanaka method [13], the method of cells [14, 15] and its variants [4, 16–18], mathematical homogenization theories [5, 19–23], finite element approaches using conventional stress analysis of representative volume elements (RVEs) [24, 25], Voronoi cell finite element method [26], and variational asymptotic method for unit cell homogenization [27, 28]. Even more structural models have been developed for composite structures which are usually based on a set of *a priori* assumptions. For composite laminates, the displacement field is usually assumed to be expressed in terms of 2D functions with known distributions through the thickness [6, 29]. For example, the classical laminated plate theory (CLPT) was derived based on the assumption that the transverse normal remains normal to the reference surface and rigid. The first-order shear-deformation theory was derived based on the assumption that the transverse normal remains straight and rigid, but does not necessarily remain normal. Many assumptions have been proposed in the literature including equivalent single-layer assumptions [30, 31], layerwise assumptions [32, 33], zigzag assumptions [34, 35]. Recently, Carrera developed a unified formulation to systematically construct all these models based on *a priori* assumptions [36, 37]. To avoid these assumptions, asymptotic models are developed [38–44] with the field variables expressed using a formal asymptotic series.

Common multiscale modeling approaches are usually a two-step approach (TSA), which carry out a micromechanical analysis followed by a structural analysis. For example, for composite laminates, a micromechanics model is first used to compute the lamina constants in terms of the microstructure, commonly called RVE or unit cell (UC), of the composite ply, then a lamination theory is used to construct a structural model for the macroscopic analysis (see Fig. 2). There are three possible issues with this approach. First, the microstructural scale is implicitly assumed to be much smaller than the structural scale which might cause significant error for structures where

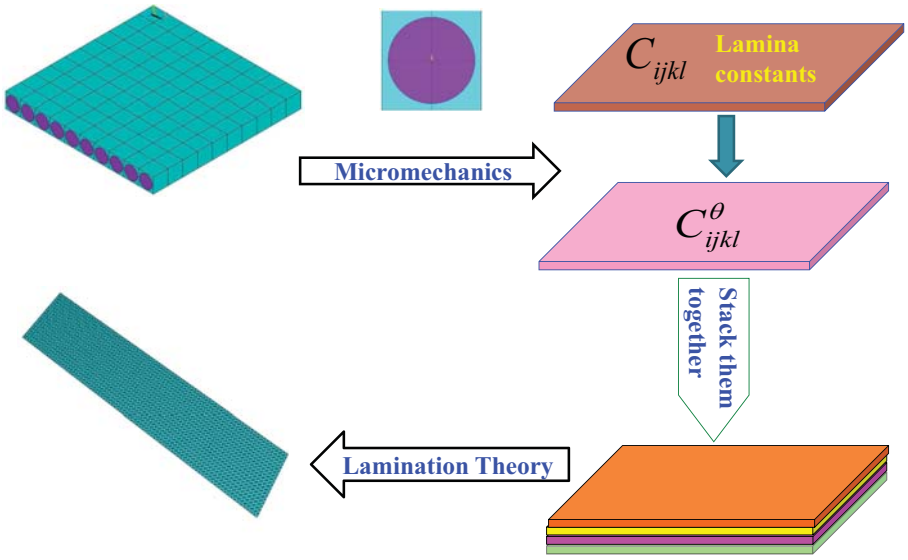

Fig. 2 Traditional multiscale modeling approach illustrated for composite laminates.

one of the dimensions has similar size as the microstructure, such as thin laminates or sandwich structures with a thick core. Second, as shown in Fig. 3, TSA creates artificial discontinuity at the layer interfaces because the original heterogeneous panel (Fig. 3a) is effectively replaced with an imaginary panel made of homogeneous layers (Fig. 3b). The real discontinuities happen at the interfaces between the fiber and matrix if perfect bonding is assumed between layers, which is normally done in lamination theories. Third, composite damage might initiate and propagate in such a way that the separation of micro scale and laminate scale in TSA is not valid any more. These issues have been noticed by Pagano and Rybicki as early as 1974 [45]. The focus of this paper is to potentially resolve these issues by developing a unified theory to link the lowest scale of interest to the structural scale.

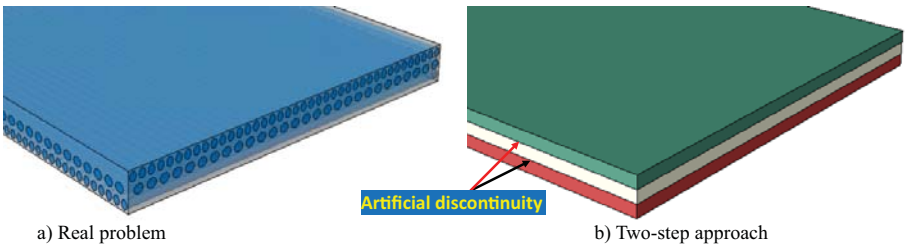

Fig. 3 Artificial discontinuity created by the lamination theory.

II. Structure Genome (SG)

A genome serves as a blueprint for an organism's growth and development. We can extrapolate this word into non-biological contexts to connote a *fundamental building block* of a system. A new concept called Structure Genome (SG) is defined as the *smallest mathematical* building block of the structure to emphasize the fact that it contains all the constitutive information needed for a structure in the same fashion as the genome contains all the genetic information for an organism's growth and development. It is noted that this work uses the continuum hypothesis and scales below the continuum scale such as the atomic scale are not considered here.

A. SG for 3D Structures

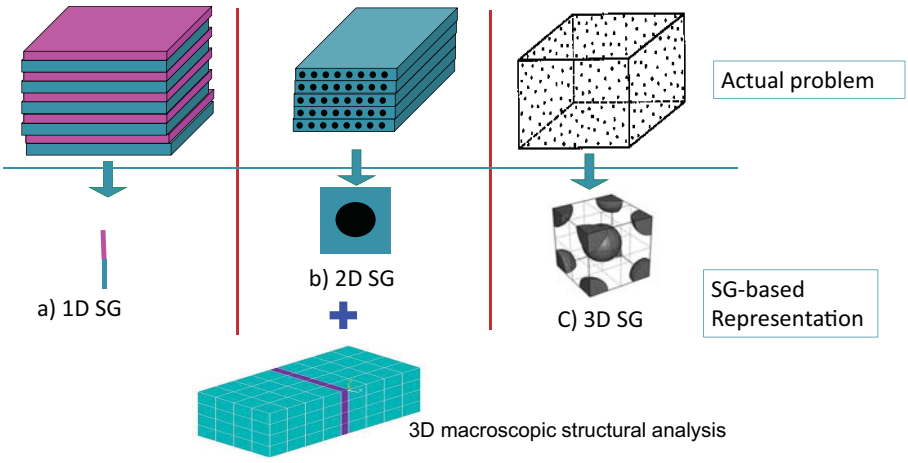

Fig. 4 Analysis of 3D heterogeneous structures approximated by a constitutive modeling over SG and a corresponding 3D macroscopic structural analysis.

As shown in Fig. 4), analyses of 3D heterogeneous structures can be approximated by a 3D macroscopic structural analysis with the material properties provided by a constitutive modeling of a SG. For 3D structures, SG serves a similar role as RVE in micromechanics. However, they are significantly different so that the new term, SG, is used to avoid confusion. For example, for a structure made of composites featuring 1D heterogeneity (e.g. binary composites made of two alternating layers, Fig. 4a), the SG will be a straight line with two segments denoting corresponding phases. One can mathematically repeat this line in-plane to build the two layers of the binary composite, and then repeat the binary composite out of plane to build the entire structure. Another

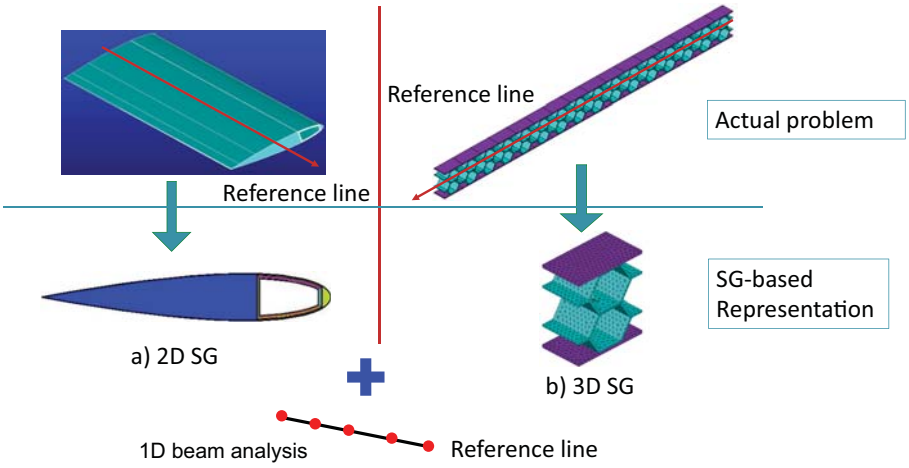

Fig. 5 Analysis of beam-like structures approximated by a constitutive modeling over SG and a corresponding 1D beam analysis.

possible application is to model a laminate as an equivalent homogeneous solid. The transverse normal line is the 1D SG for the laminate. The constitutive modeling over the 1D SG can compute the complete set of 3D properties and local fields. Such applications of SG are not equivalent to RVE. For a structure made of composites featuring 2D heterogeneity (e.g. continuous unidirectional fiber reinforced composites, Fig. 4b), the SG will be 2D. Although 2D RVEs are also used in micromechanics, only in-plane properties and local fields can be obtained from common RVE-based models. If the complete set of properties are needed for 3D structural analysis, a 3D RVE is usually required [5, 24], while a 2D domain is sufficient if it is modeled using SG-based models (Fig. 4b) or some semi-analytical models such as GMC/HFGMC [4]. For a structure made of composites featuring 3D heterogeneity (e.g. particle reinforced composites, Fig. 4c), the SG will be a 3D volume. Although 3D SG for 3D structures represents the most similar case to RVE, boundary conditions in terms of displacements and tractions indispensable in RVE-based models are not needed for SG-based models.

B. SG for Beams/Plates/Shells

SG also allows direct connection of microstructure with the beam/plate/shell analyses. For example, the structural analysis of slender (beam-like) structures can use beam elements (Fig. 5). If the beam has uniform cross-sections which could be made of homogeneous materials or composites

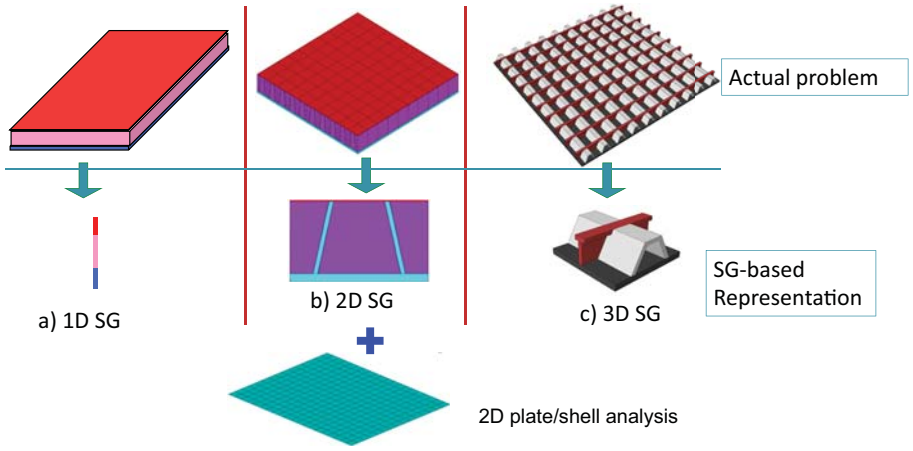

Fig. 6 Analysis of plate-like structures approximated by a constitutive modeling over SG and a corresponding 2D plate analysis.

(Fig. 5a), its SG is the 2D cross-sectional domain because the cross-section can be projected along the beam reference line to form the beam-like structure. This inspires a *new perspective* toward beam modeling [1], a traditional branch of structural mechanics. If the beam reference line is considered as a 1D continuum, every material point of this continuum has a cross-section as its microstructure. In other words, *constitutive modeling for beams can be effectively viewed as an application of micromechanics.* If the beam is also heterogeneous in the spanwise direction (Fig. 5b), a 3D SG is needed to describe the microstructure of the 1D continuum, the behavior of which is governed by the 1D beam analysis. Note that SG is different from the traditional notion of obtaining apparent material properties for a structure. For example, the flexural stiffness of an I-beam could be given by E^*I, such that an I-beam could be represented by a rectangular beam but with an apparent Young's modulus E^* so that $E^*I = E^* \times bd^3/12$ with b as the width and d as the height. Instead, using SG we can obtain the bending stiffness directly for the I-beam without referring to a geometry factor (reinterpreting it as a rectangular beam). No intermediate step such as E^* is needed. The concept of SG provides a unified treatment of structural modeling and micromechanics modeling and enables us to collapse the cross-section or a 3D beam segment into a material point for a beam analysis over the reference line with a possible, fully populated 4×4 stiffness matrix simultaneously accounting for extension, torsion, and bending in two directions.

If the structural analysis uses plate/shell elements, SG can also be chosen properly. For illustra-

tive purpose, typical SGs of plate-like structures are sketched in Fig. 6. If the plate-like structures feature no in-plane heterogeneities (Fig. 6a), the SG is the transverse normal line with each segment denoting the corresponding layer. For a sandwich panel with a core corrugated in one direction (Fig. 6b), the SG is 2D. If the panel is heterogeneous in both in-plane directions (Fig. 6c), such as a stiffened panel with stiffeners running in both directions, the SG is 3D. Despite the different dimensionalities of the SGs, the constitutive modeling should output structural properties for the corresponding structural analysis (such as the A, B, and D matrices for the Kirchhoff-Love plate model) and relations to express the original 3D fields in terms of the global behavior (e.g. moments, curvatures, etc.) obtained from the plate/shell analysis. It is known that theories of plates/shells traditionally belong to structural mechanics, but the constitutive modeling of these structures can be treated as special micromechanics applications using the SG concept. For a plate/shell-like structure, if the reference surface is considered as a 2D continuum, every material point of this continuum has an associated SG as its microstructure.

It is easy to identify SGs for periodic structures as shown in Figs. 4, 5, and 6. For structures which are not globally periodic, we usually assume that the structure is at least periodic in the neighborhood of a material point in the macroscopic structural analysis, the so-called local periodicity assumption implicit in all multiscale modeling approaches [5]. For nonlinear behavior, it is also possible that the smallest mathematical building block of the structure is not sufficient as the characteristic length scale of the nonlinear behavior may cover several building blocks. For this case, SG should be interpreted as the smallest mathematical building block necessary to represent the nonlinear behavior.

SG serves as the link between the original structure with microscopic details and the macroscopic structural analysis. Here, the terms "microstructure" and "microscopic details" are used in a general sense: any details explicitly existing in SG but not in the macroscopic structural analysis are termed microscopic details in this paper. Here and later in the paper, the real structure with microscopic details is termed as the original structure and the structure used in the macroscopic structural analysis is termed as the macroscopic structural model. It is also interesting to point out the relation between the SG concept and the idea of sub-structuring or super-element, which is commonly used

in sizing software such as HyperSizer [46]. A line element in the global analysis could correspond to a box beam made of four laminated walls, and a surface element could correspond to a sandwich panel with laminated face sheets and a corrugated core. For these cases, SG and its companion mechanics presented below provide a rigorous and systematic approach based on micromechanics to compute the constitutive models for the line and surface elements and the local fields within the original structures. A direct comparison with HyperSizer software is beyond the scope of this work. It suffices to note that HyperSizer is mainly based on a smeared properties approach to model composite beams or composite panels [46].

III. Mechanics of Structure Genome (MSG)

SG serves as the fundamental building block of a structure, no matter whether it is a 3D structure, or a beam, plate, or shell. For SG to not merely remain as a concept, it must be governed by a physics-based theory, namely mechanics of structure genome (MSG), so that there is a two-way communication between microstructural details and structural analysis: microstructural information can be rigorously passed to structural analysis to predict structural performance, and structural performance can be passed back to predict the local fields within the microstructure for failure prediction and other detailed analyses.

A structural model contains kinematics, kinetics, and constitutive relations. On the one hand, kinematics deals with strain-displacement relations and compatibility equations, on the other hand, kinetics deals with stress and equations of motion. Constitutive relations relate stress and strain. Both kinematics and kinetics can be formulated exactly within the framework of continuum mechanics and remain the same for the same structural model independent of the composition of the structure. Constitutive relations are where the difference comes from and are ultimately approximate because a hypothetical continuum is used to model the underlining atomic structure of matter. Some criterion is needed for us to minimize the loss of information between the original model describing the microscopic details and the model used for the macroscopic structural analysis. For elastic materials, this can be achieved by minimizing the difference between the strain energy of the materials stored in SG and that stored in the macroscopic structural model.

A. Kinematics

The first step in formulating MSG is to express the kinematics, including the displacement field and the strain field, of the original structures in terms of those of the macroscopic structural model. Although the SG concept is applicable to original structures made of materials admitting general continuum description such as the Cosserat continuum [47], this work focuses on materials admitting Cauchy continuum description.

1. Coordinate systems

Let us use x_i, called macro coordinates here, to denote the coordinates describing the original structure. The coordinates could be general curvilinear coordinates. However, without loss of generality, we choose an orthogonal system of arc-length coordinates. If the structure is dimensionally reducible, some of the macro coordinates x_α, called eliminated coordinates here, correspond to the dimensions eliminated in the macroscopic structural model. Here and throughout the paper, Greek indices assume values corresponding to the eliminated macro coordinates, Latin indices k, l, m assume values corresponding to the macro coordinates remaining in the macroscopic structural model, and other Latin indices assume 1, 2, 3. Repeated indices are summed over their range except where explicitly indicated.

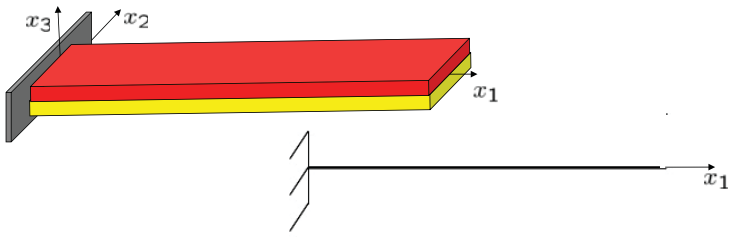

Fig. 7 Macro coordinates (x_1, x_2, x_3) and eliminated coordinates (x_2, x_3) of a beam.

For beam-like structures, only x_1, describing the beam reference line, will remain in the final beam model, while x_2, x_3, the cross-sectional coordinates, will be eliminated (see Fig. 7); for plate/shell-like structures, x_1 and x_2, describing the plate/shell reference surface, will remain in the final plate/shell model, while x_3, the thickness coordinate, will be eliminated. For this reason, the

beam model is called a 1D continuum model because all the unknown fields are functions of x_1 only. Similarly, the plate/shell model is called a 2D continuum model because all the unknown fields are functions of x_1 and x_2 only.

Since the size of a SG is much smaller than the wavelength of the macroscopic deformation, we introduce micro coordinates $y_i = x_i/\varepsilon$ to describe the SG, with ε being a small parameter. This basically enables a zoom-in view of the SG at a size similar to the macroscopic structure. If the SG is 1D, only y_3 is needed; if the SG is 2D, y_2 and y_3 are needed; if the SG is 3D, all three coordinates y_1, y_2, y_3 are needed. In multiscale structural modeling, a field function of the original structure can be generally written as a function of the macro coordinates x_k which remain in the macroscopic structural model and the micro coordinates y_j. Following [19], the partial derivative of a function $f(x_k, y_j)$ can be expressed as

$$\frac{\partial f(x_k, y_j)}{\partial x_i} = \frac{\partial f(x_k, y_j)}{\partial x_i}|_{y_j=\text{const}} + \frac{1}{\varepsilon}\frac{\partial f(x_k, y_j)}{\partial y_i}|_{x_k=\text{const}} \equiv f_{,i} + \frac{1}{\varepsilon} f_{|i} \tag{1}$$

2. *Undeformed and deformed configurations*

Let $\boldsymbol{b}_k$ denote the unit vector tangent to x_k for the undeformed configuration. Note $\boldsymbol{b}_i$ chosen this way are functions of x_k only. For example, for beam-like structures, we choose $\boldsymbol{b}_1$ to be tangent to the beam reference line x_1, and $\boldsymbol{b}_2$, $\boldsymbol{b}_3$ as unit vectors tangent to the cross-sectional coordinates x_α. As shown in Fig. 8, we can describe the position of any material point of the original structure by its position vector $\boldsymbol{r}$ relative to a point O fixed in an inertial frame such that

$$\boldsymbol{r}(x_k, y_\alpha) = \boldsymbol{r}_o(x_k) + \varepsilon y_\alpha \boldsymbol{b}_\alpha(x_k) \tag{2}$$

where $\boldsymbol{r}_o$ is the position vector from O to a material point of the macroscopic structural model. Note here x_k denote only those coordinates remaining in the macroscopic structural model, and y_α correspond to eliminated coordinates x_α. Because x_k is an arc-length coordinate, we have $\boldsymbol{b}_k = \frac{\partial \boldsymbol{r}_o}{\partial x_k}$.

When the original structure deforms, the particle that had position vector $\boldsymbol{r}$ in the undeformed configuration now has position vector $\boldsymbol{R}$ in the deformed configuration, such as

$$\boldsymbol{R}(x_k, y_j) = \boldsymbol{R}_o(x_k) + \varepsilon y_\alpha \boldsymbol{B}_\alpha(x_k) + \varepsilon w_i(x_k, y_j)\boldsymbol{B}_i(x_k) \tag{3}$$

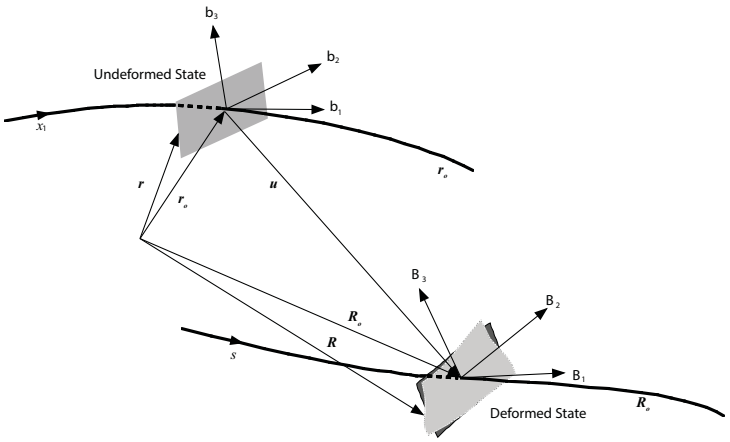

Fig. 8 Deformation of a typical beam structure.

where $\boldsymbol{R}_o$ denotes the position vector of the deformed structural model, $\boldsymbol{B}_i$ forms a new orthonormal triad for the deformed configuration, and εw_i are fluctuating functions introduced to accommodate all possible deformations other than those described by $\boldsymbol{R}_o$ and $\boldsymbol{B}_i$. $\boldsymbol{B}_i$ can be related with $\boldsymbol{b}_i$ through a direction cosine matrix, $C_{ij} = \boldsymbol{B}_i \cdot \boldsymbol{b}_j$, subject to the requirement that these two triads are the same in the undeformed configuration. $\boldsymbol{R}$ is expressed in terms of $\boldsymbol{R}_o$, $\boldsymbol{B}_i$, and w_i in Eq. (3), resulting in six times redundancy. Six constraints are needed to ensure a unique mapping. These constraints can be directly related with how we define $\boldsymbol{R}_o$ and $\boldsymbol{B}_i$ in terms of $\boldsymbol{R}$. For example, it is natural for us to define

$$\boldsymbol{R}_o = \big\langle\langle \boldsymbol{R} \rangle\big\rangle - \big\langle\langle \varepsilon y_\alpha \rangle\big\rangle \boldsymbol{B}_\alpha(x_k) \tag{4}$$

where $\big\langle\langle \cdot \rangle\big\rangle$ indicates averaging over the SG. If y_α is chosen such that $\big\langle\langle \varepsilon y_\alpha \rangle\big\rangle = 0$, $\boldsymbol{R}_o$ is defined as the average of the position vector of the original structure. Then Eq. (3) implies the following three constraints on the fluctuating functions:

$$\big\langle\langle w_i \rangle\big\rangle = 0 \tag{5}$$

Note that for 3D structures y_α disappears and no requirement for $\big\langle\langle \varepsilon y_\alpha \rangle\big\rangle = 0$ is needed but the constraints in Eq. (5) remain.

The other three constraints can be used to specify $\boldsymbol{B}_i$. For plate/shell-like structures, we can select $\boldsymbol{B}_3$ in such a way that

$$\boldsymbol{B}_3 \cdot \boldsymbol{R}_{o,1} = 0, \quad \boldsymbol{B}_3 \cdot \boldsymbol{R}_{o,2} = 0 \tag{6}$$

which provides two constraints implying that we choose $\boldsymbol{B}_3$ normal to the reference surface of the deformed plate/shell. It should be noted that this choice has nothing to do with the well-known Kirchhoff hypothesis. In the Kirchhoff assumption, the transverse normal can only rotate rigidly without any local deformation. However, in the present formulation, we allow all possible deformations, classifying all deformations other than those described by $\boldsymbol{R}_o$ and $\boldsymbol{B}_i$ in terms of the fluctuating function $w_i\boldsymbol{B}_i$. The last constraint can be specified by the rotation of $\boldsymbol{B}_\alpha$ around $\boldsymbol{B}_3$ such that

$$\boldsymbol{B}_1 \cdot \boldsymbol{R}_{o,2} = \boldsymbol{B}_2 \cdot \boldsymbol{R}_{o,1} \tag{7}$$

This constraint symmetrizes the macro strains for a plate/shell model as defined in Eq. (19) later.

For beam-like structures, we can select $\boldsymbol{B}_\alpha$ in such a way that

$$\boldsymbol{B}_2 \cdot \boldsymbol{R}_{o,1} = 0, \quad \boldsymbol{B}_3 \cdot \boldsymbol{R}_{o,1} = 0 \tag{8}$$

which provides two constraints implying that we choose $\boldsymbol{B}_1$ to be tangent to the reference line of deformed beam. Note that this choice is not the well-known Euler-Bernoulli assumption as the present formulation can describe all deformations of the cross-section. We can also prescribe the rotation of $\boldsymbol{B}_\alpha$ around $\boldsymbol{B}_1$ such that

$$\boldsymbol{B}_3 \cdot \frac{\partial \boldsymbol{R}}{\partial x_2} - \boldsymbol{B}_2 \cdot \frac{\partial \boldsymbol{R}}{\partial x_3} = 0 \tag{9}$$

which implies the following constraint on the fluctuating functions

$$\langle\langle w_{2|3} - w_{3|2} \rangle\rangle = 0 \tag{10}$$

This constraint actually defines the twist angle of the macroscopic beam model in terms of the original position vector as pointed out in [1].

Thus the fluctuating functions are constrained according to Eq. (5). For beam structures, they are additionally constrained according to Eq. (10). Other constraints for the fluctuating functions can be introduced naturally into the formulation. For example, for periodic structures, fluctuating functions should be equal on periodic boundaries.

3. Strain field

If the local rotation (the rotation of a material point of the original structure subtracting the rotation needed for bringing $\mathbf{b}_i$ to $\mathbf{B}_i$) is small, it is convenient to use the Jauman-Biot-Cauchy strain according to the decomposition of rotation tensor [48].

$$\Gamma_{ij} = \frac{1}{2}\left(F_{ij} + F_{ji}\right) - \delta_{ij} \tag{11}$$

where δ_{ij} is the Kronecker symbol and F_{ij} is the mixed-basis component of the deformation gradient tensor defined as

$$F_{ij} = \mathbf{B}_i \cdot \mathbf{G}_a \mathbf{g}^a \cdot \mathbf{b}_j = \mathbf{B}_i \cdot \left(\mathbf{G}_k \mathbf{g}^k + \mathbf{G}_\alpha \mathbf{g}^\alpha\right) \cdot \mathbf{b}_j \tag{12}$$

Here $\mathbf{g}^a$ are the 3D contravariant base vectors of the undeformed configuration and $\mathbf{G}_a$ are the 3D covariant basis vectors of the deformed configuration.

The contravariant base vector $\mathbf{g}^a$ is defined as

$$\mathbf{g}^a = \frac{1}{2\sqrt{g}} e_{aij} \boldsymbol{g}_i \times \boldsymbol{g}_j \tag{13}$$

with e_{aij} as the 3D permutation symbol and $\boldsymbol{g}_i$ as the covariant base vector of undeformed configuration and $g = \det(\boldsymbol{g}_i \cdot \boldsymbol{g}_j)$.

From the undeformed configuration in Eq. (2), corresponding to the remaining macro coordinate x_k, we obtain the covariant base vector as

$$\boldsymbol{g}_k = \frac{\partial \boldsymbol{r}}{\partial x_k} = \boldsymbol{b}_k + \varepsilon y_\alpha \frac{\partial \boldsymbol{b}_\alpha}{\partial x_k} = \boldsymbol{b}_k + \varepsilon y_\alpha \boldsymbol{k}_k \times \boldsymbol{b}_\alpha = \boldsymbol{b}_k + e_{i\alpha j} \varepsilon y_\alpha k_{ki} \boldsymbol{b}_j \tag{14}$$

Here $\boldsymbol{k}_k = k_{ki}\boldsymbol{b}_i$ is the initial curvature vector corresponding to the remaining macro coordinate x_k. This definition is consistent with that for initial curvatures of shells in [49], k_{kl}^{2D}, if we let

$$k_{kl}^{\mathrm{2D}} = \alpha_{lm} k_{km} \qquad k_{k3}^{\mathrm{2D}} = k_{k3} \tag{15}$$

with α_{lm} as the 2D permutation symbol: $\alpha_{11} = \alpha_{22} = 0, \alpha_{12} = -\alpha_{21} = 1$.

From the undeformed configuration in Eq. (2), corresponding to the eliminated macro coordinate x_α, we obtain the covariant base vector as

$$\boldsymbol{g}_\alpha = \frac{\partial \boldsymbol{r}}{\partial x_\alpha} = \frac{\partial \varepsilon y_\alpha}{\partial x_\alpha} \boldsymbol{b}_\alpha = \boldsymbol{b}_\alpha \tag{16}$$

From the deformed configuration in Eq. (3), corresponding to the remaining macro coordinate x_k, we obtain the covariant base vector $\mathbf{G}_k$ as

$$\boldsymbol{G}_k = \frac{\partial \boldsymbol{R}}{\partial x_k} = \frac{\partial \boldsymbol{R}_o}{\partial x_k} + \varepsilon y_\alpha \frac{\partial \boldsymbol{B}_\alpha}{\partial x_k} + \varepsilon \frac{\partial w_i}{\partial x_k}\boldsymbol{B}_i + \varepsilon w_i \frac{\partial \boldsymbol{B}_i}{\partial x_k} \tag{17}$$

From the deformed configuration in Eq. (3), corresponding to the eliminated macro coordinate x_α, we obtain the covariant base vector as

$$\boldsymbol{G}_\alpha = \frac{\partial \boldsymbol{R}}{\partial x_\alpha} = \frac{\partial (\varepsilon y_\beta)}{\partial x_\alpha}\boldsymbol{B}_\beta + \varepsilon \frac{\partial w_i}{\partial x_\alpha}\boldsymbol{B}_i = \boldsymbol{B}_\alpha + \frac{\partial w_i}{\partial y_\alpha}\boldsymbol{B}_i \tag{18}$$

A proper definition of the generalized strain measures for the macroscopic structural model is needed for the purpose of formulating the macroscopic structural analysis in a geometrically exact fashion. Following [1, 49, 50], we introduce the following definitions:

$$\begin{aligned} \epsilon_{kl} &= \boldsymbol{B}_l \cdot \frac{\partial \boldsymbol{R}_o}{\partial x_k} - \delta_{kl} \\ \kappa_{ki} &= \frac{1}{2} e_{iaj} \boldsymbol{B}_j \cdot \frac{\partial \boldsymbol{B}_a}{\partial x_k} - k_{ki} \end{aligned} \tag{19}$$

where ϵ_{kl} κ_{ki}

$\boldsymbol{B}_1$ $\boldsymbol{R}_o$

$\epsilon_{12} = \epsilon_{21}$

$\boldsymbol{B}_3$

is described using a Cauchy continuum, we will restrict ourselves to the Cauchy continuum model for the 3D macroscopic structural model in this paper. In other words, we are seeking a symmetric Lagrangian stretch tensor ϵ_{kl} and negligible curvature strain tensor κ_{ki}. This can be achieved by constraining the global rotation needed for bringing $\mathbf{b}_i$ to $\mathbf{B}_i$ in a specific way, which can be illustrated more clearly using an invariant form of the definitions in Eq. (19). According to [50, 53], these definitions can be rewritten as

$$\begin{aligned} \boldsymbol{\epsilon} &= \boldsymbol{C}^T \cdot \boldsymbol{F} - \boldsymbol{I} \\ \boldsymbol{\kappa}^T &= -\frac{1}{2}\boldsymbol{e} : \left(\boldsymbol{C}^T \cdot \frac{\partial \boldsymbol{C}}{\partial x_k} \boldsymbol{b}_k \right) \end{aligned} \tag{20}$$

where $\boldsymbol{\epsilon}$ is the Lagrangian stretch tensor, $\boldsymbol{\kappa}$ the Lagrangian curvature strain tensor, $\boldsymbol{C} = \boldsymbol{B}_i \boldsymbol{b}_i$ is the global rotation tensor bringing $\boldsymbol{b}_i$ to $\boldsymbol{B}_i$, $\boldsymbol{F}$ is the deformation gradient tensor, $\boldsymbol{I} = \boldsymbol{b}_i \boldsymbol{b}_i$ is the second-order identity tensor, and $\boldsymbol{e} = -\boldsymbol{I} \times \boldsymbol{I}$ is the third-order skew Ricci tensor. If the global rotation tensor $\boldsymbol{C}$ is constrained to be decomposed from $\boldsymbol{F}$ according to the polar decomposition theorem

$$\boldsymbol{F} = \boldsymbol{C} \cdot \boldsymbol{U} \tag{21}$$

where $\boldsymbol{U}$ is a second-order positive symmetric tensor, then the definitions in Eq. (20) become

$$\begin{aligned} \boldsymbol{\epsilon} &= \boldsymbol{C}^T \cdot (\boldsymbol{C} \cdot \boldsymbol{U}) - \boldsymbol{I} = \boldsymbol{U} - \boldsymbol{I} \\ \boldsymbol{\kappa}^T &= -\frac{1}{2}\boldsymbol{e} : \left(\boldsymbol{C}^T \cdot \frac{\partial \boldsymbol{C}}{\partial x_k} \boldsymbol{b}_k \right) \end{aligned} \tag{22}$$

Clearly, the Lagrangian stretch tensor $\boldsymbol{\epsilon}$ becomes symmetric and is the definition of Jauman-Biot-Cauchy strain tensor. The Lagrangian curvature strain tensor $\boldsymbol{\kappa}$ corresponds to higher-order terms (gradient of the deformation gradient) which are commonly neglected in the Cauchy continuum model. This derivation is significant because it provides a geometrically exact description for the 3D solid and has demonstrated that the Cauchy continuum description can be actually reduced from the Cosserat continuum description. It is noted that restraining the global rotation tensor according to Eq. (21) is equivalent to introducing three constraints for $\boldsymbol{B}_i$ needed for 3D structures. With this derivation, the nonlinear kinematics of beams, plates/shells, and 3D structures can be described using a single, unified formulation.

To facilitate the derivation of the covariant vectors $\boldsymbol{G}_i$, we can rewrite the definitions in Eq. (19) as

$$\begin{aligned}\frac{\partial \boldsymbol{R}_o}{\partial x_k} &= \boldsymbol{B}_k + \epsilon_{kl}\boldsymbol{B}_l \\ \frac{\partial \boldsymbol{B}_i}{\partial x_k} &= (\kappa_{kj} + k_{kj})\boldsymbol{B}_j \times \boldsymbol{B}_i\end{aligned} \tag{23}$$

Note $\epsilon_{13} = \epsilon_{23} = 0$ for plate/shell-like structures due to Eq. (6) and $\epsilon_{12} = \epsilon_{13} = 0$ for beam-like structures due to Eq. (8).

Substituting Eq. (23) into Eq. (17), we can obtain more detailed expressions for the covariant base vectors of the deformed configuration $\boldsymbol{G}_k$ as follows:

$$\begin{aligned}\boldsymbol{G}_k &= \boldsymbol{B}_k + \epsilon_{kl}\boldsymbol{B}_l + \varepsilon y_\alpha \frac{\partial \boldsymbol{B}_\alpha}{\partial x_k} + \varepsilon \frac{\partial w_l}{\partial x_k}\boldsymbol{B}_l + \varepsilon \frac{\partial w_\alpha}{\partial x_k}\boldsymbol{B}_\alpha + \varepsilon w_l \frac{\partial \boldsymbol{B}_l}{\partial x_k} + \varepsilon w_\alpha \frac{\partial \boldsymbol{B}_\alpha}{\partial x_k} \\ &= \left(\delta_{kl} + \epsilon_{kl} + \varepsilon \frac{\partial w_l}{\partial x_k}\right)\boldsymbol{B}_l + \varepsilon\left(y_\alpha + w_\alpha\right)\frac{\partial \boldsymbol{B}_\alpha}{\partial x_k} + \varepsilon \frac{\partial w_\alpha}{\partial x_k}\boldsymbol{B}_\alpha + \varepsilon w_l \frac{\partial \boldsymbol{B}_l}{\partial x_k} \\ &= \left(\delta_{kl} + \epsilon_{kl} + \varepsilon \frac{\partial w_l}{\partial x_k}\right)\boldsymbol{B}_l + \varepsilon\left[e_{ij\alpha}\left(y_\alpha + w_\alpha\right)\left(\kappa_{kj} + k_{kj}\right) + \frac{\partial w_\alpha}{\partial x_k}\delta_{\alpha i} + e_{ijl}w_l(\kappa_{kj} + k_{kj})\right]\boldsymbol{B}_i\end{aligned} \tag{24}$$

Using the expressions for $\boldsymbol{g}^a$ and $\boldsymbol{G}_a$, and dropping nonlinear terms due to the product of the curvature strains and the fluctuating functions, the 3D strain field defined in Eq. (11) can be written in the following matrix form

$$\Gamma = \Gamma_h w + \Gamma_\epsilon \bar{\epsilon} + \varepsilon \Gamma_l w + \varepsilon \Gamma_R w \tag{25}$$

where $\Gamma = \lfloor \Gamma_{11} \;\; \Gamma_{22} \;\; \Gamma_{33} \;\; 2\Gamma_{23} \;\; 2\Gamma_{13} \;\; 2\Gamma_{12} \rfloor^T$ denotes the strain field of the original structure, $w = \lfloor w_1 \;\; w_2 \;\; w_3 \rfloor^T$ the fluctuating functions, $\bar{\epsilon}$ is a column matrix containing the generalized strain measures for the macroscopic structural model. For example, if the macroscopic structural model is a beam model, we have $\bar{\epsilon} = \lfloor \epsilon_{11} \;\; \kappa_{11} \;\; \kappa_{12} \;\; \kappa_{13} \rfloor^T$ with ϵ_{11} denoting the extensional strain, κ_{11} the twist, κ_{12} and κ_{13} the bending curvatures. If the macroscopic structural model is a plate/shell model, we have $\bar{\epsilon} = \lfloor \epsilon_{11} \;\; \epsilon_{22} \;\; 2\epsilon_{12} \;\; \kappa_{11}^{\mathrm{2D}} \;\; \kappa_{22}^{\mathrm{2D}} \;\; \kappa_{12}^{\mathrm{2D}} + \kappa_{21}^{\mathrm{2D}} \rfloor^T$ with $\epsilon_{\alpha\beta}$ denoting the in-plane strains and $\kappa_{\alpha\beta}^{\mathrm{2D}}$ denoting the curvature strains. If the macroscopic structural model is a 3D continuum model, we have $\bar{\epsilon} = \lfloor \epsilon_{11} \;\; \epsilon_{22} \;\; \epsilon_{33} \;\; 2\epsilon_{23} \;\; 2\epsilon_{13} \;\; 2\epsilon_{12} \rfloor^T$ with ϵ_{ij} denoting the Biot strain measures in a Cauchy continuum. Γ_h is an operator matrix which depends on the dimensionality of the SG. Γ_ϵ and Γ_l are two operator matrices, the form of which depends on the macroscopic structural model. Γ_R is an

operator matrix existing only for those original structures featuring initial curvatures. The explicit expressions for these operators are given in the appendix for completeness.

B. Variational Statement for SG

Although the SG concept can be used to analyze structures made of various types of materials, in this paper, we illustrate its use by focusing on structures made of elastic materials. These structures are governed by the following variational statement

$$\delta U = \overline{\delta W} \tag{26}$$

where δ is the usual Lagrangean variation, U is the strain energy, and $\overline{\delta W}$ is the virtual work of the applied loads. The over bar indicates that the virtual work needs not be the variation of a functional. For a linear elastic material characterized using a 6×6 stiffness matrix D, the strain energy can be written as

$$U = \frac{1}{2} \int \frac{1}{\omega} \left\langle \Gamma^T D \Gamma \right\rangle \mathrm{d}\Omega \tag{27}$$

where Ω is the volume of the domain spanned by x_k remaining in the macroscopic structural model. The notation $\langle \bullet \rangle = \int \bullet \sqrt{g} \mathrm{d}\omega$ is used to denote a weighted integration over the domain of the SG and ω denotes the volume of the domain spanned by y_k corresponding to the coordinates x_k remaining in the macroscopic structural model. If none of y_k is needed in the SG, then $\omega = 1$. For example, if a heterogeneous beam-like structure features a 3D SG, ω is the length of the SG in the y_1 direction, corresponding to x_1 remaining in the macroscopic beam model. If the heterogeneous beam-like structure features a 2D SG (uniform cross-section), y_1 is not needed for the SG and $\omega = 1$. ω for plate/shell-like structures or 3D structures can be obtained similarly.

For a Cauchy continuum, there may exist applied loads from tractions and body forces. The virtual work done by these applied loads can be calculated as

$$\overline{\delta W} = \int \frac{1}{\omega} \left(\langle \mathbf{p} \cdot \delta \mathbf{R} \rangle + \int_s \mathbf{Q} \cdot \delta \mathbf{R} \sqrt{c} \mathrm{d}s \right) \mathrm{d}\Omega \tag{28}$$

where s denotes the boundary surfaces of the SG with applied traction force per unit area $\mathbf{Q} = Q_i \mathbf{B}_i$ and applied body force per unit volume $\mathbf{p} = p_i \mathbf{B}_i$. $\sqrt{c}$ is equal to 1 except for some degenerated cases where s is only a boundary curve of the SG and one of coordinates x_k is required to form

the physical surfaces on which the load is applied. In this case, the differential area of the physical surface is equal to $\sqrt{c}\mathrm{d}s\mathrm{d}x_k$ with $\mathrm{d}s$ as the differential arc length along the boundary curve of SG. For example for beam-like structures featuring a 2D SG, the SG boundary is the curve encircling the cross-section, and $\sqrt{c} = \sqrt{g + \left(y_2 \frac{\mathrm{d}y_2}{\mathrm{d}s} + y_3 \frac{\mathrm{d}y_3}{\mathrm{d}s}\right)^2 k_{11}^2}$.

$\delta\mathbf{R}$ is the Lagrangian variation of the displacement field in Eq. (3), such that

$$\delta\mathbf{R} = \overline{\delta q}_i \mathbf{B}_i + \varepsilon y_\alpha \delta\mathbf{B}_\alpha + \varepsilon \delta w_i \mathbf{B}_i + \varepsilon w_i \delta\mathbf{B}_i \tag{29}$$

We may safely ignore products of the fluctuating functions and virtual rotations in $\delta\mathbf{R}$, because the fluctuating functions are small. The last term of the above equation is then dropped so that

$$\delta\mathbf{R} = \overline{\delta q}_i \mathbf{B}_i + \varepsilon y_\alpha \delta\mathbf{B}_\alpha + \varepsilon \delta w_i \mathbf{B}_i \tag{30}$$

The virtual displacements and rotations of the macroscopic structural model are defined as

$$\overline{\delta q}_i = \delta\mathbf{R}_o \cdot \mathbf{B}_i, \quad \delta\mathbf{B}_\alpha = \overline{\delta\psi}_j \mathbf{B}_j \times \mathbf{B}_\alpha \tag{31}$$

where $\overline{\delta q}_i$ and $\overline{\delta\psi}_i$ contain the components of the virtual displacement and rotation in the $\mathbf{B}_i$ system, respectively. They are functions of x_k only. Note $\overline{\delta\psi}_j$ are restrained to be derivable from $\overline{\delta q}_i$ and are higher-order terms that are neglected in a 3D structure described using the Cauchy continuum.

Then we can rewrite Eq. (30) as

$$\delta\mathbf{R} = \left(\overline{\delta q}_i + \varepsilon e_{j\alpha i} y_\alpha \overline{\delta\psi}_j + \varepsilon \delta w_i\right) \mathbf{B}_i \tag{32}$$

Finally, we express the virtual work due to applied loads as

$$\overline{\delta W} = \overline{\delta W}_H + \varepsilon\, \overline{\delta W}^* \tag{33}$$

where $\overline{\delta W}_H$ is the virtual work not related with the fluctuating functions w_i and $\overline{\delta W}^*$ is the virtual work related with the fluctuating functions.

$$\overline{\delta W}_H = \int \left(f_i \overline{\delta q}_i + m_i \overline{\delta\psi}_i\right) \mathrm{d}\Omega, \quad \overline{\delta W}^* = \int \frac{1}{\omega} \left(\langle p_i \delta w_i \rangle + \oint Q_i \delta w_i \sqrt{c}\, \mathrm{d}s\right) \mathrm{d}\Omega \tag{34}$$

with the generalized forces f_i and moments m_i defined as

$$f_i = \frac{1}{\omega}\left(\langle p_i \rangle + \int Q_i \sqrt{c}\, \mathrm{d}s\right), \quad m_i = \frac{e_{i\alpha j}}{\omega}\left(\langle \varepsilon y_\alpha p_j \rangle + \int \varepsilon y_\alpha Q_j \sqrt{c}\, \mathrm{d}s\right) \tag{35}$$

If we assume that p_i and Q_i are independent of the fluctuating functions, then we can rewrite $\overline{\delta W}^*$ as

$$\overline{\delta W}^* = \delta \int \frac{1}{\omega} \left(\langle p_i w_i \rangle + \int Q_i w_i \sqrt{c} \, \mathrm{d}s \right) \mathrm{d}\Omega \tag{36}$$

In view of the strain energy in Eq. (27) and virtual work in Eq. (33) along with Eq. (34), the variational statement in Eq. (26) can be rewritten as

$$\int \frac{1}{\omega} \delta \left[\frac{1}{2} \left\langle \Gamma^T D \Gamma \right\rangle - \varepsilon \left(\langle p_i w_i \rangle + \int Q_i w_i \sqrt{c} \, \mathrm{d}s \right) \right] - \left(f_i \overline{\delta q}_i + m_i \overline{\delta \psi}_i \right) \mathrm{d}\Omega = 0 \tag{37}$$

If we attempt to solve this variational statement directly, we will meet the same difficulty as a direct analysis of the original structure. The main complexity comes from the fluctuating functions w_i which are unknown functions of both micro and macro coordinates. To reduce the original continuum model into a macroscopic structural model, the common practice in structural modeling is to assume the fluctuating functions, *a priori*, in terms of some unknown functions (displacements, rotations, and/or strains) of x_k and some known functions of y_k. However, for arbitrary structures made with general composites, use of such *a priori* assumptions may introduce significant errors. Fortunately, the variational asymptotic method (VAM) [54] provides a useful technique to obtain the fluctuating functions through an asymptotical analysis of the variational statement in Eq. (37). It does so in terms of the small parameter ε which is inherent in the composite structure to construct asymptotically correct macroscopic structural models. As the last two terms in Eq. (37) are not functions of w_i, we can conclude that the fluctuating function is governed by the following variational statement instead:

$$\delta \left[\frac{1}{2} \left\langle \Gamma^T D \Gamma \right\rangle - \varepsilon \left(\langle p_i w_i \rangle + \int Q_i w_i \sqrt{c} \, \mathrm{d}s \right) \right] = 0 \tag{38}$$

which can be considered as a variational statement for the SG as it is posed over the SG domain only. According to VAM, we can neglect the terms in the order of ε to construct the first approximation of the variational statement in Eq. (38) as

$$\delta \frac{1}{2} \left\langle (\Gamma_h w + \Gamma_\epsilon \bar{\epsilon})^T D (\Gamma_h w + \Gamma_\epsilon \bar{\epsilon}) \right\rangle = 0 \tag{39}$$

It is noted here that only small geometry parameters are considered in this work. For structures made of materials featuring significantly different properties, small material parameters should also

be introduced for the asymptotic analysis using VAM. It is also pointed out that VAM is used to discard energetically small terms which might cause difficulty in capturing some higher order local stresses. However, such loss of information is mainly governed by the macroscopic structural model. In this work, only the classical structural models including the Euler-Bernoulli beam model, Kirchhoff-Love plate/shell model, and the Cauchy continuum model are constructed using MSG. It is our future plan to derive refined models such as the Reissner-Mindlin plate/shell model, Timoshenko beam model, and Cosserat continuum model using the unified MSG framework.

For very simple cases such as isotropic beams [55], laminated plates [56], binary composites [57], the variational statement in Eq. (39) can be solved exactly and analytically, while for general cases we need to turn to numerical techniques such as the finite element method for solutions. To this end, we need to express w using shape functions defined over SG as

$$w(x_k, y_j) = S(y_j)V(x_k) \tag{40}$$

Eq. (40) is a standard way to solve Eq. (39) using the finite element method. Eq. (39) is a variational statement used to solve for w given $\bar{\epsilon}$ with V as a function of x_k because of $\bar{\epsilon}$. Such a separation of variable is inherent in multiscale modeling and structural modeling approaches. S is the standard shape functions depending on the type of elements one uses which can be found in typical finite element textbooks. V is what we need to solve for as the nodal values for the influence function based on the discretization.

Substituting Eq. (40) into Eq. (39), we obtain the the following discretized version of the strain energy functional:

$$U = \frac{1}{2}\left(V^T E V + 2V^T D_{h\epsilon}\bar{\epsilon} + \bar{\epsilon}^T D_{\epsilon\epsilon}\bar{\epsilon}\right) \tag{41}$$

where

$$E = \left\langle (\Gamma_h S)^T D (\Gamma_h S) \right\rangle, \quad D_{h\epsilon} = \left\langle (\Gamma_h S)^T D \Gamma_\epsilon \right\rangle, \quad D_{\epsilon\epsilon} = \left\langle \Gamma_\epsilon^T D \Gamma_\epsilon \right\rangle \tag{42}$$

Minimizing U in Eq. (41) subject to the constraints, gives us the following linear system

$$EV = -D_{h\epsilon}\bar{\epsilon} \tag{43}$$

It is clear that V linearly depends on $\bar{\epsilon}$, and the solution can be symbolically written as

$$V = V_0 \bar{\epsilon} \tag{44}$$

Substituting Eq. (44) back into Eq. (41), we can calculate the strain energy stored in the SG as the first approximation as

$$U = \frac{1}{2} \bar{\epsilon}^T \left(V_0^T D_{h\epsilon} + D_{\epsilon\epsilon} \right) \bar{\epsilon} \equiv \frac{\omega}{2} \bar{\epsilon}^T \bar{D} \bar{\epsilon} \tag{45}$$

where $\bar{D}$ is the effective stiffness to be used in the macroscopic structural model. For the Euler-Bernoulli beam model, $\bar{D}$ could be a fully populated 4×4 stiffness matrix, for the Kirchhoff-Love plate/shell model and Cauchy continuum model, $\bar{D}$ could be a fully populated 6×6 stiffness matrix.

Substituting the solved strain energy stored in the SG into Eq. (37), we can rewrite the variational statement governing the original structure as

$$\int \left[\delta \left(\frac{1}{2} \bar{\epsilon}^T \bar{D} \bar{\epsilon} \right) - f_i \overline{\delta q}_i - m_i \overline{\delta \psi}_i \right] \mathrm{d}\Omega = 0 \tag{46}$$

This variational statement governs the macroscopic structural model as it involves only fields which are unknown functions of the macro coordinates x_k. The first term is the variation of the strain energy of the macroscopic structural model and the rest of the terms are the virtual work done by generalized forces and moments. This variational statement governs the linear elastic behavior of structural elements (3D solid elements, 2D plate/shell elements, 1D beam elements) implemented in most commercial FEA software packages.

Often, we are also interested in computing the local fields within the original structure. With $\bar{\epsilon}$ obtained from the macroscopic structural analysis, the fluctuating function can be obtained as

$$w = S V_0 \bar{\epsilon} \tag{47}$$

The local displacement field can be obtained as

$$u_i = \bar{u}_i + x_\alpha (C_{\alpha i} - \delta_{\alpha i}) + \varepsilon w_j C_{ji} \tag{48}$$

where u_i is the local displacement, $\bar{u}_i$ is the macroscopic displacement. For SGs having coordinates y_k with corresponding x_k existing in the macroscopic structural model, $\bar{u}_i$ should be interpreted as

$$\bar{u}_i = \bar{u}_i(x_{k_0}) + x_k \bar{u}_{i,k} \tag{49}$$

where x_{k_0} is the center of the SG and $\bar{u}_{i,k}$ is the gradient along x_k evaluated at x_{k_0}.

The local strain field can be obtained as

$$\Gamma = \left(\Gamma_h S V_0 + \Gamma_\epsilon\right) \bar{\epsilon}. \tag{50}$$

The local stress field can be obtained directly using the Hooke's law as

$$\sigma = D\Gamma. \tag{51}$$

IV. An Analytical Example: Deriving the Kirchhoff-Love Model for Composite Laminates

MSG presented above is very general so that it can handle a geometrically exact analysis for all types of structures with arbitrary heterogeneity. For the sake of simplicity, the above formulation will be specialized to derive the linear elastic Kirchhoff-Love model for composite laminates.

If we assume that the composite laminate is made of anisotropic homogeneous layers, the linear elastic behavior is governed by 3D elasticity in terms of 3D displacements u_i, strains ε_{ij}, and stresses σ_{ij}. To construct a plate model, we need to first express the 3D displacements in terms of 2D plate displacements:

$$\begin{aligned} u_1(x_1, x_2, y_3) &= \bar{u}_1(x_1, x_2) - y_3 \bar{u}_{3,1} + w_1(x_1, x_2, y_3) \\ u_2(x_1, x_2, y_3) &= \bar{u}_2(x_1, x_2) - y_3 \bar{u}_{3,2} + w_2(x_1, x_2, y_3) \\ u_3(x_1, x_2, y_3) &= \bar{u}_3(x_1, x_2) + w_3(x_1, x_2, y_3) \end{aligned} \tag{52}$$

Here $u_i(x_1, x_2, y_3)$ are 3D displacements, while $\bar{u}_i(x_1, x_2)$ are plate displacements which are functions of x_1, x_2 only. We also introduce 3D unknown fluctuating functions $w_i(x_1, x_2, y_3)$ to describe the information of 3D displacements which cannot be described by the simpler Kirchhoff-Love plate kinematics. Note that the displacement expressions in Eq. (52) have nothing to do with the celebrated Kirchhoff-Love assumptions. It can be considered as a change of variables to express the 3D displacements in terms of the displacement variables of the Kirchhoff-Love plate model and fluctuating functions. The Kirchhoff-Love assumptions are equivalent to assuming $w_i = 0$. Since we consider that the original 3D model is our true model, we construct the plate model as an approximation to the true model. To this end, we need to define the plate displacements in terms of 3D displacements. A natural choice is:

$$h\bar{u}_3(x_1, x_2) = \langle u_3 \rangle, \quad h\bar{u}_\alpha(x_1, x_2) = \left\langle u_\alpha(x_1, x_2, y_3) \right\rangle + \langle y_3 \rangle \, \bar{u}_{3,\alpha} \tag{53}$$

which implies the following constraints on the fluctuating functions

$$\langle w_i \rangle = 0 \tag{54}$$

Note if the origin of the thickness coordinate is at the middle of the plate thickness, Eq. (53) actually defines the plate displacements to be the average of the 3D displacements.

Then the 3D strain field can be obtained as

$$\begin{aligned}
\Gamma_{11} &= \epsilon_{11} + x_3\kappa_{11} + w_{1,1} \\
2\Gamma_{12} &= 2\epsilon_{12} + 2x_3\kappa_{12} + w_{1,2} + w_{2,1} \\
\Gamma_{22} &= \epsilon_{22} + x_3\kappa_{22} + w_{2,2} \\
2\Gamma_{13} &= w_{1,3} + w_{3,1} \\
2\Gamma_{23} &= w_{2,3} + w_{3,2} \\
\Gamma_{33} &= w_{3,3}
\end{aligned}$$

with the linear plate strains defined as

$$\epsilon_{\alpha\beta}(x_1, x_2) = \frac{1}{2}(\bar{u}_{\alpha,\beta} + \bar{u}_{\beta,\alpha}); \quad \kappa^{2\mathrm{D}}_{\alpha\beta}(x_1, x_2) = -\bar{u}_{3,\alpha\beta} \tag{55}$$

Here α, β denotes subscript 1 or 2.

The 3D strain field can also be written in the following matrix form:

$$\varepsilon_e = \epsilon + x_3\kappa + I_\alpha w_{\|,\alpha}, \quad 2\varepsilon_s = {w_\|}' + e_\alpha w_{3,\alpha}, \quad \varepsilon_t = {w_3}' \tag{56}$$

with $\varepsilon_e = \lfloor \Gamma_{11} \ \Gamma_{22} \ 2\Gamma_{12} \rfloor^T, 2\varepsilon_s = \lfloor 2\Gamma_{13} \ 2\Gamma_{23} \rfloor^T, \varepsilon_t = \Gamma_{33}, \epsilon = \lfloor \epsilon_{11} \ \epsilon_{22} \ 2\epsilon_{12} \rfloor^T, \kappa = \lfloor \kappa^{2\mathrm{D}}_{11} \ \kappa^{2\mathrm{D}}_{22} \ \kappa^{2\mathrm{D}}_{12} + \kappa^{2\mathrm{D}}_{21} \rfloor^T$ and

$$I_1 = \begin{bmatrix} 1 & 0 \\ 0 & 1 \\ 0 & 0 \end{bmatrix}, \quad I_2 = \begin{bmatrix} 0 & 0 \\ 1 & 0 \\ 0 & 1 \end{bmatrix}, \quad e_1 = \begin{Bmatrix} 1 \\ 0 \end{Bmatrix}, \quad e_2 = \begin{Bmatrix} 0 \\ 1 \end{Bmatrix} \tag{57}$$

The strain energy can be used as a natural measure for information governing the linear elastic

behavior. Twice of the strain energy can be written as

$$2U = \left\langle \begin{Bmatrix} \varepsilon_e \\ 2\varepsilon_s \\ \varepsilon_t \end{Bmatrix}^{\mathrm{T}} \begin{bmatrix} C_e & C_{es} & C_{et} \\ C_{es}^{\mathrm{T}} & C_s & C_{st} \\ C_{et}^{\mathrm{T}} & C_{st}^{\mathrm{T}} & C_t \end{bmatrix} \begin{Bmatrix} \varepsilon_e \\ 2\varepsilon_s \\ \varepsilon_t \end{Bmatrix} \right\rangle \tag{58}$$

The explicit expression after dropping smaller energy contributions due to $w_{i,\alpha}$ according to VAM is

$$\begin{aligned} 2U_0 = \Big\langle & (\epsilon + x_3\kappa)^T C_e (\epsilon + x_3\kappa) + w_\parallel'^T C_s w_\parallel' + w_3'^T C_t w_3' \\ & + 2(\epsilon + x_3\kappa)^T C_{es} w_\parallel' + 2(\epsilon + x_3\kappa)^T C_{et} w_3' + 2w_\parallel'^T C_{st} w_3' \Big\rangle \end{aligned} \tag{59}$$

Minimizing this energy with respect to the fluctuating function w_i along with the constraints in Eq. (54), we reach the following Euler-Lagrange equations:

$$\Big((\epsilon + x_3\kappa)^{\mathrm{T}} C_{es} + {w_\parallel}'^{\mathrm{T}} C_s + {w_3}' C_{st}^{\mathrm{T}} \Big)' = \lambda_\parallel \tag{60}$$

$$\Big((\epsilon + x_3\kappa)^{\mathrm{T}} C_{et} + {w_\parallel}'^{\mathrm{T}} C_{st} + {w_3}' C_t \Big)' = \lambda_3 \tag{61}$$

where $\lambda_\parallel = \lfloor \lambda_1 \ \lambda_2 \rfloor^T$ and λ_3 denote the Lagrange multiplies enforcing the constraints in Eq. (54). The boundary conditions on the top and bottom surfaces are

$$(\epsilon + x_3\kappa)^{\mathrm{T}} C_{es} + {w_\parallel}'^{\mathrm{T}} C_s + {w_3}' C_{st}^{\mathrm{T}} = 0 \tag{62}$$

$$(\epsilon + x_3\kappa)^{\mathrm{T}} C_{et} + {w_\parallel}'^{\mathrm{T}} C_{st} + {w_3}' C_t = 0 \tag{63}$$

We can conclude that the above two equations should be satisfied at every point through the thickness and solve for ${w_\parallel}'^{\mathrm{T}}$ and ${w_3}'$ as

$${w_\parallel}'^{\mathrm{T}} = -(\epsilon + x_3\kappa) C_{es}^* C_s^{-1} \tag{64}$$

$${w_3}' = -(\epsilon + x_3\kappa) C_{et}^* C_t^{*-1} \tag{65}$$

with

$$C_t^* = C_t - C_{st}^{\mathrm{T}} C_s^{-1} C_{st}, \quad C_{et}^* = C_{et} - C_{es} C_s^{-1} C_{st}, \quad C_{es}^* = C_{es} - C_{et}^* C_{st}^{\mathrm{T}} / C_t^* \tag{66}$$

w_i can be solved by simply integrating through the thickness along with the interlaminar continuity.

Substituting the solved fluctuating functions into Eq. (59), we have

$$2U_0 = \left\langle (\epsilon + x_3\kappa)^T C_e^* (\epsilon + x_3\kappa) \right\rangle = \begin{Bmatrix} \epsilon \\ \kappa \end{Bmatrix}^T \begin{bmatrix} A & B \\ B & D \end{bmatrix} \begin{Bmatrix} \epsilon \\ \kappa \end{Bmatrix} \tag{67}$$

with

$$C_e^* = C_e - C_{es}^* C_s^{-1} C_{es}^{\mathrm{T}} - C_{et}^* C_{et}^{\mathrm{T}} / C_t^*, \quad A = \langle C_e^* \rangle, \quad B = \langle x_3 C_e^* \rangle, \quad D = \left\langle x_3^2 C_e^* \right\rangle \tag{68}$$

This strain energy along with the work done by applied loads can be used to solve the 2D plate problem to obtain $\bar{u}_i, \epsilon, \kappa$. 3D displacements can be obtained after we have solved for w_i.

$$\begin{aligned} u_1(x_1, x_2, x_3) &= \bar{u}_1(x_1, x_2) - x_3 \bar{u}_{3,1} + w_1(x_1, x_2, y_3) \\ u_2(x_1, x_2, x_3) &= \bar{u}_2(x_1, x_2) - x_3 \bar{u}_{3,2} + w_2(x_1, x_2, y_3) \\ u_3(x_1, x_2, x_3) &= \bar{u}_3(x_1, x_2) + w_3(x_1, x_2, y_3) \end{aligned} \tag{69}$$

It is clear that the transverse normal does not remain rigid and normal according to Kirchhoff-Love assumptions in CLPT. Instead the transverse normal can be deformed according to w_i.

3D strains can be obtained after neglecting the higher order terms $w_{i,\alpha}$ which are not contributing to the approximation of the plate energy.

$$\varepsilon_e = \epsilon + x_3\kappa, \quad 2\varepsilon_s = -(\epsilon + x_3\kappa) C_{es}^* C_s^{-1}, \quad \varepsilon_{33} = -(\epsilon + x_3\kappa) C_{et}^* C_t^{*-1} \tag{70}$$

Clearly, the strain field is not in-plane as what is traditionally assumed using Kirchhoff-Love assumptions in CLPT. Instead, transverse shear and normal strains both could exist.

3D stresses can be obtained by directly using the above strain field along with the Hooke's law of the original 3D elasticity theory.

$$\sigma_e = C_e^* (\epsilon + x_3\kappa,) \quad \sigma_s = 0, \quad \sigma_{33} = 0 \tag{71}$$

It can be observed that the Kirchhoff-Love model derived using MSG satisfies the plane-stress assumption invoked in CLPT. However, this is not assumed *a priori* but derived by using MSG.

V. Numerical Examples

The Mechanics of Structure Genome (MSG) developed in this paper is implemented into a computer code called SwiftComp. A few examples are used here to demonstrate the application

and validity of MSG and its companion code SwiftComp. As it can be theoretically shown that one can specialize MSG to reproduce the well established theory of composite beams known as Variational Asymptotic Beam Sectional analysis (VABS) [1, 58], theory of composite plates/shells known as Variational Asymptotic Plate And Shell analysis (VAPAS) [56], micromechanics theories known as Variational Asymptotic Method for Unit Cell Homogenization (VAMUCH) [27], heterogeneous plates and beams [59, 60]. We have verified that the current version of SwiftComp can reproduce all the results of VAMUCH, and the classical models of VABS and VAPAS. Particularly, an extensively benchmark study for micromechanics theories and codes has been recently carried out by cdmHUB (Composites Design and Manufacturing HUB) and the results have shown that MSG and SwiftComp can achieve the versatility and accuracy of 3D FEA with much less computational time, which clearly demonstrates the advantage of MSG in micromechanics. Interested readers are directed to the report and database of Micromechanics Simulation Challenge available at https://cdmhub.org/projects/mmsimulationchalleng. Here, a few examples which cannot be handled by current versions of VAMUCH, VABS, and VAPAS are used to demonstrate the application of MSG and SwiftComp.

A. A Cross-ply Laminate

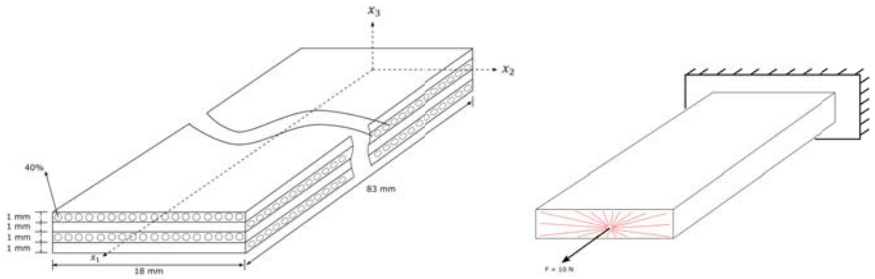

Fig. 9 Sketch of the four-layer cross-ply laminate

First, we will use a simple cross-ply laminate example to demonstrate the application of MSG. As shown in Fig. 9, a four-layer cross-ply [90°/0°/90°/0°] laminate with length 83 mm, width 18 mm, and height 4 mm is clamped at one end and loaded at the other end with a 10 N tensile force at the center of the cross-section. The composite prepreg is assumed to have square packing with 40%

fiber volume fraction. The fiber and matrix are assumed to be isotropic, with a Young's modulus of 276 GPa and a Poisson's ratio of 0.28 for the fiber and a Young's modulus of 4.76 GPa and a Poisson's ratio of 0.37 for the matrix.

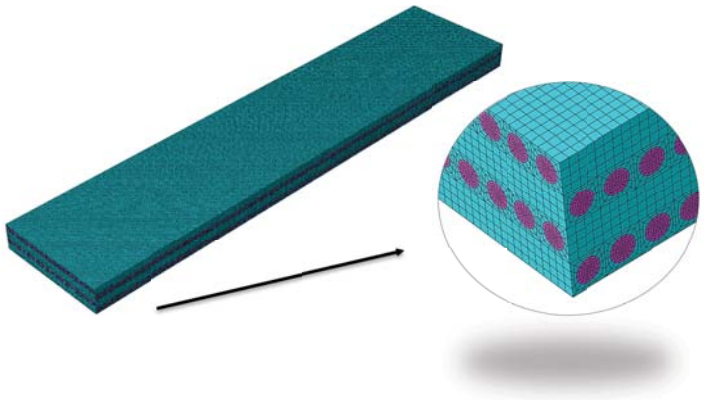

Fig. 10 3D finite element mesh of the four-layer cross-ply laminate

It is noted here that this example is not representative of a typical fiber reinforced composite laminate, as usually each layer could contain many more fibers instead of one fiber per layer thickness as assumed here for simplicity. The purpose of this example is not to question CLPT's modeling capability for conventional laminates, which could be the subject of a future publication. Instead, this example is used to demonstrate the accuracy and efficiency of alternative analysis options provided by MSG. There are two common approaches to analyze this type of structure: 3D FEA using solid elements to mesh all of the microstructural details (see Fig. 10) and lamination theory with lamina constants computed by a micromechanics approach (see Fig. 2). Using 3D FEA, the laminate is meshed with 2,294,784 C3D20R elements with a total of 9,319,562 nodes in ABAQUS to achieve a fair convergence of stress predictions. Using MSG, we can also analyze the structure as a plate with the constitutive relations provided through an analysis of the corresponding SG as shown in Fig. 11, where the SG is meshed in ABAQUS using 1,536 20-noded brick elements with 7,585 total nodes, and the reference surface is meshed with 2,988 STRI3 elements containing 1,596 nodes. Because the length is much larger than both the height and width, the structure can also be analyzed as a beam with the constitutive relations provided through an analysis of the corresponding SG as shown in Fig. 12. The SG is meshed with 27,648 20-noded brick elements with 124,409 nodes

total, and the reference line is meshed with 83 two-noded line elements with 84 nodes total.

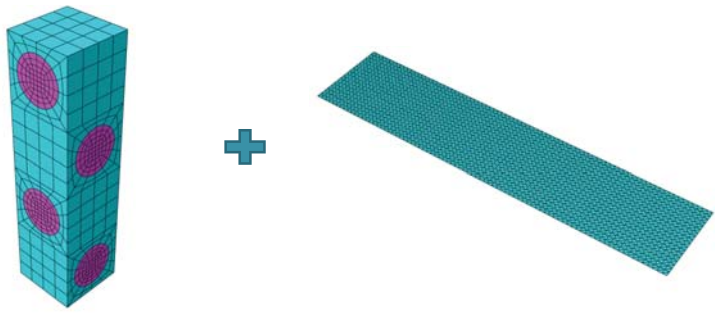

Fig. 11 SwiftComp based plate analysis

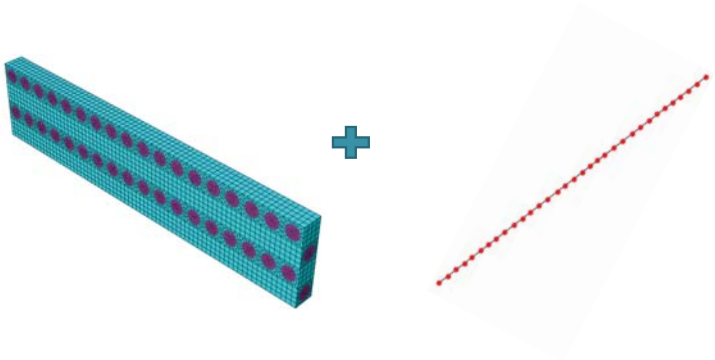

Fig. 12 SwiftComp based beam analysis

Different analysis approaches require different computing resources and time. Using 3D FEA, we used a computer with 48 cores and it took ABAQUS 7 days 11 hours and 37 minutes to finish the analysis. For the lamination theory, we used the composite layup analysis in ABAQUS with the same surface mesh as shown in Fig. 11. To compute the lamina constants, SwiftComp only requires a 2D SG which is much more efficient than other computational homogenization approaches which usually require a 3D domain to obtain the complete set of properties [5]. The micromechanics analysis and the laminate analysis are finished within 30 seconds. For SwiftComp based plate analysis, homogenization of the SG to compute the plate stiffness takes 6 seconds, the surface analysis takes 28 seconds, and dehomogenization to obtain 3D local fields takes 6 seconds. For SwiftComp based beam analysis, homogenization of SG to compute the beam stiffness takes 3 minutes and 14 seconds, the beam analysis takes 0.02 second, and dehomogenization to obtain 3D

local fields takes 1 minute 21 seconds. Except for the 3D FEA, all the other analyses were done in the same computer using only 1 core. The other analyses are several orders of magnitude more efficient than 3D FEA. SwiftComp adds small overhead for the constitutive modeling including both the homogenization and dehomogenization processes in comparison to the traditional lamination theory for this simple static analysis. However, constitutive modeling is usually done once while many global structural analyses using beam elements or plate elements are needed in the real design and analysis of composite structures. In other words, the small overhead added by SwiftComp could be negligible for most cases.

Table 1 Displacements predicted by different analyses

Analysis methods	Deflection (mm)	Extension (mm)
3D FEA	2.7124×10^{-3}	2.0849×10^{-4}
SwiftComp beam analysis	2.7146×10^{-3}	2.0873×10^{-4}
SwiftComp plate analysis	2.7084×10^{-3}	2.0832×10^{-4}
ABAQUS Composite layup	2.5264×10^{-3}	2.0804×10^{-4}

Different analysis approaches result in different predictions. The displacements at the center of the loaded tip are shown in Table 1. SwiftComp based plate analysis and beam analysis achieve an excellent agreement with 3D FEA. Lamination theory using ABAQUS layup analysis provides an excellent prediction for the minor displacement (extension), but introduces about 7% error for the major displacement (deflection) in comparison to 3D FEA. The prediction of the detailed stress distribution within composites is also very important as these quantities could be directly related with the failure of the structure. Consider the stress distribution through the thickness at $x_1 = 41.5$ mm, $x_2 = 0.5$ mm. Note at this point x_3 is passing through the diameter of one of the fibers. As shown in Figs. 13, 14, and 15, both SwiftComp based plate analysis and beam analysis achieve excellent agreement with 3D FEA for all the nontrivial stress components while the ABAQUS composite layup analysis shows significant discrepancies from 3D FEA. It is clear that the composite layup analysis predicts stress discontinuities happening at the wrong locations and the maximum stresses predicted by the composite layup analysis are also very different from 3D FEA. The composite layup

analysis cannot predict the transverse normal stress (σ_{33}) due to its inherent plane-stress assumption, while SwiftComp based plate and beam analyses still remain in very good agreement with 3D FEA, although the magnitude is small compared to the other two in-plane stress components. It can be observed that for this problem, SwiftComp can achieve similar accuracy as 3D FEA but with orders of magnitude savings in computing time and resources. Regarding the relatively larger discrepancy between SwiftComp and 3D FEA for σ_{33}, it is mainly because we could not further refine the 3D FEA model due to the limitation of the workstation we can access (56 CPUs with 256 GB RAM). We have verified that for simpler cases such as a two-layer plate of the same example, we can get a perfect match with 3D FEA. We have done mesh convergence studies for many problems and MSG consistently converges faster than 3D FEA due to the semi-analytical nature of MSG.

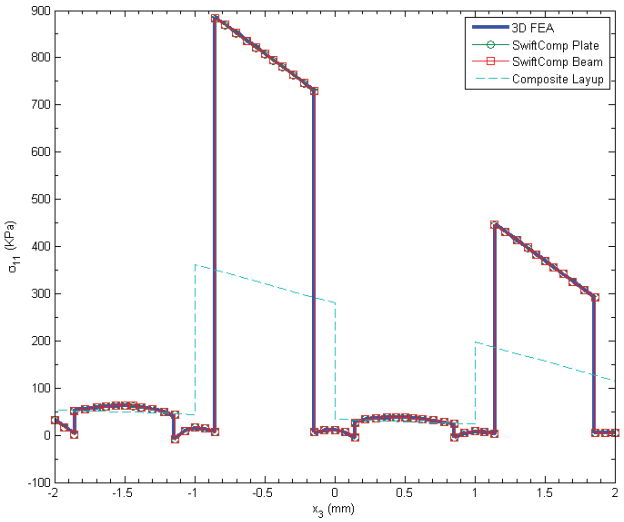

Fig. 13 σ_{11} distribution through the thickness ($x_1 = 41.5$ mm, $x_2 = 0.5$ mm)

B. Sandwich Beam with Periodically Varying Cross-Sections

The next example is used to demonstrate the application of MSG to analyze beams with spanwise heterogeneities which can be commonly found in civil engineering applications. It is a sandwich beam with periodically variable cross-section studied in [61]. The geometric parameters for each configuration are given in Fig. 16. Note that although all the SGs in Fig. 16 are uniform along y_2,

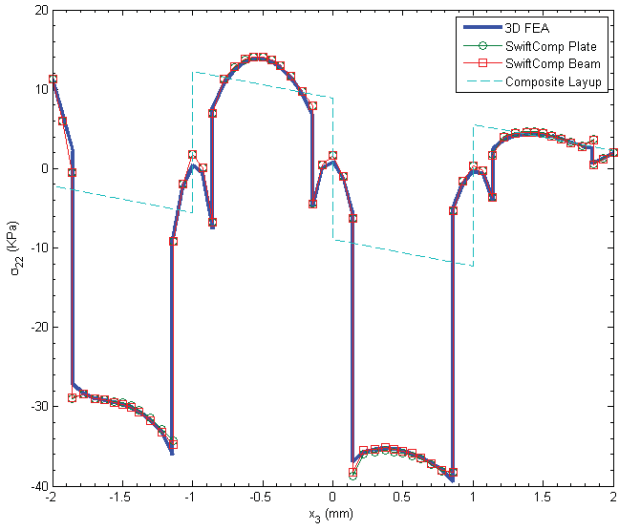

Fig. 14 σ_{22} distribution through the thickness ($x_1 = 41.5$ mm, $x_2 = 0.5$ mm)

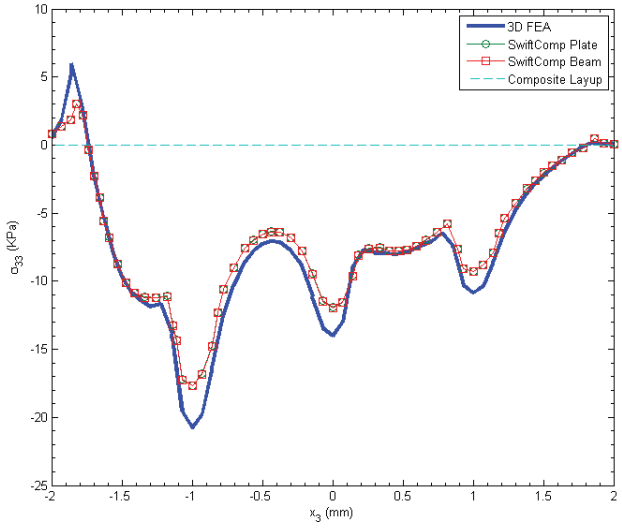

Fig. 15 σ_{33} distribution through the thickness ($x_1 = 41.5$ mm, $x_2 = 0.5$ mm)

the SG must be 3D because they are used to form a beam structure and y_2 is one of the cross-sectional coordinates (Fig. 17). All sandwich beams in the above cases have the same core material properties (material indicated by blue color in the figure) of $E_c = 3.5$ GPa, $\nu_c = 0.34$ and face

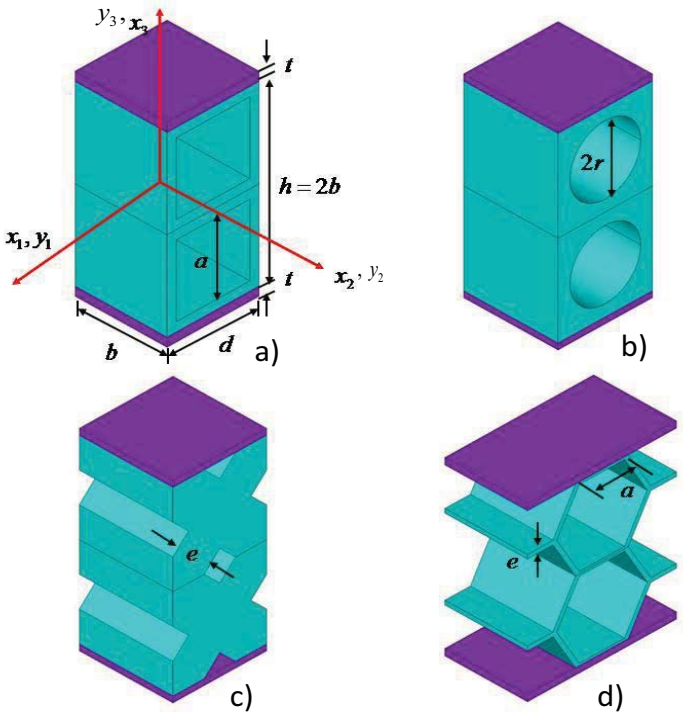

Fig. 16 The structure genome for sandwich beams with different cross-sections: a) square holes ($b = d = 1.5$ m, $t = 0.1$ m, $a = 1$ m); b)circular holes ($b = d = 1.5$ m, $t = 0.1$ m, $r = 0.5614$ m); c) cross-shaped holes ($b = d = 1.5$ m, $t = 0.1$ m, $e = 0.7071$ m); d)hexagonal holes ($b = 1.23745$ m, $d = 2b$, $t = 0.1$ m, $a = 0.7887$ m, $e = 0.6431$ m).

sheet material properties (indicated by purple color in the figure) of $E_f = 70$ GPa, $\nu_c = 0.34$. Also note that although these beams are studied in [61], only bending stiffnesses are given. In fact, the effective stiffness for the classical beam model in general should be represented by a fully populated 4×4 matrix. This example is also studied in [62] using a novel finite implementation of the asymptotic homogenization theory applied to beams. The effective bending stiffnesses predicted by the analytical formulas in [61], those of [62] denoted as NIAH standing for Novel Implementation of Asymptotic Homogenization, and SwiftComp are listed in Table 2. The details of these approaches can be found in the cited references.

As can be observed, SwiftComp predictions have an excellent agreement with NIAH and are slightly different from those in [61]. However, the present approach is more versatile than that in [61] because [61] only provides analytic formulas for the bending stiffness of beams made of materials

Table 2 Effective beam bending stiffness of sandwich beams predicted by different methods ($\times 10^{10}$ N$\cdot$ m^2)

	Ref. [61]	SwiftComp	NIAH
Square Holes	5.669	5.576	5.576
Circular Holes	5.176	5.537	5.554
Cross-shaped Holes	5.486	5.805	5.891
Hexagonal Holes	2.875	2.888	2.886

characterized only by one material constant, the Young's modulus, while SwiftComp can estimate all the engineering beam constants represented by a 4×4 stiffness matrix, possibly fully populated, for the most general anisotropic materials by factorizing the coefficient matrix in the linear system (Eq. (43)) only once. NIAH results are obtained using multiple runs of a commercial finite element code, which requires much more computing time than SwiftComp.

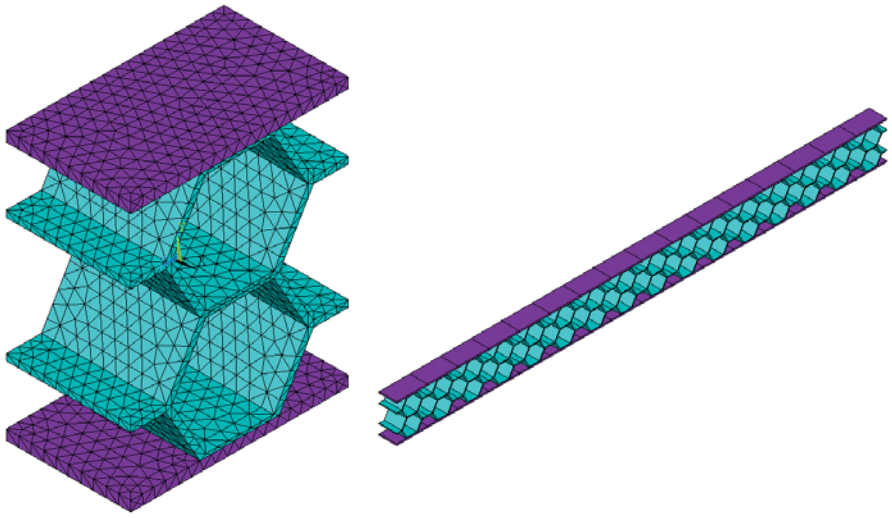

Fig. 17 A sandwich beam with hexagonal holes

C. Sandwich Panel with a Corrugated Core

The last example is to demonstrate the application of MSG to model plates with in-plane heterogeneities. It is a corrugated-core sandwich panel, a concept used for Integrated Thermal Protection System (ITPS) studied in [63]. The ITPS panel along with the details of the SG is

sketched in Fig. 18. Both materials are isotropic with $E_1 = 109.36$ GPa, $\nu_1 = 0.3$ for material 1, and $E_2 = 209.482$ GPa, $\nu_2 = 0.063$ for material 2. Although 3D unit cells are needed for the study in [63], only a 2D SG is necessary for SwiftComp as it is uniform along one of the in-plane directions. The effective stiffness for the Kirchhoff-Love plate model can be represented using the A, B and D matrices known in CLPT. Results obtained in [63] are compared with SwiftComp in Tables 3, 4 and 5. SwiftComp predictions agree very well with those in Ref. [63] with the biggest difference (around 1%) appearing for the extension-bending coupling stiffness (B_{11}). However, the present approach is much more efficient because using the approach in [63] one needs to carry out six analyses of a 3D unit cell under six different sets of boundary conditions and load conditions and postprocess the 3D stresses to compute the plate stress resultants. Using the present approach, one only needs to carry out one analysis of a 2D SG without applying carefully crafted boundary conditions and postprocessing.

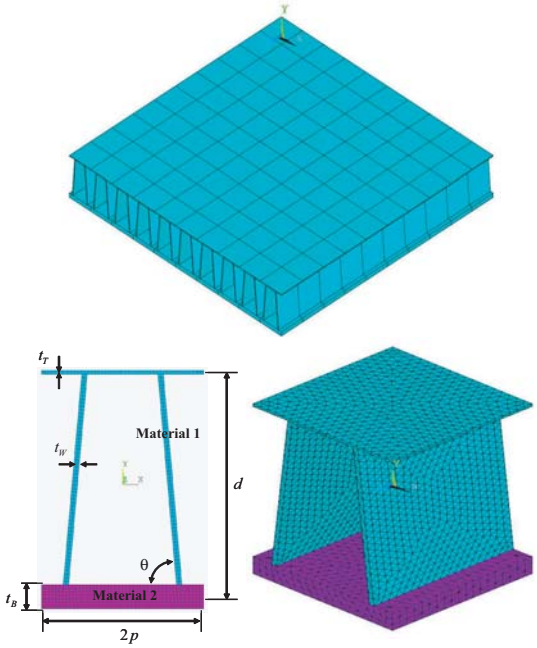

Fig. 18 Sketch of the ITPS panel and its SG ($t_T = 1.2$ mm, $t_B = 7.49$ mm, $t_W = 1.63$ mm, $p = 25$ mm, $d = 70$ mm, and $\theta = 85°$).

Table 3 Effective extension stiffness of ITPS ($\times 10^9$ N/m)

	A_{11}	A_{12}	A_{22}	A_{33}
Ref. [63]	2.83	0.18	2.33	1.07
SwiftComp	2.80	0.18	2.33	1.08

Table 4 Effective bending stiffness of ITPS ($\times 10^6$ N·m)

	D_{11}	D_{12}	D_{22}	D_{33}
Ref. [63]	3.06	0.22	2.85	1.32
SwiftComp	3.03	0.22	2.87	1.32

VI. Conclusion

This paper developed a unified theory for multiscale constitutive modeling of composites based on the concept of SG. The SG facilitates a mathematical decoupling of the original complex analysis of composite structures into a constitutive modeling over the SG and a macroscopic structural analysis. The MSG presented in this paper enables a multiscale constitutive modeling approach with the following unique features:

- Use the SG to connect microstructures and macroscopic structural analyses. Intellectually, SG enables us to view constitutive modeling for structures as applications of micromechanics. Technically, SG empowers us to systematically model complex build-up structures with heterogeneities.

- Use the VAM to avoid *a priori* assumptions commonly invoked in other approaches, providing the rigor needed to construct mathematical models with excellent tradeoffs between efficiency

Table 5 Effective coupling stiffness of ITPS ($\times 10^6$ N)

	B_{11}	B_{13}	B_{22}	B_{33}

and accuracy.

- Decouple the original problem into two sets of analyses: a constitutive modeling and a structural analysis. This allows the structural analysis to be formulated exactly as a general (1D, 2D, or 3D) continuum, the analysis of which is readily available in commercial FEA software packages. This also confines all approximations to the constitutive modeling, the accuracy of which is guaranteed to be the best by the VAM.

A general-purpose computer code called SwiftComp is developed to implement MSG along with several examples to demonstrate its application. This code can be used as a plug-in for commercial FEA software packages to accurately model structures made of anisotropic heterogeneous materials using traditional structural elements.

Although only theoretical details and implementation have been worked out for linear elastic behavior of periodic structures for which a SG can be easily identified, the basic framework is also applicable to nonlinear behavior of aperiodic heterogeneous structures, which are topics for future work.

Acknowledgments

This research is supported, in part, by the Air Force Office of Scientific Research (Agreement No. FA9550-13-1-0148) and by the Army Vertical Lift Research Center of Excellence at Georgia Institute of Technology and its affiliated program through a subcontract at Purdue University (Agreement No. W911W6-11-2-0010). The views and conclusions contained herein are those of the author and should not be interpreted as necessarily representing the official policies or endorsement, either expressed or implied, of the sponsors. The US Government is authorized to reproduce and distribute reprints notwithstanding any copyright notation thereon. The author also greatly appreciates the help from his student Ning Liu for providing results for Example 1.

Appendix

Γ_h is an operator matrix which depends on the dimensionality of the SG. If the SG is 3D, we have

$$\Gamma_h = \begin{bmatrix} \frac{1}{\sqrt{g_1}}\frac{\partial}{\partial y_1} & 0 & 0 \\ 0 & \frac{1}{\sqrt{g_2}}\frac{\partial}{\partial y_2} & 0 \\ 0 & 0 & \frac{\partial}{\partial y_3} \\ 0 & \frac{\partial}{\partial y_3} & \frac{1}{\sqrt{g_2}}\frac{\partial}{\partial y_2} \\ \frac{\partial}{\partial y_3} & 0 & \frac{1}{\sqrt{g_1}}\frac{\partial}{\partial y_1} \\ \frac{1}{\sqrt{g_2}}\frac{\partial}{\partial y_2} & \frac{1}{\sqrt{g_1}}\frac{\partial}{\partial y_1} & 0 \end{bmatrix} \tag{72}$$

where $\sqrt{g_1} = \sqrt{g_2} = 1$ for plate-like structures or 3D structures, $\sqrt{g_1} = 1 - \varepsilon y_2 k_{13} + \varepsilon y_3 k_{12}$ and $\sqrt{g_2} = 1$ for beam-like structures, $\sqrt{g_1} = 1 + \varepsilon y_3 k_{12}$ and $\sqrt{g_2} = 1 - \varepsilon y_3 k_{21}$ for shell-like structures.

If the SG is a lower-dimensional one, one just needs to vanish the corresponding term corresponding to the micro coordinates which are not used in describing the SG. For example, if the SG is 2D, we have

$$\Gamma_h = \begin{bmatrix} 0 & 0 & 0 \\ 0 & \frac{1}{\sqrt{g_2}}\frac{\partial}{\partial y_2} & 0 \\ 0 & 0 & \frac{\partial}{\partial y_3} \\ 0 & \frac{\partial}{\partial y_3} & \frac{1}{\sqrt{g_2}}\frac{\partial}{\partial y_2} \\ \frac{\partial}{\partial y_3} & 0 & 0 \\ \frac{1}{\sqrt{g_2}}\frac{\partial}{\partial y_2} & 0 & 0 \end{bmatrix} \tag{73}$$

If the SG is 1D, we have

$$\Gamma_h = \begin{bmatrix} 0 & 0 & 0 \\ 0 & 0 & 0 \\ 0 & 0 & \frac{\partial}{\partial y_3} \\ 0 & \frac{\partial}{\partial y_3} & 0 \\ \frac{\partial}{\partial y_3} & 0 & 0 \\ 0 & 0 & 0 \end{bmatrix} \tag{74}$$

Γ_ϵ is an operator matrix, the form of which depends on the macroscopic structural model. If the

macroscopic structural model is the 3D Cauchy continuum model, Γ_ϵ is the 6×6 identity matrix. If the macroscopic structural model is a beam model, we have

$$\Gamma_\epsilon = \frac{1}{\sqrt{g_1}} \begin{bmatrix} 1 & 0 & \varepsilon y_3 & -\varepsilon y_2 \\ 0 & 0 & 0 & 0 \\ 0 & 0 & 0 & 0 \\ 0 & 0 & 0 & 0 \\ 0 & \varepsilon y_2 & 0 & 0 \\ 0 & -\varepsilon y_3 & 0 & 0 \end{bmatrix} \tag{75}$$

If the macroscopic structural model is a plate/shell model, we have

$$\Gamma_\epsilon = \begin{bmatrix} \frac{1}{\sqrt{g_1}} & 0 & 0 & \frac{\varepsilon y_3}{\sqrt{g_1}} & 0 & 0 \\ 0 & \frac{1}{\sqrt{g_2}} & 0 & 0 & \frac{\varepsilon y_3}{\sqrt{g_2}} & 0 \\ 0 & 0 & 0 & 0 & 0 & 0 \\ 0 & 0 & 0 & 0 & 0 & 0 \\ 0 & 0 & 0 & 0 & 0 & 0 \\ 0 & 0 & \frac{1}{2}\left(\frac{1}{\sqrt{g_1}} + \frac{1}{\sqrt{g_2}}\right) & 0 & 0 & \frac{1}{2}\left(\frac{\varepsilon y_3}{\sqrt{g_1}} + \frac{\varepsilon y_3}{\sqrt{g_2}}\right) \end{bmatrix} \tag{76}$$

Note the above expression is obtained with the understanding that the difference between κ_{12} and κ_{21} is of higher order and negligible if we are not seeking a higher-order approximation of the initial curvatures.

Γ_l is an operator matrix, the form of which depends on the macroscopic structural model. If the macroscopic structural model is 3D, Γ_l has the same form as Γ_h in Eq. (72) with $\frac{\partial}{\partial y_k}$ replaced with $\frac{\partial}{\partial x_k}$, that is

$$\Gamma_l = \begin{bmatrix} \frac{1}{\sqrt{g_1}}\frac{\partial}{\partial x_1} & 0 & 0 \\ 0 & \frac{1}{\sqrt{g_2}}\frac{\partial}{\partial x_2} & 0 \\ 0 & 0 & \frac{\partial}{\partial x_3} \\ 0 & \frac{\partial}{\partial x_3} & \frac{1}{\sqrt{g_2}}\frac{\partial}{\partial x_2} \\ \frac{\partial}{\partial x_3} & 0 & \frac{1}{\sqrt{g_1}}\frac{\partial}{\partial x_1} \\ \frac{1}{\sqrt{g_2}}\frac{\partial}{\partial x_2} & \frac{1}{\sqrt{g_1}}\frac{\partial}{\partial x_1} & 0 \end{bmatrix} \tag{77}$$

Of course for 3D structures, we have $\sqrt{g_1} = \sqrt{g_2} = 1$.

If the macroscopic structural model is a lower-dimensional one, one just needs to vanish the corresponding term corresponding to the macro coordinates which are not used in describing the macroscopic structural model. For example, if the macroscopic structural model is a 2D plate/shell model, we have

$$\Gamma_l = \begin{bmatrix} \frac{1}{\sqrt{g_1}}\frac{\partial}{\partial x_1} & 0 & 0 \\ 0 & \frac{1}{\sqrt{g_2}}\frac{\partial}{\partial x_2} & 0 \\ 0 & 0 & 0 \\ 0 & 0 & \frac{1}{\sqrt{g_2}}\frac{\partial}{\partial x_2} \\ 0 & 0 & \frac{1}{\sqrt{g_1}}\frac{\partial}{\partial x_1} \\ \frac{1}{\sqrt{g_2}}\frac{\partial}{\partial x_2} & \frac{1}{\sqrt{g_1}}\frac{\partial}{\partial x_1} & 0 \end{bmatrix} \tag{78}$$

If the macroscopic structural model is the 1D beam model, we have

$$\Gamma_l = \begin{bmatrix} \frac{1}{\sqrt{g_1}}\frac{\partial}{\partial x_1} & 0 & 0 \\ 0 & 0 & 0 \\ 0 & 0 & 0 \\ 0 & 0 & 0 \\ 0 & 0 & \frac{1}{\sqrt{g_1}}\frac{\partial}{\partial x_1} \\ 0 & \frac{1}{\sqrt{g_1}}\frac{\partial}{\partial x_1} & 0 \end{bmatrix} \tag{79}$$

Γ_R is an operator matrix existing only for those heterogeneous structures featuring initial curvatures. For prismatic beams, plates or 3D structures, Γ_R vanishes. For those structures having initial curvatures such as initially twisted/curved beams or shells, the form of Γ_R depends on the macroscopic structural model. If the macroscopic structural model is a 1D beam model,

$$\Gamma_R = \frac{1}{\sqrt{g_1}} \begin{bmatrix} k_{11}\left(y_3\frac{\partial}{\partial y_2} - y_2\frac{\partial}{\partial y_3}\right) & -k_{13} & k_{12} \\ 0 & 0 & 0 \\ 0 & 0 & 0 \\ 0 & 0 & 0 \\ -k_{12} & k_{11} & k_{11}\left(y_3\frac{\partial}{\partial y_2} - y_2\frac{\partial}{\partial y_3}\right) \\ k_{13} & k_{11}\left(y_3\frac{\partial}{\partial y_2} - y_2\frac{\partial}{\partial y_3}\right) & -k_{11} \end{bmatrix} \tag{80}$$

If the macroscopic structural model is a 2D shell model,

$$\Gamma_R = \begin{bmatrix} 0 & \frac{-k_{13}}{\sqrt{g_1}} & \frac{k_{12}}{\sqrt{g_1}} \\ \frac{k_{23}}{\sqrt{g_2}} & 0 & \frac{-k_{21}}{\sqrt{g_2}} \\ 0 & 0 & 0 \\ 0 & \frac{k_{21}}{\sqrt{g_2}} & 0 \\ \frac{-k_{12}}{\sqrt{g_1}} & 0 & 0 \\ \frac{k_{13}}{\sqrt{g_1}} & -\frac{k_{23}}{\sqrt{g_2}} & 0 \end{bmatrix} \tag{81}$$

References

[1] Yu, W., Hodges, D. H., and Ho, J. C., "Variational Asymptotic Beam Sectional Analysis - An Updated Version," *International Journal of Engineering Science*, Vol. 59, 2012, pp. 40–64.

[2] Li, S. and Wang, G., *Introduction to Micromechanics and Nanomechanics*, World Scientific, New Jersey, 2008.

[3] Nemat-Nasser, S. and Hori, M., *Micromechanics: Overall Properties of Heterogeneous Materials*, North Holland, Amsterdam, The Netherlands, 1998.

[4] Aboudi, J., Arnold, S., and Bednarcyk, B., *Micromechanics of Composite Materials: A Generalized Multiscale Analysis Approach*, Elsevier, 2012.

[5] Fish, J., *Practical Multiscaling*, Wiley, 2013.

[6] Reddy, J. N., *Mechanics of Laminated Composite Plates and Shells: Theory and Analysis*, CRC Press, Boca Raton, Florida, 2004.

[7] Kollar, L. P., , and Springer, G. S., *Mechanics of Composite Structures*, Cambridge University Press, Cambridge, United Kingdom, 2009.

[8] Carrera, E., Cinefra, M., Petrolo, M., and Zappino, E., *Finite Element Analysis of Structures through Unified Formulation*, Wiley, 2014.

[9] Hill, R., "The Elastic Behavior of Crystalline Aggregate," *Proc. Phys. Soc. London*, Vol. A65, 1952, pp. 349–354.

[10] Hashin, Z. and Shtrikman, S., "A Variational Approach to the Theory of the Elastic Behaviour of Polycrystals," *Journal of Mechanics and Physics of Solids*, Vol. 10, 1962, pp. 343–352.

[11] Milton, G. W., *The Theory of Composites*, Cambridge University Press, Cambridge, UK, 2002.

[12] Torquato, S., *Random heterogeneous materials*, Springer New York, 2002.

[13] Mori, T. and Tanaka, K., "Average stress in matrix and average elastic energy of materials with misfitting inclusions," *Acta Metallurgica*, Vol. 21, 1973, pp. 571–574.

[14] Aboudi, J., "A Continuum Theory for Fiber-Reinforced Elastic-Visoplastic Composites," *International Journal of Engineering Science*, Vol. 20, No. 5, 1982, pp. 605 – 621.

[15] Aboudi, J., "Micromechanical Analysis of Composites by the Method of Cells," *Applied Mechanics Reviews*, Vol. 42, No. 7, 1989, pp. 193 – 221.

[16] Paley, M. and Aboudi, J., "Micromechanical Analysis of Composites by the Generalized Cells Model," *Mechanics of Materials*, Vol. 14, 1992, pp. 127–139.

[17] Aboudi, J., Pindera, M. J., and Arnold, S. M., "Linear Thermoelastic Higher-order Theory for Periodic Multiphase Materials," *Journal of Applied Mechanics*, Vol. 68, 2001, pp. 697–707.

[18] Williams, T. O., "A Two-dimensional, Higher-oder, Elasticity-based Micromechanics Model," *International Journal of Solids and Structures*, Vol. 42, 2005, pp. 1009–1038.

[19] Bensoussan, A., Lions, J., and Papanicolaou, G., *Asymptotic Analysis for Periodic Structures*, North-Holland, Amsterdam, 1978.

[20] Murakami, H. and Toledano, A., "A Higer-order Mixture Homogenization of Bi-laminated Composites," *Journal of Applied Mechanics*, Vol. 57, 1990, pp. 388–396.

[21] Guedes, J. M. and Kikuchi, N., "Preprocessing and Postprocessing for Materials Based on the Homogenization Method with Adaptive Finite Element Method," *Computer Methods in Applied Mechanics and Engineering*, Vol. 83, 1990, pp. 143–198.

[22] Michel, J. C., Moulinec, H., and Suquet, P., "Effective Properties of Composite Materials with Periodic Microstructure: a Computational Approach," *Computer Methods in Applied Mechanics and Engineering*, Vol. 172, 1999, pp. 109–143.

[23] Zhang, S. and Oskay, C., "Reduced Order Variational Multiscale Enrichment Method for Elasto-Viscoplastic Problems," *Computer Methods in Applied Mechanics and Engineering*, Vol. 300, 2016, pp. 199–224.

[24] Sun, C. T. and Vaidya, R. S., "Prediction of Composite Properties from a Representative Volume Element," *Composites Science and Technology*, Vol. 56, 1996, pp. 171 – 179.

[25] Berger, H., Kari, S., Gabbert, U., Rodriguez-Ramos, R., Bravo-Castillero, J., Guinovart-Diaz, R., Sabina, F., and Maugin, G., "Unit Cell Models of Piezoelectric Fiber Composites for Numerical and Analytical Calculation of Effective Properties," *Smart Materials and Structures*, Vol. 15, 2006, pp. 451–458.

[26] Ghosh, S., *Micromechanical Analysis and Multi-Scale Modeling Using the Voronoi Cell Finite Element Method*, Taylor & Francis US, Florida, 2010.

[27] Yu, W. and Tang, T., "Variational Asymptotic Method for Unit Cell Homogenization of Periodically Heterogeneous Materials," *International Journal of Solids and Structures*, Vol. 44, 2007, pp. 3738–3755.

[28] Zhang, L. and Yu, W., "A Micromechanics Approach to Homogenizing Elasto-viscoplastic Heterogeneous Materials," *International Journal of Solids and Structures*, Vol. 51, 2015, pp. 3878–3888.

[29] Khandan, R., Noroozi, S., Sewell, P., and Vinney, J., "The Development of Laminated composite Plate Theories: a Review," *Journal of Materials Science*, 2012, in press.

[30] Reddy, J. N., "A Simple Higher-order Theory for Laminated Composite Plates," *Journal of Applied Mechanics*, Vol. 51, No. 4, 1984, pp. 745–752.

[31] Mantari, J. L., Oktem, A. S., and Soares, C. G., "A New Trigonometric Shear Deformation Theory for Isotropic, Laminated Composite and Sandwich Plates," *International Journal of Solids and Structures*, Vol. 49, No. 1, 2011, pp. 43–53.

[32] Plagianakos, T. S. and Saravanos, D. A., "Higher-order Layerwise Laminate Theory for the Prediction of Interlaminar Shear Stresses in Thick Composite and Sandwich Composite Plates," *Composite Structures*, Vol. 87, No. 1, 2009, pp. 23–35.

[33] Icardi, U. and Ferrero, L., "Layerwise Zig-zag Model with Selective Refinement Across the Thickness," *International Journal for Numerical Methods in Engineering*, Vol. 84, No. 9, 2010, pp. 1085–1114.

[34] Carrera, E., "Historical Review of Zig-zag Theories for Multilayered Plates and Shells," *Applied Mechanics Review*, Vol. 56, No. 3, 2003, pp. 287–308.

[35] Ren, X., Chen, W., and Wu, Z., "A New Zig-zag Theory and C^0 Plate Bending Element for Composite and Sandwich Plates," *Archive of Applied Mechanics*, Vol. 81, No. 2, 2011, pp. 185–197.

[36] Demasi, L. and Yu, W., "Assess the Accuracy of the Variational Asymptotic Plate and Shell Analysis (VAPAS) Using the Generalized Unified Formulation (GUF)," *Mechanics of Advanced Materials and Structures*, 2012, in press.

[37] Carrera, E., Maiaru, M., and Petrolo, M., "Component-wise Analysis of Laminated Anisotropic Composites," *International Journal of Solids and Structures*, Vol. 49, No. 13, 2012, pp. 1839–1851.

[38] Maugin, G. A. and Attou, D., "Asymptotic theory of thin piezoelectric plates," *Quarterly Journal of Mechanics and Applied Mathematics*, Vol. 43, 1990, pp. 374 – 362.

[39] Cheng, Z. Q. and Batra, R. C., "Three-dimensional asymptotic analysis of multiple-electroded piezoelectric laminates," *AIAA Journal*, Vol. 38, No. 2, 2000, pp. 317 – 324.

[40] Kalamkarov, A. L. and Kolpakov, A. G., "A new asymptotic model for a composite piezoelastic plate,"

International journal of solids and structures, Vol. 38, No. 34-35, 2001, pp. 6027 –6044.

[41] Reddy, J. N. and Cheng, Z. Q., "Three-dimensional solutions of smart functionally graded plates," *Journal of Applied Mechanics*, Vol. 68, No. 2, 2001, pp. 234 – 241.

[42] Kalamkarov, A. L., Andrianov, I. V., and Danishevs'kyy, V. V., "Asymptotic Homogenization of Composite Materials and Structures," *Applied Mechanics Reviews*, Vol. 62, 2009, pp. 030802.

[43] Kim, J. S., "An Asymptotic Analysis of Anisotropic Heterogeneous Plates with Consideration of End Effects," *Journal of Mechanics of Materials and Structures*, Vol. 4, No. 9, 2009, pp. 1535–1553.

[44] Skoptsov, K. A. and Sheshenin, S. V., "Asymptotic Analysis of Laminated Plates and Shallow Shells," *Mechanics of Solids*, Vol. 46, No. 1, 2011, pp. 129–138.

[45] Pagano, N. J. and Rybicki, E. R., "On the Significance of Effective Modulus Solutions for Fibrous Composites," *Journal of Composite Materials*, Vol. 8, 1974, pp. 214âĂŞ228.

[46] Collier, C., Yarrington, P., and West, B. V., "Composite, Grid-Stiffened Panel Design for Post Buckling Using HyperSizer," *Proceedings of the 43rd Structures, Structural Dynamics and Materials Conference, Denver, Colorado*, AIAA, April 2002.

[47] Cosserat, B. and Cosserat, F., *Théorie des Corps Deformables*, Hermann, Paris, 1909.

[48] Danielson, D. and Hodges, D., "Nonlinear Beam Kinematics by Decomposition of the Rotation Tensor," *Journal of Applied Mechanics*, Vol. 54, 1987, pp. 258–262.

[49] Yu, W. and Hodges, D. H., "A Geometrically Nonlinear Shear Deformation Theory for Composite Shells," *Journal of Applied Mechanics*, Vol. 71, No. 1, 2004, pp. 1 – 9.

[50] Pietraszkiewicz, W. and Eremeyev, V. A., "On Natural Strain Measures of the Non-Linear Micropolar Continuum," *International Journal of Solids and Structures*, Vol. 46, 2009, pp. 774–787.

[51] Hodges, D. H., *Nonlinear Composite Beam Theory*, AIAA, Washington, D.C., 2006.

[52] Yu, W., Hodges, D. H., and Volovoi, V. V., "Asymptotic Generalization of Reissner-Mindlin Theory: Accurate Three-dimensional Recovery for Composite Shells," *Computer Methods in Applied Mechanics and Engineering*, Vol. 191, No. 44, Oct. 2002, pp. 5087 – 5109.

[53] Pietraszkiewicz, W. and Eremeyev, V. A., "On Vectorially Parameterized Natural Strain Measures of the Non-Linear Cosserat Continuum," *International Journal of Solids and Structures*, Vol. 46, 2009, pp. 2477–2480.

[54] Berdichevsky, V. L., *Variational Principles of Continuum Mechanics*, Vol. 1 and 2, Springer Berlin, 2009.

[55] Yu, W. and Hodges, D. H., "Elasticity Solutions versus Asymptotic Sectional Analysis of Homogeneous, Isotropic, Prismatic Beams," *Journal of Applied Mechanics*, Vol. 71, No. 1, 2004, pp. 15 – 23.

[56] Yu, W., "Mathematical Construction of a Reissner-Mindlin Plate Theory for Composite Laminates," *International Journal of Solids and Structures*, Vol. 42, 2005, pp. 6680–6699.

[57] Yu, W., "An Exact Solution for Micromechanical Analysis of Periodically Layered Composites," *Mechanics Research Communications*, Vol. 46, 2012, pp. 71–75.

[58] Cesnik, C. E. S. and Hodges, D. H., "VABS: A New Concept for Composite Rotor Blade Cross-Sectional Modeling," *Journal of the American Helicopter Society*, Vol. 42, No. 1, January 1997, pp. 27 – 38.

[59] Lee, C.-Y. and Yu, W., "Homogenization and Dimensional Reduction of Composite Plates with In-Plane Heterogeneity," *International Journal of Solids and Structures*, Vol. 48, No. 10, 2011, pp. 1474–1484.

[60] Lee, C.-Y. and Yu, W., "Variational Asymptotic Modeling of Composite Beams with Spanwise Heterogeneity," *Computers & Structures*, Vol. 89, 2011, pp. 1503–1511.

[61] Dai, G. M. and Zhang, W. H., "Size effects of basic cell in static analysis of sandwich beams," *International Journal of Solids and Structures*, Vol. 45, 2008, pp. 2512–2533.

[62] Yi, S., Xu, L., Cheng, G., and Cai, Y., "FEM Formulation of Homogenization Method for Effective Properties of Periodic Heterogeneous Beams and Size Effect of Basic Cell in Thickness Direction," *Computers & Structures*, Vol. 156, 2015, pp. 1 – 11.

[63] Sharma, A., Sankar, B. V., and Haftka, R. T., "Homogenization of Plates with Microstructure and Application to Corrugated Core Sandwich Panels," *Proceedings of the 51st AIAA/ASME/ASCE /AHS/ASC Structures, Structural Dynamics, and Materials Conference*, AIAA, Orlando, Florida, Apr. 12–15 2010.

AIAA SciTech
13-17 January 2014, National Harbor, Maryland
55th AIAA/ASMe/ASCE/AHS/SC Structures, Structural Dynamics, and Materials Conference

A Comprehensive Evaluation of the Predictive Capabilities of Several Advanced Micromechanics Approaches

Hamsasew Sertse*, Liang Zhang†, Wenbin Yu‡, and Zheng Ye§

The objective of this paper is to comprehensively evaluate predictive capability and efficiency of advanced micromechanics approaches such as generalized method of cells (GMC), the high fidelity generalized method of cells (HFGMC), and the variational asymptotic method for unit cell homogenization (VAMUCH) and Finite Element Analysis (FEA) based micromechanics approaches using representative examples of heterogeneous materials such as: 1. continuous fiber reinforced composite; 2. particle reinforced composite; 3. discontinuous fiber reinforced composite; 4. woven composite. The evaluation reveals that GMC experiences noticeable loss of accuracy in predicting effective properties and also ineffectively recovers the local stress fields in all cases. HFGMC shows good agreement compared to FEA and also better recovers the local stress fields while VAMUCH shows an excellent agreement with FEA for both effective properties prediction and local field recovery. The shear moduli prediction of FEA is noticed to converge to the prediction of VAMUCH as the number of unit cell increases particularly for 3D analysis. It is also found that GMC is computationally efficient however VAMUCH with fewer elements can better approximate effective properties with better efficiency.

I. Introduction

In recent decades, heterogeneous materials become increasingly used in structural components due to their capability of exhibiting designated in-plane stiffness, bending stiffness, ultimate strength, or thermal expansion coefficient. The increasing use of heterogeneous materials leads to an increasing need for knowing the effective properties of such materials. It is doable to experimentally test the effective properties of such materials, but it is expensive and time consuming to manufacture a great amount of materials and to perform various tests on them. Although possible, it is computationally prohibitive to analyze these structures with all the microstructural details because the macroscopic dimensions of these structures are usually several orders of magnitude greater than the heterogeneity length scale. Therefore, it is of great practical value to solve the problems of heterogeneous materials using a micromechanics approach.

Numerous efforts have been devoted to the homogenization of heterogeneous materials. According to Ref. [1], the homogenization generally consists of the following steps:

- Idealize the heterogeneous material as consisting of numerous periodically arranged unit cells (UCs) and identify the UC;
- Perform a micromechanical analysis on the UC and obtain the effective material properties;
- Substitute the effective material properties into the macroscopic structure to obtain the global response of the structure;

*Graduate Research Assistant, Department of Mechanical and Aerospace Engineering, Utah State University, Logan, Utah 84322-4130.
†Postdoctoral Researcher, Department of Mechanical and Aerospace Engineering, Logan, Utah 84322-4130.
‡Associate Professor, School of Aeronautics and Astronautics, Purdue University, AIAA Associate Fellow.
§Formerly, Graduate Research Assistant, Department of Mechanical and Aerospace Engineering, Utah State University, Logan, Utah 84322-4130.

- Feedback the global response to UC and recover the local fields of interest (e.g., the displacement, strain, and stress fields).

The earliest rules of mixture approaches were developed based on the Voigt-Reuss hypotheses. Hill[2] demonstrated that the Voigt-Reuss hypotheses are capable of providing rigorous lower and upper bounds of the effective material properties of the UC. However, for real heterogeneous materials, the differences between these two bounds are generally too great to be of practical value. Elaborate efforts have been devoted to overcoming these drawbacks, i.e., either to reduce the aforementioned differences or to obtain close approximations between the lower and upper bounds. Examples include the mean field homogenization (MFH),[3] Hashin and Shtrikman's variational approach,[4] the third-order bounds,[5] the recursive cell method,[6] and the mathematical homogenization theories (MHT),[7,8] and many others. Hollister and Kikuchi[9] evaluated the predictive capabilities of these approaches and concluded that, for periodic or even locally periodic heterogeneous materials, MHT is superior to the other approaches.

Numerous attempts have been made not only to obtain the effective material properties but also to recover the local fields. Aboudi and his co-workers in Ref. [10,11] developed the method of cells (MOC) and later the generalized method of cells (GMC) to achieve this goal. A detailed review on these approaches can be found in Ref. [12]. The basic ideas of these approaches are subdividing the UC into numerous cuboid subcells, solving for the average strain and stress over each subcell, and obtaining an estimation of the local fields. These approaches solve the problems to a certain extent but suffer two major drawbacks. First, using cuboid subcells to represent the UC introduces considerable domain approximation errors. This can be understood by noting that it is generally more accurate to use a finite element mesh to represent the UC. Second, using the average local strains and stresses within each subcell to represent the real ones introduces considerable approximation errors. This can be understood by noting that it is generally more accurate to use shape functions and nodal values to represent the local fields. In fact, several attempts have been made to overcome the aforementioned drawbacks. An example is the high fidelity generalized method of cells (HFGMC). Ref. [13] demonstrated that HFGMC and VAMUCH, which will be mentioned in the next paragraph, significantly outperform GMC. However, they also found that, despite higher accuracy, HFGMC is more computationally costly. In this paper, the accuracy and efficiency of GMC, HFGMC and VAMUCH will be carefully assessed.

In recent years, Yu and his co-workers Ref. [1, 14–17] developed the variational asymptotic method for unit cell homogenization (VAMUCH), a general-purpose micromechanics approach, to handle the problems of heterogeneous materials. In fact, VAMUCH is not only capable of predicting the effective material properties and recovering the local fields but also has several unique features compared with other numerical methods. One of these features is that VAMUCH has the minimum number of assumptions. Specifically, VAMUCH starts with two basic assumptions associated with the micromechanical analysis of heterogeneous materials of identifiable UCs, i.e.,

1. The exact solutions of the field have their volume averages over the UC, i.e., if u_i denotes the exact displacements within the UC, there exists a v_i such that

$$v_i = \frac{1}{\Omega}\int_\Omega u_i d\Omega \equiv \langle u_i \rangle, \tag{1}$$

   where Ω denotes the domain occupied by the UC and also its volume, and $\langle\cdot\rangle$ denotes the volume average over Ω;

2. The effective material properties obtained using the micromechanical analysis are independent of the geometry and boundary conditions of the macroscopic structure, or to say, the effective material properties are assumed to be the intrinsic properties of the material when macroscopically viewed.

These two assumptions place the fewest restrictions on the problem solving. The first assumption means that the exact solutions of the field are integrable over the UC, or to say, that the heterogeneous material can be homogenized. The second assumption basically reflects the fact that the material properties are fully described by the constitutive relations for the material and are independent of the geometry and boundary of the macroscopic structure. Of course, the micromechanical analysis of the UC is desirable and appropriate only if $\eta = h/l \ll 1$, where h denotes the characteristic size of the UC and l denotes the characteristic size of the macroscopic structure.

The objective of this paper is to comprehensively evaluate the predictive capabilities of GMC, HFGMC, and VAMUCH. The basic formulations of these approaches are presented. The accuracy and efficiency of these approaches are comprehensively evaluated using examples such as predicting the effective material properties of: 1. continuous fiber reinforced composite; 2. particle reinforced composite; 3. discontinuous fiber reinforced composite; 4. woven composite. This evaluation is expected to help scientists and engineers select appropriate micromechanics approaches to solve various problems of heterogeneous materials.

II. Generalized Method of Cells (GMC)

As mentioned above, GMC is a variant of MOC. The derivations of GMC start with discretizing a UC into numerious rectangular (2D) or cuboid (3D) subcells. Specifically, without loss of generality, consider a UC consisting of $N_\alpha \times N_\beta \times N_\gamma$ subcells (see Figure 1), where α, β, and γ denote a set of running indices taking the values of $\alpha = 1, \ldots, N_\alpha$, $\beta = 1, \ldots, N_\beta$, and $\gamma = 1, \ldots, N_\gamma$, respectively. Let the UC be of length D, width H, and height L, and let each subcell be of length d_α, width h_β, and height l_γ. Introduce two Cartesian coordinate systems, $\mathbf{x} = (x_1, x_2, x_3)$ and $\bar{\mathbf{y}} = \left(\bar{y}_1^{(\alpha)}, \bar{y}_2^{(\beta)}, \bar{y}_3^{(\gamma)}\right)$. Let $\mathbf{x}$ denote the global coordinates describing the UC, and let $\bar{\mathbf{y}}$ denote the local coordinates describing each subcell, with its origin located at the geometric center of the subcell (see Figure 1). For notational convenience, also introduce the following accessory indices:

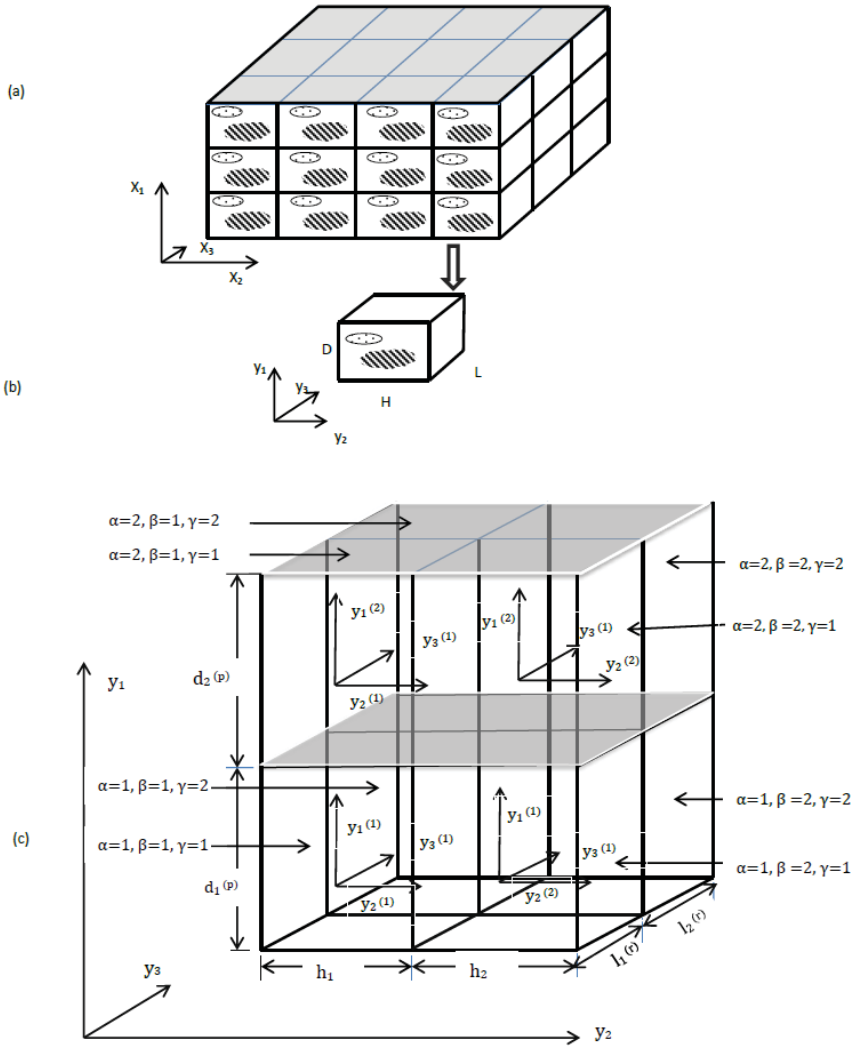

Figure 1. (a) Sketch of a heterogeneous material of identifiable UCs; (b) UC; (c) sketch of typical subcells (duplicated from Ref. [12]).

$$\hat{\alpha} = \begin{cases} \alpha+1 & \alpha < N_\alpha, \\ 1 & \alpha = N_\alpha, \end{cases} \quad \hat{\beta} = \begin{cases} \beta+1 & \beta < N_\beta, \\ 1 & \beta = N_\beta, \end{cases} \quad \hat{\gamma} = \begin{cases} \gamma+1 & \gamma < N_\alpha, \\ 1 & \gamma = N_\alpha. \end{cases} \tag{2}$$

Let the local displacements within subcell $(\alpha\beta\gamma)$ take the form of

$$u_i^{(\alpha\beta\gamma)} = w_i^{(\alpha\beta\gamma)}(\mathbf{x}) + \bar{y}_1^{(\alpha)}\chi_i^{(\alpha\beta\gamma)} + \bar{y}_2^{(\beta)}\phi_i^{(\alpha\beta\gamma)} + \bar{y}_3^{(\gamma)}\psi_i^{(\alpha\beta\gamma)} \quad i = 1,2,3, \tag{3}$$

where $w_i^{(\alpha\beta\gamma)}(\mathbf{x})$ denote the global displacements at the origin of the local coordinates, and $\chi_i^{(\alpha\beta\gamma)}$, $\phi_i^{(\alpha\beta\gamma)}$, and $\psi_i^{(\alpha\beta\gamma)}$ denote the microvariables characterizing the linear dependence of $u_i^{(\alpha\beta\gamma)}$ on $\bar{\mathbf{y}}$. It can be verified that Eq. (3) leads to a uniform strain field within the subcell. Accordingly, the local strains corresponding to $u_i^{(\alpha\beta\gamma)}$ can be obtained from Eq. (3) as

$$\epsilon_{11}^{(\alpha\beta\gamma)} = \chi_1^{(\alpha\beta\gamma)}, \quad \epsilon_{22}^{(\alpha\beta\gamma)} = \phi_2^{(\alpha\beta\gamma)}, \quad \epsilon_{33}^{(\alpha\beta\gamma)} = \psi_3^{(\alpha\beta\gamma)}, \tag{4}$$

$$2\epsilon_{23}^{(\alpha\beta\gamma)} = \phi_3^{(\alpha\beta\gamma)} + \psi_2^{(\alpha\beta\gamma)}, \quad 2\epsilon_{13}^{(\alpha\beta\gamma)} = \psi_1^{(\alpha\beta\gamma)} + \chi_3^{(\alpha\beta\gamma)}, \tag{4'}$$

$$2\epsilon_{12}^{(\alpha\beta\gamma)} = \phi_1^{(\alpha\beta\gamma)} + \chi_2^{(\alpha\beta\gamma)}, \tag{4''}$$

and the average or global strains over the UC can be expressed as

$$\bar{\epsilon}_{ij} = \frac{1}{DHL}\sum_{\alpha=1}^{N_\alpha}\sum_{\beta=1}^{N_\beta}\sum_{\gamma=1}^{N_\gamma} d_\alpha h_\beta l_\gamma \epsilon_{ij}^{(\alpha\beta\gamma)}. \tag{5}$$

Without loss of generality, let each constituent exhibit a temperature-dependent, inelastic behavior. In this case, the constitutive relations for a constituent can take the following general form:

$$\sigma_{ij}^{(\alpha\beta\gamma)} = \mathcal{C}_{ijkl}^{(\alpha\beta\gamma)}\left(\epsilon_{kl}^{(\alpha\beta\gamma)} - \epsilon_{kl}^{I(\alpha\beta\gamma)} - \epsilon_{kl}^{T(\alpha\beta\gamma)}\right), \tag{6}$$

where $\mathcal{C}_{ijkl}$ denotes the fourth-order elasticity tensor, $\epsilon_{kl}^{I(\alpha\beta\gamma)}$ denotes the inelastic strains, and $\epsilon_{kl}^{T(\alpha\beta\gamma)}$ denotes the thermal strains. Similarly to Eq. (5), the average or global stresses over the UC can be expressed as

$$\bar{\sigma}_{ij} = \frac{1}{DHL}\sum_{\alpha=1}^{N_\alpha}\sum_{\beta=1}^{N_\beta}\sum_{\gamma=1}^{N_\gamma} d_\alpha h_\beta l_\gamma \sigma_{ij}^{(\alpha\beta\gamma)}. \tag{7}$$

The local displacements must satisfy the continuity conditions and the periodic boundary conditions between neighboring unit cells. This leads to the following relations:

$$\sum_{\alpha=1}^{N_\alpha} d_\alpha \epsilon_{11}^{(\alpha\beta\gamma)} = d\bar{\epsilon}_{11}, \quad \sum_{\beta=1}^{N_\beta} h_\beta \epsilon_{22}^{(\alpha\beta\gamma)} = h\bar{\epsilon}_{22}, \quad \sum_{\gamma=1}^{N_\gamma} l_\gamma \epsilon_{33}^{(\alpha\beta\gamma)} = l\bar{\epsilon}_{33}, \tag{8}$$

$$\sum_{\alpha=1}^{N_\alpha}\sum_{\beta=1}^{N_\beta} d_\alpha h_\beta \epsilon_{12}^{(\alpha\beta\gamma)} = dh\bar{\epsilon}_{12}, \quad \sum_{\beta=1}^{N_\beta}\sum_{\gamma=1}^{N_\gamma} h_\beta l_\gamma \epsilon_{23}^{(\alpha\beta\gamma)} = hl\bar{\epsilon}_{23}, \tag{8'}$$

$$\sum_{\alpha=1}^{N_\alpha}\sum_{\gamma=1}^{N_\gamma} d_\alpha l_\gamma \epsilon_{13}^{(\alpha\beta\gamma)} = dl\bar{\epsilon}_{13}. \tag{8''}$$

Eq. (8) can be rewritten in a matrix form as

$$\mathbf{A}_G \boldsymbol{\epsilon}_s = \mathbf{J}\bar{\boldsymbol{\epsilon}}, \tag{9}$$

where $\boldsymbol{\epsilon}_s$ denotes the $6N_\alpha N_\beta N_\gamma$-order subcell strain column matrix, $\bar{\boldsymbol{\epsilon}}$ denotes the sixth-order global stain column matrix, $\mathbf{A}_G$ is a $N_\alpha(N_\beta+N_\gamma+1)+N_\beta(N_\gamma+1)+N_\gamma$ by $6N_\alpha N_\beta N_\gamma$ matrix, and $\mathbf{J}$ is a $N_\alpha(N_\beta+N_\gamma+1)+N_\beta(N_\gamma+1)+N_\gamma$ by 6 matrix.

Similarly to the local displacements, the local tractions also must satisfy the continuity conditions in an average sense between neighboring subcells. This leads to the following relations.

$$\sigma_{11}^{(\alpha\beta\gamma)} = \sigma_{11}^{(\hat{\alpha}\beta\gamma)} \quad \alpha = 1,\ldots,N_\alpha - 1, \quad \beta = 1,\ldots,N_\beta, \quad \gamma = 1,\ldots,N_\gamma, \tag{10}$$

$$\sigma_{22}^{(\alpha\beta\gamma)} = \sigma_{22}^{(\alpha\hat{\beta}\gamma)} \quad \alpha = 1,\ldots,N_\alpha, \quad \beta = 1,\ldots,N_\beta - 1, \quad \gamma = 1,\ldots,N_\gamma, \tag{10'}$$

$$\sigma_{33}^{(\alpha\beta\gamma)} = \sigma_{33}^{(\alpha\beta\hat{\gamma})} \quad \alpha = 1,\ldots,N_\alpha, \quad \beta = 1,\ldots,N_\beta, \quad \gamma = 1,\ldots,N_\gamma - 1. \tag{10''}$$

$$\sigma_{23}^{(\alpha\beta\gamma)} = \sigma_{23}^{(\alpha\hat{\beta}\gamma)} \quad \alpha = 1,\ldots,N_\alpha, \quad \beta = 1,\ldots,N_\beta - 1, \quad \gamma = 1,\ldots,N_\gamma, \tag{11}$$

$$\sigma_{32}^{(\alpha\beta\gamma)} = \sigma_{32}^{(\alpha\beta\hat{\gamma})} \quad \alpha = 1,\ldots,N_\alpha, \quad \beta = N_\beta, \quad \gamma = 1,\ldots,N_\gamma - 1. \tag{11'}$$

$$\sigma_{13}^{(\alpha\beta\gamma)} = \sigma_{13}^{(\hat{\alpha}\beta\gamma)} \quad \alpha = 1,\ldots,N_\alpha - 1, \quad \beta = 1,\ldots,N_\beta, \quad \gamma = 1,\ldots,N_\gamma, \tag{12}$$

$$\sigma_{31}^{(\alpha\beta\gamma)} = \sigma_{31}^{(\alpha\beta\hat{\gamma})} \quad \alpha = N_\alpha, \quad \beta = 1,\ldots,N_\beta, \quad \gamma = 1,\ldots,N_\gamma - 1. \tag{12'}$$

$$\sigma_{12}^{(\alpha\beta\gamma)} = \sigma_{12}^{(\hat{\alpha}\beta\gamma)} \quad \alpha = 1,\ldots,N_\alpha - 1, \quad \beta = 1,\ldots,N_\beta, \quad \gamma = 1,\ldots,N_\gamma, \tag{13}$$

$$\sigma_{21}^{(\alpha\beta\gamma)} = \sigma_{21}^{(\alpha\hat{\beta}\gamma)} \quad \alpha = N_\alpha, \quad \beta = 1,\ldots,N_\beta - 1, \quad \gamma = 1,\ldots,N_\gamma. \tag{13'}$$

Eqs. (10) - (13) can be rewritten in terms of $\epsilon_{ij}^{(\alpha\beta\gamma)}$, $\epsilon_{ij}^{I(\alpha\beta\gamma)}$, and $\epsilon_{ij}^{T(\alpha\beta\gamma)}$ using Eq. (6). The resulting equations can be further rewritten in a matrix form as

$$\mathbf{A}_M \left(\boldsymbol{\epsilon}_s - \boldsymbol{\epsilon}_s^I - \boldsymbol{\epsilon}_s^T\right) = \mathbf{O}, \tag{14}$$

where $\boldsymbol{\epsilon}_s^I$ and $\boldsymbol{\epsilon}_s^T$ denote the $6N_\alpha N_\beta N_\gamma$-order subcell inelastic and thermal strain column matrix, respectively, and $\mathbf{A}_M$ is a $6N_\alpha N_\beta N_\gamma - (N_\alpha N_\beta + N_\alpha N_\gamma + N_\beta N_\gamma) - (N_\alpha + N_\beta + N_\gamma)$ by $6N_\alpha N_\beta N_\gamma$ matrix.

Combining Eqs. (9) and (14) gives

$$\tilde{\mathbf{A}}\boldsymbol{\epsilon}_s - \tilde{\mathbf{D}}\left(\boldsymbol{\epsilon}_s^I + \boldsymbol{\epsilon}_s^T\right) = \mathbf{K}\bar{\epsilon}, \tag{15}$$

where

$$\tilde{\mathbf{A}} = \begin{bmatrix} \mathbf{A}_M \\ \mathbf{A}_G \end{bmatrix}, \quad \tilde{\mathbf{D}} = \begin{bmatrix} \mathbf{A}_M \\ \mathbf{O} \end{bmatrix}, \quad \mathbf{K} = \begin{bmatrix} \mathbf{O} \\ \mathbf{J} \end{bmatrix}. \tag{16}$$

Rearranging Eq. (15) gives

$$\boldsymbol{\epsilon}_s = \mathbf{A}\bar{\boldsymbol{\epsilon}} + \mathbf{D}\left(\boldsymbol{\epsilon}_s^I + \boldsymbol{\epsilon}_s^T\right), \tag{17}$$

where

$$\mathbf{A} = \tilde{\mathbf{A}}^{-1}\mathbf{K}, \quad \mathbf{D} = \tilde{\mathbf{A}}^{-1}\tilde{\mathbf{D}}. \tag{18}$$

Till now, $\boldsymbol{\epsilon}_s$ and $\boldsymbol{\epsilon}^{(\alpha\beta\gamma)}$ can be uniquely determined. In addition, the local stresses can be recovered as

$$\boldsymbol{\sigma}^{(\alpha\beta\gamma)} = \mathbf{C}^{(\alpha\beta\gamma)}\left[\mathbf{A}^{(\alpha\beta\gamma)}\bar{\boldsymbol{\epsilon}} + \mathbf{D}^{(\alpha\beta\gamma)}\left(\boldsymbol{\epsilon}_s^I + \boldsymbol{\epsilon}_s^T\right) - \left(\boldsymbol{\epsilon}_s^{I(\alpha\beta\gamma)} + \boldsymbol{\epsilon}_s^{T(\alpha\beta\gamma)}\right)\right], \tag{19}$$

and the global stresses can be obtained using

$$\bar{\boldsymbol{\sigma}} = \mathbf{C}^*\left(\bar{\boldsymbol{\epsilon}} - \bar{\boldsymbol{\epsilon}}^I - \bar{\boldsymbol{\epsilon}}^T\right), \tag{20}$$

where $\mathbf{C}^*$ denotes the effective elasticity matrix, and $\bar{\boldsymbol{\epsilon}}^I$ and $\bar{\boldsymbol{\epsilon}}^T$ denote the global inelastic and thermal strains, respectively. Interested readers can refer to Ref. [18] for more details on the GMC theory.

III. High Fidelity Generalized Method of Cells

As mentioned above, HFGMC is a variant of MOC and GMC. The basic concept of HFGMC is quite similar with that of GMC except that HFGMC adopts a second-order expansion of the local displacements, $u_i^{(\alpha\beta\gamma)}$. Specifically, for HFGMC, $u_i^{(\alpha\beta\gamma)}$ take the form of

$$\begin{aligned} u_i^{(\alpha\beta\gamma)} = {} & \bar{\epsilon}_{ij}x_j + w_{i(000)}^{(\alpha\beta\gamma)} + \bar{y}_1^{(\alpha)} w_{i(100)}^{(\alpha\beta\gamma)} + \bar{y}_2^{(\beta)} w_{i(010)}^{(\alpha\beta\gamma)} + \bar{y}_3^{(\gamma)} w_{i(001)}^{(\alpha\beta\gamma)} \\ & + \frac{1}{2}\left(3\bar{y}_1^{(\alpha)2} - \frac{d_\alpha^2}{4}\right) w_{i(200)}^{(\alpha\beta\gamma)} + \frac{1}{2}\left(3\bar{y}_2^{(\beta)2} - \frac{h_\beta^2}{4}\right) w_{i(020)}^{(\alpha\beta\gamma)} + \frac{1}{2}\left(3\bar{y}_3^{(\gamma)2} - \frac{l_\gamma^2}{4}\right) w_{i(002)}^{(\alpha\beta\gamma)}, \end{aligned} \tag{21}$$

where $w_{i(000)}^{(\alpha,\beta,\gamma)}$ denotes the volume-averaged displacements over the UC, and $w_{i(lmn)}^{(\alpha\beta\gamma)}$ are higher-order terms to be determined by interfacial and periodic conditions. Recall that, for GMC, $u_i^{(\alpha\beta\gamma)}$ merely represents a linear displacement field within the subcell. Here Eq. (21) introduces several second-order terms, which implies higher accuracy but also higher computational costs. To avoid redundancy, the derivations of HFGMC will not be presented in this paper. Interested readers can refer to Ref. [18] for more details on the HFGMC theory.

IV. Variational Asymptotic Method for Unit Cell Homogenization

VAMUCH is a general-purpose micromechanics approach that is capable of predicting the effective properties of heterogeneous materials and recovering the local fields. The derivations of VAMUCH start from the variational statement of a heterogeneous continuum. Note that the macroscopic dimensions of these structures are usually several orders of magnitude greater than the heterogeneity length scale. This leads one to formulate the problem of homogenization as a problem of constrained minimization on a single UC and to perform an asymptotic analysis of the variational statement. Specifically, consider a heterogeneous material of an identifiable UC. Introduce two Cartesian coordinate systems, $\mathbf{x} = (x_1, x_2, x_3)$ and $\mathbf{y} = (y_1, y_2, y_3)$. Let x_i denote the global coordinates describing the macroscopic structure, and let y_i denote the local coordinates describing the UC. The variational statement of the problem can be formulated as seeking the minimum of the functional

$$\Pi_\Omega = \frac{1}{2\Omega}\int_\Omega \left[\bar{\epsilon}_{ij} + \chi_{(i|j)}\right] \mathcal{C}_{ijkl} \left[\bar{\epsilon}_{kl} + \chi_{(k|l)}\right] d\Omega \tag{22}$$

within a UC, where $\mathcal{C}_{ijkl}$ denote the fourth-order elasticity tensor, $\bar{\epsilon}_{ij}$ denotes the components of the global strain tensor for the homogenized structure, χ_i denotes the components of the fluctuation functions and must satisfy the periodic boundary conditions along with constraint

$$\langle \chi_i \rangle = 0, \tag{23}$$

and

$$\chi_{(i|j)} = \frac{1}{2}\left(\frac{\partial \chi_i}{\partial y_j} + \frac{\partial \chi_j}{\partial y_i}\right). \tag{24}$$

Introduce the following matrix notations:

$$\bar{\epsilon} = \begin{bmatrix} \bar{\epsilon}_{11} & 2\bar{\epsilon}_{12} & \bar{\epsilon}_{22} & 2\bar{\epsilon}_{13} & 2\bar{\epsilon}_{23} & \bar{\epsilon}_{33} \end{bmatrix}^T, \tag{25}$$

$$\begin{Bmatrix} \frac{\partial \chi_1}{\partial y_1} \\ \frac{\partial \chi_1}{\partial y_2} + \frac{\partial \chi_2}{\partial y_1} \\ \frac{\partial \chi_2}{\partial y_2} \\ \frac{\partial \chi_1}{\partial y_3} + \frac{\partial \chi_3}{\partial y_1} \\ \frac{\partial \chi_2}{\partial y_3} + \frac{\partial \chi_3}{\partial y_2} \\ \frac{\partial \chi_3}{\partial y_3} \end{Bmatrix} = \begin{bmatrix} \frac{\partial}{\partial y_1} & 0 & 0 \\ \frac{\partial}{\partial y_2} & \frac{\partial}{\partial y_1} & 0 \\ 0 & \frac{\partial}{\partial y_2} & 0 \\ \frac{\partial}{\partial y_3} & 0 & \frac{\partial}{\partial y_1} \\ 0 & \frac{\partial}{\partial y_3} & \frac{\partial}{\partial y_2} \\ 0 & 0 & \frac{\partial}{\partial y_3} \end{bmatrix} \begin{Bmatrix} \chi_1 \\ \chi_2 \\ \chi_3 \end{Bmatrix} \equiv \Gamma_h \chi, \tag{28'}$$

where Γ_h denotes an operator matrix, and χ denotes a column matrix containing the three components of the fluctuation functions. Let χ be discretized using finite elements as

$$\chi\left(x_i;y_i\right)=S\left(y_i\right)\mathrm{X}\left(x_i\right), \tag{26}$$

where S denotes the shape functions, and X denotes a column matrix of the nodal values of the fluctuation functions for all the active nodes. The discretized version of Eq. (22) can then be obtained as

$$\Pi_\Omega=\frac{1}{2\Omega}\left(\mathrm{X}^T E\mathrm{X}+2\mathrm{X}^T D_{h\epsilon}\bar{\epsilon}+\bar{\epsilon}^T D_{\epsilon\epsilon}\bar{\epsilon}\right), \tag{27}$$

where

$$E=\int_\Omega\left(\Gamma_h S\right)^T D\left(\Gamma_h S\right)d\Omega,\quad D_{h\epsilon}=\int_\Omega\left(\Gamma_h S\right)^T Dd\Omega,\quad D_{\epsilon\epsilon}=\int_\Omega Dd\Omega \tag{28}$$

with D denoting the 6×6 stiffness matrix condensed from $\mathcal{C}_{ijkl}$. It can be derived from Eq. (27) that Π_Ω attains its minimum only if

$$E\mathrm{X}=-D_{h\epsilon}\bar{\epsilon} \tag{29}$$

which can be used to solve for X as;

$$\mathrm{X}=\mathrm{X}_0\bar{\epsilon}. \tag{30}$$

Eq. (30) implies that X is linearly dependent on $\bar{\epsilon}$. Substituting Eq. (30) into Eq. (27) gives the minimum of Π_Ω as

$$\Pi_\Omega=\frac{1}{2\Omega}\bar{\epsilon}^T\left(\mathrm{X}_0^T D_{h\epsilon}+D_{\epsilon\epsilon}\right)\bar{\epsilon}\equiv\frac{1}{2}\bar{\epsilon}^T\bar{D}\bar{\epsilon}, \tag{31}$$

where $\bar{D}$ denotes the so-called effective stiffness matrix, and $\bar{\epsilon}$ denotes the global strain column matrix.

Till now, the effective material properties can be fully determined. In addition, if the local fields are of interest, they can be recovered using the global displacements, v, the global strains, $\bar{\epsilon}$, and the fluctuation functions, χ. Specifically, the local displacements can be recovered as

$$u=v+\begin{bmatrix}\dfrac{\partial v_1}{\partial x_1} & \dfrac{\partial v_1}{\partial x_2} & \dfrac{\partial v_1}{\partial x_3}\\ \dfrac{\partial v_2}{\partial x_1} & \dfrac{\partial v_2}{\partial x_2} & \dfrac{\partial v_2}{\partial x_3}\\ \dfrac{\partial v_3}{\partial x_1} & \dfrac{\partial v_3}{\partial x_2} & \dfrac{\partial v_3}{\partial x_3}\end{bmatrix}\begin{Bmatrix}y_1\\ y_2\\ y_3\end{Bmatrix}+S\bar{\mathrm{X}}_0\bar{\epsilon}, \tag{32}$$

where u and v denote the local and global displacement column matrices, respectively, and $\bar{\mathrm{X}}_0$ denotes the nodal values of fluctuation functions modified from X_0 by the periodic boundary conditions and Eq. (23). The local strains can be recovered as

$$\epsilon=\bar{\epsilon}+\Gamma_h S\bar{\mathrm{X}}_0\bar{\epsilon}, \tag{33}$$

where ϵ denotes the the local strain column matrix. The local stresses can be recovered from the local strains as

$$\sigma=D\epsilon. \tag{34}$$

It is worth notice that, although VAMUCH seems as verstile as the finite element method, it is by no means an extension of the traditional displacement-based finite element method. In fact, the VAMUCH code has the following distinctive features:

- The complete set of effective material properties can be obtain within one analysis, without the application of any external loads;
- The fluctuation functions and the displacements are uniquely determined;
- The effective material properties and the recovered local fields are directly obtained with the same accuracy of the fluctuation functions, without any postprocessing-type calculations (e.g., averaging the stresses or the strains),
- The dimensionality of the problem is determined by that of the periodicity of the UC.

Interested readers can refer to Refs. [1] for more details on the VAMUCH theory.

V. Results and Discussions

In this section, the accuracy and efficiency of GMC, HFGMC and VAMUCH will be comprehensively evaluated using representative examples of heterogeneous materials such as: 1. continuous fiber reinforced composite; 2. particle reinforced composite; 3. discontinuous fiber reinforced composite; 4. woven composite. The outputs of GMC and HFGMC will be obtained using micromechanics analysis code MAC/GMC 4.0 developed by NASA Glenn Research Center.[18] Finite Element Analysis (FEA) based micromechanics approach proposed by Sun and Vaidya[19] is considered for all subsequent analyses as a benchmark for comparison of effective properties and local stress field prediction of GMC, HFGMC and VAMUCH. The computing time will also be studied for all the approaches including FEA using the ANSYS software. For consistency, the same computer is used to obtain the FEA elapsed time spent for computing solution of the analysis. Finally the outputs of GMC, HFGMC and VAMUCH will be compared with converged results of FEA.

It should be noted that the application of FEA for predicting effective properties of composite materials[19] does not rigorously simulate the periodic boundary conditions adopted in GMC, HFGMC and VAMUCH. Some differences are expected between the results of FEA and other approaches. But considering a RVE containing multiple unit cells should reduce the effects due to boundary conditions and converge to those approaches using periodic boundary conditions.

A. Continuous Fiber Reinforced Composite

First, let the unit cell of the continuous fiber reinforced composite be identified as a square matrix embedded with a circular fiber. Let the fiber be located at the center of the unit cell arranged in a square array and also let the fiber volume ratio be 40%. The local Cartesian coordinates can be introduced at the center of unit cell as $y = (y_1, y_2, y_3)$ with y_1 parallel to the fiber direction as depicted in Figure 2. Second, let material of the matrix and fiber be boron and aluminum, respectively, with the material parameters listed in Table 1, where E and ν are the Young's elastic modulus and Poisson's ratio, respectively.

Table 1. Material parameters of Boron and Aluminium

Material	E(GPa)	ν
Boron	379.3	0.1
Aluminium	68.3	0.3

A 66×66 subcell grid is used for GMC and HFGMC, and a mesh of 4500 8-noded quadrilateral elements is used for VAMUCH and FEA. FEA is conducted using PLANE82 element for G_{23} and SOLID95 elements for remaining effective properties. The comparison of the predicted results in Table 2 reveals that GMC slightly underpredicts both normal and shear moduli but HFGMC sufficiently estimates most of predicted properties except G_{23}. On the contrary, VAMUCH shows an excellent agreement with converged FEA results for all the predicted effective properties.

Table 2. Predicted effective properties of the fiber reinforced composite

	E_{11}(MPa)	E_{22}(MPa)	G_{12}(MPa)	G_{23}(MPa)	ν_{12}	ν_{23}
GMC	193300	125100	45270	39740	0.2119	0.2809
HFGMC	193500	127500	48320	42580	0.2090	0.2789
VAMUCH	193530	127676	48303	41702	0.2090	0.2777
FEA	193530	127680	48295	41702	0.2090	0.2777

The computing time has also been obtained for GMC, HFGMC, VAMUCH, and FEA for different element numbers. The computing times verse the number of elements are plotted for each approach as shown in Figure 3. To critically investigate the computing time verses the accuracy of these approaches, it is worthwhile to evaluate their effectiveness for different element numbers. From this study, it is learned that GMC and HFGMC (with 4356 elements) run for 0.118 seconds and 12.33 minutes, respectively, while FEA and VAMUCH take approximately 8.2 seconds and 28.65 seconds for 4500 elements, respectively. It is clear to observe that GMC is more efficient however, as shown in Table 3, the loss of accuracy of GMC is greater compared to the others, for instance, the losses of accuracy of GMC for longitudinal moduli E_{11} and E_{22} are

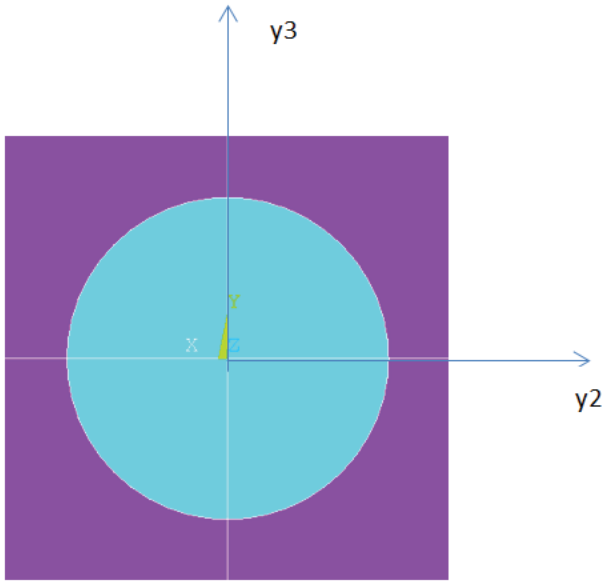

Figure 2. Unit cell for continuous fiber reinforced composite

0.118% and 2.02% , respectively, while HFGMC shows relatively better agreement resulting in 0.0156% and 0.142% losses of accuracy for E_{11} and E_{22}, respectively. These losses of accuracy (of GMC and HFGMC) are observed to be significant compared to VAMUCH (with 4500 elements) that has a capability of predicting E_{11} and E_{22} with 0.00% and 0.0031% losses of accuracy, respectively. Moreover, GMC experiences greater loss of accuracy for longitudinal shear modulus, G_{12}, which is approximated to be 6.26% compared with converged FEA results. On the contrary, HFGMC and VAMUCH show better agreement with FEA. From Table 3, it is generally noticed that the losses of accuracy of VAMUCH with 80 elements are much lower than that of GMC and HFGMC compared to FEA results. VAMUCH takes approximately 0.0467 seconds to complete the run which makes VAMUCH faster than GMC. The computing time with respect to number of elements is also plotted in Figure 3, which shows that HFGMC takes significantly more time than VAMUCH, particularly so when the number of elements is large.

The predicted effective properties are used to obtain the local stress recovery of GMC, HFGMC and VAMUCH for continuous reinforced composite. Considering a plane strain problem, it is assumed that the homogenized medium is subjected to a normal load in the x_2 direction that generates global strain $\bar{\varepsilon}_{22}$=0.1%, and the corresponding strain $\bar{\varepsilon}_{33}$ in the x_3 direction obtained based on the predicted Poisson's ratios of each approach. All other strains would be zero, i.e, $\bar{\varepsilon}_{11} = \bar{\varepsilon}_{12} = \bar{\varepsilon}_{23} = \bar{\varepsilon}_{13}$=0. These strains are fed back to the model to recover the local stresses both along y_2 ($y_3 = 0$) and y_3 ($y_2 = 0$).

Table 3. Comparison of accuracy of GMC, HFGMC and VAMUCH

	Elements	E_{11}(MPa)	E_{22}(MPa)	G_{12}(MPa)	G_{23}(MPa)	ν_{12}	ν_{23}
GMC	4356	0.119%	2.02%	5.70%	4.70%	1.38%	1.13%
HFGMC	4356	0.015%	0.14%	0.64%	-2.10%	0.0054%	-0.432%
VAMUCH	80	0.00244%	-0.035%	0.62%	0.10%	0.006%	0.071%

As it can be seen from Figure 4, GMC and HFGMC poorly recover the local stress fields σ_{11} along y_2 ($y_3 = 0$) for fiber section and at the interface but both roughly capture stress in the matrix. On the contrary, VAMUCH fully recovers the local stress σ_{11} with the same level of accuracy as FEA for fiber section, at interface and for matrix section of continuous fiber reinforced composite. The local stress σ_{22}

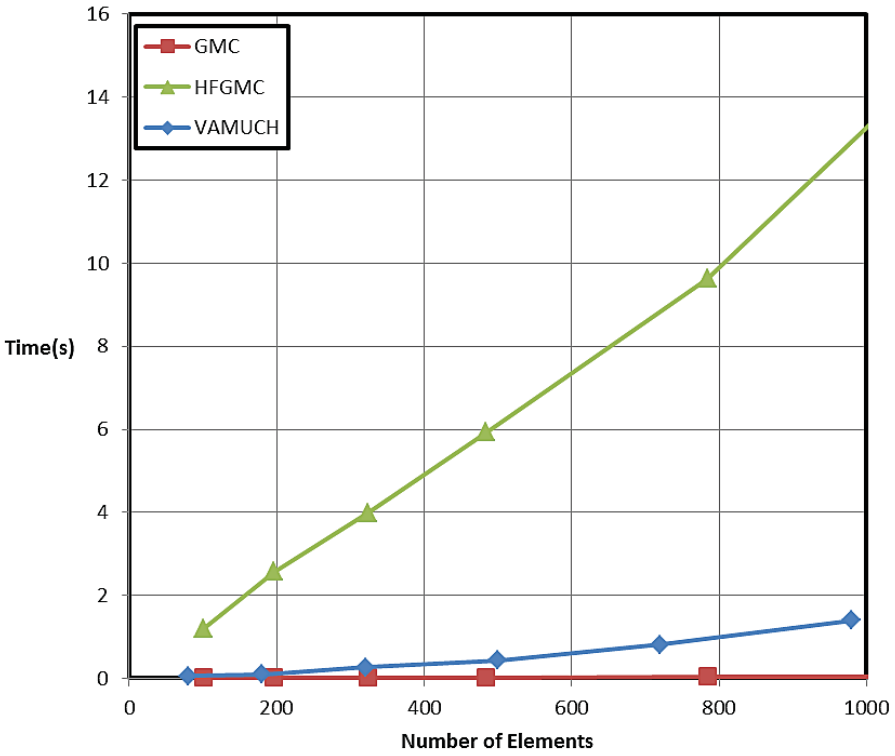

Figure 3. Computing time for GMC, HFGMC and VAMUCH

along y_3 ($y_2 = 0$), as depicted in Figure 5, is fairly recovered by both GMC and HFGMC specifically at the fiber section compared with FEA result however GMC is unable to well capture the stress disturbance at the interface. Conversely as indicated on the same figure, the local stress σ_{22} is well recovered by VAMUCH with the same level of accuracy as FEA. From Figure 6, it is evident that GMC is unable to sufficiently recover the local stress σ_{33} along y_3 ($y_2 = 0$). This is mainly due to its inherent shear coupling problem, yet HFGMC roughly captures the local stresses. Generally speaking, it is clear to observe that VAMUCH well recovers the local stress fields for both along y_2 ($y_3 = 0$) and y_3 ($y_2 = 0$) with same level of accuracy as FEA for all local stress field recovery as seen from Figures 4 to 6.

B. Particle Reinforced Composite

In this case, let a spherical inclusion with 40% fiber volume be embedded at the center of cuboidal matrix to be used as a unit cell for particle reinforced composite. Let the local Cartesian coordinates be set at the center of sphere. The particle and the matrix are made of boron and aluminium, respectively, with the material parameters listed in Table 1.

For GMC, a built-in spherical particle reinforced model with 343 elements is used as a unit cell. The current version of MAC/GMC 4.0 does not support 3D analysis for HFGMC thus it is omitted in all subsequent 3D analyses. A cuboidal unit cell with 7776 elements is used for VAMUCH and FEA. Further refining of the mesh does not have any significant improvement on the output of GMC, however it may slightly change the outputs of VAMUCH and FEA. The result of FEA analysis is obtained by using SOLID95 elements.

The prediction outputs of particle reinforced composite in Table 4 show that GMC underpredicts longitudinal moduli approximately by 3.095%, while VAMUCH shows an excellent agreement with converged FEA outputs. For particle reinforced composite, the effect of boundary conditions are found to be more observable on the prediction of axial shear modulus as learned from various analyses with multiple number of unit cells. It is timely noted that the boundary conditions in Ref. [19] was developed for continuous fiber reinforced composites, not necessarily suitable for other composites. However, as the number of unit cells

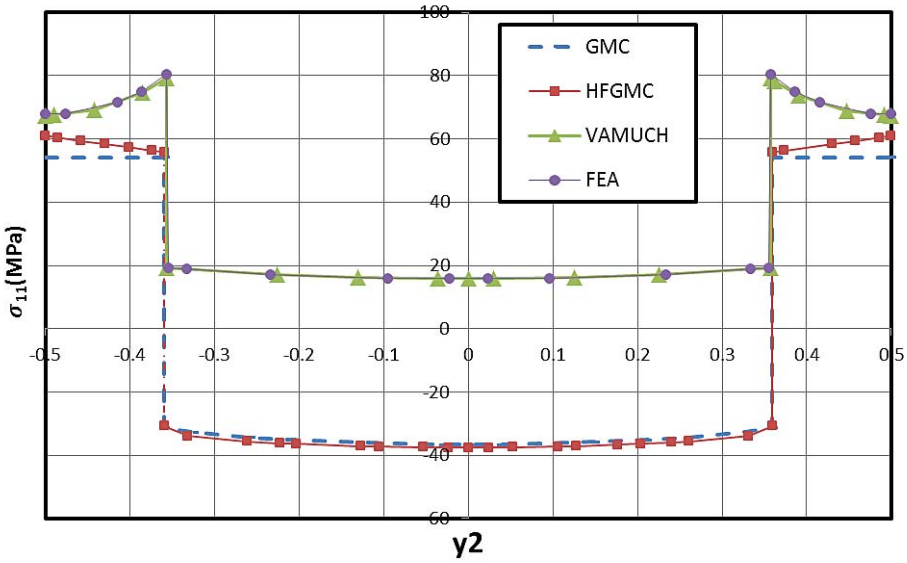

Figure 4. Comparison of recovered local stress σ_{11} along y_2 $(y_3 = 0)$

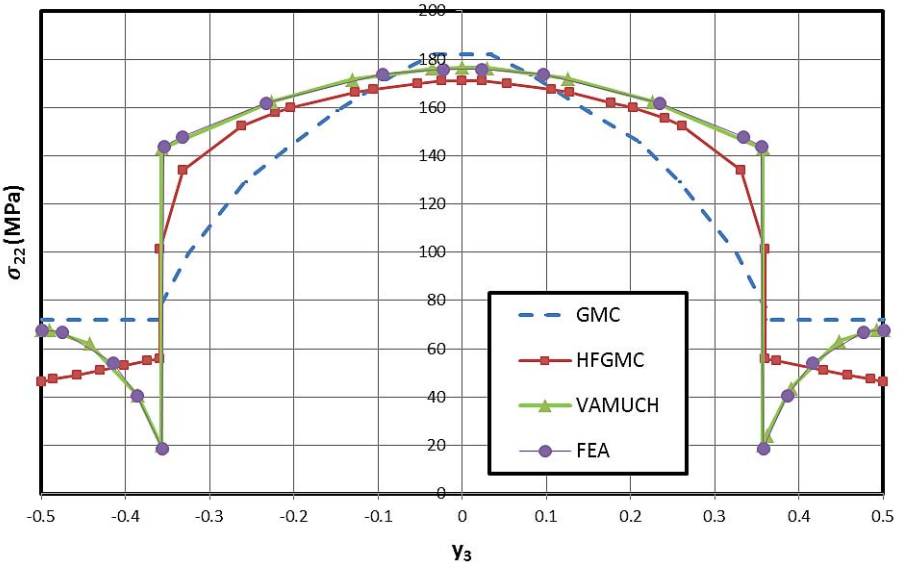

Figure 5. Comparison of recovered local stress σ_{22} along y_3 $(y_2 = 0)$

Table 4. Predicted effective properties of the particle reinforced composite.

	E_{11}(MPa)	E_{22}(MPa)	G_{12}(MPa)	G_{23}(MPa)	ν_{12}	ν_{23}
GMC	134800	134800	43340	43340	0.2229	0.2229
VAMUCH	139106	139106	46797	46797	0.2167	0.2167
FEA	139106	139106	47439	46755	0.2167	0.2167

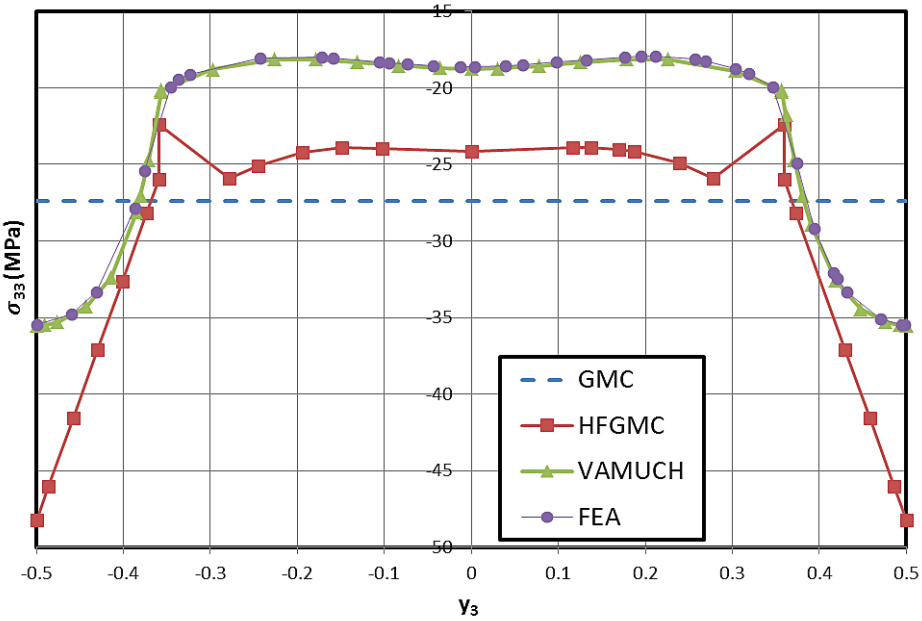

Figure 6. Comparison of recovered local stress σ_{33} along y_3 ($y_2 = 0$)

Table 5. Computing time for particle reinforced composite

	GMC	VAMUCH	FEA
Elements	343	7776	7776
Time(s)	0.052	982.52	145.4

included in the RVE increases, we can effectively avoid the boundary effect. FEA predicts G_{12} to be 49471 (MPa) for a single unit cell. As number of unit cell increases to 27 ($3 \times 3 \times 3$) unit cells, the prediction of FEA for G_{12} lowered to 47750 (MPa) based on global shear strains and shear stresses. It is believed that the middle unit cell is generally less affected by the boundary conditions and thus it is also used to predict the axial shear modulus. We first use Eqs. (35) and (36) to obtain average shear stress and average shear strain in the middle UC, respectively. The effective axial shear modulus G_{12} is then calculated as the ratio of average shear stress and average shear strain.

$$\bar{\sigma}_{12} = \frac{1}{\Omega} \sum \sigma_{12_i} \Omega_i, \tag{35}$$

where $\bar{\sigma}_{12}$ denotes average shear stress in the middle unit cell, Ω denotes the volume occupied by the middle UC and Ω_i denotes volume of subcell i within middle UC and σ_{12_i} denotes the shear stress of Ω_i.

$$\bar{\varepsilon}_{12} = \frac{1}{\Omega} \sum \varepsilon_{12_i} \Omega_i, \tag{36}$$

where $\bar{\varepsilon}_{12}$ denotes average shear strain in the middle unit cell. This approach gives more reasonable result as the number of unit cell increases. For this particular case, G_{12} is 47439 (MPa) when we use a RVE contains 125 unit cells ($5 \times 5 \times 5$). From Figure 7, it is clear to see that as the number of unit cell increases the prediction of FEA gets closer to a single unit cell prediction of VAMUCH whereas VAMUCH is confirmed to have consistent prediction for different number of unit cells. It should be noted that the remaining effective properties predicted by FEA are negligibly affected by the number of unit cells. For instance, the prediction of G_{23} using 27 ($3 \times 3 \times 3$) unit cells is observed to have less than 0.5% difference compared to single unit cell.

Based on the prediction of FEA, GMC significantly under predicts shear modulus G_{23} and G_{12} approximately by 7.30% and 8.64%, respectively. On the contrary, VAMUCH predicts G_{12} and G_{23} approximately with 1.35% and 0.089% difference from FEA results, respectively.

Computing time for particle reinforced composite is also evaluated as shown in Table 5. Although the GMC appears to be faster in this case, it achieves this efficiency at the expense of considerable loss of accuracy of predicted shear and longitudinal moduli. Moreover, these loss of accuracy and computing time are obtained under considerable difference of element numbers between GMC and VAMUCH, thus it is of interest to evaluate VAMUCH with fewer number of elements. From Table 6, it is evident to see that VAMUCH predicts the required effective properties with significantly less error than its counterpart GMC. VAMUCH takes approximately 0.14 seconds to complete the run which is of similar efficiency as GMC.

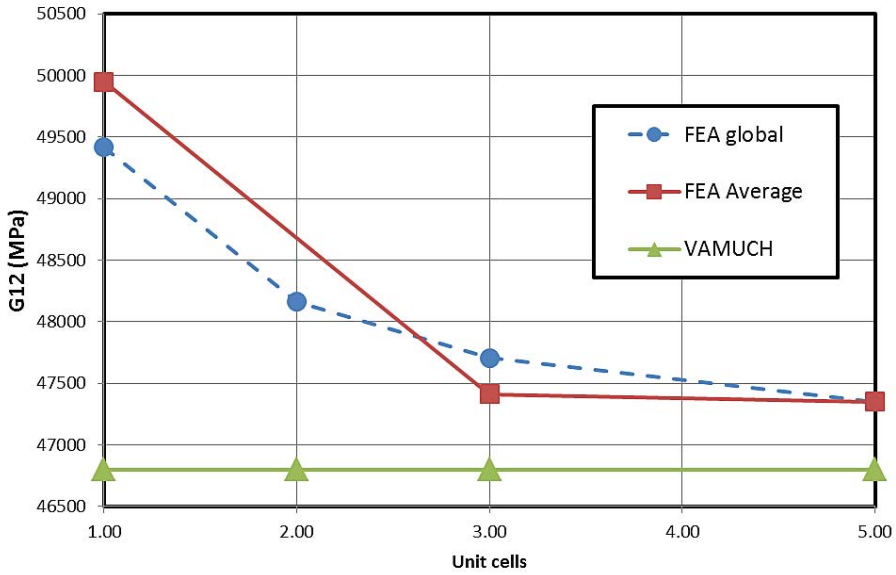

Figure 7. Convergency study of FEA for different unit cells for G_{12}

Table 6. Prediction error of GMC and VAMUCH for particle reinforced composite.

	Elements	E_{11}(MPa)	E_{22}(MPa)	G_{12}(MPa)	G_{23}(MPa)	ν_{12}	ν_{23}
GMC	343	3.095%	3.095%	8.58%	7.12%	-0.62%	0.62%
VAMUCH	52	0.44%	0.44%	0.64%	-0.42%	-0.034%	-0.034%

The recovery of the local fields for particle reinforced composite is also analyzed. It is assumed that a normal load applied in the x_2 direction of homogenized medium generates global strain of $\bar{\varepsilon}_{22} = 0.2\%$ in the x_2 direction and the corresponding strain in the x_3 direction also calculated based on the predicted Poisson's ratios of each approach. All other strains are zero. The global strains are then fed back to the model for recovering the local stress field. In this recovery of the local fields, finer meshes are used for VAMUCH and FEA for better clarity at the interface.

From this local stress recovery analysis, as depicted from Figures 8-10, it is noticed that GMC is not fully capable of capturing the local stress fields. This may be primarily due to its inherent lack of shear coupling effect. It should also be noted that MAC/GMC 4.0 software package provides only elemental average stresses for 3D analysis, thus local stress of GMC for 3D analysis is plotted using an average elemental stresses. As it can be seen from all subsequent figures, these plots fail to hit the boundary of the unit cell for the reason that the stresses are plotted at the element center. On the other hand, local stresses of VAMUCH and FEA are plotted using average nodal stresses. It is obvious to note that plots with nodal values would better capture the local fields. As shown in Figure 8, the recovered local stress σ_{22} of GMC along y_2 $(y_1 = y_3 = 0)$ is found to be the same in the matrix, fiber and interface which is not actually true. GMC again ineffectively recovers the local stress σ_{11} along y_2 $(y_1 = y_3 = 0)$ as shown in Figure 9. Conversely, VAMUCH well recovers the local stress with the same level of accuracy as FEA. Moreover, GMC poorly captures local stress σ_{33} along y_2 $(y_1 = y_3 = 0)$ as shown in Figure 10. It is also observed that VAMUCH well captures the local stress σ_{33} equivalent to FEA. In general, the outputs of the recovery analyses sufficiently demonstrates that VAMUCH is fully capable of recovering all local stresses equivalent to FEA.

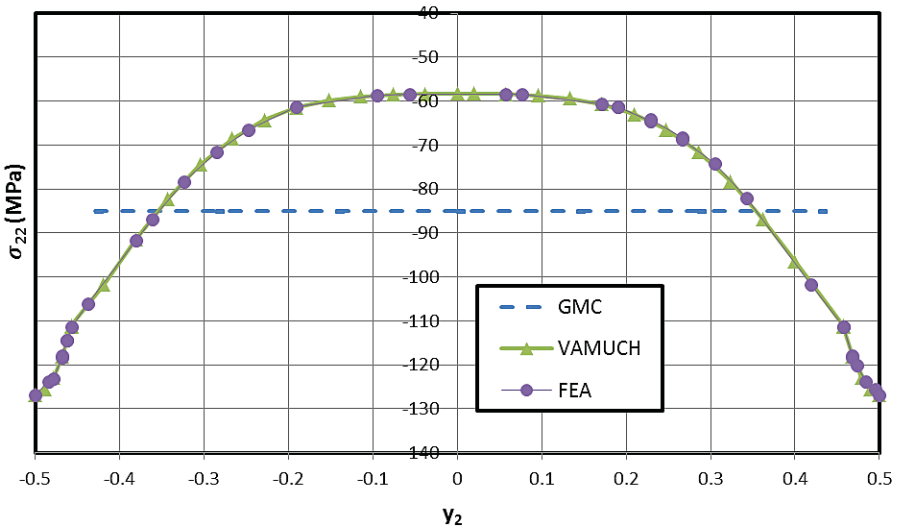

Figure 8. Comparison of recovered local stress σ_{22} along y_2 $(y_1 = y_3 = 0)$

C. Discontinuous Fiber Reinforced Composite

For a discontinuous fiber reinforced composite, first, let a quarter of circular fiber be embedded at the two opposite corners of hexagonal array matrix. Let the array be symmetric with respect to its width and height. This arrangement produces hexagonal array with circular fiber at the center and quarter circular fiber at the corners of the array as shown in Figures 11 and 13. Moreover, let the local Cartesian coordinates

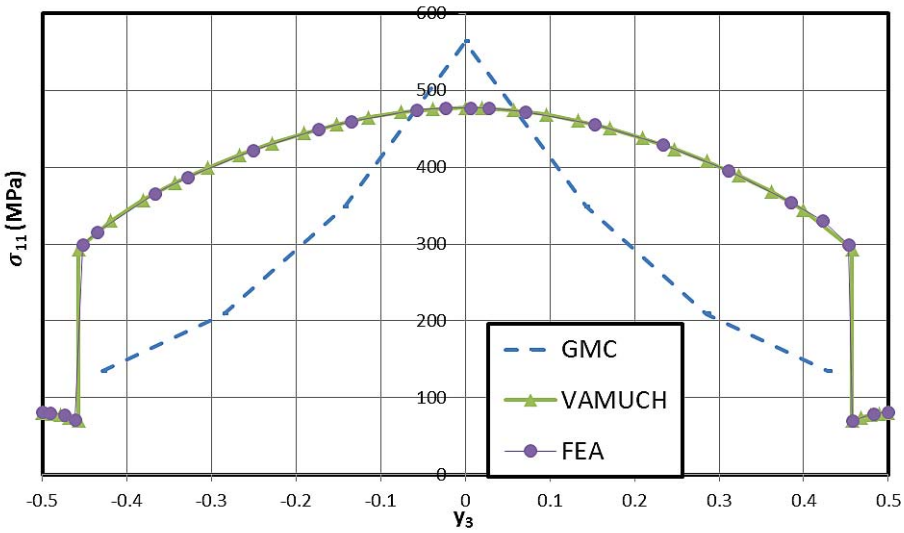

Figure 9. Comparison of recovered local stress σ_{11} along y_3 $(y_1 = y_2 = 0)$

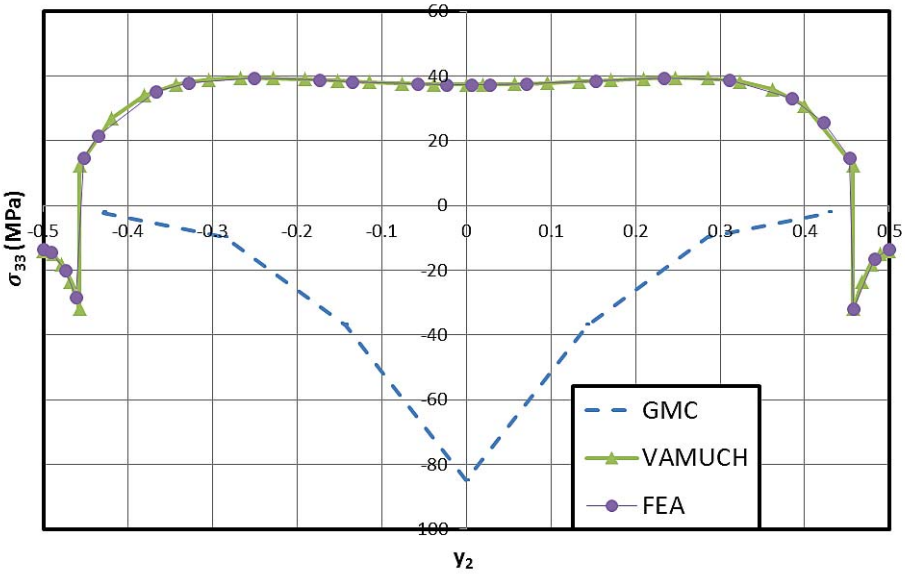

Figure 10. Comparison of recovered local stress σ_{33} along y_2 $(y_1 = y_3 = 0)$

be introduced as $y = (y_1, y_2, y_3)$ at the center of unit cell, where y_1 is in the fiber direction. The fibers are generally shorter compared to the unit cell in y_1 direction. Second, let the cross-sectional area of the hexagonal array be generated based on the common relation, $a = \beta b$, where a is the width and b the height of the unit cell and $\beta = \sqrt{3}$ for hexagonal array. The fiber aspect ratio (length/diameter) is assumed to be 5. By assuming any values of a and total length of the unit cell, it is possible to determine the diameter of the circular fiber for any required fiber volume. In this analysis, 40% of fiber volume ratio is assumed to sufficient to test the predictive capability of the models. Two variants of discontinuous fiber reinforced composites are considered for testing predictive capability of these approaches. The first one is transversely aligned regular array, called aligned-regular array here, where all the fibers are arranged in aligned pattern as shown in Figure 11 and the second one is transversely aligned staggered array, call aligned-staggered array here, where fibers are arranged in offset pattern as seen from Figure 13. Both regular and staggered array are used for predicting effective properties and local field recovery of discontinuous fiber reinforced composite using GMC, VAMUCH, and FEA.

For FEA, SOLID95 elements are used for both aligned regular and staggered arrays. The unit cell is first modeled using plane element (Mesh200) in 2D model and then the corresponding 3D model is generated by extrusion of 2D element based material type and the desired fiber volume. Material parameters may also play a vital role for evaluating the responses of GMC and VAMUCH, therefore, it is of great interest to evaluate the predictive capability of these models with higher property mismatch between fiber and matrix material. The material parameters are listed in Table 7.

1. *Aligned-Regular Array*

In this analysis, a $3 \times 44 \times 42$ (y_1, y_2, y_3) subcell grid is used for GMC, and 20-noded elements are employed for VAMUCH and FEA. In this case, considerable differences in the number of elements are observed due to specific nature of the approaches. GMC and VAMUCH/FEA have 5544 and 45000 elements, respectively. One of the reason for this difference is GMC can have only three elements in the y_1 direction and further refining of the mesh in this direction does not improve the output of GMC. The unit cell of VAMUCH and FEA is shown in the Figure 11. GMC has similar shape and size of unit cell with cuboidal meshing style. FEA can be obtained by the same unit cell as VAMUCH or one-eighth of it may also be used for prediction of effective longitudinal moduli and Poisson's ratios.

Table 7. Material parameters

	Fiber	Matrix
E(GPa)	300	10
ν	0.17	0.33

Table 8. Predicted effective properties for aligned-regular discontinuous fiber reinforced composite

	E_{11}(MPa)	E_{22}(MPa)	E_{33}(MPa)	G_{12}(MPa)	G_{23}(MPa)	ν_{12}	ν_{23}
GMC	49130	21370	19020	6955	6278	0.2482	0.4268
VAMUCH	65752	22594	22608	8199	8052	0.2366	0.4060
FEA	65753	22595	22608	8248	8048	0.2366	0.4060

The output of the analyses in Table 8 indicates that GMC significantly underpredicts longitudinal modulus, E_{11}, approximately by 25.28% compared to converged FEA output. This result is fairly consistent with the result obtained by Pahr and Arnold[20] where GMC suffers maximum of 35% prediction error. Conversely, VAMUCH shows an excellent agreement with all predicted effective properties. As described for particle reinforced composite, the prediction of G_{12} is also executed for different number of unit cells. In this case, FEA predicts G_{12} to be 8602 (MPa) and 8363 (MPa) using single unit cell and 27 $(3 \times 3 \times 3)$ unit cells, respectively. This output can further be improved using Eqs. (35) and (36) for determining the average shear stress and average shear strain of the middle unit cell, respectively. Effective shear modulus, G_{12}, can then be calculated as the ratio of average shear stress and average strain which is found to be 8248 (MPa). Similar to particle reinforced composite, in this case also, it is learned that as the number of unit cell

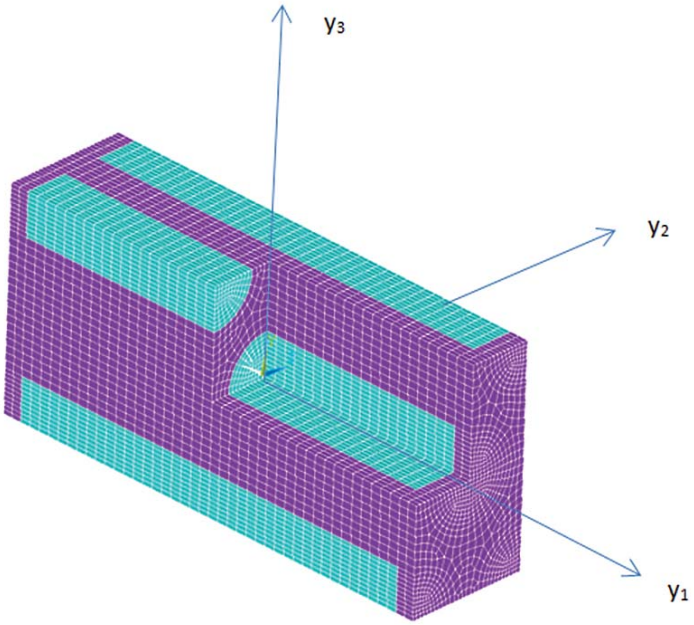

Figure 11. Aligned-regular discontinuous fiber reinforced composite

increases the prediction of FEA converges to the single unit cell prediction of VAMUCH. It is also confirmed that VAMUCH shows consistent prediction of all effective properties for any number of unit cells. It should also be noted that other effective properties predicted by FEA are negligibly affected by the number of unit cells. Other elastic properties such as E_{22} and E_{33} are fairly under predicted by GMC as shown in Table 8. However, GMC considerably underestimates G_{12} and G_{23} by 15.67% and 21.99% error, respectively, as compared to converged FEA results while VAMUCH again predicts G_{12} and G_{23} approximately with 0.59% and -0.049% error, respectively.

For local stress recovery of transversely aligned discontinuous fiber reinforced composite, a normal global load is assumed to be applied in the x_2 direction of homogenized medium. This load generates global strain $\bar{\varepsilon}_{22} = 0.1\%$ in the x_2 direction. The global strains in the x_3 directions calculated based on the predicted Poisson's ratios of each approach. All other strains are zero. The global strains are then fed back to the model for recovering the local stress field. From the recovered local stress as shown in Figure 12, it is evident to see that GMC is not fully capable of capturing the local stress σ_{22} along y_3 ($y_1 = y_2 = 0$) compared with FEA but VAMUCH recovers the local stress equivalent to FEA.

The computing times for predicting effective properties are found to be 3.53 seconds, 326.3 seconds, 2192.46 seconds, for GMC, FEA and VAMUCH, respectively. It is reasonable to notice that GMC is the fastest one as it has obviously much less number of elements, i.e. FEA and VAMUCH have eleven times more elements than GMC. Thus, it is of great importance to critically investigate the response of VAMUCH for fewer number of elements. From prediction error analysis as indicated in Table 10, it is observed that VAMUCH, with 1152 elements, predicts all effective properties except for G_{23} with less error compared to GMC where VAMUCH takes approximately 6.84 seconds to complete the run.

Table 9. Prediction error for discontinuous fiber reinforced composite (aligned regular array).

	Elements	E_{11}(MPa)	E_{22}(MPa)	E_{33}(MPa)	G_{12}(MPa)	G_{23}(MPa)	ν_{12}	ν_{23}
GMC	5544	25.17%	4.93%	15.87 %	15.36 %	21.99 %	-4.35 %	-5.32%
VAMUCH	1152	-1.89%	-1.31%	-2.00%	-13.37%	-24.68%	1.31%	1.19%

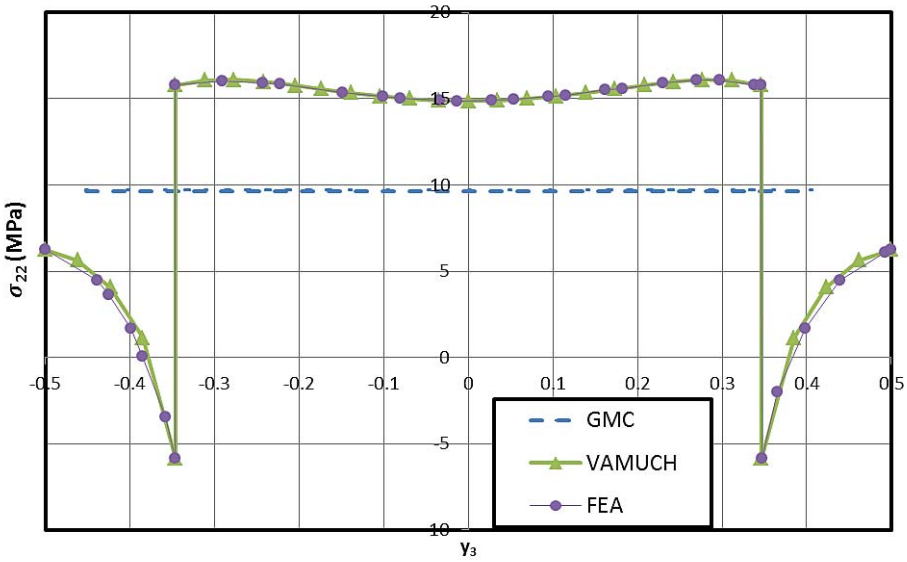

Figure 12. Comparison of recovered local stress σ_{22} along y_3 ($y_1 = y_2 = 0$)

2. Aligned-Staggered Array

In aligned staggered array case, it is similar to the regular array discontinuous fiber reinforced composite but in this case the fibers in the unit cell are arranged in staggered pattern, i.e. fibers overlap within the unit cell. Let 76% of fiber length be overlapped in the unit cell. For this case, a $6 \times 42 \times 42$ (y_1, y_2, y_3) subcell grid is used for GMC, and 34608 20-noded elements are used for VAMUCH and FEA. The unit cell of VAMUCH and FEA is shown in the Figure 13. GMC has similar unit cell with cuboidal meshing pattern.

Table 10. Predicted effective elastic properties for aligned staggered discontinuous fiber composite

	E_{11}(MPa)	E_{22}(MPa)	E_{33}(MPa)	G_{12}(MPa)	G_{23}(MPa)	ν_{12}	ν_{23}
GMC	30190	22450	19250	6729	6360	0.2388	0.3813
VAMUCH	59830	23208	24129	8792	8277	0.2853	0.3731
FEA	59831	23208	24129	8808	8246	0.2835	0.3723

The prediction outputs of discontinuous fiber reinforced composite (aligned staggered) in Table 11 indicate that GMC more significantly underpredicts E_{11} and E_{33} approximately by 49.54% and 20.22%, respectively, compared to converged FEA results. On the contrary, VAMUCH shows an excellent agreement with converged results of FEA. For this case also, as described for regular aligned array, the axial shear modulus is predicted using multiple unit cells. FEA approximately predicts G_{12} to be 9049 (MPa) and 8877 (MPa) using single and 27 ($3 \times 3 \times 3$) unit cells, respectively. To further refine this prediction, the middle unit cell is used to evaluate the axial shear modulus based on average shear stress and average shear strain obtained using Eqs. (35) and (36). The refined prediction of FEA is found to be 8808 (MPa). This output indicates that the perdition of FEA converges to single unit cell prediction of VAMUCH as the number of unit cell increases. The remaining effective properties are negligibly affected by the number of unit cells. For instance, the prediction of G_{23} using 27 ($3 \times 3 \times 3$) unit cells results in approximately less than 0.3% difference compared to the prediction of single unit cell. Based on the prediction of FEA, the axial shear modulus, G_{12}, is significantly underpredicted by GMC approximately by 23.60%. Other effective properties are fairly predicted by GMC whereas VAMUCH shows good agreement.

For analyzing the local stress recovery of staggard array, the load assumptions used for regular array are used here too but in this case the local stress σ_{33} is recovered. From Figure 14, it is clear to see that GMC is not fully able to recover the local stress σ_{33} along y_1 ($y_2 = y_3 = 0$) compared with FEA, while VAMUCH

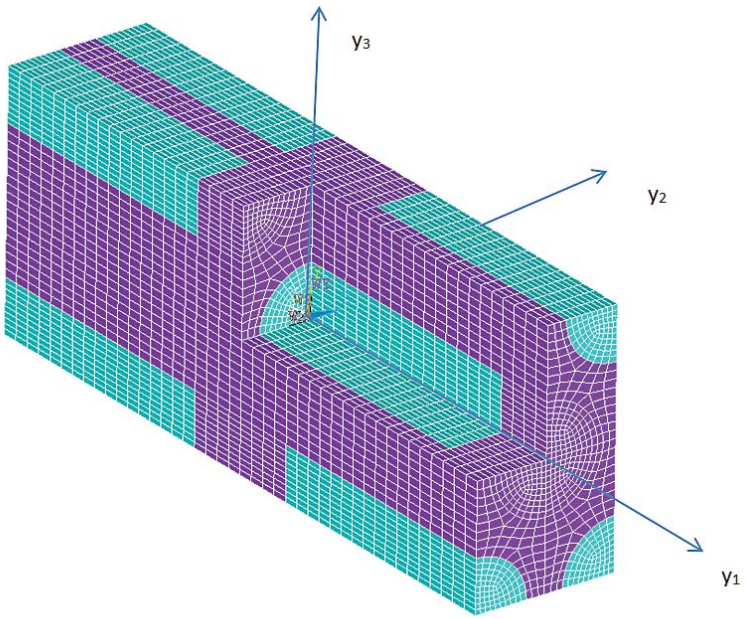

Figure 13. Aligned staggered discontinuous fiber composite

captures the local fields equivalent to FEA. The computing times of these models are found to be 7.756 seconds, 193.1 seconds, 1008.43 seconds for GMC, FEA and VAMUCH, respectively. Note that GMC has significantly few elements as compared with FEA and VAMUCH. Thus, it is worthwhile to investigate the response of VAMUCH with fewer elements. The prediction error verse element number study, as indicated in Table 11, reveals that VAMUCH sufficiently predicts all effective properties with less error compared to its counterpart GMC. VAMUCH takes approximately 1.90 seconds to complete the run which is even faster than GMC.

Table 11. Prediction error for discontinuous fiber reinforced composite (staggered array)

	Elements	E_{11}(MPa)	E_{22}(MPa)	E_{33}(MPa)	G_{12}(MPa)	G_{23}(MPa)	ν_{12}	ν_{23}
GMC	10584	49.61%	6.74%	20.22 %	23.6 %	22.87 %	16.30 %	- 2.41%
VAMUCH	1512	0.50%	-0.58%	-4.47%	-13.37%	-24.68%	0.79%	11.73%

D. Woven Composite

There are various shapes and sizes of unit cell for woven composite, for simplicity as depicted in the Figure 15, woven composite is modeled as an ellipsoidal cross section with major axis radius, c, and minor axis radius is $\frac{c}{4}$, elliptical curvature radius, $r = 2.5c$, and also matrix thickness of $\frac{c}{8}$ is assumed on the top and bottom of the side of the unit cell. The ellipsoidal cross section center to center distance is $2c$. The overall unit cell length, width and height are $4c$, $4c$ and $\frac{5c}{4}$ respectively. GMC uses the similar shape of unit cell with cuboidal meshing pattern.

As listed in Table 12, four different materials parameters with corresponding volume ratio are used for predicting effective properties of woven composite. As shown in Figure 15, material 1 and 2 are oriented in the y_1 and y_2 directions, respectively, waving through the center of unit cell in respective directions. Material 3 is oriented in both y_1 and y_2 directions waving in the outer side of the unit cell and finally material 4 is assumed to be matrix, it also covers the top and bottom sides of the unit cell.

In MAC/GMC 4.0 software package, there are two approaches of predicting effective properties of woven composite, namely single step GMC and two step GMC, both of them are used for predictions of effective properties. GMC inherently uses only cuboidal element type in the unit cell and also further meshing of the

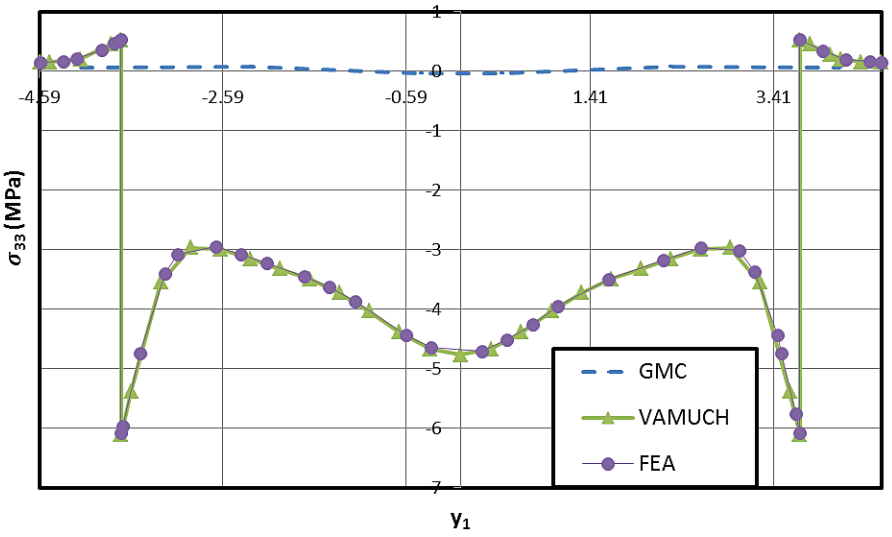

Figure 14. Comparison of recovered local stress σ_{33} along y_1 $(y_2 = y_3 = 0)$

unit cell does not add any accuracy for predicted output. Thus, GMC can only have as few as 64 elements while FEA (SOLID95 element) and VAMUCH are meshed to have 18432 elements. It is obvious that this results in significant difference in the computing time between GMC and VAMUCH.

Table 12. Material parameters and volume ratio for woven composite

	Mat.1	Mat.2	Mat.3	Mat.4
E(GPa)	413	400	73	68.3
ν	0.24	0.20	0.22	0.30
Volume ratio	12.96%	12.96%	25.96%	48.12%

The prediction output of the woven composite in Table 13 reveals that single step GMC method significantly underestimates most of effective properties except E_{22} which is fairly over predicted. The two step GMC slightly underpredicts longitudinal modulus E_{11} and E_{33} compared with converged FEA results. FEA predictions of G_{12} and G_{13} are preformed using single and multiple unit cells. From this prediction, it is observed that the prediction of G_{12} improved from 41046 (MPa) to 40089 (MPa) using single and 27 $(3 \times 3 \times 3)$ unit cells, respectively. Similarly, the prediction of G_{13} is found to be 52565 (MPa) and 50637 (MPa) for single and 27 $(3 \times 3 \times 3)$ unit cells, respectively. These two predictions can further be refined using Eqs. (35) and (36) considering only the middle unit cell as described for particle reinforced composite. The refined predictions for G_{12} and G_{13} are found to be 39961 (MPa) and 49710 (MPa), respectively. It is also noticed that FEA predictions of G_{12} and G_{13} converge to the single unit cell prediction of VAMUCH as the number of unit cell increases. Other effective properties are negligibly affected by the number of unit cells, for instance, G_{23} refined only by 0.26% using 27 $(3 \times 3 \times 3)$ unit cells. Based on the prediction of FEA, single step GMC significantly under predicts the shear moduli G_{12} and G_{13} approximately with 10.04% and 25.86% loss of accuracy, respectively, as shown in Table 13 while the two step GMC predicts G_{12} and G_{13} with 13.25% and 21.60% loss of accuracy, respectively. On the contrary, VAMUCH sufficiently predicts G_{12} and G_{13} with 0.92% and 0.0014% loss of accuracy, respectively.

For local stress recovery of woven composite, a global normal load applied in the x_1 direction is assumed to generate 0.1% of global strains in the x_1 direction and the corresponding strains in the x_2 can be obtained using the predicted Poisson's ratio of each approach and all other strains are assumed to be zero. As shown in the Figure 16, a single step GMC is not able to fully capture the local stress σ_{11} along y_2 $(y_1 = y_3 = 0)$ in woven composite while VAMUCH effectively recoveries the local stress σ_{11} equivalent to FEA.

The computing times for all approaches are evaluated. As it can be seen from Table 14, GMC is very fast for the reason that it has only 64 elements to analyze the modeled woven composite. Single step GMC takes

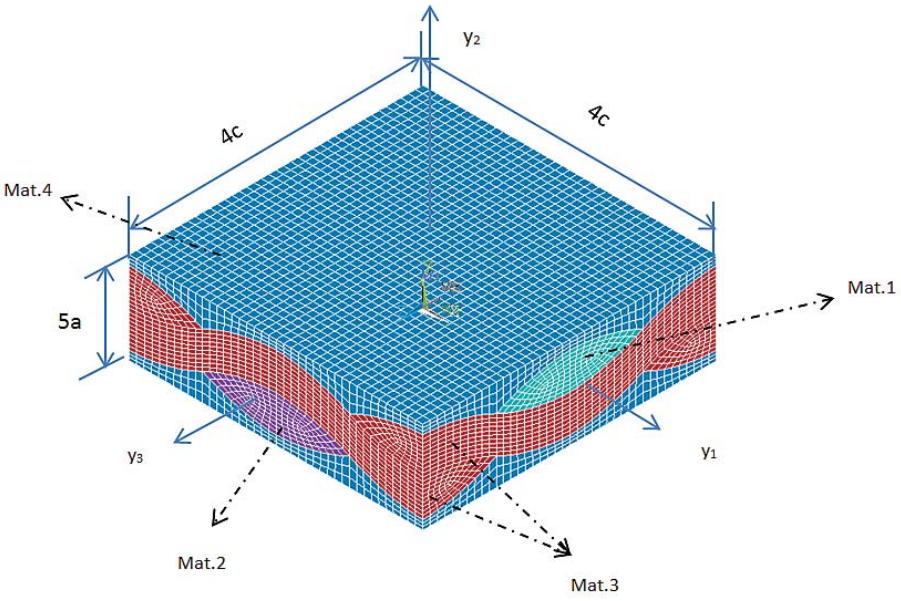

Figure 15. Unit cell for woven composite

Table 13. Predicted effective properties of woven composite

	E_{11}(MPa)	E_{22}(MPa)	E_{33}(MPa)	G_{12}(MPa)	G_{13}(MPa)	G_{23}(MPa)	ν_{12}	ν_{23}
GMC Single Step	129100	99380	129000	35590	38970	35590	0.2779	0.2145
GMC Two Step	130100	108500	129000	35590	38970	38370	0.2516	0.2333
VAMUCH	135995	97965	134766	39590	49693	39574	0.2186	0.1570
FEA	136152	98008	134824	39961	49710	39565	0.2219	0.1591

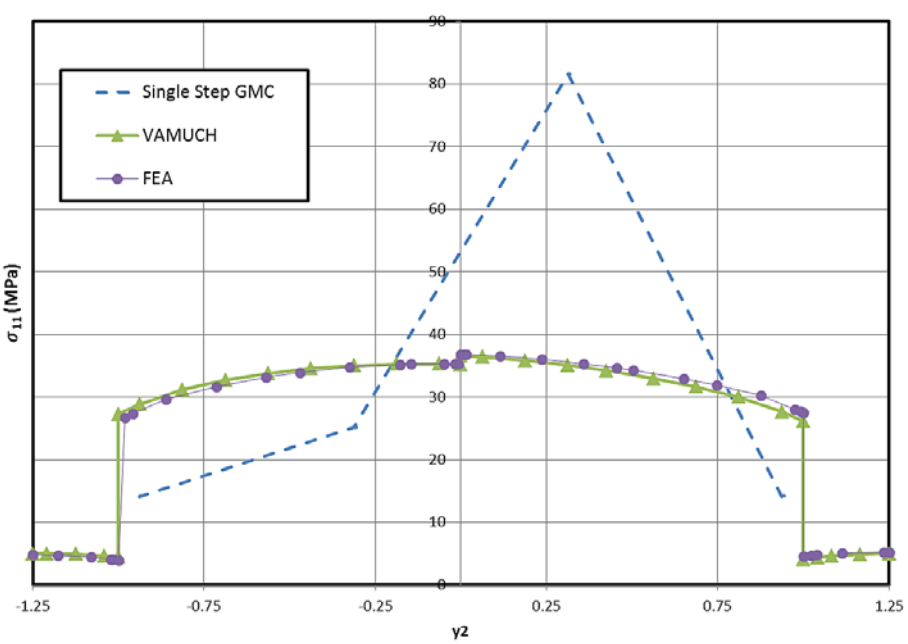

Figure 16. Comparison of recovered local stress σ_{11} along y_2 $(y_1 = y_3 = 0)$

only 0.025 seconds to produce the required effective properties. Both FEA and VAMUCH have the same number of elements but VAMUCH experiences significantly longer time to compute the required effective properties. The level of accuracy that the two step method GMC accomplishes looks better compared to single step which takes approximately 0.95 seconds to complete the run. Using VAMUCH with coarse mesh of 576 elements, we predict E_{11} and G_{23} with -0.29% and 0.76% loss of accuracy, respectively, as indicated in Table 15. VAMUCH approximately takes 16.582 seconds to complete the analysis which is slower than GMC due to the fact that VAMUCH has still relatively larger number of elements.

Table 14. Computing time for woven composites

	Single Step GMC	Two Step GMC	VAMUCH	FEM
Elements	64	16/64	18432/576	18432
Time(s)	0.025	0.95	3412.16/16.582	654.5

Table 15. Loss of accuracy of GMC, VAMUCH for woven composite

	Elements	E_{11}(MPa)	E_{22}(MPa)	E_{33}(MPa)	G_{12}(MPa)	G_{13}(MPa)	G_{23}(MPa)
GMC Single Step	64	5.18%	-1.39%	4.32%	10.93%	25.86%	10.04%
GMC Two Step	16	4.44%	-10.70%	4.32%	13.29%	21.60%	3.87%
VAMUCH	576	-0.29%	-0.04%	-0.39%	0.91%	0.034%	0.76%

VI. Conclusion

The comprehensive evaluation of advanced micromechanics approaches indicates that VAMUCH and FEA agree well both in prediction of effective properties and recovering local stress fields. For continuous fiber reinforced composites, HFGMC also better agrees with FEA however it is computationally more demanding. GMC is observed to be computationally efficient however it comes with significant losses of accuracy for predictions of effective properties and recovery of local fields. On the contrary, VAMUCH can better predict with fewer number of elements with better efficiency for some cases. From 3D analysis of particle reinforced composite, discontinuous fiber reinforced composite, and woven composite, it is observed that FEA over predicts the effective shear moduli. However, as the number of unit cell increases, the prediction of FEA converge to the single unit cell prediction of VAMCUH. Finally, the overall results of this assessment will give insight to researchers looking for predictive capability and efficiency of the GMC, HFGMC and VAMCUH compared to converged results of FEA. However still many more complex cases need to be investigated to further evaluate predictive capability of these approaches and also including other micromechanics models.

References

[1]Yu, W. and Tang, T., "Variational asymptotic method for unit cell homogenization of periodically heterogeneous materials," *International Journal of Solids and Structures*, Vol. 44, No. 11-12, 2007, pp. 3738–3755.

[2]Hill, R., "The elastic behaviour of a crystalline aggregate," *Proceedings of the Physical Society. Section A*, Vol. 65, No. 5, 1952, pp. 349.

[3]Hill, R., "A self-consistent mechanics of composite materials," *Journal of the Mechanics of Physics and Solids*, Vol. 13, 1965, pp. 213–222.

[4]Hashin, Z. and Shtrikman, S., "A variational approach to the theory of the elastic behaviour of multiphase materials," *Journal of the Mechanics and Physics of Solids*, Vol. 11, No. 2, 1963, pp. 127–140.

[5]Milton, G., "Bounds on the electromagnetic, elastic, and other properties of two-component composites," *Physical Review Letters*, Vol. 46, No. 8, 1981, pp. 542–545.

[6]Banerjee, B. and Adams, D. O., "On predicting the effective elastic properties of polymer bonded explosives using the recursive cell method," *International Journal of Solids and Structures*, Vol. 41, No. 2, 2004, pp. 481–509.

[7]Bensoussan, A., Lions, J., and Papanicolaou, G., *Asymptotic analysis for periodic structures*, North-Holland, Amsterdam, 1978.

[8]Murakami, H. and Toledano, A., "A high-order mixture homogenization of bi-laminated composites," *Transactions of the ASME Journal of Applied Mechanics*, Vol. 57, No. 2, 1990, pp. 388–397.

[9]Hollister, S. J. and Kikuchi, N., "A comparison of homogenization and standard mechanics analyses for periodic porous composites," *Computational Mechanics*, Vol. 10, No. 2, 1992, pp. 73–95.

[10]Aboudi, J., "Elastoplasticity theory for composite materials," *Solid Mechanics Archives*, Vol. 11, 1986, pp. 141–183.

[11]Aboudi, J., "Micromechanical prediction of initial and subsequent yield surfaces of metal matrix composites," *International Journal of Plasticity*, Vol. 6, 1990, pp. 471–484.

[12]Adoudi, J., "The generalized method of cells and high-fidelity generalized method of cells micromechanical models-a review," *Mechanics of Advanced Materials and Structures*, Vol. 11, No. 4-5, 2004, pp. 329–366.

[13]Williams, T., Yu, W., Aboudi, J., and Bednarcyk, B., "A critical evaluation of the predictive capabilities of various advanced micromechanics models," *Proceedings of the 48th Structures, Structural Dynamics, and Materials Conference*, Waikiki, 2007.

[14]Yu, W. and Tang, T., "A variational asymptotic micromechanics model for predicting thermoelastic properties of heterogeneous materials," *International Journal of Solids and Structures*, Vol. 44, No. 22-23, 2007, pp. 7510–7525.

[15]Tang, T. and Yu, W., "A variational asymptotic micromechanics model for predicting conductivity of composite materials," *Journal of Mechanics of Materials and Structures*, Vol. 2, 2007, pp. 1813–1830.

[16]Tang, T. and Yu, W., "Variational asymptotic homogenization of heterogeneous electromagnetoelastic materials," *International Journal of Engineering Science*, Vol. 46, No. 8, 2008, pp. 741–757.

[17]Tang, T. and Yu, W., "Variational asymptotic micromechanics modeling of heterogeneous piezoelectric materials," *Mechanics of Materials*, Vol. 40, No. 10, 2008, pp. 812–824.

[18]Aboudi, J., Arnold, S. M., and Bednarcyk, B. A., *Micromechanics of composite materials: a generalized multiscale analysis approach*, Butterworth-Heinemann, 2012.

[19]Sun, C. and Vaidya, R., "Prediction of composite properties from a Representative Volume Element," *Composites Science and Technoloy*, Vol. 56, 1996, pp. 171–179.

[20]Pahr, D. and Arnold, S., "The applicability of the generalized method of cells for analyzing discontinuously reinforced composite," *International Journal of Solids and Structures*, Vol. 33, 2002, pp. 153 – 170.

Challenge Problems for the Benchmarking of Micromechanics Analysis

A. J. RITCHEY, J. GOODSELL, H. M. SERTSE, W. YU and R. B. PIPES

ABSTRACT

Because of the inherent heterogeneity in composites, the field of micromechanics provides essential tools for the understanding and analyzing composite materials and structures. Micromechanics can serve two purposes: homogenization or prediction of effective properties and dehomogenization or recovery of the local fields in the original heterogeneous material. Many micromechanical tools have been developed and codified, including many commercially-available software packages that offer micromechanical analyses as either a stand-alone tool or as part of a chain of analyses. However, with the increasing number of tools available, the practitioner must determine which tool(s) provides the most value for the problem at hand given budget, time and resource constraints. To date, simple benchmarking examples have been reported in the literature. The present paper suggests a series of comprehensive benchmarking exercises in the field of micromechanics against which such tools can be compared. The microstructures include aligned, continuous fibers in a matrix, with and without an interphase; a 0/90 laminate; spherical inclusions; a plain-weave fabric; and a "random" short-fiber microstructure. In each case, the material constitutive relations are restricted to linear-elastic. Results from DIGMAT-MF, MAC/GMC, FVDAM, Altair MDS, SwiftComp, and 3D finite element analysis are reported.

Andrew J. Ritchey, Materials and Process Modeling Engineer, Rolls-Royce Corporation, 450 South Meridian Street, Indianapolis, IN 46225 USA
Johnathan Goodsell, Visiting Assistant Professor, School of Aeronautics and Astronautics, Purdue University, 701 W Stadium Ave, West Lafayette, IN, 47907
Hamsasew M. Sertse, Graduate Research Assistant, School of Aeronautics and Astronautics, Purdue University, 701 W Stadium Ave, West Lafayette, IN, 47907
Wenbin Yu, Associate Professor, School of Aeronautics and Astronautics, Purdue University, 701 W Stadium Ave, West Lafayette, IN, 47907
R. Byron Pipes, John Bray Distinguished Professor of Engineering, Purdue University, 701 W Stadium Ave, West Lafayette, IN, 47907

INTRODUCTION

As the number of commercial modeling tools for manufacturing and designing composite materials is large and keeps growing, it becomes more important to identify the cost-versus-value of each potential software solution. This necessitates the need for a thorough look at each software candidate to correctly identify the range of applications and limitations of the product as well as provide comparison between competing codes. In addition, as each software increases in sophistication, so does the training time required to use or even evaluate a solution against a specific application. As such, adaption of state-of-the-art integrated computational materials engineering tools by industry can be hampered.

One approach that is successfully being used to accelerate technology development is the adoption of standard benchmarking problems. On the commercial side, software vendors will often distribute releases of software with relevant benchmarking solutions. However, it is not always possible to directly compare competing software using these benchmarking studies because there is no guarantee that the same problem will be solved. On the academic side, many such benchmarking efforts are currently ongoing or available in the literature. Two such examples are the seminal work lead by Hinton, Kaddour and Soden known as the World Wide Failure Exercise [1] and the quarterly benchmark magazine from NAFEMS (the International Association of the Engineering Modelling, Analysis and Simulation Community) [2]. However, these efforts only provide a snapshot of the state-of-the-art at the time of publication. Given that the current norm is for engineering software to be developed and released on a 12 or 6 month cycle, these studies can quickly lose relevance to the engineer in industry.

Because of the rapid pace of scientific and software development, it is the authors' opinion that the research, industrial and governmental communities interested in composites would be better served by a living archive of benchmarking examples that are updated in parallel with publications and software revisions. Such an effort will require a digital collaboration environment that is accessible to the relevant stakeholders. In particular, we propose the composite micromechanics challenge problems, hosted by the Composite Design and Manufacturing Hub (cdmHub.org) as a preliminary example of such a living archive concept. It is envisioned that the cdmHub will host the results provided by the challenge participants and, to some extent, the software tools themselves. This will allow the community at large to run some of the analyses, vary the inputs and interpret results.

The Micromechanics Challenge consists of three levels. The problems specified in Level I consider linear thermoelastic behavior. Prediction of effective properties (homogenization) and local fields (dehomogenization or localization) are specified. Level II extends the challenge by introducing non-linear phase properties, including inelastic (elastic-plastic, creep, viscoplastic) constitutive relations. Finally, damage and failure prediction including fatigue file prediction under combined mechanical and environmental effects will be addressed in Level III. In addition to effective properties and local fields, the computational efficiency will be an important metric in comparing the tools. It is anticipated that the results from the challenge will compare the relative strengths and trade-offs of the participating tools and identify areas currently unaddressed by the field.

Level I microstructures are highly idealized representation of real heterogeneous materials. Nevertheless, these idealizations are constantly used in the micromechanics field. The microstructures examined in level I include aligned, continuous fibers in a matrix, with and without an interphase; a 0/90 laminate; spherical inclusions; a plain-weave fabric; and a "random" short-fiber microstructure.

In the reminder of this paper we will provide the results from the initial set of simulation tool participants completed to date. The problems and results, including data files, will be hosted on cdmHUB as a project entitled *Micromechanics Simulation Challenge*. Interested parties are invited to participate at any time by accessing and contributing to the live database on cdmHUB.

PARTICIPATING MICROMECHANICS TOOLS

In this paper, various advanced micromechanics tools are used to analyze the stated micromechanics challenge problems which are briefly described below.

DIGIMAT is a commercial code that is used to solve various engineering problems, many with a micromechanical-theme [4]. DIGIMAT uses two main approaches for homogenization: 1. Mean-field approaches (DIGIMAT-MF) such as the Mori-Tanaka (MT) approach and Double Inclusion (DI) approach; 2. FEA-based homogenization approaches (DIGIMAT-FE). In this paper only DIGIMAT-MF approaches are used to analyze the challenge problems due to difficulties we experienced with DIGIMAT-FE. Further, as the mean-field approaches (no discretization needed) are implemented for homogenization in DIGIMAT-MF, only homogenization results are available.

MAC/GMC is a well-known micromechanics code developed by NASA Glenn Research Center based on Aboudi's micromechanics theories [5] that provides a wide range of capabilities for modeling continuous, discontinuous, woven, and smart (piezo-electo-magnetic) composites. Libraries of nonlinear deformation, damage, failure, and fiber/matrix debonding models, continuous and discontinuous repeating unit cells (UCs), and material properties are provided, and the software is available from NASA Glenn [6, 7]. The software includes both GMC (generalized method of cells) and HFGMC (high-fidelity generalized method of cells) semi-analytical models. The basic idea of these two approaches is subdividing the microstructure into numerous cuboid subcells and solving for the average strain and stress over each subcell. GMC uses a first-order expansion of the local displacement field while HFGMC utilizes a second-order expansion of the local displacements. The linear displacement expansion limits GMC to uniform states of stress and strain in the subcells, which results in a lack of normal/shear coupling. Both macro and micro fields along with effective composite and laminate properties are available outputs. A detailed description of both theory and application of GMC and HFGMC is given in [5]. In the current version, MAC/GMC 4.0, HFGMC can only handle continuous reinforced (doubly periodic) microstructures.

FVDAM (Finite Volume Direct Averaging Method) uses the finite volume method [8]. The development of FVDAM took place in three stages. In the first stage, the linear thermo-elastic higher-order theory for periodic multiphase materials (HFGMC) originally developed by Aboudi et al [9] was reconstructed by Bansal and Pindera [10]. The equivalence of this approach with GMC was demonstrated by

Arnold et al [11]. The theory's further development leveraged the parametric mapping [12] into the rectangular subvolume-based finite volume theory, which was implemented in [13, 14]. This, in turn, facilitated the recent incorporation of the cohesive zone model capability [15]. The third phase of FVDAM's development involved incorporation of enriched subvolume displacement field description which resulted in enhanced interfacial traction and displacement continuity [16]. Currently, FVDAM can only handle doubly periodic microstructures.

Altair recently acquired *Multiscale Design System for linking Continuum scales* (MDS-C) developed by Jacob Fish [17]. MDS focused on the creation of practical yet rigorous tools for seamless integration of engineering modeling, simulation, testing and optimization of products involving multiple spatial and temporal scales. MDS, is a plug-in to commercial finite element software (ABAQUS, ANSYS, LS–DYNA) that provides multiscale capabilities for commercial codes. Distinguishing features of the MDS-C software are: (1) a systematic model reduction technology that reduces complex UCs having hundreds of thousands of finite elements to a manageable number of deformation modes and state variables; (2) an extensible library of parametric UCs; and (3) advanced features such as microstructural optimization, multiscale fatigue and multiphysics analyses.

SwiftComp is a general-purpose multiscale constitutive modeling code for composites which provides unified modeling for 1D (beams), 2D (plates/shells), or 3D composite structures. This is accomplished using the concept of a structure genome that unifies structural mechanics and micromechanics [18]. SwiftComp can perform homogenization and dehomogenization for a wide variety of periodic, partially periodically or aperiodic composites structures and materials including laminates, woven composites, stiffened structures, sandwich structures, corrugated structures, and other buildup structures which could be made into form of beams, plates/shells, or 3D structures. Level I problems only tests SwiftComp's capability for 3D structures made of materials featuring doubly periodic or triply periodic microstructures.

3D FEA is also used to analyze the challenge problems because it can be proven that the exact solutions of linear thermoelastic micromechanics problems can be provided by 3D FEA of a UC with periodic BCs with a sufficient fine mesh. The predictions of 3D FEA are used as references for evaluating accuracy and efficiency of other approaches. Mesh refinement study was undertaken (not shown herein) to ensure appropriate solution convergence. ANSYS is used for all the cases except for case 2 which is analyzed using ABAQUS because ANSYS has difficulty to generate a quality mesh to provide a converged local stress distribution at the thin interface.

Prof. Pindera and his team of University of Virginia obtained FVDAM results on a machine with Windows 7 64-bit operating system (Intel(R) Core(TM) i7-2760QM CPU @ 2.4 GHZ, 8G RAM). Mr. Jeffery Wollschlager at Altair provided MDS results. cdmHUB representatives generated MAC/GMC/HFGMC results independently, subsequent to review of results, input files were provided by Dr. Steven Arnold and his team at NASA Glenn, and run by cdmHUB, which are believed to provide a better tradeoff between accuracy and efficiency. cdmHUB representative also obtained DIGIMAT, SwiftComp and 3D FEA results. cdmHUB representative used a computer with Window 8.1 64-bit operating system, (Intel (R) Xeno(R) CPU E5-2697 v3 @2.6GHz, 256G RAM). Note FVDAM and MAC/GMC do not have parallel computing capability while DIGIMAT, SwiftComp, and 3D FEA can use multiple cores. Consequently, in the results reported below, only one core is used for

all the approaches to facilitate runtime comparisons. At the time of writing, the machine information, discretization, and running time of MDS are not reported. Except that it is known that current FVDAM and MAC/HFGMC (version 4.0) cannot handle triply periodic (discontinuous) cases and DIGIMAT-MF cannot provide local fields, it is expected that all the other codes can provide all the required results for the level I problems, but some results are missing for various reasons at the time of writing. Particularly, the capability of dehomogenization (localization) is important as prediction of local fields greatly influences the nonlinear behavior (including strength and failure) prediction which will be benchmarked in level II and level III challenge problems. To strive for objectivity and neutrality, we: 1) let the tool providers review the results and input/output files well in advance of deadline if cdmHUB generated the results (this applies to MAC/GMC and DIGIMAT); 2) make all the model files, inputs/outputs, result files publically available through cdmHUB; 3) make SwiftComp, a code developed by one of the co-authors, Prof. Yu, globally accessible to anybody who wants to verify the results; 4) keep a live copy of the report for anybody to question and correct the results.

RESULTS OF LEVEL I CHALLENGE PROBLEMS

For Level I problems, the effective properties reported are either in engineering constants or the stiffness matrix according to the symmetry of the composites. The local fields are computed along paths specified in each problem statement and values in the problem coordinate system (x_1, x_2, x_3) are reported. The local field cases examined consist of applying pure strain controlled problems; wherein a constant (unit) strain is applied in the a) x_1 direction, b) x_2 direction, c) shearing strain in the x_2-x_3 plane, d) shearing strain in the x_1-x_3 plane, and e) combined unit axial strain in the x_1 direction and shearing strain in the x_1-x_3 plane, while all other components of strain are constrained at zero. These constraints cause stresses to arise in the constrained directions. Note, strain control was chosen to isolate loss of accuracy in homogenization and dehomogenization, since if stress control is used effective properties (computed by various methods) will be used to compute the macroscopic strain for the purpose to compute the local fields. Particularly for multiscale modeling, strains are readily available from the macroscopic analysis. Due to page restrictions only a representative portion of the results are presented here. The complete sets of results are available on cdmHUB. Results and computing time are clearly influenced by UC discretization, particularly for numerical based methods like FEA. Only brief descriptions of the mesh are given and pictures showing the details of discretization can be found on cdmHUB.

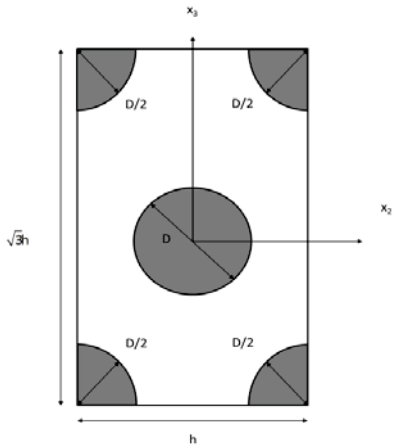

FIGURE 1.0. Hexagonal pack of fiber reinforced composites.

Case 1: Hexagonal Pack Microstructure

The first microstructure is a hexagonal pack UC shown in Figure 1.0 (not to scale). It can be

used to describe a continuous fiber reinforced composites. For this case, the effective properties are predicted assuming a fiber volume fraction of 60%. Constituent properties utilized are given by set 1 in Table I.0. Note matrix is assumed isotropic while the fiber is transversely isotropic. All nontrivial local stress components are reported along the linear path from $(-1/2h, -\sqrt{3}/2h)$ to $(1/2h, \sqrt{3}/2h)$.

TABLE I.0. Material properties

	Set 1, Carbon/Epoxy		Set 2, Low Contrast Isotropic Fiber	
Property	Matrix	Fiber	Matrix	Fiber
E_1 (GPa)	4.76	276	350	400
$E_2=E_3$ (GPa)	4.76	19.5	350	400
$\nu_{12}=\nu_{13}$	0.37	0.28	0.18	0.17
ν_{23}	0.37	0.70	0.18	0.17
$G_{12}=G_{13}$ (GPa)	1.74	70	148	171
G_{23} (GPa)	1.74	5.74	148	171
α_1 (μ/°C)	64.8	-0.4	30	20
α_2 (μ/°C)	64.8	5.6	30	20
α_3 (μ/°C)	64.8	5.6	30	20

For FVDAM, GMC, HFGMC and SwiftComp, since the material is doubly periodic, a 2D domain is sufficient to predict the full set of effective properties for this case. The 2D UC is discretized to form a 36×62 grid for GMC and HFGMC, and a 38×62 grid for FVDAM. For SwiftComp, the UC is meshed with 2300 quadrilateral elements. For 3D FEA to obtain the full set of effective properties, 3D domain is needed to model this doubly periodic material which can be obtained by extruding the mesh of SwiftComp along the fiber direction. The thickness does not matter as we applied periodic BCs in 3D FEA. However, to maintain a quality mesh, it is assumed that the UC has a thickness equal to 10% of it's the shorter side with four element in the thickness directions. The 3D UC has 10,925 hexagonal elements.

TABLE I.I. Predicted effective elastic properties

Approach	E_1 (GPa)	E_2 (GPa)	E_3 (GPa)	G_{12} (GPa)	G_{13} (GPa)	G_{23} (GPa)	υ_{12}	υ_{13}	υ_{23}
FVDAM	167.30	10.67	10.67	6.38	6.39	3.33	0.310	0.310	0.600
GMC	167.40	10.46	10.08	5.33	4.45	3.00	0.312	0.312	0.612
HFGMC	167.40	10.71	10.69	6.58	6.54	3.36	0.312	0.312	0.603
DIGIMAT-MF/MT	167.52	10.53	10.53	6.36	6.36	3.27	0.312	0.312	0.605
DIGIMAT-MF/DI	167.77	10.99	10.99	9.51	9.51	3.36	0.306	0.306	0.632
Altair MDS	166.31	10.88	10.88	6.89	6.89	3.42	0.312	0.312	0.594
SwiftComp	167.33	10.67	10.67	6.38	6.39	3.33	0.312	0.312	0.600
3D FEA	167.33	10.67	10.67	6.38	6.39	3.33	0.312	0.312	0.600

TABLE I.II. Predicted effective CTEs

Approach	FVDAM	GMC	HFGMC	DIGIMAT-MF/MT	DIGIMAT-MF/DI	SwiftComp	3D FEA
α_1 (μ/°C)	0.410	0.364	0.408	0.404	0.503	0.405	0.405
α_2 (μ/°C)	35.20	35.03	34.99	35.13	29.52	35.10	35.10
α_3 (μ/°C)	35.13	40.08	35.30	35.13	29.52	35.10	35.10

According to Table I.I, all tools predict essentially the same effective elastic properties except GMC under predicts E_3 by 6%, G_{12} by 15%, G_{13} by 30%, and G_{23} by

10%, MDS over predicts shear moduli (8% for G_{12} and G_{13}), and DIGIMAT-MF/DI over predicts shear moduli (49% for G_{12} and G_{13}) and over predicts υ_{23} by 5% as compared to 3D FEA. The discrepancy between the two DIGIMAT mean field approaches is surprising. The effective CTEs (Table I.II) are well predicted by all the tools except GMC under predicts α_1 by 10% and over predicts α_3 by 12% and DIGIMAT-MF/DI over predicts α_1 by 24% and under predicts α_2, α_3 by 16%. MDS CTEs were not reported.

The local stresses are computed using the described loading options along the specified path. For ε_{11} loading, the non-trivial stresses along the specified path are σ_{11}, σ_{22}, σ_{33}, and σ_{23}. There are similar results for the various different loading options examined, however here only representative local stress field distributions are shown. As it can be seen from Figure 1.1, all tools provide excellent agreement for σ_{11} under ε_{11}. Such excellent agreement is not observed however for Figures 1.2-1.4 where we observe GMC does not predict local fields as well as HFGMC, FVDAM, and SwiftComp. It can also been seen for these cases, HFGMC's prediction is not as good as FVDAM and SwiftComp, particularly at the interfaces or boundaries. Local fields from MDS were not reported.

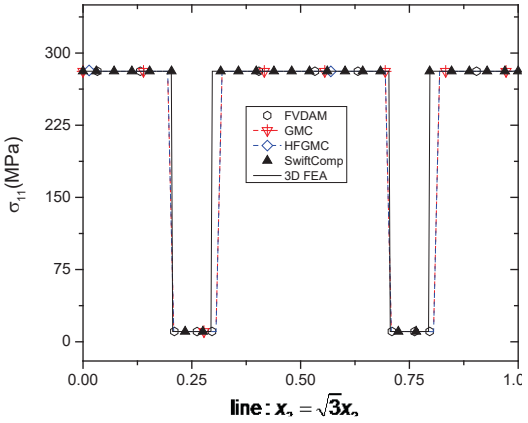

FIGURE 1.1. σ_{11} under ε_{11}

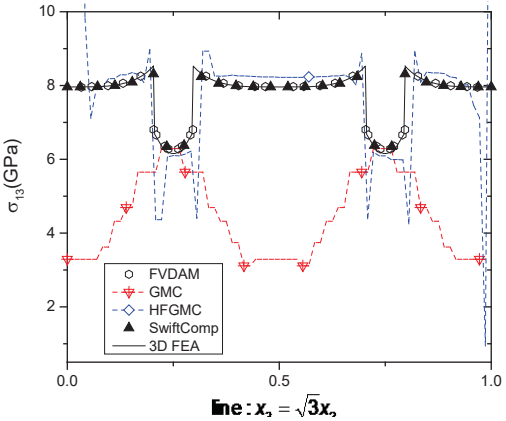

FIGURE 1.2. σ_{13} under ε_{13}

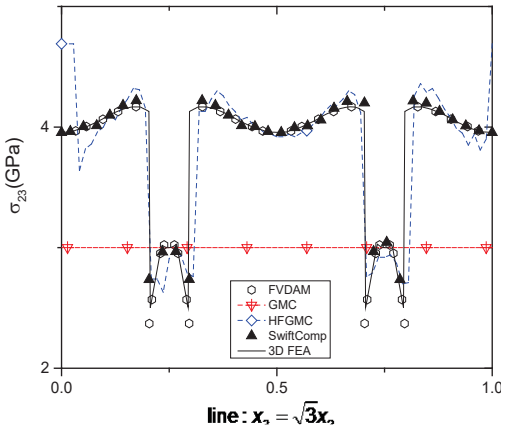

FIGURE 1.3. σ_{23} under ε_{23}

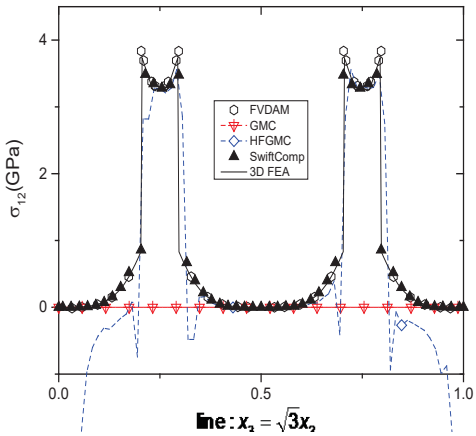

FIGURE 1.4. σ_{12} under ε_{11} & ε_{13}

The computing time of each tool is shown in Table I.III with dehomogenization is only for one load case. The time shown in the table for FVDAM and SwiftComp shows both for homogenization and dehomogenization time. Note these time are just a rough measurement as there might be some background processes affecting the time.

We assume it will affect all the tools the same fashion. It is also noted that computing time is significantly affected by mesh which is greatly related with accuracy. It is suggested that interested readers obtain the various codes to run the problems themselves to get a feeling of efficiency. Table I.III indicates that DIGIMAT-MF, GMC, HFGMC, SwiftComp and FVDAM are more efficient compared with 3D FEA, with DIGIMAT-MF being the most efficient, followed by GMC, then HFGMC, SwiftComp, and FVDAM.

TABLE I.III. Computing time for case 1

Approach	FVDAM	GMC	HFGMC	DIGIMAT-MF/MT	DIGIMAT-MF/DI	SwiftComp	3D FEA
Homo. (sec)	4	N/A	N/A	N/A	N/A	0.26	N/A
Dehomo. (sec)	0.88					0.93	
Total (sec)	4.88	0.292	1.151	0.03	0.03	1.19	42.00

Case 2: Three-Phase Interphase Microstructure

The second microstructure is a square pack array with an interphase region between the fiber and matrix. The microstructure geometry (not to scale) is shown in Figure 2.0. For the prediction of effective properties, let the volume fraction of the fiber phase be 60% and a very small interphase volume fraction be 1%. One set of fiber, matrix and interphase properties, representative of a generic CMC, is given in Table II.0. Note, this problem is purposely designed to test the capability of tools to handle microstructures with possibly very thin interfaces and may not represent any real CMCs as the chosen fiber volume fraction is significantly higher, and the interphase volume fraction an order of magnitude lower, than typical CMCs. Further, it should be noted that the fiber properties are orthotropic, despite the fact that all three Young's moduli and all three Poisson's ratios have been chosen to be the same. For dehomogenization, all nontrivial stress components should be reported along the path of $x_3 = 0$.

TABLE I.0. Material properties

	Set 3, Three phase microstructure		
Property	Matrix	Fiber	Interphase
E (GPa)	350	450	5.0
ν	0.18	0.17	0.22
G (GPa)	148	171	2.0
α_1 (μ/°C)	64.8	-0.4	5.0
α_2 (μ/°C)	64.8	5.6	5.0
α_3 (μ/°C)	64.8	5.6	5.0

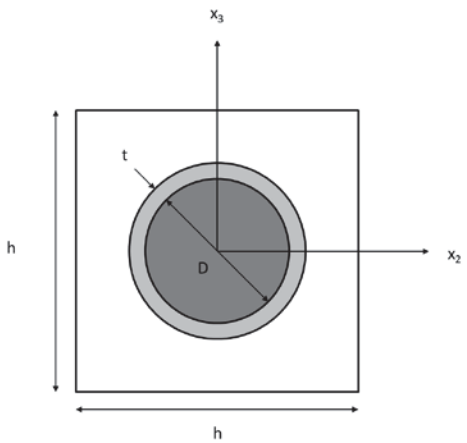

FIGURE 2.0. Circular fiber and interphase embedded in matrix.

A 56×56 grid is used for FVDAM, a 7x7 grid is used for GMC (more refined grid being unnecessary based on the approximate nature of GMC according to the tool authors), and a 240x240 grid (due to the overly thin interface) is used for HFGMC. Note to use a coarse grid in GMC, the UC must be modified in such a way that the

fiber volume fraction remains the same. For SwiftComp, the UC is meshed with 3,072 quadrilateral elements. For 3D FEA, the UC is meshed with 11,372 brick elements.

TABLE II.I. Predicted effective properties

Approach	E_1 (GPa)	$E_2 = E_3$ (GPa)	$G_{12} = G_{13}$ (GPa)	G_{23} (GPa)	$\upsilon_{12} = \upsilon_{13}$	υ_{23}	α_1 (μ/°C)	$\alpha_2 = \alpha_3$ (μ/°C)
FVDAM	406.54	276.64	116.77	110.36	0.175	0.203	21.63	32.10
GMC	406.70	295.90	114.40	93.98	0.174	0.138	21.60	30.63
HFGMC	406.40	278.40	118.00	117.00	0.175	0.193	21.47	32.00
DIGIMAT-MF/MT	406.56	271.87	83.11	111.56	0.174	0.218	25.61	30.43
DIGIMAT-MF/DI	406.08	391.15	20.70	166.4	0.173	0.175	25.63	26.65
Altair MDS	406.13	280.80	118.41	112.99	0.175	0.199	N/A	N/A
SwiftComp	406.56	276.85	117.58	115.69	0.174	0.203	21.61	32.08
3D FEA	406.55	276.85	117.58	115.49	0.174	0.203	21.61	32.08

Table II.I shows that all the tools achieve an excellent prediction for E_1, υ_{12} ($=\upsilon_{13}$). GMC over predicts E_2 ($=E_3$) by 7%, while under predicts G_{23} by 19% and υ_{23} by 32%. DIGIMAT-MF/MT under predicts G_{12} ($=G_{13}$) by 29%, over predicts υ_{23} by 7% and α_1 by 19%. DIGIMAT-MF/DI over predicts E_2 ($=E_3$) by 41%, G_{23} by 44% and α_1 by 19% while under predicts G_{12} ($=G_{13}$) by 82%, υ_{23} by 14%, and α_2 ($=\alpha_3$) by 17%. Generally speaking, FVDAM, HFGMC, MDS, and SwiftComp have excellent agreement with 3D FEA with SwiftComp being the best.

Representative local stress distributions are shown in Figures 2.1-2.4. As it can be seen from Figure 2.1, all tools provide excellent agreement for σ_{11} under ε_{11} loading. This type of problem, where a vanishingly-thin, very compliant material is sandwiched between two stiff materials is known to be challenging for GMC [19], which is also demonstrated by the properties predictions in Table II.I and local field prediction in Figures. 2.2-2.4. For more realistic interphase thicknesses, like those in real CMCs, GMC has been shown to provide good approximations of the properties and local fields [20, 21]. HFGMC prediction of local fields is significantly better than GMC, although not as good as FVDAM and SwiftComp.

The computing time of each tool is shown in the Table II.II. It is noticed that DIGIMAT-MF and GMC are three orders of magnitude faster than FEA, followed by SwiftComp two orders, FVDAM an order of magnitude faster, and HFGMC being only a factor 2.8 times faster than 3D FEA.

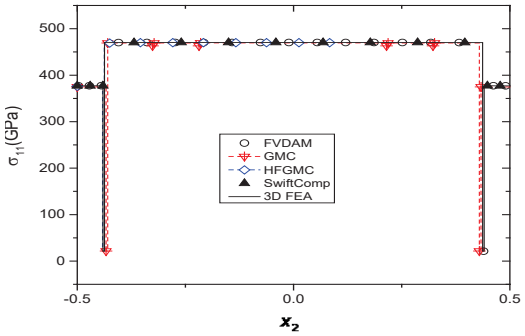

FIGURE 2.1. σ_{11} under ε_{11}

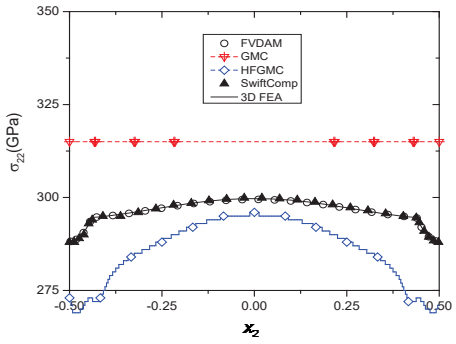

FIGURE 2.2. σ_{22} under ε_{22}

TABLE II.II. Computing time for case 2

Approach	FVDAM	GMC	HFGMC	DIGIMAT-MF/MT	DIGIMAT-MF/DI	SwiftComp	3D FEA
Homo. (sec)	5.92	N/A	N/A	N/A	N/A	0.45	N/A

Dehomo. (sec)	0.43					1.26	
Total (sec)	6.35	0.08	94.00	0.03	0.03	1.71	271

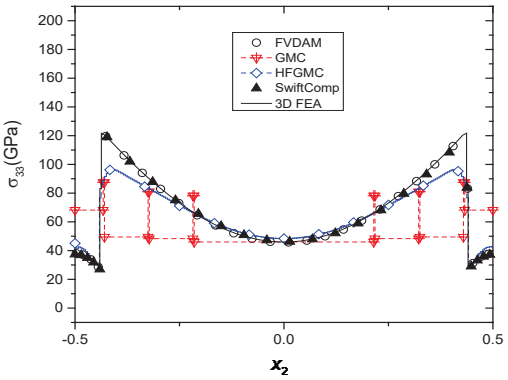

FIGURE 2.3. σ_{33} under ε_{22}

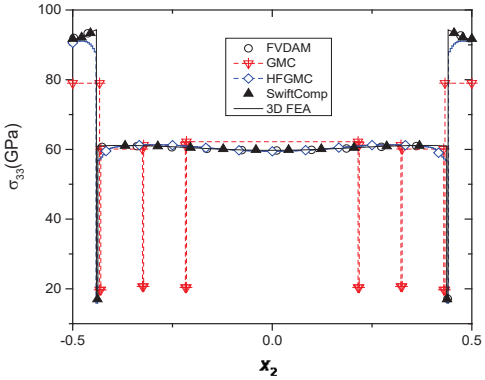

FIGURE 2.4. σ_{33} under ε_{11} & ε_{13}

Case 3: 0/90 Microstructure

The third problem, shown in Figure 3.0, is a 0/90 microstructure characterized by two perpendicular rows of 3 fibers each, with fibers having diameter, D = 5 microns. This microstructure is assumed to be periodic in the x_1 and x_2 directions, representative of a 0/90 lamina interface. Though not representative of typical composite laminate microstructures, boundary conditions on the x_3 faces are assumed to be periodic. The fiber volume fraction determines the thickness T and length L. Elastic properties for the fiber and matrix are given in the set 1 properties in Table I.0. The fiber volume fraction is 60%. All nontrivial stress components are reported along the path defined by (L/2, L/2, x_3). It is noted that the same microstructure can be represented by two UCs with one fiber each stacked on top of each other. Any methods with periodic BCs should predict the same results no matter which microstructure is used.

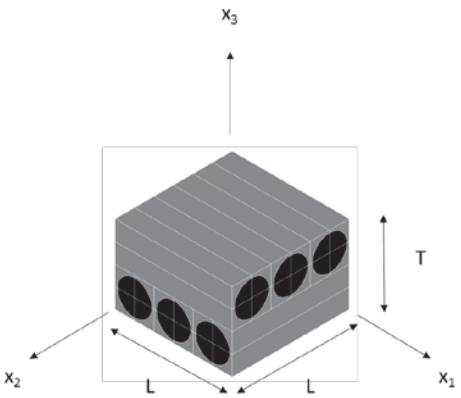

FIGURE 3.0. 0/90 microstructure

A 4×6×6 grid is used for GMC as more refined mesh is believed to be excessive by the authors of the code. For SwiftComp and 3D FEA, the UC is meshed to have 140,400 brick elements to achieve a converged solution. The predicted effective properties are shown Table III.I. It is noticed that all approaches show excellent predictions for E_1 (=E_2). GMC under predicts G_{12} by 15% and G_{13} (=G_{23}) by 11%. DIGIMAT-MF/MT under predicts G_{12} and υ_{12} by 8% while over predicts G_{13} (=G_{23}) by 14%. DIGIMAT-MF/DI over predicts E_3 by 7%, G_{12} by 37%, G_{13} (=G_{23}) by 52%, while under predicts α_1(=α_2) by 13% and α_3 by 14%. MDS over predicts G_{12} by 7%, and G_{13} (=G_{23}) by 26%.

TABLE III.I Predictions of effective properties

Approach	E_1=E_2 (GPa)	E_3 (GPa)	G_{12} (GPa)	G_{13} =G_{23} (GPa)	υ_{12}	υ_{13}= υ_{23}	α_1= α_2 (μ/°C)	α_3 (μ/°C)

GMC	89.78	15.12	5.89	3.76	0.039	0.528	3.05	55.30
DIGIMAT-MF/MT	89.50	15.30	6.36	4.82	0.036	0.539	3.00	53.60
DIGIMAT-MF/DI	89.88	16.65	9.51	6.43	0.039	0.550	2.74	45.62
Altair MDS	89.45	15.88	7.40	5.31	0.04	0.517	N/A	N/A
SwiftComp	89.51	15.52	6.93	4.23	0.039	0.526	3.12	53.10
3D FEA	89.51	15.53	6.94	4.23	0.039	0.526	3.15	52.77

As can be observed from Figures 3.1 and 3.3, GMC achieves decent predictions for these two local stress distributions, whereas for the other two cases, GMC predicts, due to the known lack of normal/shear coupling, a uniform state of shear stress along the path as shown in Figures 3.2 and 3.4. On the contrary, SwiftComp maintains consistent agreements with 3D FEA.

GMC achieves similar efficiency as DIGIMAT-MF. SwiftComp and 3D FEA are orders of magnitude slower due to the fine mesh needed for numerical convergence. SwiftComp is about 10 times more efficient than 3D FEA although exactly the same mesh is used and similar accuracy is achieved.

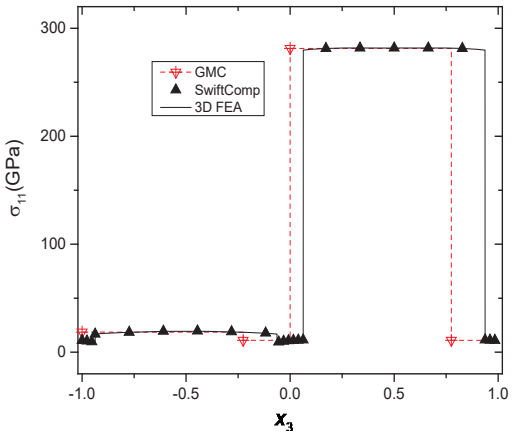

FIGURE 3.1. σ_{11} under ε_{11}

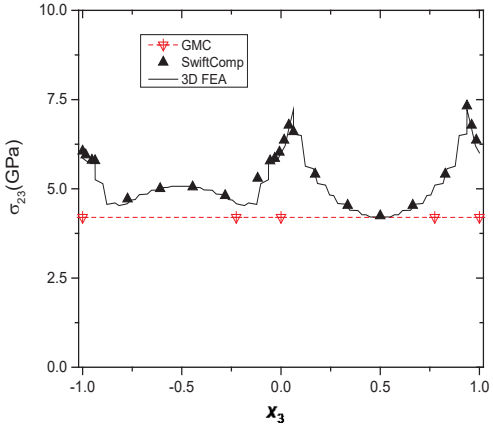

FIGURE 3.2. σ_{23} under ε_{23}

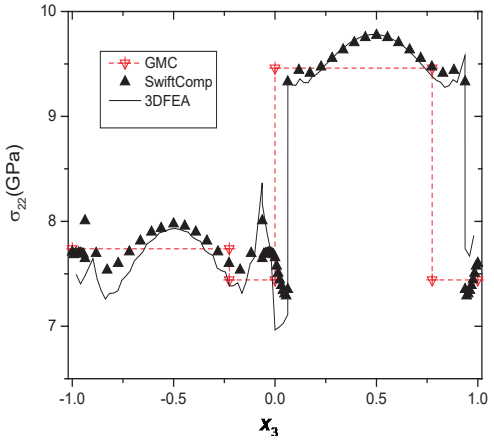

FIGURE 3.3. σ_{22} under ε_{11} & ε_{13}

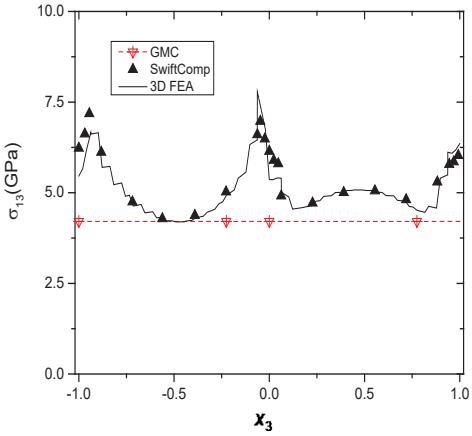

FIGURE 3.4. σ_{13} under ε_{11} & ε_{13}

TABLE III.II. Computing time for case 3

Approach	GMC	DIGIMAT-MF/MT	DIGIMAT-MF/DI	SwiftComp	3D FEA
Homo. (sec)	N/A	N/A	N/A	69.5	N/A
Dehomo. (sec)				120	
Total (sec)	0.08	0.03	0.03	324	3521

Case 4: Spherical Inclusions Microstructure

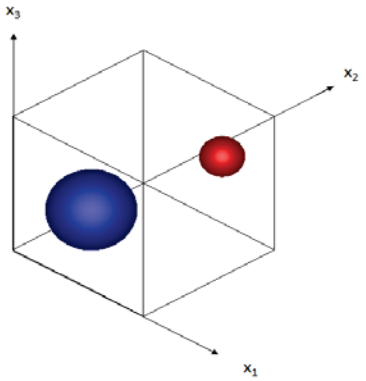

FIGURE 4.0. Spherical inclusions microstructure

A spherical-inclusion microstructure is shown in Figure 4.0. The spheres may represent particles or voids. The diameter of the 2 spheres is 1 micron and 0.5 microns, respectively. The dimensions of the UC are 2x2x2 microns. The larger sphere is centered at (0.6, 0.6, 0.6) and the smaller sphere is centered at (1.5, 1.7, 1.3). The matrix elastic properties are listed in Table IV.0. For the case where the spheres represent particles, the elastic properties of the particles are listed in Table IV.0.

Predict the elastic properties of the microstructure for the case where the spheres represent particles, and the case (not shown here) where the larger sphere represents a particle and the smaller sphere represents a void. Local field recovery should also be performed for both cases. All nontrivial stress components should be reported along the linear path from (0,0,0) to (2,2,2). Only the first (non-voided) case is presented here. The complete results will be available at cdmHUB.

TABLE IV.0. Constituent properties

	Set 4	
Property	Matrix	Particle
E (GPa)	45	450
ν	0.18	0.17
α (μ /°C)	64.8	-0.4

The UC is meshed with a 5×5×5 grid for GMC and 36,694 tetrahedral elements for SwiftComp and 3D FEA. This material is not orthotropic thus the predicted elastic properties are shown here in the form of stiffness matrix. The fully populated stiffness matrix obtained by 3D FEA listed below is reproduced by SwiftComp. GMC and DIGIMAT-MF predict this material to be isotropic and the corresponding stiffness matrices are also listed below which represent noticeable difference from 3D FEA. GMC's prediction is slightly (2.5 to 6%) worse than DIGIMAT-MF, depending upon component, for this case. CTEs are listed in Table IV.I, which shows that GMC slightly (5%) over predicts while DIGIMAT-MF and SwiftComp shows an excellent agreement with 3D FEA.

GMC (MPa)

53.72E3	11.45E3	11.45E3	0	0	0
11.45E3	53.72E3	11.45E3	0	0	0
11.45E3	11.45E3	53.72E3	0	0	0
0	0	0	20.54E3	0	0
0	0	0	0	20.54E3	0
0	0	0	0	0	20.54E3

DIGIMAT-MF/MT (MPa)

55.19E3	12.18E3	12.18E3	0	0	0

12.18E3	55.19E3	12.18E3	0	0	0
12.18E3	12.18E3	55.19E3	0	0	0
0	0	0	21.50E3	0	0
0	0	0	0	21.50E3	0
0	0	0	0	0	21.50E3

DIGIMAT-MF/DI (MPa)

55.36E3	12.22E3	12.22E3	0	0	0
12.22E3	55.36E3	12.22E3	0	0	0
12.22E3	12.22E3	55.36E3	0	0	0
0	0	0	21.56E3	0	0
0	0	0	0	21.56E3	0
0	0	0	0	0	21.56E3

3D FEA and SwiftComp (MPa)

55.33E3	12.13E3	12.11E3	-7.09	0.62	-1.02
12.13E3	55.33E3	12.11E3	-1.00	7.13	-1.11
12.11E3	12.11E3	55.32E3	0.02	0.01	-2.32
-7.09	-1.00	0.02	21.44E3	-3.15	8.91
0.62	7.13	0.01	-3.15	21.44E3	-8.75
-1.02	-1.11	-2.32	8.92	-8.76	21.47E3

Table IV.I. Effective CTEs

Approach	α_1 (μ/°C)	α_2 (μ/°C)	α_3 (μ/°C)
DIGIMAT-MF/MT	56.34	56.34	56.34
DIGIMAT-MF/DI	56.14	56.14	56.14
GMC	58.82	58.82	58.82
SwiftComp	56.31	56.31	56.36
3D FEA	56.30	56.12	56.37

Regarding the local fields, Figures 4.1-4.4 show that GMC does not adequately recover the local stress field along the specified diagonal path. Conversely, the predictions of SwiftComp, for all loading options, shows decent agreement with the predictions of 3D FEA. The computing time for each tool are shown in Table IV.II. It

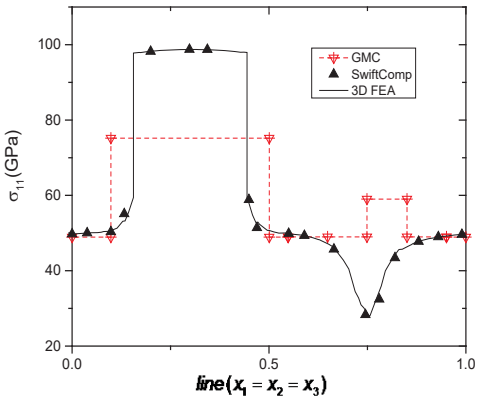

FIGURE 4.1. σ_{11} under ε_{11}

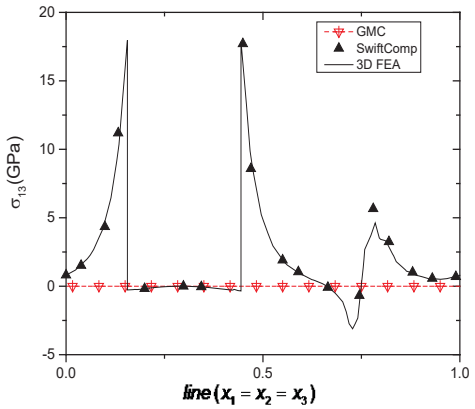

FIGURE 4.2. σ_{13} under ε_{11}

is observed that GMC achieves similar efficiency as DIGIMAT-MF (although GMC has a 6% error) which is orders of magnitude more efficient than 3D FEA. SwiftComp achieves similar accuracy as 3D FEA with 1/4 of its computing time.

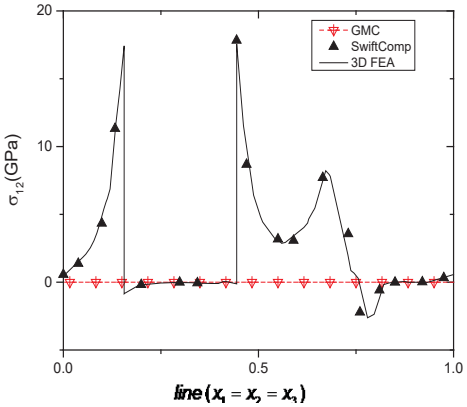

FIGURE 4.3. σ_{12} under ε_{22}

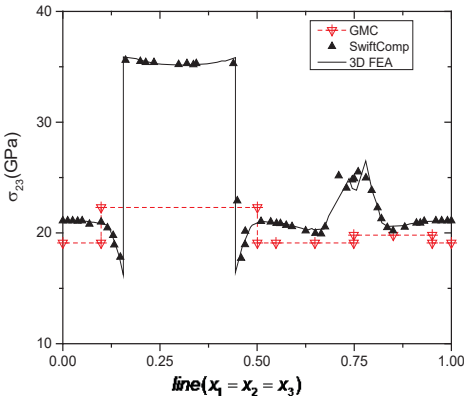

FIGURE 4.4. σ_{23} under ε_{23}

TABLE IV.II. Computing time for case 4

Approach	GMC	DIGIMAT-MF/MT	DIGIMAT-MF/DI	SwiftComp	3D FEA
Homo. (sec)	N/A	N/A	N/A	26	N/A
Dehomo. (sec)				50	
Total (sec)	0.07	0.047	0.047	76	264

Case 5: Woven-fiber microstructure

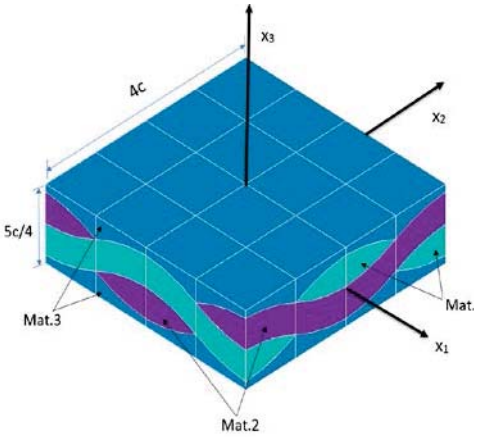

FIGURE 5.0. Woven microstructure

The woven-fiber microstructure shown in Figure 5.0 is representative of a plain weave fabric where the fibers are oriented along the x_1 and x_2-directions. To avoid the difficulty in creating pointwise anisotropy in the mesh, the constituents are assumed to be isotropic. MAT1 has elastic material properties same as those of particle listed in Table IV.0. MAT3 has the same elastic material properties as the matrix listed in Table IV.0. MAT2 has E=300 GPa, ν=0.22, α=0.8 μ/°C. The specific weave geometry of the weave is provided through an iges file. For dehomogenization, all nontrivial stress components should be reported along the paths defined by $x_2=x_3=0$ and $x_1=x_2=0$.

For GMC, the built-in woven composite template with a 4x4x4 grid is used while 3D FEA and SwiftComp are meshed to have 33,600 brick elements. The predicted effective elastic properties are listed in Table V.I. GMC predicts E_1 and Poisson's ratios well while it over predicts E_2 by 6%, G_{12} by 9%, and under predicts E_3 by 6%, G_{13} by 8%, and G_{23} by 7% as compared to 3D FEA. DIGIMAT-MF predictions for all effective properties are different from 3D FEA with the smallest error 7% for E_3 and max error 47% for G_{12}, both predicted by DIGIMAT-MF/MT. As shown in Table V.II, GMC under predicts α_1 by 11% and α_2 by 12% while over predicts α_3 by 12%. CTEs cannot be obtained from the current version of DIGIMAT 5.1.2 for this case.

TABLE V.I Predicted effective elastic properties.

Approach	E_1 (GPa)	E_2 (GPa)	E_3 (GPa)	G_{12} (GPa)	G_{13} (GPa)	G_{23} (GPa)	υ_{12}	υ_{13}	υ_{23}
GMC	208.50	208.50	86.45	87.02	34.86	34.86	0.179	0.188	0.188
DIGIMAT-MF/MT	174.63	140.11	98.75	42.75	44.86	41.88	0.201	0.131	0.158
DIGIMAT-MF/DI	179.33	147.75	111.07	51.17	48.65	47.25	0.200	0.141	0.169
SwiftComp	202.93	197.03	92.40	80.25	37.94	37.61	0.178	0.194	0.191
3D FEA	202.95	196.65	92.48	80.12	37.94	37.59	0.178	0.194	0.191

TABLE V.II Effective CTEs

Approach	α_1 (μ/°C)	α_2 (μ/°C)	α_3 (μ/°C)
GMC	6.76	6.76	41.83
SwiftComp	7.60	8.26	37.25
3D FEA	7.57	8.24	37.24

Regarding the local fields, Figures 5.1-5.4 show that GMC does not adequately recover the local stress field (except in an averaged sense) along the specified diagonal path. Conversely, the predictions of SwiftComp for all loading options show decent agreement with the predictions of 3D FEA. The computing time for each tool are shown in Table V.III. It is observed that GMC achieves similar efficiency and yet better accuracy than DIGIMAT-MF, both are orders of magnitude more efficient than 3D FEA. SwiftComp achieves similar accuracy as 3D FEA with 1/6 of its computing time.

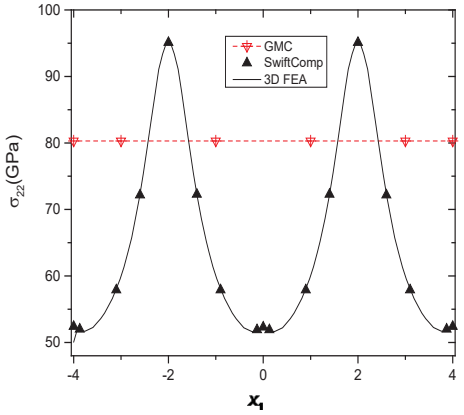

FIGURE 5.1. σ_{22} under ε_{11} (along x_1)

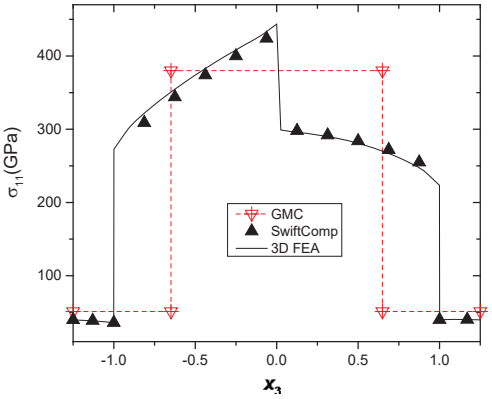

FIGURE 5.2. σ_{11} under ε_{11} (along x_3)

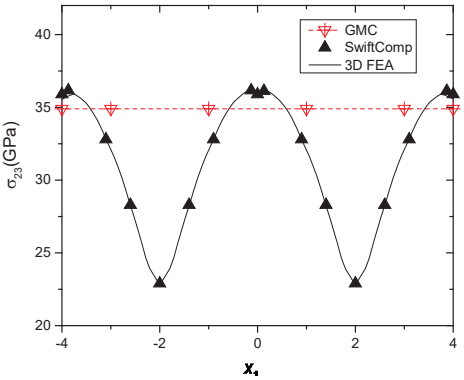

FIGURE 5.3. σ_{23} under ε_{23} (along x_1)

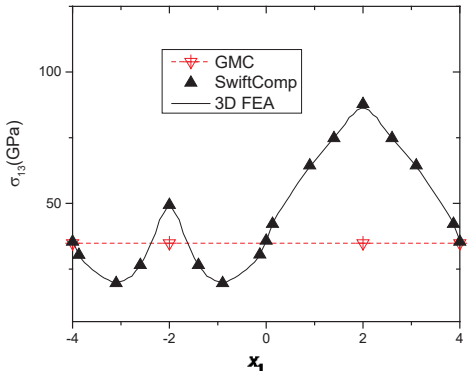

FIGURE 5.4. σ_{13} under ε_{11} & ε_{13} (along x_1)

TABLE V.III Computing time

Approach	GMC	DIGIMAT-MF/MT	DIGIMAT-MF/DI	SwiftComp	3D FEA
Homo. (sec)	N/A	N/A	N/A	27.75	N/A
Dehomo. (sec)				27.67	
Total (sec)	0.08	0.047	0.047	55.42	289.33

Case 6: Short-fiber "random" microstructure

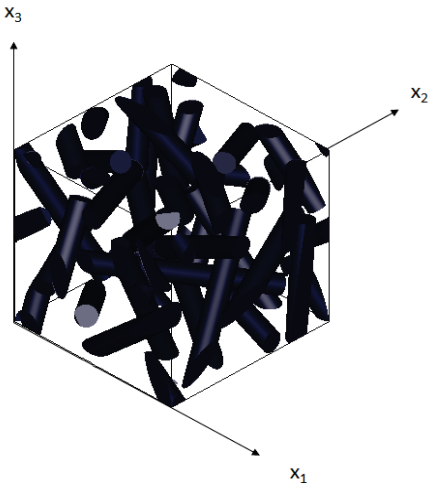

FIGURE 6.0. Short-fiber 3D random orientation microstructure

The final microstructure, shown in Figure 6.0, represents a complex triply periodic short-fiber microstructure. While much physical insight can be gained from simplification of realistic microstructures, the intent of the present microstructure is to challenge the simulation tool in treating very complex geometries. As the intent is not to test the capability of the code to reproduce complex geometries, a single geometry is generated and provided to each tool as either a step or an iges file

In this microstructure, the fibers are "randomly" oriented by rotations in each coordinate direction. The material properties of the fiber and matrix are listed in Table IV.0 with the particle properties used for fibers. For dehomogenization, all nontrivial stress components should be reported along the linear path from (0,0,0) to (L,L,L).

The UC forms a 62×62×62 grid (again believed to be excessive by the authors of the code) for GMC and 548,999 tetrahedral elements for SwiftComp and 3D FEA. The number of elements are increased to effectively capture the complex features of the short fiber microstructure. DIGIMAT-MF results are obtained by assuming the aspect ratio of the fiber to be 5 and with orientation (0.33, 0.33, 0.34) and fiber volume ratio of 7.857%. As seen from the predictions outputs, GMC and DIGIMAT-MF predict 'orthotropic' type behavior (effective properties) for the short fiber composite geometry. The prediction of 3D FEA shows fully populated matrix with anisotropic effective properties, but with the additional terms being much smaller than the orthotropic terms (maximum of 4.5%). Moreover, the predictions of GMC under predicts for all components of the stiffness matrix (with max error up to 14%) while DIGIMAT-MF shows better agreements (max error of 5.8%) with 3D FEA. The predictions of SwiftComp reproduces the prediction of 3D FEA as shown in the stiffness matrix.

GMC (GPa)

52.83	11.53	11.53	0	0	0
11.53	53.08	11.53	0	0	0
11.53	11.53	52.86	0	0	0
0	0	0	20.53	0	0
0	0	0	0	20.53	0
0	0	0	0	0	20.53

DIGIMAT-MF/MT (GPa)

57.15	12.82	12.83	0	0	0
12.82	57.15	12.83	0	0	0
12.83	12.83	57.26	0	0	0
0	0	0	22.18	0	0
0	0	0	0	22.18	0
0	0	0	0	0	21.16

DIGIMAT-MF/DI (GPa)

57.35	12.86	12.88	0	0	0
12.86	57.35	12.88	0	0	0
12.88	12.88	57.46	0	0	0
0	0	0	22.26	0	0
0	0	0	0	22.26	0
0	0	0	0	0	22.24

3D FEA/SwiftComp (GPa)

59.60	13.66	13.47	0.05	-0.60	0.56
13.66	61.70	13.47	0.55	-0.27	-0.12
13.47	13.47	58.75	0.70	-0.07	-0.45
0.05	0.55	0.70	23.24	-0.45	-0.32
-0.60	-0.27	-0.07	-0.45	23.16	0.08
0.56	-0.12	-0.45	-0.32	0.08	23.45

Regarding effective CTEs (Table VI.I), GMC over predicts α_1 by 15%, α_2 by 21%, and α_3 by 12%, and predicts the off-diagonal CTEs to be zero. DIGIMAT-MF over predicts α_2 by 10% and predicts the off-diagonal CTEs to be zero. SwiftComp shows good agreement with 3D FEA for the diagonal CTEs. Although the off diagonal terms are much smaller than the primary, diagonal terms, further investigation is needed why SwiftComp has a different prediction for coupling CTEs as this is the only case we observed a significant difference among all the effective properties and local fields between the prediction of SwiftComp and 3D FEA.

TABLE VI.I Effective CTEs

Approach	α_1 (μ/°C)	α_2 (μ/°C)	α_3 (μ/°C)	$2\alpha_{23}$ (μ/°C)	$2\alpha_{13}$ (μ/°C)	$2\alpha_{12}$ (μ/°C)
DIGIMAT-MF/MT	53.85	53.85	53.69	0.00	0.00	0.00
DIGMAT-MF/DI	53.64	53.64	53.64	0.00	0.00	0.00
GMC	59.52	59.11	59.47	0.00	0.00	0.00
SwiftComp	51.12	48.67	52.60	-3.29	2.35	0.02
3D FEA	51.68	48.75	53.00	-0.16	2.21	0.56

Regarding the local fields, Figures 6.1-6.4 show that GMC does not adequately recover the local stress field (except in an averaged sense) along the specified diagonal path. Conversely, the predictions of SwiftComp for all loading options show decent agreement with the predictions of 3D FEA. The computing time for each tool is shown in Table VI.II. It is observed that GMC is about 10 times faster than 3D FEA and SwiftComp is about six times faster than 3D FEA.

TABLE VI.II. Computing time for case 6

Approach	GMC	DIGIMAT-MF/MT	DIGIMAT-MF/DI	SwiftComp	3D FEA
Homo. (sec)	N/A	N/A	N/A	2873	N/A
Dehomo. (sec)				167	
Total (sec)	1680	0.047	0.047	3040	17496

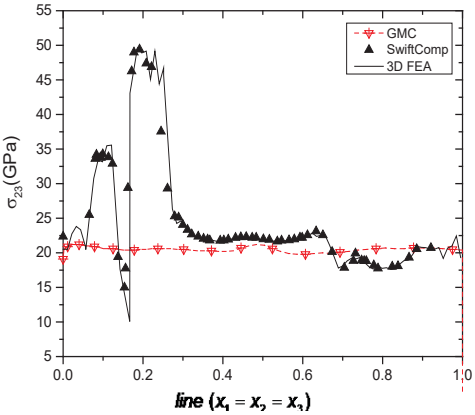

FIGURE 6.1. σ_{23} under ε_{23}

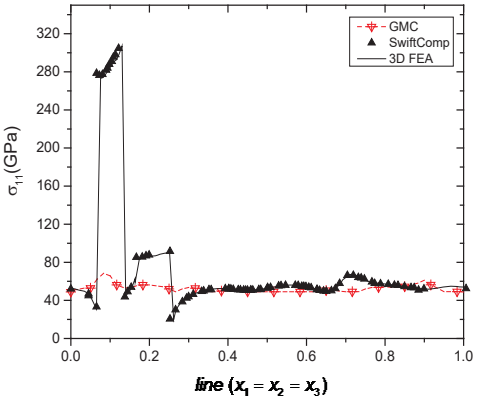

FIGURE 6.2. σ_{11} under ε_{11}

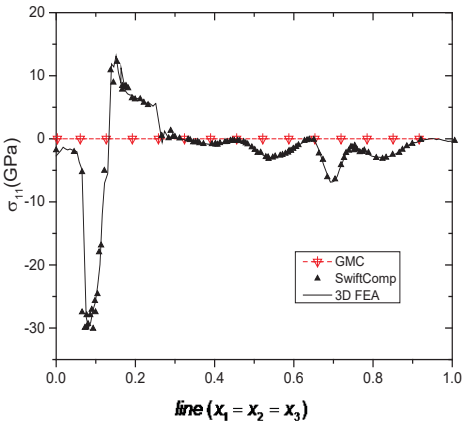

FIGURE 6.3. σ_{11} under ε_{13}

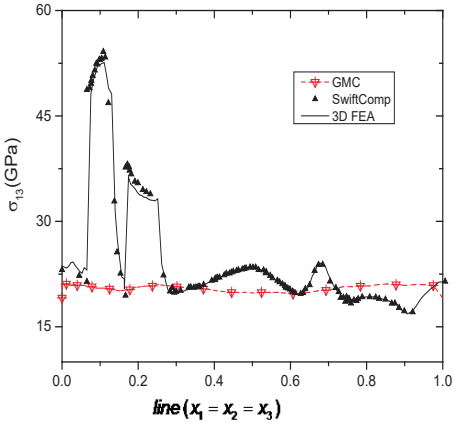

FIGURE 6.4. σ_{13} under ε_{13}

CONCLUSION

A few representative microstructures are used to evaluate existing micromechanics tools including FVDAM, MAC/GMC, DIGIMAT, Altair MDS, and SwiftComp. The results are compared with 3D FEA of a UC subject to periodic BCs. Finally, cmdHUB, utilized provided codes to obtain all results except FVDAM and MDS and all the results were reviewed by corresponding tools providers. NASA Glenn provided some revised input files for GMC and HFGMC which were believed by the tool authors to be better compromise between efficiency and accuracy within the context of each theories limitations. The following conclusion can be drawn from this exercise:

1. Not all the methods are able to accurately predict effective thermoelastic properties and local fields. Different levels of inaccuracy are observed for different quantities and different cases.
2. GMC was shown to be able to solve all problems and provide both effective thermal and mechanical properties and local fields, with minimal input demands

and high computational efficiency provided a small number of cells are used to define UC. HFGMC in general has better predictive ability than GMC, particularly for local fields. However, it is much more computationally expensive and does not handle triply periodic microstructures in MAC/GMC 4.0.

3. DIGIMAT-MF provides an efficient way to predict effective properties. Generally speaking MT provides better prediction than DI. DIGIMAT-MF cannot yet predict CTEs for case 5. No local field prediction were available. DIGIMAT-MF predicts better effective elastic constants than GMC for case 4 and case 6.
4. FVDAM can achieve similar accuracy as 3D FEA for continuous reinforced microstructures except the transverse shear modulus for Case 2. FVDAM currently can handle only doubly periodic microstructures.
5. MDS provides generally good predictions for the first three cases although 3D UCs are most likely used for all the cases. MDS over predicts all the shear moduli for the 0/90 microstructure and under predicts the transverse shear modulus for Case 2. Presently, we only received effective elastic properties for the first three microstructures from Altair, with no local field predictions.
6. SwiftComp consistently maintains excellent agreement with 3D FEA for all the microstructures analyzed in this paper including both effective properties and local fields, except the minor, coupling CTEs for the last case.
7. As far as efficiency is concerned, DIGIMAT-MF is most efficient for most cases as it does not depend on discretization of microstructure, followed by GMC, SwiftComp, FVDAM, HFGMC, and 3D FEA. Note efficiency heavily depends on the discretization of UCs. Because GMC typically requires a far coarser discretization than the other methods to arrive at its own approximate results, it will usually be significantly more efficient than other discretization-based methods. Clearly, the other methods will become more efficient as their meshes are coarsened, but neither this, nor the impact of such coarsening on the predictions, have been investigated in the present paper.
8. As far as versatility is concerned, currently only GMC, SwiftComp, and 3D FEA provide the full set of results including the complete set of thermomechanical effective properties and local fields.

However, these results provide only a snapshot of the state-of-the-art at the time of publication. Hopefully, they will provide some guidance for future development of these codes and other codes. All the results reside in a live database on cdmHUB, which will allow the community at large to run the individual analyses, vary the inputs and interpret results directly.

ACKNOWLEDGEMENT

The authors greatly appreciate 1) Dr. Steven Arnold and his team at NASA Glenn for providing MAC/GMC and providing some updated input files for GMC/HFGMC and reviewing GMC/HFGMC results presented in this paper, 2) Dr. Marek Pindera and his team at University of Virginia for providing FVDAM results, 3) Mr. Jeffery Wollschlager at Altair for providing MDS results, and 4) Dr. Roger Assaker and his team at eXstream engineering reviewing DIGIMAT results. The work is supported by the Composites Design and Manufacturing HUB (cdmHUB.org).

REFERENCES

1. Hinton, M.J., Kaddour, A.S., and Soden, P.D. (eds.) Failure Criteria in Fibre Reinforced Polymer Composites: the World-Wide Failure Exercise. A Composites Science and Technology Compendium, Elsevier, Oxford, UK, 2004.
2. NAFEMS Ltd. International Association of the Engineering Modelling, Analysis and Simulation Communitty. [online] http://www.nafems.org/ [cited 5/2/2014].
3. Yu, W., Williams, T. O., Bednarcyk, B. A., Aboudi, J. and Tang, T. A Critical Evaluation of the Predictive Capabilities of Various Advanced Micromechanics Models. Proceedings of the 48th structures, structural dynamics, and materials conference, Waikiki, Hawaii, 2007.
4. MSC Software Company, DIGIMAT User Manual, Release 5.1.2, 2014.
5. Aboudi, J., Arnold, S.M., and Bednarcyk, B.A. Micromechanics of Composite Materials A Generalized Multiscale Analysis Approach. Elsevier, New York, 2013.
6. B. A. Bednarcyk and S. M. Arnold; "MAC/GMC 4.0 User's Manual, Volume 2: Keywords Manual", TM 2002-212077/Vol 2, 2002.
7. B. A. Bednarcyk and S. M. Arnold; "MAC/GMC 4.0 User's Manual, Volume 3: Example Problem Manual", TM 2002-212077/Vol 3.
8. Cavalcante, M.A.A., Pindera, M-J. and Khatam, H. Finite-Volume Micromechanics of Periodic Materials: Past, Present and Future. Composites B, Vol. 43, No. 6, 2521-2543, 2012.
9. Aboudi, J., Pindera, M-J, and Arnold, S. M. Linear Thermoelastic Higher-Order Theory for Periodic Multiphase Materials. J. Applied Mechanics, Vol. 68, No. 5, 697-707, 2001.
10. Bansal, Y. and Pindera, M-J. A Second Look at the Higher-Order Theory for Periodic Multiphase Materials. J. Applied Mechanics, Vol. 72, No. 2, pp. 177-195, 2005.
11. Arnold S. M., Bednarcyk, B. A., Aboudi, Jacob; "Comparison of the Computational Efficiency of the Original Versus Reformulated High-Fidelity Generalized method of Cells", NASA TM-2004-213438, 2004.
12. Cavalcante, M.A.A., Marques, S.P.C., Pindera, M-J. Parametric Formulation of the Finite-Volume Theory for Functionally Graded Materials. Part I: Analysis. J. Applied Mechanics, Vol. 74, No. 5, pp. 935-945, 2007.
13. Gattu, M., Khatam, H., Drago, A.S. and Pindera, M-J. Parametric Finite-Volume Micromechanics of Uniaxial Continuously-Reinforced Periodic Materials with Elastic Phases. J. Engineering Materials & Technology, 130, No. 3, pp. 031015, 2008.
14. Khatam, H. and Pindera, M-J. Parametric Finite-Volume Micromechanics of Periodic Materials with Elastoplastic Phases. Int. J. Plasticity, Vol. 25, No. 7, pp. 1386-1411, 2009.
15. Tu, W. and Pindera, M-J.. Cohesive Zone-Based Damage Evolution in Periodic Materials Via Finite-Volume Homogenization. J. Applied Mechanics, 81(10), 01005, 2014.
16. Cavalcante, M.A.A. and Pindera, M-J. Generalized FVDAM Theory for Periodic Materials Undergoing Finite Deformation. Part I: Framework. J. Applied Mechanics 81, 021005, 2014.
17. Fish, J. and Yu, Q. Computational Mechanics of Fatigue and Life Predictions for Composite Materials and Structures. Computer Methods in Applied Mechanics, 191:4827–4849, 2002.
18. Yu, W. Structure Genome: Fill the Gap between Materials Genome and Structural Analysis. In Proceedings of the 56th Structures, Structural Dynamics and Materials Conference, Kissimmee, Florida, Jan. 5-9, 2015.
19. Pahr, D.H. and Arnold, S.M. The applicability of the generalized method of cells for analyzing discontinuous reinforced composites. Composites: Part B. 33, 2002.
20. Pineda, E.J., Bednarcyk, B.A., Mital, S.K., and Arnold, S.M. (2015) "The Effect of Stochastically Varying Creep Parameters on Residual Stresses in Ceramic Matrix Composites" 56th AIAA/ASME/ASCE/AHS/ASC Structures, Structural Dynamic, and Materials Conference, AIAA Science and Technology Forum 2015, 5-9, January, Kissimmee, FL, AIAA 2015-0389.
21. Bednarcyk, B.A, Mital, S.M., Pineda, E.J., and Arnold, S.M. (2015) "Multiscale Modeling of Ceramic Matrix Composites" 56th AIAA/ASME/ASCE/AHS/ASC Structures" Structural Dynamic, and Materials Conference, AIAA Science and Technology Forum 2015, January 5-9, Kissimmee, FL, AIAA 2015-1191.

AIAA SciTech
5-9 January 2015, Kissimmee, Florida
56th AIAA/ASCE/AHS/ASC Structures, Structural Dynamics, and Materials Conference

A Micromechanical Approach to Static Failure Prediction of Heterogeneous Materials

Hamsasew Sertse*, and Wenbin Yu†

The objective of this paper is to enable Variational Asymptotic Method for Unit Cell Homogenization (VAMUCH) to predict the static failure strength and the initial failure envelop of heterogeneous materials obeying various failure criteria. These predictions are performed using several representative examples of heterogeneous materials such as continuous fiber reinforced composite, particle reinforced composite, discontinuous fiber reinforced composite, and woven composite. The static failure predictions of VAMUCH are partially evaluated with various micromecahnics approaches such as Mori-Tanaka (MT), Double Inclusion (DI), Generalized Methods of Cells (GMC), High Fidelity Generalized Methods of Cells (HFGMC) and also Finite Element Analysis (FEA). The evaluation reveals that MT and DI insufficiently approximate the static failure compared with FEA whereas GMC and HFGMC better predict compared with MT and DI. However GMC and HFGMC poorly predict failure particularly for maximum principal stress failure criterion. GMC shows relatively better agreement with FEA for Tsai-Hill failure criterion. On the contrary, VAMUCH shows excellent agreements with FEA for all aforementioned examples of heterogeneous materials. Moreover, VAMUCH also generates the initial failure envelop for combined axial and transverse shear using maximum shear stress and Tsai-Hill failure criteria. The prediction of combined shear usually cannot be rigourously performed using commercial FEA software due to complex boundary conditions. In general, the outputs of the predictions signify that maximum principal stress criteria is more conservative compared with Tsai-Hill and Tsai-Wu failure criteria. It is also noticed that the predictions of Tsai-Hill and maximum shear stress criteria agree well for shear loading conditions except for the woven composite.

I. Introduction

Heterogeneous materials are widely used in various industrial applications due to their capability of achieving the desired performance. Despite their extensive use, there are still a number of challenges related to rigourous mathematical modeling of these materials. One of the challenges is lacking of powerful unified tools to accurately predict the failure strength and behaviors of these materials under various loading conditions. Numerous researchers have proposed various approaches to analyze the complex failure behavior of the heterogeneous materials at various levels of abstractions. For monolithic materials, failure may be modeled using Weibull's probabilistic approach. This approach, usually referred as the weakest link theory, postulates that the failure strength of the structure is governed by the weakest point in the structure. This implies that larger structures are more susceptible to failure compared with smaller structures at the same stress level. This is mainly because there is a higher probability of flaw in the larger structures. Cassenti[1] extended the weakest link theory to capture the location of failure and also to analyze the effect of loading history on the failure strength of composite materials. Sun and Yamada[2] also predicted the strength of unidirectional fiber composite under multiaxial stress state using various failure criteria. Generally, in the heterogeneous materials, failure is a complex phenomenon. It results from the interactions among various contributing factors such as the properties of the matrix, the fiber, the matrix-fiber interface, and the fiber volume fraction, and the loading conditions. The failure of a heterogeneous material is usually modeled using both macromechanical and micromechanical approaches. In macromechanical approaches,[3–5] failure analyses are performed based on the averaged/smeared properties of the heterogeneous materials. In this approach,

*Graduate Research Assistant, School of Aeronautics and Astronautics, Purdue University
†Associate Professor, School of Aeronautics and Astronautics, Purdue University, AIAA Associate Fellow.

each lamina may be treated as pseudo homogeneous orthotropic material or laminate as quasi-isotropic material. This is relatively simple for numerical analysis, but it is incapable of accurately predicting the failure strength of heterogeneous materials at the constituent level. Similarly, various micromechanics models are also employed to predict the failure strength and failure surface of heterogeneous materials. Huang[6] used the rule of mixture to predict strength of a unidirectional composite for various loading conditions. Cox and co-authors[7] also estimated the failure strength of a woven composite using this rule. Wakashima and his co-workers[8] used self-consistent approach to predict the initial yield surface and also to analyze the effect of thermal loading on the failure strength of a particle reinforced composite. Tanaka and his co-workers[9] also used the same model to predict the failure and plastic deformation of the continuous fiber reinforced composite. The mean field based micromechanical approach[6,7,9] usually uses the average stress in the matrix and the fiber to predict the strength of heterogeneous materials. This approach is capable of reasonably predicting failure strength at the constituent level compared to macromechanical approach. However, the approach is incapable of capturing the effect of the local stress and also it does not take into account the geometry of the constituents. Thus, failure analysis, using average stress approach, might considerably underestimate the overall strength of heterogeneous materials.[10] In Ref. [11, 13, 14], the method of cell (MOC) is employed to predict the failure strength, the initial and subsequent yield surfaces of composites. Bednarcky and Arnold[10] also used the generalized methods of cells (GMC) to predict the failure of viscoelastic material using the Curtin fiber breakage model and evolving complaint interfacial (ECI) model. MOC and GMC can better predict the failure strength of heterogeneous material based on the local stress fields. However, in MOC and GMC, the local stresses and strains are estimated by averaging local stresses and strains over each subcell, and moreover they inherently lack shear coupling effect, i.e, only the normal local stresses and strains are fairly approximated. These factors can affect the method to insufficiently recover the local stress field in the constituents for various loading conditions. Consequently, MOC and GMC might inadequately predict the failure strength of heterogeneous materials. Choi and Tamma[15] used FEA to analyze the damage initiation in a woven composite using stiffness degradation approach for the normal and shear loading conditions. Scida and his co-workers[16] also analyzed failure in a woven composite using a point wise lamination approach. This approach adopts classical thin-laminate theory to recover the local stresses in the woven composite. This method cannot provide a good approximation for the local stress fields.

According to Ref. [17], if failure happens locally, the load of damaged part obviously transfers to the undamaged part of the constituents. This process results in local and global load sharing through shear and tensile stresses. Hence, it is of great importance to critically investigate initial and subsequent failure of the heterogeneous material at a micro scale level. At a micro scale, failure can be analyzed using the local stress in the constituents and the local interfacial stresses or any combination of these. The local interactions determine the dominating factors that control the failure strength and behavior of the material. For example, the failure strength of Silicon-carbide-fiber/titanium-matrix (SiC/T) composite is governed by the fiber volume fractions. For fiber volume fraction greater than 20%, the fiber mainly controls the failure of the composite otherwise the matrix governs the failure of SiC/T.[10] Dvorak and his co-workers[18] demonstrated that, for transversely loaded composite, matrix properties will mainly govern yielding conditions whereas for longitudinally loaded composite, the ratio of the Young's moduli of the constituents controls the yielding of the composite materials. In Ref. [19, 20], FEA is used to analyze the strength of continuous fiber reinforced composite and woven composite, respectively, using various failure criteria. In these works, failure is evaluated at numerical integration points (Gauss points) for approximating failure strength of the material. This approach is found to be reasonable for critically analyzing failure at constituent level. Generally, it is evident to notice that the local fields will play a vital role in the failure strength prediction of heterogeneous materials. Thus, it is of great interest to use a micromechanical approach with efficient capability of recovering the local fields for better predicting the failure strength and failure envelop of heterogeneous materials. This initiates the present study to predict the static failure strength and the initial failure envelop of heterogeneous materials using variational asymptotic method for unit cell homogenization (VAMUCH).[21] VAMUCH is a recently developed general-purposed micromechanics approach framework by carrying out an asymptotic analysis of the variational statement, synthesizing the merits of both variational methods and asymptotic methods. It has the advantages of analytical micromechanics approaches and the versatile modeling capability of the finite element analysis. VAMUCH is proven to have an outstanding capability of recovering the local stress fields of heterogeneous materials.[22,23] Moreover, Tang and Yu[24] also demonstrated the capability of VAMUCH by producing the yield surface for a continuous fiber reinforced

composite under biaxial loading conditions. Thus, VAMUCH is the natural choice for the prediction of the static failure strength and the initial failure envelop of heterogeneous materials.

Failure, at the constituents level, may be predicted using numerous failure criteria. It is usually postulated that failure is initiated in a multiaxial stress state when the effective stress or maximum stress reaches a limiting or failure value. So far, no single unified failure criterion has been fully developed that can accurately predict the failure of materials. However, several failure criteria are commonly used to predict the failure strength and the failure envelop of heterogeneous materials. These are; maximum principal stress criterion, maximum shear stress criterion, maximum principal strain criterion, Tsai-Hill criterion, Tsai-Wu criterion, and many others. The first three criteria are usually used to identify the failure mode in the material but they fail to capture the stress interactions for multiaxial loading. Tsai-Wu criterion[25] is the most comprehensive failure criterion that uses tensor polynomial failure criterion. The tensor strength has the advantage of rotational invariance, symmetric properties and it is also governed by tensor transformation laws similar to elastic stiffness tensor or compliance tensor. Tasi-Wu failure criterion has also the advantage of capturing stress interactions for various multiaxial stress state conditions but it is unable to predict the mode of failure of the materials. For the details of the failure criteria, interested reader may refer to Ref. [26].

The objective of this paper is to enable VAMUCH to predict the static failure strength of heterogeneous materials and the initial failure envelop using various failure criteria such as maximum principal stress criterion, Tsai-Hill criterion, and Tsai-Wu criterion, maximum shear stress criterion, and maximum principal strain criterion. The failure analyses are performed under uniaxial and combined loading conditions using several representative examples of heterogeneous materials such as continuous fiber reinforced composite, particle reinforced composite, discontinuous fiber reinforced composite, and woven composite. The unit cell (UC) of the heterogeneous material is sufficiently discretized and then the failure is evaluated at numerical integration point (Gauss point). Finally, the prediction of VAMUCH is then compared with MT, DI, GMC, HFGMC, and FEA. A detailed review on GMC and HFGMC can be found in Ref. [27–29]. These analyses not only demonstrate the static failure and the initial failure envelop predictive capability of VAMUCH but also help engineers to use appropriate models for related problems based on the capability of corresponding approaches. Moreover, the analyses will give a general direction for inception of damage in heterogeneous material.

II. Variational Asymptotic Method for Unit Cell Homogenization

VAMUCH is a general-purpose micromechanics approach that is capable of predicting the effective properties of heterogeneous materials and recovering the local fields. Different micromechanical approaches adopt different assumptions in the literature, however there are only two essential assumptions associated with the micromechanical analysis of heterogeneous materials with identifiable UCs. These assumptions are:

1. The exact solutions of the field have their volume averages over the UC, i.e., if u_i denotes the exact displacements within the UC, there exists a v_i such that

$$v_i = \frac{1}{\Omega}\int_\Omega u_i d\Omega \equiv \langle u_i \rangle, \tag{1}$$

   where Ω denotes the domain occupied by a UC and also its volume, and $\langle\cdot\rangle$ denotes the volume average over Ω;

2. The effective material properties obtained using the micromechanical analysis are independent of the geometry and boundary conditions of the macroscopic structure, or to say, the effective material properties are assumed to be the intrinsic properties of the material when macroscopically viewed.

These two essential assumptions are the basis for the formulation of VAMUCH. VAMUCH does not depend on any other ad hoc assumptions. In general, the derivation of VAMUCH starts from the variational statement of a heterogeneous continuum. Note that the macroscopic dimensions of these structures are usually several orders of magnitude greater than the heterogeneity length scale. This leads one to formulate the problem of homogenization as a problem of constrained minimization on a single UC and to perform an asymptotic analysis of the variational statement. Introduce two Cartesian coordinate systems, $\mathbf{x} = (x_1, x_2, x_3)$ and $\mathbf{y} = (y_1, y_2, y_3)$. Let x_i denote the global coordinates describing the macroscopic structure,

and let y_i denote the local coordinates describing the UC. The variational statement of the problem can be formulated as seeking the minimum of the functional

$$\Pi_\Omega = \frac{1}{2\Omega}\int_\Omega \left[\bar{\epsilon}_{ij} + \chi_{(i|j)}\right] \mathcal{C}_{ijkl} \left[\bar{\epsilon}_{kl} + \chi_{(k|l)}\right] d\Omega \tag{2}$$

within a UC, where $\mathcal{C}_{ijkl}$ denote the fourth-order elasticity tensor, $\bar{\epsilon}_{ij}$ denotes the components of the global strain tensor for the homogenized structure, χ_i denotes the components of the fluctuation functions and must satisfy the periodic boundary conditions along with constraint

$$\langle \chi_i \rangle = 0, \tag{3}$$

and

$$\chi_{(i|j)} = \frac{1}{2}\left(\frac{\partial \chi_i}{\partial y_j} + \frac{\partial \chi_j}{\partial y_i}\right). \tag{4}$$

This minimization problem can be solved analytically for very simple cases; however, to handle general case, finite element method is the common choice for solving this problem. Eq. (2) can be discretized as follows. Introduce the following matrix notations:

$$\bar{\epsilon} = \begin{bmatrix} \bar{\epsilon}_{11} & 2\bar{\epsilon}_{12} & \bar{\epsilon}_{22} & 2\bar{\epsilon}_{13} & 2\bar{\epsilon}_{23} & \bar{\epsilon}_{33} \end{bmatrix}^T, \tag{5}$$

$$\begin{Bmatrix} \frac{\partial \chi_1}{\partial y_1} \\ \frac{\partial \chi_1}{\partial y_2} + \frac{\partial \chi_2}{\partial y_1} \\ \frac{\partial \chi_2}{\partial y_2} \\ \frac{\partial \chi_1}{\partial y_3} + \frac{\partial \chi_3}{\partial y_1} \\ \frac{\partial \chi_2}{\partial y_3} + \frac{\partial \chi_3}{\partial y_2} \\ \frac{\partial \chi_3}{\partial y_3} \end{Bmatrix} = \begin{bmatrix} \frac{\partial}{\partial y_1} & 0 & 0 \\ \frac{\partial}{\partial y_2} & \frac{\partial}{\partial y_1} & 0 \\ 0 & \frac{\partial}{\partial y_2} & 0 \\ \frac{\partial}{\partial y_3} & 0 & \frac{\partial}{\partial y_1} \\ 0 & \frac{\partial}{\partial y_3} & \frac{\partial}{\partial y_2} \\ 0 & 0 & \frac{\partial}{\partial y_3} \end{bmatrix} \begin{Bmatrix} \chi_1 \\ \chi_2 \\ \chi_3 \end{Bmatrix} \equiv \Gamma_h \chi, \tag{6}$$

where Γ_h denotes an operator matrix, and χ denotes a column matrix containing the three components of the fluctuation functions. Let χ be discretized using finite elements as

$$\chi(x_i; y_i) = S(y_i)\,\mathrm{X}(x_i), \tag{7}$$

where S denotes the shape functions, and X denotes a column matrix of the nodal values of the fluctuation functions for all the active nodes. The discretized version of Eq. (2) can then be obtained as

$$\Pi_\Omega = \frac{1}{2\Omega}\left(\mathrm{X}^T E \mathrm{X} + 2\mathrm{X}^T D_{h\epsilon}\bar{\epsilon} + \bar{\epsilon}^T D_{\epsilon\epsilon}\bar{\epsilon}\right), \tag{8}$$

where

$$E = \int_\Omega (\Gamma_h S)^T D (\Gamma_h S)\, d\Omega, \quad D_{h\epsilon} = \int_\Omega (\Gamma_h S)^T D d\Omega, \quad D_{\epsilon\epsilon} = \int_\Omega D d\Omega \tag{9}$$

with D denoting the 6×6 stiffness matrix condensed from $\mathcal{C}_{ijkl}$. It can be derived from Eq. (8) that Π_Ω attains its minimum only if

$$E\mathrm{X} = -D_{h\epsilon}\bar{\epsilon} \tag{10}$$

which can be used to solve for x as;

$$\mathrm{X} = \mathrm{X}_0\bar{\epsilon}. \tag{11}$$

Eq. (11) implies that X is linearly dependent on $\bar{\epsilon}$. Substituting Eq. (11) into Eq. (8) gives the minimum of Π_Ω as

$$\Pi_\Omega = \frac{1}{2\Omega}\bar{\epsilon}^T\left(\mathrm{X}_0^T D_{h\epsilon} + D_{\epsilon\epsilon}\right)\bar{\epsilon} \equiv \frac{1}{2}\bar{\epsilon}^T\bar{D}\bar{\epsilon}, \tag{12}$$

where $\bar{D}$ denotes the so-called effective stiffness matrix, and $\bar{\epsilon}$ denotes the global strain column matrix.

Till now, the effective material properties can be fully determined. In addition, if the local fields are of interest, they can be recovered using the global displacements, v, the global strains, $\bar{\epsilon}$, and the fluctuation functions, χ. Specifically, the local displacements can be recovered as

$$u = v + \begin{bmatrix} \frac{\partial v_1}{\partial x_1} & \frac{\partial v_1}{\partial x_2} & \frac{\partial v_1}{\partial x_3} \\ \frac{\partial v_2}{\partial x_1} & \frac{\partial v_2}{\partial x_2} & \frac{\partial v_2}{\partial x_3} \\ \frac{\partial v_3}{\partial x_1} & \frac{\partial v_3}{\partial x_2} & \frac{\partial v_3}{\partial x_3} \end{bmatrix} \begin{Bmatrix} y_1 \\ y_2 \\ y_3 \end{Bmatrix} + S\bar{\mathrm{X}}_0\bar{\epsilon}, \tag{13}$$

where u and v denote the local and global displacement column matrices, respectively, and $\bar{\mathrm{X}}_0$ denotes the nodal values of fluctuation functions modified from X_0 by the periodic boundary conditions and Eq. (3). The local strains can be recovered as

$$\epsilon = \bar{\epsilon} + \Gamma_h S\bar{\mathrm{X}}_0\bar{\epsilon}, \tag{14}$$

where ϵ denotes the the local strain column matrix. The local stresses can be recovered from the local strains as

$$\sigma = D\epsilon. \tag{15}$$

It is worth notice that, although VAMUCH seems as versatile as the finite element method, it is by no means an extension of the traditional displacement-based finite element method. In fact, the VAMUCH code has the following distinctive features:

- The complete set of effective material properties can be obtained within one analysis, without the application of any external loads or displacement boundary conditions;
- The fluctuation functions and the displacements are uniquely determined;
- The effective material properties and the recovered local fields are directly obtained with the same accuracy of the fluctuation functions, without any postprocessing-type calculations (e.g., averaging the stresses or the strains),
- The dimensionality of the problem is determined by that of the periodicity of the UC.

Interested readers can refer to Ref. [21] for more details on the VAMUCH theory.

III. Brief Review of Failure Criteria

There are various failure criteria in literature, the most common ones are: maximum principal stress criterion, maximum shear stress criterion, Tsai-Hill criterion, and Tsai-Wu criterion. The maximum principal stress criterion, usually known as Rankine's criterion, postulates that failure begins at a given point where the maximum principal stress reaches a value equal to the tensile (or compressive) yield stress which can be expressed as

$$|\frac{\sigma}{Y_T}| = 1 \qquad if \qquad \sigma > 0 \qquad or \qquad |\frac{\sigma}{Y_C}| = 1 \qquad if \qquad \sigma < 0, \tag{16}$$

where σ is the principal stress, Y_T and Y_C are the tensile and compressive failure strength of the material, respectively.

The maximum shear stress criterion, also known as the Tresca criterion, is based on the principal shear stress in the material; the maximum shear stress of a material point will be compared to the shear strength of the material. The yield function for the maximum shear stress criterion may be defined by

$$f(\tau) = \tau - \frac{Y}{2}, \tag{17}$$

where τ is the maximum shear stress, and Y is failure limit of the material.

Tsai-Hill failure criterion is more general type of failure criteria compared with maximum principal stress and maximum shear stress criteria. It includes both tensile and shear failure strength of the material to

predict the failure in the material. For two dimensional (2D) stress state, Tsai-Hill failure criterion can be expressed as

$$f_A = \sqrt{f_A(\sigma)}, \tag{18}$$

$$f_A(\sigma) = \frac{(\sigma_{11})^2}{X^2} - \frac{\sigma_{11}\sigma_{22}}{X^2} + \frac{(\sigma_{22})^2}{Y^2} + \frac{(\sigma_{12})^2}{S^2}, \tag{19}$$

where X and Y denote axial and transverse tensile strength, S denotes transverse shear strength, and σ_{11}, σ_{22}, and σ_{12} denote stress in the respective direction. In this criterion, failure is assumed to be initiated if $f_A \geq 1$.

Tsai-Wu Failure criterion[25] assumes that the failure envelop can be expressed using scalar form by Eq. (20),

$$f(\sigma_k) = F_i\sigma_i + F_{ij}\sigma_i\sigma_j = 1, \qquad i, j, k = 1, 2, ..6 \tag{20}$$

where F_i and F_{ij} are the strength tensor of second and fourth order tensor, respectively. F_{ij} is symmetric and governed by tensor transformational law. A material is assumed to be failed if the value of $f \geq 1$. In this case, there are two constraints applied to Eq. (20). The first one is stability condition. This ensures none negativity of the diagonal terms in F_{ij} tensor to be consistent with physical condition and second constraint is inadmissibility of hydrostatic failure. Interested readers may refer to Ref. [25]. The detail review of the prediction capability of various failure criteria may be obtained from Ref. [14, 26, 30].

IV. Static Failure Prediction

In this section, the predictions of static failure and initial failure envelop of the heterogeneous materials are performed using various micromechanics approaches such as MT, DI, GMC, HFGMC, VAMUCH and FEA. These approaches employ different methods of analyzing failure in heterogeneous materials. In MT and DI, failure is generally assumed to occur when the average stress in the matrix or in the fiber reaches the maximum values. The outputs of MT and DI are obtained using DIGIMAT 5.1.1 software from MSC Software and e-Xstream engineering. In GMC and HFGMC, failure is assumed to be initiated when the local stress averaged over the subcell reaches its limiting point. The results of GMC and HFGMC are obtained using micromechanics analysis code MAC 4.0/GMC developed by NASA Glenn Research Center. For VAMUCH and FEA, failure is assumed to be initiated when the stress at a numerical integration point (Gauss Point) reaches its maximum limiting value based on the failure criterion. The results of FEA are obtained using ANSYS by employing the micromechanics approach proposed by Sun and Vaidya.[31] These predictions are performed using several representative examples of heterogeneous materials such as continuous fiber reinforced composite, particle reinforced composite, discontinuous fiber reinforced composite, and woven composite. The static failure strength and initial failure envelop are analyzed using various failure criteria such as maximum principal stress criterion, Tsai-Hill criterion, Tsai-Wu criterion, maximum shear stress criterion, and maximum principal strain criterion. Finally, the predictions of VAMUCH are compared with the predictions of MT, DI, GMC, HFGMC, and FEA for all aforementioned examples of heterogeneous material. It should be noted that the proposed FEA appraoch[31] does not rigorously simulate the periodic boundary conditions adopted in MT, DI, GMC, HFGMC and VAMUCH. Thus, some differences are obviously expected between the results of FEA and other approaches. All failure analyses are performed using material properties listed in the Table 1.

Table 1. Material property for failure analysis (Ref. [19,32])

Type		$E(GPa)$	ν	Strength (GPa)	Shear strength (GPa)
1	Fiber	130	0.3	2.8	-
	Matrix	3.5	0.35	0.07	-
2	Fiber	86	0.22	4.8	2.4
	Matrix	4.3	0.34	0.083	0.04

A. Continuous fiber reinforced composite

The unit cell of continuous fiber reinforced composite is generated by assuming that a circular fiber is embedded in a square matrix. Let the local Cartesian coordinate be introduced at the center of unit cell as $y = (y_1, y_2, y_3)$ with y_1 is parallel to the fiber direction as depicted in Figure 1. A 26×26 subcell grid is used for GMC and HFGMC, and a mesh of 45008-noded quadrilateral and SOLID95 elements are used for VAMUCH and FEA, respectively. First, let the material property listed in the Table 1 (type 1) be used to predict the static failure strength of continuous fiber reinforced composite and also let the fiber volume of 63% be used for this prediction. Using maximum principal stress criterion, the following predictions are obtained. MT and DI predict the axial static failure strength to be 1.64 GPa and 1.60 GPa, respectively. GMC and HFGMC predict the the static failure strength to be 1.62 GPa and 1.76 GPa. The predictions of VAMUCH and FEA are found to be 1.61 GPa and 1.60 GPa, respectively. All approaches except HFGMC show a good agreement with the prediction of FEA. This prediction is consistent with the suggested failure strength in Ref [19] which was estimated to be 1.61 GPa. However, this is not found to be the case for the transverse static failure strength of the composite. MT and DI predict 89.36 MPa and 140.91 MPa, respectively, while GMC and HFGMC estimate the transverse static failure to be 40.26 MPa and 41.16 MPa, respectively. The predictions of VAMUCH and FEA are found to be 34.21 GPa and 34.21 MPa, respectively. From this analysis, it is clear to notice that the predictions of transverse static failure strength are not well approximated by all approaches except VAMUCH compared with FEA.

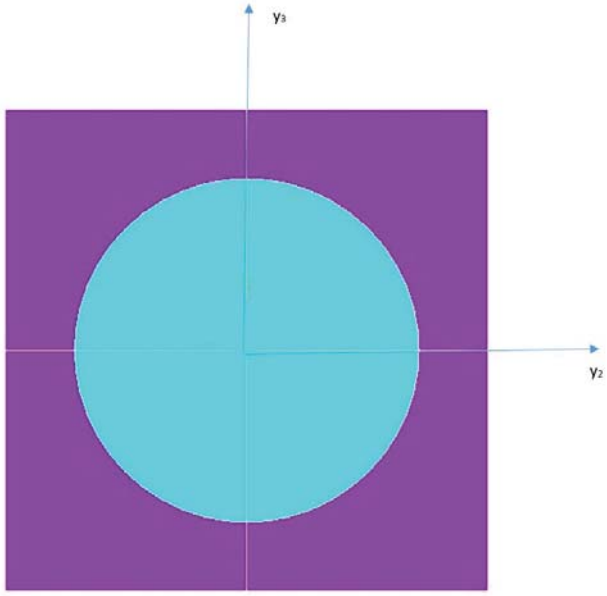

Figure 1. Unit cell for continuous fiber reinforced composite

The predictions of the axial and transverse failure strength are also analyzed for material property of type 2 using maximum principal stress and Tsai-Hill failure criteria. As shown in Tables 2 and 3, the prediction results show that MT and DI produce roughly close predictions of the axial failure strength for maximum principal stress and Tsai-Hill failure criteria compared with FEA particularly for small fiber volume fraction. As the fiber volume fraction increases, the two approaches overpredict the axial failure strength for both failure criteria. The transverse failure predictions of MT and DI are observed to be significantly overpredicted compared with FEA for both maximum principal stress and Tsai-Hill failure criteria. GMC fairly approximates the axial failure strength using both maximum principal stress and Tsai-Hill failure criteria, while HFGMC overpredicts the failure strength of the composite for both failure criteria. For transverse failure strength, GMC poorly approximates for lower fiber volume fraction for maximum principal stress criterion but shows better agreement for up to 40% fiber volume. The predictions of GMC for transverse failure strength shows relatively better agreement with FEA for Tsai-Hill failure criterion, whereas HFGMC significantly overpredicts the transverse failure strength for both maximum principal stress and Tsai-Hill failure criteria. Conversely, the predictions of VAMUCH shows excellent agreements for both failure criteria

and different fiber volume fractions.

Table 2. Axial and transverse failure strength of continuous fiber reinforced using maximum principal stress criterion

	Axial strength (MPa)						Transverse strength (MPa)					
Vof(%)	MT	DI	GMC	HFGMC	VAMUCH	FEA	MT	DI	GMC	HFGMC	VAMUCH	FEA
1	99.00	98.92	100.00	100.00	95.37	95.37	83.64	83.76	74.88	74.00	51.51	50.24
10	240.12	239.56	240.00	268.00	235.85	235.85	86.76	87.58	61.62	72.00	51.93	50.88
20	339.11	393.98	392.00	440.00	389.19	389.19	90.16	92.79	56.94	82.00	52.26	51.45
40	700.58	688.63	688.00	860.00	686.58	686.58	97.15	110.63	53.82	119.00	50.85	50.75
60	1001.5	956.43	970.00	1200.00	963.26	963.26	103.91	146.1	50.70	170.00	44.20	44.09

Table 3. Axial and transverse failure strength of continuous fiber reinforced using Tsai-Hill failure criterion

	Axial strength (MPa)						Transverse strength (MPa)					
Vof(%)	MT	DI	GMC	HFGMC	VAMUCH	FEA	MT	DI	GMC	HFGMC	VAMUCH	FEA
1	98.89	98.89	100.00	100.00	97.59	97.32	85.69	85.69	77.60	77.60	67.98	67.92
10	242.39	242.39	240.00	268.00	238.78	237.84	96.72	97.11	70.50	78.40	68.84	68.51
20	402.26	402.26	399.00	440.00	395.60	395.27	102.84	105.96	69.30	96.00	67.51	67.53
40	722.03	729.47	710.00	800.00	708.96	708.96	114.6	130.86	73.50	173.25	68.88	68.88
60	1047.7	1073.00	1022.00	1200.00	999.08	998.74	124.95	178.72	74.70	269.5	73.11	72.97

The initial failure envelops are also generated using maximum principal stress, Tsai-Hill and Tsai-Wu failure criteria. For maximum stress failure criteria, Figure 2 shows that GMC overpredicts the failure limit of the composite for the combined loading conditions, i.e, the axial and transverse loading conditions. On the other hand, VAMUCH shows an excellent agreement with FEA. For Tsai-Hill failure criterion, Figure 3, GMC predicts well except slight deviation from FEA for larger combined loading condition. The initial failure envelop generated by VAMUCH agrees well with the prediction of FEA. The failure envelop generated by Tsai-Wu failure criteria is found to same as the one generated by the Tsai-Hill failure criteria thus it is not necessary to repeat it here.

In this failure strength prediction, it can easily be noticed that the axial strength of continuous fiber reinforced composite increases with fiber volume fraction for both failure criteria. On the contrary, except for MT, DI, and HFGMC, the transverse strength decreases for maximum principal stress criterion. In the transverse direction, failure is mainly governed by matrix and the stress disturbance at the fiber-matrix interface. The increase of fiber volume will increase the area of stress disturbance thereby increases the chance of failure of the composite, i.e., consistent with the weakest link theory. But this is not observed to be the same for Tsai-Hill failure criterion where transverse failure strength also increases with fiber volume fractions. Generally, all approaches produce close prediction of the axial failure strength for relatively lower fiber volume fractions for both failure criteria, but the prediction of transverse failure strength is found to be significantly different. It is also clear to observe that the mean field homogenization approaches, MT and DI, poorly estimate both the axial and transverse failure strength. The main reason for the poor predictions of the failure strength may be due to that fact that these approaches are evaluating failure based on the average stress in the matrix and fiber. They fail to accurately recover the local stress and strain fields within the matrix, fiber and particularly in the fiber-matrix interface where the stress disturbance is most likely to occur. The capability of local field recovery remarkably influences the failure analysis in the heterogeneous material at micro level.

The shear failure strength is also predicted using axial and transverse shear loading conditions. In this case, failure is mainly caused by shear stress. This ensures that the shear failure strength of the continuous fiber reinforced composite could better be predicted using Tsai-Hill, maximum shear stress, and Tsai-Wu failure criteria. The axial and transverse shear loading are applied as proposed in the Ref. [31]. The material properties of type 2 listed in the Table 1 are used for this analysis. Please note that the current version of DIGMAT 5.1.1 does not support shear loading option thus the results of MT and DI are omitted. As shown

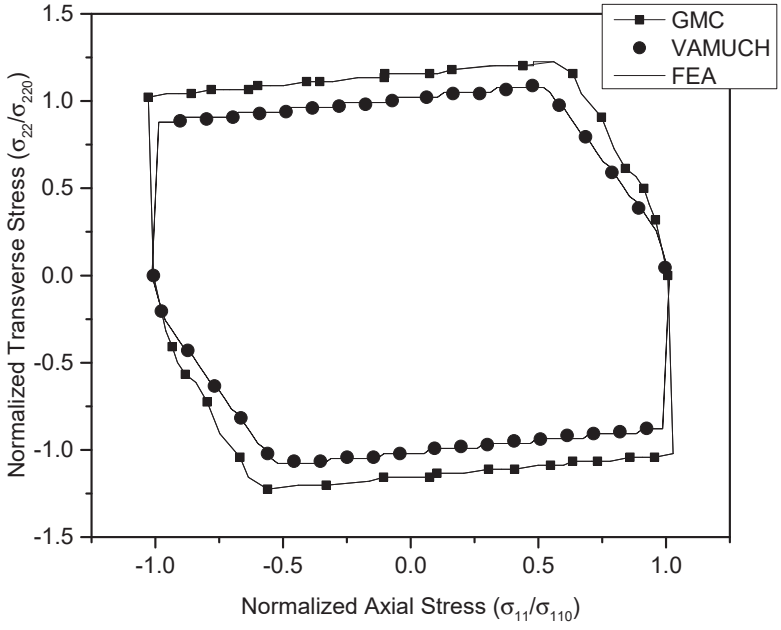

Figure 2. Initial failure envelop of continuous fiber reinforced composite (Maximum Principal Stress for 60% vof)

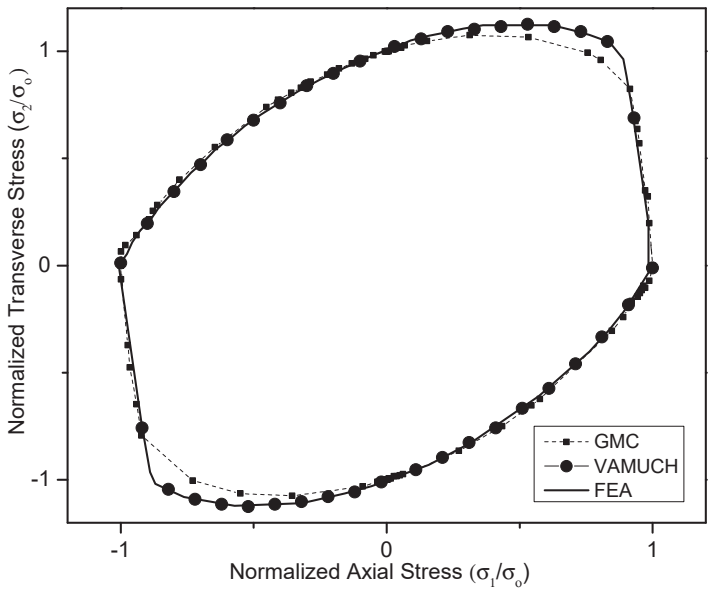

Figure 3. Initial failure envelop of continuous fiber reinforced composite (Tsai-Hill for 60% vof)

in the Table 4, the predictions of shear failure strength indicate that GMC fairly overpredicts the axial shear strength of the composite for lower fiber volume but shows better for relatively larger fiber volume fraction, while HFGMC significantly overpredicts for larger fiber volume fractions compared with the predictions of FEA. The predictions of transverse shear failure strength of GMC remains to be invariant for all fiber volume fractions. On the other hand, HFGMC predicts the transverse shear strength fairly well compared with FEA for Tsai-Hill failure criteria. On the contrary, VAMUCH shows excellent agreements with the predictions of FEA. The axial and transverse shear strength are also evaluated using maximum shear stress and Tsai-Wu failure criteria as shown in Table 5. The current version of MAC/GMC 4.0 does not support maximum shear stress criterion. As it can be seen from Table 5, the axial and transverse shear strength failure predictions of VAMUCH show excellent agreements with the predictions of FEA for both maximum shear stress and Tsai-Wu failure criteria for different fiber volume fractions. Moreover, the combined shear loading conditions may also be used to generate the initial failure envelop of the continuous fiber reinforced composite. But the application of boundary conditions for the combined axial and transverse shear loading conditions are very difficult. Thus, ANSYS is not used for this prediction. The output of MT, DI, GMC, and HFGMC are also omitted as they do not provide options of this type of loading conditions. But, VAMUCH can be used to generate the initial failure envelop for any possible combined loading options. As depicted in the Figure 4, the initial failure envelop of axial and transverse shear looks identical for maximum principal stress and Tsai-Hill failure criteria. It is also learned that these failure criteria yield very close predictions for unidirectional shear failure analyses.

Table 4. Axial and transverse shear failure strength of continuous fiber reinforced using Tsai-Hill criterion

	Axial shear strength (MPa)				Transverse shear strength (MPa)			
Vof(%)	GMC	HFGMC	VAMUCH	FEA	GMC	HFGMC	VAMUCH	FEA
1	36.62	33.95	25.52	25.52	40.02	34.92	34.04	34.00
10	29.97	35.64	23.87	23.88	40.02	29.10	32.94	33.08
20	27.30	37.20	24.60	24.61	40.02	28.13	31.84	31.85
40	24.92	46.50	24.96	24.95	40.02	27.44	31.06	31.04
60	21.85	68.60	22.10	22.08	40.02	30.07	28.23	28.18

Table 5. Axial and transverse shear failure strength of continuous fiber reinforced using maximum shear stress and Tsai-Wu criterion

	Maximum shear stress				Tsai-Wu			
	Axial shear strength (MPa)		Transverse shear strength (MPa)		Axial shear strength(MPa)		Transverse shear strength (MPa)	
Vof(%)	VAMUCH	FEA	VAMUCH	FEA	VAMUCH	FEA	VAMUCH	FEA
1	25.51	25.52	34.05	34.00	30.57	30.57	40.71	40.76
10	23.87	23.87	32.94	33.07	28.6	28.6	39.46	39.62
20	24.60	24.60	31.85	31.83	29.47	29.47	38.13	38.15
40	24.95	24.95	31.04	31.06	29.89	29.9	37.18	37.21
60	22.09	22.08	28.22	28.18	26.45	26.47	33.75	33.81

Finally, maximum principal strain failure criterion is employed to predict the strength of the continuous fiber reinforced composite using strain or displacement loading conditions. In this case, an interesting result is observed for the axial failure strain, all approaches including FEA produce the same prediction of axial failure strain approximated to be 0.019 for the material property (type 2) irrespective of the fiber volume. Since the allowable strains of the fiber is greater than the matrix, the matrix controls the failure of the composite. However, this is not observed to be the same for the transverse failure strain prediction. As it can be seen from the Table 6, MT and DI overestimate the failure strain compared with FEA. GMC and HFGMC also fairly overpredict compared with FEA. On the other hand, VAMUCH shows excellent agreement with FEA for all fiber volume fractions. The initial failure envelop is also generated using maximum principal strain

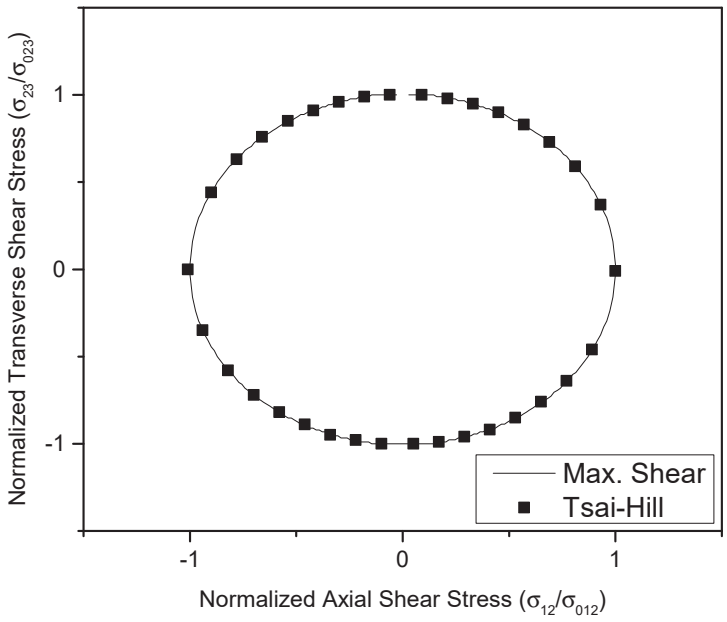

Figure 4. Initial failure envelop of axial and transverse shear predicted using VAMUCH (for 60% vof)

failure criteria. As depicted in the Figure 6, MT and DI overpredict the initial failure envelop nearly by more than 2.5 times compared to FEA. GMC shows a better prediction of the envelop, although not as good as VAMUCH compared with FEA.

Table 6. Transverse shear failure strength of continuous fiber reinforced using maximum strain failure criterion

Vof(%)	MT	DI	GMC	HFGMC	VAMUCH	FEA
1	0.019	0.019	0.0173	0.0174	0.0149	0.0149
10	0.018	0.018	0.0130	0.0156	0.0117	0.0119
20	0.016	0.016	0.0103	0.0155	0.0095	0.0098
40	0.012	0.012	0.0067	0.0157	0.0060	0.0060
60	0.009	0.009	0.0037	0.0152	0.0033	0.0033

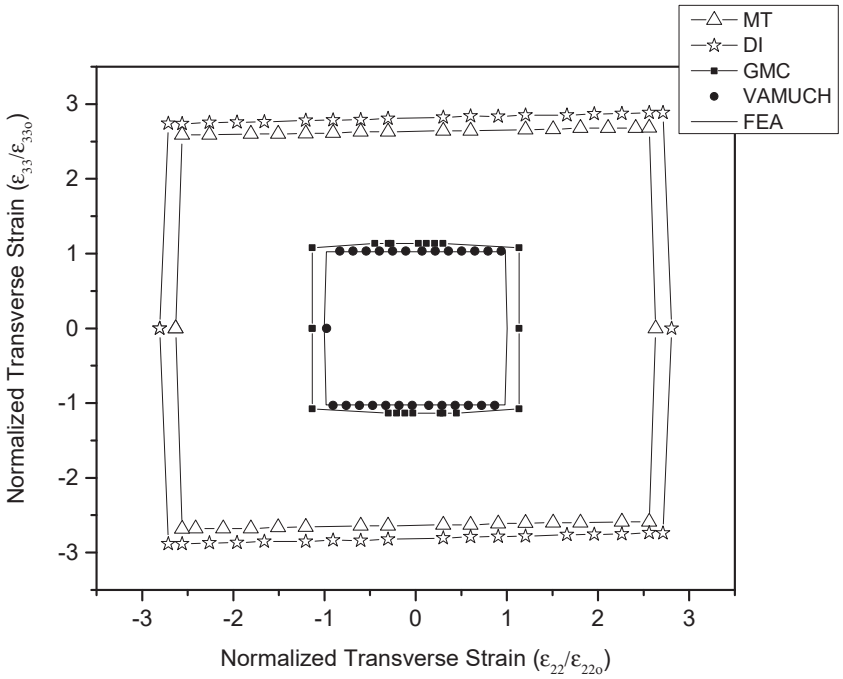

Figure 5. Initial failure envelop of continuous fiber reinforced composite (maximums principal strain for 60% vof)

B. Particle reinforced composite

In this case, let a spherical inclusion with 40% fiber volume be embedded at the center of cuboidal matrix to be used as a unit cell for particle reinforced composite. Let the local Cartesian coordinates be set at the center of sphere. The material properties of particle and the matrix are listed in the Table 1 (type 2). For MT and DI, a built in model is used, and for GMC a built-in spherical particle reinforced model with 343 elements is used. The current version of MAC/GMC 4.0 does not support 3D analysis for HFGMC. A cuboidal unit cell with 7776 elements is used for VAMUCH and FEA. Further refining of the mesh does not have any significant improvement on the outputs of GMC, however it may slightly change the outputs of VAMUCH and FEA. The results of FEA analysis are obtained by using SOLID95 elements. The static failure strength of the particle reinforced composite is predicted using MT, DI, GMC, VAMUCH and FEA. The predictions using maximum principal stress failure criterion, Table 7, reveal that both MT and DI significantly overestimate the axial failure strength of the particle reinforced composite approximately by more than 9 and 12 times, respectively, compared with FEA for 50% particle volume. GMC significantly overpredicts compared with FEA, while VAMUCH shows an excellent agreement. For Tsai-Hill and Tsai-Wu failure criteria, Table 8, both MT and DI significantly overpredict the axial failure strength of particle reinforced composite particularly for large particle volume. GMC slightly overpredicts compared with FEA using Tsai-Hill criteria while VAMUCH shows excellent agreements. Please note that GMC does not support Tsai-Wu failure criterion. Except for MT, the prediction of Tsai-Hill and Tsai-Wu are found to similar for all other approaches. It is clear to notice that as particle volume increases the static failure strength decreases for GMC, VAMUCH and FEA for all failure criteria, this is due to the fact that as particle size increases the area of stress disturbance also increases, consequently the chance of failure of the composite increases, i.e., consistent of weakest link theory. This is not found to valid for MT and DI, this is because MT and DI are inherently not capable of recovering the local stress concentrations or disturbances which mainly contribute to the failure of the composite. The over-prediction of GMC might be due to that fact that GMC does not accurately recover the local stress field.[22,23]

The initial failure envelope, for axial and transverse loading condition, is also generated using maximum stress failure criterion as shown in the Figure 6. GMC significantly overestimate the initial failure envelop

while VAMUCH shows an excellent agreement with FEA. GMC provides a better estimate for the initial failure envelop using Tsai-Hill failure criterion as shown in the Figure 7 in comparison its own prediction using the maximum stress failure criterion.

Table 7. Axial failure strength using maximum principal stress criterion

Vof(%)	MT	DI	GMC	VAMUCH	FEA
10	90.00	91.00	42.50	39.02	38.59
20	96.96	99.96	36.00	33.89	33.63
40	109.96	127.47	29.10	21.76	20.91
50	116.51	148.81	24.40	12.02	11.27

Table 8. Axial failure strength of particle reinforced composite using Tsai-Hill and Tsai-Wu critera

	MT (MPa)		DI (MPa)		GMC(MPa)		VAMUCH(MPa)		FEA(MPa)	
Vof(%)	Tsai-Hill	Tsai-Wu	Tsai-Hill	Tsai-Wu	Tsai-Hill	Tsai-Wu	Tsai-Wu	Tsai-Hill	Tsai-Wu	Tsai-Hill
10	92.04	91.80	92.63	92.91	47.00	-	46.49	46.50	44.97	44.97
20	91.77	100.41	104.50	104.32	42.50	-	39.97	39.97	38.84	38.84
40	100.56	117.84	138.08	138.23	36.50	-	34.67	34.67	32.68	32.68
50	100.95	126.98	164.91	164.48	31.20	-	24.89	24.89	23.49	23.49

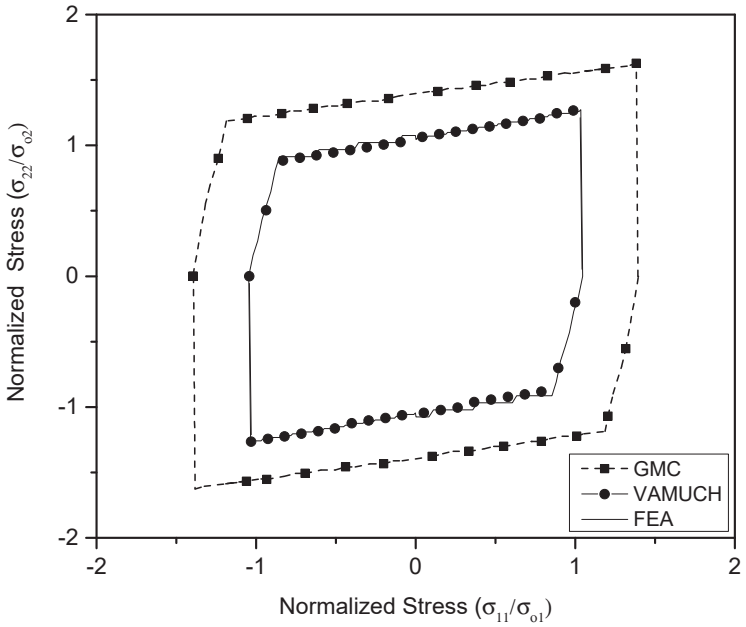

Figure 6. Initial failure envelop for axial and transverse loading condition (maximum principal stress for 40% vof)

The axial and transverse shear failure strength of the particle reinforced composite are also analyzed using Tsai-Hill and maximum shear stress criteria. The outputs of the two criteria are very much close to each other similar to what we observed for continuous fiber reinforced composite. Thus, in this case, the predictions of Tsai-Hill criterion are listed in the Table 9. It is obvious to notice that GMC significantly

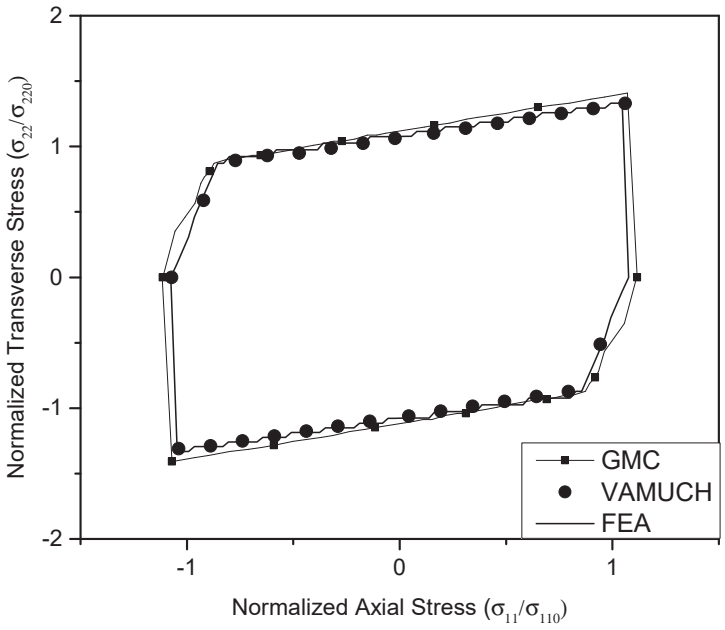

Figure 7. Initial failure envelop for axial and transverse loading condition (Tsai-Hill for 40% vof)

overpredicts both axial and transverse shear strength of particle reinforced composite, while VAMUCH shows excellent agreements with FEA. The combined axial and transverse shear loading conditions are also used to generate the initial failure envelop using maximum shear and Tsai-Hill failure criteria, the generated plots are qualitatively similar to the one generated for continuous fiber reinforced composite. Thus, it is not necessary to repeat them here.

Table 9. Axial and transverse shear failure strength of particle reinforced composite using Tsai-Hill criterion

	Axial shear strength (MPa)			Transverse shear strength (MPa)		
Vof(%)	GMC	VAMUCH	FEA	GMC	VAMUCH	FEA
10	33.60	25.70	25.12	34.00	24.48	25.70
20	30.80	25.99	25.55	31.60	25.00	25.99
40	27.20	17.03	17.22	28.00	17.14	17.03

The maximum principal strain failure criteria is also used to analyze the failure strength of the particle reinforced composite for strain or displacement loading conditions. The predictions in the Table 10 show that MT and DI significantly overpredict the failure strain compared with FEA while GMC slightly overestimates failure strains. On the other hand, VAMUCH shows an excellent agreement with the results of FEA. The initial failure envelop, Figure 9, indicates that MT and DI significantly overpredicts the failure strain. The prediction of MT and DI are plotted by dividing the actual predicted values by two for better clarity of the other figures. GMC predicts much better compared with MT and DI, but it fairly overpredicts the failure strains compared with FEA whereas VAMUCH shows an excellent agreement.

Table 10. Axial strain failure strength of particle reinforced composite using maximum strain criterion

Vof(%)	MT	DI	GMC	VAMUCH	FEA
10	0.0176	0.0176	0.0088	0.0083	0.0082
20	0.0158	0.0159	0.0061	0.0056	0.0055
40	0.0124	0.0126	0.0027	0.0023	0.0022
50	0.0106	0.0110	0.0014	0.0009	0.0010

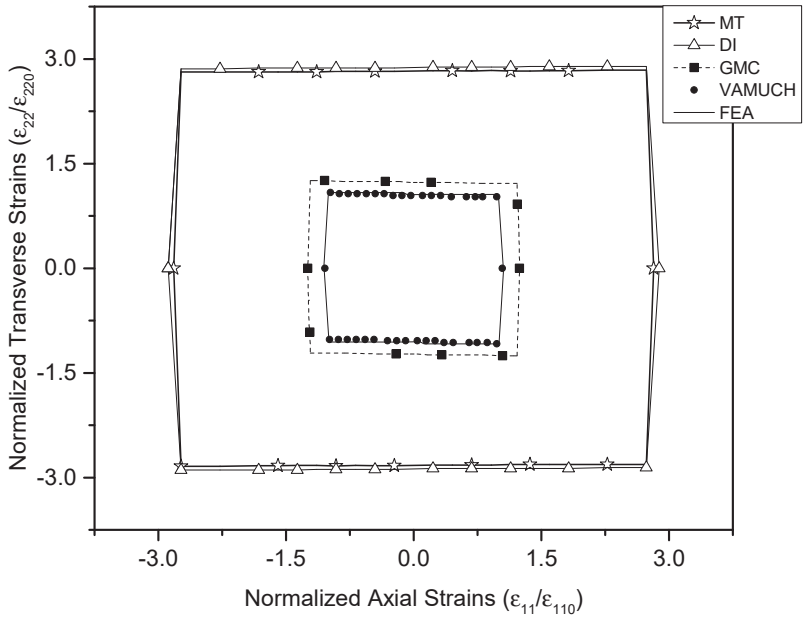

Figure 8. Initial failure envelop of particle reinforced composite (maximum principal strain for 40% vof)

C. Discontinuous Fiber Reinforced Composite

Two variants of discontinuous fiber reinforced composites are considered for predicting the static failure strength of the composite. The first one is aligned-regular array, where all the fibers are arranged in aligned pattern and the second one is aligned-staggered array, where fibers are arranged in an offset pattern. To generate the unit cell, first, let a quarter of circular fiber be embedded at the two opposite corners of hexagonal array matrix. Let the array be symmetric with respect to its width and height. This arrangement produces hexagonal array with circular fiber at the center and quarter circular fiber at the corners of the array as shown in Figures 9 and 14. Second, let the cross-sectional area of the hexagonal array be generated based on the common relation, $a = \beta b$, where a is the width and b the height of the unit cell and $\beta = \sqrt{3}$ for hexagonal array. Moreover, let the local Cartesian coordinate be introduced as $y = (y_1, y_2, y_3)$ at the center of unit cell, where y_1 is in the fiber direction. The fibers are generally shorter compared to the unit cell in y_1 direction. For detailed geometric constructions of discontinuous fiber reinforced composite, interested reader may refer to Ref. [33]. In this failure analysis, the fiber volume and fiber aspect ratio (length/diamater) are assumed to be 40% and 5, respectively. For FEA, the unit cell is first modeled using plane element (Mesh200) in 2D model and then the corresponding 3D model is generated by extrusion of the 2D model. VAMUCH uses the mesh used for FEA. The failure analysis is conducted using material properties of type 1 listed in the Table 1 for both types of discontinuous fiber reinforced composite.

1. *Aligned-Regular Array*

In this failure analysis, a $3 \times 44 \times 42$ (y_1, y_2, y_3) subcell grid is used for GMC, and 20-noded elements are used for VAMUCH and FEA. GMC and VAMUCH/FEA have 5544 and 45000 elements, respectively. This large difference of elements number comes from the modeling nature of unit cell for GMC, it may have only three elements in the y_1 direction and further refining of the mesh in this direction does not improve the output of GMC. The unit cell of VAMUCH and FEA is shown in the Figure 9. The static failure of the aligned regular array discontinuous fiber reinforced composite is conducted using various failure criteria and loading conditions. The axial and transverse failure prediction of GMC, VAMUCH and FEA using various failure criteria are shown in Table 11. These predictions indicate that GMC poorly estimates the axial failure strength for maximum principals stress and Tsai-Hill failure criteria. It also shows poor agreement with FEA for transverse failure strength for maximum principal stress criterion, however, the transverse failure predictions of GMC show good agreement for Tsai-Hill criterion. The predictions of VAMUCH very well agree with the results of FEA for both axial and transverse loading conditions using both failure criteria. GMC fairly predicts the axial failure strain using maximum principal strain failure criteria but poorly overestimates the transverse failure strain. VAMUCH produces the axial failure strain equivalent to FEA and also yields a very close prediction for the transverse strains. The slight discrepancy between the FEA and VAMUCH may be due to the applied boundary conditions in FEA.

Table 11. Axial and transverse failure strength of aligned regular array discontinuous fiber reinforced composite

	Axial strength 1			Transverse strength 2			Transverse strength 3		
Vof(%)	GMC	VAMUCH	FEA	GMC	VAMUCH	FEA	GMC	VAMUCH	FEA
Max.Prn.stress (MPa)	41.28	49.59	47.50	63.70	56.65	57.42	49.50	45.69	43.87
Tsai-Hill (MPa)	50.92	77.66	78.27	58.10	58.15	57.00	57.54	56.80	55.80
Tsai-Wu (MPa)	-	80.83	82.00	-	63.32	64.35	-	61.08	59.80
Max.Prn.strain	0.00258	0.00218	0.00218	0.0087	0.00455	0.00573	0.0062	0.00424	0.00533

As shown in the Figures 10 -13, the initial failure envelops, using different loading options, depict that GMC poorly predicts the failure strength for both maximum principal stress and Tsai-Hill criteria. On the contrary, the predictions of VAMUCH show an excellent agreement with FEA for both failure criteria and loading options. In an other analysis, the initial failure envelop of GMC shows good agreement for the biaxial transverse loading conditions using Tsai-Hill failure criteria as depicted in the Figure 12. In this case, the prediction is much closer to the FEA except slight deviation at large combined loads, whereas VAMUCH shows an excellent agreement with the prediction of FEA. In general, the prediction of maximum principal

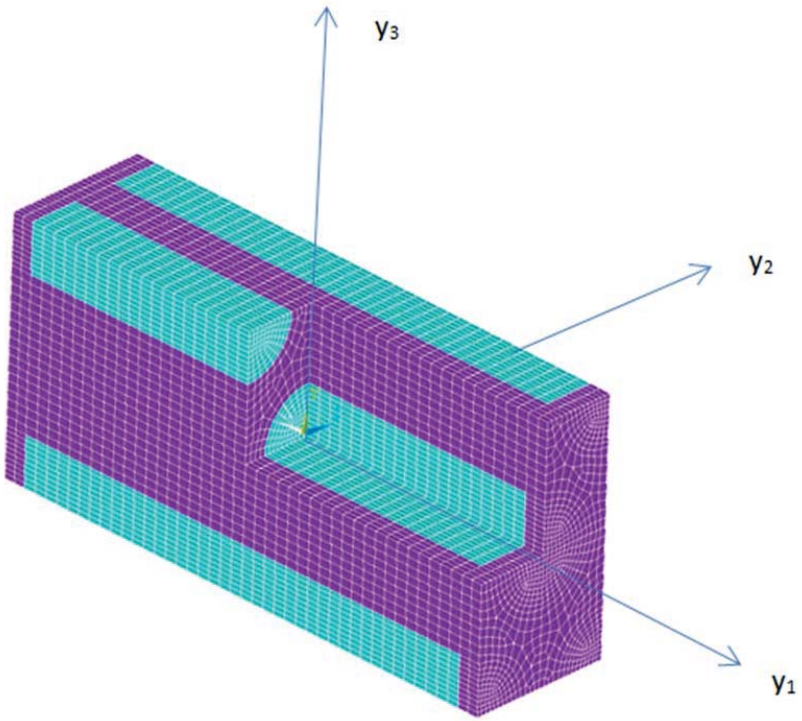

Figure 9. Unit cell aligned regular array discontinuous fiber reinforced composite

stress failure criteria is found to be conservative compared with other failure criteria.

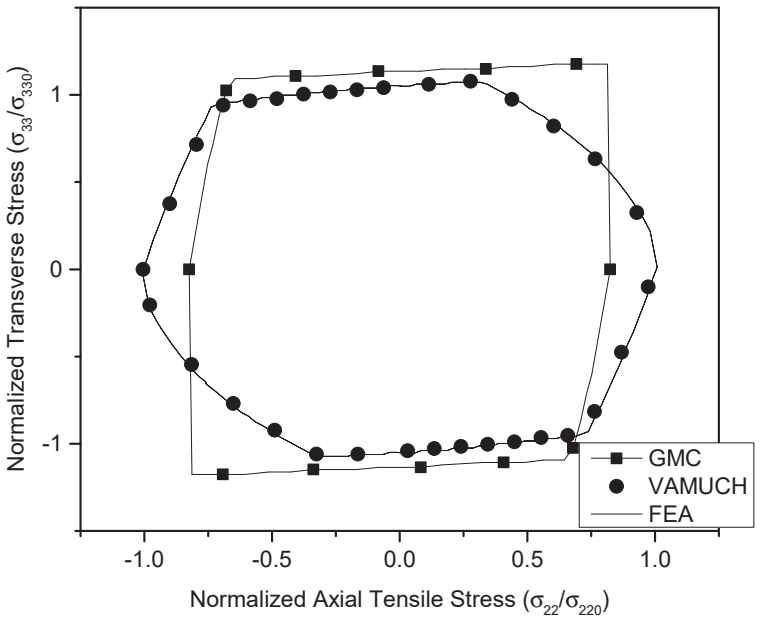

Figure 10. Initial failure envelop for axial and transverse loading (Maximum Principal stress criterion for 40% vof)

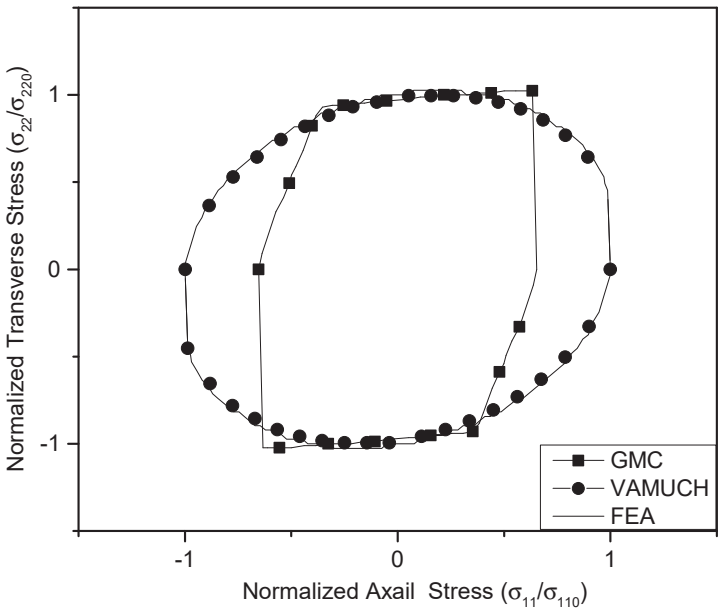

Figure 11. Initial failure envelop for axial and transverse loading (Tsai-Hill criterion for 40% vof)

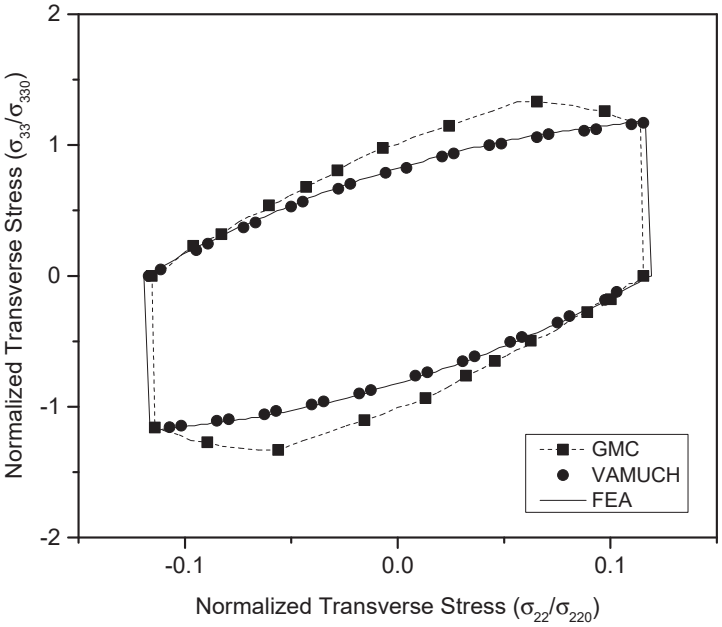

Figure 12. Initial failure envelop for transverse loading (Tsai-Hill criterion for 40% vof)

VAMUCH produces the initial failure envelop for axial and transverse shear loading using both maximum shear stress and Tsai-Hill failure criteria as shown in the Figure 13. Similar to continuous fiber reinforced and particle reinforced composite, in this case also, the two failure criteria produce very much close prediction

for combined shear failure analysis.

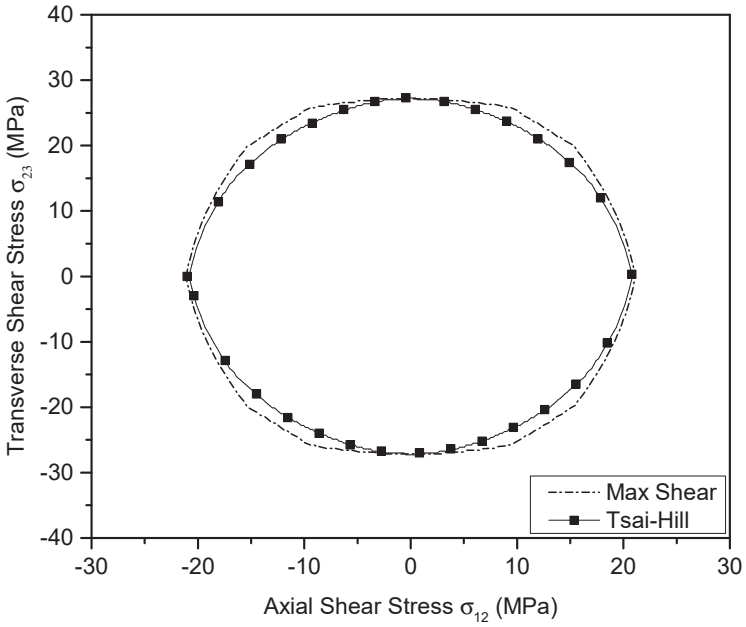

Figure 13. Initial failure envelop for axial and transverse shear loading (combined shear for 40% vof)

2. Aligned-Staggered Array

Aligned staggered array type of discontinuous fiber reinforced composite is similar to the regular aligned array but, in this case, the fibers in the unit cell are arranged in a staggered pattern, i.e., fibers overlap within the unit cell. Let 76% of fiber length overlap within a unit cell for this analysis. A $6 \times 42 \times 42$ (y_1, y_2, y_3) subcell grid is used for GMC, 34608 20-noded elements are used for VAMUCH and FEA. The unit cell of FEA/VAMUCH is shown in the Figure 14. GMC has similar unit cell with cuboidal meshing pattern. The predictions of static failure strength are performed using different failure criteria. The results of axial and transverse failure strength, Table 12, indicate that GMC insufficiently approximates the axial failure strength using all failure criteria. However, the predictions of the transverse failure strength show relatively better agreements with FEA while VAMUCH shows an excellent agreement for transverse failure strength. For axial strength, VAMUCH prediction is much better than GMC but also show slight discrepancy with FEA. This might be due to the applied boundary conditions. GMC fairly overpredicts the axial and the transverse failure strain, while VAMUCH shows better agreement.

Table 12. Axial and transverse failure strength of aligned staggered array discontinuous fiber reinforced composite

	Axial strength 1			Transverse strength 2			Transverse strength 3		
Vof(%)	GMC	VAMUCH	FEA	GMC	VAMUCH	FEA	GMC	VAMUCH	FEA
Max.Prn.stress (MPa)	49.50	67.96	61.56	53.35	47.29	47.50	48.00	43.97	44.50
Tsai-Hill (MPa)	59.40	87.36	79.81	61.38	56.40	57.66	56.84	57.52	57.60
Tsai-Wu (MPa)		93.27	84.82		60.97	61.81		57.53	57.60
Max.Prn.strain	0.0046	0.0027	0.0033	0.0073	0.0041	0.0052	0.0058	0.0052	0.0055

The axial and transverse shear failure prediction of GMC, Table 13, is observed to be overpredicted using

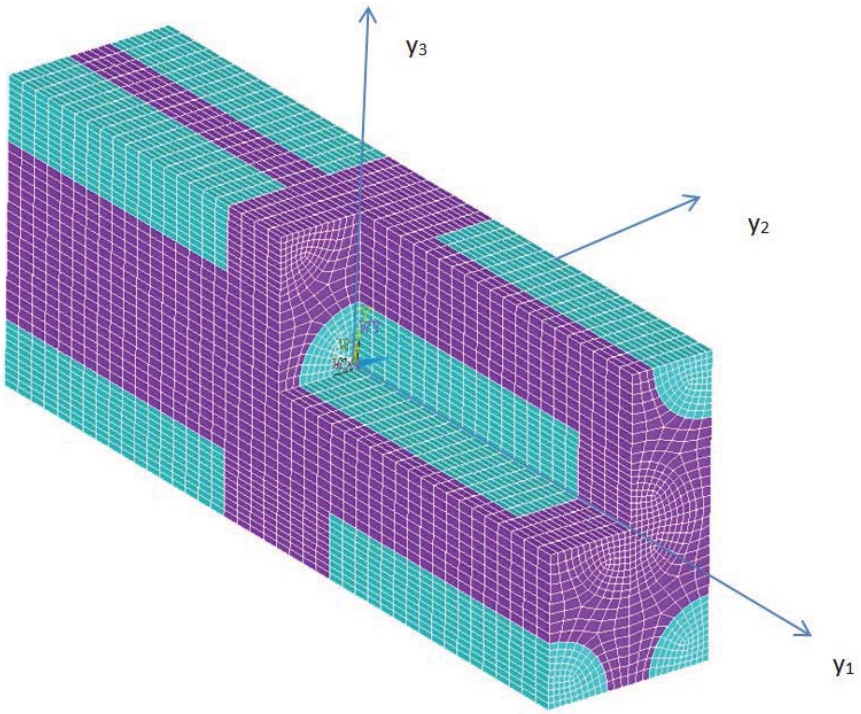

Figure 14. Unit cell aligned staggered array discontinuous fiber reinforced composite

Tsai-Hill failure criteria compared with FEA. On the contrary, VAMUCH shows excellent agreements with the predictions of FEA for axial shear failure strength using both failure criteria. But the predictions of transverse shear failure strength are slightly under predicted compared with FEA, this might be due to the effect of boundary conditions and remains to be studied. In an other analysis, GMC poorly predicts the initial failure envelop for axial transverse loading using maximum principal stress failure criteria as shown in the Figure 15. The predictions of VAMUCH well agree with FEA. As also depicted in the Figure 16, VAMUCH predicts the failure strength equivalent to FEA using Tsai-Wu failure criteria. Please note that the current version of GMC does not support the Tsai-Wu failure criteria. Similarly, Figure 17, the initial failure envelop for the transverse loading condition, i.e, σ_{22} vs σ_{33}, indicates that the failure predictions of GMC well agree with the predictions of FEA except slight deviation at larger combined loading conditions. Conversely, VAMUCH shows an excellent agreements with the prediction of FEA for all the cases.

Table 13. Axial and transverse shear failure strength of aligned staggered array discontinuous fiber reinforced composite (40% of vof)

	Max. shear stress (MPa)			Tsai-Hill (MPa)		
Vof(%)	S_{12}	S_{13}	S_{23}	S_{12}	S_{13}	S_{23}
GMC	-	-	-	29.70	32.67	35.28
VAMUCH	24.87	23.74	22.93	24.51	23.74	22.93
FEA	25.17	24.59	26.52	24.99	24.59	26.53

The predictions of the initial failure envelop for combined shear loading, i.e, σ_{12} vs σ_{23}, indicate that the maximum shear and Tsai-Hill failure criteria produce slightly different prediction unlike the continuous fiber reinforced and particle reinforced case. But it is still observable that the two failure criteria yield close prediction for the combined shear loading failure analysis as shown in the Figure 18.

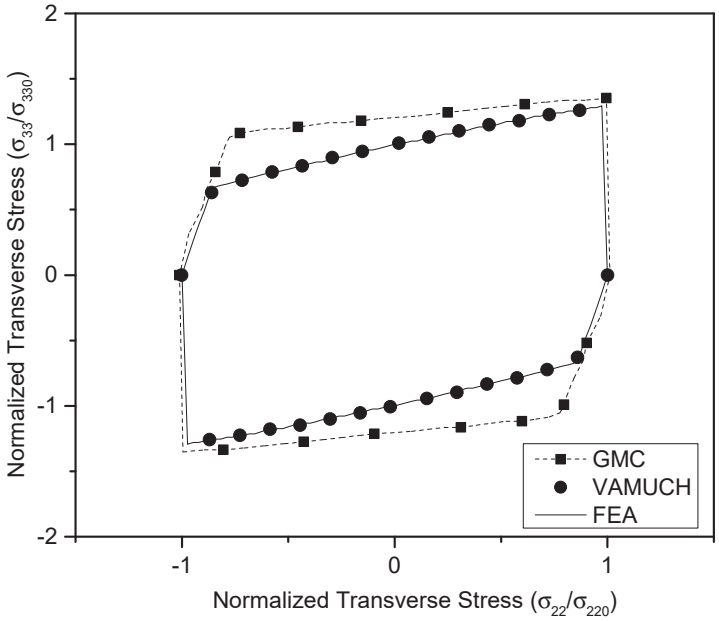

Figure 15. Initial failure envelop for transverse loading (maximum principal stress criteria vof 40%)

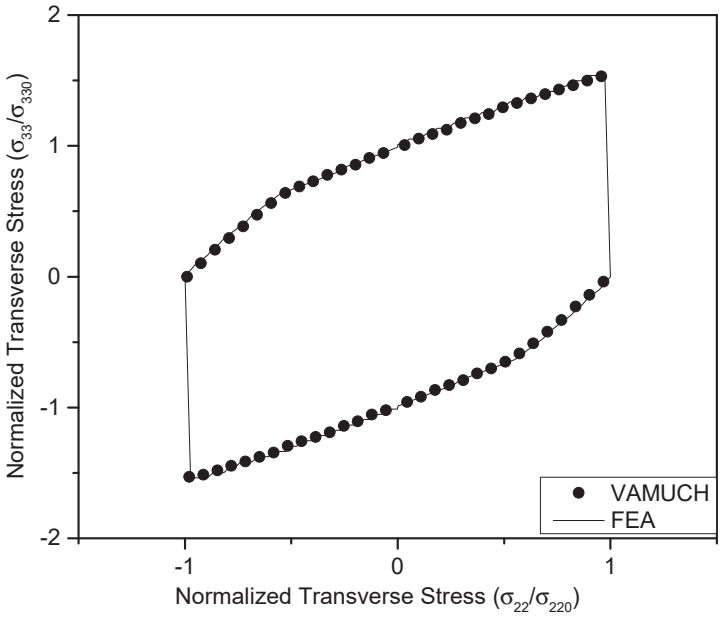

Figure 16. Initial failure envelop for transverse loading (Tsai-Wu vof 40%)

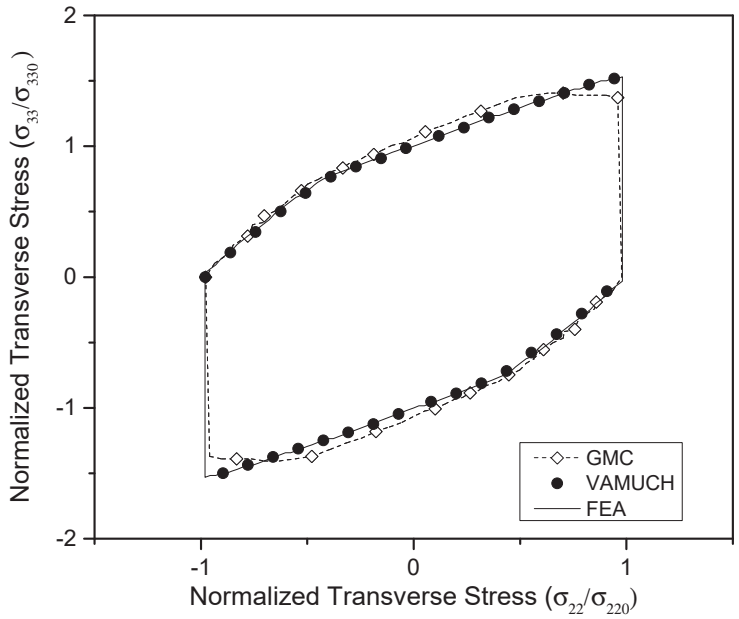

Figure 17. Initial failure envelop for transverse loading (Tsai-Hill vof 40%)

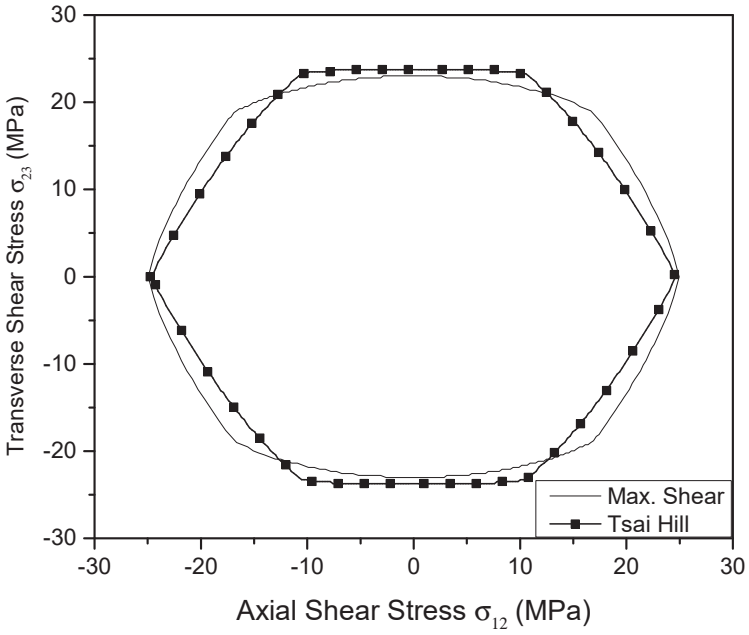

Figure 18. Initial failure envelop for axial and transverse shear loading (vof 40%)

D. Woven Composite

The woven composite is modeled as depicted in the Figure 19. The ellipsoidal cross section of major axis radius, c, and minor axis radius, $c = 4$, elliptical curvature radius, $r = 2.5c$, and also matrix thickness of $\frac{c}{8}$ is assumed on the top and bottom of the side of the unit cell. The ellipsoidal cross section center to center distance is $2c$. The overall unit cell length, width and height are $4c$, $4c$ and $\frac{5c}{4}$, respectively. GMC uses the similar shape of unit cell with cuboidal meshing pattern. A single-step GMC approach is employed for this analysis. A 64 sub cell grid is used for GMC. The basic type of woven microstructure is used from DIGIMAT for MT and DI. The unit cell of FEA/VAMUCH is meshed to have 18432 elements. It is obvious to see large element difference between the GMC and FEA/VAMUCH. This is because, GMC inherently uses only cuboidal element type in the unit cell and also further meshing of the subcell does not improve accuracy for the predicted values. The static failure strength prediction of woven composite is performed using various failure criteria. The warp and weft are assumed to have the material properties of fiber listed under type 1 and type 2, respectively. The matrix of woven is assumed to have the matrix in type 2 of the material properties shown in the Table 1. The volume of warp, weft and the matrix are assumed to be 25.95%, 25.95% and 48.10%, respectively.

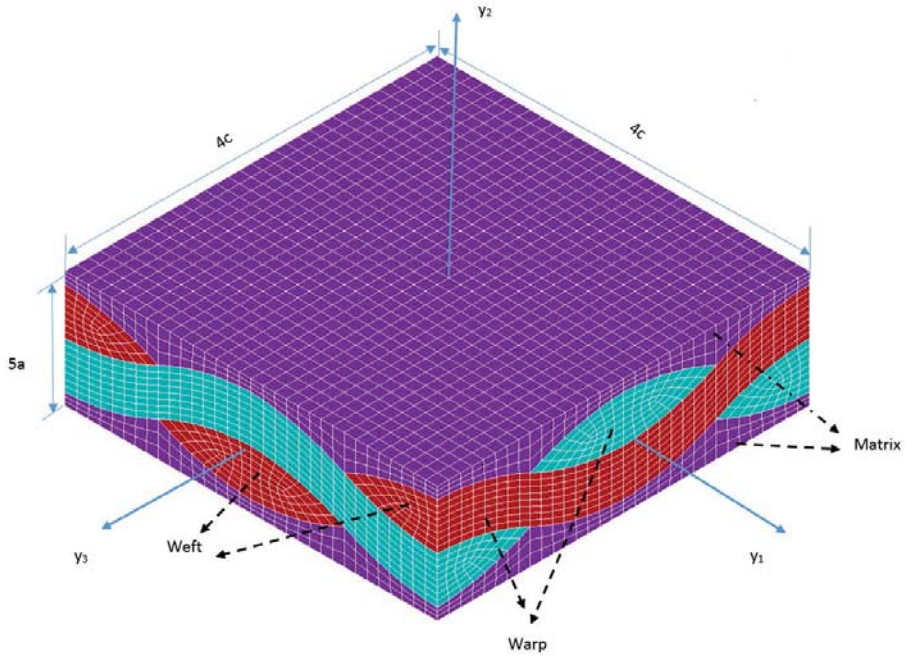

Figure 19. Unit cell of woven composite)

The axial (S_{11}) and transverse (S_{22}, S_{33}) static failure predictions of woven composite are conducted using various failure criteria. As shown in the Table 14, MT and DI significantly underpredict axial failure strength stress for maximum principal stress and Tsai-Hill criteria but overpredicts for maximum principal strain failure criterion. Conversely, these approaches significantly overpredict the transverse failure strength for all failure criterion. Similarly, GMC also significantly overestimates the axial failure strength for all failure criteria. However, the prediction of GMC is pretty good for S_{33} using Tsai-Hill failure criteria. On the other hand, VAMUCH shows good agreements for both axial and transverse failure strength. The failure strain predictions of MT, DI, and GMC are observed to be significantly greater than the prediction of FEA. VAMUCH produces the failure strains of the woven composite that agree well with the predictions of FEA.

The initial failure envelop for transverse loading, i.e., σ_{22} and σ_{33}, as depicted in the Figure 20, shows that GMC significantly overpredicts the combined failure load using maximum stress criterion approximately by more than 54%. Moreover, for Tsai-Hill failure criterion as shown in the Figure 21, the prediction of GMC is way off from the prediction of FEA and VAMUCH although VAMUCH has a good agreement with FEA. The inability of GMC for prediction the failure strength of woven composite may be due to the cuboidal shape of the sub cell. The cuboidal shape may affect the approach not to accurately recover the local fields

Table 14. Axial and transverse failure strength of woven composite

	Max. principal stress			Tsai-Hill			Max. principal strain		
Vof(%)	S_{11}	S_{22}	S_{33}	S_{11}	S_{22}	S_{33}	ϵ_{11}	ϵ_{22}	ϵ_{33}
MT(MPa)	465.41	103.57	465.41	554.01	162.35	592.52	0.01313	0.01306	0.01313
DI (MPa)	492.50	140.92	592.52	592.52	204.55	592.52	0.01339	0.01326	0.01339
GMC (MPa)	1046.64	83.30	1046.64	1094.40	159.60	194.40	0.01931	0.01010	0.01931
VAMUCH (MPa)	728.24	51.97	225.10	769.81	88.60	209.18	0.00652	0.00236	0.00219
FEA (MPa)	776.61	47.73	211.00	647.17	88.60	198.05	0.00552	0.00222	0.00281

along the wave of the warp, weft and the matrix. In general, from these predictions, it is easily noticeable that VAMUCH can predict the initial failure envelop of woven composite equivalent to FEA.

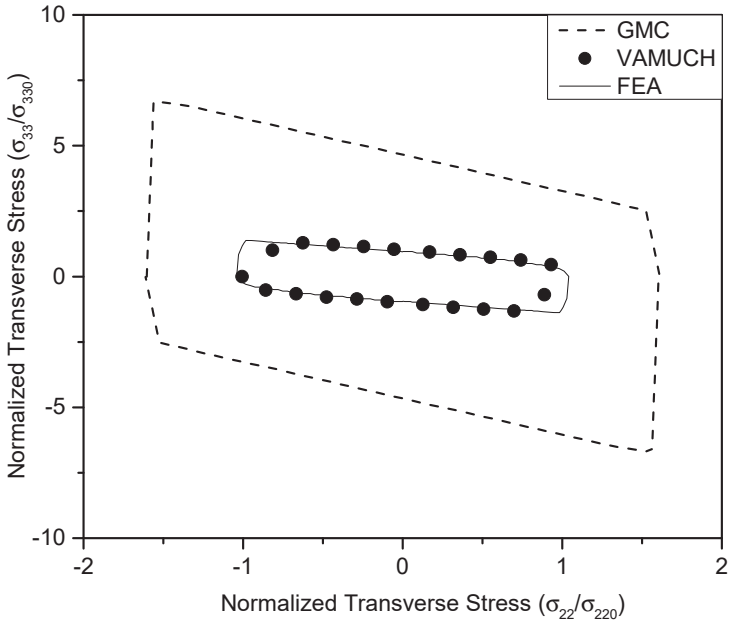

Figure 20. Initial failure envelop for σ_{22} and σ_{33} (Maximum principal stress criterion)

The initial failure envelops of woven composite for axial and transverse shear appear to be significantly different for maximum shear stress and Tsai-Hill failure criteria. It is clear to see from the Figure 22 that the Tsai-Hill failure criterion is more conservative than the maximum shear stress criterion.

V. Conclusion

The static failure prediction of several examples of heterogeneous material has been analyzed using VAMUCH obeying various failure criteria. The prediction of VAMUCH is partially evaluated with the prediction from various micromechanics approaches. The mean field based homogenization approaches, i.e, MT and DI, cannot accurately predict the static failure strength and initial failure envelop of the heterogeneous materials. GMC and HFGMC predict better compared with the mean field theory, but this approach also poorly predict the static failure strength for both uniaxial and biaxial loading using maximum principal stress and strain failure criteria. The predictions of these approaches agree relatively

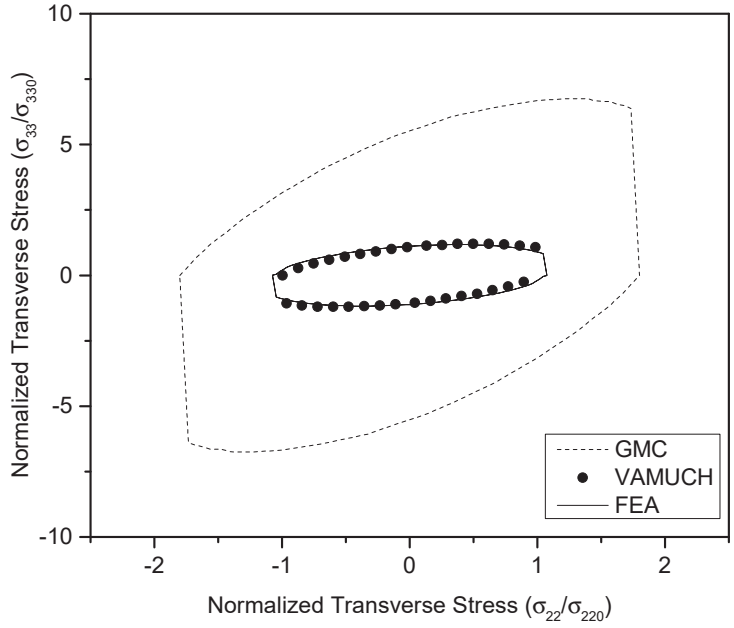

Figure 21. Initial failure envelop for σ_{22} and σ_{33} (Tsai-Hill)

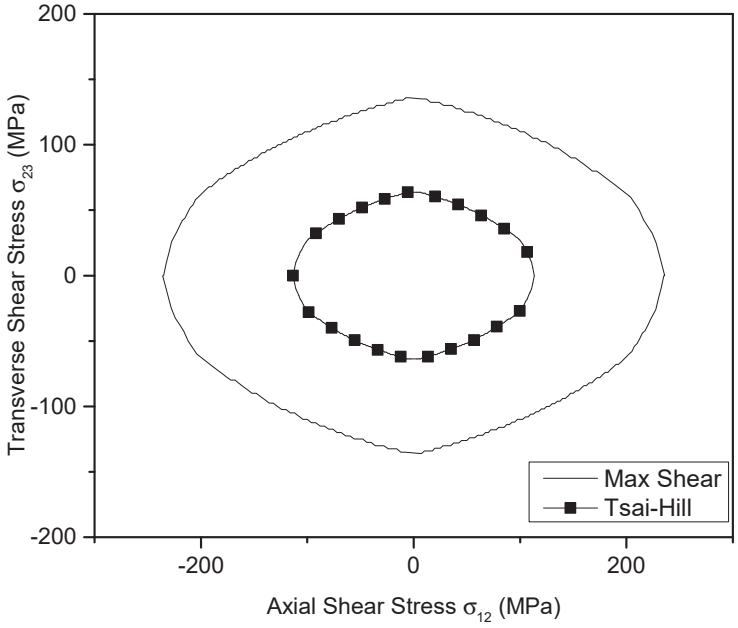

Figure 22. Initial failure envelop for σ_{12} and σ_{23} predicted using VAMUCH

better with FEA predictions for Tsai-Hill failure criterion. VAMUCH shows an excellent agreement with the prediction of FEA for both uniaxial and biaxial loading conditions using all considered failure criteria. Moreover, VAMUCH also demonstrates the capability of analyzing failure in the heterogeneous material for any possible loading condition. This capability is not usually available in commercial FEA software package due to the complexity of applying the required boundary conditions. VAMUCH can generate the initial failure envelop for combined axial and transverse shear loading conditions using maximum shear stress and Tsai-Hill failure criteria. These predictions produce the close results for the two criteria for the examples of the heterogeneous material except for woven composite. It is also known that maximum principal stress failure criteria produces conservative results compared to other failure criteria for most of the cases we have studied. Generally speaking, VAMUCH is found to be a consistent and accurate micromechanics approach to analyze the static failure of heterogeneous material for any possible loading options.

References

[1]Cassenti, B., "Probabilistic static failure of composite material," *AIAA Journal*, Vol. 22, No. 1, 1984, pp. 58.

[2]Sun, C. and Yamada, S., "Strength distribution of a unidirectional fiber composites," *Journal of Composite Materials*, Vol. 12, 1978, pp. 169.

[3]McDanels, D. L., "Analysis of stress-strain, fracture, and ductility behavior of Aluminum matrix composites containing discontinuus Silicon carbide reinforcement," *Metallurgical Transactions A*, Vol. 16, June, 1985, pp. 1105–115.

[4]Halpin, J. and Kardos, J., "Strength of discointinuous reinforced composite: I. fiber reinforced composite," *Polymer Engineering and Science*, Vol. 18, No. 6, 1978, pp. 496–504.

[5]Wang, J., Callus, P., and Bannister, M., "Experimental and numerical investigation of the tension and compression strength of un-notched and notched qusai-isoropic laminates," *Composite Structures*, Vol. 64, No. 3-4, 2004, pp. 297–306.

[6]Zheng-ming, H., "Micromechanical prediction of ultimate strength of transversely isotropic fibrous compoiste," *International Journal of Solids and Structures*, Vol. 38, 2001, pp. 4147–4172.

[7]Cox, B. N., Dadkhah, M. S., Morris, W. L., and Flintoff, J. G., "Failure mechanisms of 3d woven composites in tension, compression, and bending," *Acta Metallurgica et Materialia*.

[8]Wakashima, K., Suzuki, Y., and Umekawa, S., "A Micromechanical prediction of initial yield surfaces of unidirectional composites," *Journal of Composite Materials*, Vol. 13, 1979, pp. 288.

[9]Tanaka, K., Wakashima, K., and Moiu, T., "Plastic deformation anisotropy and workhardening of composite materials," *Journal of the Mechanics and Physics of Solids*, Vol. 21, 1973, pp. 207–214.

[10]Bednarcyk, A. and Arnold, M., "Micromechanics based deformation and failure prediction for longitudinally reinforced Titanium composites," *Journal of Composite Science and Technology*, Vol. 61, No. 2, 2001, pp. 705–729.

[11]Pindera, M. J. and Aboudi, J., "Micromechanical anlaysis of yeilding of metal matric composites," *International Journal of Plasticity*, Vol. 4, 1988, pp. 195–214.

[12]Aboudi, J., "Elastoplasticity theory for composite materials," *Solid Mech.Arch.*, Vol. 11, 1986, pp. 141–183.

[13]Aboudi, J., "Micromechanical prediction of initial and subsequent yield surfaces of metal matrix composites," *International Journal of Plasticity*, Vol. 6, 1990, pp. 471–484.

[14]Kwon, Y. and Berner, J., "Micromechanis model for damage and failure analysis of laminated fibrous composites," *Engineering Fracture Mechanics*, Vol. 52, No. 2, 1995, pp. 231–242.

[15]Choi, J. and Tamma, K. K., "Woven fabric composites-part I: predictions of homogenized elastic properties and micromechanical damage analysis," *International Journal for Numerical Methods in Engineering*.

[16]Scida, D., Abouraa, Z., Benzeggagh, M., and Bocherens, E., "A micromechanics model for 3D elasticity and failure of woven-fibre composite materials," *Composites Science and Technology*, Vol. 59, 1999, pp. 505–517.

[17]Gundel, D. and Wawner, F. E., "Experimenal and thoeretical assesment of longutidinal tensile stregnth of unidirectional SiC-fiber/Titanium matrix," *Composites Science and Technology*, Vol. 57, 1997, pp. 471–481.

[18]Dvorak, G., Rao, M., and Tarn, J., "Yielding in unidirectional composites under external loads and temperature change," *Journal of Composite Materials*, Vol. 7, 1973, pp. 194–216.

[19]Zhu, H. and Sankar, B., "Evaluation of failure failure criteria for fiber composites using finite element micromechanics," *Journal of Composite Materials*.

[20]Mayes, J. S. and Hansenb, A. C., "Composite laminate failure analysis using multicontinuum theory," *Composites Science and Technology*, Vol. 64, 2004, pp. 379–394.

[21]Yu, W. and Tang, T., "Variational asymptotic method for unit cell homogenization of periodically heterogeneous materials," *International Journal of Solids and Structures*, Vol. 44, No. 11-12, 2007, pp. 3738–3755.

[22]Yu, W., W. T., Aboudi, J., and Bednarcyk, B., "A critical evaluation of the predictive capabilities of various advanced micromechanics models," *Proceedings of the 48th Structures, Structural Dynamics and Materials Conference*, April. 23-26, 2007.

[23]Sertse, H., Zhang, L., Yu, W., and Ye, Z., "A comprehensive evaluation of the predictive capabilities of several advanced micromechanics approaches," *Proceedings of the 48th Structures, Structural Dynamics and Materials Conference*, Jan. 13-17, 2014.

[24]Tang, T. and Yu, W., "Asymptotical approach to initial yielding surface and elastoplasticity of heterogeneous materials," *Mechanics of Advanced Materials and Structures*, Vol. 18, No. 4, 2011, pp. 244–254.

[25]Tsai, S. W. and Wu, M., "A Genereal theory of strength for ansiotropic materials," *Journal of Composite Materials*, Vol. 5, 1971, pp. 58.

[26]Reddy, J. N. and Pandey, A. K., "A first-ply failure analysis of composite laminates," *Computers and Structures*, Vol. 25, No. 3, 1987, pp. 371–393.

[27]Adoudi, J., "The generalized method of cells and high-fidelity generalized method of cells micromechanical models-a review," *Mechanics of Advanced Materials and Structures*, Vol. 11, No. 4-5, 2004, pp. 329–366.

[28]Aboudi, J., Pindera, M., and Arnold, S., "High-fidelity generalization method of cells for inelastic periodic multiphase materials," *NASA/TM-2002-211469*, Vol. 2, 2002.

[29]Aboudi, J., Arnold, S. M., and Bednarcyk, B. A., *Micromechanics of composite materials: a generalized multiscale analysis approach*, Butterworth-Heinemann, 2012.

[30]Mayes, J. and Hansen, A., "A comparion of multicontinuum theory based failure simulation with experimental results," *Composites Science and Technology*, Vol. 64, No. 64, 2004, pp. 517–527.

[31]Sun, C. and Vaidya, R., "Prediction of composite properties from a Representative Volume Element," *Composites Science and Technololy*, Vol. 56, 1996, pp. 171–179.

[32]Adams, D. and Crane, D., "Combined loading of micromechanical analysis of unidirectional composite," *Composites*, Vol. 15, 1984, pp. 181–192.

[33]Pahr, D. and Arnold, S., "The applicability of the generalized method of cells for analyzing discontinuously reinforced composite," *International Journal of Solids and Structures*, Vol. 33, 2002, pp. 153–170.

AIAA SciTech
5-9 January 2015, Kissimmee, Florida
56th AIAA/ASCE/AHS/ASC Structures, Structural Dynamics, and Materials Conference

A Micromechanical Approach to Imperfect Interface Analysis of Heterogeneous Materials

Hamsasew Sertse*, and Wenbin Yu†

The objective of this paper is to extend the capability of the Variational Asymptotic Method for Unit Cell Homogenization (VAMUCH) to predict the elastic effective properties and the failure strength of heterogeneous materials with imperfect interface. The imperfect interface is modeled using linear elastic traction displacement model obeying small infinitesimal displacement jump across the interfaces. A cohesive zone model with zero thickness is introduced at the interface to simulate the imperfect interface for predictions of elastic effective properties. These predictions are performed using several representative examples of heterogeneous materials such as binary composite, continuous fiber reinforced composite, particle reinforced composite, discontinuous fiber reinforced composite, and woven composite. The predictions reveal that VAMUCH and Finite Element Analysis (FEA) agree well with exact solutions for binary composite except that FEA has difficulty to predict the axial shear modulus. The two approaches show excellent agreements for all the other aforementioned example heterogeneous materials except that FEA cannot predict the axial shear modulus for continuous fiber reinforced composite. The predictions of VAMUCH are also observed to be within the upper and lower bounds of imperfect interface effective properties proposed in the literature. The interfacial stiffness is also observed to significantly reduce the static failure strength of the material, however, the static failure may not necessarily initiate at the interface.

I. Introduction

In recent decades, various advanced micromechanics approaches have been proposed and widely used for the predictions of effective properties, local fields and the overall responses of the heterogeneous materials under various thermomechanical loadings. However, the majority of these models were developed by assuming a perfect interface among constituents. This assumption adopts continuous displacement and traction across the interface of the constituents, but this might not be obviously valid due to various reasons such as manufacturing defects, inherent properties of the constituents and bonding agents. Numerous efforts have been devoted to develop constitutive models that adequately capture the effect of imperfect interface on the effective properties and the failure strength of the heterogeneous materials. Jones and Whittter[1] proposed linear interface model, where the interfacial traction is proportional to the displacement jumps across the interface. This hypothesis is adopted by numerous researchers to formulate the imperfect interface using continuum model.[2–4] Needleman[5–7] proposed a cohesive zone model that exponentially relates the interfacial traction with displacement jump across the interface. The normal traction increases with displacement jump, reaches maximum and then finally drops to vanish at the complete debonding of the interface. In these works, it has also been demonstrated that the tangential traction shows a periodic function with displacement jump along the interface plane. These models do not explicitly indicate a finite traction value that initiates the debonding in the fiber-matrix interface. Lissenden[8] proposed a three dimensional (3D) polynomial traction displacement model. This model incorporates the effect of friction between the debonded fiber and matrix in the interface. Generally, it is evident to notice that interfacial debonding is a local phenomena. It is mainly influenced by the local stress fields in the heterogeneous material, particularly at the interface of constituents. It is also demonstrated that the imperfect interface significantly affects the effective properties of the heterogeneous material.[9,10] Hashin[11] used a thin elastic interface, as an imperfect fiber-matrix interface, to obtain the effective properties of the composite. In Ref. [3, 12],

*Graduate Research Assistant, School of Aeronautics and Astronautics, Purdue University
†Associate Professor, School of Aeronautics and Astronautics, Purdue University, AIAA Associate Fellow.

variational approach is adopted to predict the upper and lower bounds of elastic properties of a particle reinforced composite with imperfect interface. In the latter reference, the prediction is performed using stress interface model that assumes discontinuous stress across interface. The static interfacial equilibrium is maintained by generalized Young-Laplace equation. The variational approach can better predict the upper and lower bounds of elastic effective properties with imperfect interface. However, the predicted bounds may be wide enough for practical use. Moreover, this method is also incapable of rigourously obtaining the local stress fields in the heterogeneous material. Thus, the effect of imperfect interface may not be sufficiently captured for the prediction of the effective properties of the heterogeneous material. Andrianova and co-workers[13] analyzed the interfacial debonding of continuous fiber reinforced composite under axial shear loading condition. In this work, a thin elastic bond with finite volume and rigidity is introduced between the fiber and the matrix, and the asymptotic limit for the ratio of the rigidity and volume is used for the prediction of the interfacial debonding using linear interfacial model. Liu and Sun[14] analyzed the effect of imperfect fiber-matrix interface in a particle reinforced composite by adopting the Eshelby's micromechanical approach. This approach can not effectively capture the local stress fields in the composite either. Thus, the prediction may not be adequate. Tvergaard[15] used the cohesive zone model to analyze the imperfect interface and whiskers breakage in the composite using cell-model analysis approach. Aboudi[2] and Lissenden[8] used the method of cells (MOC) to analyzing the effect of imperfect interface by adopting the linear spring model and polynomial traction displacement model, respectively. In Ref. [16, 17], generalized methods of cells (GMC) is employed to predict the interfacial debonding in the continuous fiber composites under transverse loading condition. In these works, various traction displacement models such as flexible interfacial model, evolving interfacial model, statistical interfacial model and Needleman cohesive zone model are incorporated in GMC to predict interfacial decohesion in the composite. MOC and GMC can better predict the interfacial debonding. However, these methods may not sufficiently approximate the local stress field due to normal shear coupling problem and also the local stresses are obtained by averaging over each subcell. Hence, the approach might inadequately predict the interfacial debonding in the heterogeneous materials. In Ref. [18–21], FEA is used to analyze the effect of imperfect fiber-matrix interface and the fiber breakage of various heterogeneous material by adopting linear traction displacement model. This approach can give a reasonable predictions for the interfacial debonding and also the failure strength. This is because in the FEA, the local fields can be accurately recovered in the composites. This, in turn, helps to predict the effect of imperfect interface. In general, it is rational to use a micromechanical approach with outstanding predictive capability of both effective properties and local fields to better analyze the effect of imperfect interface on the effective properties, the static failure strength, and the interfacial debonding of the heterogenous materials. This initiates the present study to investigate the effect of imperfect interface on the effective properties and the static strength of the heterogeneous materials using variational asymptotic method for unit cell homogenization (VAMUCH).[22] VAMUCH is a recently developed general-purposed micromechanics approach framework by carrying out an asymptotic analysis of the variational statement, synthesizing the merits of both variational methods and asymptotic methods. It has the advantages of analytical micromechanics approaches and the versatile modeling capability of the finite element analysis. VAMUCH is proven to have an outstanding capability of predicting effective properties and recovering the local stress fields of heterogeneous materials.[23,24] Thus, VAMUCH is the natural choice for the prediction of the effective properties and the static failure of heterogenous material with imperfect interfaces. The failure strength of the heterogeneous material can be predicted using various failure criteria such as maximum principal stress criterion, Tasi-Hill, and Tasi-Wu criterion. These failure criteria will be used to critically analyze the failure strength of the heterogeneous material with imperfect interface.

The objective of this paper is to extend the capability of the VAMUCH to predict the effective properties and the failure strength of heterogeneous materials with imperfect interface. The imperfect interface will be modeled using linear elastic traction displacement model obeying small infinitesimal displacement jump across the interface. The predictions of effective properties and the static failure strength, for imperfect interface, are performed using several representative examples of heterogeneous materials such as binary composite, continuous fiber reinforced composite, particle reinforced composite, discontinuous fiber reinforced composite, and woven composite. The unit cell (UC) of the heterogeneous material is sufficiently discretized to better predict the effective properties and the failure strength of the materials. The failure strength of this materials is evaluated at numerical integration point (Gauss point) using various failure criteria such as maximum principal stress criterion, Tsai-Hill failure criterion, and Tsai-Wu failure criterion. Finally, the prediction of VAMUCH is then compared with FEA and the predictions from published papers. These

analyses not only demonstrate the predictive capability of VAMUCH for imperfect interface of heterogeneous materials but also help engineers to use appropriate models for related problems based on the capability of corresponding approaches. Moreover, the analyses will give a general direction for inception of interfacial debonding and damage in heterogeneous materials.

II. Interfacial Constitutive Model

There are various models for the imperfect interface of the heterogeneous materials in the literature.[16] These models may be categorized as linear and nonlinear interfacial models. Let the interfaces among the different constituents be subjected to infinitesimal displacement jumps across the interface. The linear traction displacement model can then sufficiently capture the effect of imperfect interface on the predictions of elastic effective properties and static failure strength of these materials. The linear traction displacement model may be expressed as[25]

$$T_i = D^*_{ij}[u_j], \qquad [u_j] = u^2 - u^1, \tag{1}$$

where T_i denote interfacial tractions, and $[u_j]$ denote displacement jumps cross the interface between constituent 1 and 2, and D^*_{ij} denote the second order interface constitutive tensor. As described by the Eq. (1), the interfacial displacement jump or failure can be expressed by three modes of failure. Let the displacement jump normal to the interface be represented as Model I failure with the corresponding interfacial stiffness, D^*_I, and let the two tangential displacement jumps be presented as Mode II and Mode III failures with the corresponding interfacial stiffness D^*_{II} and D^*_{III}, respectively, as shown in the Figure 1. For the

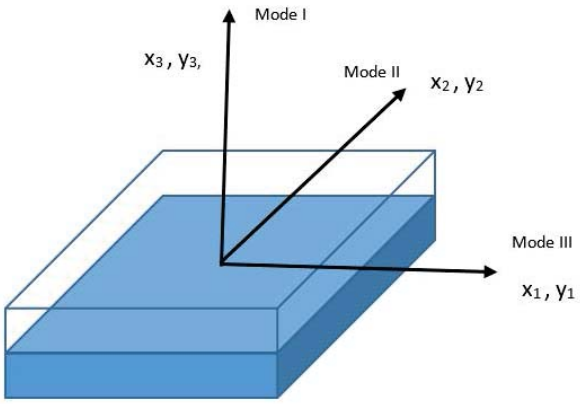

Figure 1. Interface failure modes for unit cell of binary composite

normal displacement jump, using matrix notation, we can obtain from Eq. (1) the interfacial constitutive modeling as

$$T_1 = D^*_I \begin{bmatrix} -1 & 1 \end{bmatrix} \begin{bmatrix} w^1 \\ w^2 \end{bmatrix}$$

where w^i denotes displacement jump in the normal direction. Let the displacement jumps in all directions are decoupled, i.e, tangential displacement in one direction does not affect affect the other tangential displacement jump and/or the normal displacement jump. This leads to a free sliding of one layer over the other without experiencing any normal displacement jump. Thus, Eq. (1) can be written as

$$\begin{bmatrix} T_1 \\ T_2 \\ T_3 \end{bmatrix} = \begin{bmatrix} D_I^* & 0 & 0 \\ 0 & D_{II}^* & 0 \\ 0 & 0 & D_{III}^* \end{bmatrix} \begin{bmatrix} -1 & 0 & 0 & 1 & 0 & 0 \\ 0 & -1 & 0 & 0 & 1 & 0 \\ 0 & 0 & -1 & 0 & 0 & 1 \end{bmatrix} \begin{bmatrix} w^1 \\ v^1 \\ u^1 \\ w^2 \\ v^2 \\ u^2 \end{bmatrix}$$

where v^i and u^i denote the displacement in the Mode II and Mode III direction, respectively. Let the interface undergoes infinitesimal displacement jump across the interface. The strain energy due to interfacial displacement jumps can be expressed as

$$W_{int} = \frac{1}{2} \int_{\Gamma} X^T \overline{D}^* X \, d\Gamma \tag{2}$$

where W_{int} denotes interfacial strain energy and Γ denotes interface area, X and $\overline{D}^*$ are the displacement vector of the interface and interface stiffness expressed as

$$X = \begin{bmatrix} w^1 & u^1 & v^1 & w^2 & u^2 & v^2 \end{bmatrix}$$

and

$$\left[\overline{D}^*\right] = \begin{bmatrix} D_I^* & 0 & 0 & -D_I^* & 0 & 0 \\ 0 & D_{II}^* & 0 & 0 & -D_{II}^* & 0 \\ 0 & 0 & D_{III}^* & 0 & 0 & -D_{III}^* \\ -D_I^* & 0 & 0 & D_I^* & 0 & 0 \\ 0 & -D_{II}^* & 0 & 0 & D_{II}^* & 0 \\ 0 & 0 & -D_{III}^* & 0 & 0 & D_{III}^* \end{bmatrix}$$

Here, it should be noted that this stiffness, $\overline{D}^*$, represents a spring type element between two physically contacting surfaces or interface. Thus, the interface has a zero thickness with the corresponding stiffness. Since the two points of the interface is on different materials, it is also noticeable that the interface energy equation, Eq. (2), is in the discretized form.

III. Variational Asymptotic Method for Unit Cell Homogenization

VAMUCH is a general-purpose micromechanics approach that is capable of predicting the effective properties of heterogeneous materials and recovering the local fields. Different micromechanical approaches adopt different assumptions in the literature, however there are only two essential assumptions associated with the micromechanical analysis of heterogeneous materials with identifiable UCs. These assumptions are:

1. The exact solutions of the field have their volume averages over the UC, i.e., if u_i denotes the exact displacements within the UC, there exists a v_i such that

$$v_i = \frac{1}{\Omega} \int_{\Omega} u_i d\Omega \equiv \langle u_i \rangle, \tag{3}$$

   where Ω denotes the domain occupied by a UC and also its volume, and $\langle \cdot \rangle$ denotes the volume average over Ω;

2. The effective material properties obtained using the micromechanical analysis are independent of the geometry and boundary conditions of the macroscopic structure, or to say, the effective material properties are assumed to be the intrinsic properties of the material when macroscopically viewed.

The variational statement of the micromechanical analysis of a UC has been formulated as constrained minimization problem for a perfect interface by Yu and Tang.[22] Using Eq. (1) for imperfect interface,

the proposed variational statement can be modified for imperfect interface as minimizing the value of the functional

$$\Pi_\Omega = \frac{1}{2\Omega}\int_\Omega C_{ijkl}(\bar{\epsilon}_{(i|j)} + \chi_{(i|j)})(\bar{\epsilon}_{(k|l)} + \chi_{(k|l)})d\Omega + \frac{1}{2\Omega}\int_\Gamma D^*_{ij}[\chi_i][\chi_j]d\Gamma, \tag{4}$$

subjected to the following constrains

$$\langle \chi_i \rangle = 0. \tag{5}$$

where D^*_{ij} denote the interface constitutive tensor for the current local coordinate, $[\chi_i] = u^2 - u^1$. The above equation can be discretized using the finite element method as follows. Introduce the following matrix notations:

$$\bar{\epsilon} = \begin{bmatrix} \bar{\epsilon}_{11} & 2\bar{\epsilon}_{12} & \bar{\epsilon}_{22} & 2\bar{\epsilon}_{13} & 2\bar{\epsilon}_{23} & \bar{\epsilon}_{33} \end{bmatrix}^T, \tag{6}$$

$$\begin{Bmatrix} \frac{\partial \chi_1}{\partial y_1} \\ \frac{\partial \chi_1}{\partial y_2} + \frac{\partial \chi_2}{\partial y_1} \\ \frac{\partial \chi_2}{\partial y_2} \\ \frac{\partial \chi_1}{\partial y_3} + \frac{\partial \chi_3}{\partial y_1} \\ \frac{\partial \chi_2}{\partial y_3} + \frac{\partial \chi_3}{\partial y_2} \\ \frac{\partial \chi_3}{\partial y_3} \end{Bmatrix} = \begin{bmatrix} \frac{\partial}{\partial y_1} & 0 & 0 \\ \frac{\partial}{\partial y_2} & \frac{\partial}{\partial y_1} & 0 \\ 0 & \frac{\partial}{\partial y_2} & 0 \\ \frac{\partial}{\partial y_3} & 0 & \frac{\partial}{\partial y_1} \\ 0 & \frac{\partial}{\partial y_3} & \frac{\partial}{\partial y_2} \\ 0 & 0 & \frac{\partial}{\partial y_3} \end{bmatrix} \begin{Bmatrix} \chi_1 \\ \chi_2 \\ \chi_3 \end{Bmatrix} \equiv \Gamma_h \chi \tag{7}$$

where Γ_h denotes an operator matrix, and χ denotes a column matrix containing the three components of the fluctuation functions. Let χ be discretized using finite elements as

$$\chi(x_i; y_i) = S(y_i)\,\mathrm{X}(x_i), \tag{8}$$

where S denotes the shape functions, and X denotes a column matrix of the nodal values of the fluctuation functions for all the active nodes. The discretized version of Eq. (4) can then be obtained as

$$\Pi_\Omega = \frac{1}{2\Omega}\left(\mathrm{X}^T E \mathrm{X} + 2\mathrm{X}^T D_{h\epsilon}\bar{\epsilon} + \bar{\epsilon}^T D_{\epsilon\epsilon}\bar{\epsilon} + \mathrm{X}^T D_{tt}\mathrm{X}\right), \tag{9}$$

where

$$E = \int_\Omega (\Gamma_h S)^T D (\Gamma_h S)\, d\Omega, \quad D_{h\epsilon} = \int_\Omega (\Gamma_h S)^T D d\Omega, \quad D_{\epsilon\epsilon} = \int_\Omega D d\Omega, \quad D_{tt} = \int_\Gamma \overline{D}^* d\Gamma \tag{10}$$

with D denoting the 6×6 stiffness matrix condensed from $\mathcal{C}_{ijkl}$ and $\overline{D}^*$ denote interface stiffness. The discretized version of the second part of Eq. (4) is shown in Eq. (2). The above Eq. (9) can then be modified as

$$\Pi_\Omega = \frac{1}{2\Omega}\left(\mathrm{X}^T(E + D_{tt})\mathrm{X} + 2\mathrm{X}^T D_{h\epsilon}\bar{\epsilon} + \bar{\epsilon}^T D_{\epsilon\epsilon}\bar{\epsilon}\right), \tag{11}$$

It can be derived from Eq. (11) that Π_Ω attains its minimum only if

$$(E + D_{tt})\mathrm{X} = -D_{h\epsilon}\bar{\epsilon} \tag{12}$$

which can be used to solve for X as;

$$\mathrm{X} = \mathrm{X}_0\bar{\epsilon}. \tag{13}$$

Eq. (13) implies that X is linearly dependent on $\bar{\epsilon}$. Substituting Eq. (12) into Eq. (11) gives the minimum of Π_Ω as

$$\Pi_\Omega = \frac{1}{2\Omega}\bar{\epsilon}^T\left(\mathrm{X}_0^T D_{h\epsilon} + D_{\epsilon\epsilon}\right)\bar{\epsilon} \equiv \frac{1}{2}\bar{\epsilon}^T\bar{D}\bar{\epsilon}, \tag{14}$$

where $\bar{D}$ denotes the so-called effective stiffness matrix, and $\bar{\epsilon}$ denotes the global strain column matrix. Till now, the effective material properties can be fully determined. In addition, if the local fields are of interest,

they can be recovered using the global displacements, v, the global strains, $\bar{\epsilon}$, and the fluctuation functions, χ. Specifically, the local displacements can be recovered as

$$u = v + \begin{bmatrix} \frac{\partial v_1}{\partial x_1} & \frac{\partial v_1}{\partial x_2} & \frac{\partial v_1}{\partial x_3} \\ \frac{\partial v_2}{\partial x_1} & \frac{\partial v_2}{\partial x_2} & \frac{\partial v_2}{\partial x_3} \\ \frac{\partial v_3}{\partial x_1} & \frac{\partial v_3}{\partial x_2} & \frac{\partial v_3}{\partial x_3} \end{bmatrix} \begin{Bmatrix} y_1 \\ y_2 \\ y_3 \end{Bmatrix} + S\bar{\mathrm{X}}_0\bar{\epsilon}, \tag{15}$$

where u and v denote the local and global displacement column matrices, respectively, and $\bar{\mathrm{X}}_0$ denotes the nodal values of fluctuation functions modified from X_0 by the periodic boundary conditions and Eq. (5). The local strains can be recovered as

$$\epsilon = \bar{\epsilon} + \Gamma_h S\bar{\mathrm{X}}_0\bar{\epsilon}, \tag{16}$$

where ϵ denotes the the local strain column matrix. The local stresses can be recovered from the local strains as

$$\sigma = D\epsilon. \tag{17}$$

It is worth to notice that, although VAMUCH is as versatile as the finite element method to discretized the microstructure, it is by no means an extension of the traditional displacement-based finite element method. In fact, the VAMUCH code has the following distinctive features:

- The complete set of effective material properties can be obtained within one analysis, without the application of any external loads or displacement boundary conditions;
- The fluctuation functions and the displacements are uniquely determined;
- The effective material properties and the recovered local fields are directly obtained with the same accuracy of the fluctuation functions, without any postprocessing-type calculations (e.g., averaging the stresses or the strains),
- The dimensionality of the problem is determined by that of the periodicity of the UC.

Interested readers can refer to Ref. [22] for more details on the VAMUCH theory.

IV. Effective Properties and Static Failure Predictions

In this section, a bilinear cohesive zone material model shown in the Figure 2, is employed to analyze the effects of imperfect interface on the elastic effective properties of heterogeneous materials. In this analysis, a mixed-mode fracture is assumed, i.e. both normal and tangential displacement jumps contribute for the overall displacement jumps across the interface. Here, it is also assumed that the interface undergoes infinitesimal displacement jump. This helps to bound the analysis within elastic limit. δ_n^* denotes displacement jump at the maximum interfacial stress and δ_n^c denotes the interfacial displacement at complete debonding as shown the Figure 2. This assumption ensures the displacement jumps occurs within recoverable limits. The positive slope of on the Figure shows the stiffness of the interface.

This cohesive zone material mode is used for both normal and tangential displacement jumps to analyze the effects of imperfect interface on the effective properties and also static failure strength of heterogeneous materials. The interfacial stiffness shown in Eq. (2) with this material model is incorporated into VAMUCH to analyze the effective properties and also static failure of heterogeneous materials. The predictions of VAMUCH are performed using several examples of heterogeneous materials such as binary composite, continuous fiber reinforced composite, particle reinforced composite, discontinuous fiber reinforced composite, and woven composite. These predictions are validated using exact solutions for binary composite, FEA and published data. The results of FEA are obtained using ANSYS by employing the micromechanics approach proposed by Sun and Vaidya.[26] Interface element INTER204 is used in ANSYS for all the examples analysis using FEA.

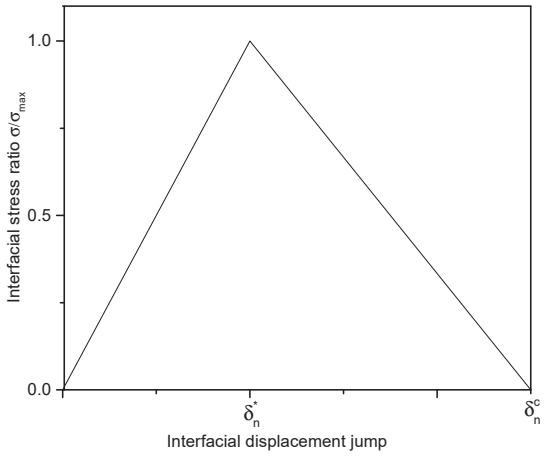

Figure 2. Sketch of cohesive zone material model

A. Binary Composite

As thoroughly discussed in the Ref. [22, 27, 28], VAMUCH theory can be used to obtain analytical the exact solution for both effective properties and local fields of binary composites, although both the effective properties of binary composite are obtained for perfectly bonded interface, i.e, both displacement and stress are continuous across the interface. Here, it should be noted that VAMUCH provides the 3D effective properties and local fields from a 1D analysis. In the current analysis, it is assumed that the interface undergoes infinitesimal displacement jumps and the stress across the interface is assumed to be continuous. The effective properties of binary composite can then be obtained by analytically solving Eq. (4) using Eq. (5) and boundary conditions as constraints as well stated in the Ref. [27, 28]. Thus, the perfect interface of the first part of Eq. (9) of Ref. [27] is modified as

$$D_I[\chi_3] - \sigma_{33} = 0, \quad D_{II}[\chi_3] - \sigma_{13} = 0, \quad D_{III}[\chi_3] - \sigma_{23} = 0, \tag{18}$$

where $[\chi_i]$ denote displacement jump across the interface, and σ_{i3} denote interfacial stress in y_i direction. For isotropic material, the effective properties for imperfect interface can be obtained as

$$G_{12} = \frac{1}{2}\frac{(1+\nu^{(2)})E^1\phi_1 + (1+\nu^{(1)}E^2\phi_2}{(1+\nu^{(1)})(1+\nu^{(2)})}$$

$$\begin{aligned} G_{13} = {} & \frac{D_{III}^2 E^{(1)}{E^{(2)}}^2(1+\nu^{(1)})^2(\frac{1}{2}+\frac{1}{2}\nu^{(2)})\phi_1}{m} \\ & + \frac{D_{III}{E^{(1)}}^2 E^{(2)}(E^{(2)}(\frac{1}{4}+\nu^{(1)}(\frac{1}{4}+\frac{1}{4}\nu^{(2)})+\frac{1}{4}\nu^{(2)}))}{m} \\ & + \frac{D_{III}^2{E^{(1)}}^2 E^{(2)}(\frac{1}{2}+\frac{1}{2}\nu^{(1)})(1+\nu^{(2)})^2\phi_2)}{m} \end{aligned}$$

$$m = (1+\nu^{(1)})(1+\nu^{(2)})(-\frac{1}{2}E^{(1)}E^{(2)} + D_{III}(E^{(1)}\phi_1(1+\nu^{(2)}) - E^{(2)}(1+\nu^{(1)})\phi_1 - E^{(1)}(1+\nu^{(2)}))^2$$

$$G_{23} = \frac{D_{II}^2 E^{(1)} {E^{(2)}}^2 (1+\nu^{(1)})^2 (\frac{1}{2}+\frac{1}{2}\nu^{(2)})\phi_1}{nn} + \frac{D_{II} {E^{(1)}}^2 E^{(2)} (E^{(2)} (\frac{1}{4}+\nu^{(1)} (\frac{1}{4}+\frac{1}{4}\nu^{(2)}) + \frac{1}{4}\nu^{(2)}))}{nn} + \frac{D_{II}^2 {E^{(1)}}^2 E^{(2)} ((\frac{1}{2}+\frac{1}{2}\nu^{(1)})(1+\nu^{(2)})^2 \phi_2)}{nn}$$

$$nn = (1+\nu^{(1)})(1+\nu^{(2)})(-\frac{1}{2}E^{(1)}E^{(2)} + D_{II}(E^{(1)}\phi_1(1+\nu^{(2)}) - E^{(2)}(1+\nu^{(1)})\phi_1 - E^{(1)}(1+\nu^{(2)}))^2$$

where $E^{(1)}$ and $E^{(2)}$ denote elastic moduli of material 1 and 2, $\nu^{(1)}$ and $\nu^{(2)}$ denote the Poisson's ratios of material 1 and 2, and $\phi 1$ and ϕ_2 denote the volume of material. The solutions for E_1, E_2, E_3 and Poisson's ratios are very lengthy, thus it is not shown here. The effective properties obtained from these equations are compared with the prediction of VAMUCH and FEA. In this analysis, VAMUCH uses only two elements. FEA uses 6400 (Solid186) elements. The FEA unit cell of binary composite is shown in the Figure 1.

The elastic modulus and Poisson's ratio of layer 1 is assumed to 86 GPa and 0.22, respectively and layer 2 has an elastic modulus of 4.3 GPa and Poisson's ratio of 0.34. The effective properties are predicted for various interfacial stiffness. Here, it is also assumed that D_{II} and D_{III} are equal. From the analyses, it is noticed that the predictions of E_1, E_2, G_{12}, and all Poisson's ratio are found to be invariant with the interfacial stiffness for VAMUCH, FEA and exact solutions. These predictions are found to be reasonable. However, as shown in the Figure 3, the predictions of E_3 are significantly affected by interfacial stiffness, D_{11}, that corresponds to the failure mode I. Note from hereon, we let $D_{11} = D_I^*$, $D_{22} = D_{II}^*$, $D_{33} = D_{III}^*$. As the interfacial stiffness decreases, the prediction reduces to very small value. These predictions are found to be consistent with the debonding strength of the layers. It is obvious to see that all approaches show an excellent agreement. The interfacial stiffness D_{II} and D_{III} also affect the shear moduli, G_{23} and G_{13}, respectively, as depicted in the Figures 4 and 5.

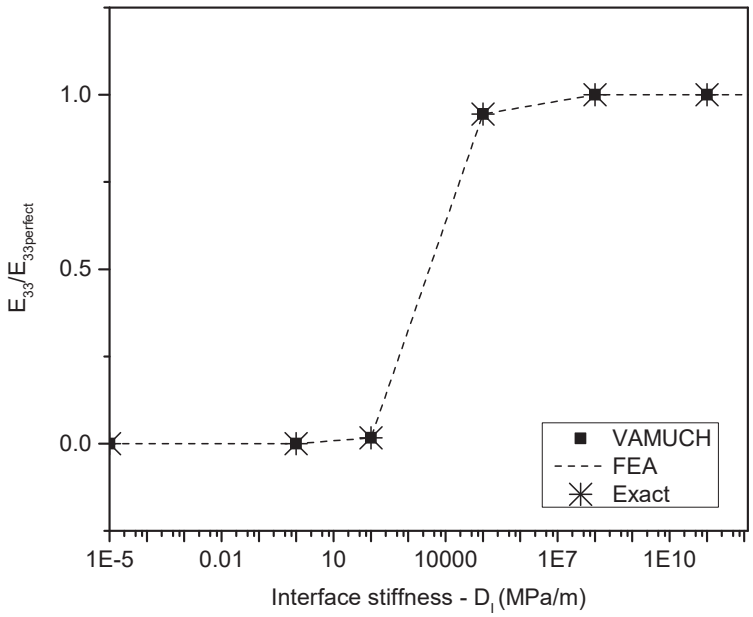

Figure 3. Predictions of E_{33}.

For this case, the FEA cohesive zone treatment is limited to only two basic failure mode, i.e, Mode I and Mode II, thus, the predictions of FEA for G_{13} shows negligible deviation from the predictions of the perfect interface (not shown here). However, as depicted in the Figure 5, the interfacial stiffness, D_{22}, can significantly affect the axial shear modulus G_{13}. Thus, it is of significant importance not to neglect the effect

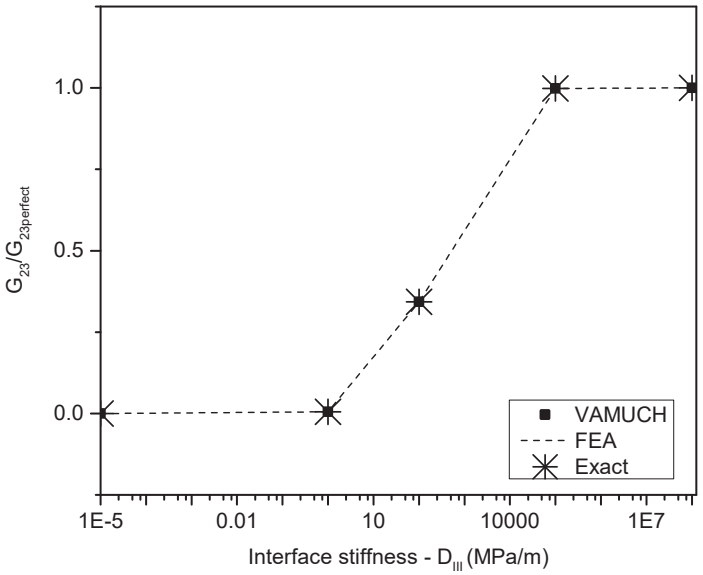

Figure 4. Predictions of G_{23}.

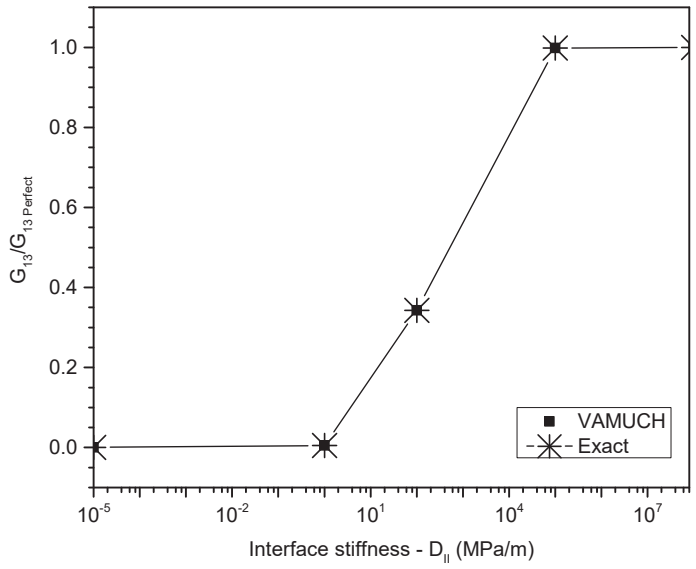

Figure 5. Predictions of G_{13}.

of the interfacial stiffness, D_{22}, particularly for the prediction of shear modulus, G_{13}, in binary composite.

The effect of the interfacial stiffness on the failure strength of the binary composite is also analyzed using maximum principal stress and maximum shear stress criteria. It is also assumed the axial and shear strength of layer are 4.8 GPa and 2.4 GPa, respectively, for layer 2 the axial and shear strength are 83 MPa and 40 MPa, respectively. These failure strength are used for all subsequent failure analyses. As it can be seen from the Figures 6 and 7, it is clear to notice that the failure strength is considerably dependent on the interfacial strength of the composite. Both VAMUCH and FEA show an excellent agreement with exact solutions. The interfacial stiffness mainly controls the failure of the composite, i.e, failure usually initiates at the interface.

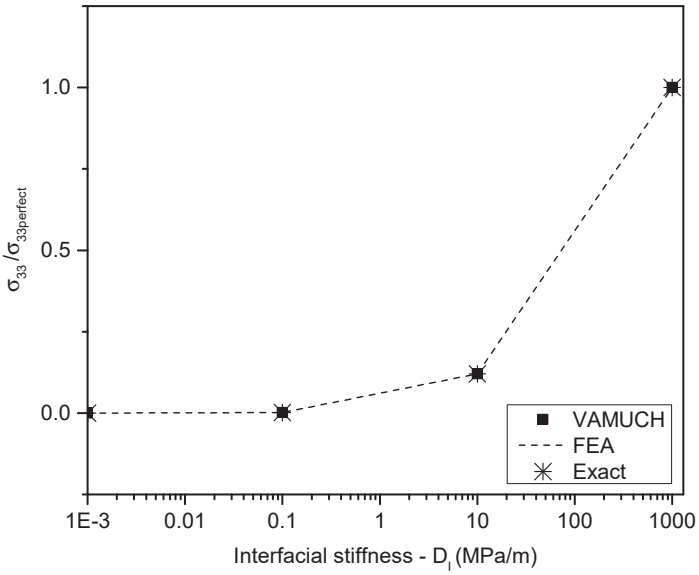

Figure 6. Predictions of failure strength σ_{33} using maximum principal stress criterion.

B. Continuous Fiber Reinforced Composite

In this case, first, let a circular fiber be embedded in a square matrix, and also let the local Cartesian coordinate be introduced at the center of unit cell as $y = (y_1, y_2, y_3)$ with y_1 is parallel to the fiber direction as depicted in Figure 8. Second, a mesh of 4500 8-noded quadrilateral and SOLID95 elements are used for VAMUCH and FEA, respectively. The material properties are listed in the Table 1. In this analysis, a fiber volume of 40% is assumed.

Table 1. Material property for imperfect interface.

Mat	E (GPa)	ν
Fiber	379.3	0.10
Matrix	68.3	0.30

The interfacial debonding can happen in three possible directions at fiber and matrix interface: normal to the contacting surface, tangent to the interface along the fiber direction which corresponds to the mode II failure, and tangent along the the interface corresponds to mode III failure. These modes of failure may be represented by three interfacial stiffness D_{11}, D_{22}, and D_{33} to analyze the effect of imperfect interface on the elastic effective properties of continuous fiber reinforced composite. Let the two tangential interface stiffness,

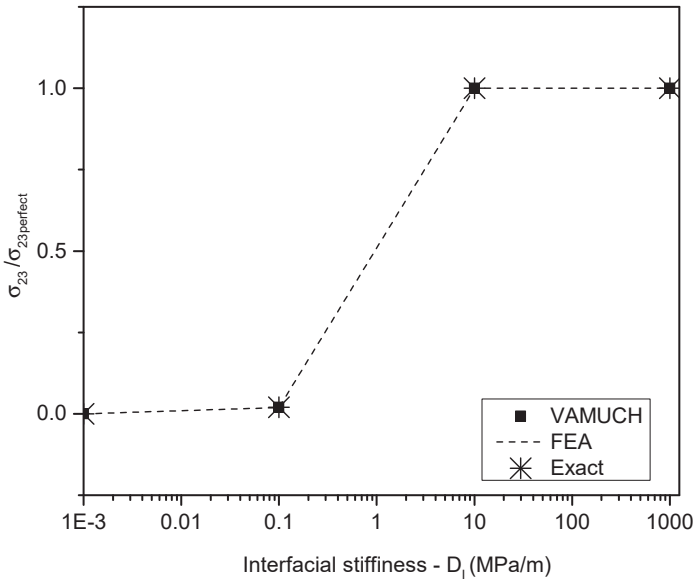

Figure 7. Predictions of failure strength σ_{23} using maximum shear stress criterion

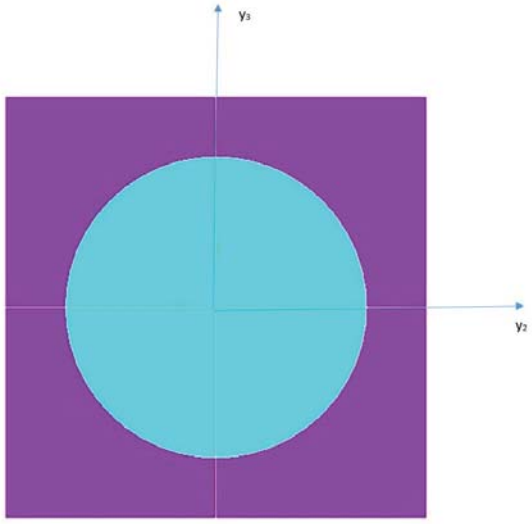

Figure 8. Unit cell of continuous fiber reinforced composite.

i.e, D_{22} and D_{33}, be equal. The predictions of this analysis reveal that the axial effective elastic modulus, E_1, is negligibly affected by the interfacial stiffness, while the transverse elastic modulus, E_2, is significantly dependent on the normal interfacial stiffness, D_{11}, as depicted in the Figure 9. However, the interfacial stiffness, D_{11}, doesn't influence the predictions of transverse elastic modulus, whereas the prediction of the transverse shear modulus, G_{23}, is found to be highly dependent on the interfacial stiffness, D_{33}, as shown the Figure 10.

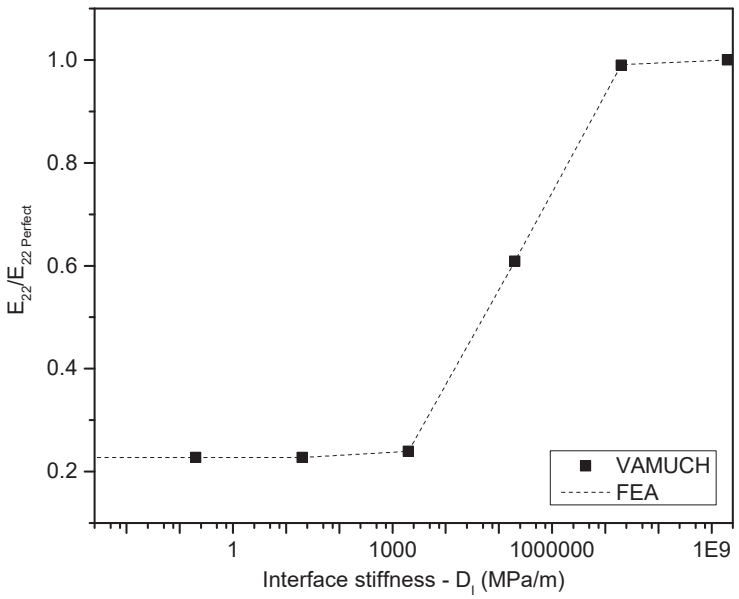

Figure 9. Predictions of E_{22}.

The axial shear modulus, G_{12}, is significantly affected by the interfacial stiffness, D_{22}, as shown in the Figure 11. However, it is not considerably affected by the the other interfacial stiffness. The current version of ANSYS 15.1 does not support the interfacial stiffness, D_{22}, which corresponds to the model II failure for continuous fiber reinforced composite. Finally, it is found to be important to analyze the influence of the interfacial stiffness on the Poisson's ratio. It is also noted that the interfacial stiffness, D_{11}, can influence the effective Poisson's ratio. As it can be seen from the Figure 12, the Poisson's ratio ν_{12} is observed to be larger for imperfect interface with negligible stiffness. This prediction appears to be reasonable. The weaker the interface is the larger the global strain at the boundary in corresponding direction. For instance, the transverse global strain, ε_{22}, is not mainly affected by axial external load along the fiber but the axial strain ε_{11} slightly affected. Thus, it results in the larger Poisson's ratio. Conversely, for transverse poisson ratio, the global strain increases in the direction of the external load application while it nearly remain the same in the other direction which results in reducing effective poisson ratio for lower interfacial stiffness.

Finally, the static failure strength of the composite is analyzed. It is learned that the failure strength in axial direction is not affected, while the failure in the transverse direction is significantly dependent of the interfacial stiffness as depicted in the Figures 13 and 14. The transverse shear failure strength is also evaluated using Tsai-Hill failure criterion as shown in the Figure 15. It is clear to notice that the interfacial stiffness control the transverse shear failure of the composite. Here, it should be noted that the failure strength of the interface is assumed to be the same as the its corresponding stiffness. Consequently, failure may usually be initiated in matrix, however, if the interfacial failure strength is assumed lower than the corresponding interfacial stiffness, then the interface mainly controls the failure strength of the composite.

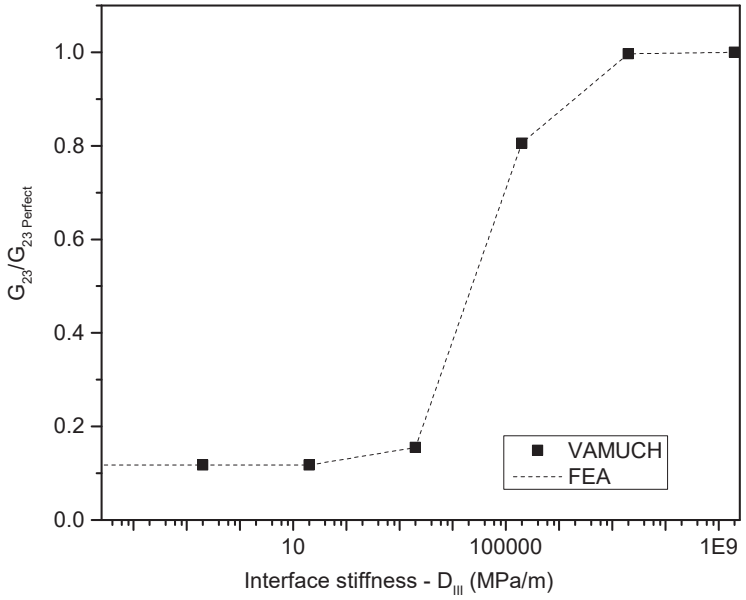

Figure 10. Predictions of G_{23}.

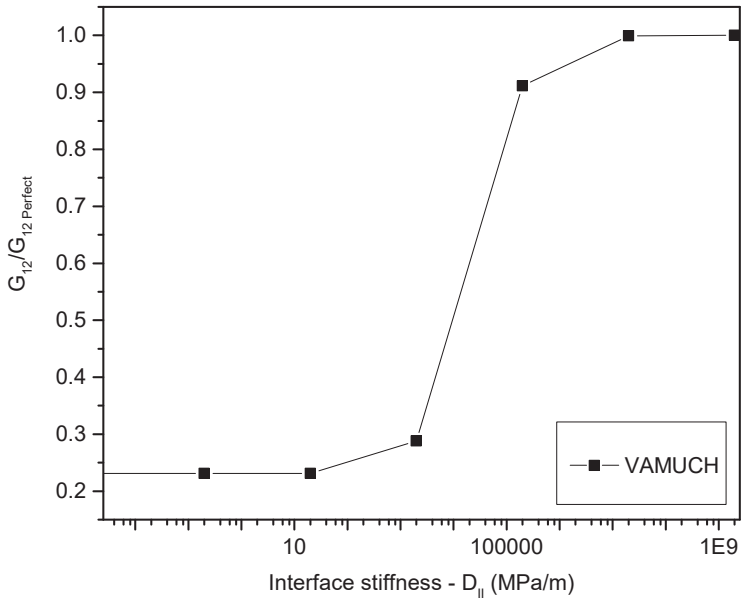

Figure 11. Predictions of G_{12}.

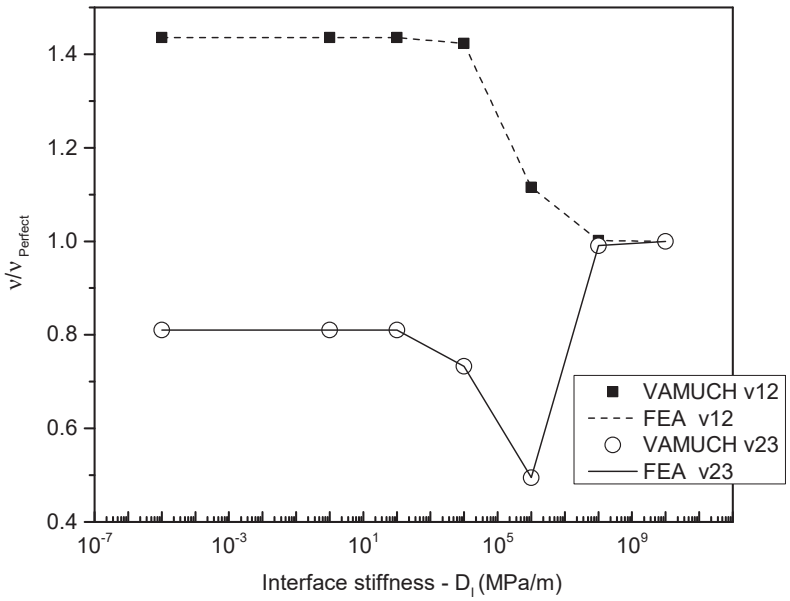

Figure 12. Predictions of ν_{12} and ν_{23}.

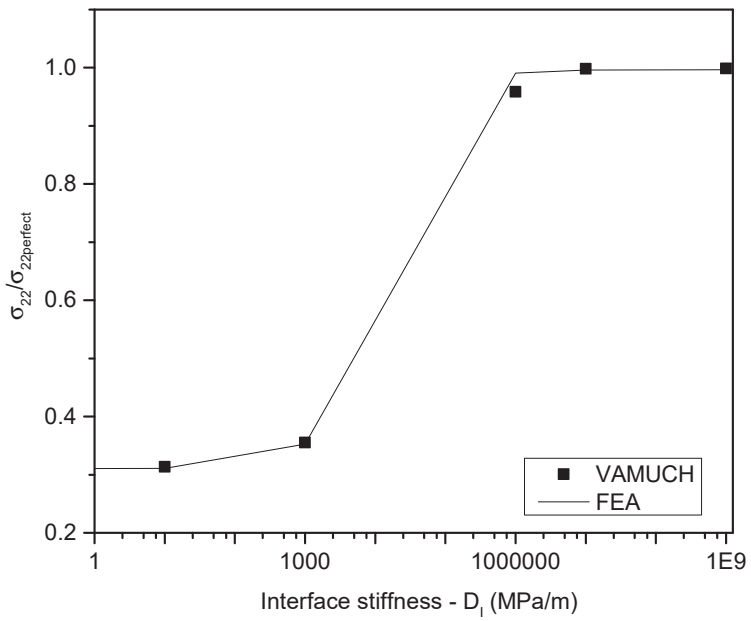

Figure 13. Predictions of failure strength for σ_{22} using maximum principal stress criterion.

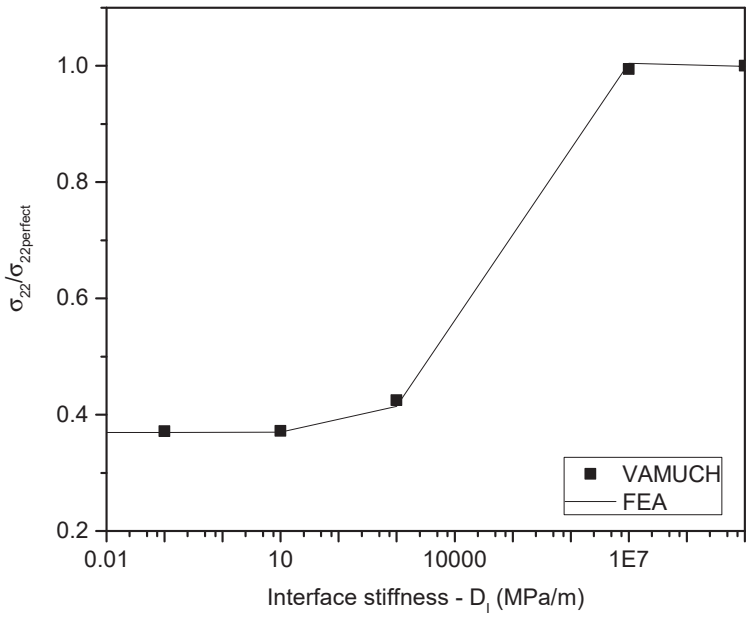

Figure 14. Predictions of failure strength for σ_{22} using Tsai-Hill criterion.

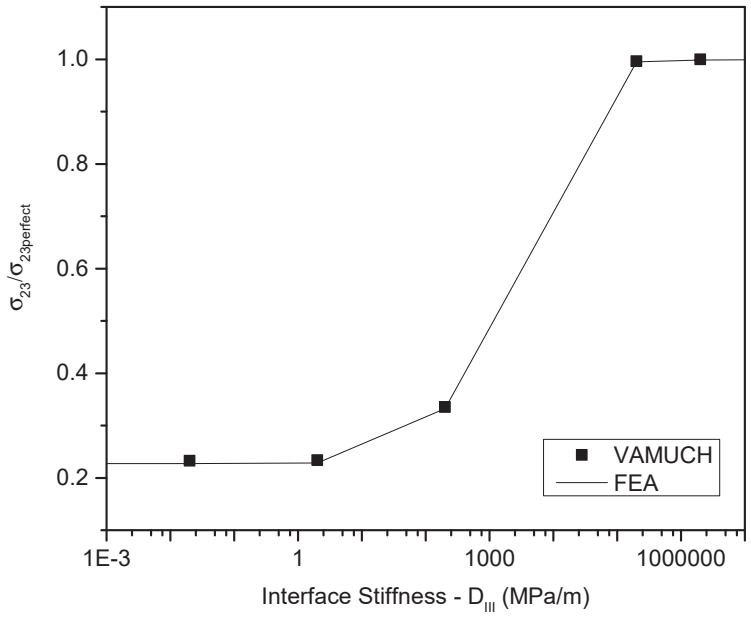

Figure 15. Predictions of failure strength for σ_{23} using Tsai-Hill criterion.

C. Particle Reinforced Composite

The unit cell of particle reinforced composite can be generated as follows. Let a spherical inclusion with 40% fiber volume be embedded at the center of cuboidal matrix. Let the local Cartesian coordinates be set at the center of sphere. The inclusion particle and matrix are assumed to have an elastic modulus 703.45 GPa and 206.94 GPa, respectively, and with the corresponding Poisson ratios of 0.2199 and 0.2999, respectively. The interface stiffness in this case is assumed to have a relation, $D_{11} = 5D_{22}$, and $D_{22} = D_{33}$, and $\frac{G_2}{aD_{22}} = 10$, where G_2 is the shear modulus of the matrix, and a is the radius of the sphere. The elastic effective properties are predicted using upper and lower bounds proposed by Hashin.[25] The upper and lower bounds for the effective elastic modulus, E, are found to be 187.86 GPa and 61.6 GPa, respectively, and similarly, for the effective shear modulus, G, the upper and the lower bounds are predicted to be 75.71 GPa and 22.50 GPa, respectively. The current predictions using VAMUCH and FEA are 140.85 GPa and 142.63 GPa for effective elastic modulus, respectively. VAMUCH and FEA also predict the effective shear modulus to be 51.89 GPa and 55.61 GPa, respectively. It appears that the prediction of VAMUCH and FEA for both elastic and shear moduli are within the within the proposed upper and lower bounds. The predictions of VAMUCH and FEA compared with the upper and lower bounds of elastic moduli are analyzed for various interfacial stiffness. As shown in the Figures 16 and 17, the prediction of both effective elastic and shear moduli is observed to be much closer to the upper bounds.

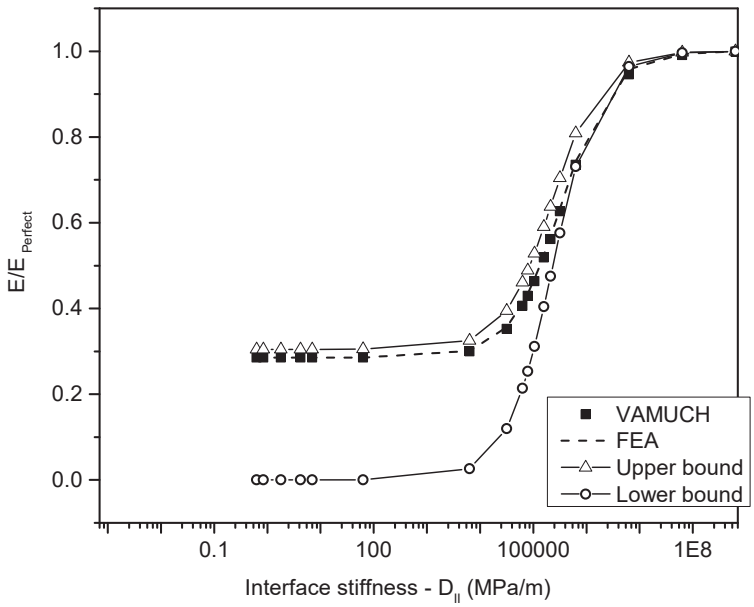

Figure 16. Predictions of effective elastic modulus E.

The failure strength of the particle reinforced composite is also analyzed for different interfacial stiffness. As depicted in the Figure 18, the predictions of failure strength using maximum principal stress criterion shows that the imperfect interface negligibly affect the failure strength of the composite. However, the Tsai-Hill failure criterion shows the failure strength of the composite can be compromised due to the imperfect interface that may go up to 25% loss of its original strength.

D. Discontinuous Fiber Reinforced Composite

To generate the unit cell for discontinuous fiber reinforced composite, first, let a quarter of circular fiber be embedded at the two opposite corners of hexagonal array matrix. Let the array be symmetric with respect to its width and height. This arrangement produces hexagonal array with circular fiber at the center and quarter circular fiber at the corners of the array as shown in Figures 19 and 26. Second, let the cross-sectional area of

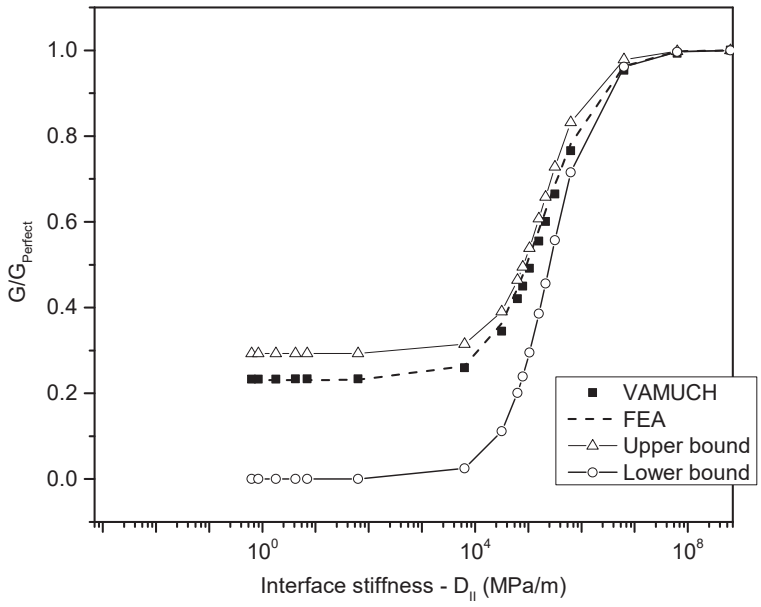

Figure 17. Predictions of effective shear modulus G.

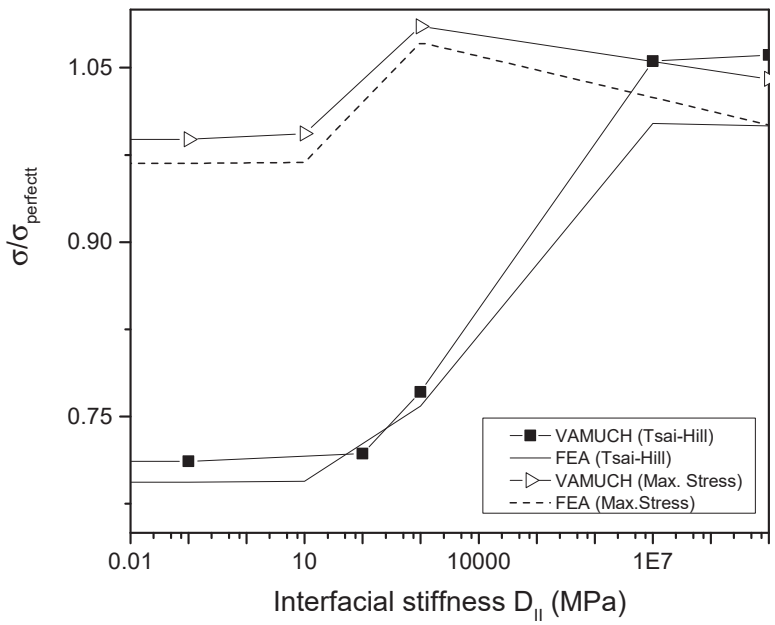

Figure 18. Predictions of failure strength of particle reinforced composite σ.

the hexagonal array be generated based on the common relation, $a = \beta b$, where a is the width and b the height of the unit cell and $\beta = \sqrt{3}$ for hexagonal array. Moreover, let the local Cartesian coordinate be introduced as $y = (y_1, y_2, y_3)$ at the center of unit cell, where y_1 is in the fiber direction. The fibers are generally shorter compared to the unit cell in y_1 direction. For detail geometric constructions of discontinuous fiber reinforced composite, interested reader may refer to Ref. [29]. Two variants of discontinuous fiber reinforced composites are considered for predicting the effective elastic properties and static failure strength of the composite with imperfect interface. The first one is aligned-regular array, where all the fibers are arranged in aligned pattern and the second one is aligned-staggered array, where fibers are arranged in offset pattern. In this analysis, the fiber volume and fiber aspect ratio (length/diamater) are assumed to be 40% and 5, respectively. For FEA, the unit cell is first modeled using plane element (Mesh200) in 2D model and then the corresponding 3D model is generated by extrusion of the 2D model. VAMUCH uses the same mesh used for FEA. The material properties for this analysis are listed in the Table 2 for both types of discontinuous fiber reinforced composite.

Table 2. Material property (Ref. [29]).

Mat	E (GPa)	ν
Fiber	300	0.17
Matrix	10	0.33

1. Aligned-Regular Array

In this imperfect interface analysis, 20-noded elements are used for VAMUCH and FEA with 10624 elements. The unit cell of VAMUCH and FEA is shown in the Figure 19. The prediction of effective properties with various interfacial stiffness are performed using VAMUCH and FEA. In this case, the interfacial stiffness, $D_{22} = 5D_{11}$ and $D_{22} = D_{33}$, are assumed. Please note that ANSYS does not support stiffness, D_{22}. Thus, this analysis also helps to critically investigate the effect of D_{22} on the prediction of effective properties. The predictions of elastic modulus E_1, using VAMUCH shows a slight deviation from ANSYS as depicted in the Figure 20. This deviation may be due the interfacial stiffness in the model II direction. In another analysis, as shown in the Figures 21 and 22, VAMUCH and FEA agree well in estimating the effects of interfacial stiffness on the effective elastic moduli, E_2 and E_3.

The prediction of both effective axial and transverse shear moduli are also performed for different interfacial stiffness. As depicted in the Figure 23, the axial shear modulus predictions of VAMUCH show slight deviation from FEA, as described in the continuous fiber reinforced composite, this deviation may be due to the stiffness in mode II direction. Similar observation has been also seen for binary composite for G_{13}. The predictions of VAMUCH for the effective transverse shear modulus agree well with the prediction of VAMUCH as shown in the Figure 24. The effect of interfacial stiffness on the effective Poisson's ratio also predicted as shown in the Figure 25. VAMUCH and FEA show good agreement except small deviation for small interfacial stiffness. In general, the imperfect interface analyses for discontinuous fiber reinforced composite reveal that the stiffness in mode II direction does not affect the predictions of the transverse axial, E_2, and transverse shear modulus, G_{23}. However, it significantly affects axial elastic modulus, E_1 and axial shear modulus, G_{12}.

2. Aligned-Staggered Array

Aligned staggered array type of discontinuous fiber reinforced composite is similar to the aligned regular array but, in this case, the fibers in the unit cell are arranged in staggered pattern, i.e., fibers overlap within the unit cell. Let 76% of fiber length overlap within a unit cell for this analysis. 9120 20-noded elements are used for VAMUCH and FEA. The unit cell of FEA and VAMUCH is shown in the Figure 26. In this case, it is assumed that the interfacial stiffness $D_{22} = D_{33}$ and also $D_{22} = 5D_{11}$.

From the analyses, it is observed that VAMUCH shows excellent agreements for all elastic moduli as depicted in the Figures 27-29. The axial and transverse shear moduli are also well predicted by VAMUCH compared with FEA as shown in the Figures 30 and 31. It is clear to notice that the interfacial stiffness, D_{22}, does not noticeably affect the axial shear moduli. This may be due to the arrangement of the fibers in the unit cell. The fibers are not fully embedded in the matrix along the axial direction, i.e., exposed to

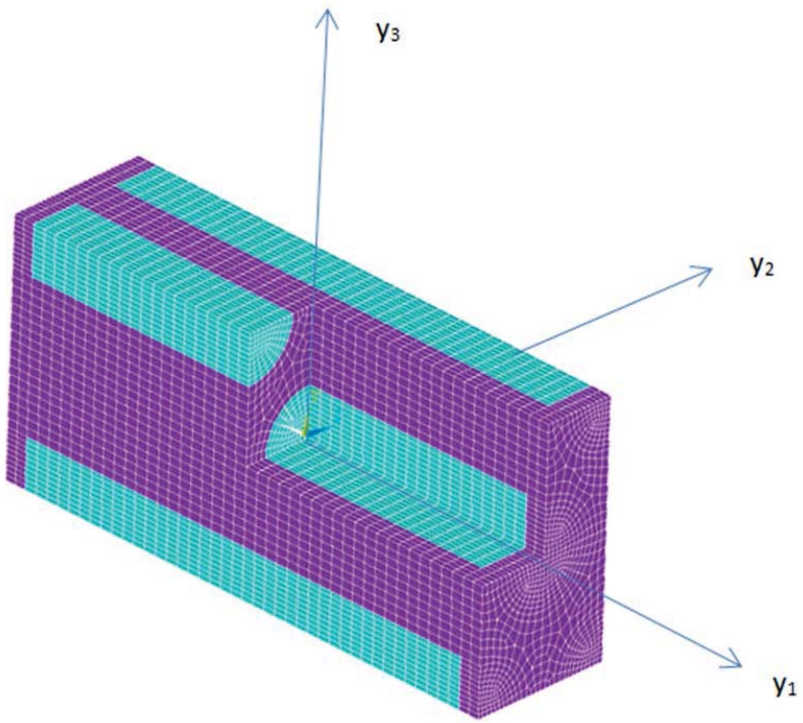

Figure 19. unit cell aligned discontinuous fiber reinforced composite.

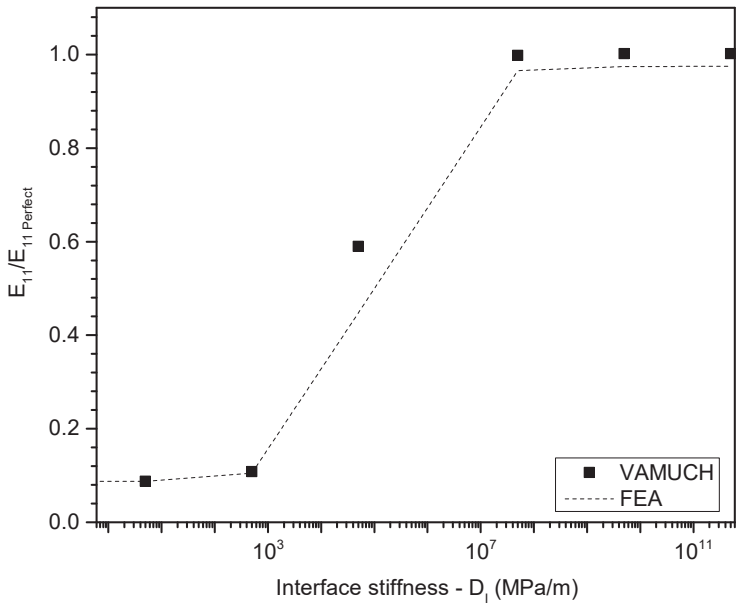

Figure 20. Predictions of effective elastic modulus E_1

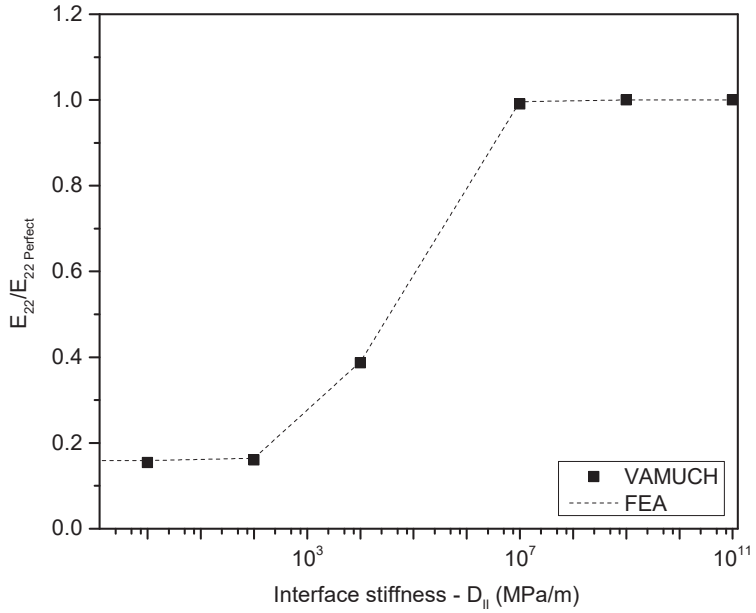

Figure 21. Predictions of effective elastic modulus E_2.

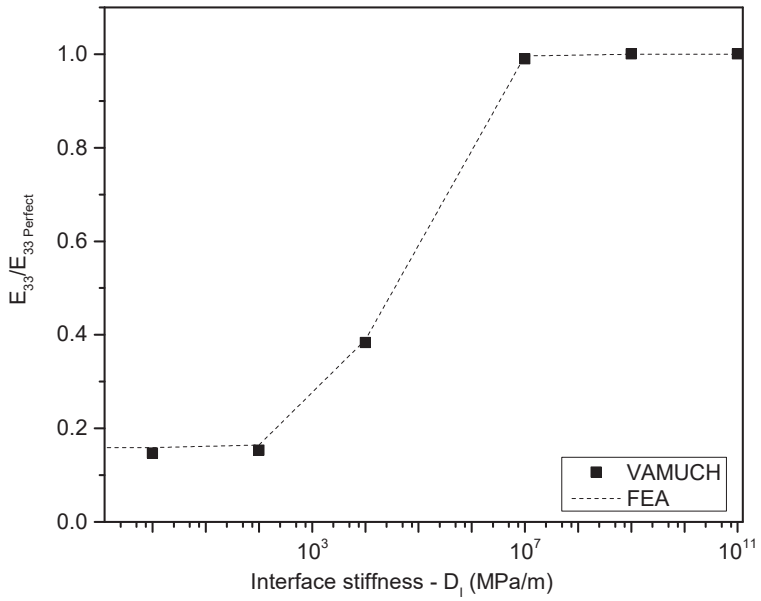

Figure 22. Predictions of effective elastic modulus E_3.

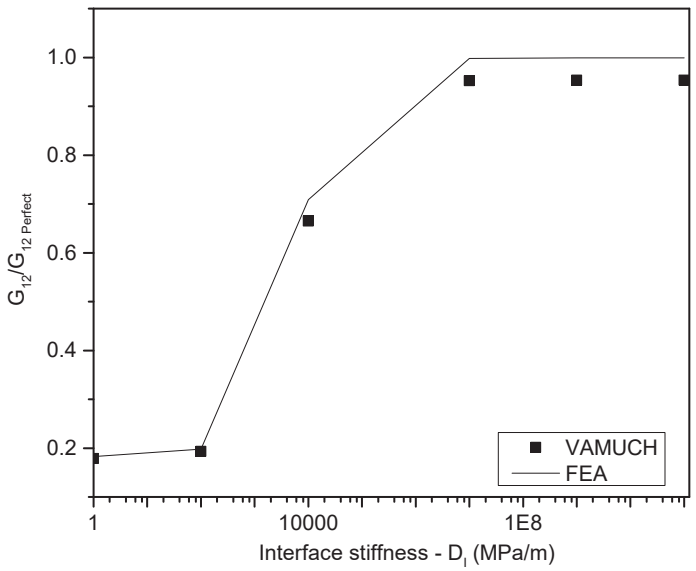

Figure 23. Predictions of effective axial shear modulus G_{12}.

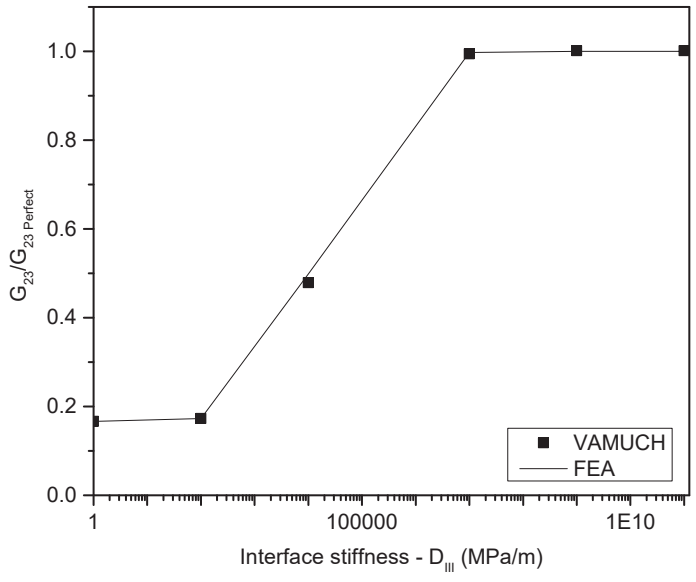

Figure 24. Predictions of effective transverse shear modulus G_{23}.

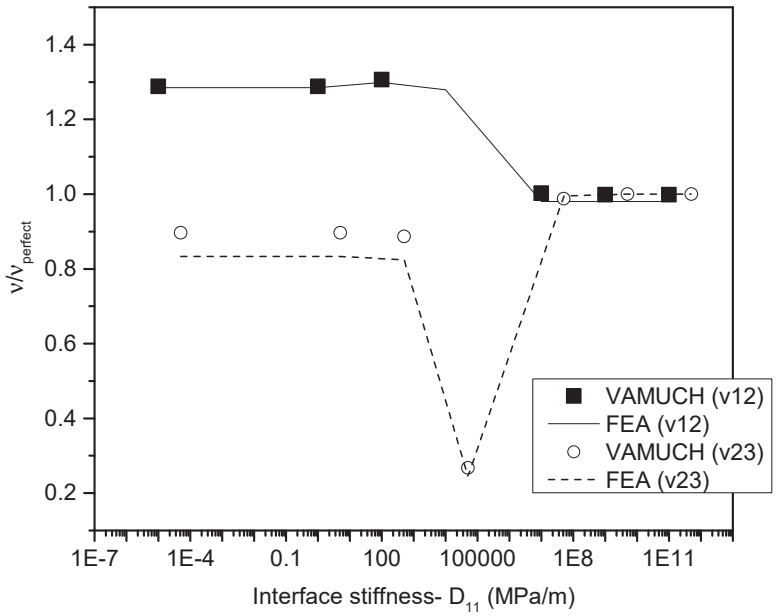

Figure 25. Predictions of effective Poisson's ratio ν_{23}.

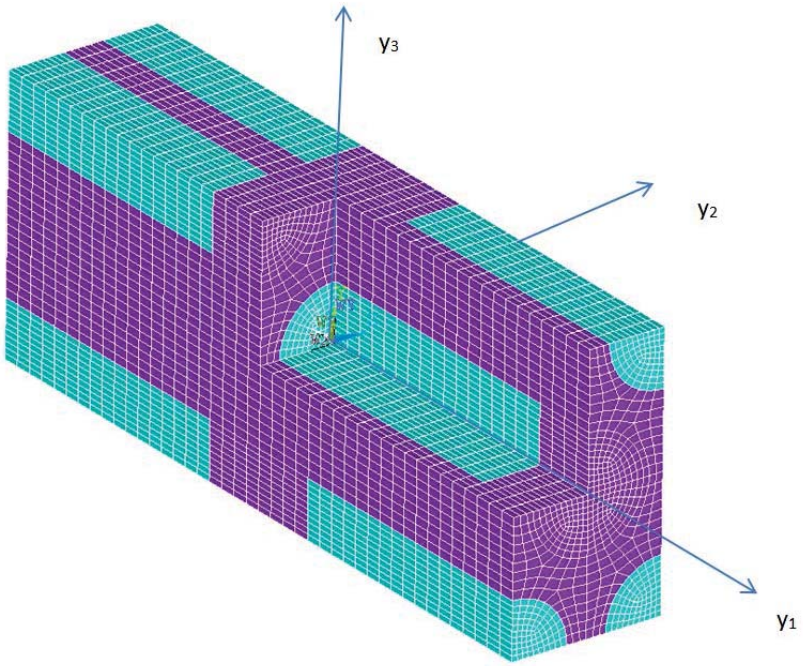

Figure 26. Unit cell aligned staggered discontinuous fiber reinforced composite.

any external boundary conditions, in the unit cell. Finally, the prediction of Poisson ratios is also evaluated. As it can be seen from Figure 32, it is noticed that VAMUCH shows excellent agreements with FEA except slight deviation for ν_{23} for smaller interface stiffness.

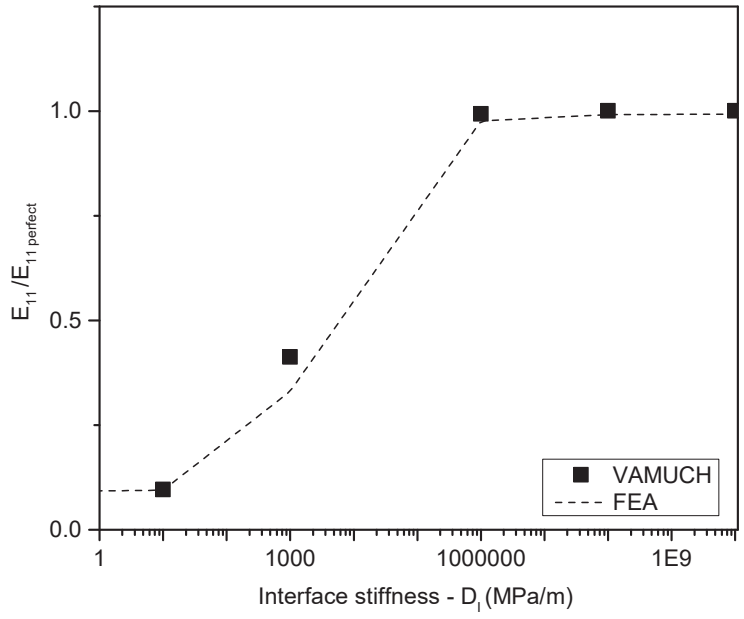

Figure 27. Predictions of effective elastic modulus E_1.

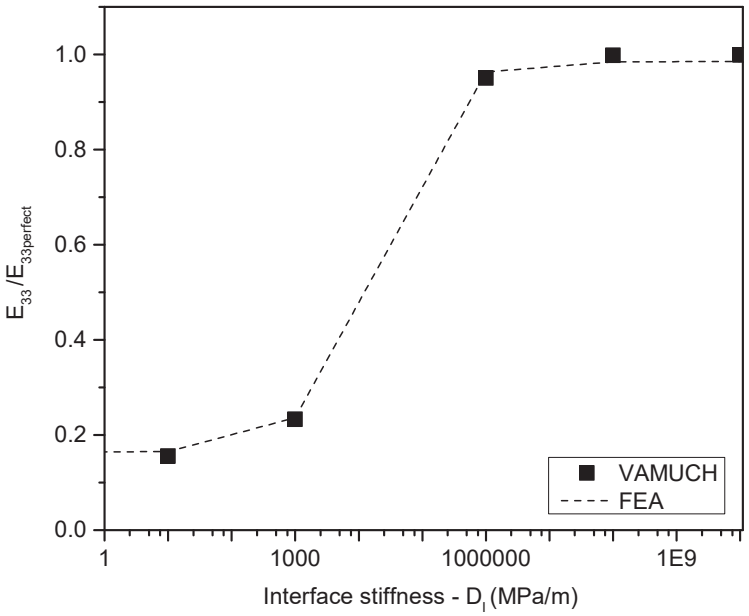

Figure 28. Predictions of effective elastic modulus E_2.

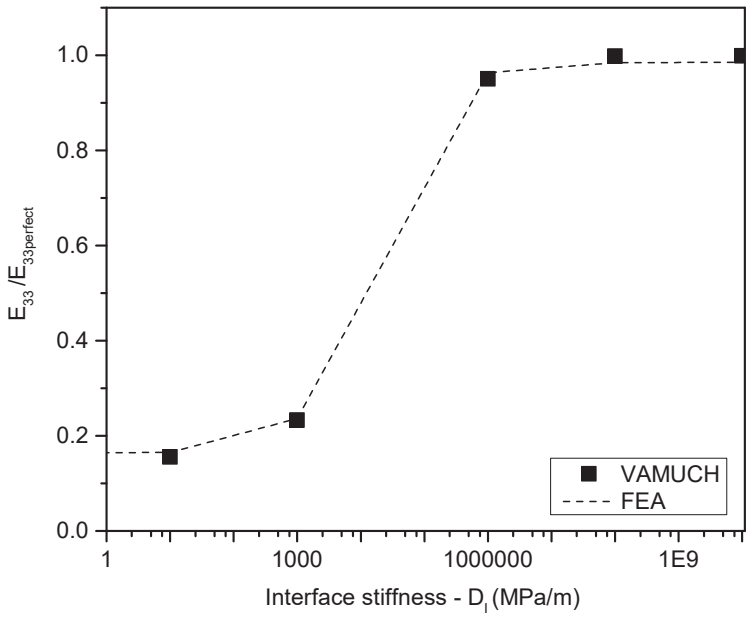

Figure 29. Predictions of effective elastic modulus E_3.

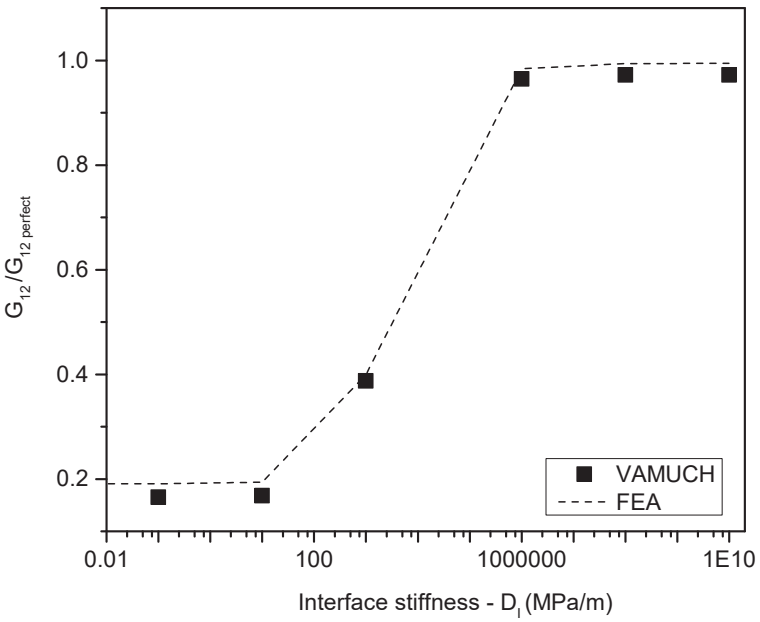

Figure 30. Predictions of effective axial shear modulus G_{12}.

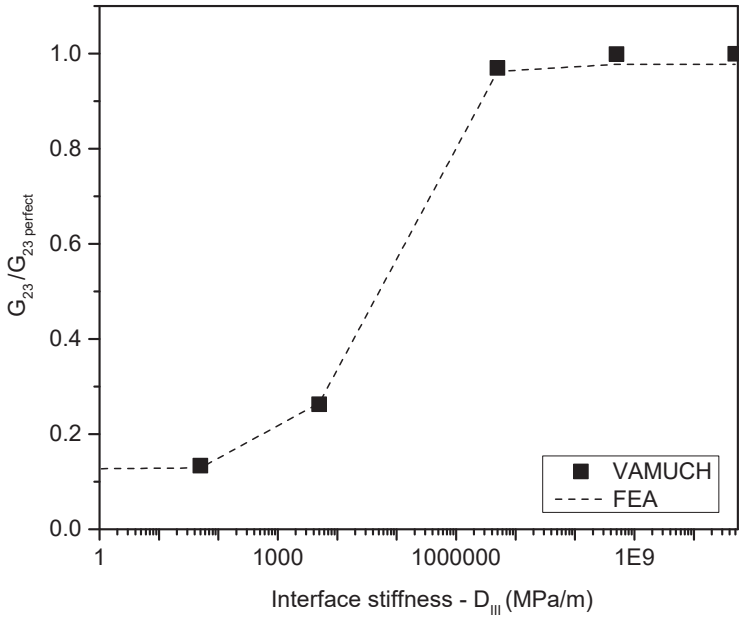

Figure 31. Predictions of effective transverse shear modulus G_{23}.

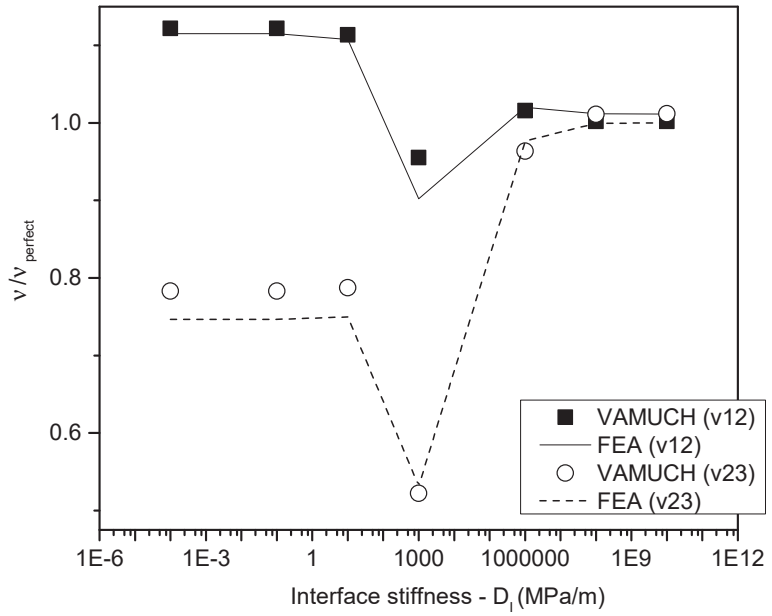

Figure 32. Predictions of effective Poisson'sratio ν_{12} and ν_{23}.

E. Woven Composite

There are various models of woven composite. For the current analysis, the woven composite is modeled with ellipsoidal cross section as depicted in the Figure 33. The ellipsoidal cross section of major axis radius, c, and minor axis radius, $\frac{c}{4}$, elliptical curvature radius, $r = 2.5c$, and also matrix thickness of $\frac{c}{8}$ is assumed on the top and bottom of the side of the unit cell. The ellipsoidal cross section center to center distance is $2c$. The overall unit cell length, width and height are $4c$, $4c$ and $\frac{5c}{4}$, respectively. The unit cell of FEA/VAMUCH is meshed to have 8640 elements. The material properties and the corresponding volume of warp, weft and the matrix are listed in the Table 3. The effects of interfacial stiffness on the effective properties of woven composite are analyzed using cohesive zone element similar to the above cases. In this case also, it is assumed that $D_{22} = 5D_{11}$ and also $D_{22} = D_{33}$. Moreover, it is also assumed that the interfacial stiffness among different material properties are the same.

Table 3. Material property (Ref. [29])

Mat	E (GPa)	ν	vol(%)
Warp	130	0.30	25.95
Weft	86	0.22	25.95
Matrix	4.30	0.34	48.10

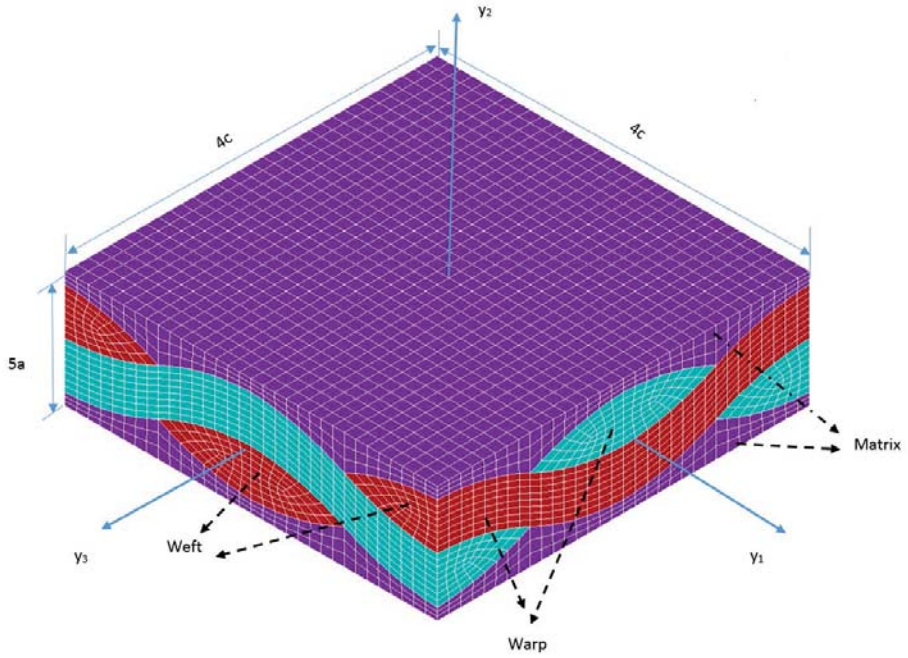

Figure 33. unit cell woven.

The predictions of effective properties of woven composite for imperfect interface are shown in the Figures 34-37. It is clear to notice that VAMUCH agrees well with the predictions of FEA for axial moduli E_{11}. However, the predictions of shear moduli are observed to significantly different particularly for smaller interfacial stiffness. This difference in general may be due to the effect of applied boundary conditions in FEA. Thus, it is of interest to analyze the effect of the boundary conditions by using $3 \times 3 \times 3$ unit cells. The middle unit cell will then be used to analyze the effective properties based on the average stress and average strain. As depicted in the Figure 36, the predictions of G_{12} using global stress and global strain nearly the same as the one generated using single unit cell, however, the predictions using the average stress and average strain, for the middle unit cell, is significantly different compared with others. To further analyze these difference, again, let the axial effective moduli, E_{11}, using the multiple unit cell be analyzed. It is interesting to observe that the prediction of axial modulus nearly the same as the predictions obtained

with the single unit cell, while the predictions based on the average stress and average strain in the the middle unit cell yields 62% greater than the single unit cell prediction. Generally, the average stress and strain approach yields better predictions. However, the current predictions of elastic modulus, E_{11} appears to be not reasonable. The over prediction may be due to the complex geometry of the woven composite contributing to interfacial stiffness D_{22} that is missing in ANSYS and also due to the cohesive element type employed. From the imperfect interface analysis of woven composite, it is also noticed that the introduction of imperfect interface with different material properties will make the woven composite to exhibit anisotropic material property, i.e, the stiffness matrix is fully populated, for relativity smaller stiffness. However, as the interfacial stiffness increases orthotopic material property will be obtained.

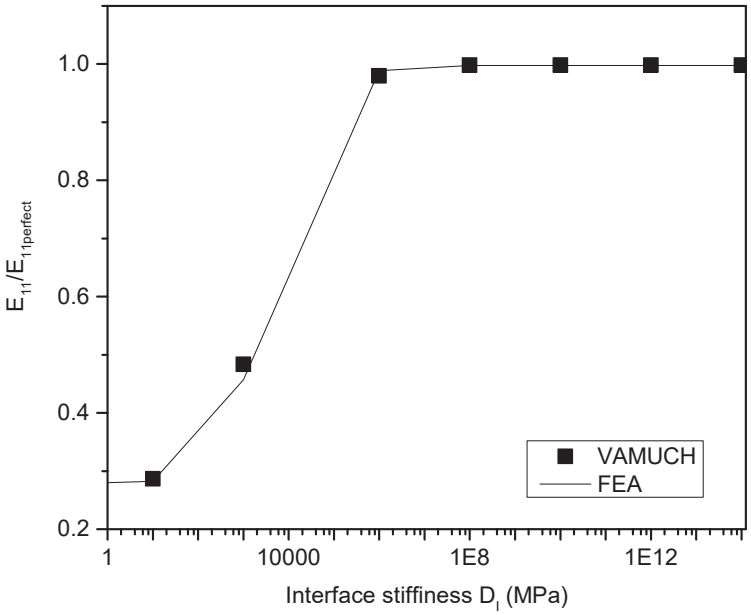

Figure 34. Prediction of E_1.

V. Conclusion

A discrete cohesive zone model is introduced into VAMUCH for the predictions of effective properties of heterogeneous material with imperfect interface. The predictions of VAMUCH are evaluated with exact solution for binary composite, the predictions of FEA and the upper and lower bounds proposed in the literature. The evaluations show that VAMUCH is capable of predicting effective properties with various interfacial stiffness. Moreover, it is learned that VAMUCH can sufficiently predict the axial shear for binary and continuous fiber reinforced composite where ANSYS can not due to the cohesive zone mode used in ANSYS. The static failure strength of heterogeneous material is found to be significantly affected by the interfacial stiffness. However, this effect will be lesser as the interface gets stiffer. The failure analysis demonstrates that the initial failure may not necessarily occur at the interface. In general, the application of external load or displacement boundary condition is mandatory in FEA to obtain effective properties. In the current analysis where the imperfect interfaces is assumed, the application of external load may lead to interpenetration of constituents across the interface. Moreover, for some cases, the output of analyses may not be easily obtained due to convergence problem. These problems can not be encountered by using VAMUCH. VAMUCH does not use any external load or displacement boundary condition to predict the effective properties for both perfect and imperfect interface. As seen for the current analyses, a simple linear

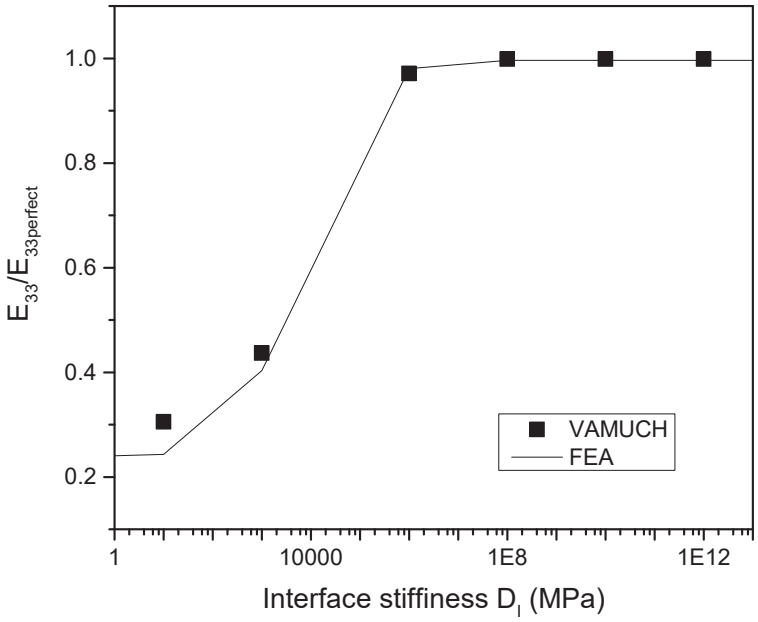

Figure 35. Prediction of E_3.

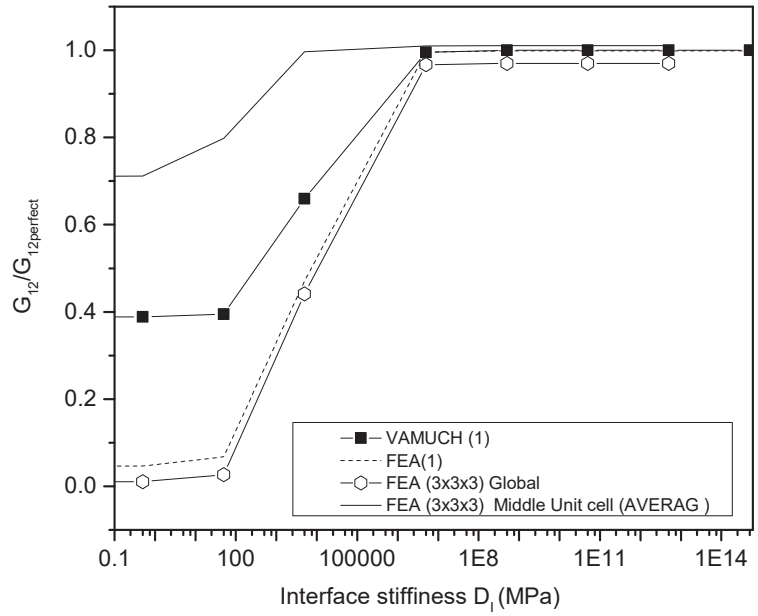

Figure 36. Prediction of G_{12}.

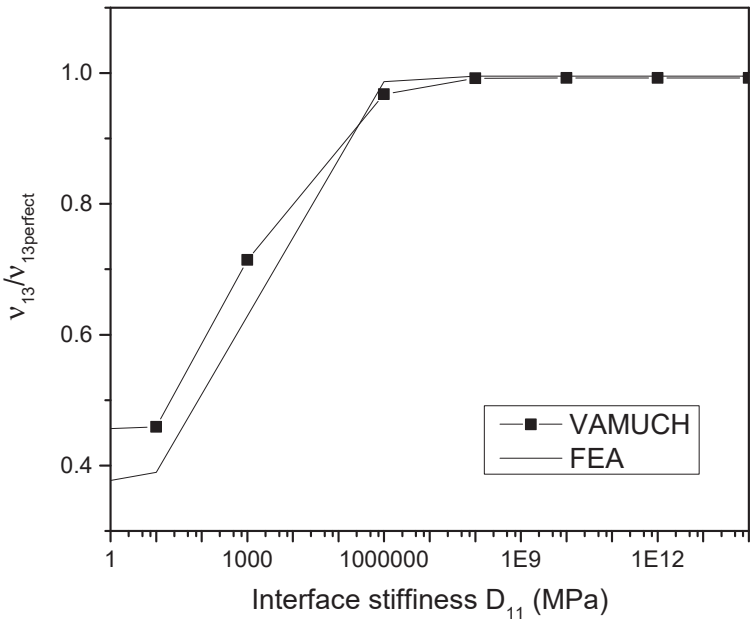

Figure 37. Prediction of ν_{13}.

analyses leads to optimal results. Finally, further studies need to be performed using nonlinear cohesive model for prediction of both elastic and inelastic material properties.

References

[1]Jone, J. P. and Whittier, J. S., "Waves at a Flexible Bonded Interface," *Journal of Applied Mechanics*, Vol. 28, 1967, pp. 103–128.

[2]Aboudi, J., "Damage in Composite-Modeling of Imperfect Bonding," *Composite Science and Technology*, Vol. 28, 1987, pp. 103–128.

[3]Hashin, Z., "Thermoelastic Properties of Particulate Composites with Imperfect Interface," *Journal of the Mechanics and Physics of Solids*, Vol. 36, No. 6, 1991, pp. 745–762.

[4]Aboudi, J., "Constitutive Equations for Elastoplastic Composites with Imperfect Interface," *Composite Science and Technology*, Vol. 4, 1988, pp. 103–125.

[5]Needleman, A., "Micromechanical Modelling of Intefacial Decohesion," *Ultramicroscopy*, Vol. 40, 1992, pp. 203–214.

[6]Xu, X. P. and Needleman, A., "Void Nucleation by Inclusion Debonding in a Crystal Matrix," *Modelling and Simulation in Materials Science and Engineering*, Vol. 1, 1993, pp. 111–132.

[7]Needleman, A., "An Analysis of Tensile Decohesion Along an Interface," *Journal of the Mechanics and Physics of Solids*, Vol. 38, No. 3, 1990, pp. 289–324.

[8]Lissenden, C., "Fiber-Matrix Interfacial Constitutive Relations for Metal Matrix Composites," *Journal of Composite; Part B Engineering*, Vol. 30, 1999, pp. 267–278.

[9]Warrier, S. H., Rangaswamy, P., Bourke, M. A., and Krishnamurthy, S., "Assessment of the Fiber: Matrix Interface Bond Strength in SiC/Ti-6Al-4V Composites," *Journal of Materials Science and Engineering*, Vol. 259A, 1999, pp. 220–227.

[10]Pagano, N. J. and Tandon, G. P., "Modeling of Imperfect Bonding in Fiber Reinforced Brittle Matrix Composites," *Journal of Mechanics of Materials*, Vol. 9, 1990, pp. 49–64.

[11]Hashin, Z., "Thin Interphase Imperfect Interface in Elasticity with Application to Coated Fiber Composites," *Journal of the Mechanics and Physics of Solids*, Vol. 36, No. 6, 1991, pp. 2509–2537.

[12]Quang, H. L. and He, Q. C., "Variational Principles and Bounds for Elastic Inhomogeneous Materials with Coherent Imperfect Interfaces," *Journal of Mechanics of Materials*, Vol. 40, 2008, pp. 865–884.

[13]Andrianova, I. V., Bolshakovb, V., Danishevs, V. V., and Weichert, D., "Asymptotic Simulation of Imperfect Bonding in Periodic Fibre-Reinforced Composite Materials under Axial Shear," *International Journal of Mechanical Sciences*, Vol. 49, 2007, pp. 1344–1354.

[14]Liu, H. T. and Sun, L. Z., "An Interfacial Debonding Model for Particle-Reinforced Composites," *International Journal of Damage Mechanics*, Vol. 13, No. 2, 2004, pp. 163–185.

[15]Tvergaard, V., "Fiber Debonding and Breakage in a Whisker-Reinforced Metal," *Journal of Material Science and Engineering*, Vol. 190A, 1995, pp. 215–222.

[16]Bednarcyk, A. B. and Arnold, M. S., "Micromechanics Based Deformation and Failure Prediction for Longitudinally Reinforced Titanium Composites," *Journal of Composite Science and Technology*, Vol. 61, No. 2, 2001, pp. 705–729.

[17]Duva, J., Aboudi, J., and Herakovich, C. T., "A Probabilistic Micromechanics Model for Damaged Composites," *Journal of Engineering Materiais and Technology*, Vol. 118, No. 4, 1996, pp. 548–553.

[18]Lene, F. and Leguillon, D., "Homogenized Constitutive Law for a Partially Cohesive Composite Material," *International Journal of Solids and Structures*, Vol. 18, No. 5, 1982, pp. 443–458.

[19]Caporale, A., Luciano, R., and Sacco, E., "Micromechanical Analysis of Interfacial Debonding in Unidirectional Fiber-Reinforced Composites," *Journal of Computers and Structures*, Vol. 84, 2006, pp. 2200–2211.

[20]Bonora, N. and Ruggiero, A., "Micromechanical Modeling of Composites with Mechanical Interface Part II: Damage Mechanics Assessment," *Journal of Composites Science and Technology*, Vol. 9, 1990, pp. 49–64.

[21]Zhu, H. and Sankar, B. V., "Evaluation of Various Failure Criteria for Fiber Composites using Finite Element Micromechanics," *Journal of Composite Materials*, Vol. 32, No. 8, 1998, pp. 766–782.

[22]Yu, W. and Tang, T., "Variational Asymptotic Method for Unit cell Homogenization of Periodically Heterogeneous Materials," *International Journal of Solids and Structures*, Vol. 44, No. 11-12, 2007, pp. 3738–3755.

[23]Yu, W., Williams, T. O., Bednarcyk, B. A., Aboudi, J., and Tang, T., "A Critical Evaluation of the Predictive Capabilities of Various Advanced Micromechanics Models," *Proceedings of the 48th Structures, Structural Dynamics and Materials Conference, 48th AIAA/ASME/ASCE/AHS/AS, Honolulu, Hawaii*, April. 23-26, 2007.

[24]Sertse, H., Zhang, L., Yu, W., and Ye, Z., "A Comprehensive Evaluation of the Predictive Capabilities of Several Advanced Micromechanics Approaches," *Proceedings of the 48th Structures, Structural Dynamics and Materials Conference, AIAA SciTech, National Harbor, Maryland*, Jan. 13-17, 2014.

[25]Hashin, Z., "Extremum Principles for Elastic Heterogeneous Media with Imperfect Interfaces and their Application to Bounding of Effective Moduli," *Journal of the Mechanics and Physics of Solids*, Vol. 40, No. 4, 1991, pp. 767–781.

[26]Sun, C. T. and Vaidya, R. S., "Prediction of Composite Properties from a Representative Volume Element," *Composites Science and Technology*, Vol. 56, 1996, pp. 171–179.

[27]Yu, W., "An Exact Solution for Micromechanical Analysis of Periodically Layered Composites," *Mechanics Research Communications*, Vol. 46, 2012, pp. 71–75.

[28]Yu, W., "A Varaitional Asymptotic Cell Method for Periodically Heterogeneuos Materials," *ASME 2005 International Mechanical Engineering Congress and Exposition Materials, ASME, Orlando, Florida*, Nov. 5-11, 2005.

[29]Pahr, D. and Arnold, S. M., "The Applicability of the Generalized Method of Cells for Analyzing Discontinuously Reinforced Composite," *International Journal of Solids and Structures*, Vol. 33, 2002, pp. 153–170.

AIAA SciTech
13-17 January 2014, National Harbor, Maryland
55th AIAA/ASMe/ASCE/AHS/SC Structures, Structural Dynamics, and Materials Conference

A Micromechanics Model for Homogenizing Hyperelastic Heterogeneous Materials

Liang Zhang*
Utah State University, Logan, UT 84322-4130, USA
Wenbin Yu†
Purdue University, West Lafayette, IN 47907-2045, USA

The variational asymptotic method for unit cell homogenization (VAMUCH) has emerged as a general-purpose micromechanics code that is capable of predicting the effective properties of heterogeneous materials and recovering the local fields. The objective of this paper is to develop a new micromechanics model which can enable VAMUCH to handle various problems of hyperelastic heterogeneous materials undergoing finite deformation. The rate form of the constitutive relations for a constituent, which is amendable to various hyperelastic material models, is derived. The rate form of the VAMUCH formulations is derived, while the corresponding code structure is developed. The application of the this new model is demonstrated using a simple example of predicting the stress-strain curves of binary composites consisting of compressible and quasi-incompressible hyperelastic constituents. The current VAMUCH is found to be capable of handling the problems involving complex constitutive relations for the constituents and complex loading conditions. More sophisticated user-defined material models can be implemented into it and more realistic examples should be used to validate this new model.

I. Introduction

Hyperelastic heterogeneous materials play an important role in numerous industrial and biological applications. Industrial products such as rubber tires are often reinforced with carbon-black particles in a small length scale and with steel or other fibers in a larger length scale such that they can exhibit designated mechanical properties,[1] while biological tissues such as human arteries are observed to be reinforced with collagen fibers.[2] Although possible, it is challenging to evaluate the mechanical behaviors of such materials because their deformation is often accompanied by material and geometrical nonlinearities. Moreover, it is difficult and time consuming to manufacture a great amount of heterogeneous materials and to perform various tests on them, while it is also computationally prohibitive to analyze them with all the microstructural details because the macroscopic dimensions of these structures are usually several orders of magnitude greater than the heterogeneity length scale. Therefore, it is of great practical value to solve the problems of hyperelastic heterogeneous materials using a micromechanics approach.

In recent decades, numerous efforts have been devoted to micromechanics. According to Ref. [3], a micromechanics approach generally consists of the following steps:

- Idealize the heterogeneous material as consisting of numerous periodically arranged unit cells (UCs) and identify the UC;
- Perform a constitutive modeling of the UC and obtain the effective material properties;
- Substitute the effective material properties into the macroscopic structure and obtain the global response of the structure;

*Postdoctoral Researcher, Department of Mechanical and Aerospace Engineering.
†Associate Professor, School of Aeronautics and Astronautics, AIAA Associate Fellow.

- Feedback the global response to the local scale and recover the local fields of interest (e.g., the displacement, strain, and stress fields).

If the deformation is restricted in the linearly elastic regime, the constitutive relations for the constituents are path-independent. In this case, the effective material properties of the UC remain the same throughout continued deformation, and the constitutive modeling just needs to be performed once. The micromechanics theories of linearly elastic heterogeneous materials have been well established. These theories include the self-consistent model,[4] Hashin and Shtrikman's variational approach,[5] the third-order bounds,[6] the method of cells (MOC) and its variants,[7] the recursive cell method,[8] and the mathematical homogenization theories,[9,10] and etc. If both material and geometrical nonlinearities are involved, one has to seek for proper stress and strain measures, derive the correspondence principal between the rates of these measures, and iteratively perform the aforementioned four steps of micromechanics.

Elaborate efforts have been devoted to predicting the global response of a hyperelastic heterogeneous material. Hill[11] and Hill and Rice[12] constructed the framework of the homogenization of linearly elastic heterogeneous materials undergoing finite deformation. Ogden[13] and Ponte Castañeda[14] later derived a Voigt-type upper bound and several Reuss-type lower bounds for general hyperelastic heterogeneous materials, respectively. Although mathematically rigorous, these upper and lower bounds do not vary with the microstructure and are hereby of limited applicabilities. Ponte Castañeda and Tiberio[15] and Lahellec et al.[16] proposed a second-order homogenization approach for particle-reinforced rubbers, which is capable of taking into account some high-order statistical information on the initial microstructure such as the particle stiffness, shape, volume fraction, and distribution. Several authors[17–20] later enabled this approach to handle the problems of particle-reinforced rubbers of random microstructure, porous elastomers of random and periodic microstructure, and fiber-reinforced elastomers of random microstructure and found good agreements between their predictions and the finite element analysis. deBotton et al.[21] also successfully homogenized a fiber-reinforced elastomer consisting of two incompressible neo-Hookean constituents, and deBotton and Shmuel[22] later extended the neo-Hookean constituents to more general ones. Despite success, all of these approaches are incapable of either dealing with designated microstructure or recovering the local fields. Therefore, there is a need for a more powerful approach.

Numerous attempts have been made not only to predict the global response but also to recover the local fields. Aboudi and his co-workers[23–25] developed the method of cells (MOC) and later the generalized method of cells (GMC) to achieve this goal. A detailed review on these approaches can be found in Ref. [26]. The basic ideas of these approaches are subdividing the UC into numerous cuboid subcells, solving for the average strain and stress over each subcell, and obtaining an estimation of the local fields. These approaches are capable of solving the problems to a certain extent but suffer two major drawbacks. Specifically, discretizing the UC using cuboid subcells may introduce considerable domain approximation errors, while describing the local fields using the average local strains and stresses may introduce considerable approximation errors. In fact, it is always more accurate to discretizing the UC using a finite element mesh and to describe the local fields using shape functions and nodal values. Meanwhile, Yvonnet and his co-workers[27,28] developed an incremental non-concurrent multiscale method to achieve the same goal and found good agreements between their predictions and the finite element analysis results. The basic ideas of this method are discretizing the UC using a finite element mesh, decomposing the problem for each iteration into a limited number of subproblems associated with different kinematic boundary conditions using the proper orthogonal decomposition, and obtaining the instantaneous effective stiffness by solving all the subproblems. Despite success, this method assumes that the UC is subject to kinematic rather than periodic boundary conditions and hereby tends to overestimate the instantaneous effective stiffness. All these lead one to seek for a more accurate and efficient approach.

Recently, Yu and his co-workers[3,29–32] developed the variational asymptotic method for unit cell homogenization (VAMUCH), a general-purpose micromechanics approach, to handle the problems of heterogeneous materials. In fact, VAMUCH is not only capable of predicting the global response and recovering the local fields but also has several unique features compared with other numerical methods. One of these features is that VAMUCH has the minimum number of assumptions. Specifically, VAMUCH starts with two basic assumptions associated with the micromechanical analysis of heterogeneous materials of identifiable UCs. For hyperelastic heterogeneous materials, these two assumptions are modified as follows:

1. The exact solutions of the field have their volume averages over the UC, i.e., if $\dot{u}_i$ denotes the exact

velocity vector in the Lagrange description within the UC, there exists a $\dot{v}_i$ such that

$$\dot{v}_i = \frac{1}{\Omega}\int_\Omega \dot{u}_i d\Omega \equiv \langle \dot{u}_i \rangle \,, \tag{1}$$

where Ω denotes the domain occupied by the UC (with boundary $\partial\Omega$) and also its volume in the Lagrange description, and $\langle\cdot\rangle$ denotes the volume average of the quantity over Ω;

2. The effective material properties obtained using the micromechanical analysis are independent of the geometry and boundary conditions of the macroscopic structure, or to say, they are assumed to be the intrinsic properties of the material when macroscopically viewed.

These two assumptions place the fewest restrictions on the problem solving. The first assumption means that the exact solutions of the field are integrable over the UC, or to say, that the heterogeneous material can be homogenized. The second assumption basically reflects the fact that the material properties are fully described by the constitutive relations for the material and are independent of the geometry and boundary of the macroscopic structure. Of course, the micromechanical analysis of the UC is desirable and appropriate only if the characteristic size of the UC is much smaller than that of the macroscopic structure.

The objective of this paper is to enable VAMUCH to handle various problems of hyperelastic heterogeneous materials undergoing finite deformation. The rate form of the constitutive relations for a constituent, which is amendable to various hyperelastic material models, is derived. The rate form of the VAMUCH formulations is derived, while the corresponding code structure is developed. The application of this capability in current VAMUCH is validated using simple examples such as predicting the stress-strain curves of binary composites consisting of compressible and quasi-incompressible hyperelastic constituents.

II. Constitutive Relations

Consider a heterogeneous material consisting of one or more hyperelastic constituents. In this section, the rate form of a constitutive relations for the hyperelastic constituent will be derived first.

Introduce a material coordinate system $\mathbf{X} = (X_1, X_2, X_3)$ and a spatial coordinate system $\mathbf{x} = (x_1, x_2, x_3)$. Without loss of generality, assume that the orthonormal basis of these two coordinate systems coincide with each other. Let $\mathbf{u}(\mathbf{X}, t)$ denote the displacement vector in the Lagrange description, where t denotes the time. $\mathbf{x}$ can be expressed as a function of $\mathbf{X}$ and t as

$$\mathbf{x}(\mathbf{X}, t) = \mathbf{X} + \mathbf{u}(\mathbf{X}, t)\,. \tag{2}$$

The deformation gradient tensor, $\mathbf{F}$, can then be defined as

$$\mathbf{F} = \frac{\partial \mathbf{x}}{\partial \mathbf{X}} = \mathbf{I} + \frac{\partial \mathbf{u}}{\partial \mathbf{X}}, \tag{3}$$

where $\mathbf{I}$ denotes the second-order identity tensor. The right Cauchy-Green deformation tensor, $\mathbf{C}$, is related to $\mathbf{F}$ by

$$\mathbf{C} = \mathbf{F}^T \cdot \mathbf{F}. \tag{4}$$

There are three widely used stress measures in continuum mechanics, i.e., the Cauchy stress, the first Piola-Kirchhoff stress, and the second Piola-Kirchhoff stress. The first Piola-Kirchhoff stress tensor, $\mathbf{P}$, can be related to the Cauchy stress tensor, $\boldsymbol{\sigma}$, by

$$\mathbf{P} = J\boldsymbol{\sigma} \cdot \mathbf{F}^{-T}, \tag{5}$$

where $J = \det \mathbf{F}$, and $(\cdot)^{-T}$ denotes the inverse of the transpose of the tensor, while the second Piola-Kirchhoff stress tensor, $\mathbf{S}$, can be related to $\mathbf{P}$ and $\boldsymbol{\sigma}$ by

$$\mathbf{S} = \mathbf{F}^{-1} \cdot \mathbf{P} = J\mathbf{F}^{-1} \cdot \boldsymbol{\sigma} \cdot \mathbf{F}^{-T}. \tag{6}$$

Among these stress and strain measures, $\mathbf{C}$, $\boldsymbol{\sigma}$, and $\mathbf{S}$ are always symmetric, while $\mathbf{F}$ and $\mathbf{P}$ are generally not.

According to continuum mechanics, a material is said to be hyperelastic only if:

- There exists a the strain energy density function, say W;
- W is locally a function of $\mathbf{F}$ in the Lagrange description, i.e., $W = W(\mathbf{X}, \mathbf{F})$.

The constitutive relations for a hyperelastic material can be defined as

$$\mathbf{P} = \frac{\partial W}{\partial \mathbf{F}}. \tag{7}$$

It can be verified that an alternative form of Eq. (7) writes

$$\mathbf{S} = 2\frac{\partial W}{\partial \mathbf{C}}. \tag{8}$$

In fact, the constitutive relations often take the form of Eq. (8) because it is more convenient to express W as a function of the invariants of $\mathbf{C}$.

It is beneficial to derive the rate forms of Eqs. (7) and (8). Following Ref. [33], taking material derivatives on both sides of Eq. (7) gives

$$\dot{\mathbf{P}} = \frac{\partial}{\partial t}\left(\frac{\partial W}{\partial \mathbf{F}}\right) = \frac{\partial}{\partial \mathbf{F}}\left(\frac{\partial W}{\partial t}\right) = \frac{\partial}{\partial \mathbf{F}}\left(\frac{\partial W}{\partial \mathbf{F}} : \dot{\mathbf{F}}\right) = \frac{\partial^2 W}{\partial \mathbf{F}\partial \mathbf{F}} : \dot{\mathbf{F}} + \frac{\partial W}{\partial \mathbf{F}} : \frac{\partial \dot{\mathbf{F}}}{\partial \mathbf{F}}. \tag{9}$$

Note that

$$\frac{\partial \dot{\mathbf{F}}}{\partial \mathbf{F}} = \frac{\partial}{\partial t}\left(\frac{\partial \mathbf{F}}{\partial \mathbf{F}}\right) = \frac{\partial \boldsymbol{\mathcal{I}}}{\partial t} = 0, \tag{10}$$

where $\boldsymbol{\mathcal{I}}$ denotes the fourth-order identity tensor. Substituting Eq. (10) into Eq. (9) gives the rate form of Eq. (7) as

$$\dot{\mathbf{P}} = \frac{\partial^2 W}{\partial \mathbf{F}\partial \mathbf{F}} : \dot{\mathbf{F}} \equiv \boldsymbol{\mathcal{A}} : \dot{\mathbf{F}}, \tag{11}$$

where $\boldsymbol{\mathcal{A}}$ is often referred to the fourth-order first elasticity tensor. It can be verified that $\boldsymbol{\mathcal{A}}$ fulfills the major symmetries (i.e., $\mathcal{A}_{ijkl} = \mathcal{A}_{klji}$) but not the minor symmetries (i.e., $\mathcal{A}_{ijkl} \neq \mathcal{A}_{jikl}$ and $\mathcal{A}_{ijkl} \neq \mathcal{A}_{ijlk}$). Similarly to Eq. (11), the rate form of Eq. (8) can be obtained as

$$\dot{\mathbf{S}} = 4\frac{\partial^2 W}{\partial \mathbf{C}\partial \mathbf{C}} : \frac{1}{2}\dot{\mathbf{C}} \equiv \boldsymbol{\mathcal{C}} : \frac{1}{2}\dot{\mathbf{C}}, \tag{12}$$

where $\boldsymbol{\mathcal{C}}$ is often referred to the fourth-order second elasticity tensor. It can also be verified that $\boldsymbol{\mathcal{C}}$ fulfills both the major and minor symmetries.

Although the rate form of the constitutive relations often takes the form of Eq. (12) for the reason mentioned above, for the convenience of unit cell homogenization, it is better to take the form of Eq. (11) (see Section III). This leads one to relate $\boldsymbol{\mathcal{A}}$ to $\boldsymbol{\mathcal{C}}$. Following Ref. [33], rewrite Eq. (6) as

$$\mathbf{P} = \mathbf{F} \cdot \mathbf{S}. \tag{13}$$

Taking material derivatives on both sides of Eq. (13) gives

$$\dot{\mathbf{P}} = \dot{\mathbf{F}} \cdot \mathbf{S} + \mathbf{F} \cdot \dot{\mathbf{S}} = \dot{\mathbf{F}} \cdot \mathbf{S} + \frac{1}{2}\mathbf{F} \cdot \left(\boldsymbol{\mathcal{C}} : \dot{\mathbf{C}}\right). \tag{14}$$

Also taking material derivatives on both sides of Eq. (4) gives

$$\dot{\mathbf{C}} = \dot{\mathbf{F}}^T \cdot \mathbf{F} + \mathbf{F}^T \cdot \dot{\mathbf{F}}. \tag{15}$$

Substituting Eq. (15) into Eq. (14) gives

$$\dot{\mathbf{P}} = \dot{\mathbf{F}} \cdot \mathbf{S} + \frac{1}{2}\mathbf{F} \cdot \left[\boldsymbol{\mathcal{C}} : \left(\dot{\mathbf{F}}^T \cdot \mathbf{F} + \mathbf{F}^T \cdot \dot{\mathbf{F}}\right)\right]. \tag{16}$$

It can be verified that

$$\boldsymbol{\mathcal{C}} : \left(\dot{\mathbf{F}}^T \cdot \mathbf{F}\right) = \boldsymbol{\mathcal{C}} : \left(\mathbf{F}^T \cdot \dot{\mathbf{F}}\right). \tag{17}$$

due to symmetry of $\mathcal{C}$. Substituting Eq. (17) into Eq. (16) gives

$$\dot{\mathbf{P}} = \dot{\mathbf{F}} \cdot \mathbf{S} + \mathbf{F} \cdot \left[\boldsymbol{\mathcal{C}} : \left(\mathbf{F}^T \cdot \dot{\mathbf{F}} \right) \right] \tag{18}$$

or

$$\dot{P}_{ij} = \dot{F}_{il} S_{lj} + F_{im} \mathcal{C}_{mjnl} F_{kn} \dot{F}_{kl} = S_{lj} \delta_{ik} \dot{F}_{kl} + F_{im} \mathcal{C}_{mjnl} F_{kn} \dot{F}_{kl} = \left(S_{lj} \delta_{ik} + F_{im} \mathcal{C}_{mjnl} F_{kn} \right) \dot{F}_{kl}. \tag{19}$$

Comparing Eq. (19) with Eq. (11) gives

$$\mathcal{A}_{ijkl} = S_{lj} \delta_{ik} + F_{im} \mathcal{C}_{mjnl} F_{kn}. \tag{20}$$

Once the hyperelastic material model is specified, the explicit expressions for $\boldsymbol{\mathcal{C}}$ and $\boldsymbol{\mathcal{A}}$ can be fully determined. More details on the derivation in this paragraph can be found in Ref. [33].

A hyperelastic material model specifies the relation between W and $\mathbf{F}$, or more frequently, the relation between W and the invariants of $\mathbf{C}$, i.e.,

$$W = W\left(I_1, I_2, I_3\right) = W\left(I_1, I_2, J\right), \tag{21}$$

where

$$I_1 = \mathrm{tr}\mathbf{C}, \quad I_2 = \frac{1}{2}\left[\mathrm{tr}^2\mathbf{C} - \mathrm{tr}\left(\mathbf{C}^2\right)\right], \quad I_3 = \det\mathbf{C} = J^2 \tag{22}$$

denote the first, second, and third invariants of $\mathbf{C}$, respectively. Moreover, according to numerous experimental observations, many hyperelastic materials exhibit uncoupled volumetric and isochoric behaviors. This leads one to seek for an alternative expression for W consisting of uncoupled volumetric and isochoric parts. Specifically, according to Ref. [34], the volumetric part of $\mathbf{C}$ can be obtained as $J^{\frac{2}{3}}\mathbf{I}$, while the isochoric part, $\bar{\mathbf{C}}$, can be obtained as

$$\bar{\mathbf{C}} = J^{-\frac{2}{3}}\mathbf{C}. \tag{23}$$

Let $\bar{I}_1$, $\bar{I}_2$, and $\bar{I}_3$ denote the first, second, and third invariants of $\bar{\mathbf{C}}$, respectively. Note that, by definition,

$$\bar{I}_1 = \mathrm{tr}\bar{\mathbf{C}}, \quad \bar{I}_2 = \frac{1}{2}\left[\mathrm{tr}^2\bar{\mathbf{C}} - \mathrm{tr}\left(\bar{\mathbf{C}}^2\right)\right], \quad \bar{I}_3 = \det\bar{\mathbf{C}} = 1. \tag{24}$$

Till now, W can be expressed as a function of $\bar{I}_1$, $\bar{I}_2$, and J, i.e.,

$$W = W\left(\bar{I}_1, \bar{I}_2, J\right). \tag{25}$$

In addition, W can further be expressed as the sum of its volumetric part, W^v, and its isochoric part, W^i, i.e.,

$$W\left(\bar{I}_1, \bar{I}_2, J\right) = W^v\left(J\right) + W^i\left(\bar{I}_1, \bar{I}_2\right). \tag{26}$$

In this paper, W is set to take the general form of Eq. (26) with the corresponding explicit expression for $\boldsymbol{\mathcal{C}}$ being derived in Appendix A, while Eq. (26) can always be replaced by a more general one as needed.

The polynomial hyperelastic model is among the most general hyperelastic material models proposed in the literature. It suggests that W takes the form of

$$W = \sum_{i,j=0}^{n} C_{ij}\left(\bar{I}_1 - 3\right)^i\left(\bar{I}_2 - 3\right)^j + \sum_{k=0}^{m} D_k(J-1)^{2k}, \tag{27}$$

which implies that the material is compressible. If $n = 1$, $C_{11} = 0$, and $m = 1$, the polynomial hyperelastic model reduces to the Mooney-Rivlin model, for which W takes the form of

$$W = C_{01}\left(\bar{I}_2 - 3\right) + C_{10}\left(\bar{I}_1 - 3\right) + D_1(J-1)^2; \tag{28}$$

if $C_{01} = 0$, the Mooney-Rivlin model further reduces to the neo-Hookean model, for which W takes the form of

$$W = C_{10}\left(\bar{I}_1 - 3\right) + D_1(J-1)^2. \tag{29}$$

Once the hyperelastic material model is specified, the explicit expression for $\boldsymbol{\mathcal{C}}$ can be fully determined (see Appendix A).

Till now, the rate form of the constitutive relations for a constituent have been derived. In the next section, the rate form of the VAMUCH formulations will be derived.

III. Variational Asymptotic Method for Unit Cell Homogenization

Consider a heterogeneous material with an identifiable UC. Introduce a global material coordinate system $\mathbf{X} = (X_1, X_2, X_3)$ and a local material coordinate system $\mathbf{Y} = (Y_1, Y_2, Y_3)$, where $\mathbf{Y}$ is related to $\mathbf{X}$ by

$$\mathbf{Y} = \mathbf{X}/\epsilon \tag{30}$$

with ϵ denoting a scale ratio and $0 < \epsilon \ll 1$. Let $\mathbf{X}$ describe the macroscopic structure, and let $\mathbf{Y}$ describe the UC with its origin located at the geometric center of the UC. Suppose that, at a given instant of time t:

- The UC is in a state of static equilibrium;
- All the state variables are known;
- All the periodic boundary conditions are satisfied.

The task is to solve for the exact velocity vector, $\dot{u}_i$, at this instant of time (see Eq. (1)).

According to Ref. [35], $\dot{u}_i$ can be expressed as the sum of its volume average over Ω, $\dot{v}_i$ (see Eq. (1)), and a fluctuation function, χ_i, i.e.,

$$\dot{u}_i(\mathbf{Y}, \mathbf{X}) = \dot{v}_i(\mathbf{X}) + \epsilon\chi_i(\mathbf{Y}, \mathbf{X}), \tag{31}$$

where χ_i is a periodic function of $\mathbf{Y}$ and may also depend on $\mathbf{X}$, and $\epsilon\chi_i$ should be asymptotically smaller than $\dot{v}_i$ such that a heterogeneous material can be homogenized. Without loss of generality, let

$$\langle \chi_i \rangle = 0. \tag{32}$$

In fact, although $\epsilon\chi_i$ negligibly contributes to $\dot{u}_i$, it does affect the derivatives of $\dot{u}_i$. Specifically,

$$\frac{\partial \dot{u}_i}{\partial X_j} = \frac{1}{\epsilon}\frac{\partial \dot{u}_i}{\partial Y_j}\bigg|_{\mathbf{X}=\text{const}} + \frac{\partial \dot{u}_i}{\partial X_j}\bigg|_{\mathbf{Y}=\text{const}} = \frac{\partial \dot{v}_i}{\partial X_j} + \frac{\partial \chi_i}{\partial Y_j} + \epsilon\frac{\partial \chi_i}{\partial X_j}, \tag{33}$$

where $\epsilon\partial\chi_i/\partial X_j$ is a high-order term and can be omitted. Recall that, by definition,

$$F_{ij} = \frac{\partial x_i}{\partial X_j} = \delta_{ij} + \frac{\partial u_i}{\partial X_j}. \tag{34}$$

Taking material derivatives on both sides of Eq. (34) gives

$$\dot{F}_{ij} = \frac{\partial \dot{u}_i}{\partial X_j}. \tag{35}$$

Also let

$$\dot{\bar{F}}_{ij} = \frac{\partial \dot{v}_i}{\partial X_j} \quad \text{and} \quad \chi_{i,j} = \frac{\partial \chi_i}{\partial Y_j}. \tag{36}$$

It can be verified that $\dot{\bar{F}}_{ij} = \left\langle \dot{F}_{ij} \right\rangle$. $\dot{\bar{F}}_{ij}$ hereby denotes the global rate of deformation gradient tensor. Combining Eqs. (33), (35), and (36) gives

$$\dot{F}_{ij} = \dot{\bar{F}}_{ij} + \chi_{i,j}. \tag{37}$$

The strong form of the problem can be formulated as seeking χ_i satisfying

$$\dot{P}_{ij,j} = 0 \quad \text{in } \Omega \tag{38}$$

subject to constraint Eq. (32) and periodic boundary conditions

$$\chi_i(\mathbf{Y}) = \chi_i(\mathbf{Y} + \mathbf{L}) \quad \text{and} \quad \left(\dot{P}_{ij}N_j\right)(\mathbf{Y}) + \left(\dot{P}_{ij}N_j\right)(\mathbf{Y} + \mathbf{L}) = 0 \quad \text{on } \partial\Omega, \tag{39}$$

where $\mathbf{L}$ denotes the periodicity vector of the UC, and N_i denotes the unit normal vector in the Lagrange description. Let $\delta\chi_i$ denotes the virtual fluctuation function which is arbitrary in Ω and satisfies periodic boundary conditions

$$\delta\chi_i(\mathbf{Y}) = \delta\chi_i(\mathbf{Y} + \mathbf{L}) \quad \text{on } \partial\Omega. \tag{40}$$

The rate form of the principle of virtual work can be expressed using arbitrary periodic functions $\delta\chi_i$ as

$$-\frac{1}{\Omega}\int_\Omega \dot{P}_{ij,j}\delta\chi_i dV = \frac{1}{\Omega}\int_\Omega \dot{P}_{ij}\delta\chi_{i,j}dV - \frac{1}{\Omega}\int_{\partial\Omega}\dot{P}_{ij}N_j\delta\chi_i dS = 0. \tag{41}$$

Substituting the second equation of Eq. (39) into Eq. (41) $\delta\chi_i$ gives

$$\frac{1}{\Omega}\int_\Omega \dot{P}_{ij}\delta\chi_{i,j}dV = 0. \tag{42}$$

The weak form of the problem can then be formulated as seeking χ_i satisfying Eq. (42) subject to constraint Eq. (32) and periodic boundary conditions

$$\chi_i(\mathbf{Y}) = \chi_i(\mathbf{Y}+\mathbf{L}) \quad \text{on } \partial\Omega. \tag{43}$$

Substituting Eq. (37) into Eq. (11) gives

$$\dot{P}_{ij} = \mathcal{A}_{ijkl}\left(\dot{\bar{F}}_{kl} + \chi_{k,l}\right). \tag{44}$$

Substituting Eq. (44) into Eq. (42) gives

$$\delta\Pi_\Omega = \frac{1}{\Omega}\int_\Omega \delta\chi_{i,j}\mathcal{A}_{ijkl}\left(\dot{\bar{F}}_{kl} + \chi_{k,l}\right)dV = 0. \tag{45}$$

Eq. (45) implies that, once $\dot{\bar{F}}_{ij}$ and $\mathcal{A}_{ijkl}$ are specified, χ_i can be uniquely determined.

It is beneficial to also relate the local first Piola-Kirchhoff stress rate tensor and the local rate of deformation gradient tensor to the global ones. Specifically, $\left\langle \dot{P}_{ij}\dot{F}_{ij}\right\rangle$ can be expressed as

$$\frac{1}{\Omega}\int_\Omega \dot{P}_{ij}\dot{F}_{ij}dV = \frac{1}{\Omega}\int_\Omega \dot{P}_{ij}\dot{\bar{F}}_{ij}dV + \frac{1}{\Omega}\int_\Omega \dot{P}_{ij}\chi_{i,j}dV. \tag{46}$$

Eq. (46), together with Eq. (42), implies that

$$\frac{1}{\Omega}\int_\Omega \dot{P}_{ij}\dot{F}_{ij}dV = \frac{1}{\Omega}\int_\Omega \dot{P}_{ij}\dot{\bar{F}}_{ij}dV = \dot{\bar{F}}_{ij}\left(\frac{1}{\Omega}\int_\Omega \dot{P}_{ij}dV\right) \equiv \dot{\bar{P}}_{ij}\dot{\bar{F}}_{ij}, \tag{47}$$

In fact, Eq. (47) is a variation of the Hill-Mandel lemma for unit cell homogenization.

Till now, the rate form of the VAMUCH formulation has been derived and has been proven valid. In the next section, this formulation will be discretized using finite elements to solve for χ_i.

IV. Finite Element Implementation of VAMUCH

Introduce the following matrix notations:

$$\dot{\bar{F}} = \left\lfloor \begin{array}{ccccccccc} \dot{\bar{F}}_{11} & \dot{\bar{F}}_{12} & \dot{\bar{F}}_{22} & \dot{\bar{F}}_{13} & \dot{\bar{F}}_{23} & \dot{\bar{F}}_{33} & \dot{\bar{F}}_{21} & \dot{\bar{F}}_{31} & \dot{\bar{F}}_{32} \end{array} \right\rfloor^T, \tag{48}$$

$$\left\{\begin{array}{c} \frac{\partial\chi_1}{\partial Y_1} \\ \frac{\partial\chi_1}{\partial Y_2} \\ \frac{\partial\chi_2}{\partial Y_2} \\ \frac{\partial\chi_1}{\partial Y_3} \\ \frac{\partial\chi_2}{\partial Y_3} \\ \frac{\partial\chi_3}{\partial Y_3} \\ \frac{\partial\chi_2}{\partial Y_1} \\ \frac{\partial\chi_3}{\partial Y_1} \\ \frac{\partial\chi_3}{\partial Y_2} \end{array}\right\} = \left[\begin{array}{ccc} \frac{\partial}{\partial Y_1} & 0 & 0 \\ \frac{\partial}{\partial Y_2} & 0 & 0 \\ 0 & \frac{\partial}{\partial Y_2} & 0 \\ \frac{\partial}{\partial Y_3} & 0 & 0 \\ 0 & \frac{\partial}{\partial Y_3} & 0 \\ 0 & 0 & \frac{\partial}{\partial Y_3} \\ 0 & \frac{\partial}{\partial Y_1} & 0 \\ 0 & 0 & \frac{\partial}{\partial Y_1} \\ 0 & 0 & \frac{\partial}{\partial Y_2} \end{array}\right] \left\{\begin{array}{c} \chi_1 \\ \chi_2 \\ \chi_3 \end{array}\right\} \equiv \Gamma_h\chi, \tag{48'}$$

where Γ_h denotes an operator matrix, and χ denotes a column matrix containing the three components of the fluctuation functions. Let χ be discretized using finite elements as

$$\chi\left(Y_i, X_i\right) = S\left(Y_i\right) \mathrm{X}\left(X_i\right), \tag{49}$$

where S denotes the shape functions, and X denotes a column matrix of the nodal values of the fluctuation functions for all the active nodes. The discretized version of Eq. (45) can then be obtained as

$$\delta\Pi_\Omega = \frac{1}{\Omega}\delta\mathrm{X}^T\left(D_{hh}\mathrm{X} + D_{hF}\dot{\bar{F}}\right) = 0, \tag{50}$$

where

$$D_{hh} = \int_\Omega \left(\Gamma_h S\right)^T D\left(\Gamma_h S\right) dV \quad \text{and} \quad D_{hF} = \int_\Omega \left(\Gamma_h S\right)^T D dV \tag{51}$$

with D denoting the 9×9 instantaneous stiffness matrix condensed from $\mathcal{A}_{ijkl}$. In Eq. (50), equality holds only if

$$D_{hh}\mathrm{X} = -D_{hF}\dot{\bar{F}} \quad \text{or} \quad \mathrm{X} = \mathrm{X}_0\dot{\bar{F}}. \tag{52}$$

Eq. (52) implies that X is proportional to $\dot{\bar{F}}$. In addition, Eq. (47) can be rewritten as

$$\dot{\bar{F}}_{ij}\dot{\bar{P}}_{ij} = \frac{1}{\Omega}\int_\Omega \dot{\bar{F}}_{ij}\dot{P}_{ij}dV = \frac{1}{\Omega}\int_\Omega \dot{\bar{F}}_{ij}\mathcal{A}_{ijkl}\left(\dot{\bar{F}}_{kl} + \chi_{k,l}\right) dV. \tag{53}$$

The discretized version of Eq. (53) can be obtained as

$$\dot{\bar{F}}^T\dot{\bar{P}} = \frac{1}{\Omega}\left(\dot{\bar{F}}^T D_{Fh}\mathrm{X} + \dot{\bar{F}}^T D_{FF}\dot{\bar{F}}\right) = \frac{1}{\Omega}\dot{\bar{F}}^T\left(D_{Fh}\mathrm{X}_0 + D_{FF}\right)\dot{\bar{F}} \equiv \dot{\bar{F}}^T\bar{D}\dot{\bar{F}}, \tag{54}$$

where $\dot{\bar{P}}$ denotes the global first Piola-Kirchhoff stress rate column matrix, $D_{Fh} = D_{hF}^T$, and $D_{FF} = \int_\Omega D dV$. It can be obtained from Eq. (54) that

$$\dot{\bar{P}} = \bar{D}\dot{\bar{F}}, \tag{55}$$

which is the rate form of the global constitutive relations, and $\bar{D}$ hereby denotes the so-called instantaneous effective stiffness matrix. This rate form of the global constitutive relations can be used in the macroscopic structural analysis at a certain load step to obtain the global rate of deformation gradient column matrix, $\dot{\bar{F}}$, which can be used to recover the local fields, which will be used to obtain the rate form of the global constitutive relations for the next step. Specifically, the local rates of deformation gradient can be recovered as

$$\dot{F} = \dot{\bar{F}} + \Gamma_h S\bar{\mathrm{X}}_0\dot{\bar{F}}, \tag{56}$$

where $\dot{F}$ denotes the the local rate of deformation gradient column matrix, and $\bar{\mathrm{X}}_0$ denotes the nodal values of the fluctuation functions modified from X_0 by Eqs. (32) and (43). The local first Piola-Kirchhoff stress rates can be recovered from the local rates of deformation gradient as

$$\dot{P} = D\dot{F}. \tag{57}$$

V. VAMUCH Code Structure

Figure 1 depicts the current VAMUCH code structure. The code starts with reading the finite element model and initializing all the state variables (e.g., the deformation gradients and the first Piola-Kirchhoff stresses). After this, it will iteratively complete the following steps in sequence:

- Perform the constitutive modeling to obtain the instantaneous effective material properties and the fluctuation functions;
- Impose the global stress/gradient increments;
- Perform the recovery to recover the local fields;
- Save the updated state variables as the inputs for the next iteration;

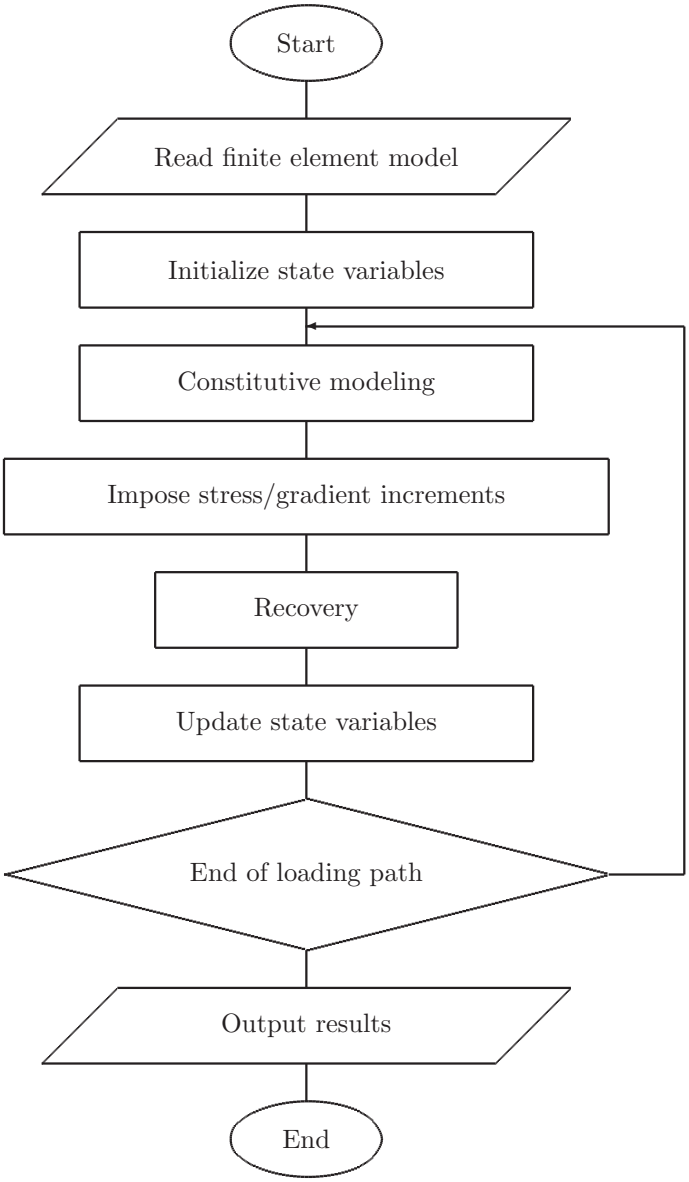

Figure 1. Current VAMUCH code structure.

- Check whether to continue the iteration.

The code will continue the iteration till the end of the loading path. After this, it will output the results as needed. Currently, the second-order Runge-Kutta method is employed as the time integration method.

VI. Validation Examples

In this section, several examples are presented to validate the applicability, power, and accuracy of the current VAMUCH. The examples include predicting the stress-strain curves of binary composites consisting of compressible and quasi-incompressible hyperelastic constituents. The results predicted by VAMUCH are compared with those predicted by ANSYS.

A. Compressible Hyperelastic Constituents

Without loss of generality, let the volume factions of the two constituents of the binary composite be 25% and 75%, respectively, and let both of these two constituents be Mooney-Rivlin solids whose behaviors are characterized by Eq. (28). According to continuum mechanics, the initial bulk and shear moduli of a Mooney-Rivlin solid, κ and μ, can be related to C_{01}, C_{10}, and D_1 as

$$\kappa = 2D_1 \quad \text{and} \quad \mu = 2\left(C_{01} + C_{10}\right), \tag{58}$$

respectively. Let the material parameters of the two constituents take the values listed in Table 1. Table 1, together with Eq. (58), implies that the first constituent is four times stiffer than the second one. In addition, here the constituents are actually highly compressible, while in the next section, they will be set to be quasi-incompressible. The UC of this composite can be identified as a line segment consisting of two connecting sub-line segments with the ratio of their lengths being 1 : 3. Recall that y_i denotes the local coordinates describing the UC with its origin located at the geometric center of the UC (see Section III). Here let the y_1-axis parallel to the line segment representing the UC, and let the y_2- and y_3-axes perpendicular to it. For notational convenience, let F_{ij} and P_{ij} denote the global gradient of deformation and first Piola-Kirchhoff stress tensors, respectively. For comparison with ANSYS, let the off-diagonal components of F_{ij} vanish in all the validation examples. In this case, periodic boundary conditions Eq. (43) reduce to homogeneous boundary conditions, and can be easily handled by ANSYS.

Table 1. Material parameters of the compressible hyperelastic constituents.

	C_{01} (Pa)	C_{10} (Pa)	D_1 (Pa)
Constituent 1	5	5	7.5
Constituent 2	1	1	1.5

Figure 2 shows the stress-strain curves of the composite subject to uniaxial tension in the y_1- and y_2-directions, respectively. It can be seen that the composite exhibits nonlinear stress-strain relations when loaded in both the y_1- and y_2-directions but is stiffer when loaded in the y_2-direction. This indicates that the first constituent more significantly reinforces the composite in the y_2-direction. In addition, it can be seen that the tangent stiffness of the composite monotonically decreases with increasing F. It is hereby of interest whether this is always the case for all the loading conditions. The answer to this question will become clear later this section. At last, it can be seen that the results predicted by VAMUCH perfectly agree with those predicted by ANSYS. This indicates that VAMUCH is capable of handling the problems involving compressible hyperelastic constituents.

Figure 3 shows the stress-strain curves of the composite subject to equal-biaxial extension in the y_1- and y_2-directions. It can be seen that the composite exhibits approximately linear stress-strain relations in different directions, or to say, as F increases, the tangent stiffness of the composite almost remains constant. Recall that, in Figure 2, the tangent stiffness monotonically decreases with increasing F. All these imply that the trend of the stress-strain curve varies with the loading condition. In addition, it can be seen that the composite here is approximately one time stiffer than that in Figure 2. This implies that the stiffness of the composite also varies with the loading condition. At last, it can be seen that the results predicted

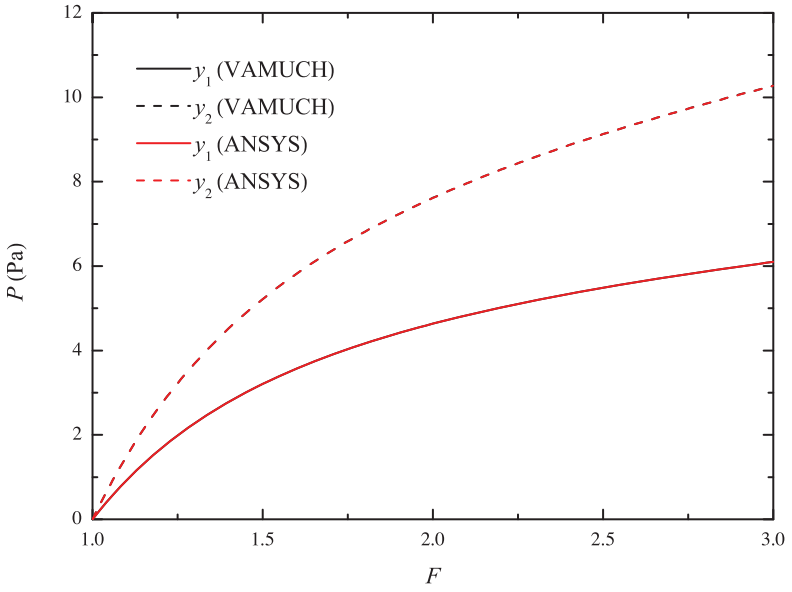

Figure 2. Stress-strain curves of the composite subject to uniaxial tension in the y_1- and y_2-direction.

by VAMUCH perfectly agree with those predicted by ANSYS. This indicates that VAMUCH is capable of handling the problems involving complex loading conditions.

Figure 4 shows the stress-strain curves of the composite subject to equal-triaxial extension. It can be seen that the tangent stiffness of the composite rapidly increases with increasing F. In fact, the tangent stiffness increases so rapidly that, as F attains 1.5, P_{11} and P_{22} both attain very high values. This not only validates the findings obtained above but also implies that, even though the composite is compressible, it is not easily deformed to a large extent when subject to equal-triaxial extension. At last, it can be seen that the results predicted by VAMUCH perfectly agree with those predicted by ANSYS. This again indicates that VAMUCH is capable of handling the problems involving complex loading conditions.

B. Quasi-Incompressible Hyperelastic Constituents

According to numerous experimental observations, many hyperelastic materials are nearly incompressible. It is hereby of great practical value to solve the problems involving incompressible or quasi-incompressible hyperelastic constituents. Recall that κ and μ are related to C_{01}, C_{10}, and D_1 by Eq. (58). It is easy to see that, for a quasi-incompressible Mooney-Rivlin solid, D_1 is much greater than C_{01} and C_{10}. This requires a homogenization approach to be of high accuracy. It is hereby of interest whether VAMUCH can meet this high standard. Specifically, let the two constituents of the binary composite become quasi-incompressible, and let the material parameters of the two constituents take the values listed in Table 2, where D_1 is set to be a penalty parameter here.

Table 2. Material parameters of the constituents.

	C_{01} (Pa)	C_{10} (Pa)	D_1 (Pa)
Constituent 1	5	5	1000
Constituent 2	1	1	1000

Figure 5 shows the stress-strain curves of the composite subject to uniaxial tension in the y_1- and y_2-directions, respectively. It can be seen that the stress-strain curves here are of similar trends as those in Figure 2 except that the composite is much stiffer here and exhibits almost the same stress-strain relation

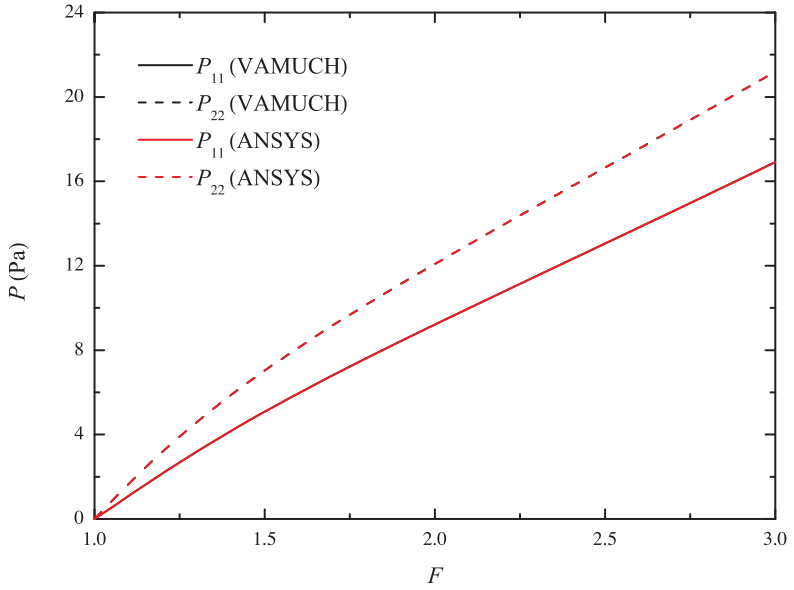

Figure 3. Stress-strain curves of the composite subject to equal-biaxial extension in the y_1- and y_2-directions.

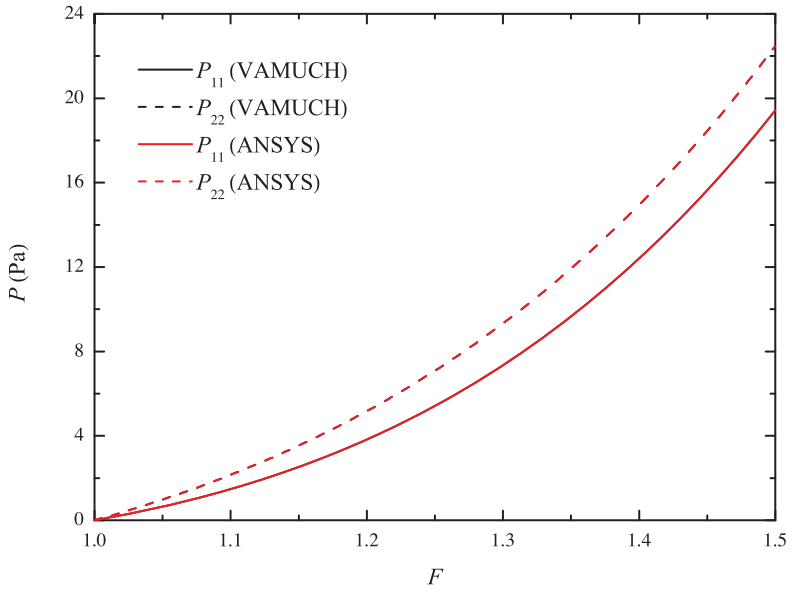

Figure 4. Stress-strain curves of the composite subject to equal-triaxial extension.

when loaded in different directions. This indicates that, as the constituents are set to be quasi-incompressible, the composite becomes more isotropic. In addition, it can be seen that the results predicted by VAMUCH agree well with those predicted by ANSYS. This indicates that VAMUCH is capable of handling the problems involving quasi-incompressible hyperelastic constituents. Last but not least, as addressed in Appendix A, the explicit expression for the second elasticity tensor, $\boldsymbol{\mathcal{C}}$, remains valid for all the hyperelastic material models for which Eq. (66) is applicable. This enables VAMUCH to handle the problems involving many other constitutive relations for the constituents, which might be very complex.

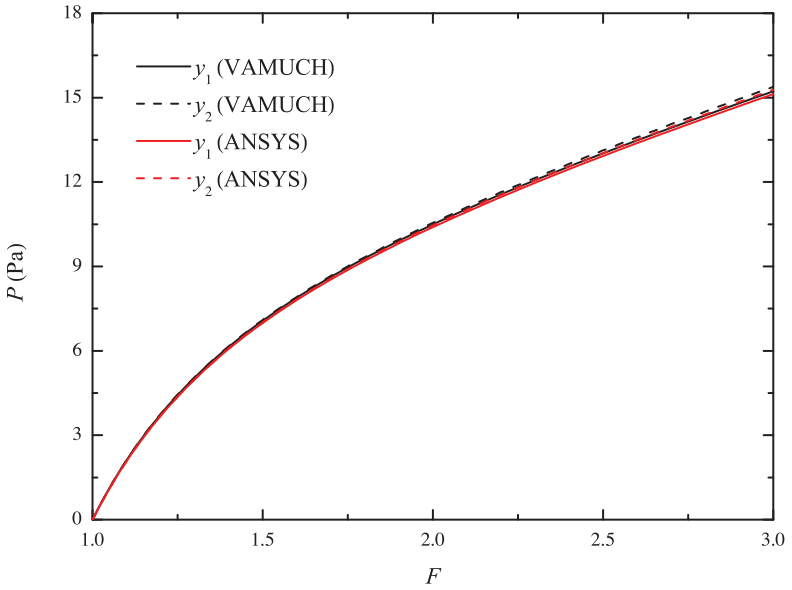

Figure 5. Stress-strain curves of the composite subject to uniaxial tension in the y_1-direction.

VII. Conclusions

In this paper, VAMUCH, a general-purpose micromechanics approach, has been enabled to handle various problems of hyperelastic heterogeneous materials undergoing finite deformation. The rate form of the constitutive relations for a constituent, which is amendable to various hyperelastic material models, is derived. The rate form of the VAMUCH formulation is derived, while the corresponding code structure is developed. The applicability, power, and accuracy of the current VAMUCH are validated using examples such as predicting the stress-strain curves of binary composites consisting of compressible and quasi-incompressible hyperelastic constituents. The current VAMUCH is found to be capable of handling the problems involving complex constitutive relations for the constituents and complex loading conditions. VAMUCH provides a powerful and convenient tool for scientists and engineers to efficiently and accurately solve the problems of hyperelastic heterogeneous materials. More sophisticated user-defined material models can be implemented into it.

Acknowledgements

This work is supported by the US AFOSR Multiscale Structural Mechanics and Prognosis Program. The views and conclusions contained herein are those of the authors and should not be interpreted as necessarily representing the official policies or endorsement, either expressed or implied, of the sponsor.

Appendix

A. Second Elasticity Tensor

It is beneficial to first introduce some fundamentals of tensor calculus. Specifically, let $\mathbf{A}$, $\mathbf{B}$, and $\mathbf{C}$ denote three arbitrary second-order tensors. It can be verified that

$$(\mathbf{A}\otimes\mathbf{B}):\mathbf{C}=(\mathbf{A}:\mathbf{B})\,\mathbf{C}=(\mathbf{B}:\mathbf{C})\,\mathbf{A}. \tag{59}$$

Let $\mathbf{A}$ further be invertible. It can be verified that

$$\frac{\partial}{\partial\mathbf{A}}\left(\det\mathbf{A}\right)=\left(\det\mathbf{A}\right)\mathbf{A}^{-T}. \tag{60}$$

In addition, let I_1, I_2, and I_3 denote the first, second, and third invariants of $\mathbf{A}$, respectively. Note that, by definition,

$$I_1=\mathrm{tr}\mathbf{A},\quad I_2=\frac{1}{2}\left[\mathrm{tr}^2\mathbf{A}-\mathrm{tr}\left(\mathbf{A}^2\right)\right],\quad I_3=\det\mathbf{A}. \tag{61}$$

It can be verified that

$$\frac{\partial I_1}{\partial\mathbf{A}}=\mathbf{I},\quad \frac{\partial I_2}{\partial\mathbf{A}}=I_1\mathbf{I}-\mathbf{A}^T,\quad \frac{\partial I_3}{\partial\mathbf{A}}=\left(\det\mathbf{A}\right)\mathbf{A}^{-T}. \tag{62}$$

At last, it can be verified that

$$\frac{\partial A^{-1}_{ji}}{\partial A_{kl}}=-A^{-1}_{li}A^{-1}_{jk}. \tag{63}$$

In addition, if $\mathbf{A}$ is symmetric, Eq. (63) can be rewritten as

$$\frac{\partial A^{-1}_{ij}}{\partial A_{kl}}=-\frac{1}{2}\left(A^{-1}_{ik}A^{-1}_{jl}+A^{-1}_{il}A^{-1}_{jk}\right)\equiv-\left(\mathbf{A}^{-1}\odot\mathbf{A}^{-1}\right)_{ijkl}. \tag{64}$$

Moreover, it can also be verified that

$$\frac{\partial\mathbf{A}^{-1}}{\partial\mathbf{A}}:\mathbf{A}\otimes\mathbf{A}^{-1}=-\mathbf{A}^{-1}\otimes\mathbf{A}^{-1}. \tag{65}$$

The details on the derivation of Eqs. (59)–(65) can be found in Ref. [34].

Recall that, if the constituent exhibits uncoupled volumetric and isochoric behaviors, W can be expressed as

$$W\left(\bar{I}_1,\bar{I}_2,J\right)=W^v\left(J\right)+W^i\left(\bar{I}_1,\bar{I}_2\right), \tag{66}$$

where

$$\bar{I}_1=\mathrm{tr}\bar{\mathbf{C}},\quad \bar{I}_2=\frac{1}{2}\left[\mathrm{tr}^2\bar{\mathbf{C}}-\mathrm{tr}\left(\bar{\mathbf{C}}^2\right)\right],\quad \bar{I}_3=\det\bar{\mathbf{C}}=1. \tag{67}$$

According to Eq. (62),

$$\frac{\partial\bar{I}_1}{\partial\bar{\mathbf{C}}}=\mathbf{I}\quad\text{and}\quad\frac{\partial I_2}{\partial\bar{\mathbf{C}}}=I_1\mathbf{I}-\bar{\mathbf{C}}^T=I_1\mathbf{I}-\bar{\mathbf{C}}. \tag{68}$$

It can be verified that

$$\frac{\partial J}{\partial\mathbf{C}}=\frac{J}{2}\mathbf{C}^{-T}=\frac{J}{2}\mathbf{C}^{-1}, \tag{69}$$

while it is beneficial to write

$$\frac{\partial J^{-\frac{2}{3}}}{\partial\mathbf{C}}=-\frac{J^{-\frac{2}{3}}}{3}\mathbf{C}^{-1} \tag{70}$$

and

$$\frac{\partial\bar{\mathbf{C}}}{\partial\mathbf{C}}=\frac{\partial}{\partial\mathbf{C}}\left(J^{-\frac{2}{3}}\mathbf{C}\right)=J^{-\frac{2}{3}}\boldsymbol{\mathcal{I}}+\mathbf{C}\otimes\frac{\partial J^{-\frac{2}{3}}}{\partial\mathbf{C}}=J^{-\frac{2}{3}}\left(\boldsymbol{\mathcal{I}}-\frac{1}{3}\mathbf{C}\otimes\mathbf{C}^{-1}\right)\equiv J^{-\frac{2}{3}}\boldsymbol{\mathcal{K}}^T, \tag{71}$$

where $\boldsymbol{\mathcal{I}}$ denotes the fourth-order identity tensor, and

$$\boldsymbol{\mathcal{K}}=\boldsymbol{\mathcal{I}}-\frac{1}{3}\mathbf{C}^{-1}\otimes\mathbf{C} \tag{72}$$

is a fourth-order projection operator with respect to the reference configuration.[34]

Following Ref. [34], substituting Eq. (26) into Eq. (26) gives

$$\mathbf{S} = 2\frac{\partial W}{\partial \mathbf{C}} = 2\frac{\partial W^v}{\partial \mathbf{C}} + 2\frac{\partial W^i}{\partial \mathbf{C}} \equiv \mathbf{S}^v + \mathbf{S}^i, \tag{73}$$

where $\mathbf{S}^v$ and $\mathbf{S}^i$ denote the volumetric and isochoric parts of $\mathbf{S}$, respectively. For notational convenience, let

$$p = -\frac{dW^v}{dJ} \tag{74}$$

and

$$\bar{\mathbf{S}} = 2\frac{\partial W^i}{\partial \bar{\mathbf{C}}} = 2\left(\frac{\partial W^i}{\partial \bar{I}_1}\frac{\partial \bar{I}_1}{\partial \bar{\mathbf{C}}} + \frac{\partial W^i}{\partial \bar{I}_2}\frac{\partial \bar{I}_2}{\partial \bar{\mathbf{C}}}\right) = 2\left[\left(\frac{\partial W^i}{\partial \bar{I}_1} + \bar{I}_1\frac{\partial W^i}{\partial \bar{I}_2}\right)\mathbf{I} - \frac{\partial W^i}{\partial \bar{I}_2}\bar{\mathbf{C}}\right]. \tag{75}$$

It can be verified that p actually denotes the hydrostatic pressure.[34] $\mathbf{S}^v$ and $\mathbf{S}^i$ can be expressed using the chain rule as

$$\mathbf{S}^v = 2\frac{\partial W^v}{\partial \mathbf{C}} = -2p\frac{\partial J}{\partial \mathbf{C}} = -Jp\mathbf{C}^{-1} \tag{76}$$

and

$$\mathbf{S}^i = 2\frac{\partial W^i}{\partial \mathbf{C}} = \bar{\mathbf{S}} : \frac{\partial \bar{\mathbf{C}}}{\partial \mathbf{C}} = J^{-\frac{2}{3}}\bar{\mathbf{S}} : \boldsymbol{\mathcal{K}}^T = J^{-\frac{2}{3}}\boldsymbol{\mathcal{K}} : \bar{\mathbf{S}}, \tag{77}$$

respectively.

Recall that, by definition,

$$\boldsymbol{\mathcal{C}} = 4\frac{\partial^2 W}{\partial \mathbf{C}\partial \mathbf{C}} = 2\frac{\partial \mathbf{S}}{\partial \mathbf{C}}. \tag{78}$$

Following Ref. [34], substituting Eq. (73) into Eq. (79) gives

$$\boldsymbol{\mathcal{C}} = 2\frac{\partial \mathbf{S}}{\partial \mathbf{C}} = 2\frac{\partial \mathbf{S}^v}{\partial \mathbf{C}} + 2\frac{\partial \mathbf{S}^i}{\partial \mathbf{C}} \equiv \boldsymbol{\mathcal{C}}^v + \boldsymbol{\mathcal{C}}^i, \tag{79}$$

where $\boldsymbol{\mathcal{C}}^v$ and $\boldsymbol{\mathcal{C}}^i$ denote the volumetric and isochoric parts of $\boldsymbol{\mathcal{C}}$, respectively. $\boldsymbol{\mathcal{C}}^v$ can be expressed as

$$\boldsymbol{\mathcal{C}}^v = 2\frac{\partial \mathbf{S}^v}{\partial \mathbf{C}} = 2\frac{\partial}{\partial \mathbf{C}}\left(-Jp\mathbf{C}^{-1}\right) = -2\mathbf{C}^{-1} \otimes \left(p\frac{\partial J}{\partial \mathbf{C}} + J\frac{\partial p}{\partial \mathbf{C}}\right) - 2Jp\frac{\partial \mathbf{C}^{-1}}{\partial \mathbf{C}}. \tag{80}$$

Eqs. (66) and (74) implies that p is a function of J. $\partial p/\partial \mathbf{C}$ can hereby be expressed using the chain rule as

$$\frac{\partial p}{\partial \mathbf{C}} = \frac{dp}{dJ}\frac{\partial J}{\partial \mathbf{C}} = \frac{1}{2}J\frac{dp}{dJ}\mathbf{C}^{-1}. \tag{81}$$

In addition, replacing $\mathbf{A}$ in Eq. (64) with $\mathbf{C}$ gives

$$\frac{\partial \mathbf{C}^{-1}}{\partial \mathbf{C}} = -\mathbf{C}^{-1} \odot \mathbf{C}^{-1}. \tag{82}$$

Substituting Eqs. (81) and (82) into (80) gives

$$\boldsymbol{\mathcal{C}}^v = -J\left(p + J\frac{dp}{dJ}\right)\mathbf{C}^{-1} \otimes \mathbf{C}^{-1} + 2Jp\mathbf{C}^{-1} \odot \mathbf{C}^{-1}. \tag{83}$$

$\boldsymbol{\mathcal{C}}^i$ can be expressed as

$$\boldsymbol{\mathcal{C}}^i = 2\frac{\partial \mathbf{S}^i}{\partial \mathbf{C}} = 2\frac{\partial}{\partial \mathbf{C}}\left(J^{-\frac{2}{3}}\boldsymbol{\mathcal{K}} : \bar{\mathbf{S}}\right) = 2\left(\boldsymbol{\mathcal{K}} : \bar{\mathbf{S}}\right) \otimes \frac{\partial J^{-\frac{2}{3}}}{\partial \mathbf{C}} + 2J^{-\frac{2}{3}}\frac{\partial}{\partial \mathbf{C}}\left(\boldsymbol{\mathcal{K}} : \bar{\mathbf{S}}\right). \tag{84}$$

The first term to the right of the last equal sign in Eq. (84) can be expressed as

$$2\left(\boldsymbol{\mathcal{K}} : \bar{\mathbf{S}}\right) \otimes \frac{\partial J^{-\frac{2}{3}}}{\partial \mathbf{C}} = -\frac{2}{3}\left(J^{-\frac{2}{3}}\boldsymbol{\mathcal{K}} : \bar{\mathbf{S}}\right) \otimes \mathbf{C}^{-1} = -\frac{2}{3}\mathbf{S}^i \otimes \mathbf{C}^{-1}, \tag{85}$$

while the second term can be expressed using Eq. (59) and the chain rule as

$$\begin{aligned} 2J^{-\frac{2}{3}}\frac{\partial}{\partial\mathbf{C}}\left(\boldsymbol{\mathcal{K}}:\bar{\mathbf{S}}\right) &= 2J^{-\frac{2}{3}}\frac{\partial}{\partial\mathbf{C}}\left[\bar{\mathbf{S}}-\frac{1}{3}\left(\mathbf{C}^{-1}\otimes\mathbf{C}\right):\bar{\mathbf{S}}\right] = 2J^{-\frac{2}{3}}\frac{\partial}{\partial\bar{\mathbf{C}}}\left[\bar{\mathbf{S}}-\frac{1}{3}\left(\mathbf{C}:\bar{\mathbf{S}}\right)\mathbf{C}^{-1}\right]:\frac{\partial\bar{\mathbf{C}}}{\partial\mathbf{C}}. \\ &= 2J^{-\frac{4}{3}}\left\{\frac{\partial\bar{\mathbf{S}}}{\partial\bar{\mathbf{C}}}-\frac{1}{3}\frac{\partial}{\partial\bar{\mathbf{C}}}\left[\left(\mathbf{C}:\bar{\mathbf{S}}\right)\mathbf{C}^{-1}\right]\right\}:\boldsymbol{\mathcal{K}}^{T}. \end{aligned} \tag{86}$$

For notational convenience, let

$$\bar{\boldsymbol{\mathcal{C}}} = 2J^{-\frac{4}{3}}\frac{\partial\bar{\mathbf{S}}}{\partial\bar{\mathbf{C}}}. \tag{87}$$

The second term in the bracket to the right of the last equal sign in Eq. (86) can be expressed as

$$\frac{\partial}{\partial\bar{\mathbf{C}}}\left[\left(\mathbf{C}:\bar{\mathbf{S}}\right)\mathbf{C}^{-1}\right] = \mathbf{C}^{-1}\otimes\frac{\partial}{\partial\bar{\mathbf{C}}}\left(\mathbf{C}:\bar{\mathbf{S}}\right)+\left(\mathbf{C}:\bar{\mathbf{S}}\right)\frac{\partial\mathbf{C}^{-1}}{\partial\bar{\mathbf{C}}}. \tag{88}$$

The first term to the right of the equal sign in Eq. (88) can be expressed as

$$\mathbf{C}^{-1}\otimes\frac{\partial}{\partial\bar{\mathbf{C}}}\left(\mathbf{C}:\bar{\mathbf{S}}\right) = \mathbf{C}^{-1}\otimes\left(\frac{\partial\mathbf{C}}{\partial\bar{\mathbf{C}}}:\bar{\mathbf{S}}\right)+\mathbf{C}^{-1}\otimes\mathbf{C}:\frac{\partial\bar{\mathbf{S}}}{\partial\bar{\mathbf{C}}} = J^{\frac{2}{3}}\mathbf{C}^{-1}\otimes\bar{\mathbf{S}}+\frac{J^{\frac{4}{3}}}{2}\mathbf{C}^{-1}\otimes\mathbf{C}:\bar{\boldsymbol{\mathcal{C}}}, \tag{89}$$

while the second term can be expressed using the chain rule as

$$\left(\mathbf{C}:\bar{\mathbf{S}}\right)\frac{\partial\mathbf{C}^{-1}}{\partial\bar{\mathbf{C}}} = \left(\mathbf{C}:\bar{\mathbf{S}}\right)\frac{\partial\mathbf{C}^{-1}}{\partial\mathbf{C}}:\frac{\partial\mathbf{C}}{\partial\bar{\mathbf{C}}} = -J^{\frac{2}{3}}\left(\mathbf{C}:\bar{\mathbf{S}}\right)\mathbf{C}^{-1}\odot\mathbf{C}^{-1}. \tag{90}$$

Substituting Eqs. (87), (89), and (90) into Eq. (86) and rearranging the equation give

$$\begin{aligned} 2J^{-\frac{2}{3}}\frac{\partial}{\partial\mathbf{C}}\left(\boldsymbol{\mathcal{K}}:\bar{\mathbf{S}}\right) = &\left(\boldsymbol{\mathcal{I}}-\frac{1}{3}\mathbf{C}^{-1}\otimes\mathbf{C}\right):\bar{\boldsymbol{\mathcal{C}}}:\boldsymbol{\mathcal{K}}^{T}-\frac{2}{3}J^{-\frac{2}{3}}\mathbf{C}^{-1}\otimes\bar{\mathbf{S}}:\boldsymbol{\mathcal{K}}^{T} \\ &+\frac{2}{3}J^{-\frac{2}{3}}\left(\mathbf{C}:\bar{\mathbf{S}}\right)\mathbf{C}^{-1}\odot\mathbf{C}^{-1}:\boldsymbol{\mathcal{K}}^{T}. \end{aligned} \tag{91}$$

It can be obtained from Eq. (65) that

$$\mathbf{C}^{-1}\odot\mathbf{C}^{-1}:\boldsymbol{\mathcal{K}}^{T} = -\frac{\partial\mathbf{C}^{-1}}{\partial\mathbf{C}}:\left(\boldsymbol{\mathcal{I}}-\frac{1}{3}\mathbf{C}\otimes\mathbf{C}^{-1}\right) = \mathbf{C}^{-1}\odot\mathbf{C}^{-1}-\frac{1}{3}\mathbf{C}^{-1}\otimes\mathbf{C}^{-1}\equiv\boldsymbol{\mathcal{L}}, \tag{92}$$

where $\boldsymbol{\mathcal{L}}$ is a fourth-order modified projection operator defined in Ref. [34]. Substituting Eqs. (72), (77), and (92) into Eq. (91) gives

$$2J^{-\frac{2}{3}}\frac{\partial}{\partial\mathbf{C}}\left(\boldsymbol{\mathcal{K}}:\bar{\mathbf{S}}\right) = \boldsymbol{\mathcal{K}}:\bar{\boldsymbol{\mathcal{C}}}:\boldsymbol{\mathcal{K}}^{T}-\frac{2}{3}\mathbf{C}^{-1}\otimes\mathbf{S}^{i}+\frac{2}{3}J^{-\frac{2}{3}}\left(\mathbf{C}:\bar{\mathbf{S}}\right)\boldsymbol{\mathcal{L}}. \tag{93}$$

Substituting Eqs. (86) and (93) into Eq. (84) and rearranging the equation give

$$\boldsymbol{\mathcal{C}}^{i} = \boldsymbol{\mathcal{K}}:\bar{\boldsymbol{\mathcal{C}}}:\boldsymbol{\mathcal{K}}^{T}+\frac{2}{3}J^{-\frac{2}{3}}\left(\mathbf{C}:\bar{\mathbf{S}}\right)\boldsymbol{\mathcal{L}}-\frac{2}{3}\left(\mathbf{C}^{-1}\otimes\mathbf{S}^{i}+\mathbf{S}^{i}\otimes\mathbf{C}^{-1}\right). \tag{94}$$

Substituting Eqs. (83) and (94) into Eq. (79) gives the explicit expression for $\boldsymbol{\mathcal{C}}$ as

$$\begin{aligned} \boldsymbol{\mathcal{C}} = &-J\left(p+J\frac{dp}{dJ}\right)\mathbf{C}^{-1}\otimes\mathbf{C}^{-1}+2Jp\mathbf{C}^{-1}\odot\mathbf{C}^{-1} \\ &+\boldsymbol{\mathcal{K}}:\bar{\boldsymbol{\mathcal{C}}}:\boldsymbol{\mathcal{K}}^{T}+\frac{2}{3}J^{-\frac{2}{3}}\left(\mathbf{C}:\bar{\mathbf{S}}\right)\boldsymbol{\mathcal{L}}-\frac{2}{3}\left(\mathbf{C}^{-1}\otimes\mathbf{S}^{i}+\mathbf{S}^{i}\otimes\mathbf{C}^{-1}\right). \end{aligned} \tag{95}$$

More details on the derivation of Eq. (95) can be found in Ref. [34].

It is worth notice that Eq. (95) remains valid for all the hyperelastic material models for which Eq. (66) is applicable. Once the hyperelastic material model is specified, the expressions for the unknowns in Eq. (95) (i.e., p, dp/dJ, $\bar{\mathbf{S}}$, and $\bar{\boldsymbol{\mathcal{C}}}$) can be easily obtained. For example, for the Mooney-Rivlin model,

$$p = -2D_1\left(J-1\right), \quad \frac{dp}{dJ} = -2D_1, \tag{96}$$

$$\bar{\mathbf{S}} = 2\left[\left(C_{10}+\bar{I}_1C_{01}\right)\mathbf{I}-C_{01}\bar{\mathbf{C}}\right], \quad \bar{\mathbf{C}} = 4C_{01}J^{-\frac{4}{3}}\left(\mathbf{I}\otimes\mathbf{I}-\boldsymbol{\mathcal{I}}\right). \tag{96'}$$

This enables VAMUCH to handle the problems involving complex constitutive relations for the constituents.

References

[1]Lopez-Pamies, O. and Ponte Castañeda, P., "On the overall behavior, microstructure evolution, and macroscopic stability in reinforced rubbers at large deformations: I–Theory," *Journal of the Mechanics and Physics of Solids*, Vol. 54, No. 4, 2006, pp. 807–830.

[2]Finlay, H. M., Whittaker, P., and Canham, P. B., "Collagen organization in the branching region of human brain arteries," *Stroke*, Vol. 29, No. 8, 1998, pp. 1595–1601.

[3]Yu, W. and Tang, T., "Variational asymptotic method for unit cell homogenization of periodically heterogeneous materials," *International Journal of Solids and Structures*, Vol. 44, No. 11-12, 2007, pp. 3738–3755.

[4]Hill, R., "A self-consistent mechanics of composite materials," *Journal of the Mechanics of Physics and Solids*, Vol. 13, 1965, pp. 213–222.

[5]Hashin, Z. and Shtrikman, S., "A variational approach to the theory of the elastic behaviour of multiphase materials," *Journal of the Mechanics and Physics of Solids*, Vol. 11, No. 2, 1963, pp. 127–140.

[6]Milton, G., "Bounds on the electromagnetic, elastic, and other properties of two-component composites," *Physical Review Letters*, Vol. 46, No. 8, 1981, pp. 542–545.

[7]Aboudi, J., "Generalized effective stiffness theory for the modeling of fiber-reinforced composites," *International Journal of Solids and Structures*, Vol. 17, No. 10, 1981, pp. 1005 – 1018.

[8]Banerjee, B. and Adams, D. O., "On predicting the effective elastic properties of polymer bonded explosives using the recursive cell method," *International Journal of Solids and Structures*, Vol. 41, No. 2, 2004, pp. 481–509.

[9]Bensoussan, A., Lions, J., and Papanicolaou, G., *Asymptotic analysis for periodic structures*, North-Holland, Amsterdam, 1978.

[10]Murakami, H. and Toledano, A., "A high-order mixture homogenization of bi-laminated composites," *Transactions of the ASME. Journal of Applied Mechanics*, Vol. 57, No. 2, 1990, pp. 388–397.

[11]Hill, R., "On constitutive macro-variables for heterogeneous solids at finite strain," *Proceedings of the Royal Society of London. A. Mathematical and Physical Sciences*, Vol. 326, No. 1565, 1972, pp. 131–147.

[12]Hill, R. and Rice, J. R., "Elastic potentials and the structure of inelastic constitutive laws," *SIAM Journal on Applied Mathematics*, Vol. 25, No. 3, 1973, pp. 448–461.

[13]Ogden, R. W., "Extremum principles in non-linear elasticity and their application to composites–I: Theory," *International Journal of Solids and Structures*, Vol. 14, No. 4, 1978, pp. 265–282.

[14]Ponte Castañeda, P., "The overall constitutive behaviour of nonlinearly elastic composites," *Proceedings of the Royal Society of London. A. Mathematical and Physical Sciences*, Vol. 422, No. 1862, 1989, pp. 147–171.

[15]Ponte Castañeda, P. and Tiberio, E., "A second-order homogenization method in finite elasticity and applications to black-filled elastomers," *Journal of the Mechanics and Physics of Solids*, Vol. 48, No. 6, 2000, pp. 1389–1411.

[16]Lahellec, N., Mazerolle, F., and Michel, J.-C., "Second-order estimate of the macroscopic behavior of periodic hyperelastic composites: theory and experimental validation," *Journal of the Mechanics and Physics of Solids*, Vol. 52, No. 1, 2004, pp. 27–49.

[17]Lopez-Pamies, O. and Ponte Castañeda, P., "Second-order estimates for the macroscopic response and loss of ellipticity in porous rubbers at large deformations," *Journal of Elasticity*, Vol. 76, No. 3, 2004, pp. 247–287.

[18]Lopez-Pamies, O. and Ponte Castañeda, P., "On the overall behavior, microstructure evolution, and macroscopic stability in reinforced rubbers at large deformations: II–Application to cylindrical fibers," *Journal of the Mechanics and Physics of Solids*, Vol. 54, No. 4, 2006, pp. 831–863.

[19]Michel, J.-C., Lopez-Pamies, O., Ponte Castañeda, P., and Triantafyllidis, N., "Microscopic and macroscopic instabilities in finitely strained porous elastomers," *Journal of the Mechanics and Physics of Solids*, Vol. 55, No. 5, 2007, pp. 900–938.

[20]Brun, M., Lopez-Pamies, O., and Ponte Castañeda, P., "Homogenization estimates for fiber-reinforced elastomers with periodic microstructures," *International Journal of Solids and Structures*, Vol. 44, No. 18, 2007, pp. 5953–5979.

[21]deBotton, G., Hariton, I., and Socolsky, E. A., "Neo-Hookean fiber-reinforced composites in finite elasticity," *Journal of the Mechanics and Physics of Solids*, Vol. 54, No. 3, 2006, pp. 533–559.

[22]deBotton, G. and Shmuel, G., "A new variational estimate for the effective response of hyperelastic composites," *Journal of the Mechanics and Physics of Solids*, Vol. 58, No. 4, 2010, pp. 466–483.

[23]Aboudi, J., "Overall finite deformation of elastic and elastoplastic composites," *Mechanics of Materials*, Vol. 5, No. 1, 1986, pp. 73–86.

[24]Aboudi, J. and Arnold, S. M., "Micromechanical modeling of the finite deformation of thermoelastic multiphase composites," *Mathematics and Mechanics of Solids*, Vol. 5, No. 1, 2000, pp. 75–99.

[25]Aboudi, J., "Micromechanical prediction of the finite thermoelastic response of rubberlike matrix composites," *Journal of Applied Mathematics and Physics (ZAMP)*, Vol. 52, No. 5, 2001, pp. 823–846.

[26]Adoudi, J., "The generalized method of cells and high-fidelity generalized method of cells micromechanical models-a review," *Mechanics of Advanced Materials and Structures*, Vol. 11, No. 4-5, 2004, pp. 329–366.

[27]Yvonnet, J. and He, Q.-C., "The reduced model multiscale method (R3M) for the non-linear homogenization of hyperelastic media at finite strains," *Journal of Computational Physics*, Vol. 223, No. 1, 2007, pp. 341–368.

[28]Yvonnet, J., Gonzalez, D., and He, Q.-C., "Numerically explicit potentials for the homogenization of nonlinear elastic heterogeneous materials," *Computer Methods in Applied Mechanics and Engineering*, Vol. 198, No. 33, 2009, pp. 2723–2737.

[29]Yu, W. and Tang, T., "A variational asymptotic micromechanics model for predicting thermoelastic properties of heterogeneous materials," *International Journal of Solids and Structures*, Vol. 44, No. 22-23, 2007, pp. 7510–7525.

[30]Tang, T. and Yu, W., "A variational asymptotic micromechanics model for predicting conductivity of composite materials," *Journal of Mechanics of Materials and Structures*, Vol. 2, 2007, pp. 1813–1830.

[31]Tang, T. and Yu, W., "Variational asymptotic homogenization of heterogeneous electromagnetoelastic materials," *International Journal of Engineering Science*, Vol. 46, No. 8, 2008, pp. 741–757.

[32]Tang, T. and Yu, W., "Variational asymptotic micromechanics modeling of heterogeneous piezoelectric materials," *Mechanics of Materials*, Vol. 40, No. 10, 2008, pp. 812–824.

[33]Spencer, A. J. M., *Continuum mechanics*, Dover Publications, Mineola, 2004.

[34]Holzapfel, G. A., *Nonlinear solid mechanics: a continuum approach for engineering*, John Wiley & Sons Ltd., Chichester, 2000.

[35]Berdichevsky, L. V., *Variational principles of continuum mechanics: II. Applications*, Springer, New York, 2009.

Composite Structures 133 (2015) 947–958

Contents lists available at ScienceDirect

Composite Structures

journal homepage: www.elsevier.com/locate/compstruct

Variational asymptotic homogenization of elastoplastic composites

Liang Zhang *, Wenbin Yu

Purdue University, West Lafayette, IN 47907-2045, USA

ARTICLE INFO

Article history:
Available online 5 August 2015

Keywords:
Metal matrix composite
Radial return algorithm
Elastic and plastic anisotropy
Nonlinear kinematic hardening
Multilevel Newton–Raphson method

ABSTRACT

The objective of this paper is to develop a micromechanics approach to homogenizing elastoplastic composites. A rigorous second-order radial return algorithm, which can handle elastic and plastic anisotropy and nonlinear kinematic hardening, is developed. A variational statement for homogenization is formulated using the variational asymptotic method, discretized in a finite-dimensional space, and solved using a multilevel Newton–Raphson method. The versatility and accuracy of the present approach are demonstrated through homogenizing long fiber-, particle-, and short fiber-reinforced metal matrix composites (MMCs). Different types of reinforcement are found to differently affect the response of MMCs. The present approach is found to be capable of handling various microstructures, complex material models, complex loading conditions, and complex loading paths. More sophisticated material models can be implemented in it.

1. Introduction

Composites are widely used in structural components due to their capability of exhibiting low strength-to-weight ratio, improved thermal conductivity, improved permittivity, or even negative Poisson's ratio. Many of them (e.g., metal matrix composites (MMCs), reinforced concrete, and metal foams) consist of elastoplastic constituents, whose deformation is often accompanied by material nonlinearity and history dependency. One major challenge is to predict their global response from the microstructural details: first, it is often difficult or expensive to experimentally measure such response; second, the scales of macroscopic structures are usually several orders of magnitude greater than those of heterogeneities, making it computationally prohibitive to capture all the microstructural details. All these lead one to seek for a micromechanics approach to solving such problems on the microscopic scale.

Elaborate efforts have been devoted to developing various analytical micromechanics approaches. The mean-field homogenization (MFH) is a popular one. Its nonlinear variants are classified into two groups: the tangent approach [23,35,27] and the secant approach [8,45]. The tangent approach involves linearizing the local constitutive relations with the stress rates, the strain rates, and a tangent modulus, and the secant approach with the stresses, the strains, and a secant modulus (sometimes plus pre-stresses/strains). Unfortunately, both approaches tend to make too stiff predictions because they assume uniform local constitutive relations over each phase. Suquet and Ponte Castañeda [44,38] developed a second-order variational homogenization method, which involves minimizing a second-order estimate of the strain energy potential of a properly selected "linear comparison composite", and made close predictions for high-contrast composites (e.g., rigidly reinforced composites and porous materials). Several authors [14,10,11,4] implemented the radial return algorithm in this method and made it more versatile. Despite success, these approaches require a two-phase composite embedded with sparsely distributed inclusions and are hereby incapable of homogenizing composites with more complex microstructures (e.g., woven composites and open-cell foams). Meanwhile, they do not recover the local fields, either.

Several semi-analytical and computational approaches have been developed to overcome these drawbacks. Such approaches often involve finely discretizing a unit cell (UC) in a finite-dimensional space such that the microstructural details are better captured. The transformation field analysis (TFA) [15,16] is a popular semi-analytical approach. It involves treating the plastic strain as a uniform eigenstrain over each phase, computing the local fields from a predetermined eignenstain field (just like solving a thermoelastic problem), and updating the plastic strain with the flow rule. Dvorak et al. [17] and Fish et al. [19] implemented TFA in the finite element method (FEM) and made TFA very versatile. Michel and Suquet [32,33] later developed the nonuniform TFA, which allows a nonuniform eigenstrain over each phase, and made closer predictions. Despite success, TFA and its variations still

* Corresponding author. Tel.: +1 979 618 6481.
E-mail addresses: zhangliang115@hotmail.com (L. Zhang), wenbinyu@purdue.edu (W. Yu).

http://dx.doi.org/10.1016/j.compstruct.2015.07.117
0263-8223/

cannot perfectly handle nonlinear kinematic hardening, complex loading conditions, and complex loading paths [26]. The method of cells (MOC) or the generalized method of cells (GMC) [1,2] is another semi-analytical approach. It involves treating the plastic strain as an eigenstrain, discretizing a UC into numerous rectangular (2D) or parallelepiped (3D) subcells, and approximating the local quantities with their averages over each subcell. Despite some advantages, MOC or GMC does not make very accurate predictions because their microstructural details and local fields are captured without sufficient accuracies.

The formal asymptotic homogenization method [5] is a popular computational approach. It involves asymptotically expanding the displacements on multiple scales and solving the resulting partial differential equation (PDE) on each scale. It possesses two major advantages: first, the asymptotic expansion allows periodic boundary conditions rigorously to be applied (see Michel et al. [30] for more details); second, although solving PDEs makes it not straightforward to implement this method in FEM, Guedes and Kikuchi [22] still accomplished it, making the method very versatile. Suquet [43] extended its applications to the nonlinear regime. Several authors [46,21] developed its nonlinear variants with continuum tangent operators and explicit time integration methods, but neither continuum tangent operators nor explicit time integration methods behave well in elastoplastic problems. Jansson [25] developed another nonlinear variant with the Newton–Raphson method and made close predictions.

The fast Fourier transform (FFT)-based approach [36] is another popular computational approach. It allows the direct use of a digital image of microstructure by discretizing the UC into numerous so-called "voxels" (a combination of "volume" and "pixel"). Eyre and Milton [18] and Michel et al. [31] enabled it to homogenize high-contrast composites with satisfactory convergence speed. Despite success, this approach requires elastically isotropic phases, for which a Green operator is explicitly known in Fourier space. Meanwhile, its capability of handling nonlinear kinematic hardening has not been demonstrated yet.

Several authors also developed computational approaches based on the displacement-based finite element analysis (FEA). Here it becomes challenging to apply periodic boundary conditions because the displacements are not necessarily periodic. Markovic and Ibrahimbegovic [29] developed an approach to handling the micro–macro transitions in multiscale FEA, yet requiring kinematic or static boundary conditions at the UC level. Sun and Vaidya [42] developed an approach to applying periodic boundary conditions to the UCs of long fiber-reinforced composites, and Smit et al. [41] developed a similar approach applicable to axisymmetric 2D UCs undergoing finite deformation. Miehe [34] developed an implicit approach applicable to 3D UCs undergoing finite deformation, requiring the Newton–Raphson iteration, and Xia and his coworkers [49,50] developed an explicit approach applicable to 3D UCs, requiring solving a master stiffness equation for six times. Despite success, neither approach applicable to 3D UCs can be straightforwardly implemented in implicit time integration methods.

The variational asymptotic homogenization method [7,51] is another computational approach. It involves asymptotically analyzing a variational statement of a composite and solving the resulting simplified functional equation governing the response of the UC. Its first-order approximation is actually mathematically equivalent to the formal asymptotic homogenization method and hereby possesses similar advantages. Moreover, since both this method and FEM are inherently variational approaches, it is more straightforward to implement this method in FEM. Zhang and Yu [52] enabled it to homogenize elasto-viscoplastic composites, and it can be further extended to homogenize elastoplastic composites.

The objective of this paper is to develop a micromechanics approach to homogenizing elastoplastic composites. A rigorous second-order radial return algorithm, which can handle elastic and plastic anisotropy and nonlinear kinematic hardening, is developed. A variational statement for homogenization is formulated using the variational asymptotic method, discretized in a finite-dimensional space, and solved using a multilevel Newton–Raphson method. The versatility and accuracy of the present approach are demonstrated through homogenizing long fiber-, particle-, and short fiber-reinforced MMCs. The effect of the type of reinforcement on the response of an MMC will be evaluated.

2. Thermodynamics and plasticity model

Let ψ denote the Helmholtz free energy per unit mass of a material. It can be treated as a function of a suitable set of independent state variables characterizing the elastic and plastic behavior of the material, e.g.,

$$\psi = \psi(\boldsymbol{\epsilon}^e, \boldsymbol{\alpha}, r), \tag{1}$$

where $\boldsymbol{\epsilon}^e$ denotes the elastic strain tensor, $\boldsymbol{\alpha}$ is a second-order tensor accounting for kinematic hardening, and r is a scalar accounting for isotropic hardening. Assume that the material exhibits uncoupled elastic and plastic behavior. ψ can then be decomposed into its elastic and plastic hardening parts, i.e.,

$$\psi(\boldsymbol{\epsilon}^e, \boldsymbol{\alpha}, r) = \psi_e(\boldsymbol{\epsilon}^e) + \psi_p(\boldsymbol{\alpha}, r). \tag{2}$$

The thermodynamic forces conjugate to the state variables in Eq. (1) are defined as

$$\boldsymbol{\sigma} = \rho\frac{\partial\psi}{\partial\boldsymbol{\epsilon}^e} = \rho\frac{\partial\psi_e}{\partial\boldsymbol{\epsilon}^e}, \quad \boldsymbol{X} = \rho\frac{\partial\psi}{\partial\boldsymbol{\alpha}} = \rho\frac{\partial\psi_p}{\partial\boldsymbol{\alpha}}, \quad R = \rho\frac{\partial\psi}{\partial r} = \rho\frac{\partial\psi_p}{\partial r}, \tag{3}$$

where $\boldsymbol{\sigma}$ denotes the stress tensor, $\boldsymbol{X}$ denotes the back stress tenor, R is related to the current yield stress, and ρ denotes the density of the material.

For isothermal deformation, the Clausius–Duhem inequality writes

$$\Phi = \boldsymbol{\sigma} : \dot{\boldsymbol{\epsilon}} - \rho\dot{\psi} \geqslant 0, \tag{4}$$

where Φ denotes the dissipation per unit volume, and the overdot denotes the time derivative of a quantity. The strain tensor, $\boldsymbol{\epsilon}$, can be decomposed into its elastic and plastic parts, i.e.,

$$\boldsymbol{\epsilon} = \boldsymbol{\epsilon}^e + \boldsymbol{\epsilon}^p. \tag{5}$$

Combining Eqs. (2)–(5) gives

$$\Phi = \boldsymbol{\sigma} : \dot{\boldsymbol{\epsilon}}^p - \boldsymbol{X} : \dot{\boldsymbol{\alpha}} - R\dot{r} \geqslant 0. \tag{6}$$

Let the yield criterion write

$$f(\boldsymbol{\sigma}, \boldsymbol{X}, R) \leqslant 0. \tag{7}$$

Assume a pseudo-plastic potential, $F(\boldsymbol{\sigma}, \boldsymbol{X}, R)$, and a plastic multiplier, $\dot{\lambda}$, yielding plastic evolution laws [9]

$$\dot{\boldsymbol{\epsilon}}^p = \dot{\lambda}\frac{\partial F}{\partial\boldsymbol{\sigma}}, \quad \dot{\boldsymbol{\alpha}} = -\dot{\lambda}\frac{\partial F}{\partial\boldsymbol{X}}, \quad \dot{r} = -\dot{\lambda}\frac{\partial F}{\partial R}. \tag{8}$$

Once $\rho\psi_p$, f, and F are specified, the plastic evolution laws can be fully determined.

Without loss of generality, let the material obey Hill's yield criterion,

$$f(\boldsymbol{\sigma}, \boldsymbol{X}, R) = \beta_{eq} - \sigma_y - R \leqslant 0, \tag{9}$$

where

$$\beta_{eq} = \sqrt{\frac{3}{2}\boldsymbol{\beta}' : \boldsymbol{\mathcal{H}} : \boldsymbol{\beta}'} \tag{10}$$

denotes a Hill measure of $\boldsymbol{\beta} = \boldsymbol{\sigma} - \boldsymbol{X}$ with $(\cdot)'$ denoting the deviatoric part of the tensor and $\mathcal{H}$ denoting the fourth-order anisotropy tensor, and σ_y denotes the initial yield stress. Note that $\mathcal{H}$ can be obtained from the so-called R-value (see Appendix A for more details). Meanwhile, set [9]

$$F = f + \frac{3a}{4C}\boldsymbol{X} : \boldsymbol{X} + \frac{R^2}{2Q}, \tag{11}$$

where C and a are two kinematic hardening parameters, and Q is an isotropic hardening parameter. Substituting Eq. (11) into Eq. (8) gives

$$\dot{\boldsymbol{\epsilon}}^p = \dot{\lambda}\boldsymbol{n}, \quad \dot{\boldsymbol{\alpha}} = \dot{\boldsymbol{\epsilon}}^p - \frac{3a}{2C}\boldsymbol{X}\dot{\lambda}, \quad \dot{r} = \left(1 - \frac{R}{Q}\right)\dot{\lambda}, \tag{12}$$

where $\boldsymbol{n} = \partial f/\partial\boldsymbol{\sigma} = \partial F/\partial\boldsymbol{\sigma}$ denotes the normal to the yield surface. Substituting Eq. (10) into the modified plastic work equivalence principle,

$$\boldsymbol{\beta} : \dot{\boldsymbol{\epsilon}}^p = \beta_{eq}\dot{p}, \tag{13}$$

gives the accumulated plastic strain rate as [6]

$$\dot{p} = \sqrt{\frac{2}{3}\dot{\boldsymbol{\epsilon}}^p : \mathcal{H}^{-1} : \dot{\boldsymbol{\epsilon}}^p}. \tag{14}$$

It is beneficial to find the relation between $\dot{\lambda}$ and $\dot{p}$. $\boldsymbol{n}$ can be expressed as [6]

$$\begin{aligned}\boldsymbol{n} &= \frac{\partial f}{\partial\boldsymbol{\sigma}} = \frac{\partial\beta_{eq}}{\partial\boldsymbol{\sigma}} = \frac{1}{2\beta_{eq}}\frac{\partial\beta_{eq}^2}{\partial\boldsymbol{\sigma}} \\ &= \frac{1}{2\beta_{eq}}\left(\frac{3}{2}2\frac{\partial}{\partial\boldsymbol{\sigma}}\boldsymbol{\beta}' : \mathcal{H} : \boldsymbol{\beta}'\right) = \frac{3}{2\beta_{eq}}\mathcal{J} : \mathcal{H} : \boldsymbol{\beta}'.\end{aligned} \tag{15}$$

where $\mathcal{J} = \mathcal{I} - \frac{1}{3}\boldsymbol{I}\otimes\boldsymbol{I}$ denotes the fourth-order deviatoric projection operator with $\mathcal{I}$ and $\boldsymbol{I}$ denoting the fourth- and second-order identity tensors, respectively. Substituting the first equation of Eq. (12) into Eq. (13) gives

$$\boldsymbol{\beta} : \left(\dot{\lambda}\boldsymbol{n}\right) = \beta_{eq}\dot{p}. \tag{16}$$

Substituting Eq. (15) into Eq. (16) gives

$$\beta_{eq}\dot{\lambda} = \beta_{eq}\dot{p} \quad \text{or} \quad \dot{\lambda} = \dot{p}, \tag{17}$$

which implies that plastic deformation is irreversible [40]. The Kuhn–Tucker conditions,

$$f \leqslant 0, \quad \dot{\lambda} \geqslant 0, \quad \dot{\lambda}f = 0, \tag{18}$$

also characterize this nature.

Also set [9]

$$\rho\psi_p = \frac{1}{3}C\boldsymbol{\alpha} : \boldsymbol{\alpha} + \frac{1}{2}bQr^2, \tag{19}$$

where b is another isotropic hardening parameter. Substituting Eq. (19) into the last two equations of Eq. (3) gives

$$\boldsymbol{X} = \frac{2}{3}C\boldsymbol{\alpha} \quad \text{and} \quad R = bQr. \tag{20}$$

Substituting the last two equations of Eq. (12) into the rate form of Eq. (20) and noting that $\dot{\lambda} = \dot{p}$ give

$$\dot{\boldsymbol{X}} = \frac{2}{3}C\dot{\boldsymbol{\epsilon}}^p - a\boldsymbol{X}\dot{p} \quad \text{and} \quad \dot{R} = b(Q - R)\dot{p}, \tag{21}$$

which are the Chaboche hardening law [12] and the rate form of the Voce hardening law [47], respectively. Integrating the second equation of Eq. (21) with respect to time gives the Voce hardening law,

$$R = Q[1 - \exp(-bp)]. \tag{22}$$

Till now, some fundamentals of thermodynamics have been briefly introduced, and the plasticity model has been specified. In the next section, a rigorous second-order radial return algorithm will be developed.

3. Radial return algorithm

The radial return algorithm is a widely used integration scheme for elastoplastic constitutive relations. If there does not exist nonlinear kinematic hardening, it is implicit and unconditionally stable; if there does, it has to explicitly update its variables and becomes semi-implicit and conditionally stable. In the latter case, a second-order algorithm is supposed to behave better than a first-order one because high order generally means high accuracy and rapid convergence. The traditional second-order algorithm (based on the midpoint rule), however, was found to behave worse than the first-order one (based on the backward Euler method) for long-time integration [3]. This is probably because the traditional algorithm imprecisely updates the back stresses. In this section, a rigorous second-order algorithm, which can handle elastic and plastic anisotropy and nonlinear kinematic hardening, will be developed.

Suppose that all the variables at a given instant of time, t_n, are known. The task is to find the variables at $t_{n+1} = t_n + \Delta t$, where $\Delta(\cdot)$ denotes the increment in a quantity over this time interval. For notational convenience, omit the subscript $n+1$ on each quantity at t_{n+1}. The trial stress tensor, $\boldsymbol{\sigma}^{tr}$, is defined as

$$\boldsymbol{\sigma}^{tr} = \mathcal{C}^e : (\boldsymbol{\epsilon} - \boldsymbol{\epsilon}_n^p), \tag{23}$$

where $\mathcal{C}^e$ denotes the fourth-order elastic stiffness tensor. The integration scheme can be formulated as solving the following equation set for $\boldsymbol{\sigma}$ and Δp:

$$\boldsymbol{\sigma} = \boldsymbol{\sigma}^{tr} - \mathcal{C}^e : \Delta\boldsymbol{\epsilon}^p, \tag{24}$$

$$f = \beta_{eq} - \sigma_y - R = 0, \tag{24'}$$

where

$$\Delta\boldsymbol{\epsilon}^p = \frac{\Delta p}{2}(\boldsymbol{n}_n + \boldsymbol{n}), \tag{25}$$

$$\dot{\boldsymbol{X}} = \frac{2}{3}C\dot{\boldsymbol{\epsilon}}^p - a\boldsymbol{X}\dot{p}. \tag{25'}$$

Its major distinction from the traditional one is that $\boldsymbol{X}$ is a solution to an ordinary differential equation (ODE) rather than [3]

$$\Delta\boldsymbol{X} = \frac{2}{3}C\Delta\boldsymbol{\epsilon}^p - a\boldsymbol{X}\Delta p. \tag{26}$$

Note that, even if $\Delta\boldsymbol{\epsilon}^p$ and Δp are second-order accurate, Eq. (26) relates $\Delta\boldsymbol{X}$ to them via a first-order method and hereby provides an imprecise second-order approximation of $\boldsymbol{X}$. This can make an algorithm inaccurate and instable for long-time integration.

Note that the solution to

$$\frac{dy}{dx} + P(x)y = Q(x) \tag{27}$$

is

$$y = e^{-\int P(x)dx}\left[\int e^{\int P(x)dx}Q(x)dx + C_1\right]. \tag{28}$$

Combining the second equation of Eqs. (25), (27), and (28) gives

$$\boldsymbol{X} = e^{-ap}\left[\frac{2}{3}C\int_0^t e^{ap(\tau)}\dot{\boldsymbol{\epsilon}}^p(\tau)d\tau + C_2\right]. \tag{29}$$

Setting $t = t_n$ in Eq. (29) and rearranging the equation give

$$C_2 = e^{ap_n}\boldsymbol{X}_n - \frac{2}{3}C\int_0^{t_n} e^{ap(\tau)}\dot{\epsilon}^p(\tau)d\tau. \tag{30}$$

Substituting Eq. (30) into Eq. (29) gives

$$\boldsymbol{X} = e^{-a\Delta p}\boldsymbol{X}_n + \frac{2}{3}Ce^{-ap}\int_{t_n}^{t} e^{ap(\tau)}\dot{\epsilon}^p(\tau)d\tau. \tag{31}$$

The integral in Eq. (31) can be approximated using the midpoint method as

$$\int_{t_n}^{t} e^{ap(\tau)}\dot{\epsilon}^p(\tau)d\tau = e^{a\left(p_n+\frac{\Delta p}{2}\right)}\dot{\epsilon}^p\left(t_n+\frac{\Delta t}{2}\right)\Delta t = e^{a\left(p_n+\frac{\Delta p}{2}\right)}\Delta\epsilon^p. \tag{32}$$

Substituting Eq. (32) into Eq. (31) gives

$$\boldsymbol{X} = e^{-a\Delta p}\boldsymbol{X}_n + \frac{2}{3}Ce^{-\frac{a\Delta p}{2}}\Delta\epsilon^p. \tag{33}$$

Substituting the first equation of Eq. (25) into Eq. (33) gives

$$\boldsymbol{X}(\boldsymbol{\beta},\Delta p) = e^{-a\Delta p}\boldsymbol{X}_n + \frac{C}{3}e^{-\frac{a\Delta p}{2}}\Delta p(\boldsymbol{n}_n+\boldsymbol{n}). \tag{34}$$

Note that the only additional approximation involved in the above derivation arises in Eq. (32) and is second-order accurate. Eq. (34) hereby provides a rigorous second-order approximation of $\boldsymbol{X}$. In addition, it is beneficial to write

$$\frac{\partial\boldsymbol{X}}{\partial\boldsymbol{\beta}} = \frac{C}{3}e^{-\frac{a\Delta p}{2}}\Delta p\frac{\partial\boldsymbol{n}}{\partial\boldsymbol{\beta}}, \tag{35}$$

$$\frac{\partial\boldsymbol{X}}{\partial\Delta p} = -ae^{-a\Delta p}\boldsymbol{X}_n + \frac{C}{3}\left(1-\frac{a\Delta p}{2}\right)e^{-\frac{a\Delta p}{2}}(\boldsymbol{n}_n+\boldsymbol{n}), \tag{35'}$$

where

$$\begin{aligned}\frac{\partial\boldsymbol{n}}{\partial\boldsymbol{\beta}} &= \frac{\partial}{\partial\boldsymbol{\beta}}\left(\frac{3}{2\beta_{eq}}\mathcal{J}:\mathcal{H}:\boldsymbol{\beta}'\right)\\ &= \frac{3}{2}\frac{\partial}{\partial\boldsymbol{\beta}}\left(\frac{1}{\beta_{eq}}\right)\otimes\mathcal{J}:\mathcal{H}:\boldsymbol{\beta}' + \frac{3}{2\beta_{eq}}\mathcal{J}:\mathcal{H}:\frac{\partial\boldsymbol{\beta}'}{\partial\boldsymbol{\beta}}\\ &= \frac{3}{2}\left(-\frac{1}{\beta_{eq}^2}\frac{\partial\beta_{eq}}{\partial\boldsymbol{\beta}}\right)\otimes\mathcal{J}:\mathcal{H}:\boldsymbol{\beta}' + \frac{3}{2\beta_{eq}}\mathcal{J}:\mathcal{H}:\mathcal{J}\\ &= \frac{1}{\beta_{eq}}\left(\frac{3}{2}\mathcal{J}:\mathcal{H}:\mathcal{J}-\boldsymbol{n}\otimes\boldsymbol{n}\right).\end{aligned} \tag{36}$$

The task can then be reformulated as solving the following equation set for $\boldsymbol{\beta}$ and Δp:

$$\boldsymbol{\Psi}(\boldsymbol{\beta},\Delta p) = \boldsymbol{\beta} - \boldsymbol{\sigma}^{tr} + \frac{\Delta p}{2}\mathcal{C}^e:(\boldsymbol{n}_n+\boldsymbol{n}) + \boldsymbol{X}(\boldsymbol{\beta},\Delta p) = \boldsymbol{0}, \tag{37}$$

$$f(\boldsymbol{\beta},\Delta p) = \beta_{eq} - \sigma_y - R = 0. \tag{37'}$$

Despite similarities, Eq. (37) is distinct to the corresponding equation set in Doghri [13] from the following three aspects:

1. it involves elastic anisotropy because $\mathcal{C}^e$ takes a general form;
2. it involves plastic anisotropy because β_{eq} is a Hill (rather than von Mises) measure of $\boldsymbol{\beta}$;
3. it is rigorously second-order (rather than first-order) accurate.

Here the Newton–Raphson method is used for problem solving. Require

$$\boldsymbol{\Psi}(\boldsymbol{\beta}_{\text{old}}+d\boldsymbol{\beta},\Delta p_{\text{old}}+d\Delta p) = \boldsymbol{\Psi}(\boldsymbol{\beta}_{\text{old}},\Delta p_{\text{old}}) + \frac{\partial\boldsymbol{\Psi}}{\partial\boldsymbol{\beta}}:d\boldsymbol{\beta} + \frac{\partial\boldsymbol{\Psi}}{\partial\Delta p}d\Delta p = \boldsymbol{0}, \tag{38}$$

$$f(\boldsymbol{\beta}_{\text{old}}+d\boldsymbol{\beta},\Delta p_{\text{old}}+d\Delta p) = f(\boldsymbol{\beta}_{\text{old}},\Delta p_{\text{old}}) + \boldsymbol{n}:d\boldsymbol{\beta} - \frac{dR}{d\Delta p}d\Delta p = 0, \tag{38'}$$

where

$$\frac{\partial\boldsymbol{\Psi}}{\partial\boldsymbol{\beta}} = \mathcal{I} + \frac{\Delta p}{2}\mathcal{C}^e:\frac{\partial\boldsymbol{n}}{\partial\boldsymbol{\beta}} + \frac{\partial\boldsymbol{X}}{\partial\boldsymbol{\beta}}, \tag{39}$$

$$\frac{\partial\boldsymbol{\Psi}}{\partial\Delta p} = \frac{1}{2}\mathcal{C}^e:(\boldsymbol{n}_n+\boldsymbol{n}) + \frac{\partial\boldsymbol{X}}{\partial\Delta p}. \tag{39'}$$

Introduce matrix notation

$$\beta = \lfloor\,\beta_{11}\quad\beta_{12}\quad\beta_{22}\quad\beta_{13}\quad\beta_{23}\quad\beta_{33}\,\rfloor^T. \tag{40}$$

The matrix form of Eq. (38) writes

$$\begin{Bmatrix}\Psi(\beta_{\text{old}},\Delta p_{\text{old}})\\ f(\beta_{\text{old}},\Delta p_{\text{old}})\end{Bmatrix} + J\begin{Bmatrix}d\beta\\ \frac{dR}{d\Delta p}d\Delta p\end{Bmatrix} = 0, \tag{41}$$

where

$$J = \begin{bmatrix}\frac{\partial\Psi}{\partial\beta} & \frac{\frac{\partial\Psi}{\partial\Delta p}}{\frac{dR}{d\Delta p}}\\ n^T & -1\end{bmatrix} \tag{42}$$

is a 7×7 Jacobian matrix. Note that Eq. (41) is arranged so that J is well-conditioned. Rearranging Eq. (41) gives

$$\begin{Bmatrix}d\beta\\ \frac{dR}{d\Delta p}d\Delta p\end{Bmatrix} = -J^{-1}\begin{Bmatrix}\Psi(\beta_{\text{old}},\Delta p_{\text{old}})\\ f(\beta_{\text{old}},\Delta p_{\text{old}})\end{Bmatrix}. \tag{43}$$

The corrections can then be computed and added to the solutions, i.e.,

$$\boldsymbol{\beta}_{\text{new}} = \boldsymbol{\beta}_{\text{old}} + d\boldsymbol{\beta} \quad\text{and}\quad \Delta p_{\text{new}} = \Delta p_{\text{old}} + d\Delta p. \tag{44}$$

Once the process is iterated to convergence, the variables are updated as

$$\Delta\boldsymbol{\epsilon}^p = \frac{\Delta p}{2}(\boldsymbol{n}_n+\boldsymbol{n}), \tag{45}$$

$$\boldsymbol{X} = e^{-a\Delta p}\boldsymbol{X}_n + e^{-\frac{a\Delta p}{2}}\frac{2}{3}C\Delta\boldsymbol{\epsilon}^p, \tag{45'}$$

$$\boldsymbol{\sigma} = \boldsymbol{\beta} + \boldsymbol{X}. \tag{45''}$$

The consistent tangent operator awaits determination. Totally differentiating both sides of Eq. (37) with respect to $\boldsymbol{\beta}, \Delta p$, and $\boldsymbol{\epsilon}$ gives

$$d\boldsymbol{\Psi} = \frac{\partial\boldsymbol{\Psi}}{\partial\boldsymbol{\beta}}:d\boldsymbol{\beta} + \frac{\partial\boldsymbol{\Psi}}{\partial\Delta p}d\Delta p - \mathcal{C}^e:d\boldsymbol{\epsilon} = \boldsymbol{0}, \tag{46}$$

$$df = \boldsymbol{n}:d\boldsymbol{\beta} - \frac{dR}{d\Delta p}d\Delta p = 0. \tag{46'}$$

Solving Eq. (46) for $d\boldsymbol{\beta}$ and $d\Delta p$ gives

$$d\boldsymbol{\beta} = \left[\frac{\partial\boldsymbol{\Psi}}{\partial\boldsymbol{\beta}} + \frac{\frac{\partial\boldsymbol{\Psi}}{\partial\Delta p}\otimes\boldsymbol{n}}{\frac{dR}{d\Delta p}}\right]^{-1}:\mathcal{C}^e:d\boldsymbol{\epsilon}, \tag{47}$$

$$d\Delta p = \frac{\boldsymbol{n}:d\boldsymbol{\beta}}{\frac{dR}{d\Delta p}}. \tag{47'}$$

Meanwhile, one has

$$d\boldsymbol{\sigma} = d\boldsymbol{\beta} + d\boldsymbol{X}, \tag{48}$$

$$d\boldsymbol{X} = \frac{\partial\boldsymbol{X}}{\partial\boldsymbol{\beta}}:d\boldsymbol{\beta} + \frac{\partial\boldsymbol{X}}{\partial\Delta p}d\Delta p. \tag{48'}$$

Combining Eqs. (47) and (48) gives

$$d\boldsymbol{\sigma} = d\boldsymbol{\beta} + \frac{\partial \boldsymbol{X}}{\partial \boldsymbol{\beta}} : d\boldsymbol{\beta} + \frac{\partial \boldsymbol{X}}{\partial \Delta p} d\Delta p = \left[\mathcal{I} + \frac{\partial \boldsymbol{X}}{\partial \boldsymbol{\beta}} + \frac{\frac{\partial \boldsymbol{X}}{\partial \Delta p} \otimes \boldsymbol{n}}{\frac{dR}{d\Delta p}} \right] : d\boldsymbol{\beta}$$
$$= \left[\mathcal{I} + \frac{\partial \boldsymbol{X}}{\partial \boldsymbol{\beta}} + \frac{\frac{\partial \boldsymbol{X}}{\partial \Delta p} \otimes \boldsymbol{n}}{\frac{dR}{d\Delta p}} \right] : \left[\frac{\partial \boldsymbol{\Psi}}{\partial \boldsymbol{\beta}} + \frac{\frac{\partial \boldsymbol{\Psi}}{\partial \Delta p} \otimes \boldsymbol{n}}{\frac{dR}{d\Delta p}} \right]^{-1} : \mathcal{C}^e : d\boldsymbol{\epsilon}$$
$$\equiv \mathcal{C}^{alg} : d\boldsymbol{\epsilon} \tag{49}$$

where $\mathcal{C}^{alg}$ denotes the fourth-order consistent tangent operator. It can be verified that $\mathcal{C}^{alg}$ fulfills the major and minor symmetries (i.e., $\mathcal{C}^{alg}_{ijkl} = \mathcal{C}^{alg}_{klij} = \mathcal{C}^{alg}_{jikl} = \mathcal{C}^{alg}_{ijlk}$).

Till now, a rigorous second-order radial return algorithm has been developed. In the next section, a variational statement for homogenizing elastoplasic composites will be formulated using the variational asymptotic method, discretized in a finite-dimensional space, and solved using a multilevel Newton–Raphson method.

4. Variational asymptotic homogenization method

Consider an elastoplasic composite having an identifiable UC. Note that an elastic constituent can be treated as an elastoplastic one with an infinite initial yield stress. Introduce global coordinates $\boldsymbol{x} = (x_1, x_2, x_3)$ describing the macroscopic structure and local coordinates $\boldsymbol{y} = (y_1, y_2, y_3)$ describing the UC, and let $\boldsymbol{y}$ be related to $\boldsymbol{x}$ by

$$\boldsymbol{y} = \boldsymbol{x}/\epsilon, \tag{50}$$

where $\epsilon \ll 1$ denotes a scale ratio. Suppose that all the global and local variables at t_n are known. The task is to find the current displacements within the UC, u_i.

That a composite can be homogenized implies that u_i has its volume average over the UC, say $\bar{u}_i$, i.e., [51]

$$\bar{u}_i = \frac{1}{\Omega} \int_\Omega u_i dV \equiv \langle\langle u_i \rangle\rangle, \tag{51}$$

where Ω denotes the domain occupied by the UC (with boundary $\partial\Omega$) and also its volume, and $\langle\langle\cdot\rangle\rangle$ denotes the volume average of a quantity over Ω. u_i can be asymptotically expanded into the sum of $\bar{u}_i$ and a fluctuation function, χ_i, i.e.,

$$u_i(\boldsymbol{y}, \boldsymbol{x}) = \bar{u}_i(\boldsymbol{x}) + \epsilon \chi_i(\boldsymbol{y}, \boldsymbol{x}), \tag{52}$$

where χ_i is a periodic function of $\boldsymbol{y}$ and may also depend on $\boldsymbol{x}$, and $\epsilon\chi_i$ must be asymptotically smaller than $\bar{u}_i$. Note that Eq. (52) is not assumed a priori but can be derived using the variational asymptotic method [7]. Combining Eqs. (51) and (52) gives

$$\langle\langle \chi_i \rangle\rangle = 0. \tag{53}$$

Although $\epsilon\chi_i$ negligibly affects u_i, it may significantly affect the derivatives of u_i. Specifically,

$$\frac{\partial u_i}{\partial x_j} = \frac{1}{\epsilon} \frac{\partial u_i}{\partial y_j}\bigg|_{\boldsymbol{x}=\text{const}} + \frac{\partial u_i}{\partial x_j}\bigg|_{\boldsymbol{y}=\text{const}} = \frac{\partial \bar{u}_i}{\partial x_j} + \frac{\partial \chi_i}{\partial y_j} + \epsilon \frac{\partial \chi_i}{\partial x_j}, \tag{54}$$

where $\epsilon \partial \chi_i / \partial X_j$ is omissible because it negligibly contributes to the integral of a state function over the UC (see Eq. (60)). By definition,

$$\epsilon_{ij} = \frac{1}{2} \left(\frac{\partial u_i}{\partial x_j} + \frac{\partial u_j}{\partial x_i} \right). \tag{55}$$

Let

$$\bar{\epsilon}_{ij} = \frac{1}{2} \left(\frac{\partial \bar{u}_i}{\partial x_j} + \frac{\partial \bar{u}_j}{\partial x_i} \right) \quad \text{and} \quad \chi_{(ij)} = \frac{1}{2} \left(\frac{\partial \chi_i}{\partial y_j} + \frac{\partial \chi_j}{\partial y_i} \right). \tag{56}$$

Note that $\bar{\epsilon}_{ij}$ actually denotes the global strain tenor. Combining Eqs. (52), (55), and (56) gives

$$\epsilon_{ij} = \bar{\epsilon}_{ij} + \chi_{(ij)}. \tag{57}$$

Define a state function, W, as

$$W(\dot{\epsilon}_{ij}) = \frac{1}{2} \dot{\epsilon}_{ij} \mathcal{C}^{alg}_{ijkl} \dot{\epsilon}_{kl}, \tag{58}$$

such that

$$\delta W = \dot{\sigma}_{ij} \delta \dot{\epsilon}_{ij}. \tag{59}$$

It can be verified that external forces negligibly contribute to the integral of W over the UC (see Eq. (60)). A variational principle can then be created for elastoplastic heterogenous materials as: among all the admissible velocities, the actual velocities make functional

$$U = \int_\Omega W dV \equiv \langle W \rangle \tag{60}$$

an absolute minimum (see Washizu [48] for more details), i.e.,

$$\delta U = \left\langle \frac{\partial W}{\partial \dot{\epsilon}_{ij}} \delta \dot{\epsilon}_{ij} \right\rangle = \langle \dot{\sigma}_{ij} \delta \dot{\chi}_{(ij)} \rangle = \langle \dot{\sigma}_{ij} \delta \dot{\chi}_{i,j} \rangle = 0 \tag{61}$$

and

$$\delta^2 U = \left\langle \frac{\partial^2 W}{\partial \dot{\epsilon}_{ij} \partial \dot{\epsilon}_{kl}} \delta \dot{\epsilon}_{ij} \delta \dot{\epsilon}_{kl} \right\rangle = \left\langle \mathcal{C}^{alg}_{ijkl} \delta \dot{\epsilon}_{ij} \delta \dot{\epsilon}_{kl} \right\rangle \geqslant 0, \tag{62}$$

where $\langle\cdot\rangle$ denotes the integral of a quantity over Ω. Note that the inequality in Eq. (62) holds because $\mathcal{C}^{alg}_{ijkl}$ is positive-definite.

Introduce the following matrix notations:

$$\bar{\epsilon} = \lfloor \bar{\epsilon}_{11} \quad 2\bar{\epsilon}_{12} \quad \bar{\epsilon}_{22} \quad 2\bar{\epsilon}_{13} \quad 2\bar{\epsilon}_{23} \quad \bar{\epsilon}_{33} \rfloor^T, \tag{63}$$

$$\begin{Bmatrix} \frac{\partial \chi_1}{\partial y_1} \\ \frac{\partial \chi_1}{\partial y_2} + \frac{\partial \chi_2}{\partial y_1} \\ \frac{\partial \chi_2}{\partial y_2} \\ \frac{\partial \chi_1}{\partial y_3} + \frac{\partial \chi_3}{\partial y_1} \\ \frac{\partial \chi_2}{\partial y_3} + \frac{\partial \chi_3}{\partial y_2} \\ \frac{\partial \chi_3}{\partial y_3} \end{Bmatrix} = \begin{bmatrix} \frac{\partial}{\partial y_1} & 0 & 0 \\ \frac{\partial}{\partial y_2} & \frac{\partial}{\partial y_1} & 0 \\ 0 & \frac{\partial}{\partial y_2} & 0 \\ \frac{\partial}{\partial y_3} & 0 & \frac{\partial}{\partial y_1} \\ 0 & \frac{\partial}{\partial y_3} & \frac{\partial}{\partial y_2} \\ 0 & 0 & \frac{\partial}{\partial y_3} \end{bmatrix} \begin{Bmatrix} \chi_1 \\ \chi_2 \\ \chi_3 \end{Bmatrix} \equiv \Gamma_h \chi, \tag{63'}$$

where Γ_h denotes an operator matrix, and χ denotes a column matrix containing the components of the fluctuation function. Let χ be discretized in a finite-dimensional space as

$$\chi(y_i, x_i) = S(y_i) \mathrm{X}(x_i), \tag{64}$$

where S denotes the shape function, and X denotes a column matrix containing the nodal values of the fluctuation function at all the active nodes. Eq. (57) can be discretized as

$$\epsilon = \bar{\epsilon} + \Gamma_h \mathrm{S} \mathrm{X}. \tag{65}$$

The task then becomes finding $\bar{\epsilon}$ and X. Here a multilevel Newton–Raphson method [39] is used for problem solving because:

1. $\bar{\epsilon}$ and X are implicitly coupled, making it numerically prohibitive to solve for them simultaneously;
2. this method fits a multiscale simulation well.

The method consists of an inner and an outer loop: in the inner loop, $\bar{\epsilon}$ is held fixed, and X is the variable; in the outer one, X is held fixed, and some global unknowns are the variables. Note that, if $\bar{\epsilon}$ is fully prescribed (this is usually the case in multiscale simulations), only the inner loop is needed. First consider the inner loop. The incremental form of Eq. (61) writes

$$\delta U^* = \left\langle \Delta\sigma_{ij}\delta\left(\Delta\chi_{i,j}\right)\right\rangle = 0 \tag{66}$$

or

$$\delta U^* = \left\langle \left[\sigma_{ij} - (\sigma_n)_{ij}\right]\delta\left[\chi_{i,j} - (\chi_n)_{i,j}\right]\right\rangle = \left\langle \left[\sigma_{ij} - (\sigma_n)_{ij}\right]\delta\chi_{i,j}\right\rangle = 0. \tag{67}$$

Eq. (67) can be discretized as

$$\delta U^* = \delta \mathrm{X}^T\left\langle (\Gamma_h S)^T[\sigma(\mathrm{X}) - \sigma_n]\right\rangle = 0, \tag{68}$$

where σ denotes the local stress column matrix. The second equality in Eq. (68) holds only if

$$\Psi_{\text{in}}(\mathrm{X}) = \left\langle (\Gamma_h S)^T[\sigma(\mathrm{X}) - \sigma_n]\right\rangle = 0. \tag{69}$$

Suppose that Eq. (69) is zeroed within each previous step. This implies that

$$\left\langle (\Gamma_h S)^T\sigma_n\right\rangle = 0. \tag{70}$$

Substituting Eq. (70) into Eq. (69) gives

$$\Psi_{\text{in}}(\mathrm{X}) = \left\langle (\Gamma_h S)^T\sigma(\mathrm{X})\right\rangle = 0. \tag{71}$$

The task of the inner loop is hereby solving Eq. (71) (rather than Eq. (69) to eliminate the accumulation of errors) for X. Requiring

$$\Psi_{\text{in}}(\mathrm{X}_{\text{old}} + \delta\mathrm{X}) = \Psi_{\text{in}}(\mathrm{X}_{\text{old}}) + \frac{\partial\Psi_{\text{in}}}{\partial\mathrm{X}}\delta\mathrm{X} = 0 \tag{72}$$

gives

$$\frac{\partial\Psi_{\text{in}}}{\partial\mathrm{X}}\delta\mathrm{X} = -\Psi_{\text{in}}(\mathrm{X}_{\text{old}}), \tag{73}$$

where

$$\frac{\partial\Psi_{\text{in}}}{\partial\mathrm{X}} = \left\langle (\Gamma_h S)^T\frac{\partial\sigma}{\partial\mathrm{X}}\right\rangle = \left\langle (\Gamma_h S)^T D(\Gamma_h S)\right\rangle \equiv D_{hh} \tag{74}$$

with D denoting the 6×6 instantaneous stiffness matrix condensed from $\mathcal{C}^{alg}$. The corrections can then be computed and added to the solution, i.e.,

$$\mathrm{X}_{\text{new}} = \mathrm{X}_{\text{old}} + d\mathrm{X}. \tag{75}$$

By definition, the global stress column matrix, $\bar{\sigma}$, is given by

$$\dot{\bar{\sigma}} = \frac{\partial}{\partial\dot{\bar{\epsilon}}}\langle\langle W\rangle\rangle = \left\langle\left\langle\frac{\partial W}{\partial\dot{\bar{\epsilon}}}\right\rangle\right\rangle = \left\langle\left\langle\left(\frac{\partial\dot{\epsilon}}{\partial\dot{\bar{\epsilon}}}\right)^T\frac{\partial W}{\partial\dot{\epsilon}}\right\rangle\right\rangle$$
$$= \left\langle\left\langle\left(I + \Gamma_h S\frac{\partial\mathrm{X}}{\partial\bar{\epsilon}}\right)^T\dot{\sigma}\right\rangle\right\rangle = \langle\langle\dot{\sigma}\rangle\rangle + \left(\frac{\partial\mathrm{X}}{\partial\bar{\epsilon}}\right)^T\left\langle\left\langle(\Gamma_h S)^T\dot{\sigma}\right\rangle\right\rangle, \tag{76}$$

where I denotes an identity matrix. Substituting the rate form of Eq. (71) into Eq. (76) gives

$$\dot{\bar{\sigma}} = \langle\langle\dot{\sigma}\rangle\rangle \quad \text{or} \quad \bar{\sigma} = \int_0^t\dot{\bar{\sigma}}dt = \int_0^t\langle\langle\dot{\sigma}\rangle\rangle dt = \langle\langle\sigma\rangle\rangle. \tag{77}$$

Next consider the outer loop. $\bar{\sigma}$ and $\bar{\epsilon}$ can be partitioned as

$$\bar{\sigma} = \begin{Bmatrix}\bar{\sigma}_u\\ \bar{\sigma}_k\end{Bmatrix} \quad \text{and} \quad \bar{\epsilon} = \begin{Bmatrix}\bar{\epsilon}_k\\ \bar{\epsilon}_u\end{Bmatrix}, \tag{78}$$

respectively, where the subscripts k and u denote the known and unknown components, respectively. Let

$$\bar{\sigma}^* = \begin{Bmatrix}\bar{\sigma}_u\\ \bar{\epsilon}_u\end{Bmatrix} \quad \text{and} \quad \bar{\epsilon}^* = \begin{Bmatrix}\bar{\epsilon}_k\\ \bar{\sigma}_k\end{Bmatrix}, \tag{79}$$

respectively. Set $\bar{\sigma}^*$ to be the variable, and choose

$$\Psi_{\text{out}}(\bar{\sigma}^*) = \bar{\epsilon}^*(\bar{\sigma}^*) - \bar{\varepsilon}^* \tag{80}$$

as the function to be zeroed in the outer loop, where $\bar{\varepsilon}^*$ denotes the prescribed value of $\bar{\epsilon}^*$ within the current load increment. Requires

$$\Psi_{\text{out}}\left(\bar{\sigma}^*_{\text{old}} + d\bar{\sigma}^*\right) = \bar{\epsilon}^*\left(\bar{\sigma}^*_{\text{old}}\right) + d\bar{\epsilon}^* - \bar{\varepsilon}^* = 0. \tag{81}$$

Substituting Eq. (80) into Eq. (81) gives

$$d\bar{\epsilon}^* = -\Psi_{\text{out}}\left(\bar{\sigma}^*_{\text{old}}\right). \tag{82}$$

It is beneficial to relate $d\bar{\sigma}^*$ to $d\bar{\epsilon}^*$. Combining Eqs. (49) and (77) gives

$$d\bar{\sigma} = \langle\langle d\sigma\rangle\rangle = \left\langle\left\langle\frac{\partial\sigma}{\partial\epsilon}\frac{\partial\epsilon}{\partial\bar{\epsilon}}\right\rangle\right\rangle d\bar{\epsilon} = \langle\langle D\rangle\rangle d\bar{\epsilon} \equiv \bar{D}d\bar{\epsilon}, \tag{83}$$

where the third equality holds because X is held fixed. Eq. (83) can be partitioned as

$$\begin{Bmatrix}d\bar{\sigma}_u\\ d\bar{\sigma}_k\end{Bmatrix} = \begin{bmatrix}\bar{D}_{uk} & \bar{D}_{uu}\\ \bar{D}_{kk} & \bar{D}_{ku}\end{bmatrix}\begin{Bmatrix}d\bar{\epsilon}_k\\ d\bar{\epsilon}_u\end{Bmatrix}. \tag{84}$$

Rearranging Eq. (84) gives

$$\begin{Bmatrix}d\bar{\sigma}_u\\ d\bar{\epsilon}_u\end{Bmatrix} = \begin{bmatrix}\bar{D}_{uk} - \bar{D}_{uu}\bar{D}_{ku}^{-1}\bar{D}_{kk} & \bar{D}_{uu}\bar{D}_{ku}^{-1}\\ -\bar{D}_{ku}^{-1}\bar{D}_{kk} & \bar{D}_{ku}^{-1}\end{bmatrix}\begin{Bmatrix}d\bar{\epsilon}_k\\ d\bar{\sigma}_k\end{Bmatrix} \tag{85}$$

or

$$d\bar{\sigma}^* = \bar{D}^*d\bar{\epsilon}^*. \tag{86}$$

Multiplying both sides of Eq. (82) by $\bar{D}^*$ gives

$$d\bar{\sigma}^* = -\bar{D}^*\Psi_{\text{out}}\left(\bar{\sigma}^*_{\text{old}}\right). \tag{87}$$

The corrections can then be computed and added to the solution, i.e.,

$$\bar{\sigma}^*_{\text{new}} = \bar{\sigma}^*_{\text{old}} + d\bar{\sigma}^*. \tag{88}$$

The whole process is iterated to convergence.

The multilevel Newton–Raphson method is not guaranteed to converge to the solution and often gets "lost" if started far from the solution. Fortunately, it can be embedded in a Euler–Newton predictor–corrector method [20] for improved convergence. This method consists of the following steps:

1. Euler predictor step—proceed in the tangent direction of the loading path;
2. Newton corrector step—bring the predictions back to the loading path.

More details on the Euler predictor step can be found in Appendix B.

5. Numerical examples

In this section, the versatility and accuracy of the present approach are demonstrated through homogenizing binary, long fiber-reinforced, and particle-reinforced MMCs. For validation purposes, the predictions by the present approach will be compared with those by ANSYS.

5.1. Long fiber-reinforced MMC

First consider a long fiber-reinforced MMC consisting of an elastoplastic aluminum matrix and numerous cylindrical, elastic SiC long fibers arranged in a square array, with a volume fraction of fibers of 10%. Here let aluminum only exhibit combined isotropic-kinematic hardening (see Eqs. (21) and (22)), and following Zhao and Lee [53], let the material parameters of SiC and aluminum take the values listed in Table 1, where E and ν denote Young's modulus and Poisson's ratio, respectively. Let the UC of this composite consist of a square matrix and a circular fiber located at its center. Choose the center of the UC as the origin of the local coordinates, y_i, and the fiber direction and the length

Table 1
Material parameters of SiC and aluminum.

Elastic constants				
	E(GPa)			v
SiC	490			0.17
Aluminum	65			0.3
Plastic parameters of aluminum				
σ_y(MPa)	Q(MPa)	b	C(MPa)	a
154	140.2	7.094	7019	118.6

and width directions of the UC as the y_1-, y_2-, and y_3-directions, respectively.

In the present approach, the 2D UC is meshed with 4-node quadrilateral elements having 3 degrees of freedom (DOFs) at each node, and the meshed UC consists of 1216 elements (see Fig. 1(a)). In ANSYS, a 3D UC is meshed with 8-node hexahedra elements (SOLID45), and the meshed UC also consists of 1216 elements (see Fig. 1(b)). Both finite element models are found to be capable of producing converged results.

Fig. 2 shows the stress–strain hysteresis loops of the composite undergoing uniaxial deformation in the y_1- and y_2-directions, respectively. Let each loading path consist of the following steps:

1. initial loading—the major strain is increased from 0 to 0.005;
2. initial unloading—the major strain is decreased from 0.005 to 0;
3. reverse loading—the major strain is decreased from 0.0 to −0.005;
4. reverse unloading—the major strain is increased from −0.005 to 0.

It can be seen that the composite exhibits a bilinear stress–strain relationship when loaded in the y_1-direction and a nonlinear one when loaded in the y_2-direction. This can be understood by investigating the stress distribution in the matrix. Specifically, in the former case, this stress distribution remains approximately uniform during continued deformation, causing the matrix to yield simultaneously everywhere; in the latter case, it remains highly nonuniform, causing the matrix to yield successively at different locations. In addition, in Fig. 2, the composite exhibits a pseudo Bauschinger effect. This effect is said to be "pseudo" because its cause is not metallurgical but the local residual stresses due to initial loading [37]. At last, in Fig. 2, the predictions by the present approach perfectly agree with those by ANSYS. This indicates that the present approach can handle complex loading paths.

Fig. 3 shows the stress–strain hysteresis loops of the composite undergoing longitudinal shear deformation. It can be seen that the stress–strain relationship here is also nonlinear. Therefore, the corresponding discussion for Fig. 2 holds here. Meanwhile, the present approach actually makes the same predictions using a 2D and a 3D UC, while ANSYS has to use a 3D UC to handle out-of-plane loads and displacements. In Fig. 3, the predictions by the present approach agree well with those by ANSYS. Figs. 2 and 3 indicate that the present approach can homogenize long fiber-reinforced MMCs using 2D UCs.

Next let aluminum also exhibit plastic transverse isotropy in the y_2y_3 plane with its R_i's taking the three sets of values listed in Table 2 in three cases (see Appendix A for more details).

Fig. 4 shows the stress–strain hysteresis loops of the composite undergoing uniaxial deformation in the y_2-direction. In fact, the following findings can be obtained after some calculation:

1. all sets of values yield the same initial yield stress in the y_1-direction;

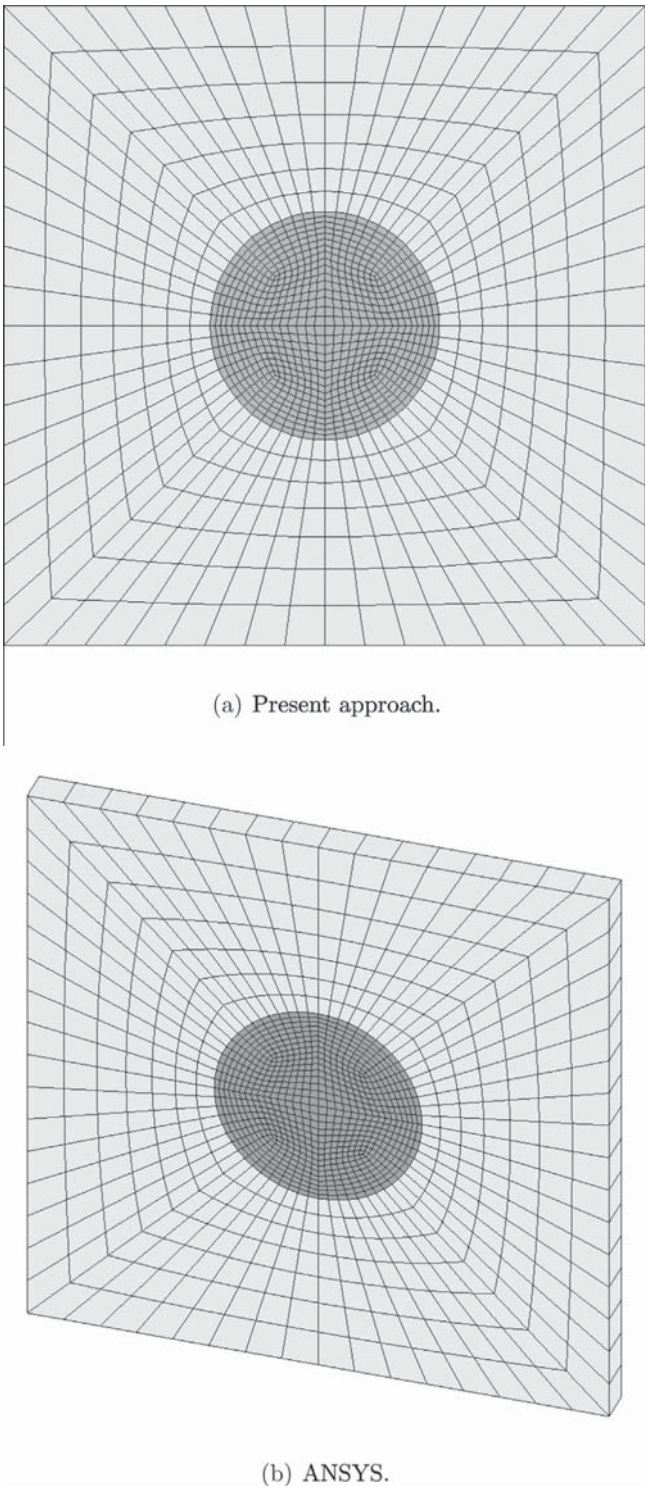

(a) Present approach.

(b) ANSYS.

Fig. 1. Meshed UCs of a long fiber-reinforced MMC.

2. the initial yield stress in the y_2-direction decreases with increasing R_3.

Accordingly, in Fig. 4, as R_3 increases, the composite becomes more flexible. Meanwhile, in Fig. 4, the predictions by the present approach agree well with those by ANSYS. Figs. 2 and 4 indicate that the present approach can handle complex material models.

Fig. 5 shows the initial yield surfaces of the composite, where $\bar{\sigma}_{11} = 0$. It can be seen that these yield surfaces all have prominent

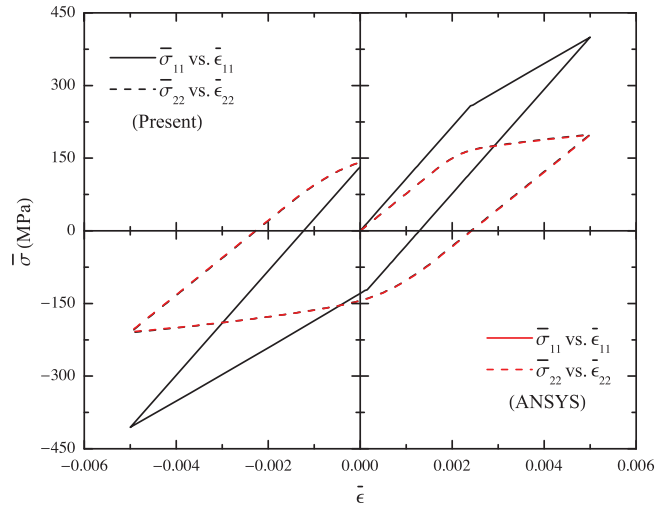

Fig. 2. Stress–strain hysteresis loops of a long fiber-reinforced MMC undergoing uniaxial deformation in the y_1- and y_2-directions, respectively.

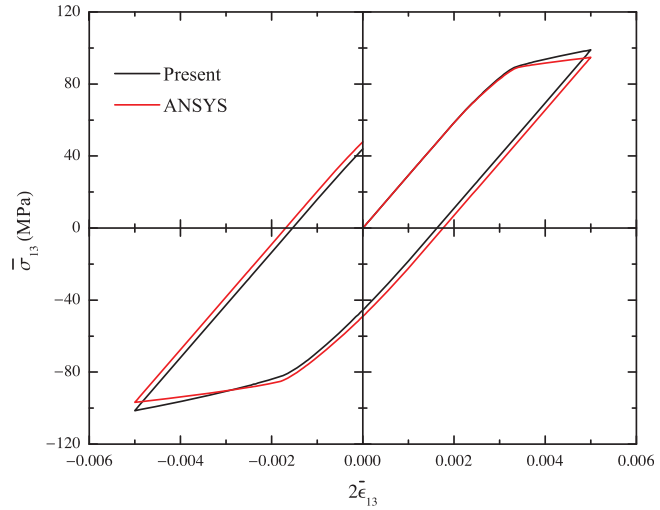

Fig. 3. Stress–strain hysteresis loops of a long fiber-reinforced MMC undergoing longitudinal shear deformation.

Table 2
R_i's in three cases.

	R_1	R_2	R_3	R_4	R_5	R_6
1	1	1	0.5	1	0.5	2
2	1	1	1	1	1	1
3	1	1	2	1	2	0.5

vertices. In fact, a point on a yield surface here is determined by finding the location where the matrix starts yielding and the global stresses at the onset of initial yielding, both of which depend on the stress distribution in the matrix. Let θ denote the inclination angle of a proportional loading path in the $\bar{\sigma}_{22}\bar{\sigma}_{33}$-plane. The numerical results indicates that the stress distribution is highly nonuniform and very sensitive to θ. This causes the location of an aforementioned point to irregularly vary with varying θ. The class of such points, an initial yield surface, hereby tends to be non-smooth. In addition, for aluminum, as R_3 increases, the yield surface remains unchanged at $\theta = 45^\circ$ but shrinks along $\theta = 135^\circ$.

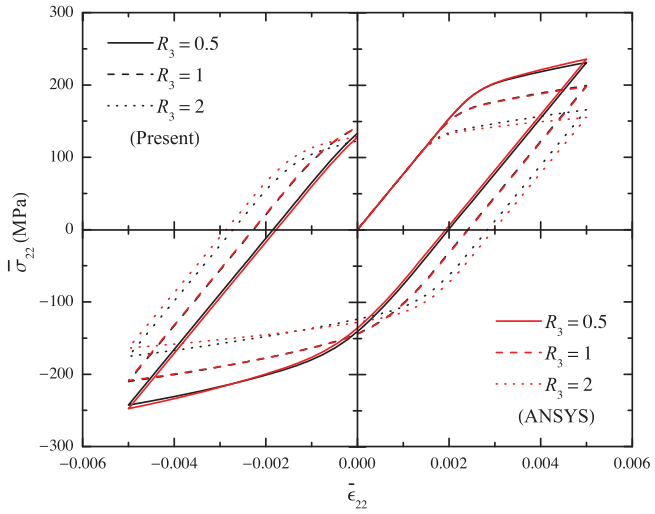

Fig. 4. Stress–strain hysteresis loops of a long fiber-reinforced MMC with a plastically anisotropic matrix, undergoing uniaxial deformation in the y_2-direction.

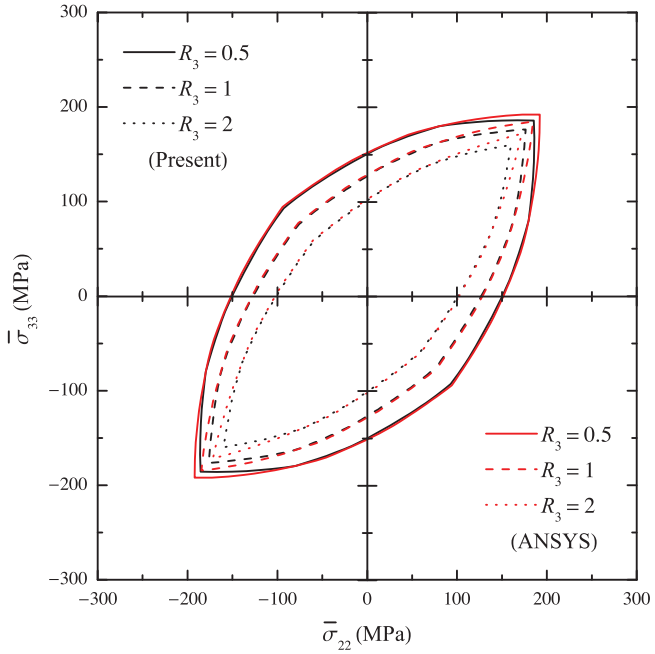

Fig. 5. Initial yield surfaces of a long fiber-reinforced MMC with a plastically anisotropic matrix, where $\bar{\sigma}_{11} = 0$.

Accordingly, for the composite, as R_3 increases, the yield surface exhibits a similar trend except that it slightly shrinks along $\theta = 45^\circ$ due to the existence of fibers (see Fig. 5). At last, in Fig. 5, the predictions by the present approach agree well with those by ANSYS. This indicates that the present approach can handle complex loading conditions and recover the local fields.

5.2. Particle-reinforced MMC

Next consider a particle-reinforced MMC consisting of an aluminum matrix and numerous spherical SiC particles arranged in a cubic array, with a volume fraction of particles of 10%. Let the material parameters of SiC and aluminum take the values listed in Table 1, and let the UC of this composite consist of a cubic matrix and a spherical particle located at its center. Here choose the

length, width, and height directions of the UC as the y_1-, y_2-, and y_3-directions, respectively.

In the present approach and ANSYS, the same UC is meshed with 8-node hexahedra elements having 3 DOFs at each node, and the meshed UC consists of 1512 elements (see Fig. 6). This finite element model is found to be capable of producing converged results.

Fig. 7 shows the stress–strain hysteresis loops of the composite undergoing uniaxial deformation in the y_1-direction. It can be seen that the stress–strain relationship here is also nonlinear. Therefore, the corresponding discussion for Fig. 2 holds here. Meanwhile, in Fig. 7, the predictions by the present approach agree well with those by ANSYS.

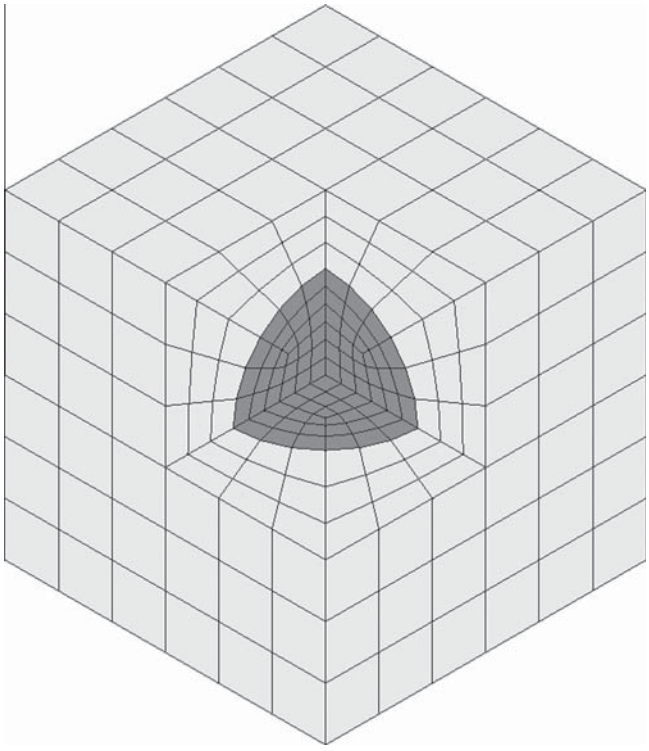

Fig. 6. Meshed UC of a particle-reinforced MMC.

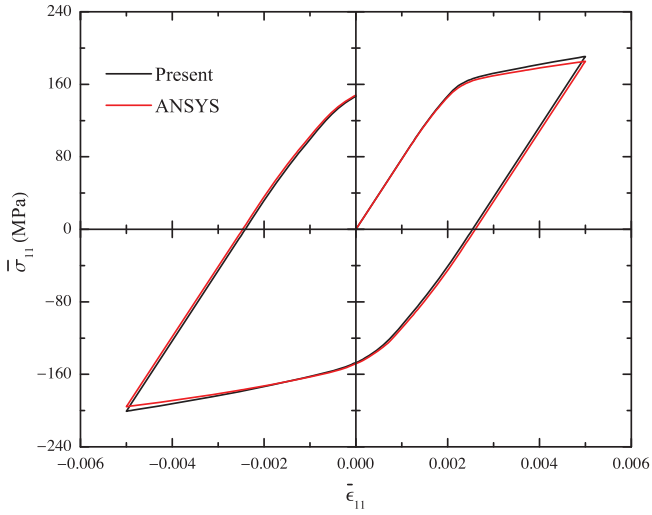

Fig. 7. Stress–strain hysteresis loops of a particle-reinforced MMC undergoing uniaxial deformation in the y_1-direction.

5.3. Short fiber-reinforced MMC

Last consider a short fiber-reinforced MMC consisting of an aluminum matrix and numerous cylindrical SiC short fibers arranged in a cuboid array, with a volume fraction of fibers of 10%. Let the material parameters of SiC and aluminum take the values listed in Table 1. Let the UC of this composite consist of a cuboid matrix and a cylindrical short fiber located at its center. Following Levy and Papazian [28],

1. define the aspect ratio of a short fiber as the ratio of the fiber length to the fiber diameter;
2. define the aspect ratio of a UC as the ratio of the UC length to the UC width;
3. set these two ratios to be equal.

Following Hom [24], set the aspect ratio of the short fiber to be 5. Here choose the length, width, and height directions of the UC as the y_1-, y_2-, and y_3-directions, respectively.

In the present approach and ANSYS, the same UC is meshed with 8-node hexahedra elements having 3 DOFs at each node, and the meshed UC consists of 4080 elements (see Fig. 8). This finite element model is found to be capable of producing converged results.

Fig. 9 shows the stress–strain hysteresis loops of the composite undergoing uniaxial deformation in the y_1- and y_2-directions, respectively. It can be seen that the composite exhibits nonlinear stress–strain relationships when loaded in both directions. This is because, in each case, the stress distribution in the matrix remains highly nonuniform, causing the matrix to yield successively at different locations. Meanwhile, in Fig. 9, the predictions by the present approach agree well with those by ANSYS. Figs. 7 and 9 indicate that the present approach can homogenize composites of 3D heterogeneities such as particle- and short fiber-reinforced MMCs.

It is beneficial to evaluate the effect of the type of reinforcement on the response of an MMC. Fig. 10 compares the predictions by the present approach in Figs. 2, 7, and 9. As expected, in Fig. 10 (a), long fibers most significantly strengthen MMCs in the y_1-direction, and short fibers come second. Meanwhile, in Fig. 10(b), different types of reinforcement similarly strengthen MMCs in the y_2-direction. This indicates that the type of reinforcement negligibly affects the response of an MMC perpendicular to the fiber direction. In fact, numerical tests indicate that the volume fraction of reinforcement plays a more important role here.

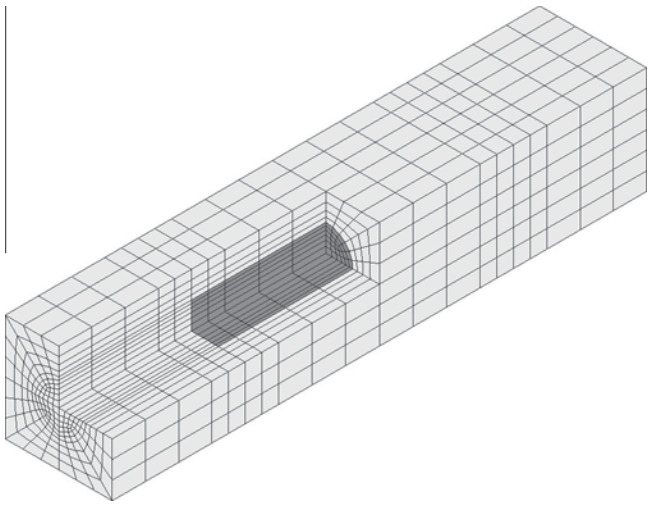

Fig. 8. Meshed UC of a short fiber-reinforced MMC.

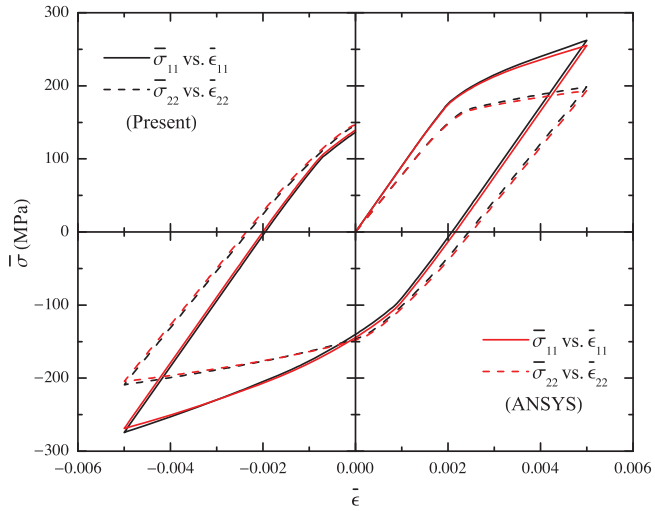

Fig. 9. Stress–strain hysteresis loops of a short fiber-reinforced MMC undergoing uniaxial deformation in the y_1- and y_2-directions, respectively.

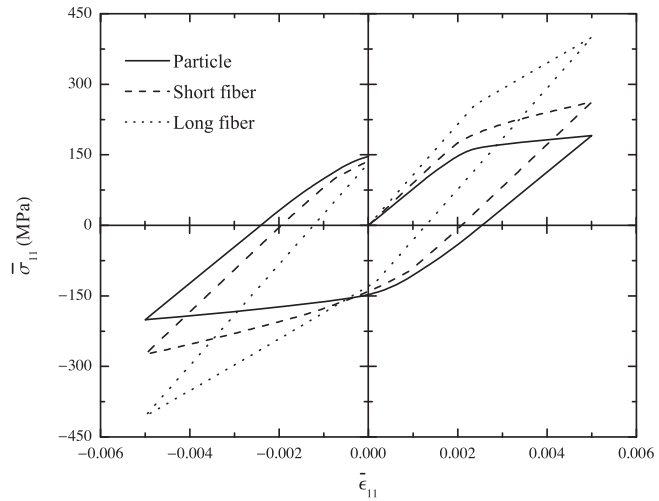

(a) y_1-direction.

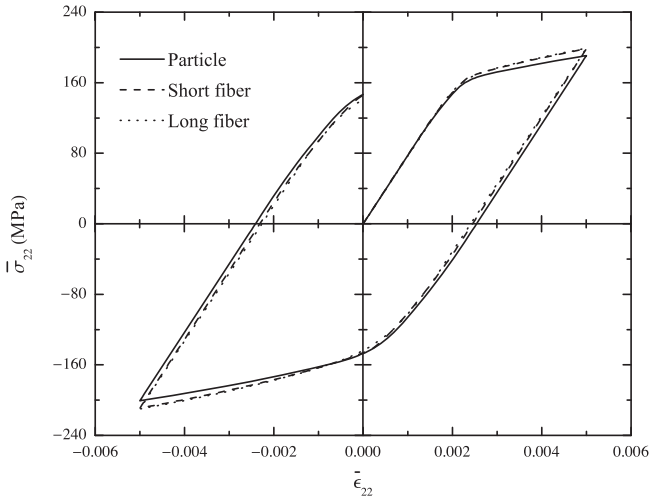

(b) y_2-direction.

Fig. 10. Stress–strain hysteresis loops of MMCs with different types of reinforcement, undergoing uniaxial deformation in the y_1- and y_2-directions, respectively.

6. Conclusions

In this paper, a micromechanics approach to homogenizing elastoplastic composites is developed. A rigorous second-order radial return algorithm, which can handle elastic and plastic anisotropy and nonlinear kinematic hardening, is developed. A simplified functional equation governing the response of the UC is derived using the variational asymptotic method, discretized in a finite-dimensional space, and solved using a multilevel Newton–Raphson method. The versatility and accuracy of the present approach are demonstrated through homogenizing long fiber-, particle-, and short fiber-reinforced MMCs. Different types of reinforcement are found to differently affect the response of MMCs. The present approach is found to be capable of handling various microstructures, complex material models, complex loading conditions, and complex loading paths.

The following conclusions can be drawn from the above findings:

1. the present approach can be embedded in a multiscale finite element code to make predictions on the microscopic scale;
2. more sophisticated material models can be implemented in it;
3. the present radial return algorithm can be implemented in various finite element codes, while various integration schemes for elastoplastic constitutive relations (e.g., a first-order radial return algorithm) can be implemented in the present homogenization approach.

Acknowledgements

This work is supported by the US AFOSR Multiscale Structural Mechanics and Prognosis Program. The views and conclusions contained herein are those of the authors and should not be interpreted as necessarily representing the official policies or endorsement, either expressed or implied, of the sponsor.

Appendix A. Plastic anisotropy parameters

The R-value is commonly used to describe the plastic anisotropy of rolled sheet metals. It can be measured in a uniaxial tensile test. The R-value of a tensile specimen cut from a sheet is defined as the ratio of the plastic strain in the width direction to that in the thickness direction, i.e.,

$$R = \frac{\epsilon_W}{\epsilon_T}. \tag{A.1}$$

Since the R-value generally varies with the cut angle with respect to the rolling direction of the sheet, α, an averaged R-value,

$$\bar{R} = \frac{R_0 + 2R_{45} + R_{90}}{4}, \tag{A.2}$$

is often adopted, where R_α denotes the R-value measured in a tensile specimen of cut angle α.

Benzerga and Besson [6] introduced six strain rate ratios, R_{ij}'s, to fully describe the plastic anisotropy of a 3D structure. These ratios can be measured in a series of uniaxial tensile and simple shear tests. Introduce Cartesian coordinates $\boldsymbol{x} = (x_1, x_2, x_3)$ with its three axes parallel to the orthotropic axes of a material. These ratios are defined as

$$R_{11} = \frac{\dot{\epsilon}_{22}}{\dot{\epsilon}_{33}}, \quad R_{12} = \frac{\dot{\epsilon}_{12}}{\dot{\epsilon}_{33}}, \quad R_{22} = \frac{\dot{\epsilon}_{33}}{\dot{\epsilon}_{11}}, \tag{A.3}$$

$$R_{13} = \frac{\dot{\epsilon}_{13}}{\dot{\epsilon}_{22}}, \quad R_{23} = \frac{\dot{\epsilon}_{23}}{\dot{\epsilon}_{11}}, \quad R_{33} = \frac{\dot{\epsilon}_{11}}{\dot{\epsilon}_{22}} \tag{A.3′}$$

and can be written in the Voigt notation as

$$R_1 = R_{11}, \quad R_2 = R_{12}, \quad R_3 = R_{22}, \tag{A.4}$$

$$R_4 = R_{13}, \quad R_5 = R_{23}, \quad R_6 = R_{33}. \tag{A.4′}$$

Eq. (A.3) implies that $R_6 = 1/R_1R_3$. Therefore, only five out of six R_i's are independent.

$\mathcal{H}_{ijkl}$ can be written in the Voigt notation as H_{ij}. The diagonal components of H_{ij} can be related to R_i by

$$H_{11} = -\frac{2}{3}\frac{R_1R_3 - 2R_1 - 2}{R_1 + 1}, \quad \frac{H_{22}}{H_{11}} = -\frac{1}{2}\frac{(2R_2 + 1)(R_1R_3 + 1)}{R_1R_3 - 2R_1 - 2}, \tag{A.5}$$

$$\frac{H_{33}}{H_{11}} = 1 - \frac{3(R_1R_3 - 1)}{R_1R_3 - 2R_1 - 2}, \quad \frac{H_{44}}{H_{11}} = -\frac{1}{2}\frac{(2R_4 + 1)(R_3 + 1)R_1}{R_1R_3 - 2R_1 - 2}, \tag{A.5′}$$

$$\frac{H_{55}}{H_{11}} = -\frac{1}{2}\frac{(2R_5 + 1)(R_1 + 1)}{R_1R_3 - 2R_1 - 2}, \quad \frac{H_{66}}{H_{11}} = 1 - \frac{3R_1(R_3 - 1)}{R_1R_3 - 2R_1 - 2}, \tag{A.5″}$$

while the off-diagonal components vanish (see more details on $\mathcal{H}$ in Benzerga and Besson [6], Appendix A).

A special case of plastic anisotropy is plastic transverse isotropy, in which case only two out of six R_i's are independent. Let the x_2x_3 plane be the plane of plastic isotropy. The correlation among R_i's is given by

$$R_3 = R_5 = \frac{1}{R_6} \equiv R \quad \text{and} \quad R_2 = R_4 \equiv R'. \tag{A.6}$$

Substituting Eq. (A.6) into Eq. (A.5) and rearranging the equations give

$$H_{11} = \frac{1}{3}(4 - R), \quad H_{22} = H_{44} = \frac{1}{6}(R + 1)(2R' + 1), \tag{A.7}$$

$$H_{33} = H_{55} = H_{66} = \frac{1}{3}(2R + 1). \tag{A.7′}$$

Appendix B. Euler predictor step

Here the task becomes finding the current velocities within the UC, $\dot{u}_i$. Note that the rate of a quantity can be converted to its corresponding increment by multiplying it by Δt. Eq. (60) can be discretized as

$$U = \frac{1}{2}\left(\dot{\mathrm{X}}^T D_{hh}\dot{\mathrm{X}} + 2\dot{\mathrm{X}}^T D_{h\epsilon}\dot{\bar{\epsilon}} + \dot{\bar{\epsilon}}^T D_{\epsilon\epsilon}\dot{\bar{\epsilon}}\right), \tag{B.1}$$

where

$$D_{hh} = \left\langle (\Gamma_h S)^T D (\Gamma_h S) \right\rangle, \quad D_{h\epsilon} = \left\langle (\Gamma_h S)^T D \right\rangle, \quad D_{\epsilon\epsilon} = \langle D \rangle. \tag{B.2}$$

Minimizing U in Eq. (B.1) gives

$$D_{hh}\dot{\mathrm{X}} = -D_{h\epsilon}\dot{\bar{\epsilon}} \quad \text{or} \quad \dot{\mathrm{X}} = \mathrm{X}_0\dot{\bar{\epsilon}}, \tag{B.3}$$

which implies that $\dot{\mathrm{X}}$ is proportional to $\dot{\bar{\epsilon}}$. Substituting Eq. (B.3) into Eq. (B.1) gives

$$U = \frac{1}{2}\dot{\bar{\epsilon}}^T\left(\mathrm{X}_0^T D_{h\epsilon} + D_{\epsilon\epsilon}\right)\dot{\bar{\epsilon}} \equiv \frac{\Omega}{2}\dot{\bar{\epsilon}}^T\bar{D}\dot{\bar{\epsilon}}, \tag{B.4}$$

where here $\bar{D}$ denotes the instantaneous effective stiffness matrix rather than a variant of a Jacobian matrix (see Section 4). By definition,

$$\dot{\bar{\sigma}} = \frac{\partial}{\partial\dot{\bar{\epsilon}}}\langle\langle W \rangle\rangle = \bar{D}\dot{\bar{\epsilon}}. \tag{B.5}$$

Eq. (B.5) can be partitioned as

$$\begin{Bmatrix} \dot{\bar{\sigma}}_u \\ \dot{\bar{\sigma}}_k \end{Bmatrix} = \begin{bmatrix} \bar{D}_{uk} & \bar{D}_{uu} \\ \bar{D}_{kk} & \bar{D}_{ku} \end{bmatrix} \begin{Bmatrix} \dot{\bar{\epsilon}}_k \\ \dot{\bar{\epsilon}}_u \end{Bmatrix}. \tag{B.6}$$

Rearranging Eq. (B.6) gives

$$\begin{Bmatrix} \dot{\bar{\sigma}}_u \\ \dot{\bar{\epsilon}}_u \end{Bmatrix} = \begin{bmatrix} \bar{D}_{uk} - \bar{D}_{uu}\bar{D}_{ku}^{-1}\bar{D}_{kk} & \bar{D}_{uu}\bar{D}_{ku}^{-1} \\ -\bar{D}_{ku}^{-1}\bar{D}_{kk} & \bar{D}_{ku}^{-1} \end{bmatrix} \begin{Bmatrix} \dot{\bar{\epsilon}}_k \\ \dot{\bar{\sigma}}_k \end{Bmatrix}, \tag{B.7}$$

from which the global response of the UC can be determined. After this, the local deformation gradient rates can be obtained as

$$\dot{\epsilon} = \dot{\bar{\epsilon}} + \Gamma_h S \mathrm{X}_0 \dot{\bar{\epsilon}}. \tag{B.8}$$

References

[1] Aboudi J. Elastoplasticity theory for composite materials. Solid Mech Arch 1986;11:141–83.
[2] Aboudi J. Micromechanical prediction of initial and subsequent yield surfaces of metal matrix composites. Int J Plast 1990;6:471–84.
[3] Artioli E, Auricchio F, Beirão da Veiga L. Second-order accurate integration algorithms for von-mises plasticity with a nonlinear kinematic hardening mechanism. Comput Methods Appl Mech Eng 2007;196:1827–46.
[4] Azoti WL, Tchalla A, Koutsawa Y, Makradi A, Rauchs G, Belouettar S, et al. Mean-field constitutive modeling of elasto-plastic composites using two (2) incremental formulations. Compos Struct 2013;105:256–62.
[5] Bensoussan A, Lions JL, Papanicolau G. Asymptotic analysis for periodic structures. Elsevier; 1978.
[6] Benzerga AA, Besson J. Plastic potentials for anisotropic porous solids. Eur J Mech A/Solids 2001;20:397–434.
[7] Berdichevsky LV. Variational principles of continuum mechanics: II. Applications. New York: Springer; 2009.
[8] Berveiller M, Zaoui A. An extension of the self-consistent scheme to plastically-flowing polycrystals. J Mech Phys Solids 1978;26:325–44.
[9] Besson J, Cailletaud G, Chaboche JL, Forest S. Non-linear mechanics of materials. Solid mechanics and its applications, vol. 167. New York: Springer; 2010.
[10] Brassart L, Stainier L, Doghri I, Delannay L. A variational formulation for the incremental homogenization of elasto-plastic composites. J Mech Phys Solids 2011;59:2455–75.
[11] Brassart L, Stainier L, Doghri I, Delannay L. Homogenization of elasto-(visco) plastic composites based on an incremental variational principle. Int J Plast 2012;36:86–112.
[12] Chaboche JL. Constitutive equations for cyclic plasticity and cyclic viscoplasticity. Int J Plast 1989;5:247–302.
[13] Doghri I. Fully implicit integration and consistent tangent modulus in elasto-plasticity. Int J Numer Methods Eng 1993;36:3915–32.
[14] Doghri I, Brassart L, Adam L, Gerard JS. A second-moment incremental formulation for the mean-field homogenization of elasto-plastic composites. Int J Plast 2011;27:352–71.
[15] Dvorak GJ. Transformation field analysis of inelastic composite materials. Proc R Soc London Ser A Math Phys Sci 1992;437:311–27.
[16] Dvorak GJ, Benveniste Y. On transformation strains and uniform fields in multiphase elastic media. Proc R Soc London Ser A Math Phys Sci 1992;437:291–310.
[17] Dvorak GJ, Wafa AM, Bahei-El-Din YA. Implementation of the transformation field analysis for inelastic composite materials. Comput Mech 1994;14:201–28.
[18] Eyre DJ, Milton GW. A fast numerical scheme for computing the response of composites using grid refinement. Eur Phys J Appl Phys 1999;6:41–7.
[19] Fish J, Shek K, Pandheeradi M, Shephard MS. Computational plasticity for composite structures based on mathematical homogenization: theory and practice. Comput Methods Appl Mech Eng 1997;148:53–73.
[20] Garcia CB, Zangwill WI. Pathways to solutions, fixed points, and equilibria. Englewood Cliffs, NJ: Prentice-Hall; 1981.
[21] Ghosh S, Lee K, Moorthy S. Two scale analysis of heterogeneous elastic-plastic materials with asymptotic homogenization and voronoi cell finite element model. Comput Methods Appl Mech Eng 1996;132:63–116.
[22] Guedes J, Kikuchi N. Preprocessing and postprocessing for materials based on the homogenization method with adaptive finite element methods. Comput Methods Appl Mech Eng 1990;83:143–98.
[23] Hill R. Continuum micro-mechanics of elastoplastic polycrystals. J Mech Phys Solids 1965;13:89–101.
[24] Hom CL. Three-dimensional finite element analysis of plastic deformation in a whisker-reinforced metal matrix composite. J Mech Phys Solids 1992;40:991–1008.
[25] Jansson S. Homogenized nonlinear constitutive properties and local stress concentrations for composites with periodic internal structure. Int J Solids Struct 1992;29:2181–200.
[26] Kanouté P, Boso DP, Chaboche JL, Schrefler BA. Multiscale methods for composites: a review. Arch Comput Methods Eng 2009;16:31–75.

[27] Lebensohn RA, Tome CN. A self-consistent anisotropic approach for the simulation of plastic deformation and texture development of polycrystals: application to zirconium alloys. Acta Metall Mater 1993;41:2611–24.
[28] Levy A, Papazian JM. Tensile properties of short fiber-reinforced sic/al composites: part ii. finite-element analysis. Metall Trans A 1990;21:411–20.
[29] Markovic D, Ibrahimbegovic A. On micro–macro interface conditions for micro scale based fem for inelastic behavior of heterogeneous materials. Comput Methods Appl Mech Eng 2004;193:5503–23.
[30] Michel JC, Moulinec H, Suquet P. Effective properties of composite materials with periodic microstructure: a computational approach. Comput Methods Appl Mech Eng 1999;172:109–43.
[31] Michel JC, Moulinec H, Suquet P. A computational method based on augmented lagrangians and fast fourier transforms for composites with high contrast. Comput Modell Eng Sci 2000;1:79–88.
[32] Michel JC, Suquet P. Nonuniform transformation field analysis. Int J Solids Struct 2003;40:6937–55.
[33] Michel JC, Suquet P. Computational analysis of nonlinear composite structures using the nonuniform transformation field analysis. Comput Methods Appl Mech Eng 2004;193:5477–502.
[34] Miehe C. Computational micro-to-macro transitions for discretized micro-structures of heterogeneous materials at finite strains based on the minimization of averaged incremental energy. Comput Methods Appl Mech Eng 2003;192:559–91.
[35] Molinari A, Canova GR, Ahzi S. A self consistent approach of the large deformation polycrystal viscoplasticity. Acta Metall 1987;35:2983–94.
[36] Moulinec H, Suquet P. A numerical method for computing the overall response of nonlinear composites with complex microstructure. Comput Methods Appl Mech Eng 1998;157:69–94.
[37] Pettermann HE, Plankensteiner AF, Böhm HJ, Rammerstorfer FG. A thermo-elasto-plastic constitutive law for inhomogeneous materials based on an incremental mori-tanaka approach. Comput Struct 1999;71:197–214.
[38] Ponte Castañeda P. Exact second-order estimates for the effective mechanical properties of nonlinear composite materials. J Mech Phys Solids 1996;44:827–62.
[39] Rabbat N, Sangiovanni-Vincentelli AL, Hsieh H. A multilevel newton algorithm with macromodeling and latency for the analysis of large-scale nonlinear circuits in the time domain. IEEE Trans Circ Syst 1979;26:733–41.
[40] Simo JC, Hughes TJR. Computational inelasticity. Interdisciplinary applied mathematics, vol. 7. New York: Springer; 1998.
[41] Smit RJM, Brekelmans WAM, Meijer HEH. Prediction of the mechanical behavior of nonlinear heterogeneous systems by multi-level finite element modeling. Comput Methods Appl Mech Eng 1998;155:181–92.
[42] Sun CT, Vaidya RS. Prediction of composite properties from a representative volume element. Compos Sci Technol 1996;56:171–9.
[43] Suquet P. Elements of homogenization theory for inelastic solid mechanics. In: Sanchez-Palencia E, Zaoui A, editors. Homogenization techniques for composite media. Springer-Verlag; 1987. p. 194–278.
[44] Suquet P. Overall properties of nonlinear composites: a modified secant moduli theory and its link with ponte castañeda's nonlinear variational procedure. CR Acad Sci Ser II Mec Phys Chim Astron 1995;320:563–71.
[45] Tandon GP, Weng GJ. A theory of particle-reinforced plasticity. Trans ASME J Appl Mech 1988;55:126–35.
[46] Terada K, Kikuchi N. Nonlinear homogenization method for practical applications. In: Ghosh S, Ostoja-Starzewski M, editors. Computational methods in micromechanics, vol. AMD-212/MD-62. AMSE; 1995. p. 1–16.
[47] Voce E. A practical strain-hardening function. Metallurgia 1955;51:219–26.
[48] Washizu K. Variational methods in elasticity and plasticity. Pergamon press; 1975.
[49] Xia Z, Zhang Y, Ellyin F. A unified periodical boundary conditions for representative volume elements of composites and applications. Int J Solids Struct 2003;40:1907–21.
[50] Xia Z, Zhou C, Yong Q, Wang X. On selection of repeated unit cell model and application of unified periodic boundary conditions in micro-mechanical analysis of composites. Int J Solids Struct 2006;43:266–78.
[51] Yu W, Tang T. Variational asymptotic method for unit cell homogenization of periodically heterogeneous materials. Int J Solids Struct 2007;44:3738–55.
[52] Zhang L, Yu W. A micromechanics approach to homogenizing elasto-viscoplastic heterogeneous materials. Int J Solids Struct 2014;51:3878–88.
[53] Zhao KM, Lee JK. Material properties of aluminum alloy for accurate draw-bend simulation. J Eng Mater Technol 2001;123:287–92.

Structures, Structural Dynamics, and Materials and Co-located Conferences
April 8-11, 2013, Boston, Massachusetts
54th AIAA/ASME/ASCE/AHS/ASC Structures, Structural Dynamics, and Materials Conference

A Variational Asymptotic Method for Unit Cell Homogenization of Elasto-Viscoplastic Heterogeneous Materials

Liang Zhang* and Wenbin Yu†
Utah State University, Logan, UT 84322-4130, USA

The variational asymptotic method for unit cell homogenization (VAMUCH) is a general-purpose micromechanics approach that is capable of predicting the effective properties of heterogeneous materials and recovering the local fields. The objective of this paper is to extend VAMUCH by enabling it to handle the problems of elasto-viscoplastic heterogeneous materials. An affine formulation of the constitutive relations for the constituents is derived. The Perzyna model, Hill's yield criterion, the Voce hardening law, and the Chaboche model are implemented into the affine formulation to enable it to couple the effects of viscoplasticity, plastic anisotropy, nonlinear isotropic hardening, and nonlinear kinematic hardening. The affine formulation is implemented into the incremental formulations of VAMUCH. A nonlinear algorithm is developed for the VAMUCH code. The applicability, power, and accuracy of the current version of VAMUCH are validated using examples such as predicting the stress-strain hysteresis loops of fiber reinforced composites consisting of matrices of various material properties, subject to various loading conditions. The current version of VAMUCH is found to be capable of handling the problems involving complex constitutive relations for the constituents, complex loading conditions, and complex loading histories. More sophisticated user-defined material models can be implemented into it.

I. Introduction

Heterogeneous materials are widely used in structural components due to their capability of exhibiting designated in-plane stiffness, bending stiffness, ultimate strength, or thermal expansion coefficient. However, when they undergo a certain extent of deformation at high temperatures, their constituents often exhibit a viscoplastic behavior, which limits their performance. It is doable to evaluate the performance of such heterogeneous materials by performing a series of tests, in which the viscoplastic behavior can be detected. However, it is expensive and time consuming to manufacture a great amount of materials and to perform various tests on them. Although possible, it is computationally prohibitive to analyze these structures with all the microstructural details because the macroscopic dimensions of these materials are usually several orders of magnitude greater than the heterogeneity length scale. Therefore, it is of great practical value to solve the problems of elasto-viscoplastic heterogeneous materials using an efficient, powerful, and accurate numerical approach, i.e., the homogenization of heterogeneous materials.

In recent decades, numerous efforts have been devoted to the homogenization of heterogeneous materials. According to Ref. [1], such homogenization generally consists of the following steps:

- Idealize the heterogeneous material as consisting of numerous periodically arranged unit cells (UCs) and identify the UC;
- Perform a micromechanical analysis on the UC and obtain the effective material properties;
- Substitute the effective material properties into the macroscopic structure and obtain the global response of the structure;

*Postdoctoral Researcher, Department of Mechanical and Aerospace Engineering.
†Associate Professor, Department of Mechanical and Aerospace Engineering, AIAA Associate Fellow.

- Feedback the global response to the local scale and recover the local fields of interest (e.g., the displacement, strain, and stress fields).

If the deformation is restricted in the linearly elastic region, the constitutive relations for the constituents are stress-, history-, and rate-independent. In this case, the effective material properties of the UC remain the same throughout continued deformation, and the aforementioned homogenization just needs to be performed once. The theories of the homogenization of linearly elastic heterogeneous materials have been well established. These theories include the self-consistent model,[2] Hashin and Shtrikman's variational approach,[3] the third-order bounds,[4] the method of cells (MOC),[5] the recursive cell method,[6] and the mathematical homogenization theories (MHT),[7,8] and etc. If the deformation is extended to the viscoplastic region, the constitutive relations for one or more than one constituents become stress-, history-, and rate-dependent, and there does not exist a correspondence principal between the stress and strain rates. This leads one to linearize the instantaneous effective material properties and to iteratively perform homogenization.

There are two major approaches to obtaining the instantaneous effective material properties, i.e., the tangent approach and the secant approach. As the name suggests, the tangent approach treats the tangent effective material properties as the instantaneous effective material properties,[2,9] while the secant approach treats the secant effective material properties as the instantaneous effective material properties.[10–12] Hutchinson[13] first extended the tangent approach to the viscoplastic region by proposing a self-consistent model of rigid-viscoplastic polycrystal. Weng[14] also extended the secant approach to the viscoplastic region by treating the inelastic strain rates as some stress free eigenvalues to linearize the constitutive relations. Nemat-Nasser and Obata[15] later extended this approach by taking account into finite deformation. These early approaches did not take account into the viscoplastic interactions among different constituents and tend to overestimate the instantaneous effective material stiffness.

To overcome these drawbacks, several authors[16–23] proposed a set of secant and affine approaches. Li and Weng[16] extended the secant approach by transform the elasto-viscoplastic problem to a viscoelastic one. Molinari et al.[17,18] proposed a non-incremental approach in which they transformed the problem to a linearly thermoelastic one. Despite improvement, these two approaches either require a two-phase heterogeneous material or tend to underestimate the instantaneous effective material stiffness. Masson et al.[19,20] proposed an affine approach in which they linearized the constitutive relations in the time domain and transformed the problem to a linearly thermoelastic one using the Laplace transformation. Pierard et al.[21,22] later extended this approach by enabling it to solve the problems of two-phase hetergeneous materials. Although the affine approach is capable of generating close predictions, it requires the inverse Laplace transformation, which is computationally costly. To overcome this drawback, Doghri et al.[23] proposed an incrementally affine apporach in which they discretized the time domine into numerous intervals, linearized the constitutive relations in each interval, and avoided the Laplace transformation. Despite success, all the aforementioned approaches are incapable of recovering the local fields or truly coupling the effects of viscoplasticity, plastic anisotropy, nonlinear isotropic hardening, and nonlinear kinematic hardening. Therefore, there is a need for a more powerful approach.

Numerous attempts have been made not only to obtain the instantaneous effective material properties but also to recover the local fields. Aboudi and his co-workers[24,25] developed the so-called method of cells (MOC) and later the generalized method of cells (GMC) of elasto-viscoplastic heterogeneous materials to achieve this goal. A detailed review on these approaches can be found in Ref. [26]. The basic ideas of these approaches are subdividing the UC into numerous cuboid subcells, solving for the average strains and stresses over each subcell, and obtaining an estimation of the local fields. These approaches solve the problems to a certain extent but suffer two major drawbacks. First, representing the UC by cuboid subcells introduces considerable domain approximation errors. This can be understood by noting that it is generally more accurate to represent the UC by a finite element mesh. Second, representing the local strains and stresses within each subcell by the average ones introduces considerable approximation errors. This can be understood by noting that it is generally more accurate to represent the local fields using shape functions and nodal values. In fact, several attempts have been made to overcome these two drawbacks. An example is the so-called high fidelity generalized method of cells (HFGMC).[27] Williams et al.[28] demonstrated that HFGMC and VAMUCH, which will be mentioned in the next paragraph, significantly outperform GMC. However, they also found that, despite higher accuracy, HFGMC is quite computationally costly. Therefore, there is a need for a more accurate and efficient approach.

In recent years, Yu and his co-workers[1,29–33] developed the variational asymptotic method for unit cell homogenization (VAMUCH), a general-purpose micromechanics approach, to handle the problems of het-

erogeneous materials. In fact, VAMUCH is not only capable of predicting the effective properties of heterogeneous materials and recovering the local fields but also has several unique features compared with other numerical methods. One of these features is that VAMUCH has the minimum number of assumptions. Specifically, VAMUCH starts with two basic assumptions associated with the micromechanical analysis of heterogeneous materials of identifiable UCs. For the problems of elasto-viscoplastic heterogeneous materials, these two assumptions are modified as follows:

- Assumption 1. The exact solutions of the field have their volume averages over the UC, i.e., if $d\mathbf{u}$ denotes the exact displacement increments within the UC, there exists a $d\mathbf{v}$ such that

$$d\mathbf{v} = \frac{1}{\Omega}\int_{\Omega} d\mathbf{u} d\Omega \equiv \langle d\mathbf{u} \rangle , \tag{1}$$

  where Ω denotes the domain occupied by a UC and also its volume and $\langle \cdot \rangle$ denotes the volume average over Ω;

- Assumption 2. The affine instantaneous effective material properties obtained using the micromechanical analysis are independent of the geometry and boundary conditions of the macroscopic structure, or to say, the affine instantaneous effective material properties are assumed to be the intrinsic properties of the material when macroscopically viewed.

These two assumptions place the fewest restrictions on the problem solving. The first assumption mathematically means that the exact solutions of the field are integrable over the UC. In other words, the heterogeneous material can be homogenized. The second assumption basically reflects the fact that material properties are part of the constitutive relations of the matter, not related with the geometry and boundary of the macroscopic structure. Of course, the micromechanical analysis of the UC is desirable and appropriate only if $\eta = h/l \ll 1$, where h denotes the characteristic size of the UC and l denotes the characteristic size of the macroscopic structure.

The objective of this paper is to extend VAMUCH by enabling it to handle the problems of elasto-viscoplastic heterogeneous materials. An affine formulation of the constitutive relations for the constituents is derived. The Perzyna model, Hill's yield criterion, the Voce hardening law, and the Chaboche model are implemented into the affine formulation to enable it to couple the effects of viscoplasticity, plastic anisotropy, nonlinear isotropic hardening, and nonlinear kinematic hardening. The affine formulation is implemented into the incremental formulations of VAMUCH. A nonlinear algorithm is developed for the VAMUCH code. The applicability, power, and accuracy of the current version of VAMUCH are validated using examples such as predicting the stress-strain hysteresis loops of fiber reinforced composites consisting of matrices of various material properties, subject to various loading conditions.

II. Constitutive Relations

A. Perzyna Model

Consider a heterogeneous material consisting of several constituents. Note that an elastic constituent can be treated as an elasto-viscoplastic one with its initial yield stress, σ_0, being infinity. Therefore, each constituent can be treated as exhibiting elasto-viscoplasticity, plastic anisotropy, and combined isotropic and kinematic hardening.

Before yielding occurs, the yield function of a constituent can take the general form of

$$f(\boldsymbol{\sigma} - \boldsymbol{\alpha}) = F(\boldsymbol{\sigma} - \boldsymbol{\alpha}) - \sigma_0; \tag{2}$$

if $f \geq 0$, yielding occurs, and f becomes

$$f(\boldsymbol{\sigma} - \boldsymbol{\alpha}, \sigma_Y) = F(\boldsymbol{\sigma} - \boldsymbol{\alpha}) - \sigma_Y , \tag{3}$$

where $\boldsymbol{\sigma}$ denotes the stress tensor, $\boldsymbol{\alpha}$ denotes the back stress tensor and accounts for kinematic hardening, and σ_Y denotes the current yield stress with σ_0 being its initial value.

For an isotropic hardening material, the evolution of σ_Y over continued deformation can be characterized by the so-called isotropic hardening law. This hardening law can be extracted from the monotonic uniaxial stress-strain relations of the constituent. Specifically, introduce a Cartesian coordinate system

$\mathbf{x} = (x_1, x_2, x_3)$ with its three axes parallel to the orthotropic axes of the constituent, and let the x_1-direction denote the loading direction. The hardening law can be expressed as

$$\sigma_Y = \kappa\left(\epsilon_1^{vp}\right), \tag{4}$$

where σ_Y equals the normal stress in the x_1-direction, σ_1, ϵ_1^{vp} denotes the viscoplastic normal strain along the x_1-direction, and κ is a monotonically increasing function of ϵ_1^{vp}. ϵ_1^{vp} can be related to its rate, $\dot{\epsilon}_1^{vp}$, by

$$\epsilon_1^{vp} = \int_0^t \dot{\epsilon}_1^{vp} dt, \tag{5}$$

where t denotes the current time.

Decomposing the total strain rate tensor, $\dot{\boldsymbol{\epsilon}}$, into its elastic and viscoplastic parts gives

$$\dot{\boldsymbol{\epsilon}} = \dot{\boldsymbol{\epsilon}}^e + \dot{\boldsymbol{\epsilon}}^{vp}, \tag{6}$$

where $\dot{\boldsymbol{\epsilon}}^e$ is related to $\dot{\boldsymbol{\sigma}}$ by the rate form of Hooke's law as

$$\dot{\boldsymbol{\sigma}} = \boldsymbol{\mathcal{C}}^e : \dot{\boldsymbol{\epsilon}}^e \quad \text{or} \quad \dot{\boldsymbol{\epsilon}}^e = \left(\boldsymbol{\mathcal{C}}^e\right)^{-1} : \dot{\boldsymbol{\sigma}} \tag{7}$$

with $\boldsymbol{\mathcal{C}}^e$ denoting the fourth-order elastic stiffness tensor, and $\dot{\boldsymbol{\epsilon}}^{vp}$ is given by the flow rule as

$$\dot{\boldsymbol{\epsilon}}^{vp} = \dot{\lambda}\frac{\partial g}{\partial \boldsymbol{\sigma}} \tag{8}$$

with g denoting the plastic potential function and $\dot{\lambda}$ being a positive scalar multiplier. The Perzyna model suggests that

$$\dot{\lambda} = \begin{cases} \gamma\Phi\left(f\right) & f > 0, \\ 0 & f \leq 0, \end{cases} \tag{9}$$

where γ denotes a fluidity parameter, and Φ denotes an overstress function and takes the form of

$$\Phi\left(f\right) = \left(\frac{f}{\sigma_Y}\right)^N \tag{10}$$

with N denoting a rate-sensitivity parameter.[34]

B. Hill's Yield Function

Without loss of generality, let the constituent obey Hill's yield function along with an associated flow rule. For notational convenience, let $\tilde{\boldsymbol{\sigma}} = \boldsymbol{\sigma} - \boldsymbol{\alpha}$. The yield function can take the form of

$$f\left(\tilde{\boldsymbol{\sigma}}, \sigma_Y\right) = \tilde{\sigma}_e - \sigma_Y, \tag{11}$$

where

$$\tilde{\sigma}_e = \sqrt{\frac{3}{2}\tilde{\boldsymbol{\sigma}}' : \boldsymbol{\mathcal{H}} : \tilde{\boldsymbol{\sigma}}'} \tag{12}$$

with $(\cdot)'$ denoting the deviatoric part of the tensor and $\boldsymbol{\mathcal{H}}$ denoting the fourth-order anisotropy tensor. According to Ref. [35], if $\boldsymbol{\alpha}$ vanishes, $\tilde{\boldsymbol{\sigma}} = \boldsymbol{\sigma}$, and $\tilde{\sigma}_e$ reduces to the Hill equivalent stress. Substituting Eq. (12) into the modified plastic work equivalence principle,

$$\tilde{\boldsymbol{\sigma}}' : \dot{\boldsymbol{\epsilon}}^{vp\prime} = \tilde{\sigma}_e \dot{\epsilon}_e^{vp}, \tag{13}$$

gives the Hill equivalent strain rate, $\dot{\epsilon}_e^{vp}$, as

$$\dot{\epsilon}_e^{vp} = \sqrt{\frac{2}{3}\dot{\boldsymbol{\epsilon}}^{vp\prime} : \hat{\boldsymbol{\mathcal{H}}} : \dot{\boldsymbol{\epsilon}}^{vp\prime}}, \tag{14}$$

where the fourth-order tensor $\hat{\boldsymbol{\mathcal{H}}}$ is the formal inverse of $\boldsymbol{\mathcal{H}}$ ($\boldsymbol{\mathcal{H}} : \hat{\boldsymbol{\mathcal{H}}} = \boldsymbol{\mathcal{I}}$ with $\boldsymbol{\mathcal{I}}$ denoting the fourth-order identity tensor).[35] $\boldsymbol{\mathcal{H}}$ and $\hat{\boldsymbol{\mathcal{H}}}$ can be obtained from the R-values that characterize plastic anisotropy and can be measured from experiments. More details on $\boldsymbol{\mathcal{H}}$ and $\hat{\boldsymbol{\mathcal{H}}}$ can be found in appendix A.

It can be derived from Eq. (13) that, for the assumed constituent, $\dot{\epsilon}_1^{vp} = \dot{\epsilon}_e^{vp}$. Eq. (15) can hereby be rewritten as

$$\epsilon_e^{vp} = \int_0^t \dot{\epsilon}_e^{vp} dt, \tag{15}$$

where ϵ_e^{vp} is referred to as the cumulative equivalent viscoplastic strain. In this paper, the Voce hardening law and the Chaboche model are employed as the isotropic and kinematic hardening laws, respectively. Specifically, the Voce hardening laws writes

$$\sigma_Y = \sigma_0 + K\left[1 - \exp\left(-n\epsilon_e^{vp}\right)\right], \tag{16}$$

where K and n are material constants;[36] the Chaboche model writes

$$\boldsymbol{\alpha} = \sum \boldsymbol{\alpha}_i, \tag{17}$$

where

$$\dot{\boldsymbol{\alpha}}_i = \frac{2}{3} C_i \dot{\boldsymbol{\epsilon}}^{vp} - \gamma_i \dot{\epsilon}_e^{vp} \boldsymbol{\alpha}_i \tag{18}$$

with C_i and γ_i being material constants.[37]

Last but not least, if $\boldsymbol{\mathcal{H}} = \boldsymbol{\mathcal{I}}$, Hill's yield function reduces to the von Mises yield function. In this case, $\tilde{\sigma}_e$ becoms

$$\tilde{\sigma}_e = \sqrt{\frac{3}{2}\tilde{\boldsymbol{\sigma}}' : \boldsymbol{\mathcal{I}} : \tilde{\boldsymbol{\sigma}}'} = \sqrt{\frac{3}{2}\tilde{\boldsymbol{\sigma}}' : \tilde{\boldsymbol{\sigma}}'}. \tag{19}$$

If $\boldsymbol{\alpha}$ vanishes, $\tilde{\sigma}_e$ reduces to the von Mises equivalent stress.

III. Affine Formulation of the Constitutive Relations

Following Ref. [23], discretize the time domain into numerous intervals, and let $[t_n, t_{n+1}]$ be the interval of interest. Suppose that all the state variables at t_n are known, and let $\Delta(\cdot)$ denotes the increment in a quantity over this time interval, e.g., $\Delta t = t_{n+1} - t_n$ and $\Delta\boldsymbol{\epsilon} = \boldsymbol{\epsilon}(t_{n+1}) - \boldsymbol{\epsilon}(t_n)$. The task is hereby to find the relations between $\Delta\boldsymbol{\sigma}$ and $\Delta\boldsymbol{\epsilon}$. Note that $\Delta\boldsymbol{\epsilon}$ can be decomposed into its elastic and viscoplastic parts, $\Delta\boldsymbol{\epsilon}^e$ and $\Delta\boldsymbol{\epsilon}^{vp}$, where $\Delta\boldsymbol{\epsilon}^e$ can be related to $\Delta\boldsymbol{\sigma}$ by Eq. (7). The task hereby becomes finding the relations between $\Delta\boldsymbol{\sigma}$ and $\Delta\boldsymbol{\epsilon}^{vp}$. According to Ref. [23], $\Delta\boldsymbol{\epsilon}^{vp}$ can be related to $\dot{\boldsymbol{\epsilon}}^{vp}(t_{n+1})$ using the backward Euler method by

$$\Delta\boldsymbol{\epsilon}^{vp} = \dot{\boldsymbol{\epsilon}}^{vp}(t_{n+1})\,\Delta t. \tag{20}$$

Remember that ϵ_e^{vp} and $\boldsymbol{\alpha}$ are the internal variables accounting for isotropic and kinematic hardening, respectively. Without loss of generality, let $\dot{\boldsymbol{\epsilon}}^{vp}$, $\dot{\epsilon}_e^{vp}$, and $\dot{\boldsymbol{\alpha}}$ be functions of $\boldsymbol{\sigma}$, ϵ_e^{vp} and $\boldsymbol{\alpha}$, respectively, i.e.,

$$\dot{\boldsymbol{\epsilon}}^{vp}(t) = \dot{\boldsymbol{\epsilon}}^{vp}\left(\boldsymbol{\sigma}(t), \epsilon_e^{vp}(t), \boldsymbol{\alpha}(t)\right), \quad \dot{\epsilon}_e^{vp}(t) = \dot{\epsilon}_e^{vp}\left(\boldsymbol{\sigma}(t), \epsilon_e^{vp}(t), \boldsymbol{\alpha}(t)\right), \tag{21}$$

$$\dot{\boldsymbol{\alpha}}(t) = \dot{\boldsymbol{\alpha}}\left(\boldsymbol{\sigma}(t), \epsilon_e^{vp}(t), \boldsymbol{\alpha}(t)\right). \tag{21'}$$

Following Ref. [23], let the evolution equations of $\dot{\boldsymbol{\epsilon}}^{vp}$, $\dot{\epsilon}_e^{vp}$, and $\dot{\boldsymbol{\alpha}}$ take the following forms:

$$\dot{\boldsymbol{\epsilon}}^{vp}(t_{n+1}) = \dot{\boldsymbol{\epsilon}}^{vp}(t_n) + \boldsymbol{\mathcal{K}}(t_{n+1}) : \Delta\boldsymbol{\sigma} + \mathbf{L}(t_{n+1})\,\Delta\epsilon_e^{vp} + \boldsymbol{\mathcal{M}}(t_{n+1}) : \Delta\boldsymbol{\alpha}, \tag{22}$$

$$\dot{\epsilon}_e^{vp}(t_{n+1}) = \dot{\epsilon}_e^{vp}(t_n) + \mathbf{N}(t_{n+1}) : \Delta\boldsymbol{\sigma} + P(t_{n+1})\,\Delta\epsilon_e^{vp} + \mathbf{Q}(t_{n+1}) : \Delta\boldsymbol{\alpha}, \tag{22'}$$

$$\dot{\boldsymbol{\alpha}}(t_{n+1}) = \dot{\boldsymbol{\alpha}}(t_n) + \boldsymbol{\mathcal{R}}(t_{n+1}) : \Delta\boldsymbol{\sigma} + \mathbf{S}(t_{n+1})\,\Delta\epsilon_e^{vp} + \boldsymbol{\mathcal{T}}(t_{n+1}) : \Delta\boldsymbol{\alpha}, \tag{22''}$$

where

$$\boldsymbol{\mathcal{K}} = \frac{\partial\dot{\boldsymbol{\epsilon}}^{vp}}{\partial\boldsymbol{\sigma}}, \quad \mathbf{L} = \frac{\partial\dot{\boldsymbol{\epsilon}}^{vp}}{\partial\dot{\epsilon}_e^{vp}}, \quad \boldsymbol{\mathcal{M}} = \frac{\partial\dot{\boldsymbol{\epsilon}}^{vp}}{\partial\boldsymbol{\alpha}}, \quad \mathbf{N} = \frac{\partial\dot{\epsilon}_e^{vp}}{\partial\boldsymbol{\sigma}}, \quad P = \frac{\partial\dot{\epsilon}_e^{vp}}{\partial\dot{\epsilon}_e^{vp}}, \quad \mathbf{Q} = \frac{\partial\dot{\epsilon}_e^{vp}}{\partial\boldsymbol{\alpha}}, \tag{23}$$

$$\boldsymbol{\mathcal{R}} = \frac{\partial\dot{\boldsymbol{\alpha}}}{\partial\boldsymbol{\sigma}}, \quad \mathbf{S} = \frac{\partial\dot{\boldsymbol{\alpha}}}{\partial\dot{\epsilon}_e^{vp}}, \quad \boldsymbol{\mathcal{T}} = \frac{\partial\dot{\boldsymbol{\alpha}}}{\partial\boldsymbol{\alpha}} \tag{23'}$$

with $\boldsymbol{\mathcal{K}}$, $\boldsymbol{\mathcal{M}}$, $\boldsymbol{\mathcal{R}}$, and $\boldsymbol{\mathcal{T}}$ being fourth-order tensors, $\mathbf{L}$, $\mathbf{N}$, $\mathbf{Q}$, and $\mathbf{S}$ being second-order tensors, and P being a scalar. Note that $\Delta\epsilon_e^{vp}$ and $\Delta\boldsymbol{\alpha}$ can also be related to $\dot{\epsilon}_e^{vp}$ and $\dot{\boldsymbol{\alpha}}$ using the backward Euler method by

$$\Delta\epsilon_e^{vp} = \dot{\epsilon}_e^{vp}(t_{n+1})\,\Delta t \quad \text{and} \quad \Delta\boldsymbol{\alpha} = \dot{\boldsymbol{\alpha}}(t_{n+1})\,\Delta t, \tag{24}$$

respectively. Substituting Eq. (24) into the second and third equations of Eq. (22) and rearranging the equations gives

$$A_{11}\dot{\epsilon}_e^{vp}\left(t_{n+1}\right)+\mathbf{A}_{12}:\dot{\boldsymbol{\alpha}}\left(t_{n+1}\right)=B_1, \tag{25}$$

$$\mathbf{A}_{21}\dot{\epsilon}_e^{vp}\left(t_{n+1}\right)+\boldsymbol{\mathcal{A}}_{22}:\dot{\boldsymbol{\alpha}}\left(t_{n+1}\right)=\mathbf{B}_2, \tag{25'}$$

where

$$A_{11}=1-P\left(t_{n+1}\right)\Delta t,\quad \mathbf{A}_{12}=-\mathbf{Q}\left(t_{n+1}\right)\Delta t,\quad \mathbf{A}_{21}=-\mathbf{S}\left(t_{n+1}\right)\Delta t,\quad \boldsymbol{\mathcal{A}}_{22}=\boldsymbol{\mathcal{I}}-\boldsymbol{\mathcal{T}}\left(t_{n+1}\right)\Delta t, \tag{26}$$

$$B_1=\dot{\epsilon}_e^{vp}\left(t_n\right)+\mathbf{N}\left(t_{n+1}\right):\Delta\boldsymbol{\sigma},\quad \mathbf{B}_2=\dot{\boldsymbol{\alpha}}\left(t_n\right)+\boldsymbol{\mathcal{R}}\left(t_{n+1}\right):\Delta\boldsymbol{\sigma}. \tag{26'}$$

Rearranging the second equation of Eq. (25) gives

$$\dot{\boldsymbol{\alpha}}\left(t_{n+1}\right)=\boldsymbol{\mathcal{A}}_{22}^{-1}:\left[\mathbf{B}_2-\mathbf{A}_{21}\dot{\epsilon}_e^{vp}\left(t_{n+1}\right)\right], \tag{27}$$

where $\boldsymbol{\mathcal{A}}_{22}^{-1}$ is the formal inverse of $\boldsymbol{\mathcal{A}}_{22}$. Substituting Eq. (27) into the first equation of Eq. (25) and rearranging the equation give

$$\dot{\epsilon}_e^{vp}\left(t_{n+1}\right)=\frac{B_1-\mathbf{A}_{12}:\boldsymbol{\mathcal{A}}_{22}^{-1}:\mathbf{B}_2}{A_{11}-\mathbf{A}_{12}:\boldsymbol{\mathcal{A}}_{22}^{-1}:\mathbf{A}_{21}}. \tag{28}$$

Substituting Eq. (28) into Eq. (27) gives

$$\dot{\boldsymbol{\alpha}}\left(t_{n+1}\right)=\boldsymbol{\mathcal{A}}_{22}^{-1}:\left(\mathbf{B}_2-\frac{B_1-\mathbf{A}_{12}:\boldsymbol{\mathcal{A}}_{22}^{-1}:\mathbf{B}_2}{A_{11}-\mathbf{A}_{12}:\boldsymbol{\mathcal{A}}_{22}^{-1}:\mathbf{A}_{21}}\mathbf{A}_{21}\right). \tag{29}$$

Substituting Eqs. (28) and (29) into Eq. (24), substituting the equation into the first equation of Eq. (22), and rearranging the equation give

$$\dot{\boldsymbol{\epsilon}}^{vp}\left(t_{n+1}\right)=\dot{\tilde{\boldsymbol{\epsilon}}}\left(t_{n+1}\right)+\tilde{\boldsymbol{\mathcal{C}}}^{-1}\left(t_{n+1}\right):\Delta\boldsymbol{\sigma}, \tag{30}$$

where

$$\begin{aligned}\dot{\tilde{\boldsymbol{\epsilon}}}\left(t_{n+1}\right)=&\dot{\boldsymbol{\epsilon}}^{vp}\left(t_n\right)+\boldsymbol{\mathcal{M}}\left(t_{n+1}\right):\boldsymbol{\mathcal{A}}_{22}^{-1}:\dot{\boldsymbol{\alpha}}\left(t_n\right)\Delta t\\&+\frac{\dot{\epsilon}_e^{vp}\left(t_n\right)-\mathbf{A}_{12}:\boldsymbol{\mathcal{A}}_{22}^{-1}:\dot{\boldsymbol{\alpha}}\left(t_n\right)}{A_{11}-\mathbf{A}_{12}:\boldsymbol{\mathcal{A}}_{22}^{-1}:\mathbf{A}_{21}}\left[\mathbf{L}\left(t_{n+1}\right)-\boldsymbol{\mathcal{M}}\left(t_{n+1}\right):\boldsymbol{\mathcal{A}}_{22}^{-1}:\mathbf{A}_{21}\right]\Delta t\end{aligned} \tag{31}$$

and

$$\begin{aligned}\tilde{\boldsymbol{\mathcal{C}}}^{-1}\left(t_{n+1}\right)=&\boldsymbol{\mathcal{K}}\left(t_{n+1}\right)+\boldsymbol{\mathcal{M}}\left(t_{n+1}\right):\boldsymbol{\mathcal{A}}_{22}^{-1}:\boldsymbol{\mathcal{R}}\left(t_{n+1}\right)\Delta t\\&+\frac{\left[\mathbf{L}\left(t_{n+1}\right)-\boldsymbol{\mathcal{M}}\left(t_{n+1}\right):\boldsymbol{\mathcal{A}}_{22}^{-1}:\mathbf{A}_{21}\right]\otimes\left[\mathbf{N}\left(t_{n+1}\right)-\mathbf{A}_{12}:\boldsymbol{\mathcal{A}}_{22}^{-1}:\boldsymbol{\mathcal{R}}\left(t_{n+1}\right)\right]}{A_{11}-\mathbf{A}_{12}:\boldsymbol{\mathcal{A}}_{22}^{-1}:\mathbf{A}_{21}}\Delta t.\end{aligned} \tag{32}$$

Substituting Eq. (30) into Eq. (20) gives

$$\Delta\boldsymbol{\epsilon}^{vp}=\Delta\tilde{\boldsymbol{\epsilon}}+\left[\tilde{\boldsymbol{\mathcal{C}}}^{-1}\left(t_{n+1}\right)\Delta t\right]:\Delta\boldsymbol{\sigma}, \tag{33}$$

where $\Delta\tilde{\boldsymbol{\epsilon}}=\dot{\tilde{\boldsymbol{\epsilon}}}\left(t_{n+1}\right)\Delta t$. Substituting Eq. (33) and the incremental form of Eq. (7) into the incremental form of Eq. (6) gives

$$\Delta\boldsymbol{\epsilon}=\Delta\boldsymbol{\epsilon}^e+\Delta\boldsymbol{\epsilon}^{vp}=\left(\boldsymbol{\mathcal{C}}^e\right)^{-1}:\Delta\boldsymbol{\sigma}+\Delta\tilde{\boldsymbol{\epsilon}}+\left[\tilde{\boldsymbol{\mathcal{C}}}^{-1}\left(t_{n+1}\right)\Delta t\right]:\Delta\boldsymbol{\sigma}. \tag{34}$$

Rearranging Eq. (34) gives a general affine formulation of the constitutive relations for the constituent as

$$\Delta\boldsymbol{\epsilon}-\Delta\tilde{\boldsymbol{\epsilon}}=\left[\left(\boldsymbol{\mathcal{C}}^e\right)^{-1}+\tilde{\boldsymbol{\mathcal{C}}}^{-1}\left(t_{n+1}\right)\Delta t\right]:\Delta\boldsymbol{\sigma} \tag{35}$$

or

$$\Delta\boldsymbol{\sigma}=\boldsymbol{\mathcal{C}}^{evp}\left(t_{n+1}\right):\left(\Delta\boldsymbol{\epsilon}-\Delta\tilde{\boldsymbol{\epsilon}}\right), \tag{36}$$

where $\boldsymbol{\mathcal{C}}^{evp}$ denotes the fourth-order affine instantaneous elasto-viscoplastic stiffness tensor and is given by

$$\boldsymbol{\mathcal{C}}^{evp}\left(t_{n+1}\right)=\left[\left(\boldsymbol{\mathcal{C}}^{e}\right)^{-1}+\tilde{\boldsymbol{\mathcal{C}}}^{-1}\left(t_{n+1}\right)\Delta t\right]^{-1}. \tag{37}$$

Once the partial derivatives in Eq. (23) are specified, $\boldsymbol{\mathcal{C}}^{evp}$ is uniquely determined.

Till now, a general affine formulation of the constitutive relations has been derived. In this paper, the Perzyna model, Hill's yield function, the Voce hardening law, and the Chaboche model (see sections II.A and II.B) are implemented into the affine formulation with the corresponding explicit expressions for the partial derivatives in Eq. (23) being derived in appendix B, while either of these material models can be replaced by a more sophisticated one as needed. In addition, if a constituent merely exhibits either isotropic or kinematic hardening, its affine formulation can reduce to a simpler form. More details on this can be found in appendix C.

IV. Variational Asymptotic Method for Unit Cell Homogenization

In this section, the general affine formulation is implemented into the incremental formulations of VAMUCH to yield the formulations for elasto-viscoplastic heterogeneous materials. In this case, some formulations of VAMUCH remain unchanged, while the others are subject to modification. To avoid redundancy, only the derivations of the latter formulations are presented here. Interested readers can refer to Refs. [1] and [33] for more details on the VAMUCH theory.

Consider a heterogeneous material consisting of numerous UCs. Introduce two Cartesian coordinate systems $\mathbf{x}=(x_1,x_2,x_3)$ and $\mathbf{y}=(y_1,y_2,y_3)$. Let x_i denote the global coordinates describing the macroscopic structure, and let y_i denote the local coordinates describing the UC. For a heterogeneous material consisting of elasto-viscoplastic constituents, the total strain energy dissipation in a UC at time t_{n+1}, $\Pi\left(t_{n+1}\right)$, is defined as

$$\Pi\left(t_{n+1}\right)=\int_{\Omega}\boldsymbol{\sigma}\left(t_{n+1}\right):\Delta\boldsymbol{\epsilon}\left(t_{n+1}\right)d\Omega, \tag{38}$$

while its increment, $\Delta\Pi$, can be obtained as

$$\begin{aligned}\Delta\Pi&=\int_{\Omega}\Delta\boldsymbol{\sigma}:\Delta\boldsymbol{\epsilon}d\Omega+\int_{\Omega}\boldsymbol{\sigma}\left(t_{n+1}\right):\Delta\left(\Delta\boldsymbol{\epsilon}\right)d\Omega=\int_{\Omega}\Delta\boldsymbol{\sigma}:\Delta\boldsymbol{\epsilon}d\Omega\\&=\int_{\Omega}\Delta\boldsymbol{\epsilon}:\boldsymbol{\mathcal{C}}^{evp}\left(t_{n+1}\right):\left(\Delta\boldsymbol{\epsilon}-\Delta\tilde{\boldsymbol{\epsilon}}\right)d\Omega,\end{aligned} \tag{39}$$

where the high-order terms are omitted. The variational statement of the problem can hereby be formulated as seeking the minimum of the functional

$$\Delta\Pi_{\Omega}=\frac{1}{\Omega}\int_{\Omega}\mathcal{C}^{evp}_{ijkl}\left[\Delta\bar{\epsilon}_{ij}+\chi_{(i|j)}\right]\left[\Delta\bar{\epsilon}_{kl}+\chi_{(k|l)}-\Delta\tilde{\epsilon}_{kl}\right]d\Omega \tag{40}$$

within a UC, where $\Delta\bar{\epsilon}_{ij}$ denotes the components of the global strain increment tensor for the homogenized structure, χ_i denotes the components of the fluctuation functions and must satisfy the periodic boundary conditions associated with Eq. (40) along with constraint

$$\langle\chi_i\rangle=0, \tag{41}$$

and

$$\chi_{(i|j)}=\frac{1}{2}\left(\frac{\partial\chi_i}{\partial y_j}+\frac{\partial\chi_j}{\partial y_i}\right). \tag{42}$$

Introduce the following matrix notations:

$$\Delta\bar{\epsilon} = \begin{bmatrix} \Delta\bar{\epsilon}_{11} & 2\Delta\bar{\epsilon}_{12} & \Delta\bar{\epsilon}_{22} & \Delta\bar{\epsilon}_{13} & 2\Delta\bar{\epsilon}_{23} & \Delta\bar{\epsilon}_{33} \end{bmatrix}^T, \tag{43}$$

$$\begin{Bmatrix} \frac{\partial\chi_1}{\partial y_1} \\ \frac{\partial\chi_1}{\partial y_2}+\frac{\partial\chi_2}{\partial y_1} \\ \frac{\partial\chi_2}{\partial y_2} \\ \frac{\partial\chi_1}{\partial y_3}+\frac{\partial\chi_3}{\partial y_1} \\ \frac{\partial\chi_2}{\partial y_3}+\frac{\partial\chi_3}{\partial y_2} \\ \frac{\partial\chi_3}{\partial y_3} \end{Bmatrix} = \begin{bmatrix} \frac{\partial}{\partial y_1} & 0 & 0 \\ \frac{\partial}{\partial y_2} & \frac{\partial}{\partial y_1} & 0 \\ 0 & \frac{\partial}{\partial y_2} & 0 \\ \frac{\partial}{\partial y_3} & 0 & \frac{\partial}{\partial y_1} \\ 0 & \frac{\partial}{\partial y_3} & \frac{\partial}{\partial y_2} \\ 0 & 0 & \frac{\partial}{\partial y_3} \end{bmatrix} \begin{Bmatrix} \chi_1 \\ \chi_2 \\ \chi_3 \end{Bmatrix} \equiv \Gamma_h \chi, \tag{46'}$$

where Γ_h denotes an operator matrix and χ denotes a column matrix containing the three components of the fluctuation functions. Let χ be discretized using finite elements as

$$\chi\left(x_i; y_i\right) = S\left(y_i\right) \mathrm{X}\left(x_i\right), \tag{44}$$

where S denotes the shape functions and X denotes a column matrix of the nodal values of the fluctuation functions for all the active nodes. The discretized version of Eq. (40) can then be obtained as

$$\Delta\Pi_\Omega = \frac{1}{\Omega}\left[\mathrm{X}^T E \mathrm{X} + \mathrm{X}^T\left(D_{h\epsilon} + D_{\epsilon h}^T\right)\Delta\bar{\epsilon} + \Delta\bar{\epsilon}^T D_{\epsilon\epsilon}\Delta\bar{\epsilon} - \mathrm{X}^T\Delta\sigma_h - \Delta\bar{\epsilon}^T\Delta\sigma_\epsilon\right], \tag{45}$$

where

$$E = \int_\Omega \left(\Gamma_h S\right)^T D\left(\Gamma_h S\right) d\Omega, \quad D_{h\epsilon} = \int_\Omega \left(\Gamma_h S\right)^T D d\Omega, \tag{46}$$

$$D_{\epsilon h} = \int_\Omega D\left(\Gamma_h S\right) d\Omega, \quad D_{\epsilon\epsilon} = \int_\Omega D d\Omega, \tag{46'}$$

$$\Delta\sigma_h = \int_\Omega \left(\Gamma_h S\right)^T D\Delta\tilde{\epsilon} d\Omega, \quad \Delta\sigma_\epsilon = \int_\Omega D\Delta\tilde{\epsilon} d\Omega \tag{46''}$$

with D denoting the 6×6 affine instantaneous stiffness matrix condensed from $\boldsymbol{\mathcal{C}}^{evp}$. It can be derived from Eq. (45) that $\Delta\Pi_\Omega$ attains its minimum only if

$$E\mathrm{X} + \frac{1}{2}\left(D_{h\epsilon} + D_{\epsilon h}^T\right)\Delta\bar{\epsilon} - \frac{\Delta\sigma_h}{2} = 0 \quad \text{or} \quad \mathrm{X} = \mathrm{X}_0\Delta\bar{\epsilon} + \mathrm{X}_1, \tag{47}$$

where

$$E\mathrm{X}_0 = \frac{1}{2}\left(D_{h\epsilon} + D_{\epsilon h}^T\right) \quad \text{and} \quad E\mathrm{X}_1 = \frac{\Delta\sigma_h}{2}. \tag{48}$$

Eq. (47) implies that X is linearly dependent on $d\bar{\epsilon}$. Substituting Eq. (47) into Eq. (45) gives the minimum of $d\Pi_\Omega$ as

$$\begin{aligned} \Delta\Pi_\Omega &= \frac{1}{\Omega}\left\{\Delta\bar{\epsilon}^T\left[\frac{1}{2}\mathrm{X}_0^T\left(D_{h\epsilon} + D_{\epsilon h}^T\right) + D_{\epsilon\epsilon}\right]\Delta\bar{\epsilon} - \Delta\bar{\epsilon}^T\mathrm{X}_0^T\Delta\sigma_h - \frac{1}{2}\mathrm{X}_1^T\Delta\sigma_h - \Delta\bar{\epsilon}^T\Delta\sigma_\epsilon\right\} \\ &\equiv \Delta\bar{\epsilon}^T\bar{D}\Delta\bar{\epsilon} - \Delta\bar{\epsilon}^T\mathrm{X}_0^T\Delta\bar{\sigma}_h - \Delta\bar{\epsilon}^T\Delta\bar{\sigma}_\epsilon - \frac{1}{2}\mathrm{X}_1^T\Delta\bar{\sigma}_h, \end{aligned} \tag{49}$$

where $\bar{D}$ denotes the so-called affine instantaneous effective stiffness matrix, $\Delta\bar{\epsilon}$ denotes the global strain increment column matrix, $\Delta\bar{\sigma}_h = \Delta\sigma_h/\Omega$, and $\Delta\bar{\sigma}_\epsilon = \Delta\sigma_\epsilon/\Omega$.

Till now, the affine instantaneous effective material properties can be fully determined. In addition, if the local fields are of interest, they can be recovered using the global displacement increments, Δv, the global

strain increments, $\Delta\bar{\epsilon}$, and the fluctuation functions, χ. Specifically, the local displacement increments can be recovered as

$$\Delta u = \Delta v + \begin{bmatrix} \frac{\partial \Delta v_1}{\partial x_1} & \frac{\partial \Delta v_1}{\partial x_2} & \frac{\partial \Delta v_1}{\partial x_3} \\ \frac{\partial \Delta v_2}{\partial x_1} & \frac{\partial \Delta v_2}{\partial x_2} & \frac{\partial \Delta v_2}{\partial x_3} \\ \frac{\partial \Delta v_3}{\partial x_1} & \frac{\partial \Delta v_3}{\partial x_2} & \frac{\partial \Delta v_3}{\partial x_3} \end{bmatrix} \begin{Bmatrix} y_1 \\ y_2 \\ y_3 \end{Bmatrix} + S\left(\bar{\mathrm{X}}_0 \Delta\bar{\epsilon} + \bar{\mathrm{X}}_1\right), \tag{50}$$

where Δu and Δv denote the local and global displacement increment column matrices, respectively, $\bar{\mathrm{X}}_0$ denotes the nodal values of fluctuation functions modified from X_0 by the periodic conditions and Eq. (41), and $\bar{\mathrm{X}}_1$ is determined similarly to $\bar{\mathrm{X}}_0$. The local strain increments can be recovered as

$$\Delta\epsilon = \Delta\bar{\epsilon} + \Gamma_h S\left(\bar{\mathrm{X}}_0 \Delta\bar{\epsilon} + \bar{\mathrm{X}}_1\right), \tag{51}$$

where $\Delta\epsilon$ denotes the the local strain increment column matrix. The local stress increments can be recovered from the local strain increments as

$$\Delta\sigma = D\left(\Delta\epsilon - \Delta\tilde{\epsilon}\right). \tag{52}$$

In addition, the global stress increments, $\Delta\bar{\sigma}$, can be obtained from Eq. (49) as

$$\Delta\bar{\sigma} = \bar{D}\Delta\bar{\epsilon} - \mathrm{X}_0^T \Delta\bar{\sigma}_h - \Delta\bar{\sigma}_\epsilon. \tag{53}$$

V. Elasto-Viscoplastic Algorithms

Figure 1 depicts the VAMUCH code structure for the problems of elasto-viscoplastic heterogeneous materials. The code starts with reading the finite element model and initializing all the state variables (i.e., the displacements, the strains, the stresses, and their increments). After this, it will iteratively perform the following steps in sequence:

- Perform the constitutive modeling to obtain the affine instantaneous effective material properties and the fluctuation functions;
- Impose the stress/strain increments;
- Perform the recovery to recover the local fields using the output of the constitutive modeling and the imposed stress/strain increments as the input;
- Save the updated state variables as the inputs for the next iteration;
- Check whether to continue the iteration.

The code will continue the iteration till the end of the loading history. After this, it will generate the history or field output as needed.

In addition, the code also needs a subroutine calculating the affine instantaneous stiffness matrix at each integration point. The algorithm of this subroutine can be described as follows:

- Read the material data and state variables at the integration point;
- Check whether the constituent exhibits an elasto-viscoplasticity;
- If yes, check whether $\sigma_e \geq \sigma_Y$;
- If $\sigma_e \geq \sigma_Y$, set the loading flag at the integration point to be true and calculate the affine instantaneous stiffness matrix using Eq. (37);
- If any of the above two criteria is not met, save the inputting elastic stiffness matrix as the affine instantaneous stiffness matrix;
- Return the resulting affine instantaneous stiffness matrix.

Especially, during the recovery, once this subroutine is called, the code will check the status of the loading flag. If the loading flag is true, the code will also update ϵ_e^{vp}, σ_Y, and $\boldsymbol{\alpha}$ at the integration point.

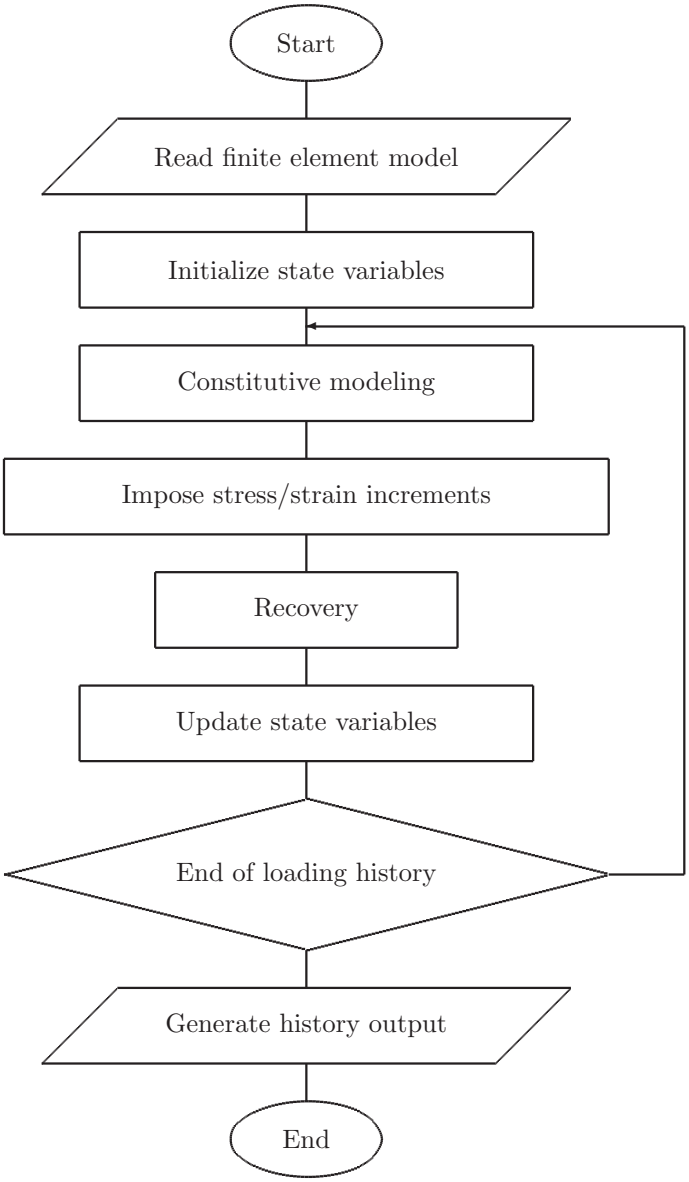

Figure 1. VAMUCH code structure for the problems of elasto-viscoplastic heterogeneous materials.

VI. Validation Examples

In this section, several examples are presented to validate the applicability, power, and accuracy of the current version of VAMUCH. The examples include predicting the stress-strain hysteresis loops of fiber reinforced composites consisting of matrices of various material properties, subject to various loading conditions. The results predicted by VAMUCH are compared with those predicted by ANSYS.

A. Isotropic Hardening

Let the composite be consist of an elasto-viscoplastic aluminum matrix embedded with numerous cylindrical, linearly elastic SiC fibers arranged in a square array and of volume fraction of fibers (VOF) 9.2%, and first let the aluminum matrix merely exhibit isotropic hardening with a hardening law taking the form of Eq. (16). Following Refs. [16] and [23], let the material parameters of aluminum and SiC take the values listed in table 1, where E and ν denote Young's modulus and Poisson's ratio, respectively. The UC of this composite can be identified as consisting of a square matrix embedded with a circular fiber located at its center. Introduce a local Cartesian coordinate system $\mathbf{y} = (y_1, y_2, y_3)$ with the origin located at the center of the UC and the y_1 axis parallel to the fiber direction. For notational convenience, let ϵ_{ij}, σ_{ij}, and $\dot{\epsilon}_{ij}$ denote the global strains, stresses, and strain rates, respectively.

Table 1. Material parameters of aluminum and SiC.

	E (GPa)	ν	σ_0 (MPa)	K (MPa)	n	$\gamma\left(\mathrm{s}^{-1}\right)$	m
Aluminum	70	0.33	60	40	54.9	4.4×10^{-6}	4.61
SiC	490	0.17	-	-	-	-	-

Figures 2 and 3 shows the stress-strain hysteresis loops of the composite subject to uniaxial loading along the y_1- and y_2-directions, respectively, where $\dot{\epsilon}$ denotes the major strain rate and equals $\dot{\epsilon}_{11}$ and $\dot{\epsilon}_{22}$ in figures 2 and 3, respectively. In the validation examples, the loading histories for the hysteresis loops are set to consist of the following steps:

- Initial loading: the major strain(s) is increased from 0 to 0.01;
- Initial unloading: the major strain(s) is decreased from 0.01 to 0;
- Reverse loading: the major strain(s) is decreased from 0.0 to -0.01;
- Reverse unloading: the major strain(s) is increased from -0.01 to 0.

As can be seen in figures 2 and 3, the composite exhibits a rate-dependent behavior in both the fiber and transverse directions, i.e., as the major strain rate increases, the composite becomes stiffer. However, due to the existence of the fiber, in figure 2, the composite approximately exhibits a bilinear stress-strain relationship, while in figure 3, it exhibit a highly nonlinear one. In addition, in figures 2 and 3, the results predicted by VAMUCH are in good agreement with those predicted by ANSYS. This indicates that VAMUCH is capable of handling the problems involving isotropic hardening and complex loading histories.

Figures 4 shows the stress-strain hysteresis loops of the composite subject to equal biaxial loading along the y_2- and y_3-directions, where $\dot{\epsilon}$ becomes $\dot{\epsilon}_{22}$ and $\dot{\epsilon}_{33}$ here. Similarly to figure 2, the composite approximately exhibits a bilinear stress-strain relationship here. However, compared to figure 2, it becomes stiffer here due to equal biaxial loading. In addition, in figure 4, the results predicted by VAMUCH are in good agreement with those predicted by ANSYS. This indicates that VAMUCH is capable of handling the problems involving complex loading conditions.

B. Plastic Anisotropy

Next let the aluminum matrix also exhibit plastic anisotropy. Specifically, consider three aluminum matrices of the material parameters listed in table 1 but of different R-values. For simplicity, let the three matrices all exhibit plastic transverse isotropy in the y_2-y_3 plane but of different values of R (see table 2). More details on plastic transverse isotropy can be found in appendix A.

Figure 5 shows the stress-strain hysteresis loops of three composites consisting of the aforementioned three matrices, respectively, where the composites are subject to uniaxial loading along the y_2-direction

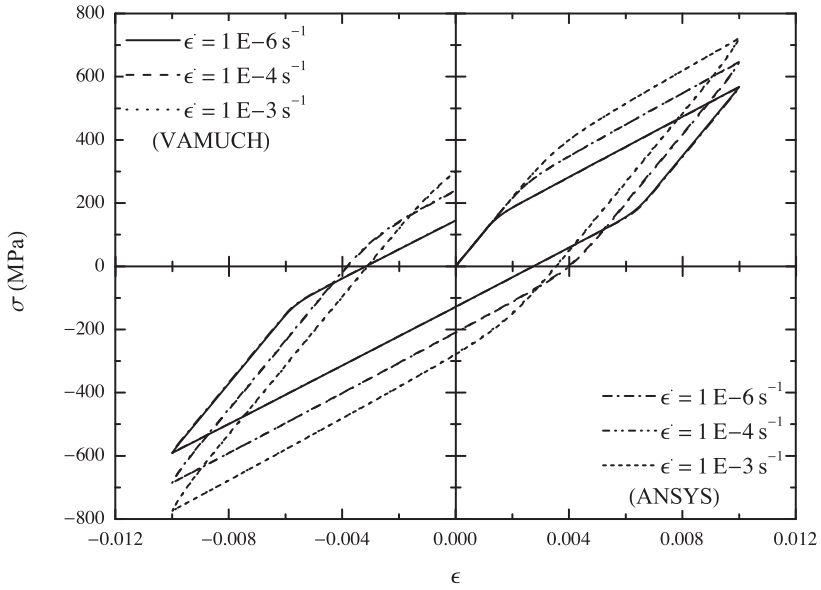

Figure 2. Stress-strain hysteresis loops of the composite subject to uniaxial loading along the y_1-direction.

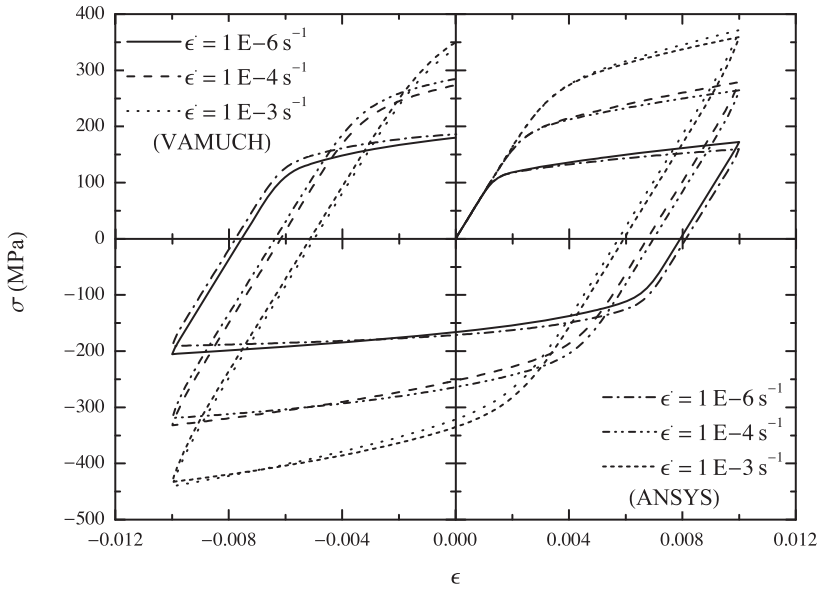

Figure 3. Stress-strain hysteresis loops of the composite subject to uniaxial loading along the y_2-direction.

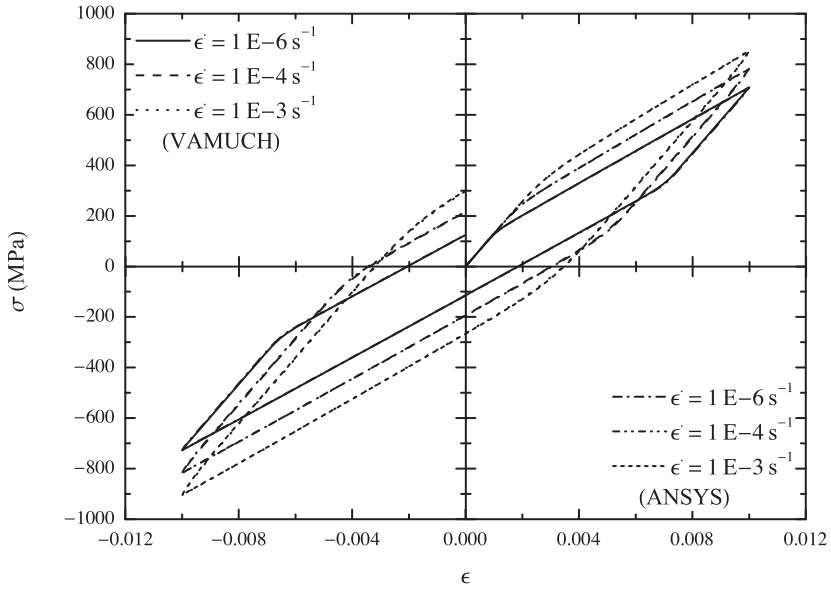

Figure 4. Stress-strain hysteresis loops of the composite subject to equal biaxial loading along the y_2- and y_3-directions.

Table 2. R-values of the three aluminum matrices.

	R_1	R_2	R_3	R_4	R_5	R_6
1	1	1	0.5	1	0.5	2
2	1	1	1	1	1	1
3	1	1	2	1	2	0.5

and $\dot{\epsilon} = 1 \times 10^{-4}\text{s}^{-1}$. Further investigation will show that the three matrices are of the same yield stress along the y_1-direction but of different yield stresses along the y_2- and y_3-directions and that the matrices of lower values of R are of higher yield stresses along the y_2- and y_3-directions. Accordingly, in figure 5, the composites of lower values of R are stiffer. In addition, in figure 5, the results predicted by VAMUCH are in good agreement with those predicted by ANSYS. This indicates that VAMUCH is also capable of handling the problems involving plastic anisotropy.

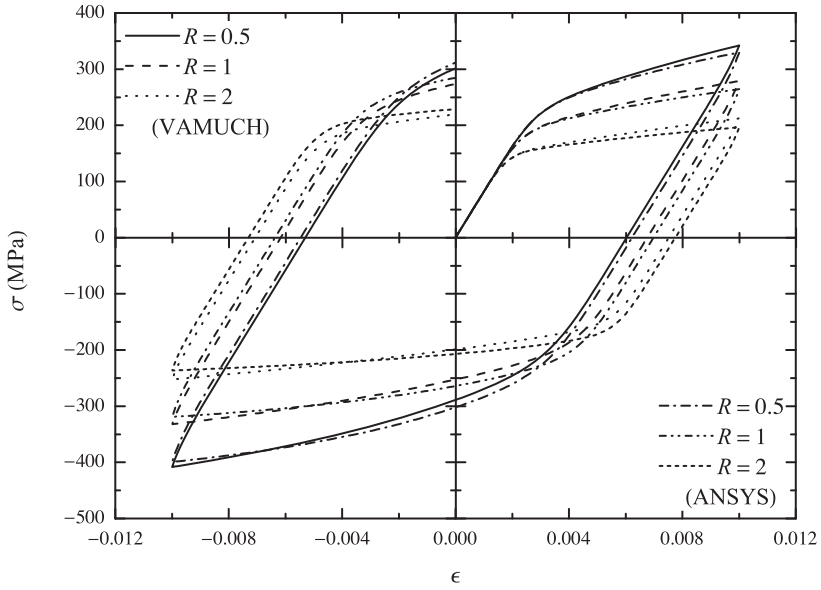

Figure 5. Stress-strain hysteresis loops of composites consisting of matrices of different values of R.

C. Kinematic Hardening

Last let the aluminum matrix further exhibit combined isotropic and kinematic hardening. Specifically, let the aluminum matrix be of the material parameters listed in table 1 and also exhibit kinematic hardening with $\dot{\boldsymbol{\alpha}}$ being given by

$$\dot{\boldsymbol{\alpha}} = \frac{2}{3} C_1 \dot{\boldsymbol{\epsilon}}^{vp} - \gamma_1 \dot{\epsilon}_e^{vp} \boldsymbol{\alpha}. \tag{54}$$

Following Ref. [38], let $C_1 = 7019\text{MPa}$ and $\gamma_1 = 118.6$.

Figure 6 shows the stress-strain hysteresis loops of the composite consisting of the aforementioned matrix, where the composite is subject to uniaxial loading along the y_2-direction and $\dot{\epsilon} = 1 \times 10^{-4}\text{s}^{-1}$. Similarly to figure 3, the composite exhibits a highly nonlinear stress-strain relationship here. To illustrate the effect of kinematic hardening on the hysteresis loops, figure 7 compares the results in figure 3 with those in figure 6. Figure 7 indicates that the composite consisting of a combined isotropic and kinematic hardening matrix is stiffer than that consisting of an isotropic hardening matrix. This is in agreement with the theory of viscoplasticity. In addition, in figure 6, the results predicted by VAMUCH are in good agreement with those predicted by ANSYS. This indicates that VAMUCH is also capable of handling the problems involving kinematic hardening.

VII. Conclusions

In this paper, VAMUCH, a general-purpose micromechanics approach, has been extended to handle the problems of elasto-viscoplastic heterogeneous materials. An affine formulation of the constitutive relations for the constituents is derived. The Perzyna model, Hill's yield criterion, the Voce hardening law, and

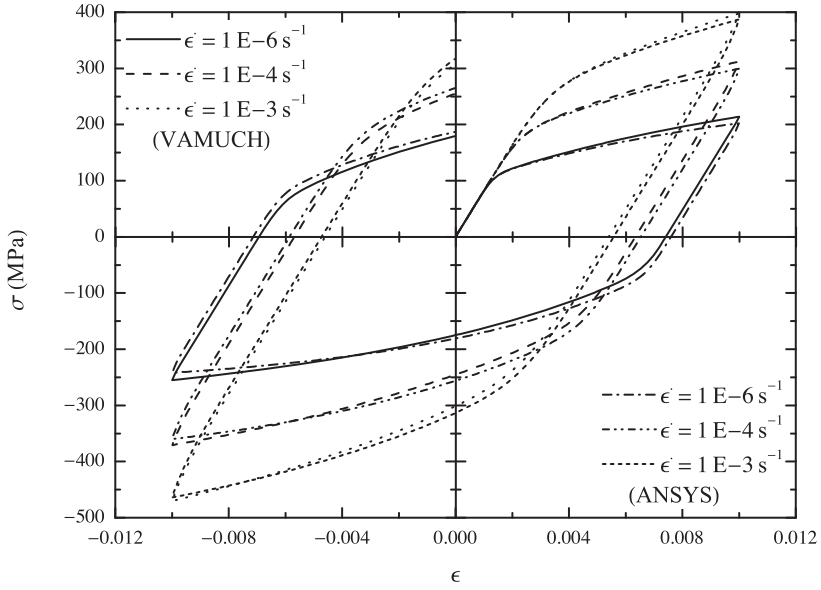

Figure 6. Stress-strain hysteresis loops of a composite consisting of a combined isotropic and kinematic hardening matrix.

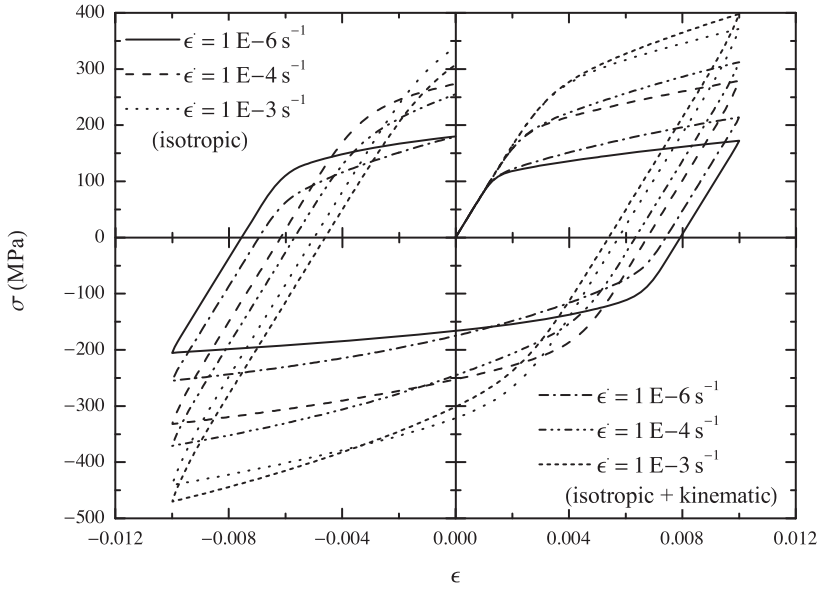

Figure 7. Comparison between the stress-strain hysteresis loops of a composite consisting of an isotropic hardening matrix and those of a composite consisting of a combined isotropic and kinematic hardening matrix.

the Chaboche model are implemented into the affine formulation to enable it to couple the effects of viscoplasticity, plastic anisotropy, nonlinear isotropic hardening, and nonlinear kinematic hardening. The affine formulation is implemented into the incremental formulations of VAMUCH. A nonlinear algorithm is developed for the VAMUCH code. The applicability, power, and accuracy of the current version of VAMUCH have been extensively validated using examples such as predicting the stress-strain hysteresis loops of fiber reinforced composites consisting of matrices of various material properties, subject to uniaxial/biaxial loading. The current version of VAMUCH is found to be capable of handling the problems involving complex constitutive relations for the constituents, complex loading conditions, and complex loading histories. VAMUCH provides an powerful and convenient tool for scientists and engineers to efficiently and accurately solve the problems of elasto-viscoplastic heterogeneous materials. More sophisticated user-defined material models can be implemented into it.

Appendix

A. Plastic Anisotropic Parameters

The R-value is widely used to characterize the plastic anisotropy of rolled sheet metals. It can be measured from a series of uniaxial tensile tests. Specifically, when a tensile specimen cut from a sheet is stretched, its R-value is defined as the ratio of the plastic strain in the width direction to that in the thickness direction, that is,

$$R = \frac{\epsilon_W}{\epsilon_T}. \tag{55}$$

In general, the R-value varies with the cut angle relative to the rolling direction of the sheet, α. In this case, an averaged R-value is often adopted. It is defined as

$$\bar{R} = \frac{R_0 + 2R_{45} + R_{90}}{4}, \tag{56}$$

where R_α denotes the R-value obtained using a tensile specimen of cut angle α.

Benzerga and Besson[35] extended the concept of the R-value by introducing six strain rate ratios, R_{ij}. These six R_{ij}'s are capable of fully characterizing the plastic anisotropy of a 3D structure, and each of them can be measured from a uniaxial tensile or simple shear test. Specifically, introduce a Cartesian coordinate system $\mathbf{x} = (x_1, x_2, x_3)$ with its three axes parallel to the orthotropic axes of the constituent, and the six R_{ij}'s can be defined as the following strain rate ratios:

$$R_{11} = \frac{\dot{\epsilon}_{22}}{\dot{\epsilon}_{33}}, \quad R_{12} = \frac{\dot{\epsilon}_{12}}{\dot{\epsilon}_{33}}, \quad R_{22} = \frac{\dot{\epsilon}_{33}}{\dot{\epsilon}_{11}}, \tag{57}$$

$$R_{13} = \frac{\dot{\epsilon}_{13}}{\dot{\epsilon}_{22}}, \quad R_{23} = \frac{\dot{\epsilon}_{23}}{\dot{\epsilon}_{11}}, \quad R_{33} = \frac{\dot{\epsilon}_{11}}{\dot{\epsilon}_{22}}. \tag{57'}$$

Let R_{ij} be written in the the Voigt notation as

$$R_1 = R_{11}, \quad R_2 = R_{12}, \quad R_3 = R_{22}, \tag{58}$$

$$R_4 = R_{13}, \quad R_5 = R_{23}, \quad R_6 = R_{33}. \tag{58'}$$

It can be obtained from Eq. (57) that $R_6 = 1/R_1R_3$. This implies that only five out of the six R_i's are independent of each other. Without loss of generality, let R_6 be expressed in terms of R_1 and R_3 in following derivations.

The components of $\boldsymbol{\mathcal{H}}$ in the material coordinate system, $\mathcal{H}_{ijkl}$, can be written in the Voigt notation as H_{ij}. According to Ref. [35], the diagonal components of H_{ij} can be related to R_i by

$$H_{11} = -\frac{2}{3}\frac{R_1R_3 - 2R_1 - 2}{R_1 + 1}, \quad \frac{H_{22}}{H_{11}} = -\frac{1}{2}\frac{(2R_2 + 1)(R_1R_3 + 1)}{R_1R_3 - 2R_1 - 2}, \tag{59}$$

$$\frac{H_{33}}{H_{11}} = 1 - \frac{3(R_1R_3 - 1)}{R_1R_3 - 2R_1 - 2}, \quad \frac{H_{44}}{H_{11}} = -\frac{1}{2}\frac{(2R_4 + 1)(R_3 + 1)R_1}{R_1R_3 - 2R_1 - 2}, \tag{59'}$$

$$\frac{H_{55}}{H_{11}} = -\frac{1}{2}\frac{(2R_5 + 1)(R_1 + 1)}{R_1R_3 - 2R_1 - 2}, \quad \frac{H_{66}}{H_{11}} = 1 - \frac{3R_1(R_3 - 1)}{R_1R_3 - 2R_1 - 2}, \tag{59''}$$

while the off-diagonal components vanish. More details on $\boldsymbol{\mathcal{H}}$ can be found in Ref. [35], appendix A.

A special case of plastic anisotropy is plastic transverse isotropy, that is, there exists a plane of plastic isotropy in which the plastic material properties are equal in all directions. For example, if the x_2-x_3 plane is the plane of plastic isotropy, the R_i's can be expressed as

$$R_3 = R_5 = \frac{1}{R_6} = R, \quad R_2 = R_4 = R', \tag{60}$$

where R and R' can be measured from two uniaxial tensile tests. Accordingly, substituting Eq. (60) into Eq. (59) and rearranging the equations give

$$H_{11} = \frac{1}{3}(4 - R), \quad H_{22} = H_{44} = \frac{1}{6}(R + 1)(2R' + 1), \tag{61}$$

$$H_{33} = H_{55} = H_{66} = \frac{1}{3}(2R + 1). \tag{61'}$$

B. Partial Derivatives

Recall that the partial derivatives whose explicit expressions are to be derived are

$$\boldsymbol{\mathcal{K}} = \frac{\partial \dot{\boldsymbol{\epsilon}}^{vp}}{\partial \boldsymbol{\sigma}}, \quad \mathbf{L} = \frac{\partial \dot{\boldsymbol{\epsilon}}^{vp}}{\partial \epsilon_e^{vp}}, \quad \boldsymbol{\mathcal{M}} = \frac{\partial \dot{\boldsymbol{\epsilon}}^{vp}}{\partial \boldsymbol{\alpha}}, \quad \mathbf{N} = \frac{\partial \dot{\epsilon}_e^{vp}}{\partial \boldsymbol{\sigma}}, \quad P = \frac{\partial \dot{\epsilon}_e^{vp}}{\partial \epsilon_e^{vp}}, \quad \mathbf{Q} = \frac{\partial \dot{\epsilon}_e^{vp}}{\partial \boldsymbol{\alpha}}, \tag{62}$$

$$\boldsymbol{\mathcal{R}} = \frac{\partial \dot{\boldsymbol{\alpha}}}{\partial \boldsymbol{\sigma}}, \quad \mathbf{S} = \frac{\partial \dot{\boldsymbol{\alpha}}}{\partial \epsilon_e^{vp}}, \quad \boldsymbol{\mathcal{T}} = \frac{\partial \dot{\boldsymbol{\alpha}}}{\partial \boldsymbol{\alpha}}. \tag{62'}$$

Let $\boldsymbol{\mathcal{K}}$, $\mathbf{L}$, and $\boldsymbol{\mathcal{M}}$ be the first set of partial derivatives of interest. Eq. (8) shows that $\dot{\boldsymbol{\epsilon}}^{vp}$ is proportional to $\partial g/\partial \boldsymbol{\sigma}$. This leads one to seek for $\partial g/\partial \boldsymbol{\sigma}$. Note that the constituent obeys Hill's yield criterion along with an associated flow rule. This implies that $\partial g/\partial \boldsymbol{\sigma} = \partial f/\partial \boldsymbol{\sigma}$. In addition, Eqs. (11) and (12) also imply that $\partial f/\partial \boldsymbol{\sigma} = \partial \tilde{\sigma}_e/\partial \boldsymbol{\sigma}$. The task hereby becomes finding $\partial \tilde{\sigma}_e/\partial \boldsymbol{\sigma}$. Eq. (12) implies that $\tilde{\sigma}_e$ can be treated as an explicit function of neither $\boldsymbol{\sigma}$ nor $\boldsymbol{\alpha}$ but $\tilde{\boldsymbol{\sigma}}$, where $\tilde{\boldsymbol{\sigma}} = \boldsymbol{\sigma} - \boldsymbol{\alpha}$. It is beneficial to first find the relations among $\partial \tilde{\sigma}_e/\partial \tilde{\boldsymbol{\sigma}}$, $\partial \tilde{\sigma}_e/\partial \boldsymbol{\sigma}$, and $\partial \tilde{\sigma}_e/\partial \boldsymbol{\alpha}$. Specifically, $\partial \tilde{\sigma}_e/\partial \boldsymbol{\sigma}$ and $\partial \tilde{\sigma}_e/\partial \boldsymbol{\alpha}$ can be related to $\partial \tilde{\sigma}_e/\partial \tilde{\boldsymbol{\sigma}}$ using the chain rule by

$$\frac{\partial \tilde{\sigma}_e}{\partial \boldsymbol{\sigma}} = \frac{\partial \tilde{\sigma}_e}{\partial \tilde{\boldsymbol{\sigma}}} : \frac{\partial \tilde{\boldsymbol{\sigma}}}{\partial \boldsymbol{\sigma}} = \frac{\partial \tilde{\sigma}_e}{\partial \tilde{\boldsymbol{\sigma}}} : \boldsymbol{\mathcal{I}} = \frac{\partial \tilde{\sigma}_e}{\partial \tilde{\boldsymbol{\sigma}}} \quad \text{and} \quad \frac{\partial \tilde{\sigma}_e}{\partial \boldsymbol{\alpha}} = \frac{\partial \tilde{\sigma}_e}{\partial \tilde{\boldsymbol{\sigma}}} : \frac{\partial \tilde{\boldsymbol{\sigma}}}{\partial \boldsymbol{\alpha}} = \frac{\partial \tilde{\sigma}_e}{\partial \tilde{\boldsymbol{\sigma}}} : (-\boldsymbol{\mathcal{I}}) = -\frac{\partial \tilde{\sigma}_e}{\partial \tilde{\boldsymbol{\sigma}}}, \tag{63}$$

respectively. In fact, if a variable can be treated as an explicit function of neither $\boldsymbol{\sigma}$ nor $\boldsymbol{\alpha}$ but $\tilde{\boldsymbol{\sigma}}$, its partial derivatives with respect to $\tilde{\boldsymbol{\sigma}}$, $\boldsymbol{\sigma}$, and $\boldsymbol{\alpha}$ can always be related to each other by a relation similar to Eq. (63). This finding will help to simplify the derivations. According to Ref. [35], the explicit expression for $\partial \tilde{\sigma}_e/\partial \tilde{\boldsymbol{\sigma}}$ (also $\partial \tilde{\sigma}_e/\partial \boldsymbol{\sigma}$ and $-\partial \tilde{\sigma}_e/\partial \boldsymbol{\alpha}$) can be derived as

$$\frac{\partial \tilde{\sigma}_e}{\partial \tilde{\boldsymbol{\sigma}}} = \frac{1}{2\tilde{\sigma}_e}\frac{\partial \tilde{\sigma}_e^2}{\partial \tilde{\boldsymbol{\sigma}}} = \frac{1}{2\tilde{\sigma}_e}\left(\frac{3}{2}2\frac{\partial \tilde{\boldsymbol{\sigma}}'}{\partial \tilde{\boldsymbol{\sigma}}} : \boldsymbol{\mathcal{H}} : \tilde{\boldsymbol{\sigma}}'\right) = \frac{3}{2\tilde{\sigma}_e}\boldsymbol{\mathcal{J}} : \boldsymbol{\mathcal{H}} : \tilde{\boldsymbol{\sigma}}' = \frac{3}{2\tilde{\sigma}_e}\left(\boldsymbol{\mathcal{H}} : \tilde{\boldsymbol{\sigma}}'\right)', \tag{64}$$

where $\boldsymbol{\mathcal{J}}$ denotes the fourth-order deviatoric projection operator and takes the form of $\boldsymbol{\mathcal{J}} = \boldsymbol{\mathcal{I}} - \frac{1}{3}\mathbf{I} \otimes \mathbf{I}$ with $\mathbf{I}$ denoting the second-order identity tensor. Eq. (9) indicates that $\dot{\lambda}$ is proportional to Φ, which is given by Eq. (10). Substituting Eq. (11) into Eq. (10) gives

$$\Phi(\tilde{\boldsymbol{\sigma}}, \sigma_Y) = \left(\frac{\tilde{\sigma}_e}{\sigma_Y} - 1\right)^N. \tag{65}$$

Eqs. (8), (9), (64), and (65) imply that $\dot{\boldsymbol{\epsilon}}^{vp}$ can also be treated as an explicit function of neither $\boldsymbol{\sigma}$ nor $\boldsymbol{\alpha}$ but $\tilde{\boldsymbol{\sigma}}$. As mentioned above, this implies that

$$\frac{\partial \dot{\boldsymbol{\epsilon}}^{vp}}{\partial \tilde{\boldsymbol{\sigma}}} = \frac{\partial \dot{\boldsymbol{\epsilon}}^{vp}}{\partial \boldsymbol{\sigma}} = -\frac{\partial \dot{\boldsymbol{\epsilon}}^{vp}}{\partial \boldsymbol{\alpha}} \quad \text{or} \quad \boldsymbol{\mathcal{M}} = -\boldsymbol{\mathcal{K}}. \tag{66}$$

By definition, $\boldsymbol{\mathcal{K}}$ can be expressed as

$$\boldsymbol{\mathcal{K}} = \frac{\partial \dot{\boldsymbol{\epsilon}}^{vp}}{\partial \tilde{\boldsymbol{\sigma}}} = \frac{\partial}{\partial \tilde{\boldsymbol{\sigma}}}\left(\dot{\lambda}\frac{\partial g}{\partial \boldsymbol{\sigma}}\right) = \gamma\frac{\partial}{\partial \tilde{\boldsymbol{\sigma}}}\left(\Phi\frac{\partial \tilde{\sigma}_e}{\partial \tilde{\boldsymbol{\sigma}}}\right) = \gamma\left[\frac{\partial \Phi}{\partial \tilde{\boldsymbol{\sigma}}} \otimes \frac{\partial \tilde{\sigma}_e}{\partial \tilde{\boldsymbol{\sigma}}} + \Phi\frac{\partial}{\partial \tilde{\boldsymbol{\sigma}}}\left(\frac{\partial \tilde{\sigma}_e}{\partial \tilde{\boldsymbol{\sigma}}}\right)\right], \tag{67}$$

where

$$\frac{\partial \Phi}{\partial \tilde{\boldsymbol{\sigma}}} = N\left(\frac{\tilde{\sigma}_e}{\sigma_Y} - 1\right)^{N-1} \frac{\partial}{\partial \tilde{\boldsymbol{\sigma}}}\left(\frac{\tilde{\sigma}_e}{\sigma_Y} - 1\right) = \frac{N}{\sigma_Y}\left(\frac{\tilde{\sigma}_e}{\sigma_Y} - 1\right)^{N-1} \frac{\partial \tilde{\sigma}_e}{\partial \tilde{\boldsymbol{\sigma}}} \tag{68}$$

and

$$\begin{aligned} \frac{\partial}{\partial \tilde{\boldsymbol{\sigma}}}\left(\frac{\partial \tilde{\sigma}_e}{\partial \tilde{\boldsymbol{\sigma}}}\right) &= \frac{\partial}{\partial \tilde{\boldsymbol{\sigma}}}\left(\frac{3}{2\tilde{\sigma}_e}\boldsymbol{\mathcal{J}} : \boldsymbol{\mathcal{H}} : \tilde{\boldsymbol{\sigma}}'\right) = \frac{3}{2}\frac{\partial}{\partial \tilde{\boldsymbol{\sigma}}}\left(\frac{1}{\tilde{\sigma}_e}\right) \otimes \boldsymbol{\mathcal{J}} : \boldsymbol{\mathcal{H}} : \tilde{\boldsymbol{\sigma}}' + \frac{3}{2\tilde{\sigma}_e}\boldsymbol{\mathcal{J}} : \boldsymbol{\mathcal{H}} : \frac{\partial \tilde{\boldsymbol{\sigma}}'}{\partial \tilde{\boldsymbol{\sigma}}} \\ &= \frac{3}{2}\left(-\frac{1}{\tilde{\sigma}_e^2}\frac{\partial \tilde{\sigma}_e}{\partial \tilde{\boldsymbol{\sigma}}}\right) \otimes \boldsymbol{\mathcal{J}} : \boldsymbol{\mathcal{H}} : \tilde{\boldsymbol{\sigma}}' + \frac{3}{2\tilde{\sigma}_e}\boldsymbol{\mathcal{J}} : \boldsymbol{\mathcal{H}} : \boldsymbol{\mathcal{J}} = -\frac{1}{\tilde{\sigma}_e}\frac{\partial \tilde{\sigma}_e}{\partial \tilde{\boldsymbol{\sigma}}} \otimes \frac{\partial \tilde{\sigma}_e}{\partial \tilde{\boldsymbol{\sigma}}} + \frac{3}{2\tilde{\sigma}_e}\boldsymbol{\mathcal{J}} : \boldsymbol{\mathcal{H}} : \boldsymbol{\mathcal{J}}. \end{aligned} \tag{69}$$

Substituting Eqs. (68) and (69) into Eq. (67) gives and rearranging the equation give

$$\boldsymbol{\mathcal{K}} = \frac{\partial \dot{\boldsymbol{\epsilon}}^{vp}}{\partial \tilde{\boldsymbol{\sigma}}} = \gamma\left(\frac{\tilde{\sigma}_e}{\sigma_Y} - 1\right)^{N-1}\left[\left(\frac{N-1}{\sigma_Y} + \frac{1}{\tilde{\sigma}_e}\right)\frac{\partial \tilde{\sigma}_e}{\partial \tilde{\boldsymbol{\sigma}}} \otimes \frac{\partial \tilde{\sigma}_e}{\partial \tilde{\boldsymbol{\sigma}}} + \frac{3}{2}\left(\frac{1}{\sigma_Y} - \frac{1}{\tilde{\sigma}_e}\right)\boldsymbol{\mathcal{J}} : \boldsymbol{\mathcal{H}} : \boldsymbol{\mathcal{J}}\right]. \tag{70}$$

Similarly to $\boldsymbol{\mathcal{K}}$, $\mathbf{L}$ can be expressed as

$$\mathbf{L} = \frac{\partial \dot{\boldsymbol{\epsilon}}^{vp}}{\partial \epsilon_e^{vp}} = \frac{\partial}{\partial \epsilon_e^{vp}}\left(\dot{\lambda}\frac{\partial g}{\partial \boldsymbol{\sigma}}\right) = \gamma\frac{\partial}{\partial \epsilon_e^{vp}}\left(\Phi\frac{\partial \tilde{\sigma}_e}{\partial \tilde{\boldsymbol{\sigma}}}\right) = \gamma\frac{\partial \Phi}{\partial \epsilon_e^{vp}}\frac{\partial \tilde{\sigma}_e}{\partial \tilde{\boldsymbol{\sigma}}}, \tag{71}$$

where

$$\frac{\partial \Phi}{\partial \epsilon_e^{vp}} = N\left(\frac{\tilde{\sigma}_e}{\sigma_Y} - 1\right)^{N-1}\frac{\partial}{\partial \epsilon_e^{vp}}\left(\frac{\tilde{\sigma}_e}{\sigma_Y} - 1\right) = -N\frac{\tilde{\sigma}_e}{\sigma_Y^2}\left(\frac{\tilde{\sigma}_e}{\sigma_Y} - 1\right)^{N-1}\frac{d\sigma_Y}{d\epsilon_e^{vp}}. \tag{72}$$

Substituting Eqs. (72) into Eq. (71) gives and rearranging the equation give

$$\mathbf{L} = \frac{\partial \dot{\epsilon}^{vp}}{\partial \epsilon_e^{vp}} = -\gamma N\frac{\tilde{\sigma}_e}{\sigma_Y^2}\left(\frac{\tilde{\sigma}_e}{\sigma_Y} - 1\right)^{N-1}\frac{d\sigma_Y}{d\epsilon_e^{vp}}\frac{\partial \tilde{\sigma}_e}{\partial \tilde{\boldsymbol{\sigma}}}. \tag{73}$$

Let $\mathbf{N}$, P, and $\mathbf{Q}$ be the next set of partial derivatives of interest. Substituting Eqs. (8), (12) and (64) into the term to the right of the equal sign of Eq. (13) gives

$$\tilde{\boldsymbol{\sigma}}' : \dot{\boldsymbol{\epsilon}}^{vp\prime} = \tilde{\boldsymbol{\sigma}}' : \dot{\lambda}\frac{\partial g}{\partial \boldsymbol{\sigma}} = \dot{\lambda}\frac{3}{2\tilde{\sigma}_e}\tilde{\boldsymbol{\sigma}}' : \boldsymbol{\mathcal{J}} : \boldsymbol{\mathcal{H}} : \tilde{\boldsymbol{\sigma}}' = \dot{\lambda}\frac{3}{2\tilde{\sigma}_e}\tilde{\boldsymbol{\sigma}}' : \boldsymbol{\mathcal{H}} : \tilde{\boldsymbol{\sigma}}' = \dot{\lambda}\frac{\tilde{\sigma}_e^2}{\tilde{\sigma}_e} = \tilde{\sigma}_e\dot{\lambda}. \tag{74}$$

Comparing Eq. (74) with Eq. (13) gives $\dot{\lambda} = \dot{\epsilon}_e^{vp}$, which has been proven valid for a material obeying the von Mises yield criterion along with an associated flow rule. Eqs. (9) and (65) imply that ϵ_e^{vp} can also be treated as an explicit function of neither $\boldsymbol{\sigma}$ nor $\boldsymbol{\alpha}$ but $\tilde{\boldsymbol{\sigma}}$. This implies that

$$\frac{\partial \dot{\epsilon}_e^{vp}}{\partial \tilde{\boldsymbol{\sigma}}} = \frac{\partial \dot{\epsilon}_e^{vp}}{\partial \boldsymbol{\sigma}} = -\frac{\partial \dot{\epsilon}_e^{vp}}{\partial \boldsymbol{\alpha}} \quad \text{or} \quad \mathbf{Q} = -\mathbf{N}. \tag{75}$$

By definition, $\mathbf{N}$ and P can be expressed as

$$\mathbf{N} = \frac{\partial \dot{\epsilon}_e^{vp}}{\partial \tilde{\boldsymbol{\sigma}}} = \frac{\partial \dot{\lambda}}{\partial \tilde{\boldsymbol{\sigma}}} = \gamma\frac{\partial \Phi}{\partial \tilde{\boldsymbol{\sigma}}} = \gamma\frac{N}{\sigma_Y}\left(\frac{\tilde{\sigma}_e}{\sigma_Y} - 1\right)^{N-1}\frac{\partial \tilde{\sigma}_e}{\partial \tilde{\boldsymbol{\sigma}}} \tag{76}$$

and

$$P = \frac{\partial \dot{\epsilon}_e^{vp}}{\partial \epsilon_e^{vp}} = \frac{\partial \dot{\lambda}}{\partial \epsilon_e^{vp}} = \gamma\frac{\partial \Phi}{\partial \epsilon_e^{vp}} = -\gamma N\frac{\tilde{\sigma}_e}{\sigma_Y^2}\left(\frac{\tilde{\sigma}_e}{\sigma_Y} - 1\right)^{N-1}\frac{d\sigma_Y}{d\epsilon_e^{vp}}, \tag{77}$$

respectively.

Now the remaining partial derivatives become $\boldsymbol{\mathcal{R}}$, $\mathbf{S}$, and $\boldsymbol{\mathcal{T}}$. Recall that the Chaboche model writes

$$\boldsymbol{\alpha} = \sum \boldsymbol{\alpha}_i, \tag{78}$$

where

$$\dot{\boldsymbol{\alpha}}_i = \frac{2}{3}C_i\dot{\boldsymbol{\epsilon}}^{vp} - \gamma_i\dot{\epsilon}_e^{vp}\boldsymbol{\alpha}_i. \tag{79}$$

Substituting Eqs. (78) and (79) into the last three equations of Eq. (62) gives

$$\boldsymbol{\mathcal{R}} = \frac{\partial \dot{\boldsymbol{\alpha}}}{\partial \boldsymbol{\sigma}} = \frac{\partial \sum \dot{\boldsymbol{\alpha}}_i}{\partial \boldsymbol{\sigma}} = \sum \frac{\partial \dot{\boldsymbol{\alpha}}_i}{\partial \boldsymbol{\sigma}} = \sum \left(\frac{2}{3} C_i \frac{\partial \dot{\boldsymbol{\epsilon}}^{vp}}{\partial \boldsymbol{\sigma}} - \gamma_i \frac{\partial \dot{\epsilon}_e^{vp}}{\partial \boldsymbol{\sigma}} \otimes \boldsymbol{\alpha}_i \right) = \sum \left(\frac{2}{3} C_i \boldsymbol{\mathcal{K}} - \gamma_i \mathbf{N} \otimes \boldsymbol{\alpha}_i \right), \tag{80}$$

$$\mathbf{S} = \frac{\partial \dot{\boldsymbol{\alpha}}}{\partial \epsilon_e^{vp}} = \sum \frac{\partial \dot{\boldsymbol{\alpha}}_i}{\partial \epsilon_e^{vp}} = \sum \left(\frac{2}{3} C_i \frac{\partial \dot{\boldsymbol{\epsilon}}^{vp}}{\partial \epsilon_e^{vp}} - \gamma_i \frac{\partial \dot{\epsilon}_e^{vp}}{\partial \epsilon_e^{vp}} \boldsymbol{\alpha}_i \right) = \sum \left(\frac{2}{3} C_i \mathbf{L} - \gamma_i P \boldsymbol{\alpha}_i \right), \tag{80'}$$

$$\begin{aligned} \boldsymbol{\mathcal{T}} = \frac{\partial \dot{\boldsymbol{\alpha}}}{\partial \boldsymbol{\alpha}} &= \sum \frac{\partial \dot{\boldsymbol{\alpha}}_i}{\partial \boldsymbol{\alpha}} = \sum \left[\frac{2}{3} C_i \frac{\partial \dot{\boldsymbol{\epsilon}}^{vp}}{\partial \boldsymbol{\alpha}} - \gamma_i \left(\frac{\partial \dot{\epsilon}_e^{vp}}{\partial \boldsymbol{\alpha}} \otimes \boldsymbol{\alpha}_i + \dot{\epsilon}_e^{vp} \frac{\partial \boldsymbol{\alpha}_i}{\partial \boldsymbol{\alpha}} \right) \right] \\ &= -\sum \left(\frac{2}{3} C_i \frac{\partial \dot{\boldsymbol{\epsilon}}^{vp}}{\partial \boldsymbol{\sigma}} - \gamma_i \frac{\partial \dot{\epsilon}_e^{vp}}{\partial \boldsymbol{\sigma}} \otimes \boldsymbol{\alpha}_i \right) - \sum \gamma_i \dot{\epsilon}_e^{vp} \boldsymbol{\mathcal{I}} = -\boldsymbol{\mathcal{R}} - \sum \gamma_i \dot{\epsilon}_e^{vp} \boldsymbol{\mathcal{I}}. \end{aligned} \tag{80''}$$

Note that, in Eq. (80), $\boldsymbol{\mathcal{T}} \neq -\boldsymbol{\mathcal{R}}$ because $\dot{\boldsymbol{\alpha}}$ can merely be treated as an explicit function of both $\tilde{\boldsymbol{\sigma}}$ and $\boldsymbol{\alpha}$.

Till now, the explicit expressions for all the partial derivatives in Eq. (62) (or Eq. (23)) have been derived and are ready to be substituted into the general affine formulation.

C. Affine Formulations for Isotropic/Kinematic Hardening Constituents

First let the constituent merely exhibit isotropic hardening, and accordingly, let $\dot{\boldsymbol{\epsilon}}^{vp}$ and $\dot{\epsilon}_e^{vp}$ be functions of $\boldsymbol{\sigma}$ and ϵ_e^{vp}, respectively, i.e.,

$$\dot{\boldsymbol{\epsilon}}^{vp}(t) = \dot{\boldsymbol{\epsilon}}^{vp}\left(\boldsymbol{\sigma}(t), \epsilon_e^{vp}(t)\right) \quad \text{and} \quad \dot{\epsilon}_e^{vp}(t) = \dot{\epsilon}_e^{vp}\left(\boldsymbol{\sigma}(t), \epsilon_e^{vp}(t)\right), \tag{81}$$

and accordingly, the evolution equations of $\dot{\boldsymbol{\epsilon}}^{vp}$ and $\dot{\epsilon}_e^{vp}$ become

$$\dot{\boldsymbol{\epsilon}}^{vp}(t_{n+1}) = \dot{\boldsymbol{\epsilon}}^{vp}(t_n) + \boldsymbol{\mathcal{K}}(t_{n+1}) : \Delta\boldsymbol{\sigma} + \mathbf{L}(t_{n+1}) \Delta\epsilon_e^{vp}, \tag{82}$$

$$\dot{\epsilon}_e^{vp}(t_{n+1}) = \dot{\epsilon}_e^{vp}(t_n) + \mathbf{N}(t_{n+1}) : \Delta\boldsymbol{\sigma} + P(t_{n+1}) \Delta\epsilon_e^{vp}, \tag{82'}$$

where $\boldsymbol{\mathcal{K}}$, $\mathbf{L}$, $\mathbf{N}$, and P are still given by Eq. (23). Substituting $\Delta\epsilon_e^{vp} = \dot{\epsilon}_e^{vp}(t_{n+1})\Delta t$ into the second equation of Eq. (82) and rearranging the equation give

$$\dot{\epsilon}_e^{vp}(t_{n+1}) = \frac{\dot{\epsilon}_e^{vp}(t_n) + \mathbf{N}(t_{n+1}) : \Delta\sigma}{1 - P(t_{n+1})\Delta t}. \tag{83}$$

Substituting Eq. (83) into the first equation of Eq. (81) and rearranging the equation give

$$\dot{\boldsymbol{\epsilon}}^{vp}(t_{n+1}) = \dot{\tilde{\boldsymbol{\epsilon}}}(t_{n+1}) + \tilde{\boldsymbol{\mathcal{C}}}^{-1}(t_{n+1}) : \Delta\boldsymbol{\sigma}, \tag{84}$$

where

$$\dot{\tilde{\boldsymbol{\epsilon}}}(t_{n+1}) = \dot{\boldsymbol{\epsilon}}^{vp}(t_n) + \frac{\dot{\epsilon}_e^{vp}(t_n)}{1 - P(t_{n+1})\Delta t} \mathbf{L}(t_{n+1}) \Delta t \tag{85}$$

and

$$\tilde{\boldsymbol{\mathcal{C}}}^{-1}(t_{n+1}) = \boldsymbol{\mathcal{K}}(t_{n+1}) + \frac{\mathbf{L}(t_{n+1}) \otimes \mathbf{N}(t_{n+1})}{1 - P(t_{n+1})\Delta t} \Delta t. \tag{86}$$

Since Eq. (84) is almost the same as Eq. (30) except that $\dot{\tilde{\boldsymbol{\epsilon}}}(t_{n+1})$ and $\tilde{\boldsymbol{\mathcal{C}}}^{-1}(t_{n+1})$ take different forms, Eqs. (33) - (37) remain valid here.

Next let the constituent merely exhibit kinematic hardening, and accordingly, let $\dot{\boldsymbol{\epsilon}}^{vp}$ and $\dot{\boldsymbol{\alpha}}$ be functions of $\boldsymbol{\sigma}$ and $\boldsymbol{\alpha}$, respectively, i.e.,

$$\dot{\boldsymbol{\epsilon}}^{vp}(t) = \dot{\boldsymbol{\epsilon}}^{vp}\left(\boldsymbol{\sigma}(t), \boldsymbol{\alpha}(t)\right) \quad \text{and} \quad \dot{\boldsymbol{\alpha}}(t) = \dot{\boldsymbol{\alpha}}\left(\boldsymbol{\sigma}(t), \boldsymbol{\alpha}(t)\right), \tag{87}$$

and accordingly, the evolution equations of $\dot{\boldsymbol{\epsilon}}^{vp}$ and $\dot{\boldsymbol{\alpha}}$ become

$$\dot{\boldsymbol{\epsilon}}^{vp}(t_{n+1}) = \dot{\boldsymbol{\epsilon}}^{vp}(t_n) + \boldsymbol{\mathcal{K}}(t_{n+1}) : \Delta\boldsymbol{\sigma} + \boldsymbol{\mathcal{M}}(t_{n+1}) : \Delta\boldsymbol{\alpha}, \tag{88}$$

$$\dot{\boldsymbol{\alpha}}(t_{n+1}) = \dot{\boldsymbol{\alpha}}(t_n) + \boldsymbol{\mathcal{R}}(t_{n+1}) : \Delta\boldsymbol{\sigma} + \boldsymbol{\mathcal{T}}(t_{n+1}) : \Delta\boldsymbol{\alpha}, \tag{88'}$$

where $\boldsymbol{\mathcal{K}}$, $\boldsymbol{\mathcal{M}}$, $\boldsymbol{\mathcal{R}}$, and $\boldsymbol{\mathcal{T}}$ are still given by Eq. (23). Substituting $\Delta\boldsymbol{\alpha} = \dot{\boldsymbol{\alpha}}\left(t_{n+1}\right)\Delta t$ into the second equation of Eq. (88) and rearranging the equation give

$$\dot{\boldsymbol{\alpha}}\left(t_{n+1}\right) = \left[\boldsymbol{\mathcal{I}} - \boldsymbol{\mathcal{T}}\left(t_{n+1}\right)\Delta t\right]^{-1} : \left[\dot{\boldsymbol{\alpha}}\left(t_n\right) + \boldsymbol{\mathcal{R}}\left(t_{n+1}\right) : \Delta\boldsymbol{\sigma}\right], \tag{89}$$

Substituting Eq. (89) into the first equation of Eq. (87) and rearranging the equation give

$$\dot{\boldsymbol{\epsilon}}^{vp}\left(t_{n+1}\right) = \dot{\tilde{\boldsymbol{\epsilon}}}\left(t_{n+1}\right) + \tilde{\boldsymbol{\mathcal{C}}}^{-1}\left(t_{n+1}\right) : \Delta\boldsymbol{\sigma}, \tag{90}$$

where

$$\dot{\tilde{\boldsymbol{\epsilon}}}\left(t_{n+1}\right) = \dot{\boldsymbol{\epsilon}}^{vp}\left(t_n\right) + \boldsymbol{\mathcal{M}}\left(t_{n+1}\right) : \left[\boldsymbol{\mathcal{I}} - \boldsymbol{\mathcal{T}}\left(t_{n+1}\right)\Delta t\right]^{-1} : \dot{\boldsymbol{\alpha}}\left(t_n\right)\Delta t \tag{91}$$

and

$$\tilde{\boldsymbol{\mathcal{C}}}^{-1}\left(t_{n+1}\right) = \boldsymbol{\mathcal{K}}\left(t_{n+1}\right) + \boldsymbol{\mathcal{M}}\left(t_{n+1}\right) : \left[\boldsymbol{\mathcal{I}} - \boldsymbol{\mathcal{T}}\left(t_{n+1}\right)\Delta t\right]^{-1} : \boldsymbol{\mathcal{R}}\left(t_{n+1}\right)\Delta t. \tag{92}$$

Similarly to the case of an isotropic hardening constituent, Eqs. (33) - (37) also remain valid here.

References

[1]Yu, W. and Tang, T., "Variational asymptotic method for unit cell homogenization of periodically heterogeneous materials," *International Journal of Solids and Structures*, Vol. 44, No. 11-12, 2007, pp. 3738–3755.

[2]Hill, R., "A self-consistent mechanics of composite materials," *Journal of the Mechanics of Physics and Solids*, Vol. 13, 1965, pp. 213–222.

[3]Hashin, Z. and Shtrikman, S., "A variational approach to the theory of the elastic behaviour of multiphase materials," *Journal of the Mechanics and Physics of Solids*, Vol. 11, No. 2, 1963, pp. 127–140.

[4]Milton, G., "Bounds on the electromagnetic, elastic, and other properties of two-component composites," *Physical Review Letters*, Vol. 46, No. 8, 1981, pp. 542–545.

[5]Aboudi, J., "Generalized effective stiffness theory for the modeling of fiber-reinforced composites," *International Journal of Solids and Structures*, Vol. 17, No. 10, 1981, pp. 1005 – 1018.

[6]Banerjee, B. and Adams, D. O., "On predicting the effective elastic properties of polymer bonded explosives using the recursive cell method," *International Journal of Solids and Structures*, Vol. 41, No. 2, 2004, pp. 481–509.

[7]Bensoussan, A., Lions, J., and Papanicolaou, G., *Asymptotic analysis for periodic structures*, North-Holland, Amsterdam, 1978.

[8]Murakami, H. and Toledano, A., "A high-order mixture homogenization of bi-laminated composites," *Transactions of the ASME. Journal of Applied Mechanics*, Vol. 57, No. 2, 1990, pp. 388–397.

[9]Lebensohn, R. and Tom, C., "A self-consistent anisotropic approach for the simulation of plastic deformation and texture development of polycrystals: Application to zirconium alloys," *Acta Metallurgica et Materialia*, Vol. 41, No. 9, 1993, pp. 2611–2624.

[10]Berveiller, M. and Zaoui, A., "An extension of the self-consistent scheme to plastically-flowing polycrystals," *Journal of the Mechanics and Physics of Solids*, Vol. 26, No. 5-6, 1978, pp. 325–344.

[11]Tandon, G. and Weng, G., "A theory of particle-reinforced plasticity," *Transactions of the ASME. Journal of Applied Mechanics*, Vol. 55, No. 1, 1988, pp. 126–135.

[12]Suquet, P., "Overall properties of nonlinear composites: a modified secant moduli theory and its link with Ponte Castaeda's nonlinear variational procedure," *Comptes rendus de l'Acadmie des sciences. Srie II, Mcanique, physique, chimie, astronomie*, Vol. 320, No. 11, 1995, pp. 563–571.

[13]Hutchinson, J., "Bounds and self-consistent estimates for creep of polycrystalline materials," *Proceedings of the Royal Society of London. Series A: Mathematical and Physical Sciences*, Vol. 348, No. 1652, 1976, pp. 101–127.

[14]Weng, G., "A unified, self-consistent theory for the plastic-creep deformation of metals," *Transactions of the ASME. Journal of Applied Mechanics*, Vol. 49, No. 4, 1982, pp. 728–734.

[15]Nemat-Nasser, S. and Obata, M., "Rate-dependent, finite elasto-plastic deformation of polycrystals," *Proceedings of the Royal Society of London. A. Mathematical and Physical Sciences*, Vol. 407, No. 1833, 1986, pp. 343–375.

[16]Li, J. and Weng, G., "A unified approach from elasticity to viscoelasticity to viscoplasticity of particle-reinforced solids," *International Journal of Plasticity*, Vol. 14, No. 1-3, 1998, pp. 193–208.

[17]Molinari, A., Canova, G., and Ahzi, S., "A self consistent approach of the large deformation polycrystal viscoplasticity," *Acta Metallurgica*, Vol. 35, No. 12, 1987, pp. 2983–2994.

[18]Molinari, A., Ahzi, S., and Kouddane, R., "On the self-consistent modeling of elastic-plastic behavior of polycrystals," *Mechanics of Materials*, Vol. 26, No. 1, 1997, pp. 43–62.

[19]Masson, R. and Zaoui, A., "Self-consistent estimates for the rate-dependent elastoplastic behaviour of polycrystalline materials," *Journal of the Mechanics and Physics of Solids*, Vol. 47, No. 7, 1999, pp. 1543–1568.

[20]Masson, R., Bornert, M., Suquet, P., and Zaoui, A., "An affine formulation for the prediction of the effective properties of nonlinear composites and polycrystals," *Journal of the Mechanics and Physics of Solids*, Vol. 48, No. 6-7, 2000, pp. 1203–1227.

[21]Pierard, O. and Doghri, I., "An enhanced affine formulation and the corresponding numerical algorithms for the mean-field homogenization of elasto-viscoplastic composites," *International Journal of Plasticity*, Vol. 22, No. 1, 2006, pp. 131–157.

[22]Pierard, O., LLorca, J., Segurado, J., and Doghri, I., "Micromechanics of particle-reinforced elasto-viscoplastic composites: finite element simulations versus affine homogenization," *International Journal of Plasticity*, Vol. 23, No. 6, 2007, pp. 1041–1060.

[23]Doghri, I., Adam, L., and Bilger, N., "Mean-field homogenization of elasto-viscoplastic composites based on a general incrementally affine linearization method," *International Journal of Plasticity*, Vol. 26, No. 2, 2010, pp. 219–238.

[24]Aboudi, J., "A continuum theory for fiber-reinforced elastic-viscoplastic composites," *International Journal of Engineering Science*, Vol. 20, No. 5, 1982, pp. 605–621.

[25]Paley, M. and Aboudi, J., "Micromechanical analysis of composites by the generalized cells model," *Mechanics of Materials*, Vol. 14, 1992, pp. 127–139.

[26]Adoudi, J., "The generalized method of cells and high-fidelity generalized method of cells micromechanical models-a review," *Mechanics of Advanced Materials and Structures*, Vol. 11, No. 4-5, 2004, pp. 329–366.

[27]Aboudi, J., "Micromechanical analysis of the finite elastic-viscoplastic response of multiphase composites," *International Journal of Solids and Structures*, Vol. 40, 2003, pp. 2793–2817.

[28]Williams, T., Yu, W., Aboudi, J., and Bednarcyk, B., "A critical evaluation of the predictive capabilities of various advanced micromechanics models," *Proceedings of the 48th Structures, Structural Dynamics, and Materials Conference*, Waikiki, 2007.

[29]Yu, W. and Tang, T., "A variational asymptotic micromechanics model for predicting thermoelastic properties of heterogeneous materials," *International Journal of Solids and Structures*, Vol. 44, No. 22-23, 2007, pp. 7510–7525.

[30]Tang, T. and Yu, W., "A variational asymptotic micromechanics model for predicting conductivity of composite materials," *Journal of Mechanics of Materials and Structures*, Vol. 2, 2007, pp. 1813–1830.

[31]Tang, T. and Yu, W., "Variational asymptotic homogenization of heterogeneous electromagnetoelastic materials," *International Journal of Engineering Science*, Vol. 46, No. 8, 2008, pp. 741–757.

[32]Tang, T. and Yu, W., "Variational asymptotic micromechanics modeling of heterogeneous piezoelectric materials," *Mechanics of Materials*, Vol. 40, No. 10, 2008, pp. 812–824.

[33]Tang, T. and Yu, W., "Asymptotical approach to initial yielding surface and elastoplasticity of heterogeneous materials," *Mechanics of Advanced Materials and Structures*, Vol. 18, No. 4, 2011, pp. 244–254.

[34]Perzyna, P., "Fundamental problems in viscoplasticity," *Advances in Applied Mechanics*, Vol. 9, Academic Press, 1966, pp. 243–377.

[35]Benzerga, A. A. and Besson, J., "Plastic potentials for anisotropic porous solids," *European Journal of Mechanics, A/Solids*, Vol. 20, No. 3, 2001, pp. 397–434.

[36]Voce, E., "A practical strain-hardening function," *Metallurgia*, Vol. 51, No. 307, 1955, pp. 219–226.

[37]Lemaitre, J. and Chaboche, J.-L., *Mechanics of solid materials*, Cambridge University Press, 1994.

[38]Zhao, K. M. and Lee, J. K., "Material properties of aluminum alloy for accurate draw-bend simulation," *Journal of Engineering Materials and Technology*, Vol. 123, No. 3, 2001, pp. 287–292.

International Journal of Solids and Structures 51 (2014) 3878–3888

Contents lists available at ScienceDirect

International Journal of Solids and Structures

journal homepage: www.elsevier.com/locate/ijsolstr

A micromechanics approach to homogenizing elasto-viscoplastic heterogeneous materials

Liang Zhang *, Wenbin Yu

Purdue University, West Lafayette, IN 47907-2045, USA

ARTICLE INFO

Article history:
Received 3 May 2013
Received in revised form 27 March 2014
Available online 29 July 2014

Keywords:
VAMUCH
Nonlinear homogenization
Affine formulation
Viscoplastic anisotropy
Combined isotropic–kinematic hardening

ABSTRACT

The variational asymptotic method for unit cell homogenization (VAMUCH) has emerged as a general-purpose micromechanics code capable of predicting the effective properties of heterogeneous materials and recovering the local fields. The objective of this paper is to propose a micromechanics approach enabling VAMUCH to homogenize elasto-viscoplastic heterogeneous materials. An affine formulation of the constitutive relations for an elasto-viscoplastic constituent, which exhibits viscoplastic anisotropy and combined isotropic–kinematic hardening, is derived. The weak form of the problem is derived using an asymptotic method, discretized using finite elements, and implemented into VAMUCH. The new features of VAMUCH are validated with examples such as homogenizing binary, fiber-reinforced, and particle-reinforced composites. VAMUCH is found to be capable of handling various microstructure, complex material models, complex loading conditions, and complex loading paths. More sophisticated material models can be implemented into it.

1. Introduction

Heterogeneous materials are widely used in structural components due to their capabilities of exhibiting designated in-plane stiffness, bending stiffness, ultimate strength, or thermal expansion coefficient. When they are deformed to certain extents at high temperatures, their constituents often exhibit elasto-viscoplastic behaviors. It is challenging to evaluate their mechanical responses because their deformations are often accompanied by material nonlinearity, history dependency, and rate dependency. Moreover, it is difficult and time consuming to manufacture a great amount of specimens and to perform various tests on them, while it is computationally prohibitive to analyze them with all the micro-structural details because the dimensions of the macroscopic structures are usually several orders of magnitude greater than the heterogeneity length scale. Therefore, it is of great practical value to solve such problems using a micromechanics approach.

In recent decades, numerous efforts have been devoted to micromechanics. A micromechanics approach generally consists of the following steps (Yu and Tang, 2007a):

1. Identify the unit cell (UC) of a heterogeneous material.
2. Compute the effective material properties through the constitutive modeling of the UC.
3. Assign these properties to the macroscopic structure and obtain the global response.
4. Feedback the global response to the local scale and recover the local fields (e.g., the displacement, strain, and stress fields).

If the deformation is restricted in the linearly elastic regime it is history- and rate-independent. In this case, the effective material properties remain constant all the time, and one just needs to perform the constitutive modeling. The micromechanics theories of linearly elastic heterogeneous materials are well established. These theories include the mean-field homogenization (MFH) (Hill, 1965a; Mori and Tanaka, 1973), Hashin and Shtrikman's variational approach (Hashin and Shtrikman, 1963), the third-order bounds (Milton, 1981), the method of cells (MOC) (Aboudi, 1981), the recursive cell method (Banerjee and Adams, 2004), and the mathematical homogenization theories (MHT) (Bensoussan et al., 1978; Murakami and Toledano, 1990), and some others. If the deformation is extended to the viscoplastic regime, it becomes history- and rate-dependent. In this case, there does not exist a correspondence principal between the stress and strain rates, and one must linearize the constitutive relations and perform an incremental analysis.

MFH is among the most popular micromechanics approaches and consists of two major approaches, i.e., the tangent and secant

* Corresponding author. Tel.: +1 979 618 6481.
E-mail addresses: zhangliang115@hotmail.com (L. Zhang), wenbinyu@purdue.edu (W. Yu).

http://dx.doi.org/10.1016/j.ijsolstr.2014.07.003
0020-7683/

approaches. As the name suggests, the tangent approach is based on a tangent linearization of the constitutive relations (Hill, 1965b; Lebensohn and TomT, 1993), while the secant approach is based on a secant linearization (Berveiller and Zaoui, 1978; Tandon and Weng, 1988; Suquet, 1995). Hutchinson (1976) first enabled Hill's incremental approach to homogenize rigid-viscoplastic polycrystals. Weng (1982) proposed a secant approach to homogenizing elasto-viscoplastic polycrystals, in which the inelastic strain is treated as a stress-free eigenstrain such that the problem is transformed to an elastic one. Nemat-Nasser and Obata (1986) later improved this approach by taking account into finite deformation. These early approaches are unable to take account into the viscoplastic interactions among different constituents and tend to generate too stiff predictions.

Elaborate efforts have been devoted to overcoming these drawbacks. Li and Weng (1998) improved the secant approach by transforming the problem to a viscoelastic one, while Molinari et al. (1987, 1997) improved the tangent approach by transforming the problem to a thermoelastic one. Despite improvements, these two approaches either require a two-phase heterogeneous material or tend to underestimate the flow stress. Masson and his coworkers (Masson and Zaoui, 1999; Masson et al., 2000) proposed an affine approach, in which the constitutive relations are first linearized in the time domain and then transformed to the Laplace domain such that the problem is transformed to a thermoelastic one, and Pierard and his coworkers (Pierard and Doghri, 2006; Pierard et al., 2007) later enabled this approach to handle two-phase heterogeneous materials. Although the affine approach is capable of generating close predictions, it requires the inverse Laplace transformation, which is computationally costly. To overcome this drawback, Doghri et al. (2010) proposed an incrementally affine approach, in which the constitutive relations are linearized in numerous discrete time intervals such that the inverse Laplace transformation is avoided. Despite success, none of the aforementioned approaches can either recover the local fields or incorporate viscoplastic anisotropy and combined isotropic–kinematic hardening. Therefore, there is a need for a more powerful approach.

Numerous attempts have been made not only to linearize the constitutive relations but also to recover the local fields. Aboudi and his co-workers (Aboudi, 1982; Paley and Aboudi, 1992) developed the method of cells (MOC) and later the generalized method of cells (GMC) to achieve this goal. A detailed review on these approaches can be found in Adoudi (2004). The basic ideas of these approaches include subdividing the UC into numerous cuboid subcells, solving for the average strains and stresses over each subcell, and estimating the local fields. Despite improvements, these approaches suffer two major drawbacks: first, discretizing the UC using cuboid subcells may introduce considerable domain approximation errors; second, approximating the local fields using the average local strains and stresses may introduce considerable approximation errors. In fact, it is always more accurate to discretize the UC using a finite element mesh and to approximate the local fields using shape functions and nodal values. To overcome these drawbacks, Aboudi et al. (2002) developed the high fidelity generalized method of cells (HFGMC). Despite high accuracy, HFGMC is found to be quite computationally costly (Williams et al., 2007). All these lead one to seek for a more accurate and efficient approach.

In recent years, Yu and his co-workers (Yu and Tang, 2007a,b; Tang and Yu, 2007, 2008a,b) developed the variational asymptotic method for unit cell homogenization (VAMUCH). VAMUCH is a general-purpose micromechanics code capable of predicting the effective material properties and recovering the local fields. One of its unique features is that it has the minimum number of assumptions:

1. The heterogeneous material can be homogenized.
2. The effective material properties of a UC are independent of the geometry and boundary conditions of the macroscopic structure.

These two assumptions place the fewest restrictions on problem solving. Although VAMUCH seems as versatile as the traditional finite element method (FEM), it is distinct to FEM at least in the following aspects:

1. VAMUCH is specially developed for the constitutive modeling, while FEM is not, or to say, VAMUCH directly solves for the constitutive relations, while FEM directly solves for the displacements, strains, and stresses under certain load conditions.
2. VAMUCH can model the UC using the smallest mathematical building block, not necessarily a 3D volume, while FEM cannot (e.g., VAMUCH can use 1D and 2D UCs to compute the complete set of 3D properties of binary and fiber-reinforced composites, respectively (Yu and Tang, 2007a), while FEM has to use 3D UCs to achieve this).
3. VAMUCH solves for the fluctuation functions (see Eq. (49)), while FEM solves for the displacements.
4. VAMUCH deals with periodic boundary conditions, while FEM mostly deals with displacement and traction boundary conditions.
5. VAMUCH can obtain the complete set of effective material properties through one analysis, while FEM cannot (e.g., for linearly elastic materials, FEM has to run six times to do this (Xia et al., 2003)).

The objective of this paper is to propose a micromechanics approach enabling VAMUCH to homogenize elasto-viscoplastic heterogeneous materials. An affine formulation of the constitutive relations for an elasto-viscoplastic constituent, which exhibits viscoplastic anisotropy and combined isotropic–kinematic hardening, is derived. The weak form of the problem is derived using an asymptotic method, discretized using finite elements, and implemented into VAMUCH. The new features of VAMUCH are validated with examples such as homogenizing binary, fiber-reinforced, and particle-reinforced composites.

2. Thermodynamic formulations

Consider a heterogeneous material of an identifiable UC. Without loss of generality, let its constituents all be elasto-viscoplastic. Note that an elastic constituent can be treated as an elasto-viscoplastic one with infinite yield stress. In this section, some fundamentals of thermodynamics will be briefed.

Let ψ denote the Helmholtz free energy per unit mass of the constituent. According to the theory of thermodynamics, ψ can be expressed as a function of a suitable set of independent state variables characterizing the elastic and viscoplastic behaviors of the constituent, e.g.,

$$\psi = \psi(\boldsymbol{\epsilon}^e, \boldsymbol{\alpha}, r), \tag{1}$$

where $\boldsymbol{\epsilon}^e$ denotes the elastic strain tensor, $\boldsymbol{\alpha}$ is a second-order tensor accounting for kinematic hardening, and r is a scalar accounting for isotropic hardening. Assume that the constituent exhibits uncoupled elastic and viscoplastic behaviors. In this case, ψ can be decomposed into its elastic part, ψ^e, and its hardening part, ψ^{vp}, i.e.,

$$\psi(\boldsymbol{\epsilon}^e, \boldsymbol{\alpha}, r) = \psi^e(\boldsymbol{\epsilon}^e) + \psi^{vp}(\boldsymbol{\alpha}, r). \tag{2}$$

The thermodynamic forces conjugate to the state variables in Eq. (1) can be defined as

$$\boldsymbol{\sigma} = \rho\frac{\partial\psi}{\partial\boldsymbol{\epsilon}^e} = \rho\frac{\partial\psi^e}{\partial\boldsymbol{\epsilon}^e}, \quad \mathbf{X} = \rho\frac{\partial\psi}{\partial\boldsymbol{\alpha}} = \rho\frac{\partial\psi^{vp}}{\partial\boldsymbol{\alpha}}, \quad R = \frac{\partial\psi}{\partial r} = \rho\frac{\partial\psi^{vp}}{\partial r}, \tag{3}$$

where $\boldsymbol{\sigma}$ denotes the stress tensor, $\mathbf{X}$ denotes the back stress tenor, R is related to the current yield stress, and ρ denotes the density of the constituent.

If the deformation is isothermal, the Clausius–Duhem inequality writes

$$\phi = \boldsymbol{\sigma} : \dot{\boldsymbol{\epsilon}} - \rho\dot{\psi} \geqslant 0, \tag{4}$$

where ϕ denotes the dissipation per unit volume, and the overdot denotes the time derivative of the quantity. Note that the strain tensor, $\boldsymbol{\epsilon}$, can be decomposed into its elastic and viscoplastic parts, i.e.,

$$\boldsymbol{\epsilon} = \boldsymbol{\epsilon}^e + \boldsymbol{\epsilon}^{vp}. \tag{5}$$

Combining Eqs. (2)–(5) gives

$$\phi = \boldsymbol{\sigma} : \dot{\boldsymbol{\epsilon}}^{vp} - \mathbf{X} : \dot{\boldsymbol{\alpha}} - R\dot{r} \geqslant 0. \tag{6}$$

Assume that there exists a viscoplastic potential, Φ, which is a function of the thermodynamic forces and governs the evolution of the state variables, i.e.,

$$\dot{\boldsymbol{\epsilon}}^{vp} = \frac{\partial\Phi}{\partial\boldsymbol{\sigma}}, \quad \dot{\boldsymbol{\alpha}} = -\frac{\partial\Phi}{\partial\mathbf{X}}, \quad \dot{r} = -\frac{\partial\Phi}{\partial R}. \tag{7}$$

Without loss of generality, let

$$f = f(\boldsymbol{\sigma}, \mathbf{X}, R) \tag{8}$$

denote the yield function, and let

$$\Phi = \Phi(f) \quad \text{and} \quad \dot{\lambda} = \frac{\partial\Phi}{\partial f}. \tag{9}$$

Eq. (7) can then be rewritten using the chain rule as

$$\dot{\boldsymbol{\epsilon}}^{vp} = \dot{\lambda}\frac{\partial f}{\partial\boldsymbol{\sigma}}, \quad \dot{\boldsymbol{\alpha}} = -\dot{\lambda}\frac{\partial f}{\partial\mathbf{X}}, \quad \dot{r} = -\dot{\lambda}\frac{\partial f}{\partial R}, \tag{10}$$

where the specific forms of $\dot{\lambda}$ and f are to be determined.

Till now, some fundamentals of thermodynamics have been briefed. In the next section, the viscoplasticity model will be specified.

3. Viscoplasticity model

For notational convenience, let $\tilde{\boldsymbol{\sigma}} = \boldsymbol{\sigma} - \mathbf{X}$. Without loss of generality, let f take the form of Hill's yield function, i.e.,

$$f(\boldsymbol{\sigma}, \mathbf{X}, R) = \tilde{\sigma}_e - \sigma_Y, \tag{11}$$

where

$$\tilde{\sigma}_e = \sqrt{\frac{3}{2}\tilde{\boldsymbol{\sigma}}' : \mathcal{H} : \tilde{\boldsymbol{\sigma}}'}, \tag{12}$$

with $(\cdot)'$ denoting the deviatoric part of the tensor and $\mathcal{H}$ denoting the fourth-order anisotropy tensor, and σ_Y denotes the current yield stress and is related to R by

$$\sigma_Y = \sigma_0 + R, \tag{13}$$

where σ_0 denotes the initial yield stress. Substituting Eq. (12) into the modified viscoplastic work equivalence principle,

$$\tilde{\boldsymbol{\sigma}} : \dot{\boldsymbol{\epsilon}}^{vp} = \tilde{\sigma}_e\dot{p}, \tag{14}$$

gives the Hill equivalent viscoplastic strain rate as

$$\dot{p} = \sqrt{\frac{2}{3}\dot{\boldsymbol{\epsilon}}^{vp} : \mathcal{H}^{-1} : \dot{\boldsymbol{\epsilon}}^{vp}}, \tag{15}$$

where $\mathcal{H} : \mathcal{H}^{-1} = \mathcal{I}$ with $\mathcal{I}$ denoting the fourth-order identity tensor (Benzerga and Besson, 2001). $\mathcal{H}$ can be obtained from the R-values, which characterize viscoplastic anisotropy and can be measured from experiments (see Appendix A for more details).

It is beneficial to find the relation between $\dot{\lambda}$ and $\dot{p}$. Specifically, substituting the first equation of Eq. (10) into Eq. (14) gives

$$\tilde{\boldsymbol{\sigma}} : \left(\dot{\lambda}\frac{\partial f}{\partial\boldsymbol{\sigma}}\right) = \tilde{\sigma}_e\dot{p}. \tag{16}$$

The explicit expression for $\partial f/\partial\boldsymbol{\sigma}$ can be derived as (Benzerga and Besson, 2001)

$$\frac{\partial f}{\partial\boldsymbol{\sigma}} = \frac{\partial\tilde{\sigma}_e}{\partial\tilde{\boldsymbol{\sigma}}} = \frac{1}{2\tilde{\sigma}_e}\frac{\partial\tilde{\sigma}_e^2}{\partial\tilde{\boldsymbol{\sigma}}} = \frac{1}{2\tilde{\sigma}_e}\left(\frac{3}{2}2\frac{\partial\tilde{\boldsymbol{\sigma}}'}{\partial\tilde{\boldsymbol{\sigma}}} : \mathcal{H} : \tilde{\boldsymbol{\sigma}}'\right) = \frac{3}{2\tilde{\sigma}_e}\mathcal{J} : \mathcal{H} : \tilde{\boldsymbol{\sigma}}', \tag{17}$$

where $\mathcal{J}$ denotes the fourth-order deviatoric projection operator and takes the form of $\mathcal{J} = \mathcal{I} - \frac{1}{3}\mathbf{I}\otimes\mathbf{I}$ with $\mathbf{I}$ denoting the second-order identity tensor. Substituting Eq. (17) into Eq. (16) gives

$$\tilde{\sigma}_e\dot{\lambda} = \tilde{\sigma}_e\dot{p} \quad \text{or} \quad \dot{\lambda} = \dot{p}. \tag{18}$$

Eq. (10), together with Eq. (11), implies that nonlinear kinematic hardening is inadmissible. This indicates that Eq. (10) places too strict restrictions (Chaboche, 1997). To overcome this drawback, introduce a pseudo-potential g, which is related to f by

$$g = f + \frac{3}{4}\frac{\gamma}{C}\mathbf{X} : \mathbf{X} + \frac{R^2}{2K} \tag{19}$$

with C and γ being two constants accounting for nonlinear kinematic hardening and K being a constant accounting for isotropic hardening, and rewrite Eq. (10) as

$$\dot{\boldsymbol{\epsilon}}^{vp} = \dot{\lambda}\frac{\partial g}{\partial\boldsymbol{\sigma}}, \quad \dot{\boldsymbol{\alpha}} = -\dot{\lambda}\frac{\partial g}{\partial\mathbf{X}} = \dot{\boldsymbol{\epsilon}}^{vp} - \frac{3}{2}\frac{\gamma}{C}\mathbf{X}\dot{\lambda}, \tag{20}$$

$$\dot{r} = -\dot{\lambda}\frac{\partial g}{\partial R} = \left(1 - \frac{R}{K}\right)\dot{\lambda}. \tag{20'}$$

Since $\partial g/\partial\boldsymbol{\sigma} = \partial f/\partial\boldsymbol{\sigma}$, Eq. (18) remains valid here. Let $\rho\psi^{vp}$ take the form of

$$\rho\psi^{vp} = \frac{1}{3}C\boldsymbol{\alpha} : \boldsymbol{\alpha} + \frac{1}{2}Knr^2, \tag{21}$$

where n is another constant accounting for isotropic hardening. Substituting Eq. (21) into the last two equations of Eq. (3) gives

$$\mathbf{X} = \frac{2}{3}C\boldsymbol{\alpha} \quad \text{and} \quad R = Knr. \tag{22}$$

Substituting the last two equations of Eq. (20) into the rate form of Eq. (22) and noting that $\dot{\lambda} = \dot{p}$ give

$$\dot{\mathbf{X}} = \frac{2}{3}C\dot{\boldsymbol{\epsilon}}^{vp} - \gamma\mathbf{X}\dot{p} \quad \text{and} \quad \dot{R} = (K - R)n\dot{p}, \tag{23}$$

which are the Chaboche hardening law (Chaboche, 1989) and the rate form of the Voce hardening law (Voce, 1955), respectively. Note that the second equation of Eq. (23) can be further integrated into the Voce hardening law as

$$R = K[1 - \exp(-np)]. \tag{24}$$

More details on the derivation in this paragraph can be found in Besson et al. (2010).

The Perzyna model (Perzyna, 1966) suggests that

$$\Phi = \begin{cases} \frac{1}{\eta}\frac{\sigma_Y}{N+1}\left(\frac{f}{\sigma_Y}\right)^{N+1} & f > 0, \\ 0 & f \leqslant 0 \end{cases} \tag{25}$$

or

$$\dot{\lambda} = \begin{cases} \frac{1}{\eta}\left(\frac{f}{\sigma_Y}\right)^{N} & f > 0, \\ 0 & f \leqslant 0, \end{cases} \tag{26}$$

where η denotes a fluidity parameter, and N denotes a rate-sensitivity parameter. Substituting Eq. (26) into Eq. (20) fully specifies the viscoplasticity model.

Till now, the viscoplasticity model has been specified. In the next section, an affine formulation of the constitutive relations for a constituent will be derived.

4. Affine formulation of the constitutive relations

Suppose that all the variables at time t_n are known. The task is to find the variables at time $t_{n+1} = t_n + \Delta t$, where $\Delta(\cdot)$ denotes the increment in a quantity over this time interval. This leads one to derive the correspondence principal between $\Delta\boldsymbol{\sigma}$ and $\Delta\boldsymbol{\epsilon}$.

Note that Hooke's law writes

$$\boldsymbol{\sigma} = \mathcal{C}^e : \boldsymbol{\epsilon}^e, \tag{27}$$

where $\mathcal{C}^e$ denotes the fourth-order elasticity tensor. Substituting the incremental form of Eq. (27) into the incremental form of Eq. (5) gives

$$\Delta\boldsymbol{\epsilon} = \Delta\boldsymbol{\epsilon}^e + \Delta\boldsymbol{\epsilon}^{vp} = (\mathcal{C}^e)^{-1} : \Delta\boldsymbol{\sigma} + \Delta\boldsymbol{\epsilon}^{vp}. \tag{28}$$

Eq. (28) leads one to first derive the correspondence principal between $\Delta\boldsymbol{\sigma}$ and $\Delta\boldsymbol{\epsilon}^{vp}$. Without loss of generality, let $\dot{\boldsymbol{\epsilon}}^{vp}$, $\dot{p}$, and $\dot{\mathbf{X}}$ be functions of $\boldsymbol{\sigma}$, p, and $\mathbf{X}$, respectively, i.e.,

$$\dot{\boldsymbol{\epsilon}}^{vp}(t) = \dot{\boldsymbol{\epsilon}}^{vp}(\boldsymbol{\sigma}(t), p(t), \mathbf{X}(t)), \quad \dot{p}(t) = \dot{p}(\boldsymbol{\sigma}(t), p(t), \mathbf{X}(t)), \tag{29}$$

$$\dot{\mathbf{X}}(t) = \dot{\mathbf{X}}(\boldsymbol{\sigma}(t), p(t), \mathbf{X}(t)). \tag{29'}$$

Following Doghri et al. (2010), let $\Delta\boldsymbol{\epsilon}^{vp}$ be related to $\dot{\boldsymbol{\epsilon}}^{vp}(t_{n+1})$ using the backward Euler method by

$$\Delta\boldsymbol{\epsilon}^{vp} = \dot{\boldsymbol{\epsilon}}^{vp}(t_{n+1})\Delta t, \tag{30}$$

and let the evolution of $\dot{\boldsymbol{\epsilon}}^{vp}$, $\dot{p}$, and $\dot{\mathbf{X}}$ be governed by

$$\dot{\boldsymbol{\epsilon}}^{vp}(t_{n+1}) = \dot{\boldsymbol{\epsilon}}^{vp}(t_n) + \mathcal{K}(t_{n+1}) : \Delta\boldsymbol{\sigma} + \mathbf{L}(t_{n+1})\Delta p + \mathcal{M}(t_{n+1}) : \Delta\mathbf{X}, \tag{31}$$

$$\dot{p}(t_{n+1}) = \dot{p}(t_n) + \mathbf{N}(t_{n+1}) : \Delta\boldsymbol{\sigma} + P(t_{n+1})\Delta p + \mathbf{Q}(t_{n+1}) : \Delta\mathbf{X}, \tag{31'}$$

$$\dot{\mathbf{X}}(t_{n+1}) = \dot{\mathbf{X}}(t_n) + \mathcal{R}(t_{n+1}) : \Delta\boldsymbol{\sigma} + \mathbf{S}(t_{n+1})\Delta p + \mathcal{T}(t_{n+1}) : \Delta\mathbf{X}, \tag{31''}$$

where

$$\mathcal{K} = \frac{\partial\dot{\boldsymbol{\epsilon}}^{vp}}{\partial\boldsymbol{\sigma}}, \quad \mathbf{L} = \frac{\partial\dot{\boldsymbol{\epsilon}}^{vp}}{\partial p}, \quad \mathcal{M} = \frac{\partial\dot{\boldsymbol{\epsilon}}^{vp}}{\partial\mathbf{X}}, \tag{32}$$

$$\mathbf{N} = \frac{\partial\dot{p}}{\partial\boldsymbol{\sigma}}, \quad P = \frac{\partial\dot{p}}{\partial p}, \quad \mathbf{Q} = \frac{\partial\dot{p}}{\partial\mathbf{X}}, \tag{32'}$$

$$\mathcal{R} = \frac{\partial\dot{\mathbf{X}}}{\partial\boldsymbol{\sigma}}, \quad \mathbf{S} = \frac{\partial\dot{\mathbf{X}}}{\partial p}, \quad \mathcal{T} = \frac{\partial\dot{\mathbf{X}}}{\partial\mathbf{X}} \tag{32''}$$

with $\mathcal{K}$, $\mathcal{M}$, $\mathcal{R}$, and $\mathcal{T}$ being fourth-order tensors, $\mathbf{L}$, $\mathbf{N}$, $\mathbf{Q}$, and $\mathbf{S}$ being second-order tensors, and P being a scalar (see Appendix B for more details on the derivation of the explicit expressions for these partial derivatives). Also let Δp and $\Delta\mathbf{X}$ be related to $\dot{p}$ and $\dot{\mathbf{X}}$ using the backward Euler method by

$$\Delta p = \dot{p}(t_{n+1})\Delta t \quad \text{and} \quad \Delta\mathbf{X} = \dot{\mathbf{X}}(t_{n+1})\Delta t, \tag{33}$$

respectively. Substituting Eq. (33) into the last two equations of Eq. (31) and rearranging the equations gives

$$A_{11}\dot{p}(t_{n+1}) + \mathbf{A}_{12} : \dot{\mathbf{X}}(t_{n+1}) = B_1, \tag{34}$$

$$\mathbf{A}_{21}\dot{p}(t_{n+1}) + \mathcal{A}_{22} : \dot{\mathbf{X}}(t_{n+1}) = \mathbf{B}_2, \tag{34'}$$

where

$$A_{11} = 1 - P(t_{n+1})\Delta t, \quad \mathbf{A}_{12} = -\mathbf{Q}(t_{n+1})\Delta t, \tag{35}$$

$$\mathbf{A}_{21} = -\mathbf{S}(t_{n+1})\Delta t, \quad \mathcal{A}_{22} = \mathcal{I} - \mathcal{T}(t_{n+1})\Delta t, \tag{35'}$$

$$B_1 = \dot{p}(t_n) + \mathbf{N}(t_{n+1}) : \Delta\boldsymbol{\sigma}, \quad \mathbf{B}_2 = \dot{\mathbf{X}}(t_n) + \mathcal{R}(t_{n+1}) : \Delta\boldsymbol{\sigma}. \tag{35''}$$

Rearranging the second equation of Eq. (34) gives

$$\dot{\mathbf{X}}(t_{n+1}) = \mathcal{A}_{22}^{-1} : [\mathbf{B}_2 - \mathbf{A}_{21}\dot{p}(t_{n+1})]. \tag{36}$$

Substituting Eq. (36) into the first equation of Eq. (34) and rearranging the equation give

$$\dot{p}(t_{n+1}) = \frac{B_1 - \mathbf{A}_{12} : \mathcal{A}_{22}^{-1} : \mathbf{B}_2}{A_{11} - \mathbf{A}_{12} : \mathcal{A}_{22}^{-1} : \mathbf{A}_{21}}. \tag{37}$$

Substituting Eq. (37) into Eq. (36) gives

$$\dot{\mathbf{X}}(t_{n+1}) = \mathcal{A}_{22}^{-1} : \left(\mathbf{B}_2 - \frac{B_1 - \mathbf{A}_{12} : \mathcal{A}_{22}^{-1} : \mathbf{B}_2}{A_{11} - \mathbf{A}_{12} : \mathcal{A}_{22}^{-1} : \mathbf{A}_{21}}\mathbf{A}_{21}\right). \tag{38}$$

Substituting Eqs. (37) and (38) into Eq. (33), substituting the equation into the first equation of Eq. (31), and rearranging the equation give

$$\dot{\boldsymbol{\epsilon}}^{vp}(t_{n+1}) = \dot{\tilde{\boldsymbol{\epsilon}}}(t_{n+1}) + \tilde{\mathcal{C}}^{-1}(t_{n+1}) : \Delta\boldsymbol{\sigma}, \tag{39}$$

where

$$\dot{\tilde{\boldsymbol{\epsilon}}}(t_{n+1}) = \dot{\boldsymbol{\epsilon}}^{vp}(t_n) + \mathcal{M}(t_{n+1}) : \mathcal{A}_{22}^{-1} : \dot{\mathbf{X}}(t_n)\Delta t + \frac{\dot{p}(t_n) - \mathbf{A}_{12} : \mathcal{A}_{22}^{-1} : \dot{\mathbf{X}}(t_n)}{A_{11} - \mathbf{A}_{12} : \mathcal{A}_{22}^{-1} : \mathbf{A}_{21}}\left[\mathbf{L}(t_{n+1}) - \mathcal{M}(t_{n+1}) : \mathcal{A}_{22}^{-1} : \mathbf{A}_{21}\right]\Delta t \tag{40}$$

and

$$\tilde{\mathcal{C}}^{-1}(t_{n+1}) = \mathcal{K}(t_{n+1}) + \mathcal{M}(t_{n+1}) : \mathcal{A}_{22}^{-1} : \mathcal{R}(t_{n+1})\Delta t + \frac{\left[\mathbf{L}(t_{n+1}) - \mathcal{M}(t_{n+1}) : \mathcal{A}_{22}^{-1} : \mathbf{A}_{21}\right] \otimes \left[\mathbf{N}(t_{n+1}) - \mathbf{A}_{12} : \mathcal{A}_{22}^{-1} : \mathcal{R}(t_{n+1})\right]}{A_{11} - \mathbf{A}_{12} : \mathcal{A}_{22}^{-1} : \mathbf{A}_{21}}\Delta t. \tag{41}$$

Substituting Eq. (39) into Eq. (30) gives

$$\Delta\boldsymbol{\epsilon}^{vp} = \Delta\tilde{\boldsymbol{\epsilon}} + \left[\tilde{\mathcal{C}}^{-1}(t_{n+1})\Delta t\right] : \Delta\boldsymbol{\sigma}, \tag{42}$$

where $\Delta\tilde{\boldsymbol{\epsilon}} = \dot{\tilde{\boldsymbol{\epsilon}}}(t_{n+1})\Delta t$. Substituting Eq. (42) into Eq. (28) gives

$$\Delta\boldsymbol{\epsilon} = \Delta\boldsymbol{\epsilon}^e + \Delta\boldsymbol{\epsilon}^{vp} = (\mathcal{C}^e)^{-1} : \Delta\boldsymbol{\sigma} + \Delta\tilde{\boldsymbol{\epsilon}} + \left[\tilde{\mathcal{C}}^{-1}(t_{n+1})\Delta t\right] : \Delta\boldsymbol{\sigma}. \tag{43}$$

Rearranging Eq. (43) gives an affine formulation of the constitutive relations for the constituent as

$$\Delta\boldsymbol{\epsilon} - \Delta\tilde{\boldsymbol{\epsilon}} = \left[(\mathcal{C}^e)^{-1} + \tilde{\mathcal{C}}^{-1}(t_{n+1})\Delta t\right] : \Delta\boldsymbol{\sigma} \tag{44}$$

or

$$\Delta\boldsymbol{\sigma} = \mathcal{C}^{evp}(t_{n+1}) : (\Delta\boldsymbol{\epsilon} - \Delta\tilde{\boldsymbol{\epsilon}}), \tag{45}$$

where $\mathcal{C}^{evp}$ denotes the fourth-order affine instantaneous elasto-viscoplastic stiffness tensor and is given by

$$\mathcal{C}^{evp}(t_{n+1}) = \left[(\mathcal{C}^e)^{-1} + \tilde{\mathcal{C}}^{-1}(t_{n+1})\Delta t\right]^{-1}. \tag{46}$$

Till now, an affine formulation of the constitutive relations has been derived. In the next section, the weak form of the problem will be derived.

5. Weak form

Introduce global coordinates $\mathbf{x} = (x_1, x_2, x_3)$ describing the macroscopic structure and local coordinates $\mathbf{y} = (y_1, y_2, y_3)$ describing the UC, and let $\mathbf{y}$ be related to $\mathbf{x}$ by (Berdichevsky, 2009)

$$\mathbf{y} = \mathbf{x}/\epsilon, \tag{47}$$

where $\epsilon \ll 1$ denotes a scale ratio. Suppose that, at time t_n:

1. The UC is in a state of static equilibrium.
2. The global and local variables are known.
3. Periodic boundary conditions are satisfied.

Also note that the rate of a quantity can be converted to its increment by multiplying it by Δt. The task hereby becomes solving for the exact velocity vector within the UC, $\dot{u}_i$, at t_{n+1}.

$\dot{u}_i$ must have its volume average over the UC, say $\dot{v}_i$, such that the heterogeneous material can be homogenized (Yu and Tang, 2007a). By definition, $\dot{v}_i$ is related to $\dot{u}_i$ by

$$\dot{v}_i = \frac{1}{\Omega}\int_\Omega \dot{u}_i dV \equiv \langle \dot{u}_i \rangle, \tag{48}$$

where Ω denotes the domain occupied by the UC (with boundary $\partial\Omega$) and also its volume, and $\langle\cdot\rangle$ denotes the volume average of a quantity over Ω. $\dot{u}_i$ can be decomposed into $\dot{v}_i$ and a fluctuation function, χ_i, i.e., (Berdichevsky, 2009)

$$\dot{u}_i(\mathbf{y},\mathbf{x}) = \dot{v}_i(\mathbf{x}) + \epsilon\chi_i(\mathbf{y},\mathbf{x}), \tag{49}$$

where χ_i is a periodic function of $\mathbf{y}$ and may also depend on $\mathbf{x}$, and $\epsilon\chi_i$ should be asymptotically smaller than $\dot{v}_i$. Eqs. (48) and (49) imply that

$$\langle \chi_i \rangle = 0. \tag{50}$$

In fact, although $\epsilon\chi_i$ negligibly affects $\dot{u}_i$, it can significantly affect the derivatives of $\dot{u}_i$. Specifically,

$$\frac{\partial \dot{u}_i}{\partial x_j} = \frac{1}{\epsilon}\frac{\partial \dot{u}_i}{\partial y_j}\bigg|_{\mathbf{x}=\text{const}} + \frac{\partial \dot{u}_i}{\partial x_j}\bigg|_{\mathbf{y}=\text{const}} = \frac{\partial \dot{v}_i}{\partial x_j} + \frac{\partial \chi_i}{\partial y_j} + \epsilon\frac{\partial \chi_i}{\partial x_j}, \tag{51}$$

where $\epsilon\partial\chi_i/\partial x_j$ is a high-order term and can be omitted. Note that, by definition,

$$\dot{\epsilon}_{ij} = \frac{1}{2}\left(\frac{\partial \dot{u}_i}{\partial x_j} + \frac{\partial \dot{u}_j}{\partial x_i}\right). \tag{52}$$

Let

$$\dot{\bar{\epsilon}}_{ij} = \frac{1}{2}\left(\frac{\partial \dot{v}_i}{\partial x_j} + \frac{\partial \dot{v}_j}{\partial x_i}\right) \quad \text{and} \quad \chi_{(i|j)} = \frac{1}{2}\left(\frac{\partial \chi_i}{\partial y_j} + \frac{\partial \chi_j}{\partial y_i}\right), \tag{53}$$

where $\dot{\bar{\epsilon}}_{ij}$ actually denotes the global strain rate tenor. Combining Eqs. (49), (52), and (53) gives

$$\dot{\epsilon}_{ij} = \dot{\bar{\epsilon}}_{ij} + \chi_{(i|j)}. \tag{54}$$

The strong form of the problem can be formulated as seeking χ_i satisfying

$$\dot{\sigma}_{ij,j} = 0 \quad \text{in } \Omega \tag{55}$$

subject to constraint Eq. (50) and periodic boundary conditions

$$\chi_i(\mathbf{y}) = \chi_i(\mathbf{y}+\mathbf{l}) \quad \text{and} \quad (\dot{\sigma}_{ij}n_j)(\mathbf{y}) = -(\dot{\sigma}_{ij}n_j)(\mathbf{y}+\mathbf{l}) \quad \text{on } \partial\Omega, \tag{56}$$

where $\mathbf{l}$ denotes the periodicity vector of the UC, and n_i denotes the unit normal vector. Let $\delta\chi_i$ denote the virtual fluctuation function being arbitrary in Ω and satisfying periodic boundary conditions

$$\delta\chi_i(\mathbf{y}) = \delta\chi_i(\mathbf{y}+\mathbf{l}) \quad \text{on } \partial\Omega. \tag{57}$$

The rate form of the principle of virtual work can be expressed in terms of $\delta\chi_i$ as

$$\delta\Pi_\Omega = -\frac{1}{\Omega}\int_\Omega \dot{\sigma}_{ij,j}\delta\chi_i dV = \frac{1}{\Omega}\int_\Omega \dot{\sigma}_{ij}\delta\chi_{(i|j)}dV - \frac{1}{\Omega}\int_\Omega \dot{\sigma}_{ij}n_j\delta\chi_i dS = 0. \tag{58}$$

Substituting Eq. (57) and the second equation of Eq. (56) into Eq. (58) gives

$$\delta\Pi_\Omega = \frac{1}{\Omega}\int_\Omega \dot{\sigma}_{ij}\delta\chi_{(i|j)}dV = 0. \tag{59}$$

The weak form of the problem can then be formulated as seeking χ_i satisfying Eq. (59) subject to constraint Eq. (50) and periodic boundary conditions

$$\chi_i(\mathbf{y}) = \chi_i(\mathbf{y}+\mathbf{l}) \quad \text{on } \partial\Omega. \tag{60}$$

Substituting Eq. (54) into the rate form of Eq. (45) gives

$$\dot{\sigma}_{ij} = \mathcal{C}^{evp}_{ijkl}\left[\dot{\bar{\epsilon}}_{kl} + \chi_{(k|l)} - \dot{\bar{\epsilon}}_{kl}\right]. \tag{61}$$

Substituting Eq. (61) into Eq. (59) gives

$$\delta\Pi_\Omega = \frac{1}{\Omega}\int_\Omega \delta\chi_{(i|j)}\mathcal{C}^{evp}_{ijkl}\left[\dot{\bar{\epsilon}}_{kl} + \chi_{(k|l)} - \dot{\bar{\epsilon}}_{kl}\right]dV = 0. \tag{62}$$

Eq. (62) implies that, once $\dot{\bar{\epsilon}}_{ij}$ and $\mathcal{C}^{evp}_{ijkl}$ are specified, χ_i can be uniquely determined.

It is beneficial to also relate the local stress and strain rate tensors to the global ones. Specifically, $\langle\dot{\sigma}_{ij}\dot{\epsilon}_{ij}\rangle$ can be expressed as

$$\frac{1}{\Omega}\int_\Omega \dot{\sigma}_{ij}\dot{\epsilon}_{ij}dV = \frac{1}{\Omega}\int_\Omega \dot{\sigma}_{ij}\dot{\bar{\epsilon}}_{ij}dV + \frac{1}{\Omega}\int_\Omega \dot{\sigma}_{ij}\chi_{(i|j)}dV. \tag{63}$$

Eq. (63), together with Eq. (59), implies that

$$\frac{1}{\Omega}\int_\Omega \dot{\sigma}_{ij}\dot{\epsilon}_{ij}dV = \frac{1}{\Omega}\int_\Omega \dot{\sigma}_{ij}\dot{\bar{\epsilon}}_{ij}dV = \dot{\bar{\epsilon}}_{ij}\left(\frac{1}{\Omega}\int_\Omega \dot{\sigma}_{ij}dV\right) \equiv \dot{\bar{\sigma}}_{ij}\dot{\bar{\epsilon}}_{ij}, \tag{64}$$

In fact, Eq. (64) is a variation of the Hill–Mandel lemma.

Till now, the weak form of the problem has been derived. In the next section, it will be discretized using finite elements such that the fluctuation functions can be determined.

6. Finite element implementation

Introduce the following matrix notations:

$$\dot{\bar{\epsilon}} = \lfloor \dot{\bar{\epsilon}}_{11} \quad 2\dot{\bar{\epsilon}}_{12} \quad \dot{\bar{\epsilon}}_{22} \quad 2\dot{\bar{\epsilon}}_{13} \quad 2\dot{\bar{\epsilon}}_{23} \quad \dot{\bar{\epsilon}}_{33} \rfloor^T, \tag{65}$$

$$\begin{Bmatrix} \frac{\partial\chi_1}{\partial y_1} \\ \frac{\partial\chi_1}{\partial y_2} + \frac{\partial\chi_2}{\partial y_1} \\ \frac{\partial\chi_2}{\partial y_2} \\ \frac{\partial\chi_1}{\partial y_3} + \frac{\partial\chi_3}{\partial y_1} \\ \frac{\partial\chi_2}{\partial y_3} + \frac{\partial\chi_3}{\partial y_2} \\ \frac{\partial\chi_3}{\partial y_3} \end{Bmatrix} = \begin{bmatrix} \frac{\partial}{\partial y_1} & 0 & 0 \\ \frac{\partial}{\partial y_2} & \frac{\partial}{\partial y_1} & 0 \\ 0 & \frac{\partial}{\partial y_2} & 0 \\ \frac{\partial}{\partial y_3} & 0 & \frac{\partial}{\partial y_1} \\ 0 & \frac{\partial}{\partial y_3} & \frac{\partial}{\partial y_2} \\ 0 & 0 & \frac{\partial}{\partial y_3} \end{bmatrix} \begin{Bmatrix} \chi_1 \\ \chi_2 \\ \chi_3 \end{Bmatrix} \equiv \Gamma_h\chi, \tag{65'}$$

where Γ_h denotes an operator matrix, and χ denotes a column matrix containing the three components of the fluctuation functions. Let χ be discretized using finite elements as

$$\chi(y_i, x_i) = S(y_i)\mathrm{X}(x_i), \tag{66}$$

where S denotes the shape functions, and X denotes a column matrix of the nodal values of the fluctuation functions at all the active nodes. The discretized version of Eq. (62) can then be obtained as

$$\delta\Pi_\Omega = \frac{1}{\Omega}\delta\mathrm{X}^T\left(D_{hh}\mathrm{X} + D_{h\epsilon}\dot{\bar{\epsilon}} - \dot{\sigma}_h\right) = 0, \tag{67}$$

where

$$D_{hh} = \int_\Omega (\Gamma_h S)^T D(\Gamma_h S)dV, \quad D_{h\epsilon} = \int_\Omega (\Gamma_h S)^T D dV, \tag{68}$$

$$\dot{\sigma}_h = \int_\Omega (\Gamma_h S)^T D\dot{\bar{\epsilon}}dV \tag{68'}$$

with D denoting the 6×6 instantaneous stiffness matrix condensed from C^{evp}_{ijkl}. In Eq. (67), equality holds only if

$$D_{hh}\mathrm{X} = -D_{h\epsilon}\dot{\bar{\epsilon}} + \dot{\sigma}_h \quad \text{or} \quad \mathrm{X} = \mathrm{X}_0\dot{\bar{\epsilon}} + \mathrm{X}_1, \tag{69}$$

where

$$D_{hh}\mathrm{X}_0 = -D_{h\epsilon} \quad \text{and} \quad D_{hh}\mathrm{X}_1 = \dot{\sigma}_h. \tag{70}$$

Eq. (69) implies that X is linearly dependent on $\dot{\bar{\epsilon}}$. In addition, Eq. (64) can be rewritten as

$$\dot{\bar{\epsilon}}_{ij}\dot{\bar{\sigma}}_{ij} = \frac{1}{\Omega}\int_\Omega \dot{\epsilon}_{ij}\dot{\sigma}_{ij}dV = \frac{1}{\Omega}\int_\Omega \dot{\epsilon}_{ij}C^{evp}_{ijkl}\left[\dot{\bar{\epsilon}}_{kl} + \chi_{(k|l)} - \dot{\epsilon}_{kl}\right]dV. \tag{71}$$

The discretized version of Eq. (71) can be obtained as

$$\begin{aligned}\dot{\bar{\epsilon}}^T\dot{\bar{\sigma}} &= \frac{1}{\Omega}\left(\dot{\bar{\epsilon}}^T D_{\epsilon h}\mathrm{X} + \dot{\bar{\epsilon}}^T D_{\epsilon\epsilon}\dot{\bar{\epsilon}} - \dot{\bar{\epsilon}}^T\dot{\sigma}_\epsilon\right)\\ &= \frac{1}{\Omega}\dot{\bar{\epsilon}}^T\left[(D_{\epsilon h}\mathrm{X}_0 + D_{\epsilon\epsilon})\dot{\bar{\epsilon}} + D_{\epsilon h}\mathrm{X}_1 - \dot{\sigma}_\epsilon\right]\\ &\equiv \dot{\bar{\epsilon}}^T\left[\bar{D}\dot{\bar{\epsilon}} + \frac{1}{\Omega}(D_{\epsilon h}\mathrm{X}_1 - \dot{\sigma}_\epsilon)\right],\end{aligned} \tag{72}$$

where $\dot{\bar{\sigma}}$ denotes the global stress rate column matrix, and

$$D_{\epsilon h} = \int_\Omega D(\Gamma_h S)dV, \quad D_{\epsilon\epsilon} = \int_\Omega DdV, \quad \dot{\sigma}_\epsilon = \int_\Omega D\dot{\epsilon}dV. \tag{73}$$

The rate form of the global constitutive relations can then be obtained from Eq. (72) as

$$\dot{\bar{\sigma}} = \bar{D}\dot{\bar{\epsilon}} + \frac{1}{\Omega}(D_{\epsilon h}\mathrm{X}_1 - \dot{\sigma}_\epsilon), \tag{74}$$

where $\bar{D}$ denotes the affine instantaneous effective stiffness matrix. Once $\dot{\bar{\epsilon}}$, $\dot{\bar{\sigma}}$, or a suitable combination of the components of $\dot{\bar{\epsilon}}$ and $\dot{\bar{\sigma}}$ is specified, the global response of the UC can be fully determined using Eq. (74). In addition, the real value of X_0, say $\bar{\mathrm{X}}_0$, can be obtained by modifying X_0 such that χ satisfies Eqs. (50) and (60). Once $\dot{\bar{\epsilon}}$ and $\bar{\mathrm{X}}_0$ are specified, the local fields can be fully recovered. Specifically, the local strain rates can be recovered as

$$\dot{\epsilon} = \dot{\bar{\epsilon}} + \Gamma_h S\left(\bar{\mathrm{X}}_0\dot{\bar{\epsilon}} + \bar{\mathrm{X}}_1\right), \tag{75}$$

where $\dot{\epsilon}$ denotes the local strain rate column matrix, and $\bar{\mathrm{X}}_1$ is obtained similarly to $\bar{\mathrm{X}}_0$. The local stress rates can be recovered from the local strain rates as

$$\dot{\sigma} = D\left(\dot{\epsilon} - \dot{\bar{\epsilon}}\right). \tag{76}$$

Till now, the fluctuation functions can be determined. In the next section, the code structure will be presented.

7. Code structure

VAMUCH employs the second-order implicit Runge–Kutta method as its time integration method (see Fig. 1 for its code structure). It starts with reading the finite element model and initializing the global and local variables. After this, it will perform the following steps within each load increment:

1. Compute the effective material properties and the fluctuation functions.
2. Impose the global stress/strain increments.
3. Recover the local fields.
4. Update the global and local variables.
5. Continue to the next increment if needed.

At last, it will output the results as needed.

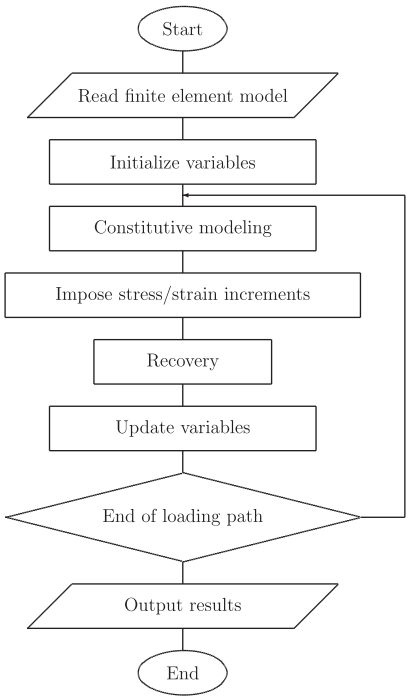

Fig. 1. Code structure.

VAMUCH uses the Gaussian quadrature to compute the element stiffness matrices. The corresponding algorithm is described as follows:

1. Read the data associated with an integration point.
2. Check whether the constituent is elasto-viscoplastic.
3. If yes, check whether $f > 0$.
4. If yes, compute the stiffness matrix using Eq. (46) and return it.
5. If either of the two criteria is not met, return the elastic stiffness matrix.

Especially, if $f > 0$, VAMUCH will update the corresponding p and $\mathbf{X}$ during the recovery.

8. Validation examples

In this section, the new features of VAMUCH will be validated with examples such as homogenizing binary, fiber-reinforced, and particle-reinforced composites. For validation purposes, the results obtained using VAMUCH will be compared with those obtained using ANSYS.

8.1. Fiber-reinforced composite

First consider a fiber-reinforced composite consisting of an elasto-viscoplastic aluminum matrix and numerous cylindrical, elastic SiC fibers arranged in a square array with the volume fraction of fibers being 10%. With loss of generality, let aluminum exhibit combined isotropic–kinematic hardening (see Eqs. (23)–(25)). Following Li and Weng (1998), Doghri et al. (2010) and Zhao and Lee (2001), let the material parameters of SiC and aluminum take the values listed in Table 1, where E and v denote Young's modulus and Poisson's ratio, respectively. Let the UC of this composite consist of a square matrix and a circular fiber located at its center. Recall that y_i denotes the local coordinates describing the UC with its origin located at the geometric center of the UC (see Section 5). Here let the y_1-axis be parallel to the fiber direction, and let the

Table 1
Material parameters of SiC and aluminum.

(a) Elastic constants

	E(GPa)	v
SiC	490	0.17
Aluminum	70	0.33

(b) Viscoplastic material parameters of aluminum

σ_0(MPa)	K(MPa)	n	η(s)	m	C(MPa)	γ
60	40	54.9	2.27×10^5	4.61	7019	118.6

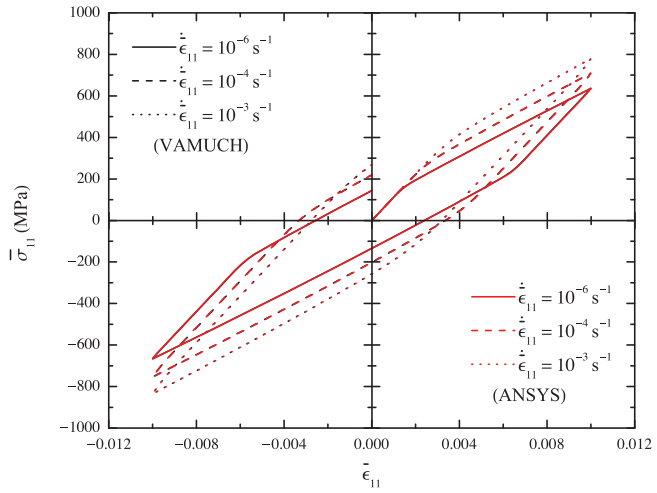

(a) y_1-direction.

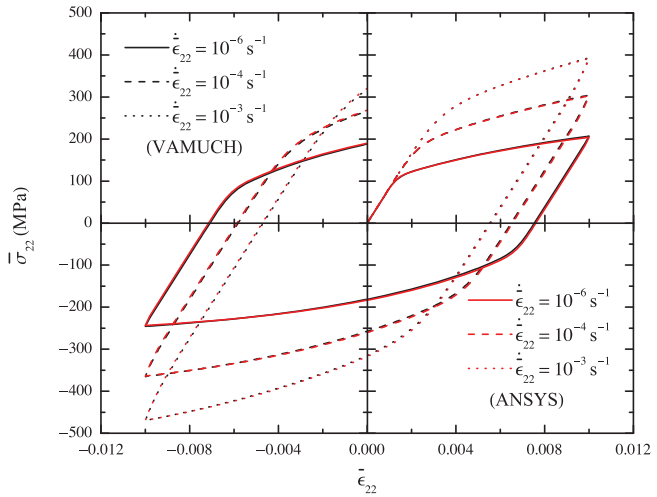

(b) y_2-direction.

Fig. 2. Stress–strain hysteresis loops of a fiber-reinforced composite undergoing uniaxial extension.

y_2- and y_3-axes be parallel to the length and width directions of the UC, respectively.

In VAMUCH, a 2D UC is meshed using 4-node quadrilateral elements having 3 degrees of freedom (DOFs) at each node, and the meshed UC consists of 1216 elements. Periodic boundary conditions are applied using the master–slave elimination method. In ANSYS, a 3D UC is meshed using 8-node hexahedra elements (SOLID185), and the meshed UC consists of 2432 elements. For validation purposes, the UC is set to undergo uniaxial or biaxial extension in which cases periodic boundary conditions becomes homogeneous ones. Both finite element models are found to be capable of producing converged results.

Fig. 2 shows the stress–strain hysteresis loops of the composite undergoing uniaxial extension in the y_1- and y_2-directions, respectively. For illustration purposes, let the loading path in each example consist of the following steps:

1. Initial loading: the major strain(s) is increased from 0 to 0.01.
2. Initial unloading: the major strain(s) is decreased from 0.01 to 0.
3. Reverse loading: the major strain(s) is decreased from 0.0 to −0.01.
4. Reverse unloading: the major strain(s) is increased from −0.01 to 0.

It can be seen that the composite exhibits an approximately bilinear stress-strain relationship when loaded in the y_1-direction and a highly nonlinear one when loaded in the y_2-direction. This can be understood by investigating the stress distribution in the matrix. Specifically, in Fig. 2(a), the stress distribution in the matrix remains approximately uniform during continued deformation, causing yielding to simultaneously occur at different locations in the matrix; in Fig. 2(b), it remains highly nonuniform, causing yielding to subsequently occur. In addition, in Fig. 2, the composite becomes stiffer as the major strain rate increases. This agrees with the theory of viscoplasticity. At last, in Fig. 2, the results obtained using VAMUCH perfectly agree with those obtained using ANSYS. In fact, VAMUCH can generate the same predictions using 2D and 3D UCs, while ANSYS has to use a 3D UC to handle the out-of-plane loads and displacements. All these indicate that VAMUCH is capable of homogenizing fiber-reinforced composites using 2D UCs and handling complex loading paths.

Fig. 3 shows the stress–strain hysteresis loops of the composite undergoing equal biaxial extension in the y_2- and y_3-directions. It can be seen that the stress–strain relationships here are similar to those in Fig. 2(a). Therefore, the discussion for Fig. 2(a) holds here. In addition, in Fig. 3, the results obtained using VAMUCH perfectly agree with those obtained using ANSYS. This indicates that VAMUCH is capable of handling complex loading conditions.

Next let aluminum exhibit viscoplastic transverse isotropy in the y_2-y_3 plane here, and allow its R_i's to take three sets of values listed in Table 2 for three cases (see Appendix A for more details). For validation purposes, let aluminum exhibit no kinematic hardening here such that ANSYS can handle the material model.

Fig. 4 shows the stress–strain hysteresis loops of the composite undergoing uniaxial extension in the y_2-direction,

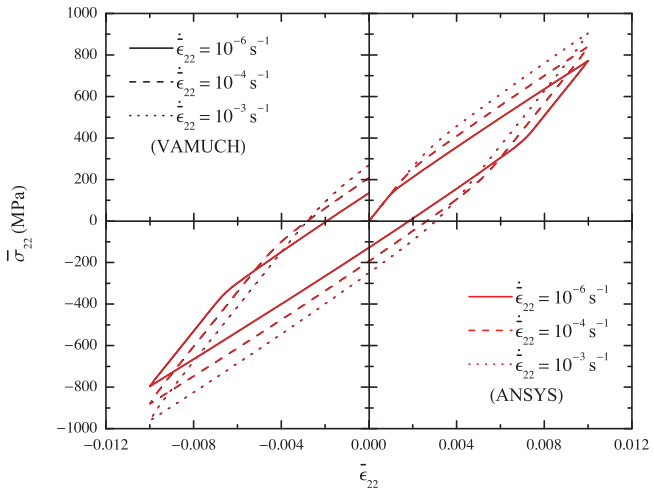

Fig. 3. Stress–strain hysteresis loops of a fiber-reinforced composite undergoing equal biaxial extension in the y_2- and y_3-directions.

$\dot{\bar{\epsilon}}_{22} = 10^{-4}\ s^{-1}$. In fact, the following findings can be obtained after some calculation:

1. All three sets of the values yield the same yield stress in the y_1-direction.
2. The set of values with the lowest value of R_3 yields the lowest yield stress in the y_2- (or y_3-) direction and vice versa.

Accordingly, in Fig. 4, as R_3 increases, the composite becomes more flexible. In addition, in Fig. 4, the results obtained using VAMUCH perfectly agree with those obtained using ANSYS. This indicates that VAMUCH is capable of handling complex material models.

8.2. Binary composite

Next consider a binary composite consisting of a SiC constituent and an aluminum constituent with their volume fractions being 10% and 90%, respectively. Let the material parameters of SiC and aluminum take the values listed in Table 1. Let the UC of this composite be a line segment consisting of two connecting sub-line segments. Here let the y_1-axis be parallel to the line segment representing the UC.

In VAMUCH, a 1D UC is meshed using 2-node line elements having 3 DOFs at each node, and the meshed UC consists of 2 elements. In ANSYS, a 3D UC is meshed using SOLID185, and the meshed UC consists of 64 elements. Both finite element models are found to be capable of producing converged results.

Fig. 5 shows the stress–strain hysteresis loops of the composite undergoing uniaxial extension in the y_1- and y_2-directions, . It can be seen that the stress–strain relationships here are similar to those in Fig. 2(a). Therefore, the discussion for Fig. 2(a) holds here. In addition, in Fig. 5, the results obtained using VAMUCH perfectly agree with those obtained using ANSYS. This indicates that VAMUCH is capable of homogenizing binary composites using 1D UCs.

8.3. Particle-reinforced composite

Last consider a particle-reinforced composite consisting of an aluminum matrix and numerous spherical SiC particles arranged in a cubic array with the volume fraction of particles being 10%. Let the material parameters of SiC and aluminum take the values listed in Table 1. Let the UC of this composite consist of a cubic matrix and a spherical particle located at its center. Here let the y_1-, y_2-, and y_3-axes be parallel to the length, width, and height directions of the UC, respectively.

In VAMUCH and ANSYS, the same UC is meshed using 8-node hexahedra elements having 3 DOFs at each node, and the meshed UC consists of 1512 elements. Both finite element models are found to be capable of producing converged results.

Fig. 6 shows the stress–strain hysteresis loops of the composite undergoing uniaxial extension in the y_1-direction. It can be seen that the stress–strain relationships here are similar to those in Fig. 2(b). Therefore, the discussion for Fig. 2(b) holds here. In addition, in Fig. 6, the results obtained using VAMUCH agree well with those obtained using ANSYS. This indicates that VAMUCH is capable of homogenizing heterogeneous materials of 3D heterogeneity such as particle-reinforced composites.

Table 2
R_i's for different cases.

	R_1	R_2	R_3	R_4	R_5	R_6
1	1	1	0.5	1	0.5	2
2	1	1	1	1	1	1
3	1	1	2	1	2	0.5

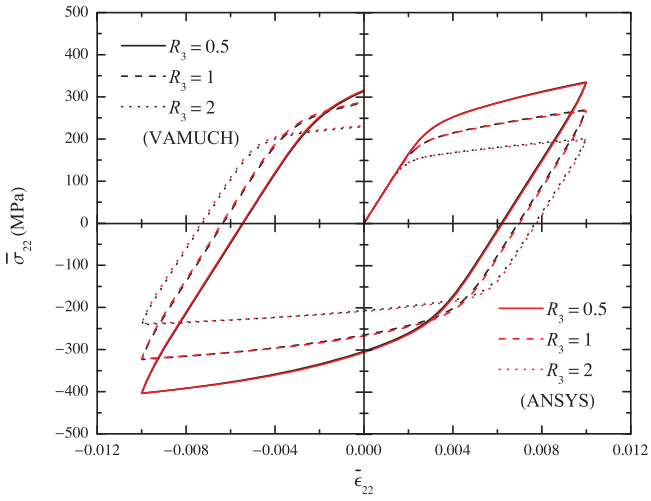

Fig. 4. Stress–strain hysteresis loops of a fiber-reinforced composite with a viscoplastically anisotropic matrix undergoing uniaxial extension in the y_2-direction.

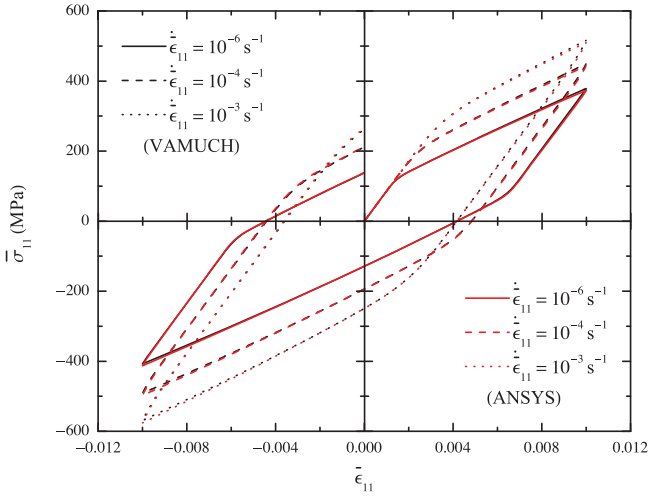

(a) y_1-direction.

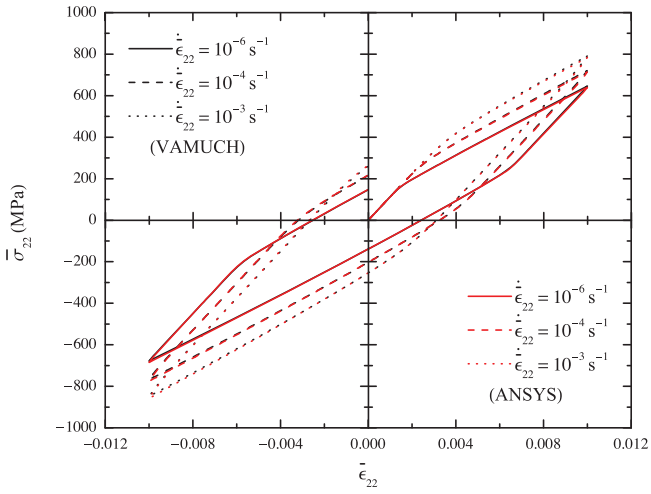

(b) y_2-direction.

Fig. 5. Stress–strain hysteresis loops of a binary composite undergoing uniaxial extension.

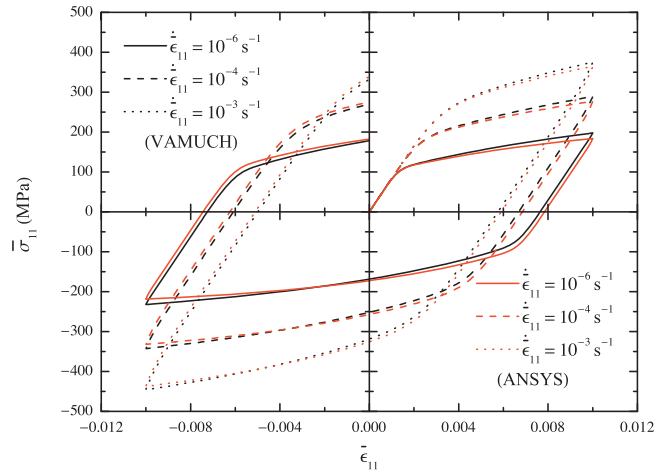

Fig. 6. Stress–strain hysteresis loops of a particle-reinforced composite undergoing uniaxial extension in the y_1-direction.

9. Conclusions

VAMUCH has emerged as a general-purpose micromechanics code capable of predicting the effective properties of heterogeneous materials and recovering the local fields. In this paper, a micromechanics approach is proposed to enable VAMUCH to homogenize elasto-viscoplastic heterogeneous materials. An affine formulation of the constitutive relations for an elasto-viscoplastic constituent, which exhibits viscoplastic anisotropy and combined isotropic–kinematic hardening, is derived. The weak form of the problem is derived using an asymptotic method, discretized using finite elements, and implemented into VAMUCH. The new features of VAMUCH are validated with examples such as homogenizing binary, fiber-reinforced, and particle-reinforced composites. VAMUCH is found to be capable of handling various microstructure, complex material models, complex loading conditions, and complex loading paths. It provides a versatile and convenient tool allowing scientists and engineers to accurately and efficiently homogenize elasto-viscoplastic heterogeneous materials. More sophisticated material models can be implemented into it.

Acknowledgements

This work is supported by the US AFOSR Multiscale Structural Mechanics and Prognosis Program. The views and conclusions contained herein are those of the authors and should not be interpreted as necessarily representing the official policies or endorsement, either expressed or implied, of the sponsor.

Appendix A. Viscoplastic anisotropy parameters

The R-value is widely used to characterize the viscoplastic anisotropy of rolled sheet metals and can be measured from a series of uniaxial tensile tests. Specifically, when a tensile specimen cut from a sheet is stretched, its R-value is defined as the ratio of the viscoplastic strain in the width direction to that in the thickness direction, i.e.,

$$R = \frac{\epsilon_W}{\epsilon_T}. \tag{A.1}$$

In general, the R-value varies with the cut angle with respect to the rolling direction of the sheet, α. In this case, an averaged R-value is often adopted. It is defined as

$$\bar{R} = \frac{R_0 + 2R_{45} + R_{90}}{4}, \tag{A.2}$$

where R_α denotes the R-value obtained from a tensile specimen of cut angle α.

Benzerga and Besson (2001) enriched the concept of the R-value by introducing six strain rate ratios, R_{ij}, which are capable of fully characterizing the viscoplastic anisotropy of a 3D structure. Similarly to the R-value, each of these ratios can be measured from either a uniaxial tensile test or a simple shear test. Specifically, introduce Cartesian coordinates $\mathbf{x} = (x_1, x_2, x_3)$ with its three axes parallel to the orthotropic axes of the constituent. These ratios can then be defined as

$$R_{11} = \frac{\dot{\epsilon}_{22}}{\dot{\epsilon}_{33}}, \quad R_{12} = \frac{\dot{\epsilon}_{12}}{\dot{\epsilon}_{33}}, \quad R_{22} = \frac{\dot{\epsilon}_{33}}{\dot{\epsilon}_{11}}, \tag{A.3}$$

$$R_{13} = \frac{\dot{\epsilon}_{13}}{\dot{\epsilon}_{22}}, \quad R_{23} = \frac{\dot{\epsilon}_{23}}{\dot{\epsilon}_{11}}, \quad R_{33} = \frac{\dot{\epsilon}_{11}}{\dot{\epsilon}_{22}}. \tag{A.3′}$$

R_{ij} can be written in the Voigt notation as

$$R_1 = R_{11}, \quad R_2 = R_{12}, \quad R_3 = R_{22}, \tag{A.4}$$

$$R_4 = R_{13}, \quad R_5 = R_{23}, \quad R_6 = R_{33}. \tag{A.4′}$$

It can be obtained from Eq. (A.3) that $R_6 = 1/R_1R_3$. This implies that only five out of the six R_i's are independent.

$\mathcal{H}_{ijkl}$ can be written in the Voigt notation as H_{ij}. The diagonal components of H_{ij} can be related to R_i by (Benzerga and Besson, 2001)

$$H_{11} = -\frac{2}{3}\frac{R_1R_3 - 2R_1 - 2}{R_1 + 1}, \quad \frac{H_{22}}{H_{11}} = -\frac{1}{2}\frac{(2R_2 + 1)(R_1R_3 + 1)}{R_1R_3 - 2R_1 - 2}, \tag{A.5}$$

$$\frac{H_{33}}{H_{11}} = 1 - \frac{3(R_1R_3 - 1)}{R_1R_3 - 2R_1 - 2}, \quad \frac{H_{44}}{H_{11}} = -\frac{1}{2}\frac{(2R_4 + 1)(R_3 + 1)R_1}{R_1R_3 - 2R_1 - 2}, \tag{A.5′}$$

$$\frac{H_{55}}{H_{11}} = -\frac{1}{2}\frac{(2R_5 + 1)(R_1 + 1)}{R_1R_3 - 2R_1 - 2}, \quad \frac{H_{66}}{H_{11}} = 1 - \frac{3R_1(R_3 - 1)}{R_1R_3 - 2R_1 - 2}, \tag{A.5″}$$

while the off-diagonal components vanish. More details on $\mathcal{H}$ can be found in Benzerga and Besson (2001), Appendix A.

A special case of viscoplastic anisotropy is viscoplastic transverse isotropy, in which case there exists a plane of viscoplastic isotropy. Without loss of generality, let the $x_2 - x_3$ plane be the plane of viscoplastic isotropy. R_i can then be expressed as

$$R_3 = R_5 = \frac{1}{R_6} = R \quad \text{and} \quad R_2 = R_4 = R', \tag{A.6}$$

where R and R' can be measured from a uniaxial tensile test and a simple shear test, respectively. Substituting Eq. (A.6) into Eq. (A.5) and rearranging the equations give

$$H_{11} = \frac{1}{3}(4 - R), \quad H_{22} = H_{44} = \frac{1}{6}(R + 1)(2R' + 1), \tag{A.7}$$

$$H_{33} = H_{55} = H_{66} = \frac{1}{3}(2R + 1). \tag{A.7′}$$

Appendix B. Partial derivatives

Recall that the partial derivatives whose explicit expressions are to be derived are

$$\mathcal{K} = \frac{\partial \dot{\boldsymbol{\epsilon}}^{vp}}{\partial \boldsymbol{\sigma}}, \quad \mathbf{L} = \frac{\partial \dot{\boldsymbol{\epsilon}}^{vp}}{\partial p}, \quad \mathcal{M} = \frac{\partial \dot{\boldsymbol{\epsilon}}^{vp}}{\partial \mathbf{X}}, \tag{B.1}$$

$$\mathbf{N} = \frac{\partial \dot{p}}{\partial \boldsymbol{\sigma}}, \quad P = \frac{\partial \dot{p}}{\partial p}, \quad \mathbf{Q} = \frac{\partial \dot{p}}{\partial \mathbf{X}}, \tag{B.1′}$$

$$\mathcal{R} = \frac{\partial \dot{\mathbf{X}}}{\partial \boldsymbol{\sigma}}, \quad \mathbf{S} = \frac{\partial \dot{\mathbf{X}}}{\partial p}, \quad \mathcal{T} = \frac{\partial \dot{\mathbf{X}}}{\partial \mathbf{X}}. \tag{B.1''}$$

Let $\mathcal{K}, \mathbf{L}$, and $\mathcal{M}$ be the first set of partial derivatives of interest. Recall that

$$\frac{\partial f}{\partial \boldsymbol{\sigma}} = \frac{\partial g}{\partial \boldsymbol{\sigma}} = \frac{\partial \tilde{\sigma}_e}{\partial \tilde{\boldsymbol{\sigma}}} = \frac{3}{2\tilde{\sigma}_e} \mathcal{J} : \mathcal{H} : \tilde{\boldsymbol{\sigma}}'. \tag{B.2}$$

In addition, Eq. (12) indicates that $\tilde{\sigma}_e = \tilde{\sigma}_e(\tilde{\boldsymbol{\sigma}})$. Also recall that $\tilde{\boldsymbol{\sigma}} = \boldsymbol{\sigma} - \mathbf{X}$. It can then be obtained using the chain rule that

$$\frac{\partial \tilde{\sigma}_e}{\partial \boldsymbol{\sigma}} = \frac{\partial \tilde{\sigma}_e}{\partial \tilde{\boldsymbol{\sigma}}} : \frac{\partial \tilde{\boldsymbol{\sigma}}}{\partial \boldsymbol{\sigma}} = \frac{\partial \tilde{\sigma}_e}{\partial \tilde{\boldsymbol{\sigma}}} : \mathcal{I} = \frac{\partial \tilde{\sigma}_e}{\partial \tilde{\boldsymbol{\sigma}}}, \tag{B.3}$$

$$\frac{\partial \tilde{\sigma}_e}{\partial \mathbf{X}} = \frac{\partial \tilde{\sigma}_e}{\partial \tilde{\boldsymbol{\sigma}}} : \frac{\partial \tilde{\boldsymbol{\sigma}}}{\partial \mathbf{X}} = \frac{\partial \tilde{\sigma}_e}{\partial \tilde{\boldsymbol{\sigma}}} : (-\mathcal{I}) = -\frac{\partial \tilde{\sigma}_e}{\partial \tilde{\boldsymbol{\sigma}}}. \tag{B.3'}$$

Recall that, when $f > 0, \dot{\lambda}$ is given by

$$\dot{\lambda} = \frac{1}{\eta}\left(\frac{f}{\sigma_Y}\right)^N = \frac{1}{\eta}\left(\frac{\tilde{\sigma}_e}{\sigma_Y} - 1\right)^N. \tag{B.4}$$

The first equation of Eq. (20), together with Eqs. (B.2) and (B.4), implies that $\dot{\boldsymbol{\epsilon}}^{vp} = \dot{\boldsymbol{\epsilon}}^{vp}(\tilde{\boldsymbol{\sigma}}, p)$. Similarly to Eq. (B.3), one obtains

$$\frac{\partial \dot{\boldsymbol{\epsilon}}^{vp}}{\partial \tilde{\boldsymbol{\sigma}}} = \frac{\partial \dot{\boldsymbol{\epsilon}}^{vp}}{\partial \boldsymbol{\sigma}} = -\frac{\partial \dot{\boldsymbol{\epsilon}}^{vp}}{\partial \mathbf{X}} \quad \text{or} \quad \mathcal{M} = -\mathcal{K}. \tag{B.5}$$

By definition, $\mathcal{K}$ can be expressed as

$$\mathcal{K} = \frac{\partial \dot{\boldsymbol{\epsilon}}^{vp}}{\partial \tilde{\boldsymbol{\sigma}}} = \frac{\partial}{\partial \tilde{\boldsymbol{\sigma}}}\left(\dot{\lambda}\frac{\partial g}{\partial \boldsymbol{\sigma}}\right) = \left[\frac{\partial \dot{\lambda}}{\partial \tilde{\boldsymbol{\sigma}}} \otimes \frac{\partial \tilde{\sigma}_e}{\partial \tilde{\boldsymbol{\sigma}}} + \dot{\lambda}\frac{\partial}{\partial \tilde{\boldsymbol{\sigma}}}\left(\frac{\partial \tilde{\sigma}_e}{\partial \tilde{\boldsymbol{\sigma}}}\right)\right], \tag{B.6}$$

where

$$\frac{\partial \dot{\lambda}}{\partial \tilde{\boldsymbol{\sigma}}} = \frac{N}{\eta}\left(\frac{\tilde{\sigma}_e}{\sigma_Y} - 1\right)^{N-1} \frac{\partial}{\partial \tilde{\boldsymbol{\sigma}}}\left(\frac{\tilde{\sigma}_e}{\sigma_Y} - 1\right) = \frac{N}{\eta\sigma_Y}\left(\frac{\tilde{\sigma}_e}{\sigma_Y} - 1\right)^{N-1} \frac{\partial \tilde{\sigma}_e}{\partial \tilde{\boldsymbol{\sigma}}}, \tag{B.7}$$

and

$$\begin{aligned}
\frac{\partial}{\partial \tilde{\boldsymbol{\sigma}}}\left(\frac{\partial \tilde{\sigma}_e}{\partial \tilde{\boldsymbol{\sigma}}}\right) &= \frac{\partial}{\partial \tilde{\boldsymbol{\sigma}}}\left(\frac{3}{2\tilde{\sigma}_e}\mathcal{J} : \mathcal{H} : \tilde{\boldsymbol{\sigma}}'\right) = \frac{3}{2}\frac{\partial}{\partial \tilde{\boldsymbol{\sigma}}}\left(\frac{1}{\tilde{\sigma}_e}\right) \otimes \mathcal{J} : \mathcal{H} \\
&= \tilde{\boldsymbol{\sigma}}' + \frac{3}{2\tilde{\sigma}_e}\mathcal{J} : \mathcal{H} : \frac{\partial \tilde{\boldsymbol{\sigma}}'}{\partial \tilde{\boldsymbol{\sigma}}} = \frac{3}{2}\left(-\frac{1}{\tilde{\sigma}_e^2}\frac{\partial \tilde{\sigma}_e}{\partial \tilde{\boldsymbol{\sigma}}}\right) \otimes \mathcal{J} : \mathcal{H} \\
&= \tilde{\boldsymbol{\sigma}}' + \frac{3}{2\tilde{\sigma}_e}\mathcal{J} : \mathcal{H} : \mathcal{J} = -\frac{1}{\tilde{\sigma}_e}\frac{\partial \tilde{\sigma}_e}{\partial \tilde{\boldsymbol{\sigma}}} \otimes \frac{\partial \tilde{\sigma}_e}{\partial \tilde{\boldsymbol{\sigma}}} + \frac{3}{2\tilde{\sigma}_e}\mathcal{J} \\
&= \mathcal{H} : \mathcal{J}.
\end{aligned} \tag{B.8}$$

Substituting Eqs. (B.7) and (B.8) into Eq. (B.6) and rearranging the equation give

$$\begin{aligned}
\mathcal{K} = \frac{\partial \dot{\boldsymbol{\epsilon}}^{vp}}{\partial \tilde{\boldsymbol{\sigma}}} &= \frac{1}{\eta}\left(\frac{\tilde{\sigma}_e}{\sigma_Y} - 1\right)^{N-1} \\
&\times \left[\left(\frac{N-1}{\sigma_Y} + \frac{1}{\tilde{\sigma}_e}\right)\frac{\partial \tilde{\sigma}_e}{\partial \tilde{\boldsymbol{\sigma}}} \otimes \frac{\partial \tilde{\sigma}_e}{\partial \tilde{\boldsymbol{\sigma}}} + \frac{3}{2}\left(\frac{1}{\sigma_Y} - \frac{1}{\tilde{\sigma}_e}\right)\mathcal{J} : \mathcal{H} : \mathcal{J}\right].
\end{aligned} \tag{B.9}$$

Similarly to $\mathcal{K}$, $\mathbf{L}$ can be expressed as

$$\mathbf{L} = \frac{\partial \dot{\boldsymbol{\epsilon}}^{vp}}{\partial p} = \frac{\partial}{\partial p}\left(\dot{\lambda}\frac{\partial g}{\partial \boldsymbol{\sigma}}\right) = \frac{\partial \dot{\lambda}}{\partial p}\frac{\partial \tilde{\sigma}_e}{\partial \tilde{\boldsymbol{\sigma}}}, \tag{B.10}$$

where

$$\begin{aligned}
\frac{\partial \dot{\lambda}}{\partial p} &= \frac{N}{\eta}\left(\frac{\tilde{\sigma}_e}{\sigma_Y} - 1\right)^{N-1} \frac{\partial}{\partial p}\left(\frac{\tilde{\sigma}_e}{\sigma_Y} - 1\right) \\
&= -\frac{N}{\eta}\frac{\tilde{\sigma}_e}{\sigma_Y^2}\left(\frac{\tilde{\sigma}_e}{\sigma_Y} - 1\right)^{N-1}\frac{dR}{dp}.
\end{aligned} \tag{B.11}$$

Substituting Eq. (B.11) into Eq. (B.10) and rearranging the equation give

$$\mathbf{L} = \frac{\partial \dot{\boldsymbol{\epsilon}}^{vp}}{\partial p} = -\frac{N}{\eta}\frac{\tilde{\sigma}_e}{\sigma_Y^2}\left(\frac{\tilde{\sigma}_e}{\sigma_Y} - 1\right)^{N-1}\frac{dR}{dp}\frac{\partial \tilde{\sigma}_e}{\partial \tilde{\boldsymbol{\sigma}}}. \tag{B.12}$$

Let $\mathbf{N}$, P, and $\mathbf{Q}$ be the next set of partial derivatives of interest. Recall that $\dot{p} = \dot{\lambda}$. This, together with Eq. (B.4), implies that $\dot{p} = \dot{p}(\tilde{\boldsymbol{\sigma}}, p)$. Similarly to Eq. (B.3), one obtains

$$\frac{\partial \dot{p}}{\partial \tilde{\boldsymbol{\sigma}}} = \frac{\partial \dot{p}}{\partial \boldsymbol{\sigma}} = -\frac{\partial \dot{p}}{\partial \mathbf{X}} \quad \text{or} \quad \mathbf{Q} = -\mathbf{N}. \tag{B.13}$$

By definition, $\mathbf{N}$ and P can be expressed as

$$\mathbf{N} = \frac{\partial \dot{p}}{\partial \tilde{\boldsymbol{\sigma}}} = \frac{\partial \dot{\lambda}}{\partial \tilde{\boldsymbol{\sigma}}} = \frac{N}{\eta\sigma_Y}\left(\frac{\tilde{\sigma}_e}{\sigma_Y} - 1\right)^{N-1}\frac{\partial \tilde{\sigma}_e}{\partial \tilde{\boldsymbol{\sigma}}} \tag{B.14}$$

and

$$P = \frac{\partial \dot{p}}{\partial p} = \frac{\partial \dot{\lambda}}{\partial p} = -\frac{N}{\eta}\frac{\tilde{\sigma}_e}{\sigma_Y^2}\left(\frac{\tilde{\sigma}_e}{\sigma_Y} - 1\right)^{N-1}\frac{dR}{dp}, \tag{B.15}$$

respectively.

Now the remaining partial derivatives are $\mathcal{R}$, $\mathbf{S}$, and $\mathcal{T}$. Recall that

$$\dot{\mathbf{X}} = \frac{2}{3}C\dot{\boldsymbol{\epsilon}}^{vp} - \gamma\mathbf{X}\dot{p}. \tag{B.16}$$

Substituting Eq. (B.16) into the last three equations of Eq. (B.1) gives

$$\mathcal{R} = \frac{\partial \dot{\mathbf{X}}}{\partial \boldsymbol{\sigma}} = \frac{2}{3}C\frac{\partial \dot{\boldsymbol{\epsilon}}^{vp}}{\partial \boldsymbol{\sigma}} - \gamma\frac{\partial \dot{p}}{\partial \boldsymbol{\sigma}} \otimes \mathbf{X} = \frac{2}{3}C\mathcal{K} - \gamma\mathbf{N} \otimes \mathbf{X}, \tag{B.17}$$

$$\mathbf{S} = \frac{\partial \dot{\mathbf{X}}}{\partial p} = \frac{2}{3}C\frac{\partial \dot{\boldsymbol{\epsilon}}^{vp}}{\partial p} - \gamma\frac{\partial \dot{p}}{\partial p}\mathbf{X} = \frac{2}{3}C\mathbf{L} - \gamma P\mathbf{X}, \tag{B.17'}$$

$$\begin{aligned}
\mathcal{T} = \frac{\partial \dot{\mathbf{X}}}{\partial \mathbf{X}} &= \frac{2}{3}C\frac{\partial \dot{\boldsymbol{\epsilon}}^{vp}}{\partial \mathbf{X}} - \gamma\left(\frac{\partial \dot{p}}{\partial \mathbf{X}} \otimes \mathbf{X} + \dot{p}\frac{\partial \mathbf{X}}{\partial \mathbf{X}}\right) \\
&= -\left(\frac{2}{3}C\frac{\partial \dot{\boldsymbol{\epsilon}}^{vp}}{\partial \boldsymbol{\sigma}} - \gamma\frac{\partial \dot{p}}{\partial \boldsymbol{\sigma}} \otimes \mathbf{X}\right) - \gamma\dot{p}\mathcal{I} = -\mathcal{R} - \gamma\dot{p}\mathcal{I}.
\end{aligned} \tag{B.17''}$$

Note that, in Eq. (B.17), $\mathcal{T} \neq -\mathcal{R}$ because $\dot{\mathbf{X}} = \dot{\mathbf{X}}(\boldsymbol{\sigma}, \mathbf{X}, p) \neq \dot{\mathbf{X}}(\tilde{\boldsymbol{\sigma}}, p)$.

Till now, the explicit expressions for all the partial derivatives in Eq. (B.1) (or Eq. (32)) have been derived.

References

Aboudi, J., 1981. Generalized effective stiffness theory for the modeling of fiber-reinforced composites. Int. J. Solids Struct., 1005–1018.

Aboudi, J., 1982. A continuum theory for fiber-reinforced elastic-viscoplastic composites. Int. J. Eng. Sci. 20, 605–621.

Aboudi, J., Pindera, M., Arnold, S., 2002. High-fidelity generalization method of cells for inelastic periodic multiphase materials. NASA/TM-2002-211469 2.

Adoudi, J., 2004. The generalized method of cells and high-fidelity generalized method of cells micromechanical models-a review. Mech. Adv. Mater. Struct. 11, 329–366.

Banerjee, B., Adams, D.O., 2004. On predicting the effective elastic properties of polymer bonded explosives using the recursive cell method. Int. J. Solids Struct. 41, 481–509.

Bensoussan, A., Lions, J., Papanicolaou, G., 1978. Asymptotic Analysis for Periodic Structures. North-Holland, Amsterdam.

Benzerga, A.A., Besson, J., 2001. Plastic potentials for anisotropic porous solids. Eur. J. Mech. A/Solids 20, 397–434.

Berdichevsky, L.V., 2009. Variational Principles of Continuum Mechanics: II. Applications. Springer, New York.

Berveiller, M., Zaoui, A., 1978. An extension of the self-consistent scheme to plastically-flowing polycrystals. J. Mech. Phys. Solids 26, 325–344.

Besson, J., Cailletaud, G., Chaboche, J.L., Forest, S., 2010. Non-linear mechanics of materials. Solid Mechanics and its Applications, vol. 167. Springer, New York.

Chaboche, J.L., 1989. Constitutive equations for cyclic plasticity and cyclic viscoplasticity. Int. J. Plast. 5, 247–302.

Chaboche, J.L., 1997. Thermodynamic formulation of constitutive equations and application to the viscoplasticity and viscoelasticity of metals and polymers. Int. J. Solids Struct. 34, 2239–2254.

Doghri, I., Adam, L., Bilger, N., 2010. Mean-field homogenization of elasto-viscoplastic composites based on a general incrementally affine linearization method. Int. J. Plast. 26, 219–238.

Hashin, Z., Shtrikman, S., 1963. A variational approach to the theory of the elastic behaviour of multiphase materials. J. Mech. Phys. Solids 11, 127–140.
Hill, R., 1965a. A self-consistent mechanics of composite materials. J. Mech. Phys. Solids 13, 213–222.
Hill, R., 1965b. A self-consistent mechanics of composite materials. J. Mech. Phys. Solids 13, 213–222.
Hutchinson, J., 1976. Bounds and self-consistent estimates for creep of polycrystalline materials. Proc. R. Soc. London. Ser. A: Math. Phys. Sci. 348, 101–127.
Lebensohn, R., TomT, C., 1993. A self-consistent anisotropic approach for the simulation of plastic deformation and texture development of polycrystals: application to zirconium alloys. Acta Metal. Mater. 41, 2611–2624.
Li, J., Weng, G., 1998. A unified approach from elasticity to viscoelasticity to viscoplasticity of particle-reinforced solids. Int. J. Plast. 14, 193–208.
Masson, R., Zaoui, A., 1999. Self-consistent estimates for the rate-dependent elastoplastic behaviour of polycrystalline materials. J. Mech. Phys. Solids 47, 1543–1568.
Masson, R., Bornert, M., Suquet, P., Zaoui, A., 2000. An affine formulation for the prediction of the effective properties of nonlinear composites and polycrystals. J. Mech. Phys. Solids 48, 1203–1227.
Milton, G., 1981. Bounds on the electromagnetic, elastic, and other properties of two-component composites. Phys. Rev. Lett. 46, 542–545.
Molinari, A., Canova, G., Ahzi, S., 1987. A self consistent approach of the large deformation polycrystal viscoplasticity. Acta Metal. 35, 2983–2994.
Molinari, A., Ahzi, S., Kouddane, R., 1997. On the self-consistent modeling of elastic-plastic behavior of polycrystals. Mech. Mater. 26, 43–62.
Mori, T., Tanaka, K., 1973. Average stress in matrix and average elastic energy of materials with misfitting inclusions. Acta Metal. 21, 571–574.
Murakami, H., Toledano, A., 1990. A high-order mixture homogenization of bi-laminated composites. Transactions of the ASME. J. Appl. Mech. 57, 388–397.
Nemat-Nasser, S., Obata, M., 1986. Rate-dependent, finite elasto-plastic deformation of polycrystals. Proc. R. Soc. London. A. Math. Phys. Sci. 407, 343–375.
Paley, M., Aboudi, J., 1992. Micromechanical analysis of composites by the generalized cells model. Mech. Mater. 14, 127–139.
Perzyna, P., 1966. Fundamental problems in viscoplasticity. Advances in Applied Mechanics, vol. 9. Academic Press, pp. 243–377.
Pierard, O., Doghri, I., 2006. An enhanced affine formulation and the corresponding numerical algorithms for the mean-field homogenization of elasto-viscoplastic composites. Int. J. Plast. 22, 131–157.
Pierard, O., LLorca, J., Segurado, J., Doghri, I., 2007. Micromechanics of particle-reinforced elasto-viscoplastic composites: finite element simulations versus affine homogenization. Int. J. Plast. 23, 1041–1060.
Suquet, P., 1995. Overall properties of nonlinear composites: a modified secant moduli theory and its link with ponte castaeda's nonlinear variational procedure. Comptes rendus de l'AcadTmie des sciences STrie II, MTcanique, physique, chimie, astronomie 320, 563–571.
Tandon, G., Weng, G., 1988. A theory of particle-reinforced plasticity. Transactions of the ASME. J. Appl. Mech. 55, 126–135.
Tang, T., Yu, W., 2007. A variational asymptotic micromechanics model for predicting conductivity of composite materials. J. Mech. Mater. Struct. 2, 1813–1830.
Tang, T., Yu, W., 2008a. Variational asymptotic homogenization of heterogeneous electromagnetoelastic materials. Int. J. Eng. Sci. 46, 741–757.
Tang, T., Yu, W., 2008b. Variational asymptotic micromechanics modeling of heterogeneous piezoelectric materials. Mech. Mater. 40, 812–824.
Voce, E., 1955. A practical strain-hardening function. Metallurgia 51, 219–226.
Weng, G., 1982. A unified, self-consistent theory for the plastic-creep deformation of metals. Transactions of the ASME. J. Appl. Mech. 49, 728–734.
Williams, T., Yu, W., Aboudi, J., Bednarcyk, B., 2007. A critical evaluation of the predictive capabilities of various advanced micromechanics models. In: Proceedings of the 48th Structures, Structural Dynamics, and Materials Conference. Waikiki.
Xia, Z., Zhang, Y., Ellyin, F., 2003. A unified periodical boundary conditions for representative volume elements of composites and applications. Int. J. Solids Struct. 40, 1907–1921.
Yu, W., Tang, T., 2007a. Variational asymptotic method for unit cell homogenization of periodically heterogeneous materials. Int. J. Solids Struct. 44, 3738–3755.
Yu, W., Tang, T., 2007b. A variational asymptotic micromechanics model for predicting thermoelastic properties of heterogeneous materials. Int. J. Solids Struct. 44, 7510–7525.
Zhao, K.M., Lee, J.K., 2001. Material properties of aluminum alloy for accurate draw-bend simulation. J. Eng. Mater. Technol. 123, 287–292.

AIAA SciTech
13-17 January 2014, National Harbor, Maryland
55th AIAA/ASMe/ASCE/AHS/SC Structures, Structural Dynamics, and Materials Conference

On the Constitutive Relations for Damaged Elastoplastic Materials Coupling Anisotropic Damage and Plasticity

Liang Zhang*
Utah State University, Logan, UT 84322-4130, USA
Wenbin Yu†
Purdue University, West Lafayette, IN 47907-2045, USA

The objective of this paper is to propose the constitutive relations for damaged elastoplastic materials, which are capable of coupling anisotropic damage, damage hardening, plastic anisotropy, and isotropic/kinematic hardening. Some fundamentals of continuum damage mechanics and thermodynamics are briefed, and the conventional damage tensors are modified to be of more concise forms and clearer physical meanings. The constitutive relations in the undamaged configuration, the damage evolution law, and the constitutive relations in the damaged configuration are subsequently derived. The applicability and power of the proposed constitutive relations are validated using examples such as predicting the stress-strain and damage factor-strain curves of damaged elastoplastic materials of various material properties. More sophisticated material properties can be incorporated.

I. Introduction

Microscopic defects, such as microcracks, microvoids, and dislocations, are inevitable in real materials. As a material undergoes a certain extent of deformation, the microscopic defects within the material will start propagating, nucleating, growing, coalescing, or moving. Such activities of the defects often cause irreversible microstructure changes in the microstructure of the material, most of which are harmful and should be avoided or monitored. It is doable to experimentally monitor the activities of microscopic defects, in which the microstructure change can be detected. However, it is expensive and time consuming to manufacture a great amount of materials and to perform various tests on them. Although possible, it is computationally prohibitive to analyze a material with all the microstructural details because the macroscopic dimensions of the material are usually several orders of magnitude greater than the microscopic length scale. Therefore, it is of great practical value to seek for a precise and concise mathematical description of the behaviors of a damaged material, i.e., the constitutive relations for the damaged material.

Microscopic defects can be classified into three categories, i.e., line defects (dislocations), planar defects (macrocracks and grain doundries), and volume defects (microvoids). The theory of plasticity deals with the macroscopic effect of dislocation motion, while continuum damage mechanics deals with the macroscopic effect of microcrack propagation and microvoid growth. Continuum damage mechanics, which combines the internal state variable theory and the theory of irreversible thermodynamics, provides a solid framework for the derivation of the constitutive relations for damaged materials. In recent decades, elaborate efforts have been devoted to enabling it to handle more and more complex problems, such as those involving complex material behaviors, complex loading conditions, and complex loading histories. Some authors[1–7] have extensively enriched the framework based on isotropic damage, while some others[8–23] extended the framework by considering anisotropic damage.

The theory of plasticity has been well established and is capable of perfectly solving various problems involving dislocation motion. However, neither continuum damage mechanics nor the theory of plasticity is

*Postdoctoral Researcher, Department of Mechanical and Aerospace Engineering.
†Associate Professor, School of Aeronautics and Astronautics, AIAA Associate Fellow.

capable of perfectly handling the problems of damaged elastoplastic materials alone. This leads numerous researchers to seek for a suitable combination of these two theories. The related works can be classified into two groups. Specifically, one group of works is formulated based on the stress-based theory of plasticity, in the undamaged (effective) configuration, in which the so-called effective stresses are defined as the average microscopic stresses acting on the undamaged materials among the microscopic defects.[4,6,7,12–14,17,22,23] In contrast, the other group is formulated also based on stress-based theory of plasticity, but in the damaged (nominal) configuration, in which the so-called nominal stresses are defined as the macroscopic stresses acting on both the damaged and undamaged materials.[2,11,20] More details on the undamaged and damaged configurations can be found in Section II). However, due to the complexity of the problem, there is still a lack of theories capable of perfectly coupling anisotropic damage and plasticity. Therefore, there is a need for such powerful theories.

The objective of this paper is to propose the constitutive relations for damaged elastoplastic materials, which are capable of coupling anisotropic damage, damage hardening, plastic anisotropy, and isotropic/kinematic hardening. Some fundamentals of continuum damage mechanics and thermodynamics are briefed, and the conventional damage tensors are modified to be of more concise forms and clearer physical meanings. The constitutive relations in the undamaged configuration, the damage evolution law, and the constitutive relations in the damaged configuration are subsequently derived. The applicability and power of the proposed constitutive relations are validated using examples such as predicting the stress-strain and damage factor-strain curves of damaged elastoplastic materials of various material properties.

II. Undamaged Configuration and Damage Tensors

In this section, some fundamentals of continuum damage mechanics will be briefed, while the conventional damage tensors will be modified to be of more concise forms and clearer physical meanings. Specifically, the derivation of the constitutive relations for a damaged material generally starts with two basic but important assumptions:

1. Each damaged material has an equivalent undamaged material;
2. There exists a one-to-one correspondence between each pair of physical quantities in the damaged and undamaged (effective) configurations.

As these two assumption are made, the task can be accomplished by subsequently deriving the constitutive relations in the undamaged configuration, the damage evolution law, and the constitutive relations in the damaged configuration.

The stress tensor in the undamaged configuration can be related to that in the damaged configuration, $\boldsymbol{\sigma}$, by

$$\bar{\boldsymbol{\sigma}} = \boldsymbol{\mathcal{M}} : \boldsymbol{\sigma} \quad \text{or} \quad \boldsymbol{\sigma} = \boldsymbol{\mathcal{M}}^{-1} : \bar{\boldsymbol{\sigma}}, \tag{1}$$

where the overbar denotes the quantity in the undamaged configuration, $\boldsymbol{\mathcal{M}}$ denotes the fourth-order damage effect tensor, and $\bar{\boldsymbol{\sigma}}$ is often referred to as the effective stress tensor. Without loss of generality, let $\boldsymbol{\omega}$ and $\boldsymbol{\mathcal{D}}$ denotes the second- and fourth-order damage tensors, respectively. Also let $\boldsymbol{\omega}$ be symmetric, and let $\boldsymbol{\mathcal{D}}$ be related to $\boldsymbol{\omega}$ by

$$\boldsymbol{\mathcal{D}} = \sum_{i=1}^{3}\sum_{j=1}^{3} \omega_{ij} \mathbf{e}_i \otimes \mathbf{e}_j \otimes \mathbf{e}_i \otimes \mathbf{e}_j, \tag{2}$$

where $\mathbf{e}_i$ denotes the unit vector. It can be verified that $\boldsymbol{\mathcal{D}}$ fulfills both the major and minor symmetries (i.e., $\mathcal{D}_{ijkl} = \mathcal{D}_{klij}$, $\mathcal{D}_{ijkl} = \mathcal{D}_{jikl}$, and $\mathcal{D}_{ijkl} = \mathcal{D}_{ijlk}$). Moreover, $\mathcal{D}_{ijkl}$ can be written in the Voigt notation as D_{ij} with the diagonal components of D_{ij} being ω_i (ω_{ij} in the Voigt notation) and the off-diagonal components vanishing. At last, for the special case of isotropic damage, $\boldsymbol{\omega} = \omega \mathbf{I}$, where ω denotes the damage factor, and $\mathbf{I}$ denotes the second-order identity tensor. Let $\boldsymbol{\mathcal{M}}^{-1}$ be related to $\boldsymbol{\mathcal{D}}$ by

$$\boldsymbol{\mathcal{M}}^{-1} = \boldsymbol{\mathcal{I}} - \boldsymbol{\mathcal{D}}, \tag{3}$$

where $\boldsymbol{\mathcal{I}}$ denotes the fourth-order identity tensor. It can be verified that $\boldsymbol{\mathcal{M}}^{-1}$ also fulfills both the major and minor symmetries.

Let Ψ^e and $\boldsymbol{\epsilon}^e$ denote the elastic strain energy density and the elastic strain tensor, respectively. The correspondence between the stress and elastic strain tensors in the damaged configuration and those in the undamaged configuration can be defined as

$$\Psi^e\left(\boldsymbol{\epsilon}^e, \boldsymbol{\omega}\right) = \Psi^e\left(\bar{\boldsymbol{\epsilon}}^e\right) \quad \text{or} \quad \frac{1}{2}\boldsymbol{\sigma} : \boldsymbol{\epsilon}^e = \frac{1}{2}\bar{\boldsymbol{\sigma}} : \bar{\boldsymbol{\epsilon}}^e, \tag{4}$$

where $\bar{\boldsymbol{\epsilon}}^e$ is often referred to as the effective elastic strain tensor. Substituting Eq. (1) into Eq. (4) gives

$$\bar{\boldsymbol{\epsilon}}^e = \boldsymbol{\mathcal{M}}^{-1} : \boldsymbol{\epsilon}^e \quad \text{or} \quad \boldsymbol{\epsilon}^e = \boldsymbol{\mathcal{M}} : \bar{\boldsymbol{\epsilon}}^e. \tag{5}$$

Hooke's law can be expressed in the damaged and undamaged configurations as

$$\boldsymbol{\sigma} = \boldsymbol{\mathcal{C}}^e : \boldsymbol{\epsilon}^e \quad \text{and} \quad \bar{\boldsymbol{\sigma}} = \bar{\boldsymbol{\mathcal{C}}}^e : \bar{\boldsymbol{\epsilon}}^e, \tag{6}$$

respectively, where $\boldsymbol{\mathcal{C}}^e$ and $\bar{\boldsymbol{\mathcal{C}}}^e$ denotes the fourth-order elastic stiffness tensor and the fourth-order undamaged elastic stiffness tensor with $\bar{\boldsymbol{\mathcal{C}}}^e$ being constant. Substituting Eqs. (1), (5), and (6) into Eq. (4) gives

$$\boldsymbol{\mathcal{C}}^e = \boldsymbol{\mathcal{M}}^{-1} : \bar{\boldsymbol{\mathcal{C}}}^e : \boldsymbol{\mathcal{M}}^{-1} \quad \text{or} \quad \left(\boldsymbol{\mathcal{C}}^e\right)^{-1} = \boldsymbol{\mathcal{M}} : \left(\bar{\boldsymbol{\mathcal{C}}}^e\right)^{-1} : \boldsymbol{\mathcal{M}}. \tag{7}$$

Recall that $\boldsymbol{\mathcal{M}}^{-1}$ fulfills both the major and minor symmetries. This, together with Eqs. (1), (5), and (7), implies that, if $\boldsymbol{\sigma}$ and $\boldsymbol{\epsilon}$ are symmetric, $\bar{\boldsymbol{\sigma}}$ and $\bar{\boldsymbol{\epsilon}}$ are also symmetric and that, if $\bar{\boldsymbol{\mathcal{C}}}^e$ fulfills both the major and minor symmetries, $\boldsymbol{\mathcal{C}}^e$ also fulfills both the major and minor symmetries. In addition, Eqs. (1), (5), and (7) also imply that each component of $\boldsymbol{\omega}$ actually provides a measure of the damages associated with the corresponding components of $\boldsymbol{\sigma}$ and $\boldsymbol{\epsilon}$.

Till now, some fundamentals of continuum damage mechanics have been briefed, while the conventional damage tensors have been modified to be of more concise forms and clearer physical meanings. In the next section, some fundamentals of thermodynamics will be briefed.

III. Thermodynamic Formulations

Let ψ denote the Helmholtz free energy per unit mass of the constituent. According to the theory of thermodynamics, ψ can be expressed as a function of a suitable set of independent state variables characterizing the elastic, plastic, and damage behaviors of the material, e.g.,

$$\psi = \psi\left(\boldsymbol{\epsilon}^e, \boldsymbol{\omega}, \boldsymbol{\alpha}, r, s\right), \tag{8}$$

where $\boldsymbol{\alpha}$ is a second-order tensor accounting for kinematic hardening, and r and s are two scalars accounting for isotropic and damage hardening, respectively. Assume that the material exhibits uncoupled elastic, plastic, and damage behaviors. In this case, ψ can be expressed as the sum of its elastic part, ψ^e, and its plastic hardening part, ψ^p, and its damage hardening part, ψ^d, i.e.,

$$\psi\left(\boldsymbol{\epsilon}^e, \boldsymbol{\omega}, \boldsymbol{\alpha}, p, q\right) = \psi^e\left(\boldsymbol{\epsilon}^e, \boldsymbol{\omega}\right) + \psi^p\left(\boldsymbol{\alpha}, r\right) + \psi^d\left(s\right). \tag{9}$$

The thermodynamic forces conjugate to the state variables in Eq. (8) can be defined as

$$\boldsymbol{\sigma} = \rho\frac{\partial\psi}{\partial\boldsymbol{\epsilon}^e} = \rho\frac{\partial\psi^e}{\partial\boldsymbol{\epsilon}^e}, \quad \mathbf{Y} = -\rho\frac{\partial\psi}{\partial\boldsymbol{\omega}} = -\rho\frac{\partial\psi^e}{\partial\boldsymbol{\omega}}, \tag{10}$$

$$\mathbf{X} = \rho\frac{\partial\psi}{\partial\boldsymbol{\alpha}} = \rho\frac{\partial\psi^p}{\partial\boldsymbol{\alpha}}, \quad R = \rho\frac{\partial\psi}{\partial r} = \rho\frac{\partial\psi^p}{\partial r}, \quad S = \rho\frac{\partial\psi}{\partial s} = \rho\frac{d\psi^d}{ds}, \tag{10'}$$

where $\mathbf{Y}$ denotes the damage conjugate force tensor, $\mathbf{X}$ denotes the back stress tensor, and R and S are related to the current yield stress and the current damage threshold, respectively.

If the deformation is isothermal, the Clausius-Duhem inequality writes

$$\phi = \boldsymbol{\sigma} : \dot{\boldsymbol{\epsilon}} - \rho\dot{\psi} \geq 0, \tag{11}$$

where ϕ denotes the dissipation per unit volume, and the overdot denotes the time derivative of the quantity. Note that the strain tensor, $\boldsymbol{\epsilon}$, can be decomposed into its elastic and plastic parts, i.e.,

$$\boldsymbol{\epsilon} = \boldsymbol{\epsilon}^e + \boldsymbol{\epsilon}^p. \tag{12}$$

Combining Eqs. (9)–(12) gives

$$\phi = \boldsymbol{\sigma} : \dot{\boldsymbol{\epsilon}}^p + \mathbf{Y} : \dot{\boldsymbol{\omega}} - \mathbf{X} : \dot{\boldsymbol{\alpha}} - R\dot{r} - S\dot{s} \geq 0, \tag{13}$$

Similarly to ψ, ϕ can be decomposed into its plastic hardening and damage hardening parts, ϕ^p and ϕ^d, i.e.,

$$\phi = \phi^p + \phi^d, \tag{14}$$

where

$$\phi^p = \boldsymbol{\sigma} : \dot{\boldsymbol{\epsilon}}^p - \mathbf{X} : \dot{\boldsymbol{\alpha}} - R\dot{r} \geq 0 \quad \text{and} \quad \phi^d = \mathbf{Y} : \dot{\boldsymbol{\omega}} - S\dot{s} \geq 0. \tag{15}$$

Let the yield and damage criteria take the forms of

$$f^p\left(\sigma, \mathbf{X}, R\right) = 0 \quad \text{and} \quad f^d\left(\mathbf{Y}, S\right) = 0, \tag{16}$$

respectively. The maximum dissipation principle states that the actual state of the thermodynamic forces should maximize ϕ subject to constraint Eq. (16).[24] This implies that the actual state of the thermodynamic forces should maximize Lagrange functions

$$\Lambda^p = \phi^p - \dot{\lambda}^p f^p \quad \text{and} \quad \Lambda^d = \phi^d - \dot{\lambda}^d f^d, \tag{17}$$

where $\dot{\lambda}^p$ and $\dot{\lambda}^d$ are two Lagrange multipliers. Λ^p and Λ^d reach their respective maximums only if

$$\frac{\partial \Lambda^p}{\partial \boldsymbol{\sigma}} = 0, \quad \frac{\partial \Lambda^p}{\partial \mathbf{X}} = 0, \quad \frac{\partial \Lambda^p}{\partial R} = 0, \quad \frac{\partial \Lambda^d}{\partial \mathbf{Y}} = 0, \quad \frac{\partial \Lambda^d}{\partial S} = 0. \tag{18}$$

Substituting Eqs. (13)–(17) into Eq. (18) gives

$$\dot{\boldsymbol{\epsilon}}^p = \dot{\lambda}^p \frac{\partial f^p}{\partial \boldsymbol{\sigma}}, \quad \dot{\boldsymbol{\alpha}} = -\dot{\lambda}^p \frac{\partial f^p}{\partial \mathbf{X}}, \quad \dot{r} = -\dot{\lambda}^p \frac{\partial f^p}{\partial R}, \quad \dot{\boldsymbol{\omega}} = \dot{\lambda}^d \frac{\partial f^d}{\partial \mathbf{Y}}, \quad \dot{s} = -\dot{\lambda}^d \frac{\partial f^d}{\partial S}, \tag{19}$$

which governs the evolution of the state variables.

Till now, some fundamentals of thermodynamics will have been briefed. In the next section, the constitutive relations in the undamaged configuration will be derived.

IV. Constitutive Relations in the Undamaged Configuration

Note that the plastic deformation can only occur in the undamaged part of the material. This implies that

$$f^p\left(\boldsymbol{\sigma}, \mathbf{X}, R\right) = f^p\left(\bar{\boldsymbol{\sigma}}, \bar{\mathbf{X}}, \bar{R}\right). \tag{20}$$

Eq. (20) leads one to first derive the constitutive relations in the undamaged configuration. In this section, this task will be accomplished.

For notational convenience, let $\tilde{\bar{\boldsymbol{\sigma}}} = \bar{\boldsymbol{\sigma}} - \bar{\mathbf{X}}$. Without loss of generality, let the material obey Hill's yield criterion. i.e.,

$$f^p\left(\bar{\boldsymbol{\sigma}}, \bar{\mathbf{X}}, \bar{R}\right) = \tilde{\bar{\sigma}}_e - \bar{\sigma}_Y = 0, \tag{21}$$

where

$$\tilde{\bar{\sigma}}_e = \sqrt{\frac{3}{2}\tilde{\bar{\boldsymbol{\sigma}}}' : \bar{\boldsymbol{\mathcal{H}}} : \tilde{\bar{\boldsymbol{\sigma}}}'}, \tag{22}$$

with $(\cdot)'$ denoting the deviatoric part of the tensor and $\bar{\boldsymbol{\mathcal{H}}}$ denoting the fourth-order anisotropy tensor, and $\bar{\sigma}_Y$ denotes the current yield stress and is related to $\bar{R}$ by

$$\bar{\sigma}_Y = \bar{\sigma}_0 + \bar{R} \tag{23}$$

with $\bar{\sigma}_0$ denoting the initial yield stress. Note that, if $\bar{\mathbf{X}}$ vanishes, $\tilde{\bar{\boldsymbol{\sigma}}} = \bar{\boldsymbol{\sigma}}$, and $\tilde{\bar{\sigma}}_e$ reduces to the Hill equivalent stress.[25] Substituting Eq. (22) into the modified plastic work equivalence principle,

$$\tilde{\bar{\boldsymbol{\sigma}}} : \dot{\boldsymbol{\epsilon}}^p = \tilde{\bar{\sigma}}_e \dot{\bar{p}}, \tag{24}$$

gives the Hill equivalent plastic strain rate as

$$\dot{\bar{p}} = \sqrt{\frac{2}{3}\dot{\bar{\boldsymbol{\epsilon}}}^p : \bar{\boldsymbol{\mathcal{H}}}^{-1} : \dot{\bar{\boldsymbol{\epsilon}}}^p}, \tag{25}$$

where $\bar{\boldsymbol{\mathcal{H}}} : \bar{\boldsymbol{\mathcal{H}}}^{-1} = \boldsymbol{\mathcal{I}}$.[25] $\bar{\boldsymbol{\mathcal{H}}}$ can be obtained from the R-values, which characterize plastic anisotropy and can be measured from experiments. More details on $\bar{\boldsymbol{\mathcal{H}}}$ can be found in Appendix A.

It is beneficial to find the relation between $\dot{\bar{\lambda}}^p$ and $\dot{\bar{p}}$. Similarly to the first three equations of Eq. (19), one can obtain that

$$\dot{\bar{\boldsymbol{\epsilon}}}^p = \dot{\bar{\lambda}}^p \frac{\partial f^p}{\partial \bar{\boldsymbol{\sigma}}}, \quad \dot{\bar{\boldsymbol{\alpha}}} = -\dot{\bar{\lambda}}^p \frac{\partial f^p}{\partial \bar{\mathbf{X}}}, \quad \dot{\bar{r}} = -\dot{\bar{\lambda}}^p \frac{\partial f^p}{\partial \bar{R}} \tag{26}$$

in the undamaged configuration. Substituting the first equation of Eq. (26) into Eq. (24) gives

$$\tilde{\bar{\boldsymbol{\sigma}}} : \left(\dot{\bar{\lambda}}^p \frac{\partial f^p}{\partial \bar{\boldsymbol{\sigma}}} \right) = \tilde{\bar{\sigma}}_e \dot{\bar{p}}. \tag{27}$$

According to Ref. [25], the explicit expression for $\partial f^p / \partial \bar{\boldsymbol{\sigma}}$ can be derived as

$$\frac{\partial f^p}{\partial \bar{\boldsymbol{\sigma}}} = \frac{\partial \tilde{\bar{\sigma}}_e}{\partial \tilde{\bar{\boldsymbol{\sigma}}}} = \frac{1}{2\tilde{\bar{\sigma}}_e} \frac{\partial \tilde{\bar{\sigma}}_e^2}{\partial \tilde{\bar{\boldsymbol{\sigma}}}} = \frac{1}{2\tilde{\bar{\sigma}}_e} \left(\frac{3}{2} 2 \frac{\partial \tilde{\bar{\boldsymbol{\sigma}}}'}{\partial \tilde{\bar{\boldsymbol{\sigma}}}} : \bar{\boldsymbol{\mathcal{H}}} : \tilde{\bar{\boldsymbol{\sigma}}}' \right) = \frac{3}{2\tilde{\bar{\sigma}}_e} \boldsymbol{\mathcal{J}} : \bar{\boldsymbol{\mathcal{H}}} : \tilde{\bar{\boldsymbol{\sigma}}}', \tag{28}$$

where $\boldsymbol{\mathcal{J}}$ denotes the fourth-order deviatoric projection operator and takes the form of $\boldsymbol{\mathcal{J}} = \boldsymbol{\mathcal{I}} - \frac{1}{3}\mathbf{I} \otimes \mathbf{I}$. Substituting Eq. (28) into Eq. (27) gives

$$\tilde{\bar{\sigma}}_e \dot{\bar{\lambda}}^p = \tilde{\bar{\sigma}}_e \dot{\bar{p}} \quad \text{or} \quad \dot{\bar{\lambda}}^p = \dot{\bar{p}}. \tag{29}$$

Accordingly, the Kuhn-Tucker conditions (loading/unloading conditions) write

$$f^p \leq 0, \quad \dot{\bar{\lambda}}^p \geq 0, \quad \dot{\bar{\lambda}}^p f^p = 0. \tag{30}$$

Eq. (26), together with Eq. (21), implies that nonlinear kinematic hardening is inadmissible. This indicates that Eq. (26) places too strict restrictions.[26] To overcome this drawback, introduce a pseudo-potential g^p, which is related to f^p by

$$g^p = f^p + \frac{3}{4}\frac{\bar{\gamma}}{\bar{C}} \bar{\mathbf{X}} : \bar{\mathbf{X}} + \frac{\bar{R}^2}{2\bar{K}} \tag{31}$$

with $\bar{C}$ and $\bar{\gamma}$ being two constants accounting for kinematic hardening and $\bar{K}$ being a constant accounting for isotropic hardening, and rewrite Eq. (26) as

$$\dot{\bar{\boldsymbol{\epsilon}}}^p = \dot{\bar{\lambda}}^p \frac{\partial g^p}{\partial \bar{\boldsymbol{\sigma}}}, \quad \dot{\bar{\boldsymbol{\alpha}}} = -\dot{\bar{\lambda}}^p \frac{\partial g^p}{\partial \bar{\mathbf{X}}} = \dot{\bar{\boldsymbol{\epsilon}}}^p - \frac{3}{2}\frac{\bar{\gamma}}{\bar{C}} \bar{\mathbf{X}} \dot{\bar{\lambda}}^p, \quad \dot{\bar{r}} = -\dot{\bar{\lambda}}^p \frac{\partial g^p}{\partial \bar{R}} = \left(1 - \frac{\bar{R}}{\bar{K}} \right) \dot{\bar{\lambda}}^p. \tag{32}$$

Since $\partial g^p / \partial \bar{\boldsymbol{\sigma}} = \partial f^p / \partial \bar{\boldsymbol{\sigma}}$, Eq. (29) remains valid here. Let $\rho\psi^p$ take the form of

$$\rho\psi^p = \frac{1}{3}\bar{C}\bar{\boldsymbol{\alpha}} : \bar{\boldsymbol{\alpha}} + \frac{1}{2}\bar{K}\bar{n}\bar{r}^2, \tag{33}$$

where $\bar{n}$ is another constant accounting for isotropic hardening. Note that, by definition,

$$\bar{\mathbf{X}} = \frac{2}{3}\bar{C}\bar{\boldsymbol{\alpha}} \quad \text{and} \quad \bar{R} = \bar{K}\bar{n}\bar{r}. \tag{34}$$

Substituting the last two equations of Eq. (32) into the rate form of Eq. (34) and noting that $\dot{\bar{\lambda}}^p = \dot{\bar{p}}$ give

$$\dot{\bar{\mathbf{X}}} = \frac{2}{3}\bar{C}\dot{\bar{\boldsymbol{\epsilon}}}^p - \bar{\gamma}\bar{\mathbf{X}}\dot{\bar{p}} \quad \text{and} \quad \dot{\bar{R}} = \left(\bar{K} - \bar{R} \right) \bar{n}\dot{\bar{p}}, \tag{35}$$

which are the Chaboche hardening law[27] and the rate form of the Voce hardening law,[28] respectively. Note that the second equation of Eq. (35) can be further integrated into the Voce hardening law as

$$\bar{R} = \bar{K} \left[1 - \exp\left(-\bar{n}\bar{p} \right) \right]. \tag{36}$$

More details on the derivation in this paragraph can be found in Ref. [29].

The consistency condition can be obtained from Eq. (21) as

$$\dot{f}^p = \frac{\partial f^p}{\partial \bar{\boldsymbol{\sigma}}} : \dot{\bar{\boldsymbol{\sigma}}} + \frac{\partial f^p}{\partial \bar{\mathbf{X}}} : \dot{\bar{\mathbf{X}}} + \frac{\partial f^p}{\partial \bar{R}} \frac{d\bar{R}}{d\bar{p}} \dot{\bar{p}} = 0. \tag{37}$$

Combining Eqs. (32), (35), and (37) and noting that $\partial f^p / \partial \bar{\mathbf{X}} = -\partial f^p / \partial \bar{\boldsymbol{\sigma}}$, $\partial f^p / \partial \bar{R} = -1$, and $\dot{\bar{\lambda}}^p = \dot{\bar{p}}$ give

$$\frac{\partial f^d}{\partial \bar{\boldsymbol{\sigma}}} : \dot{\bar{\boldsymbol{\sigma}}} = \frac{2}{3} \bar{C} \dot{\bar{\lambda}}^p \frac{\partial f^p}{\partial \bar{\boldsymbol{\sigma}}} : \frac{\partial g^p}{\partial \bar{\boldsymbol{\sigma}}} - \left(\bar{\gamma} \frac{\partial f^p}{\partial \bar{\boldsymbol{\sigma}}} : \bar{\mathbf{X}} - \frac{d\bar{R}}{d\bar{p}} \right) \dot{\bar{\lambda}}^p. \tag{38}$$

Note that $\dot{\bar{\boldsymbol{\epsilon}}}$ can be expressed as

$$\dot{\bar{\boldsymbol{\epsilon}}} = \dot{\bar{\boldsymbol{\epsilon}}}^e + \dot{\bar{\boldsymbol{\epsilon}}}^p = \left(\bar{\boldsymbol{\mathcal{C}}}^e \right)^{-1} : \dot{\bar{\boldsymbol{\sigma}}} + \dot{\bar{\lambda}}^p \frac{\partial g^p}{\partial \bar{\boldsymbol{\sigma}}}. \tag{39}$$

Multiplying both sides of Eq. (39) by $\partial f^p / \partial \bar{\boldsymbol{\sigma}} : \bar{\boldsymbol{\mathcal{C}}}^e$ gives

$$\frac{\partial f^p}{\partial \bar{\boldsymbol{\sigma}}} : \bar{\boldsymbol{\mathcal{C}}}^e : \dot{\bar{\boldsymbol{\epsilon}}} = \frac{\partial f^p}{\partial \bar{\boldsymbol{\sigma}}} : \dot{\bar{\boldsymbol{\sigma}}} + \dot{\bar{\lambda}}^p \frac{\partial f^p}{\partial \bar{\boldsymbol{\sigma}}} : \bar{\boldsymbol{\mathcal{C}}}^e : \frac{\partial g^p}{\partial \bar{\boldsymbol{\sigma}}}. \tag{40}$$

Substituting Eq. (38) into Eq. (39) gives

$$\frac{\partial f^p}{\partial \bar{\boldsymbol{\sigma}}} : \bar{\boldsymbol{\mathcal{C}}}^e : \dot{\bar{\boldsymbol{\epsilon}}} = \frac{2}{3} \bar{C} \dot{\bar{\lambda}}^p \frac{\partial f^p}{\partial \bar{\boldsymbol{\sigma}}} : \frac{\partial g^p}{\partial \bar{\boldsymbol{\sigma}}} - \left(\bar{\gamma} \frac{\partial f^p}{\partial \bar{\boldsymbol{\sigma}}} : \bar{\mathbf{X}} - \frac{d\bar{R}}{d\bar{p}} \right) \dot{\bar{\lambda}}^p + \dot{\bar{\lambda}}^p \frac{\partial f^p}{\partial \bar{\boldsymbol{\sigma}}} : \bar{\boldsymbol{\mathcal{C}}}^e : \frac{\partial g^p}{\partial \bar{\boldsymbol{\sigma}}}. \tag{41}$$

$\dot{\bar{\lambda}}^p$ can hereby be obtained as

$$\dot{\bar{\lambda}}^p = \frac{\dfrac{\partial f^p}{\partial \bar{\boldsymbol{\sigma}}} : \bar{\boldsymbol{\mathcal{C}}}^e : \dot{\bar{\boldsymbol{\epsilon}}}}{\dfrac{2}{3} \bar{C} \dfrac{\partial f^p}{\partial \bar{\boldsymbol{\sigma}}} : \dfrac{\partial g^p}{\partial \bar{\boldsymbol{\sigma}}} - \bar{\gamma} \dfrac{\partial f^p}{\partial \bar{\boldsymbol{\sigma}}} : \bar{\mathbf{X}} + \dfrac{d\bar{R}}{d\bar{p}} + \dfrac{\partial f^p}{\partial \bar{\boldsymbol{\sigma}}} : \bar{\boldsymbol{\mathcal{C}}}^e : \dfrac{\partial g^p}{\partial \bar{\boldsymbol{\sigma}}}}. \tag{42}$$

Substituting Eq. (42) into Eq. (39), multiplying both sides of the equation by $\bar{\boldsymbol{\mathcal{C}}}^e$, and rearranging the equation give the rate form of the constitutive relations in the undamaged configuration as

$$\dot{\bar{\boldsymbol{\sigma}}} = \bar{\boldsymbol{\mathcal{C}}}^{ep} : \dot{\bar{\boldsymbol{\epsilon}}}, \tag{43}$$

where $\bar{\boldsymbol{\mathcal{C}}}^{ep}$ denotes the fourth-order instantaneous elastoplastic stiffness tensor in the undamaged configuration and is given by

$$\bar{\boldsymbol{\mathcal{C}}}^{ep} = \bar{\boldsymbol{\mathcal{C}}}^e - \frac{\left(\bar{\boldsymbol{\mathcal{C}}}^e : \dfrac{\partial g^p}{\partial \bar{\boldsymbol{\sigma}}} \right) \otimes \left(\dfrac{\partial f^p}{\partial \bar{\boldsymbol{\sigma}}} : \bar{\boldsymbol{\mathcal{C}}}^e \right)}{\dfrac{2}{3} \bar{C} \dfrac{\partial f^p}{\partial \bar{\boldsymbol{\sigma}}} : \dfrac{\partial g^p}{\partial \bar{\boldsymbol{\sigma}}} - \bar{\gamma} \dfrac{\partial f^p}{\partial \bar{\boldsymbol{\sigma}}} : \bar{\mathbf{X}} + \dfrac{d\bar{R}}{d\bar{p}} + \dfrac{\partial f^p}{\partial \bar{\boldsymbol{\sigma}}} : \bar{\boldsymbol{\mathcal{C}}}^e : \dfrac{\partial g^p}{\partial \bar{\boldsymbol{\sigma}}}}. \tag{44}$$

Till now, the constitutive relations in the undamaged configuration have been derived. In the next section, the damage evolution law will be derived.

V. Damage Evolution Law

Following Ref. [30], let the damage criterion take a Hill-type form, i.e.,

$$f^d(\mathbf{Y}, S) = Y_e - Y_T = 0, \tag{45}$$

where Y_e denotes a Hill-type equivalent damage conjugate force and takes the form of

$$Y_e = \sqrt{\mathbf{Y} : \boldsymbol{\mathcal{L}} : \mathbf{Y}} \tag{46}$$

with $\boldsymbol{\mathcal{L}}$ denoting a fourth-order tensor accounting for anisotropic damage, and Y_T denotes the current damage threshold and is related to S by

$$Y_T = Y_0 + S, \tag{47}$$

with Y_0 denoting the initial damage threshold. $\mathcal{L}_{ijkl}$ can be written in the Voigt notation as L_{ij}. According to Ref. [30], the diagonal components of L_{ij} are around 1, while the off-diagonal components are smaller than the diagonal ones. More details on $\boldsymbol{\mathcal{L}}$ can be found in Ref. [30]. One can write the damage dissipation equivalence principle as

$$\mathbf{Y} : \dot{\boldsymbol{\omega}} = Y_e \dot{q}, \tag{48}$$

where $\dot{q}$ denotes a Hill-type equivalent damage rate. Following to Ref. [25], taking the partial derivatives with respect to $\mathbf{Y}$ on both sides of Eq. (48) gives

$$\dot{\boldsymbol{\omega}} = \frac{\partial Y_e}{\partial \mathbf{Y}} \dot{q}. \tag{49}$$

Similarly to Eq. (28), $\partial Y_e / \partial \mathbf{Y}$ can be obtained as

$$\frac{\partial Y_e}{\partial \mathbf{Y}} = \frac{1}{2Y_e} \frac{\partial Y_e^2}{\partial \mathbf{Y}} = \frac{1}{2Y_e} \left(2 \frac{\partial \mathbf{Y}}{\partial \mathbf{Y}} : \boldsymbol{\mathcal{L}} : \mathbf{Y} \right) = \frac{\boldsymbol{\mathcal{L}} : \mathbf{Y}}{Y_e}. \tag{50}$$

Substituting Eq. (50) into Eq. (49) gives

$$\dot{\boldsymbol{\omega}} = \frac{\boldsymbol{\mathcal{L}} : \mathbf{Y}}{Y_e} \dot{q} \quad \text{or} \quad \mathbf{Y} = \frac{\boldsymbol{\mathcal{L}}^{-1} : \dot{\boldsymbol{\omega}}}{\dot{q}} Y_e, \tag{51}$$

where $\boldsymbol{\mathcal{L}} : \boldsymbol{\mathcal{L}}^{-1} = \boldsymbol{\mathcal{I}}$. Substituting the second equation of Eq. (51) into Eq. (48) and rearranging the equation give

$$\dot{q}^2 = \dot{\boldsymbol{\omega}} : \boldsymbol{\mathcal{L}}^{-1} : \dot{\boldsymbol{\omega}} \quad \text{or} \quad \dot{q} = \sqrt{\dot{\boldsymbol{\omega}} : \boldsymbol{\mathcal{L}}^{-1} : \dot{\boldsymbol{\omega}}}. \tag{52}$$

Similarly to Section IV, it is beneficial to find the relation between $\dot{\lambda}^d$ and $\dot{q}$. Recall that the last two equations of Eq. (19) writes

$$\dot{\boldsymbol{\omega}} = \dot{\lambda}^d \frac{\partial f^d}{\partial \mathbf{Y}} \quad \text{and} \quad \dot{s} = -\dot{\lambda}^d \frac{\partial f^d}{\partial S}. \tag{53}$$

Substituting the first equation of Eq. (53) into Eq. (48) gives

$$\mathbf{Y} : \left(\dot{\lambda}^d \frac{\partial f^d}{\partial \mathbf{Y}} \right) = Y_e \dot{q}. \tag{54}$$

Note that $\partial f^d / \partial \mathbf{Y} = \partial Y_e / \partial \mathbf{Y}$. Substituting Eq. (50) into Eq. (54) gives

$$Y_e \dot{\lambda}^d = Y_e \dot{q} \quad \text{or} \quad \dot{\lambda}^d = \dot{q}. \tag{55}$$

Accordingly, the Kuhn-Tucker condition (loading/unloading conditions) write

$$f^d \leq 0, \quad \dot{\lambda}^d \geq 0, \quad \dot{\lambda}^d f^d = 0. \tag{56}$$

Similarly to Section IV, introduce a pseudo-potential g^d, which is related to f^d by

$$g^d = f^d + \frac{S^2}{2L} \tag{57}$$

with L being a constant accounting for damage hardening, and rewrite Eq. (53) as

$$\dot{\boldsymbol{\omega}} = \dot{\lambda}^d \frac{\partial g^d}{\partial \mathbf{Y}} \quad \text{and} \quad \dot{s} = -\dot{\lambda}^d \frac{\partial g^d}{\partial S}. \tag{58}$$

Since $\partial g^d / \partial \mathbf{Y} = \partial f^d / \partial \mathbf{Y}$, Eq. (55) remains valid here. Let $\rho \psi^d$ take the form of

$$\rho \psi^d = \frac{1}{2} L o s^2, \tag{59}$$

where o is another constant accounting for damage hardening. Substituting Eq. (59) into the last equation of Eq. (10) gives

$$S = Los. \tag{60}$$

Substituting the last equation of Eq. (58) into the rate form of Eq. (60) and noting that $\dot{\lambda}^d = \dot{q}$ give

$$\dot{S} = (L - S)\, o\dot{q} \quad \text{or} \quad S = L\left[1 - \exp\left(-oq\right)\right]. \tag{61}$$

The consistency condition can be obtained from Eq. (45) as

$$\dot{f}^d = \frac{\partial f^d}{\partial \mathbf{Y}} : \dot{\mathbf{Y}} + \frac{\partial f^d}{\partial S}\frac{dS}{dq}\dot{q} = 0. \tag{62}$$

Rearranging Eq. (62) and noting that $\partial f^d / \partial S = -1$ and $\dot{\lambda}^d = \dot{q}$ and give

$$\dot{\lambda}^d = \frac{\dfrac{\partial f^d}{\partial \mathbf{Y}} : \dot{\mathbf{Y}}}{\dfrac{dS}{dq}}. \tag{63}$$

Substituting Eq. (63) into the first equation of Eq. (58) gives

$$\dot{\boldsymbol{\omega}} = \frac{\dfrac{\partial f^d}{\partial \mathbf{Y}} : \dot{\mathbf{Y}}}{\dfrac{dS}{dq}}\frac{\partial g^d}{\partial \mathbf{Y}} = \frac{\dfrac{\partial g^d}{\partial \mathbf{Y}} \otimes \dfrac{\partial f^d}{\partial \mathbf{Y}}}{\dfrac{dS}{dq}} : \dot{\mathbf{Y}} \equiv \boldsymbol{\mathcal{S}}^d : \dot{\mathbf{Y}}, \tag{64}$$

which is the damage evolution law. It is worth notice that $\boldsymbol{\mathcal{S}}^d$ is not always invertible.

Till now, the damage evolution law has been derived. In the next section, the constitutive relations in the damaged configuration will be derived from those in the undamaged configuration and the damage evolution law.

VI. Constitutive Relations in the Damaged Configuration

The constitutive relations in the damaged configuration can be derived by subsequently accomplishing the following tasks:

1. Relate $\dot{\bar{\boldsymbol{\epsilon}}}^e$ to $\dot{\boldsymbol{\epsilon}}^e$;
2. Relate $\dot{\bar{\boldsymbol{\sigma}}}$ to $\dot{\boldsymbol{\sigma}}$;
3. Relate $\dot{\bar{\boldsymbol{\epsilon}}}^p$ to $\dot{\boldsymbol{\epsilon}}^p$, and complete the derivation.

In this section, these tasks will be accomplished in turn.

To relate $\dot{\bar{\boldsymbol{\epsilon}}}^e$ to $\dot{\boldsymbol{\epsilon}}^e$, recall that

$$\bar{\boldsymbol{\epsilon}}^e = \boldsymbol{\mathcal{M}}^{-1} : \boldsymbol{\epsilon}^e. \tag{65}$$

Taking time derivatives on both sides of Eq. (65) gives

$$\dot{\bar{\boldsymbol{\epsilon}}}^e = \dot{\boldsymbol{\mathcal{M}}}^{-1} : \boldsymbol{\epsilon}^e + \boldsymbol{\mathcal{M}}^{-1} : \dot{\boldsymbol{\epsilon}}^e. \tag{66}$$

The first term to the right of the equal sign in Eq. (71) can be further expressed as

$$\dot{\mathcal{M}}^{-1}_{ijmn}\epsilon^e_{mn} = \left(\frac{\partial \mathcal{M}^{-1}_{ijmn}}{\partial \omega_{kl}}\dot{\omega}_{kl}\right)\epsilon^e_{mn} = \left(\frac{\partial \mathcal{M}^{-1}_{ijmn}}{\partial \omega_{kl}}\epsilon^e_{mn}\right)\dot{\omega}_{kl}. \tag{67}$$

For notational convenience, let

$$\mathscr{K}_{ijklmn} = -\frac{\partial \mathcal{M}^{-1}_{ijmn}}{\partial \omega_{kl}} = -\frac{\partial}{\partial \omega_{kl}}\left(\mathcal{I}_{ijmn} - \mathcal{D}_{ijmn}\right) = \frac{\partial \mathcal{D}_{ijmn}}{\partial \omega_{kl}}. \tag{68}$$

Substituting Eq. (2) into Eq. (68) gives

$$\mathscr{K} = \sum_{i=1}^{3}\sum_{j=1}^{3} \mathbf{e}_i \otimes \mathbf{e}_j \otimes \mathbf{e}_i \otimes \mathbf{e}_j \otimes \mathbf{e}_i \otimes \mathbf{e}_j. \tag{69}$$

Substituting Eq. (68) into Eq. (67) gives

$$\dot{\mathcal{M}}^{-1}_{ijmn}\epsilon^e_{mn} = -\mathscr{K}_{ijklmn}\dot{\omega}_{kl}\epsilon^e_{mn} = -\left(\mathscr{K}_{ijklmn}\epsilon^e_{mn}\right)\dot{\omega}_{kl} \quad \text{or} \quad \dot{\boldsymbol{\mathcal{M}}}^{-1} : \boldsymbol{\epsilon}^e = -\left(\mathscr{K} : \boldsymbol{\epsilon}^e\right) : \dot{\boldsymbol{\omega}}. \tag{70}$$

Substituting Eq. (70) into Eq. (66) gives

$$\dot{\bar{\boldsymbol{\epsilon}}}^e = -\left(\mathscr{K} : \boldsymbol{\epsilon}^e\right) : \dot{\boldsymbol{\omega}} + \boldsymbol{\mathcal{M}}^{-1} : \dot{\boldsymbol{\epsilon}}^e. \tag{71}$$

Eq. (71) implies that, to relate $\dot{\bar{\boldsymbol{\epsilon}}}^e$ to $\dot{\boldsymbol{\epsilon}}^e$, one needs to first relate $\dot{\boldsymbol{\omega}}$ to $\dot{\boldsymbol{\epsilon}}^e$. Note that ψ^e can be expressed as

$$\psi^e = \frac{1}{2}\boldsymbol{\sigma} : \boldsymbol{\epsilon}^e = \frac{1}{2}\boldsymbol{\epsilon}^e : \boldsymbol{\mathcal{C}}^e : \boldsymbol{\epsilon}^e = \frac{1}{2}\boldsymbol{\epsilon}^e : \left(\boldsymbol{\mathcal{M}}^{-1} : \bar{\boldsymbol{\mathcal{C}}}^e : \boldsymbol{\mathcal{M}}^{-1}\right) : \boldsymbol{\epsilon}^e. \tag{72}$$

Substituting Eq. (72) into the second equation of Eq. (10) gives

$$\mathbf{Y} = -\frac{\partial \psi^e}{\partial \boldsymbol{\omega}} = \frac{1}{2}\boldsymbol{\epsilon}^e : \left(\mathscr{K} : \bar{\boldsymbol{\mathcal{C}}}^e : \boldsymbol{\mathcal{M}}^{-1} + \boldsymbol{\mathcal{M}}^{-1} : \bar{\boldsymbol{\mathcal{C}}}^e : \mathscr{K}\right) : \boldsymbol{\epsilon}^e. \tag{73}$$

Eq. (73) implies that $\mathbf{Y}$ can be treated as a function of $\boldsymbol{\epsilon}^e$ and $\boldsymbol{\omega}$. Accordingly, $\dot{\mathbf{Y}}$ can be expressed in terms of $\dot{\boldsymbol{\epsilon}}^e$ and $\dot{\boldsymbol{\omega}}$ using the chain rule as

$$\dot{\mathbf{Y}} = \frac{\partial \mathbf{Y}}{\partial \boldsymbol{\epsilon}^e} : \dot{\boldsymbol{\epsilon}}^e + \frac{\partial \mathbf{Y}}{\partial \boldsymbol{\omega}} : \dot{\boldsymbol{\omega}}, \tag{74}$$

where the expressions for $\partial \mathbf{Y}/\partial \boldsymbol{\epsilon}^e$ and $\partial \mathbf{Y}/\partial \boldsymbol{\omega}$ can be obtained from Eq. (73) as

$$\frac{\partial \mathbf{Y}}{\partial \boldsymbol{\epsilon}^e} = \frac{1}{2}\left[\left(\mathscr{K} : \bar{\boldsymbol{\mathcal{C}}}^e : \boldsymbol{\mathcal{M}}^{-1} + \boldsymbol{\mathcal{M}}^{-1} : \bar{\boldsymbol{\mathcal{C}}}^e : \mathscr{K}\right) : \boldsymbol{\epsilon}^e + \boldsymbol{\epsilon}^e : \left(\mathscr{K} : \bar{\boldsymbol{\mathcal{C}}}^e : \boldsymbol{\mathcal{M}}^{-1} + \boldsymbol{\mathcal{M}}^{-1} : \bar{\boldsymbol{\mathcal{C}}}^e : \mathscr{K}\right)\right] \tag{75}$$

and

$$\frac{\partial \mathbf{Y}}{\partial \boldsymbol{\omega}} = -\frac{1}{2}\boldsymbol{\epsilon}^e : \left(\mathscr{K} : \bar{\boldsymbol{\mathcal{C}}}^e : \mathscr{K} + \mathscr{K} : \bar{\boldsymbol{\mathcal{C}}}^e : \mathscr{K}\right) : \boldsymbol{\epsilon}^e = -\boldsymbol{\epsilon}^e : \mathscr{K} : \bar{\boldsymbol{\mathcal{C}}}^e : \mathscr{K} : \boldsymbol{\epsilon}^e, \tag{76}$$

respectively. Substituting Eq. (74) into Eq. (64) and rearranging the equation give

$$\dot{\boldsymbol{\omega}} = \left[\left(\boldsymbol{\mathcal{I}} - \boldsymbol{\mathcal{S}}^d : \frac{\partial \mathbf{Y}}{\partial \boldsymbol{\omega}}\right)^{-1} : \left(\boldsymbol{\mathcal{S}}^d : \frac{\partial \mathbf{Y}}{\partial \boldsymbol{\epsilon}^e}\right)\right] : \dot{\boldsymbol{\epsilon}}^e \equiv \boldsymbol{\mathcal{A}} : \dot{\boldsymbol{\epsilon}}^e, \tag{77}$$

which relates $\dot{\boldsymbol{\omega}}$ to $\dot{\boldsymbol{\epsilon}}^e$. Substituting Eq. (77) into Eq. (71) gives

$$\dot{\bar{\boldsymbol{\epsilon}}}^e = -\left(\mathscr{K} : \boldsymbol{\epsilon}^e\right) : \boldsymbol{\mathcal{A}} : \dot{\boldsymbol{\epsilon}}^e + \boldsymbol{\mathcal{M}}^{-1} : \dot{\boldsymbol{\epsilon}}^e = \left[-\left(\mathscr{K} : \boldsymbol{\epsilon}^e\right) : \boldsymbol{\mathcal{A}} + \boldsymbol{\mathcal{M}}^{-1}\right] : \dot{\boldsymbol{\epsilon}}^e \equiv \tilde{\boldsymbol{\mathcal{N}}}^{-1} : \dot{\boldsymbol{\epsilon}}^e, \tag{78}$$

which relates $\dot{\bar{\boldsymbol{\epsilon}}}^e$ to $\dot{\boldsymbol{\epsilon}}^e$.

To relate $\dot{\boldsymbol{\sigma}}$ to $\dot{\boldsymbol{\sigma}}$, recall that

$$\boldsymbol{\sigma} = \boldsymbol{\mathcal{C}}^e : \boldsymbol{\epsilon}^e. \tag{79}$$

Taking time derivatives on both sides of Eq. (79) gives

$$\dot{\boldsymbol{\sigma}} = \dot{\boldsymbol{\mathcal{C}}}^e : \boldsymbol{\epsilon}^e + \boldsymbol{\mathcal{C}}^e : \dot{\boldsymbol{\epsilon}}^e. \tag{80}$$

Recall that

$$\boldsymbol{\mathcal{C}}^e = \boldsymbol{\mathcal{M}}^{-1} : \bar{\boldsymbol{\mathcal{C}}}^e : \boldsymbol{\mathcal{M}}^{-1}. \tag{81}$$

The first term to the right of the equal sign in Eq. (71) can be further expressed as

$$\begin{aligned}
\dot{\mathcal{C}}^e_{ijrs}\epsilon^e_{rs} &= \left(\dot{\mathcal{M}}^{-1}_{ijmn}\bar{\mathcal{C}}^e_{mnpq}\mathcal{M}^{-1}_{pqrs} + \mathcal{M}^{-1}_{ijmn}\bar{\mathcal{C}}^e_{mnpq}\dot{\mathcal{M}}^{-1}_{pqrs}\right)\epsilon^e_{rs} \\
&= -\left(\mathscr{K}_{ijklmn}\dot{\omega}_{kl}\bar{\mathcal{C}}^e_{mnpq}\mathcal{M}^{-1}_{pqrs} + \mathcal{M}^{-1}_{ijmn}\bar{\mathcal{C}}^e_{mnpq}\mathscr{K}_{pqklrs}\dot{\omega}_{kl}\right)\epsilon^e_{rs} \\
&= -\left[\left(\mathscr{K}_{ijklmn}\bar{\mathcal{C}}^e_{mnpq}\mathcal{M}^{-1}_{pqrs} + \mathcal{M}^{-1}_{ijmn}\bar{\mathcal{C}}^e_{mnpq}\mathscr{K}_{pqklrs}\right)\epsilon^e_{rs}\right]\dot{\omega}_{kl} \equiv -\left(\mathscr{B}_{ijklrs}\epsilon^e_{rs}\right)\dot{\omega}_{kl}
\end{aligned} \tag{82}$$

or

$$\dot{\boldsymbol{\mathcal{C}}}^e : \boldsymbol{\epsilon}^e = -\left[\left(\boldsymbol{\mathscr{K}} : \bar{\boldsymbol{\mathcal{C}}}^e : \boldsymbol{\mathcal{M}}^{-1} + \boldsymbol{\mathcal{M}}^{-1} : \bar{\boldsymbol{\mathcal{C}}}^e : \boldsymbol{\mathscr{K}}\right) : \boldsymbol{\epsilon}^e\right] : \dot{\boldsymbol{\omega}} \equiv -\left(\boldsymbol{\mathscr{B}} : \boldsymbol{\epsilon}^e\right) : \dot{\boldsymbol{\omega}}. \tag{83}$$

Substituting Eq. (83) into Eq. (80) gives

$$\dot{\boldsymbol{\sigma}} = -\left(\boldsymbol{\mathscr{B}} : \boldsymbol{\epsilon}^e\right) : \dot{\boldsymbol{\omega}} + \boldsymbol{\mathcal{C}}^e : \dot{\boldsymbol{\epsilon}}^e = -\left(\boldsymbol{\mathscr{B}} : \boldsymbol{\epsilon}^e\right) : \boldsymbol{\mathcal{A}} : \dot{\boldsymbol{\epsilon}}^e + \boldsymbol{\mathcal{C}}^e : \dot{\boldsymbol{\epsilon}}^e = \left[-\left(\boldsymbol{\mathscr{B}} : \boldsymbol{\epsilon}^e\right) : \boldsymbol{\mathcal{A}} + \boldsymbol{\mathcal{C}}^e\right] : \dot{\boldsymbol{\epsilon}}^e. \tag{84}$$

Note that

$$\dot{\bar{\boldsymbol{\sigma}}} = \bar{\boldsymbol{\mathcal{C}}}^e : \dot{\bar{\boldsymbol{\epsilon}}}^e. \tag{85}$$

$\dot{\boldsymbol{\epsilon}}^e$ can hereby be related to $\dot{\bar{\boldsymbol{\sigma}}}$ by

$$\dot{\boldsymbol{\epsilon}}^e = \tilde{\boldsymbol{\mathcal{N}}} : \dot{\bar{\boldsymbol{\epsilon}}}^e = \tilde{\boldsymbol{\mathcal{N}}} : \left(\bar{\boldsymbol{\mathcal{C}}}^e\right)^{-1} : \dot{\bar{\boldsymbol{\sigma}}}. \tag{86}$$

Substituting Eq. (86) into Eq. (84) gives

$$\dot{\boldsymbol{\sigma}} = \left\{\left[-\left(\boldsymbol{\mathscr{B}} : \boldsymbol{\epsilon}^e\right) : \boldsymbol{\mathcal{A}} + \boldsymbol{\mathcal{C}}^e\right] : \tilde{\boldsymbol{\mathcal{N}}} : \left(\bar{\boldsymbol{\mathcal{C}}}^e\right)^{-1}\right\} : \dot{\bar{\boldsymbol{\sigma}}} \equiv \boldsymbol{\mathcal{N}}^{-1} : \dot{\bar{\boldsymbol{\sigma}}}, \tag{87}$$

which relates $\dot{\bar{\boldsymbol{\sigma}}}$ to $\dot{\boldsymbol{\sigma}}$.

To relate $\dot{\bar{\boldsymbol{\epsilon}}}^p$ to $\dot{\boldsymbol{\epsilon}}^p$, let

$$\boldsymbol{\sigma} : \dot{\boldsymbol{\epsilon}}^p = \bar{\boldsymbol{\sigma}} : \dot{\bar{\boldsymbol{\epsilon}}}^p. \tag{88}$$

Substituting Eq. (1) into Eq. (88) gives

$$\dot{\bar{\boldsymbol{\epsilon}}}^p = \boldsymbol{\mathcal{M}}^{-1} : \dot{\boldsymbol{\epsilon}}^p \quad \text{or} \quad \dot{\boldsymbol{\epsilon}}^p = \boldsymbol{\mathcal{M}} : \dot{\bar{\boldsymbol{\epsilon}}}^p. \tag{89}$$

Eq. (44) can be written as

$$\dot{\bar{\boldsymbol{\sigma}}} = \bar{\boldsymbol{\mathcal{C}}}^{ep} : \dot{\bar{\boldsymbol{\epsilon}}} = \bar{\boldsymbol{\mathcal{C}}}^{ep} : \dot{\bar{\boldsymbol{\epsilon}}}^e + \bar{\boldsymbol{\mathcal{C}}}^{ep} : \dot{\bar{\boldsymbol{\epsilon}}}^p. \tag{90}$$

Substituting Eqs. (78), (79), and (89) into Eq. (90) gives

$$\begin{aligned} \boldsymbol{\mathcal{N}} : \dot{\boldsymbol{\sigma}} &= \bar{\boldsymbol{\mathcal{C}}}^{ep} : \tilde{\boldsymbol{\mathcal{N}}}^{-1} : \dot{\boldsymbol{\epsilon}}^e + \bar{\boldsymbol{\mathcal{C}}}^{ep} : \boldsymbol{\mathcal{M}}^{-1} : \dot{\boldsymbol{\epsilon}}^p = \bar{\boldsymbol{\mathcal{C}}}^{ep} : \tilde{\boldsymbol{\mathcal{N}}}^{-1} : \dot{\boldsymbol{\epsilon}}^e + \bar{\boldsymbol{\mathcal{C}}}^{ep} : \boldsymbol{\mathcal{M}}^{-1} : \left(\dot{\boldsymbol{\epsilon}} - \dot{\boldsymbol{\epsilon}}^e\right) \\ &= \bar{\boldsymbol{\mathcal{C}}}^{ep} : \boldsymbol{\mathcal{M}}^{-1} : \dot{\boldsymbol{\epsilon}} + \bar{\boldsymbol{\mathcal{C}}}^{ep} : \left(\tilde{\boldsymbol{\mathcal{N}}}^{-1} - \boldsymbol{\mathcal{M}}^{-1}\right) : \dot{\boldsymbol{\epsilon}}^e. \end{aligned} \tag{91}$$

Note that $\dot{\boldsymbol{\epsilon}}^e$ can be related to $\dot{\boldsymbol{\sigma}}$ by

$$\dot{\boldsymbol{\epsilon}}^e = \tilde{\boldsymbol{\mathcal{N}}} : \dot{\bar{\boldsymbol{\epsilon}}}^e = \tilde{\boldsymbol{\mathcal{N}}} : \left(\bar{\boldsymbol{\mathcal{C}}}^e\right)^{-1} : \dot{\bar{\boldsymbol{\sigma}}} = \tilde{\boldsymbol{\mathcal{N}}} : \left(\bar{\boldsymbol{\mathcal{C}}}^e\right)^{-1} : \boldsymbol{\mathcal{N}} : \dot{\boldsymbol{\sigma}}. \tag{92}$$

Substituting Eq. (92) into Eq. (91) and rearranging the equation give

$$\left[\boldsymbol{\mathcal{I}} - \bar{\boldsymbol{\mathcal{C}}}^{ep} : \left(\tilde{\boldsymbol{\mathcal{N}}}^{-1} - \boldsymbol{\mathcal{M}}^{-1}\right) : \tilde{\boldsymbol{\mathcal{N}}} : \left(\bar{\boldsymbol{\mathcal{C}}}^e\right)^{-1}\right] : \boldsymbol{\mathcal{N}} : \dot{\boldsymbol{\sigma}} = \bar{\boldsymbol{\mathcal{C}}}^{ep} : \boldsymbol{\mathcal{M}}^{-1} : \dot{\boldsymbol{\epsilon}}. \tag{93}$$

Rearranging Eq. (93) gives the rate form of the constitutive relations in the damaged configuration as

$$\dot{\boldsymbol{\sigma}} = \left\{\boldsymbol{\mathcal{N}}^{-1} : \left[\boldsymbol{\mathcal{I}} - \bar{\boldsymbol{\mathcal{C}}}^{ep} : \left(\tilde{\boldsymbol{\mathcal{N}}}^{-1} - \boldsymbol{\mathcal{M}}^{-1}\right) : \tilde{\boldsymbol{\mathcal{N}}} : \left(\bar{\boldsymbol{\mathcal{C}}}^e\right)^{-1}\right]^{-1} : \bar{\boldsymbol{\mathcal{C}}}^{ep} : \boldsymbol{\mathcal{M}}^{-1}\right\} : \dot{\boldsymbol{\epsilon}} \equiv \boldsymbol{\mathcal{C}}^{ep} : \dot{\boldsymbol{\epsilon}}, \tag{94}$$

where $\boldsymbol{\mathcal{C}}^{ep}$ denotes the fourth-order instantaneous elastoplastic stiffness tensor in the damaged configuration.

VII. Validation Examples

In this section, several examples are presented to validate the applicability and power of the proposed constitutive relations and also to investigate some characteristics of damaged elastoplastic materials. The examples include predicting the stress-strain curves of damaged elastoplastic materials exhibiting various material properties.

Table 1. Material parameters of aluminum and SiC.

E (GPa)	ν	σ_0 (MPa)	K (MPa)	n	C (MPa)	γ	Y_0 (MPa)	o
71	0.32	142	40	54.9	7019	118.6	0.071	5

A. Damage Hardening

Without loss of generality, first let the damaged elastoplastic material merely exhibit isotropic hardening, kinematic hardening, and damage hardening. Specifically, let the material parameters take the values listed in Table 1, where E and ν denote Young's modulus and Poisson's ratio, respectively, and let the diagonal and off-diagonal components of L_{ij} take the values of 1 and 0.32, respectively. In this section, allow L in Eq. (61) to take the values of $2.5Y_0$, $5Y_0$, and $10Y_0$ for different cases. Introduce a Cartesian coordinate system $\mathbf{x} = (x_1, x_2, x_3)$, and let its three axes coincide with the three axes of damage orthotropy. It can be obtained from Table 1 that the material becomes damaged at $\epsilon_{11} = 0.001$ and yields at $\epsilon_{11} = 0.002$ when subject to uniaxial tension in the x_1-direction.

Figures 1 and 2 show the stress-strain and ω_{11}-ϵ_{11} curves of the material subject to uniaxial tension in the x_1-direction, respectively. For illustration purposes, the loading path here is set to consist of the following steps:

- Initial loading: ϵ_{11} is increased from 0 to 0.002;
- Unloading I: ϵ_{11} is decreased from 0.002 till σ_{11} is decreased to 0MPa, or to say, ϵ_{11} is decreased to ϵ_{11}^p at $\epsilon_{11} = 0.002$ (a residual strain);
- Reloading I: ϵ_{11} is increased to 0.004;
- ...
- Reloading IV: ϵ_{11} is increased to 0.01.

As can be seen, as damages initiate and evolve, the material exhibits a nonlinear stress-strain relation in the elastic regime and even exhibits strain softening in case L is sufficiently small, and as L decreases, the stress-strain curve of the damaged material more significantly shifts downward with respect to that of the undamaged one. In addition, it is worth notice that, for different values of L, the ω_{11}-ϵ_{11} curves exhibit quite different trends. Note that the residual strains in Figure 1 actually characterize how much plastic deformation is induced at different stages of the deformation. Figure 1 indicates that, for $L = 2.5Y_0$, negligible plastic deformation is induced. In this case, damages initiate at a very low stress level and evolve rapidly, and the subsequent damage evolution further inhibits the increase in the modified Hill equivalent stress in the undamaged configuration, $\tilde{\bar{\sigma}}_e$, and hereby the plastic deformation. Accordingly, the corresponding ω_{11}-ϵ_{11} curve exhibits an approximately monotonically increasing, which is typical for a damaged elastic material. Meanwhile, Figure 1 also indicates that, for $L = 10Y_0$, considerable plastic deformation is induced. In this case, the plastic deformation is induced just after damages initiate, and the subsequent plastic deformation inhibit the increases in the stresses and hereby the damage evolution. Accordingly, the corresponding ω_{11}-ϵ_{11} curve exhibits an approximately bilinear trend. At last, it is interesting to note that the stress-strain curve for $L = 5Y_0$ exhibits a trend different from those for $L = 2.5Y_0$ and $L = 10Y_0$. In fact, its trend is similar to that for $L = 10Y_0$ before ϵ_{11} attains 0.006 and to that $L = 2.5Y_0$ after ϵ_{11} attains 0.008. The reason for such a transition of the trend is that the damage evolution gradually takes the place of the plastic deformation and becomes dominant within $0.006 < \epsilon_{11} < 0.008$. Accordingly, the corresponding ω_{11}-ϵ_{11} curve exhibits an unexpected nonlinear trend within this interval.

Figures 3 and 4 show the stress-strain and ω_{11}-ϵ_{11} curves of the material subject to pure shear in the x_1-x_2 plane, respectively. The loading path here is similar to that in the last paragraph:

- Initial loading: ϵ_{12} is increased from 0 to 0.002;
- Unloading I: ϵ_{12} is decreased from 0.002 till σ_{12} is decreased to 0MPa;
- Reloading I: ϵ_{12} is increased to 0.004;
- ...

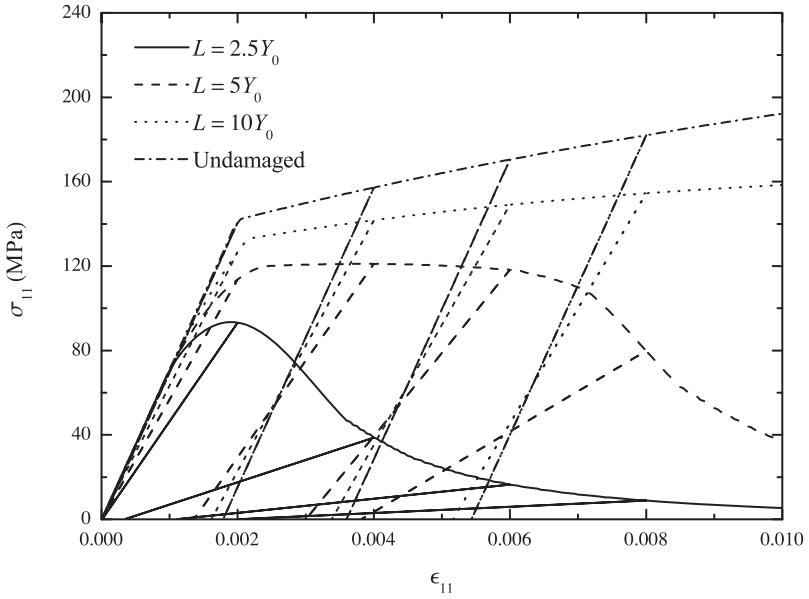

Figure 1. Stress-strain curves of the material subject to uniaxial tension in the x_1-direction.

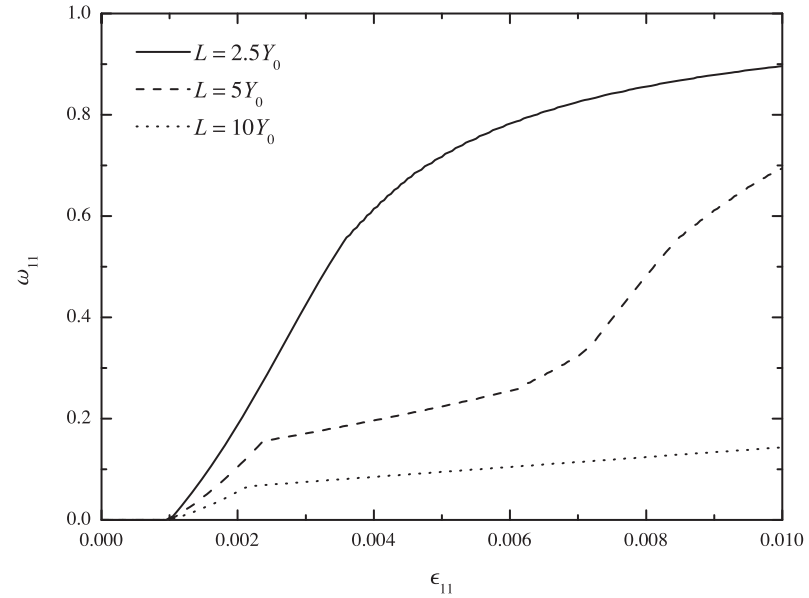

Figure 2. ω_{11}-ϵ_{11} curves of the material subject to uniaxial tension in the x_1-direction.

It can be seen that the trends of the curves here are quite similar to those in Figure 1 and 2. Therefore, most discussion in the last paragraph holds here. In addition, it is worth notice that, even if L is small, considerable plastic deformation can still be induced here. This can be understood by noting that the mean and deviatoric stresses (or strictly speaking, their increments) differently affects the damage evolution and the plastic deformation. Specifically, both the mean and deviatoric stresses contribute the damage evolution, while only the deviatoric stresses contributes to $\tilde{\bar{\sigma}}_e$ and hereby the plastic deformation. Therefore, when the material is subject to uniaxial tension, the damage evolution is easier to become dominant; when the material is subject to pure shear, the plastic deformation is easier to become dominant. In fact, Figure 4 also indicates that ω_{12} increases very slowly over continued deformation here. This again demonstrates that, relatively speaking, the damage evolution is inhibited here.

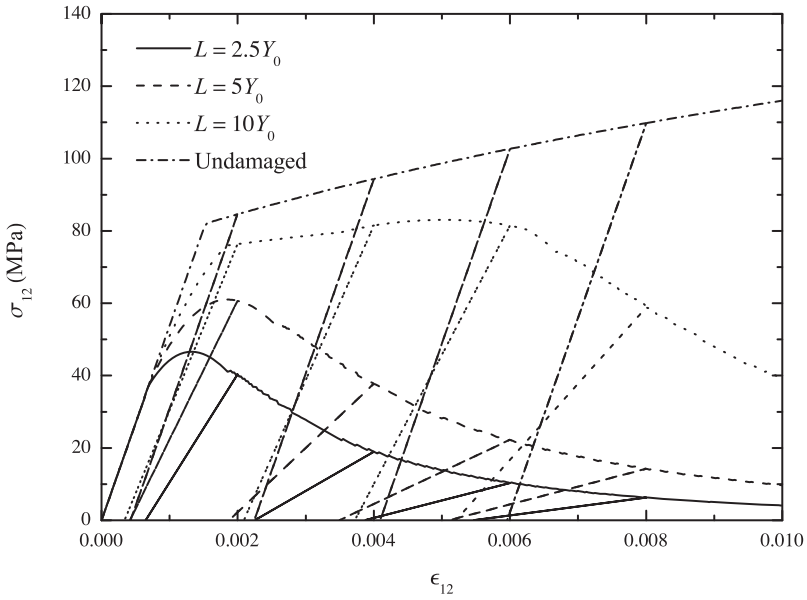

Figure 3. Stress-strain curves of the material subject to pure shear in the x_1-x_2 plane.

Figures 5 and 6 show the stress-strain and ω_{11}-ϵ_{11} curves of the material subject to equal triaxial tension, respectively. The loading path here is similar to that in the last paragraph:

- Initial loading: ϵ_{11}, ϵ_{22}, and ϵ_{33} are increased from 0 to 0.001;
- Unloading I: ϵ_{11}, ϵ_{22}, and ϵ_{33} are decreased from 0.001 till σ_{11}, σ_{22}, and σ_{33} are decreased to 0MPa;
- Reloading I: ϵ_{11}, ϵ_{22}, and ϵ_{33} are increased to 0.002;
- ...

Note that, since all the diagonal components of L_{ij} all equal 1, the stresses in the undamaged configuration are purely hydrostatic, or to say, $\tilde{\bar{\sigma}}_e$ always vanishes. This implies that on plastic deformation is induced, or to say, that the material behaves like a damaged elastic material. Therefore, all the discussion for $L = 2.5Y_0$ in the paragraph before last holds here. In addition, it is worth notice that the damages evolution here is more rapid than that in Figures 2. Note that the off-diagonal components of L_{ij} are non-zero. This implies that, for example, an increase σ_{11} may induce not only an increase ω_{11} but also those in σ_{22} and σ_{33}. In fact, it can be verified that the speed of the damage evolution here is at least 1.64 times of that in Figures 2. At last, if the diagonal components of L_{ij} becomes highly distinct to each other, it is possible that $\tilde{\bar{\sigma}}_e$ attains such a high value that the yield criterion is met, or to say, it is possible that some plastic deformation is induced here.

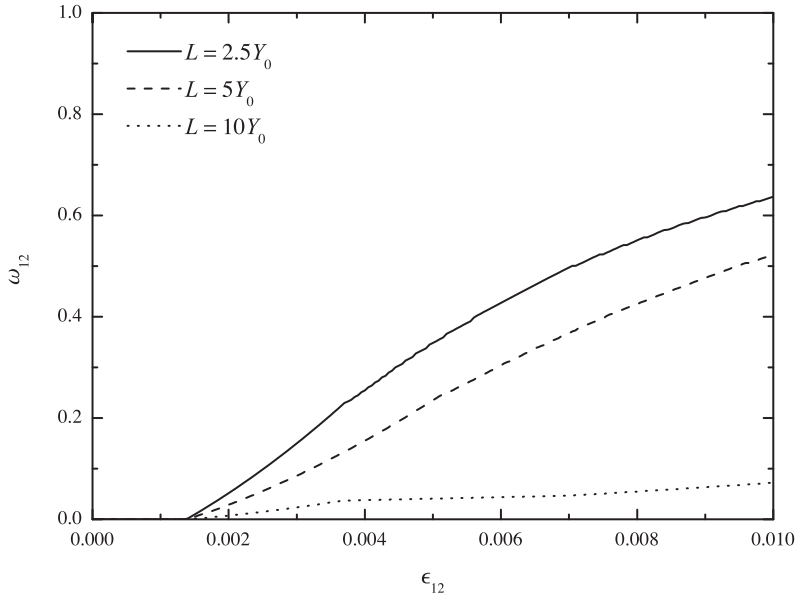

Figure 4. ω_{12}-ϵ_{12} **curves of the material subject to pure shear in the** x_1-x_2 **plane.**

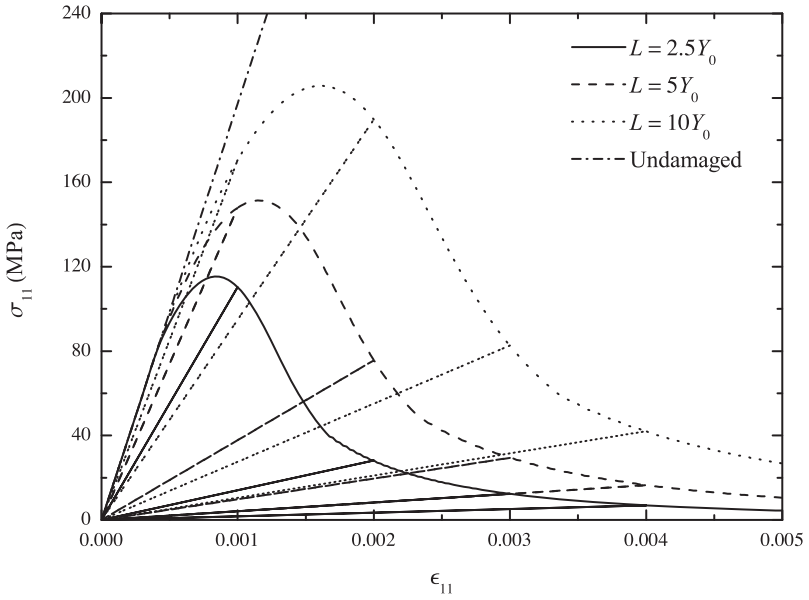

Figure 5. Stress-strain curves of the material subject to equal triaxial tension.

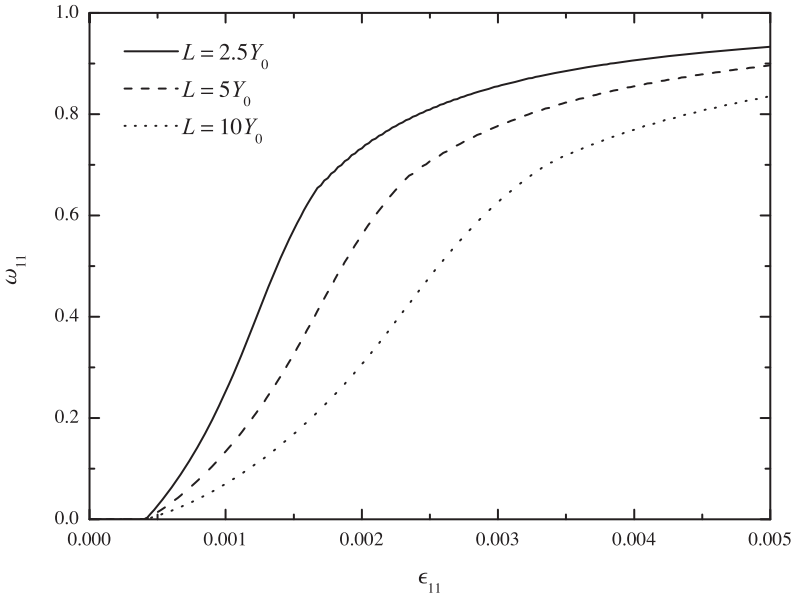

Figure 6. ω_{11}-ϵ_{11} **curves of the material subject to equal triaxial tension.**

B. General Damage Anisotropy

Next let the material also exhibit a more general type of damage anisotropy, where the term "more general" means that the diagonal components of L_{ij} can be distinct. Specifically, let the material parameters take the values listed in Table 1 with $L = 5Y_0$, and let the components of L_{ij} here except L_{11} be the same as those in Section VII-A. In this section, allow L_{11} to take the values of 0.707, 1, and 1.414 for different cases.

Figures 7 and 8 show the stress-strain and ω_{11}-ϵ_{11} curves of the material subject to uniaxial tension in the x_1-direction, respectively. The loading path here is set to be the same as that for uniaxial tension in Section VII-A. In fact, it can be obtained from Eqs. (45) and (46) that, as L_{11} increases, the material become more vulnerable to σ_{11}, while similar findings can be obtained for some other cases of damage anisotropy. For this reason, in Figure 7, as L_{11} increases, the stress-strain curve of the damaged material more significantly shifts downward with respect to that of the undamaged one. Other than this, it can be seen that the trends of the curves here are quite similar to those in Figures 1 and 2. Therefore, most discussion in the second paragraph of Section VII-A holds here.

C. Plastic Anisotropy

At last, let the material exhibit plastic anisotropy instead of general damage anisotropy. Specifically, let the material parameters take the values listed in Table 1 with $L = 5Y_0$, and let L_{ij} here be the same as that in Section VII-A. In this section, let the material exhibit plastic transverse isotropy in the x_2-x_3 plane, and allow the R-values of the material to take the three sets of values listed in Table 2 for different cases. More details on plastic transverse isotropy can be found in Appendix A.

Table 2. R**-values of the three matrices.**

	R_1	R_2	R_3	R_4	R_5	R_6
1	1	1	0.5	1	0.5	2
2	1	1	1	1	1	1
3	1	1	2	1	2	0.5

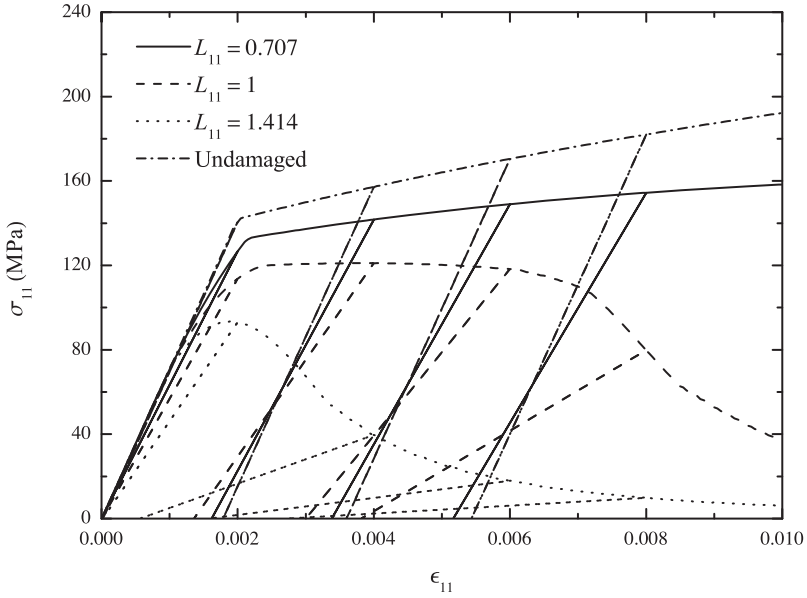

Figure 7. Stress-strain curves of the material exhibiting general damage anisotropy subject to uniaxial tension in the x_1-direction.

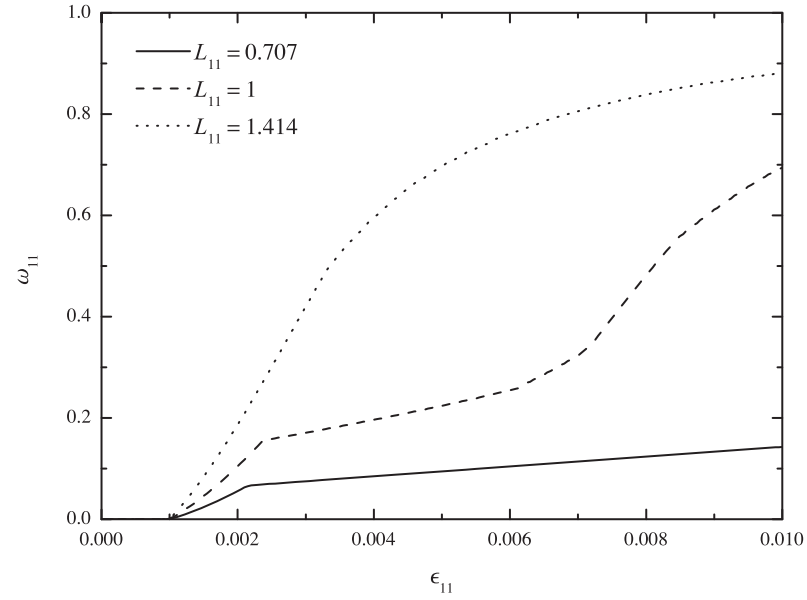

Figure 8. ω_{11}-ϵ_{11} curves of the material exhibiting general damage anisotropy subject to uniaxial tension in the x_1-direction.

Figures 9 and 10 show the stress-strain and ω_{22}-ϵ_{22} curves of the material subject to uniaxial tension in the x_2-direction, respectively. The loading path here is set to be almost the same as that in the second paragraph of Section VII-A except that ϵ_{22} and σ_{22} take the places of ϵ_{11} and σ_{11}. As can be seen, the trends of the stress-strain and ω-ϵ curves for $R_3 = R_5 = 0.5$ here are quite similar with those for $L = 2.5Y_0$ in Figures 9 and 10 except that the stress-strain curve here seems to be scaled-up, while those for $R_3 = R_5 = 2$ here are quite similar with those for $L = 10Y_0$ in Figures 9 and 10 except that the stress-strain curve here seems to be scaled-down. This can be understood by noting that the R-values can affect the initial yield stress and hereby the damage evolution and the plastic deformation. Specifically, one can obtain the following findings first by substituting the R-values in Table 2 into Eq. (99) and then by substituting the resulting values of H_{ij} into Eq. (22):

- Different sets of the R-values yields the same yield stress of the material loaded in the y_1-direction;
- The set of the R-values of lowest value of R_3 (or R_5) yields at the lowest yield stress of the material loaded in the y_2- (or y_3-) direction and vice versa.

Therefore, for $R_3 = R_5 = 0.5$, damages can evolve to a considerable extent before the yield criterion, which becomes more restrictive in this case, is met, and the subsequent damage evolution further inhibits the plastic deformation. This leads the material to behave like a damaged elastic one. Accordingly, the corresponding ω_{22}-ϵ_{22} curve exhibits an approximately monotonically increasing trend. In contrast, for $R_3 = R_5 = 2$, the yield criterion, which becomes less restrictive in this case, can be met just after damages initiate, and the subsequent plastic deformation further inhibits the damage evolution. This leads the material to behave like an elastoplastic one. Accordingly, the corresponding ω_{22}-ϵ_{22} curve exhibits an approximately bilinear trend.

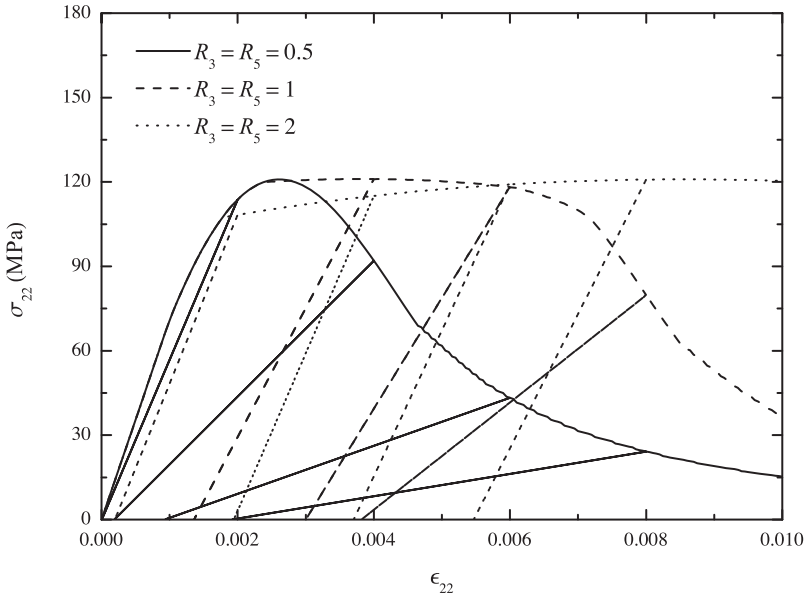

Figure 9. Stress-strain curves of the material exhibiting plastic anisotropy subject to uniaxial tension in the x_2-direction.

VIII. Conclusions

In this paper, the constitutive relations for damaged elastoplastic materials, which are capable of coupling anisotropic damage, damage hardening, plastic anisotropy, and isotropic/kinematic hardening, are proposed. Some fundamentals of continuum damage mechanics and thermodynamics are briefed, and the conventional

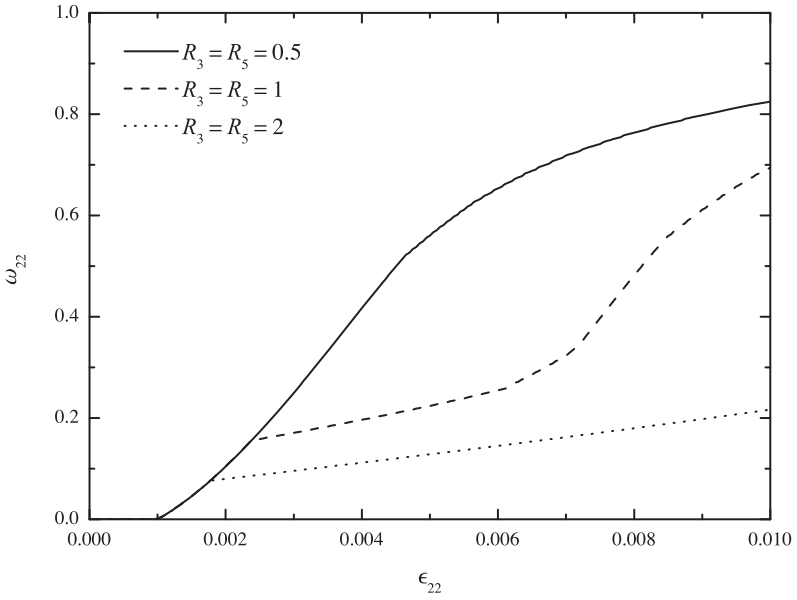

Figure 10. ω_{11}-ϵ_{11} **curves of the material exhibiting plastic anisotropy subject to uniaxial tension in the** x_2**-direction.**

damage tensors are modified to be of more concise forms and clearer physical meanings. The constitutive relations in the undamaged configuration, the damage evolution law, and the constitutive relations in the damaged configuration are subsequently derived. The applicability and power of the proposed constitutive relations are validated using examples such as predicting the stress-strain and damage factor-strain curves of damaged elastoplastic materials of various material properties. More sophisticated material properties can be incorporated.

Acknowledgements

This work is supported by the US AFOSR Multiscale Structural Mechanics and Prognosis Program. The views and conclusions contained herein are those of the authors and should not be interpreted as necessarily representing the official policies or endorsement, either expressed or implied, of the sponsor.

Appendix

A. Plastic Anisotropic Parameters

The R-value is widely used to characterize the plastic anisotropy of rolled sheet metals. It can be measured from a series of uniaxial tensile tests. Specifically, when a tensile specimen cut from a sheet is stretched, its R-value is defined as the ratio of the plastic strain in the width direction to that in the thickness direction, that is,

$$R = \frac{\epsilon_W}{\epsilon_T}. \tag{95}$$

In general, the R-value varies with the cut angle relative to the rolling direction of the sheet, α. In this case, an averaged R-value is often adopted. It is defined as

$$\bar{R} = \frac{R_0 + 2R_{45} + R_{90}}{4}, \tag{96}$$

where R_α denotes the R-value obtained using a tensile specimen of cut angle α.

Benzerga and Besson[25] extended the concept of the R-value by introducing six strain rate ratios, R_{ij}. These six R_{ij}'s are capable of fully characterizing the plastic anisotropy of a 3D structure, and each of them can be measured from a uniaxial tensile or simple shear test. Specifically, introduce a Cartesian coordinate system $\mathbf{x} = (x_1, x_2, x_3)$ with its three axes parallel to the orthotropic axes of the material, and the six R_{ij}'s can be defined as the following strain rate ratios:

$$R_{11} = \frac{\dot{\epsilon}_{22}}{\dot{\epsilon}_{33}}, \quad R_{12} = \frac{\dot{\epsilon}_{12}}{\dot{\epsilon}_{33}}, \quad R_{22} = \frac{\dot{\epsilon}_{33}}{\dot{\epsilon}_{11}}, \tag{97}$$

$$R_{13} = \frac{\dot{\epsilon}_{13}}{\dot{\epsilon}_{22}}, \quad R_{23} = \frac{\dot{\epsilon}_{23}}{\dot{\epsilon}_{11}}, \quad R_{33} = \frac{\dot{\epsilon}_{11}}{\dot{\epsilon}_{22}}. \tag{97'}$$

Let R_{ij} be written in the the Voigt notation as

$$R_1 = R_{11}, \quad R_2 = R_{12}, \quad R_3 = R_{22}, \tag{98}$$

$$R_4 = R_{13}, \quad R_5 = R_{23}, \quad R_6 = R_{33}. \tag{98'}$$

It can be obtained from Eq. (97) that $R_6 = 1/R_1R_3$. This implies that only five out of the six R_i's are independent of each other. Without loss of generality, let R_6 be expressed in terms of R_1 and R_3 in following derivations.

$\mathcal{H}_{ijkl}$ can be written in the Voigt notation as H_{ij}. According to Ref. [25], the diagonal components of H_{ij} can be related to R_i by

$$H_{11} = -\frac{2}{3}\frac{R_1R_3 - 2R_1 - 2}{R_1 + 1}, \quad \frac{H_{22}}{H_{11}} = -\frac{1}{2}\frac{(2R_2 + 1)(R_1R_3 + 1)}{R_1R_3 - 2R_1 - 2}, \tag{99}$$

$$\frac{H_{33}}{H_{11}} = 1 - \frac{3(R_1R_3 - 1)}{R_1R_3 - 2R_1 - 2}, \quad \frac{H_{44}}{H_{11}} = -\frac{1}{2}\frac{(2R_4 + 1)(R_3 + 1)R_1}{R_1R_3 - 2R_1 - 2}, \tag{99'}$$

$$\frac{H_{55}}{H_{11}} = -\frac{1}{2}\frac{(2R_5 + 1)(R_1 + 1)}{R_1R_3 - 2R_1 - 2}, \quad \frac{H_{66}}{H_{11}} = 1 - \frac{3R_1(R_3 - 1)}{R_1R_3 - 2R_1 - 2}, \tag{99''}$$

while the off-diagonal components vanish. More details on $\boldsymbol{\mathcal{H}}$ can be found in Ref. [25], Appendix A.

A special case of plastic anisotropy is plastic transverse isotropy, in which case there exists a plane of plastic isotropy. Without loss of generality, let the x_2-x_3 plane be the plane of plastic isotropy. R_i can then be expressed as

$$R_3 = R_5 = \frac{1}{R_6} = R \quad \text{and} \quad R_2 = R_4 = R', \tag{100}$$

where R and R' can be measured from a uniaxial tensile test and a simple shear test, respectively. Substituting Eq. (100) into Eq. (99) and rearranging the equations give

$$H_{11} = \frac{1}{3}(4 - R), \quad H_{22} = H_{44} = \frac{1}{6}(R + 1)(2R' + 1), \tag{101}$$

$$H_{33} = H_{55} = H_{66} = \frac{1}{3}(2R + 1). \tag{101'}$$

References

[1]Krajcinovic, D., "Continuous damage mechanics," *Applied Mechanics Reviews*, Vol. 37, No. 1, 1984, pp. 1–6.

[2]Lubliner, J., Oliver, J., Oller, S., and Oñate, E., "A plastic-damage model for concrete," *International Journal of Solids and Structures*, Vol. 25, No. 3, 1989, pp. 299–326.

[3]Faria, R., Oliver, J., and Cervera, M., "A strain-based plastic viscous-damage model for massive concrete structures," *International Journal of Solids and Structures*, Vol. 35, No. 14, 1998, pp. 1533–1558.

[4]Lee, J. and Fenves, G. L., "Plastic-damage model for cyclic loading of concrete structures," *Journal of Engineering Mechanics*, Vol. 124, No. 8, 1998, pp. 892–900.

[5]Peerlings, R., De Borst, R., Brekelmans, W., and Geers, M., "Gradient-enhanced damage modelling of concrete fracture," *Mechanics of Cohesive-frictional Materials*, Vol. 3, No. 4, 1998, pp. 323–342.

[6]Jason, L., Huerta, A., Pijaudier-Cabot, G., and Ghavamian, S., "An elastic plastic damage formulation for concrete: application to elementary tests and comparison with an isotropic damage model," *Computer Methods in Applied Mechanics and Engineering*, Vol. 195, No. 52, 2006, pp. 7077–7092.

[7]Wu, J. Y., Li, J., and Faria, R., "An energy release rate-based plastic-damage model for concrete," *International Journal of Solids and Structures*, Vol. 43, No. 3, 2006, pp. 583–612.

[8]Krajcinovic, D. and Fonseka, G., "The continuous damage theory of brittle materials. Part I: General theory." *Journal of Applied Mechanics*, Vol. 48, No. 4, 1981, pp. 809.

[9]Murakami, S. and Ohno, N., "A continuum theory of creep and creep damage," *Creep in Structures*, Springer, 1981, pp. 422–444.

[10]Chaboche, J.-L., "Continuous damage mechanicsa tool to describe phenomena before crack initiation," *Nuclear Engineering and Design*, Vol. 64, No. 2, 1981, pp. 233–247.

[11]Ortiz, M., "A constitutive theory for the inelastic behavior of concrete," *Mechanics of Materials*, Vol. 4, No. 1, 1985, pp. 67–93.

[12]Simo, J. and Ju, J., "Strain- and stress-based continuum damage modelsII. Computational aspects," *International Journal of Solids and Structures*, Vol. 23, No. 7, 1987, pp. 841–869.

[13]Ju, J., "Isotropic and anisotropic damage variables in continuum damage mechanics," *Journal of Engineering Mechanics*, Vol. 116, No. 12, 1990, pp. 2764–2770.

[14]Yazdani, S. and Schreyer, H., "Combined plasticity and damage mechanics model for plain concrete," *Journal of Engineering Mechanics*, Vol. 116, No. 7, 1990, pp. 1435–1450.

[15]Chaboche, J.-L., "Development of continuum damage mechanics for elastic solids sustaining anisotropic and unilateral damage," *International Journal of Damage Mechanics*, Vol. 2, No. 4, 1993, pp. 311–329.

[16]Lubarda, V. and Krajcinovic, D., "Damage tensors and the crack density distribution," *International Journal of Solids and Structures*, Vol. 30, No. 20, 1993, pp. 2859–2877.

[17]Govindjee, S., Kay, G. J., and Simo, J. C., "Anisotropic modelling and numerical simulation of brittle damage in concrete," *International Journal for Numerical Methods in Engineering*, Vol. 38, No. 21, 1995, pp. 3611–3633.

[18]Halm, D. and Dragon, A., "A model of anisotropic damage by mesocrack growth; unilateral effect," *International Journal of Damage Mechanics*, Vol. 5, No. 4, 1996, pp. 384–402.

[19]Gatuingt, F. and Pijaudier-Cabot, G., "Coupled damage and plasticity modelling in transient dynamic analysis of concrete," *International Journal for Numerical and Analytical Methods in Geomechanics*, Vol. 26, No. 1, 2002, pp. 1–24.

[20]Abu Al-Rub, R. K. and Voyiadjis, G. Z., "On the coupling of anisotropic damage and plasticity models for ductile materials," *International Journal of Solids and Structures*, Vol. 40, No. 11, 2003, pp. 2611–2643.

[21]Menzel, A., Ekh, M., Runesson, K., and Steinmann, P., "A framework for multiplicative elastoplasticity with kinematic hardening coupled to anisotropic damage," *International Journal of Plasticity*, Vol. 21, No. 3, 2005, pp. 397–434.

[22]Cicekli, U., Voyiadjis, G. Z., and Abu Al-Rub, R. K., "A plasticity and anisotropic damage model for plain concrete," *International Journal of Plasticity*, Vol. 23, No. 10, 2007, pp. 1874–1900.

[23]Voyiadjis, G. Z., Taqieddin, Z. N., and Kattan, P. I., "Anisotropic damage-plasticity model for concrete," *International Journal of Plasticity*, Vol. 24, No. 10, 2008, pp. 1946–1965.

[24]Simo, J. C. and Hughes, T. J. R., *Computational Inelasticity*, Vol. 7 of *Interdisciplinary Applied Mathematics*, Springer, New York, 1998.

[25]Benzerga, A. A. and Besson, J., "Plastic potentials for anisotropic porous solids," *European Journal of Mechanics, A/Solids*, Vol. 20, No. 3, 2001, pp. 397–434.

[26]Chaboche, J.-L., "Thermodynamic formulation of constitutive equations and application to the viscoplasticity and viscoelasticity of metals and polymers," *International Journal of Solids and Structures*, Vol. 34, No. 18, 1997, pp. 2239–2254.

[27]Chaboche, J.-L., "Constitutive equations for cyclic plasticity and cyclic viscoplasticity," *International Journal of Plasticity*, Vol. 5, No. 3, 1989, pp. 247–302.

[28]Voce, E., "A practical strain-hardening function," *Metallurgia*, Vol. 51, No. 307, 1955, pp. 219–226.

[29]Besson, J., Cailletaud, G., Chaboche, J.-L., and Forest, S., *Non-linear mechanics of materials*, Vol. 167 of *Solid mechanics and its applications*, Springer, New York, 2010.

[30]Chow, C. and Wang, J., "An anisotropic theory of elasticity for continuum damage mechanics," *International Journal of Fracture*, Vol. 33, No. 1, 1987, pp. 3–16.

AIAA SciTech
5-9 January 2015, Kissimmee, Florida
56th AIAA/ASCE/AHS/ASC Structures, Structural Dynamics, and Materials Conference

On the Closed-Form Constitutive Relations for Damageable Elasto-Viscoplastic Materials

Liang Zhang* and Wenbin Yu†
Purdue University, West Lafayette, IN 47907-2045, USA

The objective of this paper is to derive the closed-form constitutive relations for damageable elasto-viscoplastic materials exhibiting damage anisotropy, damage hardening, viscoplastic anisotropy, and combined isotropic-kinematic hardening. Some fundamentals of continuum damage mechanics and thermodynamics are briefed, and the second-order damage tensor is redefined with an emphasis on a clear physical meaning. An affine formulation of the constitutive relations in the undamaged configuration, the damage evolution law, and the constitutive relations in the damaged configuration are subsequently derived. The use of the current constitutive relations is demonstrated by modeling an aluminium alloy exhibiting various material behaviors. The current constitutive relations are found to be capable of handling complex material models. More sophisticated material behaviors can be incorporated.

I. Introduction

Microscopic defects, such as microcracks, microvoids, and dislocations, are inevitable in real materials. When a material is deformed to a certain extent at a high temperature, its deformation often becomes nonlinear, history dependent, and rate dependent due to the propagation, nucleation, growth, coalescence, or motion of its microscopic defects. Such activities of microscopic defects often cause irreversible changes in the microstructure of a material, most of which are harmful and should be avoided or monitored. One major challenge is to predict the responses of damageable elasto-viscoplastic materials based on the microstructural details: on the one hand, it is often difficult or expensive to measure their responses; on the other hand, the scales of the macroscopic materials are usually several orders of magnitude greater than those of microscopic defects, making it computationally prohibitive to capture all the microstructural details. All these lead one to derive the closed-form constitutive relations for such materials.

Microscopic defects can be classified into three categories, i.e., line defects (dislocations), planar defects (macrocracks and grain doundries), and volume defects (microvoids). Continuum damage mechanics deals with the macroscopic effect of microcrack propagation and microvoid growth. It combines the internal state variable theory and the theory of irreversible thermodynamics and enables one to derive the constitutive relations for damaged materials. Elaborate efforts have been devoted to enabling it to handle complex material behaviors, complex loading conditions, and complex loading histories. Some authors[1–7] extensively enriched its framework based on isotropic damage, while some others[8–23] extended its framework by incorporating anisotropic damage. The theory of viscoplasticity deals with the macroscopic effect of dislocation motion at high temperatures. Masson and his coworkers[24,25] linearized the constitutive relations for viscoplastic materials in the Laplace domain and obtained an affine formulation similar to the constitutive relations for thermoelastic materials, while Doghri et al.[26] later derived an affine formulation in the time domain and avoided the computationally costly inverse Laplace transformation required by Refs. [24,25]. Unfortunately, neither continuum damage mechanics nor the theory of viscoplasticity can perfectly deal with damageable elasto-viscoplastic materials alone. This leads numerous researchers to seek for a suitable combination of these two theories.

Elaborated efforts have been devoted to deriving the constitutive relations for damageable elastoplastic materials. Most authors derived their constitutive relations in two different ways: some of them[4,6,7,12–14,17,22,23]

*Postdoctoral Researcher, School of Aeronautics and Astronautics.
†Associate Professor, School of Aeronautics and Astronautics, AIAA Associate Fellow.

formulated their plasticity models in terms of the so-called effective stresses, i.e., the average microscopic stresses acting on the undamaged microbonds of the material, while the others[2,11,20] formulated their models in terms of the so-called nominal stresses, i.e., the macroscopic stresses acting on the macroscopic material. It is more challenging to derive the theory for damageable elasto-viscoplastic materials because the deformations become rate-dependent. Although several authors[27–30] provided valuable insights into the problem, there is still a need for the closed-form constitutive relations capable of handling damage anisotropy, damage hardening, viscoplastic anisotropy, and combined isotropic-kinematic hardening.

The objective of this paper is to derive the closed-form constitutive relations for damageable elasto-viscoplastic materials exhibiting damage anisotropy, damage hardening, viscoplastic anisotropy, and combined isotropic-kinematic hardening. Some fundamentals of continuum damage mechanics and thermodynamics are briefed, and the second-order damage tensor is redefined with an emphasis on a clear physical meaning. An affine formulation of the constitutive relations in the undamaged configuration, the damage evolution law, and the constitutive relations in the damaged configuration are subsequently derived. The use of the current constitutive relations is demonstrated by by modeling an aluminium alloy exhibiting various material behaviors.

II. Basic Concepts of Continuum Damage Mechanics

In this section, some fundamentals of continuum damage mechanics will be briefed, while the second-order damage tensor will be redefined with an emphasis on a clear physical meaning.

The derivation of the constitutive relations for a damaged material generally starts with two assumptions:

1. Each damaged material can be idealized as an equivalent undamaged material;
2. There exists a one-to-one correspondence between each pair of physical quantities in the damaged and undamaged configurations.

With these two assumptions, one can subsequently derive an affine formulation of the constitutive relations in the undamaged configurations, the damage evolution law, and the constitutive relations in the damaged configuration.

Let an overbar denote the quantity in the effective material. The stress tensor in the undamaged configuration, $\bar{\boldsymbol{\sigma}}$, can be related to that in the damaged configuration, $\boldsymbol{\sigma}$, by

$$\bar{\boldsymbol{\sigma}} = \boldsymbol{\mathcal{M}} : \boldsymbol{\sigma} \quad \text{or} \quad \boldsymbol{\sigma} = \boldsymbol{\mathcal{M}}^{-1} : \bar{\boldsymbol{\sigma}}, \tag{1}$$

where $\boldsymbol{\mathcal{M}}$ denotes the fourth-order damage effect tensor, and $\bar{\boldsymbol{\sigma}}$ is often referred to as the effective stress tensor. Without loss of generality, let $\boldsymbol{\omega}$ and $\boldsymbol{\mathcal{D}}$ denote the second- and fourth-order damage tensors, respectively. Also let $\boldsymbol{\omega}$ be symmetric, and let $\boldsymbol{\mathcal{D}}$ be related to $\boldsymbol{\omega}$ by

$$\boldsymbol{\mathcal{D}} = \sum_{i=1}^{3}\sum_{j=1}^{3} \omega_{ij} \mathbf{e}_i \otimes \mathbf{e}_j \otimes \mathbf{e}_i \otimes \mathbf{e}_j, \tag{2}$$

where $\mathbf{e}_i$ denotes the unit vector. It can be verified that:

1. $\boldsymbol{\mathcal{D}}$ fulfills the major and minor symmetries (i.e., $\mathcal{D}_{ijkl} = \mathcal{D}_{klij}$, $\mathcal{D}_{ijkl} = \mathcal{D}_{jikl}$, and $\mathcal{D}_{ijkl} = \mathcal{D}_{ijlk}$);
2. $\mathcal{D}_{ijkl}$ can be written in the Voigt notation as D_{ij} with its diagonal components being ω_i (ω_{ij} in the Voigt notation) and its off-diagonal components vanishing.

Let $\boldsymbol{\mathcal{M}}^{-1}$ take the form of

$$\boldsymbol{\mathcal{M}}^{-1} = \boldsymbol{\mathcal{I}} - \boldsymbol{\mathcal{D}} \tag{3}$$

where $\boldsymbol{\mathcal{I}}$ denotes the fourth-order identity tensor. It can be verified that $\boldsymbol{\mathcal{M}}^{-1}$ also fulfills the major and minor symmetries.

Let ρ, ψ^e, and $\boldsymbol{\epsilon}^e$ denote the density of the material, the elastic strain energy per unit mass of the material, and the elastic strain tensor, respectively. For the effective material to be equivalent to the damaged material, the elastic strain energy of the damaged material should equal that of the equivalent undamaged material, i.e.,[31]

$$\rho\psi^e\left(\boldsymbol{\epsilon}^e, \boldsymbol{\omega}\right) = \rho\psi^e\left(\bar{\boldsymbol{\epsilon}}^e\right) \quad \text{or} \quad \frac{1}{2}\boldsymbol{\sigma} : \boldsymbol{\epsilon}^e = \frac{1}{2}\bar{\boldsymbol{\sigma}} : \bar{\boldsymbol{\epsilon}}^e. \tag{4}$$

Substituting Eq. (1) into Eq. (4) gives

$$\bar{\boldsymbol{\epsilon}}^e = \boldsymbol{\mathcal{M}}^{-1} : \boldsymbol{\epsilon}^e \quad \text{or} \quad \boldsymbol{\epsilon}^e = \boldsymbol{\mathcal{M}} : \bar{\boldsymbol{\epsilon}}^e. \tag{5}$$

Hooke's law can be expressed in the damaged and undamaged configurations as

$$\boldsymbol{\sigma} = \boldsymbol{\mathcal{C}}^e : \boldsymbol{\epsilon}^e \quad \text{and} \quad \bar{\boldsymbol{\sigma}} = \bar{\boldsymbol{\mathcal{C}}}^e : \bar{\boldsymbol{\epsilon}}^e, \tag{6}$$

respectively, where $\boldsymbol{\mathcal{C}}^e$ denotes the fourth-order elastic stiffness tensor, and $\bar{\boldsymbol{\mathcal{C}}}^e$ denotes the fourth-order undamaged elastic stiffness tensor. Combining Eqs. (1), (4), (5), and (6) gives

$$\boldsymbol{\mathcal{C}}^e = \boldsymbol{\mathcal{M}}^{-1} : \bar{\boldsymbol{\mathcal{C}}}^e : \boldsymbol{\mathcal{M}}^{-1} \quad \text{or} \quad (\boldsymbol{\mathcal{C}}^e)^{-1} = \boldsymbol{\mathcal{M}} : \left(\bar{\boldsymbol{\mathcal{C}}}^e\right)^{-1} : \boldsymbol{\mathcal{M}}. \tag{7}$$

Recall that $\boldsymbol{\mathcal{M}}^{-1}$ fulfills the major and minor symmetries. This, together with Eqs. (1), (5), and (7), implies that

1. If $\boldsymbol{\sigma}$ and $\boldsymbol{\epsilon}^e$ are symmetric, so do $\bar{\boldsymbol{\sigma}}$ and $\bar{\boldsymbol{\epsilon}}^e$;
2. If $\bar{\boldsymbol{\mathcal{C}}}^e$ fulfills the major and minor symmetries, so does $\boldsymbol{\mathcal{C}}^e$;
3. ω_{ij} provides a measure of the damage associated with σ_{ij} or ϵ^e_{ij}.

Till now, some fundamentals of continuum damage mechanics have been briefed, while the second-order damage tensor has been redefined with an emphasis on a clear physical meaning. In the next section, some fundamentals of thermodynamics will be briefed.

III. Thermodynamics

Let ψ denote the Helmholtz free energy per unit mass of the constituent. According to the theory of thermodynamics, ψ can be expressed as a function of a suitable set of independent state variables characterizing the elastic, viscoplastic, and damage behaviors of the material, e.g.,

$$\psi = \psi\left(\boldsymbol{\epsilon}^e, \boldsymbol{\omega}, \boldsymbol{\alpha}, r, s\right), \tag{8}$$

where $\boldsymbol{\alpha}$ is a second-order tensor accounting for kinematic hardening, and r and s are two scalars accounting for isotropic and damage hardening, respectively. Assume that the material exhibits uncoupled elastic, viscoplastic, and damage behaviors. In this case, ψ can be decomposed into its elastic, viscoplastic hardening, and damage hardening parts, i.e.,

$$\psi\left(\boldsymbol{\epsilon}^e, \boldsymbol{\omega}, \boldsymbol{\alpha}, r, s\right) = \psi^e\left(\boldsymbol{\epsilon}^e, \boldsymbol{\omega}\right) + \psi^{vp}\left(\boldsymbol{\alpha}, r\right) + \psi^d\left(s\right). \tag{9}$$

The thermodynamic forces conjugate to the state variables in Eq. (8) can be defined as

$$\boldsymbol{\sigma} = \rho\frac{\partial\psi}{\partial\boldsymbol{\epsilon}^e} = \rho\frac{\partial\psi^e}{\partial\boldsymbol{\epsilon}^e}, \quad \mathbf{Y} = -\rho\frac{\partial\psi}{\partial\boldsymbol{\omega}} = -\rho\frac{\partial\psi^e}{\partial\boldsymbol{\omega}}, \tag{10}$$

$$\mathbf{X} = \rho\frac{\partial\psi}{\partial\boldsymbol{\alpha}} = \rho\frac{\partial\psi^{vp}}{\partial\boldsymbol{\alpha}}, \quad R = \rho\frac{\partial\psi}{\partial r} = \rho\frac{\partial\psi^{vp}}{\partial r}, \quad S = \rho\frac{\partial\psi}{\partial s} = \rho\frac{d\psi^d}{ds}, \tag{10$'$}$$

where $\mathbf{Y}$ denotes the damage conjugate force tensor, $\mathbf{X}$ denotes the back stress tensor, and R and S are related to the current yield stress and damage threshold, respectively.

If the deformation is isothermal, the Clausius-Duhem inequality writes

$$\phi = \boldsymbol{\sigma} : \dot{\boldsymbol{\epsilon}} - \rho\dot{\psi} \geq 0, \tag{11}$$

where ϕ denotes the dissipation per unit volume, and the overdot denotes the time derivative of the quantity. Note that the strain tensor, $\boldsymbol{\epsilon}$, can be decomposed into its elastic and viscoplastic parts, i.e.,

$$\boldsymbol{\epsilon} = \boldsymbol{\epsilon}^e + \boldsymbol{\epsilon}^{vp}. \tag{12}$$

Combining Eqs. (9)–(12) gives

$$\phi = \boldsymbol{\sigma} : \dot{\boldsymbol{\epsilon}}^{vp} + \mathbf{Y} : \dot{\boldsymbol{\omega}} - \mathbf{X} : \dot{\boldsymbol{\alpha}} - R\dot{r} - S\dot{s} \geq 0, \tag{13}$$

Similarly to ψ, ϕ can be decomposed into its viscoplastic hardening and damage hardening parts, ϕ^{vp} and ϕ^d, i.e.,

$$\phi = \phi^{vp} + \phi^d, \tag{14}$$

where

$$\phi^{vp} = \boldsymbol{\sigma} : \dot{\boldsymbol{\epsilon}}^{vp} - \mathbf{X} : \dot{\boldsymbol{\alpha}} - R\dot{r} \geq 0 \quad \text{and} \quad \phi^d = \mathbf{Y} : \dot{\boldsymbol{\omega}} - S\dot{s} \geq 0. \tag{15}$$

Assume that there exists a viscoplastic potential, Φ^{vp}, which is a function of the corresponding thermodynamic forces and governs the evolution of the corresponding state variables, i.e.,

$$\dot{\boldsymbol{\epsilon}}^{vp} = \frac{\partial \Phi^{vp}}{\partial \boldsymbol{\sigma}}, \quad \dot{\boldsymbol{\alpha}} = -\frac{\partial \Phi^{vp}}{\partial \mathbf{X}}, \quad \dot{r} = -\frac{\partial \Phi^{vp}}{\partial R}. \tag{16}$$

Without loss of generality, let

$$f^{vp} = f^{vp}\left(\boldsymbol{\sigma}, \mathbf{X}, R\right) \tag{17}$$

denote the yield function, and let

$$\Phi^{vp} = \Phi^{vp}\left(f^{vp}\right) \quad \text{and} \quad \dot{\lambda}^{vp} = \frac{\partial \Phi^{vp}}{\partial f^{vp}}. \tag{18}$$

Eq. (16) can then be rewritten using the chain rule as

$$\dot{\boldsymbol{\epsilon}}^{vp} = \dot{\lambda}^{vp}\frac{\partial f^{vp}}{\partial \boldsymbol{\sigma}}, \quad \dot{\boldsymbol{\alpha}} = -\dot{\lambda}^{vp}\frac{\partial f^{vp}}{\partial \mathbf{X}}, \quad \dot{r} = -\dot{\lambda}^{vp}\frac{\partial f^{vp}}{\partial R}. \tag{19}$$

Also let the damage criterion take the form of

$$f^d\left(\mathbf{Y}, S\right) = 0. \tag{20}$$

The maximum dissipation principle states that the actual thermodynamic forces should maximize ϕ^d subject to constraint Eq. (20);[32] or to say, that the actual thermodynamic forces should maximize Lagrange function

$$\Lambda^d = \phi^d - \dot{\lambda}^d f^d, \tag{21}$$

where $\dot{\lambda}^d$ is a Lagrange multiplier. Λ^d reaches its maximum only if

$$\frac{\partial \Lambda^d}{\partial \mathbf{Y}} = 0 \quad \text{and} \quad \frac{\partial \Lambda^d}{\partial S} = 0. \tag{22}$$

This gives

$$\dot{\boldsymbol{\omega}} = \dot{\lambda}^d\frac{\partial f^d}{\partial \mathbf{Y}} \quad \text{and} \quad \dot{s} = -\dot{\lambda}^d\frac{\partial f^d}{\partial S}. \tag{23}$$

Till now, some fundamentals of thermodynamics have been briefed. In the next section, the viscoplasticity model will be specified.

IV. Viscoplasticity Model

The so-called effective stress space (visco)plasticity states that the (visco)plastic deformation can only occur within the undamaged microbonds of the material;[33] This allows one to derive the constitutive relations in the undamaged configuration.

For notational convenience, let $\tilde{\bar{\boldsymbol{\sigma}}} = \bar{\boldsymbol{\sigma}} - \bar{\mathbf{X}}$. Without loss of generality, let the undamaged material obey Hill's yield function, i.e.,

$$f^{vp}\left(\bar{\boldsymbol{\sigma}}, \bar{\mathbf{X}}, \bar{R}\right) = \tilde{\bar{\sigma}}_e - \bar{\sigma}_Y, \tag{24}$$

where

$$\tilde{\bar{\sigma}}_e = \sqrt{\frac{3}{2}\tilde{\bar{\boldsymbol{\sigma}}}' : \bar{\boldsymbol{\mathcal{H}}} : \tilde{\bar{\boldsymbol{\sigma}}}'}, \tag{25}$$

denotes the Hill equivalent stress with $(\cdot)'$ denoting the deviatoric part of the tensor and $\bar{\boldsymbol{\mathcal{H}}}$ denoting the fourth-order anisotropy tensor, and

$$\bar{\sigma}_Y = \bar{\sigma}_0 + \bar{R} \tag{26}$$

denotes the current yield stress with $\bar{\sigma}_0$ denoting the initial yield stress. Substituting Eq. (25) into the modified viscoplastic work equivalence principle,

$$\tilde{\bar{\boldsymbol{\sigma}}} : \dot{\bar{\boldsymbol{\epsilon}}}^{vp} = \tilde{\bar{\sigma}}_e \dot{\bar{p}}, \tag{27}$$

gives the Hill equivalent viscoplastic strain rate as[34]

$$\dot{\bar{p}} = \sqrt{\frac{2}{3}\dot{\bar{\boldsymbol{\epsilon}}}^{vp} : \bar{\boldsymbol{\mathcal{H}}}^{-1} : \dot{\bar{\boldsymbol{\epsilon}}}^{vp}}. \tag{28}$$

Note that $\bar{\boldsymbol{\mathcal{H}}}$ can be obtained from the so-called R-values (see Appendix A for more details).

It is beneficial to find the relation between $\dot{\bar{\lambda}}^{vp}$ and $\dot{\bar{p}}$. Similarly to Eq. (19), one can obtain that

$$\dot{\bar{\boldsymbol{\epsilon}}}^{vp} = \dot{\bar{\lambda}}^{vp} \frac{\partial f^{vp}}{\partial \bar{\boldsymbol{\sigma}}}, \quad \dot{\bar{\boldsymbol{\alpha}}} = -\dot{\bar{\lambda}}^{vp} \frac{\partial f^{vp}}{\partial \bar{\mathbf{X}}}, \quad \dot{\bar{r}} = -\dot{\bar{\lambda}}^{vp} \frac{\partial f^{vp}}{\partial \bar{R}}. \tag{29}$$

Substituting the first equation of Eq. (29) into Eq. (27) gives

$$\tilde{\bar{\boldsymbol{\sigma}}} : \left(\dot{\bar{\lambda}}^{vp} \frac{\partial f^{vp}}{\partial \bar{\boldsymbol{\sigma}}} \right) = \tilde{\bar{\sigma}}_e \dot{\bar{p}}. \tag{30}$$

The explicit expression for $\partial f^{vp}/\partial \bar{\boldsymbol{\sigma}}$ can be derived as[34]

$$\frac{\partial f^{vp}}{\partial \bar{\boldsymbol{\sigma}}} = \frac{\partial \tilde{\bar{\sigma}}_e}{\partial \tilde{\bar{\boldsymbol{\sigma}}}} = \frac{1}{2\tilde{\bar{\sigma}}_e} \frac{\partial \tilde{\bar{\sigma}}_e^2}{\partial \tilde{\bar{\boldsymbol{\sigma}}}} = \frac{1}{2\tilde{\bar{\sigma}}_e} \left(\frac{3}{2} 2 \frac{\partial \tilde{\bar{\boldsymbol{\sigma}}}'}{\partial \tilde{\bar{\boldsymbol{\sigma}}}} : \bar{\boldsymbol{\mathcal{H}}} : \tilde{\bar{\boldsymbol{\sigma}}}' \right) = \frac{3}{2\tilde{\bar{\sigma}}_e} \boldsymbol{\mathcal{J}} : \bar{\boldsymbol{\mathcal{H}}} : \tilde{\bar{\boldsymbol{\sigma}}}', \tag{31}$$

where $\boldsymbol{\mathcal{J}} = \boldsymbol{\mathcal{I}} - \frac{1}{3}\mathbf{I} \otimes \mathbf{I}$ with $\mathbf{I}$ denotes the fourth-order deviatoric projection operator with $\mathbf{I}$ denoting the second-order identity tensor. Substituting Eq. (31) into Eq. (30) gives

$$\tilde{\bar{\sigma}}_e \dot{\bar{\lambda}}^{vp} = \tilde{\bar{\sigma}}_e \dot{\bar{p}} \quad \text{or} \quad \dot{\bar{\lambda}}^{vp} = \dot{\bar{p}}, \tag{32}$$

which implies that the viscoplastic deformation is irreversible.

Eq. (29), together with Eq. (24), implies that nonlinear kinematic hardening is inadmissible. This indicates that Eq. (29) places too strict restrictions.[35] To overcome this drawback, introduce a pseudo-potential g^{vp}, which is related to f^{vp} by

$$g^{vp} = f^{vp} + \frac{3}{4}\frac{\bar{\gamma}}{\bar{C}} \bar{\mathbf{X}} : \bar{\mathbf{X}} + \frac{\bar{R}^2}{2\bar{K}} \tag{33}$$

with $\bar{C}$ and $\bar{\gamma}$ being two constants accounting for kinematic hardening and $\bar{K}$ being a constant accounting for isotropic hardening, and rewrite Eq. (29) as

$$\dot{\bar{\boldsymbol{\epsilon}}}^{vp} = \dot{\bar{\lambda}}^{vp} \frac{\partial g^{vp}}{\partial \bar{\boldsymbol{\sigma}}}, \quad \dot{\bar{\boldsymbol{\alpha}}} = -\dot{\bar{\lambda}}^{vp} \frac{\partial g^{vp}}{\partial \bar{\mathbf{X}}} = \dot{\bar{\boldsymbol{\epsilon}}}^{vp} - \frac{3}{2}\frac{\bar{\gamma}}{\bar{C}} \bar{\mathbf{X}} \dot{\bar{\lambda}}^{vp}, \quad \dot{\bar{r}} = -\dot{\bar{\lambda}}^{vp} \frac{\partial g^{vp}}{\partial \bar{R}} = \left(1 - \frac{\bar{R}}{\bar{K}}\right) \dot{\bar{\lambda}}^{vp}. \tag{34}$$

Note that Eq. (32) remains valid because $\partial g^{vp}/\partial \bar{\boldsymbol{\sigma}} = \partial f^{vp}/\partial \bar{\boldsymbol{\sigma}}$. Let $\rho\psi^{vp}$ take the form of

$$\rho\psi^{vp} = \frac{1}{3}\bar{C}\bar{\boldsymbol{\alpha}} : \bar{\boldsymbol{\alpha}} + \frac{1}{2}\bar{K}\bar{n}\bar{r}^2, \tag{35}$$

where $\bar{n}$ is another constant accounting for isotropic hardening. Accordingly,

$$\bar{\mathbf{X}} = \frac{2}{3}\bar{C}\bar{\boldsymbol{\alpha}} \quad \text{and} \quad \bar{R} = \bar{K}\bar{n}\bar{r}. \tag{36}$$

Substituting the last two equations of Eq. (34) into the rate form of Eq. (36) and noting that $\dot{\bar{\lambda}}^{vp} = \dot{\bar{p}}$ give

$$\dot{\bar{\mathbf{X}}} = \frac{2}{3}\bar{C}\dot{\bar{\boldsymbol{\epsilon}}}^{vp} - \bar{\gamma}\bar{\mathbf{X}}\dot{\bar{p}} \quad \text{and} \quad \dot{\bar{R}} = \left(\bar{K} - \bar{R}\right)\bar{n}\dot{\bar{p}}, \tag{37}$$

which are the Chaboche hardening law[36] and the rate form of the Voce hardening law,[37] respectively. The second equation of Eq. (37) can be further integrated into the Voce hardening law as

$$\bar{R} = \bar{K}\left[1 - \exp\left(-\bar{n}\bar{p}\right)\right]. \tag{38}$$

More details on the derivation in this paragraph can be found in Ref. [38].

The Perzyna model[39] suggests that

$$\Phi^{vp} = \begin{cases} \dfrac{1}{\bar{\eta}} \dfrac{\bar{\sigma}_Y}{\bar{N}+1} \left(\dfrac{f^{vp}}{\bar{\sigma}_Y} \right)^{\bar{N}+1} & f^{vp} > 0, \\ 0 & f^{vp} \leq 0 \end{cases} \tag{39}$$

or

$$\dot{\bar{\lambda}}^{vp} = \begin{cases} \dfrac{1}{\bar{\eta}} \left(\dfrac{f^{vp}}{\bar{\sigma}_Y} \right)^{\bar{N}} & f^{vp} > 0, \\ 0 & f^{vp} \leq 0, \end{cases} \tag{40}$$

where $\bar{\eta}$ denotes a fluidity parameter, and $\bar{N}$ denotes a rate-sensitivity parameter. Substituting Eq. (40) into Eq. (34) fully specifies the viscoplasticity model.

Till now, the viscoplasticity model has be specified. In the next section, an affine formulation of the constitutive relations in the undamaged configuration will be derived.

V. Affine Formulation of the Constitutive Relations in the Undamaged Configuration

Suppose that all the variables at time t_n are known. The task is to find the variables at time $t_{n+1} = t_n + \Delta t$, where $\Delta(\cdot)$ denotes the increment in a quantity over this time interval. This leads one to derive the correspondence principle between $\Delta\bar{\boldsymbol{\sigma}}$ and $\Delta\bar{\boldsymbol{\epsilon}}$.

Recall that

$$\bar{\boldsymbol{\sigma}} = \bar{\boldsymbol{\mathcal{C}}}^e : \bar{\boldsymbol{\epsilon}}^e. \tag{41}$$

Substituting the incremental form of Eq. (41) into the incremental form of Eq. (12) gives

$$\Delta\bar{\boldsymbol{\epsilon}} = \Delta\bar{\boldsymbol{\epsilon}}^e + \Delta\bar{\boldsymbol{\epsilon}}^{vp} = \left(\bar{\boldsymbol{\mathcal{C}}}^e\right)^{-1} : \Delta\bar{\boldsymbol{\sigma}} + \Delta\bar{\boldsymbol{\epsilon}}^{vp}. \tag{42}$$

Eq. (42) leads one first to derive the correspondence principle between $\Delta\bar{\boldsymbol{\sigma}}$ and $\Delta\bar{\boldsymbol{\epsilon}}^{vp}$. Without loss of generality, let $\dot{\bar{\boldsymbol{\epsilon}}}^{vp}$, $\dot{\bar{p}}$, and $\dot{\bar{\mathbf{X}}}$ all be functions of $\bar{\boldsymbol{\sigma}}$, $\bar{p}$, and $\bar{\mathbf{X}}$, i.e.,

$$\dot{\bar{\boldsymbol{\epsilon}}}^{vp}(t) = \dot{\bar{\boldsymbol{\epsilon}}}^{vp}\left(\bar{\boldsymbol{\sigma}}(t), \bar{p}(t), \bar{\mathbf{X}}(t)\right), \quad \dot{\bar{p}}(t) = \dot{\bar{p}}\left(\bar{\boldsymbol{\sigma}}(t), \bar{p}(t), \bar{\mathbf{X}}(t)\right), \tag{43}$$

$$\dot{\bar{\mathbf{X}}}(t) = \dot{\bar{\mathbf{X}}}\left(\bar{\boldsymbol{\sigma}}(t), \bar{p}(t), \bar{\mathbf{X}}(t)\right). \tag{43'}$$

Following Ref. [26], let $\Delta\bar{\boldsymbol{\epsilon}}^{vp}$ be related to $\dot{\bar{\boldsymbol{\epsilon}}}^{vp}(t_{n+1})$ using the backward Euler method by

$$\Delta\bar{\boldsymbol{\epsilon}}^{vp} = \dot{\bar{\boldsymbol{\epsilon}}}^{vp}(t_{n+1})\,\Delta t, \tag{44}$$

and let the evolution of $\dot{\bar{\boldsymbol{\epsilon}}}^{vp}$, $\dot{\bar{p}}$, and $\dot{\bar{\mathbf{X}}}$ be governed by

$$\dot{\bar{\boldsymbol{\epsilon}}}^{vp}(t_{n+1}) = \dot{\bar{\boldsymbol{\epsilon}}}^{vp}(t_n) + \boldsymbol{\mathcal{K}}(t_{n+1}) : \Delta\bar{\boldsymbol{\sigma}} + \mathbf{L}(t_{n+1})\,\Delta\bar{p} + \boldsymbol{\mathcal{M}}(t_{n+1}) : \Delta\bar{\mathbf{X}}, \tag{45}$$

$$\dot{\bar{p}}(t_{n+1}) = \dot{\bar{p}}(t_n) + \mathbf{N}(t_{n+1}) : \Delta\bar{\boldsymbol{\sigma}} + P(t_{n+1})\,\Delta\bar{p} + \mathbf{Q}(t_{n+1}) : \Delta\bar{\mathbf{X}}, \tag{45'}$$

$$\dot{\bar{\mathbf{X}}}(t_{n+1}) = \dot{\bar{\mathbf{X}}}(t_n) + \boldsymbol{\mathcal{R}}(t_{n+1}) : \Delta\bar{\boldsymbol{\sigma}} + \mathbf{S}(t_{n+1})\,\Delta\bar{p} + \boldsymbol{\mathcal{T}}(t_{n+1}) : \Delta\bar{\mathbf{X}}, \tag{45''}$$

where

$$\boldsymbol{\mathcal{K}} = \frac{\partial\dot{\bar{\boldsymbol{\epsilon}}}^{vp}}{\partial\bar{\boldsymbol{\sigma}}}, \quad \mathbf{L} = \frac{\partial\dot{\bar{\boldsymbol{\epsilon}}}^{vp}}{\partial\bar{p}}, \quad \boldsymbol{\mathcal{M}} = \frac{\partial\dot{\bar{\boldsymbol{\epsilon}}}^{vp}}{\partial\bar{\mathbf{X}}}, \quad \mathbf{N} = \frac{\partial\dot{\bar{p}}}{\partial\bar{\boldsymbol{\sigma}}}, \quad P = \frac{\partial\dot{\bar{p}}}{\partial\bar{p}}, \quad \mathbf{Q} = \frac{\partial\dot{\bar{p}}}{\partial\bar{\mathbf{X}}}, \tag{46}$$

$$\boldsymbol{\mathcal{R}} = \frac{\partial\dot{\bar{\mathbf{X}}}}{\partial\bar{\boldsymbol{\sigma}}}, \quad \mathbf{S} = \frac{\partial\dot{\bar{\mathbf{X}}}}{\partial\bar{p}}, \quad \boldsymbol{\mathcal{T}} = \frac{\partial\dot{\bar{\mathbf{X}}}}{\partial\bar{\mathbf{X}}} \tag{46'}$$

with $\boldsymbol{\mathcal{K}}$, $\boldsymbol{\mathcal{M}}$, $\boldsymbol{\mathcal{R}}$, and $\boldsymbol{\mathcal{T}}$ being fourth-order tensors, $\mathbf{L}$, $\mathbf{N}$, $\mathbf{Q}$, and $\mathbf{S}$ being second-order tensors, and P being a scalar (see Appendix B for more details on the derivation of the explicit expressions for these partial derivatives). Also let $\Delta\bar{p}$ and $\Delta\bar{\mathbf{X}}$ be related to $\dot{\bar{p}}$ and $\dot{\bar{\mathbf{X}}}$ using the backward Euler method by

$$\Delta\bar{p} = \dot{\bar{p}}(t_{n+1})\,\Delta t \quad \text{and} \quad \Delta\bar{\mathbf{X}} = \dot{\bar{\mathbf{X}}}(t_{n+1})\,\Delta t, \tag{47}$$

respectively. Substituting Eq. (47) into the last two equations of Eq. (45) and rearranging the equations give

$$A_{11}\dot{\bar{p}}\left(t_{n+1}\right)+\mathbf{A}_{12}:\dot{\bar{\mathbf{X}}}\left(t_{n+1}\right)=B_1, \tag{48}$$

$$\mathbf{A}_{21}\dot{\bar{p}}\left(t_{n+1}\right)+\boldsymbol{\mathcal{A}}_{22}:\dot{\bar{\mathbf{X}}}\left(t_{n+1}\right)=\mathbf{B}_2, \tag{48'}$$

where

$$A_{11}=1-P\left(t_{n+1}\right)\Delta t,\quad \mathbf{A}_{12}=-\mathbf{Q}\left(t_{n+1}\right)\Delta t,\quad \mathbf{A}_{21}=-\mathbf{S}\left(t_{n+1}\right)\Delta t,\quad \boldsymbol{\mathcal{A}}_{22}=\boldsymbol{\mathcal{I}}-\boldsymbol{\mathcal{T}}\left(t_{n+1}\right)\Delta t, \tag{49}$$

$$B_1=\dot{\bar{p}}\left(t_n\right)+\mathbf{N}\left(t_{n+1}\right):\Delta\bar{\boldsymbol{\sigma}},\quad \mathbf{B}_2=\dot{\bar{\mathbf{X}}}\left(t_n\right)+\boldsymbol{\mathcal{R}}\left(t_{n+1}\right):\Delta\bar{\boldsymbol{\sigma}}. \tag{49'}$$

Rearranging the second equation of Eq. (48) gives

$$\dot{\bar{\mathbf{X}}}\left(t_{n+1}\right)=\boldsymbol{\mathcal{A}}_{22}^{-1}:\left[\mathbf{B}_2-\mathbf{A}_{21}\dot{\bar{p}}\left(t_{n+1}\right)\right]. \tag{50}$$

Substituting Eq. (50) into the first equation of Eq. (48) and rearranging the equation give

$$\dot{\bar{p}}\left(t_{n+1}\right)=\frac{B_1-\mathbf{A}_{12}:\boldsymbol{\mathcal{A}}_{22}^{-1}:\mathbf{B}_2}{A_{11}-\mathbf{A}_{12}:\boldsymbol{\mathcal{A}}_{22}^{-1}:\mathbf{A}_{21}}. \tag{51}$$

Substituting Eq. (51) into Eq. (50) gives

$$\dot{\bar{\mathbf{X}}}\left(t_{n+1}\right)=\boldsymbol{\mathcal{A}}_{22}^{-1}:\left(\mathbf{B}_2-\frac{B_1-\mathbf{A}_{12}:\boldsymbol{\mathcal{A}}_{22}^{-1}:\mathbf{B}_2}{A_{11}-\mathbf{A}_{12}:\boldsymbol{\mathcal{A}}_{22}^{-1}:\mathbf{A}_{21}}\mathbf{A}_{21}\right). \tag{52}$$

Substituting Eqs. (51) and (52) into Eq. (47), substituting the equation into the first equation of Eq. (45), and rearranging the equation give

$$\dot{\bar{\boldsymbol{\epsilon}}}^{vp}\left(t_{n+1}\right)=\dot{\bar{\boldsymbol{\epsilon}}}\left(t_{n+1}\right)+\tilde{\boldsymbol{\mathcal{C}}}^{-1}\left(t_{n+1}\right):\Delta\bar{\boldsymbol{\sigma}}, \tag{53}$$

where

$$\begin{aligned}\dot{\bar{\boldsymbol{\epsilon}}}\left(t_{n+1}\right)=&\dot{\bar{\boldsymbol{\epsilon}}}^{vp}\left(t_n\right)+\boldsymbol{\mathcal{M}}\left(t_{n+1}\right):\boldsymbol{\mathcal{A}}_{22}^{-1}:\dot{\bar{\mathbf{X}}}\left(t_n\right)\Delta t\\&+\frac{\dot{\bar{p}}\left(t_n\right)-\mathbf{A}_{12}:\boldsymbol{\mathcal{A}}_{22}^{-1}:\dot{\bar{\mathbf{X}}}\left(t_n\right)}{A_{11}-\mathbf{A}_{12}:\boldsymbol{\mathcal{A}}_{22}^{-1}:\mathbf{A}_{21}}\left[\mathbf{L}\left(t_{n+1}\right)-\boldsymbol{\mathcal{M}}\left(t_{n+1}\right):\boldsymbol{\mathcal{A}}_{22}^{-1}:\mathbf{A}_{21}\right]\Delta t,\end{aligned} \tag{54}$$

and

$$\begin{aligned}\tilde{\boldsymbol{\mathcal{C}}}^{-1}\left(t_{n+1}\right)=&\boldsymbol{\mathcal{K}}\left(t_{n+1}\right)+\boldsymbol{\mathcal{M}}\left(t_{n+1}\right):\boldsymbol{\mathcal{A}}_{22}^{-1}:\boldsymbol{\mathcal{R}}\left(t_{n+1}\right)\Delta t\\&+\frac{\left[\mathbf{L}\left(t_{n+1}\right)-\boldsymbol{\mathcal{M}}\left(t_{n+1}\right):\boldsymbol{\mathcal{A}}_{22}^{-1}:\mathbf{A}_{21}\right]\otimes\left[\mathbf{N}\left(t_{n+1}\right)-\mathbf{A}_{12}:\boldsymbol{\mathcal{A}}_{22}^{-1}:\boldsymbol{\mathcal{R}}\left(t_{n+1}\right)\right]}{A_{11}-\mathbf{A}_{12}:\boldsymbol{\mathcal{A}}_{22}^{-1}:\mathbf{A}_{21}}\Delta t.\end{aligned} \tag{55}$$

Substituting Eq. (53) into Eq. (44) gives

$$\Delta\bar{\boldsymbol{\epsilon}}^{vp}=\Delta\tilde{\boldsymbol{\epsilon}}+\left[\tilde{\boldsymbol{\mathcal{C}}}^{-1}\left(t_{n+1}\right)\Delta t\right]:\Delta\bar{\boldsymbol{\sigma}}, \tag{56}$$

where $\Delta\tilde{\boldsymbol{\epsilon}}=\dot{\bar{\boldsymbol{\epsilon}}}\left(t_{n+1}\right)\Delta t$. Substituting Eq. (56) into Eq. (42) gives

$$\Delta\bar{\boldsymbol{\epsilon}}=\Delta\bar{\boldsymbol{\epsilon}}^{e}+\Delta\bar{\boldsymbol{\epsilon}}^{vp}=\left(\bar{\boldsymbol{\mathcal{C}}}^{e}\right)^{-1}:\Delta\bar{\boldsymbol{\sigma}}+\Delta\tilde{\boldsymbol{\epsilon}}+\left[\tilde{\boldsymbol{\mathcal{C}}}^{-1}\left(t_{n+1}\right)\Delta t\right]:\Delta\bar{\boldsymbol{\sigma}}. \tag{57}$$

Rearranging Eq. (57) gives an affine formulation of the constitutive relations in the undamaged configuration as

$$\Delta\bar{\boldsymbol{\epsilon}}-\Delta\tilde{\boldsymbol{\epsilon}}=\left[\left(\bar{\boldsymbol{\mathcal{C}}}^{e}\right)^{-1}+\tilde{\boldsymbol{\mathcal{C}}}^{-1}\left(t_{n+1}\right)\Delta t\right]:\Delta\bar{\boldsymbol{\sigma}} \tag{58}$$

or

$$\Delta\bar{\boldsymbol{\sigma}}=\bar{\boldsymbol{\mathcal{C}}}^{evp}\left(t_{n+1}\right):\left(\Delta\bar{\boldsymbol{\epsilon}}-\Delta\tilde{\boldsymbol{\epsilon}}\right), \tag{59}$$

where

$$\bar{\boldsymbol{\mathcal{C}}}^{evp}\left(t_{n+1}\right)=\left[\left(\bar{\boldsymbol{\mathcal{C}}}^{e}\right)^{-1}+\tilde{\boldsymbol{\mathcal{C}}}^{-1}\left(t_{n+1}\right)\Delta t\right]^{-1} \tag{60}$$

denotes the fourth-order affine instantaneous elasto-viscoplastic stiffness tensor in the undamaged configuration.

Till now, an affine formulation of the constitutive relations in the undamaged configuration has been derived. In the next section, the damage evolution law will be derived.

VI. Damage Evolution Law

Without loss of generality, let the damage criterion take a Hill-type form, i.e.,

$$f^d(\mathbf{Y}, S) = Y_e - Y_T = 0, \tag{61}$$

where

$$Y_e = \sqrt{\mathbf{Y} : \boldsymbol{\mathcal{L}} : \mathbf{Y}} \tag{62}$$

denotes a Hill-type equivalent damage conjugate force with $\boldsymbol{\mathcal{L}}$ denoting a fourth-order damage anisotropy tensor, and

$$Y_T = Y_0 + S, \tag{63}$$

denotes the current damage threshold with Y_0 denoting the initial damage threshold. $\mathcal{L}_{ijkl}$ can be written in the Voigt notation as L_{ij}. In general, the diagonal components of L_{ij} are around 1, while the off-diagonal components are smaller than the diagonal ones (see Ref. [40] for more details on $\boldsymbol{\mathcal{L}}$). Similarly to Eq. (27), one can write the damage dissipation equivalence principle as

$$\mathbf{Y} : \dot{\boldsymbol{\omega}} = Y_e \dot{q}, \tag{64}$$

where $\dot{q}$ denotes a Hill-type equivalent damage rate. Following Ref. [34], taking the partial derivatives with respect to $\mathbf{Y}$ on both sides of Eq. (64) gives

$$\dot{\boldsymbol{\omega}} = \frac{\partial Y_e}{\partial \mathbf{Y}} \dot{q}. \tag{65}$$

Similarly to Eq. (31), $\partial Y_e / \partial \mathbf{Y}$ can be obtained as

$$\frac{\partial Y_e}{\partial \mathbf{Y}} = \frac{1}{2Y_e} \frac{\partial Y_e^2}{\partial \mathbf{Y}} = \frac{1}{2Y_e} \left(2 \frac{\partial \mathbf{Y}}{\partial \mathbf{Y}} : \boldsymbol{\mathcal{L}} : \mathbf{Y} \right) = \frac{\boldsymbol{\mathcal{L}} : \mathbf{Y}}{Y_e}. \tag{66}$$

Substituting Eq. (66) into Eq. (65) gives

$$\dot{\boldsymbol{\omega}} = \frac{\boldsymbol{\mathcal{L}} : \mathbf{Y}}{Y_e} \dot{q} \quad \text{or} \quad \mathbf{Y} = \frac{\boldsymbol{\mathcal{L}}^{-1} : \dot{\boldsymbol{\omega}}}{\dot{q}} Y_e. \tag{67}$$

Substituting the second equation of Eq. (67) into Eq. (64) and rearranging the equation give

$$\dot{q}^2 = \dot{\boldsymbol{\omega}} : \boldsymbol{\mathcal{L}}^{-1} : \dot{\boldsymbol{\omega}} \quad \text{or} \quad \dot{q} = \sqrt{\dot{\boldsymbol{\omega}} : \boldsymbol{\mathcal{L}}^{-1} : \dot{\boldsymbol{\omega}}}. \tag{68}$$

It is also beneficial to find the relation between $\dot{\lambda}^d$ and $\dot{q}$. Recall that Eq. (23) writes

$$\dot{\boldsymbol{\omega}} = \dot{\lambda}^d \frac{\partial f^d}{\partial \mathbf{Y}} \quad \text{and} \quad \dot{s} = -\dot{\lambda}^d \frac{\partial f^d}{\partial S}. \tag{69}$$

Substituting the first equation of Eq. (69) into Eq. (64) gives

$$\mathbf{Y} : \left(\dot{\lambda}^d \frac{\partial f^d}{\partial \mathbf{Y}} \right) = Y_e \dot{q}. \tag{70}$$

Note that $\partial f^d / \partial \mathbf{Y} = \partial Y_e / \partial \mathbf{Y}$. Substituting Eq. (66) into Eq. (70) gives

$$Y_e \dot{\lambda}^d = Y_e \dot{q} \quad \text{or} \quad \dot{\lambda}^d = \dot{q}, \tag{71}$$

which implies that the damage evolution is irreversible. One can also write the damage evolution conditions as

$$f^d \leq 0, \quad \dot{\lambda}^d \geq 0, \quad \dot{\lambda}^d f^d = 0. \tag{72}$$

Also introduce a pseudo-potential g^d, which is related to f^d by

$$g^d = f^d + \frac{S^2}{2L} \tag{73}$$

with L being a constant accounting for damage hardening, and rewrite Eq. (69) as

$$\dot{\boldsymbol{\omega}} = \dot{\lambda}^d \frac{\partial g^d}{\partial \mathbf{Y}} \quad \text{and} \quad \dot{s} = -\dot{\lambda}^d \frac{\partial g^d}{\partial S}. \tag{74}$$

Note that Eq. (71) remains valid because $\partial g^d / \partial \mathbf{Y} = \partial f^d / \partial \mathbf{Y}$. Let $\rho\psi^d$ take the form of

$$\rho\psi^d = \frac{1}{2} L o s^2, \tag{75}$$

where o is another constant accounting for damage hardening. Substituting Eq. (75) into the last equation of Eq. (10) gives

$$S = Los. \tag{76}$$

Substituting the last equation of Eq. (74) into the rate form of Eq. (76) and noting that $\dot{\lambda}^d = \dot{q}$ give

$$\dot{S} = (L - S)\, o\dot{q} \quad \text{or} \quad S = L\left[1 - \exp\left(-oq\right)\right]. \tag{77}$$

The consistency condition can be obtained from Eq. (61) as

$$\dot{f}^d = \frac{\partial f^d}{\partial \mathbf{Y}} : \dot{\mathbf{Y}} + \frac{\partial f^d}{\partial S} \frac{dS}{dq} \dot{q} = 0. \tag{78}$$

Rearranging Eq. (78) and noting that $\partial f^d / \partial S = -1$ and $\dot{\lambda}^d = \dot{q}$ give

$$\dot{\lambda}^d = \frac{\dfrac{\partial f^d}{\partial \mathbf{Y}} : \dot{\mathbf{Y}}}{\dfrac{dS}{dq}}. \tag{79}$$

Substituting Eq. (79) into the first equation of Eq. (74) gives

$$\dot{\boldsymbol{\omega}} = \frac{\dfrac{\partial f^d}{\partial \mathbf{Y}} : \dot{\mathbf{Y}}}{\dfrac{dS}{dq}} \frac{\partial g^d}{\partial \mathbf{Y}} = \frac{\dfrac{\partial g^d}{\partial \mathbf{Y}} \otimes \dfrac{\partial f^d}{\partial \mathbf{Y}}}{\dfrac{dS}{dq}} : \dot{\mathbf{Y}} \equiv \boldsymbol{\mathcal{S}}^d : \dot{\mathbf{Y}}, \tag{80}$$

which is the damage evolution law. Note that $\boldsymbol{\mathcal{S}}^d$ is generally non-invertible.

Till now, the damage evolution law has been derived. In the next section, the constitutive relations in the damaged configuration will be derived.

VII. Affine Formulation in the Damaged Configuration

Note that the rate of a quantity can be converted to its increment by multiplying it by Δt. The constitutive relations in the damaged configuration can be derived by subsequently finding the $\dot{\bar{\boldsymbol{\epsilon}}}^e$-$\dot{\boldsymbol{\epsilon}}^e$, $\dot{\bar{\boldsymbol{\sigma}}}$-$\dot{\boldsymbol{\sigma}}$, and $\dot{\bar{\boldsymbol{\epsilon}}}^p$-$\dot{\boldsymbol{\epsilon}}^p$ relations.

Recall that

$$\bar{\boldsymbol{\epsilon}}^e = \boldsymbol{\mathcal{M}}^{-1} : \boldsymbol{\epsilon}^e. \tag{81}$$

Taking time derivatives on both sides of Eq. (81) gives

$$\dot{\bar{\boldsymbol{\epsilon}}}^e = \dot{\boldsymbol{\mathcal{M}}}^{-1} : \boldsymbol{\epsilon}^e + \boldsymbol{\mathcal{M}}^{-1} : \dot{\boldsymbol{\epsilon}}^e. \tag{82}$$

The first term to the right of the equal sign in Eq. (88) can further be expressed as

$$\dot{\mathcal{M}}^{-1}_{ijmn} \epsilon^e_{mn} = \left(\frac{\partial \mathcal{M}^{-1}_{ijmn}}{\partial \omega_{kl}} \dot{\omega}_{kl} \right) \epsilon^e_{mn} = \left(\frac{\partial \mathcal{M}^{-1}_{ijmn}}{\partial \omega_{kl}} \epsilon^e_{mn} \right) \dot{\omega}_{kl}. \tag{83}$$

For notational convenience, let

$$\mathscr{I}_{ijklmn} = -\frac{\partial \mathcal{M}^{-1}_{ijmn}}{\partial \omega_{kl}} = -\frac{\partial}{\partial \omega_{kl}} \left(\mathcal{I}_{ijmn} - \mathcal{D}_{ijmn} \right) = \frac{\partial \mathcal{D}_{ijmn}}{\partial \omega_{kl}}. \tag{84}$$

Substituting Eq. (2) into Eq. (84) gives

$$\boldsymbol{\mathscr{I}} = \sum_{i=1}^{3}\sum_{j=1}^{3} \mathbf{e}_i \otimes \mathbf{e}_j \otimes \mathbf{e}_i \otimes \mathbf{e}_j \otimes \mathbf{e}_i \otimes \mathbf{e}_j. \tag{85}$$

Substituting Eq. (84) into Eq. (83) gives

$$\dot{\mathcal{M}}^{-1}_{ijmn}\epsilon^e_{mn} = -\mathscr{I}_{ijklmn}\dot{\omega}_{kl}\epsilon^e_{mn} = -\left(\mathscr{I}_{ijklmn}\epsilon^e_{mn}\right)\dot{\omega}_{kl} \tag{86}$$

or

$$\dot{\boldsymbol{\mathcal{M}}}^{-1} : \boldsymbol{\epsilon}^e = -\left(\boldsymbol{\mathscr{I}} : \boldsymbol{\epsilon}^e\right) : \dot{\boldsymbol{\omega}}. \tag{87}$$

Substituting Eq. (87) into Eq. (82) gives

$$\dot{\bar{\boldsymbol{\epsilon}}}^e = -\left(\boldsymbol{\mathscr{I}} : \boldsymbol{\epsilon}^e\right) : \dot{\boldsymbol{\omega}} + \boldsymbol{\mathcal{M}}^{-1} : \dot{\boldsymbol{\epsilon}}^e. \tag{88}$$

Eq. (88) leads one first to find the relation between $\dot{\boldsymbol{\omega}}$ and $\dot{\boldsymbol{\epsilon}}^e$. Note that $\rho\psi^e$ can be expressed as

$$\rho\psi^e = \frac{1}{2}\boldsymbol{\sigma} : \boldsymbol{\epsilon}^e = \frac{1}{2}\boldsymbol{\epsilon}^e : \boldsymbol{\mathcal{C}}^e : \boldsymbol{\epsilon}^e = \frac{1}{2}\boldsymbol{\epsilon}^e : \left(\boldsymbol{\mathcal{M}}^{-1} : \bar{\boldsymbol{\mathcal{C}}}^e : \boldsymbol{\mathcal{M}}^{-1}\right) : \boldsymbol{\epsilon}^e. \tag{89}$$

Substituting Eq. (89) into the second equation of Eq. (10) gives

$$\mathbf{Y} = -\rho\frac{\partial\psi^e}{\partial\boldsymbol{\omega}} = \frac{1}{2}\boldsymbol{\epsilon}^e : \left(\boldsymbol{\mathscr{I}} : \bar{\boldsymbol{\mathcal{C}}}^e : \boldsymbol{\mathcal{M}}^{-1} + \boldsymbol{\mathcal{M}}^{-1} : \bar{\boldsymbol{\mathcal{C}}}^e : \boldsymbol{\mathscr{I}}\right) : \boldsymbol{\epsilon}^e. \tag{90}$$

Eq. (90) implies that $\mathbf{Y}$ is a function of $\boldsymbol{\epsilon}^e$ and $\boldsymbol{\omega}$. $\dot{\mathbf{Y}}$ can hereby be expressed using the chain rule as

$$\dot{\mathbf{Y}} = \frac{\partial\mathbf{Y}}{\partial\boldsymbol{\epsilon}^e} : \dot{\boldsymbol{\epsilon}}^e + \frac{\partial\mathbf{Y}}{\partial\boldsymbol{\omega}} : \dot{\boldsymbol{\omega}}, \tag{91}$$

where the explicit expressions for $\partial\mathbf{Y}/\partial\boldsymbol{\epsilon}^e$ and $\partial\mathbf{Y}/\partial\boldsymbol{\omega}$ can be obtained as

$$\frac{\partial\mathbf{Y}}{\partial\boldsymbol{\epsilon}^e} = \frac{1}{2}\left[\left(\boldsymbol{\mathscr{I}} : \bar{\boldsymbol{\mathcal{C}}}^e : \boldsymbol{\mathcal{M}}^{-1} + \boldsymbol{\mathcal{M}}^{-1} : \bar{\boldsymbol{\mathcal{C}}}^e : \boldsymbol{\mathscr{I}}\right) : \boldsymbol{\epsilon}^e + \boldsymbol{\epsilon}^e : \left(\boldsymbol{\mathscr{I}} : \bar{\boldsymbol{\mathcal{C}}}^e : \boldsymbol{\mathcal{M}}^{-1} + \boldsymbol{\mathcal{M}}^{-1} : \bar{\boldsymbol{\mathcal{C}}}^e : \boldsymbol{\mathscr{I}}\right)\right] \tag{92}$$

and

$$\frac{\partial\mathbf{Y}}{\partial\boldsymbol{\omega}} = -\frac{1}{2}\boldsymbol{\epsilon}^e : \left(\boldsymbol{\mathscr{I}} : \bar{\boldsymbol{\mathcal{C}}}^e : \boldsymbol{\mathscr{I}} + \boldsymbol{\mathscr{I}} : \bar{\boldsymbol{\mathcal{C}}}^e : \boldsymbol{\mathscr{I}}\right) : \boldsymbol{\epsilon}^e = -\boldsymbol{\epsilon}^e : \boldsymbol{\mathscr{I}} : \bar{\boldsymbol{\mathcal{C}}}^e : \boldsymbol{\mathscr{I}} : \boldsymbol{\epsilon}^e, \tag{93}$$

respectively. Substituting Eq. (91) into Eq. (80) and rearranging the equation give

$$\dot{\boldsymbol{\omega}} = \left[\left(\boldsymbol{\mathcal{I}} - \boldsymbol{\mathcal{S}}^d : \frac{\partial\mathbf{Y}}{\partial\boldsymbol{\omega}}\right)^{-1} : \left(\boldsymbol{\mathcal{S}}^d : \frac{\partial\mathbf{Y}}{\partial\boldsymbol{\epsilon}^e}\right)\right] : \dot{\boldsymbol{\epsilon}}^e \equiv \boldsymbol{\mathcal{A}} : \dot{\boldsymbol{\epsilon}}^e, \tag{94}$$

Substituting Eq. (94) into Eq. (88) gives

$$\dot{\bar{\boldsymbol{\epsilon}}}^e = -\left(\boldsymbol{\mathscr{I}} : \boldsymbol{\epsilon}^e\right) : \boldsymbol{\mathcal{A}} : \dot{\boldsymbol{\epsilon}}^e + \boldsymbol{\mathcal{M}}^{-1} : \dot{\boldsymbol{\epsilon}}^e = \left[-\left(\boldsymbol{\mathscr{I}} : \boldsymbol{\epsilon}^e\right) : \boldsymbol{\mathcal{A}} + \boldsymbol{\mathcal{M}}^{-1}\right] : \dot{\boldsymbol{\epsilon}}^e \equiv \tilde{\boldsymbol{\mathcal{N}}}^{-1} : \dot{\boldsymbol{\epsilon}}^e. \tag{95}$$

Recall that

$$\boldsymbol{\sigma} = \boldsymbol{\mathcal{C}}^e : \boldsymbol{\epsilon}^e \tag{96}$$

and that

$$\boldsymbol{\mathcal{C}}^e = \boldsymbol{\mathcal{M}}^{-1} : \bar{\boldsymbol{\mathcal{C}}}^e : \boldsymbol{\mathcal{M}}^{-1}. \tag{97}$$

Taking time derivatives on both sides of Eq. (96) gives

$$\dot{\boldsymbol{\sigma}} = \dot{\boldsymbol{\mathcal{C}}}^e : \boldsymbol{\epsilon}^e + \boldsymbol{\mathcal{C}}^e : \dot{\boldsymbol{\epsilon}}^e. \tag{98}$$

The first term to the right of the equal sign in Eq. (98) can further be expressed as

$$\begin{aligned}
\dot{\mathcal{C}}^e_{ijrs}\epsilon^e_{rs} &= \left(\dot{\mathcal{M}}^{-1}_{ijmn}\bar{\mathcal{C}}^e_{mnpq}\mathcal{M}^{-1}_{pqrs} + \mathcal{M}^{-1}_{ijmn}\bar{\mathcal{C}}^e_{mnpq}\dot{\mathcal{M}}^{-1}_{pqrs}\right)\epsilon^e_{rs} \\
&= -\left(\mathscr{I}_{ijklmn}\dot{\omega}_{kl}\bar{\mathcal{C}}^e_{mnpq}\mathcal{M}^{-1}_{pqrs} + \mathcal{M}^{-1}_{ijmn}\bar{\mathcal{C}}^e_{mnpq}\mathscr{I}_{pqklrs}\dot{\omega}_{kl}\right)\epsilon^e_{rs} \\
&= -\left[\left(\mathscr{I}_{ijklmn}\bar{\mathcal{C}}^e_{mnpq}\mathcal{M}^{-1}_{pqrs} + \mathcal{M}^{-1}_{ijmn}\bar{\mathcal{C}}^e_{mnpq}\mathscr{I}_{pqklrs}\right)\epsilon^e_{rs}\right]\dot{\omega}_{kl} \equiv -\left(\mathscr{B}_{ijklrs}\epsilon^e_{rs}\right)\dot{\omega}_{kl}
\end{aligned} \tag{99}$$

or

$$\dot{\boldsymbol{\mathcal{C}}}^e : \boldsymbol{\epsilon}^e = -\left[\left(\boldsymbol{\mathscr{I}} : \bar{\boldsymbol{\mathcal{C}}}^e : \boldsymbol{\mathcal{M}}^{-1} + \boldsymbol{\mathcal{M}}^{-1} : \bar{\boldsymbol{\mathcal{C}}}^e : \boldsymbol{\mathscr{I}}\right) : \boldsymbol{\epsilon}^e\right] : \dot{\boldsymbol{\omega}} \equiv -\left(\boldsymbol{\mathscr{B}} : \boldsymbol{\epsilon}^e\right) : \dot{\boldsymbol{\omega}}. \tag{100}$$

Combining Eqs. (94), (98), and (100) gives

$$\begin{aligned} \dot{\boldsymbol{\sigma}} = & -\left(\boldsymbol{\mathscr{B}} : \boldsymbol{\epsilon}^e\right) : \dot{\boldsymbol{\omega}} + \boldsymbol{\mathcal{C}}^e : \dot{\boldsymbol{\epsilon}}^e = -\left(\boldsymbol{\mathscr{B}} : \boldsymbol{\epsilon}^e\right) : \boldsymbol{\mathcal{A}} : \dot{\boldsymbol{\epsilon}}^e + \boldsymbol{\mathcal{C}}^e : \dot{\boldsymbol{\epsilon}}^e \\ = & \left[-\left(\boldsymbol{\mathscr{B}} : \boldsymbol{\epsilon}^e\right) : \boldsymbol{\mathcal{A}} + \boldsymbol{\mathcal{C}}^e\right] : \dot{\boldsymbol{\epsilon}}^e \equiv \tilde{\boldsymbol{\mathcal{C}}}^e : \dot{\boldsymbol{\epsilon}}^e. \end{aligned} \tag{101}$$

Recall that

$$\dot{\bar{\boldsymbol{\sigma}}} = \bar{\boldsymbol{\mathcal{C}}}^e : \dot{\bar{\boldsymbol{\epsilon}}}^e. \tag{102}$$

Combining Eqs. (95) and (102) gives

$$\dot{\boldsymbol{\epsilon}}^e = \tilde{\boldsymbol{\mathcal{N}}} : \dot{\bar{\boldsymbol{\epsilon}}}^e = \tilde{\boldsymbol{\mathcal{N}}} : \left(\bar{\boldsymbol{\mathcal{C}}}^e\right)^{-1} : \dot{\bar{\boldsymbol{\sigma}}}. \tag{103}$$

Substituting Eq. (103) into Eq. (101) gives

$$\dot{\boldsymbol{\sigma}} = \left[\tilde{\boldsymbol{\mathcal{C}}}^e : \tilde{\boldsymbol{\mathcal{N}}} : \left(\bar{\boldsymbol{\mathcal{C}}}^e\right)^{-1}\right] : \dot{\bar{\boldsymbol{\sigma}}} \equiv \boldsymbol{\mathcal{N}}^{-1} : \dot{\bar{\boldsymbol{\sigma}}}. \tag{104}$$

The (visco)plastic dissipation equivalence hypothesis states that the (visco)plastic dissipation of a damaged material should equal that of its equivalent undamaged material, i.e.,[41]

$$\boldsymbol{\sigma} : \dot{\boldsymbol{\epsilon}}^{vp} = \bar{\boldsymbol{\sigma}} : \dot{\bar{\boldsymbol{\epsilon}}}^{vp}. \tag{105}$$

Substituting Eq. (1) into Eq. (105) gives

$$\dot{\bar{\boldsymbol{\epsilon}}}^{vp} = \boldsymbol{\mathcal{M}}^{-1} : \dot{\boldsymbol{\epsilon}}^{vp} \quad \text{or} \quad \dot{\boldsymbol{\epsilon}}^{vp} = \boldsymbol{\mathcal{M}} : \dot{\bar{\boldsymbol{\epsilon}}}^{vp}. \tag{106}$$

The rate form of Eq. (59) can be written as

$$\dot{\bar{\boldsymbol{\sigma}}} = \bar{\boldsymbol{\mathcal{C}}}^{evp} : \left(\dot{\bar{\boldsymbol{\epsilon}}} - \dot{\tilde{\boldsymbol{\epsilon}}}\right) = \bar{\boldsymbol{\mathcal{C}}}^{evp} : \dot{\bar{\boldsymbol{\epsilon}}}^e + \bar{\boldsymbol{\mathcal{C}}}^{evp} : \dot{\bar{\boldsymbol{\epsilon}}}^{vp} - \bar{\boldsymbol{\mathcal{C}}}^{evp} : \dot{\tilde{\boldsymbol{\epsilon}}}. \tag{107}$$

Substituting Eqs. (95), (96), and (106) into Eq. (107) gives

$$\begin{aligned} \boldsymbol{\mathcal{N}} : \dot{\boldsymbol{\sigma}} &= \bar{\boldsymbol{\mathcal{C}}}^{evp} : \tilde{\boldsymbol{\mathcal{N}}}^{-1} : \dot{\boldsymbol{\epsilon}}^e + \bar{\boldsymbol{\mathcal{C}}}^{evp} : \boldsymbol{\mathcal{M}}^{-1} : \dot{\boldsymbol{\epsilon}}^{vp} - \bar{\boldsymbol{\mathcal{C}}}^{evp} : \dot{\tilde{\boldsymbol{\epsilon}}} \\ &= \bar{\boldsymbol{\mathcal{C}}}^{evp} : \tilde{\boldsymbol{\mathcal{N}}}^{-1} : \dot{\boldsymbol{\epsilon}}^e + \bar{\boldsymbol{\mathcal{C}}}^{evp} : \boldsymbol{\mathcal{M}}^{-1} : \left(\dot{\boldsymbol{\epsilon}} - \dot{\boldsymbol{\epsilon}}^e\right) - \bar{\boldsymbol{\mathcal{C}}}^{evp} : \dot{\tilde{\boldsymbol{\epsilon}}} \\ &= \bar{\boldsymbol{\mathcal{C}}}^{evp} : \boldsymbol{\mathcal{M}}^{-1} : \dot{\boldsymbol{\epsilon}} + \bar{\boldsymbol{\mathcal{C}}}^{evp} : \left(\tilde{\boldsymbol{\mathcal{N}}}^{-1} - \boldsymbol{\mathcal{M}}^{-1}\right) : \dot{\boldsymbol{\epsilon}}^e - \bar{\boldsymbol{\mathcal{C}}}^{evp} : \dot{\tilde{\boldsymbol{\epsilon}}}. \end{aligned} \tag{108}$$

Eq. (101) can be rewritten as

$$\dot{\boldsymbol{\epsilon}}^e = \left(\tilde{\boldsymbol{\mathcal{C}}}^e\right)^{-1} : \dot{\boldsymbol{\sigma}}. \tag{109}$$

Substituting Eq. (109) into Eq. (108) and rearranging the equation give

$$\left[\boldsymbol{\mathcal{N}} - \bar{\boldsymbol{\mathcal{C}}}^{evp} : \left(\tilde{\boldsymbol{\mathcal{N}}}^{-1} - \boldsymbol{\mathcal{M}}^{-1}\right) : \left(\tilde{\boldsymbol{\mathcal{C}}}^e\right)^{-1}\right] : \dot{\boldsymbol{\sigma}} = \bar{\boldsymbol{\mathcal{C}}}^{evp} : \boldsymbol{\mathcal{M}}^{-1} : \dot{\boldsymbol{\epsilon}} - \bar{\boldsymbol{\mathcal{C}}}^{evp} : \dot{\tilde{\boldsymbol{\epsilon}}}. \tag{110}$$

Multiplying both sides of Eq. (110) by Δt and rearranging the equation give the constitutive relations in the damaged configuration as

$$\begin{aligned} \Delta\boldsymbol{\sigma} &= \left\{\left[\boldsymbol{\mathcal{N}} - \bar{\boldsymbol{\mathcal{C}}}^{evp} : \left(\tilde{\boldsymbol{\mathcal{N}}}^{-1} - \boldsymbol{\mathcal{M}}^{-1}\right) : \left(\tilde{\boldsymbol{\mathcal{C}}}^e\right)^{-1}\right]^{-1} : \bar{\boldsymbol{\mathcal{C}}}^{evp} : \boldsymbol{\mathcal{M}}^{-1}\right\} : \left(\Delta\boldsymbol{\epsilon} - \boldsymbol{\mathcal{M}} : \Delta\tilde{\boldsymbol{\epsilon}}\right) \\ &\equiv \boldsymbol{\mathcal{C}}^{evp} : \left(\Delta\boldsymbol{\epsilon} - \boldsymbol{\mathcal{M}} : \Delta\tilde{\boldsymbol{\epsilon}}\right), \end{aligned} \tag{111}$$

where $\boldsymbol{\mathcal{C}}^{evp}$ denotes the fourth-order affine instantaneous elasto-viscoplastic stiffness tensor in the damaged configuration.

VIII. Validation Examples

In this section, the use of the current constitutive relations will be demonstrated by modeling an aluminium alloy exhibiting various material behaviors.

A. Damage Hardening

First consider an aluminium alloy exhibiting combined isotropic-kinematic hardening and damage hardening. Following Refs. [26], [42], and [43], let its material parameters take the values listed in Table 1, where $\bar{E}$ and $\bar{\nu}$ denote the undamaged Young's modulus and Poisson's ratio, respectively, and allow L to take the values of $10Y_0$ and $20Y_0$ in different cases. Recall that $\mathcal{L}_{ijkl}$ can be written in the Voigt notation as L_{ij}. Following Ref. [40], let L_{ij} take the form of

$$L_{ij} = \begin{cases} 1 & i = j, \\ 0.32 & i \neq j. \end{cases} \tag{112}$$

Table 1 and Eq. (112) imply that the material yields and becomes damaged simultaneously under uniaxial extension. Introduce a Cartesian coordinate system $\mathbf{x} = (x_1, x_2, x_3)$, and let its three axes coincide with the three axes of damage orthotropy.

11.5

Table 1. Material parameters.

(a) Elastic constants.

$\bar{E}$ (GPa)	$\bar{\nu}$
70	0.33

(b) Viscoplastic constants.

$\bar{\sigma}_0$ (MPa)	$\bar{K}$ (MPa)	$\bar{n}$	$\bar{\eta}$ (s)	$\bar{m}$	$\bar{C}$ (MPa)	$\bar{\gamma}$
60	40	54.9	2.27×10^5	4.61	7019	118.6

(c) Damage constants.

Y_0 (MPa)	L (MPa)	o
0.0514	–	5

Figures 1 shows the stress-strain curves of a perfect material undergoing uniaxial extension in the x_1-direction. It can be seen that, as the major strain rate increases, the material becomes stiffer. This agrees with the theory of viscoplasticity. In the rest of the examples, the major strain rate will be set to equal 10^{-4} s^{-1} with an emphasis of the damage behavior of the material.

Figure 2 shows the stress-strain and ω_{11}-ϵ_{11} curves of the damageable material undergoing uniaxial extension in the x_1-direction. Note that L provides a measure of the resistance of a material to damages, i.e., a low value of L corresponds to a material vulnerable to damages and vice versa. Accordingly, in Figure 2, as L decreases, the stress-strain curve shifts downwards, while the ω_{11}-ϵ_{11} shifts upwards. In addition, in Figure 2(b), both ω_{11}-ϵ_{11} curves exhibit highly nonlinear trends. Such trends actually result from the interactions among the elastic, viscoplastic, and damage behaviors of the material. Especially, for $L = 10Y_0$, the material exhibits strain softening at an early stage of deformation. The numerical results shows that, as the material is further deformed, the damage evolution gradually takes the place of the viscoplastic deformation and becomes dominant. Figure 2 indicates that, after this, the material behaves like a damagable elastic one exhibiting an asymptotic behavior near fracture.

B. General Damage Anisotropy

Next let the material also exhibit general damage anisotropy, where the term "general" means that the components of L_{ij} are independent of each other. Specifically, let the material parameters take the values listed in Table 1 with $L = 20Y_0$, and let Eq. (112) hold except that L_{11} can take the values of 0.707, 1, and 1.414 in three cases.

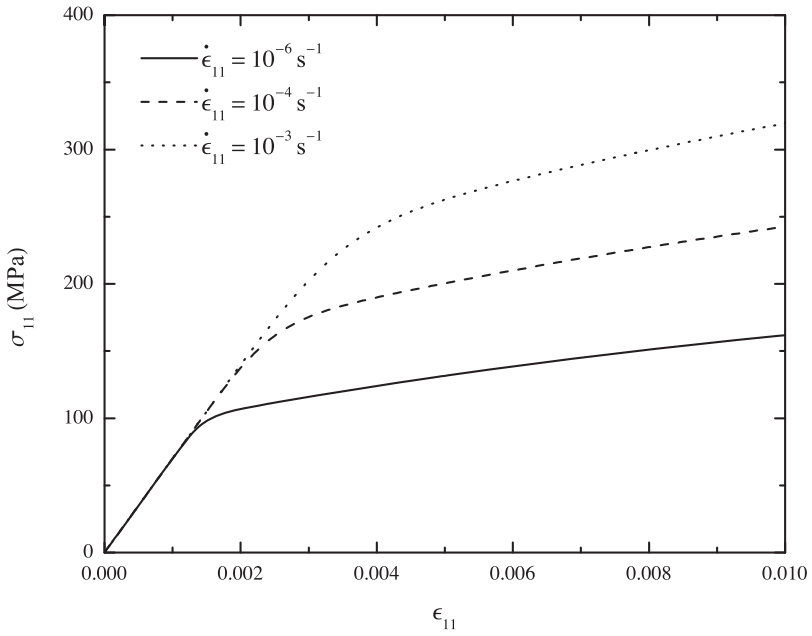

Figure 1. Stress-strain curves of a perfect alloy undergoing uniaxial extension in the x_1-direction.

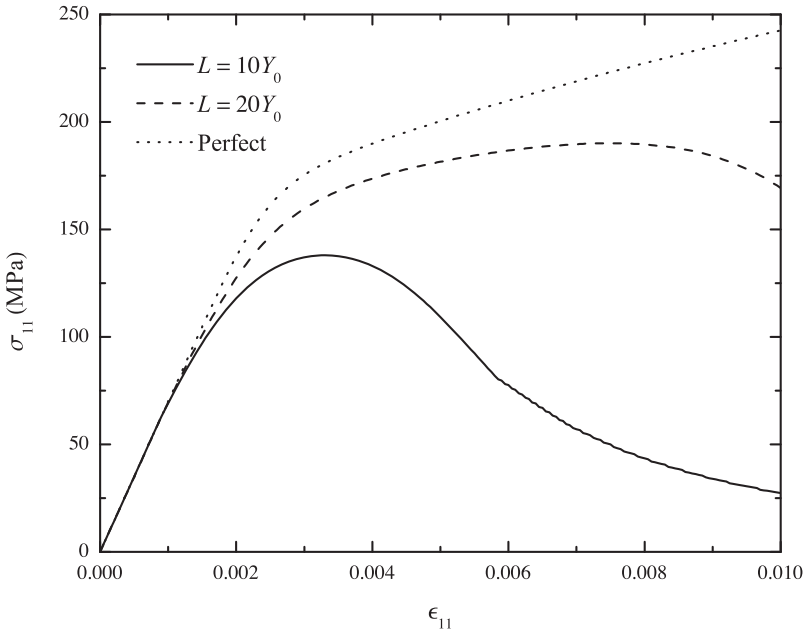

(a) Stress-strain curves.

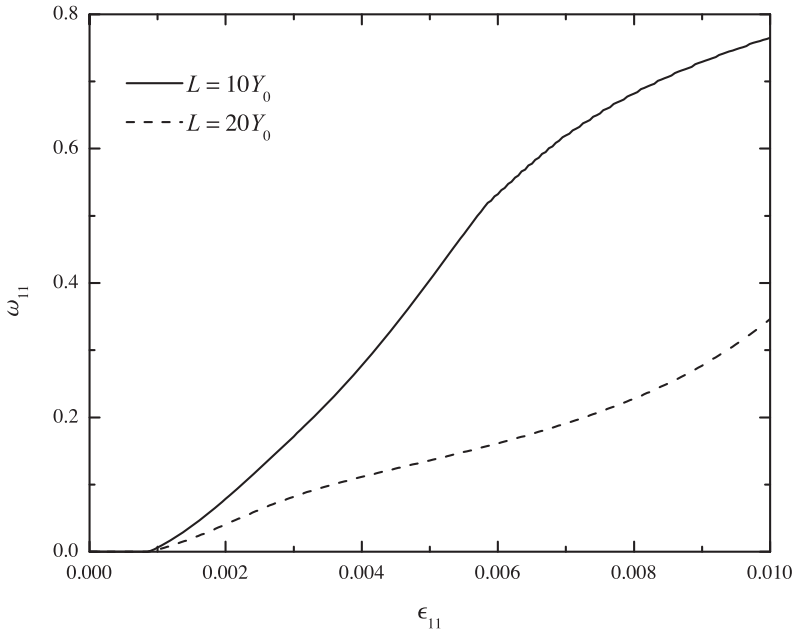

(b) ω_{11}-ϵ_{11} curves.

Figure 2. Stress-strain and ω_{11}-ϵ_{11} curves of a damageable alloy undergoing uniaxial extension in the x_1-direction.

Figures B shows the stress-strain and ω_{11}-ϵ_{11} curves of the material undergoing uniaxial extension in the x_1-direction. It can be verified that, as L_{11} increases, the material becomes more vulnerable to σ_{11}. Accordingly, in Figure B, as L_{11} increases, the stress-strain curve shifts downwards, while the ω_{11}-ϵ_{11} curve shifts upwards. Meanwhile, it can be seen that the curves here exhibit trends similar to those in Figures 2(a). Therefore, the corresponding discussion for Figures 2(a) holds here.

C. Viscoplastic Anisotropy

At last, let the material exhibit viscoplastic transverse isotropy in the x_2-x_3 plane. Specifically, let the material parameters take the values listed in Table 1 with $L = 20Y_0$, and let Eq. (112) hold here. Also let the R_i's of the material take three sets of values listed in Table 2 in three cases (see Appendix A for more details).

Table 2. R_i's in three cases.

	R_1	R_2	R_3	R_4	R_5	R_6
1	1	1	0.707	1	0.707	1.414
2	1	1	1	1	1	1
3	1	1	1.414	1	1.414	0.707

Figures 4 shows the stress-strain and ω_{11}-ϵ_{11} curves of the material undergoing uniaxial extension in the x_2-direction. In fact, the following findings can be obtained after some calculation:

1. All sets of values yield the same initial yield stress in the x_1-direction;

2. The initial yield stress in the x_2-direction decreases with increasing R_3.

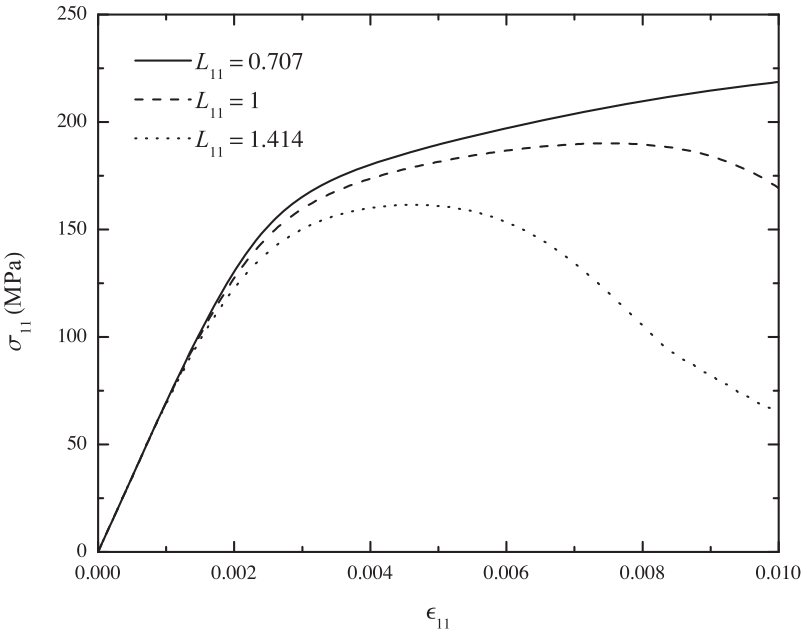

(a) Stress-strain curves.

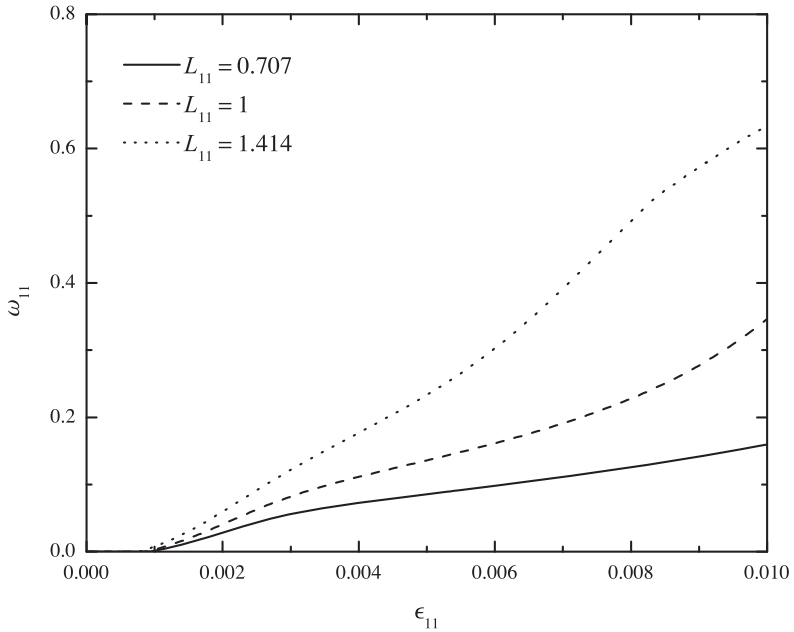

(b) ω_{11}-ϵ_{11} curves.

Figure 3. Stress-strain and ω_{11}-ϵ_{11} curves of an alloy exhibiting general damage anisotropy, undergoing uniaxial extension in the x_1-direction (continued).

Accordingly, for $R_3 = R_5 = 0.707$, σ_{22} attains a high level at an early stage of deformation, enabling damages to evolve to a considerable extent. This leads the material to behave like a damageable elastic one afterwards. In contrast, for $R_3 = R_5 = 1.414$, σ_{22} remains at a low level during continued deformation, prohibiting damages from evolving. This leads the material to behave like a perfect elasto-viscoplastic one.

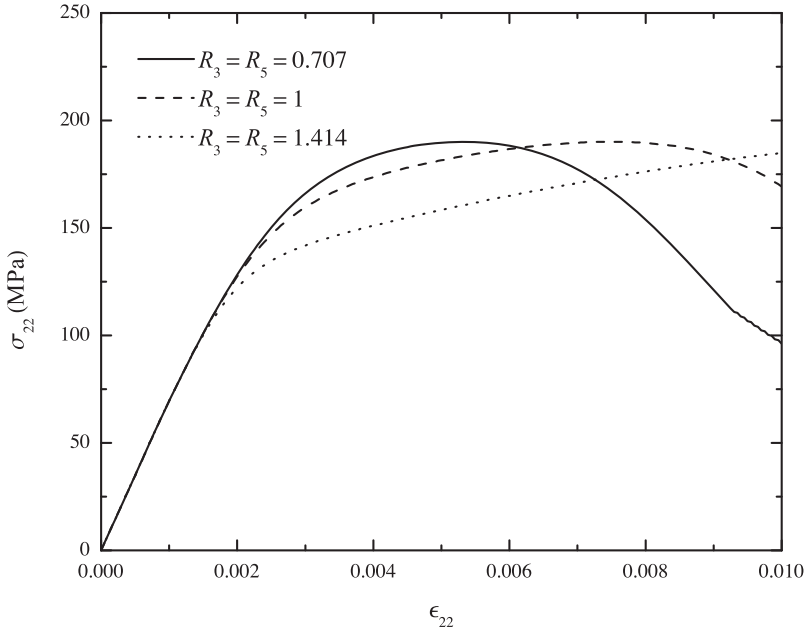

(a) Stress-strain curves.

IX. Conclusions

In this paper, the closed-form constitutive relations for damageable elasto-viscoplastic materials, which exhibit damage anisotropy, damage hardening, viscoplastic anisotropy, and combined isotropic-kinematic hardening, are derived. Some fundamentals of continuum damage mechanics and thermodynamics are briefed, and the second-order damage tensor is redefined with an emphasis on a clear physical meaning. An affine formulation of the constitutive relations in the undamaged configuration, the damage evolution law, and the constitutive relations in the damaged configuration are subsequently derived. The current constitutive relations are validated by modeling an aluminium alloy exhibiting various material behaviors. They are found to be capable of handling complex material models.

The following conclusions can be drawn:

1. The interaction between the rate dependency and damage behavior of a material can also be evaluated;
2. More complex loading conditions and loading paths can be involved;
3. More sophisticated material behaviors can be incorporated into the current constitutive relations.

Acknowledgements

This work is supported by the US AFOSR Multiscale Structural Mechanics and Prognosis Program. The views and conclusions contained herein are those of the authors and should not be interpreted as necessarily representing the official policies or endorsement, either expressed or implied, of the sponsor.

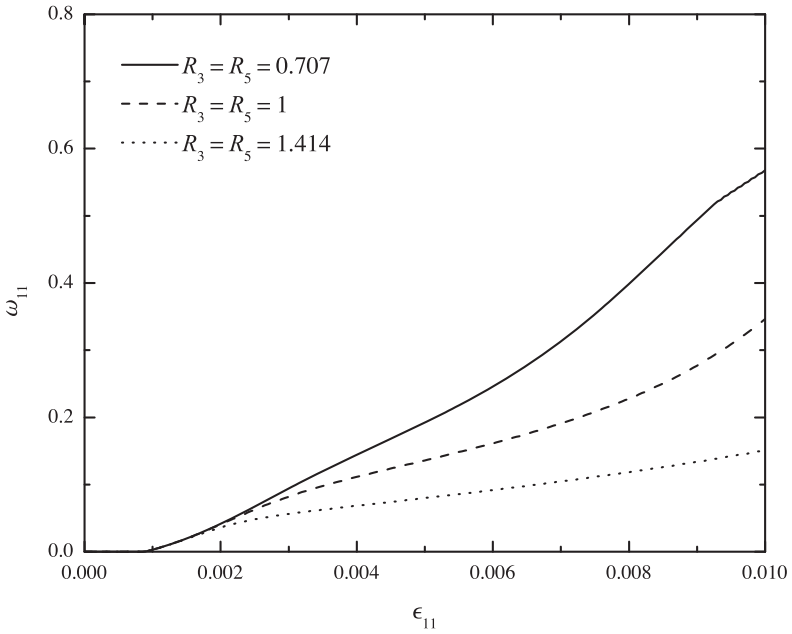

(b) ω_{22}-ϵ_{22} curves.

Figure 4. Stress-strain and ω_{22}-ϵ_{22} curves of a damageable alloy exhibiting viscoplastic anisotropy, undergoing uniaxial extension in the x_2-direction.

Appendix

A. Viscoplastic Anisotropic Parameters

The R-value is widely used to characterize the viscoplastic anisotropy of rolled sheet metals and can be measured in a series of uniaxial tensile tests. Specifically, when a tensile specimen cut from a sheet is stretched, its R-value is defined as the ratio of the viscoplastic strain in the width direction to that in the thickness direction, i.e.,

$$R = \frac{\epsilon_W}{\epsilon_T}. \tag{113}$$

In general, the R-value varies with the cut angle with respect to the rolling direction of the sheet, α. In this case, an averaged R-value is often adopted. It is defined as

$$\bar{R} = \frac{R_0 + 2R_{45} + R_{90}}{4}, \tag{114}$$

where R_α denotes the R-value measured in a tensile specimen of cut angle α.

Benzerga and Besson[34] enriched the concept of the R-value by introducing six strain rate ratios, R_{ij}, which are capable of fully characterizing the viscoplastic anisotropy of a 3D structure. Similarly to the R-value, each of these ratios can be measured in either a uniaxial tensile test or a simple shear test. Specifically, introduce Cartesian coordinates $\mathbf{x} = (x_1, x_2, x_3)$ with its three axes parallel to the orthotropic axes of the constituent. These ratios can then be defined as

$$R_{11} = \frac{\dot{\epsilon}_{22}}{\dot{\epsilon}_{33}}, \quad R_{12} = \frac{\dot{\epsilon}_{12}}{\dot{\epsilon}_{33}}, \quad R_{22} = \frac{\dot{\epsilon}_{33}}{\dot{\epsilon}_{11}}, \tag{115}$$

$$R_{13} = \frac{\dot{\epsilon}_{13}}{\dot{\epsilon}_{22}}, \quad R_{23} = \frac{\dot{\epsilon}_{23}}{\dot{\epsilon}_{11}}, \quad R_{33} = \frac{\dot{\epsilon}_{11}}{\dot{\epsilon}_{22}}. \tag{115$'$}$$

R_{ij} can be written in the Voigt notation as

$$R_1 = R_{11}, \quad R_2 = R_{12}, \quad R_3 = R_{22}, \tag{116}$$

$$R_4 = R_{13}, \quad R_5 = R_{23}, \quad R_6 = R_{33}. \tag{116'}$$

It can be obtained from Eq. (115) that $R_6 = 1/R_1R_3$. This implies that only five out of the six R_i's are independent.

$\mathcal{H}_{ijkl}$ can be written in the Voigt notation as H_{ij}. The diagonal components of H_{ij} can be related to R_i by[34]

$$H_{11} = -\frac{2}{3}\frac{R_1R_3 - 2R_1 - 2}{R_1 + 1}, \quad \frac{H_{22}}{H_{11}} = -\frac{1}{2}\frac{(2R_2 + 1)(R_1R_3 + 1)}{R_1R_3 - 2R_1 - 2}, \tag{117}$$

$$\frac{H_{33}}{H_{11}} = 1 - \frac{3(R_1R_3 - 1)}{R_1R_3 - 2R_1 - 2}, \quad \frac{H_{44}}{H_{11}} = -\frac{1}{2}\frac{(2R_4 + 1)(R_3 + 1)R_1}{R_1R_3 - 2R_1 - 2}, \tag{117'}$$

$$\frac{H_{55}}{H_{11}} = -\frac{1}{2}\frac{(2R_5 + 1)(R_1 + 1)}{R_1R_3 - 2R_1 - 2}, \quad \frac{H_{66}}{H_{11}} = 1 - \frac{3R_1(R_3 - 1)}{R_1R_3 - 2R_1 - 2}, \tag{117''}$$

while the off-diagonal components vanish. More details on $\boldsymbol{\mathcal{H}}$ can be found in Ref. [34], Appendix A.

A special case of viscoplastic anisotropy is viscoplastic transverse isotropy, in which case there exists a plane of viscoplastic isotropy. Without loss of generality, let the x_2-x_3 plane be the plane of viscoplastic isotropy. R_i can then be expressed as

$$R_3 = R_5 = \frac{1}{R_6} = R \quad \text{and} \quad R_2 = R_4 = R', \tag{118}$$

where R and R' can be measured in a uniaxial tensile test and a simple shear test, respectively. Substituting Eq. (118) into Eq. (117) and rearranging the equations give

$$H_{11} = \frac{1}{3}(4 - R), \quad H_{22} = H_{44} = \frac{1}{6}(R + 1)(2R' + 1), \tag{119}$$

$$H_{33} = H_{55} = H_{66} = \frac{1}{3}(2R + 1). \tag{119'}$$

B. Partial Derivatives

Recall that the partial derivatives whose explicit expressions are to be derived are

$$\boldsymbol{\mathcal{K}} = \frac{\partial \dot{\bar{\boldsymbol{\epsilon}}}^{vp}}{\partial \bar{\boldsymbol{\sigma}}}, \quad \mathbf{L} = \frac{\partial \dot{\bar{\boldsymbol{\epsilon}}}^{vp}}{\partial \bar{p}}, \quad \boldsymbol{\mathcal{M}} = \frac{\partial \dot{\bar{\boldsymbol{\epsilon}}}^{vp}}{\partial \bar{\mathbf{X}}}, \quad \mathbf{N} = \frac{\partial \dot{\bar{p}}}{\partial \bar{\boldsymbol{\sigma}}}, \quad P = \frac{\partial \dot{\bar{p}}}{\partial \bar{p}}, \quad \mathbf{Q} = \frac{\partial \dot{\bar{p}}}{\partial \bar{\mathbf{X}}}, \tag{120}$$

$$\boldsymbol{\mathcal{R}} = \frac{\partial \dot{\bar{\mathbf{X}}}}{\partial \bar{\boldsymbol{\sigma}}}, \quad \mathbf{S} = \frac{\partial \dot{\bar{\mathbf{X}}}}{\partial \bar{p}}, \quad \boldsymbol{\mathcal{T}} = \frac{\partial \dot{\bar{\mathbf{X}}}}{\partial \bar{\mathbf{X}}}. \tag{120'}$$

Let $\boldsymbol{\mathcal{K}}$, $\mathbf{L}$, and $\boldsymbol{\mathcal{M}}$ be the first set of partial derivatives of interest. Recall that $\tilde{\bar{\sigma}}_e = \tilde{\bar{\sigma}}_e(\tilde{\bar{\boldsymbol{\sigma}}}) = \tilde{\bar{\sigma}}_e(\bar{\boldsymbol{\sigma}} - \bar{\mathbf{X}})$ (see Eq. (25)). It can then be obtained using the chain rule that

$$\frac{\partial \tilde{\bar{\sigma}}_e}{\partial \bar{\boldsymbol{\sigma}}} = \frac{\partial \tilde{\bar{\sigma}}_e}{\partial \tilde{\bar{\boldsymbol{\sigma}}}} : \frac{\partial \tilde{\bar{\boldsymbol{\sigma}}}}{\partial \bar{\boldsymbol{\sigma}}} = \frac{\partial \tilde{\bar{\sigma}}_e}{\partial \tilde{\bar{\boldsymbol{\sigma}}}} : \boldsymbol{\mathcal{I}} = \frac{\partial \tilde{\bar{\sigma}}_e}{\partial \tilde{\bar{\boldsymbol{\sigma}}}}, \tag{121}$$

$$\frac{\partial \tilde{\bar{\sigma}}_e}{\partial \bar{\mathbf{X}}} = \frac{\partial \tilde{\bar{\sigma}}_e}{\partial \tilde{\bar{\boldsymbol{\sigma}}}} : \frac{\partial \tilde{\bar{\boldsymbol{\sigma}}}}{\partial \bar{\mathbf{X}}} = \frac{\partial \tilde{\bar{\sigma}}_e}{\partial \tilde{\bar{\boldsymbol{\sigma}}}} : (-\boldsymbol{\mathcal{I}}) = -\frac{\partial \tilde{\bar{\sigma}}_e}{\partial \tilde{\bar{\boldsymbol{\sigma}}}}. \tag{121'}$$

Recall that, when $f^{vp} > 0$, $\dot{\bar{\lambda}}^{vp}$ is given by

$$\dot{\bar{\lambda}}^{vp} = \frac{1}{\bar{\eta}}\left(\frac{f^{vp}}{\bar{\sigma}_Y}\right)^{\bar{N}} = \frac{1}{\bar{\eta}}\left(\frac{\tilde{\bar{\sigma}}_e}{\bar{\sigma}_Y} - 1\right)^{\bar{N}} \tag{122}$$

and that

$$\frac{\partial f^{vp}}{\partial \bar{\boldsymbol{\sigma}}} = \frac{\partial g^{vp}}{\partial \bar{\boldsymbol{\sigma}}} = \frac{\partial \tilde{\bar{\sigma}}_e}{\partial \tilde{\bar{\boldsymbol{\sigma}}}} = \frac{3}{2\tilde{\bar{\sigma}}_e}\boldsymbol{\mathcal{J}} : \boldsymbol{\mathcal{H}} : \tilde{\bar{\boldsymbol{\sigma}}}'. \tag{123}$$

The first equation of Eq. (34), together with Eqs. (122) and (123), implies that $\dot{\tilde{\boldsymbol{\epsilon}}}^{vp} = \dot{\tilde{\boldsymbol{\epsilon}}}^{vp}(\tilde{\boldsymbol{\sigma}}, \bar{p})$. Similarly to Eq. (121), one obtains

$$\frac{\partial \dot{\tilde{\boldsymbol{\epsilon}}}^{vp}}{\partial \tilde{\boldsymbol{\sigma}}} = \frac{\partial \dot{\tilde{\boldsymbol{\epsilon}}}^{vp}}{\partial \bar{\boldsymbol{\sigma}}} = -\frac{\partial \dot{\tilde{\boldsymbol{\epsilon}}}^{vp}}{\partial \bar{\mathbf{X}}} \quad \text{or} \quad \boldsymbol{\mathcal{M}} = -\boldsymbol{\mathcal{K}}. \tag{124}$$

By definition, $\boldsymbol{\mathcal{K}}$ can be expressed as

$$\boldsymbol{\mathcal{K}} = \frac{\partial \dot{\tilde{\boldsymbol{\epsilon}}}^{vp}}{\partial \tilde{\boldsymbol{\sigma}}} = \frac{\partial}{\partial \tilde{\boldsymbol{\sigma}}}\left(\dot{\tilde{\lambda}}^{vp}\frac{\partial g}{\partial \bar{\boldsymbol{\sigma}}}\right) = \left[\frac{\partial \dot{\tilde{\lambda}}^{vp}}{\partial \tilde{\boldsymbol{\sigma}}} \otimes \frac{\partial \tilde{\bar{\sigma}}_e}{\partial \tilde{\boldsymbol{\sigma}}} + \dot{\tilde{\lambda}}^{vp}\frac{\partial}{\partial \tilde{\boldsymbol{\sigma}}}\left(\frac{\partial \tilde{\bar{\sigma}}_e}{\partial \tilde{\boldsymbol{\sigma}}}\right)\right], \tag{125}$$

where

$$\frac{\partial \dot{\tilde{\lambda}}^{vp}}{\partial \tilde{\boldsymbol{\sigma}}} = \frac{\bar{N}}{\bar{\eta}}\left(\frac{\tilde{\bar{\sigma}}_e}{\bar{\sigma}_Y} - 1\right)^{\bar{N}-1}\frac{\partial}{\partial \tilde{\boldsymbol{\sigma}}}\left(\frac{\tilde{\bar{\sigma}}_e}{\bar{\sigma}_Y} - 1\right) = \frac{\bar{N}}{\bar{\eta}\bar{\sigma}_Y}\left(\frac{\tilde{\bar{\sigma}}_e}{\bar{\sigma}_Y} - 1\right)^{\bar{N}-1}\frac{\partial \tilde{\bar{\sigma}}_e}{\partial \tilde{\boldsymbol{\sigma}}}, \tag{126}$$

and

$$\begin{aligned}\frac{\partial}{\partial \tilde{\boldsymbol{\sigma}}}\left(\frac{\partial \tilde{\bar{\sigma}}_e}{\partial \tilde{\boldsymbol{\sigma}}}\right) &= \frac{\partial}{\partial \tilde{\boldsymbol{\sigma}}}\left(\frac{3}{2\tilde{\bar{\sigma}}_e}\boldsymbol{\mathcal{J}} : \boldsymbol{\mathcal{H}} : \tilde{\boldsymbol{\sigma}}'\right) = \frac{3}{2}\frac{\partial}{\partial \tilde{\boldsymbol{\sigma}}}\left(\frac{1}{\tilde{\bar{\sigma}}_e}\right) \otimes \boldsymbol{\mathcal{J}} : \boldsymbol{\mathcal{H}} : \tilde{\boldsymbol{\sigma}}' + \frac{3}{2\tilde{\bar{\sigma}}_e}\boldsymbol{\mathcal{J}} : \boldsymbol{\mathcal{H}} : \frac{\partial \tilde{\boldsymbol{\sigma}}'}{\partial \tilde{\boldsymbol{\sigma}}} \\ &= \frac{3}{2}\left(-\frac{1}{\tilde{\bar{\sigma}}_e^2}\frac{\partial \tilde{\bar{\sigma}}_e}{\partial \tilde{\boldsymbol{\sigma}}}\right) \otimes \boldsymbol{\mathcal{J}} : \boldsymbol{\mathcal{H}} : \tilde{\boldsymbol{\sigma}}' + \frac{3}{2\tilde{\bar{\sigma}}_e}\boldsymbol{\mathcal{J}} : \boldsymbol{\mathcal{H}} : \boldsymbol{\mathcal{J}} = -\frac{1}{\tilde{\bar{\sigma}}_e}\frac{\partial \tilde{\bar{\sigma}}_e}{\partial \tilde{\boldsymbol{\sigma}}} \otimes \frac{\partial \tilde{\bar{\sigma}}_e}{\partial \tilde{\boldsymbol{\sigma}}} + \frac{3}{2\tilde{\bar{\sigma}}_e}\boldsymbol{\mathcal{J}} : \boldsymbol{\mathcal{H}} : \boldsymbol{\mathcal{J}}.\end{aligned} \tag{127}$$

Substituting Eqs. (126) and (127) into Eq. (125) and rearranging the equation give

$$\boldsymbol{\mathcal{K}} = \frac{\partial \dot{\tilde{\boldsymbol{\epsilon}}}^{vp}}{\partial \tilde{\boldsymbol{\sigma}}} = \frac{1}{\bar{\eta}}\left(\frac{\tilde{\bar{\sigma}}_e}{\bar{\sigma}_Y} - 1\right)^{\bar{N}-1}\left[\left(\frac{\bar{N}-1}{\bar{\sigma}_Y} + \frac{1}{\tilde{\bar{\sigma}}_e}\right)\frac{\partial \tilde{\bar{\sigma}}_e}{\partial \tilde{\boldsymbol{\sigma}}} \otimes \frac{\partial \tilde{\bar{\sigma}}_e}{\partial \tilde{\boldsymbol{\sigma}}} + \frac{3}{2}\left(\frac{1}{\bar{\sigma}_Y} - \frac{1}{\tilde{\bar{\sigma}}_e}\right)\boldsymbol{\mathcal{J}} : \boldsymbol{\mathcal{H}} : \boldsymbol{\mathcal{J}}\right]. \tag{128}$$

Similarly to $\boldsymbol{\mathcal{K}}$, $\mathbf{L}$ can be expressed as

$$\mathbf{L} = \frac{\partial \dot{\tilde{\boldsymbol{\epsilon}}}^{vp}}{\partial \bar{p}} = \frac{\partial}{\partial \bar{p}}\left(\dot{\tilde{\lambda}}^{vp}\frac{\partial g}{\partial \bar{\boldsymbol{\sigma}}}\right) = \frac{\partial \dot{\tilde{\lambda}}^{vp}}{\partial \bar{p}}\frac{\partial \tilde{\bar{\sigma}}_e}{\partial \tilde{\boldsymbol{\sigma}}}, \tag{129}$$

where

$$\frac{\partial \dot{\tilde{\lambda}}^{vp}}{\partial \bar{p}} = \frac{\bar{N}}{\bar{\eta}}\left(\frac{\tilde{\bar{\sigma}}_e}{\bar{\sigma}_Y} - 1\right)^{\bar{N}-1}\frac{\partial}{\partial \bar{p}}\left(\frac{\tilde{\bar{\sigma}}_e}{\bar{\sigma}_Y} - 1\right) = -\frac{\bar{N}}{\bar{\eta}}\frac{\tilde{\bar{\sigma}}_e}{\bar{\sigma}_Y^2}\left(\frac{\tilde{\bar{\sigma}}_e}{\bar{\sigma}_Y} - 1\right)^{\bar{N}-1}\frac{d\bar{R}}{d\bar{p}}. \tag{130}$$

Substituting Eqs. (130) into Eq. (129) gives and rearranging the equation give

$$\mathbf{L} = \frac{\partial \dot{\tilde{\boldsymbol{\epsilon}}}^{vp}}{\partial \bar{p}} = -\frac{\bar{N}}{\bar{\eta}}\frac{\tilde{\bar{\sigma}}_e}{\bar{\sigma}_Y^2}\left(\frac{\tilde{\bar{\sigma}}_e}{\bar{\sigma}_Y} - 1\right)^{\bar{N}-1}\frac{d\bar{R}}{d\bar{p}}\frac{\partial \tilde{\bar{\sigma}}_e}{\partial \tilde{\boldsymbol{\sigma}}}. \tag{131}$$

Let $\mathbf{N}$, P, and $\mathbf{Q}$ be the next set of partial derivatives of interest. Recall that $\dot{\bar{p}} = \dot{\tilde{\lambda}}^{vp}$. This, together with Eq. (122), implies that $\dot{\bar{p}} = \dot{\bar{p}}(\tilde{\boldsymbol{\sigma}}, \bar{p})$. Similarly to Eq. (121), one obtains

$$\frac{\partial \dot{\bar{p}}}{\partial \tilde{\boldsymbol{\sigma}}} = \frac{\partial \dot{\bar{p}}}{\partial \bar{\boldsymbol{\sigma}}} = -\frac{\partial \dot{\bar{p}}}{\partial \bar{\mathbf{X}}} \quad \text{or} \quad \mathbf{Q} = -\mathbf{N}. \tag{132}$$

By definition, $\mathbf{N}$ and P can be expressed as

$$\mathbf{N} = \frac{\partial \dot{\bar{p}}}{\partial \tilde{\boldsymbol{\sigma}}} = \frac{\partial \dot{\tilde{\lambda}}^{vp}}{\partial \tilde{\boldsymbol{\sigma}}} = \frac{\bar{N}}{\bar{\eta}\bar{\sigma}_Y}\left(\frac{\tilde{\bar{\sigma}}_e}{\bar{\sigma}_Y} - 1\right)^{\bar{N}-1}\frac{\partial \tilde{\bar{\sigma}}_e}{\partial \tilde{\boldsymbol{\sigma}}} \tag{133}$$

and

$$P = \frac{\partial \dot{\bar{p}}}{\partial \bar{p}} = \frac{\partial \dot{\tilde{\lambda}}^{vp}}{\partial \bar{p}} = -\frac{\bar{N}}{\bar{\eta}}\frac{\tilde{\bar{\sigma}}_e}{\bar{\sigma}_Y^2}\left(\frac{\tilde{\bar{\sigma}}_e}{\bar{\sigma}_Y} - 1\right)^{\bar{N}-1}\frac{d\bar{R}}{d\bar{p}}, \tag{134}$$

respectively.

Now the remaining partial derivatives are $\boldsymbol{\mathcal{R}}$, $\mathbf{S}$, and $\boldsymbol{\mathcal{T}}$. Recall that

$$\dot{\bar{\mathbf{X}}} = \frac{2}{3}\bar{C}\dot{\tilde{\boldsymbol{\epsilon}}}^{vp} - \bar{\gamma}\bar{\mathbf{X}}\dot{\bar{p}}. \tag{135}$$

Substituting Eq. (135) into the last three equations of Eq. (120) gives

$$\boldsymbol{\mathcal{R}} = \frac{\partial \dot{\bar{\mathbf{X}}}}{\partial \bar{\boldsymbol{\sigma}}} = \frac{2}{3}\bar{C}\frac{\partial \dot{\bar{\boldsymbol{\epsilon}}}^{vp}}{\partial \bar{\boldsymbol{\sigma}}} - \bar{\gamma}\frac{\partial \dot{\bar{p}}}{\partial \bar{\boldsymbol{\sigma}}} \otimes \bar{\mathbf{X}} = \frac{2}{3}\bar{C}\boldsymbol{\mathcal{K}} - \bar{\gamma}\mathbf{N} \otimes \bar{\mathbf{X}}, \tag{136}$$

$$\mathbf{S} = \frac{\partial \dot{\bar{\mathbf{X}}}}{\partial \bar{p}} = \frac{2}{3}\bar{C}\frac{\partial \dot{\bar{\boldsymbol{\epsilon}}}^{vp}}{\partial \bar{p}} - \bar{\gamma}\frac{\partial \dot{\bar{p}}}{\partial \bar{p}}\bar{\mathbf{X}} = \frac{2}{3}\bar{C}\mathbf{L} - \bar{\gamma}P\bar{\mathbf{X}}, \tag{136$'$}$$

$$\begin{aligned}\boldsymbol{\mathcal{T}} = \frac{\partial \dot{\bar{\mathbf{X}}}}{\partial \bar{\mathbf{X}}} &= \frac{2}{3}\bar{C}\frac{\partial \dot{\bar{\boldsymbol{\epsilon}}}^{vp}}{\partial \bar{\mathbf{X}}} - \bar{\gamma}\left(\frac{\partial \dot{\bar{p}}}{\partial \bar{\mathbf{X}}} \otimes \bar{\mathbf{X}} + \dot{\bar{p}}\frac{\partial \bar{\mathbf{X}}}{\partial \bar{\mathbf{X}}}\right) \\ &= -\left(\frac{2}{3}\bar{C}\frac{\partial \dot{\bar{\boldsymbol{\epsilon}}}^{vp}}{\partial \bar{\boldsymbol{\sigma}}} - \bar{\gamma}\frac{\partial \dot{\bar{p}}}{\partial \bar{\boldsymbol{\sigma}}} \otimes \bar{\mathbf{X}}\right) - \bar{\gamma}\dot{\bar{p}}\boldsymbol{\mathcal{I}} = -\boldsymbol{\mathcal{R}} - \bar{\gamma}\dot{\bar{p}}\boldsymbol{\mathcal{I}}.\end{aligned} \tag{136$''$}$$

Note that, in Eq. (136), $\boldsymbol{\mathcal{T}} \neq -\boldsymbol{\mathcal{R}}$ because $\dot{\bar{\mathbf{X}}} \neq \dot{\bar{\mathbf{X}}}\left(\tilde{\bar{\boldsymbol{\sigma}}}, \bar{p}\right)$.

Till now, the explicit expressions for all the partial derivatives in Eq. (120) (or Eq. (46)) have been derived.

References

[1]Krajcinovic, D., "Continuous damage mechanics," *Applied Mechanics Reviews*, Vol. 37, No. 1, 1984, pp. 1–6.

[2]Lubliner, J., Oliver, J., Oller, S., and Oñate, E., "A plastic-damage model for concrete," *International Journal of Solids and Structures*, Vol. 25, No. 3, 1989, pp. 299–326.

[3]Faria, R., Oliver, J., and Cervera, M., "A strain-based plastic viscous-damage model for massive concrete structures," *International Journal of Solids and Structures*, Vol. 35, No. 14, 1998, pp. 1533–1558.

[4]Lee, J. and Fenves, G. L., "Plastic-damage model for cyclic loading of concrete structures," *Journal of Engineering Mechanics*, Vol. 124, No. 8, 1998, pp. 892–900.

[5]Peerlings, R., De Borst, R., Brekelmans, W., and Geers, M., "Gradient-enhanced damage modelling of concrete fracture," *Mechanics of Cohesive-frictional Materials*, Vol. 3, No. 4, 1998, pp. 323–342.

[6]Jason, L., Huerta, A., Pijaudier-Cabot, G., and Ghavamian, S., "An elastic plastic damage formulation for concrete: application to elementary tests and comparison with an isotropic damage model," *Computer Methods in Applied Mechanics and Engineering*, Vol. 195, No. 52, 2006, pp. 7077–7092.

[7]Wu, J. Y., Li, J., and Faria, R., "An energy release rate-based plastic-damage model for concrete," *International Journal of Solids and Structures*, Vol. 43, No. 3, 2006, pp. 583–612.

[8]Krajcinovic, D. and Fonseka, G., "The continuous damage theory of brittle materials. Part I: General theory." *Journal of Applied Mechanics*, Vol. 48, No. 4, 1981, pp. 809.

[9]Murakami, S. and Ohno, N., "A continuum theory of creep and creep damage," *Creep in Structures*, Springer, 1981, pp. 422–444.

[10]Chaboche, J.-L., "Continuous damage mechanicsa tool to describe phenomena before crack initiation," *Nuclear Engineering and Design*, Vol. 64, No. 2, 1981, pp. 233–247.

[11]Ortiz, M., "A constitutive theory for the inelastic behavior of concrete," *Mechanics of Materials*, Vol. 4, No. 1, 1985, pp. 67–93.

[12]Simo, J. and Ju, J., "Strain- and stress-based continuum damage modelsII. Computational aspects," *International Journal of Solids and Structures*, Vol. 23, No. 7, 1987, pp. 841–869.

[13]Ju, J., "Isotropic and anisotropic damage variables in continuum damage mechanics," *Journal of Engineering Mechanics*, Vol. 116, No. 12, 1990, pp. 2764–2770.

[14]Yazdani, S. and Schreyer, H., "Combined plasticity and damage mechanics model for plain concrete," *Journal of Engineering Mechanics*, Vol. 116, No. 7, 1990, pp. 1435–1450.

[15]Chaboche, J.-L., "Development of continuum damage mechanics for elastic solids sustaining anisotropic and unilateral damage," *International Journal of Damage Mechanics*, Vol. 2, No. 4, 1993, pp. 311–329.

[16]Lubarda, V. and Krajcinovic, D., "Damage tensors and the crack density distribution," *International Journal of Solids and Structures*, Vol. 30, No. 20, 1993, pp. 2859–2877.

[17]Govindjee, S., Kay, G. J., and Simo, J. C., "Anisotropic modelling and numerical simulation of brittle damage in concrete," *International Journal for Numerical Methods in Engineering*, Vol. 38, No. 21, 1995, pp. 3611–3633.

[18]Halm, D. and Dragon, A., "A model of anisotropic damage by mesocrack growth; unilateral effect," *International Journal of Damage Mechanics*, Vol. 5, No. 4, 1996, pp. 384–402.

[19]Gatuingt, F. and Pijaudier-Cabot, G., "Coupled damage and plasticity modelling in transient dynamic analysis of concrete," *International Journal for Numerical and Analytical Methods in Geomechanics*, Vol. 26, No. 1, 2002, pp. 1–24.

[20]Abu Al-Rub, R. K. and Voyiadjis, G. Z., "On the coupling of anisotropic damage and plasticity models for ductile materials," *International Journal of Solids and Structures*, Vol. 40, No. 11, 2003, pp. 2611–2643.

[21]Menzel, A., Ekh, M., Runesson, K., and Steinmann, P., "A framework for multiplicative elastoplasticity with kinematic hardening coupled to anisotropic damage," *International Journal of Plasticity*, Vol. 21, No. 3, 2005, pp. 397–434.

[22]Cicekli, U., Voyiadjis, G. Z., and Abu Al-Rub, R. K., "A plasticity and anisotropic damage model for plain concrete," *International Journal of Plasticity*, Vol. 23, No. 10, 2007, pp. 1874–1900.

[23]Voyiadjis, G. Z., Taqieddin, Z. N., and Kattan, P. I., "Anisotropic damage-plasticity model for concrete," *International Journal of Plasticity*, Vol. 24, No. 10, 2008, pp. 1946–1965.

[24]Masson, R. and Zaoui, A., "Self-consistent estimates for the rate-dependent elastoplastic behaviour of polycrystalline materials," *Journal of the Mechanics and Physics of Solids*, Vol. 47, No. 7, 1999, pp. 1543–1568.

[25]Masson, R., Bornert, M., Suquet, P., and Zaoui, A., "An affine formulation for the prediction of the effective properties of nonlinear composites and polycrystals," *Journal of the Mechanics and Physics of Solids*, Vol. 48, No. 6-7, 2000, pp. 1203–1227.

[26]Doghri, I., Adam, L., and Bilger, N., "Mean-field homogenization of elasto-viscoplastic composites based on a general incrementally affine linearization method," *International Journal of Plasticity*, Vol. 26, No. 2, 2010, pp. 219–238.

[27]Voyiadjis, G. Z., Abu Al-Rub, R. K., and Palazotto, A. N., "Thermodynamic framework for coupling of non-local viscoplasticity and non-local anisotropic viscodamage for dynamic localization problems using gradient theory," *International Journal of Plasticity*, Vol. 20, No. 6, 2004, pp. 981–1038.

[28]Zaïri, F., Naït-Abdelaziz, M., Woznica, K., and Gloaguen, J.-M., "Constitutive equations for the viscoplastic-damage behaviour of a rubber-modified polymer," *European Journal of Mechanics-A/Solids*, Vol. 24, No. 1, 2005, pp. 169–182.

[29]Zaïri, F., Naït-Abdelaziz, M., Gloaguen, J.-M., and Lefebvre, J.-M., "Modelling of the elasto-viscoplastic damage behaviour of glassy polymers," *International Journal of Plasticity*, Vol. 24, No. 6, 2008, pp. 945–965.

[30]Balieu, R., Lauro, F., Bennani, B., Delille, R., Matsumoto, T., and Mottola, E., "A fully coupled elastoviscoplastic damage model at finite strains for mineral filled semi-crystalline polymer," *International Journal of Plasticity*, Vol. 51, 2013, pp. 241–270.

[31]Cordebois, J. and Sidoroff, F., "Anisotropic damage in elasticity and plasticity," *Journal de Mécanique Théorique et Appliquée*, 1982, pp. 45–60.

[32]Simo, J. C. and Hughes, T. J. R., *Computational Inelasticity*, Vol. 7 of *Interdisciplinary Applied Mathematics*, Springer, New York, 1998.

[33]Ju, J., "On energy-based coupled elastoplastic damage theories: constitutive modeling and computational aspects," *International Journal of Solids and Structures*, Vol. 25, No. 7, 1989, pp. 803–833.

[34]Benzerga, A. A. and Besson, J., "Plastic potentials for anisotropic porous solids," *European Journal of Mechanics, A/Solids*, Vol. 20, No. 3, 2001, pp. 397–434.

[35]Chaboche, J.-L., "Thermodynamic formulation of constitutive equations and application to the viscoplasticity and viscoelasticity of metals and polymers," *International Journal of Solids and Structures*, Vol. 34, No. 18, 1997, pp. 2239–2254.

[36]Chaboche, J.-L., "Constitutive equations for cyclic plasticity and cyclic viscoplasticity," *International Journal of Plasticity*, Vol. 5, No. 3, 1989, pp. 247–302.

[37]Voce, E., "A practical strain-hardening function," *Metallurgia*, Vol. 51, No. 307, 1955, pp. 219–226.

[38]Besson, J., Cailletaud, G., Chaboche, J.-L., and Forest, S., *Non-linear mechanics of materials*, Vol. 167 of *Solid mechanics and its applications*, Springer, New York, 2010.

[39]Perzyna, P., "Fundamental problems in viscoplasticity," *Advances in Applied Mechanics*, Vol. 9, Academic Press, 1966, pp. 243–377.

[40]Chow, C. and Wang, J., "An anisotropic theory of elasticity for continuum damage mechanics," *International Journal of Fracture*, Vol. 33, No. 1, 1987, pp. 3–16.

[41]Voyiadjis, G. Z. and Thiagarajan, G., "Micro and macro anisotropic cyclic damage-plasticity models for MMCS," *International Journal of Engineering Science*, Vol. 35, No. 5, 1997, pp. 467–484.

[42]Li, J. and Weng, G., "A unified approach from elasticity to viscoelasticity to viscoplasticity of particle-reinforced solids," *International Journal of Plasticity*, Vol. 14, No. 1-3, 1998, pp. 193–208.

[43]Zhao, K. M. and Lee, J. K., "Material properties of aluminum alloy for accurate draw-bend simulation," *Journal of Engineering Materials and Technology*, Vol. 123, No. 3, 2001, pp. 287–292.

AIAA SciTech
5-9 January 2015, Kissimmee, Florida
56th AIAA/ASCE/AHS/ASC Structures, Structural Dynamics, and Materials Conference

A Micromechanics Approach to Homogenizing Damageable Elastoplastic Heterogeneous Materials

Liang Zhang* and Wenbin Yu†
Purdue University, West Lafayette, IN 47907-2045, USA

The objective of this paper is to propose a micromechanics approach to homogenizing damageable elastoplastic heterogeneous materials. The derivation of the constitutive relations for a constituent, which exhibits damage anisotropy, damage hardening, plastic anisotropy, and combined isotropic-kinematic hardening, is briefed. The weak form of the problem is derived using an asymptotic method, discretized using finite elements, and solved using the second-order Runge-Kutta method. The capability of the proposed approach is demonstrated by homogenizing a binary composite with a constituent exhibiting various mechanical behaviors. The proposed approach is found to be capable of handling complex material models. More sophisticated material models can be implemented into the proposed approach.

I. Introduction

Heterogeneous materials are widely used in structural components due to their capability of exhibiting designated in-plane or bending stiffness, ultimate strength, thermal conductivity, or even negative Poisson's ratio. Unfortunately, many of their constituents have plenty of microscopic defects (e.g., microcracks, microvoids, and dislocations), whose evolution often causes harmful changes in the microstructure of such materials. One major challenge is to predict the global responses of damageable elastoplastic heterogeneous materials based on the constituent properties and the microstructural details: on the one hand, it is often difficult or expensive to measure such responses; on the other hand, the scales of the resulting structures are usually several orders of magnitude greater than those of the heterogeneities, making it computationally prohibitive to capture all the microstructural details. All these lead one to seek for a micromechanics approach to solve such problems on the microscopic scale.

The mean field approach is a popular analytical micromechanics approach. Its nonlinear version consists of two major branches, i.e., the tangent and secant approaches. As the name suggests, the tangent approach is based on a tangent linearization of the local constitutive relations,[1–3] while the secant approach is based on a secant linearization.[4,5] Unfortunately, both approaches tend to generate too stiff predictions because they assume uniform linearized constitutive relations in each constituent. To overcome this drawback, several authors[6–9] made use of the second-order moment of the stress or strain within each constituent of a linear comparison composite. The so-call second-order method is capable of generating close predictions and homogenizing high-contrast composites (e.g., rigidly reinforced composites and porous materials). Recently, Wu et al.[10] implemented a so-called gradient-enhanced damage model into the mean field approach and enabled it to homogenize damageable elastoplastic composites. Despite success, the mean field approach suffers from two drawbacks. First, it requires randomly distributed Eshelby-type inclusions. This restricts its application to many realistic materials (e.g., woven composites and open-cell foams). Second, it cannot recover the local fields. This may lead to inaccurate predictions if complex loading paths are involved or prohibit engineers from inspecting the local fields if necessary.

Several computational approaches have been developed to overcome the aforementioned drawbacks. Such an approach often involves a fine discretization of the unit cell (UC) of a heterogeneous material to better capture the microstructural details. The asymptotic homogenization is a popular computational approach.

*Postdoctoral Researcher, School of Aeronautics and Astronautics.
†Associate Professor, School of Aeronautics and Astronautics, AIAA Associate Fellow.

Bensoussan et al.[11] developed its fundamental theory, and Ref. [12] appears as the first implementation of this theory using the finite element method. This approach is based on an asymptotic expansion of the displacement into its average over the UC and a periodic fluctuating part, making it capable of easily applying periodic boundaries conditions using the master-slave elimination method. Fish and his coworkers[13,14] further enabled this approach to homogenize damageable elastic composites. Aboudi[15,16] developed another computational approach, the method of cells (MOC) or the generalized method of cells (GMC), which involves a discretization of the UC into rectangular (2D) or parallelepiped (3D) subcells and an approximation of the local quantities using their averages over each subcell. Despite improvements, MOC or GMC cannot generate very accurate predictions because their microstructural details and local fields are captured without sufficient accuracies.

Several authors also developed computational approaches based on the displacement-based finite element method (no asymptotic expansion of the displacement). Unlike the asymptotic homogenization, here it becomes challenging to apply periodic boundary conditions because the displacement itself is aperiodic. Markovic and Ibrahimbegovic[17] proposed an approach to handling the micro-macro transitions in multiscale finite element models, yet requiring displacement or traction boundary conditions at the UC level. Sun and Vaidya[18] successfully applied periodic boundary conditions to the UC of a long fiber-reinforced composite, while Smit et al.[19] used a similar approach in their multiscale finite element models. Miehe[20] proposed an implicit approach to applying periodic boundary conditions, requiring a Newton-Raphson iteration, while Xia and his coworkers[21,22] proposed an explicit approach in which a master stiffness equation has to be solved for six times. Despite success, both approaches are more computationally costly than those in the asymptotic homogenization.

Microscopic defects can be classified into three categories, i.e., line defects (dislocations), planar defects (microcracks and grain boundaries), and volume defects (microvoids). Continuum damage mechanics deals with the macroscopic effect of microcrack propagation and microvoid growth. It combines the internal state variable theory and the theory of irreversible thermodynamics and enables one to derive the constitutive relations for damaged materials. The theory of plasticity deals with the macroscopic effect of dislocation motion and is well established. Unfortunately, neither continuum damage mechanics nor the theory of plasticity can perfectly deal with damageable elastoplastic materials alone. Elaborated efforts have been devoted to deriving the constitutive relations for such materials. Most authors derived their constitutive relations in two different ways: some of them[23–31] formulated their plasticity models in terms of the so-called effective stresses, i.e., the average microscopic stresses acting on the undamaged microbonds of the material, while the others[32–34] formulated their models in terms of the so-called nominal stresses, i.e., the macroscopic stresses acting on the macroscopic material. Recently, Zhang and Yu[35] derived closed-form constitutive relations capable of handling damage anisotropy, damage hardening, plastic anisotropy, and combined isotropic-kinematic hardening. In this paper, such constitutive relations will be adopted to characterize the mechanical behavior of a damageable elastoplastic constituent.

The objective of this paper is to propose a micromechanics approach to homogenizing damageable elastoplastic heterogeneous materials. The derivation of the constitutive relations for a constituent, which exhibits damage anisotropy, damage hardening, plastic anisotropy, and combined isotropic-kinematic hardening, is briefed. The weak form of the problem is derived using an asymptotic method, discretized using finite elements, and solved using the second-order Runge-Kutta method. The capability of the proposed approach is demonstrated by homogenizing a binary composite with a constituent exhibiting various mechanical behaviors.

II. Constitutive Relations

Consider a heterogeneous material having an identifiable UC. Without loss of generality, let its constituents all be elastoplastic and damageable. Note that an perfect elastic constituent can be treated as a damageable elastoplastic one of infinite initial yield stress and damage threshold. In this section, the derivation of the constitutive relations for a constituent will be briefed. More details on the derivation in this section can be found in Ref. [35].

The derivation of the constitutive relations for a damaged material generally starts with two assumptions:

1. Each damaged material can be idealized as an equivalent undamaged material;

2. There exists a one-to-one correspondence between each pair of physical quantities in the damaged and

undamaged configurations.

Let an overbar denote the quantity in the undamaged configuration. The stress tensor in the undamaged configuration (or the effective stress tensor), $\bar{\boldsymbol{\sigma}}$, can be related to that in the damaged configuration, $\boldsymbol{\sigma}$, by

$$\bar{\boldsymbol{\sigma}} = \boldsymbol{\mathcal{M}} : \boldsymbol{\sigma} \quad \text{or} \quad \boldsymbol{\sigma} = \boldsymbol{\mathcal{M}}^{-1} : \bar{\boldsymbol{\sigma}}, \tag{1}$$

where $\boldsymbol{\mathcal{M}}$ denotes the fourth-order damage effect tensor whose form varies with the form of the damage tensor (see Refs. [36–38] for example). Let $\boldsymbol{\omega}$ and $\boldsymbol{\mathcal{D}}$ denote the second- and fourth-order damage tensors, respectively. Also let $\boldsymbol{\omega}$ be symmetric, and let $\boldsymbol{\mathcal{D}}$ be related to $\boldsymbol{\omega}$ by

$$\boldsymbol{\mathcal{D}} = \sum_{i=1}^{3}\sum_{j=1}^{3} \omega_{ij} \mathbf{e}_i \otimes \mathbf{e}_j \otimes \mathbf{e}_i \otimes \mathbf{e}_j, \tag{2}$$

where $\mathbf{e}_i$ denotes the unit vector. It can be verified tha $\boldsymbol{\mathcal{D}}$ fulfills the major and minor symmetries (i.e., $\mathcal{D}_{ijkl} = \mathcal{D}_{klij}$, $\mathcal{D}_{ijkl} = \mathcal{D}_{jikl}$, and $\mathcal{D}_{ijkl} = \mathcal{D}_{ijlk}$). Let $\boldsymbol{\mathcal{M}}^{-1}$ take the form of

$$\boldsymbol{\mathcal{M}}^{-1} = \boldsymbol{\mathcal{I}} - \boldsymbol{\mathcal{D}} \tag{3}$$

throughout this paper, where $\boldsymbol{\mathcal{I}}$ denotes the fourth-order identity tensor. It can be verified that $\boldsymbol{\mathcal{M}}^{-1}$ also fulfills both the major and minor symmetries. Let ρ, ψ^e, and $\boldsymbol{\epsilon}^e$ denote the density of the material, the elastic strain energy per unit mass of the material, and the elastic strain tensor, respectively. The elastic strain energy equivalence hypothesis states that the elastic strain energy of a damaged material should equal that of its equivalent undamaged material, i.e.,[37]

$$\rho\psi^e\left(\boldsymbol{\epsilon}^e, \boldsymbol{\omega}\right) = \rho\psi^e\left(\bar{\boldsymbol{\epsilon}}^e\right) \quad \text{or} \quad \frac{1}{2}\boldsymbol{\sigma} : \boldsymbol{\epsilon}^e = \frac{1}{2}\bar{\boldsymbol{\sigma}} : \bar{\boldsymbol{\epsilon}}^e. \tag{4}$$

Substituting Eq. (1) into Eq. (4) gives

$$\bar{\boldsymbol{\epsilon}}^e = \boldsymbol{\mathcal{M}}^{-1} : \boldsymbol{\epsilon}^e \quad \text{or} \quad \boldsymbol{\epsilon}^e = \boldsymbol{\mathcal{M}} : \bar{\boldsymbol{\epsilon}}^e. \tag{5}$$

Hooke's law can be expressed in the damaged and undamaged configurations as

$$\boldsymbol{\sigma} = \boldsymbol{\mathcal{C}}^e : \boldsymbol{\epsilon}^e \quad \text{and} \quad \bar{\boldsymbol{\sigma}} = \bar{\boldsymbol{\mathcal{C}}}^e : \bar{\boldsymbol{\epsilon}}^e, \tag{6}$$

respectively, where $\boldsymbol{\mathcal{C}}^e$ denotes the fourth-order elastic stiffness tensor, and $\bar{\boldsymbol{\mathcal{C}}}^e$ denotes the fourth-order undamaged elastic stiffness tensor and is constant. Combining Eqs. (1), (4), (5), and (6) gives

$$\boldsymbol{\mathcal{C}}^e = \boldsymbol{\mathcal{M}}^{-1} : \bar{\boldsymbol{\mathcal{C}}}^e : \boldsymbol{\mathcal{M}}^{-1} \quad \text{or} \quad \left(\boldsymbol{\mathcal{C}}^e\right)^{-1} = \boldsymbol{\mathcal{M}} : \left(\bar{\boldsymbol{\mathcal{C}}}^e\right)^{-1} : \boldsymbol{\mathcal{M}}. \tag{7}$$

It can be verified that ω_{ij} provides a measure of the damage associated with σ_{ij} or ϵ^e_{ij}.

Let ψ denote the Helmholtz free energy per unit mass of the constituent. According to the theory of thermodynamics, ψ can be expressed as a function of a suitable set of independent state variables characterizing the elastic, plastic, and damage behaviors of the constituent, e.g.,

$$\psi = \psi\left(\boldsymbol{\epsilon}^e, \boldsymbol{\omega}, \boldsymbol{\alpha}, r, s\right), \tag{8}$$

where $\boldsymbol{\alpha}$ is a second-order tensor accounting for kinematic hardening, and r and s are two scalars accounting for isotropic and damage hardening, respectively. Assume that the constituent exhibits uncoupled elastic, plastic, and damage behaviors. In this case, ψ can be decomposed into its elastic, plastic hardening, and damage hardening parts, i.e.,

$$\psi\left(\boldsymbol{\epsilon}^e, \boldsymbol{\omega}, \boldsymbol{\alpha}, r, s\right) = \psi^e\left(\boldsymbol{\epsilon}^e, \boldsymbol{\omega}\right) + \psi^p\left(\boldsymbol{\alpha}, r\right) + \psi^d\left(s\right). \tag{9}$$

The thermodynamic forces conjugate to the state variables in Eq. (8) can be defined as

$$\boldsymbol{\sigma} = \rho\frac{\partial\psi}{\partial\boldsymbol{\epsilon}^e} = \rho\frac{\partial\psi^e}{\partial\boldsymbol{\epsilon}^e}, \quad \mathbf{Y} = -\rho\frac{\partial\psi}{\partial\boldsymbol{\omega}} = -\rho\frac{\partial\psi^e}{\partial\boldsymbol{\omega}}, \tag{10}$$

$$\mathbf{X} = \rho\frac{\partial\psi}{\partial\boldsymbol{\alpha}} = \rho\frac{\partial\psi^p}{\partial\boldsymbol{\alpha}}, \quad R = \rho\frac{\partial\psi}{\partial r} = \rho\frac{\partial\psi^p}{\partial r}, \quad S = \rho\frac{\partial\psi}{\partial s} = \rho\frac{d\psi^d}{ds}, \tag{10'}$$

where $\mathbf{Y}$ denotes the damage conjugate force tensor, $\mathbf{X}$ denotes the back stress tensor, and R and S are related to the current yield stress and the current damage threshold, respectively. Let the yield and damage criteria take the forms of

$$f^p\left(\boldsymbol{\sigma}, \mathbf{X}, R\right) = 0 \quad \text{and} \quad f^d\left(\mathbf{Y}, S\right) = 0, \tag{11}$$

respectively. It can be verified that the evolution of the state variables are governed by

$$\dot{\boldsymbol{\epsilon}}^p = \dot{\lambda}^p \frac{\partial f^p}{\partial \boldsymbol{\sigma}}, \quad \dot{\boldsymbol{\alpha}} = -\dot{\lambda}^p \frac{\partial f^p}{\partial \mathbf{X}}, \quad \dot{r} = -\dot{\lambda}^p \frac{\partial f^p}{\partial R}, \quad \dot{\boldsymbol{\omega}} = \dot{\lambda}^d \frac{\partial f^d}{\partial \mathbf{Y}}, \quad \dot{s} = -\dot{\lambda}^d \frac{\partial f^d}{\partial S}, \tag{12}$$

where $\boldsymbol{\epsilon}^p$ denotes the plastic strain, and $\dot{\lambda}^p$ and $\dot{\lambda}^d$ are two Lagrange multipliers.

The so-called effective stress space plasticity states that the plastic deformation can only occur within the undamaged microbonds of the material.[39] This allows one to derive the constitutive relations in the undamaged configuration. Let $\tilde{\bar{\boldsymbol{\sigma}}} = \bar{\boldsymbol{\sigma}} - \bar{\mathbf{X}}$, and let the constituent obey Hill's yield criterion,

$$f^p\left(\bar{\boldsymbol{\sigma}}, \bar{\mathbf{X}}, \bar{R}\right) = \tilde{\bar{\sigma}}_e - \bar{\sigma}_Y = 0, \tag{13}$$

where

$$\tilde{\bar{\sigma}}_e = \sqrt{\frac{3}{2}\tilde{\bar{\boldsymbol{\sigma}}}' : \bar{\boldsymbol{\mathcal{H}}} : \tilde{\bar{\boldsymbol{\sigma}}}'} \tag{14}$$

denotes the Hill equivalent stress with $(\cdot)'$ denoting the deviatoric part of the tensor and $\bar{\boldsymbol{\mathcal{H}}}$ denoting the fourth-order anisotropy tensor, and

$$\bar{\sigma}_Y = \bar{\sigma}_0 + \bar{R} \tag{15}$$

denotes the current yield stress with $\bar{\sigma}_0$ denoting the initial yield stress. Substituting Eq. (14) into the modified plastic work equivalence principle,

$$\tilde{\bar{\boldsymbol{\sigma}}} : \dot{\bar{\boldsymbol{\epsilon}}}^p = \tilde{\bar{\sigma}}_e \dot{\bar{p}}, \tag{16}$$

gives the Hill equivalent plastic strain rate as

$$\dot{\bar{p}} = \sqrt{\frac{2}{3}\dot{\bar{\boldsymbol{\epsilon}}}^p : \bar{\boldsymbol{\mathcal{H}}}^{-1} : \dot{\bar{\boldsymbol{\epsilon}}}^p}. \tag{17}$$

Note that $\bar{\boldsymbol{\mathcal{H}}}$ can be obtained from the so-called R-values (see Appendix A for more details). It can be verified that

$$\dot{\bar{\lambda}}^p = \dot{\bar{p}}. \tag{18}$$

Let the constituent obey the Chaboche hardening law,[40]

$$\dot{\bar{\mathbf{X}}} = \frac{2}{3}\bar{C}\dot{\bar{\boldsymbol{\epsilon}}}^p - \bar{\gamma}\bar{\mathbf{X}}\dot{\bar{p}}, \tag{19}$$

and the Voce hardening law,[41]

$$\bar{R} = \bar{K}\left[1 - \exp\left(-\bar{n}\bar{p}\right)\right], \tag{20}$$

where $\bar{C}$ and $\bar{\gamma}$ are two constants accounting for kinematic hardening, and $\bar{K}$ and $\bar{n}$ are two constants accounting for isotropic hardening. The rate form of the constitutive relations in the undamaged configuration can then be derived as

$$\dot{\bar{\boldsymbol{\sigma}}} = \bar{\boldsymbol{\mathcal{C}}}^{ep} : \dot{\bar{\boldsymbol{\epsilon}}}, \tag{21}$$

where

$$\bar{\boldsymbol{\mathcal{C}}}^{ep} = \bar{\boldsymbol{\mathcal{C}}}^{e} - \frac{\left(\bar{\boldsymbol{\mathcal{C}}}^e : \dfrac{\partial f^p}{\partial \bar{\boldsymbol{\sigma}}}\right) \otimes \left(\dfrac{\partial f^p}{\partial \bar{\boldsymbol{\sigma}}} : \bar{\boldsymbol{\mathcal{C}}}^e\right)}{\dfrac{2}{3}\bar{C}\dfrac{\partial f^p}{\partial \bar{\boldsymbol{\sigma}}} : \dfrac{\partial f^p}{\partial \bar{\boldsymbol{\sigma}}} - \bar{\gamma}\dfrac{\partial f^p}{\partial \bar{\boldsymbol{\sigma}}} : \bar{\mathbf{X}} + \dfrac{d\bar{R}}{d\bar{p}} + \dfrac{\partial f^p}{\partial \bar{\boldsymbol{\sigma}}} : \bar{\boldsymbol{\mathcal{C}}}^e : \dfrac{\partial f^p}{\partial \bar{\boldsymbol{\sigma}}}} \tag{22}$$

denotes the fourth-order instantaneous elastoplastic stiffness tensor in the undamaged configuration. The explicit expression for $\partial f^p / \partial \bar{\boldsymbol{\sigma}}$ can be derived as[42]

$$\frac{\partial f^p}{\partial \bar{\boldsymbol{\sigma}}} = \frac{\partial \tilde{\bar{\sigma}}_e}{\partial \tilde{\bar{\boldsymbol{\sigma}}}} = \frac{1}{2\tilde{\bar{\sigma}}_e}\frac{\partial \tilde{\bar{\sigma}}_e^2}{\partial \tilde{\bar{\boldsymbol{\sigma}}}} = \frac{1}{2\tilde{\bar{\sigma}}_e}\left(\frac{3}{2}2\frac{\partial \tilde{\bar{\boldsymbol{\sigma}}}'}{\partial \tilde{\bar{\boldsymbol{\sigma}}}} : \bar{\boldsymbol{\mathcal{H}}} : \tilde{\bar{\boldsymbol{\sigma}}}'\right) = \frac{3}{2\tilde{\bar{\sigma}}_e}\boldsymbol{\mathcal{J}} : \bar{\boldsymbol{\mathcal{H}}} : \tilde{\bar{\boldsymbol{\sigma}}}', \tag{23}$$

where $\boldsymbol{\mathcal{J}}$ denotes the fourth-order deviatoric projection operator and takes the form of $\boldsymbol{\mathcal{J}} = \boldsymbol{\mathcal{I}} - \frac{1}{3}\mathbf{I}\otimes\mathbf{I}$ with $\mathbf{I}$ denoting the second-order identity tensor. At last, the Kuhn-Tucker loading/unloading conditions write

$$f^p \leq 0, \quad \dot{\lambda}^p \geq 0, \quad \dot{\lambda}^p f^p = 0. \tag{24}$$

Also let the damage criterion take a Hill-type form,[43]

$$f^d(\mathbf{Y}, S) = Y_e - Y_T = 0, \tag{25}$$

where

$$Y_e = \sqrt{\mathbf{Y} : \boldsymbol{\mathcal{L}} : \mathbf{Y}} \tag{26}$$

denotes a Hill-type equivalent damage conjugate force with $\boldsymbol{\mathcal{L}}$ denoting a fourth-order damage anisotropy tensor, and

$$Y_T = Y_0 + S \tag{27}$$

denotes the current damage threshold with Y_0 denoting the initial damage threshold. $\mathcal{L}_{ijkl}$ can be written in the Voigt notation as L_{ij}. In general, the diagonal components of L_{ij} are around 1, while the off-diagonal components are smaller than the diagonal ones (see Ref. [43] for more details on $\boldsymbol{\mathcal{L}}$). It can be verified that here the equivalent damage rate writes

$$\dot{q} = \sqrt{\dot{\boldsymbol{\omega}} : \boldsymbol{\mathcal{L}}^{-1} : \dot{\boldsymbol{\omega}}} \tag{28}$$

and that

$$\dot{\lambda}^d = \dot{q}. \tag{29}$$

Let the constituent obey a Voce-type damage hardening law,

$$\dot{S} = (L - S)\, o\dot{q} \quad \text{or} \quad S = L\left[1 - \exp\left(-oq\right)\right]. \tag{30}$$

The damage evolution law can then be derived as

$$\dot{\boldsymbol{\omega}} = \frac{\dfrac{\partial f^d}{\partial \mathbf{Y}} : \dot{\mathbf{Y}}}{\dfrac{dS}{dq}} \frac{\partial f^d}{\partial \mathbf{Y}} = \frac{\dfrac{\partial f^d}{\partial \mathbf{Y}} \otimes \dfrac{\partial f^d}{\partial \mathbf{Y}}}{\dfrac{dS}{dq}} : \dot{\mathbf{Y}} \equiv \boldsymbol{\mathcal{S}}^d : \dot{\mathbf{Y}}, \tag{31}$$

where

$$\frac{\partial f^d}{\partial \mathbf{Y}} = \frac{\partial Y_e}{\partial \mathbf{Y}} = \frac{1}{2Y_e}\frac{\partial Y_e^2}{\partial \mathbf{Y}} = \frac{1}{2Y_e}\left(2\frac{\partial \mathbf{Y}}{\partial \mathbf{Y}} : \boldsymbol{\mathcal{L}} : \mathbf{Y}\right) = \frac{\boldsymbol{\mathcal{L}} : \mathbf{Y}}{Y_e}. \tag{32}$$

Note that $\boldsymbol{\mathcal{S}}^d$ is generally non-invertible. At last, the damage evolution conditions write

$$f^d \leq 0, \quad \dot{\lambda}^d \geq 0, \quad \dot{\lambda}^d f^d = 0. \tag{33}$$

The constitutive relations in the damaged configuration can be derived using those in the undamaged configuration and the damage evolution law. Specifically, $\dot{\boldsymbol{\omega}}$ can be related to $\dot{\boldsymbol{\epsilon}}^e$ using Eq. (31) by

$$\dot{\boldsymbol{\omega}} = \left[\left(\boldsymbol{\mathcal{I}} - \boldsymbol{\mathcal{S}}^d : \frac{\partial \mathbf{Y}}{\partial \boldsymbol{\omega}}\right)^{-1} : \left(\boldsymbol{\mathcal{S}}^d : \frac{\partial \mathbf{Y}}{\partial \boldsymbol{\epsilon}^e}\right)\right] : \dot{\boldsymbol{\epsilon}}^e \equiv \boldsymbol{\mathcal{A}} : \dot{\boldsymbol{\epsilon}}^e, \tag{34}$$

where

$$\frac{\partial \mathbf{Y}}{\partial \boldsymbol{\epsilon}^e} = \frac{1}{2}\left[\left(\boldsymbol{\mathcal{I}} : \bar{\boldsymbol{\mathcal{C}}}^e : \boldsymbol{\mathcal{M}}^{-1} + \boldsymbol{\mathcal{M}}^{-1} : \bar{\boldsymbol{\mathcal{C}}}^e : \boldsymbol{\mathcal{I}}\right) : \boldsymbol{\epsilon}^e + \boldsymbol{\epsilon}^e : \left(\boldsymbol{\mathcal{I}} : \bar{\boldsymbol{\mathcal{C}}}^e : \boldsymbol{\mathcal{M}}^{-1} + \boldsymbol{\mathcal{M}}^{-1} : \bar{\boldsymbol{\mathcal{C}}}^e : \boldsymbol{\mathcal{I}}\right)\right] \tag{35}$$

and

$$\frac{\partial \mathbf{Y}}{\partial \boldsymbol{\omega}} = -\frac{1}{2}\boldsymbol{\epsilon}^e : \left(\boldsymbol{\mathcal{I}} : \bar{\boldsymbol{\mathcal{C}}}^e : \boldsymbol{\mathcal{I}} + \boldsymbol{\mathcal{I}} : \bar{\boldsymbol{\mathcal{C}}}^e : \boldsymbol{\mathcal{I}}\right) : \boldsymbol{\epsilon}^e = -\boldsymbol{\epsilon}^e : \boldsymbol{\mathcal{I}} : \bar{\boldsymbol{\mathcal{C}}}^e : \boldsymbol{\mathcal{I}} : \boldsymbol{\epsilon}^e \tag{36}$$

with

$$\boldsymbol{\mathcal{I}} = \sum_{i=1}^{3}\sum_{j=1}^{3} \mathbf{e}_i \otimes \mathbf{e}_j \otimes \mathbf{e}_i \otimes \mathbf{e}_j \otimes \mathbf{e}_i \otimes \mathbf{e}_j. \tag{37}$$

$\dot{\bar{\boldsymbol{\epsilon}}}^e$ can be related to $\dot{\boldsymbol{\epsilon}}^e$ using Eq. (34) by

$$\dot{\bar{\boldsymbol{\epsilon}}}^e = -\left(\boldsymbol{\mathscr{I}} : \boldsymbol{\epsilon}^e\right) : \boldsymbol{\mathcal{A}} : \dot{\boldsymbol{\epsilon}}^e + \boldsymbol{\mathcal{M}}^{-1} : \dot{\boldsymbol{\epsilon}}^e = \left[-\left(\boldsymbol{\mathscr{I}} : \boldsymbol{\epsilon}^e\right) : \boldsymbol{\mathcal{A}} + \boldsymbol{\mathcal{M}}^{-1}\right] : \dot{\boldsymbol{\epsilon}}^e \equiv \tilde{\boldsymbol{\mathcal{N}}}^{-1} : \dot{\boldsymbol{\epsilon}}^e. \tag{38}$$

It can be verified that

$$\dot{\boldsymbol{\mathcal{C}}}^e : \boldsymbol{\epsilon}^e = -\left[\left(\boldsymbol{\mathscr{I}} : \bar{\boldsymbol{\mathcal{C}}}^e : \boldsymbol{\mathcal{M}}^{-1} + \boldsymbol{\mathcal{M}}^{-1} : \bar{\boldsymbol{\mathcal{C}}}^e : \boldsymbol{\mathscr{I}}\right) : \boldsymbol{\epsilon}^e\right] : \dot{\boldsymbol{\omega}} \equiv -\left(\boldsymbol{\mathscr{B}} : \boldsymbol{\epsilon}^e\right) : \dot{\boldsymbol{\omega}}. \tag{39}$$

$\dot{\boldsymbol{\sigma}}$ can be related to $\dot{\boldsymbol{\epsilon}}^e$ using Eqs. (34) and (39) by

$$\dot{\boldsymbol{\sigma}} = -\left(\boldsymbol{\mathscr{B}} : \boldsymbol{\epsilon}^e\right) : \dot{\boldsymbol{\omega}} + \boldsymbol{\mathcal{C}}^e : \dot{\boldsymbol{\epsilon}}^e = -\left(\boldsymbol{\mathscr{B}} : \boldsymbol{\epsilon}^e\right) : \boldsymbol{\mathcal{A}} : \dot{\boldsymbol{\epsilon}}^e + \boldsymbol{\mathcal{C}}^e : \dot{\boldsymbol{\epsilon}}^e = \left[-\left(\boldsymbol{\mathscr{B}} : \boldsymbol{\epsilon}^e\right) : \boldsymbol{\mathcal{A}} + \boldsymbol{\mathcal{C}}^e\right] : \dot{\boldsymbol{\epsilon}}^e \equiv \tilde{\boldsymbol{\mathcal{C}}}^e : \dot{\boldsymbol{\epsilon}}^e. \tag{40}$$

$\dot{\bar{\boldsymbol{\sigma}}}$ can be related to $\dot{\boldsymbol{\sigma}}$ using Eqs. (38) and (40) by

$$\dot{\boldsymbol{\sigma}} = \left[\tilde{\boldsymbol{\mathcal{C}}}^e : \tilde{\boldsymbol{\mathcal{N}}} : \left(\bar{\boldsymbol{\mathcal{C}}}^e\right)^{-1}\right] : \dot{\bar{\boldsymbol{\sigma}}} \equiv \boldsymbol{\mathcal{N}}^{-1} : \dot{\bar{\boldsymbol{\sigma}}}. \tag{41}$$

The plastic dissipation equivalence hypothesis states that the plastic dissipation of a damaged material should equal that of its equivalent undamaged material, i.e.,[44]

$$\boldsymbol{\sigma} : \dot{\boldsymbol{\epsilon}}^p = \bar{\boldsymbol{\sigma}} : \dot{\bar{\boldsymbol{\epsilon}}}^p. \tag{42}$$

Substituting Eq. (1) into Eq. (42) gives

$$\dot{\bar{\boldsymbol{\epsilon}}}^p = \boldsymbol{\mathcal{M}}^{-1} : \dot{\boldsymbol{\epsilon}}^p \quad \text{or} \quad \dot{\boldsymbol{\epsilon}}^p = \boldsymbol{\mathcal{M}} : \dot{\bar{\boldsymbol{\epsilon}}}^p. \tag{43}$$

Combining Eqs. (22), (38), (40), (41), and (43) gives the rate form of the constitutive relations in the damaged configuration as

$$\dot{\boldsymbol{\sigma}} = \left\{\left[\boldsymbol{\mathcal{N}} - \bar{\boldsymbol{\mathcal{C}}}^{ep} : \left(\tilde{\boldsymbol{\mathcal{N}}}^{-1} - \boldsymbol{\mathcal{M}}^{-1}\right) : \left(\tilde{\boldsymbol{\mathcal{C}}}^e\right)^{-1}\right]^{-1} : \bar{\boldsymbol{\mathcal{C}}}^{ep} : \boldsymbol{\mathcal{M}}^{-1}\right\} : \dot{\boldsymbol{\epsilon}} \equiv \boldsymbol{\mathcal{C}}^{ep} : \dot{\boldsymbol{\epsilon}}, \tag{44}$$

where $\boldsymbol{\mathcal{C}}^{ep}$ denotes the fourth-order instantaneous elastoplastic stiffness tensor in the damaged configuration.

Till now, the derivation of the constitutive relations for a constituent has been briefed. In the next section, the weak form of the problem will be derived.

III. Weak Form

Introduce global coordinates $\mathbf{x} = (x_1, x_2, x_3)$ describing the macroscopic structure and local coordinates $\mathbf{y} = (y_1, y_2, y_3)$ describing the UC, and let $\mathbf{y}$ be related to $\mathbf{x}$ by[45]

$$\mathbf{y} = \mathbf{x}/\epsilon, \tag{45}$$

where $\epsilon \ll 1$ denotes a scale ratio. Suppose that, at time t_n:

1. The UC is in a state of static equilibrium;
2. The global and local variables are known;
3. Periodic boundary conditions are satisfied.

The task is to solve for the exact velocity vector within the UC, $\dot{u}_i$, at t_{n+1}.

$\dot{u}_i$ must have its volume average over the UC, say $\dot{v}_i$, such that the heterogeneous material can be homogenized.[46] By definition, $\dot{v}_i$ is related to $\dot{u}_i$ by

$$\dot{v}_i = \frac{1}{\Omega}\int_\Omega \dot{u}_i dV \equiv \langle \dot{u}_i \rangle, \tag{46}$$

where Ω denotes the domain occupied by the UC (with boundary $\partial\Omega$) and also its volume, and $\langle\cdot\rangle$ denotes the volume average of a quantity over Ω. $\dot{u}_i$ can be decomposed into $\dot{v}_i$ and a fluctuation function, say χ_i, i.e.,[45]

$$\dot{u}_i(\mathbf{y}, \mathbf{x}) = \dot{v}_i(\mathbf{x}) + \epsilon\chi_i(\mathbf{y}, \mathbf{x}), \tag{47}$$

where χ_i is a periodic function of $\mathbf{y}$ and may also depend on $\mathbf{x}$, and $\epsilon\chi_i$ should be asymptotically smaller than $\dot{v}_i$. Combining Eqs. (46) and (47) gives

$$\langle \chi_i \rangle = 0. \tag{48}$$

Although $\epsilon\chi_i$ negligibly affects $\dot{u}_i$, it can significantly affect the derivatives of $\dot{u}_i$. Specifically,

$$\frac{\partial \dot{u}_i}{\partial x_j} = \frac{1}{\epsilon}\frac{\partial \dot{u}_i}{\partial y_j}\bigg|_{\mathbf{x}=\text{const}} + \frac{\partial \dot{u}_i}{\partial x_j}\bigg|_{\mathbf{y}=\text{const}} = \frac{\partial \dot{v}_i}{\partial x_j} + \frac{\partial \chi_i}{\partial y_j} + \epsilon\frac{\partial \chi_i}{\partial x_j}, \tag{49}$$

where $\epsilon\partial\chi_i/\partial x_j$ is a high-order term and can be omitted. Note that, by definition,

$$\dot{\epsilon}_{ij} = \frac{1}{2}\left(\frac{\partial \dot{u}_i}{\partial x_j} + \frac{\partial \dot{u}_j}{\partial x_i}\right). \tag{50}$$

Let

$$\dot{\bar{\epsilon}}_{ij} = \frac{1}{2}\left(\frac{\partial \dot{v}_i}{\partial x_j} + \frac{\partial \dot{v}_j}{\partial x_i}\right) \quad \text{and} \quad \chi_{(i|j)} = \frac{1}{2}\left(\frac{\partial \chi_i}{\partial y_j} + \frac{\partial \chi_j}{\partial y_i}\right), \tag{51}$$

where $\dot{\bar{\epsilon}}_{ij}$ actually denotes the global strain rate tenor. Combining Eqs. (47), (50), and (51) gives

$$\dot{\epsilon}_{ij} = \dot{\bar{\epsilon}}_{ij} + \chi_{(i|j)}. \tag{52}$$

The strong form of the problem can be formulated as seeking χ_i satisfying

$$\dot{\sigma}_{ij,j} = 0 \quad \text{in } \Omega \tag{53}$$

subject to constraint Eq. (48) and periodic boundary conditions

$$\chi_i(\mathbf{y}) = \chi_i(\mathbf{y}+\mathbf{l}) \quad \text{and} \quad (\dot{\sigma}_{ij}n_j)(\mathbf{y}) = -(\dot{\sigma}_{ij}n_j)(\mathbf{y}+\mathbf{l}) \quad \text{on } \partial\Omega, \tag{54}$$

where $\mathbf{l}$ denotes the periodicity vector of the UC, and n_i denotes the unit normal vector. Let $\delta\chi_i$ denote the virtual fluctuation function being arbitrary in Ω and satisfying periodic boundary conditions

$$\delta\chi_i(\mathbf{y}) = \delta\chi_i(\mathbf{y}+\mathbf{l}) \quad \text{on } \partial\Omega. \tag{55}$$

The rate form of the principle of virtual work can be expressed in terms of $\delta\chi_i$ as

$$\delta\Pi_\Omega = -\frac{1}{\Omega}\int_\Omega \dot{\sigma}_{i,j}\delta\chi_i dV = \frac{1}{\Omega}\int_\Omega \dot{\sigma}_{ij}\delta\chi_{(i|j)}dV - \frac{1}{\Omega}\int_\Omega \dot{\sigma}_{ij}n_j\delta\chi_i dS = 0. \tag{56}$$

Substituting Eq. (55) and the second equation of Eq. (54) into Eq. (56) gives

$$\delta\Pi_\Omega = \frac{1}{\Omega}\int_\Omega \dot{\sigma}_{ij}\delta\chi_{(i|j)}dV = 0. \tag{57}$$

The weak form of the problem can then be formulated as seeking χ_i satisfying Eq. (57) subject to constraint Eq. (48) and periodic boundary conditions

$$\chi_i(\mathbf{y}) = \chi_i(\mathbf{y}+\mathbf{l}) \quad \text{on } \partial\Omega. \tag{58}$$

Substituting Eq. (52) into Eq. (44) gives

$$\dot{\sigma}_{ij} = \mathcal{C}^{ep}_{ijkl}\left[\dot{\bar{\epsilon}}_{kl} + \chi_{(k|l)}\right]. \tag{59}$$

Substituting Eq. (59) into Eq. (57) gives

$$\delta\Pi_\Omega = \frac{1}{\Omega}\int_\Omega \delta\chi_{(i|j)}\mathcal{C}^{ep}_{ijkl}\left[\dot{\bar{\epsilon}}_{kl} + \chi_{(k|l)}\right]dV = 0. \tag{60}$$

Eq. (60) implies that, once $\dot{\bar{\epsilon}}_{ij}$ and $\mathcal{C}^{ep}_{ijkl}$ are specified, χ_i can be uniquely determined.

It is beneficial to also relate the local stress and strain rate tensors to the global ones. Specifically, $\langle \dot{\sigma}_{ij}\dot{\epsilon}_{ij} \rangle$ can be expressed as

$$\frac{1}{\Omega}\int_\Omega \dot{\sigma}_{ij}\dot{\epsilon}_{ij}dV = \frac{1}{\Omega}\int_\Omega \dot{\sigma}_{ij}\dot{\bar{\epsilon}}_{ij}dV + \frac{1}{\Omega}\int_\Omega \dot{\sigma}_{ij}\chi_{(i|j)}dV. \tag{61}$$

Eq. (61), together with Eq. (57), implies that

$$\frac{1}{\Omega}\int_\Omega \dot{\sigma}_{ij}\dot{\epsilon}_{ij}dV = \frac{1}{\Omega}\int_\Omega \dot{\sigma}_{ij}\dot{\bar{\epsilon}}_{ij}dV = \dot{\bar{\epsilon}}_{ij}\left(\frac{1}{\Omega}\int_\Omega \dot{\sigma}_{ij}dV\right) \equiv \dot{\bar{\sigma}}_{ij}\dot{\bar{\epsilon}}_{ij}, \tag{62}$$

In fact, Eq. (62) is a variation of the Hill-Mandel lemma.

Till now, the weak form of the problem has been derived. In the next section, it will be discretized using finite elements such that the fluctuation function can be determined.

IV. Finite Element Implementation

Introduce the following matrix notations:

$$\dot{\bar{\epsilon}} = \begin{bmatrix} \dot{\bar{\epsilon}}_{11} & 2\dot{\bar{\epsilon}}_{12} & \dot{\bar{\epsilon}}_{22} & 2\dot{\bar{\epsilon}}_{13} & 2\dot{\bar{\epsilon}}_{23} & \dot{\bar{\epsilon}}_{33} \end{bmatrix}^T, \tag{63}$$

$$\begin{Bmatrix} \dfrac{\partial\chi_1}{\partial y_1} \\ \dfrac{\partial\chi_1}{\partial y_2}+\dfrac{\partial\chi_2}{\partial y_1} \\ \dfrac{\partial\chi_2}{\partial y_2} \\ \dfrac{\partial\chi_1}{\partial y_3}+\dfrac{\partial\chi_3}{\partial y_1} \\ \dfrac{\partial\chi_2}{\partial y_3}+\dfrac{\partial\chi_3}{\partial y_2} \\ \dfrac{\partial\chi_3}{\partial y_3} \end{Bmatrix} = \begin{bmatrix} \dfrac{\partial}{\partial y_1} & 0 & 0 \\ \dfrac{\partial}{\partial y_2} & \dfrac{\partial}{\partial y_1} & 0 \\ 0 & \dfrac{\partial}{\partial y_2} & 0 \\ \dfrac{\partial}{\partial y_3} & 0 & \dfrac{\partial}{\partial y_1} \\ 0 & \dfrac{\partial}{\partial y_3} & \dfrac{\partial}{\partial y_2} \\ 0 & 0 & \dfrac{\partial}{\partial y_3} \end{bmatrix} \begin{Bmatrix} \chi_1 \\ \chi_2 \\ \chi_3 \end{Bmatrix} \equiv \Gamma_h \chi, \tag{63$'$}$$

where Γ_h denotes an operator matrix, and χ denotes a column matrix containing the three components of the fluctuation function. Let χ be discretized using finite elements as

$$\chi(y_i, x_i) = S(y_i)\,\mathrm{X}(x_i), \tag{64}$$

where S denotes the shape functions, and X denotes a column matrix of the nodal values of the fluctuation function at all the active nodes. The discretized version of Eq. (60) can then be obtained as

$$\delta\Pi_\Omega = \frac{1}{\Omega}\delta\mathrm{X}^T\left(D_{hh}\mathrm{X} + D_{h\epsilon}\dot{\bar{\epsilon}}\right) = 0, \tag{65}$$

where

$$D_{hh} = \int_\Omega (\Gamma_h S)^T D\,(\Gamma_h S)\,dV \quad \text{and} \quad D_{h\epsilon} = \int_\Omega (\Gamma_h S)^T D dV \tag{66}$$

with D denoting the 6×6 instantaneous stiffness matrix condensed from $\mathcal{C}^{ep}_{ijkl}$. In Eq. (65), equality holds only if

$$D_{hh}\mathrm{X} = -D_{h\epsilon}\dot{\bar{\epsilon}} \quad \text{or} \quad \mathrm{X} = \mathrm{X}_0\dot{\bar{\epsilon}}. \tag{67}$$

Eq. (67) implies that X is proportional to $\dot{\bar{\epsilon}}$. In addition, Eq. (62) can be rewritten as

$$\dot{\bar{\epsilon}}_{ij}\dot{\bar{\sigma}}_{ij} = \frac{1}{\Omega}\int_\Omega \dot{\bar{\epsilon}}_{ij}\dot{\sigma}_{ij}dV = \frac{1}{\Omega}\int_\Omega \dot{\bar{\epsilon}}_{ij}\mathcal{C}^{ep}_{ijkl}\left[\dot{\bar{\epsilon}}_{kl} + \chi_{(k|l)}\right]dV. \tag{68}$$

The discretized version of Eq. (68) can be obtained as

$$\dot{\bar{\epsilon}}^T\dot{\bar{\sigma}} = \frac{1}{\Omega}\left(\dot{\bar{\epsilon}}^T D_{\epsilon h}\mathrm{X} + \dot{\bar{\epsilon}}^T D_{\epsilon\epsilon}\dot{\bar{\epsilon}}\right) = \frac{1}{\Omega}\dot{\bar{\epsilon}}^T\left(D_{\epsilon h}\mathrm{X}_0 + D_{\epsilon\epsilon}\right)\dot{\bar{\epsilon}} \equiv \dot{\bar{\epsilon}}^T\bar{D}\dot{\bar{\epsilon}}, \tag{69}$$

where $\dot{\bar{\sigma}}$ denotes the global stress strain rate column matrix, and

$$D_{\epsilon h} = \int_{\Omega} D\left(\Gamma_h S\right) dV \quad \text{and} \quad D_{\epsilon\epsilon} = \int_{\Omega} D dV. \tag{70}$$

The rate form of the global constitutive relations can then be obtained from Eq. (69) as

$$\dot{\bar{\sigma}} = \bar{D}\dot{\bar{\epsilon}}, \tag{71}$$

where $\bar{D}$ denotes the instantaneous effective stiffness matrix. Once $\dot{\bar{\epsilon}}$, $\dot{\bar{\sigma}}$, or a suitable combination of the components of $\dot{\bar{\epsilon}}$ and $\dot{\bar{\sigma}}$ is specified, the global response of the UC can be fully determined using Eq. (71). In addition, the real value of X_0, say $\bar{\mathrm{X}}_0$, can be obtained by modifying X_0 such that χ satisfies Eqs. (48) and (58). Once $\dot{\bar{\epsilon}}$ and $\bar{\mathrm{X}}_0$ are specified, the local fields can be fully recovered. Specifically, the local strain rates can be recovered as

$$\dot{\epsilon} = \dot{\bar{\epsilon}} + \Gamma_h S \bar{\mathrm{X}}_0 \dot{\bar{\epsilon}}, \tag{72}$$

where $\dot{\epsilon}$ denotes the local strain rate column matrix. The local stress rates can be recovered from the local strain rates as

$$\dot{\sigma} = D\dot{\epsilon}. \tag{73}$$

Till now, the fluctuation function have been determined. In the next section, the code structure will be presented.

V. Code Structure

The code employs the second-order Runge-Kutta method as its time integration method (see Figure 1 for its structure). It starts with reading the finite element model and initializing the global and local stresses and strains. After this, it will perform the following steps within each load increment:

1. Compute the effective material properties and the fluctuation function;
2. Impose the global stress/strain increments;
3. Recover the local fields;
4. Update the global and local variables;
5. Continue to the next increment if needed.

At last, it will output the results as needed.

The code uses the Gaussian quadrature to compute the element stiffness matrices. The corresponding algorithm is described as follows:

1. Read the data associated with an integration point;
2. Check whether the constituent is damageable elastoplastic;
3. If yes, check whether Eqs. (24) and (33) is satisfied;
4. If yes, compute the stiffness matrix using Eq. (44) and return it;
5. If either of the two criteria is not met, return the elastic stiffness matrix;

Especially, if either Eq. (24) or Eq. (33) is satisfied, the code will update the corresponding local variables during the recovery.

VI. Results and Discussion

In this section, the capability of the proposed approach will be demonstrated by homogenizing a binary composite with a constituent exhibiting various mechanical behaviors.

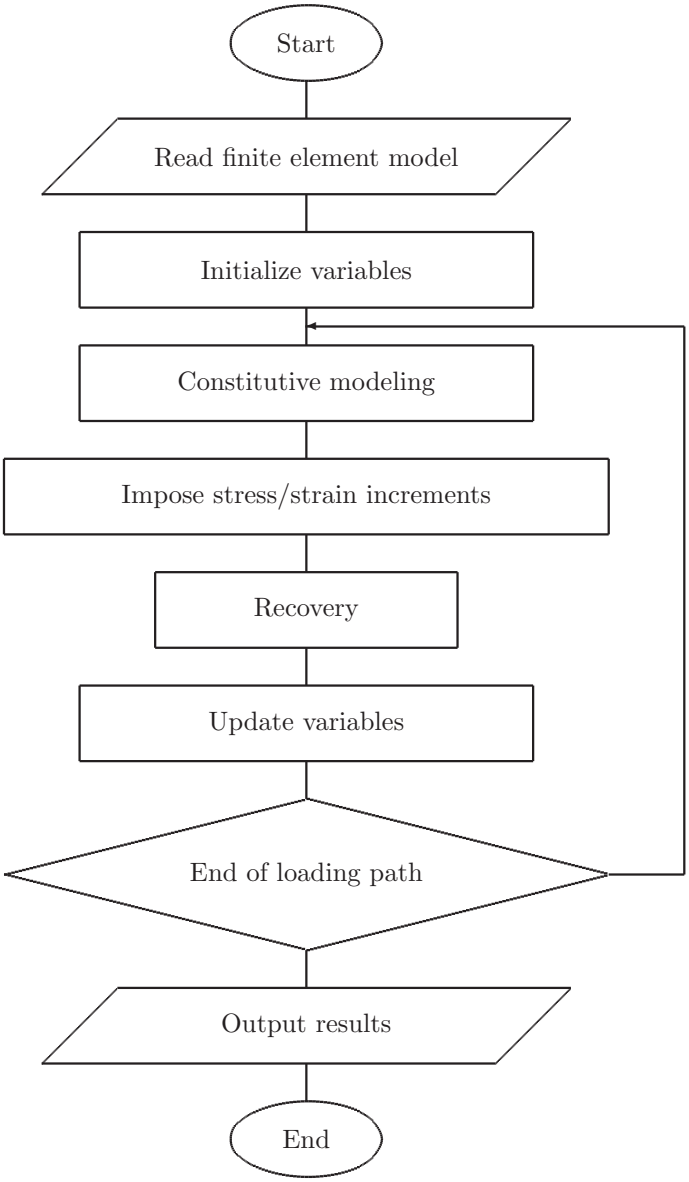

Figure 1. Code structure.

A. Damage Hardening

Consider a binary composite consisting of an elastic SiC constituent and a damageable elastoplastic aluminum constituent with their volume fractions being 10% and 90%, respectively. With loss of generality, let aluminum exhibit combined isotropic-kinematic hardening (see Eqs. (19) and (20)). Following Refs. [47] and [48], let the material parameters of SiC and aluminum take the values listed in Table 1, where $\bar{E}$ and $\bar{\nu}$ denote the undamaged Young's modulus and Poisson's ratio, respectively. Recall that $\mathcal{L}_{ijkl}$ can be written in the Voigt notation as L_{ij}. Following Ref. [43], let the L_{ij}'s of aluminum take the form of

$$L_{ij} = \begin{cases} 1 & i = j, \\ 0.32 & i \neq j. \end{cases} \tag{74}$$

Let the UC of this composite be a line segment consisting of two connecting sub-line segments. Recall that y_i denotes the local coordinates describing the UC with its origin located at the geometric center of the UC (see Section III). Here let the y_1-axis be parallel to the line segment representing the UC.

Table 1. Material parameters of SiC and aluminum.

(a) Elastic constants.

	$\bar{E}$ (GPa)	$\bar{\nu}$
SiC	490	0.17
Aluminum	65	0.3

(b) Plastic constants of aluminum.

$\bar{\sigma}_0$ (MPa)	$\bar{K}$ (MPa)	$\bar{n}$	$\bar{C}$ (MPa)	$\bar{\gamma}$
154	140.2	54.9	7019	118.6

(c) Damage constants of aluminum.

Y_0 (MPa)	L (MPa)	o
0.0912	1.824	5

In the proposed approach, a 1D UC is meshed using 2-node line elements having 3 degrees of freedom at each node, and the meshed UC consists of 2 elements. Note that this finite element model is much simpler than a 3D one in a commercial finite element software.

Figure 2 shows the stress-strain curve of the damageable composite undergoing uniaxial extension in the y_1-direction. For comparison purposes, it also shows a similar curve of a perfect composite. It can be seen that the damageable composite becomes more and more flexible compared with the perfect one during continued deformation and even exhibits strain softening to the end of deformation. This is because here aluminum is severely deformed and becomes heavily damaged. Moreover, the numerical results show that, as aluminum is deformed to a certain extent, the damage evolution gradually takes the place of the plastic deformation and becomes dominant within it and that, after this, the composite will exhibit an asymptotic behavior near fracture, just like a damageable elastic material.

Figure 3 shows the stress-strain curves of the composite undergoing uniaxial extension in the y_1-directions. It can be seen that the two curves here are very close to easy other. This is because here aluminum is not severely deformed and remains almost undamaged. As can be seen in Figures 2 and 3, the global stress state determines the local stress distribution and hereby the local responses of damageable constituents, while such responses can further react to the global response of the UC. Therefore, it is of great significance to accurately recover the local fields within the UC.

B. General Damage Anisotropy

Next let aluminum also exhibit general damage anisotropy, where the term "general" means that the components of L_{ij} are independent of each other. Specifically, let the material parameters of aluminum still take the values listed in Table 1, and let Eq. (74) hold except that L_{11} can take the values of 0.707, 1, and 1.414 in three cases.

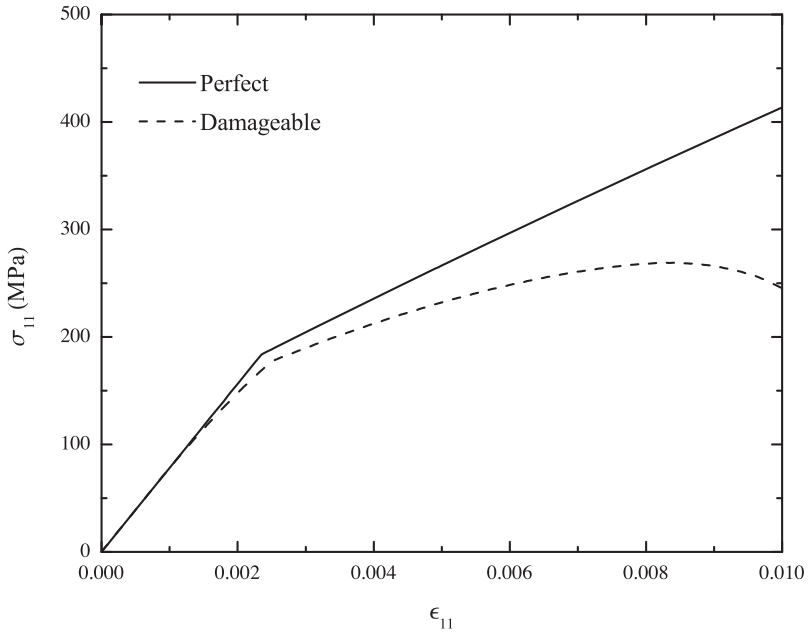

Figure 2. Stress-strain curves of perfect and damageable binary composites undergoing uniaxial extension in the y_1-direction.

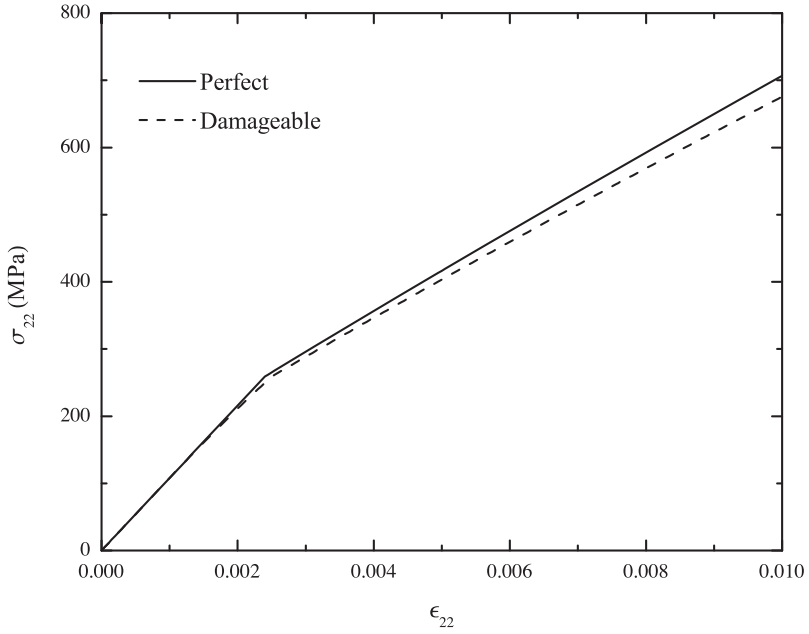

Figure 3. Stress-strain curves of perfect and damageable binary composites undergoing uniaxial extension in the y_2-direction.

Figures 4 shows the stress-strain curves of the composite undergoing uniaxial extension in the Y_1-direction, respectively. It can be verified that, as L_{11} increases, the material becomes more vulnerable to σ_{11}. Accordingly, in Figure 4, as L_{11} increases, the stress-strain curve shifts downwards. Meanwhile, it can be seen that the curves here exhibit trends similar to that for the damageable composite in Figures 2. Therefore, the corresponding discussion for Figures 2 holds here.

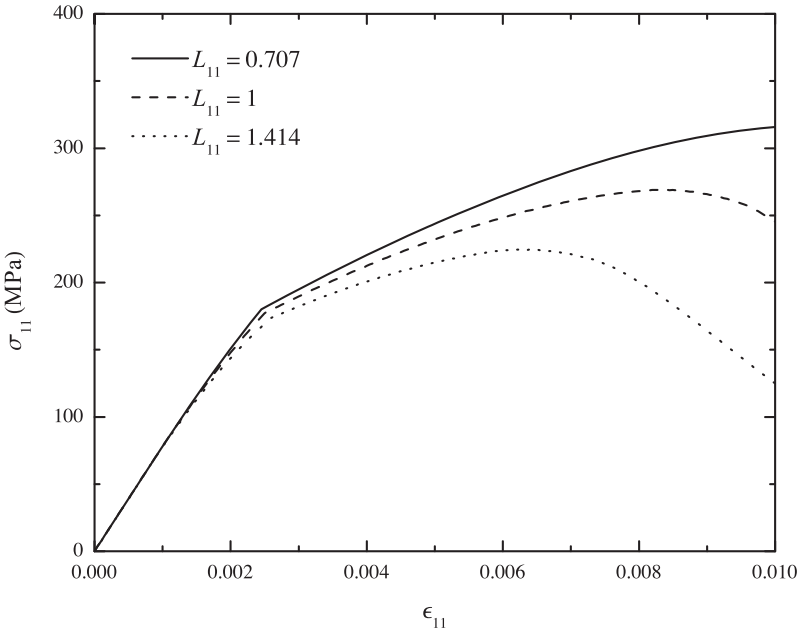

Figure 4. Stress-strain curves of a binary composite with a constituent exhibiting general damage anisotropy, undergoing uniaxial extension in the y_1-direction.

C. Plastic Anisotropy

At last, let aluminum exhibit plastic transverse isotropy in the x_2-x_3 plane. Specifically, let aluminum parameters take the values listed in Table 1 with its initial yield stresses in the y_2- and y_3-directions remaining unchanged, and let Eq. (74) hold here. Also let the R_i's of aluminum take three sets of values listed in Table 2 in three cases (see Appendix A for more details).

Table 2. R_i's in three cases.

	R_1	R_2	R_3	R_4	R_5	R_6
1	1	1	0.5	1	0.5	2
2	1	1	1	1	1	1
3	1	1	2	1	2	0.5

Figures 5 shows the stress-strain curves of the composite undergoing uniaxial extension in the x_2-direction. It can be verified from Table 2 that, if the initial yield stresses in the y_2- and y_3-directions remain unchanged, that in the x_2-direction increases with increasing R_3. Accordingly, for $R_3 = R_5 = 2$, σ_{11} attains a high level at an early stage of deformation, enabling damages to evolve to a considerable extent. This leads the composite to behave like a damageable elastic material afterwards. In contrast, for $R_3 = R_5 = 0.5$, σ_{11} increases more slowly, prohibiting damages from evolving too early. This leads the composite not to exhibit strain softening very soon.

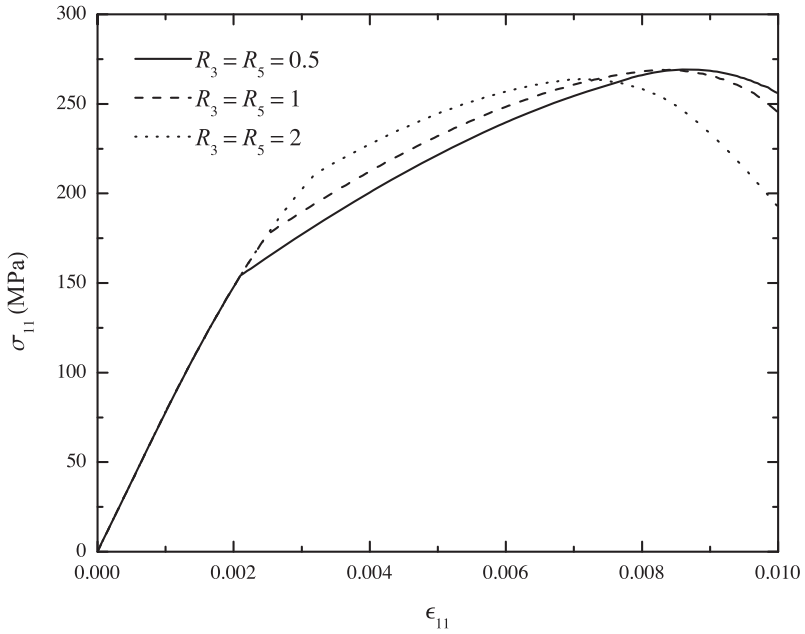

Figure 5. Stress-strain curves of a binary composite with a plastically anisotropic matrix, undergoing uniaxial extension in the y_1-direction.

VII. Conclusions

In this paper, a micromechanics approach to homogenizing damageable elastoplastic heterogeneous materials is proposed. The derivation of the constitutive relations for a constituent, which exhibits damage anisotropy, damage hardening, plastic anisotropy, and combined isotropic-kinematic hardening, is briefed. The weak form of the problem is derived using an asymptotic method, discretized using finite elements, and solved using the second-order Runge-Kutta method. The capability of the proposed approach is demonstrated by homogenizing a binary composite with a constituent exhibiting various mechanical behaviors. The proposed approach is found to be capable of handling complex material models. More sophisticated material models can be implemented into the proposed approach.

The following conclusions can be drawn:

1. More complex microstructure can be modeled;
2. More complex loading conditions and loading paths can be involved;
3. More sophisticated material models can be incorporated into the proposed approach.

Acknowledgements

This work is supported by the US AFOSR Multiscale Structural Mechanics and Prognosis Program. The views and conclusions contained herein are those of the authors and should not be interpreted as necessarily representing the official policies or endorsement, either expressed or implied, of the sponsor.

Appendix

A. Plastic Anisotropic Parameters

The R-value is widely used to characterize the plastic anisotropy of rolled sheet metals and can be measured in a series of uniaxial tensile tests. Specifically, when a tensile specimen cut from a sheet is stretched, its R-value is defined as the ratio of the plastic strain in the width direction to that in the thickness direction, i.e.,

$$R = \frac{\epsilon_W}{\epsilon_T}. \tag{75}$$

In general, the R-value varies with the cut angle with respect to the rolling direction of the sheet, α. In this case, an averaged R-value is often adopted. It is defined as

$$\bar{R} = \frac{R_0 + 2R_{45} + R_{90}}{4}, \tag{76}$$

where R_α denotes the R-value measured in a tensile specimen of cut angle α.

Benzerga and Besson[42] enriched the concept of the R-value by introducing six strain rate ratios, R_{ij}, which are capable of fully characterizing the plastic anisotropy of a 3D structure. Similarly to the R-value, each of these ratios can be measured in either a uniaxial tensile test or a simple shear test. Specifically, introduce Cartesian coordinates $\mathbf{x} = (x_1, x_2, x_3)$ with its three axes parallel to the orthotropic axes of the constituent. These ratios can then be defined as

$$R_{11} = \frac{\dot{\epsilon}_{22}}{\dot{\epsilon}_{33}}, \quad R_{12} = \frac{\dot{\epsilon}_{12}}{\dot{\epsilon}_{33}}, \quad R_{22} = \frac{\dot{\epsilon}_{33}}{\dot{\epsilon}_{11}}, \tag{77}$$

$$R_{13} = \frac{\dot{\epsilon}_{13}}{\dot{\epsilon}_{22}}, \quad R_{23} = \frac{\dot{\epsilon}_{23}}{\dot{\epsilon}_{11}}, \quad R_{33} = \frac{\dot{\epsilon}_{11}}{\dot{\epsilon}_{22}}. \tag{77$'$}$$

R_{ij} can be written in the Voigt notation as

$$R_1 = R_{11}, \quad R_2 = R_{12}, \quad R_3 = R_{22}, \tag{78}$$

$$R_4 = R_{13}, \quad R_5 = R_{23}, \quad R_6 = R_{33}. \tag{78$'$}$$

It can be obtained from Eq. (77) that $R_6 = 1/R_1R_3$. This implies that only five out of the six R_i's are independent.

$\mathcal{H}_{ijkl}$ can be written in the Voigt notation as H_{ij}. The diagonal components of H_{ij} can be related to R_i by[42]

$$H_{11} = -\frac{2}{3}\frac{R_1R_3 - 2R_1 - 2}{R_1 + 1}, \quad \frac{H_{22}}{H_{11}} = -\frac{1}{2}\frac{(2R_2 + 1)(R_1R_3 + 1)}{R_1R_3 - 2R_1 - 2}, \tag{79}$$

$$\frac{H_{33}}{H_{11}} = 1 - \frac{3(R_1R_3 - 1)}{R_1R_3 - 2R_1 - 2}, \quad \frac{H_{44}}{H_{11}} = -\frac{1}{2}\frac{(2R_4 + 1)(R_3 + 1)R_1}{R_1R_3 - 2R_1 - 2}, \tag{79$'$}$$

$$\frac{H_{55}}{H_{11}} = -\frac{1}{2}\frac{(2R_5 + 1)(R_1 + 1)}{R_1R_3 - 2R_1 - 2}, \quad \frac{H_{66}}{H_{11}} = 1 - \frac{3R_1(R_3 - 1)}{R_1R_3 - 2R_1 - 2}, \tag{79$''$}$$

while the off-diagonal components vanish. More details on $\boldsymbol{\mathcal{H}}$ can be found in Ref. [42], Appendix A.

A special case of plastic anisotropy is plastic transverse isotropy, in which case there exists a plane of plastic isotropy. Without loss of generality, let the x_2-x_3 plane be the plane of plastic isotropy. R_i can then be expressed as

$$R_3 = R_5 = \frac{1}{R_6} = R \quad \text{and} \quad R_2 = R_4 = R', \tag{80}$$

where R and R' can be measured in a uniaxial tensile test and a simple shear test, respectively. Substituting Eq. (80) into Eq. (79) and rearranging the equations give

$$H_{11} = \frac{1}{3}(4 - R), \quad H_{22} = H_{44} = \frac{1}{6}(R + 1)(2R' + 1), \tag{81}$$

$$H_{33} = H_{55} = H_{66} = \frac{1}{3}(2R + 1). \tag{81$'$}$$

References

[1]Hill, R., "Continuum micro-mechanics of elastoplastic polycrystals," *Journal of the Mechanics and Physics of Solids*, Vol. 13, No. 2, 1965, pp. 89–101.

[2]Molinari, A., Canova, G., and Ahzi, S., "A self consistent approach of the large deformation polycrystal viscoplasticity," *Acta Metallurgica*, Vol. 35, No. 12, 1987, pp. 2983–2994.

[3]Lebensohn, R. and Tom, C., "A self-consistent anisotropic approach for the simulation of plastic deformation and texture development of polycrystals: Application to zirconium alloys," *Acta Metallurgica et Materialia*, Vol. 41, No. 9, 1993, pp. 2611–2624.

[4]Berveiller, M. and Zaoui, A., "An extension of the self-consistent scheme to plastically-flowing polycrystals," *Journal of the Mechanics and Physics of Solids*, Vol. 26, No. 5-6, 1978, pp. 325–344.

[5]Tandon, G. and Weng, G., "A theory of particle-reinforced plasticity," *Transactions of the ASME. Journal of Applied Mechanics*, Vol. 55, No. 1, 1988, pp. 126–135.

[6]Suquet, P., "Overall properties of nonlinear composites: a modified secant moduli theory and its link with Ponte Castaeda's nonlinear variational procedure," *Comptes rendus de l'Acadmie des sciences. Srie II, Mcanique, physique, chimie, astronomie*, Vol. 320, No. 11, 1995, pp. 563–571.

[7]Doghri, I., Brassart, L., Adam, L., and Gerard, J.-S., "A second-moment incremental formulation for the mean-field homogenization of elasto-plastic composites," *International Journal of Plasticity*, Vol. 27, No. 3, 2011, pp. 352–371.

[8]Brassart, L., Stainier, L., Doghri, I., and Delannay, L., "A variational formulation for the incremental homogenization of elasto-plastic composites," *Journal of the Mechanics and Physics of Solids*, Vol. 59, No. 12, 2011, pp. 2455–2475.

[9]Brassart, L., Stainier, L., Doghri, I., and Delannay, L., "Homogenization of elasto-(visco) plastic composites based on an incremental variational principle," *International Journal of Plasticity*, Vol. 36, No. 0, 2012, pp. 86–112.

[10]Wu, L., Noels, L., Adam, L., and Doghri, I., "A multiscale mean-field homogenization method for fiber-reinforced composites with gradient-enhanced damage models," *Computer Methods in Applied Mechanics and Engineering*, Vol. 233, 2012, pp. 164–179.

[11]Bensoussan, A., Lions, J., and Papanicolaou, G., *Asymptotic analysis for periodic structures*, North-Holland, Amsterdam, 1978.

[12]Guedes, J. and Kikuchi, N., "Preprocessing and postprocessing for materials based on the homogenization method with adaptive finite element methods," *Computer Methods in Applied Mechanics and Engineering*, Vol. 83, No. 2, 1990, pp. 143–198.

[13]Fish, J., Yu, Q., and Shek, K., "Computational damage mechanics for composite materials based on mathematical homogenization," *International Journal for Numerical Methods in Engineering*, Vol. 45, No. 11, 1999, pp. 1657–1679.

[14]Fish, J. and Yu, Q., "Multiscale damage modelling for composite materials: theory and computational framework," *International Journal for Numerical Methods in Engineering*, Vol. 52, No. 1-2, 2001, pp. 161–191.

[15]Aboudi, J., "Damage in compositesmodeling of imperfect bonding," *Composites Science and Technology*, Vol. 28, No. 2, 1987, pp. 103–128.

[16]Aboudi, J., "Constitutive equations for elastoplastic composites with imperfect bonding," *International Journal of Plasticity*, Vol. 4, No. 2, 1988, pp. 103–125.

[17]Markovic, D. and Ibrahimbegovic, A., "On micro–macro interface conditions for micro scale based FEM for inelastic behavior of heterogeneous materials," *Computer Methods in Applied Mechanics and Engineering*, Vol. 193, No. 48, 2004, pp. 5503–5523.

[18]Sun, C. and Vaidya, R., "Prediction of composite properties from a Representative Volume Element," *Composites Science and Technololy*, Vol. 56, 1996, pp. 171–179.

[19]Smit, R., Brekelmans, W., and Meijer, H., "Prediction of the mechanical behavior of nonlinear heterogeneous systems by multi-level finite element modeling," *Computer Methods in Applied Mechanics and Engineering*, Vol. 155, No. 1, 1998, pp. 181–192.

[20]Miehe, C., "Computational micro-to-macro transitions for discretized micro-structures of heterogeneous materials at finite strains based on the minimization of averaged incremental energy," *Computer Methods in Applied Mechanics and Engineering*, Vol. 192, No. 5, 2003, pp. 559–591.

[21]Xia, Z., Zhang, Y., and Ellyin, F., "A unified periodical boundary conditions for representative volume elements of composites and applications," *International Journal of Solids and Structures*, Vol. 40, No. 8, 2003, pp. 1907–1921.

[22]Xia, Z., Zhou, C., Yong, Q., and Wang, X., "On selection of repeated unit cell model and application of unified periodic boundary conditions in micro-mechanical analysis of composites," *International Journal of Solids and Structures*, Vol. 43, No. 2, 2006, pp. 266–278.

[23]Simo, J. and Ju, J., "Strain- and stress-based continuum damage modelsII. Computational aspects," *International Journal of Solids and Structures*, Vol. 23, No. 7, 1987, pp. 841–869.

[24]Ju, J., "Isotropic and anisotropic damage variables in continuum damage mechanics," *Journal of Engineering Mechanics*, Vol. 116, No. 12, 1990, pp. 2764–2770.

[25]Yazdani, S. and Schreyer, H., "Combined plasticity and damage mechanics model for plain concrete," *Journal of Engineering Mechanics*, Vol. 116, No. 7, 1990, pp. 1435–1450.

[26]Lee, J. and Fenves, G. L., "Plastic-damage model for cyclic loading of concrete structures," *Journal of Engineering Mechanics*, Vol. 124, No. 8, 1998, pp. 892–900.

[27]Govindjee, S., Kay, G. J., and Simo, J. C., "Anisotropic modelling and numerical simulation of brittle damage in concrete," *International Journal for Numerical Methods in Engineering*, Vol. 38, No. 21, 1995, pp. 3611–3633.

[28]Jason, L., Huerta, A., Pijaudier-Cabot, G., and Ghavamian, S., "An elastic plastic damage formulation for concrete: application to elementary tests and comparison with an isotropic damage model," *Computer Methods in Applied Mechanics and Engineering*, Vol. 195, No. 52, 2006, pp. 7077–7092.

[29]Wu, J. Y., Li, J., and Faria, R., "An energy release rate-based plastic-damage model for concrete," *International Journal of Solids and Structures*, Vol. 43, No. 3, 2006, pp. 583–612.

[30]Cicekli, U., Voyiadjis, G. Z., and Abu Al-Rub, R. K., "A plasticity and anisotropic damage model for plain concrete," *International Journal of Plasticity*, Vol. 23, No. 10, 2007, pp. 1874–1900.

[31]Voyiadjis, G. Z., Taqieddin, Z. N., and Kattan, P. I., "Anisotropic damage-plasticity model for concrete," *International Journal of Plasticity*, Vol. 24, No. 10, 2008, pp. 1946–1965.

[32]Ortiz, M., "A constitutive theory for the inelastic behavior of concrete," *Mechanics of Materials*, Vol. 4, No. 1, 1985, pp. 67–93.

[33]Lubliner, J., Oliver, J., Oller, S., and Oñate, E., "A plastic-damage model for concrete," *International Journal of Solids and Structures*, Vol. 25, No. 3, 1989, pp. 299–326.

[34]Abu Al-Rub, R. K. and Voyiadjis, G. Z., "On the coupling of anisotropic damage and plasticity models for ductile materials," *International Journal of Solids and Structures*, Vol. 40, No. 11, 2003, pp. 2611–2643.

[35]Zhang, L. and Yu, W., "On the constitutive relations for damaged elastoplastic materials coupling anisotropic damage and plasticity," *Proceedings of the 55th Structures, Structural Dynamics, and Materials Conference*, National Harbor, 2014.

[36]Murakami, S. and Ohno, N., "A continuum theory of creep and creep damage," *Creep in Structures*, Springer, 1981, pp. 422–444.

[37]Cordebois, J. and Sidoroff, F., "Anisotropic damage in elasticity and plasticity," *J. de Mecanique Theorique et Appliquee*, 1982, pp. 45–60.

[38]Voyiadjis, G. Z. and Kattan, P. I., *Advances in damage mechanics: metals and metal matrix composites*, Elsevier Science, 1999.

[39]Ju, J., "On energy-based coupled elastoplastic damage theories: constitutive modeling and computational aspects," *International Journal of Solids and Structures*, Vol. 25, No. 7, 1989, pp. 803–833.

[40]Chaboche, J.-L., "Constitutive equations for cyclic plasticity and cyclic viscoplasticity," *International Journal of Plasticity*, Vol. 5, No. 3, 1989, pp. 247–302.

[41]Voce, E., "A practical strain-hardening function," *Metallurgia*, Vol. 51, No. 307, 1955, pp. 219–226.

[42]Benzerga, A. A. and Besson, J., "Plastic potentials for anisotropic porous solids," *European Journal of Mechanics, A/Solids*, Vol. 20, No. 3, 2001, pp. 397–434.

[43]Chow, C. and Wang, J., "An anisotropic theory of elasticity for continuum damage mechanics," *International Journal of Fracture*, Vol. 33, No. 1, 1987, pp. 3–16.

[44]Voyiadjis, G. Z. and Thiagarajan, G., "Micro and macro anisotropic cyclic damage-plasticity models for MMCS," *International Journal of Engineering Science*, Vol. 35, No. 5, 1997, pp. 467–484.

[45]Berdichevsky, L. V., *Variational principles of continuum mechanics: II. Applications*, Springer, New York, 2009.

[46]Yu, W. and Tang, T., "Variational asymptotic method for unit cell homogenization of periodically heterogeneous materials," *International Journal of Solids and Structures*, Vol. 44, No. 11-12, 2007, pp. 3738–3755.

[47]Zhao, K. M. and Lee, J. K., "Material properties of aluminum alloy for accurate draw-bend simulation," *Journal of Engineering Materials and Technology*, Vol. 123, No. 3, 2001, pp. 287–292.

[48]Doghri, I., Adam, L., and Bilger, N., "Mean-field homogenization of elasto-viscoplastic composites based on a general incrementally affine linearization method," *International Journal of Plasticity*, Vol. 26, No. 2, 2010, pp. 219–238.

AIAA SciTech
13-17 January 2014, National Harbor, Maryland
55th AIAA/ASMe/ASCE/AHS/SC Structures, Structural Dynamics, and Materials Conference

A Thermodynamically Consistent Cohesive Zone Model for Mixed-Mode Fracture

Liang Zhang*
Utah State University, Logan, UT 84322-4130, USA
Wenbin Yu†
Purdue University, West Lafayette, IN 47907-2045, USA

The objective of this paper is to propose a thermodynamically consistent cohesive zone model for mixed-mode fracture, which enables a cohesive element to exhibit designated behaviors when subject to mixed-mode loading. Some fundamentals of the cohesive zone model, continuum damage mechanics, and thermodynamics are briefed, and the concept of the irreversible deformation is introduced. The cohesive law in the undamaged configuration, the damage evolution law, and the cohesive law in the damaged configuration are subsequently derived, and a novel delamination criterion is proposed. The applicability and power of the proposed cohesive zone model are demonstrated using examples such as predicting the traction-relative displacement and damage factor-relative displacement curves of cohesive elements of various cohesive properties. More sophisticated cohesive properties can be incorporated into the proposed model.

I. Introduction

Cohesive zone models are among the most powerful tools for solving the problems of material fracture. A self-contained cohesive zone model should consist of a geometric representation, a cohesive law, and a delamination criterion. Specifically, the geometric representation of a cohesive zone can be a finite element, often named as a cohesive zone element. A cohesive element is generally a line (2D) or surface (3D) element, or to say, it is of zero thickness. This is because the microscopic length scale associated with material fracture is a priori infinitely smaller than the scale of the macroscopic structure. In addition, this also implies that the model is intrinsically a multiscale approach.[1] The cohesive law relates the traction vector acting across the line/surface cohesive element to the so-call relative displacement vector (or displacement discontinuities). It brings the model a great advantage, i.e., it enables the model to be implemented into some sophisticated user-defined traction-separation relations such that the model is capable of handling the problems involving mixed-mode fracture, complex loading conditions, and complex loading histories. The delamination criterion is generally first experimentally determined and then implemented into the model. It enables the results predicted by the model to agree with those predicted by linear elastic fracture mechanics (LEFM) in case LEFM applies.[2] Till now, it becomes clear that the selection or determination of these three components is crucial to the development of a powerful cohesive zone model.

The facts that the cohesive zone model is a multiscale approach and that its predictions must agree with the LEFM results imply that the model should be thermodynamically consistent. In recent decades, elaborate efforts have been devoted to developing powerful cohesive zone models.[1–16] However, few of them have been validated to be a thermodynamically consistent model for mixed-mode fracture. One reason for this is that some of the cohesive laws are not thermodynamically consistent. Note that, most likely, the constraints imposed by the principles of thermodynamics are not automatically satisfied and require special attention. However, since these constraints are easy to be ignored, the cohesive laws are often derived in an ad-hoc manner. Another reason is that some of the cohesive laws have difficulties in being associated with a delamination criterion in the presence of mixed-mode fracture. Specifically, for mixed-mode fracture,

*Postdoctoral Researcher, Department of Mechanical and Aerospace Engineering.
†Associate Professor, School of Aeronautics and Astronautics, AIAA Associate Fellow.

both the cohesive law and the experimentally determined delamination criterion should be anisotropic. But unfortunately, they are generally not anisotropic in the same manner, i.e., they are governed by different sets of anisotropic parameters, and it is quite challenging to relate one to another. Moreover, in this case, it is even more difficult to simultaneously enable the model to handling the problems involving non-proportional loading/unloading. All in all, there is a need for a powerful cohesive zone model.

The objective of this paper is to propose a thermodynamically consistent cohesive zone model for mixed-mode fracture, which enables a cohesive element to exhibit designated behaviors when subject to mixed-mode loading. Some fundamentals of the cohesive zone model, continuum damage mechanics, and thermodynamics are briefed, and the concept of the irreversible deformation are introduced. The cohesive law in the undamaged configuration, the damage evolution law, and the cohesive law in the damaged configuration are subsequently derived, and a novel delamination criterion is proposed. The applicability and power of the proposed cohesive zone model are demonstrated using examples such as predicting the traction-relative displacement and damage factor-relative displacement curves of cohesive elements of various cohesive properties.

II. Cohesive Zone Model

Cohesive elements are a group of elements developed for the cohesive zone model. A cohesive element is a line (2D) or surface (3D) element whose constitutive relation relates the so-call relative displacement vector (or displacement discontinuities) to the traction vector across the tangential line/plane of the element, while the constitutive relation for a cohesive element is often called the cohesive law (see Figure 1).

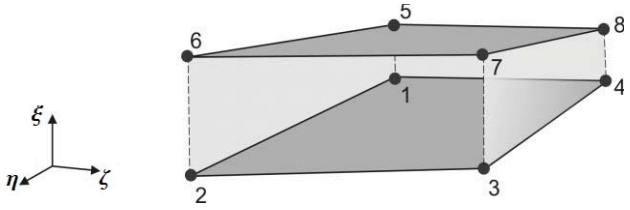

Figure 1. Sketch of a 8-node cohesive element (reproduced from Ref. [11]).

Without loss of generality, consider the linear cohesive element for a 3D problem depicted in Figure 1. Introduce two Cartesian coordinate systems, (x, y, z) and (ξ, η, ζ). Let (x, y, z) denote the global coordinates describing the global structure, and let (ξ, η, ζ) denote the local coordinates describing the element, with its origin located at the geometric center of the element and the ξ-direction normal to the tangential plane of the element (see Figure 1). Let u, v, and w denote the displacements in the x-, y-, and z-directions, respectively. The displacements within the element can be expressed in terms of the standard Lagrangian shape functions, N_i, and the nodal displacements, u_i, v_i, and w_i, as

$$u = \sum_i N_i u_i, \quad v = \sum_i N_i v_i, \quad w = \sum_i N_i w_i, \tag{1}$$

where i denotes the node number. Let the superscripts $+$ and $-$ denote the quantities on the top and bottom surfaces of the element, respectively. The displacements on the top and bottom surfaces can hereby be expressed as

$$u^+ = \sum_i N_i u_i^+, \quad v^+ = \sum_i N_i v_i^+, \quad w^+ = \sum_i N_i w_i^+ \quad i \in \{\text{top nodes}\}, \tag{2}$$

$$u^- = \sum_i N_i u_i^-, \quad v^- = \sum_i N_i v_i^-, \quad w^- = \sum_i N_i w_i^- \quad i \in \{\text{bottom nodes}\}, \tag{2'}$$

respectively. Following Refs. [17] and [18], define the relative displacement vector as follows:

$$[\![u]\!] = u^+ - u^- = \sum_i N_i \left(u_i^+ - u_i^-\right), \quad [\![v]\!] = v^+ - v^- = \sum_i N_i \left(v_i^+ - v_i^-\right), \tag{3}$$

$$[\![w]\!] = w^+ - w^- = \sum_i N_i \left(w_i^+ - w_i^-\right). \tag{3'}$$

In general, the relative displacement vector and the traction vector must be determined in the local coordinate system. This leads one to seek for the transformation matrix from (x, y, z) to (ξ, η, ζ). Specifically, let $\mathbf{V}$ be a arbitrary vector lying in the tangential plane of the element, and let $\mathbf{V} = x\mathbf{i}+y\mathbf{j}+z\mathbf{k}$ in the global coordinate system, where $\mathbf{i}$, $\mathbf{j}$, and $\mathbf{k}$ denote the unit vectors in the x-, y-, and z-directions, respectively. Also let $\mathbf{n}$, $\mathbf{s}$, and $\mathbf{t}$ denote the unit vectors in the ξ-, η-, and ζ-directions, respectively. Note that the vector projections of $\mathbf{V}$ on $\mathbf{s}$ and $\mathbf{t}$, $\mathbf{V}_\eta$ and $\mathbf{V}_\zeta$, can be expressed as

$$\mathbf{V}_\eta = \frac{\partial \mathbf{V}}{\partial \eta} d\eta = \frac{\partial x}{\partial \eta} d\eta \mathbf{i} + \frac{\partial y}{\partial \eta} d\eta \mathbf{j} + \frac{\partial z}{\partial \eta} d\eta \mathbf{k}, \tag{4}$$

$$\mathbf{V}_\zeta = \frac{\partial \mathbf{V}}{\partial \zeta} d\zeta = \frac{\partial x}{\partial \zeta} d\zeta \mathbf{i} + \frac{\partial y}{\partial \zeta} d\zeta \mathbf{j} + \frac{\partial z}{\partial \zeta} d\zeta \mathbf{k}, \tag{4'}$$

respectively. $\mathbf{n}$, $\mathbf{s}$, and $\mathbf{t}$ can then be obtained from $\mathbf{V}_\eta$ and $\mathbf{V}_\zeta$ as

$$\mathbf{n} = \frac{\mathbf{V}_\eta \times \mathbf{V}_\zeta}{|\mathbf{V}_\eta \times \mathbf{V}_\zeta|}, \quad \mathbf{s} = \frac{\mathbf{V}_\eta}{|\mathbf{V}_\eta|}, \quad \mathbf{t} = \frac{\mathbf{V}_\zeta}{|\mathbf{V}_\zeta|}, \tag{5}$$

and the transformation matrix from the global coordinate system to the local one can be obtained from $\mathbf{n}$, $\mathbf{s}$, and $\mathbf{t}$ as

$$\Omega = \begin{bmatrix} n_1 & s_1 & t_1 \\ n_2 & s_2 & t_2 \\ n_3 & s_3 & t_3 \end{bmatrix}. \tag{6}$$

Let $[\![v]\!]$, $[\![\varpi]\!]$, and $[\![\omega]\!]$ denote the relative displacement vector in (ξ, η, ζ), respectively. $[\![v]\!]$, $[\![\varpi]\!]$, and $[\![\omega]\!]$ can be related to $[\![u]\!]$, $[\![v]\!]$, and $[\![w]\!]$ by

$$\begin{bmatrix} [\![v]\!] & [\![\varpi]\!] & [\![\omega]\!] \end{bmatrix}^T = \Omega \begin{bmatrix} [\![u]\!] & [\![v]\!] & [\![w]\!] \end{bmatrix}^T. \tag{7}$$

For notational convenience, let $\boldsymbol{\gamma}$ denote the relative displacement vector in (ξ, η, ζ) with its components being

$$\boldsymbol{\gamma} = \begin{bmatrix} [\![v]\!] & [\![\varpi]\!] & [\![\omega]\!] \end{bmatrix}^T, \tag{8}$$

and let $\boldsymbol{\tau}$ denote the traction vector in (ξ, η, ζ). The cohesive law, which relates $\boldsymbol{\gamma}$ to $\boldsymbol{\tau}$, will be derived later in this paper.

There are two types of interface boundary conditions in the cohesive zone, i.e., the relative displacement boundary conditions and the traction boundary conditions. As the name suggests, for the former boundary conditions, the relative displacement vector is prescribed on the relative displacement boundaries, while for the latter ones, the traction vector is prescribed on the traction boundaries. For notational convenience, let $\mathbf{u}$, $[\![\mathbf{u}]\!]$, and $\mathbf{T}$ denote the displacement vector, the relative displacement vector, and the traction vector in (x, y, z), respectively. The aforementioned two types of boundary conditions can be expressed as

$$[\![\mathbf{u}]\!] = [\![\bar{\mathbf{u}}]\!] \quad \text{on } \Gamma_{[\![\mathbf{u}]\!]}, \tag{9}$$

$$\mathbf{T} = \bar{\mathbf{T}} \quad \text{on } \Gamma_{\mathbf{T}} \tag{4'}$$

respectively, where $\Gamma_{[\![\mathbf{u}]\!]}$ and $\Gamma_{\mathbf{T}}$ denote the relative displacement and traction boundaries, respectively, and $[\![\bar{\mathbf{u}}]\!]$ and $\bar{\mathbf{T}}$ denote the prescribed values of $[\![\mathbf{u}]\!]$ and $\mathbf{T}$, respectively. Also note that $\boldsymbol{\gamma}$ and $\boldsymbol{\tau}$ are related to $[\![\mathbf{u}]\!]$and $\mathbf{T}$ by

$$\boldsymbol{\gamma} = \boldsymbol{\Omega} \cdot [\![\mathbf{u}]\!] \quad \text{and} \quad \boldsymbol{\tau} = \boldsymbol{\Omega} \cdot \mathbf{T}, \tag{10}$$

respectively.

Introduce a local coordinate system $\mathbf{x} = (x_1, x_2, x_3)$, and let the x_1-, x_2-, and x_3-axes correspond to modes I, II, and III loading, respectively. According to Ref. [11], the modes I, II, and III energy release rates can be expressed as

$$G_{\mathrm{I}} = \int_0^{\gamma_1} \tau_1 d\gamma_1, \quad G_{\mathrm{II}} = \int_0^{\gamma_2} \tau_2 d\gamma_2, \quad G_{\mathrm{III}} = \int_0^{\gamma_3} \tau_3 d\gamma_3, \tag{11}$$

respectively, and the mixed-mode energy release rate can be expressed as

$$G = G_{\mathrm{I}} + G_{\mathrm{II}} + G_{\mathrm{III}}. \tag{12}$$

$\boldsymbol{\gamma}$ and $\boldsymbol{\tau}$ actually take the forms of

$$\boldsymbol{\gamma} = \begin{bmatrix} \langle\gamma_1\rangle & \gamma_2 & \gamma_3 \end{bmatrix}^T \quad \text{and} \quad \boldsymbol{\tau} = \begin{bmatrix} \langle\tau_1\rangle & \tau_2 & \tau_3 \end{bmatrix}^T, \tag{13}$$

where $\langle\cdot\rangle$ denotes the Macaulay bracket, i.e.,

$$\langle x\rangle = \begin{cases} x & x > 0, \\ 0 & x \leq 0. \end{cases} \tag{14}$$

This can be understood by noting that negative γ_1 and τ_1 do not contribute to G_{I} and are hereby physically meaningless. As mentioned above, the cohesive law relates $\boldsymbol{\tau}$ to $\boldsymbol{\gamma}$. This, together with Eq. (11), implies that, once the cohesive law is specified, the variations of G_{I}, G_{II}, and G_{III} during continued deformation are fully determined.

It is often assumed that delamination occurs as G attains a critical value, say G_c. According to Ref. [19], the mixed-mode critical energy release rate, G_c, can be expressed as

$$G_c = G_c\left(G_{\mathrm{I}c}, G_{\mathrm{II}c}, G_{\mathrm{III}c}, \boldsymbol{\beta}\right), \tag{15}$$

where $G_{\mathrm{I}c}$, $G_{\mathrm{II}c}$, and $G_{\mathrm{III}c}$ denote the modes I, II, and III critical energy release rates, respectively, which are known as material constants, and $\boldsymbol{\beta}$ denotes a mode mixity vector with its form being specified later, while the specific form of Eq. (15) can be determined by finding an expression fitting the experimental results well. Since Eq. (15) specifies the delamination conditions, it is also referred to as the delamination criterion. It is worth notice that Eq. (15) is not the only option of the delamination criterion. In this paper, a novel delamination criterion will be proposed.

As mentioned above, a self-contained cohesive zone model should consist of a geometric representation, a cohesive law, and a delamination criterion. Since the geometric representation is well developed, the major tasks become specifying the cohesive law and the delamination criterion. These two tasks will be accomplished in the next several sections. In the next section, some fundamentals of continuum damage mechanics will be briefed. This will help the understanding of the problem from the perspective of continuum damage mechanics.

III. Undamaged Configuration and Damage Factor

Tan and his coworkers[20] have demonstrated that the delamination of a cohesive zone is always accompanied by a monotonic traction decrease with increasing relative displacement vector. Meanwhile, several authors[1,2,11,13,15,16,21] also introduced a damage factor to describe this phenomenon and formulated the cohesive law in the framework of continuum damage mechanics. For this reason, it is beneficial to brief some fundamentals of continuum damage mechanics here.

Without loss of generality, let $\boldsymbol{\gamma}$ consist of a reversible part, $\boldsymbol{\gamma}^e$, and an irreversible part, $\boldsymbol{\gamma}^p$, i.e.,

$$\boldsymbol{\gamma} = \boldsymbol{\gamma}^e + \boldsymbol{\gamma}^p. \tag{16}$$

Also let $\boldsymbol{\tau}$ be related to $\boldsymbol{\gamma}^e$ by

$$\boldsymbol{\tau} = \mathbf{C}^e \cdot \boldsymbol{\gamma}^e, \tag{17}$$

where $\mathbf{C}^e$ denotes the second-order reversible stiffness tensor. In this paper, the off-diagonal components of $\mathbf{C}^e$ are set to be vanish. This physically means that different modes of fracture do not interfere each other.

There are two basic but important assumptions in continuum damage mechanics:

1. Each damaged material has an equivalent undamaged material;
2. There exists a one-to-one correspondence between each pair of physical quantities in the damaged and undamaged (effective) configurations.

As these two assumption are made, the task can be accomplished by subsequently deriving the cohesive law in the undamaged configuration, the damage evolution law, and the cohesive law in the damaged configuration.

The traction vector in the undamaged configuration can be related to that in the damaged configuration, $\boldsymbol{\tau}$, by

$$\bar{\boldsymbol{\tau}} = \mathbf{M} \cdot \boldsymbol{\tau} \quad \text{or} \quad \boldsymbol{\tau} = \mathbf{M}^{-1} \cdot \bar{\boldsymbol{\tau}}, \tag{18}$$

where the overbar denotes the quantity in the undamaged configuration, $\mathbf{M}$ denotes the second-order damage effect tensor, and $\bar{\boldsymbol{\tau}}$ can be referred to as the effective traction vector. Without loss of generality, let $\boldsymbol{\omega}$ and $\mathbf{D}$ denote the damage vector and the second-order damage tensors, respectively, and let $\mathbf{D}$ be related to $\boldsymbol{\omega}$ by

$$\mathbf{D} = \sum_{i=1}^{3} \omega_i \mathbf{e}_i \otimes \mathbf{e}_i, \tag{19}$$

where $\mathbf{e}_i$ denotes the unit vector. Eq. (19) implies that the off-diagonal components of $\mathbf{D}$ vanish. Let $\mathbf{M}^{-1}$ be related to $\mathbf{D}$ by

$$\mathbf{M}^{-1} = \mathbf{I} - \mathbf{D}, \tag{20}$$

where $\mathbf{I}$ denotes the second-order identity tensor. Similarly to $\mathbf{D}$, the off-diagonal components of $\mathbf{M}^{-1}$ also vanish.

Let ψ^e denote the reversible free energy density. The correspondence between the traction vector and relative displacement vector in the damaged configuration and those in the undamaged configuration can be defined as

$$\rho\psi^e\left(\boldsymbol{\gamma}^e, \boldsymbol{\omega}\right) = \rho\psi^e\left(\bar{\boldsymbol{\gamma}}^e\right) \quad \text{or} \quad \frac{1}{2}\boldsymbol{\tau}\cdot\boldsymbol{\gamma}^e = \frac{1}{2}\bar{\boldsymbol{\tau}}\cdot\bar{\boldsymbol{\gamma}}^e. \tag{21}$$

Substituting Eq. (18) into Eq. (21) gives

$$\bar{\boldsymbol{\gamma}}^e = \mathbf{M}^{-1}\cdot\boldsymbol{\gamma}^e \quad \text{or} \quad \boldsymbol{\gamma}^e = \mathbf{M}\cdot\bar{\boldsymbol{\gamma}}^e. \tag{22}$$

Eq. (17) can be expressed in the undamaged configuration as

$$\bar{\boldsymbol{\tau}} = \bar{\mathbf{C}}^e\cdot\bar{\boldsymbol{\gamma}}^e, \tag{23}$$

where $\bar{\mathbf{C}}^e$ denotes the second-order reversible stiffness tensor and is constant. Substituting Eqs. (17), (18), (22), and (101) into Eq. (21) gives

$$\mathbf{C}^e = \mathbf{M}^{-1}\cdot\bar{\mathbf{C}}^e\cdot\mathbf{M}^{-1} \quad \text{or} \quad \left(\mathbf{C}^e\right)^{-1} = \mathbf{M}\cdot\left(\bar{\mathbf{C}}^e\right)^{-1}\cdot\mathbf{M}. \tag{24}$$

Recall that the off-diagonal components of $\mathbf{M}^{-1}$ vanish. This, together with Eqs. (18), (22), and (24), implies that each component of $\boldsymbol{\omega}$ actually provides a measure of the damages associated with the corresponding components of $\boldsymbol{\tau}$ and $\boldsymbol{\gamma}^e$.

Till now, some fundamentals of continuum damage mechanics have been briefed. In the next section, some fundamentals of thermodynamics will be briefed.

IV. Thermodynamic Formulations

Let ψ denote the Helmholtz free energy per unit area of the cohesive element. According to the theory of thermodynamics, ψ can be expressed as a function of a suitable set of independent state variables characterizing the reversible, irreversible, and damage behaviors of the element, e.g.,

$$\psi = \psi\left(\boldsymbol{\gamma}, \boldsymbol{\omega}, r, s\right), \tag{25}$$

where r and s are two scalars accounting for the isotropic hardening due to the irreversible deformation and damage hardening, respectively. Assume that the element exhibits uncoupled reversible, irreversible, and damage behaviors. In this case, ψ can be expressed as the sum of its reversible part, ψ^e, its irreversible hardening part, ψ^p, and its damage hardening part, ψ^d, i.e.,

$$\psi\left(\boldsymbol{\gamma}, \boldsymbol{\omega}, r, s\right) = \psi^e\left(\boldsymbol{\gamma}^e, \boldsymbol{\omega}\right) + \psi^p\left(r\right) + \psi^d\left(s\right), \tag{26}$$

where ψ^p and ψ^d denote the free energy densities due to isotropic hardening and damage hardening, respectively. The thermodynamic forces conjugate to the state variables in Eq. (25) can be defined as

$$\boldsymbol{\tau} = \frac{\partial\psi}{\partial\boldsymbol{\gamma}^e} = \frac{\partial\psi^e}{\partial\boldsymbol{\gamma}^e}, \quad \mathbf{Y} = -\frac{\partial\psi}{\partial\boldsymbol{\omega}} = -\frac{\partial\psi^e}{\partial\boldsymbol{\omega}}, \quad R = \frac{\partial\psi}{\partial r} = \frac{d\psi^p}{dr}, \quad S = \frac{\partial\psi}{\partial s} = \frac{d\psi^d}{ds}, \tag{27}$$

where $\mathbf{Y}$ denotes the damage conjugate force vector, and R and S are related to the current yield traction and the current damage threshold.

If the deformation is isothermal, the Clausius-Duhem inequality writes

$$\phi = \boldsymbol{\tau} \cdot \dot{\boldsymbol{\gamma}} - \dot{\psi} \geq 0, \tag{28}$$

where ϕ denotes the dissipation per unit area, and the overdot denotes the time derivative of the quantity. Combining Eq. (16) and Eqs. (26)–(28) gives

$$\phi = \boldsymbol{\tau} \cdot \dot{\boldsymbol{\gamma}}^p + \mathbf{Y} \cdot \dot{\boldsymbol{\omega}} - R\dot{r} - S\dot{s} \geq 0, \tag{29}$$

Similarly to ψ, ϕ can be decomposed into its plastic hardening and damage hardening parts, ϕ^p and ϕ^d, i.e.,

$$\phi = \phi^p + \phi^d, \tag{30}$$

where

$$\phi^p = \boldsymbol{\tau} \cdot \dot{\boldsymbol{\gamma}}^p - R\dot{r} \geq 0 \quad \text{and} \quad \phi^d = \mathbf{Y} \cdot \dot{\boldsymbol{\omega}} - S\dot{s} \geq 0. \tag{31}$$

Let the yield and damage criteria take the forms of

$$f^p(\boldsymbol{\tau}, R) = 0 \quad \text{and} \quad f^d(\mathbf{Y}, S) = 0, \tag{32}$$

respectively. The maximum dissipation principle states that the actual state of the thermodynamic forces should maximize ϕ subject to constraint Eq. (32).[22] This implies that the actual state of the thermodynamic forces should maximize Lagrange functions

$$\Lambda^p = \phi^p - \dot{\lambda}^p f^p \quad \text{and} \quad \Lambda^d = \phi^d - \dot{\lambda}^d f^d, \tag{33}$$

where $\dot{\lambda}^p$ and $\dot{\lambda}^d$ are two Lagrange multipliers. Λ^p and Λ^d reach their respective maximums only if

$$\frac{\partial \Lambda^p}{\partial \boldsymbol{\tau}} = 0, \quad \frac{\partial \Lambda^p}{\partial R} = 0, \quad \frac{\partial \Lambda^d}{\partial \mathbf{Y}} = 0, \quad \frac{\partial \Lambda^d}{\partial S} = 0. \tag{34}$$

Substituting Eqs. (29)–(33) into Eq. (34) gives

$$\dot{\boldsymbol{\gamma}}^p = \dot{\lambda}^p \frac{\partial f^p}{\partial \boldsymbol{\tau}}, \quad \dot{r} = -\dot{\lambda}^p \frac{\partial f^p}{\partial R}, \quad \dot{\boldsymbol{\omega}} = \dot{\lambda}^d \frac{\partial f^d}{\partial \mathbf{Y}}, \quad \dot{s} = -\dot{\lambda}^d \frac{\partial f^d}{\partial S}, \tag{35}$$

which governs the evolution of the state variables.

Till now, some fundamentals of thermodynamics have been briefed. In the next section, the cohesive law in the undamaged configuration will be derived.

V. Cohesive Law in the Undamaged Configuration

It is reasonable that the irreversible deformation can only occur in the undamaged part of the cohesive element. This implies that

$$f^p(\boldsymbol{\tau}, R) = f^p\left(\bar{\boldsymbol{\tau}}, \bar{R}\right). \tag{36}$$

Eq. (36) leads one to first derive the cohesive law in the undamaged configuration. In this section, this task will be accomplished.

Without loss of generality, let the cohesive element obey a Hill-type yield criterion, which writes

$$f^p\left(\bar{\boldsymbol{\tau}}, \bar{R}\right) = \bar{\tau}_e - \bar{\tau}_Y = 0, \tag{37}$$

where $\bar{\tau}_e$ denotes a Hill-type equivalent traction and takes the form of

$$\bar{\tau}_e = \sqrt{\bar{\boldsymbol{\tau}} \cdot \bar{\mathbf{H}} \cdot \bar{\boldsymbol{\tau}}} \tag{38}$$

with $\bar{\mathbf{H}}$ denoting a second-order anisotropy tensor, and $\bar{\tau}_Y$ denotes the current yield traction and is related to $\bar{R}$ by

$$\bar{\tau}_Y = \bar{\tau}_0 + \bar{R} \tag{39}$$

with $\bar{\tau}_0$ denoting the initial yield stress. In this paper, the off-diagonal components of $\bar{\mathbf{H}}$ are set to vanish. One can write the irreversible work equivalence principle as

$$\bar{\boldsymbol{\tau}} \cdot \dot{\bar{\boldsymbol{\gamma}}}^p = \bar{\tau}_e \dot{\bar{p}}, \tag{40}$$

where $\dot{\bar{p}}$ denotes a Hill-type irreversible equivalent velocity. Following Ref. [23], taking the partial derivatives with respect to $\bar{\boldsymbol{\tau}}$ on both sides of Eq. (40) gives

$$\dot{\bar{\boldsymbol{\gamma}}}^p = \frac{\partial \bar{\tau}_e}{\partial \bar{\boldsymbol{\tau}}} \dot{\bar{p}}. \tag{41}$$

The explicit expression for $\partial \bar{\tau}_e / \partial \bar{\boldsymbol{\tau}}$ can be derived as

$$\frac{\partial \bar{\tau}_e}{\partial \bar{\boldsymbol{\tau}}} = \frac{1}{2\bar{\tau}_e} \frac{\partial \bar{\boldsymbol{\tau}}_e^2}{\partial \bar{\boldsymbol{\tau}}} = \frac{1}{2\bar{\tau}_e} \left(2 \frac{\partial \bar{\boldsymbol{\tau}}}{\partial \bar{\boldsymbol{\tau}}} \cdot \bar{\mathbf{H}} \cdot \bar{\boldsymbol{\tau}} \right) = \frac{\bar{\mathbf{H}} \cdot \bar{\boldsymbol{\tau}}}{\bar{\tau}_e}. \tag{42}$$

Substituting Eq. (42) into Eq. (41) gives

$$\dot{\bar{\boldsymbol{\gamma}}}^p = \frac{\bar{\mathbf{H}} \cdot \bar{\boldsymbol{\tau}}}{\bar{\tau}_e} \dot{\bar{p}} \quad \text{or} \quad \bar{\boldsymbol{\tau}} = \frac{\bar{\mathbf{H}}^{-1} \cdot \dot{\bar{\boldsymbol{\gamma}}}^p}{\dot{\bar{p}}} \bar{\tau}_e, \tag{43}$$

where $\bar{\mathbf{H}} \cdot \bar{\mathbf{H}}^{-1} = \mathbf{I}$. Substituting the second equation of Eq. (43) into Eq. (40) and rearranging the equation give

$$\dot{\bar{p}}^2 = \dot{\bar{\boldsymbol{\gamma}}}^p \cdot \bar{\mathbf{H}}^{-1} \cdot \dot{\bar{\boldsymbol{\gamma}}}^p \quad \text{or} \quad \dot{\bar{p}} = \sqrt{\dot{\bar{\boldsymbol{\gamma}}}^p \cdot \bar{\mathbf{H}}^{-1} \cdot \dot{\bar{\boldsymbol{\gamma}}}^p}. \tag{44}$$

It is beneficial to find the relation between $\dot{\bar{\lambda}}^p$ and $\dot{\bar{p}}$. Similarly to the first three equations of Eq. (35), one can obtain that

$$\dot{\bar{\boldsymbol{\gamma}}}^p = \dot{\bar{\lambda}}^p \frac{\partial f^p}{\partial \bar{\boldsymbol{\tau}}}, \quad \text{or} \quad \dot{\bar{r}} = -\dot{\bar{\lambda}}^p \frac{\partial f^p}{\partial \bar{R}} \tag{45}$$

in the undamaged configuration. Substituting the first equation of Eq. (45) into Eq. (40) gives

$$\bar{\boldsymbol{\tau}} \cdot \left(\dot{\bar{\lambda}}^p \frac{\partial f^p}{\partial \bar{\boldsymbol{\tau}}} \right) = \bar{\tau}_e \dot{\bar{p}}. \tag{46}$$

Note that $\partial f^p / \partial \bar{\boldsymbol{\tau}} = \partial \bar{\tau}_e / \partial \bar{\boldsymbol{\tau}}$. Substituting Eq. (42) into Eq. (46) gives

$$\bar{\tau}_e \dot{\bar{\lambda}}^p = \bar{\tau}_e \dot{\bar{p}} \quad \text{or} \quad \dot{\bar{\lambda}}^p = \dot{\bar{p}}. \tag{47}$$

Accordingly, the Kuhn-Tucker conditions (loading/unloading conditions) write

$$f^p \leq 0, \quad \dot{\bar{\lambda}}^p \geq 0, \quad \dot{\bar{\lambda}}^p f^p = 0. \tag{48}$$

According to Ref. [24], Eq. (45) sometime places too strict restriction. Following Ref. [25], introduce a pseudo-potential g^p, which is related to f^p by

$$g^p = f^p + \frac{\bar{R}^2}{2\bar{K}} \tag{49}$$

with $\bar{K}$ being a constant accounting for isotropic hardening, and rewrite Eq. (45) as

$$\dot{\bar{\boldsymbol{\gamma}}}^p = \dot{\bar{\lambda}}^p \frac{\partial g^p}{\partial \bar{\boldsymbol{\tau}}} \quad \text{and} \quad \dot{\bar{r}} = -\dot{\bar{\lambda}}^p \frac{\partial g^p}{\partial \bar{R}} = \left(1 - \frac{\bar{R}}{\bar{K}} \right) \dot{\bar{\lambda}}^p. \tag{50}$$

Since $\partial g^p / \partial \bar{\boldsymbol{\tau}} = \partial f^p / \partial \bar{\boldsymbol{\tau}}$, Eq. (47) remains valid here. Let ψ^p take the form of

$$\psi^p = \frac{1}{2} \bar{K} \bar{n} \bar{r}^2, \tag{51}$$

where $\bar{n}$ is another constant accounting for isotropic hardening. Note that, by definition,

$$\bar{R} = \bar{K} \bar{n} \bar{r}. \tag{52}$$

Substituting the last equation of Eq. (50) into the rate form of Eq. (52) and noting that $\dot{\bar{\lambda}}^p = \dot{\bar{p}}$ give

$$\dot{\bar{R}} = \left(\bar{K} - \bar{R}\right) \bar{n} \dot{\bar{p}} \quad \text{or} \quad \bar{R} = \bar{K} \left[1 - \exp\left(-\bar{n}\bar{p}\right)\right]. \tag{53}$$

The consistency condition can be obtained from Eq. (37) as

$$\dot{f}^p = \frac{\partial f^p}{\partial \bar{\boldsymbol{\tau}}} \cdot \dot{\bar{\boldsymbol{\tau}}} + \frac{\partial f^p}{\partial \bar{R}} \frac{d\bar{R}}{d\bar{p}} \dot{\bar{p}} = 0. \tag{54}$$

Rearranging Eq. (54) and noting that $\partial f / \partial \bar{R} = -1$ and $\dot{\bar{\lambda}}^p = \dot{\bar{p}}$ give

$$\frac{\partial f^p}{\partial \bar{\boldsymbol{\tau}}} \cdot \dot{\bar{\boldsymbol{\tau}}} = \frac{d\bar{R}}{d\bar{p}} \dot{\bar{\lambda}}^p. \tag{55}$$

Note that $\dot{\bar{\boldsymbol{\gamma}}}$ can be expressed as

$$\dot{\bar{\boldsymbol{\gamma}}} = \dot{\bar{\boldsymbol{\gamma}}}^e + \dot{\bar{\boldsymbol{\gamma}}}^p = \left(\bar{\mathbf{C}}^e\right)^{-1} \cdot \dot{\bar{\boldsymbol{\tau}}} + \dot{\bar{\lambda}}^p \frac{\partial g^p}{\partial \bar{\boldsymbol{\tau}}}. \tag{56}$$

Multiplying both sides of Eq. (56) by $\partial f^p / \partial \bar{\boldsymbol{\tau}} \cdot \bar{\mathbf{C}}^e$ gives

$$\frac{\partial f^p}{\partial \bar{\boldsymbol{\tau}}} \cdot \bar{\mathbf{C}}^e \cdot \dot{\bar{\boldsymbol{\gamma}}} = \frac{\partial f^p}{\partial \bar{\boldsymbol{\tau}}} \cdot \dot{\bar{\boldsymbol{\tau}}} + \dot{\bar{\lambda}}^p \frac{\partial f^p}{\partial \bar{\boldsymbol{\tau}}} \cdot \bar{\mathbf{C}}^e \cdot \frac{\partial g^p}{\partial \bar{\boldsymbol{\tau}}}. \tag{57}$$

Substituting Eq. (55) into Eq. (56) gives

$$\frac{\partial f^p}{\partial \bar{\boldsymbol{\tau}}} \cdot \bar{\mathbf{C}}^e \cdot \dot{\bar{\boldsymbol{\gamma}}} = \frac{d\bar{R}}{d\bar{p}} \dot{\bar{\lambda}}^p + \dot{\bar{\lambda}}^p \frac{\partial f^p}{\partial \bar{\boldsymbol{\tau}}} \cdot \bar{\mathbf{C}}^e \cdot \frac{\partial g^p}{\partial \bar{\boldsymbol{\tau}}}. \tag{58}$$

$\dot{\bar{\lambda}}^p$ can hereby be obtained as

$$\dot{\bar{\lambda}}^p = \frac{\dfrac{\partial f^p}{\partial \bar{\boldsymbol{\tau}}} \cdot \bar{\mathbf{C}}^e \cdot \dot{\bar{\boldsymbol{\gamma}}}}{\dfrac{d\bar{R}}{d\bar{p}} + \dfrac{\partial f^p}{\partial \bar{\boldsymbol{\tau}}} \cdot \bar{\mathbf{C}}^e \cdot \dfrac{\partial g^p}{\partial \bar{\boldsymbol{\tau}}}}. \tag{59}$$

Substituting Eq. (59) into Eq. (56), multiplying both sides of the equation by $\bar{\boldsymbol{\mathcal{C}}}^e$, and rearranging the equation give the rate form of the cohesive law in the undamaged configuration as

$$\dot{\bar{\boldsymbol{\tau}}} = \bar{\mathbf{C}}^{ep} \cdot \dot{\bar{\boldsymbol{\gamma}}}, \tag{60}$$

where $\bar{\mathbf{C}}^{ep}$ denotes the second-order instantaneous cohesive stiffness tensor in the undamaged configuration and is given by

$$\bar{\mathbf{C}}^{ep} = \bar{\mathbf{C}}^e - \frac{\left(\bar{\mathbf{C}}^e \cdot \dfrac{\partial g^p}{\partial \bar{\boldsymbol{\tau}}}\right) \otimes \left(\dfrac{\partial f^p}{\partial \bar{\boldsymbol{\tau}}} \cdot \bar{\mathbf{C}}^e\right)}{\dfrac{d\bar{R}}{d\bar{p}} + \dfrac{\partial f^p}{\partial \bar{\boldsymbol{\tau}}} \cdot \bar{\mathbf{C}}^e \cdot \dfrac{\partial g^p}{\partial \bar{\boldsymbol{\tau}}}}. \tag{61}$$

Till now, the cohesive law in the undamaged configuration has been derived. In the next section, the damage evolution law will be derived.

VI. Damage Evolution Law

Let the damage criterion take a Hill-type form, i.e.,

$$f^d\left(\mathbf{Y}, S\right) = Y_e - Y_T = 0, \tag{62}$$

where Y_e denotes a Hill-type equivalent damage conjugate force and takes the form of

$$Y_e = \sqrt{\mathbf{Y} \cdot \mathbf{L} \cdot \mathbf{Y}} \tag{63}$$

with $\mathbf{L}$ denoting a second-order damage anisotropy tensor, and Y_T denotes the current damage threshold and is related to S by

$$Y_T = Y_0 + S \tag{64}$$

with Y_0 denoting the initial damage threshold. Following to Ref. [26], let the diagonal components of L_{ij} be greater than the off-diagonal ones. More details on the damage anisotropy tensor can be found in Ref. [26]. One can write the damage dissipation equivalence principle as

$$\mathbf{Y} \cdot \dot{\boldsymbol{\omega}} = Y_e \dot{q}, \tag{65}$$

where $\dot{q}$ denotes a Hill-type equivalent damage rate. Similarly to Section V, taking the partial derivatives with respect to $\mathbf{Y}$ on both sides of Eq. (65) gives

$$\dot{\boldsymbol{\omega}} = \frac{\partial Y_e}{\partial \mathbf{Y}} \dot{q}. \tag{66}$$

$\partial Y_e / \partial \mathbf{Y}$ can be obtained as

$$\frac{\partial Y_e}{\partial \mathbf{Y}} = \frac{1}{2Y_e} \frac{\partial Y_e^2}{\partial \mathbf{Y}} = \frac{1}{2Y_e} \left(2 \frac{\partial \mathbf{Y}}{\partial \mathbf{Y}} \cdot \mathbf{L} \cdot \mathbf{Y} \right) = \frac{\mathbf{L} \cdot \mathbf{Y}}{Y_e}. \tag{67}$$

Substituting Eq. (67) into Eq. (66) gives

$$\dot{\boldsymbol{\omega}} = \frac{\mathbf{L} \cdot \mathbf{Y}}{Y_e} \dot{q} \quad \text{or} \quad \mathbf{Y} = \frac{\mathbf{L}^{-1} \cdot \dot{\boldsymbol{\omega}}}{\dot{q}} Y_e, \tag{68}$$

where $\mathbf{L} \cdot \mathbf{L}^{-1} = \mathbf{I}$. Substituting the second equation of Eq. (68) into Eq. (65) and rearranging the equation give

$$\dot{q}^2 = \dot{\boldsymbol{\omega}} \cdot \mathbf{L}^{-1} \cdot \dot{\boldsymbol{\omega}} \quad \text{or} \quad \dot{q} = \sqrt{\dot{\boldsymbol{\omega}} \cdot \mathbf{L}^{-1} \cdot \dot{\boldsymbol{\omega}}}. \tag{69}$$

Similarly to Section V, it is beneficial to find the relation between $\dot{\lambda}^d$ and $\dot{q}$. Recall that the last two equations of Eq. (35) writes

$$\dot{\boldsymbol{\omega}} = \dot{\lambda}^d \frac{\partial f^d}{\partial \mathbf{Y}} \quad \text{and} \quad \dot{s} = -\dot{\lambda}^d \frac{\partial f^d}{\partial S}. \tag{70}$$

Substituting the first equation of Eq. (70) into Eq. (65) gives

$$\mathbf{Y} \cdot \left(\dot{\lambda}^d \frac{\partial f^d}{\partial \mathbf{Y}} \right) = Y_e \dot{q}. \tag{71}$$

Note that $\partial f^d / \partial \mathbf{Y} = \partial Y_e / \partial \mathbf{Y}$. Substituting Eq. (67) into Eq. (71) gives

$$Y_e \dot{\lambda}^d = Y_e \dot{q} \quad \text{or} \quad \dot{\lambda}^d = \dot{q}. \tag{72}$$

Accordingly, the Kuhn-Tucker condition (loading/unloading conditions) write

$$f^d \leq 0, \quad \dot{\lambda}^d \geq 0, \quad \dot{\lambda}^d f^d = 0. \tag{73}$$

Similarly to Section V, introduce a pseudo-potential g^d, which is related to f^d by

$$g^d = f^d + \frac{S^2}{2L} \tag{74}$$

with L being a constant accounting for damage hardening, and rewrite Eq. (70) as

$$\dot{\boldsymbol{\omega}} = \dot{\lambda}^d \frac{\partial g^d}{\partial \mathbf{Y}} \quad \text{and} \quad \dot{s} = -\dot{\lambda}^d \frac{\partial g^d}{\partial S}. \tag{75}$$

Since $\partial g^d / \partial \mathbf{Y} = \partial f^d / \partial \mathbf{Y}$, Eq. (72) remains valid here. Let ψ^d take the form of

$$\psi^d = \frac{1}{2} L o s^2, \tag{76}$$

where o is another constant accounting for damage hardening. Substituting Eq. (76) into the last equation of Eq. (27) gives

$$S = Los. \tag{77}$$

Substituting the last equation of Eq. (75) into the rate form of Eq. (77) and noting that $\dot{\lambda}^d = \dot{q}$ give

$$\dot{S} = (L - S)\, o\dot{q} \quad \text{or} \quad S = L\left[1 - \exp\left(-oq\right)\right]. \tag{78}$$

The consistency condition can be obtained from Eq. (62) as

$$\dot{f}^d = \frac{\partial f^d}{\partial \mathbf{Y}} \cdot \dot{\mathbf{Y}} + \frac{\partial f^d}{\partial S}\frac{dS}{dq}\dot{q} = 0. \tag{79}$$

Rearranging Eq. (79) and noting that $\partial f^d / \partial S = -1$ and $\dot{\lambda}^d = \dot{q}$ and give

$$\dot{\lambda}^d = \frac{\dfrac{\partial f^d}{\partial \mathbf{Y}} \cdot \dot{\mathbf{Y}}}{\dfrac{dS}{dq}}. \tag{80}$$

Substituting Eq. (80) into the first equation of Eq. (75) gives

$$\dot{\boldsymbol{\omega}} = \frac{\dfrac{\partial f^d}{\partial \mathbf{Y}} \cdot \dot{\mathbf{Y}}}{\dfrac{dS}{dq}}\frac{\partial g^d}{\partial \mathbf{Y}} = \frac{\dfrac{\partial g^d}{\partial \mathbf{Y}} \otimes \dfrac{\partial f^d}{\partial \mathbf{Y}}}{\dfrac{dS}{dq}} \cdot \dot{\mathbf{Y}} \equiv \mathbf{S}^d \cdot \dot{\mathbf{Y}}, \tag{81}$$

which is the damage evolution law. It is worth notice that $\mathbf{S}^d$ is not always invertible.

Till now, the damage evolution law has been derived. In the next section, the cohesive law in the damaged configuration will be derived.

VII. Cohesive Law in the Damaged Configuration

The cohesive law in the damaged configuration can be derived by subsequently accomplishing the following tasks:

1. Relate $\dot{\bar{\boldsymbol{\gamma}}}^e$ to $\dot{\boldsymbol{\gamma}}^e$;
2. Relate $\dot{\bar{\boldsymbol{\tau}}}$ to $\dot{\boldsymbol{\tau}}$;
3. Relate $\dot{\bar{\boldsymbol{\gamma}}}^p$ to $\dot{\boldsymbol{\gamma}}^p$, and complete the derivation.

To relate $\dot{\bar{\boldsymbol{\gamma}}}^e$ to $\dot{\boldsymbol{\gamma}}^e$, recall that

$$\bar{\boldsymbol{\gamma}}^e = \mathbf{M}^{-1} \cdot \boldsymbol{\gamma}^e. \tag{82}$$

Taking time derivatives on both sides of Eq. (82) gives

$$\dot{\bar{\boldsymbol{\gamma}}}^e = \dot{\mathbf{M}}^{-1} \cdot \boldsymbol{\gamma}^e + \mathbf{M}^{-1} \cdot \dot{\boldsymbol{\gamma}}^e. \tag{83}$$

The first term to the right of the equal sign in Eq. (88) can be further expressed as

$$\dot{M}^{-1}_{ij}\gamma^e_j = \left(\frac{\partial M^{-1}_{ij}}{\partial \omega_k}\dot{\omega}_k\right)\gamma^e_j = \left(\frac{\partial M^{-1}_{ij}}{\partial \omega_k}\gamma^e_j\right)\dot{\omega}_k. \tag{84}$$

Let

$$\mathcal{K}_{ikj} = -\frac{\partial M^{-1}_{ij}}{\partial \omega_k} = -\frac{\partial}{\partial \omega_k}\left(I_{ij} - D_{ij}\right) = \frac{\partial D_{ij}}{\partial \omega_k}. \tag{85}$$

Substituting Eq. (19) into Eq. (85) gives

$$\boldsymbol{\mathcal{K}} = \sum_{i=1}^{3} \mathbf{e}_i \otimes \mathbf{e}_i \otimes \mathbf{e}_i. \tag{86}$$

Substituting Eq. (85) into Eq. (84) gives

$$\dot{M}_{ij}^{-1}\gamma_j^e = -\left(\mathcal{K}_{ikj}\gamma_j^e\right)\dot{\omega}_k \quad \text{or} \quad \dot{\mathbf{M}}^{-1}\cdot\boldsymbol{\gamma}^e = -\left(\boldsymbol{\mathcal{K}}\cdot\boldsymbol{\gamma}^e\right)\cdot\dot{\boldsymbol{\omega}}. \tag{87}$$

Substituting Eq. (87) into Eq. (83) gives

$$\dot{\bar{\boldsymbol{\gamma}}}^e = -\left(\boldsymbol{\mathcal{K}}\cdot\boldsymbol{\gamma}^e\right)\cdot\dot{\boldsymbol{\omega}} + \mathbf{M}^{-1}\cdot\dot{\boldsymbol{\gamma}}^e. \tag{88}$$

Eq. (88) implies that, to relate $\dot{\bar{\boldsymbol{\gamma}}}^e$ to $\dot{\boldsymbol{\gamma}}^e$, one needs to first relate $\dot{\boldsymbol{\omega}}$ to $\dot{\boldsymbol{\gamma}}^e$. Note that ψ^e can be expressed as

$$\psi^e = \frac{1}{2}\boldsymbol{\tau}\cdot\boldsymbol{\gamma}^e = \frac{1}{2}\boldsymbol{\gamma}^e\cdot\mathbf{C}^e\cdot\boldsymbol{\gamma}^e = \frac{1}{2}\boldsymbol{\gamma}^e\cdot\left(\mathbf{M}^{-1}\cdot\bar{\mathbf{C}}^e\cdot\mathbf{M}^{-1}\right)\cdot\boldsymbol{\gamma}^e. \tag{89}$$

Substituting Eq. (89) into the second equation of Eq. (27) gives

$$\mathbf{Y} = -\frac{\partial\psi^e}{\partial\boldsymbol{\omega}} = \frac{1}{2}\boldsymbol{\gamma}^e\cdot\left(\boldsymbol{\mathcal{K}}\cdot\bar{\mathbf{C}}^e\cdot\mathbf{M}^{-1} + \mathbf{M}^{-1}\cdot\bar{\mathbf{C}}^e\cdot\boldsymbol{\mathcal{K}}\right)\cdot\boldsymbol{\gamma}^e. \tag{90}$$

Eq. (90) implies that $\mathbf{Y}$ can be treated as a function of $\boldsymbol{\gamma}^e$ and $\boldsymbol{\omega}$. Accordingly, $\dot{\mathbf{Y}}$ can be expressed in terms of $\dot{\boldsymbol{\gamma}}^e$ and $\dot{\boldsymbol{\omega}}$ using the chain rule as

$$\dot{\mathbf{Y}} = \frac{\partial\mathbf{Y}}{\partial\boldsymbol{\gamma}^e}\cdot\dot{\boldsymbol{\gamma}}^e + \frac{\partial\mathbf{Y}}{\partial\boldsymbol{\omega}}\cdot\dot{\boldsymbol{\omega}}, \tag{91}$$

where the expressions for $\partial\mathbf{Y}/\partial\boldsymbol{\gamma}^e$ and $\partial\mathbf{Y}/\partial\boldsymbol{\omega}$ can be obtained from Eq. (90) as

$$\frac{\partial\mathbf{Y}}{\partial\boldsymbol{\gamma}^e} = \frac{1}{2}\left[\left(\boldsymbol{\mathcal{K}}\cdot\bar{\mathbf{C}}^e\cdot\mathbf{M}^{-1} + \mathbf{M}^{-1}\cdot\bar{\mathbf{C}}^e\cdot\boldsymbol{\mathcal{K}}\right)\cdot\boldsymbol{\gamma}^e + \boldsymbol{\gamma}^e\cdot\left(\boldsymbol{\mathcal{K}}\cdot\bar{\mathbf{C}}^e\cdot\mathbf{M}^{-1} + \mathbf{M}^{-1}\cdot\bar{\mathbf{C}}^e\cdot\boldsymbol{\mathcal{K}}\right)\right] \tag{92}$$

and

$$\frac{\partial\mathbf{Y}}{\partial\boldsymbol{\omega}} = -\frac{1}{2}\boldsymbol{\gamma}^e\cdot\left(\boldsymbol{\mathcal{K}}\cdot\bar{\mathbf{C}}^e\cdot\boldsymbol{\mathcal{K}} + \boldsymbol{\mathcal{K}}\cdot\bar{\mathbf{C}}^e\cdot\boldsymbol{\mathcal{K}}\right)\cdot\boldsymbol{\gamma}^e = -\boldsymbol{\gamma}^e\cdot\boldsymbol{\mathcal{K}}\cdot\bar{\mathbf{C}}^e\cdot\boldsymbol{\mathcal{K}}\cdot\boldsymbol{\gamma}^e, \tag{93}$$

respectively. Substituting Eq. (91) into Eq. (81) and rearranging the equation give

$$\dot{\boldsymbol{\omega}} = \left[\left(\mathbf{I} - \mathbf{S}^d\cdot\frac{\partial\mathbf{Y}}{\partial\boldsymbol{\omega}}\right)^{-1}\cdot\left(\mathbf{S}^d\cdot\frac{\partial\mathbf{Y}}{\partial\boldsymbol{\gamma}^e}\right)\right]\cdot\dot{\boldsymbol{\gamma}}^e \equiv \mathbf{A}\cdot\dot{\boldsymbol{\gamma}}^e, \tag{94}$$

which relates $\dot{\boldsymbol{\omega}}$ to $\dot{\boldsymbol{\gamma}}^e$. Substituting Eq. (94) into Eq. (88) gives

$$\dot{\bar{\boldsymbol{\gamma}}}^e = -\left(\boldsymbol{\mathcal{K}}\cdot\boldsymbol{\gamma}^e\right)\cdot\mathbf{A}\cdot\dot{\boldsymbol{\gamma}}^e + \mathbf{M}^{-1}\cdot\dot{\boldsymbol{\gamma}}^e = \left[-\left(\boldsymbol{\mathcal{K}}\cdot\boldsymbol{\gamma}^e\right)\cdot\mathbf{A} + \mathbf{M}^{-1}\right]\cdot\dot{\boldsymbol{\gamma}}^e \equiv \tilde{\mathbf{N}}^{-1}\cdot\dot{\boldsymbol{\gamma}}^e, \tag{95}$$

which relates $\dot{\bar{\boldsymbol{\gamma}}}^e$ to $\dot{\boldsymbol{\gamma}}^e$.

To relate $\dot{\boldsymbol{\tau}}$ to $\dot{\boldsymbol{\tau}}$, recall that

$$\boldsymbol{\tau} = \mathbf{C}^e\cdot\boldsymbol{\gamma}^e. \tag{96}$$

Taking time derivatives on both sides of Eq. (96) gives

$$\dot{\boldsymbol{\tau}} = \dot{\mathbf{C}}^e\cdot\boldsymbol{\gamma}^e + \mathbf{C}^e\cdot\dot{\boldsymbol{\gamma}}^e. \tag{97}$$

The first term to the right of the equal sign in Eq. (88) can be further expressed as

$$\begin{aligned}\dot{C}_{ijm}\gamma_m^e &= \left(\dot{M}_{ik}^{-1}\bar{C}_{kl}^e M_{lm}^{-1} + M_{ik}^{-1}\bar{C}_{kl}^e\dot{M}_{lm}^{-1}\right)\gamma_m^e = -\left(\mathcal{K}_{ijk}\dot{\omega}_j\bar{C}_{kl}^e M_{lm}^{-1} + M_{ik}^{-1}\bar{C}_{kl}^e\mathcal{K}_{ljm}\dot{\omega}_j\right)\gamma_m^e \\ &= -\left[\left(\mathcal{K}_{ijk}\bar{C}_{kl}^e M_{lm}^{-1} + M_{ik}^{-1}\bar{C}_{kl}^e\mathcal{K}_{ljm}\right)\gamma_m^e\right]\dot{\omega}_j \equiv -\left(\mathcal{B}_{ijm}\gamma_m^e\right)\dot{\omega}_j\end{aligned} \tag{98}$$

or

$$\dot{\mathbf{C}}^e\cdot\boldsymbol{\gamma}^e = -\left[\left(\boldsymbol{\mathcal{K}}\cdot\bar{\mathbf{C}}^e\cdot\mathbf{M}^{-1} + \mathbf{M}^{-1}\cdot\bar{\mathbf{C}}^e\cdot\boldsymbol{\mathcal{K}}\right)\cdot\boldsymbol{\gamma}^e\right]\cdot\dot{\boldsymbol{\omega}} \equiv -\left(\boldsymbol{\mathcal{B}}\cdot\boldsymbol{\gamma}^e\right)\cdot\dot{\boldsymbol{\omega}}. \tag{99}$$

Substituting Eq. (99) into Eq. (97) gives

$$\dot{\boldsymbol{\tau}} = -\left(\boldsymbol{\mathcal{B}}\cdot\boldsymbol{\gamma}^e\right)\cdot\dot{\boldsymbol{\omega}} + \mathbf{C}^e\cdot\dot{\boldsymbol{\gamma}}^e = -\left(\boldsymbol{\mathcal{B}}\cdot\boldsymbol{\gamma}^e\right)\cdot\mathbf{A}\cdot\dot{\boldsymbol{\gamma}}^e + \mathbf{C}^e\cdot\dot{\boldsymbol{\gamma}}^e = \left[-\left(\boldsymbol{\mathcal{B}}\cdot\boldsymbol{\gamma}^e\right)\cdot\mathbf{A} + \mathbf{C}^e\right]\cdot\dot{\boldsymbol{\gamma}}^e. \tag{100}$$

Note that

$$\dot{\boldsymbol{\tau}} = \bar{\mathbf{C}}^e\cdot\dot{\bar{\boldsymbol{\gamma}}}^e. \tag{101}$$

$\dot{\boldsymbol{\gamma}}^e$ can hereby be related to $\dot{\tilde{\boldsymbol{\tau}}}$ by

$$\dot{\boldsymbol{\gamma}}^e = \tilde{\mathbf{N}} \cdot \dot{\tilde{\boldsymbol{\gamma}}}^e = \tilde{\mathbf{N}} \cdot \left(\bar{\mathbf{C}}^e\right)^{-1} \cdot \dot{\tilde{\boldsymbol{\tau}}}. \tag{102}$$

Substituting Eq. (102) into Eq. (100) gives

$$\dot{\boldsymbol{\tau}} = \left\{ \left[- \left(\boldsymbol{\mathcal{B}} \cdot \boldsymbol{\gamma}^e \right) \cdot \mathbf{A} + \mathbf{C}^e \right] \cdot \tilde{\mathbf{N}} \cdot \left(\bar{\mathbf{C}}^e\right)^{-1} \right\} \cdot \dot{\tilde{\boldsymbol{\tau}}} \equiv \mathbf{N}^{-1} \cdot \dot{\tilde{\boldsymbol{\tau}}}, \tag{103}$$

which relates $\dot{\tilde{\boldsymbol{\tau}}}$ to $\dot{\boldsymbol{\tau}}$.

To relate $\dot{\tilde{\boldsymbol{\gamma}}}^p$ to $\dot{\boldsymbol{\gamma}}^p$, further let

$$\boldsymbol{\tau} \cdot \dot{\boldsymbol{\gamma}}^p = \bar{\boldsymbol{\tau}} \cdot \dot{\tilde{\boldsymbol{\gamma}}}^p. \tag{104}$$

Substituting Eq. (18) into Eq. (104) gives

$$\dot{\tilde{\boldsymbol{\gamma}}}^p = \mathbf{M}^{-1} \cdot \dot{\boldsymbol{\gamma}}^p \quad \text{or} \quad \dot{\boldsymbol{\gamma}}^p = \mathbf{M} \cdot \dot{\tilde{\boldsymbol{\gamma}}}^p. \tag{105}$$

Eq. (61) can be written as

$$\dot{\tilde{\boldsymbol{\tau}}} = \bar{\mathbf{C}}^{ep} \cdot \dot{\tilde{\boldsymbol{\gamma}}} = \bar{\mathbf{C}}^{ep} \cdot \dot{\tilde{\boldsymbol{\gamma}}}^e + \bar{\mathbf{C}}^{ep} \cdot \dot{\tilde{\boldsymbol{\gamma}}}^p. \tag{106}$$

Substituting Eqs. (95), (96), and (105) into Eq. (106) gives

$$\begin{aligned} \mathbf{N} \cdot \dot{\boldsymbol{\tau}} &= \bar{\mathbf{C}}^{ep} \cdot \tilde{\mathbf{N}}^{-1} \cdot \dot{\boldsymbol{\gamma}}^e + \bar{\mathbf{C}}^{ep} \cdot \mathbf{M}^{-1} \cdot \dot{\boldsymbol{\gamma}}^p = \bar{\mathbf{C}}^{ep} \cdot \tilde{\mathbf{N}}^{-1} \cdot \dot{\boldsymbol{\gamma}}^e + \bar{\mathbf{C}}^{ep} \cdot \mathbf{M}^{-1} \cdot \left(\dot{\boldsymbol{\gamma}} - \dot{\boldsymbol{\gamma}}^e\right) \\ &= \bar{\mathbf{C}}^{ep} \cdot \mathbf{M}^{-1} \cdot \dot{\boldsymbol{\gamma}} + \bar{\mathbf{C}}^{ep} \cdot \left(\tilde{\mathbf{N}}^{-1} - \mathbf{M}^{-1}\right) \cdot \dot{\boldsymbol{\gamma}}^e. \end{aligned} \tag{107}$$

Note that $\dot{\boldsymbol{\gamma}}^e$ can be related to $\dot{\boldsymbol{\tau}}$ by

$$\dot{\boldsymbol{\gamma}}^e = \tilde{\mathbf{N}} \cdot \dot{\tilde{\boldsymbol{\gamma}}}^e = \tilde{\mathbf{N}} \cdot \left(\bar{\mathbf{C}}^e\right)^{-1} \cdot \dot{\tilde{\boldsymbol{\tau}}} = \tilde{\mathbf{N}} \cdot \left(\bar{\mathbf{C}}^e\right)^{-1} \cdot \mathbf{N} \cdot \dot{\boldsymbol{\tau}}. \tag{108}$$

Substituting Eq. (108) into Eq. (107) and rearranging the equation give

$$\left[\mathbf{I} - \bar{\mathbf{C}}^{ep} \cdot \left(\tilde{\mathbf{N}}^{-1} - \mathbf{M}^{-1}\right) \cdot \tilde{\mathbf{N}} \cdot \left(\bar{\mathbf{C}}^e\right)^{-1} \right] \cdot \mathbf{N} \cdot \dot{\boldsymbol{\tau}} = \bar{\mathbf{C}}^{ep} \cdot \mathbf{M}^{-1} \cdot \dot{\boldsymbol{\gamma}}. \tag{109}$$

Rearranging Eq. (109) gives the rate form of the cohesive law in the damaged configuration as

$$\dot{\boldsymbol{\tau}} = \left\{ \mathbf{N}^{-1} \cdot \left[\mathbf{I} - \bar{\mathbf{C}}^{ep} \cdot \left(\tilde{\mathbf{N}}^{-1} - \mathbf{M}^{-1}\right) \cdot \tilde{\mathbf{N}} \cdot \left(\bar{\mathbf{C}}^e\right)^{-1} \right]^{-1} \cdot \bar{\mathbf{C}}^{ep} \cdot \mathbf{M}^{-1} \right\} \cdot \dot{\boldsymbol{\gamma}} \equiv \mathbf{C}^{ep} \cdot \dot{\boldsymbol{\gamma}}, \tag{110}$$

where $\mathbf{C}^{ep}$ denotes the second-order instantaneous cohesive stiffness tensor in the damaged configuration.

Till now, the cohesive law in the damaged configuration has been derived. In the next section, a novel delamination criterion will be proposed.

VIII. Delamination Criterion

As mentioned above, the conventional delamination criterion states that delamination occurs as G attains a critical value, G_c, which can be expressed as

$$G_c = G_c \left(G_{\mathrm{Ic}}, G_{\mathrm{IIc}}, G_{\mathrm{IIIc}}, \boldsymbol{\beta} \right), \tag{111}$$

while the specific form of the delamination criterion can be determined by finding an expression fitting the experimental results well. Eq. (111) enables a cohesive zone model to provide close predictions and is definitely very powerful. However, there exists several reasons for which it cannot be directly adopted here. First of all, specify the mode mixity vector, $\boldsymbol{\beta}$, and define the term "proportional loading". Specifically, let $\boldsymbol{\beta}$ denote a dimensionless vector obtained by normalizing $\boldsymbol{\gamma}$, using a nonzero component of $\boldsymbol{\gamma}$ as a measure of scale, and let proportional loading denote a loading process in which $\boldsymbol{\beta}$ remains constant, or to say, in which all the components of $\boldsymbol{\gamma}$ proportionally vary. According to Ref. [11], Eq. (111) is applicable to proportional loading and performs well. However, it remains unclear that whether Eq. (111) is applicable to non-proportional loading/unloading. In addition, it is commonly assumed that, as the delamination criterion is met, the scalar-valued damage factor is smoothly increased to 1.[1–4,11,13,15,16] This assumption seems reasonable but places too strict restrictions. Specifically, it requires that the damage factor can only

be a scalar, or to say, that no damage anisotropy is allowed. In addition, the numerical results indicate that, if a cohesive element obeying the proposed cohesive law is subject to proportional loading, one or more components of the damage vector tend to approach but never to attain 1 during continued deformation. This finding may seem odd but is actually very common in continuum damage mechanics, and it also leads one to seek for an alternative delamination criterion.

In this paper, let the delamination criterion state that delamination occurs as the cumulative equivalent damage factor, q, attains a critical value, say q_c, which can be expressed as

$$q_c = q_c\left(\boldsymbol{\beta}\right). \tag{112}$$

Note that q is related to its rate by

$$q = \int_0^t \dot{q} dt \tag{113}$$

and that $\dot{q}$ is related to $\dot{\boldsymbol{\omega}}$ by Eq. (69). Eq. (112) has several advantages. First, it has a clear physical meaning. Note that q_c is intrinsically a measure of damages. Eq. (69) hereby implies that delamination occurs as an equivalent measure of damages attains a critical value. Second, it is also physically admissible. This is because q_c can always take a certain value such that only a negligible traction discontinuity arises at the onset of delamination. On the one hand, this treatment eliminates the strict restrictions placed by the thermodynamic formulations and it almost has no impacts on the predictions. Third, it allows damage anisotropy. In fact, if damage isotropy is assumed, the coupling among different modes of fracture are strong. In contrast, if damage anisotropy is assumed, this coupling becomes adjustable. Last but not least, it is applicable to non-proportional loading/unloading. Moreover, it can even be expected that G_c is no longer a function of $\boldsymbol{\beta}$ but also becomes path-dependent. Of course, all the element parameters and the specific form of Eq. (112) should be properly selected to fit the experimental results.

IX. Demonstration Examples

In this section, several examples are presented to validate the applicability and power of the proposed model and also to investigate some characteristics of the cohesive element. The examples include predicting the traction-relative displacement and damage factor-relative displacement curves of cohesive elements of various cohesive properties.

A. Damage Hardening

Without loss of generality, first let the element merely exhibit irreversible hardening and damage hardening. For illustration purposes, let the element exhibit the same response when subject to purely modes I, II, and III loading. This implies that the diagonal components of C_{ij} take the same value, say C. Of course, these components can take distinct values to incorporate more realistic responses. Following Ref. [1], let the element parameters take the values listed in Table 1 such that the resulting values of $\boldsymbol{\gamma}$ and $\boldsymbol{\tau}$ will be in realistic orders of magnitude. In addition, let $\bar{\mathbf{H}} = \mathbf{I}$, and let the diagonal and off-diagonal components of L_{ij} take the values of 1 and 0.32, respectively. In this section, allow L in Eq. (78) to take the values of $2.5Y_0$, $5Y_0$, and $10Y_0$ for different cases. It can be obtained from Table 1 that the element becomes damaged at $\gamma_1 = 0.005$mm and yields at $\gamma_1 = 0.01$mm when subject to mode I loading.

Table 1. Element parameters.

C (MPa/mm)	τ_0 (MPa)	K (MPa)	n	Y_0 (J/m^2)	o
500	5	1.5	50	12.5	5

Figures 2 and 3 show the τ_1-γ_1 and ω_1-γ_1 curves of the element subject to mode I loading, respectively. For illustration purposes, the loading path here is set to consist of the following steps:

- Initial loading: γ_1 is increased from 0 to 0.02mm;
- Unloading I: γ_1 is decreased from 0.02mm till τ_1 is decreased to 0MPa, or to say, γ_1 is decreased to γ_1^p at $\gamma_1 = 0.02$mm (a residual relative displacement);

- Reloading I: γ_1 is increased to 0.04mm;
- ...
- Reloading IV: γ_1 is increased to 0.1mm.

According to Ref. [1], there exist three commonly used τ-γ relations, i.e., linear softening, power-law hardening/softening, and softening with a traction plateau. As can be seen, for $L = 2.5Y_0$, the τ_1-γ_1 curve exhibits a typical power-law hardening/softening trend, while the ω_1-γ_1 curve exhibits an approximately monotonically increasing trend; for $L = 5Y_0$, the τ_1-γ_1 curve exhibits a softening with a traction plateau trend with a plateau located in $0.01 < \gamma_1 < 0.03$, while the ω_1-γ_1 curve has a plateau located in the same interval; for $L = 10Y_0$, the τ_1-γ_1 and ω_1-γ_1 curves both have wider plateaus. It is of interest to investigate the cause of the plateaus. Specifically, note that the residual relative displacements in Figure 2 actually characterize how much irreversible deformation is induced at different stages of the deformation. Figure 2 indicates that, for $L = 2.5Y_0$, negligible irreversible deformation is induced. In this case, damages initiate at a very low traction level and evolve rapidly, and the subsequent damage evolution further inhibits the increase in the Hill equivalent traction in the undamaged configuration, $\bar{\tau}_e$, and hereby the irreversible deformation. Accordingly, the element behaves like a damaged elastic material. Meanwhile, Figure 2 also indicates that, for $L = 5Y_0$, considerable irreversible deformation is induced. In this case, the irreversible deformation is induced just after damages initiate, and the subsequent irreversible deformation inhibit the increases in the tractions and hereby the damage evolution. This causes the corresponding τ_1-γ_1 and ω_1-γ_1 curves to have plateaus. In this case, the element behaves like a damaged elastoplastic material. Accordingly, for $L = 10Y_0$, the irreversible deformation is easier to become dominant. At last, it is worth notice that, although the τ_1-γ_1 curves here all exhibit commonly used trends, they are actually differently obtained. Specifically, since the commonly used relations are assumed a priori, their corresponding cohesive laws are not necessarily thermodynamically consistent and may not be applicable to non-proportional loading/unloading (or additional assumptions have to be made). In contrast, the proposed cohesive law is strictly thermodynamically consistent, and since Eqs. (48) and (73) fully specify the irreversible and damage loading/unloading conditions, it is also applicable to non-proportional loading/unloading.

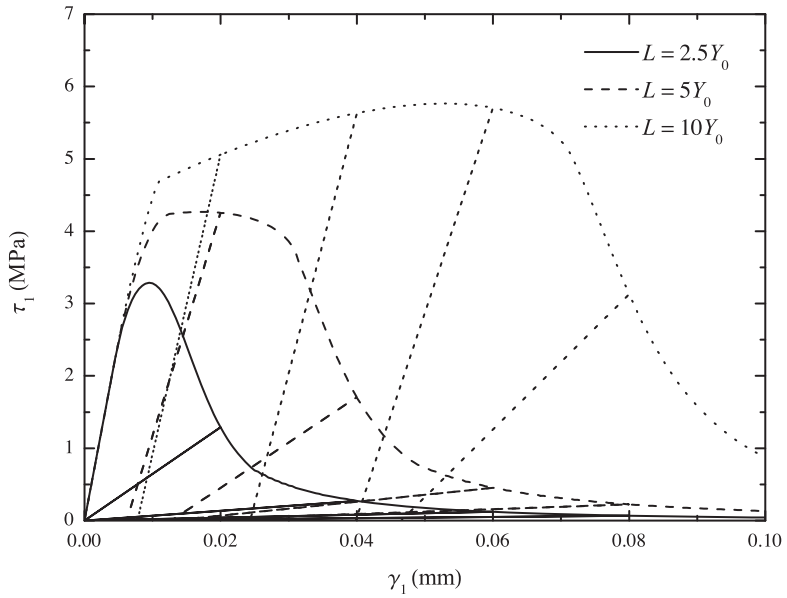

Figure 2. τ_1-γ_1 curves of the element subject to mode I loading.

Figures 4 and 5 show the τ_1-γ_1 and ω_1-γ_1 curves of the element subject to mixed-mode loading, respectively, where $L = 5Y_0$. The loading path here is similar to that in the last paragraph:

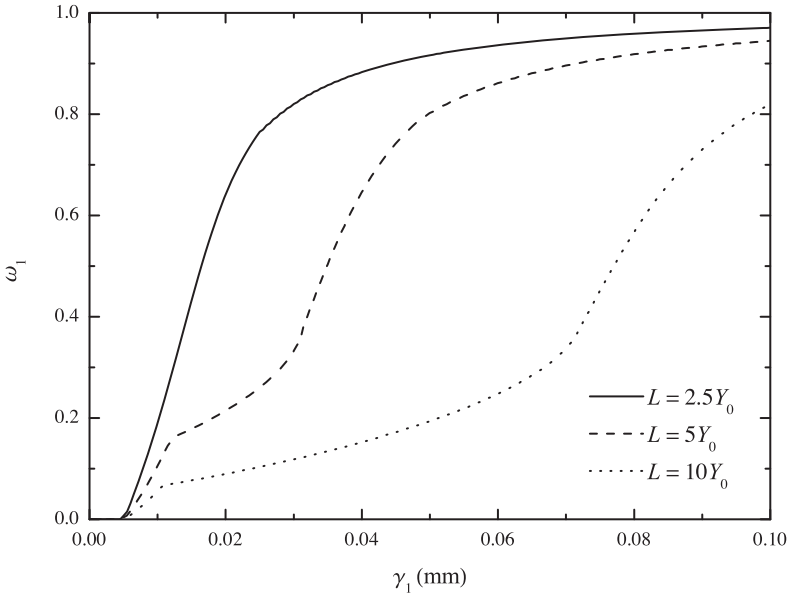

Figure 3. ω_1-γ_1 curves of the element subject to mode I loading.

- Initial loading: γ_1, γ_2, and γ_3 are increased from 0 to 0.02mm;
- Unloading I: γ_1, γ_2, and γ_3 are decreased from 0.02mm till τ_1, τ_2, and τ_3 are decreased to 0MPa;
- Reloading I: γ_1, γ_2, and γ_3 are increased to 0.04mm;
- ...

It can be seen that all the τ_1-γ_1 and ω_1-γ_1 curves here exhibit trends similar to those for $L = 5Y_0$ in Figures 2 and 3. Therefore, all the discussion for $L = 5Y_0$ in the last paragraph holds here. In addition, it is worth notice that the element seems more vulnerable to mixed-mode loading. This can be understood by noting that the off-diagonal components of L_{ij} are non-zero. For example, it can be verified that an increase in τ_1 may induce not only an increase in ω_1 but also those in ω_2 and ω_3. In fact, if all the off-diagonal components of L_{ij} approach to 1, the element would approximately exhibit damage isotropy.

B. General Damage Anisotropy

Next let the element also exhibit a more general type of damage anisotropy, where the term "more general" means that the diagonal components of L_{ij} can be distinct. Specifically, let the element parameters take the values listed in Table 1 with $L = 5Y_0$, and let the components of H_{ij} and L_{ij} here except L_{11} be the same as those in Section IX-A. In this section, allow L_{11} to take the values of 0.707, 1, and 1.414 for different cases.

Figures 6 and 7 show the τ_1-γ_1 and ω_1-γ_1 curves of the element subject to mode I loading, respectively. The loading path here is set to be the same as that for mode I loading in Section IX-A. In fact, it can be obtained from Eqs. (62) and (63) that, as L_{11} increases, the element becomes more vulnerable to mode I loading, while similar findings can be obtained for some other cases of damage anisotropy. For this reason, in Figure 6, as L_{11} increases, the τ_1-γ_1 curve shifts downward. Other than this, it can be seen that all the τ_1-γ_1 and ω_1-γ_1 curves here exhibit trends similar to those for $L = 5Y_0$ in Figures 2 and 3. Therefore, all the discussion $L = 5Y_0$ in the second paragraph of Section IX-A holds here.

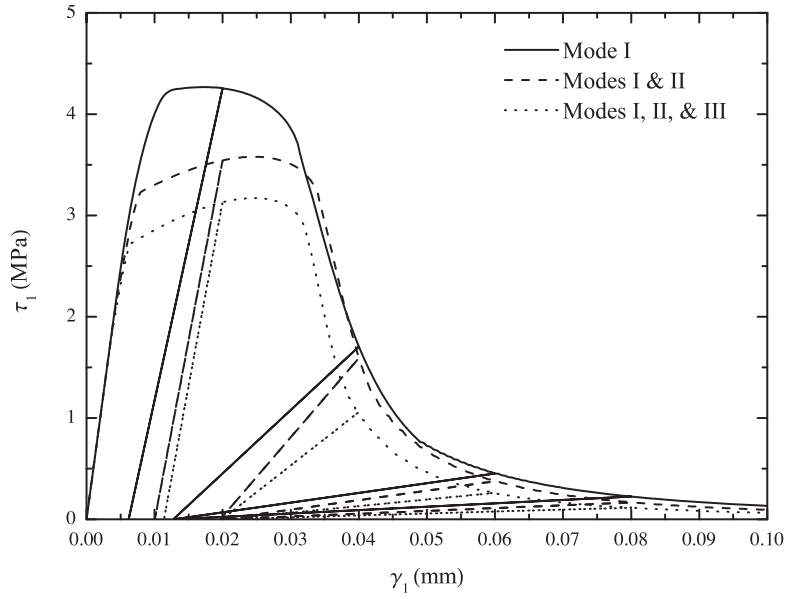

Figure 4. Stress-strain curves of the element subject to mixed-mode loading, where $L = 5Y_0$.

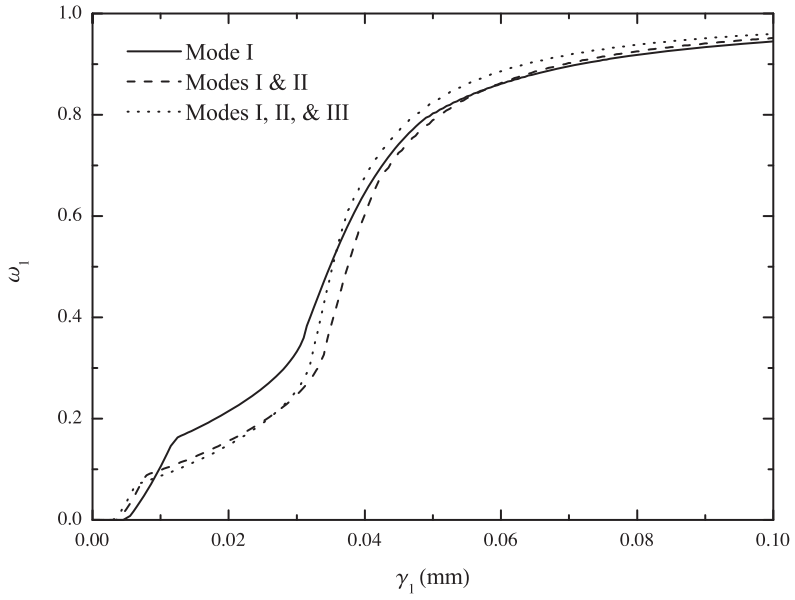

Figure 5. ω_1-γ_1 curves of the element subject to mixed-mode loading, where $L = 5Y_0$.

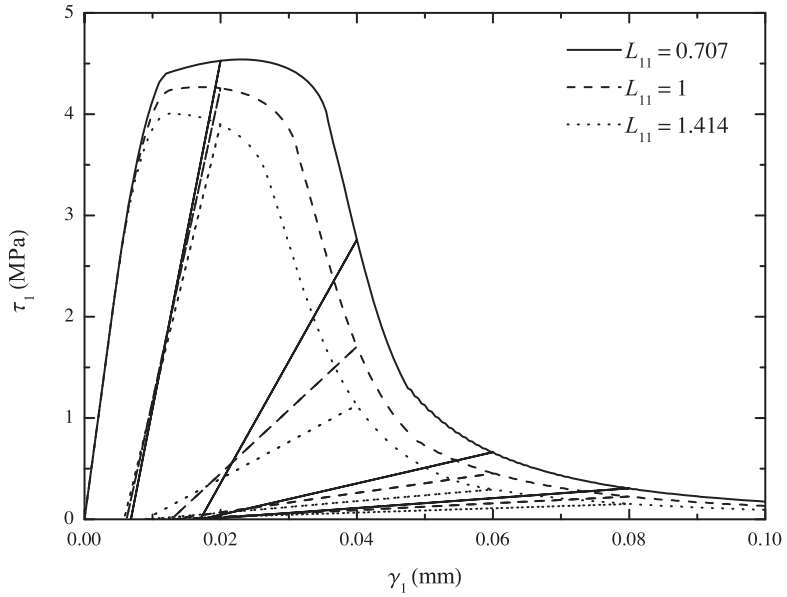

Figure 6. τ_1-γ_1 **curves of the element exhibiting general damage anisotropy subject to mode I loading.**

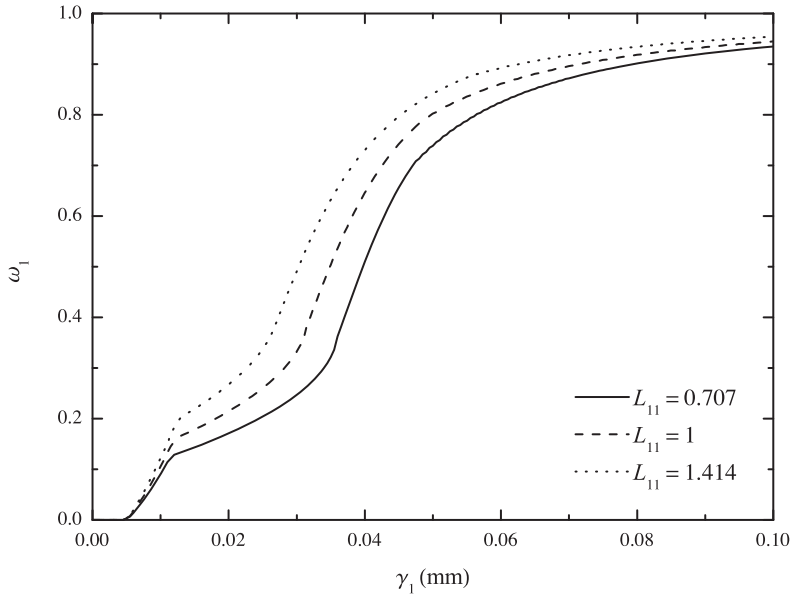

Figure 7. ω_1-γ_1 **curves of the element exhibiting general damage anisotropy subject to mode I loading.**

C. Irreversible Anisotropy

At last, let the element exhibit irreversible anisotropy instead of general damage anisotropy. Specifically, let the element parameters take the values listed in Table 1 with $L = 5Y_0$, and let the components of H_{ij} and L_{ij} here except H_{11} be the same as those in Section IX-A. In this section, allow H_{11} to take the values of 0.707, 1, and 1.414 for different cases.

Figures 8 and 9 show the τ_1-γ_1 and ω_1-γ_1 curves of the element subject to mode I loading, respectively. The loading path here is set to be the same as that in the second paragraph of Section IX-A. As can be seen, the τ_1-γ_1 and ω_1-γ_1 curves for $H_{11} = 0.707$ exhibit trends similar to those for $L = 2.5Y_0$ in Figures 8 and 9 except that the τ_1-γ_1 curve here seems to be scaled-up, while those for $H_{11} = 1.414$ exhibit trends similar to those for $L = 10Y_0$ in Figures 8 and 9 except that the τ_1-γ_1 curve here seems to be scaled-down. In fact, this can be understood by noting that the value of H_{ij} can affect the initial yield traction. Specifically, one can obtain the following findings by substituting the values of H_{11} here into Eq. (38):

- The value of H_{11} does not affect the yield traction of the element subject to purely mode II or III loading;
- The lowest value of H_{11} yields the lowest yield traction of the element subject to purely mode I loading and vice versa.

Therefore, for $H_{11} = 0.707$, damages can evolve to a considerable extent before the yield criterion, which becomes more restrictive here, is met, and the subsequent damage evolution further inhibits the irreversible deformation. This leads the element to behave like a damaged elastic material. Accordingly, the corresponding ω_1-γ_1 curve exhibits an approximately monotonically increasing trend. In contrast, for $H_{11} = 1.414$, the yield criterion, which becomes less restrictive here, can be met just after damages initiate, and the subsequent irreversible deformation further inhibits the damage evolution. This leads the element to more significantly behave like a damaged elastoplastic material. Accordingly, the corresponding ω_1-γ_1 curve has a wide plateau.

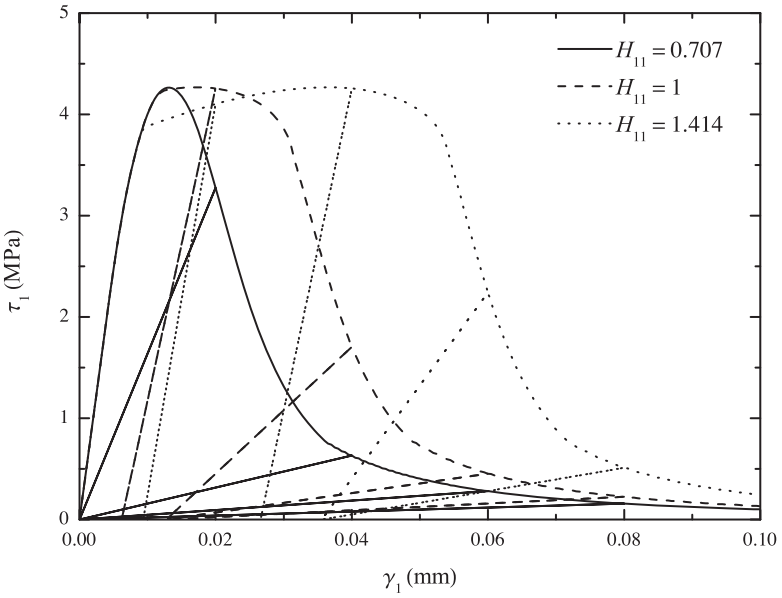

Figure 8. τ_1-γ_1 curves of the element exhibiting irreversible anisotropy subject to mode I loading.

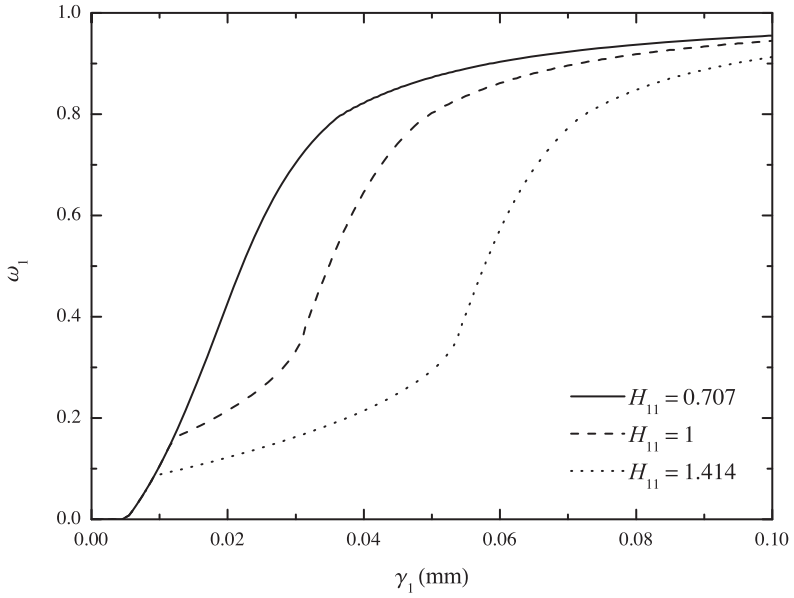

Figure 9. ω_1-γ_1 curves of the element exhibiting irreversible anisotropy subject to mode I loading.

X. Conclusions

In this paper, a thermodynamically consistent cohesive zone model for mixed-mode fracture, which enables a cohesive element to exhibit designated behaviors when subject to mixed-mode loading, is proposed. Some fundamentals of the cohesive zone model, continuum damage mechanics, and thermodynamics are briefed, and the concept of the irreversible deformation is introduced. The cohesive law in the undamaged configuration, the damage evolution law, and the cohesive law in the damaged configuration are subsequently derived, and a novel delamination criterion is proposed. The applicability and power of the proposed cohesive zone model are validated using examples such as predicting the traction-relative displacement and damage factor-relative displacement curves of cohesive elements of various cohesive properties. More sophisticated cohesive properties can be incorporated into the proposed model.

Acknowledgements

This work is supported by the US AFOSR Multiscale Structural Mechanics and Prognosis Program. The Program Manager is Dr. David Stargel. The views and conclusions contained herein are those of the authors and should not be interpreted as necessarily representing the official policies or endorsement, either expressed or implied, of the sponsor.

References

[1]Mosler, J. and Scheider, I., "A thermodynamically and variationally consistent class of damage-type cohesive models," *Journal of the Mechanics and Physics of Solids*, Vol. 59, No. 8, 2011, pp. 1647–1668.

[2]Turon, A., Camanho, P., Costa, J., and Renart, J., "Accurate simulation of delamination growth under mixed-mode loading using cohesive elements: definition of interlaminar strengths and elastic stiffness," *Composite Structures*, Vol. 92, No. 8, 2010, pp. 1857–1864.

[3]Needleman, A., "A continuum model for void nucleation by inclusion debonding," *Journal of Applied Mechanics*, Vol. 54, No. 3, 1987, pp. 525–531.

[4]Tvergaard, V. and Hutchinson, J. W., "The relation between crack growth resistance and fracture process parameters in elastic-plastic solids," *Journal of the Mechanics and Physics of Solids*, Vol. 40, No. 6, 1992, pp. 1377–1397.

[5]Cui, W. and Wisnom, M., "A combined stress-based and fracture-mechanics-based model for predicting delamination in

composites," *Composites*, Vol. 24, No. 6, 1993, pp. 467–474.

[6]Schellekens, J. and De Borst, R., "A non-linear finite element approach for the analysis of mode-I free edge delamination in composites," *International Journal of Solids and Structures*, Vol. 30, No. 9, 1993, pp. 1239–1253.

[7]Xu, X.-P. and Needleman, A., "Numerical simulations of fast crack growth in brittle solids," *Journal of the Mechanics and Physics of Solids*, Vol. 42, No. 9, 1994, pp. 1397–1434.

[8]Mi, Y., Crisfield, M., Davies, G., and Hellweg, H., "Progressive delamination using interface elements," *Journal of Composite Materials*, Vol. 32, No. 14, 1998, pp. 1246–1272.

[9]Chen, M. Crisfield, A. K. E. B. F. M. Y. Q. J., "Predicting progressive delamination of composite material specimens via interface elements," *Mechanics of Composite Materials and Structures*, Vol. 6, No. 4, 1999, pp. 301–317.

[10]Alfano, G. and Crisfield, M., "Finite element interface models for the delamination analysis of laminated composites: mechanical and computational issues," *International journal for numerical methods in engineering*, Vol. 50, No. 7, 2001, pp. 1701–1736.

[11]Camanho, P. P., Davila, C., and De Moura, M., "Numerical simulation of mixed-mode progressive delamination in composite materials," *Journal of Composite Materials*, Vol. 37, No. 16, 2003, pp. 1415–1438.

[12]Goyal, V. K., Johnson, E. R., and Dávila, C. G., "Irreversible constitutive law for modeling the delamination process using interfacial surface discontinuities," *Composite Structures*, Vol. 65, No. 3, 2004, pp. 289–305.

[13]Turon, A., Camanho, P. P., Costa, J., and Dávila, C., "A damage model for the simulation of delamination in advanced composites under variable-mode loading," *Mechanics of Materials*, Vol. 38, No. 11, 2006, pp. 1072–1089.

[14]Jiang, W.-G., Hallett, S. R., Green, B. G., and Wisnom, M. R., "A concise interface constitutive law for analysis of delamination and splitting in composite materials and its application to scaled notched tensile specimens," *International Journal for Numerical Methods in Engineering*, Vol. 69, No. 9, 2007, pp. 1982–1995.

[15]Balzani, C. and Wagner, W., "An interface element for the simulation of delamination in unidirectional fiber-reinforced composite laminates," *Engineering Fracture Mechanics*, Vol. 75, No. 9, 2008, pp. 2597–2615.

[16]Wagner, W. and Balzani, C., "Simulation of delamination in stringer stiffened fiber-reinforced composite shells," *Computers & Structures*, Vol. 86, No. 9, 2008, pp. 930–939.

[17]Ahmad, S., Irons, B. M., and Zienkiewicz, O., "Analysis of thick and thin shell structures by curved finite elements," *International Journal for Numerical Methods in Engineering*, Vol. 2, No. 3, 1970, pp. 419–451.

[18]Bfer, G., "An isoparametric joint/interface element for finite element analysis," *International Journal for Numerical Methods in Engineering*, Vol. 21, No. 4, 1985, pp. 585–600.

[19]Benzeggagh, M. and Kenane, M., "Measurement of mixed-mode delamination fracture toughness of unidirectional glass/epoxy composites with mixed-mode bending apparatus," *Composites Science and Technology*, Vol. 56, No. 4, 1996, pp. 439–449.

[20]Tan, H., Liu, C., Huang, Y., and Geubelle, P., "The cohesive law for the particle/matrix interfaces in high explosives," *Journal of the Mechanics and Physics of Solids*, Vol. 53, No. 8, 2005, pp. 1892–1917.

[21]Camanho, P. P., Davila, C., and Pinho, S., "Fracture analysis of composite co-cured structural joints using decohesion elements," *Fatigue & Fracture of Engineering Materials & Structures*, Vol. 27, No. 9, 2004, pp. 745–757.

[22]Simo, J. C. and Hughes, T. J. R., *Computational Inelasticity*, Vol. 7 of *Interdisciplinary Applied Mathematics*, Springer, New York, 1998.

[23]Benzerga, A. A. and Besson, J., "Plastic potentials for anisotropic porous solids," *European Journal of Mechanics, A/Solids*, Vol. 20, No. 3, 2001, pp. 397–434.

[24]Chaboche, J.-L., "Thermodynamic formulation of constitutive equations and application to the viscoplasticity and viscoelasticity of metals and polymers," *International Journal of Solids and Structures*, Vol. 34, No. 18, 1997, pp. 2239–2254.

[25]Besson, J., Cailletaud, G., Chaboche, J.-L., and Forest, S., *Non-linear mechanics of materials*, Vol. 167 of *Solid mechanics and its applications*, Springer, New York, 2010.

[26]Chow, C. and Wang, J., "An anisotropic theory of elasticity for continuum damage mechanics," *International Journal of Fracture*, Vol. 33, No. 1, 1987, pp. 3–16.

Simulating the Mixed-Mode Progressive Delamination in Composite Laminates

Z. GAO, L. ZHANG and W. YU

ABSTRACT

Delamination, or interlaminar debonding, is a commonly observed failure mechanism in composite laminates. The objective of this paper is to develop a 2D and a 3D numerical approach to simulating the double-cantilever beam (DCB), the end-notched flexure (ENF), and the mixed-mode bending (MMB) tests with a commercial software, Abaqus, and to seek for appropriate simplifications of the simulations. An explicit dynamic time integration scheme and a viscosity parameter is adopted to yield close predictions of the specimen responses. The load rate and the specimen mass density are properly selected to approximate a quasi-static loading process. A linear cohesive zone model is used to characterize the mechanical response of the interface. The validity of different strategies of simplifying the finite element model is discussed. The 2D and the 3D predictions are both found to fit the experimental results well, but the 2D predictions are found to be more accurate and stable than the 3D predictions. The 2D approach is found to better handle the mixed-mode progressive delamination in composite laminates satisfying plane stress condition. Although the present approaches are developed with Abaqus/Explicit, they are also amendable to other finite element codes.

Purdue University, West Lafayette, Indiana 47907

INTRODUCTION

Delamination, or interlaminar debonding, is a commonly observed failure mechanism in composite laminates. When a composite laminate is subject to a certain extent of transverse load, either during its manufacturing or in use, progressive delamination may occur within it. Such phenomenon should be avoided because it may harm the performance of a composite structure (e.g., load-carrying capability and structural integrity). One major challenge is to predict the onset of such phenomenon: first, it is often difficult or expensive to experimentally quantify delamination, especially with mixed-mode delamination; second, the interfacial properties significantly affect delamination and vary case by case. All these lead one to seek for a comprehensive method for numerically simulating the progressive mixed-mode delamination in composite laminates.

There are three basic testing methods for measuring the progressive delamination in composite laminates, either pure mode or mixed-mode. The double-cantilever beam (DCB) and the end-notched flexure (ENF) tests are designed to measure pure mode I and II delamination, respectively (see Figure 1), and the mixed-mode bending (MMB) test the mixed-mode delamination (Figure 2) [1]. For a class of composite laminates, three tests require an identical pre-cracked composite laminate consisting of two plies glued with one layer of adhesive but different loading conditions:

1. in a DCB test, two opposite vertical forces opening the crack are applied at the free end of a cantilever beam;
2. in an ENF test, a downward force is applied at the middle of a simply supported beam;
3. in an MMB test, a downward force is applied at one end of a loading lever placed above the beam to yield an upward force at the free end of a simply supported beam and a downward force at the middle of the beam, where the loading level length is adjusted to yield designated mode-mixing ratio.

Several direct and indirect numerical approaches have been developed to model the delamination in composite laminates. A direct approach involves directly computing the strain energy release rate with the theory of fracture mechanics, from some finite element analysis (FEA) results. The virtual crack closure technique (VCCT) is a widely used direct approach. It involves making use of the crack-closure integral, or to say, the total work needed to close a crack. Rybicki and Kanninen first proposed the VCCT for 2D problems [2]. Shivakumar et al. enabled this approach to handle 3D

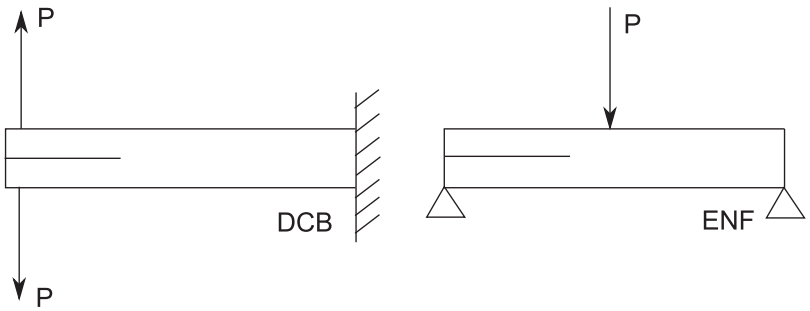

Figure 1. Schematics of the DCB and ENF tests

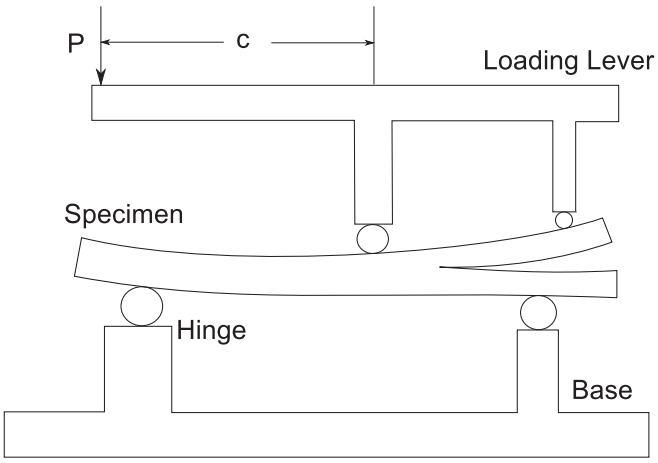

Figure 2. The mixed-mode bending test

problems [3]. It can predict the onset and stability of delamination but is incapable of predicting the damage initiation because it requires initial delamination defined a priori. Meanwhile, VCCT implicitly assumes that the crack growth is self-similar, which means the crack front remains straight throughout the delamination process. This, however, is often not the case because even in DCB tests, the crack surfaces will become curved after crack propagation [4]. In contrast, the indirect approaches, which make use of some idealization of the interface (e.g., a cohesive zone model), can overcome these drawbacks.

Researchers have used different finite element models to simulate the delamination of composite laminates with cohesive elements and cohesive laws. A cohesive element acts as a geometric representation of the interface and is often placed between two glued plies, where delamination is expected to occur. A set of cohesive elements can be modeled by the usual elements provided in existing finite element packages and form into a continuous adhesive layer, where in the thickness direction there is only one element. While one can model a composite laminate as a 3D body, this significantly increases computation cost compared with other models with simplifications. Dávila et al. [5] have described using shell elements to model delamination with cohesive elements in implicit time integration. Borg et al. [6], and Balzani and Wagner [7], simulated the DCB, the ENF, and the MMB tests with shell element model. A more common used and more simplified way to model the delamination is to idealize the composite laminate as one under plane stress conditions where the delamination specimen only has length and thickness directions [8]. The reduction in degrees of freedom of the whole model can further reduce the computation cost.

Cohesive elements can be implemented into both 2D and 3D finite element models. In a 2D model, one can identify these delamination tests as plane stress problems and mesh the model with 2D plane stress elements. In a 3D model, one can mesh the body with 3D brick elements. In this case, some issues may arise and await resolution:

1. an implicit static integration scheme may not give converged results, and one has to use an explicit dynamic one to solve the problems of non-uniqueness of solution and snap-back instability in the presence of high interface strength and

TABLE I. SPECIMEN GEOMETRY

	length	width	thickness
dimension (mm)	102	25.4	3.12

mixed-mode delamination [9];
2. once an explicit dynamic integration scheme is adopted, the laminate mass density and the load rate have to be properly selected to yield converged and accurate results;
3. some viscosity terms and fine meshes around the interface need to be introduced to improve load-displacement curve quality.

The objective of this paper is to develop a 2D and a 3D numerical approach to simulating the DCB, the ENF, and the MMB tests with a commercial software, Abaqus, and to seek for appropriate simplifications of the simulations. An explicit dynamic time integration scheme and a viscosity parameter is adopted to yield close predictions of the specimen responses. The load rate and the specimen mass density are properly selected to approximate a quasi-static loading process. A linear cohesive zone model is used to characterize the mechanical response of the interface. The validity of different strategies of simplifying the finite element model is discussed. The 2D and 3D predictions are compared with the experimental results. The stabilities and accuracy of the 2D and 3D predictions are evaluated.

NUMERICAL METHODS

In this section, a 2D and a 3D numerical approach will be developed following the experimental setups of DCB, ENF, and MMB tests in Ref. [1]. The method of properly selecting the time integration scheme, the viscosity parameter and the mass-scaling factor will be presented such that the numerical approaches can produce converged and accurate results.

Experimental Setups and Finite Element Model

In this paper, the finite element models are developed with reference to the experiment setups in Ref. [1]. Table I lists the specimen dimensions. In the DCB and the ENF tests, the load is directly applied to the specimen, while in the MMB test, the load is applied at one end of a loading lever placed above the specimen. The experiment results on such tests plot the relation between the load acting on the arm and the displacement at the loading point. For different mode-mixing ratios, different initial crack lengths are used, which is obtained from experiments. Table II lists the crack length for different tests and mode-mixing ratios. The loading level length is adjusted to yield designated mode-mixing ratio. The weight of the lever is negligible. To get a specimen model that can lead to converged and accurate results, some model parameters need to be adjusted and tested.

TABLE II. CRACK LENGTH

mode-mixing ratio	0% (DCB)	20%	50%	80%	100% (ENF)
crack length (mm)	33	34	34	31	39

The MMB test apparatus can be modeled with Abaqus in a 2D finite element model by modeling the arm as a rigid body, tying the end of the arm to the specimen, and defining a contact pair in the middle (Figure 3). To simplify the finite element model, the two loading arm branches shown in Figure 2 are removed. The crack is on the right for all figures. The MMB test can be simulated by prescribing a displacement at the end of the arm varying from 0 to desired value (Figure 4). The specimen is simply supported at the cracked end, and roller supported at the other end, allowing it to move in the longitudinal direction. A 3D finite element model can be obtained from a 2D one with the same boundary conditions and loading method by extruding along the width direction.

Time Integration Scheme and Viscosity

Simulations with cohesive elements often experience convergence difficulties after cracks start propagating. Specially, an implicit integration scheme often fails to converge after the traction in a cohesive element reaches its maximum. Fortunately, one can avoid most of these convergence problems with an explicit integration scheme, Abaqus/Explicit, with which the real time process of delamination can be simulated. Due to the dynamic nature of delamination problems and the required small load rate of the delamination tests, one has to solve the problem in a quasi-static set-up. A standard is that the kinetic energy should not be greater than 5% of the total energy at most times during the analysis. Otherwise, the results will be unrealistic and

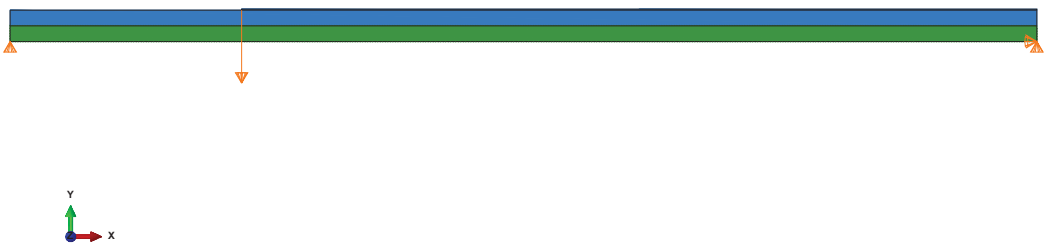

Figure 3. 2D model for the MMB test

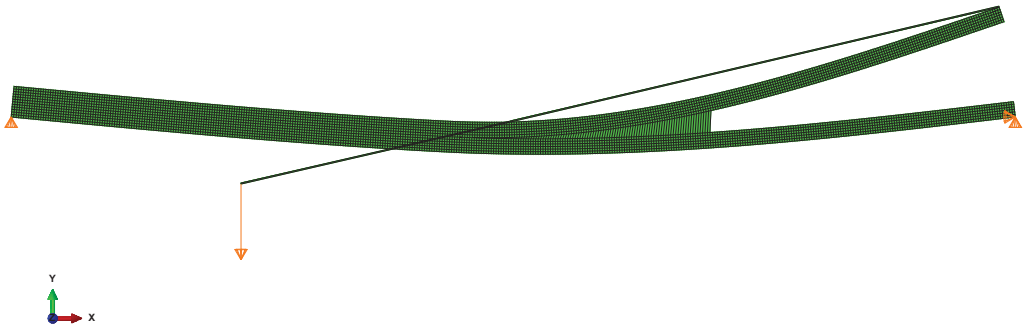

Figure 4. Deformed MMB test apparatus

thus inaccurate. As long as the dynamic steps are quasi-static, an explicit integration scheme can make close predictions for the load-displacement curves.

To alleviate the fluctuation in an explicit analysis, an effective way is to include a small viscosity parameter in the cohesive law, which is simple and productive. The viscosity parameter should be sufficiently great to guarantee curve quality, but sufficiently small to maintain reasonable solving time. In summary, one can guarantee the convergence of the finite element analysis by adopting an explicit integration scheme, and by applying viscosity to simulation, one can get better curve quality when modeling with 3D elements. To further improve the results, other parameters need to be considered.

Mass Scaling and Load Rate

The requirement of the quasi-static set-up can be fulfilled by adjusting load rates and material densities. But applying a real material mass density may lead to much more computation time. By increasing the mass density, one can also reduce the solving time. This is often referred to as mass scaling for explicit dynamic analysis. Mass scaling can affect the computation time because Abaqus approximates the stable time increment as [10]:

$$\Delta t = \frac{L_c}{c_d} \tag{1}$$

where Δt is the stable time increment, L_c is the element characteristic length, and c_d is the dilatational wave speed, which is approximated as:

$$c_d = \sqrt{\frac{E}{\rho}} \tag{2}$$

where E is the elastic modulus and ρ is the mass density of material. This shows that increasing the mass density of material (applying mass scaling) causes the stable time increment to increase and the number of increments to decrease. The mass scaling

factor (or the material mass density of model) should be sufficiently great to ensure analysis efficiency, but sufficiently small to keep the kinetic energy less than 5% of the total energy throughout the process. Because of the raise in kinetic energy ratio when increasing mass scaling factor, one needs to adjust load rate to keep the quasi-static set-up. The load rate should be sufficiently great to ensure analysis efficiency, but sufficiently small to guarantee a quasi-static problem state. One can significantly improve the accuracy of the finite element solution and computation efficiency at the same time by choosing suitable coupling between mass scaling and load rate.

Mesh Density

For complex finite element models, the accuracy of the solution highly depends on the mesh density because the dissipated energy during the fracture process is proportional to the volume of failed elements rather than the area of fracture surface. Models with higher mesh density can surely yield more accurate results at the cost of computation efficiency. Coarser meshes tend to over-predict the results of the load applied to the specimen or the loading lever [11]. One needs to test the mesh density of a finite element model to yield realistic results.

Cohesive Zone Model

A self-contained cohesive zone model should consist of a geometric representation, a cohesive law, and a delamination criterion, where the geometric representation is a cohesive element. Such cohesive elements can form a cohesive layer where the delamination may occur. There is a hypothesis that fracture in such a failure plane formed by the length and width of the element, fracture is caused by normal traction vector and two shear traction vectors acting on it. Thus only these traction vectors will be accounted for fracture of the element. The relative displacement (or separation), δ, is defined as the displacement of a point located on the top surface with respect to a corresponding point located on the bottom surface of the element, u_i^+ and u_i^-:

$$\delta_i = u_i^+ - u_i^- \tag{3}$$

where, for a 3D 8-node cohesive element (Figure 5(a)):

$$\begin{aligned} u_i^+ &= N_k u_{ki}^+, \quad k = 5,6,7,8 \\ u_i^- &= N_k u_{ki}^-, \quad k = 1,2,3,4 \end{aligned} \tag{4}$$

where u_{ki}^+ and u_{ki}^- are the displacements of top and bottom nodes in the element in i direction, respectively, and N_k are Lagrangian shape functions. The element tractions are defined as:

$$\boldsymbol{\sigma} = \boldsymbol{D} \cdot \boldsymbol{\delta} \tag{5}$$

throughout the loading process, where $\boldsymbol{D}$ is the constitutive relation matrix. In this paper, it writes:

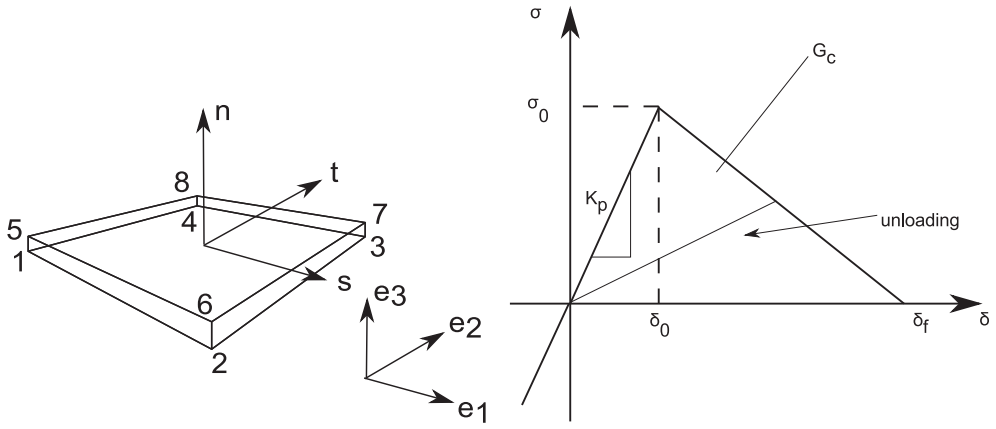

(a) 8-node cohesive element (b) Linear cohesive law

Figure 5. Cohesive zone model with linear cohesive law

$$\begin{pmatrix} \tau_1 \\ \tau_2 \\ \sigma \end{pmatrix} = \begin{pmatrix} D_{11} & 0 & 0 \\ 0 & D_{22} & 0 \\ 0 & 0 & D_{33} \end{pmatrix} \begin{pmatrix} \delta_1 \\ \delta_2 \\ \delta_3 \end{pmatrix} \tag{6}$$

where δ_i is the local relative displacement with 3 denoting the normal direction. Cohesive laws can be developed based on the relations between tractions and relative displacements [12]. D_{11}, D_{22}, and D_{33} are determined with respect to the cohesive law adopted. The cohesive law used in this paper is the linear cohesive law (Figure 5(b)), where the slope K_p of the first linear part is the penalty stiffness and the triangular area under the linear relations is the critical energy release rate G_{c}. For the linear elastic part:

$$D_{ii} = K_{pi}, \quad i = 1, 2, 3 \tag{7}$$

while for the linear softening part:

$$D_{ii} = (1 - d)K_{pi}, \quad i = 1, 2, 3 \tag{8}$$

where d is a damage parameter going from 0 to 1 as the relative displacement goes from δ_0 to δ_f for each direction. A cohesive law is always accompanied by a mixed-mode criterion such that the displacement for total decohesion δ_f for each direction can be uniquely determined because for each direction:

$$G_{\mathrm{c}} = \frac{\sigma_0 \delta_f}{2} \tag{9}$$

Following Ref. [12], the B-K criterion proposed by Benzeggagh and Kenane [13] is used here. It writes:

$$G_{\mathrm{Ic}} + (G_{\mathrm{IIc}} - G_{\mathrm{Ic}}) \left(\frac{G_{\mathrm{shear}}}{G_{\mathrm{T}}} \right)^{\eta} = G_{\mathrm{c}} \tag{10}$$

where G_{Ic} and G_{IIc} are the critical energy release rates for mode I and mode II fracture, respectively, and G_{T} and G_{shear} are the total energy release rate and shear energy

TABLE III. MATERIAL PROPERTIES

E_{11} (GPa)	E_{22}=E_{33} (GPa)	G_{12}=G_{13} (GPa)	G_{23} (GPa)	ν_{12}=ν_{13}
122.7	10.1	5.5	3.7	0.25
ν_{23}	G_{Ic} (KJ/m^2)	G_{IIc} (KJ/m^2)	σ_0 (MPa)	τ_0 (MPa)
0.45	0.969	1.719	80	100

release rate, respectively. The B-K parameter η in Eq. (10) takes the value determined in Ref. [12] which is 2.284. Note that no mode III fracture is present in the tests under consideration, which means:

$$G_{\text{shear}} = G_{\text{II}}, \quad G_{\text{T}} = G_{\text{I}} + G_{\text{II}} \tag{11}$$

In this case, the mode-mixing ratio β is defined as:

$$\beta = \frac{G_{\text{shear}}}{G_{\text{T}}} = \frac{G_{\text{II}}}{G_{\text{I}} + G_{\text{II}}} \tag{12}$$

RESULTS AND DISCUSSION

The test specimen is a 2-ply plate-shaped AS4/PEEK carbon-fiber reinforced composite laminate. Table III lists the material parameters, where σ_0 and τ_0 denote the layer strength in normal and shear directions, respectively. The laminate only consists of long fiber-reinforced plies.

While a 3D model with brick elements can simulate the tests as it is, a 2D model with elements under planes stress condition is also valid because the in-plane stresses are negligible in this problem. Both 2D model with plane stress elements and 3D model with brick elements are used to simulate the tests.

In the present approach, the specimen is meshed using 4-node plane stress elements for the 2D model and 8-node brick elements for the 3D model, with 408 elements in the longitudinal direction, 12 elements in the thickness direction, and 5 elements in the width direction for the 3D model. The cohesive layer is meshed with zero-thickness 4-node cohesive elements for the 2D model and 8-node cohesive elements for the 3D model. Geometrically, the 3D model is obtained by extruding the 2D model along the width direction.

As mentioned before, the viscosity parameter, the mass scaling factor, and the loading rate all affect the load-displacement curve quality and computation cost. Numerical tests show that the parameters listed in Table IV provide satisfactory convergence, accuracy, and efficiency for both 2D and 3D models.

Figure 6 compares load-displacement curves of the DCB, ENF and the MMB tests predicted by the present 3D finite element model with the experiment results shown in Ref. [12]. The percentages in the figure show the mode-mixing ratios defined in Eq. (12). The displacement denotes the load point displacement in the tests. The experiment was carried out by Reeder and Crews [1]. The numerical ENF curve

TABLE IV. FINITE ELEMENT MODEL PARAMETERS

mass density (ton/mm^3)	viscosity	load rate (mm/s)
10^{-4}	0.6	0.5

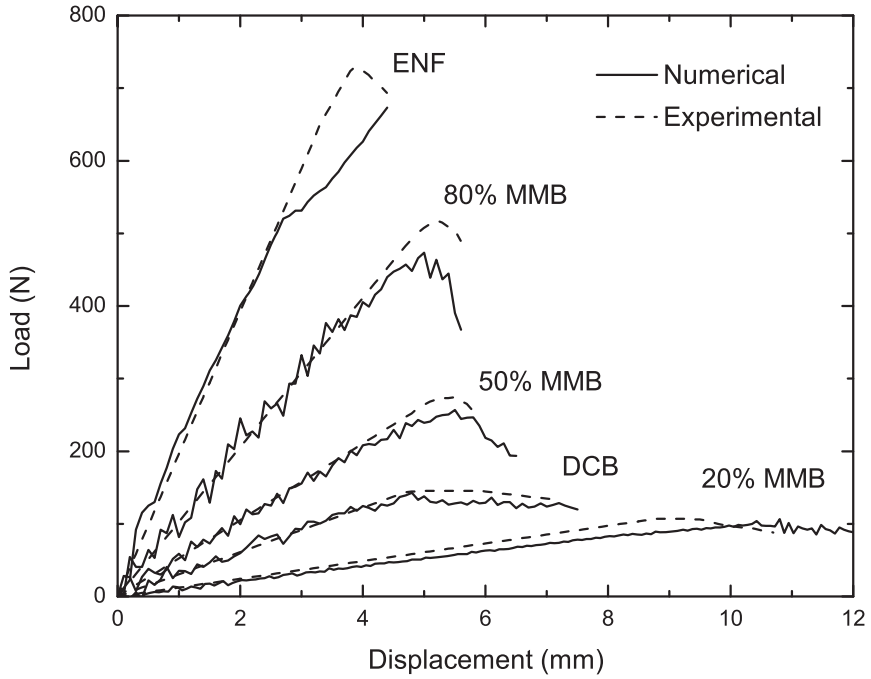

Figure 6. Load-displacement curves of the 3D model

exhibits an unexpected trend. Specifically, it becomes nonlinear at a low traction lever but exhibits no softening which arises in other cases. One possible reason is that the explicit integration scheme failed to propagate along the real loading path. It will be seen below that the 2D model, which has better convergence due to its simplicity, predicts a corresponding curve with an expected trend.

Figure 7 shows the results from all the tests using the 2D model and the comparison with experiment results. All the numerical results agree well with the experiment results. This implies that the finite element model and the parameters selected are validated.

Simulations with both 2D and 3D models give similar trends of the load-displacement curves. The 3D result roughly agrees with the experiment results, while the 2D result agrees with the experiment better. The 2D result is also prominently more accurate than the 3D result in the MMB test with a mode-mixing ratio of 20%. The 3D result significantly fluctuates especially in the MMB test with a mode-mixing ratio of 80%, which makes it hard to tell whether the 3D model is better than 2D in this test. Table V lists the differences in the maximum loads reached in loading history

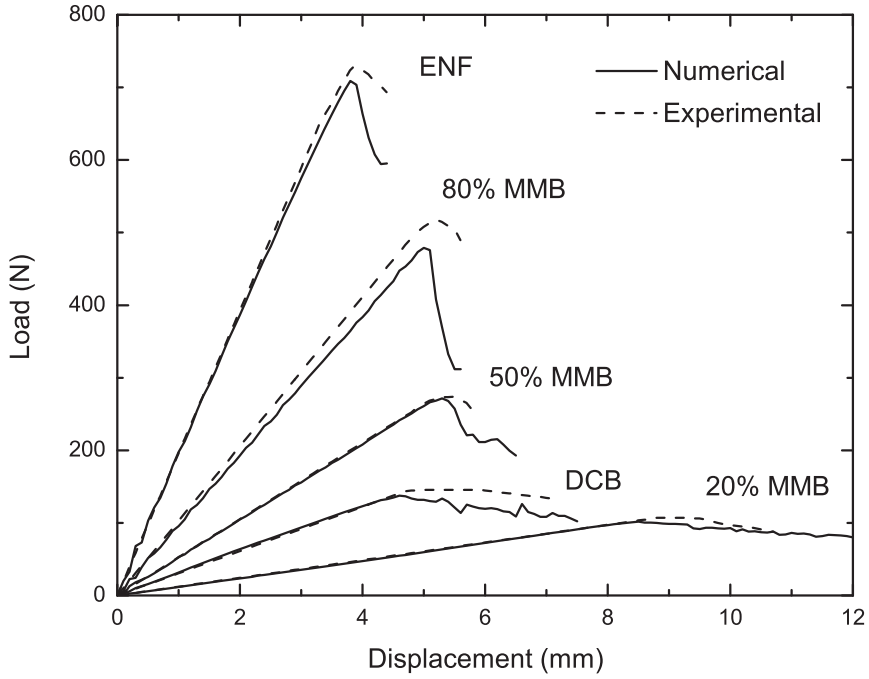

Figure 7. Load-displacement curves of the 2D model

TABLE V. MAXIMUM LOADS FOR DCB, ENF AND MMB TESTS

mode-mixing ratio	0% (DCB)	20%	50%	80%	100% (ENF)
experimental (N)	147.1	108.1	275.4	518.7	734.0
2D numerical (N)	137.4	101.5	271.7	478.9	708.9
error (%)	-6.6	-6.1	-1.3	-7.7	-3.4
3D numerical (N)	142.9	106.6	257.0	473.5	N/A
error (%)	-2.9	-1.4	-6.7	-8.7	N/A

of the tests. For the maximum load, the 3D model only shows better results than the 2D model in the DCB test and the MMB test with a mode-mixing ratio of 20%. With the large fluctuations in the load-displacement curves of the 3D model, the results of the maximum loads are also not accurate enough to show the real trend of the curves. Meanwhile, the 3D model for the specimen has 191,412 degrees of freedom in total compared with the 2D model's 15,951 degrees of freedom, and this led to considerably more solving time for the 3D model. In summary, the 2D approach is found to better handle the mixed-mode progressive delamination in composite laminates satisfying plane stress condition.

CONCLUSIONS

In this paper, a 2D and a 3D numerical approach to simulating DCB, the ENF, and the MMB tests is developed with a commercial software, Abaqus. An explicit dynamic time integration scheme and a viscosity parameter is adopted to yield close predictions of the specimen responses. The load rate and the specimen mass density are properly selected to approximate a quasi-static loading process. A linear cohesive zone model is used to characterize the mechanical response of the interface. The validity of different strategies of simplifying the finite element model is discussed.

The following findings can be obtained from the results:

1. the 2D and the 3D predictions are both found to fit the experimental results well, but the 2D predictions are found to be more accurate and stable than the 3D predictions;
2. the 2D approach is found to better handle the mixed-mode progressive delamination in composite laminates satisfying plane stress condition.

The following conclusions can be drawn from the above findings:

1. more sophisticated cohesive zone models can be implemented in the present approaches, with the user-defined material subroutine for Abaqus/Explicit, VUMAT;
2. the present approach can be further extended to handle the interfacial debonding in many other heterogeneous materials (e.g., fiber- and particle-reinforced composites);
3. although the present approaches are developed with Abaqus/Explicit, they are also applicable to other finite element codes.

REFERENCES

1. Reeder, J. R. and J. J. H. Crews. 1990, "Mixed-mode bending method for delamination testing," *AIAA Journal*, 28(7):1270–1276.
2. Rybicki, E. F. and M. F. Kanninen. 1977, "A finite element calculation of stress intensity factors by a modified crack closure integral," *Engineering Fracture Mechanics*, 9:931–938.
3. Shivakumar, K. N., P. W. Tan, and J. J. C. Newman. 1988, "A virtual crack-closure technique for calculating stress intensity factors for cracked three dimensional bodies," *International Journal of Fracture*, 36:R43–R50.
4. Nilsson, K. F., "On growth of crack fronts in the DCB test," *Composite Engineering*, 3(6).
5. Dávila, C. G., P. P. Camanho, and A. Turon. 2008, "Effective simulation of delamination in aeronautical structures using shells and cohesive elements," *Journal of Aircraft*, 45(2):663–672.
6. Borg, R., L. Nilsson, and K. Simonsson, "Simulating DCB, ENF and MMB experiments using shell elements and a cohesive zone model," *Journal of Composites Science and Technology*, 64(2).
7. Balzani, C. and W. Wagner. 2008, "An interface element for the simulation of delamination in unidirectional fiber-reinforced composite laminates," *Journal of Engineering Fracture Mechanics*, 75:2597–2615.
8. Mi, Y., M. A. Crisfield, and G. A. O. Davies, "Progressive delamination using interface elements," *Journal of Composite Materials*, 32(14).
9. Gao, Y. F. and A. F. Bower. 2004, "A simple technique for avoiding convergence problems in finite element simulations of crack nucleation and growth on cohesive interfaces," *Modelling and Simulation in Materials Science and Engineering*, 12:453–463.
10. 2011, "ABAQUS analysis user's manual," .

11. Turon, A., C. G. Dávila, P. P. Camanho, and J. Costa. 2007, "An engineering solution for mesh size effects in the simulation of delamination using cohesive zone models," *Journal of Engineering Fracture Mechanics*, 74(10):1665–1682.
12. Camanho, P. P., C. G. Dávila, and M. F. de Moura. 2003, "Numerical simulation of mixed-mde progressive delamination in composite materials," *Journal of Composite Materials*, 37(16).
13. Benzeggagh, M. L. and M. Kenane. 2003, "Measurement of mixed-mode delamination fracture toughness of unidirectional glass/epoxy composites with mixed-mode bending apparatus," *Journal of Composites Science and Technology*, 56:439–449.

Asymptotical Modelling of Thermopiezoelastic Laminates

Y. LONG and W. YU

ABSTRACT

A general anisotropic laminated plate model with thermal deformation and two-way coupled piezoelectric effect and pyroelectric effect is constructed using the variational asymptotic method, without any ad hoc assumptions. Total potential energy contains strain energy, electric potential energy and energy caused by temperature change. Three-dimensional strain field is built based on the concept of warping function and decomposition of the rotation tensor. The feature of small thickness and large in-plane dimension of plate structures helped to asymptotically simplify the three-dimensional analysis to a two-dimensional analysis on the reference surface and a one-dimensional analysis through the thickness. Several numerical examples are studied. The present model is validated by the excellent agreements between the results from 3D finite element analyses and the presented model.

INTRODUCTION

Modelling for plate structures bonded with piezoelectric materials is more and more popular in recent years because they can achieve active shape and vibration control ([1], [2]and [3]). Piezoelectric effect leads to a coupling between electric energy and mechanical energy, making the modelling more difficult than conventional plates. Besides, most piezoelectric materials also have pyroelectricity coupling the electric energy with thermal energy. Since thermal stress and strain affect the performance of laminates significantly, it is valuable to take pyroelectric effect and thermal deformation into consideration when modelling multi-layered piezoelectric plates.

Although many efforts are made to get exact 3D solutions for piezoelectric plates, they are still only available to limited cases ([4], [5], [6] and [7]). As a result, modelling is still highly relying on plate theories. However, most of the existing works are based on ad hoc assumptions for simplification, making stresses and strains in the structure unnecessarily restricted before any analyses are proceeded. Lee [8] de-

Yufei Long and Wenbin Yu, Purdue University, West Lafayette, Indiana 47907, U.S.A

veloped an isotropic laminated plate model based on Kirchhoff-Love assumptions. Chandrashekhara and Agarwal [2] modified his formulation to a Reissner-Mindlin model and used it for vibration control. Pai et al. [9] proposed a refined geometrically nonlinear model for composite plates with piezoelectric sensors and actuators, but the piezoelectricity and mechanical forces are not fully coupled. Mitchell and Reddy [10] derived a composite laminated piezoelectric plate model including the energy from electrostatic charge, using a third-order shear deformation theory [11]. Wang et al. [12] studied vibration of a piezoelectric circular plate using the Kirchhoff-Love plate model. Orthotropy of piezoelectric material is considered and electric and mechanical fields are fully coupled to ensure the satisfaction of Maxwell equation. Qu [13] derived finite element formulations for composite laminated plates with coupled direct and converse piezoelectric effects. Beginning from 3D formulations of a piezoelectric plate, Figueiredo and Leal [14] used asymptotic analysis to get a 2D piezoelectric model. By applying a hypothesis of zero elastic constants in thickness direction, the model converges to the Kirchhoff-Love theory when the thickness goes to zero. Kapuria and Achary [15] used a modified zigzag theory along with von Karman geometric nonlinearity to analyze the buckling of piezoelectric plates.

Many researchers also concern the effect of temperature load on piezoelectric plates. Since most piezoelectric materials also present pyroelectric effect, thermal expansion would not be the only effect to be considered when temperature changes [16]. Tauchert [17] proposed an analysis on thermal deformation of a piezoelectric laminated plate based on Kirchhoff assumptions. Krommer and Irschik [18] derived a Reissner-Mindlin type piezoelectric plate under thermal load. Concentration is put on the influence of direct piezoelectric and pyroelectric effect on plate stiffness. Cho and Oh [19] constructed a fully coupled thermopiezoelastic composite plate model, in which temperature and electric field are treated as variables, using a higher order zigzag theory. Kapuria and Achary [20] introduced another zigzag theory in third-order that can achieve the consistency of no shear traction on the top and bottom surfaces. Oh et al. [21] developed a lower-order shear deformation theory averaged from higher-order zigzag theory and applied it on modelling fully coupled electro-thermo-mechanical laminated plates.

Even though many results from plate models with ad hoc assumptions can provide acceptable accuracy, those assumptions can be avoided and can make the models predict wrong results when these assumptions are violated. In contrast, the variational-asymptotic method (VAM), developed by Berdichevsky [22], is a mathematical approach capable of analyzing functionals with relatively small parameters. By using the VAM, taking the advantage of small parameter of h/l in plate structures, where h is the thickness and l indicates the characteristic in-plane dimension, a model with desired accuracy can be acquired without priori assumptions.

Early application of VAM on composite plate modelling includes the work by Atilgan and Hodges [23]. Their work is extended by Sutyrin and Hodges [24, 25] to make the model practical for multi-layered composite plates by transforming the formula to a Reissner-Mindlin-like model. Yu et al. [26, 27] developed a general composite laminated plate model based on the geometrically nonlinear theory in [28]. Using a finite element approach, Yu and Hodges extended their previous work for applying on a thermopiezoelastic composite plate [29], but electric field and temper-

ature field are only one way coupled with mechanical field. Liao and Yu [30, 31] developed the model to accommodate a fully coupled piezoelectric composite plate. Recently, Chen and Yu [32] further induced magnetic field in the composite laminate model.

The purpose of this paper is to derive a model for multi-layered surfaces and interfaces electroded piezoelectric plates under thermal loads. With the help of decomposition of rotation tensor [33] and warping functions, 3D strains can be expressed in terms of 2D generalized strains. Energy expression of the plate contains potential energy, kinetic energy and virtual work from external loads. Since the main purpose is to study the deformation of plates, converse effect of pyroelectricity is not included to avoid heat conduction problem. 3D model is then reduced to a 2D formulation by applying the VAM. The reduced 2D plate model can be solved in the same way as classical or Reissner-Mindlin plate theory. 3D displacement, stress and strain fields can be recovered using warping functions derived from energy expression.

THREE-DIMENSIONAL FORMULATION

Plate kinematics

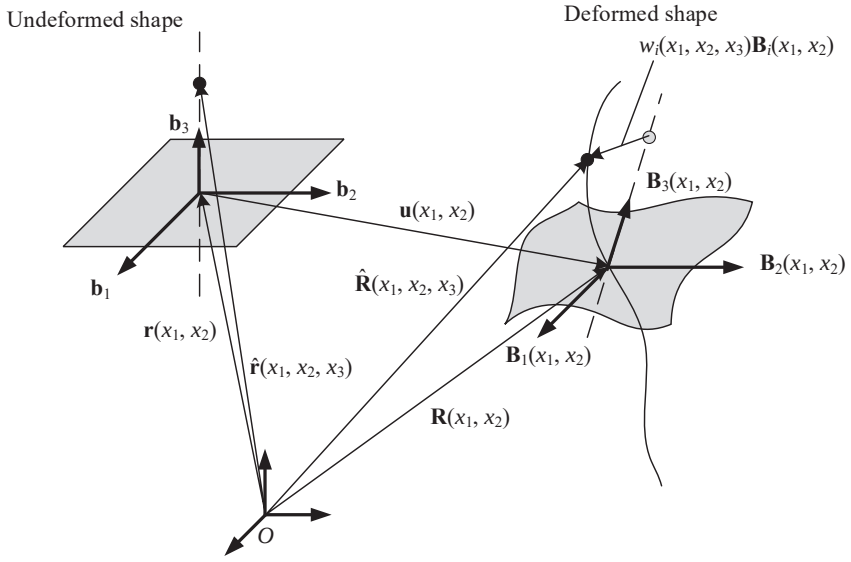

Figure 1: Schematic of plate deformation.

Position of a point in a plate can be determined by its Cartesian coordinates x_i, as shown in Figure 1, where x_α are two orthogonal coordinates in the reference surface and x_3 is the normal coordinate with the origin locating at the middle of the thickness. Greek letter indices refer to 1 and 2 while Latin letter indices refers to 1, 2 and 3 here and after. Orthogonal triad $\mathbf{b}_i$ denote the unit vectors in x_i directions of the undeformed plate, so any material point in the undeformed plate can have a position

vector $\hat{\mathbf{r}}$ from a fixed point O so that

$$\hat{\mathbf{r}}\left(x_1, x_2, x_3\right) = \mathbf{r}\left(x_1, x_2\right) + x_3\mathbf{b}_3 \tag{1}$$

where $\mathbf{r}$ denotes the position vector of intersection point of the reference surface and the normal line on which the described point is located.

When deformation happens, the material point described by vector $\hat{\mathbf{r}}$ in the undeformed state will have the position vector $\hat{\mathbf{R}}$ in the deformed state. For expression, orthogonal unit vector triad for the deformed plate $\mathbf{B}_i$ is introduced. Relation between $\mathbf{b}_i$ and $\mathbf{B}_i$ is indicated in a similar way as coordinate transformation using direction cosine matrix $\mathcal{C}_{ij}\left(x_1, x_2\right)$

$$\mathbf{B}_i = \mathcal{C}_{ij}\mathbf{b}_j, \quad \mathcal{C}_{ij} = \mathbf{B}_i \cdot \mathbf{b}_j \tag{2}$$

Now $\hat{\mathbf{R}}$ can be expanded to the following form for any definition of $\mathbf{B}_i$

$$\hat{\mathbf{R}}\left(x_1, x_2, x_3\right) = \mathbf{R}\left(x_1, x_2\right) + x_3\mathbf{B}_3\left(x_1, x_2\right) + w_i\left(x_1, x_2, x_3\right)\mathbf{B}_i\left(x_1, x_2\right) \tag{3}$$

where w_i are warping functions to ensure equation (3) to be able to describe all possible deformation. No assumption is made on the shape of warping functions and their exact expression will be solved later. In order to uniquely determine $\mathbf{B}_i$, six constraints are introduced. The first three constraints is set in the way of

$$\left\langle w_{\|}\left(x_1, x_2, x_3\right)\right\rangle = c_{\|}, \quad \left\langle w_3\left(x_1, x_2, x_3\right)\right\rangle = 0 \tag{4}$$

where $\left(\ \right)_{\|} = \left[\left(\ \right)_1 \quad \left(\ \right)_2\right]^{\mathrm{T}}$ and $c_{\|}$ is a free variable independent of x_3. Angle brackets indicate definite integral on x_3 direction from the bottom to the top of the plate.

Two more constraints can be specified by setting $\mathbf{B}_3$ normal to the reference surface of the deformed plate. Here transverse shear and thickness change are still allowed because of the warping functions, which dissociates the present work from any kinematic hypotheses. It is still possible for $\mathbf{B}_\alpha$ to rotate around $\mathbf{B}_3$, so introducing

$$\mathbf{B}_1 \cdot \mathbf{R}_{,2} = \mathbf{B}_2 \cdot \mathbf{R}_{,1} \tag{5}$$

to be the last constraint.

Terms in the deformation gradient tensor is defined as

$$F_{ij} = \mathbf{B}_i \cdot \mathbf{G}_j \tag{6}$$

where $\mathbf{G}_i$ are the covariant base vectors in the deformed state and $\mathbf{G}_i = \frac{\partial \hat{\mathbf{R}}}{\partial x_i}$. Then the 3D strain field can be derived from decomposition of the rotation tensor [34]

$$\Gamma_{ij} = \frac{1}{2}(F_{ij} + F_{ji}) - \delta_{ij} \tag{7}$$

where δ_{ij} is the Kronecker symbol.

For expressing 3D strain field in terms of 2D strains, one can define 2D generalized strains in the same way as [28]

$$\mathbf{R}_{,\alpha} = \mathbf{B}_\alpha + \varepsilon_{\alpha\beta}\mathbf{B}_\beta \tag{8}$$

$$\mathbf{B}_{i,\alpha} = (-K_{\alpha\beta}\mathbf{B}_\beta \times \mathbf{B}_3 + K_{\alpha 3}\mathbf{B}_3) \times \mathbf{B}_i \tag{9}$$

where $\varepsilon_{\alpha\beta}$ and $K_{\alpha\beta}$ are 2D generalized membrane strains and curvatures, a comma in subscript implies partial derivative. Strains are assumed to be small compared to unity and warping functions are of the similar magnitude of strain when only geometric nonlinearity is considered. Now one can derive the 3D strain field expression to be

$$\Gamma_e = \epsilon + x_3\kappa + I_\alpha w_{\|,\alpha}, \quad 2\Gamma_s = {w_\|}' + e_\alpha w_{3,\alpha}, \quad \Gamma_t = {w_3}' \tag{10}$$

where $(\,)'$ implies partial derivative with respect to x_3 and

$$\Gamma_e = [\ \Gamma_{11} \quad 2\Gamma_{12} \quad \Gamma_{22}\ ]^{\mathrm{T}}, \quad 2\Gamma_s = [\ 2\Gamma_{13} \quad 2\Gamma_{23}\ ]^{\mathrm{T}}, \quad \Gamma_t = \Gamma_{33} \tag{11}$$

and

$$\epsilon = [\ \varepsilon_{11} \quad 2\varepsilon_{12} \quad \varepsilon_{22}\ ]^{\mathrm{T}}, \quad \kappa = [\ K_{11} \quad K_{12} + K_{21} \quad K_{22}\ ]^{\mathrm{T}} \tag{12}$$

and

$$I_1 = \begin{bmatrix} 1 & 0 \\ 0 & 1 \\ 0 & 0 \end{bmatrix}, \quad I_2 = \begin{bmatrix} 0 & 0 \\ 1 & 0 \\ 0 & 1 \end{bmatrix}, \quad e_1 = \begin{Bmatrix} 1 \\ 0 \end{Bmatrix}, \quad e_2 = \begin{Bmatrix} 0 \\ 1 \end{Bmatrix} \tag{13}$$

So far kinematics of a plate is formulated. However, for a coupled piezoelectric laminated plates, electric field should also be in concern along with the mechanical field. Electric field can be defined using electric potential $\phi\,(x_1, x_2, x_3)$

$$E_s = [\ E_1 \quad E_2\ ]^{\mathrm{T}} = -[\ \phi_{,1} \quad \phi_{,2}\ ]^{\mathrm{T}}, \quad E_t = E_3 = -\phi' \tag{14}$$

In this study electrodes of the piezoelectric plate are coated on the top and bottom surfaces or interfaces between layers. Electrodes are assumed to be of negligible thickness and have no influence on mechanical properties of the plate. Then electric potential can be specified at $x_3 = h_i$, where h_i refers to the position of surface or interface and here i indicates the numbering of layers varying from 1 to $k+1$ and k is the total number of layers. Although temperature load is considered in the work, it is only one-way coupling so temperature change $T\,(x_1, x_2, x_3)$ is treated as a known function.

Energy formulation

The elastodynamic behavior of a piezoelectric laminated plate is governed by the extended Hamiltion's principle [35]

$$\int_{t_1}^{t_2} \left[\delta(\mathcal{K} - \mathcal{U}) + \overline{\delta\mathcal{W}}\right] \mathrm{d}t = 0 \tag{15}$$

where t_1 and t_2 are arbitrary fixed time; $\mathcal{K}$ is the kinetic energy; $\mathcal{U}$ is the internal potential energy related to strain, electric field and temperature; $\overline{\delta\mathcal{W}}$ is the virtual work of external loads. Kinetic energy can be neglected in static problems, and virtual work is considered in the process of dimensional reduction, so here concentration is on expressing $\mathcal{U}$ in terms of 2D plate variables.

For piezoelectric structures with thermal loads, the internal potential energy $\mathcal{U}$ can be expressed as the integral of area potential energy density

$$\mathcal{U} = \int_{\Omega} \mathcal{H} \mathrm{d}\Omega \tag{16}$$

where Ω is the area domain of the reference surface and

$$\begin{aligned}
\mathcal{H} = \frac{1}{2} &\left\langle \begin{Bmatrix} \Gamma_e \\ 2\Gamma_s \\ \Gamma_t \end{Bmatrix}^{\mathrm{T}} \begin{bmatrix} C_e & C_{es} & C_{et} \\ C_{es}^{\mathrm{T}} & C_s & C_{st} \\ C_{et}^{\mathrm{T}} & C_{st}^{\mathrm{T}} & C_t \end{bmatrix} \begin{Bmatrix} \Gamma_e \\ 2\Gamma_s \\ \Gamma_t \end{Bmatrix} \right\rangle \\
&- \left\langle \begin{Bmatrix} \Gamma_e \\ 2\Gamma_s \\ \Gamma_t \end{Bmatrix}^{\mathrm{T}} \begin{bmatrix} e_b & e_{et} \\ e_s & e_a \\ e_c & e_t \end{bmatrix} \begin{Bmatrix} E_s \\ E_t \end{Bmatrix} \right\rangle \\
&- \left\langle \begin{Bmatrix} \Gamma_e \\ 2\Gamma_s \\ \Gamma_t \end{Bmatrix}^{\mathrm{T}} \begin{bmatrix} C_e & C_{es} & C_{et} \\ C_{es}^{\mathrm{T}} & C_s & C_{st} \\ C_{et}^{\mathrm{T}} & C_{st}^{\mathrm{T}} & C_t \end{bmatrix} \begin{Bmatrix} \alpha_e \\ \alpha_s \\ a_t \end{Bmatrix} T \right\rangle \\
&- \frac{1}{2} \left\langle \begin{Bmatrix} E_s \\ E_t \end{Bmatrix}^{\mathrm{T}} \begin{bmatrix} d_s & d_{et} \\ d_{et}^{\mathrm{T}} & d_t \end{bmatrix} \begin{Bmatrix} E_s \\ E_t \end{Bmatrix} \right\rangle - \left\langle \begin{Bmatrix} E_s \\ E_t \end{Bmatrix}^{\mathrm{T}} \begin{Bmatrix} p_s \\ p_t \end{Bmatrix} T \right\rangle
\end{aligned} \tag{17}$$

where C_e, C_{es}, C_{et}, C_s, C_{st} and C_t are the submatrices of the partitioned 6×6 material's elastic constant matrix; e_b, e_{et}, e_s, e_a, e_c and e_t are the submatrices of the partitioned transpose of the 3×6 piezoelectric stress coefficient matrix; α_e, α_s and α_t are the submatrices of the partitioned 6×1 thermal expansion coefficient matrix; d_s, d_{et} and d_t are the submatrices of the partitioned 3×3 dielectric constant matrix; p_s and p_t are the submatrices of the partitioned 3×1 pyroelectric coefficient matrix.

Up to this point, the 3D continuum model of the thermopiezoelastic plate is ready to be reduced to a 2D plate model by a through-the-thickness analysis using the VAM.

DIMENSIONAL REDUCTION

Zeroth-order reduction

In the zeroth-order reduction, the energy is expanded into the order of $(hl^2)\mu\epsilon^2$. Because of the order of external loads [30], warping functions w_i and electric potential ϕ only appears in the area potential energy density, so it is more convenient to directly work on $\mathcal{H}_0$. The variation of $\mathcal{H}_0$ can be calculated to be

$$\begin{aligned}
\delta\mathcal{H}_0 = \Big\langle &\big[(\varepsilon + x_3\kappa)^{\mathrm{T}} C_{es} + {w_\parallel}'^{\mathrm{T}} C_s + {w_3}' C_{st}^{\mathrm{T}} + \phi' e_a^{\mathrm{T}} \\
&- (\alpha_e^{\mathrm{T}} C_{es} + \alpha_s^{\mathrm{T}} C_s + \alpha_t C_{st}^{\mathrm{T}}) T \big] \delta {w_\parallel}' + \lambda_\parallel \delta w_\parallel \\
&+ \big[(\varepsilon + x_3\kappa)^{\mathrm{T}} C_{et} + {w_\parallel}'^{\mathrm{T}} C_{st} + {w_3}' C_t + \phi' e_t \\
&- (\alpha_e^{\mathrm{T}} C_{et} + \alpha_s^{\mathrm{T}} C_{st} + \alpha_t C_t) T \big] \delta {w_3}' + \lambda_3 \delta w_3 \\
&+ \big[(\varepsilon + x_3\kappa)^{\mathrm{T}} e_{et} + {w_\parallel}'^{\mathrm{T}} e_a + {w_3}' e_t - \phi' d_t + p_t T \big] \delta\phi' \Big\rangle
\end{aligned} \tag{18}$$

where $\lambda_\parallel$ and λ_3 are Lagrange multipliers for introducing the constraints in equation (4). Warping functions w_i are free to vary at the top and bottom surfaces but electric potential is free to vary only when it is not prescribed at those locations. Euler-Lagrange equations of equatio (18) can be written as

$$\begin{aligned}(\epsilon + x_3\kappa)^{\mathrm{T}} C_{es} + {w_\parallel}'^{\mathrm{T}} C_s + {w_3}' C_{st}^{\mathrm{T}} + \phi' e_a^{\mathrm{T}} \\ -(\alpha_e^{\mathrm{T}} C_{es} + \alpha_s^{\mathrm{T}} C_s + \alpha_t C_{st}^{\mathrm{T}})T = 0\end{aligned} \tag{19}$$

$$\begin{aligned}(\epsilon + x_3\kappa)^{\mathrm{T}} C_{et} + {w_\parallel}'^{\mathrm{T}} C_{st} + {w_3}' C_t + \phi' e_t \\ -(\alpha_e^{\mathrm{T}} C_{et} + \alpha_s^{\mathrm{T}} C_{st} + \alpha_t C_t)T = 0\end{aligned} \tag{20}$$

$$(\epsilon + x_3\kappa)^{\mathrm{T}} e_{et} + {w_\parallel}'^{\mathrm{T}} e_a + {w_3}' e_t - \phi' d_t + p_t T = \mathcal{P} \tag{21}$$

where $\mathcal{P}$ is an arbitrary function independent of x_3 generated by indefinite integration. Expressions of the warping function and electric potential for each layer can be solved from equations (19), (20) and (21), giving

$${w_\parallel}'^{\mathrm{T}} = -(\epsilon + x_3\kappa - \alpha_e T)^{\mathrm{T}} C_{es}^{**} C_s^{-1} + \mathcal{P}\frac{e_a^{*\mathrm{T}} C_s^{-1}}{d_t^*} - p_t^* T \frac{e_a^{*\mathrm{T}} C_s^{-1}}{d_t^*} + \alpha_s^{\mathrm{T}} T \tag{22}$$

$${w_3}' = -(\epsilon + x_3\kappa - \alpha_e T)^{\mathrm{T}} C_{et}^{**} C_t^{*-1} + \mathcal{P}\frac{e_t^* C_t^{*-1}}{d_t^*} - p_t^* T \frac{e_t^* C_t^{*-1}}{d_t^*} + \alpha_t T \tag{23}$$

$$\phi' = (\epsilon + x_3\kappa - \alpha_e T)^{\mathrm{T}} \frac{e_{et}^*}{d_t^*} - \mathcal{P}\frac{1}{d_t^*} + p_t^* T \frac{1}{d_t^*} \tag{24}$$

where the starred quantities are introduced for simplifying the expression, and

$$\begin{aligned} C_{et}^* = C_{et} - C_{es} C_s^{-1} C_{st}, \quad C_t^* = C_t - C_{st}^{\mathrm{T}} C_s^{-1} C_{st}, \quad C_{es}^* = C_{es} - \frac{C_{et}^* C_{st}^{\mathrm{T}}}{C_t^*} \\ C_{et}^{**} = C_{et}^* + \frac{e_{et}^* e_t^*}{d_t^*}, \quad C_{es}^{**} = C_{es}^* + \frac{e_{et}^* e_a^{*\mathrm{T}}}{d_t^*}, \quad e_t^* = e_t - e_a^{\mathrm{T}} C_s^{-1} C_{st} \\ e_a^* = e_a - \frac{C_{st} e_t^*}{C_t^*}, \quad e_{et}^* = e_{et} - C_{es}^* C_s^{-1} e_a - \frac{C_{et}^* e_t}{C_t^*} \\ d_t^* = d_t + e_a^{*\mathrm{T}} C_s^{-1} e_a + \frac{e_t^* e_t}{C_t^*}, \quad p_t^* = p_t + \alpha_e^{\mathrm{T}} e_{et} + \alpha_s^{\mathrm{T}} e_a + \alpha_t e_t \end{aligned} \tag{25}$$

It is impossible to determine the expression of $\mathcal{P}$ without knowing the electric boundary condition, but a most general form of function $\mathcal{P}$ can be written as

$$\mathcal{P} = \epsilon^{\mathrm{T}} \mathcal{P}_\epsilon + \kappa^{\mathrm{T}} \mathcal{P}_\kappa + \mathcal{P}_\phi \tag{26}$$

Substituting equations (22), (23)and (24) into $\mathcal{H}_0$, the zeroth-order asymptotically correct expression of the potential energy density can be obtained as

$$2\mathcal{H}_0 = \begin{Bmatrix} \epsilon \\ \kappa \end{Bmatrix}^{\mathrm{T}} \begin{bmatrix} A^* & B^* \\ B^{*\mathrm{T}} & D^* \end{bmatrix} \begin{Bmatrix} \epsilon \\ \kappa \end{Bmatrix} - 2 \begin{Bmatrix} S_\epsilon \\ S_\kappa \end{Bmatrix}^{\mathrm{T}} \begin{Bmatrix} \epsilon \\ \kappa \end{Bmatrix} \tag{27}$$

with

$$A^* = \left\langle C_e^* - \frac{\mathcal{P}_\epsilon \mathcal{P}_\epsilon^{\mathrm{T}}}{d_t^*} \right\rangle, \qquad B^* = \left\langle x_3 C_e^* - \frac{\mathcal{P}_\epsilon \mathcal{P}_\kappa^{\mathrm{T}}}{d_t^*} \right\rangle$$
$$D^* = \left\langle {x_3}^2 C_e^* - \frac{\mathcal{P}_\kappa \mathcal{P}_\kappa^{\mathrm{T}}}{d_t^*} \right\rangle \tag{28}$$

and

$$S_\epsilon = \left\langle \frac{\mathcal{P}_\epsilon \mathcal{P}_\phi^{\mathrm{T}}}{d_t^*} + T\left[C_e^* \alpha_e - \frac{e_{et}^*}{d_t^*} p_t^* \right] \right\rangle$$
$$S_\kappa = \left\langle \frac{\mathcal{P}_\kappa \mathcal{P}_\phi^{\mathrm{T}}}{d_t^*} + T\left[x_3 C_e^* \alpha_e - x_3 \frac{e_{et}^*}{d_t^*} p_t^* \right] \right\rangle \tag{29}$$

where

$$C_e^* = C_e - C_{es}^* C_s^{-1} C_{es}^{\mathrm{T}} - \frac{C_{et}^* C_{et}^{\mathrm{T}}}{C_t^*} + \frac{e_{et}^* e_{et}^{*\mathrm{T}}}{d_t^*} \tag{30}$$

Terms not relating to 2D generalized strains are all dropped because they will not affect the total energy when the plate is deformed. It can be found from equation (28) that the stiffness matrices A^*, B^* and D^* not only depend on material elastic constants, but also piezoelectric coefficients and dielectric constants. Temperature change and applied electric field can affect the values of S_ϵ and S_κ, which provide additional contributions to the total potential energy.

Up to this point, the original 3D problem has been reduced to a 2D plate problem. It is obvious that even though the plate is a piezoelectric smart plate, the 2D energetics has the same form as the classical lamination theory (CLT) with thermal load except the temperature related term is extended to contain piezoelectric effect.

The stiffness matrices in equation (27) can be used in a plate analysis for prediction of global plate behavior. However, in many cases it is also valuable to acquire the 3D quantities of the plate structure. In such situations, 3D fields are required to be recovered via the 2D results. For the zeroth-order approximation, the 3D strain field and electric field can be recovered by neglecting terms with derivatives with respect to x_α in equation (10) and (14), obtaining

$$\Gamma_e^0 = \epsilon + x_3 \kappa, \quad 2\Gamma_s^0 = {w_\parallel}', \quad \Gamma_t^0 = {w_3}' \tag{31}$$

$$E_s^0 = 0, \quad E_t^0 = -\phi' \tag{32}$$

The 3D stress field and electric displacement field can be obtained using 3D constitutive relations of elasticity and piezoelectricity.

From the second equation in (31) it can be found that the transverse shear and normal strains are not zero, which means lines normal to the reference surface in the undeformed plate are deformable, differing the current model from the CLT. In zeroth-order reduction, transverse shear and normal stresses are identically zero because their expressions coincide the Euler-Lagrange equations in (19) and (20). This result is a direct deduction from the variational statement instead of an ad hoc assumption. Similarly, electric displacement in x_3 direction always equals to $\mathcal{P}$ because of Euler-Lagrange equation (21). Though at this stage transverse shear and normal stresses cannot be predicted, they can be estimated in a higher-order approximation.

First-order reduction

To improve the accuracy as well as predict transverse stresses, dimensional reduction of the first-order is required. In this reduction, strains are expanded into the order of $\frac{h}{l}\epsilon$ and the resultant energy is in the order of $(hl^2)\mu(\frac{h}{l})^2\epsilon^2$. Then warping functions and electric potential are perturbed to be

$$\begin{gathered} w_\| = w_\|^0 + v_\| + o\left(\frac{h^2}{l}\epsilon\right), \quad w_3 = w_3^0 + v_3 + o\left(\frac{h^2}{l}\epsilon\right) \\ \phi = \phi^0 + \varphi + o\left(\frac{h^2}{l}\epsilon\right) \end{gathered} \tag{33}$$

Up to this order virtual work of applied loads are not negligible, so total potential density with virtual work added can be defined as

$$\Pi = \mathcal{H} - W \tag{34}$$

with

$$W = \left\langle P_\|^{\mathrm{T}} w_\| \right\rangle + \tau_\|^{\mathrm{T}} w_\|^+ + \beta_\|^{\mathrm{T}} w_\|^- + \langle P_3 w_3 \rangle + \tau_3 w_3^+ + \beta_3 w_3^- \tag{35}$$

In the zeroth-order approximation, the formulation is for fully anisotropic materials, but it becomes tedious in higher order derivation. Since most piezoelectric and composite materials present at least monoclinic symmetry about the mid-plane, it would be enough for practical use when applying this material symmetry. Consequently, C_{es}, C_{st}, e_b, e_a, e_c, d_{et} and α_s will always vanish. Then warping functions and electric potential in each layer solved during the zeroth-order reduction can be rewritten as

$$w_\|^0 = 0, \quad w_3^0 = C_\perp \mathcal{E} + w_{3e}^0, \quad \phi^0 = C_\phi \mathcal{E} + \phi_e^0 \tag{36}$$

with $\mathcal{E} = \begin{bmatrix} \epsilon & \kappa \end{bmatrix}^{\mathrm{T}}$ and

$$\begin{aligned} C_\perp{}' &= \begin{bmatrix} -\dfrac{C_{et}^{**\mathrm{T}}}{C_t^*} + \dfrac{e_t^*}{d_t^* C_t^*}\mathcal{P}_\epsilon^{\mathrm{T}} & -x_3\dfrac{C_{et}^{**\mathrm{T}}}{C_t^*} + \dfrac{e_t^*}{d_t^* C_t^*}\mathcal{P}_\kappa^{\mathrm{T}} \end{bmatrix} \\ w_{3e}^0{}' &= T\left(\frac{C_{et}^{**\mathrm{T}}\alpha_e}{C_t^*} - \frac{e_t^* p_t^*}{d_t^* C_t^*} + \alpha_t\right) + \frac{e_t^*}{d_t^* C_t^*}\mathcal{P}_\phi \end{aligned} \tag{37}$$

$$\begin{aligned} C_\phi{}' &= \begin{bmatrix} \dfrac{e_{et}^{*\mathrm{T}}}{d_t^*} - \dfrac{1}{d_t^*}\mathcal{P}_\epsilon^{\mathrm{T}} & x_3\dfrac{e_{et}^{*\mathrm{T}}}{d_t^*} - \dfrac{1}{d_t^*}\mathcal{P}_\kappa^{\mathrm{T}} \end{bmatrix} \\ \phi_e^{0\prime} &= T\left(-\frac{e_{et}^{*\mathrm{T}}\alpha_e}{d_t^*} + \frac{p_t^*}{d_t^*}\right) - \frac{1}{d_t^*}\mathcal{P}_\phi \end{aligned} \tag{38}$$

where the "0" in superscript denotes that the quantity is from the zeroth-order reduction.

Taking the variation of the total potential density, gives

$$\begin{aligned} \delta\Pi_1 = \Big\langle & \big[(\epsilon + x_3\kappa - \alpha_e T)^{\mathrm{T}} C_e^* + (p_t^* T - \mathcal{P})\frac{e_{et}^{*\mathrm{T}}}{d_t^*}\big] I_\alpha \delta v_{\|,\alpha} \\ & + \big[(v_\|{}' + e_\alpha w_{3,\alpha}^0)^{\mathrm{T}} C_s + \phi_{,\|}^{0\mathrm{T}} e_s{}^{\mathrm{T}}\big]\delta v_\|{}' + \big[v_3{}' C_t + \varphi' e_t\big]\delta v_3{}' \\ & + \big[p_s^{\mathrm{T}} T\big]\delta\varphi_{,\|} + \big[P + v_3{}' e_t - \varphi' d_t\big]\delta\varphi' \Big\rangle \\ & - \left\langle P_\|^{\mathrm{T}}\delta v_\| \right\rangle - \tau_\|^{\mathrm{T}}\delta v_\|^+ - \beta_\|^{\mathrm{T}}\delta v_\|^- + \left\langle \bar{\lambda}_\|\delta v_\| \right\rangle + \left\langle \bar{\lambda}_3\delta v_3 \right\rangle \end{aligned} \tag{39}$$

Driving it to be zero, the simplified Euler-Lagrange equations can be derived to be

$$v_3{}'C_t + \varphi' e_t = 0 \tag{40}$$

$$v_3{}'e_t - \varphi' d_t = -\theta_\parallel^{\mathrm{T}} p_s + \hat{\mathcal{P}} \tag{41}$$

$$C_s(v_\parallel{}' + e_\alpha w_{3,\alpha}^0) + e_s \phi_{,\parallel}^0 = D_\alpha \mathcal{E}_{,\alpha} + g + \bar{\lambda}_\parallel x_3 + \bar{\Lambda}_\parallel \tag{42}$$

where $\hat{\mathcal{P}}$ is a function independent from x_3, and

$$\begin{aligned} D_\alpha{}' &= -I_\alpha^{\mathrm{T}} \begin{bmatrix} C_e^* - \dfrac{e_{et}^*}{d_t^*}\mathcal{P}_\epsilon^{\mathrm{T}} & x_3 C_e^* - \dfrac{e_{et}^*}{d_t^*}\mathcal{P}_\kappa^{\mathrm{T}} \end{bmatrix} \\ g' &= I_\alpha^{\mathrm{T}} \left(T_{,\alpha} C_e^* \alpha_e - \frac{e_{et}^*}{d_t^*}\mathcal{P}_{\phi,\alpha} + T_{,\alpha} p_t^* \frac{e_{et}^*}{d_t^*} \right) - P_\parallel, \quad \theta_\parallel{}' = T_{,\parallel} \end{aligned} \tag{43}$$

Boundary terms generated by integration by parts about the x_α coordinates is not considered as the study aims at seeking an internal solution. As a result, integration by parts with respect to the in-plane coordinates can be freely adopted when convenient in the following derivation.

From equations (40), (41) and (42), it can be found that $v_\parallel$ is decoupled from v_3 and φ, so they can be solved separately. Solving equation (40) and (41) gives

$$v_3{}' = -(\theta_\parallel^{\mathrm{T}} p_s - \hat{\mathcal{P}}) \frac{e_t}{d_t^* C_t} \tag{44}$$

$$\varphi' = (\theta_\parallel^{\mathrm{T}} p_s - \hat{\mathcal{P}}) \frac{1}{d_t^*} \tag{45}$$

Warping functions $v_\parallel$ can be solved using equation (42) to be

$$v_\parallel = (\bar{D}_\alpha + L_\alpha)\mathcal{E}_{,\alpha} + \bar{g} \tag{46}$$

with

$$\bar{D}_\alpha' = C_s^{-1} D_\alpha^*, \quad \bar{g}' = C_s^{-1} g^* \tag{47}$$

and

$$D_\alpha^* = D_\alpha - C_s e_\alpha C_\perp - e_s e_\alpha C_\phi - \left(\frac{x_3}{h} + \frac{1}{2}\right) D_\alpha^+ + \left(\frac{x_3}{h} - \frac{1}{2}\right) D_\alpha^- \tag{48}$$

$$\begin{aligned} g^* = g - C_s e_\alpha w_{3e,\alpha}^0 - e_s e_\alpha \phi_{e,\alpha}^0 + \left(\frac{x_3}{h} + \frac{1}{2}\right) \tau_\parallel + \left(\frac{x_3}{h} - \frac{1}{2}\right) \beta_\parallel \\ - \left(\frac{x_3}{h} + \frac{1}{2}\right) g^+ + \left(\frac{x_3}{h} - \frac{1}{2}\right) g^- \end{aligned} \tag{49}$$

where L_α are constants generated by integral and will be used as optimization parameters later. In order to satisfy the constraints in equation (4), coefficients in equation (46) should have $\langle \bar{D}_\alpha \rangle = 0$, $\langle \bar{g} \rangle = 0$, and $L_\alpha \mathcal{E}_{,\alpha} = c_\parallel / h$.

Substituting the solution of $v_\parallel$, v_3 and φ back, the asymptotically correct expression of the total potential density Π_1 to the second-order is

$$2\Pi_1 = \mathcal{E}^{\mathrm{T}} A \mathcal{E} + \mathcal{E}_{,1}^{\mathrm{T}} B \mathcal{E}_{,1} + 2\mathcal{E}_{,1}^{\mathrm{T}} C \mathcal{E}_{,2} + \mathcal{E}_{,2}^{\mathrm{T}} D \mathcal{E}_{,2} - 2\mathcal{E}^{\mathrm{T}} F \tag{50}$$

where

$$A = \begin{bmatrix} A^* & B^* \\ B^{*\mathrm{T}} & D^* \end{bmatrix} \tag{51}$$

$$\begin{aligned} B = \big\langle & - D_1^{*\mathrm{T}} C_s^{-1} D_1^* + C_{s(11)} C_\perp^{\mathrm{T}} C_\perp + e_{s(11)} C_\perp^{\mathrm{T}} C_\phi \\ & + e_{s(11)} C_\phi^{\mathrm{T}} C_\perp - d_{s(11)} C_\phi^{\mathrm{T}} C_\phi \big\rangle + \big\langle {D_1'}^{\mathrm{T}} \big\rangle L_1 + L_1^{\mathrm{T}} \big\langle D_1' \big\rangle \end{aligned} \tag{52}$$

$$\begin{aligned} C = \big\langle & - D_1^{*\mathrm{T}} C_s^{-1} D_2^* + C_{s(12)} C_\perp^{\mathrm{T}} C_\perp + e_{s(12)} C_\perp^{\mathrm{T}} C_\phi \\ & + e_{s(12)} C_\phi^{\mathrm{T}} C_\perp - d_{s(12)} C_\phi^{\mathrm{T}} C_\phi \big\rangle + \big\langle {D_1'}^{\mathrm{T}} \big\rangle L_2 + L_1^{\mathrm{T}} \big\langle D_2' \big\rangle \end{aligned} \tag{53}$$

$$\begin{aligned} D = \big\langle & - D_2^{*\mathrm{T}} C_s^{-1} D_2^* + C_{s(22)} C_\perp^{\mathrm{T}} C_\perp + e_{s(22)} C_\perp^{\mathrm{T}} C_\phi \\ & + e_{s(22)} C_\phi^{\mathrm{T}} C_\perp - d_{s(22)} C_\phi^{\mathrm{T}} C_\phi \big\rangle + \big\langle {D_2'}^{\mathrm{T}} \big\rangle L_2 + L_2^{\mathrm{T}} \big\langle D_2' \big\rangle \end{aligned} \tag{54}$$

$$\begin{aligned} F = S_{\epsilon\kappa} + \Big\langle & - R_{\epsilon\kappa} - D_\alpha^{*\mathrm{T}} C_s^{-1} g_{,\alpha}^* + \big[p_{s(\alpha)} C_\phi^{\mathrm{T}} T \big]_{,\alpha} \\ & + \big[C_{s(\alpha\beta)} C_\perp^{\mathrm{T}} w_{3e}^0 + e_{s(\alpha\beta)} C_\perp^{\mathrm{T}} \phi_e^0 + e_{s(\alpha\beta)} C_\phi^{\mathrm{T}} w_{3e}^0 - d_{s(\alpha\beta)} C_\phi^{\mathrm{T}} \phi_e^0 \big]_{,\alpha\beta} \Big\rangle \\ & + \big\langle C_\perp^{\mathrm{T}} P_3 \big\rangle + C_\perp^{+\mathrm{T}} \tau_3 + C_\perp^{-\mathrm{T}} \beta_3 - L_\alpha^{\mathrm{T}} \Big(\tau_\parallel + \beta_\parallel - \big\langle g' \big\rangle \Big)_{,\alpha} \end{aligned} \tag{55}$$

with

$$S_{\epsilon\kappa} = \begin{Bmatrix} S_\epsilon \\ S_\kappa \end{Bmatrix}, \quad R_{\epsilon\kappa} = \begin{Bmatrix} \mathcal{P}_\epsilon \big(\theta_\parallel^{\mathrm{T}} p_s - \hat{\mathcal{P}} \big) / d_t^* \\ \mathcal{P}_\kappa \big(\theta_\parallel^{\mathrm{T}} p_s - \hat{\mathcal{P}} \big) / d_t^* \end{Bmatrix} \tag{56}$$

and $(\alpha\beta)$ in the subscript indicates the α, βth element in the corresponding matrix.

Transformation to the Reissner-Mindlin model

Though equation (50) is asymptotically correct to the second order, it is inconvenient for practical use because it contains derivatives of the 2D generalized strain, making the boundary conditions hard to define. For practical use, we can transform it into a model having the same form as the Reissner-Mindlin theory. To do so, two transverse shear strains need to be introduced along with another orthogonal triad $\mathbf{B}_i^*$ in the deformed plate to redefine the 2D generalized strains, so that

$$\mathbf{R}_{,\alpha} = \mathbf{B}_\alpha^* + \varepsilon_{\alpha\beta}^* \mathbf{B}_\beta^* + 2\gamma_{\alpha 3} \mathbf{B}_3^* \tag{57}$$

$$\mathbf{B}_{i,\alpha}^* = (-K_{\alpha\beta}^* \mathbf{B}_\beta^* \times \mathbf{B}_3^* + K_{\alpha 3}^* \mathbf{B}_3^*) \times \mathbf{B}_i^* \tag{58}$$

with the transverse shear strains as $\gamma = \begin{bmatrix} 2\gamma_{13} & 2\gamma_{23} \end{bmatrix}^{\mathrm{T}}$.

Kinematic identity can be found between the former 2D generalized strain $\mathcal{E}$ and Reissner-Mindlin 2D generalized strain $\mathcal{R}$ as

$$\mathcal{E} = \mathcal{R} - \mathcal{D}_\alpha \gamma_{,\alpha} \tag{59}$$

where

$$\mathcal{D}_1 = \begin{bmatrix} 0 & 0 & 0 & 1 & 0 & 0 \\ 0 & 0 & 0 & 0 & 1 & 0 \end{bmatrix}^{\mathrm{T}}, \quad \mathcal{D}_2 = \begin{bmatrix} 0 & 0 & 0 & 0 & 1 & 0 \\ 0 & 0 & 0 & 0 & 0 & 1 \end{bmatrix}^{\mathrm{T}} \tag{60}$$

$$\mathcal{R} = \begin{bmatrix} \varepsilon_{11}^* & 2\varepsilon_{12}^* & \varepsilon_{22}^* & K_{11}^* & K_{12}^* + K_{21}^* & K_{22}^* \end{bmatrix}^{\mathrm{T}} \tag{61}$$

Substituting equation (59) back into equation (50) and neglecting higher-order terms, it becomes

$$\begin{aligned} 2\Pi_1 = {} & \mathcal{R}^{\mathrm{T}} A \mathcal{R} - 2\mathcal{R}^{\mathrm{T}} A \mathcal{D}_1 \gamma_{,1} - 2\mathcal{R}^{\mathrm{T}} A \mathcal{D}_2 \gamma_{,2} \\ & + \mathcal{R}_{,1}^{\mathrm{T}} B \mathcal{R}_{,1} + 2\mathcal{R}_{,1}^{\mathrm{T}} C \mathcal{R}_{,2} + \mathcal{R}_{,2}^{\mathrm{T}} D \mathcal{R}_{,2} - 2\mathcal{R}^{\mathrm{T}} F \end{aligned} \tag{62}$$

Compared to the potential energy of the Reissner-Mindlin model, which has the form of

$$2\Pi_{\mathcal{R}} = \mathcal{R}^{\mathrm{T}} A \mathcal{R} + \gamma^{\mathrm{T}} G \gamma - 2\mathcal{R}^{\mathrm{T}} F_{\mathcal{R}} - 2\gamma^{\mathrm{T}} F_{\gamma} \tag{63}$$

further derivation is still required to completely eliminate terms with partial derivatives of the 2D generalized strains in equation (62). This can be achieved by utilizing the plate equilibrium equations about in-plane moments and transverse shear forces. Then equation (62) can be rewritten as

$$2\Pi_1 = \mathcal{R}^{\mathrm{T}} A \mathcal{R} + \gamma^{\mathrm{T}} G \gamma - 2\mathcal{R}^{\mathrm{T}} F - 2\gamma^{\mathrm{T}} F_{\gamma} + U^* \tag{64}$$

where

$$F_{\gamma} = -\mathcal{D}_{\alpha}^{\mathrm{T}} S_{\epsilon\kappa,\alpha}, \quad U^* = \mathcal{R}_{,1}^{\mathrm{T}} \bar{B} \mathcal{R}_{,1} + 2\mathcal{R}_{,1}^{\mathrm{T}} \bar{C} \mathcal{R}_{,2} + \mathcal{R}_{,2}^{\mathrm{T}} \bar{D} \mathcal{R}_{,2} \tag{65}$$

and

$$\begin{aligned} \bar{B} = B + A\mathcal{D}_1 G^{-1} {\mathcal{D}_1}^{\mathrm{T}} A, \quad \bar{C} = C + A\mathcal{D}_1 G^{-1} {\mathcal{D}_2}^{\mathrm{T}} A \\ \bar{D} = D + A\mathcal{D}_2 G^{-1} {\mathcal{D}_2}^{\mathrm{T}} A \end{aligned} \tag{66}$$

In the most ideal case, U^* can be driven to be zero for any $\mathcal{R}$ and transverse shear stiffness matrix can be solved exactly, leading the asymptotically correct total potential in equation (64) to have the same form as the Reissner-Mindlin model in equation (63). However, this is impossible for most multi-layered, piezoelectric composite plate, so an optimization process is required to minimize U^* and thus minimize the error between the asymptotically correct expression and the Reissner-Mindlin form expression. The accuracy of the Reissner-Mindlin-like model is influenced by the deviation of U^* from zero. Considering symmetry, there are totally 78 quantities in $\bar{B}$, $\bar{C}$ and $\bar{D}$ that are desirable to be zero, and there are 27 optimization parameters, 3 in G and 24 in L_{α}. To make U^* as close to zero as possible under any strain field, an overdetermined linear system with 78 equations and 27 unknowns is constructed, then the least square method is implemented to solve for the 27 unknowns.

By the optimization process, the best transverse shear stiffness matrix G can be obtained to complete the transformation to the Reissner-Mindlin-like model. Similar to the zeroth-order model, the current first-order model can be directly applied in any thermopiezoelastic Reissner-Mindlin plate analyses with equivalent stiffness matrices A, G, F and F_{γ} calculated from plate geometry and material constants. Piezoelectricity, thermal expansion and pyroelectricity are coupled in the stiffness matrices along with elasticity.

From equation (3), the 3D displacement field U_i can be easily recovered using 2D displacement field u_i and warping functions w_i, that is

$$U_i = u_i + x_3(\mathcal{C}_{3i} - \delta_{3i}) + w_j \mathcal{C}_{ji} \tag{67}$$

For the first-order approximation, the 3D strain field can be recovered to be

$$\Gamma_e^1 = \epsilon + x_3\kappa, \quad 2\Gamma_s^1 = {v_\parallel}' + e_\alpha w_{3,\alpha}^0, \quad \Gamma_t^1 = {w_3^0}' + {v_3}' \tag{68}$$

Then 3D stresses up to the first-order can be obtained. The first-order model can predict the transverse shear strains and stresses, but the transverse normal stress still vanishes. For predicting transverse normal stress, the warping functions should be perturbed once more to be

$$\begin{gathered} w_\parallel = w_\parallel^0 + v_\parallel^1 + y_\parallel + o\left(\frac{h^3}{l^2}\epsilon\right), \quad w_3 = w_3^0 + v_3^1 + y_3 + o\left(\frac{h^3}{l^2}\epsilon\right) \\ \phi = \phi^0 + \varphi^1 + \psi + o\left(\frac{h^3}{l^2}\epsilon\right) \end{gathered} \tag{69}$$

Using a similar procedure as the first-order reduction, the expression of the warping functions and electric potential can be obtained. That is

$$\begin{aligned} {y_\parallel}' = & -C_s^{-1}e_s e_\alpha \varphi_{,\alpha}^1 - C_s^{-1} I_\alpha^{\mathrm{T}} e_{et}^* \varphi_{,\alpha}^1 \\ & + \left(\frac{x_3}{h} + \frac{1}{2}\right) I_\alpha^{\mathrm{T}} e_{et}^* \varphi_{,\alpha}^{1+} - \left(\frac{x_3}{h} - \frac{1}{2}\right) I_\alpha^{\mathrm{T}} e_{et}^* \varphi_{,\alpha}^{1-} \end{aligned} \tag{70}$$

$$\begin{aligned} {y_3}' = & -\frac{C_{et}^{**\mathrm{T}}}{C_t}\left[I_\beta(\bar{D}_\alpha + L_\alpha)\mathcal{E}_{,\alpha\beta} + I_\beta \bar{g}_{,\beta}\right] + \frac{e_t}{d_t^* C_t}\left(E_{\phi\alpha\beta}\mathcal{E}_{,\alpha\beta} + S_\phi + \hat{\hat{\mathcal{P}}}\right) \\ & + \frac{d_t}{d_t^* C_t}\left[E_{\perp\alpha\beta}\mathcal{E}_{,\alpha\beta} + S_\perp + \left(\frac{x_3}{h} + \frac{1}{2}\right)\tau_3 + \left(\frac{x_3}{h} - \frac{1}{2}\right)\beta_3 \right. \\ & - \left(\frac{x_3}{h} + \frac{1}{2}\right) E_{\perp\alpha\beta}^+ \mathcal{E}_{,\alpha\beta} + \left(\frac{x_3}{h} - \frac{1}{2}\right) E_{\perp\alpha\beta}^- \mathcal{E}_{,\alpha\beta} \\ & \left. - \left(\frac{x_3}{h} + \frac{1}{2}\right) S_\perp^+ + \left(\frac{x_3}{h} - \frac{1}{2}\right) S_\perp^- \right] \end{aligned} \tag{71}$$

$$\begin{aligned} \psi' = & \frac{e_{et}^{*\mathrm{T}}}{d_t^*}\left[I_\beta(\bar{D}_\alpha + L_\alpha)\mathcal{E}_{,\alpha\beta} + I_\beta \bar{g}_{,\beta}\right] - \frac{1}{d_t^*}\left(E_{\phi\alpha\beta}\mathcal{E}_{,\alpha\beta} + S_\phi + \hat{\hat{\mathcal{P}}}\right) \\ & + \frac{e_t}{d_t^* C_t}\left[E_{\perp\alpha\beta}\mathcal{E}_{,\alpha\beta} + S_\perp + \left(\frac{x_3}{h} + \frac{1}{2}\right)\tau_3 + \left(\frac{x_3}{h} - \frac{1}{2}\right)\beta_3 \right. \\ & - \left(\frac{x_3}{h} + \frac{1}{2}\right) E_{\perp\alpha\beta}^+ \mathcal{E}_{,\alpha\beta} + \left(\frac{x_3}{h} - \frac{1}{2}\right) E_{\perp\alpha\beta}^- \mathcal{E}_{,\alpha\beta} \\ & \left. - \left(\frac{x_3}{h} + \frac{1}{2}\right) S_\perp^+ + \left(\frac{x_3}{h} - \frac{1}{2}\right) S_\perp^- \right] \end{aligned} \tag{72}$$

with

$${E_{\perp\alpha\beta}}' = -\left(e_\beta^{\mathrm{T}} D_\alpha^* + C_{s(\alpha\beta)} C_\perp + e_{s(\alpha\beta)} C_\phi\right) \tag{73}$$

$${S_\perp}' = -\left(e_\beta^{\mathrm{T}} g_{,\beta}^* + C_{s(\alpha\beta)} w_{3e,\alpha\beta}^0 + e_{s(\alpha\beta)} \phi_{e,\alpha\beta}^0 + P_3\right) \tag{74}$$

$${E_{\phi\alpha\beta}}' = -\left(e_\beta^{\mathrm{T}} e_s C_s^{-1} D_\alpha^* + e_{s(\alpha\beta)} C_\perp - d_{s(\alpha\beta)} C_\phi\right) \tag{75}$$

$${S_\phi}' = -\left(e_\beta^{\mathrm{T}} e_s C_s^{-1} g_{,\beta}^* + e_{s(\alpha\beta)} w_{3e,\alpha\beta}^0 - d_{s(\alpha\beta)} \phi_{e,\alpha\beta}^0\right) \tag{76}$$

and $\hat{\hat{\mathcal{P}}}$ is an arbitrary function of x_α.

Even though it is possible to derive the energy expression to the fourth-order with warping functions and electric potential presented above, it is unnecessary to do so because it is too complex for practical use. Consequently, 2D plate model derived from first-order reduction is still adopted, while the recovery considers the strains in second-order, that is

$$\begin{gathered}\Gamma_e^2 = \varepsilon + x_3\kappa + I_\alpha v_{\|,\alpha}^1, \quad 2\Gamma_s^2 = v_\|^{1\prime} + y_\|{}' + e_\alpha(w_{3,\alpha}^0 + v_{3,\alpha}^1) \\ \Gamma_t^2 = w_3^{0\prime} + v_3^{1\prime} + y_3{}'\end{gathered} \tag{77}$$

and the electric field to be

$$E_s^2 = -\phi_{,\|}^0 - \varphi_{,\|}^1, \quad E_t^2 = -\phi^{0\prime} - \varphi^{1\prime} - \psi' \tag{78}$$

3D stress field and electric displacement can be recovered based on equation (17).

NUMERICAL EXAMPLES

Four examples are provided to verify the present work. The plates in four examples have the same in-plane dimensions, 140 mm $\times$ 140 mm, with different layups, thicknesses, or boundary conditions. Origin of the coordinate system locates at the bottom left. Materials used in the examples are shown in Table I. Results are compared with 3D finite element analysis in ABAQUS.

In example 1, the plate has two layers. The bottom layer is a PVDF piezoelectric layer, with the thickness of 0.05 mm, and the upper layer is a polyimide layer, with the thickness of 0.1 mm. Since the aspect ratio of this plate is very large, using the zeroth-order model can have enough accuracy. The plate has a simply-supported boundary. Thermal load is 5 K in the whole plate. The bottom surface is charged with 300 V, and the interface between two layers is grounded. Result of transverse normal strain is shown in Figure 2, from which it is obvious that Γ_{33} is not zero. Though not shown here, other quantities also have excellent accuracy.

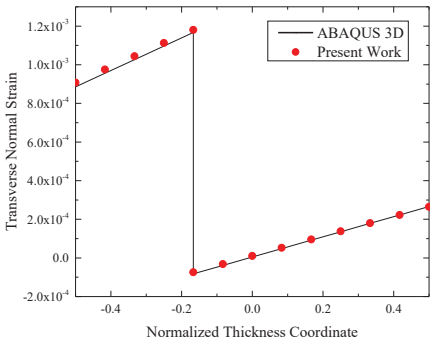

Figure 2: Distribution of transverse normal strain through thickness at the center.

In example 2, the plate consist of three layers. From the bottom to the top, the first layer is PZT-4, the second is S glass/epoxy orienting 90 degree, the third is

TABLE I: MATERIAL PROPERTIES OF THE PLATES

Properties	PVDF	Polyimide	PZT-4	S glass/epoxy
C_{11} (GPa)	3.61	3.85	139.02	48.5
C_{12} (GPa)	1.61	1.98	77.85	5.82
C_{13} (GPa)	1.42	1.98	74.33	5.82
C_{22} (GPa)	3.13	3.85	139.02	12.7
C_{23} (GPa)	1.31	1.98	74.33	6.7
C_{33} (GPa)	1.63	3.85	115.45	12.7
C_{44} (GPa)	0.55	0.93	25.6	3
C_{55} (GPa)	0.59	0.93	25.6	4.5
C_{66} (GPa)	0.69	0.93	30.6	4.5
e_{31} (C/m^2)	0.0105	0	-5.2	0
e_{32} (C/m^2)	-0.0117	0	-5.2	0
e_{33} (C/m^2)	-0.0284	0	15.08	0
$e_{24} = e_{15}$ (C/m^2)	-0.0122	0	12.72	0
d_{11} ($\times 10^{-9}$ C^2/(Nm^2))	0.0651	0.031	13.06	0.056
d_{22} ($\times 10^{-9}$ C^2/(Nm^2))	0.0821	0.031	13.06	0.056
d_{33} ($\times 10^{-9}$ C^2/(Nm^2))	0.0686	0.031	11.51	0.056
α_1 ($\times 10^{-6}$ K^{-1})	130	20	3.8	5
α_2 ($\times 10^{-6}$ K^{-1})	130	20	3.8	26
α_3 ($\times 10^{-6}$ K^{-1})	130	20	1.2	26
$p_1 = p_2$ ($\times 10^{-6}$ C/(Km^2))	30	0	0	0
p_3 ($\times 10^{-6}$ C/(Km^2))	30	0	-170	0

S glass/epoxy orienting 0 degree. Each layer has the thickness of 5 mm. As this plate is much thicker, the first-order model is adopted. Thermal load is 5 K in the whole plate. The bottom surface has a prescribed electric potential of 600 V, and the interface between the first and second layer is grounded. Representative results are shown in Figure 3 and 4. From Figure 3 it can be found that the present work can predict the quadratic distribution of transverse shear strain and stress through the thickness. From Figure 4, though relatively small, the transverse normal stress is not zero either.

In example 3, the plate is the same as the one in example 2, but with a fixed boundary condition. In addition to the thermal load and electric charge, a uniformly distributed load of 10 kPa is applied downwards on the top surface. The results are shown in Figure 5 and 6. It can be found that the accuracy of the model remains well with different boundary condition. From Figure 6 it can be seen that σ_{33} predicted by the theory can satisfy the boundary condition at the top surface.

In example 4, the plate has two PZT-4 layers with each on the top and bottom surfaces, and six S glass/epoxy layers between them, orienting $[90^\circ/0^\circ/45^\circ/-45^\circ/0^\circ/90^\circ]$. The boundary condition is simply-supported. Besides the loads in example 3, the top surface is also charged with 600 V, and interfaces between PZT-4 and contacting S glass/epoxy layers are grounded. Results are shown in Figure 7 and 8. We can see that the agreement remains well for more complex lamination.

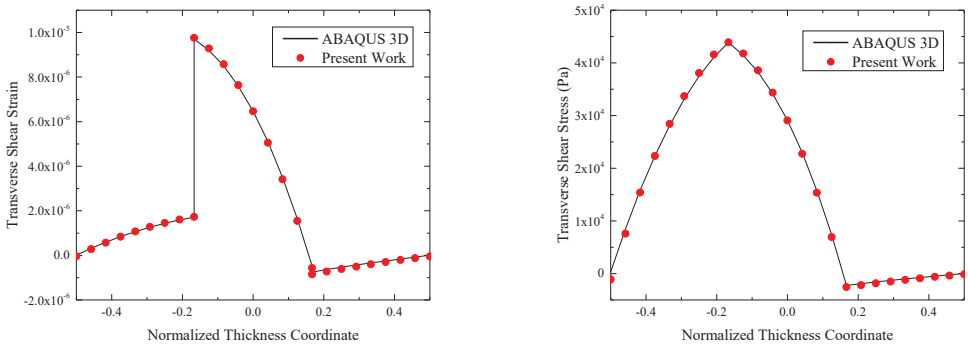

(a) Γ_{23} (b) σ_{23}

Figure 3: Distribution of transverse shear strain and stress through thickness at $x_1 = 0.07$ m, $x_2 = 0.105$.

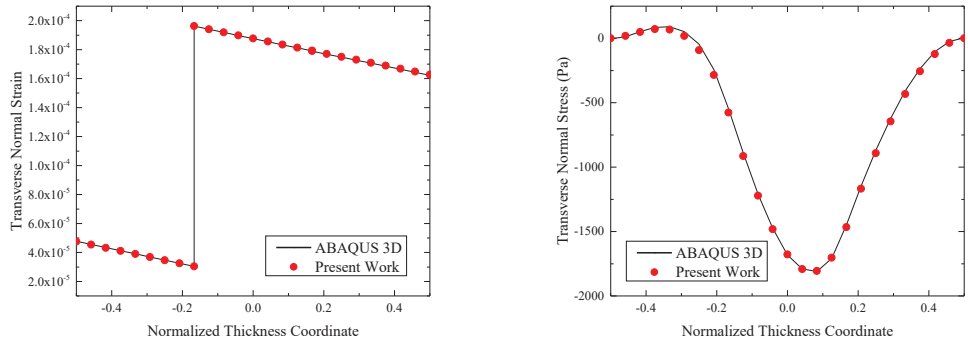

(a) Γ_{33} (b) σ_{33}

Figure 4: Distribution of transverse normal strain and stress through thickness at the center.

CONCLUSION

In this paper, a laminated anisotropic plate model with thermal expansion and piezoelectric effect is constructed based on the variational-asymptotic method. The main focus is on the interior constitutive model of the plate. For modelling, the original 3D plate problem is separated into a 1D through the thickness analysis and a 2D reference surface analysis. Recovery of 3D fields using 2D plate solution is also made possible in the model. Following accomplishments are achieved during the study:

1. In formulating the 3D strain field, warping functions are introduced to describe every possible shape in the deformed state. Then 3D strains containing 2D generalized strains and warping functions are obtained.

2. Beginning from the energy expression, the dimensional reduction is implemented by first dropping smaller terms. Then, variation of the energy is taken

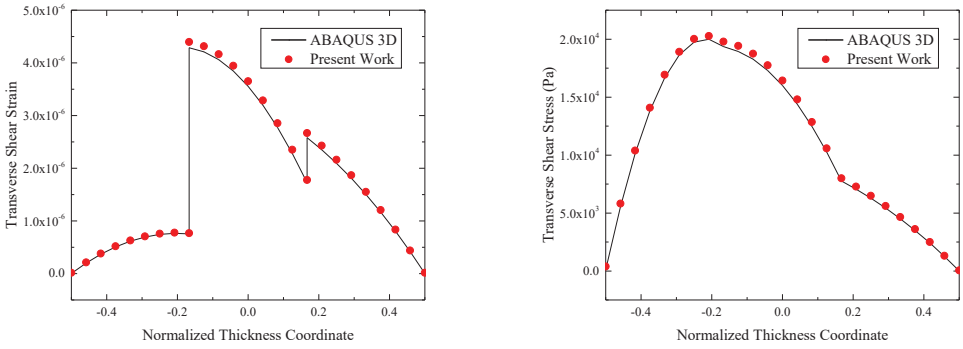

(a) Γ_{23} (b) σ_{23}

Figure 5: Distribution of transverse shear strain and stress through thickness at $x_1 = 0.07$ m, $x_2 = 0.105$.

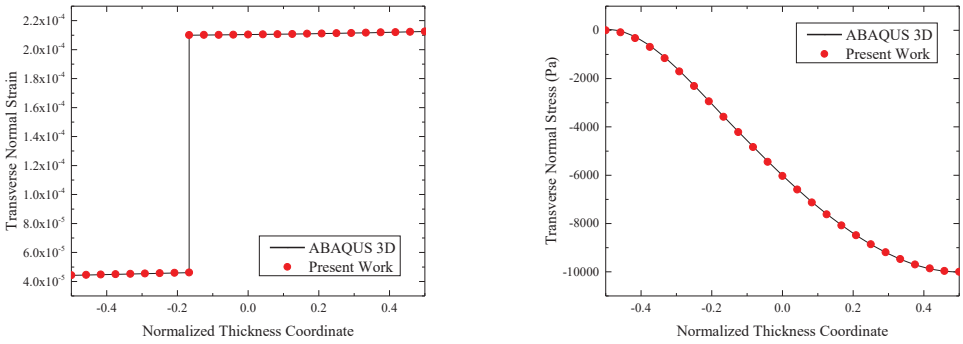

(a) Γ_{33} (b) σ_{33}

Figure 6: Distribution of transverse normal strain and stress through thickness at the center.

to solve for warping functions and electric potential, and construct equivalent constitutive relation. The warping functions are perturbed twice resulting a zeroth-order model resembling the CLT and a first-order model being transformed into the Reissner-Mindlin model.

3. Several numerical examples are studied for validating both the zeroth-order model and the first-order model. The zeroth-order model is proved to have high fidelity when analyzing thin plates. The first-order model can keep a good accuracy even though the aspect ratio of the plate goes smaller. Different laminations, boundary conditions and load combinations in the examples verify the robustness of the model.

It should be emphasized that the mathematical derivation of the present work follows a rigorous procedure that does not involves any ad hoc assumptions. Terms dropped in the current model are because of their smallness in order and will appear if the model is further derived into a higher order.

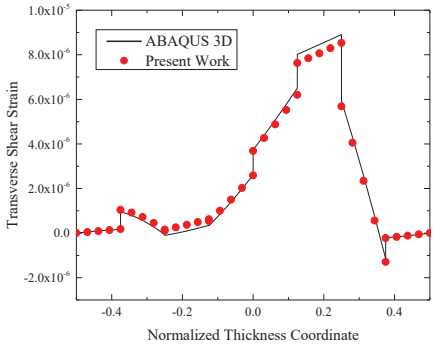

(a) Γ_{23}

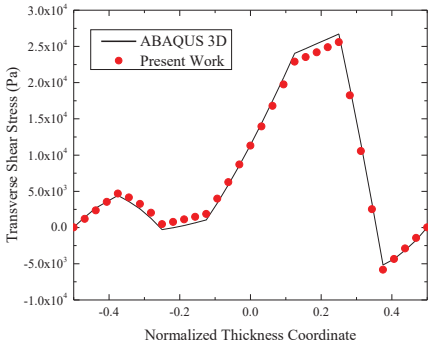

(b) σ_{23}

Figure 7: Distribution of transverse shear strain and stress through thickness at $x_1 = 0.07$ m, $x_2 = 0.105$.

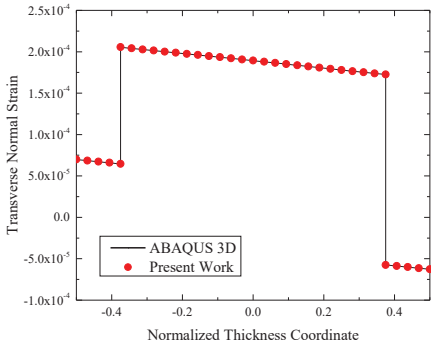

(a) Γ_{33}

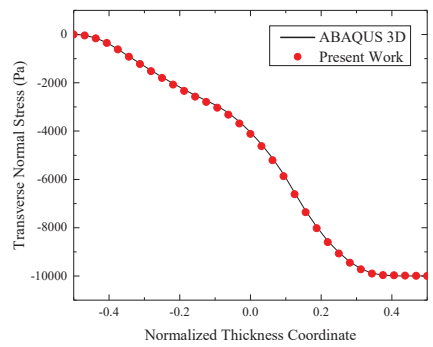

(b) σ_{33}

Figure 8: Distribution of transverse normal strain and stress through thickness at the center.

REFERENCES

1. Luo, Q. and L. Tong. 2006, "High precision shape control of plates using orthotropic piezoelectric actuators," *Finite Elements in Analysis and Design*, 42(11):1009–1020.

2. Chandrashekhara, K. and A. N. Agarwal. 1993, "Active vibration control of laminated composite plates using piezoelectric devices: a finite element approach," *Journal of Intelligent Material Systems and Structures*, 4(4):496–508.

3. Irschik, H. 2002, "A review on static and dynamic shape control of structures by piezoelectric actuation," *Engineering Structures*, 24(1):5–11.

4. Ray, M. C., K. M. Rao, and B. Samanta. 1992, "Exact analysis of coupled electroelastic behaviour of a piezoelectric plate under cylindrical bending," *Computers & Structures*, 45(4):667–677.

5. Lee, J. S. and L. Z. Jiang. 1996, "Exact electroelastic analysis of piezoelectric laminae via state space approach," *International Journal of Solids and Structures*, 33(7):977–990.

6. Zhong, Z. and E. T. Shang. 2003, "Three-dimensional exact analysis of a simply supported functionally gradient piezoelectric plate," *International Journal of Solids and Structures*, 40(20):5335–5352.

7. Xu, K., A. K. Noor, and Y. Y. Tang. 1995, "Three-dimensional solutions for coupled thermoelectroelastic response of multilayered plates," *Computer Methods in Applied Mechanics and Engineering*, 126(3):355–371.

8. Lee, C. K. 1990, "Theory of laminated piezoelectric plates for the design of distributed sensors/actuators. Part I: Governing equations and reciprocal relationships," *The Journal of the Acoustical Society of America*, 87(3):1144–1158.

9. Pai, P. F., A. H. Nayfeh, K. Oh, and D. T. Mook. 1993, "A refined nonlinear model of composite plates with integrated piezoelectric actuators and sensors," *International Journal of Solids and Structures*, 30(12):1603–1630.

10. Mitchell, J. A. and J. N. Reddy. 1995, "A refined hybrid plate theory for composite laminates with piezoelectric laminae," *International Journal of Solids and Structures*, 32(16):2345–2367.

11. Reddy, J. N. 1984, "A simple higher-order theory for laminated composite plates," *Journal of Applied Mechanics*, 51(4):745–752.

12. Wang, Q., S. T. Quek, C. T. Sun, and X. Liu. 2001, "Analysis of piezoelectric coupled circular plate," *Smart Materials and Structures*, 10(2):229.

13. Qu, Z. Q. 2001, "An efficient modelling method for laminated composite plates with piezoelectric sensors and actuators," *Smart Materials and Structures*, 10(4):807.

14. Figueiredo, I. M. N. and C. M. F. Leal. 2005, "A piezoelectric anisotropic plate model," *Asymptotic Analysis*, 44(3):327–346.

15. Kapuria, S. and G. G. S. Achary. 2006, "Nonlinear coupled zigzag theory for buckling of hybrid piezoelectric plates," *Composite Structures*, 74(3):253–264.

16. Kepler, R. G. and R. A. Anderson. 1978, "Piezoelectricity and pyroelectricity in polyvinylidene fluoride," *Journal of Applied Physics*, 49(8):4490–4494.

17. Tauchert, T. R. 1992, "Piezothermoelastic behavior of a laminated plate," *Journal of Thermal Stresses*, 15(1):25–37.

18. Krommer, M. and H. Irschik. 2000, "A Reissner-Mindlin-type plate theory including the direct piezoelectric and the pyroelectric effect," *Acta Mechanica*, 141(1-2):51–69.

19. Cho, M. and J. Oh. 2004, "Higher order zig-zag theory for fully coupled thermo-electric–mechanical smart composite plates," *International Journal of Solids and Structures*, 41(5):1331–1356.

20. Kapuria, S. and G. G. S. Achary. 2005, "A coupled consistent third-order theory for hybrid piezoelectric plates," *Composite Structures*, 70(1):120–133.

21. Oh, J., M. Cho, and J. S. Kim. 2007, "Enhanced lower-order shear deformation theory for fully coupled electro-thermo-mechanical smart laminated plates," *Smart Materials and Structures*, 16(6):2229.

22. Berdichevskii, V. L. 1979, "Variational-asymptotic method of constructing a theory of shells: PMM vol. 43, no. 4, 1979, pp. 664–687," *Journal of Applied Mathematics and Mechanics*, 43(4):711–736.

23. Atilgan, A. R. and D. H. Hodges. 1992, "On the strain energy of laminated composite plates," *International Journal of Solids and Structures*, 29(20):2527–2543.

24. Sutyrin, V. G. and D. H. Hodges. 1996, "On asymptotically correct linear laminated plate theory," *International Journal of Solids and Structures*, 33(25):3649–3671.

25. Sutyrin, V. G. 1997, "Derivation of plate theory accounting asymptotically correct shear deformation," *Journal of Applied Mechanics*, 64(4):905–915.

26. Yu, W. 2002, *Variational Asymptotic Modeling of Composite Dimensionally Reducible Structures*, Ph.D. thesis, Georgia Institute of Technology.

27. Yu, W., D. H. Hodges, and V. V. Volovoi. 2002, "Asymptotic construction of Reissner-like composite plate theory with accurate strain recovery," *International Journal of Solids and Structures*, 39(20):5185–5203.

28. Hodges, D. H., A. R. Atilgan, and D. A. Danielson. 1993, "A geometrically nonlinear theory of elastic plates," *Journal of Applied Mechanics*, 60(1):109–116.

29. Yu, W. and D. H. Hodges. 2004, "A simple thermopiezoelastic model for smart composite plates with accurate stress recovery," *Smart Materials and Structures*, 13(4):926.

30. Liao, L. and W. Yu. 2008, "Asymptotical construction of a fully coupled, Reissner–Mindlin model for piezoelectric composite plates," *Smart Materials and Structures*, 17(1):015010.

31. Liao, L. and W. Yu. 2009, "An electromechanical Reissner–Mindlin model for laminated piezoelectric plates," *Composite Structures*, 88(3):394–402.

32. Chen, H. and W. Yu. 2014, "A multiphysics model for magneto-electro-elastic laminates," *European Journal of Mechanics-A/Solids*, 47:23–44.

33. Danielson, D. A. 1991, "Finite rotation with small strain in beams and plates," in *Proceedings of the 2nd Pan American Congress of Applied Mechanics*, pp. 2–4.

34. Danielson, D. A. and D. H. Hodges. 1987, "Nonlinear beam kinematics by decomposition of the rotation tensor," *Journal of Applied Mechanics*, 54(2):258–262.

35. Reddy, J. N. 2004, *Mechanics of Laminated Composite Plates and Shells: Theory and Analysis*, CRC press.

36. Hodges, D. H. 1987, "Finite rotation and nonlinear beam kinematics," *Vertica*, 11(1/2):297–307.

Asymptotical modeling of thermopiezoelastic laminates

IOP Publishing Smart Materials and Structures
Smart Mater. Struct. 25 (2016) 015002 (13pp) doi:10.1088/0964-1726/25/1/015002

Asymptotical modeling of thermopiezoelastic laminates

Yufei Long[1] **and Wenbin Yu**[2]

School of Aeronautics and Astronautics, Purdue University, West Lafayette, Indiana 47907, USA

E-mail: wenbinyu@purdue.edu

Received 20 July 2015, revised 7 October 2015
Accepted for publication 21 October 2015
Published 17 November 2015

Abstract

A general anisotropic laminated plate model with thermal deformation and two-way coupled piezoelectric effect and pyroelectric effect is constructed using the variational asymptotic method. Total potential energy contains strain energy, electric potential energy and energy caused by temperature change and external loads. The feature of small thickness and large in-plane dimension of plate structures helps to asymptotically simplify the three-dimensional analysis to a two-dimensional analysis on the reference surface and a one-dimensional analysis through the thickness. Several numerical examples are studied. The present model is validated by the excellent agreement between the results from 3D finite element analyses and the present model.

Keywords: piezoelectric, plate, composite, variational asymptotic method

(Some figures may appear in colour only in the online journal)

1. Introduction

Modeling for plate structures bonded with piezoelectric materials is more and more popular in recent years because they can achieve active shape and vibration control [1–3]. The piezoelectric effect leads to a coupling between electric energy and mechanical energy, making the modeling more difficult than conventional plates. Besides, most piezoelectric materials also have pyroelectricity coupling the electric energy with thermal energy. Since thermal stress and strain affect the performance of laminates significantly, it is valuable to take the pyroelectric effect and thermal deformation into consideration when modeling multi-layered piezoelectric plates.

Although much effort has been applied to obtain exact 3D solutions for piezoelectric plates, they are still only available to limited cases [4–7]. As a result, modeling is still highly reliant on plate theories. However, most of the existing works are based on *ad hoc* assumptions for simplification, making stresses and strains in the structure unnecessarily restricted before any analyses can proceed. Lee [8] developed an isotropic laminated plate model based on Kirchhoff–Love assumptions. Chandrashekhara and Agarwal [2] modified his formulation to a Reissner–Mindlin model and used it for vibration control. Pai *et al* [9] proposed a refined geometrically nonlinear model for composite plates with piezoelectric sensors and actuators, but the piezoelectricity and mechanical forces are not fully coupled. Mitchell and Reddy [10] derived a composite laminated piezoelectric plate model including the energy from electrostatic charge, using a third-order shear deformation theory [11]. Wang *et al* [12] studied vibration of a piezoelectric circular plate using the Kirchhoff–Love plate model. Orthotropy of piezoelectric material is considered and electric and mechanical fields are fully coupled to ensure satisfaction of the Maxwell equation. Qu [13] derived finite element formulations for composite laminated plates with coupled direct and converse piezoelectric effects. Beginning from 3D formulations of a piezoelectric plate, Figueiredo and Leal [14] used asymptotic analysis to get a 2D piezoelectric model. By applying a hypothesis of zero elastic constants in the thickness direction, the model converges to the Kirchhoff–Love theory when the thickness goes to zero. Kapuria and Achary [15] used a modified zigzag theory along with von Karman geometric nonlinearity to analyze the buckling of piezoelectric plates.

Many researchers have also studied the effects of temperature load on piezoelectric plates. Since most piezoelectric

[1] Graduate research assistant, School of Aeronautics and Astronautics.
[2] Associate Professor, School of Aeronautics and Astronautics.

materials also display pyroelectric effects, thermal expansion would not be the only effect to be considered when temperature changes [16]. Tauchert [17] proposed an analysis on thermal deformation of a piezoelectric laminated plate based on Kirchhoff assumptions. Krommer and Irschik [18] derived a Reissner–Mindlin type piezoelectric plate under thermal load, focusing on the influence of the direct piezoelectric and pyroelectric effects on plate stiffness. Cho and Oh [19] constructed a fully coupled thermopiezoelastic composite plate model, in which temperature and electric field are treated as variables, using a higher-order zigzag theory. Kapuria and Achary [20] introduced another zigzag theory in third order that can achieve the consistency of no shear traction on the top and bottom surfaces. Oh *et al* [21] developed a lower-order shear deformation theory averaged from higher-order zigzag theory and applied it to modeling fully coupled electro-thermo-mechanical laminated plates.

Even though many results from plate models with *ad hoc* assumptions can provide acceptable accuracy, those assumptions are avoidable and can make the models predict wrong results when these assumptions are violated. In contrast, the variational-asymptotic method (VAM), developed by Berdichevsky [22], is a mathematical approach capable of analyzing functionals with relatively small parameters. By using the VAM, taking advantage of small values of h/l in plate structures, where h is the thickness and l indicates the characteristic in-plane dimension, a model with the desired accuracy can be derived without *a priori* assumptions.

Early application of the VAM on composite plate modeling includes the work by Atilgan and Hodges [23]. Their work is extended by Sutyrin and Hodges [24, 25] to allow more accurate recovery of stresses for multi-layered composite plates by transforming the formula to a Reissner–Mindlin-like model. Yu *et al* [26, 27] developed a general composite laminated plate model based on the geometrically nonlinear theory in [28]. Using a finite element approach, Yu and Hodges extended their previous work for applying to a thermopiezoelastic composite plate [29], but the electric and temperature fields are only coupled one way with the mechanical field. Liao and Yu [30, 31] developed the model to accommodate a fully coupled piezoelectric composite plate. Recently, Chen and Yu [32] further induced a magnetic field in the composite laminate model.

The purpose of this paper is to derive a model for multi-layered surface and interface electroded piezoelectric plates under thermal loads. With the aid of decomposition of the rotation tensor [33] and warping functions, 3D strains can be expressed in terms of 2D generalized strains. The energy expression of the plate contains potential energy, kinetic energy and virtual work from external loads. Since the main purpose is to study the deformation of plates, the converse effect of pyroelectricity is not included to avoid the heat conduction problem. The 3D model is then reduced to a 2D formulation by applying the VAM. The reduced 2D plate model can be solved in the same way as classical or Reissner–Mindlin plate theory. 3D displacement, stress, strain, electric potential, electric field and electric displacement can be recovered based on the global response obtained from the plate analysis.

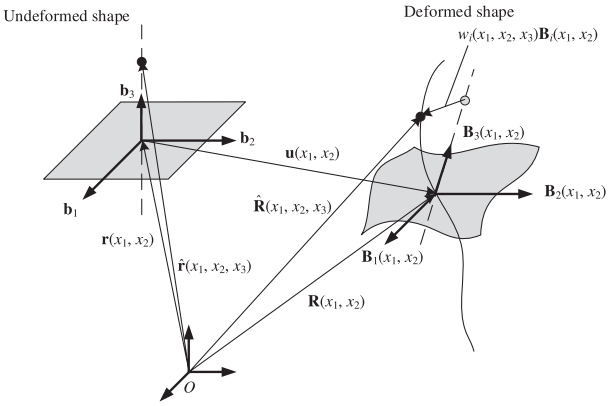

Figure 1. Schematic of plate deformation.

2. Three-dimensional formulation

2.1. Plate kinematics

The position of a point in a plate can be determined by its Cartesian coordinates x_i, as shown in figure 1, where x_α are two orthogonal coordinates in the reference surface and x_3 is the normal coordinate with the origin located at the middle of the thickness. Greek letter indices refer to 1 and 2 while Latin letter indices refer to 1, 2 and 3 hereafter. The orthogonal triad $\mathbf{b}_i$ denotes the unit vectors in x_i directions of the undeformed plate, so any material point in the undeformed plate can have a position vector $\hat{\mathbf{r}}$ from a fixed point O so that

$$\hat{\mathbf{r}}(x_1, x_2, x_3) = \mathbf{r}(x_1, x_2) + x_3\mathbf{b}_3, \tag{1}$$

where $\mathbf{r}$ denotes the position vector of the intersection point of the reference surface and the normal line on which the described point is located. Integrating both sides of equation (1), we have

$$\langle \hat{\mathbf{r}}(x_1, x_2, x_3) \rangle = h\mathbf{r}(x_1, x_2), \tag{2}$$

where h is the thickness of the plate, and angle brackets indicate the definite integral in the x_3 direction from the bottom to the top of the plate.

When deformation happens, the material point described by vector $\hat{\mathbf{r}}$ in the undeformed state will have the position vector $\hat{\mathbf{R}}$ in the deformed state. For clarity, the orthogonal unit vector triad for the deformed plate $\mathbf{B}_i$ is introduced. The relation between $\mathbf{b}_i$ and $\mathbf{B}_i$ is indicated in a similar way as the coordinate transformation using the direction cosine matrix $\mathcal{C}_{ij}(x_1, x_2)$

$$\mathbf{B}_i = \mathcal{C}_{ij}\mathbf{b}_j, \quad \mathcal{C}_{ij} = \mathbf{B}_i \cdot \mathbf{b}_j. \tag{3}$$

Now $\hat{\mathbf{R}}$ can be expanded to the following form for any definition of $\mathbf{B}_i$:

$$\hat{\mathbf{R}}(x_1, x_2, x_3) = \mathbf{R}(x_1, x_2) + x_3\mathbf{B}_3(x_1, x_2) + w_i(x_1, x_2, x_3)\mathbf{B}_i(x_1, x_2), \tag{4}$$

where w_i are warping functions to ensure equation (4) is able to describe all possible deformations. No assumption is made

on the shape of warping functions and their exact expression will be solved later. In order to uniquely determine $\mathbf{B}_i$, six constraints are introduced. The first three constraints are set in the way of

$$\left\langle w_{\|}(x_1, x_2, x_3)\right\rangle = c_{\|}, \quad \langle w_3(x_1, x_2, x_3)\rangle = 0, \tag{5}$$

where $(\,)_{\|} = [(\,)_1 \quad (\,)_2]^{\mathrm{T}}$ and $c_{\|}$ contain three free variables independent of x_3.

Two more constraints can be specified by setting $\mathbf{B}_3$ normal to the reference surface of the deformed plate. Here transverse shear and thickness change are still allowed because of the warping functions, which differentiate the present work from those based on hypotheses. It is still possible for $\mathbf{B}_\alpha$ to rotate around $\mathbf{B}_3$, so we introduce

$$\mathbf{B}_1 \cdot \mathbf{R}_{,2} = \mathbf{B}_2 \cdot \mathbf{R}_{,1} \tag{6}$$

to be the last constraint.

Terms in the deformation gradient tensor are defined as

$$F_{ij} = \mathbf{B}_i \cdot \mathbf{G}_k \mathbf{g}^k \cdot \mathbf{b}_j, \tag{7}$$

where $\mathbf{G}_i$ are the covariant base vectors in the deformed state and $\mathbf{G}_i = \frac{\partial \hat{\mathbf{R}}}{\partial x_i}$, $\mathbf{g}^i$ are the contravariant base vectors in the undeformed state and for plates, $\mathbf{g}^i = \mathbf{b}_i$. Then the 3D strain field can be derived from decomposition of the rotation tensor [34]

$$\Gamma_{ij} = \frac{1}{2}\left(F_{ij} + F_{ji}\right) - \delta_{ij}, \tag{8}$$

where δ_{ij} is the Kronecker symbol.

For expressing the 3D strain field in terms of 2D strains, one can define 2D generalized strains in the same way as [28]

$$\mathbf{R}_{,\alpha} = \mathbf{B}_\alpha + \varepsilon_{\alpha\beta}\mathbf{B}_\beta, \tag{9}$$

$$\mathbf{B}_{i,\alpha} = \left(-K_{\alpha\beta}\mathbf{B}_\beta \times \mathbf{B}_3 + K_{\alpha 3}\mathbf{B}_3\right) \times \mathbf{B}_i, \tag{10}$$

where $\varepsilon_{\alpha\beta}$ and $K_{\alpha\beta}$ are 2D generalized membrane strains and curvatures, and a comma in the subscript implies partial derivative. Strains are assumed to be small compared to unity and warping functions are of similar magnitude to strain when only geometric nonlinearity is considered. Now one can derive the 3D strain field expression to be

$$\Gamma_e = \epsilon + x_3\kappa + I_\alpha w_{\|,\alpha}, \quad 2\Gamma_s = w_{\|}' + e_\alpha w_{3,\alpha}, \quad \Gamma_t = w_3', \tag{11}$$

where $(\,)'$ implies partial derivative with respect to x_3 and

$$\Gamma_e = \left[\Gamma_{11} \quad 2\Gamma_{12} \quad \Gamma_{22}\right]^{\mathrm{T}}, \quad 2\Gamma_s = \left[2\Gamma_{13} \quad 2\Gamma_{23}\right]^{\mathrm{T}}, \quad \Gamma_t = \Gamma_{33} \tag{12}$$

and

$$\epsilon = \left[\varepsilon_{11} \quad 2\varepsilon_{12} \quad \varepsilon_{22}\right]^{\mathrm{T}}, \quad \kappa = \left[K_{11} \quad K_{12} + K_{21} \quad K_{22}\right]^{\mathrm{T}} \tag{13}$$

and

$$I_1 = \begin{bmatrix} 1 & 0 \\ 0 & 1 \\ 0 & 0 \end{bmatrix}, \quad I_2 = \begin{bmatrix} 0 & 0 \\ 1 & 0 \\ 0 & 1 \end{bmatrix}, \quad e_1 = \begin{Bmatrix} 1 \\ 0 \end{Bmatrix}, \quad e_2 = \begin{Bmatrix} 0 \\ 1 \end{Bmatrix} \tag{14}$$

So far kinematics of a plate is formulated. However, for coupled piezoelectric laminated plates, the electric field should also be taken into account along with the mechanical field. The electric field can be defined using the electric potential $\phi(x_1, x_2, x_3)$

$$E_s = \left[E_1 \quad E_2\right]^{\mathrm{T}} = -\left[\phi_{,1} \quad \phi_{,2}\right]^{\mathrm{T}}, \quad E_t = E_3 = -\phi'. \tag{15}$$

In this study the electrodes of the piezoelectric plate are coated on the top and bottom surfaces or interfaces between layers. The electrodes are assumed to be of negligible thickness and have no influence on the mechanical properties of the plate. Then the electric potential can be specified at $x_3 = h_i$, where h_i refers to the position of surface or interface and where i indicates the numbering of layers varying from 1 to $k + 1$ and k is the total number of layers. Although temperature load is considered in the work, it is only one-way coupling so temperature change $T(x_1, x_2, x_3)$ is treated as a known function.

2.2. Energy formulation

The elastodynamic behavior of a piezoelectric laminated plate is governed by the extended Hamilton's principle [35]

$$\int_{t_1}^{t_2} \left[\delta(\mathcal{K} - \mathcal{U}) + \overline{\delta\mathcal{W}}\right]\mathrm{d}t = 0, \tag{16}$$

where t_1 and t_2 are arbitrary fixed times; $\mathcal{K}$ is the kinetic energy; $\mathcal{U}$ is the internal potential energy related to strain, electric field and temperature; $\overline{\delta\mathcal{W}}$ is the virtual work of external loads. Kinetic energy can be neglected in static problems, so it is not discussed here, even though the theory developed here is also applicable to dynamic problems of plate structures vibrating at low frequencies.

For piezoelectric structures with thermal loads, the internal potential energy $\mathcal{U}$ can be expressed as the integral of the area potential energy density

$$\mathcal{U} = \int_\Omega \mathcal{H}\mathrm{d}\Omega, \tag{17}$$

where Ω is the area domain of the reference surface and

$$\begin{aligned}\mathcal{H} = \frac{1}{2}&\left\langle \begin{Bmatrix} \Gamma_e \\ 2\Gamma_s \\ \Gamma_t \end{Bmatrix}^{\mathrm{T}} \begin{bmatrix} C_e & C_{es} & C_{et} \\ C_{es}^{\mathrm{T}} & C_s & C_{st} \\ C_{et}^{\mathrm{T}} & C_{st}^{\mathrm{T}} & C_t \end{bmatrix} \begin{Bmatrix} \Gamma_e \\ 2\Gamma_s \\ \Gamma_t \end{Bmatrix} \right\rangle \\ &- \left\langle \begin{Bmatrix} \Gamma_e \\ 2\Gamma_s \\ \Gamma_t \end{Bmatrix}^{\mathrm{T}} \begin{bmatrix} e_b & e_{et} \\ e_s & e_a \\ e_c & e_t \end{bmatrix} \begin{Bmatrix} E_s \\ E_t \end{Bmatrix} \right\rangle \\ &- \left\langle \begin{Bmatrix} \Gamma_e \\ 2\Gamma_s \\ \Gamma_t \end{Bmatrix}^{\mathrm{T}} \begin{bmatrix} C_e & C_{es} & C_{et} \\ C_{es}^{\mathrm{T}} & C_s & C_{st} \\ C_{et}^{\mathrm{T}} & C_{st}^{\mathrm{T}} & C_t \end{bmatrix} \begin{Bmatrix} \alpha_e \\ \alpha_s \\ a_t \end{Bmatrix} T \right\rangle \\ &- \frac{1}{2}\left\langle \begin{Bmatrix} E_s \\ E_t \end{Bmatrix}^{\mathrm{T}} \begin{bmatrix} d_s & d_{et} \\ d_{et}^{\mathrm{T}} & d_t \end{bmatrix} \begin{Bmatrix} E_s \\ E_t \end{Bmatrix} \right\rangle \\ &- \left\langle \begin{Bmatrix} E_s \\ E_t \end{Bmatrix}^{\mathrm{T}} \begin{Bmatrix} p_s \\ p_t \end{Bmatrix} T \right\rangle, \end{aligned} \tag{18}$$

where C_e, C_{es}, C_{et}, C_s, C_{st} and C_t are the submatrices of the partitioned 6×6 material's elastic constant matrix; e_b, e_{et}, e_s, e_a, e_c and e_t are the submatrices of the partitioned transpose of the 3×6 piezoelectric stress coefficient matrix; α_e, α_s and α_t are the submatrices of the partitioned 6×1 thermal expansion coefficient matrix; d_s, d_{et} and d_t are the submatrices of the partitioned 3×3 dielectric constant matrix; p_s and p_t are the submatrices of the partitioned 3×1 pyroelectric coefficient matrix.

The virtual work in the plate due to the applied loads can be calculated as

$$\overline{\delta \mathcal{W}} = \overline{\delta \mathcal{W}}_{2\mathrm{D}} + \overline{\delta \mathcal{W}}^*, \tag{19}$$

where

$$\overline{\delta \mathcal{W}}_{2\mathrm{D}} = \int_\Omega \left(f_i \overline{\delta q}_i + m_\alpha \overline{\delta \psi}_\alpha\right) \mathrm{d}\Omega + \int_s \left(\langle Q_i \rangle \overline{\delta q}_i + \langle x_3 Q_\alpha \rangle \overline{\delta \psi}_\alpha \right) \mathrm{d}s, \tag{20}$$

$$\overline{\delta \mathcal{W}}^* = \int_\Omega \left(\langle P_i \delta w_i \rangle + \tau_i \delta w_i^+ + \beta_i \delta w_i^- \right) \mathrm{d}\Omega + \int_s \langle Q_i \delta w_i \rangle \, \mathrm{d}s \tag{21}$$

and s is the boundary of the reference surface; P_i is the applied body force; τ_i is the applied traction on the top surface and β_i is the applied traction on the bottom surface; Q_i are the applied tractions on the lateral boundary surfaces. The $+$ and $-$ signs in superscripts denote the value at the top and bottom surface respectively. The virtual displacement and rotation can be defined in a similar way as the definition of 2D general strains, so that

$$\delta \mathbf{R} = \overline{\delta q}_i \mathbf{B}_i, \quad \delta \mathbf{B}_i = \left(-\overline{\delta \psi}_2 \mathbf{B}_1 + \overline{\delta \psi}_1 \mathbf{B}_2 + \overline{\delta \psi}_3 \mathbf{B}_3 \right) \times \mathbf{B}_i, \tag{22}$$

where $\overline{\delta q}_i$ and $\overline{\delta \psi}_i$ are the virtual displacement and rotation components in the $\mathbf{B}_i$ bases respectively. Generalized forces and moments f_i and m_α are defined as

$$f_i = \langle P_i \rangle + \tau_i + \beta_i, \quad m_\alpha = \langle x_3 P_\alpha \rangle + \frac{h}{2}(\tau_\alpha - \beta_\alpha). \tag{23}$$

In this study, the goal is to obtain a constitutive relation of the interior part of the plate, so the second term in equation (21) can be safely neglected as it represents the edge effects.

Up to this point, the 3D continuum model of the thermopiezoelastic plate is ready to be reduced to a 2D plate model by a through-the-thickness analysis using the VAM.

3. Dimensional reduction

Before using the VAM, it is necessary to recognize the order of terms in the expression. Based on the definition of a plate structure, the ratio of thickness over the characteristic in-plane dimension of the reference surface is much smaller than one, that is, $h/l \ll 1$. As only geometric nonlinearity is considered, strains are assumed to be small, that is, $\Gamma_{ij} \sim \varepsilon_{\alpha\beta} \sim hK_{\alpha\beta} \sim \epsilon \ll 1$, so ϵ can represent the order of all strains. Because of the equilibrium condition for plate structures, the orders of external loads can be determined to be

$$\begin{aligned} &hP_\alpha \sim \tau_\alpha \sim \beta_\alpha \sim \mu \frac{h}{l}\epsilon, \quad Q_\alpha \sim \mu\epsilon \\ &hP_3 \sim \tau_3 \sim \beta_3 \sim \mu \left(\frac{h}{l}\right)^2 \epsilon, \\ &Q_3 \sim \mu \frac{h}{l}\epsilon, \end{aligned} \tag{24}$$

where material constants have the order of μ.

3.1. Zeroth-order reduction

In the zeroth-order reduction, the energy is expanded into the order of $(hl^2)\mu\epsilon^2$. Because of the order of external loads, warping functions w_i and electric potential ϕ only appear in the area potential energy density, so it is more convenient to directly work on $\mathcal{H}_0$. The variation of $\mathcal{H}_0$ can be calculated to be

$$\begin{aligned} \delta \mathcal{H}_0 = \Big\langle & \Big[(\varepsilon + x_3\kappa)^{\mathrm{T}} C_{es} + w_\parallel'^{\mathrm{T}} C_s + w_3' C_{st}^{\mathrm{T}} + \phi' e_a^{\mathrm{T}} \\ & - \left(\alpha_e^{\mathrm{T}} C_{es} + \alpha_s^{\mathrm{T}} C_s + \alpha_t C_{st}^{\mathrm{T}}\right) T \Big] \delta w_\parallel' + \lambda_\parallel \delta w_\parallel \\ & + \Big[(\varepsilon + x_3\kappa)^{\mathrm{T}} C_{et} + w_\parallel'^{\mathrm{T}} C_{st} + w_3' C_t + \phi' e_t \\ & - \left(\alpha_e^{\mathrm{T}} C_{et} + \alpha_s^{\mathrm{T}} C_{st} + \alpha_t C_t\right) T \Big] \delta w_3' + \lambda_3 \delta w_3 \\ & + \Big[(\varepsilon + x_3\kappa)^{\mathrm{T}} e_{et} + w_\parallel'^{\mathrm{T}} e_a + w_3' e_t - \phi' d_t + p_t T \Big] \delta \phi' \Big\rangle, \end{aligned} \tag{25}$$

where $\lambda_\parallel$ and λ_3 are Lagrange multipliers for introducing the constraints in equation (5). Warping functions w_i are free to vary at the top and bottom surfaces but electric potential is free to vary only when it is not prescribed at those locations. The Euler–Lagrange equations of equation (25) can be written as

$$\begin{aligned} & (\epsilon + x_3\kappa)^{\mathrm{T}} C_{es} + w_\parallel'^{\mathrm{T}} C_s + w_3' C_{st}^{\mathrm{T}} + \phi' e_a^{\mathrm{T}} \\ & \quad - \left(\alpha_e^{\mathrm{T}} C_{es} + \alpha_s^{\mathrm{T}} C_s + \alpha_t C_{st}^{\mathrm{T}}\right) T = 0, \end{aligned} \tag{26}$$

$$\begin{aligned} & (\epsilon + x_3\kappa)^{\mathrm{T}} C_{et} + w_\parallel'^{\mathrm{T}} C_{st} + w_3' C_t + \phi' e_t \\ & \quad - \left(\alpha_e^{\mathrm{T}} C_{et} + \alpha_s^{\mathrm{T}} C_{st} + \alpha_t C_t\right) T = 0, \end{aligned} \tag{27}$$

$$(\epsilon + x_3\kappa)^{\mathrm{T}} e_{et} + w_\parallel'^{\mathrm{T}} e_a + w_3' e_t - \phi' d_t + p_t T = \mathcal{P}, \tag{28}$$

where $\mathcal{P}$ is an arbitrary function independent of x_3 generated by indefinite integration. Expressions of the warping function and electric potential for each layer can be solved from equations (26)–(28), giving

$$\begin{aligned} w_\parallel'^{\mathrm{T}} = & -\left(\epsilon + x_3\kappa - \alpha_e T\right)^{\mathrm{T}} C_{es}^{**} C_s^{-1} \\ & + \mathcal{P} \frac{e_a^{*\mathrm{T}} C_s^{-1}}{d_t^*} - p_t^* T \frac{e_a^{*\mathrm{T}} C_s^{-1}}{d_t^*} + \alpha_s^{\mathrm{T}} T, \end{aligned} \tag{29}$$

$$\begin{aligned} w_3' = & -\left(\epsilon + x_3\kappa - \alpha_e T\right)^{\mathrm{T}} C_{et}^{**} C_t^{*-1} \\ & + \mathcal{P} \frac{e_t^* C_t^{*-1}}{d_t^*} - p_t^* T \frac{e_t^* C_t^{*-1}}{d_t^*} + \alpha_t T, \end{aligned} \tag{30}$$

$$\phi' = \left(\epsilon + x_3\kappa - \alpha_e T\right)^{\mathrm{T}} \frac{e_{et}^*}{d_t^*} - \mathcal{P}\frac{1}{d_t^*} + p_t^* T \frac{1}{d_t^*}, \tag{31}$$

where the starred quantities are introduced for simplifying the expression, and

$$C_{et}^* = C_{et} - C_{es}C_s^{-1}C_{st}, \qquad C_t^* = C_t - C_{st}^{\mathrm{T}}C_s^{-1}C_{st}$$
$$C_{es}^* = C_{es} - \frac{C_{et}^* C_{st}^{\mathrm{T}}}{C_t^*}, \qquad C_{et}^{**} = C_{et}^* + \frac{e_{et}^* e_t^*}{d_t^*}$$
$$C_{es}^{**} = C_{es}^* + \frac{e_{et}^* e_a^{*\mathrm{T}}}{d_t^*},$$
$$e_t^* = e_t - e_a^{\mathrm{T}} C_s^{-1} C_{st}$$
$$e_a^* = e_a - \frac{C_{st} e_t^*}{C_t^*},$$
$$e_{et}^* = e_{et} - C_{es}^* C_s^{-1} e_a - \frac{C_{et}^* e_t}{C_t^*}$$
$$d_t^* = d_t + e_a^{*\mathrm{T}} C_s^{-1} e_a + \frac{e_t^* e_t}{C_t^*},$$
$$p_t^* = p_t + \alpha_e^{\mathrm{T}} e_{et} + \alpha_s^{\mathrm{T}} e_a + \alpha_t e_t.$$

It is impossible to determine the expression of $\mathcal{P}$ without knowing the electric boundary condition, but a general form of function $\mathcal{P}$ can be written as

$$\mathcal{P} = \epsilon^{\mathrm{T}}\mathcal{P}_\epsilon + \kappa^{\mathrm{T}}\mathcal{P}_\kappa + \mathcal{P}_\phi. \tag{33}$$

Substituting equations (29)–(31) into $\mathcal{H}_0$, the zeroth-order asymptotically correct expression of the potential energy density can be obtained as

$$2\mathcal{H}_0 = \begin{Bmatrix} \epsilon \\ \kappa \end{Bmatrix}^{\mathrm{T}} \begin{bmatrix} A^* & B^* \\ B^{*\mathrm{T}} & D^* \end{bmatrix} \begin{Bmatrix} \epsilon \\ \kappa \end{Bmatrix} - 2 \begin{Bmatrix} S_\epsilon \\ S_\kappa \end{Bmatrix}^{\mathrm{T}} \begin{Bmatrix} \epsilon \\ \kappa \end{Bmatrix} \tag{34}$$

with

$$A^* = \left\langle C_e^* - \frac{\mathcal{P}_\epsilon \mathcal{P}_\epsilon^{\mathrm{T}}}{d_t^*} \right\rangle, \qquad B^* = \left\langle x_3 C_e^* - \frac{\mathcal{P}_\epsilon \mathcal{P}_\kappa^{\mathrm{T}}}{d_t^*} \right\rangle$$
$$D^* = \left\langle x_3^2 C_e^* - \frac{\mathcal{P}_\kappa \mathcal{P}_\kappa^{\mathrm{T}}}{d_t^*} \right\rangle$$

and

$$S_\epsilon = \left\langle \frac{\mathcal{P}_\epsilon \mathcal{P}_\phi^{\mathrm{T}}}{d_t^*} + T\left[C_e^* \alpha_e - \frac{e_{et}^*}{d_t^*} p_t^* \right] \right\rangle$$
$$S_\kappa = \left\langle \frac{\mathcal{P}_\kappa \mathcal{P}_\phi^{\mathrm{T}}}{d_t^*} + T\left[x_3 C_e^* \alpha_e - x_3 \frac{e_{et}^*}{d_t^*} p_t^* \right] \right\rangle, \tag{36}$$

where

$$C_e^* = C_e - C_{es}^* C_s^{-1} C_{es}^{\mathrm{T}} - \frac{C_{et}^* C_{et}^{\mathrm{T}}}{C_t^*} + \frac{e_{et}^* e_{et}^{*\mathrm{T}}}{d_t^*}. \tag{37}$$

Terms not relating to 2D generalized strains are all dropped because they will not affect the total energy when the plate is deformed. It can be found from equation (35) that the stiffness matrices A^*, B^* and D^* not only depend on material elastic constants, but also piezoelectric coefficients and dielectric constants. Temperature change and applied electric field can affect the values of S_ϵ and S_κ, which provide additional contributions to the total potential energy.

Up to this point, the original 3D problem has been reduced to a 2D plate problem. It is obvious that even though the plate is a piezoelectric smart plate, the 2D energetics has the same form as the classical lamination theory (CLT) with thermal load except that the temperature related term is extended to contain the piezoelectric effect.

The stiffness matrices in equation (34) can be used in a plate analysis for prediction of global plate behavior. However, in many cases it is also valuable to acquire the 3D quantities of the plate structure. In such situations, 3D fields are required to be recovered via the 2D results. For the zeroth-order approximation, the 3D strain field and electric field can be recovered by neglecting terms with derivatives with respect to x_α in equations (11) and (15), obtaining

$$\Gamma_e^0 = \epsilon + x_3\kappa, \quad 2\Gamma_s^0 = w_\parallel', \quad \Gamma_t^0 = w_3', \tag{38}$$

$$E_s^0 = 0, \quad E_t^0 = -\phi'. \tag{39}$$

The 3D stress field and electric displacement field can be obtained using 3D constitutive relations of elasticity and piezoelectricity.

From the second equation in (38) it can be found that the transverse shear and normal strains are not zero, which means lines normal to the reference surface in the undeformed plate are deformable, distinguishing the current model from the CLT. In the zeroth-order reduction, transverse shear and normal stresses are identically zero because their expressions coincide with the Euler–Lagrange equations in (26) and (27). This result is a direct deduction from the variational statement instead of an *ad hoc* assumption. Similarly, electric displacement in x_3 direction is always equal to $\mathcal{P}$ because of the Euler–Lagrange equation (28). Though at this stage transverse shear and normal stresses cannot be predicted, they can be estimated in a higher-order approximation.

3.2. First-order reduction

To improve the accuracy as well as predict transverse stresses, dimensional reduction of the first-order is required. In this reduction, strains are expanded into the order of $\frac{h}{l}\epsilon$ and the resultant energy is in the order of $(hl^2)\mu\left(\frac{h}{l}\right)^2\epsilon^2$. Then the warping functions and electric potential are perturbed to be

$$w_\parallel = w_\parallel^0 + v_\parallel + o\left(\frac{h^2}{l}\epsilon\right), \quad w_3 = w_3^0 + v_3 + o\left(\frac{h^2}{l}\epsilon\right)$$
$$\phi = \phi^0 + \varphi + o\left(\frac{h^2}{l}\epsilon\right). \tag{40}$$

Up to this order, virtual work of applied loads is not negligible, so the total potential density with virtual work added can be defined as

$$\Pi = \mathcal{H} - W, \tag{41}$$

$$W = \left\langle P_{\|}^{\mathrm{T}} w_{\|} \right\rangle + \tau_{\|}^{\mathrm{T}} w_{\|}^{+} + \beta_{\|}^{\mathrm{T}} w_{\|}^{-} + \langle P_3 w_3 \rangle + \tau_3 w_3^{+} + \beta_3 w_3^{-}. \quad (42)$$

In the zeroth-order approximation, the formulation is for fully anisotropic materials, but it becomes tedious in higher-order derivation. Since most piezoelectric and composite materials present at least monoclinic symmetry about the mid-plane, it would be adequate for practical use to consider this material symmetry. Consequently, C_{es}, C_{st}, e_b, e_a, e_c, d_{et} and α_s will always vanish. Then the warping functions and electric potential in each layer solved during the zeroth-order reduction can be rewritten as

$$w_{\|}^{0} = 0, \quad w_3^{0} = C_{\perp}\mathcal{E} + w_{3e}^{0}, \quad \phi^{0} = C_{\phi}\mathcal{E} + \phi_e^{0} \quad (43)$$

with $\mathcal{E} = [\epsilon\ \kappa]^{\mathrm{T}}$ and

$$C_{\perp}' = \left[-\frac{C_{et}^{**\mathrm{T}}}{C_t^*} + \frac{e_t^*}{d_t^* C_t^*}\mathcal{P}_{\epsilon}^{\mathrm{T}} \quad -x_3\frac{C_{et}^{**\mathrm{T}}}{C_t^*} + \frac{e_t^*}{d_t^* C_t^*}\mathcal{P}_{\kappa}^{\mathrm{T}} \right]$$

$$w_{3e}^{0\,\prime} = T\left(\frac{C_{et}^{**\mathrm{T}}\alpha_e}{C_t^*} - \frac{e_t^* p_t^*}{d_t^* C_t^*} + \alpha_t \right) + \frac{e_t^*}{d_t^* C_t^*}\mathcal{P}_{\phi}, \quad (44)$$

$$C_{\phi}' = \left[\frac{e_{et}^{*\mathrm{T}}}{d_t^*} - \frac{1}{d_t^*}\mathcal{P}_{\epsilon}^{\mathrm{T}} \quad x_3\frac{e_{et}^{*\mathrm{T}}}{d_t^*} - \frac{1}{d_t^*}\mathcal{P}_{\kappa}^{\mathrm{T}} \right]$$

$$\phi_e^{0\prime} = T\left(-\frac{e_{et}^{*\mathrm{T}}\alpha_e}{d_t^*} + \frac{p_t^*}{d_t^*} \right) - \frac{1}{d_t^*}\mathcal{P}_{\phi}, \quad (45)$$

where the '0' in the superscript denotes that the quantity is from the zeroth-order reduction.

Taking the variation of the total potential density gives

$$\begin{aligned}
\delta\Pi_{\mathrm{I}} = & \left\langle \left[(\epsilon + x_3\kappa - \alpha_e T)^{\mathrm{T}} C_e^* + \left(p_t^* T - \mathcal{P}\right)\frac{e_{et}^{*\mathrm{T}}}{d_t^*} \right] I_{\alpha}\delta v_{\|,\alpha} \right. \\
& + \left[\left(v_{\|}' + e_{\alpha} w_{3,\alpha}^{0}\right)^{\mathrm{T}} C_s + \phi_{,\|}^{0\mathrm{T}} e_s^{\mathrm{T}} \right]\delta v_{\|}' + \left[v_3' C_t + \varphi' e_t \right]\delta v_3' \\
& + \left[p_s^{\mathrm{T}} T \right]\delta\varphi_{,\|} + \left[P + v_3' e_t - \varphi' d_t \right]\delta\varphi' \Big\rangle \\
& - \left\langle P_{\|}^{\mathrm{T}}\delta v_{\|} \right\rangle - \tau_{\|}^{\mathrm{T}}\delta v_{\|}^{+} - \beta_{\|}^{\mathrm{T}}\delta v_{\|}^{-} + \left\langle \bar{\lambda}_{\|}\delta v_{\|} \right\rangle \\
& + \left\langle \bar{\lambda}_3\delta v_3 \right\rangle.
\end{aligned} \quad (46)$$

Equaling this to zero, the simplified Euler–Lagrange equations can be derived to be

$$v_3' C_t + \varphi' e_t = 0, \quad (47)$$

$$v_3' e_t - \varphi' d_t = -\theta_{\|}^{\mathrm{T}} p_s + \hat{\mathcal{P}}, \quad (48)$$

$$C_s\left(v_{\|}' + e_{\alpha} w_{3,\alpha}^{0}\right) + e_s\phi_{,\|}^{0} = D_{\alpha}\mathcal{E}_{,\alpha} + g + \bar{\lambda}_{\|}x_3 + \bar{\Lambda}_{\|}, \quad (49)$$

where $\hat{\mathcal{P}}$ is a function independent from x_3, and

$$\theta_{\|}' = T_{,\|}, \quad D_{\alpha}' = -I_{\alpha}^{\mathrm{T}}\left[C_e^* - \frac{e_{et}^*}{d_t^*}\mathcal{P}_{\epsilon}^{\mathrm{T}} \quad x_3 C_e^* - \frac{e_{et}^*}{d_t^*}\mathcal{P}_{\kappa}^{\mathrm{T}} \right]$$

$$g' = I_{\alpha}^{\mathrm{T}}\left(T_{,\alpha} C_e^*\alpha_e - \frac{e_{et}^*}{d_t^*}\mathcal{P}_{\phi,\alpha} + T_{,\alpha} p_t^*\frac{e_{et}^*}{d_t^*} \right) - P_{\|}. \quad (50)$$

Boundary terms generated by integration by parts about the x_{α} coordinates are not considered as the study aims at seeking an internal solution. As a result, integration by parts with respect to the in-plane coordinates is freely used when convenient in the following derivation.

From equations (47)–(49), it can be found that $v_{\|}$ is decoupled from v_3 and φ, so they can be solved separately. Solving equations (47) and (48) gives

$$v_3' = -\left(\theta_{\|}^{\mathrm{T}} p_s - \hat{\mathcal{P}}\right)\frac{e_t}{d_t^* C_t}, \quad (51)$$

$$\varphi' = \left(\theta_{\|}^{\mathrm{T}} p_s - \hat{\mathcal{P}}\right)\frac{1}{d_t^*}. \quad (52)$$

Warping functions $v_{\|}$ can be solved using equation (49) along with the boundary conditions of

$$\begin{aligned}
\left[C_s\left(v_{\|}' + e_{\alpha} w_{3,\alpha}^{0}\right) + e_s\phi_{,\|}^{0} \right]^{+} &= \tau_{\|}, \\
\left[C_s\left(v_{\|}' + e_{\alpha} w_{3,\alpha}^{0}\right) + e_s\phi_{,\|}^{0} \right]^{-} &= -\beta_{\|}
\end{aligned} \quad (53)$$

resulting in

$$v_{\|} = \left(\bar{D}_{\alpha} + L_{\alpha}\right)\mathcal{E}_{,\alpha} + \bar{g}, \quad (54)$$

where

$$\bar{D}_{\alpha}' = C_s^{-1} D_{\alpha}^*, \quad \bar{g}' = C_s^{-1} g^* \quad (55)$$

and

$$\begin{aligned}
D_{\alpha}^* = & D_{\alpha} - C_s e_{\alpha} C_{\perp} - e_s e_{\alpha} C_{\phi} \\
& - \left(\frac{x_3}{h} + \frac{1}{2}\right) D_{\alpha}^{+} + \left(\frac{x_3}{h} - \frac{1}{2}\right) D_{\alpha}^{-},
\end{aligned} \quad (56)$$

$$\begin{aligned}
g^* = & g - C_s e_{\alpha} w_{3e,\alpha}^{0} - e_s e_{\alpha}\phi_{e,\alpha}^{0} \\
& + \left(\frac{x_3}{h} + \frac{1}{2}\right)\tau_{\|} + \left(\frac{x_3}{h} - \frac{1}{2}\right)\beta_{\|} \\
& - \left(\frac{x_3}{h} + \frac{1}{2}\right) g^{+} + \left(\frac{x_3}{h} - \frac{1}{2}\right) g^{-},
\end{aligned} \quad (57)$$

where L_{α} are constants generated by the integral and will be used as optimization parameters to find the optimal Reissner–Mindlin model later. In order to satisfy the constraints in equation (5), the coefficients in equation (54) should have $\left\langle \bar{D}_{\alpha} \right\rangle = 0$, $\langle \bar{g} \rangle = 0$, and $L_{\alpha}\mathcal{E}_{,\alpha} = c_{\|}/h$.

Substituting the solution of $v_{\|}$, v_3 and φ, the asymptotically correct expression of the total potential density Π_1 to the second-order is

$$2\Pi_{\mathrm{I}} = \mathcal{E}^{\mathrm{T}} A\mathcal{E} + \mathcal{E}_{,1}^{\mathrm{T}} B\mathcal{E}_{,1} + 2\mathcal{E}_{,1}^{\mathrm{T}} C\mathcal{E}_{,2} + \mathcal{E}_{,2}^{\mathrm{T}} D\mathcal{E}_{,2} - 2\mathcal{E}^{\mathrm{T}} F, \quad (58)$$

where

$$A = \begin{bmatrix} A^* & B^* \\ B^{*\mathrm{T}} & D^* \end{bmatrix}, \quad (59)$$

$$\begin{aligned}
B = & \left\langle -D_1^{*\mathrm{T}} C_s^{-1} D_1^* + C_{s(11)} C_{\perp}^{\mathrm{T}} C_{\perp} + e_{s(11)} C_{\perp}^{\mathrm{T}} C_{\phi} \right. \\
& \left. + e_{s(11)} C_{\phi}^{\mathrm{T}} C_{\perp} - d_{s(11)} C_{\phi}^{\mathrm{T}} C_{\phi} \right\rangle + \left\langle D_1'^{\mathrm{T}} \right\rangle L_1 + L_1^{\mathrm{T}} \left\langle D_1' \right\rangle,
\end{aligned} \quad (60)$$

$$C = \left\langle -D_1^{*\mathrm{T}} C_s^{-1} D_2^* + C_{s(12)} C_\perp^{\mathrm{T}} C_\perp + e_{s(12)} C_\perp^{\mathrm{T}} C_\phi + e_{s(12)} C_\phi^{\mathrm{T}} C_\perp - d_{s(12)} C_\phi^{\mathrm{T}} C_\phi \right\rangle + \left\langle D_1'^{\mathrm{T}} \right\rangle L_2 + L_1^{\mathrm{T}} \left\langle D_2' \right\rangle, \tag{61}$$

$$D = \left\langle -D_2^{*\mathrm{T}} C_s^{-1} D_2^* + C_{s(22)} C_\perp^{\mathrm{T}} C_\perp + e_{s(22)} C_\perp^{\mathrm{T}} C_\phi + e_{s(22)} C_\phi^{\mathrm{T}} C_\perp - d_{s(22)} C_\phi^{\mathrm{T}} C_\phi \right\rangle + \left\langle D_2'^{\mathrm{T}} \right\rangle L_2 + L_2^{\mathrm{T}} \left\langle D_2' \right\rangle, \tag{62}$$

$$F = S_{\epsilon\kappa} + \left\langle -R_{\epsilon\kappa} - D_\alpha^{*\mathrm{T}} C_s^{-1} g_{,\alpha}^* + \left[p_{s(\alpha)} C_\phi^{\mathrm{T}} T \right]_{,\alpha} + \left[C_{s(\alpha\beta)} C_\perp^{\mathrm{T}} w_{3e}^0 + e_{s(\alpha\beta)} C_\perp^{\mathrm{T}} \phi_e^0 + e_{s(\alpha\beta)} C_\phi^{\mathrm{T}} w_{3e}^0 - d_{s(\alpha\beta)} C_\phi^{\mathrm{T}} \phi_e^0 \right]_{,\alpha\beta} \right\rangle + \left\langle C_\perp^{\mathrm{T}} P_3 \right\rangle + C_\perp^{+\mathrm{T}} \tau_3 + C_\perp^{-\mathrm{T}} \beta_3 - L_\alpha^{\mathrm{T}} \left(\tau_\parallel + \beta_\parallel - \left\langle g' \right\rangle \right)_{,\alpha} \tag{63}$$

with

$$S_{\epsilon\kappa} = \begin{Bmatrix} S_\epsilon \\ S_\kappa \end{Bmatrix}, \quad R_{\epsilon\kappa} = \begin{Bmatrix} \mathcal{P}_\epsilon \left(\theta_\parallel^{\mathrm{T}} p_s - \hat{\mathcal{P}} \right) / d_t^* \\ \mathcal{P}_\kappa \left(\theta_\parallel^{\mathrm{T}} p_s - \hat{\mathcal{P}} \right) / d_t^* \end{Bmatrix} \tag{64}$$

and $(\alpha\beta)$ in the subscript indicates the (α, β)th element in the corresponding matrix.

3.3. Transformation to the Reissner–Mindlin model

Though equation (58) is asymptotically correct to the second order, it is inconvenient for practical use because it contains derivatives of the 2D generalized strain, making the boundary conditions hard to define physically. For practical use, we can transform it into a model having the same form as the Reissner–Mindlin model. To do so, two transverse shear strains need to be introduced along with another orthogonal triad $\mathbf{B}_i^*$ in the deformed plate to redefine the 2D generalized strains, so that

$$\mathbf{R}_{,\alpha} = \mathbf{B}_\alpha^* + \varepsilon_{\alpha\beta}^* \mathbf{B}_\beta^* + 2\gamma_{\alpha 3} \mathbf{B}_3^*, \tag{65}$$

$$\mathbf{B}_{i,\alpha}^* = \left(-K_{\alpha\beta}^* \mathbf{B}_\beta^* \times \mathbf{B}_3^* + K_{\alpha 3}^* \mathbf{B}_3^* \right) \times \mathbf{B}_i^* \tag{66}$$

with the transverse shear strains as $\gamma = \left[2\gamma_{13} \;\; 2\gamma_{23} \right]^{\mathrm{T}}$.

Kinematic identity can be found between the former 2D generalized strain $\mathcal{E}$ and Reissner–Mindlin 2D generalized strain $\mathcal{R}$ as

$$\mathcal{E} = \mathcal{R} - \mathcal{D}_\alpha \gamma_{,\alpha}, \tag{67}$$

where

$$\mathcal{D}_1 = \begin{bmatrix} 0 & 0 & 0 & 1 & 0 & 0 \\ 0 & 0 & 0 & 0 & 1 & 0 \end{bmatrix}^{\mathrm{T}}, \quad \mathcal{D}_2 = \begin{bmatrix} 0 & 0 & 0 & 0 & 1 & 0 \\ 0 & 0 & 0 & 0 & 0 & 1 \end{bmatrix}^{\mathrm{T}}, \tag{68}$$

$$\mathcal{R} = \left[\varepsilon_{11}^* \;\; 2\varepsilon_{12}^* \;\; \varepsilon_{22}^* \;\; K_{11}^* \;\; K_{12}^* + K_{21}^* \;\; K_{22}^* \right]^{\mathrm{T}}. \tag{69}$$

Substituting equation (67) back into equation (58) and neglecting higher-order terms, it becomes

$$2\Pi_{\mathrm{l}} = \mathcal{R}^{\mathrm{T}} A \mathcal{R} - 2\mathcal{R}^{\mathrm{T}} A \mathcal{D}_1 \gamma_{,1} - 2\mathcal{R}^{\mathrm{T}} A \mathcal{D}_2 \gamma_{,2} + \mathcal{R}_{,1}^{\mathrm{T}} B \mathcal{R}_{,1} + 2\mathcal{R}_{,1}^{\mathrm{T}} C \mathcal{R}_{,2} + \mathcal{R}_{,2}^{\mathrm{T}} D \mathcal{R}_{,2} - 2\mathcal{R}^{\mathrm{T}} F. \tag{70}$$

Compared to the potential energy of the Reissner–Mindlin model, which has the form of

$$2\Pi_{\mathcal{R}} = \mathcal{R}^{\mathrm{T}} A \mathcal{R} + \gamma^{\mathrm{T}} G \gamma - 2\mathcal{R}^{\mathrm{T}} F_{\mathcal{R}} - 2\gamma^{\mathrm{T}} F_\gamma \tag{71}$$

further derivation is still required to completely eliminate terms with partial derivatives of the 2D generalized strains in equation (70). This can be achieved by utilizing the plate equilibrium equations about in-plane moments and transverse shear forces. Then equation (70) can be rewritten as

$$2\Pi_{\mathrm{l}} = \mathcal{R}^{\mathrm{T}} A \mathcal{R} + \gamma^{\mathrm{T}} G \gamma - 2\mathcal{R}^{\mathrm{T}} F - 2\gamma^{\mathrm{T}} F_\gamma + U^*, \tag{72}$$

where

$$F_\gamma = -\mathcal{D}_\alpha^{\mathrm{T}} S_{\epsilon\kappa,\alpha}, \quad U^* = \mathcal{R}_{,1}^{\mathrm{T}} \bar{B} \mathcal{R}_{,1} + 2\mathcal{R}_{,1}^{\mathrm{T}} \bar{C} \mathcal{R}_{,2} + \mathcal{R}_{,2}^{\mathrm{T}} \bar{D} \mathcal{R}_{,2} \tag{73}$$

and

$$\bar{B} = B + A\mathcal{D}_1 G^{-1} \mathcal{D}_1^{\mathrm{T}} A, \quad \bar{C} = C + A\mathcal{D}_1 G^{-1} \mathcal{D}_2^{\mathrm{T}} A \quad \bar{D} = D + A\mathcal{D}_2 G^{-1} \mathcal{D}_2^{\mathrm{T}} A. \tag{74}$$

In the most ideal case, U^* can be driven to be zero for any $\mathcal{R}$ and the transverse shear stiffness matrix can be solved exactly, leading the asymptotically correct total potential in equation (72) to have the same form as the Reissner–Mindlin model in equation (71). However, this is impossible for most multi-layered, piezoelectric composite plates, so an optimization process is required to minimize U^* and thus minimize the error between the asymptotically correct expression and the Reissner–Mindlin form. The accuracy of the Reissner–Mindlin model is influenced by the deviation of U^* from zero. Considering symmetry, there are totally 78 quantities in $\bar{B}$, $\bar{C}$ and $\bar{D}$ that are required to be zero, and there are 27 optimization parameters, 3 in G and 24 in L_α. To make U^* as close to zero as possible under any strain field, an overdetermined linear system with 78 equations and 27 unknowns is constructed, then the least-squares method is implemented to solve for the 27 unknowns.

By the optimization process, the best transverse shear stiffness matrix G can be obtained to complete the transformation to the Reissner–Mindlin-like model. Similar to the zeroth-order model, the current first-order model can be directly applied in any thermopiezoelastic Reissner–Mindlin plate analyses with equivalent stiffness matrices A, G, F and F_γ calculated from plate geometry and material constants. Piezoelectricity, thermal expansion and pyroelectricity are coupled in the stiffness matrices along with elasticity.

From equation (4), the 3D displacement field U_i can be easily recovered using the 2D displacement field u_i and warping functions w_i, that is

$$U_i = u_i + x_3 \left(\mathcal{C}_{3i} - \delta_{3i} \right) + w_j \mathcal{C}_{ji}. \tag{75}$$

For the first-order approximation, the 3D strain field can be recovered to be

$$\Gamma_e^1 = \epsilon + x_3\kappa, \quad 2\Gamma_s^1 = v_\parallel' + e_\alpha w_{3,\alpha}^0, \quad \Gamma_t^1 = w_3^{0\prime} + v_3'. \tag{76}$$

Then 3D stresses up to the first-order can be obtained. The first-order model can predict the transverse shear strains and stresses, but the transverse normal stress still vanishes. For predicting transverse normal stress, the warping functions should be perturbed once more to be

$$\begin{aligned} w_\parallel &= w_\parallel^0 + v_\parallel^1 + y_\parallel + o\left(\frac{h^3}{l^2}\epsilon\right), \\ w_3 &= w_3^0 + v_3^1 + y_3 + o\left(\frac{h^3}{l^2}\epsilon\right) \\ \phi &= \phi^0 + \varphi^1 + \psi + o\left(\frac{h^3}{l^2}\epsilon\right). \end{aligned} \tag{77}$$

Using a similar procedure as the first-order reduction, the expression of the warping functions and electric potential can be obtained. That is

$$\begin{aligned} y_\parallel' = &- C_s^{-1}e_s e_\alpha \varphi_{,\alpha}^1 - C_s^{-1}I_\alpha^{\mathrm{T}} e_{et}^* \varphi_{,\alpha}^1 \\ &+ \left(\frac{x_3}{h} + \frac{1}{2}\right) I_\alpha^{\mathrm{T}} e_{et}^* \varphi_{,\alpha}^{1+} - \left(\frac{x_3}{h} - \frac{1}{2}\right) I_\alpha^{\mathrm{T}} e_{et}^* \varphi_{,\alpha}^{1-}, \end{aligned} \tag{78}$$

$$\begin{aligned} y_3' = &- \frac{C_{et}^{**\mathrm{T}}}{C_t}\left[I_\beta\left(\bar{D}_\alpha + L_\alpha\right)\mathcal{E}_{,\alpha\beta} + I_\beta \bar{g}_{,\beta}\right] \\ &+ \frac{e_t}{d_t^* C_t}\left(E_{\phi\alpha\beta}\mathcal{E}_{,\alpha\beta} + S_\phi + \hat{\hat{\mathcal{P}}}\right) \\ &+ \frac{d_t}{d_t^* C_t}\left[E_{\perp\alpha\beta}\mathcal{E}_{,\alpha\beta} + S_\perp + \left(\frac{x_3}{h} + \frac{1}{2}\right)\tau_3\right. \\ &+ \left(\frac{x_3}{h} - \frac{1}{2}\right)\beta_3 \\ &- \left(\frac{x_3}{h} + \frac{1}{2}\right)E_{\perp\alpha\beta}^+ \mathcal{E}_{,\alpha\beta} + \left(\frac{x_3}{h} - \frac{1}{2}\right)E_{\perp\alpha\beta}^- \mathcal{E}_{,\alpha\beta} \\ &\left. - \left(\frac{x_3}{h} + \frac{1}{2}\right)S_\perp^+ + \left(\frac{x_3}{h} - \frac{1}{2}\right)S_\perp^-\right], \end{aligned} \tag{79}$$

$$\begin{aligned} \psi' = &\frac{e_{et}^{*\mathrm{T}}}{d_t^*}\left[I_\beta\left(\bar{D}_\alpha + L_\alpha\right)\mathcal{E}_{,\alpha\beta} + I_\beta \bar{g}_{,\beta}\right] \\ &- \frac{1}{d_t^*}\left(E_{\phi\alpha\beta}\mathcal{E}_{,\alpha\beta} + S_\phi + \hat{\hat{\mathcal{P}}}\right) \\ &+ \frac{e_t}{d_t^* C_t}\left[E_{\perp\alpha\beta}\mathcal{E}_{,\alpha\beta} + S_\perp + \left(\frac{x_3}{h} + \frac{1}{2}\right)\tau_3\right. \\ &+ \left(\frac{x_3}{h} - \frac{1}{2}\right)\beta_3 \\ &- \left(\frac{x_3}{h} + \frac{1}{2}\right)E_{\perp\alpha\beta}^+ \mathcal{E}_{,\alpha\beta} + \left(\frac{x_3}{h} - \frac{1}{2}\right)E_{\perp\alpha\beta}^- \mathcal{E}_{,\alpha\beta} \\ &\left. - \left(\frac{x_3}{h} + \frac{1}{2}\right)S_\perp^+ + \left(\frac{x_3}{h} - \frac{1}{2}\right)S_\perp^-\right] \end{aligned} \tag{80}$$

Table 1. Material properties of the plates.

Properties	PVDF	Polyimide	PZT-4	*S* glass/ epoxy
C_{11} (GPa)	3.61	3.85	139.02	48.5
C_{12} (GPa)	1.61	1.98	77.85	5.82
C_{13} (GPa)	1.42	1.98	74.33	5.82
C_{22} (GPa)	3.13	3.85	139.02	12.7
C_{23} (GPa)	1.31	1.98	74.33	6.7
C_{33} (GPa)	1.63	3.85	115.45	12.7
C_{44} (GPa)	0.55	0.93	25.6	3
C_{55} (GPa)	0.59	0.93	25.6	4.5
C_{66} (GPa)	0.69	0.93	30.6	4.5
e_{31} (C/m^2)	0.0105	0	−5.2	0
e_{32} (C/m^2)	−0.0117	0	−5.2	0
e_{33} (C/m^2)	−0.0284	0	15.08	0
$e_{24} = e_{15}$ (C/m^2)	−0.0122	0	12.72	0
d_{11} ($\times 10^{-9}$ C^2/(Nm^2))	0.0651	0.031	13.06	0.056
d_{22} ($\times 10^{-9}$ C^2/(Nm^2))	0.0821	0.031	13.06	0.056
d_{33} ($\times 10^{-9}$ C^2/(Nm^2))	0.0686	0.031	11.51	0.056
α_1 ($\times 10^{-6}$ K^{-1})	130	20	3.8	5
α_2 ($\times 10^{-6}$ K^{-1})	130	20	3.8	26
α_3 ($\times 10^{-6}$ K^{-1})	130	20	1.2	26
$p_1 = p_2$ ($\times 10^{-6}$ C/(Km^2))	30	0	0	0
p_3 ($\times 10^{-6}$ C/(Km^2))	30	0	−170	0

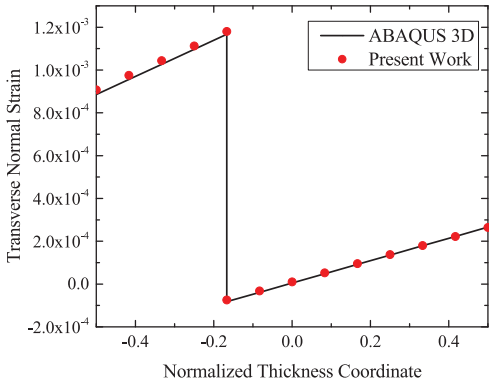

Figure 2. Distribution of transverse normal strain through thickness at the center.

with

$$\begin{aligned} E_{\perp\alpha\beta}' &= -\left(e_\beta^{\mathrm{T}} D_\alpha^* + C_{s(\alpha\beta)}C_\perp + e_{s(\alpha\beta)}C_\phi\right) \\ S_\perp' &= -\left(e_\beta^{\mathrm{T}} g_{,\beta}^* + C_{s(\alpha\beta)}w_{3e,\alpha\beta}^0 + e_{s(\alpha\beta)}\phi_{e,\alpha\beta}^0 + P_3\right), \end{aligned} \tag{81}$$

$$\begin{aligned} E_{\phi\alpha\beta}' &= -\left(e_\beta^{\mathrm{T}} e_s C_s^{-1} D_\alpha^* + e_{s(\alpha\beta)}C_\perp - d_{s(\alpha\beta)}C_\phi\right) \\ S_\phi' &= -\left(e_\beta^{\mathrm{T}} e_s C_s^{-1} g_{,\beta}^* + e_{s(\alpha\beta)}w_{3e,\alpha\beta}^0 - d_{s(\alpha\beta)}\phi_{e,\alpha\beta}^0\right) \end{aligned} \tag{82}$$

and $\hat{\hat{\mathcal{P}}}$ is an arbitrary function of x_α.

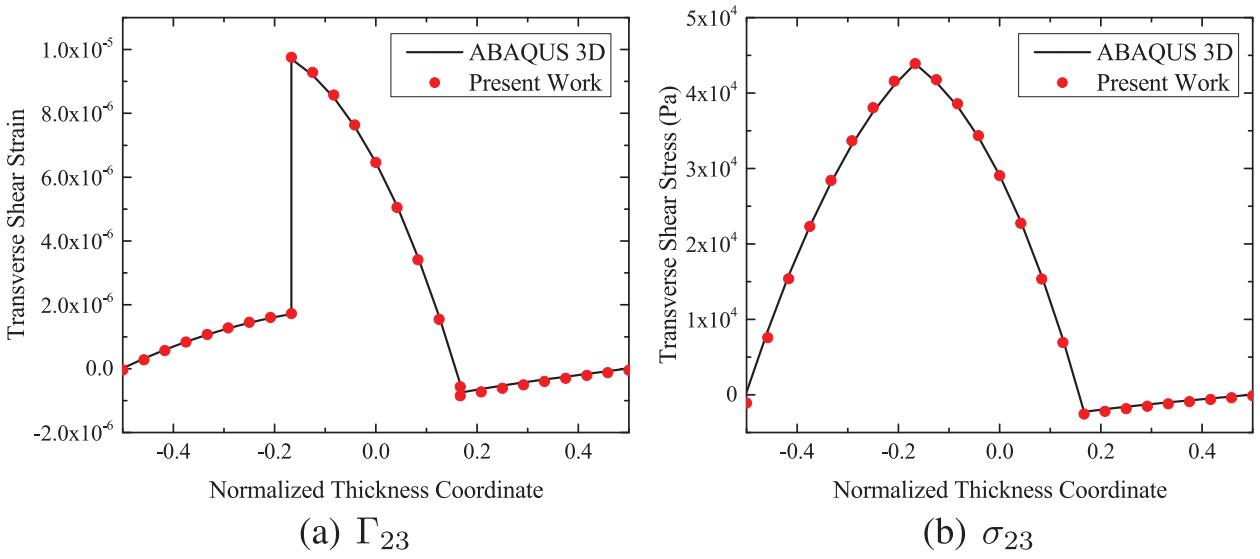

Figure 3. Distribution of transverse shear strain and stress through thickness at $x_1 = 0.07$ m, $x_2 = 0.105$.

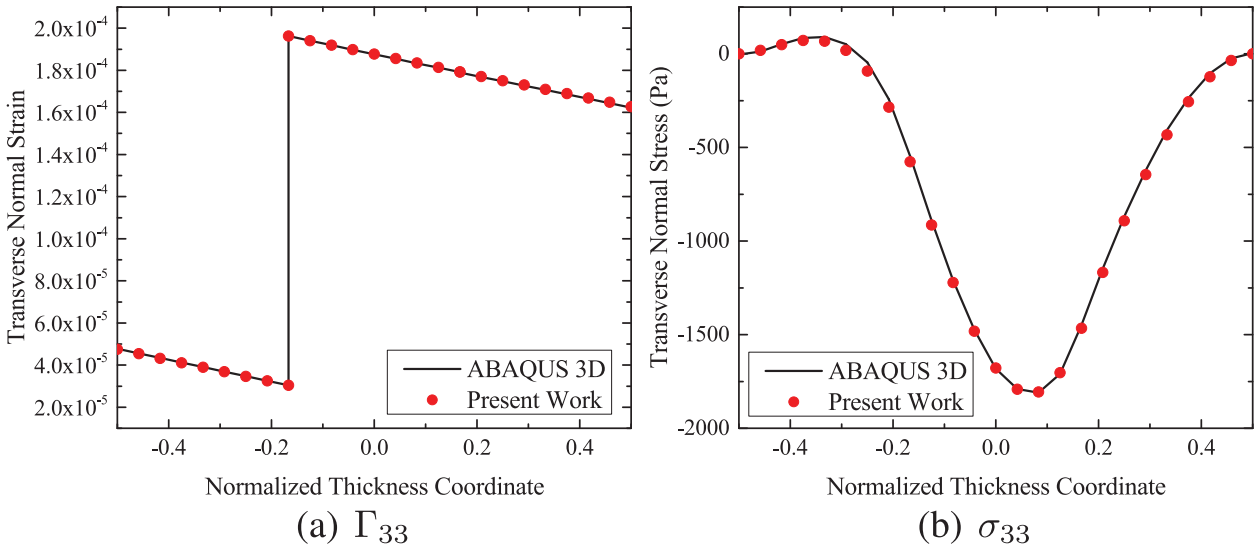

Figure 4. Distribution of transverse normal strain and stress through thickness at the center.

Even though it is possible to derive the energy expression to the fourth-order for the plate analysis with warping functions and electric potential presented above, it is unnecessary to do so because it is too complex for practical use. Consequently, 2D plate model derived from first-order reduction is still adopted, while the recovery considers the strains in second-order, that is

$$\begin{aligned} \Gamma_e^2 &= \varepsilon + x_3\kappa + I_\alpha v_{\|,\alpha}^1, \\ 2\Gamma_s^2 &= v_\|^{1\prime} + y_\|' + e_\alpha\left(w_{3,\alpha}^0 + v_{3,\alpha}^1\right) \\ \Gamma_t^2 &= w_3^{0\prime} + v_3^{1\prime} + y_3' \end{aligned} \tag{83}$$

and the electric field

$$E_s^2 = -\phi_{,\|}^0 - \varphi_{,\|}^1, \quad E_t^2 = -\phi^{0\prime} - \varphi^{1\prime} - \psi'. \tag{84}$$

The 3D stress field and electric displacement can be recovered based on equation (18).

4. Numerical examples

Four examples are provided to verify the present work. The plates in the four examples have the same in-plane dimensions, 140 mm × 140 mm, with different layups, thicknesses, or boundary conditions. The origin of the coordinate system is located at the bottom left. Materials used in the examples are shown in table 1. The model in this paper is implemented in ABAQUS using the shell element S8R, with sectional stiffness calculated using the presented theory. Results are

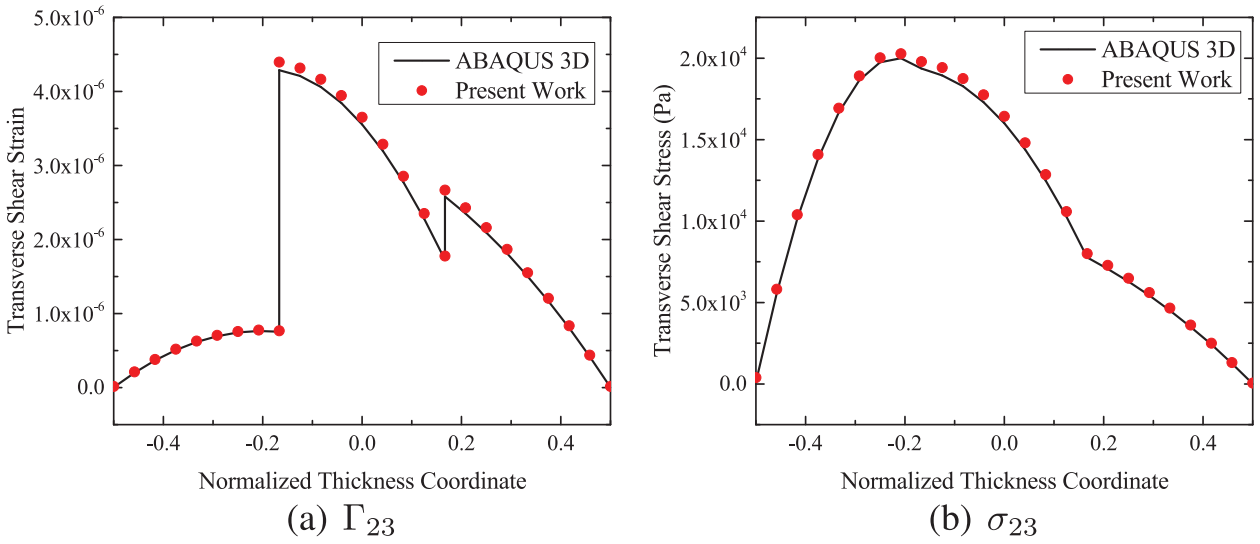

Figure 5. Distribution of transverse shear strain and stress through thickness at $x_1 = 0.07$ m, $x_2 = 0.105$.

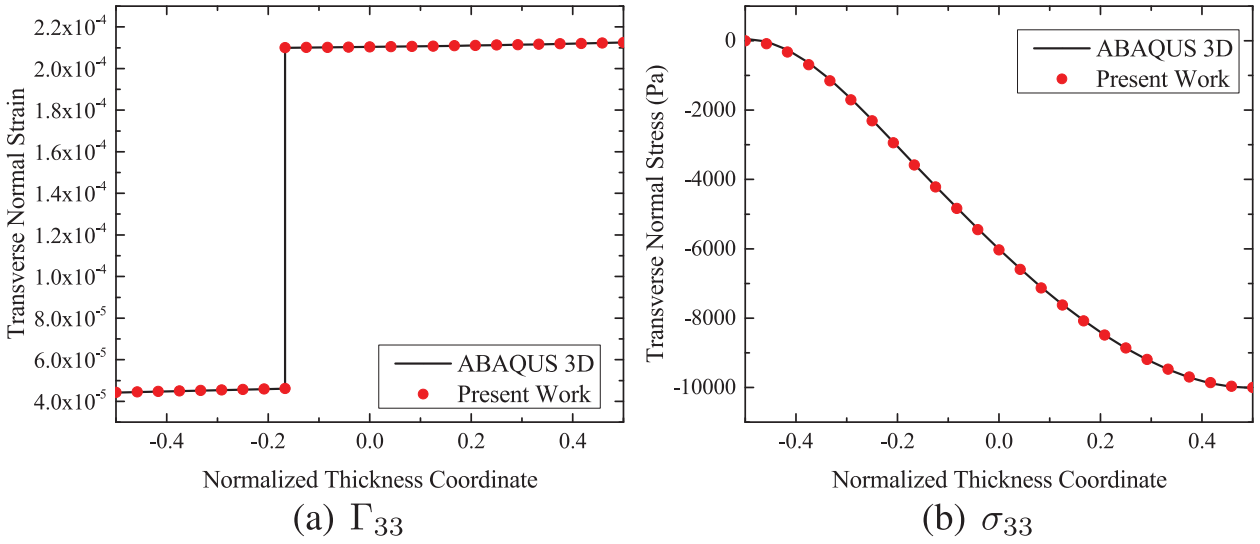

Figure 6. Distribution of transverse normal strain and stress through thickness at the center.

compared with 3D finite element analysis with detailed material properties of each layer in ABAQUS.

4.1. Two-layer plate

In example 1, the plate has two layers. The bottom layer is a PVDF piezoelectric layer, with the thickness of 0.05 mm, and the upper layer is a polyimide layer, with the thickness of 0.1 mm. Since the aspect ratio of this plate is very large, using the zeroth-order model can have sufficient accuracy. The plate has a simply supported boundary. Thermal load is 5 K in the whole plate. The bottom surface is charged with 300 V, and the interface between two layers is grounded. The 3D finite element model uses 240 000 C3D20RE 3D piezoelectric quadratic elements. In the thickness direction, 9 nodes are in the polyimide layer and 5 in the PVDF layer.

The result of transverse normal strain is shown in figure 2. Thickness coordinate x_3 is normalized by $\bar{z} = x_3/h$ in the plots. Since this plate is very thin, the strain distribution is quite linear through the thickness. Due to the large α_3 of PVDF, transverse normal strain in the PVDF layer is much larger. Note that this accurate prediction in comparison to the detailed 3D analysis, is directly obtained from the present theory and a 2D plate analysis in ABAQUS. Though not shown here, other quantities also have excellent accuracy.

4.2. Three-layer simply supported plate

In example 2, the plate consists of three layers. From the bottom to the top, the first layer is PZT-4 orienting 0°, the second is *S* glass/epoxy orienting 90° and the third is *S* glass/epoxy orienting 0°. Each layer has a thickness of 5 mm. As

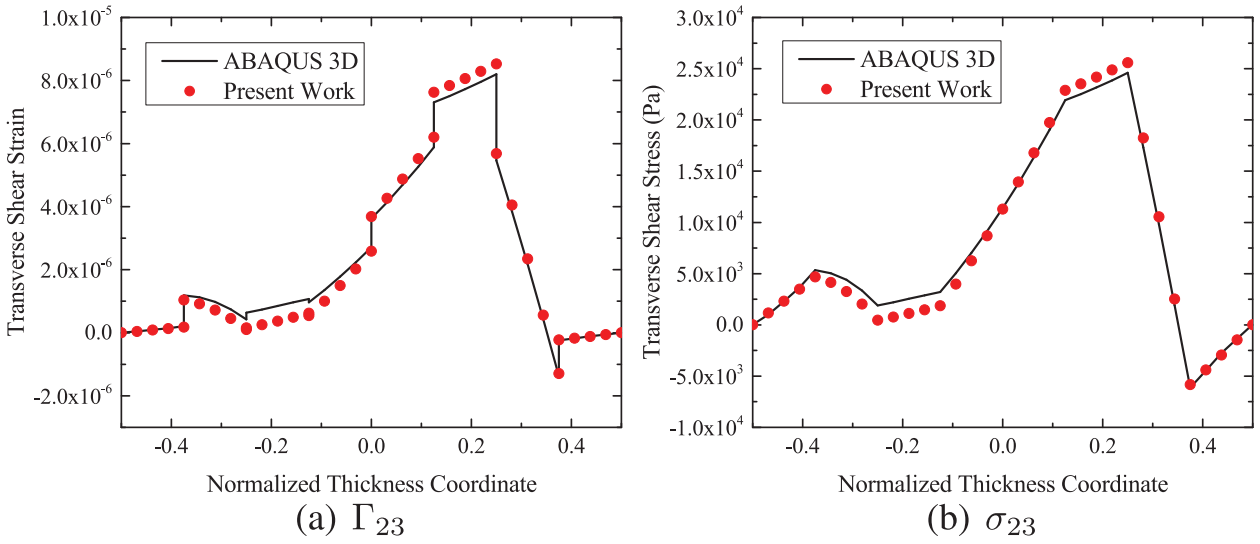

Figure 7. Distribution of transverse shear strain and stress through thickness at $x_1 = 0.07$ m, $x_2 = 0.105$.

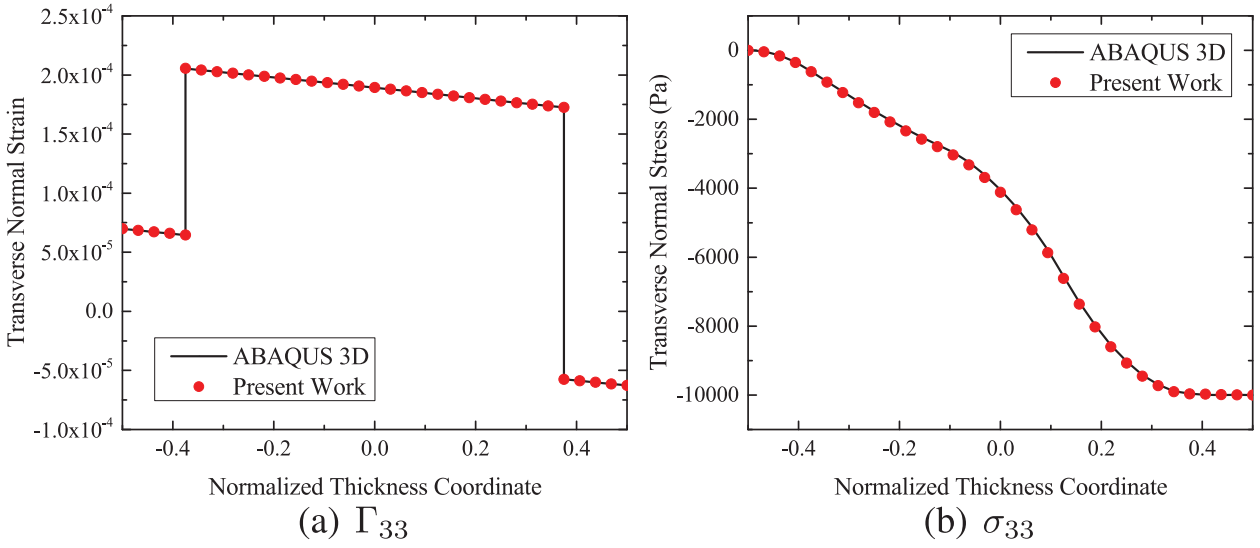

Figure 8. Distribution of transverse normal strain and stress through thickness at the center.

this plate is much thicker, the first-order model is used. Thermal load is 5 K in the whole plate. The bottom surface has a prescribed electric potential of 600 V, and the interface between the first and second layer is grounded. The 3D finite element model contains 797 970 C3D10E tetrahedron elements, with 17 nodes through the thickness in each layer.

Representative results are shown in figures 3 and 4. It can be found that the continuity of transverse shear and normal stresses through the thickness is satisfied. A quadratic distribution of transverse shear strain and stress through the thickness that is similar to a 3D theory is accurately predicted by the present single-layer equivalent model. σ_{33} is an order smaller than σ_{23} because transverse shear stresses are recovered from the first-order model while transverse normal stress is from the second-order model.

4.3. Three-layer clamped plate

In example 3, the plate is the same as the one in example 2, but with a clamped boundary condition. In addition to the thermal load and electric charge, a uniformly distributed load of 10 kPa is applied downwards on the top surface. The 3D model is also the same as the one in example 2 except for the loads, while in order to ensure the plate model to have the same boundary condition as the 3D model, its boundary region is modelled in 3D, with a solid to plate coupling with the interior region.

The results are shown in figures 5 and 6. It can be found that the accuracy of the model remains well with different boundary conditions. In this example, the pressure applied on the top surface generates a traction of $\tau_3 = -10$ kPa at

$\bar{z} = 0.5$, which is a boundary condition for σ_{33}. From figures 5 and 6 it can be observed that stresses predicted by the theory can satisfy the traction boundary conditions at the top surface.

4.4. Eight-layer plate

In example 4, the plate has two PZT-4 layers on the top and bottom surfaces, and six *S* glass/epoxy layers between them with stacking sequence as [90°/0°/45°/ −45°/0°/90°]. All layers have the same thickness of 2 mm. The boundary condition is simply supported. Temperature change is 5 K in the plate; a 10 kPa downward pressure is applied on the top; the top and bottom surfaces are charged with 600 V, and interfaces between PZT-4 and *S* glass/epoxy layers are grounded. 1 053 966 C3D10E elements are used in the 3D FEA, with 9 nodes through the thickness in each layer.

Results are shown in figures 7 and 8. It can be observed that transverse normal stresses can still satisfy the boundary condition at the top, though the distribution through the thickness is more complex. For transverse shear strains and stresses, quadratic distribution is not as obvious as in the previous two examples because the thickness of every single layer is relatively small, while discrepancies occur as the complicated layup causes a stronger 3D behavior, making the higher-order terms contribute more to the results. If more accurate results are required, higher-order models should be developed.

5. Conclusion

In this paper, a laminated anisotropic plate model with thermal and piezoelectric effect is constructed based on the VAM. The main focus is on the interior constitutive model of the plate. For modeling, the original 3D plate problem is separated into a 1D through-the-thickness analysis and a 2D reference surface analysis. Recovery of 3D fields using 2D plate behavior is also made possible in the model. The following accomplishments are achieved in this work.

(i) In formulating the 3D strain field, warping functions are introduced to describe every possible shape in the deformed state. Then 3D strains containing 2D generalized strains and warping functions are obtained.
(ii) Beginning from the energy expression, the dimensional reduction is implemented by first dropping smaller terms. Then, variation of the energy is taken to solve for warping functions and electric potential, and to construct equivalent constitutive relation. The warping functions are solved for a zeroth-order model resembling the CLT and a first-order model being transformed into the Reissner–Mindlin model. Higher-order warping functions are also solved for better recovery of the 3D fields.
(iii) Several numerical examples are studied for validating both the zeroth-order model and the first-order model. The zeroth-order model is shown to be accurate for thin plates. The first-order model can provide an accurate prediction even if the plate gets thicker. Different laminations, boundary conditions and load combinations in the examples verify the robustness of the model.

It should be emphasized that the mathematical derivation of the present work follows a rigorous procedure that does not involves any *a priori* kinemtic assumptions as commonly invoked in other approaches. Terms dropped in the current model are because of their smallness in order and will appear if the model is further derived into a higher order.

Acknowledgments

This work is supported by the US AFOSR Multiscale Structural Mechanics and Prognosis Program. The views and conclusions contained herein are those of the authors and should not be interpreted as necessarily representing the official policies or endorsement, either expressed or implied, of the sponsor. The program manager is Dr David Stargel.

References

[1] Luo Q and Tong L 2006 High precision shape control of plates using orthotropic piezoelectric actuators *Finite Elem. Anal. Des.* **42** 1009–20
[2] Chandrashekhara K and Agarwal A N 1993 Active vibration control of laminated composite plates using piezoelectric devices: a finite element approach *J. Intell. Mater. Syst. Struct.* **4** 496–508
[3] Irschik H 2002 A review on static and dynamic shape control of structures by piezoelectric actuation *Eng. Struct.* **24** 5–11
[4] Ray M C, Rao K M and Samanta B 1992 Exact analysis of coupled electroelastic behaviour of a piezoelectric plate under cylindrical bending *Comput. Struct.* **45** 667–77
[5] Lee J S and Jiang L Z 1996 Exact electroelastic analysis of piezoelectric laminae via state space approach *Int. J. Solids Struct.* **33** 977–90
[6] Zhong Z and Shang E T 2003 Three-dimensional exact analysis of a simply supported functionally gradient piezoelectric plate *Int. J. Solids Struct.* **40** 5335–52
[7] Xu K, Noor A K and Tang Y Y 1995 Three-dimensional solutions for coupled thermoelectroelastic response of multilayered plates *Comput. Methods Appl. Mech. Eng.* **126** 355–71
[8] Lee C K 1990 Theory of laminated piezoelectric plates for the design of distributed sensors/actuators: I. Governing equations and reciprocal relationships *J. Acoust. Soc. Am.* **87** 1144–58
[9] Pai P F, Nayfeh A H, Oh K and Mook D T 1993 A refined nonlinear model of composite plates with integrated piezoelectric actuators and sensors *Int. J. Solids Struct.* **30** 1603–30
[10] Mitchell J A and Reddy J N 1995 A refined hybrid plate theory for composite laminates with piezoelectric laminae *Int. J. Solids Struct.* **32** 2345–67
[11] Reddy J N 1984 A simple higher-order theory for laminated composite plates *J. Appl. Mech.* **51** 745–52
[12] Wang Q, Quek S T, Sun C T and Liu X 2001 Analysis of piezoelectric coupled circular plate *Smart Mater. Struct.* **10** 229

[13] Qu Z Q 2001 An efficient modelling method for laminated composite plates with piezoelectric sensors and actuators *Smart Mater. Struct.* **10** 807
[14] Figueiredo I M N and Leal C M F 2005 A piezoelectric anisotropic plate model *Asymptotic Anal.* **44** 327–46
[15] Kapuria S and Achary G G S 2006 Nonlinear coupled zigzag theory for buckling of hybrid piezoelectric plates *Compos. Struct.* **74** 253–64
[16] Kepler R G and Anderson R A 1978 Piezoelectricity and pyroelectricity in polyvinylidene fluoride *J. Appl. Phys.* **49** 4490–4
[17] Tauchert T R 1992 Piezothermoelastic behavior of a laminated plate *J. Therm. Stresses* **15** 25–37
[18] Krommer M and Irschik H 2000 A Reissner–Mindlin-type plate theory including the direct piezoelectric and the pyroelectric effect *Acta Mech.* **141** 51–69
[19] Cho M and Oh J 2004 Higher order zig-zag theory for fully coupled thermo-electric-mechanical smart composite plates *Int. J. Solids Struct.* **41** 1331–56
[20] Kapuria S and Achary G G S 2005 A coupled consistent third-order theory for hybrid piezoelectric plates *Compos. Struct.* **70** 120–33
[21] Oh J, Cho M and Kim J S 2007 Enhanced lower-order shear deformation theory for fully coupled electro-thermo-mechanical smart laminated plates *Smart Mater. Struct.* **16** 2229
[22] Berdichevskii V L 1979 Variational-asymptotic method of constructing a theory of shells: PMM vol 43, no. 4, pp 664–87 *J. Appl. Math. Mech.* **43** 711–36
[23] Atilgan A R and Hodges D H 1992 On the strain energy of laminated composite plates *Int. J. Solids Struct.* **29** 2527–43
[24] Sutyrin V G and Hodges D H 1996 On asymptotically correct linear laminated plate theory *Int. J. Solids Struct.* **33** 3649–71
[25] Sutyrin V G 1997 Derivation of plate theory accounting asymptotically correct shear deformation *J. Appl. Mech.* **64** 905–15
[26] Yu W 2002 Variational asymptotic modeling of composite dimensionally reducible structures *PhD Thesis* Georgia Institute of Technology
[27] Yu W, Hodges D H and Volovoi V V 2002 Asymptotic construction of Reissner-like composite plate theory with accurate strain recovery *Int. J. Solids Struct.* **39** 5185–203
[28] Hodges D H, Atilgan A R and Danielson D A 1993 A geometrically nonlinear theory of elastic plates *J. Appl. Mech.* **60** 109–16
[29] Yu W and Hodges D H 2004 A simple thermopiezoelastic model for smart composite plates with accurate stress recovery *Smart Mater. Struct.* **13** 926
[30] Liao L and Yu W 2008 Asymptotical construction of a fully coupled, Reissner–Mindlin model for piezoelectric composite plates, Smart *Mater. Struct.* **17** 015010
[31] Liao L and Yu W 2009 An electromechanical Reissner–Mindlin model for laminated piezoelectric plates *Compos. Struct.* **88** 394–402
[32] Chen H and Yu W 2014 A multiphysics model for magneto-electro-elastic laminates *Eur. J. Mech.* A **47** 23–44
[33] Danielson D A 1991 Finite rotation with small strain in beams and plates *Proc. 2nd Pan American Congress of Applied Mechanics* pp 2–4
[34] Danielson D A and Hodges D H 1987 Nonlinear beam kinematics by decomposition of the rotation tensor *J. Appl. Mech.* **54** 258–62
[35] Reddy J N 2004 *Mechanics of Laminated Composite Plates and Shells: Theory and Analysis* (Boca Raton, FL: CRC Press)

A New Micromechanics Theory for Homogenization and Dehomogenization of Heterogeneous Materials

B. PENG and W. YU*

ABSTRACT

To avoid the difficulty of applying periodic boundary conditions and deal with aperiodic heterogeneous materials, a new micromechanics theory is developed based on the mechanics of structure genome. This new theory starts with expressing the kinematics including both displacements and strains of the original heterogeneous material in terms of those of the equivalent homogeneous material and fluctuating functions with the kinematic equivalency enforced through integral constraints of the fluctuating functions. Then the principle of minimum total potential energy can be used along with the variational asymptotic method to formulate the variational statement for the micromechanics theory. As this theory does not require boundary conditions, one is free to choose the analysis domain of arbitrary shape and they need not be volumes with periodic boundaries. This theory can also handle periodic materials by enforcing the periodicity of the fluctuating functions. To demonstrate the application of this new theory, we will compare the results of different micromechanics approaches for both periodic and aperiodic materials.

INTRODUCTION

Micromechanics seeks to model heterogeneous material as an equivalent homogenous material. The first aim of micromechanics is to predict the effective macroscopic properties, commonly called homogenization. The second aim of micromechanics is to predict the local fields such as stress and strain fields within the microstructure from the macroscopic behavior. This step is commonly called dehomogenization or localization, which is very critical for evaluating the strength and failure of heteroge-

Purdue University, West Lafayette, Indiana 47907

neous materials, although usually neglected by most micromechanics models.

In addition to the governing equations established in continuum mechanics, most micromechanics models need to choose an analysis domain, commonly called representative volume element (RVE), and prescribe boundary conditions (BCs). RVE was defined as a material volume entirely typical of the whole mixture on average and contains a sufficient number of inclusions for the apparent overall properties to be effectively independent of the boundary conditions [1]. Although this definition is theoretically sound on the ergodic principle, it creates a paradox. On one hand, RVE must include a large number of heterogeneities to be representative, while on the other hand, it must be small enough to be justified as a material point for the macroscopic structural analysis. For periodic materials, the smallest RVE can be the repeating unit cell (UC) of the material if periodic boundary conditions are applied. For aperiodic materials, RVEs are usually chosen out of practical considerations despite the requirements of a rigorous RVE based on the ergodic principle.

The boundary conditions we can apply to an RVE is usually governed by the Hill-Mandel macrohomogeneity condition so that the homogenized material is energetically equivalent to the original heterogeneous material. Three types of boundary conditions satisfying Hill-Mandel macrohomogeneity condition are commonly used: statically uniform boundary conditions (SUBCs), kinematically uniform boundary conditions (KUBCs), and periodic boundary conditions (PBCs).

Pindera et al. [2] summarized the literature which numerically investigated the influence of the RVE size and boundary conditions. SUBCs and KUBCs lead to lower and upper estimates of the effective properties, respectively, compared to PBCs. In addition, predictions using SUBCs and KUBCs converge to those of PBCs with increasing analysis domain size.

In addition, Mesarovic et al. [3] proposed Minimal Kinematic Boundary Conditions (MKBCs) with linearized kinematics for simulations of disordered microstructures based on Cauchy continuum, later this theory is extended in [4] for higher-order numerical homogenization schemes. For three-dimensional (3D) problems, MKBCs include three constraints to remove rigid translation, three constraints to remove rigid rotation, and constraints corresponding to the homogenized strain definitions. Later, in [5], the three rotation constraints are removed from MKBCs for micromechanics using infinitesimal strains. It has later been proved that the first-order homogenization schemes based on the MKBCs predicts uniform traction on the boundary of RVE if no body force is included [5].

Recently, de Souza Neto et al. proposed a generalized unified micromechnics theory [6], in which the Hill-Mandel Principle is rephrased as a variational statement by requiring the total macro-scale virtual power to coincide with the volume average of its micro-scale counterpart, named the principle of multiscale virtual power. With this new principle, various problems such as dynamics, high order strain effects, material failure can be addressed.

In this paper, we will develop a new theory based on the the concept of structure genome (SG), which is defined as the smallest mathematical building block of the structure in [7]. This new theory starts with expressing the kinematics including both displacements and strains of the original heterogeneous material in terms of those of the equivalent homogeneous material and fluctuating functions with the kinematic

equivalency enforced through integral constraints of the fluctuating functions. Then the principle of minimum total potential energy is used along with the variational asymptotic method to formulate the micromechanics theory. As this theory does not require boundary conditions, one is free to choose SG of arbitrary shape and they need not be volumes with straight boundaries. This theory can also accommodate periodic materials by enforcing the periodicity of the fluctuating functions. The new theory is implemented using the finite element method into a general-purpose multiscale constitutive modeling code called SwiftComp$^{\mathrm{TM}}$. To demonstrate the application of this new theory and the companion SwiftComp$^{\mathrm{TM}}$ code, we will compare the results of different micromechanics approaches for both periodic and aperiodic materials.

THEORY OF THE NEW MICROMECHANICS

Concept of structure genome

SG is so named to emphasize the fact that it contains all the constitutive information needed for a structure the same fashion as the genome contains all the intrinsic information for an organism's growth and development. For periodic structures, it is easy to identify the SG as described later. However, for real structures in engineering, we rely on the expert opinion of the analysts to determine what will be the smallest, representative building block of the structure. This liberal definition is intended for maximizing the freedom in choosing the SG. It can be justified from the view point of material characterization using experiments. When experimentalists want to find properties of a material, they cut representative pieces of the material according to their own judgment, make a specimen out of it and do the testing to get the properties and associated statistics. As we are not doing physical experiments, SG is thus defined as the smallest *mathematical* building block.

SG generalizes from the RVE concept with two fundamental differences. First, SG allows a direct connection with the macroscopic structural analysis, particularly for dimensionally reducible structures which have one or two dimensions much smaller than the other dimensions. Second, even if the macroscopic structural analysis uses a 3D model (Figure 1), SG-based theory could be more efficient than those based on RVE. For a structure made of composites featuring one-dimensional (1D) heterogeneity (e.g. binary composites made of two alternating layers), SG will be a straight line with two segments denoting corresponding layers. Mathematically speaking, we can repeat this straight line in plane to build the two layers of the binary composite, then we can repeat the binary composite out of plane to build the entire structure. For a structure made of composites featuring 2D heterogeneity (e.g. continuous unidirectional fiber reinforced composites), the SG will be a two-dimensional (2D) domain, and for a structure made of composites featuring 3D heterogeneity (e.g. particle reinforced composites), the SG will be a 3D volume. Despite of the dimensionality of SGs, the effective properties obtained from SG are 3D. For example, for linear elastic behavior, one should be able to carry out a 1D analysis over the SG of binary composites to obtain the complete 6×6 stiffness matrix. Clearly, SG uses the lowest dimension, thus highest efficiency, to describe the heterogeneity, while RVE dimen-

sion is determined by heterogeneity and by what type of properties required for the macroscopic structural analysis. If 3D properties are needed for a 3D structural analysis of continuous unidirectional fiber reinforced composites, a 3D RVE is usually required.

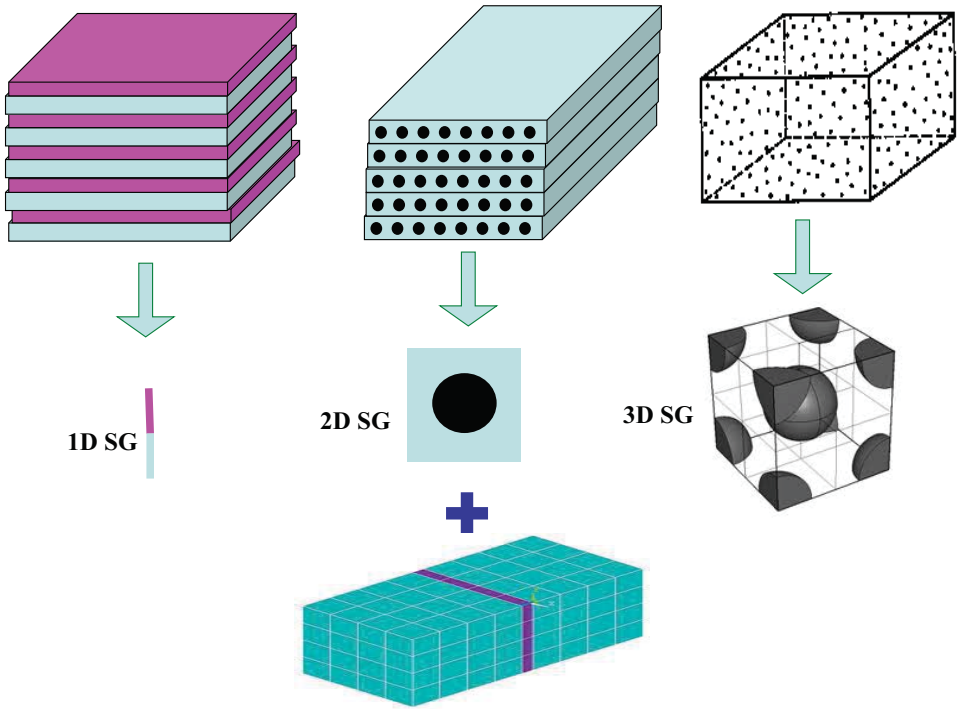

Figure 1. SG for 3D structure (cited from Ref.[7])

Theoretical formulation

To facilitate the formulation, two coordinate systems are set up. The macro coordinate system $\mathbf{x} = (x_1, x_2, x_3)$ is applied to describe the original heterogeneous structure, while micro coordinate system $\mathbf{y} = (y_1, y_2, y_3)$ is introduced to denote the rapid change in the material characteristics in SG, (Here and throughout the paper Latin indices assume 1, 2, and 3. Repeated indices are summed over their range except where explicitly indicated). As the size of SG is much smaller than the wavelength of the macroscopic deformation, we denote $y_i = x_i/\varepsilon$, with ε being a small parameter. A field function of the original heterogeneous structure can be generally written as a function of the macro coordinates x_i and the micro coordinates y_i. The partial derivative of a function $f(x_i, y_j)$ can be expressed as

$$\frac{\partial f(x_i, y_j)}{\partial x_i} = \frac{\partial f(x_i, y_j)}{\partial x_i}|_{y_j=\text{const}} + \frac{1}{\varepsilon}\frac{\partial f(x_i, y_j)}{\partial y_i}|_{x_i=\text{const}} \equiv f_{,i} + \frac{1}{\varepsilon} f_{|i} \qquad (1)$$

As stated before, SG can be 1D, 2D or 3D based on the microstructure heterogeneity. If a SG is 1D, only y_3 is needed; if a SG is 2D, y_2 and y_3 are needed; if a SG is 3D, all three coordinates y_1, y_2, y_3 are needed. For generality, we will formulate the theory for 3D SG which can be easily reduced to deal with 1D or 2D SGs. Although the proposed framework is general to handle most of micromechanics problems, this

paper focuses only on the linear, elastic, static behavior of Cauchy continuum with infinitesimal strains.

To replace the original heterogeneous material with an equivalent homogeneous material, we need to first assume that the average displacement can be represented by the equivalent homogeneous material, in other words,

$$v_i = \frac{1}{\Omega}\int_\Omega u_i \, \mathrm{d}\Omega \equiv \langle u_i \rangle \tag{2}$$

where u_i denotes the displacement of the heterogenous material, v_i denotes the displacement of the homogeneous material, Ω denotes the domain occupied by the SG and its volume, $\langle\cdot\rangle$ denotes the volume average over a SG.

We are free to express the displacement of the original heterogeneous material as

$$u_i(\mathbf{x};\mathbf{y}) = v_i(\mathbf{x}) + \varepsilon\chi_i(\mathbf{x};\mathbf{y}) \tag{3}$$

with χ_i termed as fluctuating functions. According to Eq. (2)

$$\langle \chi_i \rangle = 0 \tag{4}$$

If the original heterogeneous structure is made of materials described using a Cauchy continuum, the infinitesimal strains is defined as

$$\epsilon_{ij}(\mathbf{x};\mathbf{y}) = \frac{1}{2}\left[\frac{\partial u_i(\mathbf{x};\mathbf{y})}{\partial x_j} + \frac{\partial u_j(\mathbf{x};\mathbf{y})}{\partial x_i}\right] = \bar{\epsilon}_{ij} + \chi_{(i|j)} + \varepsilon\chi_{(i,j)} \tag{5}$$

with $\bar{\epsilon}_{ij} = v_{(i,j)}$. Here, the parenthesis in the subscripts denotes a symmetric operation, for example, $v_{(i,j)} = \frac{1}{2}\left(v_{i,j} + v_{j,i}\right)$. The last term in Eq. (5) is asymptotically smaller than the first two terms and its contribution to the energy can be neglected according to the variational asymptotic method [8]. As the equivalent homogeneous material is what we created mathematically to approximate the original heterogeneous material, we need to define the strain field in terms of that of the original heterogeneous material. For 3D structures, the natural choice is

$$\bar{\epsilon}_{ij} \equiv \langle \epsilon_{ij} \rangle \tag{6}$$

In view of Eq. (5) and (6), we have the following constraints on the fluctuating function:

$$\left\langle \chi_{(i|j)} \right\rangle = 0 \tag{7}$$

The elastic behavior of the original heterogeneous is governed by the principle of minimum total potential energy. If we are only interested in the constitutive relations, we can neglect the effects of loads and the potential energy becomes strain energy. Then we need to minimize the strain energy of the heterogeneous material along with the constraints in Eqs. (4) and (7), which means we need to minimize the following functional:

$$J = \langle \frac{1}{2} C_{ijkl}\epsilon_{ij}\epsilon_{kl} \rangle = \langle \frac{1}{2} C_{ijkl}\left(\bar{\epsilon}_{ij} + \chi_{(i|j)}\right)\left(\bar{\epsilon}_{kl} + \chi_{(k|l)}\right) \rangle - \lambda_{kl}\langle \chi_{(k|l)} \rangle - \eta_i \langle \chi_i \rangle \tag{8}$$

where λ_{kl} and η_i are Lagrange multipliers to enforce the constraints in Eqs. (7) and (4), respectively. Note $\lambda_{ij} = \lambda_{ji}$.

Finite element implementation

To solve Eq. (8) for general cases, we need to turn to numerical techniques such as the finite element method (FEM). It is possible to formulate the FEM solution based on Eq. (8) directly, however since the constraints in Eq. (4) do not affect the minimum value of J but help uniquely determine χ_i, in practice we can constrain the fluctuating functions at an arbitrary node to be zero and later use these constraints to recover the unique fluctuating functions. Introduce the following matrix notations

$$\bar{\epsilon} = \lfloor \bar{\epsilon}_{11} \;\; \bar{\epsilon}_{22} \;\; \bar{\epsilon}_{33} \;\; 2\bar{\epsilon}_{23} \;\; 2\bar{\epsilon}_{13} \;\; 2\bar{\epsilon}_{12} \rfloor^{\mathrm{T}} \tag{9}$$

$$\epsilon = \lfloor \epsilon_{11} \;\; \epsilon_{22} \;\; \epsilon_{33} \;\; 2\epsilon_{23} \;\; 2\epsilon_{13} \;\; 2\epsilon_{12} \rfloor^{\mathrm{T}} \tag{10}$$

$$\lambda = \lfloor \lambda_{11} \;\; \lambda_{22} \;\; \lambda_{33} \;\; \lambda_{23} \;\; \lambda_{13} \;\; \lambda_{12} \rfloor^{\mathrm{T}} \tag{11}$$

$$\begin{bmatrix} \frac{\partial \chi_1}{\partial y_1} \\ \frac{\partial \chi_2}{\partial y_2} \\ \frac{\partial \chi_3}{\partial y_3} \\ \frac{\partial \chi_2}{\partial y_3} + \frac{\partial \chi_3}{\partial y_2} \\ \frac{\partial \chi_1}{\partial y_3} + \frac{\partial \chi_3}{\partial y_1} \\ \frac{\partial \chi_1}{\partial y_2} + \frac{\partial \chi_2}{\partial y_1} \end{bmatrix} = \begin{bmatrix} \frac{\partial}{\partial y_1} & 0 & 0 \\ 0 & \frac{\partial}{\partial y_2} & 0 \\ 0 & 0 & \frac{\partial}{\partial y_3} \\ 0 & \frac{\partial}{\partial y_3} & \frac{\partial}{\partial y_2} \\ \frac{\partial}{\partial y_3} & 0 & \frac{\partial}{\partial y_1} \\ \frac{\partial}{\partial y_2} & \frac{\partial}{\partial y_1} & 0 \end{bmatrix} \begin{bmatrix} \chi_1 \\ \chi_2 \\ \chi_3 \end{bmatrix} = \Gamma_h \chi \tag{12}$$

where Γ_h is an operator matrix and χ is a column matrix containing the three components of the fluctuating functions. Discretize χ using the finite elements as

$$\chi(x_i; y_j) = S(y_j) V(x_i) \tag{13}$$

where S represents the shape functions and V a column matrix of the nodal values of the fluctuating functions.

Substituting Eqs. (9), (10), and (13) into Eq. (8), we obtain a discretized version of the functional J as

$$J = \frac{1}{2} \left(V^T E V + 2 V^T D_{h\epsilon} \bar{\epsilon} + \bar{\epsilon}^T D_{\epsilon\epsilon} \bar{\epsilon} \right) - \lambda^{\mathrm{T}} D_{h\lambda}^{\mathrm{T}} V \tag{14}$$

where

$$E = \left\langle (\Gamma_h S)^T D (\Gamma_h S) \right\rangle \quad D_{h\epsilon} = \left\langle (\Gamma_h S)^T D \right\rangle \quad D_{\epsilon\epsilon} = \langle D \rangle \quad D_{h\lambda} = \langle \Gamma_h S \rangle^{\mathrm{T}} \tag{15}$$

with D as the 6×6 material matrix condensed from the fourth-order elasticity tensor C_{ijkl} of the heterogeneous material. Minimizing J in Eq. (14) gives us the following linear system

$$\begin{bmatrix} E & -D_{h\lambda} \\ -D_{h\lambda}^{\mathrm{T}} & 0 \end{bmatrix} \begin{bmatrix} V \\ \lambda \end{bmatrix} = \begin{bmatrix} -D_{h\epsilon} \bar{\epsilon} \\ 0 \end{bmatrix} \tag{16}$$

It is clear that V will linearly depend on $\bar{\epsilon}$, and the solution can be symbolically written as

$$V = V_0 \bar{\epsilon} \tag{17}$$

With the solution in Eq. (17), we can calculate the strain energy storing in the SG as the first approximation as

$$U = \frac{1}{2}\bar{\epsilon}^{\mathrm{T}}\left(D_{\epsilon\epsilon} + V_0^{\mathrm{T}} D_{h\epsilon}\right)\bar{\epsilon} \equiv \frac{\Omega}{2}\bar{\epsilon}^{\mathrm{T}}\bar{D}\bar{\epsilon} \tag{18}$$

where $\bar{D}$ is the effective stiffness matrix to be used in the macroscopic structural analysis.

The local fields within the SG can also be recovered easily based on the global displacement v_i and global strain $\bar{\epsilon}$. First knowing $\bar{\epsilon}$, we can compute the fluctuating function as

$$\chi = SV_0\bar{\epsilon} \tag{19}$$

The local strain field can be recovered using Eq. (12) as

$$\epsilon = \bar{\epsilon} + \Gamma_h SV_0\bar{\epsilon} \tag{20}$$

The local stress field can be obtained directly using the Hooke's law as

$$\sigma = D\epsilon. \tag{21}$$

VALIDATION AND APPLICATION

The present theory is implemented in the general-purpose multiscale constitutive modeling code, SwiftComp$^{\mathrm{TM}}$. Note that within the framework of the proposed theory, other constraints can be easily added to Eq. (8). For example, if a microstructure has periodicity in three directions, PBCs can be used. In this case, PBCs automatically satisfy the constraints in Eq. (7). The present theory can also handle structures with partial periodicity. For example, if a composite structure has periodicity only in the in-plane directions x_1 and x_2, applying PBCs to all the three dimensions of the SG will result in significant errors which can be seen in the examples in the next section. In this case in SwiftComp$^{\mathrm{TM}}$, the user are allowed to apply periodic constraints to surfaces normal to y_1 and y_2 according to the periodicity of the material microstructure, while keep the constraints related to y_3 defined by Eq. (7) still be satisfied in SG. We name these combined constraints as 'MIX001', where the '0' at the first place denotes periodicity in x_1 direction, the '0' at the second place denotes periodicity in x_2 direction, and '1' at the third place denotes no extra constraint is applied at constraints in Eq. (7) related to y_3. Following the same way, different combination of constraints can be named as 'MIXijk', where the place of the number i, j, k denotes the corresponding axis direction, and number '0' at i denotes periodicity in x_i direction. Therefore, 'MIX011' means periodic constraints are applied to surfaces normal to x_1, 'MIX010' means periodic constraints are applied to parallel surfaces normal to x_1 and x_3 respectively.

In this section, the convergence study of effective properties calculated by introducing different constraints is first conducted to show the influence of the different constraints, and then a realistic woven composite structure is studied using the current theory and the SwiftComp$^{\mathrm{TM}}$ code. The results are compared with 3D FEA direct numerical simulation to demonstrate the effectiveness of the theory in both homogenization and dehomogenization.

Convergence study: Unidirectional fiber reinforced composite with different constraints

In order to understand the influence of the different constraints, a case study of a unidirectional fiber reinforced composite is used. It is made of an isotropic matrix material ($E = 3.54$ GPa, $\nu = 0.37$) and a transversely isotropic fiber ($E_L = 58.61$ GPa, $E_T = 14.49$ GPa, $G_{LT} = 5.38$ GPa, $\nu_{LT} = 0.250$, $\nu_{TT} = 0.247$) with volume fraction of fiber equal to 0.6. 3D SG and 2D SG are shown in Figure 2. In the convergence study, the number of SGs are increased from 1 to 3 in each direction, therefore the the total number of SGs increased from 1 to 8 and then to 27.

(a) 3D SG (b) 2D SG

Figure 2. SG of the unidirectional fiber reinforced composite

Homogenization are conducted with different constraints, including PBCs, KUBCs, SUBCs, and three combined constraints MIX011, MIX010 and MIX001. The results are presented in Figure 3, in which the vertical axis value r is the relative difference calculated by Eq. (22)

$$r = (P - P_{PBCs})/P_{PBCs} \times 100(\%) \tag{22}$$

where P is a certain effective property calculated using the considered constraints, P_{PBCs} is the corresponding effective property obtained with PBCs using 27 SGs. It is shown that E_1, E_2, G_{12}, G_{13} obtained from combined constraints MIX011, MIX010 and MIX001 lie between the bound values from using KUBCs and SUBCs. And all the effective properties P show an expected convergence to P_{PBCs}. For SG with periodicity in all three directions, results remain the same not matter how many SGs used in the analysis. In addition, if periodicity in any direction is reserved, the related effective properties will be closer to that obtained from PBCs. Apparently, this phenomenon is consistent with well accepted observation that KUBCs model gives the stiffest (most kinematically constrained solution) to the microscopic equilibrium problem, followed in order of decreasing stiffness by PBCs, and SUBCs.

It is also note worthy that in this case the 3D SG features no heterogeneity in x_1 direction, therefore a 2D SG as shown in Figure 2(b) can be used to produce exactly the same effective property values with 3D SG once the applied constraints are identical. For example, if the constraints in Eq. (7) is applied on a 2D SG, the resulting effective properties are exactly the same with that produced by 3D SG with MIX011 constraint, since the availability of 2D SG is based on the periodicity in the x_1 direction. The principle also applies to microstructures featuring 1D heterogeneity.

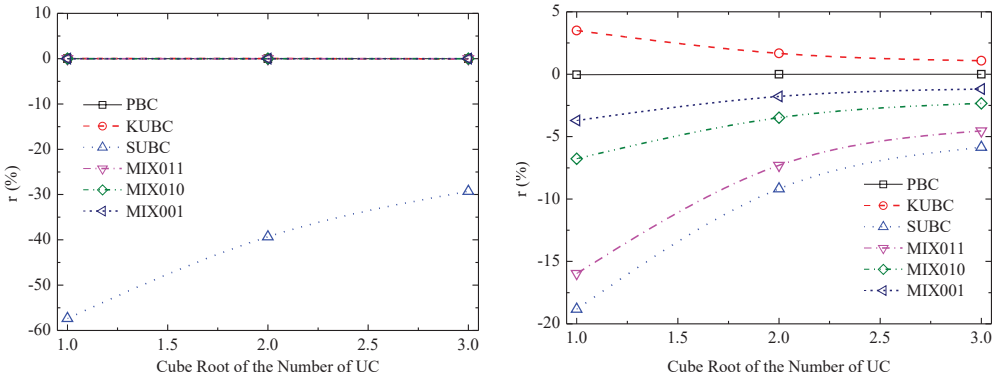

(a) Convergence of E_1 (b) Convergence of E_2

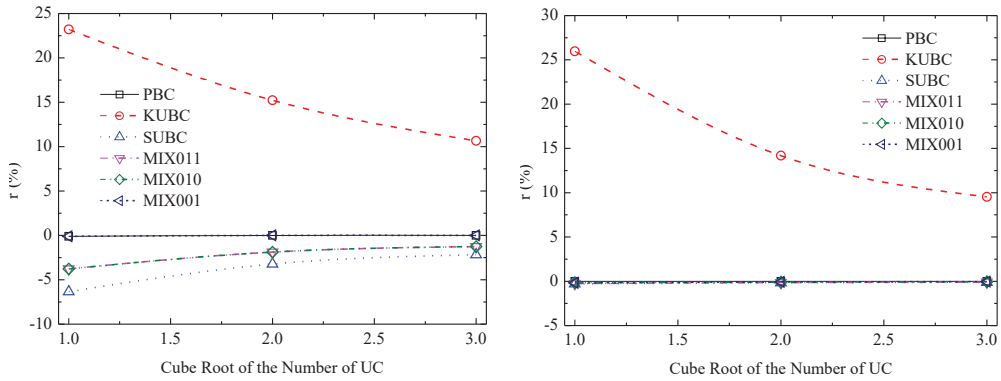

(c) Convergence of G_{12} (d) Convergence of G_{23}

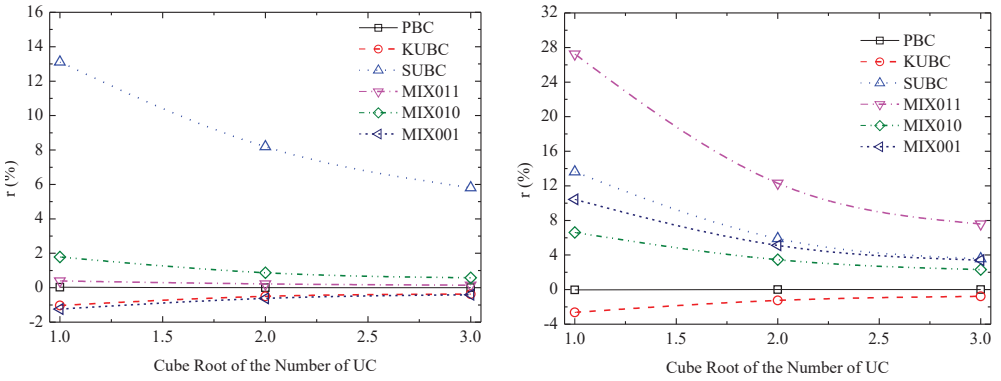

(e) Convergence of ν_{12} (f) Convergence of ν_{23}

Figure 3. Convergence study of results

It is clear that SG uses the lowest dimension, thus has the highest efficiency, as a micromechanics theory.

Example of 3D orthogonal interlock composites

To demonstrate the potential usage of the proposed theory in practice, a realistic 3D orthogonal interlock composites structure is studied under two loading cases. The composites structure is constructed by repeating the microstructure of Figure 4 only in the in-plane direction. The material properties of constituents is listed in Table I. It is important to note that there is a horizontal portion of z-tow in the upper part of the repeating SG. Hence only in-plane periodicity is preserved, PBC in the thickness direction should not be used. To deal with this partial periodicity, Ref. [9] studied this composite structure by asymptotic expansion homogenization method, predicted the lamina constants ($E_1, E_2, G_{12}, \nu_{12}$) of the composite structure and compared them with that obtained from homogenization implementing PBCs. Furthermore, local stress fields obtained from biaxial tensile loading are recovered but not compared with direct FEA results in [9]. According to [9], free traction must be ensured at the top and bottom surfaces as this is what was assumed in the derivation.

Applying the present theory for this specific case, a good choice of constraints are periodic constraints applied to the surfaces of SG normal to the micro y_1 and y_2 directions in addition to the necessary constraints in Eq. (7) (named 'MIX001'). In Table II, the 3D effective properties ($E_1, E_2, E_3, G_{23}, G_{13}, G_{12}, \nu_{23}, \nu_{13}, \nu_{12}$) predicted with this set of constraints are presented and compared with those calculated by applying PBCs to all the directions. Both sets of effective properties are calculated using the same mesh with global mesh size of 0.15 mm using SwiftComp$^{\mathrm{TM}}$. It is shown the major differences are in the properties (E_3, ν_{23}, ν_{13}) which are related to the y_3 direction.

Next, we want to carry out the dehomogenization procedure to obtain the local stress distribution and compare those using 3D FEA results. To perform dehomogenization, a 3D structure analysis using 3D elements with obtained effective material properties is carried out, from which the volume average strain $\bar{\epsilon}$ of SG is obtained and then used in dehomogenization. Local stresses from dehomogenization using constraints MIX001 and PBCs are also compared to show the capability of the current theory.

The first case has the same configuration as the biaxial loading case in [9]. The plate structure has a dimension of $75 \times 30 \times 3.576$ mm^3, which contains 25 SGs along x_1 and 5 SGs along x_2. The model configuration is shown in Figure 5. Dehomogenization is performed at the SG located at the center of the structure. The stress distributions on three sampling paths Line A, Line B and Line C shown in Figure 5 are investigated. The macro coordinates (x_1, x_2) of the three paths A, B and C are (37.5, 7.5), (37.5, 8.925) and (38.925, 6.075) respectively. Interested users can refer to Ref.[9] for specific corresponding SG constituents along thickness direction of each line. The dominant stress components σ_{11}, σ_{22} and σ_{33} at these three paths through the thickness of the plate structure are compared in (a), (c), (e) of Figure 7, Figure 8 and Figure 9.

The second case is under a uniform compression loading 1 MPa at the top and

bottom surfaces through the thickness direction. The detailed settings of the second loading cases are shown in Figure 6. Normal stresses at Line A (37.5, -7.5), Line B (37.5, -6.075) and Line C (38.925, -8.925) are compared in (b), (d), (f) of Figure 7, Figure 8 and Figure 9. It is shown that for such highly heterogeneous composite structure, the stress distributions agree well with that of 3D FEA except some minor discrepancy close to the top and bottom surfaces in the thickness direction. Particularly, σ_{33} at all the three paths predicted by MIX001 constraints show much better correspondence compared with those predicted by PBC. In the uniform compression loading case, some of the shear stress components are in the same order with the normal stress components. The shear stress components at Line C are shown in Figure 10. Similarly, the stress distributions predicted by the constraints MIX001 can capture both the variation and the magnitude compared with 3D FEA results. However while the 3D FEA took 75 minutes with 20 CPUs, the homogenization and dehomogenization process of the current case cost only 80 seconds with only 1 CPU. The present theory is clearly more efficient and accurate. Note this structure can also be analyzed as a plate with the corresponding constitutive relations obtained using a plate SG in SwiftComp, which is studied in [10].

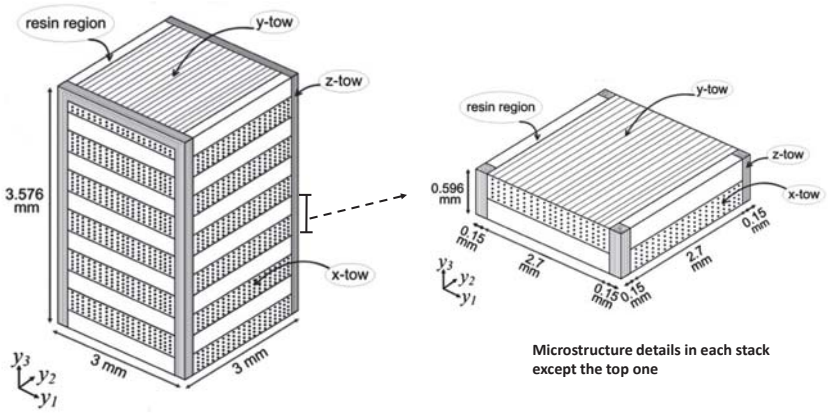

Figure 4. SG of the orthogonal interlock composites (cited from Ref.[9])

TABLE I. MATERIAL PROPERTIES OF THE ORTHOGONAL INTERLOCK COMPOSITES

Properties	X-tow	Y-tow	Z-tow	Resin region
E_1 (GPa)	122.55	7.13	4.96	3.40
E_2 (GPa)	7.13	122.55	4.96	3.40
E_3 (GPa)	7.13	7.13	148.70	3.40
G_{12} (GPa)	3.25	3.25	2.45	1.26
G_{31} (GPa)	3.25	2.53	3.21	1.26
G_{23} (GPa)	2.53	23.25	3.21	1.26
ν_{12}	0.263	0.015	0.476	0.35
ν_{31}	0.015	0.414	0.335	0.35
ν_{23}	0.414	0.263	0.011	0.35

TABLE II. COMPARISON OF EFFECTIVE PROPERTIES OF WOVEN COMPOSITE

Properties	MIX001	PBC	Diff % (based on PBC)
E_1 (GPa)	59594	59642	-0.08
E_2 (GPa)	57145	57515	-0.64
E_3 (GPa)	8576	8914	-3.79
G_{12} (GPa)	2974	2980	-0.20
G_{13} (GPa)	2658	2663	-0.16
G_{23} (GPa)	2653	2657	-0.16
ν_{12}	0.0335	0.0342	-1.86
ν_{13}	0.3661	0.3525	3.85
ν_{23}	0.3702	0.3556	4.09

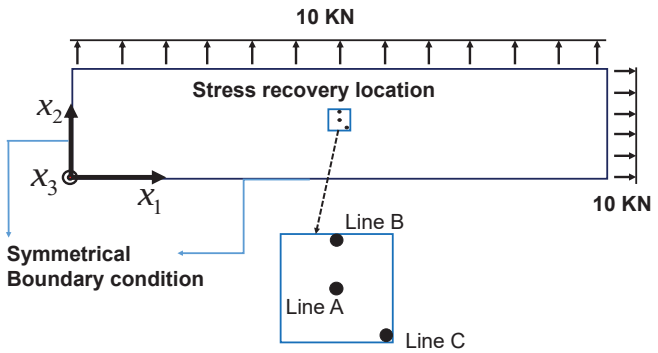

Figure 5. Configuration of the 3D orthogonal interlock composite plate under biaxial load

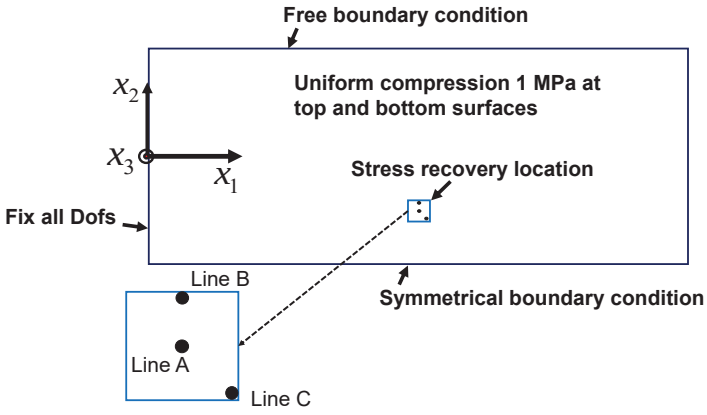

Figure 6. Configuration of the 3D orthogonal interlock composite plate under compression load

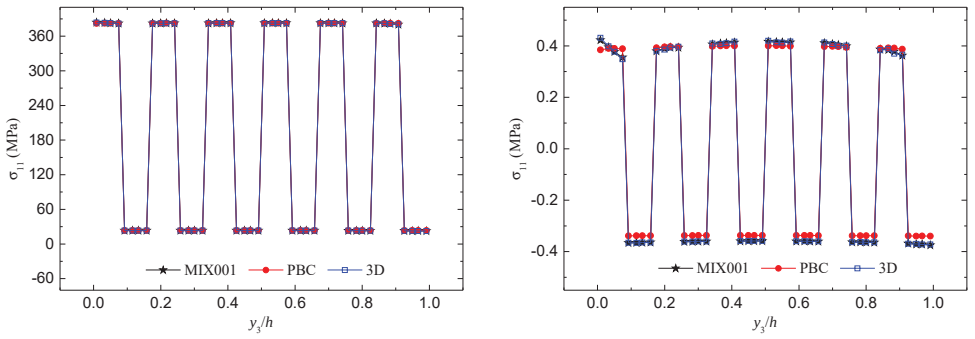

(a) σ_{11} under biaxial loading

(b) σ_{11} under compression load

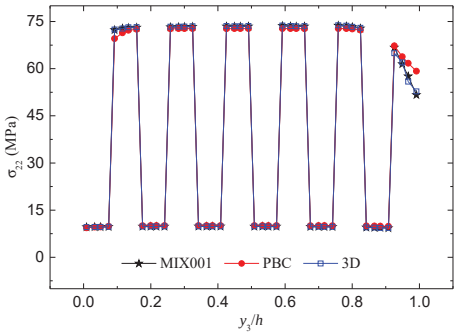

(c) σ_{22} under biaxial load

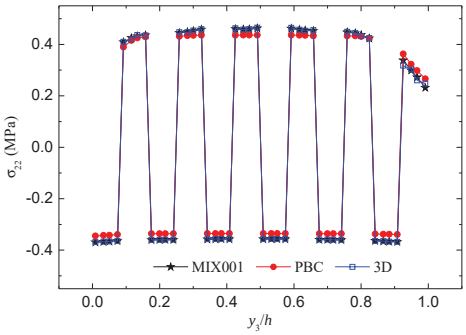

(d) σ_{22} under compression load

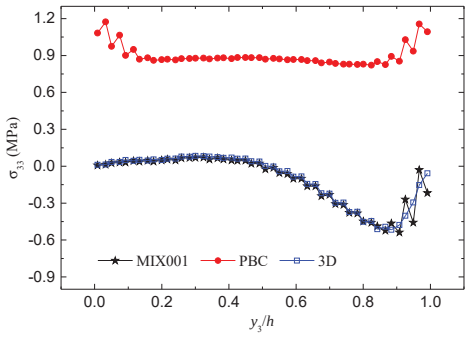

(e) σ_{33} under biaxial load

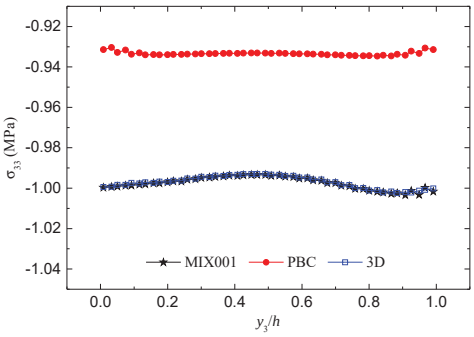

(f) σ_{33} under compression load

Figure 7. Comparison of stress distributions through the normalized thickness along line A

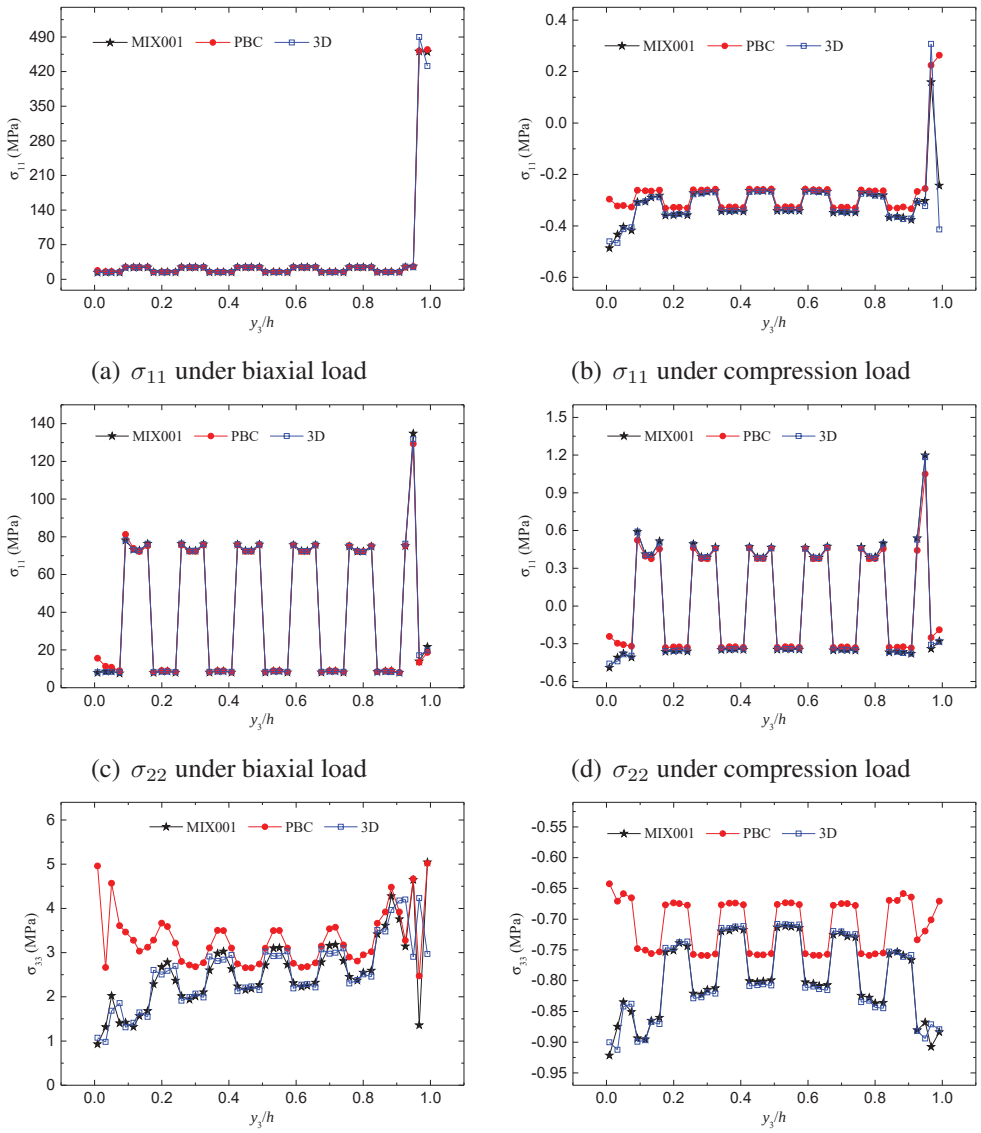

(a) σ_{11} under biaxial load

(b) σ_{11} under compression load

(c) σ_{22} under biaxial load

(d) σ_{22} under compression load

(e) σ_{33} under biaxial load

(f) σ_{33} under compression load

Figure 8. Comparison of stress distribution through the normalized thickness along line B

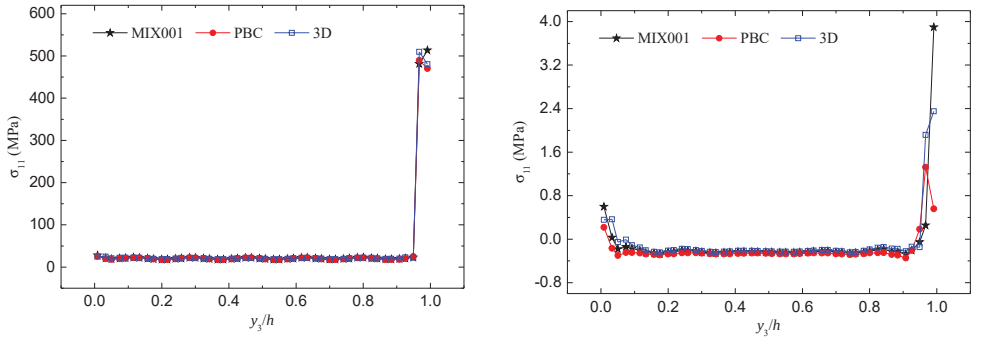

(a) σ_{11} under biaxial load

(b) σ_{11} under compression load

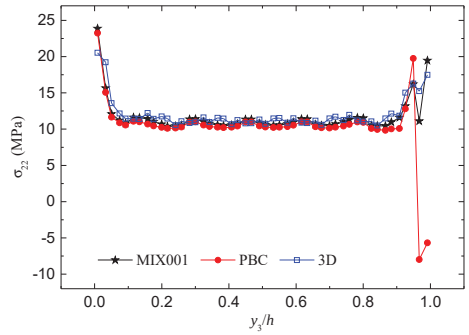

(c) σ_{22} under biaxial load

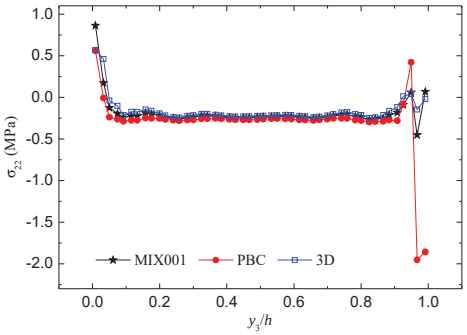

(d) σ_{22} under compression load

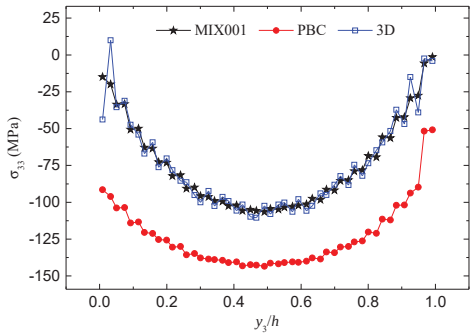

(e) σ_{33} under biaxial load

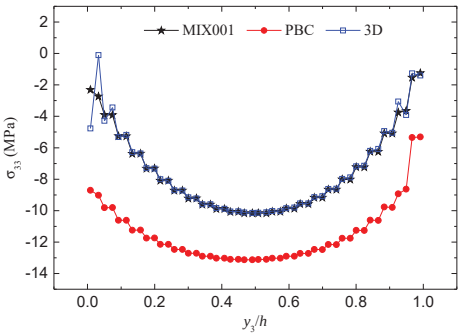

(f) σ_{33} under compression load

Figure 9. Comparison of stress distribution through the normalized thickness along line C

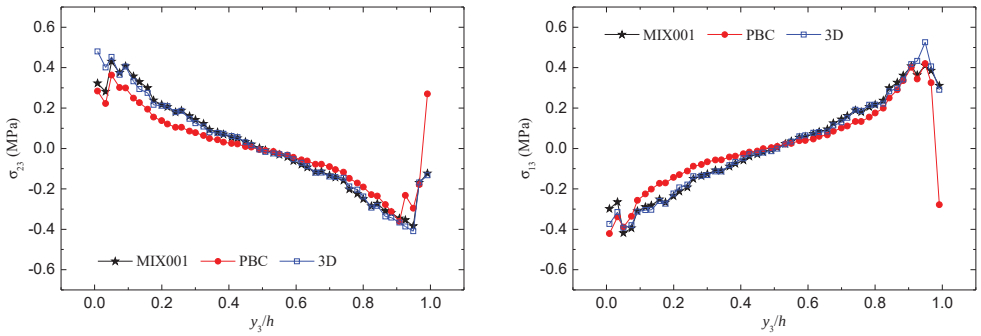

(a) σ_{23} under biaxial load (b) σ_{13} under biaxial load

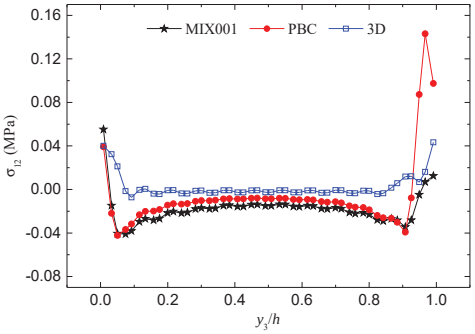

(c) σ_{12} under biaxial load

Figure 10. Shear stress distribution through the normalized thickness along line C under compressive load

CONCLUSIONS

A new micromechanics theory is developed for both homogenization and dehomogenization. The theory is based on the concept of structure genome through minimizing the energy of the original heterogeneous materials. As no boundary conditions are involved except the constraints to ensure kinematics equivalency between the heterogeneous material and the equivalent homogeneous material, the theory can be applied to SG of arbitrary shape. In addition, this theory provides a general framework for homogenization and dehomogenization of heterogeneous materials. It can handle aperiodic materials, materials with partial periodicity, or material with complete periodicity. Second, SG can use the lowest dimension to describe the heterogeneity. This theory has been implemented into a general-purpose computer code SwiftComp$^{\mathrm{TM}}$ using the finite element method. By using realistic numerical examples, it is demonstrated that the new theory shows good accuracy compared with the 3D direct FEA with meshing all the microstructural details. Although in this paper, the most simple case of linear elastic material undergo small deformation is studied, the present theory can be easily extended to handle more complex situations. The general-purpose multiscale constitutive modeling code SwiftComp$^{\mathrm{TM}}$ can be accessed in the cloud at cdmHUB.org.

ACKNOWLEDGEMENTS

This work is supported by the US AFOSR Multiscale Structural Mechanics and Prognosis Program. The views and conclusions contained herein are those of the authors and should not be interpreted as necessarily representing the official policies or endorsement, either expressed or implied, of the sponsor.

REFERENCES

1. Hill, R. 1963, "Elastic Properties of Reinforced Solids: Some Theoretical Principles," *Journal of Mechanics and Physics of Solids*, 11:357–372.
2. Pindera, M.-J., H. Khatam, A. S. Drago, and Y. Bansal. 2009, "Micromechanics of spatially uniform heterogeneous media: a critical review and emerging approaches," *Composites Part B: Engineering*, 40(5):349–378.
3. Mesarovic, S. D. and J. Padbidri. 2005, "Minimal kinematic boundary conditions for simulations of disordered microstructures," *Philosophical Magazine*, 85(1):65–78.
4. Jänicke, R. and H. Steeb. 2012, "Minimal loading conditions for higher-order numerical homogenisation schemes," *Archive of Applied Mechanics*, 82(8):1075–1088.
5. de Souza Neto, E. A. and R. Feijóo. 2011, "Variational foundations of large strain multiscale solid constitutive models: kinematical formulation," *Advanced Computational Materials Modeling: From Classical to Multi-Scale Techniques. Wiley-VCH, Weinheim*.
6. Blanco, P. J., P. J. Sánchez, E. A. de Souza Neto, and R. A. Feijóo. 2014, "Variational Foundations and Generalized Unified Theory of RVE-Based Multiscale Models," *Archives of Computational Methods in Engineering*, pp. 1–63.
7. Yu, W. 2015, "Structure Genome: Fill the Gap between Materials Genome and Structural Analysis," in *56th AIAA/ASCE/AHS/ASC Structures, Structural Dynamics, and Materials Conference*, AIAA SciTech.

8. Berdichevskii, V. 1979, "Variational-asymptotic method of constructing a theory of shells: PMM vol. 43, no. 4, 1979, pp. 664–687," *Journal of Applied Mathematics and Mechanics*, 43(4):711–736.
9. Nasution, M. R. E., N. Watanabe, A. Kondo, and A. Yudhanto. 2014, "A novel asymptotic expansion homogenization analysis for 3-D composite with relieved periodicity in the thickness direction," *Composites Science and Technology*, 97:63–73.
10. Peng, B. and W. Yu. 2015, "Remove Homogeneous Layer Assumption from Lamination Theories," in *30th American Society of Composites Technical Meeting*, DEStech Publications, Inc.

An Introduction to Micromechanics

Wenbin Yu[1,a]

[1]Purdue University, West Lafayette, Indiana, 47907-2045, USA

[a] wenbinyu@purdue.edu

Keywords: Micromechanics; Mechanics of Structure Genome; Mathematical Homogenization Theory; RVE Analysis; Rules of Mixtures

Abstract. This article provides a brief introduction to micromechanics using linear elastic materials as an example. The fundamental micromechanics concepts including homogenization and dehomogenization, representative volume element (RVE), unit cell, average stress and strain theories, effective stiffness and compliance, Hill-Mandel macrohomogeneity condition. This chapter also describes the detailed derivations of the rules of mixtures, and three full field micromechanics theories including finite element analysis of a representative volume element (RVE analysis), mathematical homogenization theory (MHT), and mechanics of structure genome (MSG). Theoretical connections among the three full field micromechanics theories are clearly shown. Particularly, it is shown that RVE analysis, MHT and MSG are governed by the same set of equations for 3D RVEs with periodic boundary conditions. RVE analysis and MSG can also handle aperiodic or partially periodic materials for which MHT is not applicable. MSG has the unique capability to obtain the complete set of 3D properties and local fields for heterogeneous materials featuring 1D or 2D heterogeneities.

Introduction

Composites by nature are anisotropic and heterogeneous while most conventional materials such as metals can be safely assumed to be isotropic and homogeneous. Anisotropy can be dealt with using coordinate transformation by transforming the material properties measured in the material coordinate into those expressed in the problem coordinates. In principle, heterogeneity can be handled by direct numerical simulation (DNS) of the composite structure containing all the microstructural details using the finite element analysis (FEA). But this requires an extremely fine scale finite element mesh with enormous numbers of degrees of freedom (DOFs). For example, using the finite element analysis to analyze epoxy/caborn fiber reinforced composites capturing the fiber details, we need the element size to be smaller than the diameter of the carbon fiber, usually a few microns. With this type of discretization, we need to have dozens of millions DOFs in our FEA model to analyze even a very tiny 1 mm^3 material block. For most realistic composite structures in engineering, trillions of DOFs are needed. Most engineers will not have access to computing hardware and software which can handle such a huge finite element model. In another hand, it is often an unnecessary waste of engineers' time and computing resources to use DNS for composite structures capturing fiber details. With properly constructed models, we can replace composites with an effective homogeneous material to achieve almost the same accuracy as DNS at a cost many orders of magnitude less, except at the places having significant changes in geometry, load conditions, material properties, or close to the boundaries. The saving of engineers' time and computing resources can be used for exploring more advanced designs and technological innovations. The concept to replace the original heterogeneous materials with homogeneous material which are imaginary, yet equivalent in some sense, is called homogenization. This concept is fundamental in engineering design and analysis because we usually characterize a material, composites or not, in terms of continuous field and neglect the underlying atomic structure of the material. For example, temperature is defined as a measurement of the average kinetic energy of the molecules in an object or system. Such a homogenization can be achieved using experiments or atomistic simulations. Particularly for composites, we deal with heterogeneities at the size of micron and larger and assume the constituents of composites can be adequately described as continuum with

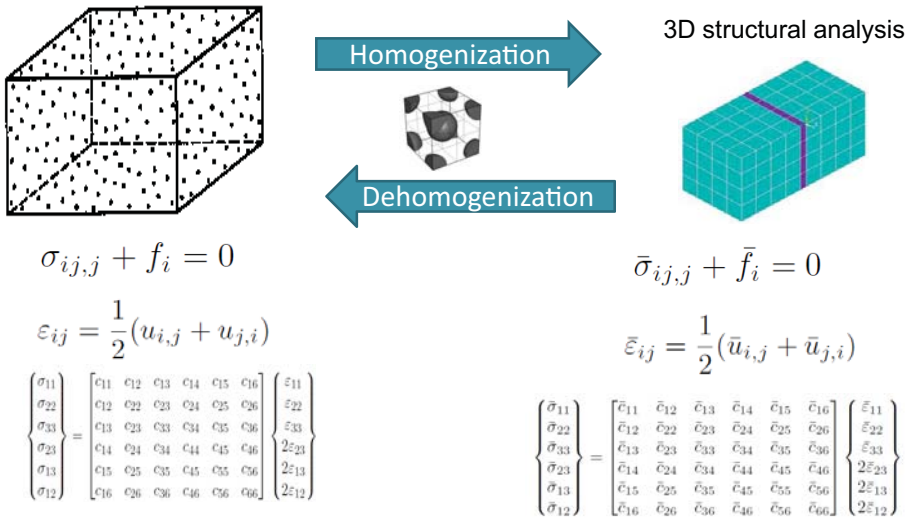

Fig. 1: Basic idea of micromechanics

the constitutive models of constituents simpler than the constitutive models we need to use to model the composite.

The basic idea of micromechanics is to replace the original heterogeneous material with an imaginary homogenous material so that the analysis of the original structure made of heterogeneous materials can be simplified (Fig. 1). The first aim of micromechanics is to theoretically predict the effective macroscopic properties of heterogeneous materials in terms of microstructure. Here microstructure contain geometry and constitutive relations of constituents. This step is also commonly called homogenization, and many early models were developed solely for this purpose [1, 2, 3, 4, 5, 6, 7]. Homogenization can be used either for virtual material characterization, i.e., simulating the overall material response under simple loading conditions, or constitutive modeling, where the complete set of effective material properties must be deduced and used as inputs for the structural analysis to predict the macroscopic behavior. The material properties obtained are usually properties for three-dimensional (3D) structural analysis. The second aim of micromechanics is to predict the microscopic fields such as displacement, stress and strain fields within the microstructure from the macroscopic behavior. This step is also commonly called localization or dehomogenization and is very critical for assessment of the strength and failure of heterogeneous materials. Dehomogenization is usually more demanding than homogenization as the local fields are very sensitive to the microstructural details. To achieve the above two aims, micromechanics has to assume that the constitutive models and material properties of the constituents are known. However, it is often difficult to measure the constituent properties but it is relatively easier to measure the composite properties. To this end, micromechanics can be used to back calculate the constituent properties from composite properties through an inverse analysis, so-called reverse engineering, the solution of which is usually not unique and the analysis can be casted as an optimization problem.

Many modeling techniques have been introduced to provide either rigorous bounds, such as the rules of mixtures [8], Hashin-Shtrikman bounds [9], third-order bounds [3], higher-order bounds [10], or approximate predictions including mean field approaches such as dilute method, Mori-Tanaka method, self-consistent method, generalized self-consistent method, or full field approaches such as the method of cells [11, 12] and its variants [13, 14, 15], mathematical homogenization theories (MHT) [16, 17, 18, 19], finite element approaches using conventional stress analysis of RVE [20, 21], Voronoi cell finite element method [22], and mechanics of structure genome (MSG) [23].

Microstructure, Representative Volume Element, and Unit Cell

We purposely neglected the microstructure of composites in our macroscopic structural analyses for efficiency. However, we need to capture the effects of microstructure on effective properties and local fields using micromechanics models. Although we can observe the physical microstructure of a material, its complexity may prevent its use in micromechanics modeling. Hence, the microstructures we use in micromechanics may or may not correspond to what we can observe in reality. This presents a direct contrast with other mechanics subject such as structural mechanics, which we usually have a well defined domain with easily recognizable boundaries to work with. The reason being that the heterogeneous material is essentially represented as a point in our macroscopic structural analysis, the size of that material point is irrelevant and it could contain one or many fundamental building blocks of the material, if such fundamental building blocks can be identified. However, we do need a microstructure to infer how the effective material properties of the heterogeneous material relate with the geometry and properties of its constituents. The fundamental requirement of a microstructure for micromechanics model is being representative of the material of which the macroscopic structure can be considered as made of.

It is the very first step of micromechanics to come up with the right microstructure. The choice of microstructure is not only related with the real material but also depends on the micromechanics model the analyst chooses to use. For example, if rules of mixtures are used, then the microstructure can be simply described using volume fractions of constituents. This is actually the simplest microstructure. As a general rule, the complexity, usually also the representativeness, of the microstructure increases with the increased complexity of micromechanics models.

Generally speaking, there are four ways to obtain a microstructure for the purpose of micromechanics modeling. First, one can idealize the observed microstructural features of the material using simple geometric models such as composite cylinders assembly, square or hexagonal pack microstructure for continuously fiber reinforced composites (CFRC), etc. Second, one can reconstruct a microstructure based on the statistical information such as correlation functions obtained from the corresponding real microstructure [10]. The one-point correlation function actually corresponds to the volume fraction of the constituent. The third approach is to reconstruct the microstructure using image data obtained using techniques such as using X-ray microtomography. Computer software tools like Simpleware can be used for this purpose. This approach has the potential to come up with the most realistic representation of the microstructure, although it usually end up with a huge finite element model for the micromechanics analysis. The four approach is to predict the microstructure from simulating the manufacturing process. With increased fidelity and predictive capability of manufacturing simulation software, this approach can obtain more and more realistic microstructures needed for micromechanics modeling.

The predictability of any micromechanics model greatly depends on whether we can accurately account for the material behavior of individual constituents and their geometry and topology. To this end, we need to first identify a microscopic domain representative of the heterogeneous material, usually called the representative volume element (RVE) in micromechanics taxonomy. RVE was originally defined as a material volume entirely typical of the whole mixture on average and contains a sufficient number of inclusions for the apparent overall properties to be effectively independent of the boundary conditions [24]. Although this definition is theoretically sound on the ergodic principle, it creates a paradox. On one hand, RVE must include a sufficient number of heterogeneities for the effective properties independent of boundary conditions, while on the other hand, it must be small enough to be justified as a material point for the macroscopic structural analysis. To resolve this dilemma, other definitions of RVE have been proposed [25, 26, 27, 6]. Most definitions are a posteriori as they mainly focus on minimizing the statistical scatter of effective properties, which are known only after one has chosen the RVE and performed the micromechanical analysis. In addition to different assumptions inherently implied by different RVE definitions, micromechanics models, particularly the earlier analytical models, also commonly make assumptions regarding geometry shape and topology of the

RVE and its constituents, such as the composite spheres model, the composite cylinder model, and the three-phase model [1]. Although different mathematically oriented definitions are given for an RVE in the literature [2], we give a practice-oriented definition for an RVE as any block of material the analyst wants to use for the micromechanical analysis to find the effective properties to replace it with an equivalent homogeneous material. This liberal definition is intended for maximizing the freedom in choosing the RVE. It can be justified from the view point of material characterization using physical experiments. When experimentalists want to find properties of a material, they cut representative pieces of the material according to their own judgment and do the testing to get the properties and associated statistics.

The term unit cell (UC) is also used extensively and sometimes interchangeably with RVE in the literature. UC refers to the fundamental building block of the material. Its use is more frequently associated with materials featuring periodic heterogeneities and UC can be clearly defined as a repeating unit cell for these materials. Fundamentally speaking, by assuming the existence of RVE, we actually implicitly assume that homogeneous material we used in the macroscopic structural analysis contains many such RVEs. In other words, we implicitly assume that the material features periodic heterogeneities, at least locally in the neighborhood of the material particle we used the effective properties computed from the RVE. In principle, if the material microstructure changes significantly, we might need to have different RVEs at different locations of the composite structure. But not matter what, at each location of the composite structure, the material are implicitly assumed to contain many same RVEs at the same location. Otherwise, micromechanics is not applicable. Therefore, it is not right to say that one micromechanics method can handle aperiodic materials yet another one cannot. Micromechanics fundamentally assumes the material is at least locally periodic where RVE or UC is defined. Another point worthy to point out is that the choice of RVE and UC is not unique, even for periodic materials. For example as shown in Figure 2, one can chose six different UCs to represent the microstructure of a CFRC. In fact, there are infinite many choices of the UC as long as this material can be assembled by composing many such UCs, neglecting the partial cells at the boundary. As we are modeling the same CFRC material, a good micromechanics theory should compute the same effective properties. It is analogous to solve the same problem using different coordinate systems. Unfortunately this is not the case for most micromechanics theories. Most micromechanics theories can only deal with UCs with straight edges normal to each other (UC1, UC2, UC3 in Fig. 2). And even for these three choices, some micromechanics theories might compute different effective properties.

To facilitate mathematical formulation, we describe the macroscopic structure using a global coordinate system x_i. As the size of RVE is much smaller than the size of the macroscopic structure, we introduce a local coordinate system $y_i = x_i/\delta$ to describe the RVE, with δ being a small parameter. This basically enables a zoom-in view of the RVE at the size similar as the macroscopic structure.

Volume Average

As the RVE is effectively considered as a material point in the macroscopic analysis, we need to come up with a single value to represent the RVE in the macroscopic analysis. For this purpose, it is natural to compute the volume average of quantities of interest over the RVE such that

$$\bar{f} = \langle f \rangle \equiv \frac{1}{V} \int_V f \mathrm{d}V \tag{1}$$

where V is the volume of RVE and the angle brackets denote the volume average. Note f could be a scalar, vector, or tensor and is in general a pointwise varying function within the RVE while $\bar{f}$ is the corresponding effective quantity.

Using the conservation of mass, the effective density can be computed as

$$\bar{\rho} = \langle \rho \rangle \tag{2}$$

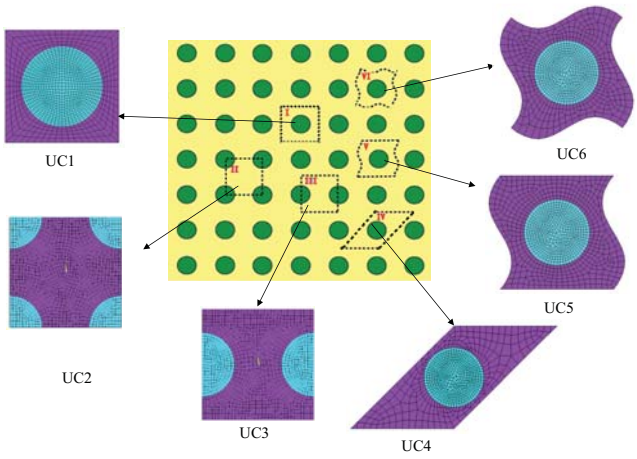

Fig. 2: Six UC choices for CFRC

Average Stress Theorem

If a heterogenous body, in static equilibrium, is subjected only to tractions along the boundary which is generated by a constant stress tensor $\bar{\sigma}_{ij}$ along the boundary. That is, the applied traction vector is $t_i^0 = \bar{\sigma}_{ij} n_j$ with n_j as the outward normal of the boundary. Then, the average of the stress field inside the body is equal to $\bar{\sigma}_{ij}$.

In general the stress field, σ_{ij}, is not constant within the body, as the body is heterogeneous. Because the body is only subjected to tractions (no body force), the stress field should satisfy the equilibrium equation

$$\sigma_{ij,j} = 0 \tag{3}$$

with comma denoting partial derivative with respect to the local coordinate system y_j. We have

$$\sigma_{ij} = \sigma_{ik}\delta_{jk} = \sigma_{ik}\frac{\partial y_j}{\partial x_k} = (\sigma_{ik}y_j)_{,k} - \sigma_{ik,k}y_j = (\sigma_{ik}y_j)_{,k} \tag{4}$$

Then we can deduce the following:

$$\begin{aligned}\langle\sigma_{ij}\rangle &= \frac{1}{V}\int_V \sigma_{ij}\mathrm{d}V = \frac{1}{V}\int_V (\sigma_{ik}y_j)_{,k}\mathrm{d}V = \frac{1}{V}\oint_{\partial V}\sigma_{ik}y_j n_k \mathrm{d}S \\ &= \frac{\bar{\sigma}_{ik}}{V}\oint_{\partial V} y_j n_k \mathrm{d}S = \frac{\bar{\sigma}_{ik}}{V}\int_V y_{j,k}\mathrm{d}V = \bar{\sigma}_{ij}\end{aligned} \tag{5}$$

where S denotes the bounding surface of the volume. This is a fundamental result in micromechanics called *Average Stress Theorem*. What this theorem tells us is that when a heterogeneous body is subjected to the traction boundary condition generated by a constant stress tensor $\bar{\sigma}_{ij}$, the stress averaged over the entire body is the same as $\bar{\sigma}_{ij}$, regardless the complexity of the stress field within the body.

Eq. (5) also implies that the average stress of an RVE can be computed by the tractions t_i^0 along the boundary such that

$$\bar{\sigma}_{ij} = \langle\sigma_{ij}\rangle = \frac{1}{V}\oint_{\partial V}\sigma_{ik}y_j n_k \mathrm{d}S = \frac{1}{V}\oint_{\partial V} t_i^0 y_j \mathrm{d}S \tag{6}$$

because we know from elasticity that the stress field must satisfy the traction boundary condition: $t_i^0 = \sigma_{ik}n_k$ although t_i^0 might not be generated from a constant stress tensor according to $t_i^0 = \bar{\sigma}_{ik}n_k$.

Average Strain Theorem

If a continuous body with perfect bonding between constituents is subjected to applied displacement boundary conditions generated by a constant strain tensor $\bar{\varepsilon}_{ij}$ along the boundary such that $u_i^0 = y_j \bar{\varepsilon}_{ij}$ with y_j as the components of the position vector of a point on the boundary, the average of the infinitesimal strain field of the body is equal to $\bar{\varepsilon}_{ij}$.

In general the strain field, ε_{ij}, is not constant within the body, as the body could be formed by different constituents. However, the following is obvious:

$$\begin{aligned}\langle \varepsilon_{ij} \rangle &\equiv \frac{1}{V}\int_V \varepsilon_{ij} \mathrm{d}V = \frac{1}{2V}\int_V (u_{i,j} + u_{j,i})\mathrm{d}V = \frac{1}{2V}\oint_{\partial V} (u_i^0 n_j + u_j^0 n_i)\mathrm{d}S \\ &= \frac{1}{2V}\oint_{\partial V} (\bar{\varepsilon}_{ik} y_k n_j + \bar{\varepsilon}_{jk} y_k n_i)\mathrm{d}S = \frac{1}{2V}\int_V (\bar{\varepsilon}_{ik}\delta_{kj} + \bar{\varepsilon}_{jk}\delta_{ki})\mathrm{d}V = \bar{\varepsilon}_{ij}\end{aligned} \tag{7}$$

This is a fundamental result in micromechanics called *Average Strain Theorem*. What this theorem tells us is that when a continuous body, let it be formed by a single constituent or multiple different constituents, is subject to a prescribed displacement distribution according to $u_i^0 = y_j \bar{\varepsilon}_{ij}$, the infinitesimal field averaged over the entire body is the same as $\bar{\varepsilon}_{ij}$, regardless the complexity of the strain field within the body.

Eq. (7) also implies that the average strain of an RVE can be computed by the displacement values along the boundary although the displacement values might not be generated by a constant strain tensor according to $u_i^0 = y_j \bar{\varepsilon}_{ij}$.

Effective Stiffness and Compliance

To achieve the first aim of micromechanics, homogenization, we need to find the constitutive relations for the imaginary homogeneous material to replace the original heterogeneous material. Let us restrict to linear elastic behavior for illustrative purpose. We assume that the constituents of the original heterogeneous material obeys the following constitutive relations

$$\sigma_{ij} = C_{ijkl}\varepsilon_{kl} \qquad \varepsilon_{ij} = S_{ijkl}\sigma_{kl} \tag{8}$$

with σ_{ij} and ε_{kl} denoting the pointwise stress field and strain field of the original material, respectively. C_{ijkl} and S_{ijkl} are the corresponding stiffness tensor and compliance tensor, respectively, which are functions of location for a heterogeneous material, assumed to be known. It is known that the inverse of the compliance is the stiffness: $C_{ijkl} = S_{ijkl}^{-1}$. σ_{ij} and ε_{kl} are also called as *microscopic stress and strain*, respectively.

Homogenization of the heterogeneous material implies that we need to obtain the following constitutive relations

$$\bar{\sigma}_{ij} = C^*_{ijkl}\bar{\varepsilon}_{kl} \qquad \bar{\varepsilon}_{ij} = S^*_{ijkl}\bar{\sigma}_{kl} \tag{9}$$

where $\bar{\sigma}_{ij}$ and $\bar{\varepsilon}_{ij}$ are the stress field and strain field of the homogeneous material, respectively, C^*_{ijkl} and S^*_{ijkl} represent the so-called effective stiffness tensor and compliance tensor, correspondingly. It is known that the inverse of the compliance is the stiffness: $C^*_{ijkl} = S^{*-1}_{ijkl}$. Note $\bar{\sigma}_{ij}$ and $\bar{\varepsilon}_{ij}$ are constant within the equivalent homogeneous material corresponding to the RVE (see Fig. 1) for the reason that they are considered as the stress and strain states of a material point in the macroscopic structural analysis. $\bar{\sigma}_{ij}$ and $\bar{\varepsilon}_{ij}$ are also called *macroscopic stress and strain*, respectively. Since the homogeneous material is imaginary, the macroscopic stress and strain are merely the volume average of the real stresses and strains within the constituents in the heterogeneous material. They are not real physical quantities experienced by the composites.

To compute C^*_{ijkl} or S^*_{ijkl}, we need to find a way to relate the microscopic stress and strain with the macroscopic stress and strain. Often in most micromechanics models, $\bar{\sigma}_{ij}$, $\bar{\varepsilon}_{ij}$, or a combination of

their components are applied to the RVE, usually in terms of boundary conditions, to solve a boundary value problem to find the stress σ_{ij} and strain ε_{ij} field within the RVE.

Hill-Mandel Macrohomogeneity Condition The celebrated Hill-Mandel macrohomogeneity condition in micromechanics addresses the following question: for a heterogenous body without body force in linear elastic static equilibrium, under what condition the average of the strain energy density is the same as the the strain energy density of homogeneous body occupying the same space with a uniform stress field and a uniform strain field? The uniform stress field and strain field of the homogeneous body is the same as the average stress field and strain field of the heterogeneous body.

For the heterogeneous body, let us denote the strain field as ε_{ij} and the stress field as σ_{ij}. They are not constant in general as the body is heterogeneous. The stress tensor is governed by the static equilibrium equations without body force. The strain energy density, $\frac{1}{2}\sigma_{ij}\varepsilon_{ij}$, is not constant. It is obvious that

$$\bar{\sigma}_{ij}\bar{\varepsilon}_{ij} = \frac{1}{V}\int\limits_V \bar{\varepsilon}_{ij}\sigma_{ij}dV = \frac{1}{V}\int\limits_V \varepsilon_{ij}\bar{\sigma}_{ij}dV = \frac{1}{V}\int\limits_V u_{i,j}\bar{\sigma}_{ij}dV \tag{10}$$

The question raised in the beginning of this section requires us to show under what condition we have $\langle\sigma_{ij}\varepsilon_{ij}\rangle = \bar{\sigma}_{ij}\bar{\varepsilon}_{ij}$. To this end we need to find under what condition the difference will vanish.

$$\begin{aligned}
\langle\sigma_{ij}\varepsilon_{ij}\rangle - \bar{\sigma}_{ij}\bar{\varepsilon}_{ij} &= \frac{1}{V}\int\limits_V \left(\sigma_{ij}u_{i,j} - \bar{\sigma}_{ij}u_{i,j} - \sigma_{ij}\bar{\varepsilon}_{ij} + \bar{\sigma}_{ij}\bar{\varepsilon}_{ij}\right)dV \\
&= \frac{1}{V}\int\limits_V \left(\sigma_{ij} - \bar{\sigma}_{ij}\right)\left(u_{i,j} - \bar{\varepsilon}_{ij}\right)dV \\
&= \frac{1}{V}\int\limits_V \left(\sigma_{ik} - \bar{\sigma}_{ik}\right)\left(u_{i,k} - \delta_{jk}\bar{\varepsilon}_{ij}\right)dV \\
&= \frac{1}{V}\int\limits_V \left(\sigma_{ik} - \bar{\sigma}_{ik}\right)\left(u_{i,k} - y_{j,k}\bar{\varepsilon}_{ij}\right)dV \\
&= \frac{1}{V}\int\limits_V \left[\left(\sigma_{ik} - \bar{\sigma}_{ik}\right)\left(u_i - y_j\bar{\varepsilon}_{ij}\right)\right]_{,k}dV \\
&= \frac{1}{V}\oint\limits_{\partial V} n_k\left(\sigma_{ik} - \bar{\sigma}_{ik}\right)\left(u_i - y_j\bar{\varepsilon}_{ij}\right)dS
\end{aligned} \tag{11}$$

Note that $\left(\sigma_{ik} - \langle\sigma_{ik}\rangle\right)\left(u_{i,k} - y_{j,k}\bar{\varepsilon}_{ij}\right) = \left[\left(\sigma_{ik} - \langle\sigma_{ik}\rangle\right)\left(u_i - y_j\bar{\varepsilon}_{ij}\right)\right]_{,k}$ due to Eq. (3). We can observe from the equation in Eq. (11) that if the surface integral on the right hand side vanishes, we have $\langle\sigma_{ij}\varepsilon_{ij}\rangle = \bar{\sigma}_{ij}\bar{\varepsilon}_{ij}$. This condition is called the *Hill-Mandel macro-homogeneity condition* in micromechanics. There are infinite many ways to vanish the surface integral. For example, the homogenous traction boundary conditions, the homogeneous displacement boundary conditions, or the periodic boundary conditions can satisfy this condition, the details of which will be later. So if such boundary conditions are applied to the RVE, the volume-averaged strain energy density of a heterogeneous material is equal to those obtained from the volume averages of the stresses and strains. Accordingly, homogenization can be interpreted as finding a homogeneous comparison material that is energetically equivalent to a given heterogeneous material. This idea can be used to define the effective properties of heterogeneous media. If the Hill-Mandel macrohomogeneity condition is satisfied, we can compute the average of strain energy of the RVE as

$$U = \frac{1}{2}\langle\sigma_{ij}\varepsilon_{ij}\rangle = \frac{1}{2}\bar{\sigma}_{ij}\bar{\varepsilon}_{ij} \tag{12}$$

which implies the following

$$\bar{\sigma}_{ij} = \frac{\partial U}{\partial\bar{\varepsilon}_{ij}} \tag{13}$$

The effective elasticity tensor can be computed as

$$C^*_{ijkl} = \frac{\partial \bar{\sigma}_{ij}}{\partial \bar{\varepsilon}_{kl}} = \frac{\partial^2 U}{\partial \bar{\varepsilon}_{ij} \partial \bar{\varepsilon}_{kl}} \tag{14}$$

Using effective stiffness and compliance, the energy equivalence according to Hill-Mandel macro-homogeneity condition can also be expressed using the following formulas

$$\langle C_{ijkl} \varepsilon_{ij} \varepsilon_{kl} \rangle = C^*_{ijkl} \bar{\varepsilon}_{ij} \bar{\varepsilon}_{kl} = S^*_{ijkl} \bar{\sigma}_{ij} \bar{\sigma}_{kl} \tag{15}$$

Rules of Mixtures

The simplest models of micromechanics are the rules of mixtures (ROMs) according to Voigt assumption and Reuss assumption, which are also frequently used in industry. Voigt assumed that the strain field within the RVE is constant, that is $\varepsilon_{ij} = \bar{\varepsilon}_{ij}$. We have the following

$$\bar{\sigma}_{ij} = \langle \sigma_{ij} \rangle = \langle C_{ijkl} \varepsilon_{kl} \rangle = \langle C_{ijkl} \bar{\varepsilon}_{kl} \rangle = \langle C_{ijkl} \rangle \, \bar{\varepsilon}_{kl} = C^*_{ijkl} \bar{\varepsilon}_{kl} \tag{16}$$

which implies

$$C^{V*}_{ijkl} = \langle C_{ijkl} \rangle \tag{17}$$

meaning that the effective stiffness is the volume average of the stiffness of the constituents. The superscript V indicates that the effective stiffness is computed according to Voigt rule of mixtures (ROM). Clearly the effective stiffness according to Voigt ROM features the same symmetry as the least symmetry of the constituent properties.

Reuss assumed that the stress field within the RVE is constant, that is $\sigma_{ij} = \bar{\sigma}_{ij}$. We have the following

$$\bar{\varepsilon}_{ij} = \langle \varepsilon_{ij} \rangle = \langle S_{ijkl} \sigma_{kl} \rangle = \langle S_{ijkl} \bar{\sigma}_{kl} \rangle = \langle S_{ijkl} \rangle \, \bar{\sigma}_{kl} = S^*_{ijkl} \bar{\sigma}_{kl} \tag{18}$$

which implies

$$S^{R*}_{ijkl} = \langle S_{ijkl} \rangle = \left\langle C^{-1}_{ijkl} \right\rangle \tag{19}$$

meaning that the effective compliance is the volume average of the compliance of the constituents. The superscript R indicates that the effective property is computed according to Reuss ROM. The Reuss ROM can also be expressed in terms of stiffness as

$$C^{R*}_{ijkl} = \left(S^{R*}_{ijkl} \right)^{-1} = \left\langle C^{-1}_{ijkl} \right\rangle^{-1} \tag{20}$$

Similarly, the effective properties, stiffness or compliance, according to Reuss ROM features the same symmetry as the least symmetry of the constituent properties.

It can be shown that the effective stiffness obtained using Voigt ROM is the upper bound and that obtained using Reuss ROM is the lower bound. In other words, if one uses another method to obtain the effective stiffess C^*_{ijkl}, it must satisfy the following

$$C^{R*}_{ijkl} \leq C^*_{ijkl} \leq C^{V*}_{ijkl} \tag{21}$$

These inequalities must be understood in the sense of the inequality for corresponding strain energy, which implies that for any set of strains ε'_{ij}, we have the following inequalities exist

$$\frac{1}{2} C^{R*}_{ijkl} \varepsilon'_{ij} \varepsilon'_{kl} \leq \frac{1}{2} C^*_{ijkl} \varepsilon'_{ij} \varepsilon'_{kl} \leq \frac{1}{2} C^{V*}_{ijkl} \varepsilon'_{ij} \varepsilon'_{kl} \tag{22}$$

It is emphatically pointed out that the inequality in Eq. (21) does not mean corresponding entries in the corresponding matrices satisfy this inequality. Nevertheless, it is easy to conclude that the corresponding eigenvalues and diagonal terms of the matrices will satisfy the inequality in Eq. (21).

The inequality in Eq. (22) can be proven as follows. Let us assume $\varepsilon_{ij} = \bar{\varepsilon}_{ij} + \varepsilon'_{ij}$, then due to the positive definiteness of C_{ijkl}, we have

$$\begin{aligned} 0 \leq \left\langle C_{ijkl}\varepsilon'_{ij}\varepsilon'_{kl} \right\rangle &= \langle C_{ijkl}(\varepsilon_{ij} - \bar{\varepsilon}_{ij})(\varepsilon_{kl} - \bar{\varepsilon}_{kl}) \rangle \\ &= \langle C_{ijkl}(\varepsilon_{ij}\varepsilon_{kl} - 2\bar{\varepsilon}_{ij}\varepsilon_{kl} + \bar{\varepsilon}_{ij}\bar{\varepsilon}_{kl}) \rangle \\ &= C^*_{ijkl}\bar{\varepsilon}_{ij}\bar{\varepsilon}_{kl} - 2\bar{\varepsilon}_{ij}\bar{\sigma}_{kl} + \langle C_{ijkl} \rangle \bar{\varepsilon}_{ij}\bar{\varepsilon}_{kl} \\ &= \left(C^{V*}_{ijkl} - C^*_{ijkl} \right) \bar{\varepsilon}_{ij}\bar{\varepsilon}_{kl} \end{aligned} \tag{23}$$

Here we used the Hill-Mandel macrohomogeneity condition in Eq. (15) and the effective properties definition in Eq. (9).

Similarly, let us assume $\sigma_{ij} = \bar{\sigma}_{ij} + \sigma'_{ij}$, then due to the positive definiteness of S_{ijkl} or C^{-1}_{ijkl}, we have

$$\begin{aligned} 0 \leq \left\langle S_{ijkl}\sigma'_{ij}\sigma'_{kl} \right\rangle &= \langle S_{ijkl}(\sigma_{ij} - \bar{\sigma}_{ij})(\sigma_{kl} - \bar{\sigma}_{kl}) \rangle \\ &= \langle S_{ijkl}(\sigma_{ij}\sigma_{kl} - 2\bar{\sigma}_{ij}\sigma_{kl} + \bar{\sigma}_{ij}\bar{\sigma}_{kl}) \rangle \\ &= S^*_{ijkl}\bar{\sigma}_{ij}\bar{\sigma}_{kl} - 2\bar{\sigma}_{ij}\bar{\varepsilon}_{kl} + \langle S_{ijkl} \rangle \bar{\sigma}_{ij}\bar{\sigma}_{kl} \\ &= \left(S^{R*}_{ijkl} - S^*_{ijkl} \right) \bar{\sigma}_{ij}\bar{\sigma}_{kl} \end{aligned} \tag{24}$$

Here we used the Hill-Mandel macrohomogeneity condition in Eq. (15) and the effective properties definition in Eq. (9). From Eq. (23) and (24), we can conclude the inequality in Eq. (22).

For a composite made of two orthotropic constituents, denoting as fiber and matrix, the effective stiffness according to the Voigt ROM can be computed as

$$C^{V*} = \begin{bmatrix} C^{V*}_{11} & C^{V*}_{12} & C^{V*}_{13} & 0 & 0 & 0 \\ C^{V*}_{12} & C^{V*}_{22} & C^{V*}_{23} & 0 & 0 & 0 \\ C^{V*}_{13} & C^{V*}_{23} & C^{V*}_{33} & 0 & 0 & 0 \\ 0 & 0 & 0 & C^{V*}_{44} & 0 & 0 \\ 0 & 0 & 0 & 0 & C^{V*}_{55} & 0 \\ 0 & 0 & 0 & 0 & 0 & C^{V*}_{66} \end{bmatrix} \tag{25}$$

where $C^{V*}_{ij} = V^f C^f_{ij} + V^m C^m_{ij}$ with V^f and V^m denoting volume fraction of fiber and matrix, respectively, and C^f_{ij} and C^m_{ij} are corresponding stiffness matrices of fiber and matrix, respectively according to the Voigt engineering notation. Note $V^f + V^m = 1$. Based on C^{V*} we can compute the corresponding engineering constants.

The effective stiffness according to the Reuss ROM can be computed as

$$C^{R*} = \begin{bmatrix} \left\langle \frac{1}{E_1} \right\rangle & -\left\langle \frac{\nu_{21}}{E_2} \right\rangle & -\left\langle \frac{\nu_{31}}{E_3} \right\rangle & 0 & 0 & 0 \\ -\left\langle \frac{\nu_{12}}{E_1} \right\rangle & \left\langle \frac{1}{E_2} \right\rangle & -\left\langle \frac{\nu_{32}}{E_3} \right\rangle & 0 & 0 & 0 \\ -\left\langle \frac{\nu_{13}}{E_1} \right\rangle & -\left\langle \frac{\nu_{23}}{E_2} \right\rangle & \left\langle \frac{1}{E_3} \right\rangle & 0 & 0 & 0 \\ 0 & 0 & 0 & \left\langle \frac{1}{G_{23}} \right\rangle & 0 & 0 \\ 0 & 0 & 0 & 0 & \left\langle \frac{1}{G_{13}} \right\rangle & 0 \\ 0 & 0 & 0 & 0 & 0 & \left\langle \frac{1}{G_{12}} \right\rangle \end{bmatrix}^{-1} \tag{26}$$

where $\left\langle \frac{\nu_{21}}{E_2} \right\rangle = V^f \frac{\nu^f_{21}}{E^f_2} + V^m \frac{\nu^m_{21}}{E^m_2}$, with $E^f_2, \nu^f_{21}, E^m_2, \nu^m_{21}$ denoting the properties for fiber and matrix, respectively.

If the composite is made of two isotropic constituents, with E^f and ν^f denoting the Young's modulus and Poisson's ratio for the fiber and with E^m and ν^m denoting the Young's modulus and Poisson's

ratio for the matrix, we can solve for the effective Young's modulus and Poisson's ratio according to the Voigt ROM from the following two equations

$$C_{12}^{V*} = \frac{V^f \nu^f E^f}{(1+\nu^f)(1-2\nu^f)} + \frac{V^m \nu^m E^m}{(1+\nu^m)(1-2\nu^m)} = \frac{\nu^{V*} E^{V*}}{(1+\nu^{V*})(1-2\nu^{V*})} \tag{27}$$

$$C_{44}^{V*} = \frac{V^f E^f}{2(1+\nu^f)} + \frac{V^m E^m}{2(1+\nu^m)} = \frac{E^{V*}}{2(1+\nu^{V*})} \tag{28}$$

which can be used to solve for E^{V*} and ν^{V*} as

$$E^{V*} = V^f E^f + V^m E^m + \frac{2V^f V^m E^f E^m (\nu^f - \nu^m)^2}{V^f E^f (1+\nu^m)(1-2\nu^m) + V^m E^m (1+\nu^f)(1-2\nu^f)} \tag{29}$$

$$\nu^{V^*} = \frac{V^f E^f \nu^f (1+\nu^m)(1-2\nu^m) + V^m E^m \nu^m (1+\nu^f)(1-2\nu^f)}{V^f E^f (1+\nu^m)(1-2\nu^m) + V^m E^m (1+\nu^f)(1-2\nu^f)} \tag{30}$$

Eq. (28) implies that the effective shear modulus can be be computed using the following formula

$$G^{V*} = V^f G^f + V^m G^m \tag{31}$$

We can easily verify that the effective bulk modulus can be computed using

$$K^{V*} = V^f K^f + V^m K^m \tag{32}$$

This means that shear modulus and bulk modulus obey the commonly known ROMs. But neither Young's modulus nor Poisson's ratio obey the simple rules given below

$$E^* = V^f E^f + V^m E^m \qquad \nu^* = V^f \nu^f + V^m \nu^m \tag{33}$$

which is a a common mistake made in many textbooks and research papers on composites [28]. Young's modulus obeys the simple ROMs only if $\nu^f = \nu^m$ for the composites made of isotropic constituents. For composites made of transversely isotropic or orthotropic constituents, it is possible to obtain analytical formulas to express effective engineering constants in terms of constituent constants similar as those in Eq. (30) for isotropic constituents, although the formulas are very lengthy and not given here.

The Young's modulus, shear modulus, bulk modulus, and Poisson's ratio for a composite containing two isotropic components according to the Reuss ROM are obtained as

$$\frac{1}{E^{R*}} = \frac{V^f}{E^f} + \frac{V^m}{E^m} \tag{34}$$

$$\frac{1}{G^{R*}} = \frac{V^f}{G^f} + \frac{V^m}{G^m} \tag{35}$$

$$\frac{1}{K^{R*}} = \frac{V^f}{K^f} + \frac{V^m}{K^m} \tag{36}$$

$$\frac{1}{\nu^{R*}} = \frac{V^f E^m + V^m E^f}{V^f E^m \nu^f + V^m E^f \nu^m} \tag{37}$$

Note that the Poisson's ratio does not obey the simplistic rule such as

$$\frac{1}{\nu^{R*}} = \frac{V^f}{\nu^f} + \frac{V^m}{\nu^m} \tag{38}$$

Assume $E^f = 73$ GPa, $E^m = 25$ GPa, $\nu^f = 0.22$, and $\nu^m = 0.45$, we can plot the prediction of Young's modulus and Poisson's ratio versus V^f using Voigt ROM, Reuss ROM, and the simple rules as shown in Figure 3 and Fig. 4. Clearly the simplistic rules might cause significant loss of accuracy.

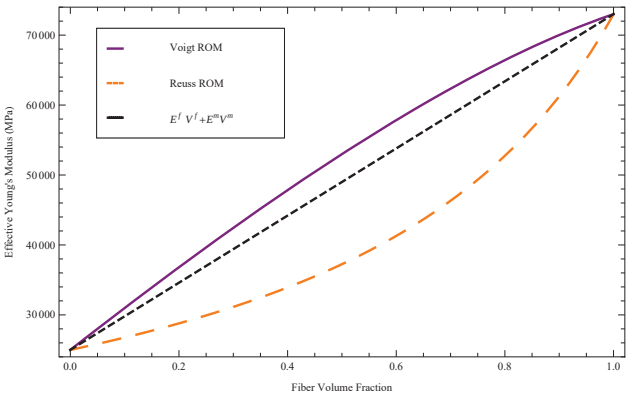

Fig. 3: Young's modulus versus fiber volume fraction

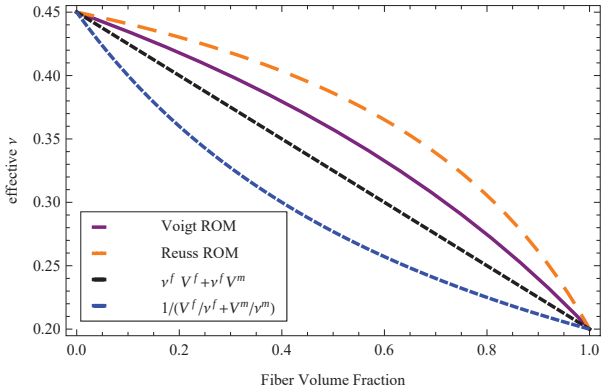

Fig. 4: Poisson's ratio versus fiber volume fraction

RVE Analysis

RVE analysis is a very popular micromechanics method, partially due to the extensive acceptance of user friendly commercial FEA software. RVE analysis is a straightforward use of readily available commercial FEA packages such as ABAQUS or ANSYS to carry out a static analysis of the RVE subjected to a carefully crafted boundary conditions in terms of displacements and tractions. As FEA has achieved the maturity that practicing engineers believe it to be the golden standard, the only thing one needs to pay attention to is the boundary conditions. Another reason of the popularity of RVE analysis is that the concept is deeply rooted in engineering. Although not as formalized as the RVE analysis in micromechanics, similar ideas have been used in practice for many decades, for example to obtain the torsional stiffness and bending stiffness needed in an aeroelastic design of a wing using beam representation, one usually subjects a segment of the wing to a unit torque or bending moment to obtain the corresponding twist or bending curvature. The sub-structuring and super-element techniques in FEA also have similar philosophical roots as the RVE analysis.

According to linear elasticity, we know the static equilibrium of the RVE without body force is given by Eq. (3). To have a well posed boundary value problem, boundary conditions in terms of displacement or traction along the RVE boundary are needed. As the objective is to compute the effective stiffness or compliance, Eq. (9), we need to apply the boundary conditions in terms of the macroscopic stress or strain $\bar{\sigma}_{ij}$, $\bar{\varepsilon}_{ij}$, then we can solve the boundary value problem using FEA to find the stress σ_{ij} and strain ε_{ij} field within the RVE which can be used to compute the effective properties. Assumed loads in terms of displacements, forces, or unit strains [29, 20], are often applied as boundary conditions to the RVE to complete the boundary value problem.

According to its definition, RVE should be chosen so that the effective properties will not depend on the boundary conditions. In other words, no matter which boundary conditions applies to the RVE, we will get the same effective properties. To be true to this definition, we need to chose RVEs with increasing sizes and subject to arbitrary boundaries to compute the effective properties until the effective properties are not changing with respect to the size of RVE and boundary conditions. However, in real practices, the size of such RVEs become so large that its computation is too expensive to exploit any advantage provided by micromechanics. Instead, the analyst chooses a RVE according to his/her own experience to carry out the analysis which usually does not satisfy the original definition of RVE. Thus the results are sensitive to the boundary conditions applied to the RVE. As RVE is essentially a material point in the macroscopic structural analysis, boundary conditions are artificially created to formulate a well-posed boundary value problem for FEA to solve. For virtual material characterization of material response under simple loading conditions, boundary conditions are usually applied in a way to mimic the real boundary conditions applied to the test coupon. For constitutive modeling needed to compute the complete set of effective material properties for the macroscopic structural analysis, many boundary conditions have been proposed in the past. Now, it is commonly accepted that the boundary conditions applied to a RVE should satisfy the Hill-Mandel macrohomogeneity condition so that the homogenized material is energetically equivalent to the original heterogeneous material.

Three types of boundary conditions are commonly applied to an RVE including homogeneous displacement boundary conditions, homogeneous traction boundary conditions, and periodic boundary conditions with details given below.

The *homogeneous displacement boundary conditions*, also called kinematically uniform boundary conditions, are given in terms of

$$u_i^0 = \bar{\varepsilon}_{ij} y_j \tag{39}$$

with $\bar{\varepsilon}_{ij}$ as constant along the boundary. Under these boundary conditions, the average strain of a perfectly bonded RVE is the same as $\bar{\varepsilon}_{ij}$ according to the average strain theorem. Clearly these boundary conditions will vanish the surface integral in Eq. (11), thus satisfying the Hill-Mandel macrohomogeneity condition.

The *homogeneous stress boundary conditions*, also called statically uniform boundary conditions, are given in terms of

$$t_i^0 = \bar{\sigma}_{ij} n_j \tag{40}$$

with $\bar{\sigma}_{ij}$ as constant along the boundary. Under these boundary conditions, the average stress of the RVE is the same as $\bar{\sigma}_{ij}$ according to the average stress theorem. Clearly these boundary conditions will vanish the surface integral in Eq. (11), thus satisfying the Hill-Mandel macrohomogeneity condition. The reason the boundary conditions in Eqs. (39) and (40) are called homogeneous boundary conditions is that these boundary conditions, when applied to a homogeneous body, will generate a homogeneous (uniform) strain or stress field in the body.

The *periodic boundary conditions* are given in terms of

$$t_i^+ = -t_i^- \qquad \chi_i^+ = \chi_i^- \tag{41}$$

where

$$\chi_i = u_i - y_j \bar{\varepsilon}_{ij} \tag{42}$$

denoting the displacement fluctuations and superscripts $+$ and $-$ denote the quantities on the corresponding periodic boundaries. Basically periodic boundary conditions require that the tractions on the corresponding periodic boundaries equal and opposite in directions, and displacement fluctuations equal to each other on the corresponding periodic boundaries. Clearly the periodic boundary conditions will vanish the surface integral in Eq. (11), thus satisfying the Hill-Mandel macrohomogeneity condition.

It is proven that homogeneous displacement boundary conditions and homogenous traction boundary conditions lead to upper and lower estimates of the effective properties, respectively, compared to periodic boundary conditions. Predictions using homogeneous displacement and traction boundary conditions converge to those of periodic boundary conditions with increasing RVE size [30, 31, 32]. It is also theoretically justified and numerically confirmed that periodic boundary conditions provide the most reasonable estimates among the class of possible boundary conditions satisfying Hill-Mandel macrohomogeneity condition [33]. In other words, PBC is the best boundary conditions to use for RVE analysis. As most FEA is displacement based, only the the displacement fluctuations are required to be periodic and the periodic traction boundary conditions are automatically satisfied for a fine enough mesh with converged stress results. The periodic boundary conditions were originally given in [30]. However, periodic boundary conditions are not extensively used in the RVE analysis using commercial FEA software until the recent arrival of coupled equation constraints in these software packages which enables convenient application of these conditions.

In summary, substituting the constitutive relations in Eq. (8) along with the infinitesimal strain definition into Eq. (3), we can obtain the following displacement-based formulation for the RVE analysis

$$\left(C_{ijkl} u_{k,l}\right)_{,j} = 0 \tag{43}$$

subject to boundary conditions $\left(u_i - y_j \bar{\varepsilon}_{ij}\right)^+ = \left(u_i - y_j \bar{\varepsilon}_{ij}\right)^-$. In real analysis, we apply unit value to one component of the macroscopic strain, say $\bar{\varepsilon}_{11} = 1$, then write out these boundary conditions explicitly for each surfaces. Run FEA using these boundary conditions to carry out the static analysis to compute the stress field σ_{ij} within the RVE. Then we can compute the volume average of the stress $\bar{\sigma}_{ij}$, which corresponds to the first column of the effective stiffness matrix according to Eq. (9). Similarly applying unit value to the rest of five macroscopic strain components, we will obtain the corresponding column of the effective stiffness matrix. Six FEA analyses are needed to compute the 6×6 stiffness matrix.

Mathematical Homogenization Theory

Mathematical homogenization theory (MHT), also called asymptotic homogenization theory, despite its arcane mathematical derivation, is another popular micromechanics method. It is an application of the formal asymptotic method through a two-scale formulation [34, 16]. Its application in engineering has been popularized by its implementation using the finite element method [35, 18, 36, 19]. Although it was originally developed for periodic media formed by a unit cell, it can be applied to RVE because the material must be locally periodic for us to replace it with an effective homogenous material in the macroscopic structural analysis. For periodic media, the unit cell can be chosen as a RVE. In fact, it will be shown later that MHT is exactly the same as RVE analysis with periodic boundary conditions. Thus, we will use RVE only in later derivations with the understanding that RVE is chosen to be a unit cell for a periodic material.

The two-scale formulation assumes that a field function of the original structure can be generally written as a function of the macro coordinates x_k and the micro coordinates y_j. Following [16], the partial derivative of a function $f(x_k, y_j)$ can be expressed as

$$\frac{\partial f(x_k,y_j)}{\partial x_i} = \frac{\partial f(x_k,y_j)}{\partial x_i}|_{y_j=\text{const}} + \frac{1}{\delta}\frac{\partial f(x_k,y_j)}{\partial y_i}|_{x_k=\text{const}} \equiv f_{|i} + \frac{1}{\delta}f_{,i} \tag{44}$$

According to 3D elasticity, the mechanical behavior of the heterogeneous material $(u_i, \varepsilon_{ij}, \sigma_{ij})$ must satisfy the following governing equations at every point of the composite body

$$\frac{\partial \sigma_{ij}}{\partial x_j} + f_i = 0 \tag{45}$$

$$\varepsilon_{ij} = \frac{1}{2}\left(\frac{\partial u_i}{\partial x_j} + \frac{\partial u_j}{\partial x_i}\right) \tag{46}$$

$$\sigma_{ij} = C_{ijkl}\varepsilon_{ij} \tag{47}$$

along with boundary conditions in terms of displacements and tractions such as $u_i = \bar{u}_i$ and $\sigma_{ij}n_j = \bar{t}_i$. It is noted that these boundary conditions are not applied on the RVE boundary but on the boundary of the macroscopic structure.

MHT starts with the assumption that the displacement field can be expanded into an asymptotic series such that

$$u_i(x,y) = u_i^0(x,y) + \delta\, u_i^1(x,y) + \delta^2 u_i^2(x,y) + O(\delta^3) \tag{48}$$

Substituting Eq. (48) into Eq. (46) and considering Eq. (44), we obtain

$$\varepsilon_{ij}(x,y) = \frac{1}{\delta}\varepsilon_{ij}^{-1}(x,y) + \varepsilon_{ij}^0(x,y) + \delta\, \varepsilon_{ij}^1(x,y) + O(\delta^2) \tag{49}$$

with

$$\varepsilon_{ij}^{-1}(x,y) = u_{(i,j)}^0 \tag{50}$$

$$\varepsilon_{ij}^0(x,y) = u_{(i|j)}^0 + u_{(i,j)}^1 \tag{51}$$

$$\varepsilon_{ij}^1(x,y) = u_{(i|j)}^1 + u_{(i,j)}^2 \tag{52}$$

where the subscript pairs with parenthesis denote the symmetric gradient defined as

$$u_{(i,j)}^0 = \frac{1}{2}(u_{i,j}^0 + u_{j,i}^0) \qquad u_{(i|j)}^0 = \frac{1}{2}(u_{i|j}^0 + u_{j|i}^0) \tag{53}$$

Substituting Eq. (49) into Eq. (47), we have

$$\sigma_{ij}(x,y) = \frac{1}{\delta}\sigma_{ij}^{-1}(x,y) + \sigma_{ij}^0(x,y) + \delta\, \sigma_{ij}^1(x,y) + O(\delta^2) \tag{54}$$

with

$$\sigma_{ij}^{-1}(x,y) = C_{ijkl}\varepsilon_{ij}^{-1} \tag{55}$$
$$\sigma_{ij}^{0}(x,y) = C_{ijkl}\varepsilon_{ij}^{0} \tag{56}$$
$$\sigma_{ij}^{1}(x,y) = C_{ijkl}\varepsilon_{ij}^{1} \tag{57}$$

Here MHT introduces the second assumption that the elasticity tensor C_{ijkl} is an order on function.

Substituting Eq. (54) into Eq. (45), we have

$$\frac{1}{\delta^2}\sigma_{ij,j}^{-1} + \frac{1}{\delta}\left(\sigma_{ij|j}^{-1} + \sigma_{ij,j}^{0}\right) + \sigma_{ij|j}^{0} + \sigma_{ij,j}^{1} + f_i + O(\delta) = 0 \tag{58}$$

Multiplying Eq. (58) by δ^2 and then taking the limit of δ approaching zero, one can obtain the leading order equilibrium. Similarly, we can obtain the equilibrium for other orders. The resulting equilibrium equations according to each asymptotic order are

$$\sigma_{ij,j}^{-1} = 0 \tag{59}$$

$$\sigma_{ij|j}^{-1} + \sigma_{ij,j}^{0} = 0 \tag{60}$$

$$\sigma_{ij|j}^{0} + \sigma_{ij,j}^{1} + f_i = 0 \tag{61}$$

Here MHT introduces the third assumption that the body force f_i and the boundary conditions $\bar{u}_i$ and $\bar{t}_i$ are order one functions.

Multiplying Eq. (59) by u_i^0, we have

$$0 = \int_V u_i^0 \sigma_{ij,j}^{-1} dV = \oint_{\partial V} u_i^0 \sigma_{ij}^{-1} n_j dS - \int_V u_{i,j}^0 \sigma_{ij}^{-1} dV \tag{62}$$

The surface integral over the boundary vanishes due to the assumption of periodic response over unit cell boundaries so that u_i^0 is equal on the corresponding periodic sides of the unit cell, while traction $\sigma_{ij}^{-1} n_j$ is equal with opposite sign on the corresponding periodic sides of the unit cell. Further substituting Eqs. (55) and (50) into Eq. (62), we have

$$\int_V u_{i,j}^0 C_{ijkl} u_{k,l}^0 dV = 0 \tag{63}$$

As C_{ijkl} is positive definite and has both minor and major symmetry, we conclude that for Eq. (63) to be satisfied, we must have $u_{i,j}^0 = 0$, which implies

$$u_i^0(x,y) = u_i^0(x) \equiv \bar{u}_i(x) \qquad \sigma_{ij}^{-1} = 0 \tag{64}$$

Here $\bar{u}_i$ is the volume average of u_i if we require

$$\left\langle u_i^1 \right\rangle = \left\langle u_i^2 \right\rangle = \ldots = 0 \tag{65}$$

Substituting Eqs. (64), (56), and (51) into Eq. (60), we have

$$\left(C_{ijkl}\left(\bar{\varepsilon}_{kl} + u_{k,l}^1\right)\right)_{,j} = 0 \tag{66}$$

with

$$\bar{\varepsilon}_{kl} = \bar{u}_{(k|l)} \tag{67}$$

Eq. (66) can be used along with the constraints in Eq. (65) to uniquely solve for u_k^1, which can be symbolically written as

$$u_k^1 = H_k^{mn} \bar{\varepsilon}_{mn} \tag{68}$$

As u_k^1 must be periodic, then H_k^{mn} must be periodic too.

The strain field ε_{ij}^1 can be obtained as

$$\varepsilon_{ij}^0(x,y) = \bar{\varepsilon}_{ij} + H_{(i,j)}^{mn} \bar{\varepsilon}_{mn} \tag{69}$$

It can be shown that

$$\bar{\varepsilon}_{ij} = \int_V \varepsilon_{ij}^0(x,y) dV \tag{70}$$

due to the periodicity of H_k^{mn}. The stress field σ_{ij}^0 can be obtained as

$$\sigma_{ij}^0(x,y) = C_{ijkl}\varepsilon_{kl}^0 = C_{ijkl}\left(\bar{\varepsilon}_{kl} + H_{(k,l)}^{mn}\bar{\varepsilon}_{mn}\right) = \left(C_{ijmn} + C_{ijkl}H_{(k,l)}^{mn}\right)\bar{\varepsilon}_{mn} \tag{71}$$

Lastly, we need to solve the equilibrium equation in Eq. (61). As the RVE is actually considered as a point in the macroscopic analysis, taking the volume average of this equation over the RVE domain and considering the periodicity of σ_{ij}^1, we have

$$\bar{\sigma}_{ij|j} + \bar{f}_i = 0 \tag{72}$$

with

$$\bar{\sigma}_{ij} = \left\langle \sigma_{ij}^0 \right\rangle = \left\langle \left(C_{ijmn} + C_{ijkl}H_{(k,l)}^{mn}\right)\bar{\varepsilon}_{mn} \right\rangle \equiv C_{ijmn}^* \bar{\varepsilon}_{mn} \tag{73}$$

with

$$C_{ijmn}^* = \left\langle C_{ijmn} + C_{ijkl}H_{(k,l)}^{mn} \right\rangle \tag{74}$$

Clearly, the 15 equations governing the macroscopic structural analysis consists of Eq. (72) for equilibrium, Eq. (73) for constitutive relations, and Eq. (67) for strain-displacement relations to solve for the 15 field variables including the macroscopic stress field $\bar{\sigma}_{ij}$, the macroscopic strain field $\bar{\varepsilon}_{ij}$, and the macroscopic displacement field $\bar{u}_i$. So according to MHT, the homogenization step is to solve Eq. (66) for a periodic u_i^1 along with the constraint in Eq. (65) to find the effective properties C_{ijkl}^* using Eq. (74). Then the effective properties can be used to solve for the macroscopic behavior including $\bar{u}_i$, $\bar{\varepsilon}_{ij}$ and $\bar{\sigma}_{ij}$. The dehomogenization step is to obtain the local displacement field using

$$u_i(x,y) = \bar{u}_i(x) + \delta\ H_i^{mn}\bar{\varepsilon}_{mn} \tag{75}$$

Note here $\bar{u}_i$ should be interpreted as

$$\bar{u}_i = \bar{u}_i(x_{k_0}) + x_k \bar{u}_{i,k} \tag{76}$$

where x_{k_0} is the center of RVE and $\bar{u}_{i,k}$ is the gradient along x_k evaluated at x_{k_0}.

The local strain field can be obtained using

$$\varepsilon_{ij} = \bar{\varepsilon}_{ij} + H_{(i,j)}^{mn}\bar{\varepsilon}_{mn} \tag{77}$$

The local stress field can be obtained using

$$\sigma_{ij} = \left(C_{ijmn} + C_{ijkl}H_{(k,l)}^{mn}\right)\bar{\varepsilon}_{mn} \tag{78}$$

Mechanics of Structure Genome

Mechanics of structure genome (MSG) is a unified approach recently introduced for multiscale constitutive modeling for all types of composites structures including beams, plates/shells, and 3D structures [23]. Structure Genome (SG) is defined as the *smallest mathematical* building block of the structure to emphasize the fact that it contains all the constitutive information needed for a structure the same fashion as the genome contains all the intrinsic information for an organism's growth and development. For 3D bodies, SG serves a similar role as the RVE concept in micromechanics (Figure 5). However, they are different. For example, for a structure made of composites featuring 1D heterogeneity (e.g. binary composites made of two alternating layers), SG will be a straight line with two segments denoting corresponding phases as one can mathematically repeat this line in plane to build the two layers of the binary composite, then repeat the binary composite out of plane to build the entire structure. For a structure made of composites featuring 2D heterogeneity (e.g. continuous fiber reinforced composites), the SG will be 2D, and for a structure made of composites featuring 3D heterogeneity (e.g. particle reinforced composites), the SG will be 3D. Despite that SG for 3D bodies could have different dimensions due to their heterogeneities, the effective properties should remain 3D for the 3D structural analysis. For example, for linear elastic analysis, one should be able to obtain the complete 6×6 stiffness matrix from an analysis of the 1D SG of the binary composite. Clearly, SG uses the lowest dimension, thus highest efficiency, to describe the heterogeneity, while RVE dimension is usually determined by heterogeneity and what type of properties required for the structural analysis. For example, if 3D properties are needed for 3D structural analysis of continuous fiber reinforced composites, a 3D RVE is usually required. Although unnecessary waste of computing resources, MSG can use SGs with higher dimensions to reproduce the results by SGs with dimensionality the same as that of the heterogeneity. For example, MSG can use 2D or 3D SGs to reproduce the results of 1D SGs for binary composites and 3D SGs to reproduce the results of 2D SGs for continuous fiber reinforced composites.

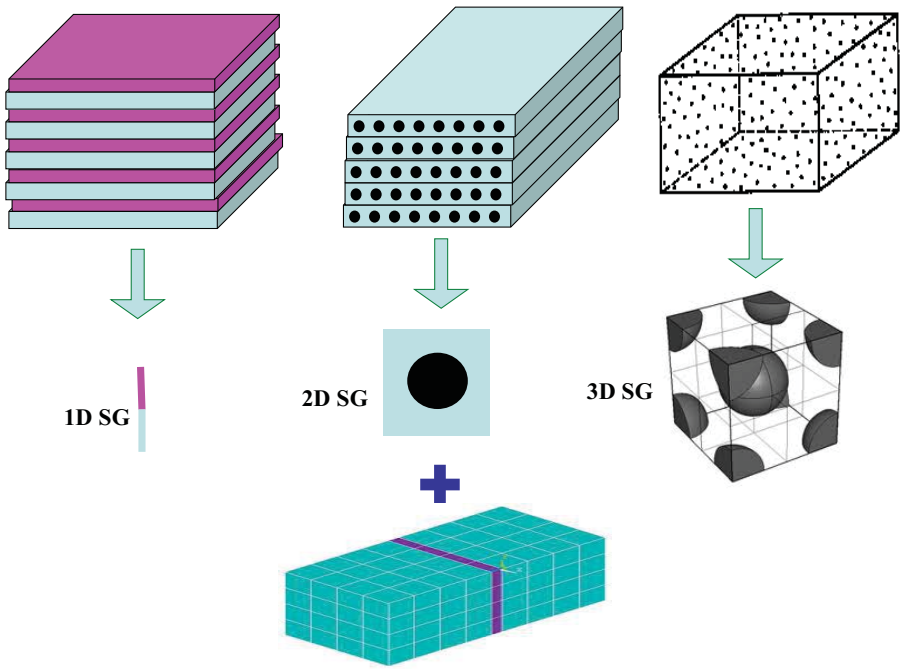

Fig. 5: SG for 3D structure

MSG is based on the principle of minimum information loss which states that the homogenized model can be constructed through minimizing the information loss between the original model and

the homogenized model. For linear elastic material, the information can be the strain energy density. According to MSG, we need to first express the kinematics of the original model in terms of the model to be constructed as

$$u_i(x,y) = \bar{u}_i(x) + \chi_i(x,y) \tag{79}$$

with u_i denoting the displacement field of the original model, $\bar{u}_i$ denoting the displacement of the homogenized model, and χ_i denoting the difference between these two fields, which is commonly called fluctuation function in micromechanics.

Then we can obtain the strain field of the original model as

$$\varepsilon_{ij}(x,y) = \bar{\varepsilon}_{ij}(x) + \frac{1}{\delta}\chi_{(i|j)} \tag{80}$$

Here the higher order term $\chi_{(i,j)}$ has been neglected according to the variational asymptotic method [37]. As we are constructing the homogenized model out of the original model, we need to define the kinematic variables of the homogenized model in terms of those of the original model. The natural choice is to define

$$\bar{u}_i = \langle u_i \rangle \qquad \bar{\varepsilon}_{ij} = \langle \varepsilon_{ij} \rangle \tag{81}$$

which implies the following constraints on the fluctuation functions

$$\langle \chi_i \rangle = 0 \qquad \left\langle \chi_{(i,j)} \right\rangle = 0 \tag{82}$$

The principle of minimum information loss seeks to minimize the difference between the strain energy of the original model and the homogenized model which is

$$\Pi = \left\langle \frac{1}{2} C_{ijkl}\varepsilon_{ij}\varepsilon_{kl} \right\rangle - \frac{1}{2} C^*_{ijkl}\bar{\varepsilon}_{ij}\bar{\varepsilon}_{kl} \tag{83}$$

To minimize Π, we consider the homogenized model as given (i.e., $C^*_{ijkl}, \bar{\varepsilon}_{ij}$ cannot be varied). Then χ_i can be solved from the following variational statement

$$\min_{\chi_i} \left\langle \frac{1}{2} C_{ijkl}\varepsilon_{ij}\varepsilon_{kl} \right\rangle = \min_{\chi_i \in \text{Eq. (82)}} \left\langle \frac{1}{2} C_{ijkl} \left(\bar{\varepsilon}_{ij} + \chi_{(i,j)}\right) \left(\bar{\varepsilon}_{kl} + \chi_{(k,l)}\right) \right\rangle \tag{84}$$

Using calculus of variations, we can conclude that χ_i must satisfy the following Euler-Lagrange equations

$$\left(C_{ijkl}\left(\bar{\varepsilon}_{kl} + \chi_{k,l}\right)\right)_{,j} = 0 \tag{85}$$

along with the constraints in Eq. (82), additional constraints can be incorporated as needed. For example, for periodic materials, χ_i must be periodic, and the second equation in Eq. (82) will be automatically satisfied. χ_i will be solved in terms of $\bar{\varepsilon}_{kl}$, which has the same symbolic form of Eq. (68).

$$\chi_k = H^{mn}_k \bar{\varepsilon}_{mn} \tag{86}$$

The volume average of the strain energy of the RVE can be obtained as

$$U = \left\langle \frac{1}{2} C_{ijkl}(\bar{\varepsilon}_{ij} + H^{mn}_{(i,j)}\bar{\varepsilon}_{mn})(\bar{\varepsilon}_{kl} + H^{st}_{(k,l)}\bar{\varepsilon}_{st}) \right\rangle \tag{87}$$

The effective stiffness can be obtained using Eq. (14) as

$$C^*_{ijkl} = \left\langle C_{ijmn} + C_{ijkl}H^{mn}_{(k,l)} \right\rangle \tag{88}$$

Theoretical Connections of RVE Analysis, MHT and MSG

To show the theoretical connections among RVE analysis, MHT, and MSG, we need to first to change the formulation of the RVE analysis with periodic boundary conditions. From Eq. (42), we can obtain

$$u_i = \chi_i + y_j \bar{\varepsilon}_{ij} \tag{89}$$

Then the strain field within the RVE can be obtained as

$$\varepsilon_{ij} = \chi_{(i,j)} + \bar{\varepsilon}_{ij} \tag{90}$$

Substituting the constitutive relations in Eq. (8) along with the infinitesimal strain in Eq. (90) into Eq. (3), we can obtain the following displacement-based formulation for the RVE analysis

$$\left(C_{ijkl}(\bar{\varepsilon}_{kl} + \chi_{k,l})\right)_{,j} = 0 \tag{91}$$

with χ_i being periodic. This differential equation is the exactly same as that obtained by MSG in Eq. (85), and that obtained by MHT in Eq. (66) with a simple change of variable $u_k^1 = \chi_k$. In other words, for a heterogeneous material featuring a 3D RVE with periodic boundary conditions, RVE analysis, MHT and MSG will provide exactly the same results for both effective properties and local fields.

As far as efficiency is concerned, computing the complete stiffness matrix, RVE analysis requires solving the six static problems because the coefficient matrix of the linear system is affected by the coupled equation constraints used to apply the periodic boundary conditions. MHT and MSG can be implemented using the finite element method so that the linear system will be factorized once and solve for six load steps. Theoretically speaking, MHT and MSG could be five to six times more efficient than RVE analysis.

However, such equivalence does not exist for situations when periodic boundary conditions cannot be applied. MHT is not appicable for such cases. RVE analysis and MSG can still use whatever boundary conditions are appropriate but the results will differ from each other.

For materials featuring lower-dimensional heterogeneities such as binary composites or continuously reinforced composites, RVE analysis and MHT can only obtain properties and local fields with the same dimensionality as that of the RVE, while MSG can still obtain the complete set of 3D properties and local fields out of a 1D or 2D analysis. The main reason is that numerical implementation of MHT and RVE are based on weak form converted from the strong form of the boundary value problem in Eq. (66) and Eq. (43), while MSG directly solve the variational statement in Eq. (84).

MSG has the capability to directly construct models for beams/plates/shells based on the same principle of minimum information loss which is different from the RVE analysis and MHT although it is possible to modify RVE analysis and MHT to construct models for beams/plates/shells.

Acknowledgments

This work is supported, in part, by the Air Force Office of Scientific Research and by the Army Vertical Lift Research Center of Excellence at Georgia Institute of Technology and its affiliate program through subcontract at Purdue University. The technical monitors are Dr. David Stargel and Dr. Mahendra J Bhagwat. The views and conclusions contained herein are those of the authors and should not be interpreted as necessarily representing the official policies or endorsement, either expressed or implied, of the sponsor.

References

[1] R. M. Christensen. *Mechanics of Composite Materials*. Wiley-Interscience, New York, 1979.

[2] S. Nemat-Nasser and M. Hori. *Micromechanics: Overall Properties of Heterogeneous Materials*. North-Holland, Amsterdam, 1993.

[3] G. W. Milton. *The Theory of Composites*. Cambridge University Press, Cambridge, UK, 2002.

[4] J. Qu and M. Cherkaoui. *Fundamentals of Micromechanics of Solids*. Wiley, New Jersey, 2006.

[5] V. Buryachenko. *Micromechanics of Heterogeneous Materials*. Springer, New York, 2007.

[6] S. Li and G. Wang. *Introduction to Micromechanics and Nanomechanics*. World Scientific, New Jersey, 2008.

[7] H. J. Bohm. A short introduction to basic aspects of continuum micromechanics. Technical Report ILSB Report/ILSB-Arbeitsbericht 206, 2012.

[8] R. Hill. The elastic behavior of crystalline aggregate. *Proc. Phys. Soc. London*, A65:349--354, 1952.

[9] Z. Hashin and S. Shtrikman. A variational approach to the theory of the elastic behaviour of polycrystals. *Journal of Mechanics and Physics of Solids*, 10:343--352, 1962.

[10] S. Torquato. *Random heterogeneous materials*. Springer New York, 2002.

[11] J. Aboudi. A continuum theory for fiber-reinforced elastic-visoplastic composites. *International Journal of Engineering Science*, 20(5):605 -- 621, 1982.

[12] J. Aboudi. Micromechanical analysis of composites by the method of cells. *Applied Mechanics Reviews*, 42(7):193 -- 221, 1989.

[13] M. Paley and J. Aboudi. Micromechanical analysis of composites by the generalized cells model. *Mechanics of Materials*, 14:127--139, 1992.

[14] J. Aboudi, M. J. Pindera, and S. M. Arnold. Linear thermoelastic higher-order theory for periodic multiphase materials. *Journal of Applied Mechanics*, 68:697--707, 2001.

[15] T. O. Williams. A two-dimensional, higher-oder, elasticity-based micromechanics model. *International Journal of Solids and Structures*, 42:1009--1038, 2005.

[16] A. Bensoussan, J. Lions, and G. Papanicolaou. *Asymptotic Analysis for Periodic Structures*. North-Holland, Amsterdam, 1978.

[17] H. Murakami and A. Toledano. A higer-order mixture homogenization of bi-laminated composites. *Journal of Applied Mechanics*, 57:388--396, 1990.

[18] J. M. Guedes and N. Kikuchi. Preprocessing and postprocessing for materials based on the homogenization method with adaptive finite element method. *Computer Methods in Applied Mechanics and Engineering*, 83:143--198, 1990.

[19] J. C. Michel, H. Moulinec, and P. Suquet. Effective properties of composite materials with periodic microstructure: a computational approach. *Computer Methods in Applied Mechanics and Engineering*, 172:109--143, 1999.

[20] C. T. Sun and R. S. Vaidya. Prediction of composite properties from a representative volume element. *Composites Science and Technology*, 56:171 -- 179, 1996.

[21] H. Berger, S. Kari, U. Gabbert, R. Rodriguez-Ramos, J. Bravo-Castillero, R. Guinovart-Diaz, F. Sabina, and G.A. Maugin. Unit cell models of piezoelectric fiber composites for numerical and analytical calculation of effective properties. *Smart Materials and Structures*, 15:451--458, 2006.

[22] S Ghosh. *Micromechanical Analysis and Multi-Scale Modeling Using the Voronoi Cell Finite Element Method*. Taylor & Francis US, Florida, 2010.

[23] W. Yu. Structure genome: Fill the gap between materials genome and structural analysis. In *Proceedings of the 56th Structures, Structural Dynamics and Materials Conference*, Kissimmee, Florida, Jan. 5-9 2015. AIAA.

[24] R. Hill. Elastic properties of reinforced solids: Some theoretical principles. *Journal of Mechanics and Physics of Solids*, 11:357--372, 1963.

[25] Z. Hashin. Analysis of composite materials-a survey. *Applied Mechanics Review*, 50:481--505, 1983.

[26] W. Drugan and J. Willis. A micromechanics-based nonlocal constitutive equations and estimates of representative volume element size for elastic composites. *Journal of Mechanics and Physics of Solids*, 44:497--524, 1996.

[27] M. Ostoja-Starzewski. Microstructural randomness verse representative volume element in thermomechanics. *Journal of Applied Mechanics*, 69:25--30, 2002.

[28] B. Liu, X. Feng, and Zhang S. M. The effective Young's modulus of composites beyond the Voigt estimation due to the Poisson effect. *Composite Science and Technology*, 69:2198 -- 2204, 2009.

[29] S. J. Hollister and N. Kikuchi. A comparison of homogenization and standard mechanics analyses for periodic porous composites. *Computational Mechanics*, 1992.

[30] Sanchez-Palencia and A. Zaoui. Elements of homogenization for inelastic solid mechanics. In *Homogenization Techniques in Composites*, pages 194--278. Springer-Verlag, 1987.

[31] A. Drago and M.-J. Pindera. Micro-macromechanical analysis of heterogeneous materials: Macroscopically homogeneous vs periodic microstructures. *Composite science and Technology*, 67:1243--1263, 2007.

[32] D. H. Pahr and H. J. Bohm. Assessment of mixed uniform boundary conditions for predicting the mechanical behavior of elastic and inelastic discontinuously reinforced composites. *CMES*, 34:117--136, 2008.

[33] K. Terada, M. Hori, T. Kyoya, and N. Kikuchi. Simulation of the multi-scale convergence in computational homogenization approaches. *International Journal of Solids and Structures*, 37:2285--2311, 2000.

[34] N. S. Bakhvalov. Homogenization of partial differential operators with rapidly oscillating coefficients. *Soviet Mathematics - Doklady*, 16:351--355, 1975.

[35] F. Devries and F. Lene. Homogenization at set macroscopic stress: Numerical implementation and application. *Recherche Aerospatiale*, 1:34--51, 1987.

[36] J. Fish, K. Shek, M. Pandheeradi, and M. Shephard. Computational plasticity for composite structures based on mathematical homogenization: Theory and practice. *Computer Methods in Applied Mechanics and Engineering*, 148:53--73, 1997.

[37] V. L. Berdichevsky. *Variational Principles of Continuum Mechanics*, volume 1 and 2. Springer Berlin, 2009.

Remove Homogeneous Layer Assumption from Lamination Theories

B. PENG and W. YU

ABSTRACT

Composite multilayer structures are often modeled using lamination theories. All lamination theories inherently assume the composite laminate is made of homogeneous layers characterized with lamina constants, which will restrict the lamination theories from capturing the real microstructural details of the composite material, and thus create artificial layer boundaries and result in many phenomena predicted by lamination theories occurred at wrong locations. Another drawback of lamination theories is that the lamina constants can not be rigorously defined. Recently a new theory called Mechanics of Structure Genome (MSG) has been developed without the homogeneous layer assumption. The variational asymptotic method (VAM) has been used to minimize the loss of information between the original 3D heterogeneous structures and the final equivalent plate model without invoking any ad hoc kinematic assumptions. To analyze multilayer plates/shells, MSG decouples the original 3D problem into a plate analysis and a constitutive modeling over a Structure Genome (SG), where SG is the mathematical smallest building block of the multilayer plate/shell structure. Through the analysis of SG, a constitutive relation between the generalized 2D strains and stress resultants is obtained for the plate analysis which can be solved at the same computational cost as Classical Laminate Theory (CLT). Dehomogenization can also be conducted to obtain the displacements, strains and stresses in the original heterogeneous structure. Several examples will be used to disclose the aforementioned flaws of lamination theories and the advantage of MSG. It is numerically demonstrated that while using the same plate elements in ABAQUS, MSG has an excellent accuracy compared to 3D FEA in terms of all the displacements and in-plane stress components, as well as a fair agreement of the transverse normal stress.

Purdue University, West Lafayette, Indiana 47907

INTRODUCTION

Composite plates and shells are widely used in engineering applications such as aerospace, naval, automotive and construction industries. They provide the merits of high strength-to-weight, high stiffness to weight ratios, good fatigue strength and resistance to corrosion, and the design flexibility of tailoring the material microstructures to achieve the ever-increasing performance requirements [1]. Composite plates are usually constructed layered structures, such as laminates, sandwich panels and part of the woven-fabric textile composites. An economical and reliable design of such plate and shell structures motivates the researchers to actively seek for efficient and accurate theories over decades.

The most investigated methods are axiomatic type approaches, which present the advantage that the important physical behaviors of the structures can be modeled using the 'intuition' of eminent scientists [2]. Axiomatic approaches take advantage of the characteristics of the plates/shells of which the thickness is at least one order smaller than the in-plane dimensions. Thus it is possible to reduce a 3D model to a 2D model, and model the multilayer structures with lamination theories. Such a dimensional reduction is enabled by some ad hoc kinematic assumptions to express the 3D displacements in terms of unknown 2D functions of the in-plane coordinates and known functions of the thickness coordinate. Different kinematic assumptions result in different theories, which are generally classified into Equivalent Single Layer (ESL) models and Layer-Wise (LW) models based on the choice of variables. In ESL model, variables are introduced for the whole plate/shell, while in LW models the number of the independent variables is dependent on the number of layers [3].

The earliest ESL theory is the Classical Laminate Theory (CLT), which can be dating back to 1960s [4]. The principal assumption in CLT is that normal lines to the reference surface before deformation remain straight rigid and normal to the reference surface after deformation. Although this assumption leads to a simple plate model, it neglects the transverse strains and stresses, which will result in the overestimation of the structural stiffness and will introduce large error for thick plates.

To overcome the limitation, transverse shear deformation is considered in the later developed theories. First-order shear-deformation theory (FOSDT) proposed by Mindlin [5] and Reissner [6] included a constant transverse shear strain in the model. Later FOSDT is significantly improved by Vlasov [7], Reddy [8], Phan [9] by enforcing zero traction on the upper and the bottom plate/shell surfaces.

Given the possibility to increase the accuracy of numerical evaluations for moderately thick plates, various higher-order shear-deformation theories (HOSDTs) based on an assumption of nonlinear stress variation through the thickness were developed in Ref. [10], [11], and [12], to name only a few. Different forms of functions, such as trigonometric functions, exponential functions, polynomials are implemented to represent shape functions determining the distribution of the transverse shear strains along the thickness [12]. Zigzag effect and interlaminar continuity(IC) can be considered in HOSDTs [11, 13]. Some of these models are numerically compared in Ref. [11, 12].

To improve the transverse shear stress prediction, LW theories implement the mentioned CLT, FOSDT, HOSDT in each layer of the multilayer plate/shell struc-

tures, which intrinsically consider the Zigzag effect but not necessarily IC. These theories are more accurate in terms of transverse stresses than ESLs, but suffer from the deficiency of expensive computation cost.

Detailed reviews on multilayered composite plates/shells can be read or referred in detail in Refs. [1, 3]. Numerical comparison of different models can be found in Ref. [2, 13, 14], etc. Especially, there are reviews on sandwich plates [13], and for woven composite [15].

In summery, most of the above mentioned lamination theories inherently assume the composite laminate is made of homogeneous layers. There are at least two consequences of this assumption. First, any lamination theory, despite of its complexity, can only approximate a 3D body made of homogeneous layers and cannot capture the real microstructural details of the composite material. As this assumption actually introduces artificial layer boundaries, many phenomena predicted by lamination theories will occur at wrong locations. For example, the maximum stress predicted by lamination theory may exist at the interlaminar surface while in fact the maximum stresses may exist at the interface of different phases of materials. Second, the lamina constants are not rigorously defined. There are two ways to obtain the lamina constants. One can measure four in-plane lamina constants ($E_1, E_2, G_{12}, \nu_{12}$) for a layer in a plane stress state. However, layers are not necessarily behave in plane stress state within a laminate. One can also numerically compute the lamina constants using micromechanics based on a unit cell [15]. However, micromechanics inherently assumes that one can repeat the same unit cell to build the entire structure, which is often not the case. For example, Ref. [16] stated that phase shift of woven-fabric textile composites will influence the effective properties of plate. In addition, the lamination theories are mainly based on various a priori assumptions. Such theories are either efficient but too simplistic to be predictive, or accurate but too computationally intensive to be used for effective design.

Very recently, a new theory called Mechanics of Structure Genome (MSG) has been developed without any apriori assumptions including the homogeneous layer assumption [17].

Applying MSG, a constitutive relation between the generalized 2D strains and stress resultants is obtained for the plate analysis, in which no ad hoc kinematic assumptions are introduced, the problem of dealing with IC does not exist. Dehomogenization can also be conducted to obtain the displacements, strains and stresses in the original heterogeneous structure. In the following sections, first the basics of MSG will be introduced, and then several examples will be used to disclose the aforementioned flaws of lamination theories and the advantage of MSG by compare their results with direct 3D finite element analysis (FEA). This study also suggests a few possible improvements for MSG including a shear refined model for better capturing transverse shear and normal stresses, and applying this new theory for failure analysis.

MECHANICS OF STRUCTURE GENOME FOR PLATES/SHELLS

MSG is a unified theory proposed to fill the gap between material microstructures and structural analysis, which is capable of dealing with homogenization and dehomogenization of 3D structures, plates/shells, and beams. Ref. [17] first introduced MSG in a systematic way, in which works focusing on plate/shells in MSG has been proposed in earlier papers [14, 18] although the term 'MSG' was not used back at that time. Therefore the current section only provides a brief introduction to MSG applying to plate/shell.

For heterogeneous plate/shell structures which have a thickness much smaller than the in-plane dimensions, MSG treats their reference surfaces as 2D continuum, and every material point of this continuum has a constitutive relation between the generalized 2D strains and stress resultants from SG analysis (such as A, B, D matrices for the CLT). Therefore, the original 3D heterogeneous body is decoupled into a plate analysis and a constitutive modeling over a SG.

SG is a very important basic concept in MSG, which acts as the basic building block of the structure connecting materials to structures. SG can be 1D, 2D or 3D which depends on the heterogeneity of the plates/shells. For example, if the plate-like structures feature no in-plane heterogeneities such as those assumed in composite lamination theories, the SG is a material line along the thickness direction with each segment denoting the corresponding material of each layer. For a sandwich panel with a core corrugated in one direction, the SG is 2D, and if the panel is heterogeneous in both in-plane directions, the SG is 3D [17].

The original heterogeneous structure can be described by macro coordinates x_i, where x_α are two orthogonal arc-length coordinates in the reference surface and x_3 is the thickness coordinate. In the final homogenized 2D plate/shell model, x_α will remain while x_3 will be delimited due to the fact that thickness h is much smaller than the in-plane dimensions. (Here and throughout the paper, Greek indices assume values 1 and 2 while Latin indices assume 1, 2, and 3. Repeated indices are summed over their range except where explicitly indicated).

A set of micro coordinates $y_i = x_i/\varepsilon$ are introduced to denotes the rapid change in the material characteristics in SG, with ε being a small parameter denoting the order of a term. If the SG is 1D, only y_3 is needed; if the SG is 2D, y_2 and y_3 are needed; if the SG is 3D, all three coordinates y_1, y_2, y_3 are needed.

Therefore a field function of the original heterogeneous structure can be generally written as a function of the macro coordinates x_α and the micro coordinates y_j. The partial derivative of a function $f(x_\alpha, y_j)$ can be expressed as

$$\frac{\partial f(x_\alpha, y_j)}{\partial x_i} = \frac{\partial f(x_\alpha, y_j)}{\partial x_i}|_{y_j=\text{const}} + \frac{1}{\varepsilon}\frac{\partial f(x_\alpha, y_j)}{\partial y_i}|_{x_\alpha=\text{const}} \equiv f_{,i} + \frac{1}{\varepsilon}f_{|i} \qquad (1)$$

Based on these definitions, the deformation of the original heterogeneous plate structures can be formulated by contributions from the reference surface, the rotation of the local deformed coordinate system and the fluctuation function $w(x_\alpha, y_j)$ in SG, where y_j are the micro coordinates used to describe the SG. Using a proper definition of strain, the strain energy U stored in the original heterogeneous plate structure can be obtained. Similarly, the virtual work δW done by the applied loads can also be calculated. Therefore a complete statement of the problem can be presented in terms of

the principle of virtual work. To this end, by exploiting the smallness of SG and plate thickness compared with the reference surface in terms of the in-plane dimension, VAM is applied to construct an asymptotically correct macroscopic plate model. By assessing the orders of all the quantities in the variational statement and neglecting the terms in the order of ε , the first approximation of the variational statement can be obtained as

$$\delta U \equiv \delta \frac{1}{2} \left\langle (\Gamma_h w + \Gamma_\epsilon \bar{\epsilon})^T D (\Gamma_h w + \Gamma_\epsilon \bar{\epsilon}) \right\rangle = 0 \tag{2}$$

where fluctuation function $w = \lfloor w_1 \; w_2 \; w_3 \rfloor^T$, $\bar{\epsilon} = \lfloor \epsilon_{11} \;\; 2\epsilon_{12} \;\; \epsilon_{22} \;\; \kappa_{11} \;\; \kappa_{12} + \kappa_{21} \;\; \kappa_{22} \rfloor^T$ with $\epsilon_{\alpha\beta}$ denoting the in-plane strains and $\kappa_{\alpha\beta}$ denoting the curvature strains of the plate model. The notation $\langle \bullet \rangle$ is used to denote a weighted integration over the domain of the SG, $D(y_1, y_2, y_3)$ is the 3D 6×6 material matrix, which consists of elements of the fourth-order elasticity tensor expressed in the y_i coordinate system. In Eq. (2), we introduce the following matrix notations for strain components:

$$\Gamma = \begin{bmatrix} \Gamma_{11} & \Gamma_{22} & \Gamma_{33} & 2\Gamma_{23} & 2\Gamma_{13} & 2\Gamma_{12} \end{bmatrix}^{\mathrm{T}} = \Gamma_\epsilon \bar{\epsilon} + \Gamma_h w \tag{3}$$

$$\Gamma_h = \begin{bmatrix} \frac{\partial}{\partial y_1} & 0 & 0 \\ 0 & \frac{\partial}{\partial y_2} & 0 \\ 0 & 0 & \frac{\partial}{\partial y_3} \\ 0 & \frac{\partial}{\partial y_3} & \frac{\partial}{\partial y_2} \\ \frac{\partial}{\partial y_3} & 0 & \frac{\partial}{\partial y_1} \\ \frac{\partial}{\partial y_2} & \frac{\partial}{\partial y_1} & 0 \end{bmatrix} \qquad \Gamma_\epsilon = \begin{bmatrix} 1 & 0 & 0 & y_3 & 0 & 0 \\ 0 & 0 & 1 & 0 & 0 & y_3 \\ 0 & 0 & 0 & 0 & 0 & 0 \\ 0 & 0 & 0 & 0 & 0 & 0 \\ 0 & 0 & 0 & 0 & 0 & 0 \\ 0 & 1 & 0 & 0 & y_3 & 0 \end{bmatrix} \tag{4}$$

To solve Eq. (2), for general cases we need to turn to numerical techniques such as finite element method. By expressing w using shape functions defined over SG as

$$w(x_\alpha; y_j) = S(y_j) V(x_\alpha) \tag{5}$$

where S represents the shape functions and V a column matrix of the nodal values of the fluctuation functions. Substituting Eq. (5) into Eq. (2), we obtain the leading terms for the zeroth-order approximation in the following discretized form as

$$U = \frac{1}{2} \left(V^T E V + 2 V^T D_{h\epsilon} \bar{\epsilon} + \bar{\epsilon}^T D_{\epsilon\epsilon} \bar{\epsilon} \right) \tag{6}$$

where

$$E = \left\langle (\Gamma_h S)^T D (\Gamma_h S) \right\rangle \quad D_{h\epsilon} = \left\langle (\Gamma_h S)^T D \Gamma_\epsilon \right\rangle \quad D_{\epsilon\epsilon} = \left\langle \Gamma_\epsilon^T D \Gamma_\epsilon \right\rangle \tag{7}$$

Minimizing U in Eq. (6) subject to the constraints, gives us the following linear system

$$E V = -D_{h\epsilon} \bar{\epsilon} \tag{8}$$

It is clear that V will linearly depend on $\bar{\epsilon}$, and the solution can be symbolically written as

$$V = V_0 \bar{\epsilon} \tag{9}$$

Substituting Eq. (9) back into Eq. (6), we can calculate the strain energy storing in the SG as the first approximation as

$$U = \frac{1}{2}\bar{\epsilon}^T \left(V_0^T D_{h\epsilon} + D_{\epsilon\epsilon}\right) \bar{\epsilon} \equiv \frac{\omega}{2}\bar{\epsilon}^T \bar{D} \bar{\epsilon} \tag{10}$$

where $\bar{D}$ is the effective plate stiffness to be used for in the classical plate model which contains the well-known A, B, and D matrices in CLT. However, unlike the standard procedure of CLT, the effective plate stiffness are calculated from knowledge of complex geometric and material characteristics in a SG at the microscopic level considering the smallness of both thickness and heterogeneity. In addition, there is no ad hoc kinematic assumptions in the derivation of MSG theory, where the only assumptions applied are the smallness of the SG in comparison to the in-plane dimensions and the existence of an effective plate constitutive model. The local fields within the SG can also be recovered easily based on the 2D global displacements, 2D global strains and curvatures $\bar{\epsilon}$. Especially, the local strain field can be obtained as

$$\Gamma = \left(\Gamma_h S V_0 + \Gamma_\epsilon\right) \bar{\epsilon}. \tag{11}$$

The local stress field can be obtained directly using the Hooke's law as

$$\sigma = D\Gamma. \tag{12}$$

The presented derivation is based on a zeroth-order approximation of the variational statement, if higher accuracy are required, a first-order approximation of the variational statement can be carried out and refined to obtain an effective constitutive relation used in FOSDT [18, 14].

EXAMPLES AND RESULTS

In this section, three examples are used to disclose the aforementioned flaws of lamination theories and the advantage of MSG. A general-purpose computer code called SwiftComp$^{\mathrm{TM}}$ implemented MSG, is applied to obtain the effective plate constants and also carry out the dehomogenization to get the 3D stresses within the original plate structure. Since currently the plate model in SwiftComp$^{\mathrm{TM}}$ is corrected to O(ϵ) which is of the same order of the CLT, the results from CLT and MSG are compared. Both the result from CLT and MSG are compared with direct 3D FEA using ABAQUS to assess the loss of accuracy of MSG and CLT. In the plate analysis, as the only element type theoretically based on Kirchhoff-Love assumption in ABAQUS, STRI3 is implemented.

Example 1: Single-layer plate

The configuration of first example is the same with the second example in section 4.2 in Ref. [18], which is a plate made of a single layer of unidirectional composites as shown in Figure 1 with $d_1 = h = 10\mu$m, $L = 200\mu$m . The unidirectional composite is constituted of epoxy matrix ($E_m = 3.5$ GPa, $v_m = 0.35$) and E-glass fiber

($E_f = 70$ GPa, $\nu_f = 0.2$) with volume fraction of fiber (vof) 0.6. Note SwiftComp$^{\text{TM}}$ can also be used as a general-purpose micromechanics code to obtain 3D properties, for instance, the lamina constants for this case. The effective lamina constants obtained using SwiftComp$^{\text{TM}}$ are given in Table I. The structure genome, which is the smallest mathematical building block of this plate can be viewed as that shown in Figure 1(b). The fiber direction is along x_1 and the plate is periodic along x_2. The non-zero items in plate stiffness matrix obtained from SwiftComp$^{\text{TM}}$ and CLT are compared in Tables II and III. Significance differences are observed in the bending stiffness.

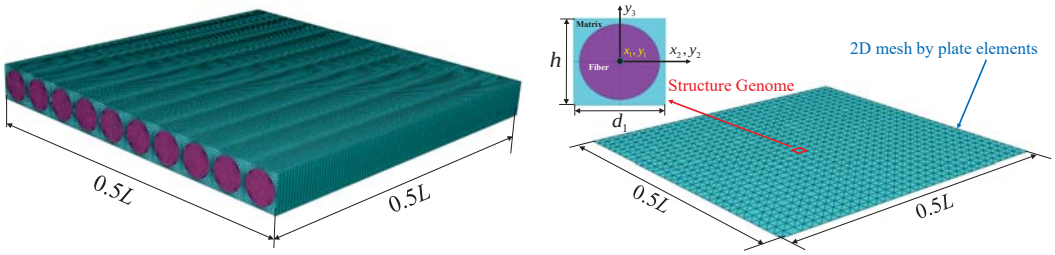

(a) 3D mesh in ABAQUS (b) 2D structure genome with plate elements

Figure 1. FEA of the plate-like structure with one ply

TABLE I. EFFECTIVE LAMINA CONSTANTS PREDICTED BY SWIFTCOMP

E_{11} (GPa)	$E_{22} = E_{33}$ (GPa)	$G_{12} = G_{13}$ (GPa)	G_{23} (GPa)	$\nu_{12} = \nu_{13}$	ν_{23}
43.43	15.23	4.71	3.37	0.250	0.266

TABLE II. COMPARISON OF THE EXTENSIONAL STIFFNESS

	A_{11} (10^3 N/m)	A_{12} (10^3 N/m)	A_{22} (10^3 N/m)	A_{33} (10^3 N/m)
CLT	444	39	156	47
SwiftComp	443	35	145	47

TABLE III. COMPARISON OF THE BENDING STIFFNESS

	D_{11} (10^{-9} Nm)	D_{12} (10^{-9} Nm)	D_{22} (10^{-9} Nm)	D_{33} (10^{-9} Nm)
CLT	3700	324	1297	1297
SwiftComp	2247	177	653	547

Consider a square plate containing 20 fibers and subjected to a uniform pressure of 1MPa. This plate is simply supported at the four edges. Only one-fourth of the

structure is analyzed because of symmetry as shown in Figure 1(a). The plate is modeled as a 2D plate as shown in Figure 1(b) in ABAQUS, using the two sets of plate constants in Tables II and III. It can be clearly observed in Table IV that the maximum deflection of the plate using plate stiffnesses prediction by using CLT is poor.

TABLE IV. COMPARISON OF THE MAXIMUM DEFLECTION

	Max Deflection (μm)	Difference (%)
3D FEA (ABAQUS)	4.792	Control Group
SwiftComp	4.755	-0.77
CLT	3.605	-24.77

The dehomogenization analysis can be carried out at any interested point of the 2D plate model by using the global plate strains as the input in SwiftComp$^{\mathrm{TM}}$. In this example, the stress dehomogenization is carried out at point (45, 45) of the plate if the origin of the plate model is set at the center of the whole plate. Figure 2 shows the stress distributions at this point through the thickness of plate from SwiftComp$^{\mathrm{TM}}$, 3D FEA using ABAQUS, and from the CLT method using the embedded composite layer-up model in ABAQUS. It can be seen that for one layer plate, the components of σ_{11}, σ_{22}, σ_{12}, results from SwiftComp$^{\mathrm{TM}}$ result in a perfect agreement with 3D FEA, while CLT cannot predict the details of the stress distribution. Although SwiftComp$^{\mathrm{TM}}$ does not predicted a very accurate σ_{33}, it did capture both the magnitude and the distribution tendency. Note that CLT can not predict this stress component. Another thing note worthy that if a 3D SG with its cross-section identical to the chosen 2D SG in this example, SwiftComp$^{\mathrm{TM}}$ produce the same plate stiffness and stress field.

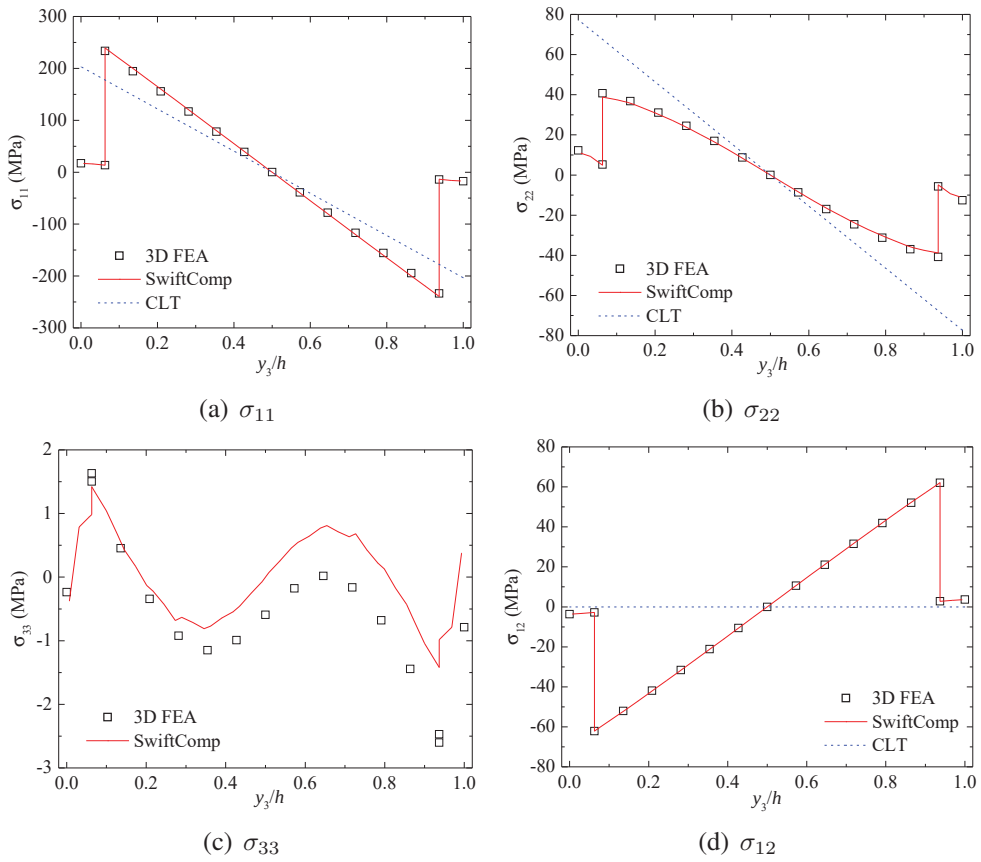

(a) σ_{11} (b) σ_{22}

(c) σ_{33} (d) σ_{12}

Figure 2. Comparison of the stress distribution through the normalized thickness

Example 2: Double-layer plate

The second example is a two-layer plate structure constructed by a 0 degree layer and 90 degree layer shown in Figure 3, where $L = 30$ m, $d_1 = d_2 = 0.5h = 1$m. The plate is simply supported and under uniform pressure of 500 KPa. Similar to the first example, only one-fourth of the plate is modeled. The material properties of the fiber are $E_1 = 58.61$ GPa, $E_2 = E_3 = 14.49$ GPa, $G_{12} = G_{13} = 5.38$ GPa, $G_{23} = 5.81$ GPa, $\nu_{12} = \nu_{13} = 0.250$, $\nu_{23} = 0.247$. For the matrix, $E = 3.45$ GPa, $\nu = 0.37$. The vof is 0.6. The effective lamina constants obtained using SwiftComp$^{\text{TM}}$ are given in Table V.

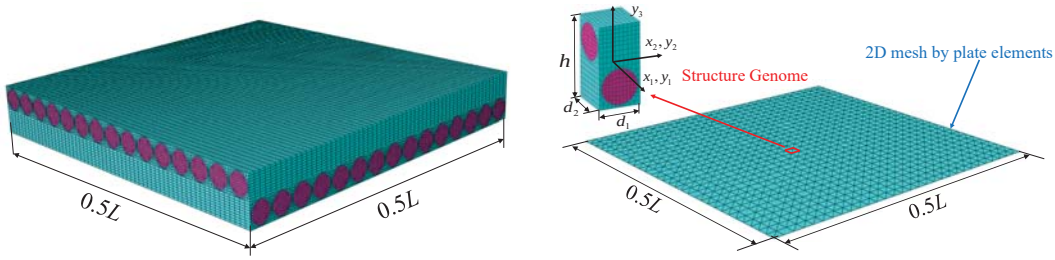

(a) 3D mesh in ABAQUS (b) 2D structure genome with plate elements

Figure 3. FEA of the plate-like structure with two plies

TABLE V. EFFECTIVE LAMINA CONSTANTS PREDICTED BY SWIFTCOMP

E_{11} (GPa)	$E_{22} = E_{33}$ (GPa)	$G_{12} = G_{13}$ (GPa)	G_{23} (GPa)	$\nu_{12} = \nu_{13}$	ν_{23}
36.56	8.59	2.79	2.49	0.294	0.362

The plate stiffnesses obtained from SwiftComp$^{\mathrm{TM}}$ and CLT are compared in the Tables VI, VII, and VIII. It is observed that the major differences of about 10% lie in the bending stiffness. The maximum deflection of the plate analysis using different models are presented in Table IX. Apparently the plate stiffnesses of MSG resulted in much more accurate global reaction compared with that from CLT.

TABLE VI. COMPARISON OF THE EXTENSIONAL STIFFNESS

	A_{11} (N/m)	A_{12} (N/m)	A_{22} (N/m)	A_{33} (N/m)
CLT	4.61E+10	5.16E+9	4.61E+10	5.58E+9
SwiftComp	4.58E+10	4.97E+9	4.58E+10	5.61E+9

TABLE VII. COMPARISON OF THE BENDING STIFFNESS

	D_{11} (Nm)	D_{12} (Nm)	D_{22} (Nm)	D_{33} (Nm)
CLT	1.54E+10	1.72E+9	1.54E+10	1.86E+9
SwiftComp	1.39E+10	1.55E+9	1.39E+10	1.78E+9

TABLE VIII. COMPARISON OF THE COUPLING STIFFNESS

	B_{11} (N)	B_{12} (N)	B_{22} (N)	B_{33} (N)
CLT	-1.43E+10	0.0	1.43E+10	0.0
SwiftComp	-1.44E+10	-2.79E+6	1.44E+10	7.98E+4

TABLE IX. DATA COMPARISON OF THE MAXIMUM DEFLECTION

	Max Deflection (m)	Difference (%)
3D FEA (ABAQUS)	0.2451	Control Group
SwiftComp	0.2471	-0.82
CLT	0.2088	-14.8

The stress distributions at location (7.5, 7.5) through the thickness are presented in Figure 4. Clearly with the same simulation effort, SwiftComp$^{\mathrm{TM}}$ can predict the stress distribution accurately, while CLT cannot predict accurate maximum stresses. Figure 4 also shows that the maximum stress discrepancy happened at the interface between fiber and matrix demonstrated by the results of 3D FEA and SwiftComp$^{\mathrm{TM}}$, instead of the layer interface shown by CLT. This result also indicates the possibility to implement a simple plate model based on SwiftComp$^{\mathrm{TM}}$ to carry out the failure analysis of composite laminate analysis effectively.

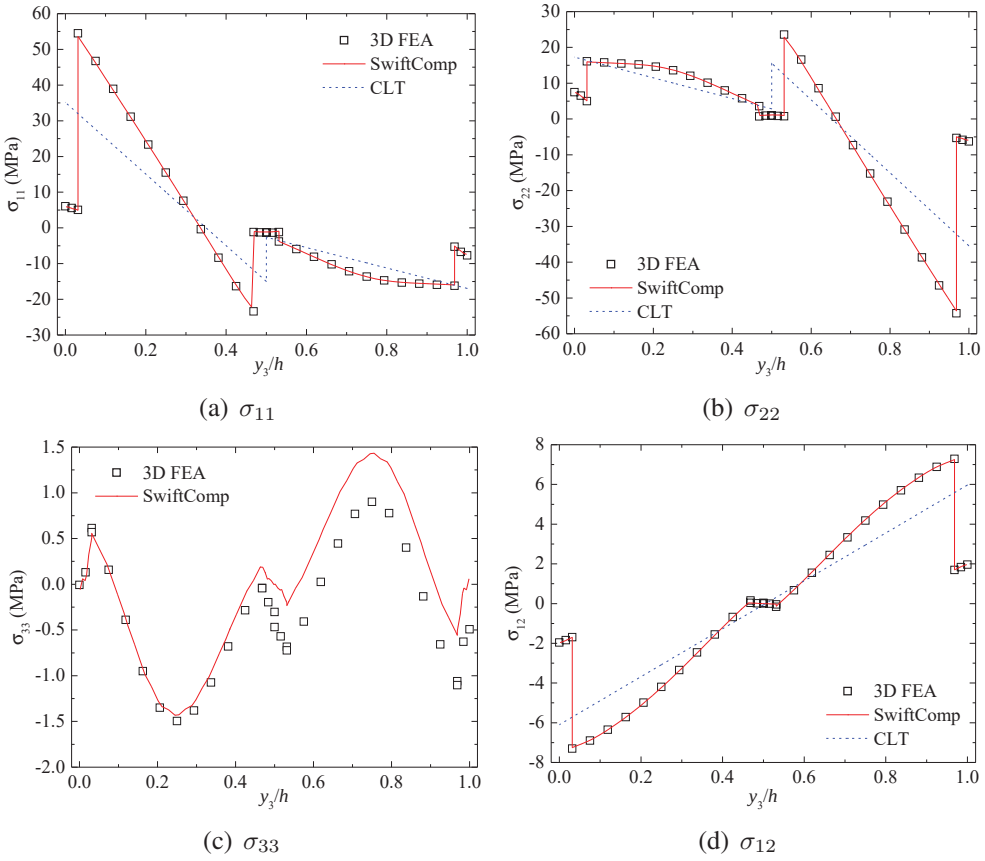

(a) σ_{11} (b) σ_{22}

(c) σ_{33} (d) σ_{12}

Figure 4. Comparison of the stress distribution through the normalized thickness

Example 3: 3D orthogonal interlock composites

This example studies a realistic 3D orthogonal interlock composites plane structures, of which the SG is shown in Figure 5. The material properties are given in Table X. The example is studied in Ref. [19] by asymptotic expansion homogenization method to obtain the lamina constants of the composite structure and local fields, however no deflection deformation can be captured due to the assumption that zeroth order deflection is zero. In contrast we investigate a bending behavior of this highly heterogeneous composite plate structure.

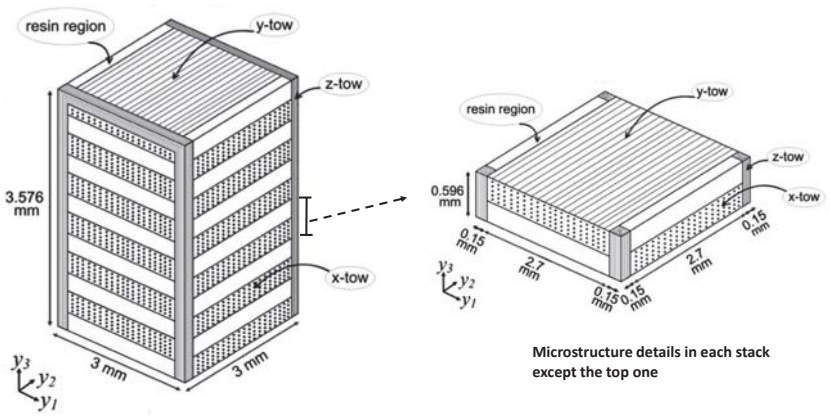

Figure 5. SG of the orthogonal interlock composites(cited from Ref. [19])

TABLE X. MATERIAL PROPERTIES OF THE ORTHOGONAL INTERLOCK COMPOSITES

Properties	X-tow	Y-tow	Z-tow	Resin region
E_1 (GPa)	122.55	7.13	4.96	3.40
E_2 (GPa)	7.13	122.55	4.96	3.40
E_3 (GPa)	7.13	7.13	148.70	3.40
G_{12} (GPa)	3.25	3.25	2.45	1.26
G_{31} (GPa)	3.25	2.53	3.21	1.26
G_{23} (GPa)	2.53	23.25	3.21	1.26
ν_{12}	0.263	0.015	0.476	0.35
ν_{31}	0.015	0.414	0.335	0.35
ν_{23}	0.414	0.263	0.011	0.35

Applying plate analysis of MSG using SwiftComp$^{\mathrm{TM}}$, the A,B,D matrices obtained from SwiftComp$^{\mathrm{TM}}$ are listed below, where the unit of extension stiffness A is 10^3 N/m, coupling stiffness B is N, and bending stiffness D is 10^{-3} Nm.

$$
\begin{aligned}
A &= \begin{bmatrix} 213339 & 6857 & 0 \\ 6857 & 204572 & 0 \\ 0 & 0 & 10635 \end{bmatrix} \\
B &= \begin{bmatrix} 357273 & 12231 & 0 \\ 12231 & 382208 & 0 \\ 0 & 0 & 19019 \end{bmatrix} \\
D &= \begin{bmatrix} 826711 & 28866 & 0 \\ 28866 & 918074 & 0 \\ 0 & 0 & 45326 \end{bmatrix}
\end{aligned} \tag{13}
$$

A direct 3D FEA is conducted using a plate structure with 25 SGs in the x_1 direction and 10 SGs along x_2 direction, therefore the plate has dimension of $75 \times 30 \times 3.576$ mm^3. The boundary condition is shown in Figure 6. The maximum deflection of the plate structure predicted by SwiftComp$^{\text{TM}}$-based plate analysis and direct 3D FEA only has a discrepancy of -1.5%. Three stress sampling paths Line A, Line B and Line C having macro coordinates (37.5, -7.5), (37.5, -6.075) and (38.925, -8.925) respectively are taken on the reference surface. Interested users can refer to Ref. [19] for specific corresponding SG constituents along thickness direction of each line. The dominant stress component σ_{11} at this three paths through the thickness of the plate are compared between SwiftComp$^{\text{TM}}$ and 3D FEA in Figure 7. It is shown that for such highly heterogeneous composite structure, the stress distributions agree well with that of 3D FEA. However while the 3D FEA took 75 minutes with 20 CPUs, SwiftComp$^{\text{TM}}$ took much less computation time within 3 minutes by only 1 CPU.

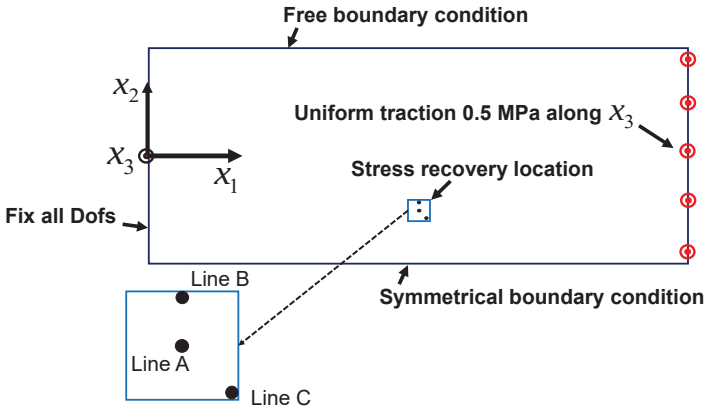

Figure 6. Boundary conditions of the 3D orthogonal interlock composite plate and stress recovery locations

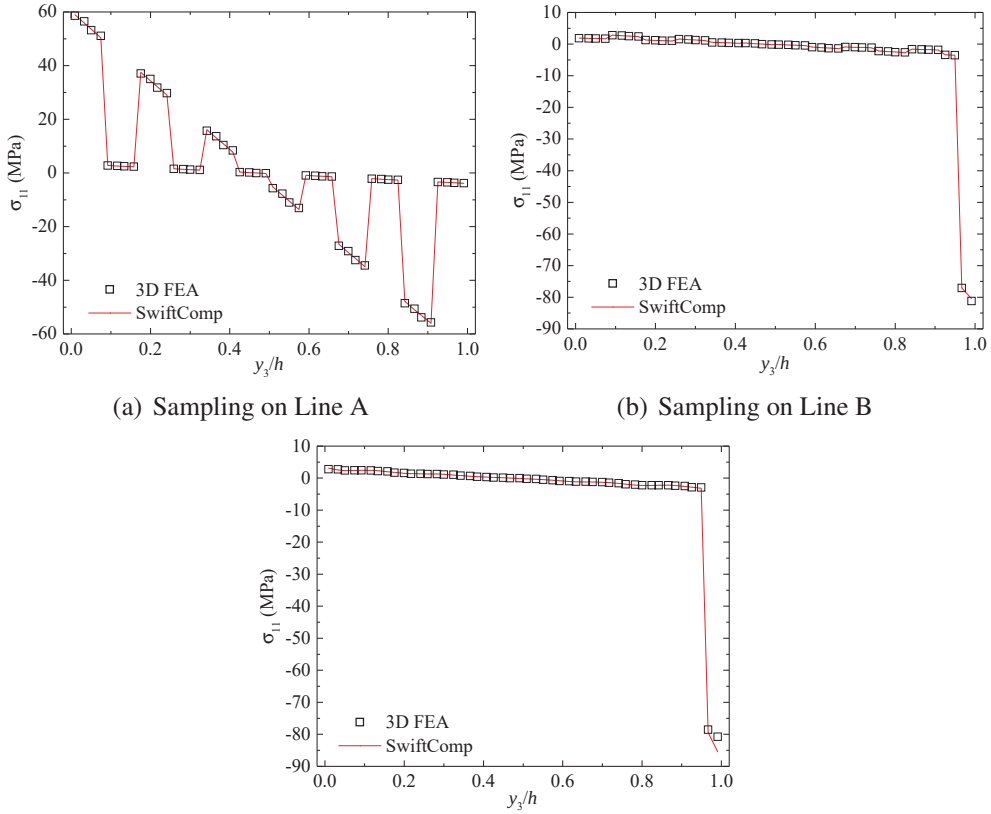

(a) Sampling on Line A

(b) Sampling on Line B

(c) Sampling on Line C

Figure 7. Comparison of the stress distribution through the normalized thickness

CONCLUSIONS

The inherent assumption that laminate is made of homogeneous layers in lamination theories, artificially created layer boundaries which do not actually exist in composite multilayer plate/shell structures, and also deprived the ability of lamination theories to predict the accurate local fields such as stress considering the complex microstructures within the plates. However, a recently developed multiscale structural modeling theory, Mechanics of Structure Genome (MSG), introduced none ad hoc kinematic assumptions in its derivation. MSG decouple the original problem of 3D composite plate structures into a 2D plate/shell problem and a constitutive modeling over a Structure Genome. Through analysis of structure genome, effective plate stiffness matrix and the local fields recovery relations can be obtained based on the information of the real microstructures of the original 3D body. Therefore artificial layer boundaries are elegantly avoided. It is proved numerically by the examples in the current study that MSG is capable of constructing high-fidelity effective plate/shell constitutive relations used for CLT for multilayer composite plate/shell structures, and also can recover accurate local fields compared with 3D direct finite element analysis. Although the zeroth-order plate model of MSG used in the current study cannot predict accurate transverse shear stress, a refined model of MSG can give better results. The accuracy of localized stress suggests a good prospect of MSG being

used in failure analysis. Another advantage of MSG is its efficiency. The computation cost of MSG is comparable with CLT, however the result using MSG is much more accurate. MSG has been implemented into a general-purpose multiscale constitutive modeling code called SwiftComp^{TM}, which can be accessed in the cloud at cdmHUB.org.

REFERENCES

1. Khandan, R., S. Noroozi, P. Sewell, and J. Vinney. 2012, "The Development of Laminated Composite Plate Theories: A Review," *Journal of Materials Science*, 47(16):5901–5910.
2. Demasi, L. and W. Yu. 2013, "Assess the Accuracy of the Variational Asymptotic Plate and Shell Analysis Using the Generalized Unified Formulation," *Mechanics of Advanced Materials and Structures*, 20(3):227–241.
3. Carrera, E. 2002, "Theories and Finite Elements for Multilayered, Anisotropic, Composite Plates and Shells," *Archives of Computational Methods in Engineering*, 9(2):87–140.
4. Reissner, E. and Y. Stavsky. 1961, "Bending and Stretching of Certain Types of Heterogeneous Aeolotropic Elastic Plates," *Journal of Applied Mechanics*, 28(3):402–408.
5. Mindlin, R. D. 1961, "Influence of rotatory inertia and shear flexural motions of isotropic elastic plates," *Journal of Applied Mechanics*, 18:31–38.
6. Reissner, E. 1945, "The Effect of Transverse Shear Deformation on the Bending of Elastic Plates," *Journal of applied Mechanics*, 12:69–77.
7. Vlasov, B. 1957, "On the Equations of Bending of Plates," *Dokla Ak Nauk Azerbeijanskoi-SSR*, 3:955–979.
8. Reddy, J. N. 1984, *Energy and Variational Methods*, John Wiley, New York.
9. Reddy, J. N. and N. D. Phan. 1985, "Stability and Vibration of Isotropic, Orthotropic and Laminated Plates According to a Higher-Order Shear Deformation Theory," *Journal of Sound and Vibration*, 98(2):157–170.
10. Reddy, J. N. and C. F. Liu. 1985, "A Higher-Order Shear Deformation Theory of Laminated Elastic Shells," *International Journal of Engineering Science*, 23(3):319–330.
11. Carrera, E. 2003, "Theories and Finite Elements for Multilayered Plates and Shells: A Unified Compact Formulation with Numerical Assessment and Benchmarking," *Archives of Computational Methods in Engineering*, 10(3):215–296.
12. Mantari, J. L. and C. G. Soares. 2012, "Analysis of Isotropic and Multilayered Plates and Shells by Using a Generalized Higher-Order Shear Deformation Theory," *Composite Structures*, 94(8):2640–2656.
13. Carrera, E. and S. Brischetto. 2009, "A Survey with Numerical Assessment of Classical and Refined Theories for the Analysis of Sandwich Plates," *Applied Mechanics Reviews*, 62(1):010803.
14. Lee, C.-Y., W. Yu, and D. H. Hodges. 2014, "Refined Modeling of Composite Plates with In-Plane Heterogeneity," *ZAMM-Journal of Applied Mathematics and Mechanics/Zeitschrift für Angewandte Mathematik und Mechanik*, 94(1-2):85–100.
15. Dixit, A. and H. S. Mali. 2013, "Modeling Techniques for Predicting the Mechanical Properties of Woven-Fabric Textile Composites: A Review," *Mechanics of Composite Materials*, 49(1):1–20.
16. Huang, H. S. 2015, "Influence of Phase Shift on the Responses of Woven Laminated Composites," *Composite Structures*, 130:143–154.
17. Yu, W. 2015, "Structure Genome: Fill the Gap between Materials Genome and Structural Analysis," in *56th AIAA/ASCE/AHS/ASC Structures, Structural Dynamics, and Materials Conference*, AIAA SciTech.
18. Lee, C.-Y. and W. Yu. 2011, "Homogenization and Dimensional Reduction of Composite Plates with In-Plane Heterogeneity," *International Journal of Solids and Structures*, 48(10):1474–1484.
19. Nasution, M. R. E., N. Watanabe, A. Kondo, and A. Yudhanto. 2014, "A Novel Asymptotic Expansion Homogenization Analysis for 3-D Composite with Relieved Periodicity in the Thickness Direction," *Composites Science and Technology*, 97:63–73.

AIAA SciTech
4-8 January 2016, San Diego, California, USA
57th AIAA/ASCE/AHS/ASC Structures, Structural Dynamics, and Materials Conference

A Micromechanical Approach to High Cycle Fatigue Analysis and Life Prediction of Composites

Hamsasew Sertse* and Wenbin Yu†

The objective of this paper is to analyze the high cycle fatigue (HCF) damage and fatigue life of composites using a micromechanical approach based on mechanics of structure genome (SG) and its companion code SwiftComp. In this study, local continuum damage mechanics approach is employed to model and analyze the evolution of fatigue damage. The constitutive law for elastic damage analysis is derived. The evolution of anisotropic fatigue damage is iteratively approximated by incremental algorithm at each numerical integration point using weighted averaged local field. The HCF fatigue damage and life are estimated for continuous fiber-reinforced composite. The predicted results are in good agreement with available experimental data. The effects of progressive fatigue damage on effective properties of the composite are also examined.

I. Introduction

In recent decades, composites are extensively used in cyclic loading working conditions due to their excellent capability of resisting fatigue failure. Despite their wide applications, there are a number of challenges related to the applications of these materials. One of the challenges is the lack of accurate tools for predictions of fatigue damage and its corresponding life under various thermo-mechanical loading conditions. A great deal of efforts have been devoted to analyze fatigue failure in homogeneous materials. However, the direct use of this approach to heterogenous materials may not lead to reasonable predictions due to higher accumulation of damage in the composites.[1] Generally speaking, fatigue damage is a multi-scale complex local phenomena that can be affected by many interacting factors.[2–4] Numerous researchers have proposed various models to analyze fatigue damage and its corresponding life. These models may be categorized as fatigue life models and phenomenological models.[5,6] The fatigue life models predict the fatigue life of a component from stress-life (S-N) or strain life (ϵ-N) curves based on a specified failure criteria. This method does not take into account the local material degradation. Recently, a new energy based fatigue life analysis is proposed to analyze fatigue life based on both elastic and plastic energy in the material. This approach correlates the energy in the material with fatigue life.[7,8] Interested reader may refer to Refs. [5, 6] for various similar fatigue models. On the other hand, the phenomenological models use the residual strength or stiffness to predict the fatigue damage. Continuum damage mechanics approach is a typical phenomenological method that is extensively used in damage and fatigue life analysis of both homogeneous and composites.[9–11] In composites, fatigue damage and life analysis are generally more complex due to the interactions among various constituents and their interfaces.[12] In these materials, fatigue damage and life prediction analysis can be performed using both macromechanical and micromechanical approaches. In macromechanical approach, fatigue damage and life analysis are performed at macro scale or with the homogenized properties.[1,13–17] In this approach, it is evident that fatigue damage analysis does not take into account the local stress disturbance to various constituents and their interfacial interactions. Thus, the approach may not reasonably predict fatigue damage and life for composites with complex microstructure. Whereas, in micromechanical approach, the local strain and stress fields are mainly employed for fatigue damage analysis. In Refs. [18, 19], fatigue damage and life are analyzed based on the average stress and strain in each constitute using damage model similar to the well-known Tsai-Hill yield criteria. Fish and his coworkers[20] analyzed fatigue life of elastic and inelastic composites using mathematical homogenization approach. This analysis is performed using continuum damage mechanics approach based on the average

*Graduate Research Assistant, School of Aeronautics and Astronautics, Purdue University
†Associate Professor, School of Aeronautics and Astronautics, Purdue University, AIAA Associate Fellow.

stresses and strains in each constituent by adopting nonlocal isotropic damage parameter. Voyiadjis and Deliktas[21] analyzed anisotropic damage in composites based on the average stress and strains in the each constitutes. The average local fields are computed using Mori-Tanaka approach. The average stress and strain approach better predicts fatigue life compared with the macromechanical approach. However, in HCF damage and life predictions, the local material damage lead to sudden fracture of the material before inducing large elastic strain, thus the material will unlikely sustain the applied load until the average stress or strain in each constituent meet the requirement of the failure particularly for the safe life design criteria. Thus, the average stress and strain approach may not rigorously predict the fatigue damage in HCF.

In continuum damage mechanics, it is commonly postulated that failure in brittle material is dominated with dissipative mechanisms where viscous, thermal or other non-mechanical effects are not taken into account and also the plastic strain is assumed to be negligible compared with the elastic strain. These assumptions lead to elastic damage analysis for HCF damage and life prediction analysis with isotropic or anisotropic damage assumption.[9,22,23] On the other hand, it is hypothesized that damage in brittle material undergoes the process of nucleation, void formation and coalescence at micro scale, this implies that the material yields plastic strain locally while the majority of the part remains elastic. On this basis, Lemaitre and his coworkers[24] proposed a two-scaled approach assuming that brittle materials experience a localized plastic strain. The local stress and strain fields approximated using Eshelby−Kröner localization law. Desmorat and his coworkers[25] extended the two-scaled approach for complex thermomechanical loading conditions. Doudard and his coworkers also analyzed the fatigue life of homogeneous materials using the two-scaled based probabilistic approach.[26] For detailed numerical implementation of the two−scaled approach, interested reader may refer to Ref. [27].

The main drawbacks of continuum damage mechanics for numerical implementation are its pathological mesh dependency and improper convergency which originate from strain localization due to strain softening, damage localization and stress singularity at crack tip. Numerous researchers proposed possible solutions to avoid these problems. Interested reader may refer to Refs. [28–30] for various proposed approaches to solve a mesh dependency problem of local damage approach. The common methods to solve the mesh dependency problems are nonlocal damage,[31,32] gradient method,[33,34] and viscous regularization.[35] The nonlocal approach described in Refs. [28, 31] proposes averaging local fields at integration points based on weighted average of the local fields near the integration point. The weighting value is a function of characteristic length expressed using Gaussian weighting function.

It is obvious that the local field recovery is a critical capability to sufficiently analyze fatigue damage and life prediction of composites. This capability is important particularly for HCF analysis where fatigue damage is highly localized and affected by the local stress and strain fields. SwiftComp is a general-purpose multiscale constitutive modeling code for composites which provides unified modeling for 1D (beams), 2D (plates/shells), or 3D composite structures. This is accomplished using the concept of structure genome that unifies structural mechanics and micromechanics.[36] The previous version of SwiftComp, VAMUCH (Variational Asymptotic Method for Unit cell Homogenization), sufficiently demonstrates excellent capability both in predicting effective properties and recovering the local fields.[37,38] Thus, SwiftComp is a natural choice to perform fatigue damage analysis and life predictions.

In the HCF, the number of cycles for fatigue life prediction are extremely large and running all these cycles is computationally demanding, thus the cycle jump methods proposed in Ref. [39] is used in this study to sufficiently obtain a reasonable predictions of the fatigue damage and life cycle.

The objective of this paper is to analyze the high cycle fatigue (HCF) damage and fatigue life of composites using a micromechanical approach based on mechanics of structure genome (SG) and its companion code SwiftComp. The fatigue damage and life analysis are performed using local continuum damage mechanics approach. The damage variables are iteratively solved using the incremental method. The HCF fatigue damage and life are estimated for continuous fiber-reinforced composite. The prediction of fatigue life of the composite shows good agreement with experimental data.

II. Basics of Damage Mechanics

The concept of continuum damage mechanics is first formulated based on the hypothesis of Kachanov[40] which postulates the gradual deterioration of the effective cross sectional area that sustain the the applied

load. Thus the damage variable can be expressed as

$$d = \frac{A - \tilde{A}}{A} \tag{1}$$

where A denotes total cross sectional area, $\tilde{A}$ denotes effective cross sectional area. The value of d shows the level of damage in the material when $d = 0$ shows undamage states (no damage) and, $d = D_c \leq 1$ shows the extent of failure, if $d = 1$ shows a complete failure. This formulation holds only for the isotropic damage however in most cases the damage may not be necessarily isotropic thus in general the damage may be better expressed using a second-order tensor which considers the directional dependency of the the damage parameter. Thus, let $\boldsymbol{d}$ denote a symmetric second-order tensor for anisotropic damage. It can be expressed as

$$\boldsymbol{d} = \begin{bmatrix} d_{11} & d_{66} & d_{55} \\ d_{66} & d_{22} & d_{44} \\ d_{55} & d_{44} & d_{33} \end{bmatrix} \tag{2}$$

The damaged second-order compliance tensor proposed in Ref. [15] is adopted here for the general multi-axial stress state with anisotropic damage. Then, the fourth-order damaged compliance tensor can be expressed as

$$\boldsymbol{\mathcal{S}}(\boldsymbol{d}) = \begin{bmatrix} \frac{S_{1111}}{1-d_{11}} & S_{1112} & S_{1113} & S_{1123} & S_{1113} & S_{1112} \\ & \frac{S_{2222}}{1-d_{22}} & S_{2223} & S_{2223} & S_{2213} & S_{2216} \\ & & \frac{S_{3333}}{1-d_{33}} & S_{3323} & S_{3313} & S_{3312} \\ & & & \frac{S_{2323}}{1-d_{44}} & S_{2313} & S_{2312} \\ & SYMM & & & \frac{S_{1313}}{1-d_{55}} & S_{1312} \\ & & & & & \frac{S_{1212}}{1-d_{66}} \end{bmatrix} \tag{3}$$

Using the strain equivalence approach, the stress in the damaged and undamaged configurations can be related as

$$\tilde{\boldsymbol{\sigma}} = \boldsymbol{\mathcal{M}}^{-1} : \boldsymbol{\sigma}, \quad \boldsymbol{\mathcal{M}}^{-1} = \boldsymbol{\mathcal{S}}^{-1} : \tilde{\boldsymbol{\mathcal{S}}} \tag{4}$$

where $\tilde{\boldsymbol{\sigma}}$ denotes effective stress in the undamaged material, $\boldsymbol{\sigma}$ denotes stress in the damaged material, and $\boldsymbol{\mathcal{M}}$ denotes the fourth-order damage effect tensor as a function of the fourth-order compliance tensor, $\tilde{\boldsymbol{\mathcal{S}}}$ denotes effective compliance in the undamaged material, and $\boldsymbol{\mathcal{S}}$ denotes compliance in the damaged material.

III. Brief Review of Thermodynamics

In the general thermomechanical problems, the phenomena of elasticity, plasticity, and the thermal effects may be modeled using irreversible thermodynamics formulation. In this case, the observable state variables can be second-order elastic strain tensor $\boldsymbol{\epsilon}^e$ and temperature T with their associated variables second-order stress $\boldsymbol{\sigma}$ and entropy S, respectively. The local or internal variables could be accumulated plastic strain r with its associated variable R and kinematic hardening variable or back stress $\boldsymbol{\alpha}$ with its associated variable $\boldsymbol{A}$, respectively. Let the Helmholtz free energy be expressed as a function of the given state variables as

$$\psi = \psi(\boldsymbol{\epsilon}^e, T, r, \boldsymbol{\alpha}, V_k) \quad (k = 1, 2, ..., n) \tag{5}$$

where ψ denotes energy per unit mass of the material and V_k denote other internal variables. For HCF analysis, it is assumed that the plastic strain is negligible and also let the internal variables V_k be the second-order damage tensor $\boldsymbol{d}$ and damage hardening parameter β. Thus, the Helmholtz free energy in Eq. (5) for an isothermal process can be rewritten as

$$\psi = \psi(\boldsymbol{\epsilon}^e, \boldsymbol{d}, \beta) \tag{6}$$

The Helmholtz free energy per unit mass for uncoupled elastic and damaged part of the material can further be decomposed as follows:

$$\psi(\boldsymbol{\epsilon}^e, \boldsymbol{d}, \beta) = \psi_e(\boldsymbol{\epsilon}^e, \boldsymbol{d}) + \psi_d(\beta) \tag{7}$$

$$\rho\psi_e(\boldsymbol{\epsilon}^e, \boldsymbol{d}) = \frac{1}{2}\boldsymbol{\epsilon}^e : \boldsymbol{\mathcal{C}}(\boldsymbol{d}) : \boldsymbol{\epsilon}^e \qquad \text{and} \qquad \rho\psi_d(\beta) = f(\beta, o, L) \tag{8}$$

where o and L denote material constants obtained from experiments. Substituting Eq. (7), in to the Clausius-Duhem inequality, the following relation is obtained

$$(\boldsymbol{\sigma} - \rho\frac{\partial\psi}{\partial\boldsymbol{\epsilon}^e}) : \dot{\boldsymbol{\epsilon}}^{\boldsymbol{e}} - \rho\frac{\partial\psi}{\partial\boldsymbol{d}} : \dot{\boldsymbol{d}} - \rho\frac{\partial\psi}{\partial\beta}\dot{\beta} \geq 0 \tag{9}$$

This inequality must be satisfied for any values of $\dot{\epsilon}^e$, $\dot{\boldsymbol{d}}$ and $\dot{\beta}$. If damage does not exist in the material, then the inequality can be satisfied only for $\boldsymbol{\sigma} = \rho\frac{\partial\psi}{\partial\epsilon^e}$ which gives the elastic constitutive equation. Let $\boldsymbol{Y}$ and B be thermodynamic conjugate force variables that denote a second-order tensor that represents elastic energy release rate due to damage and damage hardening parameter, respectively. These variables can be related to Helmholtz free energy, i.e., Eq. (7), as

$$\boldsymbol{y} \equiv -\rho\frac{\partial\psi}{\partial\boldsymbol{d}} = -\rho\frac{\partial\psi_e}{\partial\boldsymbol{d}}, \qquad \text{and} \qquad B \equiv \rho\frac{\partial\psi}{\partial\beta} = \rho\frac{\partial\psi_d}{\partial\beta} \tag{10}$$

From Eq. (9) and using Eq. (10), it can be postulated that the dissipation per unit volume can be obtained as

$$\Phi = \boldsymbol{y} : \dot{\boldsymbol{d}} - B\dot{\beta} \geq 0 \tag{11}$$

Based on this dissipation mechanism, without loss of generality, for an associated flow rule, the dissipation potential F can be expressed as[41]

$$F(\boldsymbol{y}, B; \boldsymbol{d}, \beta) = f_{\boldsymbol{d}}(\boldsymbol{y}, B; \boldsymbol{d}, \beta) \tag{12}$$

where $f_{\boldsymbol{d}}$ denotes damage yield function. Here, it is assumed that there exists the damage yield function $f_{\boldsymbol{d}} = 0$ in the space of the thermodynamic conjugate force $\boldsymbol{y}$ and B, thus, the convex surface for the damage yield function may be expressed as[42]

$$f_{\boldsymbol{d}}(\boldsymbol{y}, B) = Y_{EQ} - (B_o + B) = 0 \tag{13}$$

where $Y_{EQ} = \left[\frac{1}{2}\boldsymbol{y} : \boldsymbol{\mathcal{L}}(\boldsymbol{d}) : \boldsymbol{y}\right]^{1/2}$ denotes equivalent damage energy release rate, B_o denotes damage threshold (material dependent value). $\boldsymbol{\mathcal{L}}(\boldsymbol{d})$ denotes the fourth-order damage tensor function which can be expressed using index notation as

$$\boldsymbol{\mathcal{L}}_{ijkl} = \frac{1}{2}(\delta_{ik}\delta_{jl} + \delta_{il}\delta_{jk}) + \frac{1}{2}c^d(\delta_{ik}d_{jl} + d_{ik}\delta_{jl} + \delta_{il}d_{jk} + d_{il}\delta_{jk}) \tag{14}$$

where c^d denotes material constants. Using the damage yield function, damage evolution and the rate of change of damage parameter can be expressed as

$$\dot{\boldsymbol{d}} = \dot{\lambda}_{\boldsymbol{d}}\frac{\partial f_d}{\partial\boldsymbol{y}}, \qquad \text{and} \qquad \dot{\beta} = -\dot{\lambda}_{\boldsymbol{d}}\frac{\partial f_{\boldsymbol{d}}}{\partial B} \tag{15}$$

where $\dot{\lambda}_{\boldsymbol{d}}$ denotes damage independent multiplier and it describes the rate of damage flow, $\frac{\partial f_{\boldsymbol{d}}}{\partial y}$ denotes the direction of flow of damage. Let us assume [41, 43],

$$\rho\psi_d(\beta) = \frac{S^2}{2Lo}, \quad S = L(1 - exp(-o\beta)) \tag{16}$$

Substituting Eq (16) in Eq (10), one can obtain

$$B = L(1 - exp(-o\beta)) \tag{17}$$

where L and o are constant to be obtained from curve fitting with experimental data for monotonic loading. The loading and unloading conditions of Eq (15) can be obtained using Kuhn-Tucker conditions.

$$\dot{\lambda}_d \geq 0, \quad f_d \leq 0, \quad \dot{\lambda}_d f_d = 0 \tag{18}$$

where $\dot{\lambda}_{\boldsymbol{d}}$ is obtained from consistency condition $\dot{f}_d = 0$ as[41, 43]

$$\dot{f}_d = \frac{\partial f_d}{\partial \boldsymbol{y}} : \dot{\boldsymbol{y}} + \frac{\partial f_d}{\partial B}\frac{\partial B}{\partial \beta}\dot{\beta} + \frac{\partial f_d}{\partial \boldsymbol{\mathcal{L}}}\frac{\partial \boldsymbol{\mathcal{L}}}{\partial \boldsymbol{d}} : \dot{\boldsymbol{d}} = 0 \tag{19}$$

The rate form of the thermodynamic conjugate force may be expressed using Eq. (8) and (10)as

$$\dot{\boldsymbol{y}} = \frac{\partial \boldsymbol{y}}{\partial \boldsymbol{\epsilon^e}} : \dot{\boldsymbol{\epsilon^e}} + \frac{\partial \boldsymbol{y}}{\partial \boldsymbol{d}} : \dot{\boldsymbol{d}} \tag{20}$$

Substituting Eq. (20) and (15) in Eq (19) and after a few algebraic manipulations, one obtains

$$\dot{f}_d = \frac{1}{2Y_{EQ}}\boldsymbol{y} : \left(\boldsymbol{\mathcal{L}} : \frac{\partial \boldsymbol{y}}{\partial \boldsymbol{\epsilon^e}}\right) : \dot{\boldsymbol{\epsilon^e}} + \boldsymbol{L}\dot{\lambda}_d = 0 \tag{21}$$

where $\boldsymbol{L} = -\frac{1}{2Y_{EQ}}(\boldsymbol{y} : \boldsymbol{\mathcal{L}} : (\frac{\partial \boldsymbol{y}}{\partial \boldsymbol{d}} : \frac{\partial f_{\boldsymbol{d}}}{\partial \boldsymbol{y}})) - \frac{1}{4Y_{EQ}}(\boldsymbol{y} : (\frac{\partial \boldsymbol{\mathcal{L}}}{\partial \boldsymbol{d}} : \boldsymbol{y}) : \frac{\partial f_d}{\partial \boldsymbol{y}}) + \frac{\partial B}{\partial \beta}$. Then, the damage evolution rate can be expressed as

$$\dot{\lambda}_d = \frac{\boldsymbol{y} : \left(\boldsymbol{\mathcal{L}} : \frac{\partial \boldsymbol{y}}{\partial \epsilon^e}\right) : \dot{\boldsymbol{\epsilon^e}}}{\frac{1}{2Y_{EQ}}\boldsymbol{L}} \tag{22}$$

For a small incremental loading, one can write the stress-strain law in the rate form as

$$\dot{\sigma} = \frac{\partial \sigma}{\partial \epsilon^e}\dot{\epsilon^e} + \frac{\partial \sigma}{\partial \boldsymbol{d}}\dot{\boldsymbol{d}} \tag{23}$$

It should be noted that the plastic strain is assumed to be negligible. The damage evolution rate in Eq (15) can be obtained using Eq (22) for the strain space as

$$\dot{\boldsymbol{d}} = \frac{1}{2Y_{EQ}\boldsymbol{L}}\left(\frac{\partial f_d}{\partial \boldsymbol{y}} \otimes F_{LY\epsilon}\right)\dot{\epsilon^e} \tag{24}$$

where $F_{LY\epsilon} = \boldsymbol{y} : \left(\boldsymbol{\mathcal{L}} : \frac{\partial \boldsymbol{y}}{\partial \epsilon^e}\right)$

Substituting Eq (24) in Eq (23), the constitutive law for elastic damage analysis for a small incremental load can be found as

$$\delta\sigma = \boldsymbol{\mathcal{C}}^{ed}\delta\epsilon^e \tag{25}$$

where $\boldsymbol{\mathcal{C}}^{ed}$ denotes tangent operator for elastic damage analysis and it can be expressed as

$$\boldsymbol{\mathcal{C}}^{ed} = \boldsymbol{\mathcal{C}}(\boldsymbol{d}) + \frac{1}{2Y_{EQ}\boldsymbol{L}}\left(\frac{\partial \boldsymbol{\mathcal{C}}(\boldsymbol{d})}{\partial \boldsymbol{d}}\epsilon^e\right)\left(\frac{\partial f_d}{\partial \boldsymbol{y}} \otimes F_{LY\epsilon}\right) \tag{26}$$

where $\boldsymbol{\mathcal{C}(d)}$ denotes the fourth-order damaged stiffness tensor.

IV. Averaging Approach

The pathological mesh dependency of local continuum damage mechanics can be solved using various nonlocal approaches. The nonlocal field can be obtained by smearing damage variable or local fields over the entire material or constituents. However, for HCF failure, where localized material degradations play a major role for sudden failure of a component, it is more reasonable to consider the average local field computed within its proximity than smearing over the whole material. Thus, the weighted averaged local field for a given point can be obtained as[28,31,32]

$$< f >= \frac{\sum_i w^i \Delta v_i f_i}{\sum_i w^i \Delta v_i} \tag{27}$$

where $< f >$ denote weighted average local fields (strains/stresses) at integration point, Δv_i denote integration volume, $w(l)$ denotes Gaussian weighting functions expressed as $w(l) = e^{(\alpha_w l/\lambda_w)^2}$. The parameter λ_w denotes characteristic length which depends on the volume/area considered for averaging the local field, l denotes the location of points from a point of interest and should not be greater than the λ_w. The smallest volume/area could be averaging within an element, and α_w denote the distribution of weighing function over the characteristic length. The damage potential surface (threshold), damage evolution rate, elastic energy release rate, damage parameter can then be expressed using the pointwise local average field designated as $\bar{f}_{\boldsymbol{d}}$, $\bar{\lambda}_{\boldsymbol{d}}$, $\overline{\boldsymbol{y}}$ and $\overline{\beta}$, respectively.

V. Mechanics of Structure Genome (MSG)

MSG is a unified theory proposed to fill the gap between materials genome and macroscopic structural analysis. Structure Genome (SG) is the smallest mathematical building block (or a cell in biological contexts) of the structure containing many such building blocks. SG is not only describes the matter but also carries the information bridging materials genome and structural analysis. Although in a different way, the basic concept of the MSG is first introduced in series of papers Refs. [44–46]. Later, the proposed concept give birth to a unified and systematic approach to solve structural analysis problem called MSG. It is a general-purpose approach for multiscale structural modeling for various structures such as for 1D (beams), 2D (plates/shells), and 3D composite structures. The theory of MSG is implemented in the computer code SwiftComp.

The properties of composites varies with scale and also in view of the fact that the size of SG is much smaller than the overall size of the macroscopic structure, we introduce a set of micro coordinates $y_i = x_i/\epsilon$ with ϵ being a small parameter to describe the SG. This basically enables a zoom-in view of the SG at the size similar as the macroscopic structure. If the SG is 1D, only y_3 is needed; if the SG is 2D, y_2 and y_3 are needed; if the SG is 3D, all three coordinates y_1, y_2, y_3 are needed.

In multiscale structural modeling, it is postulated that all the information can be obtained from the SG in combination with the macroscopic structural model. In other words, a field function of the original heterogeneous structure can be generally written as a function of the macro coordinates x_k which remain in the macroscopic structural model and the micro coordinates y_j. The partial derivative of a function $f(x_k, y_j)$ can be expressed as

$$\frac{\partial f(x_k, y_j)}{\partial x_i} = \frac{\partial f(x_k, y_j)}{\partial x_i}|_{y_j=\text{const}} + \frac{1}{\epsilon}\frac{\partial f(x_k, y_j)}{\partial y_i}|_{x_k=\text{const}} \equiv f_{,i} + \frac{1}{\epsilon}f_{|i} \tag{28}$$

The deformed and undeformed configuration of structure of any type can be expressed using position vector based on the type of the structure we have, i.e., beam , plate/shell, 3D structure featuring 1D, 2D and 3D structures. Interested readers can get details of this method in Ref. [36]. Although the SG concept can be used to analyze various types of behavior of heterogeneous structures, we illustrate the basic idea of MSG using elastostatic behavior of the composites. The governing equation can be expressed using the following the variational statement

$$\delta U = \overline{\delta W} \tag{29}$$

δ is the usual Lagrangean variation, U is the strain energy and $\overline{\delta W}$ is the virtual work of applied loads. The bars over variations are used to indicate that the virtual quantity needs not be the variation of a functional. For a linear elastic material characterized using a 6×6 stiffness matrix D, the strain energy can be written as

$$U = \frac{1}{2}\int \frac{1}{\omega}\left\langle \Gamma^T D \Gamma \right\rangle \mathrm{d}\Omega \tag{30}$$

where Ω is the volume of the domain spanned by x_k remaining in the macroscopic structural model. The notation $\langle \bullet \rangle = \int \bullet \sqrt{g}\mathrm{d}\omega$ is used to denote a weighted integration over the domain of the SG, ω, where g is the determinant of the metric tensor of the undeformed configuration spanned by x_1, x_2, x_3. ω also denotes the volume of the domain spanned by y_k corresponding to the coordinates x_k, remaining in the macroscopic structural model, Γ denotes 3D strain field which can be written for 3D structures as

$$\Gamma = \Gamma_h w + \Gamma_\epsilon \bar{\epsilon} \tag{31}$$

where $\Gamma = \lfloor \Gamma_{11} \quad \Gamma_{22} \quad \Gamma_{33} \quad 2\Gamma_{23} \quad 2\Gamma_{13} \quad 2\Gamma_{12} \rfloor^T$, $w = \lfloor w_1 \quad w_2 \quad w_3 \rfloor^T$, $\bar{\epsilon}$ is a column matrix containing the generalized strain measures for the macroscopic structural model. If the macroscopic structural model is a 3D continuum model we have $\bar{\epsilon} = \lfloor \epsilon_{11} \quad \epsilon_{22} \quad \epsilon_{33} \quad 2\epsilon_{23} \quad 2\epsilon_{13} \quad 2\epsilon_{12} \rfloor^T$ with ϵ_{ij} denoting the Biot strain measures in a Cauchy continuum. Γ_h is an operator matrix which depends on the dimensionality of the SG. Γ_ϵ is an operator matrix the form of which depends on the macroscopic structural model. If the macroscopic structural model is the 3D Cauchy continuum model, Γ_ϵ is the 6×6 identity matrix. By using the variational statement in Eq. (29) and the strain energy in Eq. (30) and also by neglecting the terms with small order, the first approximation of variational statement cab be obtained as[36]

$$\delta \frac{1}{2}\left\langle (\Gamma_h w + \Gamma_\epsilon \bar{\epsilon})^T D (\Gamma_h w + \Gamma_\epsilon \bar{\epsilon}) \right\rangle = 0 \tag{32}$$

For very simple cases, this variational statement can be solved analytically, while for general cases we need to turn to numerical techniques such as the finite element method for solution which has been implemented in the computer code SwiftComp.

VI. Proposed HCF Failure and Life Prediction Approach

Anisotropic damage is adopted to analyze the fatigue life of a continuous fiber-reinforced composite. The fourth-order damaged compliance tensor described in the Eq. (3) is used to estimate damage propagation and the fatigue life in the composite. The fatigue life prediction is computationally prohibitive if the analysis is allowed to run until the failure point is reached. Thus, for simplicity, the damage is assumed to be constant for each cycle throughout the whole analysis. Consequently, without affecting the anisotropic damage growth rate in each constituent of the composite, a reasonable number of cycle increment, for a specified damage amount, $\Delta\bar{d}$, is added to the cycle number. The cycle increment can be calculated as[39]

$$\Delta N_i = \frac{\Delta\bar{d}}{\left(\delta d/\delta N\right)}, \quad N_{i+1} = N_i + \Delta N_i, \quad d_{i+1} = d_i + (\delta d/\delta N)\Delta N_i \tag{33}$$

where $(\delta d/\delta N)$ denotes the rate of change of damage per cycle, it is assumed to be constant for a certain number of cycle, N_i, $\Delta\bar{d}$ denotes the damage amount to be accounted during cycle jump, it is usually obtained as $D_c/50$, D_c denotes critical damage level in the material beyond which the material can not sustain any load. For the current analysis, $\Delta\bar{d}$ is determined based on damage rate per cycle and it ranges from 10^{-3} to 10^{-5}. For given global stress or strain loading, the maximum cycle number or fatigue life N is obtained based on the critical damage value D_c. The critical damage level is evaluated at each integration point based on the weighted averaged local field. If the damage at any give point reaches the critical damage level, then it is assumed that crack starts to propagate indefinitely resulting in the failure of the material. It should be noted that material constants such B_o, c^d, L and o in Eq. (13), (14) and (16) may be obtained by curve fitting with experimental data for monotonic loading condition.

For the fatigue life analysis, after each cycle of global loading, the homogenization and dehomogenization analyses are carried out. This is followed by evaluation of damage at each numerical integration point using weighted averaged local field based on Eq. (13). The weighted averaged field is computed using the $\lambda_w = 0.1$ and $\alpha_w = 0.005$. If $\bar{f}_{\boldsymbol{d}} > 0$, the damage evolution is estimated using incremental algorithm based on consistency conditions, i.e., $\bar{f}_{\boldsymbol{d}} = 0$, $\dot{\bar{f}}_{\boldsymbol{d}} = 0$. The stress-strain constitutive tangent operator tensor Eq. (26) are then updated for each loading. The proposed approach is summarized in the flow chart in Figure 1.

VII. Fatigue life of Continuous Fiber-Reinforced Composite

In this section, the proposed approach is partially validated using the predictions obtained from the experiments. The glass/epoxy composite is used for this prediction. The fiber and matrix are assumed to have an elastic modulus of 78.5 GPa and 3.45 GPa, respectively, and with the corresponding Poisson ratios of 0.25 and 0.35, respectively. The fiber matrix volume ratio is 0.6. The stress ratio, $R = \frac{\sigma_{min}}{\sigma_{max}}$) is 0.10. The experimental results are obtained from Ref. [47]. In the current prediction, it is assumed that the material constant in Eq. (14), $c^d = 0$. Since the monotonic loading data are not available, the calibration of the material constants, B_o, L and o are performed based on the fatigue data, i.e., minimum stress from S-N curve and its corresponding fatigue life. Finally, the fatigue life of the composite for various loads is estimated based on the calibrated data. It should be noted that since the current approach is entirely based on micromechanics analysis particularly on the local fields, the specified material constants for each constituent are required to sufficiently estimate the fatigue life of the composite. However, if these material constants are not available, it is suggested to assume the failure mode for each loading direction. For instance, for continuous fiber reinforced composite, it is reasonable to assume that the fiber controls the failure of the composite in axial/fiber direction while in the transverse direction the matrix controls the failure. Based on these assumptions, the specified material constants may be calibrated for each constituent of the composite.

The material constants B_o, L and o can easily be calibrated for uniaxial loading in the fiber direction. Let the average minimum stress at the specified fatigue life, N, be approximately 0.7375 GPa as it can be seen from S-N curve depicted in the Figure 2. Then, one can calibrate the damage threshold B_o as follows.

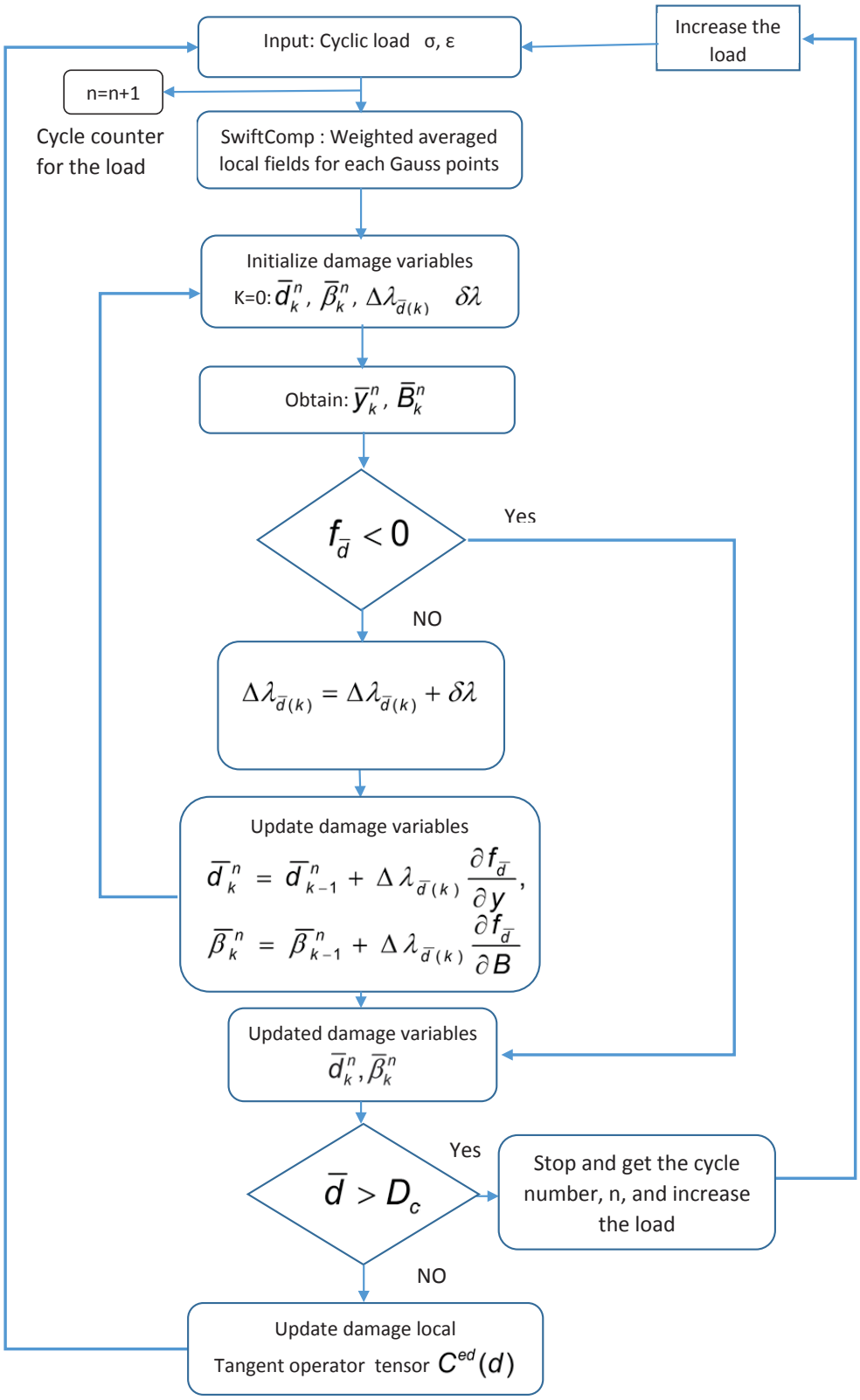

Figure 1. Summary of the proposed approach.

First, apply the global load equivalent to the minimum stress then evaluate the damage at each numerical integration points using Eq. (13). Second, it is known that the initial damage occurs whenever $Y_{EQ} = B_o$. Thus, we can freely select the value of B_o to have no damage in the composite or infinitesimally small damage for the given global load. In the current case, $B_o = 12.772$ MPa is selected for infinitesimally small damage. The material constants in Eq. (16), L and o, are also obtained using the calibrated value of B_o and minimum stress with the corresponding fatigue life, N.

In this case, the fatigue life, N, is iteratively simulated for different values of L and o by applying the global load equivalent to the minimum stress. The process is repeated until the predicted fatigue life is sufficiently equal to the prediction of experiment. If the two predictions are equal, the values of L and o are then used as calibrated material constants. These constants are in turn used to estimate the fatigue life of the composite. For the current case, the calibrated values of L and o are found to be 970 GPa and 8, respectively. It should be noted that the calibration of these three constants are based on the a single point (minimum stress). Moreover, one should notice that critical damage D_c is also a material parameter, it is usually assumed to be between $0.2 < D_c < 0.8$.[41] In this analysis, 0.35 and 0.55 are used for the fiber and matrix, respectively. Using the calibrated material constants, the fatigue life of the composite for various loads

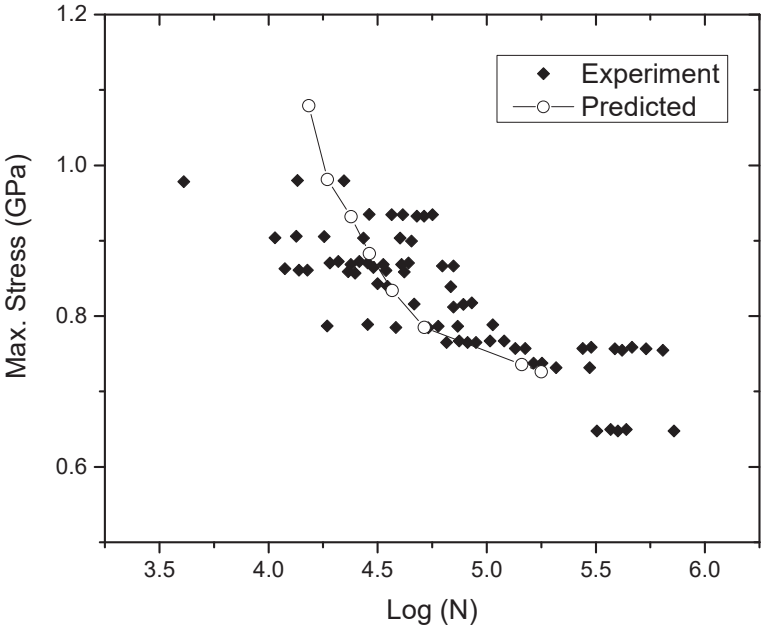

Figure 2. *S-N* **for continuous fiber-reinforced composite.**

are generated as shown using the *S-N* curve in the Figure 2. The prediction shows a good agreement with experiment. It is also noticeable to see the variation of experimental data which precipitates from various contributing factors such as variability of manufacturing process, human error, etc. In these predictions, it is noticed that, at failure, the weighted average damage in the composite does not depend on the magnitude of the applied load as shown the Figure 3. Similar predictions are also observed for all components of damage tensor. It is also noticed that the effective stiffness of the composite just before failure is found to be load independent similar to the d_{11}. It is clear that the progressive fatigue damage affects the effective stiffness of the composite. For instance, for global load, 1.079 GPA , it is observed that the progressive fatigue damage induced significant degradation of effective elastic modulus and also affect the Poisson's ratio of the composite as shown in the Figure 4. However, the transverse and the shear moduli are insignificantly affected.

In another estimation of fatigue life, the material property listed in the Table 1 are used. The fiber matrix volume ratio is 0.70. In this analysis, let the composite be loaded unidirectionally in transverse

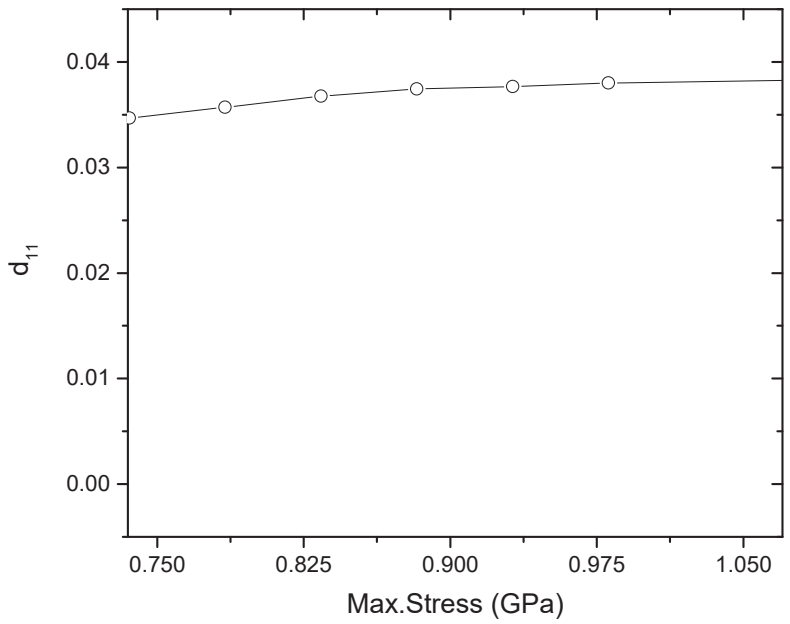

Figure 3. Weighted averaged damage at failure.

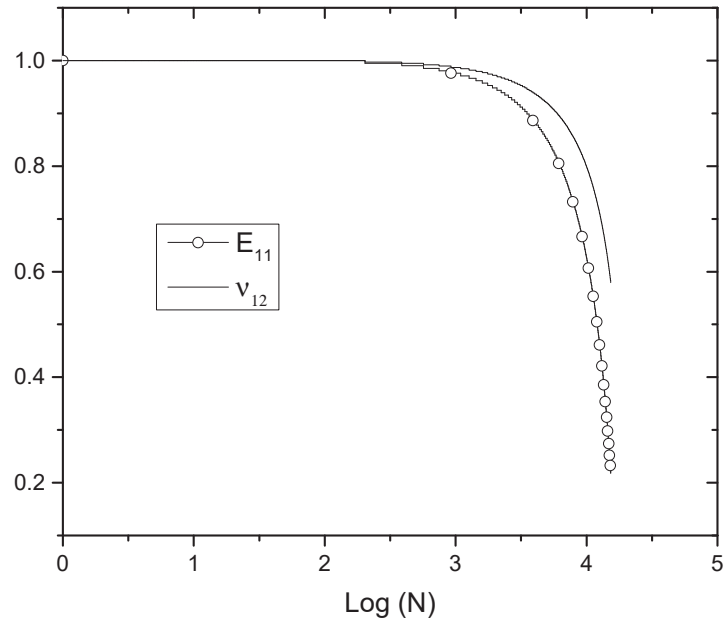

Figure 4. Degradation of effective stiffness and Poisson's ratio.

direction. Thus, it is reasonable to assume the matrix controls the failure of the composite. Consequently, the materials constants B_o, L, and o are calibrated as described for the first case based on the matrix and are approximately found to be 0.5588 MPa, 5 GPa and 6, respectively. In this case also, $c^d = 0$. The critical damage, D_c, 0.33 and 0.53 are used for the fiber and matrix, respectively. The fatigue life for transversely loaded composite is estimated based on the calibrated material. The prediction is fairly in good agreement with the experiments as shown in the Figure 5.

Table 1. Material property for fatigue analysis (Ref et al. [48])

Material	E_{22} GPa	E_{22} GPa	G_{12} GPa	ν_{12}	ν_{23}
Fiber	194.30	15.00	18.10	0.275	0.275
Matrix	3.45	3.45	-	0.350	0.350

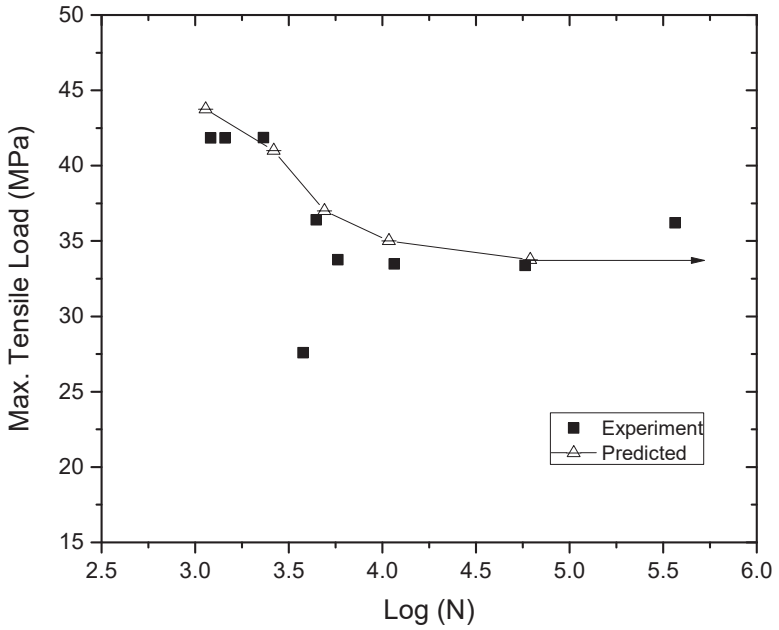

Figure 5. *S-N* **for transversely loaded continuous fiber-reinforced composite.**

For transverse load, one can expect higher stress distribution in the fiber matrix interphase due to the interaction between the two constituents with higher material property mismatch. This stress disturbance may result in significant material degradation locally. For instance, for 37 MPa transverse cyclic load, the effect of stress disturbance can be seen from the weighted averaged damage propagation in the matrix as shown in the Figure 6. It can easily be noticed that the damage propagation in the transverse direction d_{22} is significantly larger than the other damage tensor components which results from the higher stress disturbance for transversely continuous fiber-reinforced composite.

VIII. Conclusion

The damage and fatigue life of continuous fiber-reinforced composite are analyzed using micromechanical approach. The proposed method is incorporated into SwiftComp to estimate the fatigue life and anisotropic damage evolution of the composite. The fatigue life is estimated and found to be good agreement with the

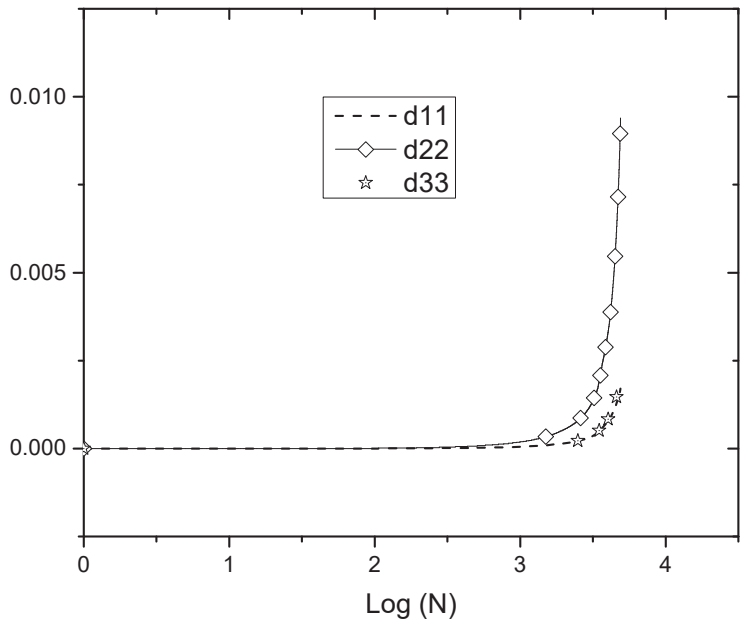

Figure 6. Weighted averaged damage propagation in the matrix.

experimental data. As the proposed approach is mainly based on micromechanics particularly on the local fields, it requires material properties specific to each constituent. The current prediction may be improved if all material data are available. The current calibration approach is limited to unidirectional loading option. It is suggested to make this approach applicable for multi directional loading conditions. Additional validations are also required to examine the capability of the current approach.

Acknowledgments

This research is supported, in part, by the Air Force Office of Scientific Research (with Dr. David Stargel as the program manager) and by the Composites Design and Manufacturing HUB at Purdue University. The views and conclusions contained herein are those of the authors and should not be interpreted as necessarily representing the official policies or endorsement, either expressed or implied, of the sponsor.

References

[1]Mao, H. and Mahadevan, S., "Fatigue Damage Modelling of Composite Materials," *Composite Structures*, Vol. 58, 2002, pp. 405–410.

[2]Sangid, J., "The Physics of Fatigue Crack Initiation," *International Journal of Fatigue*, Vol. 57, 2012, pp. 58–72.

[3]Lin, J., Liu, Y., and Dean, T., "Comparison of Nonlocal Approaches in Continuum Damage Mechanics," *International Journal of Damage Mechanics*, Vol. 14, No. 4, 2005, pp. 299–319.

[4]Mortazavian, S. and Fatemi, A., "Fatigue Behavior and Modeling of Short Fiber Reinforced Polymer Composites: A Literature Review," *International Journal of Fatigue*, Vol. 70, 2015, pp. 297–321.

[5]Degrieck, J. and Paepegem, W., "Fatigue Damage Modelling of Fiber Reinforced Composite Materials: Review," *Applied mechanics reviews: ASME*, Vol. 54, No. 4, Jul 01, 2001, pp. 279–300.

[6]Fatemi, A. and Yang, L., "Cumulative Fatigue Damage and Life Prediction Theories: A Survey of the State of the Art for Homogeneous Materials," *Int.Journal of Fatigue*, Vol. 20, No. 1, 1998, pp. 9–34.

[7]Farahani, A., Haftchenari, H., and Panbechi, M., "An Energy-Based Fatigue Damage Parameter for Off-axis Unidirectional FRP Composites," *Composite Structures*, Vol. 79, 2007, pp. 381389.

[8]Jahed, H., Farahani, A., Noban, M., and Khalaji, I., "An Energy-Based Fatigue Life Assessment Model for Various Metallic Materials Under Proportional and Non-proportional Loading Conditions," *International Journal of Fatigue*, Vol. 29, 2007, pp. 647655.

[9]PaaS, M., Schreurs, P. J., and Brekelmans, W. A., "A Continuum Approach to Brittle and Fatigue Damage: Theory and Numerical Procedures," *International Journal of Solids and Structures*, Vol. 30, 1993, pp. 579–599.

[10]Chow, C. and Wei, Y., "A Model of Continuum Damage Mechanics for Fatigue Failure," *International Journal of Fracture*, Vol. 50, 1991.

[11]Chaboche, J. and Lense, P., "A Non-Linear Continuous Fatigue Damage Model," *Fatigue and Fracture of Engineering Materials and Structures*, Vol. 11, No. 1, 1988, pp. 1–17.

[12]Gamstedt, E., Berglund, L., and Peijs, T., "Fatigue Mechanisms in Unidirectional Glass-Fibre-Reinforced polypropylene," *Composites Science and Technology*, Vol. 59, 1997, pp. 759–768.

[13]Kawai, M., "A Phenomenological Model for Off-axis Fatigue Behavior of Unidirectional Polymer Matrix Composites Under Different Stress Ratios," *Composites: Part A*, Vol. 35, 2004, pp. 955963.

[14]Chaboche, J. and Maire, J., "A New Micromechanics Based CDM Model and its Application to CMCs," *Aerospace Science and Technology*, Vol. 6, 2002, pp. 131–145.

[15]Maimi, P., Camanho, P., Mayugo, J., and Davila, C., "A Continuum Damage Model for Composite Laminates: Part I Constitutive Model," *Mechanics of Materials*, Vol. 39, 2007, pp. 897–908.

[16]Maimi, P., Camanho, P., Mayugo, J., and Davila, C., "A Continuum Damage Model for Composite Laminates: Part II Constitutive Model," *Mechanics of Materials*, Vol. 39, 2007, pp. 897–908.

[17]Mohandesi, J. and Majidi, B., "Fatigue Damage Accumulation in Carbon/Epoxy Laminated Composites," *Materials and Design*, Vol. 30, 2009, pp. 1950–1956.

[18]Barbero, E.J, A. G. and Caceres, A., "A Micromechanics Approach for Damage Modeling of Polymer Matrix Composites," *Composite Structures*, Vol. 67, 2004, pp. 427–436.

[19]Abdelal, G., Caceres, A., and Barbero, E., "A Micro-Mechanics Damage Approach for Fatigue of Composite materials," *Composite Structures*, Vol. 56, 2002, pp. 413–422.

[20]Fish, J., Bailakanavar, M., Powers, L., and Cook, T., "Multiscale fatigue Life Prediction Model for Heterogeneous Materials," *International journal for numerical methods in engineering*, Vol. 91, 2012, pp. 1087–1104.

[21]Voyiadjis, G. Z. and Deliktas, B., "A Coupled Anisotropic Damage Model for Inelastic Response of Composite Materials," *Comput. Methods Appl. Mech. Engrg*, Vol. 183, 2000, pp. 159–199.

[22]Xiao, Y., Li, S., and Gao, Z., "A Continuum Damage Mechanics Model for High Cycle Fatigue," *Smart Materials and Structures*, Vol. 20, 1998, pp. 503–508.

[23]Murakami, S. and Kamiya, K., "Constitutive and Damage Evolution Equations of Elastic-Brittle Materials Based on Irreversible Thermodynamics," *Int. J. Mech. Sci.*, Vol. 39, No. 4, 1996, pp. 473–486.

[24]Lemaiter, J., Sermage, J., and Desmorat, R., "A Two Scale Damage Concept Applied to Fatigue," *International Journal of Fracture*, Vol. 97, 1999, pp. 67–81.

[25]Desmorat, R., Kane, A., Seyedi, M., and Sermage, J., "Two scale Damage Model and Related Numerical Issues for Thermo-Mechanical High Cycle Fatigue," *European Journal of Mechanics A/Solids*, Vol. 26, 2007, pp. 909–935.

[26]Doudard, C., Calloch, S., Cugy, A., Galtier, A., and Hild, F., "A Probabilistic Two-scale Model for High-Cycle Fatigue Life Predictions," *Fatigue and Fracture of Engineering Materials and Structures*, Vol. 28, No. 3, 2005, pp. 279288.

[27]Desmorat, R., Pauget, F., Aboudi, J., and Sermage, J., "Damage-2005: A Post-Processor for High Cycle Fatigue Undex Complex Thermomechanical Loading," July 23-27, 2006.

[28]Vree, J., Brekelmans, W., and Gils, M., "Comparison of Nonlocal Approaches in Continuum Damage Mechanics," *Computers and Strucutres*, Vol. 45, No. 4, 1995, pp. 581–588.

[29]Borst, R., Sluys, L., Muhlhaus, H., and Pamin, A., "Fundamental Issues in Finite Element Analyses of Localization of Deformation," *Engineering Computations*, Vol. 26, No. 1, 1997, pp. 43–62.

[30]Pegon, P. and Anthoine, A., "Numerical Strategies for Solving Continuum Damage Problems with Softening: Application to the Homogenization of Masonry," *Comuters and Structcure*, Vol. 64, No. 1-4, 1997, pp. 623–642.

[31]Baant, Z., "Why Continuum Damage is Nonlocal: Micromechanics Arguments," *Journal of Engineering Mechanics*, Vol. 117, No. 5, 1991, pp. 10701087.

[32]Baant, Z. and Pijaudier-Cabot, G., "Nonlocal Continuum Damage, Localization Instability and Convergence," *Journal of Applied Mechanics*, Vol. 55, No. 2, 1988, pp. 287–293.

[33]Peerlings, R., Borst, R., Bekelmans, W., and De Vree, J., "Gradient Enhanced Damage for Quasi-brittle Materials," *International Journal for Numerical Methods in Engineering*, Vol. 39, 1996, pp. 3391– 3403.

[34]Masson, R., Bekelmans, W., , Borst, R., and Geers, M., "Gradient Enhanced damage for Quasi-brittle materials," *International Journal for Numerical Methods in Engineering*, Vol. 49, 2000, pp. 1547–1569.

[35]Liu, Y., Filonova, V., Hu, N., Yuan, Z., Fish, J., Yuan, Z., and Belytschko, T., "A Regularized Phenomenological Multiscale Damage Model," *International Journal for Numerical Methods in Engineering*, Vol. 99, 2014, pp. 867–887.

[36]Yu, W., "Structure Genome: Fill the Gap between Materials Genome and Structural Analysis," *Proceedings of the 56th Structures, Structural Dynamics and Materials Conference, Kissimmee, Florida*, Jan. 5-9, 2015.

[37]W. Yu, T. O. Williams, B. A. B. J. A. and T.Tang., "A critical evaluation of the predictive capabilities of various advanced micromechanics models," *Proceedings of the 48th Structures, Structural Dynamics and Materials Conference,Honolulu, Hawaii*, April. 23-26, 2007.

[38]Sertse, H., Zhang, L., Yu, W., and Ye, Z., "A Comprehensive Evaluation of the Predictive Capabilities of Several Advanced Micromechanics Approaches," *Proceedings of the 48th Structures, Structural Dynamics and Materials Conference, National Harbor, Maryland*, Jan. 13-17, 2014.

[39]Lemaitre, J., "A Course on Damage Mechanics," 1996.

[40]Kachanov, L., "On creep rupture time," *Izv. Acad. Nauk SSSR*, Vol. 8, 1958, pp. 26–31.

[41]Sumio, M., *Continuum Damage Mechanics: A Continuum Mechanics Approach to the Analysis of Damage and Fracture*, Springer, 2012.

[42]Hayakawa, K., Murakami, S., and Liu, Y., "An Irreversible Thermodynamic Theory for Elastic-Plastic Damage Materials," *Eur J Mech A/Solids*, Vol. 17, No. 2, 1998, pp. 1332.

[43]Besson, J., Cailletaud, G., Chaboche, J., and Forest, S., *Non-Linear Mechanics of Materials, Solid Mechanics and Its Applications*, Vol. 167, Springer, 2012.

[44]Tang, T. and Yu, W., "Asymptotical Approach to Initial yielding surface and elastoplasticity of heterogeneous materials," *Mechanics of Advanced Materials and Structures*, Vol. 18, No. 4, 2011, pp. 244–254.

[45]Tang, T. and Yu, W., "Variational Asymptotic Micromechanics Modeling of Heterogeneous Piezoelectric Materials," *Mechanics of Materials*, Vol. 40, No. 10, 2008, pp. 812–824.

[46]Lee, C. and Yu, W., "Homogenization and Dimensional Reduction of Composite Plates with In-Plane Heterogeneity," *International Journal of Solids and Structures*, Vol. 48, No. 10, 2011, pp. 14741484.

[47]Hashin, Z. and Rotem, A., "A Fatigue Failure Criterion for Fiber Reinforced Materials," *Journal of Composite Material*, Vol. 7, 1973, pp. 448464.

[48]Huang, Z., "Micromechanical Modeling of Fatigue Strength of Unidirectional Fibrous Composites," *International Journal of Solids and Structures*, Vol. 38, 2001, pp. 4147–4172.

AIAA SciTech
4-8 January 2016, San Diego, California, USA
57th AIAA/ASCE/AHS/ASC Structures, Structural Dynamics, and Materials Conference

A Micromechanical Approach to Low Cycle Fatigue Analysis and Life Prediction of Composites

Hamsasew Sertse* and Wenbin Yu†

The objective of this paper is to analyze low cycle fatigue (LCF) damage and fatigue life of composites using a micromechanical approach based on mechanics of structure genome (SG) and its companion code SwiftComp. In this study, the overall tangent modulus of uncoupled elastoplastic damage for negligible back stress effect is derived. The initiation of plasticity and damage in each constituent are evaluated at each numerical integration points using averaged weighted local fields. The accumulated plastic strain and anisotropic damage evolution variables are iteratively solved using incremental algorithm. The proposed approach is used to predict the stress-strain curve. The predicted stress-strain curve for monotonic loading shows good agreement with experimental data. The LCF life is estimated for continuous fiber-reinforced composite and particle reinforced composite. The combined effects of strain hardening and progressive fatigue damage on the effective properties of the composite are also examined.

I. Introduction

Recently, the application of composites in cyclic loading working conditions has gained a considerable momentum due to their excellent capability of accumulating damage compared with conventional homogeneous material. Despite its wide application, the investigation of powerful tools for accurate predictions of damage accumulation, failure and fatigue life prediction remains to be the main research topic in this area. In LCF, particularly in a ductile material, fatigue damage undergoes process of nucleation, coalescence and growth of micro cavity induced by large plastic deformation. A number of researchers have proposed various model to analyze this process of failure, usually termed as a ductile failure, in homogeneous materials.[1,2] These models may be categorized as micromechanical and phenomenological modeling approach. In micromechanical approach, both analytical tools and micromechanical based constitutive models have been proposed to model the growth and coalescence of voids, and ductile failure.[3,4] The other approach is phenomenological approach which is formulated based on a consistent thermodynamic framework called continuum damage mechanics.[5–7] A brief review of various approach may be obtained from Ref. [8]. Numerous researchers used continuum damage mechanics approach to analyze ductile fracture in homogenous material.[6,9–11] The ductile damage is more complex in composites due to interactions among various constituents and also their interfaces. Various approaches have been proposed to analyse ductile damage and LCF in the composites using continuum damage mechanics. Voyiadjis and Deliktas[12] proposed anisotropic damage model for inelastic response of composite materials for both rate-independent and rate-dependent material properties. Maire and Chaboche[13] analyzed ductile damage failure in composites with a local micro closure effect. Fish and his co-workers[14] also analyzed damage in the composites using mathematical homogenization approach for isotropic damage variable. Chaboche and his coworkers[15] also examined damage propagation in plastically deformed composite using micromechanical approaches (Mori-Tanaka and Eshelby).

According to Ref. [16], it is experimentally observed that for LCF both fiber and matrix can contribute for the failure of a composite for any loading direction. It is also further noted that fiber, matrix and interface independently or all together determine the failure of the composite based on the stress level. In Refs. [11, 17], continuum damage mechanics is adopted to analyze low cycle fatigue for various loading options. Interested readers may refer to Refs. [18–21] for additional reference for LCF analysis.

*Graduate Research Assistant, School of Aeronautics and Astronautics, Purdue University
†Associate Professor, School of Aeronautics and Astronautics, Purdue University, AIAA Associate Fellow.

The main drawbacks of continuum damage mechanics for numerical implementation are its pathological mesh dependency and improper convergency which originate from strain localization due to strain softening, damage localization and stress singularity at crack tip. Numerous researchers proposed possible solutions to avoid these problems. Interested reader may refer to Refs. [22–27] for various proposed approaches to solve a mesh dependency problem of local damage approach. In Refs. [28,29], it is demonstrated that for numerical implementation, major effect comes from stress singularity particularly at the critical damage level. It is also shown that loss of ellipticity of equilibrium equation may not be usually due to crack initiation. The nonlocal approach described in Refs. [22, 25] proposes averaging local fields at integration points based on weighted average of the local fields in the neighbourhood of each integration point. The weighting value is a function of characteristic length expressed using a Gaussian weighting function.

It should be noted that the fatigue limit of many materials may be much smaller than their yield limit in a global sense. However, locally the material undergoes a process of nucleation and void formation. This process is more significant in the composite material due to higher local stress disturbance resulting from the interaction of various constituents. This phenomena can be well captured and integrated in fatigue analysis by considering the local fields. Thus, the local field recovery is a critical capability for any micromechanics approach to sufficiently analyze the fatigue damage and life prediction of composite. SwiftComp is a general-purpose multiscale constitutive modeling code for composites which provides unified modeling for 1D (beams), 2D (plates/shells), or 3D composite structures. This is accomplished using the concept of structure genome that unifies structural mechanics and micromechanics.[30] The previous version of SwiftComp, VAMUCH (Variational Asymptotic Method for Unit cell Homogenization), sufficiently demonstrates excellent capability both in predicting effective properties and dehomogenization of the local fields.[31,32] Thus, SwiftComp is a natural choice to perform fatigue damage analysis and life predictions.

The objective of this paper is to analyze the low cycle fatigue (LCF) damage and fatigue life predictions of composites using a micromechanical approach based on mechanics of structure genome (SG) and its companion code SwiftComp. The overall uncoupled elastoplastic tangent modulus is derived by assuming the effect of back stress (kinematic hardening) to be negligible. The accumulated plastic strain and the growth of damage in each constituent are evaluated at each numerical integration points using weighted averaged local fields. The accumulation of plastic strain and evolution of damage variables are iteratively solved using the incremental method. The stress-strain curve for monotonic loading shows good agreements with the experimental data. The LCF fatigue damage and life prediction are estimated for continuous fiber-reinforced composite and particle-reinforced composite. The combined effects of strain hardening and progressive fatigue damage on effective properties are also analyzed.

II. Basics of Damage Mechanics

The concept of continuum damage mechanics is first formulated based on the hypothesis of Kachanov[33] which postulates the gradual deterioration of the effective cross sectional area that sustain the the applied load. Thus, the damage variable can be expressed as

$$d = \frac{A - \tilde{A}}{A} \tag{1}$$

where A denotes total cross sectional area, $\tilde{A}$ denotes effective cross sectional area. The value of d shows the level of damage in the material when $d = 0$ shows undamage states (no damage) and, $d = D_c \leq 1$ shows the extent of failure if $d = 1$ shows a complete failure. This formulation holds only for the isotropic damage however in most cases the damage may not be necessarily isotropic thus in general the damage may be better expressed using a second-order tensor which considers the directional dependency of the damage parameter.

First, let $\boldsymbol{d}$ and $\boldsymbol{\mathcal{D}}$ denote the second-order and fourth-order damage tensors, respectively. Let $\boldsymbol{d}$ be symmetric, then $\boldsymbol{\mathcal{D}}$ can be written as using $\boldsymbol{d}$ as

$$\boldsymbol{\mathcal{D}} = \sum_{i=1}^{3}\sum_{j=1}^{3} d_{ij} e_i \otimes e_j \otimes e_i \otimes e_j \tag{2}$$

The damage effect tensor $\boldsymbol{\mathcal{M}}$ can be expresses as

$$\boldsymbol{\mathcal{M}} = \boldsymbol{\mathcal{I}} - \boldsymbol{\mathcal{D}} \tag{3}$$

where $\boldsymbol{\mathcal{I}}$ denotes fourth-order identity tensor. Based on the elastic strain energy equivalence of the damaged and fictitious undamaged material, the stiffness of

$$\boldsymbol{\mathcal{C}} = \boldsymbol{\mathcal{M}} : \tilde{\boldsymbol{\mathcal{C}}} : \boldsymbol{\mathcal{M}} \tag{4}$$

where $\boldsymbol{\mathcal{C}}$ denotes the fourth-order damaged elasticity tensor of the material, and $\tilde{\boldsymbol{\mathcal{C}}}$ denotes the fourth-order fictitious undamaged elasticity tensor of the material.

Secondly, let the damage only affect the diagonal terms of the compliance tensor of the material then the damaged compliance matrix can be expressed as

$$\boldsymbol{\mathcal{S}}(\boldsymbol{d}) = \begin{bmatrix} \frac{S_{1111}}{1-d_{11}} & S_{1112} & S_{1113} & S_{1123} & S_{1113} & S_{1112} \\ & \frac{S_{2222}}{1-d_{22}} & S_{2223} & S_{2223} & S_{2213} & S_{2216} \\ & & \frac{S_{3333}}{1-d_{33}} & S_{3323} & S_{3313} & S_{3312} \\ & & & \frac{S_{2323}}{1-d_{44}} & S_{2313} & S_{2312} \\ & SYMM & & & \frac{S_{1313}}{1-d_{55}} & S_{1312} \\ & & & & & \frac{S_{1212}}{1-d_{66}} \end{bmatrix} \tag{5}$$

Using the strain equivalence approach, the stress in the damaged and undamaged configuration can be related as

$$\tilde{\boldsymbol{\sigma}} = \boldsymbol{\mathcal{M}}^{-1} : \boldsymbol{\sigma}, \quad \boldsymbol{\mathcal{M}}^{-1} = \boldsymbol{\mathcal{S}}^{-1} : \tilde{\boldsymbol{\mathcal{S}}} \tag{6}$$

where $\tilde{\boldsymbol{\sigma}}$ denotes effective stress in the undamaged material, $\boldsymbol{\sigma}$ denotes stress in the damaged material, and $\mathcal{M}$ denotes the fourth-order damage effect tensor as a function of the fourth-order compliance tensor, $\tilde{\boldsymbol{\mathcal{S}}}$ denotes effective compliance in the undamaged material, and $\boldsymbol{\mathcal{S}}$ denotes compliance in the damaged material. It should be noted that $\boldsymbol{\mathcal{M}}$ in Eq. (3) and Eq. (6) are different. Both types of the damage models are revisited in section VI for selecting the thermodynamically consistent model.

III. Brief Review of Thermodynamics

In the general thermomechanical problems, the phenomena of elasticity, plasticity, and the thermal effects may be modeled using irreversible thermodynamics formulation. In this case, the observable state variables can be elastic strain $\boldsymbol{\epsilon^e}$, and temperature T with their associated variables stress $\boldsymbol{\sigma}$ and entropy S, respectively. Let the Helmholtz free energy be expressed as a function of the given state variables as

$$\psi = \psi(\boldsymbol{\epsilon}, T, V_k) \quad (k = 1, 2, ..., n) \tag{7}$$

where ψ denotes energy per unit mass of the material, V_k denote other internal variables. It is usually observed that ductile damage starts after significant inelastic deformation that precipitates from accumulation of plastic damage. Thus, it is reasonable to assume the elastic strains are smaller compared with the plastic strains. From additive decompositions of strain one can have

$$\boldsymbol{\epsilon} = \boldsymbol{\epsilon}^e + \boldsymbol{\epsilon}^p \tag{8}$$

It is also observed that the effect of kinematic harding in a fatigue analysis is obsrved to be negligible.[5,34] Thus, let accumulated plastic strain r with their associated variable R, the second-order damage tensor $\boldsymbol{d}$ and damage hardening parameter β, be the internal variables. Moreover, let the material exhibit uncoupled plastic and damage behaviour. Thus, the Helmholtz free energy for isothermal process can be written as

$$\psi = \psi_e(\boldsymbol{\epsilon^e}, \boldsymbol{d}) + \psi_p(r) + \psi_d(\beta) \tag{9}$$

Substituting Eq. (9), in to the Clausius-Duhem inequality, the following relation is obtained

$$(\boldsymbol{\sigma} - \rho\frac{\partial\psi}{\partial\boldsymbol{\epsilon}^e}) : \dot{\boldsymbol{\epsilon}}^{\boldsymbol{e}} + \boldsymbol{\sigma} : \dot{\boldsymbol{\epsilon}}^p - \rho\frac{\partial\psi}{\partial r}\dot{r} - \rho\frac{\partial\psi}{\partial\boldsymbol{d}} : \dot{\boldsymbol{d}} - \rho\frac{\partial\psi}{\partial\beta}\dot{\beta} \geq 0 \tag{10}$$

This inequality must be satisfied for any values of $\boldsymbol{\epsilon}^e$, $\boldsymbol{\epsilon}^p$, $\dot{r}$, $\dot{\boldsymbol{d}}$ and $\dot{\beta}$. If the damage and plastic strains $\boldsymbol{\epsilon^p}$ do not exist in the material, then the inequality can be satisfied only for $\boldsymbol{\sigma} = \rho\frac{\partial\psi}{\partial\boldsymbol{\epsilon}^e}$ which give the elastic constitutive equation. Let $\boldsymbol{y}$ and B be thermodynamic conjugate force variables (elastic energy release rate due to damage) and damage hardening parameter, respectively. These variables can be related to Helmholtz free energy as

$$R \equiv \rho\frac{\partial\psi_p}{\partial r}, \qquad \boldsymbol{y} \equiv -\rho\frac{\partial\psi_e}{\partial\boldsymbol{d}}, \qquad B \equiv \rho\frac{\partial\psi_d}{\partial\beta} \tag{11}$$

where R denotes accumulated plastic strain associated variables. Using Eq. (10) and (11), dissipation potential per unit volume can be described as

$$\Phi = \boldsymbol{\sigma} : \dot{\boldsymbol{\epsilon}}^p - R\dot{r} + \boldsymbol{y} : \dot{\boldsymbol{d}} - B\dot{\beta} \geq 0 \tag{12}$$

For uncoupled the plastic and damage behaviour, the dissipation potential per unit volume Φ can decomposed into

$$\Phi = \Phi_p + \Phi_d \tag{13}$$

where

$$\Phi_p = \boldsymbol{\sigma} : \dot{\boldsymbol{\epsilon}}^p - R\dot{r} \qquad \text{and} \qquad \Phi_d = \boldsymbol{y} : \dot{\boldsymbol{d}} - B\dot{\beta} \tag{14}$$

Thus, the yield and damage criteria can then be expressed as

$$f_p(\boldsymbol{\sigma}, R) \leq 0 \qquad \text{and} \qquad f_d(\boldsymbol{y}, B) \leq 0 \tag{15}$$

One can assume a pseudo-plastic and damage potential to be $F_p(\sigma, R)$ and $F_d(\mathbf{d}, \beta)$, respectively. Based on the dissipation mechanism, the flow rule for uncoupled plasticity and damage can be expressed using two independent multipliers, $\dot{\lambda}_p$ and $\dot{\lambda}_d$, such that the plastic and damage evolution rate can be written as[34]

$$\dot{\boldsymbol{\epsilon}}^p = \dot{\lambda}_p\frac{\partial F_p}{\partial\boldsymbol{\sigma}}, \qquad \dot{r} = -\dot{\lambda}_p\frac{\partial F_p}{\partial R}, \qquad \dot{\boldsymbol{d}} = \dot{\lambda}_d\frac{\partial F_d}{\partial\boldsymbol{y}}, \qquad \dot{\beta} = -\dot{\lambda}_d\frac{\partial F_d}{\partial B} \tag{16}$$

Once ψ, F_p, f_p, F_d, f_d are known, the two independent multipliers can be uniquely determined. For plastically deformed part of the material, it should be noted that plastic deformation can only occur in the effective stress space, i.e., the undamaged part. Thus, Hill's yield criterion can be used to analyze yield surface of the undamaged part.

$$f_p(\boldsymbol{\sigma}, R) = \sigma_{eq} - R - \sigma_y \leq 0, \qquad \sigma_{eq} = \sqrt{\frac{3}{2}(\tilde{\boldsymbol{\sigma}})' : \mathcal{H} : (\tilde{\boldsymbol{\sigma}})'} \tag{17}$$

where f_p denotes yield function, R denotes isotropic hardening, and σ_y denotes stress threshold, $\mathcal{H}$ denotes a positive semi-definite tensor of the fourth-order characterizing the yield condition of orthotropic materials, $\tilde{\sigma}$ denotes effective stress, $()'$ denotes deviatoric part of the field. Let R be expressed using Voce hardening law as[34, 35]

$$R = Q[1 - e^{(-br)}] \tag{18}$$

where Q and b denote isotropic hardening parameters and also let the plastic flow obey the associative flow rule $F_p = f_p$. The loading and unloading conditions of Eq. (16) can be obtained using Kuhn-Tucker conditions.

$$\dot{\lambda}_p \geq 0, \quad f_p \leq 0, \quad \dot{\lambda}_p f_p = 0 \tag{19}$$

Then, independent multiplier of plasticity in Eq (16) can be uniquely obtained from consistency equation $\dot{f}_p = 0$.

$$\dot{f}_p = \frac{\partial f_p}{\partial\tilde{\boldsymbol{\sigma}}}\dot{\tilde{\boldsymbol{\sigma}}} + \frac{\partial f_p}{\partial R}\frac{\partial R}{\partial r}\dot{r} \tag{20}$$

The rate equation of effective stress space for decoupled plastic damage can be written as

$$\dot{\tilde{\boldsymbol{\sigma}}} = \boldsymbol{C}(\boldsymbol{d})\,(\dot{\boldsymbol{\epsilon}} - \dot{\boldsymbol{\epsilon}}^p) \tag{21}$$

Substituting Eq. (21) into Eq. (20) and using Eq. (16) and Eq. (17), after a few algebraic manipulations, one obtains

$$\dot{\lambda}_p = \left(\frac{\frac{\partial f_p}{\partial\tilde{\boldsymbol{\sigma}}} : \boldsymbol{C}(\boldsymbol{d}) : \dot{\boldsymbol{\epsilon}}}{\frac{\partial f_p}{\partial\tilde{\boldsymbol{\sigma}}} : \boldsymbol{C}(\boldsymbol{d}) : \frac{\partial f_p}{\partial\tilde{\boldsymbol{\sigma}}} + \frac{\partial R}{\partial r}}\right), \qquad \dot{r} = \dot{\lambda}_p \tag{22}$$

Then, the evolution of plastic strain $\dot{\epsilon}^p$ in Eq. (16) can be written using Eq. (22) as

$$\dot{\boldsymbol{\epsilon}}^p = \left(\frac{\frac{\partial f_p}{\partial \tilde{\boldsymbol{\sigma}}} : \boldsymbol{C}(\boldsymbol{d}) : \dot{\boldsymbol{\epsilon}}}{\frac{\partial f_p}{\partial \tilde{\boldsymbol{\sigma}}} : \boldsymbol{C}(\boldsymbol{d}) : \frac{\partial f_p}{\partial \tilde{\boldsymbol{\sigma}}} + \frac{\partial R}{\partial r}} \right) \frac{\partial f_p}{\partial \tilde{\boldsymbol{\sigma}}} \tag{23}$$

For damaged part, it is assumed that there exists the damage potential $f_{\boldsymbol{d}} = 0$ in the space of the thermodynamic conjugate force $\boldsymbol{y}$ and $\mathbf{B}$, thus, the convex surface for the damage criterion may be expressed as[36]

$$f_d(\boldsymbol{y}, B) = Y_{EQ} - (B_o + B) = 0 \tag{24}$$

where $Y_{EQ} = \left[\frac{1}{2}\boldsymbol{y} : \mathcal{L}(d) : \boldsymbol{y}\right]^{1/2}$ denotes equivalent damage energy release rate, B_o denotes damage threshold (material dependent value). $\mathcal{L}(d)$ denotes the fourth-order damage tensor function which can be expressed using index notation as

$$\mathcal{L}_{ijkl} = \frac{1}{2}(\delta_{ik}\delta_{jl} + \delta_{il}\delta_{jk}) + \frac{1}{2}c^d(\delta_{ik}d_{jl} + d_{ik}\delta_{jl} + \delta_{il}d_{jk} + d_{il}\delta_{jk}) \tag{25}$$

where c^d denotes material constants. Using the damage potential, damage evolution rate and the rate of change of damage parameter can be expressed as

$$\dot{\boldsymbol{d}} = \dot{\lambda}_d \frac{\partial f_d}{\partial \boldsymbol{y}}, \qquad \text{and} \qquad \dot{\beta} = -\dot{\lambda}_d \frac{\partial f_d}{\partial B} \tag{26}$$

where $\dot{\boldsymbol{d}}$ denotes the rate of damage flow, $\frac{\partial f_d}{\partial y}$ denotes the direction of flow of damage. Let $\rho\psi_d(\beta)$ be expressed as[34,35]

$$\rho\psi_d(\beta) = \frac{S^2}{2Lo}, \quad S = L(1 - exp(-o\beta)) \tag{27}$$

Substituting Eq. (27) into Eq. (11), one can obtain

$$B = L(1 - exp(-o\beta)) \tag{28}$$

where L and o are constant to be obtained from curve fitting with experimental prediction for monotonic loading. The loading and unloading conditions of Eq. (26) can be obtained using Kuhn-Tucker conditions.

$$\dot{\lambda}_d \geq 0, \quad f_d \leq 0, \quad \dot{\lambda}_d f_d = 0 \tag{29}$$

where $\dot{\lambda}_{\boldsymbol{d}}$ is obtained from consistency conditions $\dot{f}_d = 0$ as[34]

$$\dot{f}_d = \frac{\partial f_d}{\partial \boldsymbol{y}} : \dot{\boldsymbol{y}} + \frac{\partial f_d}{\partial B}\frac{\partial B}{\partial \beta}\dot{\beta} + \frac{\partial f_d}{\partial \boldsymbol{\mathcal{L}}}\frac{\partial \boldsymbol{\mathcal{L}}}{\partial d} : \dot{\boldsymbol{d}} = 0 \tag{30}$$

From Eq. (11), one can write

$$\dot{\boldsymbol{y}} = \frac{\partial \boldsymbol{y}}{\partial \boldsymbol{\epsilon^e}} : \dot{\boldsymbol{\epsilon^e}} + \frac{\partial \boldsymbol{y}}{\partial \boldsymbol{d}} : \dot{\boldsymbol{d}} \tag{31}$$

Using Eq. (31), (26) and after a few algebraic manipulations, Eq. (30) can be rewritten as

$$\dot{f}_d = \frac{1}{2Y_{EQ}}\boldsymbol{y} : \boldsymbol{\mathcal{L}} : (\frac{\partial \boldsymbol{y}}{\partial \boldsymbol{\epsilon^e}} : \dot{\boldsymbol{\epsilon^e}}) + \boldsymbol{L}\dot{\lambda}_d = 0 \tag{32}$$

where $\boldsymbol{L} = -\frac{1}{2Y_{EQ}}(\boldsymbol{y} : \boldsymbol{\mathcal{L}} : (\frac{\partial \boldsymbol{y}}{\partial d} : \frac{\partial f_d}{\partial \boldsymbol{y}})) - \frac{1}{4Y_{EQ}}(\boldsymbol{y} : (\frac{\partial \boldsymbol{\mathcal{L}}}{\partial \boldsymbol{d}} : \boldsymbol{y}) : \frac{\partial f_d}{\partial \boldsymbol{y}}) + \frac{\partial B}{\partial \beta}$. Then, the damage evolution rate can be expressed as

$$\dot{\lambda}_d = \frac{\frac{1}{2Y_{EQ}}\boldsymbol{y} : \boldsymbol{\mathcal{L}} : (\frac{\partial \boldsymbol{y}}{\partial \boldsymbol{\epsilon^e}} : \dot{\boldsymbol{\epsilon^e}})}{\boldsymbol{L}} \tag{33}$$

The rate equation for stress can be written as

$$\dot{\tilde{\boldsymbol{\sigma}}} = \frac{\partial \tilde{\boldsymbol{\sigma}}}{\partial \boldsymbol{\epsilon}_e}\dot{\boldsymbol{\epsilon}}_e + \frac{\partial \tilde{\boldsymbol{\sigma}}}{\partial \boldsymbol{d}}\dot{\boldsymbol{d}} \tag{34}$$

In the low cycle fatigue analysis, it can be postulated that the material undergoes excessive plastic deformation before failure occurs. Thus, using Eq. (8), Eq. (34) can be rewritten as

$$\dot{\tilde{\boldsymbol{\sigma}}} = \boldsymbol{C}(\boldsymbol{d})(\dot{\boldsymbol{\epsilon}} - \dot{\boldsymbol{\epsilon}}^p) + \frac{\partial \tilde{\boldsymbol{\sigma}}}{\partial \boldsymbol{d}} \dot{\boldsymbol{d}} \tag{35}$$

Substituting Eq (23) in Eq (35) and using Eq (33) and (26), The rate equation for uncoupled damaged elastoplastic constitutive equation can be expressed for small incremental loading as

$$\delta \tilde{\boldsymbol{\sigma}} = \mathcal{C}^{epd} : \delta \boldsymbol{\epsilon} \tag{36}$$

where $\mathcal{C}^{epd}$ denotes damaged elastoplastic tangent stiffness tensor and it can be expressed as

$$\mathcal{C}^{epd} = \boldsymbol{C}(\boldsymbol{d}) - \frac{\left(\boldsymbol{C}(\boldsymbol{d}) : \frac{\partial f_p}{\partial \tilde{\boldsymbol{\sigma}}}\right) \otimes \left(\frac{\partial f_p}{\partial \tilde{\boldsymbol{\sigma}}} : \boldsymbol{C}(\boldsymbol{d})\right)}{\frac{\partial f_p}{\partial \tilde{\boldsymbol{\sigma}}} : \boldsymbol{C}(\boldsymbol{d}) : \frac{\partial f_p}{\partial \tilde{\boldsymbol{\sigma}}} + \frac{\partial R}{\partial r}} + \frac{1}{Y_{EQ}\,\mathbf{L}} \left(\frac{\partial \boldsymbol{C}(\boldsymbol{d})}{\partial \boldsymbol{d}} \boldsymbol{\epsilon}\right) \left(\frac{\partial f_d}{\partial \boldsymbol{y}} \otimes (F_{Ly\epsilon})\right) + C_{pd} \tag{37}$$

where $F_{Ly\epsilon} = \boldsymbol{y} : \boldsymbol{\mathcal{L}} : \frac{\partial \boldsymbol{y}}{\partial \boldsymbol{\epsilon}^e}$, $\left(\frac{\partial \boldsymbol{C}(\boldsymbol{d})}{\partial \boldsymbol{d}} \epsilon\right) = \frac{\partial \boldsymbol{\sigma}}{\partial \boldsymbol{d}}$ and

$$C_{pd} = \frac{1}{Y_{EQ}\,\mathbf{L}} \left(\frac{\partial \boldsymbol{C}(\boldsymbol{d})}{\partial \boldsymbol{d}} \boldsymbol{\epsilon}\right) \left(\frac{\partial f_d}{\partial \boldsymbol{y}} \otimes (F_{Ly\epsilon})\right) \left(\frac{\frac{\partial f_p}{\partial \tilde{\boldsymbol{\sigma}}} \otimes \left(\frac{\partial f_p}{\partial \tilde{\boldsymbol{\sigma}}} : \boldsymbol{C}(\boldsymbol{d})\right)}{\frac{\partial f_p}{\partial \tilde{\boldsymbol{\sigma}}} : \boldsymbol{C}(\boldsymbol{d}) : \frac{\partial f_p}{\partial \tilde{\boldsymbol{\sigma}}} + \frac{\partial R}{\partial r}}\right) \tag{38}$$

where $\boldsymbol{C}(d)$ denotes the damaged fourth-ordered stiffness tensor, the first term in Eq (37) represents elastic case, the second term for plastic case, the third term is for damage, and the fourth term represents the combined effect of both plasticity and damage. It should be noted that the effect of kinematic hardening assumed to be negligible due to cyclic loading.

IV. Averaging Approach

The pathological mesh dependency of local continuum damage mechanics can be solved using various nonlocal approaches. The nonlocal field can be obtained by smearing damage variable or local fields over the entire material or constituents. However, for LCF failure, where localized material degradations play a major role for sudden failure of a component, it is more reasonable to consider the average local field computed within its proximity than smearing over the whole material domain. Thus, the weighted averaged local field for a given point can be obtained as[22, 25, 26]

$$< f >= \frac{\sum_i w^i \Delta v_i f}{\sum_i w^i \Delta v_i} \tag{39}$$

where $< f >$ denote weighted average local fields (strains/stresses) at integration point, Δv_i denote integration volume, $w(l)$ denotes Gaussian weighting functions expressed as $w(l) = e^{(\alpha l/\lambda_w)^2}$. The parameter λ_w denotes characteristic length which depends on the volume/area considered for averaging the local field, l denotes location of points from a point of interest and should not be greater than the λ_w. The smallest volume/area could be averaging within an element, and α denote the distribution of weighing function over the characteristic length. The damage potential surface (threshold), damage evolution rate, elastic energy release rate, damage parameter can then be expressed using the pointwise local average field designated as $f^{\overline{\boldsymbol{d}}}$, $\dot{\Lambda}^{\overline{\boldsymbol{d}}}$, $\overline{\boldsymbol{y}}$ and $\overline{\beta}$, respectively.

V. Mechanics of Structure Genome (MSG)

MSG is a unified theory proposed to fill the gap between materials genome and macroscopic structural analysis. Structure Genome (SG) is the smallest mathematical building block (or a cell in biological contexts) of the structure containing many such building blocks. SG not only describes the matter but also carries the information bridging materials genome and structural analysis. Although in a different way, the basic concept of the MSG is first introduced in series of papers Refs. [37–39]. Later, the proposed concept gave birth to

a unified and systematic approach to solve structural analysis problem called MSG. It is a general-purpose approach for multiscale structural modeling for various structures such as for 1D (beams), 2D (plates/shells), and 3D composite structures. The theory of MSG is implemented in the computer code SwiftComp.

The properties of composites varies with scale and also in view of the fact that the size of SG is much smaller than the overall size of the macroscopic structure, we introduce a set of micro coordinates $y_i = x_i/\epsilon$ with ϵ being a small parameter to describe the SG. This basically enables a zoom-in view of the SG at the size similar as the macroscopic structure. If the SG is 1D, only y_3 is needed; if the SG is 2D, y_2 and y_3 are needed; if the SG is 3D, all three coordinates y_1, y_2, y_3 are needed.

In multiscale structural modeling, it is postulated that all the information can be obtained from the SG in combination with the macroscopic structural model. In other words, a field function of the original heterogeneous structure can be generally written as a function of the macro coordinates x_k which remain in the macroscopic structural model and the micro coordinates y_j. The partial derivative of a function $f(x_k, y_j)$ can be expressed as

$$\frac{\partial f(x_k, y_j)}{\partial x_i} = \frac{\partial f(x_k, y_j)}{\partial x_i}|_{y_j=\text{const}} + \frac{1}{\epsilon}\frac{\partial f(x_k, y_j)}{\partial y_i}|_{x_k=\text{const}} \equiv f_{,i} + \frac{1}{\epsilon}f_{|i} \tag{40}$$

The deformed and undeformed configuration of structure of any type can be expressed using position vector based on the type of the structure we have, i.e., beam , plate/shell, 3D structure featuring 1D, 2D and 3D structures. Interested readers can get details of this method in Ref. [30]. Although the SG concept can be used to analyze various types of behavior of heterogeneous structures, we illustrate the basic idea of MSG using elastostatic behavior of the composites. The governing equation can be expressed using the following the variational statement

$$\delta U = \overline{\delta W} \tag{41}$$

δ is the usual Lagrangean variation, U is the strain energy and $\overline{\delta W}$ is the virtual work of applied loads. The bars over variations are used to indicate that the virtual quantity needs not be the variation of a functional. For a linear elastic material characterized using a 6×6 stiffness matrix D, the strain energy can be written as

$$U = \frac{1}{2}\int \frac{1}{\omega}\left\langle \Gamma^T D \Gamma \right\rangle \mathrm{d}\Omega \tag{42}$$

where Ω is the volume of the domain spanned by x_k remaining in the macroscopic structural model. The notation $\langle \bullet \rangle = \int \bullet \sqrt{g} \mathrm{d}\omega$ is used to denote a weighted integration over the domain of the SG, ω, where g is the determinant of the metric tensor of the undeformed configuration spanned by x_1, x_2, x_3. ω also denotes the volume of the domain spanned by y_k corresponding to the coordinates x_k, remaining in the macroscopic structural model, Γ denotes the 3D strain field which can be written for 3D structures as

$$\Gamma = \Gamma_h w + \Gamma_\epsilon \bar{\epsilon} \tag{43}$$

where $\Gamma = \lfloor \Gamma_{11} \quad \Gamma_{22} \quad \Gamma_{33} \quad 2\Gamma_{23} \quad 2\Gamma_{13} \quad 2\Gamma_{12} \rfloor^T$, $w = \lfloor w_1 \quad w_2 \quad w_3 \rfloor^T$, $\bar{\epsilon}$ is a column matrix containing the generalized strain measures for the macroscopic structural model. If the macroscopic structural model is a 3D continuum model we have $\bar{\epsilon} = \lfloor \epsilon_{11} \quad \epsilon_{22} \quad \epsilon_{33} \quad 2\epsilon_{23} \quad 2\epsilon_{13} \quad 2\epsilon_{12} \rfloor^T$ with ϵ_{ij} denoting the Biot strain measures in a Cauchy continuum. Γ_h is an operator matrix which depends on the dimensionality of the SG. Γ_ϵ is an operator matrix the form of which depends on the macroscopic structural model. If the macroscopic structural model is the 3D Cauchy continuum model, Γ_ϵ is the 6×6 identity matrix. By using the variational statement in Eq. (41) and the strain energy in Eq. (42) and also by neglecting the terms with small order, the first approximation of variational statement cab be obtained as[30]

$$\delta \frac{1}{2}\left\langle (\Gamma_h w + \Gamma_\epsilon \bar{\epsilon})^T D (\Gamma_h w + \Gamma_\epsilon \bar{\epsilon}) \right\rangle = 0 \tag{44}$$

For very simple cases, this variational statement can be solved analytically, while for general cases we need to turn to numerical techniques such as the finite element method for solution which has been implemented in the computer code SwiftComp.

VI. Proposed LCF Damage and Life Prediction Approach

The two damage models described in section II are considered in this study. However, the first damage model does not give the predictions of thermodynamic conjugate force $\boldsymbol{y}$ consistence with the dissipation

potential Φ_d in Eq (14) that require $\boldsymbol{y} \equiv -\rho\frac{\partial \psi_e}{\partial \boldsymbol{d}} \geq 0$. For instance, for uniaxial global loading, the model gives $y_{22} < 0$ and $y_{33} < 0$ while $y_{11} > 0$. Moreover, as one assumes large value of damage in axial direction and small values for all other damage, all components of $\boldsymbol{y} < 0$. In a global sense, this problem is partly due to the effect of Poisson's ratio. For unidirectional loading, there will be deformation particularly contractions in transverse direction. Thus, the effect of the transverse strain yields $y_{22} < 0$ and $y_{33} < 0$. However, the problem may not be encountered for multi-directional loadings. It should also be noted that the diagonal terms of damage effect tensor in Eq (3) with $\sqrt{1-d_{ij}}$ components also suffers similar problem.

For the second damage model, thermodynamic conjugate force $\boldsymbol{y}$ can alteratively be obtained from complementary energy $\boldsymbol{G}$ using the proposed damage model, Eq (5), as[40]

$$\boldsymbol{y} = \frac{\partial \boldsymbol{G}}{\partial \boldsymbol{d}}, \qquad \boldsymbol{G} = \frac{1}{2}\sigma : S(\boldsymbol{d}) : \sigma \tag{45}$$

The second damage model is adopted in this paper to analyse the LCF damage and the corresponding fatigue life of composites. Generally, for fatigue loading case, it is computational demanding to subdivide a load in one cycle in to small incremental loads. Thus, it is assumed that a single step loading for each cycle with constant plastic strain and damage. The critical damage level is evaluated at each integration point based on the weighted averaged local field. The weighted averaged fields are computed using $\lambda_w = 0.1$ and $\alpha = 0.005$. The critical damage level D_c is a material dependent constant that can be obtained from experiments. It usually assumed to be $0.2 < D_c < 0.8$.[34] The critical damage level determines the fatigue life N of the composite. The material constants, σ_y, Q, and b in Eqs. (17) and (18) and also B_o, L, and o in Eqs. (24) and (28) are obtained by curve fitting with experimental data for monotonic loading. Once the material constants are obtained. The prediction either for monotonic or fatigue loading can be performed.

The proposed fatigue life prediction approach for LCF can be summarized as follows:

1. Apply the specified load ϵ or σ.
2. Predict the effective properties of the composite and obtain the weighted averaged local fields (dehomogenization).
3. Evaluate plastic yield Eq. (17), if $f_p < 0$ go to the next step else solve for accumulated plastic strain r based on the consistency equation $\dot{f}_p = 0$ using incremental algorithm
4. Evaluate damage limit Eq. (24), if $f_d < 0$ go to the next step else using consistency $\dot{f}_d = 0$ obtain λ_d, β and $\boldsymbol{d}$ iteratively using incremental algorithm.
5. Update p, λ_d, β and $\boldsymbol{d}$.
6. Evaluate the critical damage level for each constituent, if damage level is less than D_c go to the next step else, the analysis will be terminated.
7. Update effective stiffness tensor Eq (37) damaged elastoplastic tangent stiffness tensor.
8. Repeat steps from 1 to 7.

The Step 1 to 6 are performed for all integration points where plastic strain and/or damage occur.

A. Continuous Fiber-Reinforced Composite

For the current study, the LCF life is predicted for glass/epoxy composite. Let the material constant in Eq. (25) be $c^d = 0$ and also $\mathcal{H}$ is assumed to be diagonal fourth order tensor with all its components equal to 1. The material constants for the fiber and matrix are listed in Table 1. The fiber volume fraction is 55%. The monotonic experimental data are not available. Thus, some of material constants are approximated based on the measured effective tensile strength and tensile failure strain in the composite. First, let σ_y be assumed for each constituent as shown in Table 1. The values of b and Q can be approximated using numerical simulation for a few small incremental loading just after the yield limit of each constituent.

Again, let the stress level 2.64 GPa and 1.50 GPa, for the matrix and fiber, respectively, be the limit of damage initiation due to excessive plastic strain, the corresponding values of B_o can then be estimated using Eq. (24). If $f_d < 0$, no damage. Thus, B_o is selected to have infinitesimally small damage in the each

constituent. The critical damage values are assumed to be 0.2 and 0.23 for the fiber and matrix, respectively. The values of L, and o are then estimated by numerically simulation. These simulations are performed until the predicted maximum tensile stress and tensile failure strain fits with the measured values 1.670 GPa and 3.8% of maximum tensile stress and tensile failure strain, respectively, Ref. [21]. The predicted effective tensile strength maximum tensile stress and tensile failure strain are found to be 1.65 GPa and 3.96%, respectively. The predicted and measured values maximum tensile stress and tensile failure strain show good agreements. Thus, it is believed that the calibrated material constants can be used to predict the fatigue life of the composite.

Table 1. Material constant for fatigue analysis (Ref. [21])

Material	E GPa	ν	σ_y (GPa)	b	Q (GPa)	B_o(GPa)	L(GPa)	o
Fiber	78.50	0.189	2.750*	9.5*	1000*	0.052*	120.00*	8*
Matrix	3.50	0.350	0.150*	15.5*	10000*	0.058*	0.199*	7.5*

* estimated

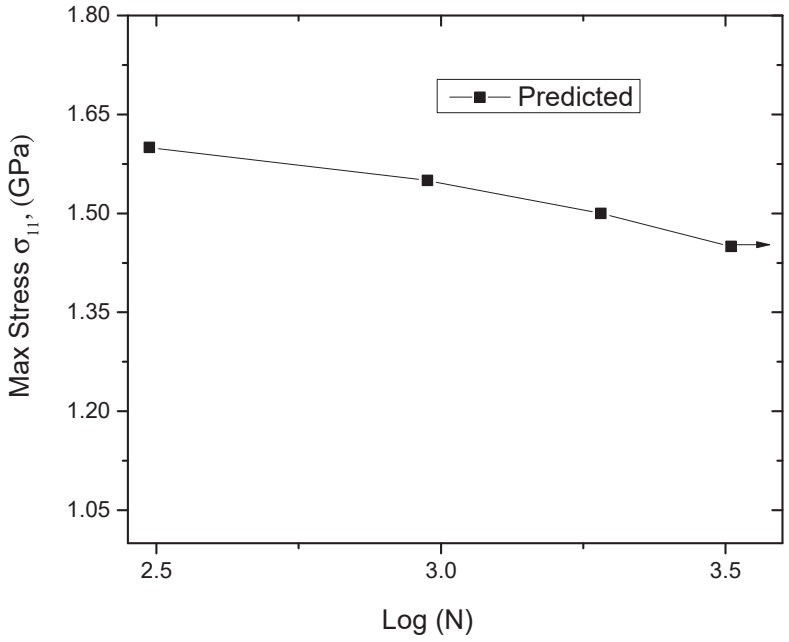

Figure 1. S-N for continuous fiber-reinforced composite.

Let the stress ratio $R = \frac{\sigma_{min}}{\sigma_{max}}$ be 0.5, the fatigue life of continuous fiber-reinforced composite is then estimated based on the calibrated material constants as shown in Figure 1.

To analyze the propagation of accumulated plastic strain and damage, let the global load 1.6 GPa be applied on the structure genome of the composite. The applied load is used to run fatigue analysis to study the growth of plastic strain and damage during cyclic loading. In this analysis, it is noticed that the fiber mainly controls the failure of the composite. The plastic strain and damage in the matrix are also observed to be negligible. The propagation of weighted averaged plastic strain in the matrix and damage growth in the fiber are depicted in Figures 2 and 3, respectively. The progressive fatigue damage also affects the effective properties of composites as shown in Figure 4. The degradation of the effective properties are observed to

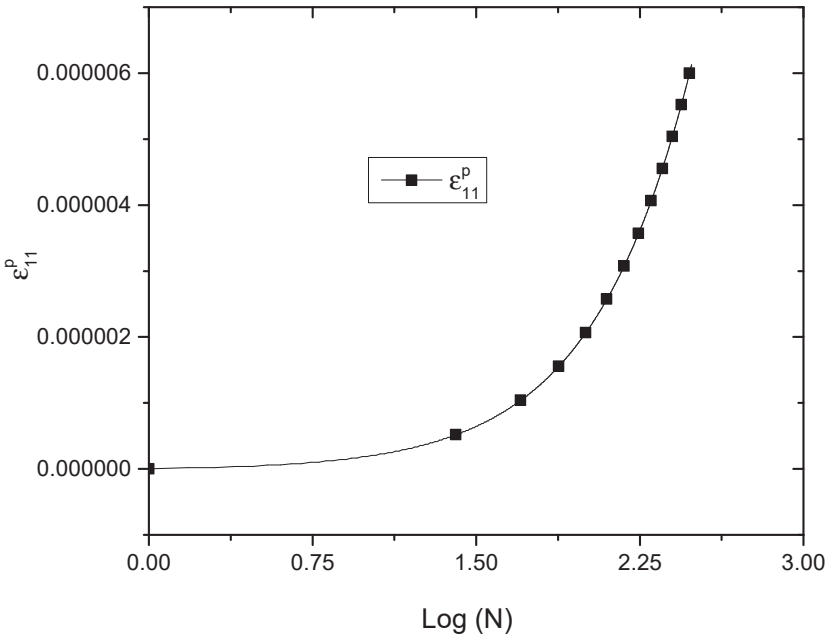

Figure 2. Weighted averaged plastic in continuous fiber-reinforced composite.

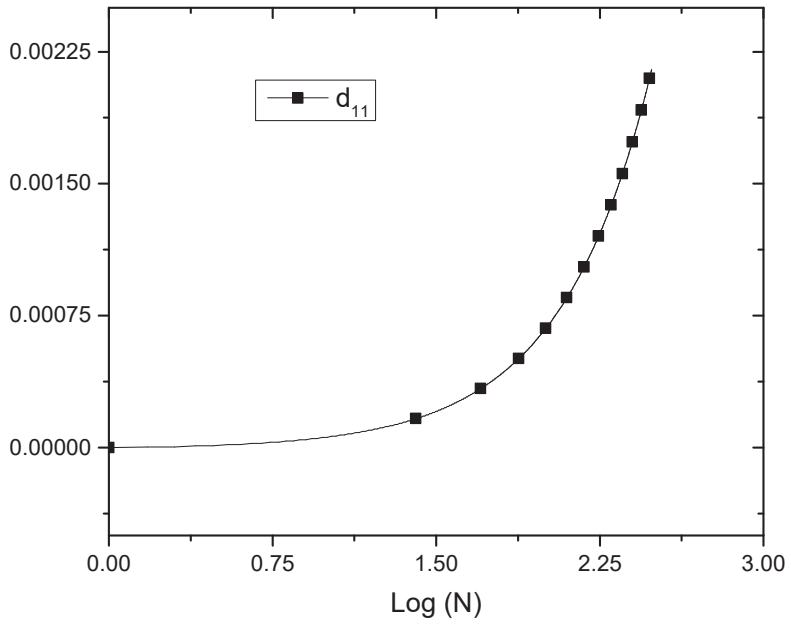

Figure 3. Weighted averaged damage in continuous fiber-reinforced composite.

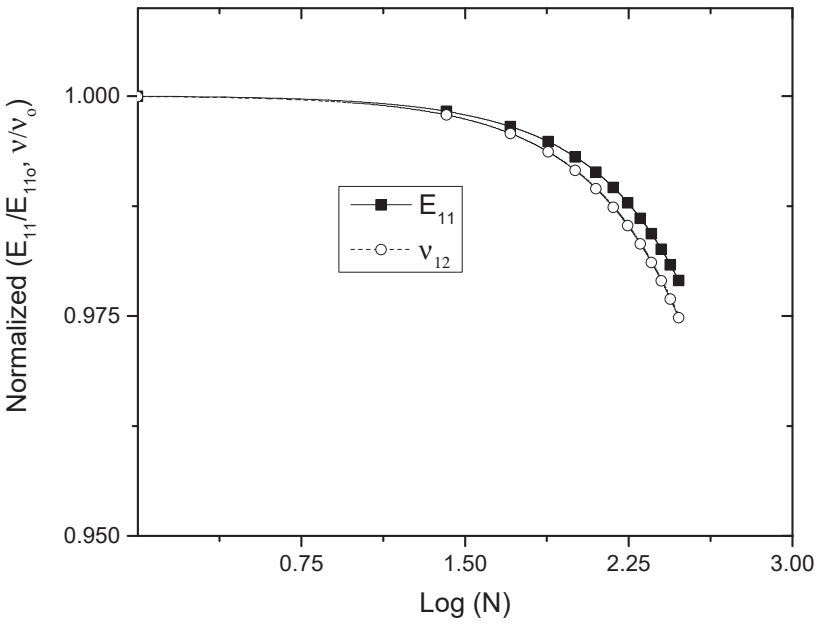

Figure 4. Effective properties of continuous fiber-reinforced composite.

be gradually decreasing unlike the high cycle fatigue where sudden failure happens. This is because the material undergoes excessive plastic strain before damage occurs.

B. Particle-Reinforced Composite

In this example, a cuboidal structure genome is used. Let the a spherical particle be embedded at the center of the structure genome and also let particle volume ratio be 10%. In this case, monotonic stress-strain experimental data of the composite are available. Thus, the material constants both for plasticity σ_y, b, and Q, and damage analysis B_o, L, and o are calibrated by numerically simulations. Let the material constant in Eq. (25) $c^d = 0$ and also $\mathcal{H}$ is assumed to be diagonal fourth-order tensor with all its components equal to 1. The simulations are performed until the predicted curve fits with the experimental data. The yield limit of the fiber is approximated, while the yield limit of the matrix and the composite is measured as shown in Table 2. Consequently, plastic strain and damage analysis constants are approximated using the yield limits of the particle and matrix. It should be noted that, for LCF, damage occurs due to excessive plastic strain. The material constants b and Q are then calibrated by curve fitting with experimental data for few small incremental load after yield limit. As the load increases, damage initiates at a specified stress level beyond the yield limit. In this analysis, let the specified stresses be approximately 2869 MPa and 208 MPa for the matrix and fiber, respectively. Based on these stresses, one can estimate the values of B_o using Eq. (24). If $f_d < 0$, no damage. Let the value of B_o be selected for infinitesimally small positive values of f_d which results in infinitesimally small damage in each constituent. The values of L and o are then estimated by numerically simulation using different values. The estimated material constants are shown in the Table 2. These material constants are then used to predict the stress-strain curve for the uniaxial loading. As shown in Figure 5, the predicted results show good agreement with the experimental data.

As seen from the predicted results for monotonic loading, it is reasonable to use estimated material constants to predict the fatigue life of the composite. In this case, let the stress ratio $R = \frac{\sigma_{min}}{\sigma_{max}}$ be 0.6. The fatigue life of the particle reinforced composite is estimated as it can be seen from Figure 6.

For LCF, the fatigue life is dependent of on the growth of local accumulated plastic strain and damage in the composite. To investigate this, let a cyclic load of 1.5 MPa be used. In this analysis, the matrix

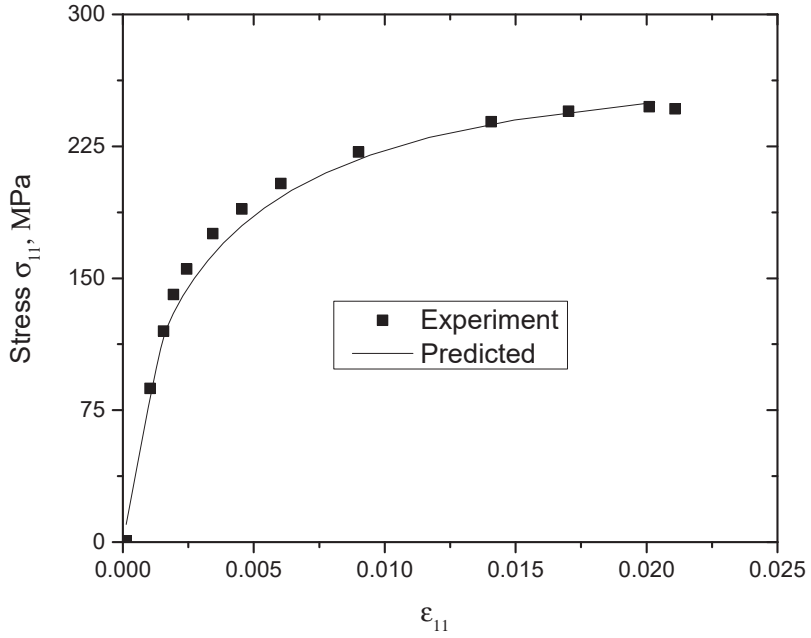

Figure 5. Stress-strain curve for particle-reinforced composite.

Table 2. Material constant for fatigue analysis (Ref. [19])

Material	E (GPa)	ν	σ_y (GPa)	b	Q (GPa)	B_o(GPa)	L(GPa)	o
Fiber	234.90	0.204	21	21*	2000*	8.2*	20*	10*
Matrix	69.90	0.330	0.135	12.5*	350*	0.8*	0.3*	5*

* estimated.

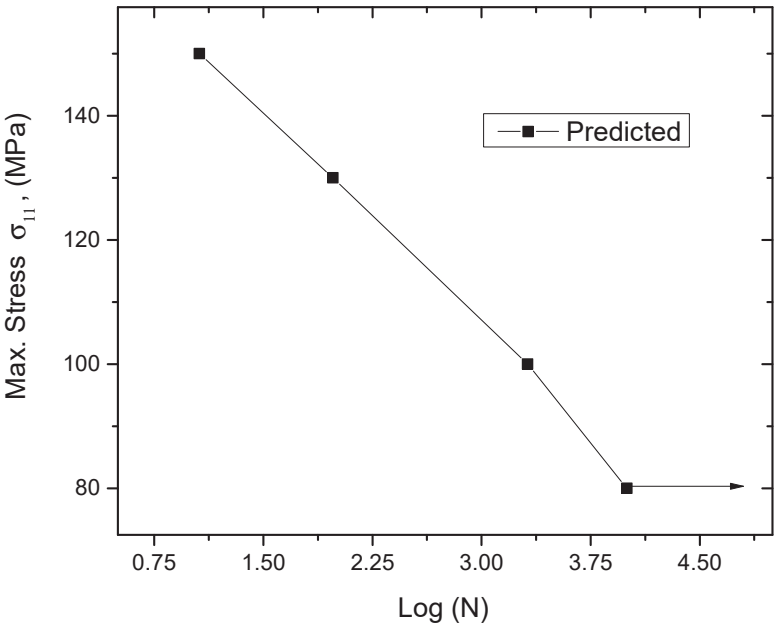

Figure 6. S-N **curve for particle-reinforced composite.**

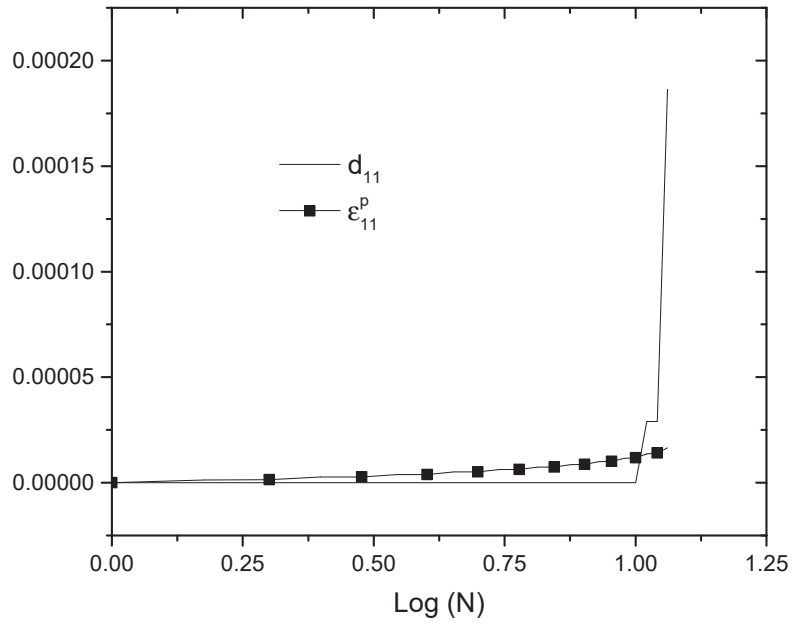

Figure 7. Weighted averaged accumulated plastic strain and damage in particle-reinforced composite.

mainly controls the failure of the composite. it is also observed that the damage starts to propagate after excessive accumulated plastic strain. However, the growth of weighted averaged damage is much greater than accumulated plastic strain as shown in Figure 7. This may be due to larger stress disturbance in each constituent particularly along the fiber-matrix interface. Morevoer, it is noticed that the progressive fatigue damage can significantly affect the effective properties of the composite as shown in Figure 8. In this analysis, the shear moduli are observed to be negligibly affected.

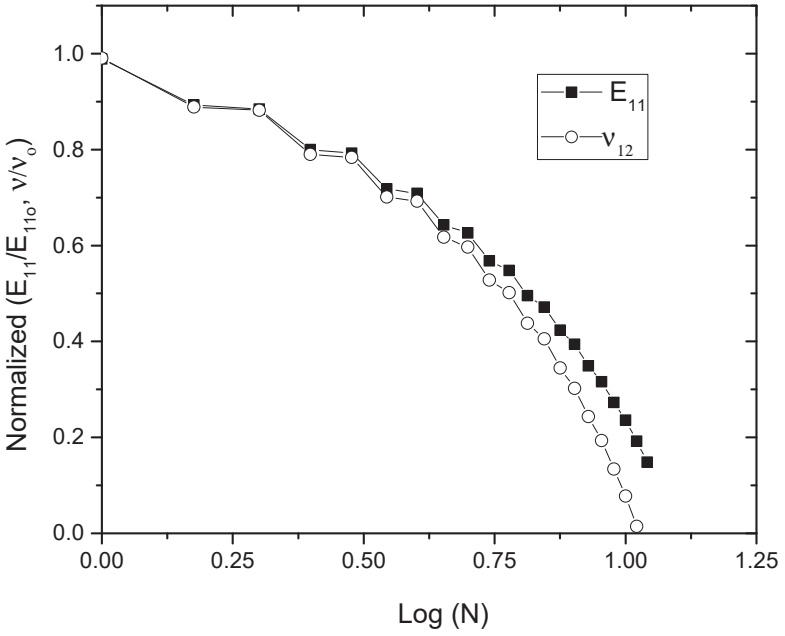

Figure 8. Degradation of effective properties of particle-reinforced composite.

VII. Conclusion

The fatigue life analysis of composite materials are studied using a micromechanics approach. The proposed method is incorporated into SwiftComp to estimate the fatigue life and anisotropic damage evolution of the composite. The stress-strain curve for monotonic loading is found to be in a good agreement with the experimental data. As the proposed approach is mainly based on micromechanics particularly on the local fields, it requires material properties specific to each constituent. The current prediction may be improved if all material data are available. The current calibration approach is limited to unidirectional loading option. It is suggested to make this approach applicable for multi directional loading conditions. Additional validations of the fatigue life with experimental data are also required to examine the capability of the current approach.

Acknowledgments

This research is supported, in part, by the Air Force Office of Scientific Research (with Dr. David Stargel as the program manager) and by the Composites Design and Manufacturing HUB at Purdue University. The views and conclusions contained herein are those of the authors and should not be interpreted as necessarily representing the official policies or endorsement, either expressed or implied, of the sponsor.

References

[1]Rice, J. and Tracy, D., "On Ductile Enlargement of Voids in Triaxial Stress ields," *Journal of Mechanics and Physics of Solids*.

[2]Needleman, A. and Tvergaard, V., "An Analysis of Ductile Rupture in Notched Bars," *Journal of Mechanics and Physics of Solids*.

[3]Gurson, A., "Continuum Theory of Ductile Rupture by Void Nucleation and Growth: Part I- Yield Criteria and Flow Rules for Porous Ductile Media," *J. Eng. Mater. Technol*, Vol. 99, 1977, pp. 2–15.

[4]Tvergaard, V. and Needleman, A., "Analysis of the Cup-cone Fracture in a Round Tensile Bar," *Acta Metall*, Vol. 32, 1984, pp. 157169.

[5]Lemaitre, J., Desmorat, R., and Sauzay, M., "Anisotropic Damage Law of Evolution," *Eur. J. Mech. A/Solids*, Vol. 19, 2000, pp. 187208.

[6]Lemaitre, J. and Desmorat, R., *Engineering Damage Mechanics*, Springer, 2005.

[7]Lemaitre, J., *A Course in Damage Mechanics*, Springer, 1996.

[8]Besson, J., "Continuum Models of Ductile Fracture: A Review," *International Journal of Damage Mechanics*.

[9]Lemaitre, J. and Chaboche, J.-L., *Mechanics of solid materials*, Cambridge University Press, 1994.

[10]Lemaitre, J., "Damage 90: A Continuous Damage Mechanics model for Ductile Fracture," *Journal of Engg Material and Technology*, Vol. 107, 1985, pp. 85.

[11]Dufailly, J. and Lemaitre, J., "Modeling Very Low Cycle Fatigue," *International Journal of Damage Mechanics*, Vol. 4, No. 2, 1995, pp. 153–170.

[12]Voyiadjis, G. and Deliktas, B., "A Coupled Anisotropic Damage Model for Inelastic Response of Composite Materials," *Comput. Methods Appl. Mech. Engrg*, Vol. 183, 2000, pp. 159–199.

[13]Maire, J. and Chaboche, J., "A New Formulation of Continuum Damage Mechanics (CDM) for Composite Materials," *Aerospace Science and Technology*, Vol. 4, No. 4-5, 1997, pp. 247–257.

[14]Fish, J. and Oskay, C., "A Nonlocal Multiscale Fatigue Model," *Mechanics of Advanced Materials and Structures*, Vol. 12, 2005, pp. 485500.

[15]Chaboche, J., Kruch, S., Maire, J., and Pottier, T., "Towards a Micromechanics based Ineleastic and Damage Modeling of Composites," *Internaltional Journal of Plasticity*, Vol. 17, 2001, pp. 411–439.

[16]Jeng, S., Alassoeur, P., and Yang, J., "Fracture Mechanisms of Fiber-Reinforced Titanium Alloy Matrix Composites Part IV:Low Cycle Fatigue," *Materials Sciene and Engineering*, Vol. A148, 1991, pp. 67–77.

[17]Pirondi, A. and Bonora, N., "Modeling Ductile Damage under Fully Reversed Cycling," *Internaltional Journal of Plasticity*, Vol. 17, 2001, pp. 411–439.

[18]Pang, J., Xiong, B., and Low, T., "Low Cycle Fatigue Models for Lead-free Solders," *Internaltional Journal of Plasticity*, Vol. 17, 2001, pp. 411–439.

[19]Koh, S., Oh, S., Li, C., and Ellyin, F., "Low-Cycle Fatigue Life of SiC-Particulate-Reinforced Al-Si Cast Alloy Composites with Tensile Mean Strain Effects," *International Journal of Fatigue*, Vol. 21, 1999, pp. 1019–1032.

[20]Srivatsan, T., "The Low-Cycle Fatigue Behaviour of an Aluminium-Alloy-Ceramic-Particle Composite," *International Journal of Fatigue*, Vol. 3, 1992, pp. 173–182.

[21]Harik, V., Klinger, J., and Bogetti, T., "Low-Cycle Fatigue of Unidirectional Composites: Bi-linear SN Curves," *International Journal of Fatigue*, Vol. 24, 2002, pp. 455–462.

[22]Vree, J., Brekelmans, W., and Gils, M., "Comparison of Nonlocal Approaches in Continuum Damage Mechanics," *Computers and Strucutres*, Vol. 45, No. 4, 1995, pp. 581–588.

[23]Borst, R., Sluys, L., Muhlhaus, H., and Pamin, A., "Fundamental Issues in Finite Element Analyses of Localization of Deformation," *Engineering Computations*, Vol. 26, No. 1, 1997, pp. 43–62.

[24]Pegon, P. and Anthoine, A., "Numerical Strategies for Solving Continuum Damage Problems with Softening: Application to the Homogenization of Masonry," *Computers and Structcure*, Vol. 64, No. 1-4, 1997, pp. 623–642.

[25]Bažant, Z., "Why Continuum Damage is Nonlocal: Micromechanics Arguments," *Journal of Engineering Mechanics*, Vol. 117, No. 5, 1991, pp. 10701087.

[26]Bažant, Z. and Pijaudier-Cabot, G., "Nonlocal Continuum Damage, Localization Instability and Convergence," *Journal of Applied Mechanics*, Vol. 55, No. 2, 1988, pp. 287–293.

[27]Liu, Y., Filonova, V., Hu, N Yuan, Z., Fihs, J., Tuan, Z., , J., and Belytschko, T., "A Regularized Phenomenological Multiscale Damage Model," *International Journal of Damage Mechanics*, Vol. 4, No. 2, 1995, pp. 153–170.

[28]Peerlings, R., Borst, R., Bekelmans, W., and De Vree, J., "Gradient Enhanced Damage for Quasi-Brittle Materials," *International Journal for Numerical Methods in Engineering*, Vol. 39, 1996, pp. 3391– 3403.

[29]Masson, R., Bekelmans, W., Borst, R., and Geers, M., "Gradient Enhanced Damage for Quasi-brittle materials," *International Journal for Numerical Methods in Engineering*, Vol. 49, 2000, pp. 1547–1569.

[30]Yu, W., "Structure Genome: Fill the Gap between Materials Genome and Structural Analysis," *Proceedings of the 56th Structures, Structural Dynamics and Materials Conference, Kissimmee, Florida*, Jan. 5-9, 2015.

[31]Yu, W., Williams, T., Bednarcyk, B., Aboudi, J., and Tang, T., "A Critical Evaluation of the Predictive Capabilities of Various Advanced Micromechanics Models," *Proceedings of the 48th Structures, Structural Dynamics and Materials Conference,Honolulu, Hawaii*, April. 23-26, 2007.

[32]Sertse, H., Zhang, L., Yu, W., and Ye, Z., "A Comprehensive Evaluation of the Predictive Capabilities of Several Advanced Micromechanics Approaches," *Proceedings of the 48th Structures, Structural Dynamics and Materials Conference, National Harbor, Maryland*, Jan. 13-17, 2014.

[33]Kachanov, L., "On Creep Rupture Time," *Izv. Acad. Nauk SSSR*, Vol. 8, 1958, pp. 26–31.

[34]Sumio, M., *Continuum Damage Mechanics: A Continuum Mechanics Approach to the Analysis of Damage and Fracture*, Springer, 2012.

[35]Besson, J., Cailletaud, G., Chaboche, J., and Forest, S., *Non-Linear Mechanics of Materials, Solid Mechanics and Its Applications*, Vol. 167, Springer, 2012.

[36]Hayakawa, K., Murakami, S., and Liu, Y., "An Irreversible Thermodynamic Theory for Elastic-Plastic Damage Materials," *Eur J Mech A/Solids*, Vol. 17, No. 2, 1998, pp. 1332.

[37]Tang, T. and Yu, W., "Asymptotical Approach to Initial Yielding Surface and Elastoplasticity of Heterogeneous Materials," *Mechanics of Advanced Materials and Structures*, Vol. 18, No. 4, 2011, pp. 244–254.

[38]Tang, T. and Yu, W., "Variational Asymptotic Micromechanics Modeling of Heterogeneous Piezoelectric Materials," *Mechanics of Materials*, Vol. 40, No. 10, 2008, pp. 812–824.

[39]Lee, C. and Yu, W., "Homogenization and Dimensional Reduction of Composite Plates with In-Plane Heterogeneity," *International Journal of Solids and Structures*, Vol. 48, No. 10, 2011, pp. 14741484.

[40]Maimi, P., Camanho, P., Mayugo, J., and Davila, C., "A Continuum Damage Model for Composite Laminates: Part I Constitutive Model," *Mechanics of Materials*, Vol. 39, 2007, pp. 897–908.

Modeling Aperiodic Dimensionally Reducible Structures Using Mechanics of Structure Genome

Bo Peng, Wenbin Yu*

* Purdue University, West Lafayette, Indiana 47907

ABSTRACT

This work systematically constructs multiscale constitutive models for aperiodic dimensionally reducible structures (beams/plates) using Mechanics of Structure Genome (MSG). MSG splits the original 3D body into a dimensionally reduced structural analysis and a constitutive modeling over the Structure Genome (SG). SG is the smallest mathematical building block of the structure, which can be used to obtain all the necessary constitutive relations for the reduced structural analysis. The approach starts with expressing the kinematics including both displacements and strains of the original heterogeneous material in terms of those of the dimensionally reduced structures and fluctuating functions. To ensure the kinematic equivalency of the original heterogeneous structures and the dimensionally reduced structures, integral constraints on the fluctuating functions are developed. Then based on the principle of minimum information loss along with the variational asymptotic method, the variational statement governing the SG only can be formulated and solved. As this theory does not require boundary conditions, one is free to choose the analysis domain of arbitrary shape and they need not to be volumes with periodic boundaries. This theory can also handle periodic microstructures by enforcing the periodicity of the fluctuating functions. To validate this new theory, the results using the current approach are compared with that obtained from using PBCs for periodic heterogeneous beam/plate structures.

INTRODUCTION

Composites are widely used in engineering applications, especially in aeronautics, which have high strength to weight and stiffness to weight ratios. These struc-

Purdue University, West Lafayette, Indiana 47907

tures are usually of complex geometries and materials, but displaying a feature that one or two dimensions of the three-dimensional (3D) body are much smaller than the remaining dimensions, referred as dimensionally reducible structures (DRS). Examples are rotor blades with complex cross-section geometries and varying geometric features along the blade length, or plates with stiffeners or other complicated buildup features. Despite the highly developed computation capability of today, 3D analysis is usually replaced with lower-dimensional models to avoid the expensive computational cost. To ensure the accuracy, the reduced models must be properly constructed from the original 3D problem, to achieve both good estimation of macroscopic deformation and 3D local fields.

Historically, numerous theories for composite beams and plates are developed as two different branches of methods. Two important types of beam structures mostly investigated in the related literatures are rotor blades and heterogeneous beam structures consisting of unit cells arranged periodically in the longitudinal direction. For rotor blades, Hodges and Yu developed the Variational Asymptotic Beam Sectional Analysis (VABS) in [1, 2], in which the beam-like structure is described by a lengthwise variation of properties associated with cross-sections, and the original 3D problem is split into a two-dimensional linear cross-sectional analysis and a one-dimensional beam analysis. In the numerical application of VABS, isoparametric 2D elements are used. Couturier [3] evaluated the cross-section stiffness matrix by analyzing six independent deformation modes corresponding to extension, torsion, bending and shear on a single element thickness slice represented by 3D solid elements with lengthwise Hermitian interpolation. Rotor blades are often not uniform in the longitudinal direction, however in these approaches the non-uniformities of the cross-section at different locations is not handled directly, instead the beam is discretized and the cross-section stiffness matrix is solved at different locations with an implicit assumption that the cross-section is almost identical in the neighborhood of the considered location of the macro model. Only Ho in [4] directly dealt with the non-uniformities effect of a tapered homogeneous beam using VABS, which demonstrated VABS has a potential to be valid for non-uniform beams composed of arbitrary materials and geometries with more work required. Heterogeneous beam structures consisting of unit cells arranged periodically in the longitudinal direction are studied in [5, 6], in both approaches periodic boundary conditions must be applied.

For heterogeneous plate and shell structures comprised of in-plane periodic unit cells, the developed theories including asymptotic homogenization method (AHM) [7, 8], variational asymptotic homogenization method [9, 10], and a novel numerical implementation of AHM [11]. These theories are for general in-plane unit cells and directly resulted in the effective plate properties for the homogenized macro plate model. There are also numerous approaches take advantage of the geometry characteristics of some specific unit cells such as sandwich structures with honeycomb core [12, 13] or woven composite plates [14]. Composite plate theories [15, 16, 17] are also used in heterogeneous plate structures following a two-step scenario. First the effective properties of the heterogeneous materials of each layer are obtained, and then the effective properties are used in the various plate theories.

However, there is still more work to do for aperiodic dimensional reducible structures, such as tapered composite beams, plates without strict in-plane periodic struc-

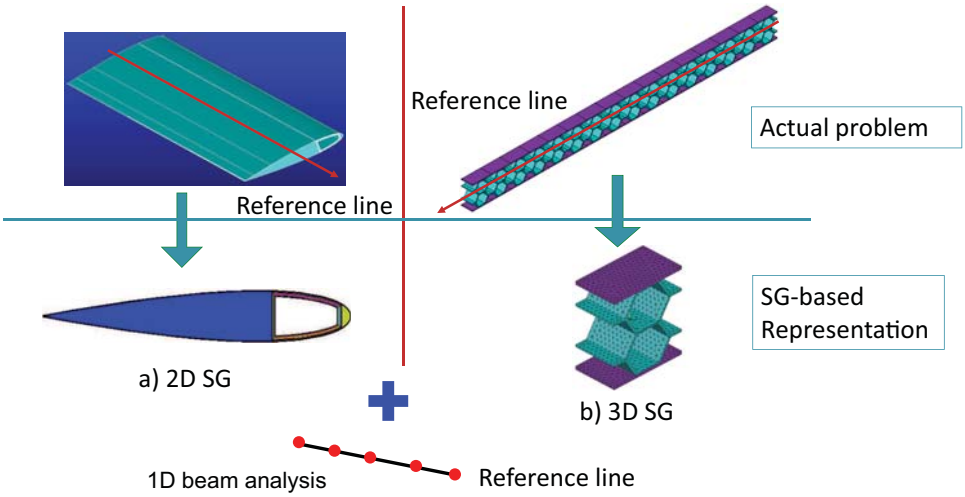

Figure 1. Analysis of beam-like structures approximated by a constitutive modeling over SG and a corresponding 1D beam analysis.

tures, or periodic structures in beams or plates which are too complicated to apply PBCs. The goal of the present paper is to use the recently discovered Mechanics of Structure Genome (MSG) [18, 19] to model these structures.

MSG allows direct connection between materials and the macroscopic structural analysis, particularly for dimensionally reducible structures in a consistent way. MSG has been proved to be very efficient and capable of predicting quite accurate results when periodic structures exist. In this work, first a basic concept structure genome(SG) in MSG is introduced on which the current theory is based on. Then we will proposed the minimum kinematic constraints (MKCs) for DRS so that the constitutive models of beams and plates with complecated heterogeneous microstructures can be systematically constructed without relying of periodic assumption. To validate this new theory, the results using the current approach are compared with that obtained from using PBCs for periodic heterogeneous beam/plate structures.

CONCEPT OF STRUCTURE GENOME

SG is defined as the smallest mathematical building block of the structure which contains all the constitutive information needed for a structure the same fashion as the genome contains all the intrinsic information for an organism's growth and development. For periodic structures, it is easy to identify the SG as shown in Figure 1 for beams and Figure 2 for plates. If the beam has uniform cross-sections which could be made of homogeneous materials or composites (Fig. 1a), its SG is the 2D cross-sectional domain because the cross-section can be projected along the beam reference line to form the beam-like structure.

If the beam is also heterogeneous in the spanwise direction (Fig. 1b), a 3D SG is needed to describe the microstructure of the 1D continuum. If the structural analysis uses plate/shell elements, SG can also be chosen properly. If the plate-like structures feature no in-plane heterogeneities (Fig. 2a), the SG is the transverse normal line

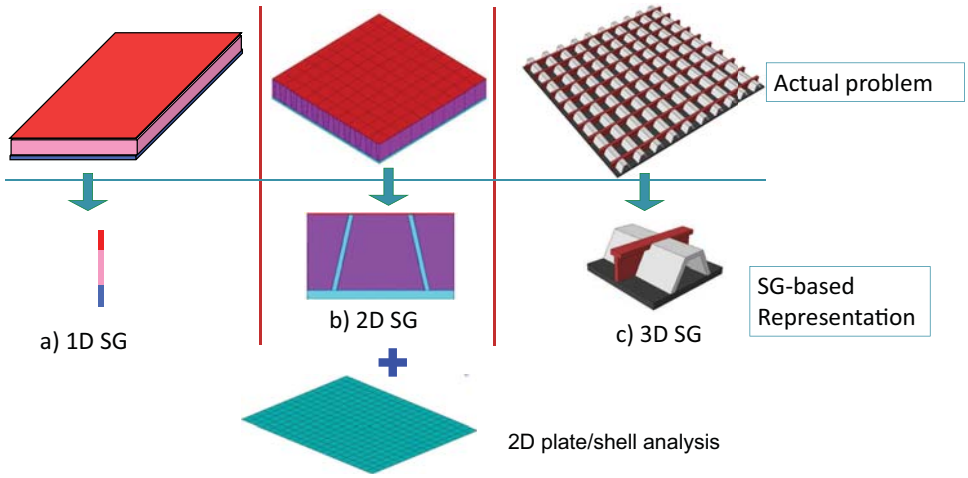

Figure 2. Analysis of plate-like structures approximated by a constitutive modeling over SG and a corresponding 2D plate analysis.

with each segment denoting the corresponding layer. For a sandwich panel with a core corrugated in one direction (Fig. 2b), the SG is 2D. If the panel is heterogeneous in both in-plane directions (Fig. 2c), such as a stiffened panel with stiffeners running in both directions, the SG is 3D.

Despite the different dimensionalities of the SGs, the constitutive modeling outputs the effective structural properties for the corresponding structural analysis and the recovery relations to express the original 3D fields in terms of the global behavior (moments, strains and curvatures, etc.) obtained from the structure analysis. If a zeroth-order approximation is performed [2], for heterogeneous beam structures the effective properties is a 4×4 stiffness matrix simultaneously accounting for extension, torsion, and bending in two directions; for plate/shells, the effective properties are composed of A, B, and D matrices. First-order approximation can also be performed [2, 10] if necessary but not considered in this work. It is known that theories of beams/plates/shells traditionally belong to structural mechanics, but the constitutive modeling of these structures can be treated as special micromechanics applications using the SG concept. For a dimensionally reducible structure, if the reference line/surface is considered as a 1D/2D continuum, every material point of this continuum has an associated SG as its microstructure.

However, in some real structures in engineering, such as rotor blades or plates with stiffeners or other complicated buildup features, periodic microstructures are not exist. In this case, we rely on the expert opinion of the analysts to determine what will be the smallest, representative building block of the structure, which is like volume representative volume (RVE) in micromechanics in the analogue sense. It can also be justified from the viewpoint of material characterization using experiments. When experimentalists want to find properties of a material, they cut representative pieces of the material according to their own judgment, make a specimen out of it and do the testing to get the properties and associated statistics through relations form strucutre analysis. In the process, the effective properties of structures are internel quantities which however, is what required in this work through modeling.

THEORY OF THE MSG FOR STRUCTURE ELEMENTS WITH APERIODICITY

Although the proposed framework is general to handle most of micromechanics problems, this paper focuses only on the linear, elastic, static behavior of dimensional reducible heterogeneous structures without initial curvatures. To facilitate the formulation, two coordinate systems are set up. The macro coordinate system $\mathbf{x} = (x_1, x_2, x_3)$ is applied to describe the original heterogeneous structure, while micro coordinate system $\mathbf{y} = (y_1, y_2, y_3)$ is introduced to denote the rapid change in the material characteristics in SG. If the structure is dimensionally reducible, some of the macro coordinates x_α, called eliminated coordinates here, correspond to the dimensions eliminated in the macroscopic structural model. Here and throughout the paper, Greek indices assume values corresponding to the eliminated macro coordinates, Latin indices k, l, m assume values corresponding to the macro coordinates remaining in the macroscopic structural model, and other Latin indices assume 1, 2, 3. Repeated indices are summed over their range except where explicitly indicated.

For beam-like structures, only x_1, describing the beam reference line, will remain in the macro beam model; for plate/shell-like structures, x_1 and x_2, describing the plate reference surface, will remain in the macro plate model.

The first step in formulating MSG is to express the kinematics, including the displacement field and the strain field, of the original structures in terms of those of the macroscopic structural model. As derived in [19], the strain fields of beams and plates can be expressed in a uniform in Eq. (1) if a zeroth-order approximation is performed

$$\Gamma = \Gamma_h w + \Gamma_\epsilon \bar{\epsilon} \tag{1}$$

where $\Gamma = \lfloor \Gamma_{11} \;\; \Gamma_{22} \;\; \Gamma_{33} \;\; 2\Gamma_{23} \;\; 2\Gamma_{13} \;\; 2\Gamma_{12} \rfloor^T$ denotes the strain field of the original structure, $w = \lfloor w_1 \;\; w_2 \;\; w_3 \rfloor^T$ the fluctuating functions, $\bar{\epsilon}$ is a column matrix containing the generalized strain measures for the macroscopic structural model. If the macroscopic structural model is a beam model, we have $\bar{\epsilon} = \lfloor \epsilon_{11} \;\; \kappa_{11} \;\; \kappa_{12} \;\; \kappa_{13} \rfloor^T$ with ϵ_{11} denoting the extensional strain, κ_{11} the twist, κ_{12} and κ_{13} the bending curvatures. If the macroscopic structural model is a plate/shell model, we have $\bar{\epsilon} = \lfloor \epsilon_{11} \;\; \epsilon_{22} \;\; 2\epsilon_{12} \;\; \kappa_{11}^{\text{2D}} \;\; \kappa_{22}^{\text{2D}} \;\; \kappa_{12}^{\text{2D}} + \kappa_{21}^{\text{2D}} \rfloor^T$ with $\epsilon_{\alpha\beta}$ denoting the in-plane strains and $\kappa_{\alpha\beta}^{\text{2D}}$ denoting the curvature strains.

Γ_h is an operator matrix which depends on the dimensionality of the SG. If the SG is 3D,

$$\Gamma_h = \begin{bmatrix} \frac{\partial}{\partial y_1} & 0 & 0 \\ 0 & \frac{\partial}{\partial y_2} & 0 \\ 0 & 0 & \frac{\partial}{\partial y_3} \\ 0 & \frac{\partial}{\partial y_3} & \frac{\partial}{\partial y_2} \\ \frac{\partial}{\partial y_3} & 0 & \frac{\partial}{\partial y_1} \\ \frac{\partial}{\partial y_2} & \frac{\partial}{\partial y_1} & 0 \end{bmatrix} \tag{2}$$

If the SG is a lower-dimensional one, one just needs to vanish the corresponding term corresponding to the micro coordinates which are not used in describing the SG.

For example, if the SG is 2D,

$$\Gamma_h = \begin{bmatrix} 0 & 0 & 0 \\ 0 & \frac{\partial}{\partial y_2} & 0 \\ 0 & 0 & \frac{\partial}{\partial y_3} \\ 0 & \frac{\partial}{\partial y_3} & \frac{\partial}{\partial y_2} \\ \frac{\partial}{\partial y_3} & 0 & 0 \\ \frac{\partial}{\partial y_2} & 0 & 0 \end{bmatrix} \tag{3}$$

If the macroscopic structural model is a beam model,

$$\Gamma_\epsilon = \begin{bmatrix} 1 & 0 & y_3 & -y_2 \\ 0 & 0 & 0 & 0 \\ 0 & 0 & 0 & 0 \\ 0 & 0 & 0 & 0 \\ 0 & y_2 & 0 & 0 \\ 0 & -y_3 & 0 & 0 \end{bmatrix} \tag{4}$$

If the macroscopic structural model is a plate/shell model,

$$\Gamma_\epsilon = \begin{bmatrix} 1 & 0 & 0 & y_3 & 0 & 0 \\ 0 & 1 & 0 & 0 & y_3 & 0 \\ 0 & 0 & 0 & 0 & 0 & 0 \\ 0 & 0 & 0 & 0 & 0 & 0 \\ 0 & 0 & 0 & 0 & 0 & 0 \\ 0 & 0 & 1 & 0 & 0 & y_3 \end{bmatrix} \tag{5}$$

Without loss of generality, we consider the origin of the coordinate system of a SG associated to a point in the of the macro model to be located at the geometric center of the SG, that is

$$\langle \varepsilon y_\alpha \rangle = 0 \tag{6}$$

where $\langle \bullet \rangle$ denotes integration over the domain of SG. To ensure the kinematics equivalency between the original heterogeneous structures and the dimensionally reduced structures (beams or plates), a unique mapping between the micro-scale kinematic fields and the macro-scale kinematic fields must be satisfied. As derived in [19], the fluctuating functions must be constrained according to Eq. (7). For beam structures, they are additionally constrained by Eq. (8).

$$\langle w_i \rangle = 0 \tag{7}$$

$$\langle w_{2|3} - w_{3|2} \rangle = 0 \tag{8}$$

These constraints only ensure the equivalency of the displacement vector of the macro model and the average displacement of the original heterogeneous structures, and thus the rigid body displacement of the SG can be eliminated. Equivalency of strain

vector of the macro model and the original heterogeneous structures should also be satisfied. For DRS with periodic microstructures, this is ensured by exerting PBCs on the fluctuating functions. In this work, MKCs of beam and plate heterogeneous structures are proposed so that the equivalency of strain can be achieved. If the macro structure is a beam, the MKCs are

$$\begin{aligned} \left\langle w_{i|1} \right\rangle &= 0 \quad (i = 1, 2, 3) \\ \left\langle y_\alpha w_{1|1} \right\rangle &= 0 \quad (\alpha = 2, 3) \\ \left\langle y_2 w_{3|1} - y_3 w_{2|1} \right\rangle &= 0 \end{aligned} \tag{9}$$

for a 3D SG. It is apparrent that the constraints in Eq. (9) will be automatically be satisfied for 1D and 2D beam SG in which y_1 is a constant.

For plates, these MKCs are

$$\begin{aligned} \left\langle w_{k|l} + w_{l|k} \right\rangle &= 0 \quad (l, k = 1, 2) \\ \left\langle y_3 (w_{k|l} + w_{l|k}) \right\rangle &= 0 \quad (l, k = 1, 2) \end{aligned} \tag{10}$$

for 3D SG. For 2D SG or 3D SG with PBCs applied on nodes on the boundary surfaces normal to y_1, the terms related to the partial derivative of y_1 disappeared. Eq. (10) is satisfied automatically for 1D SG of plate. Any solution of fluctuating functions must satify the constraints Eq. (7), Eq. (8) and Eq. (9) for beams or Eqs. (7) and (10) for plates, which define the most flexible solution space of fluctuating functions. The solution found from this solution space using the principal of minimum potential will apply least constraints on the fluctuations, which correspond to the static uniform boundary conditions on RVE. More constraints can be additionally applied if they are chosen probably according to the physical problem in question to obtain faster converging results. In fact, it is explicit the fluctuating functions periodically constrained at the periodic boudnary surfaces satisfy Eq. (9) for beams or Eq. (10) for plates automatically.

Therefore, it enlighten us at least 3 messages: (1) For aperiodic beams or plates, once the SG is chosen properly, multiscale modeling can be performed using the proposed constraints. As this theory does not involve any boundary conditions, the analyst is free to choose SGs of arbitrary shape and they need not be volumes with straight boundaries. (2) For partially periodic beam or plates, by enforcing the periodicity of the fluctuating functions on the corresponding surfaces in addition to the MKCs, the best solution can be obtained with the minimum information loss. (3) For some periodic structures, it is very difficult to generate mesh with all nodes on boundary surfaces have a corresponding periodic node, but quite often the periodic node pairs exist partially. In this case, the existed periodic constraints can be applied along with the MKCs.

For linear elastic problem, the behavior of the original heterogeneous is governed by the principle of minimum total potential energy. To minimize the loss of information between the original model describing the microscopic details and the model used for the macroscopic structural analysis, for elastic materials we minimize the difference between the strain energy of the materials stored in SG and that stored in the macroscopic structural model along with the required constraints. As pointed out

in [19], the effects of loads can be negnected if we are only interested in the constitutive relations and thus the potential energy becomes strain energy. Therefore the governing equation is only defined in the SG as

$$\delta J = \delta \left\langle \frac{1}{2}(\Gamma_h w + \Gamma_\epsilon \bar{\epsilon})^T D(\Gamma_h w + \Gamma_\epsilon \bar{\epsilon}) - \lambda \Gamma_k w - \eta \Gamma_c w \right\rangle = 0 \tag{11}$$

where D is the 6×6 material matrix of the original heterogeneous DRS. $\Gamma_k w$ is the constraints of beam (Eqs. (9) and Eq. (8)) and plate (Eqs. (10)) written in matrix form, λ is the corresponding Lagrange multiplier vector. $\Gamma_c w$ is the constraints of Eqs. (7) written in matrix form, and η is the corresponding Lagrange multiplier vector.

Finite element implementation

To solve Eq. (11) for general cases, we need to turn to numerical techniques such as the finite element method (FEM). It is possible to formulate the FEM solution based on Eq. (11) directly, however since the constraints of the last term do not affect the minimum value of J but help uniquely determine the fluctuating functions, in practice we can constrain the fluctuating functions at an arbitrary node to be zero and later use these constraints to recover the unique fluctuating functions. Discretize w using the finite elements as

$$w(x_i; y_j) = S(y_j)V(x_i) \tag{12}$$

where S represents the shape functions and V a column matrix of the nodal values of the fluctuating functions.

Substituting Eqs. (12) into Eq. (11), we obtain a discretized version of the functional J as

$$J = \frac{1}{2}\left(V^T E V + 2V^T D_{h\epsilon}\bar{\epsilon} + \bar{\epsilon}^T D_{\epsilon\epsilon}\bar{\epsilon}\right) - \lambda^{\mathrm{T}} D_{h\lambda}^{\mathrm{T}} V \tag{13}$$

where

$$E = \left\langle (\Gamma_h S)^T D (\Gamma_h S) \right\rangle \quad D_{h\epsilon} = \left\langle (\Gamma_h S)^T D \right\rangle \quad D_{\epsilon\epsilon} = \langle D \rangle \quad D_{h\lambda} = \langle \Gamma_h S \rangle^{\mathrm{T}} \tag{14}$$

Minimizing J in Eq. (13) gives us the following linear system

$$\begin{bmatrix} E & -D_{h\lambda} \\ -D_{h\lambda}^{\mathrm{T}} & 0 \end{bmatrix} \begin{bmatrix} V \\ \lambda \end{bmatrix} = \begin{bmatrix} -D_{h\epsilon}\bar{\epsilon} \\ 0 \end{bmatrix} \tag{15}$$

It is clear that V will linearly depend on $\bar{\epsilon}$, and the solution can be symbolically written as

$$V = V_0 \bar{\epsilon} \tag{16}$$

With the solution in Eq. (16), we can calculate the strain energy storing in the SG as the first approximation as

$$U = \frac{1}{2}\bar{\epsilon}^{\mathrm{T}}\left(D_{\epsilon\epsilon} + V_0^{\mathrm{T}} D_{h\epsilon}\right)\bar{\epsilon} \equiv \frac{\Omega}{2}\bar{\epsilon}^{\mathrm{T}}\bar{D}\bar{\epsilon} \tag{17}$$

where $\bar{D}$ is the effective stiffness matrix to be used in the macroscopic structural analysis.

The local fields within the SG can also be recovered easily based on the global displacement v_i and global strain $\bar{\epsilon}$. First knowing $\bar{\epsilon}$, we can compute the fluctuating function as

$$w = SV_0\bar{\epsilon} \tag{18}$$

The local strain field can be recovered using Eq. (1) as

$$\epsilon = \bar{\epsilon} + \Gamma_h SV_0\bar{\epsilon} \tag{19}$$

The local stress field can be obtained directly using the Hooke's law as

$$\sigma = D\epsilon. \tag{20}$$

VALIDATION OF BEAM AND PLATE MODEL

The present theory is implemented in the general-purpose multiscale constitutive modeling code, SwiftComp$^{\mathrm{TM}}$. Several examples are used to validate the effectiveness of the constraints for beam and plate model. In all the models the same two materials are used with properties shown in Table I. The coordinate system notation x, y, z is used instead of y_1, y_2, y_3 in this section.

TABLE I. MATERIAL PROPERTIES

Materials	E_1 (GPa)	$E_2 = E_3$ (GPa)	$G_{12} = G_{13}$(GPa)	G_{23} (GPa)	$\nu_{12} = \nu_{13}$	ν_{23}
Material 1 (Green)	50.0	15.2	4.7	3.28	0.254	0.428
Material 2 (Grey)	2.60	2.60	1.0	1.0	0.30	0.30

Validation of beam model

First a cylinder beam with a span-wise heterogeneity is considered, of which the 3D SG is shown in Figure 3. The SG has a diameter of 2 mm, and the length in x direction is 1 mm. Each material occupies the same volume in the SG. The approximate mesh size chosen for this example is 0.24 mm. Using the current configuration, the effective beam properties obtained using PBCs are presented in Table II.

The effective beam properties obtained from using the MKCs can be found to converge to the results of using PBCs in the x direction with the increasing of the number of SGs used (Figure 4). It is shown that the torsional stiffness D_{22} is not influenced by the constraints applied for a cylinder beam SG with homogeneous material properties across the cross-section in this case.

The discrepancy between using MKCs and PBCs comes from the boundary effect. When a macro strain $\epsilon_{11} = 0.1$ is applied to a beam SG composed of 4 repetitive SGs of Figure 3, the stress σ_{11} dehomogenized with MKCs and PBCs are compared in

Figure 5. If the number of repetitive SGs is increased, this boundary effect will not be elimilated but the influence to the homogelized beam model will be decreased. From Fig 6, it is shown that the increasing of the number of SGs exerted litter influence to σ_{11} distribution at the path along the x axis of the SG in the boundary region.

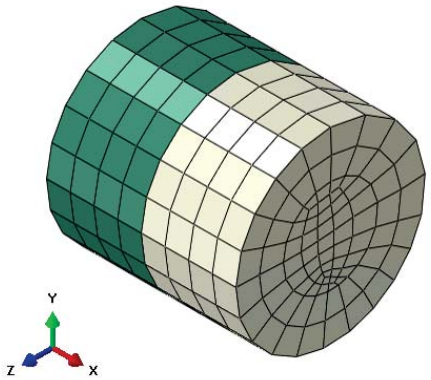

Figure 3. Beam SG 1: SG with a circular cross-section.

TABLE II. EFFECTIVE BEAM PROPERTIES OBTAINED USING SG 1 AND APPLYING PBCS

D_{11} (N)	D_{22} (N m^2)	D_{33} (N m^2)	D_{44} (N m^2)
1.6740E+4	2.503E-3	4.072E-3	4.079E-3

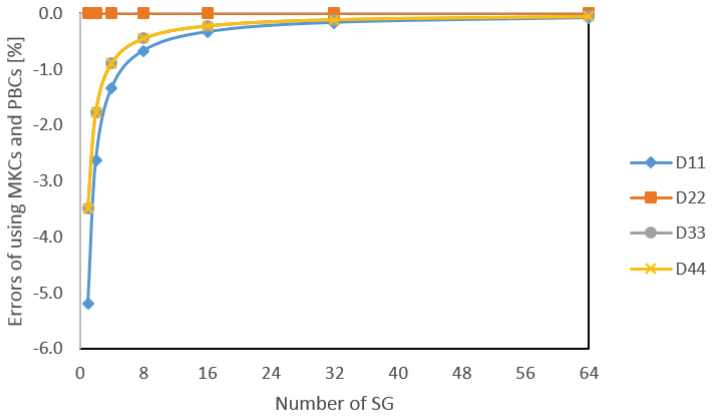

Figure 4. Convergence study of effective beam stiffness of beam SG 1.

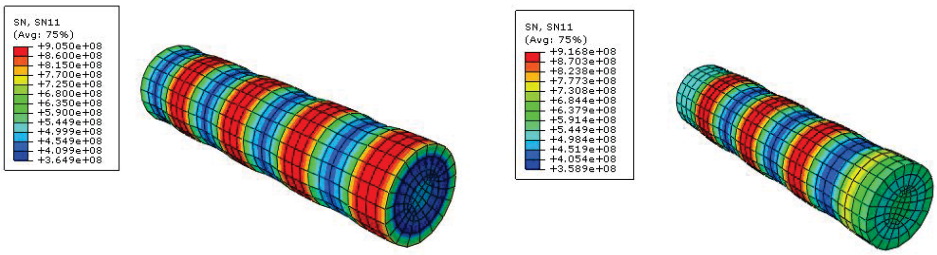

(a) Using PBCs (b) Using MIX100

Figure 5. σ_{11} obtained by dehomogenization with macro strain $\epsilon_{11} = 0.1$

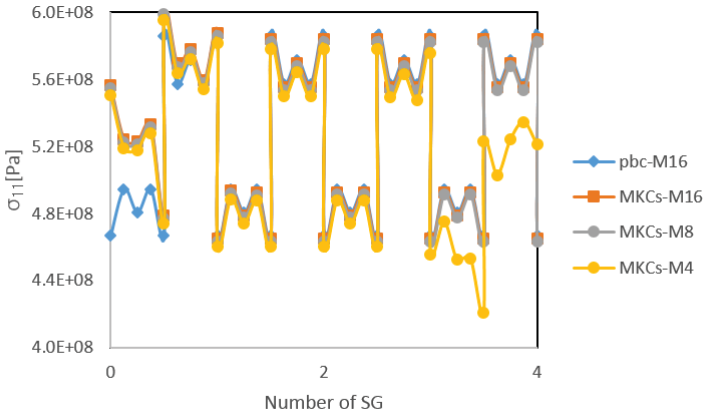

Figure 6. σ_{11} along the x axis of beam SG 1. The number after 'M' denotes the number of repetitive SGs in Figure 3 analyzed.

In the second example, a more complex beam structure with heterogeneity in all the directions is studied, the SG of which is shown in Figure 7. The SG has a length of 2 mm, and the diameters are 1 mm and 2 mm respectively for the inner cylinder and the outside tube, in which each material occupies the same volume fraction. The mesh of the SG is purposely made not periodic on the boundary surfaces, with about 16 out of 87 nodes having no periodic corresponding node on the other boundary surface to apply PBCs. Two kinds of constraints are compared in this example. The first one is that only the MKCs are applied, the second one is that MKCs are applied along with PBCs applicable for nodes on the boundary surfaces with corresponding periodic nodes on the other boundary surface (denoted as 'partial PBCs').

The converged results obtained from using 64 SGs are presented in Table IV. It is shown that with the two different set of constraints applied, the obtained effective beam stiffness properties converged to close values. The bending stiffness D_{33} and D_{44} obtained are slightly deviated from each other since the mesh is coarse and the nodes are not symmetrical with respect to the y and z axis (Figure 7(b)). From Figure 8, it can be seen by adding the applicable PBCs to the model, the effective beam properties will converge within a smaller range compared with applying only MKCs. However, one should not that adding the applicable PBCs may predict unwanted results if the nodes without corresponding periodic nodes are not evenly distributed on

the boundary surfaces.

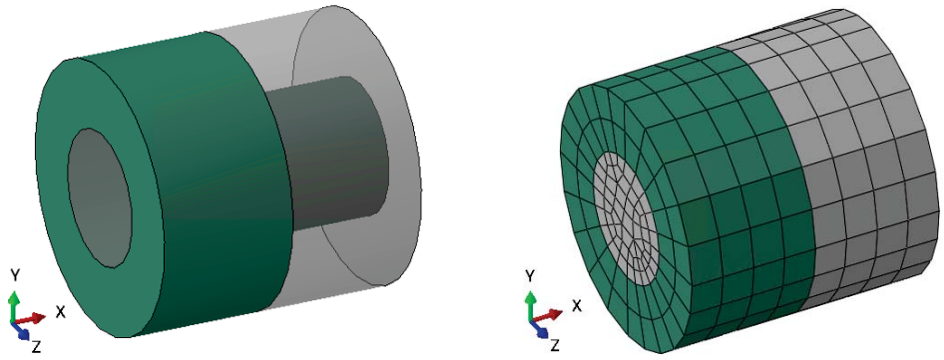

(a) Geometry and materials (b) Mesh configuration

Figure 7. Beam SG 2

TABLE III. THE CONVERGED EFFECTIVE BEAM PROPERTIES OF SG 2

	D_{11} (N)	D_{22} (N m^2)	D_{33} (N m^2)	D_{44} (N m^2)
Partial PBCs (64SGs)	2.913E+4	2.842E-3	5.623E-3	5.598E-3
MKCs (64SGs)	2.911E+4	2.844E-3	5.629E-3	5.604E-3

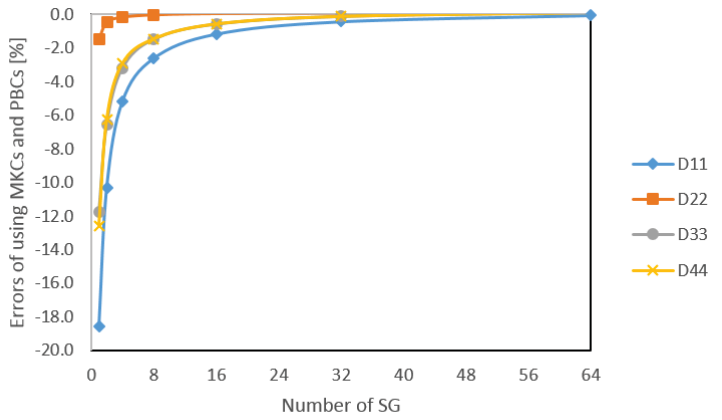

(a) beam SG applying MKCs

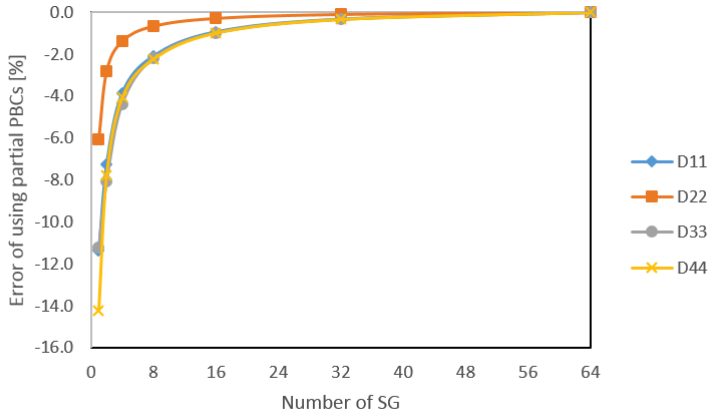

(b) beam SG applying MKCs and PBCs when available for nodes on the boundary surfaces

Figure 8. Convergence study of effective beam stiffness

Validation of plate model

A binary composite plate model is studied with SG shown in Figure 9. For this plate microstructure, the 3D SG and the 2D SG in Figure 9 both contains all the required constitutive information of the 2D plate model. The dimension of the SG in each direction are 2 mm. Four kinds of constraints are applied: (1) MIX110: only MKCs are applied,(2) MIX100: MKCs along with PBCs applied to nodes on the boundary surfaces normal to y, (3) MIX010: MKCs along with PBCs applied to nodes on the boundary surfaces normal to x, (4) PBC: PBCs are applied to boundary surfaces normal to x and y. From Figure 10, the effective plate properties obtained from using MIX110, MIX100 and MIX010 converge to the results of using PBCs with the increasing of the number of SGs in x and y directions. Since the heterogeneity is in the y direction, the effective plate stiffness converge much faster when MIX010 is applied to the SG. For the case applying MIX010, the MSG analysis using 3D SG and 2D SG will predict exactly the same results, which also proved the

consistence of the proposed MKCs.

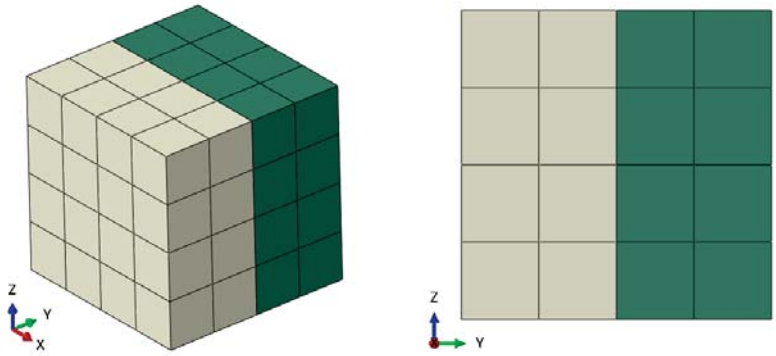

(a) 3D plate SG (b) 2D plate SG

Figure 9. Plate SG: binary composites

TABLE IV. THE CONVERGED EFFECTIVE BEAM PROPERTIES OF THE PLATE SG

	A_{11} (N/m)	A_{22} (N/m)	A_{33} (N/m)	A_{12} (N/m)	D_{11} (N m)	D_{22} (N m)	D_{33} (N m)	D_{12} (N m)
PBCs	5.341E+7	1.021E+7	3.298E+2	2.874E+2	1.785E+1	3.426	1.248	9.890E-1

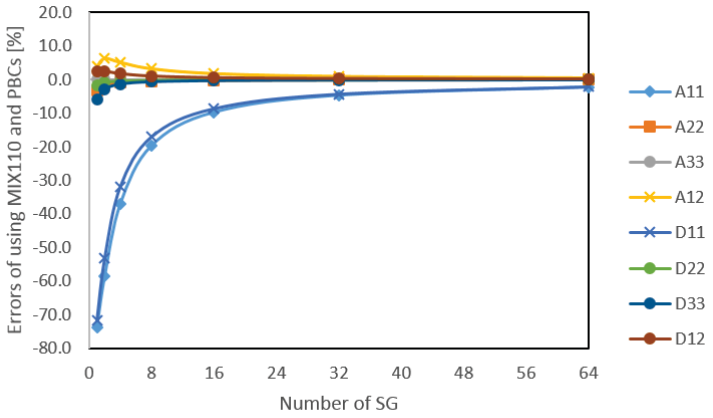

(a) Plate SG applying MIX110

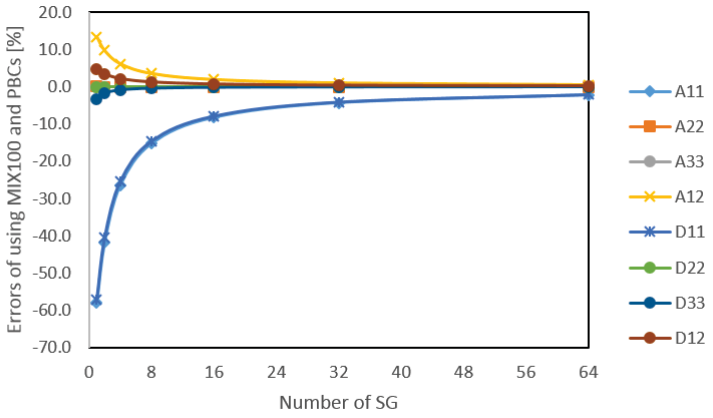

(b) Plate SG applying MIX100

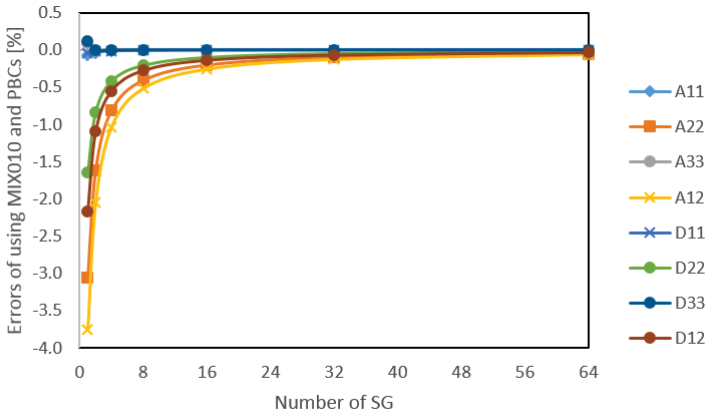

(c) Plate SG applying MIX010

Figure 10. Convergence study of effective plate stiffness

CONCLUSIONS

This paper developed a systematical solution in MSG to deal with multiscale constitutive modeling of the aperiodic dimensionally reducible structures (beams, plates/shells).The theory is based on the concept of structure genome through minimizing the energy of the original heterogeneous structures. As no boundary conditions are involved except the constraints to ensure kinematics equivalency between the heterogeneous material and the equivalent homogeneous material, the theory can be applied to SG of arbitrary shape. In addition, this theory provides a general framework for homogenization and dehomogenization of heterogeneous dimensional reducible structures. It can handle aperiodic microstructures, microstructures with partial periodicity, or microstructures with complete periodicity. For periodic structures, the effective properties obtained using MKCs or MKCs along with partial PBCs will converge consistently to that obtained from using PBCs. Second, SG can use the lowest dimension to describe the heterogeneity. This theory has been implemented into a general-purpose computer code SwiftComp$^{\mathrm{TM}}$ using the finite element method. The general-purpose multiscale constitutive modeling code SwiftComp$^{\mathrm{TM}}$ can be accessed in the cloud at cdmHUB.org.

REFERENCES

1. Hodges, D. H. 1990, "Review of composite rotor blade modeling," *AIAA journal*, 28(3):561–565.
2. Yu, W., D. H. Hodges, and J. C. Ho. 2012, "Variational asymptotic beam sectional analysis–an updated version," *International Journal of Engineering Science*, 59:40–64.
3. Couturier, P. J., S. Krenk, and J. Høgsberg. 2015, "Beam section stiffness properties using a single layer of 3D solid elements," *Computers & Structures*, 156:122–133.
4. Ho, J. C., D. H. Hodges, and W. Yu. 2010, "Energy transformation to generalized Timoshenko form for nonuniform beams," *AIAA Journal*, 48(6):1268–1272.
5. Yi, S., L. Xu, G. Cheng, and Y. Cai. 2015, "FEM formulation of homogenization method for effective properties of periodic heterogeneous beam and size effect of basic cell in thickness direction," *Computers & Structures*, 156:1–11.
6. Lee, C.-Y. and W. Yu. 2011, "Variational asymptotic modeling of composite beams with spanwise heterogeneity," *Computers & Structures*, 89(15):1503–1511.
7. Kalamkarov, A. and A. Georgiades. 2004, "Asymptotic homogenization models for smart composite plates with rapidly varying thickness: Part I-theory," *International Journal for Multiscale Computational Engineering*, 2(1).
8. Kalamkarov, A. L., I. V. Andrianov, V. V. Danishevsâ, *et al.* 2009, "Asymptotic homogenization of composite materials and structures," *Applied Mechanics Reviews*, 62(3):030802.
9. Lee, C.-Y. and W. Yu. 2011, "Homogenization and dimensional reduction of composite plates with in-plane heterogeneity," *International Journal of Solids and Structures*, 48(10):1474–1484.
10. Lee, C.-Y., W. Yu, and D. H. Hodges. 2014, "Refined modeling of composite plates with in-plane heterogeneity," *ZAMM-Journal of Applied Mathematics and Mechanics/Zeitschrift für Angewandte Mathematik und Mechanik*, 94(1-2):85–100.
11. Cai, Y., L. Xu, and G. Cheng. 2014, "Novel numerical implementation of asymptotic homogenization method for periodic plate structures," *International Journal of Solids and Structures*, 51(1):284–292.
12. Saha, G. C., A. L. Kalamkarov, and A. V. Georgiades. 2007, "Effective elastic characteristics of honeycomb sandwich composite shells made of generally orthotropic materials," *Composites Part A: Applied Science and Manufacturing*, 38(6):1533–1546.
13. Chen, D. 2011, "Equivalent flexural and torsional rigidity of hexagonal honeycomb," *Composite*

Structures, 93(7):1910–1917.
14. Dixit, A. and H. S. Mali. 2013, "Modeling techniques for predicting the mechanical properties of woven-fabric textile composites: A review," *Mechanics of Composite Materials*, 49(1):1–20.
15. Carrera, E. and S. Brischetto. 2009, "A survey with numerical assessment of classical and refined theories for the analysis of sandwich plates," *Applied mechanics reviews*, 62(1):010803.
16. Kreja, I. 2011, "A literature review on computational models for laminated composite and sandwich panels," *Open Engineering*, 1(1):59–80.
17. Khandan, R., S. Noroozi, P. Sewell, and J. Vinney. 2012, "The development of laminated composite plate theories: a review," *Journal of Materials Science*, 47(16):5901–5910.
18. Yu, W. 2015, "Structure genome: fill the gap between materials genome and structural analysis," in *56th AIAA/ASCE/AHS/ASC Structures, Structural Dynamics, and Materials Conference*, p. 0201.
19. Yu, W. 2016, "A unified theory for constitutive modeling of composites," *Journal of Mechanics of Materials and Structures*, to appear.

1.

1. Report Type

Final Report

Primary Contact E-mail

Contact email if there is a problem with the report.

ling.liu@usu.edu

Primary Contact Phone Number

Contact phone number if there is a problem with the report

+1-435-797-9149

Organization / Institution name

Utah State University

Grant/Contract Title

The full title of the funded effort.

Representative Structural Element: A New Paradigm for Multi-Scale Structural Modeling

Grant/Contract Number

AFOSR assigned control number. It must begin with "FA9550" or "F49620" or "FA2386".

FA9550-13-1-0148

Principal Investigator Name

The full name of the principal investigator on the grant or contract.

Ling Liu

Program Manager

The AFOSR Program Manager currently assigned to the award

James M. Fillerup

Reporting Period Start Date

03/27/2013

Reporting Period End Date

03/31/2016

Abstract

Under the sponsorship of AFOSR, we have successfully achieved the objective to establish a new paradigm for multiscale structural modeling to provide a systematic approach for efficient high-fidelity modeling of aerospace structures featuring multiscale heterogeneities and anisotropy. The proposed approach uses the concept of representative structural element, later renamed to be structure genome (SG) to emphasize the potential of this concept to bridge materials genome and structural analysis, and to better align with the Materials Genome Initiative (MGI). In this project, we have formulated the general theory for mechanics of structure genome (MSG), carried out a critical assessment of the proposed approach, and applied this approach to predict static failure and imperfect interfaces, construct models for hyperelastic materials, elastoplastic materials, viscoplastic materials, damaged materials, smart laminates, aperiodic materials, and last but not least, applied this approach to create new theories for laminates and micromechanics, and to provide a versatile solution for general free-edge stress problems.

Distribution Statement

This is block 12 on the SF298 form.

Distribution A - Approved for Public Release

Explanation for Distribution Statement

If this is not approved for public release, please provide a short explanation. E.g., contains proprietary information.

SF298 Form

Please attach your SF298 form. A blank SF298 can be found here. Please do not password protect or secure the PDF The maximum file size for an SF298 is 50MB.

AFD-070820-035.pdf

Upload the Report Document. File must be a PDF. Please do not password protect or secure the PDF . The maximum file size for the Report Document is 50MB.

Final_Report_New2.pdf

Upload a Report Document, if any. The maximum file size for the Report Document is 50MB.

Archival Publications (published) during reporting period:

1. Yu, W.: "Structure Genome: Fill the Gap between Materials Genome and Structural Analysis," Proceedings of the 56th Structures, Structural Dynamics, and Materials Conference, Kissimmee, Florida, Jan. 5-9, 2015.
2. Yu, W.: "A Unified Theory for Constitutive Modeling of Composites," Journal of Mechanics of Materials and Structures, to appear.
3. Sertse, H.; Zhang, L.; Yu, W. and Ye, Z. "A Comprehensive Evaluation of the Predictive Capabilities of Several Advanced Micromechanics Approaches," Proceedings of the 55th Structures, Structural Dynamics, and Materials Conference, National Harbor, Maryland, Jan. 13-17, 2014.
4. Ritchey, A.; Goodsell, J.; Sertse, H.; Yu, W.; and Pipes, R B: "Challenge Problems for the Benchmarking of Micromechanics Analysis," Proceedings of the American Society for Composites 30th Technical Conference, East Lansing, Michigan, Sept. 28-30, 2015.
5. Sertse, H. and Yu, W. "A Micromechanical Approach to Static Failure Prediction of Heterogeneous Materials," Proceedings of the 56th Structures, Structural Dynamics, and Materials Conference, Kissimmee, Florida, Jan. 5-9, 2015.
6. Sertse, H. and Yu, W. "A Micromechanical Approach to Imperfect Interface Analysis of Heterogeneous Materials," Proceedings of the 56th Structures, Structural Dynamics, and Materials Conference, Kissimmee, Florida, Jan. 5-9, 2015.
7. Zhang, L. and Yu, W.: "A Variational Asymptotic Method for Unit Cell Homogenization of Hyperelastic Heterogeneous Materials," Proceedings of the 55th Structures, Structural Dynamics, and Materials Conference, National Harbor, Maryland, Jan. 13-17, 2014.
8. Zhang, L. and Yu, W.: "Variational Asymptotic Homogenization of Elastoplastic Composites," Composite Structures, vol 133, 2015, 947-958.
9. Zhang, L. and Yu, W.: "A Variational Asymptotic Method for Unit Cell Homogenization of Elasto-Viscoplastic Heterogeneous Materials," Proceedings of the 54th Structures, Structural Dynamics, and Materials Conference, Boston, Massachusetts, Apr. 8-11, 2013.
10. Zhang, L. and Yu, W.: "A Micromechanics Approach to Homogenizing Elasto-viscoplastic Heterogeneous Materials," International Journal of Solids and Structures, vol. 51, 2014, pp. 3878-3888.
11. Zhang, L. and Yu, W.: "On the Constitutive Relations for Damaged Elastoplastic Materials Coupling Anisotropic Damage and Plasticity," Proceedings of the 55th Structures, Structural Dynamics, and Materials Conference, National Harbor, Maryland, Jan. 13-17, 2014.
12. Zhang, L. and Yu, W.: "On the Constitutive Relations for Damaged Elasto-Viscoplastic Materials Coupling Anisotropic Damage and Viscoplasticity," Proceedings of the 56th Structures, Structural Dynamics, and Materials Conference, Kissimmee, Florida, Jan. 5-9, 2015.
13. Zhang, L. and Yu, W.: "A Micromechanics Approach to Homogenizing Damaged Elastoplastic Heterogeneous Materials," Proceedings of the 56th Structures, Structural Dynamics, and Materials Conference, Kissimmee, Florida, Jan. 5-9, 2015.
14. Zhang, L. and Yu, W.: "A Thermodynamically Consistent Cohesive Zone Model for Mixed-Mode Fracture," Proceedings of the 55th Structures, Structural Dynamics, and Materials Conference, National Harbor, Maryland, Jan. 13-17, 2014.
15. Gao, Z.; Zhang, L. and Yu, W.: "Simulating the Mixed-Mode Progressive Delamination in Composite Laminates," Proceedings of the American Society for Composites 30th Technical Conference, East

Lansing, Michigan, Sept. 28-30, 2015.
16. Long, Y.; and Yu, W.: "Asymptotical Modelling of Thermopiezoelastic Laminates," Proceedings of the American Society for Composites 30th Technical Conference, East Lansing, Michigan, Sept. 28-30, 2015.
17. Long, Y. and Yu, W.: "Asymptotical Modelling of Thermopiezoelastic Laminates," Smart Materials and Structures, vol. 25, 2016, 015002.
18. Peng, B.; and Yu, W.: "A New Micromechanics Theory for Homogenization and Dehomogenization of Heterogeneous Materials," Proceedings of the American Society for Composites 30th Technical Conference, East Lansing, Michigan, Sept. 28-30, 2015.
19. Yu, W.: "An Introduction to Micromechanics," Chapter 1 of Composite Materials and Structures in Aerospace Engineering, Applied Mechanics and Materials, Volume 828, pp. 3-24, 2016, edited by Erasmo Carrera.
20. Peng, B.; and Yu, W.: "Remove Homogeneous Layer Assumption from Lamination Theories," Proceedings of the American Society for Composites 30th Technical Conference, East Lansing, Michigan, Sept. 28-30, 2015.
21. Sertse, H. and Yu, W.: "A Micromechanical Approach to Low Cycle Fatigue Analysis and Life Prediction of Heterogeneous Materials," Proceedings of the 57th Structures, Structural Dynamics, and Materials Conference, San Diego, California, Jan. 4-8, 2016.
22. Sertse, H. and Yu, W.: "A Micromechanical Approach to High Cycle Fatigue Analysis and Life Prediction of Heterogeneous Materials," Proceedings of the 57th Structures, Structural Dynamics, and Materials Conference, San Diego, California, Jan. 4-8, 2016.
23. Peng, B.; A; Goodsell, J.; Pipes, R. B. and Yu, W.: "Generalized Free-Edge Stress Analysis Using Mechanics of Structure Genome," Proceedings of the American Society for Composites 31st Technical Conference, Williamsburg, Virginia, Sept. 19-22, 2016.
24. Peng, B. and Yu, W.: "Modeling Aperiodic Dimensionally Reducible Structures Using Mechanics of Structure Genome," Proceedings of the American Society for Composites 31st Technical Conference, Williamsburg, Virginia, Sept. 19-22, 2016.

2. New discoveries, inventions, or patent disclosures:

Do you have any discoveries, inventions, or patent disclosures to report for this period?

Yes

Please describe and include any notable dates

We developed a code called SwiftComp based on Mechanics of Structure Genome, the theory discovered in this research. SwiftComp™ provides an efficient and accurate approach for modeling composite materials and structures. It can be used either independently as a tool for virtual testing of composites or as a plugin to power conventional FEA codes with high-fidelity multiscale modeling for composites. It was disclosed to Purdue Research Foundation on March 13, 2015.

Do you plan to pursue a claim for personal or organizational intellectual property?

Yes

Changes in research objectives (if any):

None

Change in AFOSR Program Manager, if any:

From David S. Stargel to James M. Fillerup

Extensions granted or milestones slipped, if any:

None

AFOSR LRIR Number

LRIR Title

Reporting Period

Laboratory Task Manager

Program Officer

Research Objectives

Technical Summary

Funding Summary by Cost Category (by FY, $K)

	Starting FY	FY+1	FY+2
Salary			
Equipment/Facilities			
Supplies			
Total			

Report Document

Report Document - Text Analysis

Report Document - Text Analysis

Appendix Documents

2. Thank You

E-mail user

Jun 29, 2016 19:36:36 Success: Email Sent to: ling.liu@usu.edu